2023 SAUPEC Conference, Johannesburg, South Africa, January 24-26, 2023

Fault Location In Electrical Power Distribution Network Using Support Vector Regression and Wavelet Packet Transform Method

Katleho Moloi and Innocent E. Davidson
Smart Grid Research Centre
Department of Electrical Power Engineering
Faculty of Engineering and the Built Environment
Durban University of Technology
Durban, 4000, South Africa.
KatlehoM@dut.ac.za, InnocentD@dut.ac.za

***Abstract*—This paper presents a fault location protection scheme in a power distribution system. The paper amplifies the importance of condition monitoring in power systems for reliability enhancement of the network. In this paper, a hybrid protection fault locating scheme based on wavelet packet transform (WPT) and support vector regression (SVR) is proposed. The proposed scheme uses the WPT to extract statistical features of the fault and subsequently, the SVR technique is employed to estimate the location of the fault. Furthermore, the proposed WPT-SVR scheme is tested using ½ cycles for signal analysis. An Eskom 132 kV power system line is modelled using the Digsilent platform. Thereafter, various types of fault cases are investigated from the modelled network. The fault classification scheme is tested using a machine learning platform WEKA. The results obtained show that the different impedance variations do not affect the efficiency of the scheme.**

Keywords*—*Fault location, Power system, Support vector regression, Wavelet packet transform

I. INTRODUCTION

The design topology of overhead power distribution lines is venerable to external interference from elements such as weather conditions and foreign objects. These interferences result is a fault within the system and thus interrupting the supply of power. The loss of power has detrimental effects on the loads depending on the reliability and availability of power supply. It is thus imperative to build control monitoring protection schemes to minimize the impact of the fault. Traditionally the fault location schemes play a significant role is estimating the position of the fault, resulting in a reduced repairing duration and network recovery [1, 2]. The general application of using a fault locating scheme is to calculate the distance between the nearest source terminal and the fault position. The objective of the scheme is to estimate the fault location with minimum errors. Although different distribution topology exists in real world application such as single and multiple terminals, the mathematical application of the scheme must be viable. The different network topology and its impact on the locating scheme is discussed in [3, 4, 5].

Different techniques have been used to find an efficient methodology for fault location. These techniques include the impedance-based method, travelling waves method and recently the intelligent based method. The impedance-based method uses both the voltage and current measurement to determine the fault position by calculating the fault impedance [6, 7]. The travelling waves methods usually uses either the current or voltage measurement to determine the fault position in the power system [8, 9]. Also, the intelligent fault location method either uses the current or voltage magnitude as input to the decision matrix of the scheme [10, 11]. Although the travelling waves technique has good advantages over the impedance-based method, the application has some complexity with the sampling rate and computational burden. Hence there has been great acceleration in using intelligent methods to solve several power system problems.

The general architectural design of an intelligent fault location scheme consists of a pre-processing and feature extraction segments. The pre-processing segment is achieved by taking measurements at the source terminals of the distribution line. For efficient fault location, the feature extraction segment is used to minimize the data spectrum and improve the computational duration. A technique based on discreet Fourie transform (DFT) for feature extraction and radial basis neural network (RBNN) for fault estimation was proposed in [12]. In [13], a hyperbolic S-transform was used to extract the energy and standard deviation features which were subsequently used to train the RBNN for fault estimation. An intelligent method based on random forest and shuffled frog leap algorithm was proposed to estimate the fault position [14]. A technique based on discrete wavelet transform (DWT) and artificial neural network (ANN) was proposed [15]. The technique utilized the DWT to decompose the fault signal and extract features and the ANN was used to estimate the position of the fault along the transmission line. The fault location phenomenon can never be over emphasized to maintain system reliability. In this paper, a hybrid technique for fault estimation is proposed. The technique comprises of a feature extraction technique based on WPT and SVR is utilized to estimate the position of the fault along the distribution line. The remaining section of this paper is organized as follow. In section II, the signal processing and feature extraction techniques using WPT is discussed, section III discusses the fault location scheme using SVR technique. In section IV, the proposed fault location scheme is discussed, the power distribution simulation study is presented in section V, the results are presented on section VI and lastly a conclusion is drawn in section VII.

II. Signal Decomposition and Feature Extraction

A. Wavelet packet transform

Signal processing tools have been widely used to solve power system problems. The DWT and WPT signal processing tool has gained much interest and has been applied in various fields such as data compression, signal tracking and feature extraction. However, in WPT the filtering processing segments are more than that of the DWT, resulting in more data even for small signal analysis. In Fig. 1. The WPT decomposition tree is depicted. The process begins with a signal going through both the low pass filter $h(k)$ and high pass filter $g(k)$, corresponding to the approximation and detail functions [16]. The coefficients of the sub-bands signal are further decomposed recursively by a factor of $2n$. At each level of decomposition, the approximation and detail function are further sub-divided into new detail and approximation coefficients.

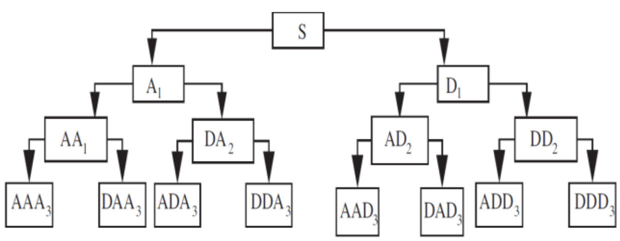

Fig. 1: Wavelet packet transform decomposition tree

The mathematical definition of the recursive functions using the $h(k)$ and $g(k)$ filters can be expressed as:

$$W_{2n}(x) = \sqrt{2}\sum_{k=0}^{2N-1} h(k)W_n\,(2x-k) \tag{1}$$

$$W_{2n+1}(x) = \sqrt{2}\sum_{k=0}^{2N-1} g(k)W_n\,(2x-k) \tag{2}$$

Where, the scaling and wavelet functions are represented by $W_0 = \phi(x)$ and $W_1 = \psi(x)$ respectively. Subsequently, the WPT function can be mathematically computed as:

$$W_{j,n,k}(x) = 2^{j/2}W^n(2^{-j}x-k) \tag{3}$$

When a fault occurs in a power system, a significant amount of data is generated. However, within the whole data spectrum there is an abundance of redundant data. The redundant data may impact the fault location scheme efficiency. In order to mitigate the impact of redundant data, a feature extraction technique is employed. Feature extraction is defined as a process of electing significant data matrix from the whole data spectrum without compromising the integrity of the signal spectrum [17]. In this paper, the signal energy and entropy features are obtained and subsequently used to train and test the fault location scheme. The energy (E) of the signal is mathematically defined as:

$$E(t_1,t_2) = \int_{t_1}^{t_2}(|y(t)|)^2\,dt \tag{4}$$

Where, $y(t)$ is the measured signal, the time intervals (t_1,t_2) represents the signal range. Generally, when a fault occurs the fault signal is usually greater than the normal current signal. Furthermore, the entropy of the signal measures the anticipated extent of the data given by categorizing the effect of the output variables. Thus, computing $(E)=0$, the entropy (EN) of the signal $y(t)$ is defined as:

$$EN(y) = \sum_i EN(y_i) \tag{5}$$

where, (y_i) is the decomposed coefficient of $y(t)$. Consequently, the entropy of the fault current signal is greater that the entropy of the normal current signal. In this paper, a total set of 24 features calculated as:

$$f = S_f \times WPT_c \tag{6}$$

Where, $S_f = 2$ is the statistical feature, $WPT_c = 12$ is the wavelet coefficients at the 3rd level of decomposition.

III. Support Vector Regression

Support vector machines (SVMs) have been widely used to solve both classification and regression problems in power systems. For distinctive reasons, in the application of SVMs for fault location a regression scheme using a loss function is applied. Support vector regression (SVR) uses structural minimization principles to estimate the output value based on the input value. Consequently, the risk of over-fitting is nullified when using SVR compared to neural network.

Assuming a training data set given by $(x_1,y_1),(x_2,y_2),\cdots(x_i,y_i)x_i\,\epsilon R^n$, x_i indicates the input variable and y_i indicates the targeted output. The non-linearity of the SVR is obtained by mapping the data into a high dimensional space. The mapping φ of the liner function can be defined as:

$$f(x) = \langle\omega,\varphi(x)\rangle + b \qquad \omega\,\epsilon\,R^n,\quad b\,\epsilon\,R \tag{7}$$

where, the dot product in R^n is indicated by $\langle,\rangle$. The optimal regression function is defined by:

$$R(\omega,b,\eta,\eta^*) = \frac{1}{2}\|\omega\|^2 + C\sum_{i=1}^{l}\big(\zeta_i(\eta_i)+\zeta_i(\eta_i^*)\big) \tag{8}$$

where, C is the pre-determined value, the loss function is given by ζ_i, the slack variables are represented by η_i. The SVR problem can be reiterated as solving a quadratic optimization problem given by:

$$R(\omega,b,\eta,\eta^*) = \frac{1}{2}\|\omega\|^2 + C\sum_{i=1}^{l}\big(\zeta_i(\eta_i)+\zeta_i(\eta_i^*)\big)\,\langle\omega,\varphi(x)\rangle + b - y_i \le \eta_i + \epsilon \tag{9}$$

Subject to $y_i - \langle\omega,\varphi(x)\rangle + b - y_i \le \eta_i + \epsilon\eta_i,\eta_i^* < 0$, this equation can be solved using the Langrange function as reported in [16]. In some real-world problems, the fault data is not always linearly separable. This impacts the efficiency of the estimation scheme. To solve this problem a kernel function is used. In this work, the radial bias function (RBF) is used to solve the non-linearity and is defined mathematically as:

$$K(X, X_i) = e^{-\frac{\|X-X_i\|^2}{2\alpha^2}} \tag{10}$$

IV. Proposed Fault Location Scheme

Fault location in power system is an imperative element to improve system reliability and restoration. In this paper, a hybrid fault locating scheme is proposed. The scheme logical sequence architecture is depicted in Fig. 2. The sequency begins with the measurements of current and voltage signal variables at the source terminal. Subsequently, the measured parameters are passed through the WPT segment for signal decomposition. Furthermore, the energy and entropy statistical features are extracted from the decomposed signal at level 3 with nodes $[AAA_3 \cdots DDD_3]$ obtained to formulate a feature matrix, the post fault measurements are taken over ¼ cycle period. Subsequently, the feature matrix is fed into the SVR scheme for training and testing purposes and lastly the position of the fault is estimated.

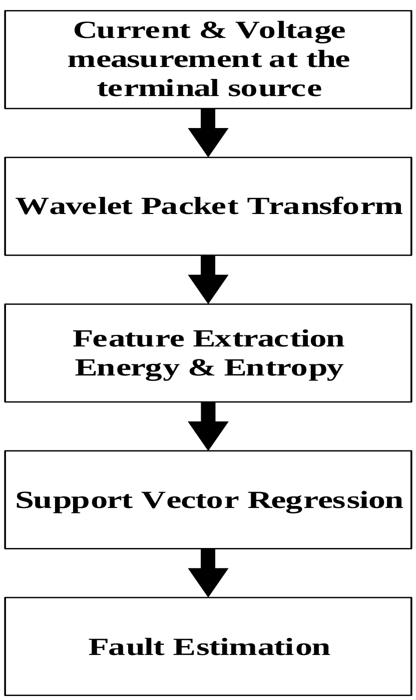

Fig. 2: Logical sequence of the fault estimation scheme.

V. Power System Study

To test the validity of the proposed scheme, a segment of an Eskom distribution network is studied (Boulders-Matsulu). The network is modelled as a pi-system at 132 kV. The substation and line parameters are depicted in Table I and II respectively. The line to ground (LG), line to line (LL) and line to line to ground (LLG) fault current signals at 40 km of the line is depicted in Fig.3, 4 and 5 respectively. The power system under study is depicted in Fig. 6. The network was modelled in Digsilent.

TABLE I. Substation Parameters

Parameters	Boulders	Matsulu
Rating (MVA)	85	80
Short circuit current (kA)	25	18.5
X/R ratio	21.3	19.1

TABLE II. Line Parameters

Description	Parameters
Line length (km)	150
Pos. sequence impedance (Ω)/km	(7+j15.3)
Neg. sequence impedance (Ω)/km	(7+j15.3)
Zero sequence impedance (Ω)/km	(4.5+j16.0)
System frequency (Hz)	50

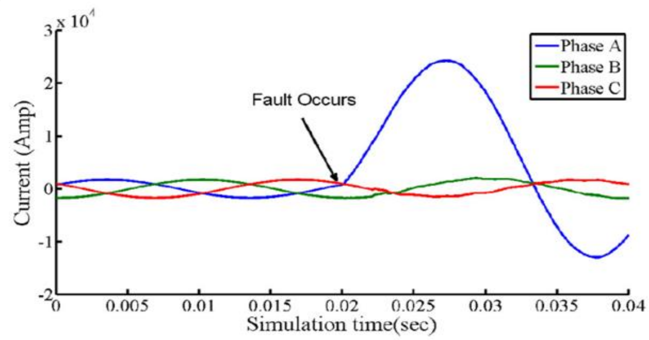

Fig. 3: LG fault signal.

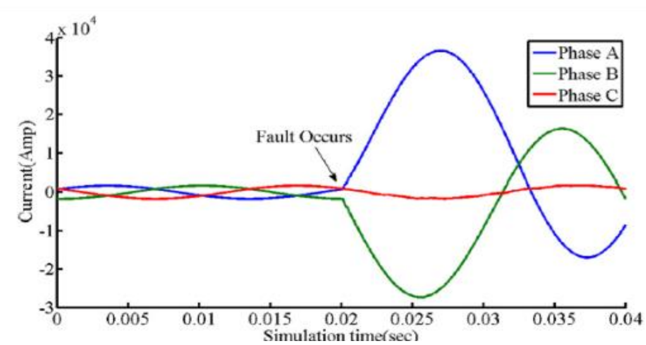

Fig. 4: LL fault signal.

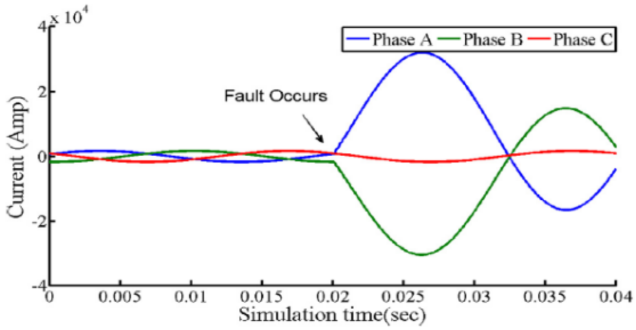

Fig. 5: LG fault signal.

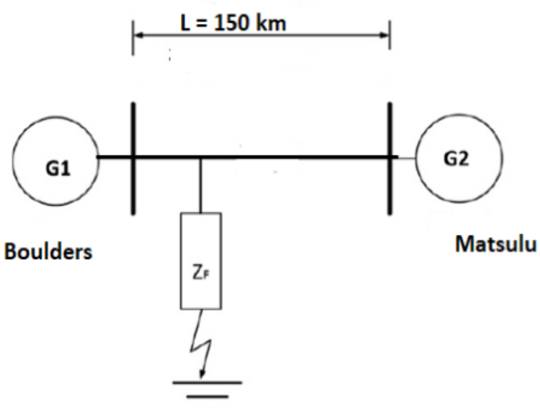

Fig. 6: Eskom power system

VI. Results and Discussion

In this section the simulation results are analyzed and discussed. As mentioned before, the selection of a mother wavelet when using WPT is an essential element for efficient signal processing. In this work, an evaluation of the mother wavelet is conducted, and the results are depicted in Table III. It is observed in the results that db4 Daubechies 4 (db4) mother wavelet has least mean error and thus selected in the present work.

TABLE III. Mother wavelet selection

Mother wavelet	Fault estimation	
	Absolute error (%)	Mean square error (%)
db7	1.10	0.50
db14	1.05	0.58
db5	1.52	0.52
db4	**0.10**	**0.11**

Furthermore, to investigate the pragmatic application of the proposed fault estimation scheme, the mean square error (MSE) and the absolute error (AE) criterions are calculated. The AE and MSE are mathematically defined as:

$$AE = |\, x - x_i| \quad (11)$$

$$MSE = \sum \left(\frac{x - x_i}{n}\right)^2 \quad (12)$$

Where, x is the actual fault position, x_i is the estimated fault position and n is the number of faults accumulated. Subsequently, in Tables IV and V the fault estimation with different fault impedance (Z_f) and angles are presented. The results presented in the two tables show that the scheme is robust for different fault positions with different fault impedance and fault angles. Furthermore, the importance of using WPT for signal processing and feature extraction is demonstrated in - Table VI. From the results it is observed that when using WPT, the results are better than when WPT is not used. To further validate the proposed fault estimation scheme, the MSE criterion is calculated for different fault location and impedances. The MSE results for different fault conditions are depicted in Tables VII and VIII respectively.

TABLE IV. Fault location estimation with $Z_f = 10\,\Omega$

Fault type	20 km			105 km		
	0°	30°	45°	0°	30°	45°
LL	20.00	20.00	20.00	105.10	105.00	105.10
LLG	20.00	20.00	20.00	105.00	105.00	105.50
LLL	20.00	20.00	20.00	104.99	105.00	104.99
LLLG	19.95	20.00	20.00	104.95	105.00	104.99

TABLE V. Fault location estimation with $Z_f = 100\,\Omega$

Fault type	20 km			105 km		
	0°	30°	45°	0°	30°	45°
LL	19.99	20.00	20.00	104.99	105.00	104.99
LLG	19.99	20.00	20.00	104.99	105.00	104.99
LLL	19.99	19.98	20.00	104.99	105.00	104.99
LLLG	20.00	19.98	20.00	104.99	105.00	104.99

TABLE VI. Fault location estimation with and without WPT

Fault type	20 km			105 km		
	With WPT			Without WPT		
	0°	30°	45°	0°	30°	45°
LL	19.99	20.00	20.00	100.99	102.00	101.99
LLG	19.99	20.00	20.00	100.99	101.00	103.99
LLL	19.99	19.98	20.00	101.99	102.00	102.99
LLLG	20.00	19.98	20.00	101.99	101.00	101.99

TABLE VII. MSE computation with different impedance

$Z_f(\Omega)$	LLG			LLL		
	0°	30°	45°	0°	30°	45°
0.2	3.02E-3	3.40E-4	3.51E-4	3.25E-3	4.01E-3	4.10E-4
1.05	2.50E-5	6.35E-3	5.25E-5	4.75E-5	4.25E-3	3.50E-3
10.3	3.05E-3	4.50E-4	5.25E-5	5.10E-5	5.50E-3	4.50E-3
15.8	3.70E-5	5.30E-3	4.85E-5	4.55E-5	5.55E-3	3.20E-4

TABLE VIII. MSE COMPUTATION WITH DIFFERENT IMPEDANCE

$Z_f(\Omega)$	LG			LL		
	0º	30º	45º	0º	30º	45º
0.2	1.20E-4	1.10E-4	1.15E-3	1.52E-3	1.10E-4	1.14E-4
1.05	1.34E-4	1.50E-3	1.25E-4	1.55E-4	1.25E-4	1.11E-3
10.3	1.90E-4	1.61E-4	1.22E-4	1.10E-4	1.50E-4	1.15E-3
15.8	2.10E-5	1.50E-3	1.85E-4	1.55E-3	1.55E-4	1.20E-4

The importance of power system fault location can never over be accentuated for system reliability and security. Fault location schemes enable power system operators to respond promptly to the adverse effects of the fault. As depicted in Tables VII and VIII, our scheme has a minimum MSE error. This indicates the robust formulation of the proposed fault location scheme. One of the major advantages of our scheme is the computational time implementation, our scheme uses ¼ cycle of the post fault data period for estimating the fault position. In Table IX our scheme is compared with some of the schemes in the literature. From the comparison results, it is observed the proposed scheme uses less data spectrum.

TABLE IX. SCHEME COMPARISON

Scheme ref	Pre-fault	During fault	Post fault	Data window
[12]	1	none	none	1 cycle
[13]	1	none	1	2 cycles
Proposed scheme	none	none	1/4	½ cycles

VII. CONCLUSION

In this paper a fault location scheme is proposed. The scheme comprises of a signal processing segment which is used to decompose the signal. Subsequently, the energy and entropy statistical features are extracted. The extracted features are then used to train and test the fault location scheme using SVR. The scheme uses ¼. cycle of the data spectrum, resulting in a much faster response and less computational burden. Furthermore, it was observed that the proposed scheme correctly identifies different types of fault with different fault impedance and angles.

REFERENCES

[1] M. Mirzaei, M. Z. A. Kadir, E. Moazami and H. Hizam, "Review of Fault Location Methods for Distribution Power System," *Australian Journal of Basic and Applied Sciences*, vol. 3, no. 3, pp. 2670-2676, 2009.

[2] K. Buthelezi, M. Kabeya and M. Leoaneka, "A Review of Fault Location Algorithms Utilising Travelling Wave, Wavelet Transform and Multi-Resolution Analysis Techniques," in *30th Southern African Universities Power Engineering Conference (SAUPEC)*, Durban, South Africa, 2022.

[3] Z. Chen and J. Maun, "Artificial neural network approach to single-ended fault locator for transmission lines," *IEEE Transactions on Power Systems*, vol. 15, no. 1, pp. 370-375, 2000.

[4] V. L. Felipe, F. K. Bernard, M. Kleber, F. D. Jr. and L. A. N. Washignton, "Fault location on transmission lines little longer than half-wavelength," *Electric Power Systems Research*, vol. 114, pp. 101-109, 2014.

[5] D. Spoor and J. Zhu, "Improved single-ended traveling-wave fault-location algorithm based on experience with conventional substation transducers," *IEEE Transaction on Power Delivery*, vol. 21, no. 3, pp. 1714-1720, 2006.

[6] A. Keshavarz, R. Dashti, M. Deljoo and H. Shaker, "Fault location in distribution networks based on SVM and impedance-based method using online databank generation," *Neural Computing and Applications*, vol. 34, p. 2375–2391, 2022.

[7] S. Das, S. Santoso, A. Gaikwad and M. Patel, "Impedance-based fault location in transmission networks: theory and application," *IEEE Access*, vol. 2, pp. 537-557, 2014.

[8] J. Ding, X. Wang, Y. Zheng and L. Li, "Distributed Traveling-Wave-Based Fault-Location Algorithm Embedded in Multiterminal Transmission Lines," *IEEE Transactions on Power Delivery*, vol. 33, no. 6, pp. 3045-3054, 2022.

[9] Y. Zhang, N. Tai and B. Xu, "Fault Analysis and Traveling-Wave Protection Scheme for Bipolar HVDC Lines," *IEEE Transactions on Power Delivery*, vol. 27, no. 3, pp. 1583-1591, 2012.

[10] S. R. Fahim, Y. Sarker, O. K. Islam, S. K. Sarker, M. F. Ishraque and S. K. Das, "An Intelligent Approach of Fault Classification and Localization of a Power Transmission Line," in *IEEE International Conference on Power, Electrical, and Electronics and Industrial Applications (PEEIACON)*, Dhaka, Bangladesh, 2019.

[11] Z. Jiao and R. Wu, "A New Method to Improve Fault Location Accuracy in Transmission Line Based on Fuzzy Multi-Sensor Data Fusion," *IEEE Transactions on Smart Grid*, vol. 10, no. 4, pp. 4211-4220, 2019.

[12] M. Joorabian, S. M. A. Taleghani and R. K. Aggarwal, "Accurate fault locator for EHV transmission lines based

on radial basis function neural networks," *Electric Power Systems Research,* vol. 71, no. 3, pp. 195-202, 2004.

[13] S. Samantaray, P. K. Dash and G. Panda, "Fault classification and location using HS-transform and Radial Basis Function Neural Network," *Electric Power Systems Research*, vol. 76, pp. 897-905, 2006.

[14] B. Chang, R. Yang, C. Guo, S. Ge and L. Li, "A New Application of Optimized Random Forest Algorithms in Intelligent Fault Location of Rudders," *IEEE Access,* vol. 7, pp. 94276-94283, 2021.

[15] A. C. Adewole, R. Tzoneva and S. Behardien, "Distribution network fault section identification and fault location using wavelet entropy and neural networks," *Applied Soft Computing,* vol. 46, pp. 296-306, 2016.

[16] K. Moloi, M. Ntombela, T. C. Mosetlhe, T. R. Ayodele and A. A. Yusuff, "Feature Extraction based Technique for Fault Classification in Power Distribution System," in *IEEE PES/IAS PowerAfrica*, Nairobi, Kenya, 2021.

[17] K. Moloi, J. A. Jordaan and Y. Hamam, "The Development of a High Impedance Fault Diagnostic Scheme on Power Distribution Network," *International Review of Electrical Engineering (IREE),* vol. 15, no. 1, pp. 69-79, 2020.

[18] A. A. Yusuff, C. Fei, A. A. Jimoh and J. L. Munda, "Fault location in a series compensated transmission line based on wavelet packet decomposition and support vector regression," *Electric Power Systems Research,* vol. 81, p. 1258–1265, 2011.

[19] M. Joorabian, S. M. A. T. Asl and R. K. Aggarwal, "Accurate fault locator for EHV transmission lines based on radial basis function neural networks," *Electric Power Systems Research,* vol. 71, p. 195–202, 2004.

[20] S. Ekici, S. Yildirim and M. Poyraz, "Energy and entropy-based feature extraction for locating fault on transmission lines by using neural network and wavelet packet decomposition," *Expert Systems with Applications*, vol. 34, pp. 2937-2944, 2008.

Parameter Estimation of a Distribution Transformer Model using Pseudo-Random Impulse Sequence Perturbation

Daniel Marc Banks
Electrical and Electronic Engineering
Stellenbosch University
Stellenbosch, South Africa
20784678@sun.ac.za

Johannes Cornelius Bekker
Electrical and Electronic Engineering
Stellenbosch University
Stellenbosch, South Africa
https://orcid.org/0000-0003-0678-4152

Hendrik Johannes Vermeulen
Electrical and Electronic Engineering
Stellenbosch University
Stellenbosch, South Africa
https://orcid.org/0000-0003-4356-4044

***Abstract*—This paper investigates the use of a Pseudo-Random Impulse Sequence (PRIS) as a perturbation signal for estimating the parameters of a wideband lumped-parameter transformer model for a 16kVA, 22kV/240V distribution transformer. The frequency responses of the open-circuit and short-circuit primary and secondary input impedances, as well as the forward and backward voltage transformation ratios, are simulated using PRIS perturbation signals, and compared with results published in literature. It is shown that the simulated frequency responses exhibit close correlation with the responses derived using analytical expressions, and that PRIS perturbation excites the model sufficiently to obtain accurate frequency responses up to 100kHz. The model parameters are subsequently estimated from these frequency response results and compared with results published in literature. The performance of particle-swarm optimisation and genetic algorithm for the parameter estimation processes are, furthermore, compared. It is shown that particle-swarm optimisation delivers improved parameter estimates and more efficient runtimes.**

***Index Terms*—Distribution Transformer Model, Wideband Perturbation, Parameter Estimation**

I. Introduction

Frequency Response Analysis (FRA) has been widely used in transformer condition monitoring to detect mechanical problems such as winding deformation [1]. FRA condition monitoring, however, requires accurate wideband model model topologies and parameter sets, such that changes in the model parameters can be related to changes within the physical transformer. Frequency responses are also of major importance for investigating the resonant behaviour of transformer windings, including characterising resonant voltage amplification and understanding interaction with external circuits.

Distributed winding models are commonly approximated using lumped-parameter equivalent-circuit models, and the topologies of these models have been studied extensively in literature [2], [3]. Many of the wideband transformer model topologies proposed in literature derive from the standard low-frequency T-equivalent transformer model [4]–[6]. Slemon [6] includes lumped representations of the inter-winding, inter-turn and winding-to-ground capacitances. Vermeulen *et al.* [7] uses the model of Slemon [6] as a basis to predict the voltage transformation ratio in the frequency range of 100Hz to 10kHz for a 110V/11kV step-up transformer. Olivier *et al.* [4] used a cascaded connection of adapted T-equivalent transformer models to predict the frequency response of a cascaded connection between two 440V/110kV high-voltage transformers up to 1.5kHz.

Wideband winding models typically represent the transformer on a layer-by-layer or turn-by-turn basis [2], [3], [8]. A cascaded two-winding transformer model can be formed by combining two lumped-parameter winding models and introducing lumped inter-winding capacitance between the sections [9]. Kheyani *et al.* [2] estimated the parameters of a two-winding transformer model by fitting the model response to that of a 15kVA, 7.62kV/240V single-phase distribution transformer. The transformer model implements a single low-voltage section and a single high-voltage section to model the frequency response measurements up to 100kHz. Brozio *et al.* [3] developed a lumped-parameter equivalent-circuit model to represent a 16kVA, 22kV/240V distribution transformer for the frequency range up to 100kHz. The parameters of the model were estimated using measured frequency responses of the open- and short-circuit input impedances and voltage transformation ratios.

This paper explores the use of a Pseudo-Random Impulse Sequence (PRIS) perturbation signal [10] for estimating the parameters of a lumped-parameter circuit model developed by Brozio *et al.* [3]. The frequency responses of the open-circuit and short-circuit primary and secondary input impedances, as well as the forward and backward voltage transformation ratios, are simulated using PRIS perturbation signals. These frequency responses are subsequently derived analytically and compared to the simulated responses. A parameter estimation methodology is implemented to derive the model parameters from the simulated frequency responses, and the results are presented and interpreted. The performance of two optimisation algorithms, namely the particle-swarm and genetic algorithms, is subsequently compared. The paper concludes by summarising the findings and presenting suggestions for further work.

II. Transformer Model

A. Lumped-Parameter Equivalent-Circuit Model

Fig. 1 presents a wideband lumped-parameter equivalent-circuit model topology for two-winding distribution transformers as proposed by Brozio [3]. The model is developed such that the parameters can be closely related to the physical elements of the transformer structure. Capacitor C_{a10} is a lumped representation of the Low-Voltage (LV) inter-turn capacitance as well as the capacitance to ground, and C_{ab1} is a lumped representation of the inter-winding capacitance. The core losses are approximated by coupling R_c to the inductances L_{a1}-L_{b4} through the inductor L_c. Capacitors C_{b1}-C_{b4} and C_{b12} represent the lumped inter-turn capacitances of the High-Voltage (HV) winding, while C_{b10} is included to represent the capacitance between the HV winding and ground. Capacitor C_{b34} is a lumped representation of both inter-turn capacitance and capacitance to ground for the HV winding. Resistors $R_{a1} - R_{b4}$ are lumped representations of the HV winding resistances. Parameters $L_{a1} - L_{b4}$ represent the self-inductances of the HV winding, and are all mutually coupled.

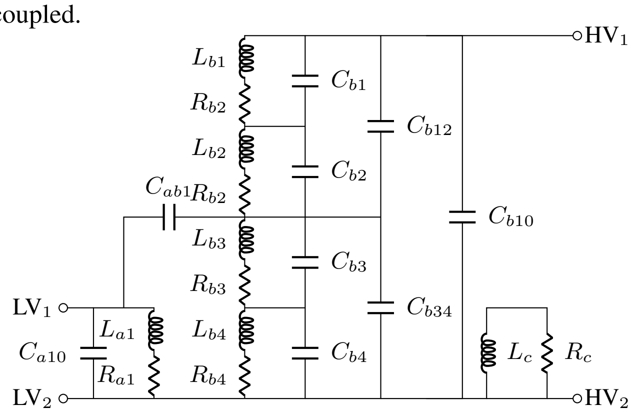

Fig. 1. Wideband lumped-parameter transformer model [3].

Table I summarises the linear model parameters estimated by Brozio [11]. The self-inductance L_c is fixed to $37.5H$, as it only serves to couple the core-loss resistance to the winding inductances.

TABLE I
Target Parameter Values for the model shown in Fig . 1 [11]

Parameter	Value	Parameter	Value	Parameter	Value
R_{a1} $[m\Omega]$	9.80	C_{b3} $[pF]$	411.0	K_{a1b4}	0.999079
R_{b1} $[k\Omega]$	2.02	C_{b4} $[pF]$	187.0	K_{b1b2}	0.9990
R_{b2} $[k\Omega]$	2.96	C_{ab1} $[pF]$	60.0	K_{b1b3}	0.997584
R_{b3} $[k\Omega]$	2.36	L_{a1} $[mH]$	358	K_{b1b4}	0.997907
R_{b4} $[k\Omega]$	1.27	L_{b1} $[H]$	144	K_{b2b3}	0.998343
R_c $[k\Omega]$	60.4	L_{b2} $[H]$	322	K_{b2b4}	0.999161
C_{a10} $[pF]$	72.0	L_{b3} $[H]$	427	K_{b3b4}	0.999321
C_{b10} $[pF]$	102.0	L_{b4} $[H]$	161	K_{a1c}	0.99
C_{b12} $[pF]$	164.0	L_c $[H]$	37.5	K_{b1c}	0.99
C_{b34} $[pF]$	269.0	K_{a1b1}	0.999043	K_{b2c}	0.99
C_{b1} $[pF]$	228.0	K_{a1b2}	0.999051	K_{b3c}	0.99
C_{b2} $[pF]$	351.0	K_{a1b3}	0.999072	K_{b4c}	0.99

All flux components that are linked by the winding inductances are assumed to be confined to the core and, therefore, contribute to the core losses. The coupling coefficient between each winding section's self-inductance and L_c is assumed to be equal and is fixed to 0.99, which in practice is not necessarily the case. The estimated parameters are able to model the 16kVA 22kV/240V distribution transformer frequency responses from approximately 1kHz up to 100kHz. Mismatches below 1kHz are attributed to the frequency dependence of the inductive and resistive model elements that are not taken into account [11]. The set of transformer frequency responses targeted in this study, Γ, can be expressed mathematically as

$$\begin{aligned}\Gamma = [&Z_{lvoc}(\omega), Z_{lvsc}(\omega), Z_{hvoc}(\omega),\\ &Z_{hvsc}(\omega), R_{lvhv}(\omega), R_{hvlv}(\omega)],\end{aligned} \tag{1}$$

where $Z_{lvoc}(\omega)$, $Z_{lvsc}(\omega)$, $Z_{hvoc}(\omega)$, $Z_{hvsc}(\omega)$, $R_{lvhv}(\omega)$ and $R_{hvlv}(\omega)$ represent the open-circuit and short-circuit input impedances of the primary winding, open-circuit and short-circuit input impedances of the secondary winding, and the forward and backward voltage transformation ratios of the transformer respectively.

B. Mathematical Derivation of the Model Frequency Response Transfer Functions

The input impedance transfer functions of the model are obtained by determining the impedance matrix, $\mathbf{Z}$, for each input impedance case through mesh current equations. The Laplace-domain mesh current equations of the circuit shown in Fig. 1 are determined individually, but can be summarised by the following general relationships:

$$\mathbf{V} = \mathbf{ZI}, \tag{2}$$

$$\mathbf{V} = [0\,,\,0\,,\,\cdots\,,\,V_{in}(s)]^T, \tag{3}$$

$$\mathbf{I} = [I_1(s)\,,\,I_2(s)\,,\,\cdots\,,\,I_{in}(s)]^T \tag{4}$$

and

$$\mathbf{Z} = \begin{bmatrix} Z_{11} & Z_{12} & \cdots & Z_{1n} \\ Z_{21} & Z_{22} & \cdots & Z_{2n} \\ \vdots & \vdots & \ddots & \vdots \\ Z_{n1} & Z_{n2} & \cdots & Z_{nn} \end{bmatrix}, \tag{5}$$

where $V_{in}(s)$ denote the Laplace transforms of input voltage, $v_{in}(t)$, and matrix $\mathbf{I}$ contains the entries of Laplace domain mesh currents from $I_1(s)$ to $I_{in}(s)$. The Laplace domain input impedance for each case, $Z_{in}(s)$, is then given by the general relationship

$$Z_{in}(s) = \frac{V_{in}(s)}{I_{in}(s)} = \frac{\Delta_{\mathbf{Z}}}{C_{\mathbf{Z}(n,n)}}, \tag{6}$$

where $\Delta_{\mathbf{Z}}$ denotes the determinant and $C_{\mathbf{Z}(n,n)}$ denotes the (n,n)-th cofactor of $\mathbf{Z}$. The general mesh current equations and matrices in (2)-(6) is applied to each input impedance case. Table II summarises the matrix sizes and orders of the analytical input impedance transfer functions derived from the model in Fig. 1.

TABLE II
Summary of the Input Impedance Transfer Functions

$Z_{in}(s)$	Matrix Size (n x n)	Numerator Order	Denominator Order
$Z_{lvoc}(s)$	11x11	10^{th}	11^{th}
$Z_{lvsc}(s)$	12x12	9^{th}	10^{th}
$Z_{hvoc}(s)$	11x11	10^{th}	11^{th}
$Z_{hvsc}(s)$	12x12	9^{th}	10^{th}

The voltage transformation ratio transfer functions, $R(s)$, are derived by assuming an input voltage of 1V. This yields

$$R(s) = \frac{V_o(s)}{V_{in}(s)} = \frac{V_o(s)}{1} = I_i(s)Z_{ij}. \tag{7}$$

The output voltage $V_o(s)$ is calculated by multiplying the mesh current in the loop of the output voltage, $I_i(s)$, with the impedance of the circuit elements across the output voltage, denoted by Z_{ij}. Table III summarises the matrix sizes and orders of the analytical voltage transformations transfer functions as well as the circuit elements used to form Z_{ij} from the model in Fig. 1.

TABLE III
SUMMARY OF THE VOLTAGE TRANSFORMATION RATIO TRANSFER FUNCTIONS

$R(s)$	Matrix Size (n x n)	Z_{ij}	Numerator Order	Denominator Order
$R_{lvhv}(s)$	11x11	$(sC_{b10})^{-1}$	10^{th}	10^{th}
$R_{hvlv}(s)$	11x11	$(sC_{a10})^{-1}$	10^{th}	10^{th}

Tables II and III present a brief summary of the derived transfer functions, as space limitations prohibit the presentation of the detailed coefficients for each of the analytical expressions.

C. Pseudo-Random Impulse Sequence Perturbation

Fig. 2 shows the topology of the perturbation arrangement as implemented in Simulink for perturbations applied to the LV winding. The PRIS perturbation source consists of the DC voltage source V_{DC}, PRBS clock source V_{PRBS}, H-bridge switching circuit and series RLC circuit, comprised of R_{pris}, L_{pris} and C_{pris} [10]. A PRBS clock frequency of $f_{clk} = 40kHz$ is selected, such that the majority of frequency response resonant points fall within the main lobe of the perturbation current Power Spectral Density (PSD), whilst maintaining a practically realisable switching frequency. The time constants τ_1 and τ_2 are chosen such that the PSD of the perturbation signal has a high Signal-to-Noise Ratio (SNR), with low low-frequency perturbation energy to avoid transformer saturation [7], [10]. The time constants can be formed with infinite combinations of RLC circuit parameters. The RLC circuit parameters should, however, be chosen such that the RLC circuit impedance magnitude is comparable to the input impedance of the device under test [12]. The set of six frequency responses, as defined in (1), are obtained through separate simulations. The variable PRIS parameters and simulation arrangements are summarised in Table IV. For LV terminal frequency response simulations terminals T_1 and T_2 are perturbed by the PRIS source, while terminals T_3 and T_4 are perturbed for HV frequency responses simulations. For open-circuit frequency response simulations switch SW_1 is open, and vice-versa for short-circuit frequency response simulations. The DC voltage and RLC circuit parameters are optimised depending on whether an HV terminal or LV terminal frequency response is being obtained.

TABLE IV
PRIS PERTURBATION ARRANGEMENTS AND PARAMETERS OF FIG. 2

Frequency Response	V_{DC} [V]	R_{pris} [Ω]	L_{pris} [H]	C_{pris} [F]	Perturbed Terminals	SW_1 State
$Z_{lvoc}(\omega)$	30	50.0	100μ	10μ	T_1, T_2	open
$Z_{lvsc}(\omega)$	30	50.0	100μ	10μ	T_1, T_2	closed
$Z_{hvoc}(\omega)$	210	4.4k	54m	40n	T_3, T_4	open
$Z_{hvsc}(\omega)$	210	4.4k	54m	40n	T_3, T_4	closed
$R_{lvhv}(\omega)$	30	50.0	100μ	10μ	T_1, T_2	open
$R_{hvlv}(\omega)$	210	4.4k	54m	40n	T_3, T_4	open

The simulations are performed using a sampling frequency of $f_s = 4MHz$. The RLC circuit parameters are chosen using an iterative selection process. The transformer HV input impedance is orders of magnitude larger compared to the LV side. Therefore, the series impedance of the RLC components is increased to obtain an impedance magnitude comparable to that of the HV winding.

D. Frequency Response Analysis

Figures 3 and 4 compare the magnitudes of the six frequency responses in the set Γ, obtained through simulated PRIS perturbations and the analytically derived transfer functions respectively. The analytical transfer functions and the responses from simulated PRIS perturbations show close correlation. The analytical responses are obtained through the derived expressions described in Section II-B, whilst the simulated responses are obtained through the six simulation arrangements presented in Section II-C. The frequency responses of the simulated waveforms are determined through the *tfestimate* function of the MATLAB Signal Processing Toolbox [13], using the general relationship

$$H_{xy}(\omega) = \frac{P_{xy}(\omega)}{P_{xx}(\omega)}, \tag{8}$$

where $H_{xy}(\omega)$ denotes the transfer function being calculated, $P_{xy}(\omega)$ denotes the cross PSD of the input signal x and the output signal y, and $P_{xx}(\omega)$ denotes the PSD of the

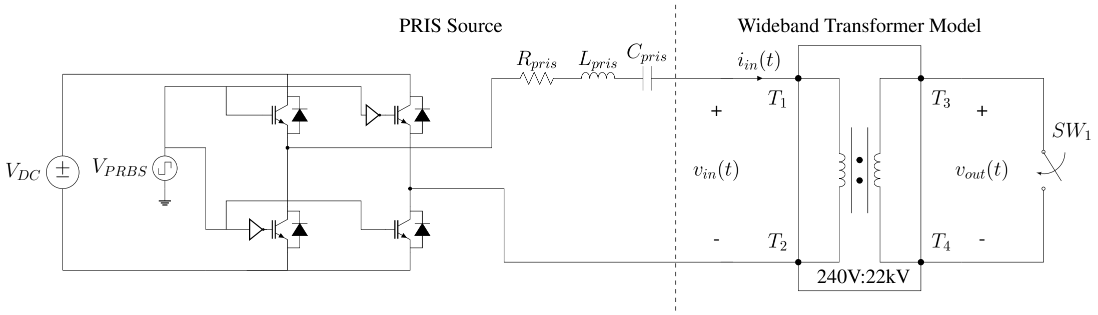

Fig. 2. PRIS arrangement for perturbing the LV terminals of the wideband lumped-parameter transformer model in simulation.

input signal x. The PSDs are determined through spectral estimation using the Welch averaged periodogram with a Hanning window size of 50% of the discrete time-series data points and an overlap percentage of 62.5%.

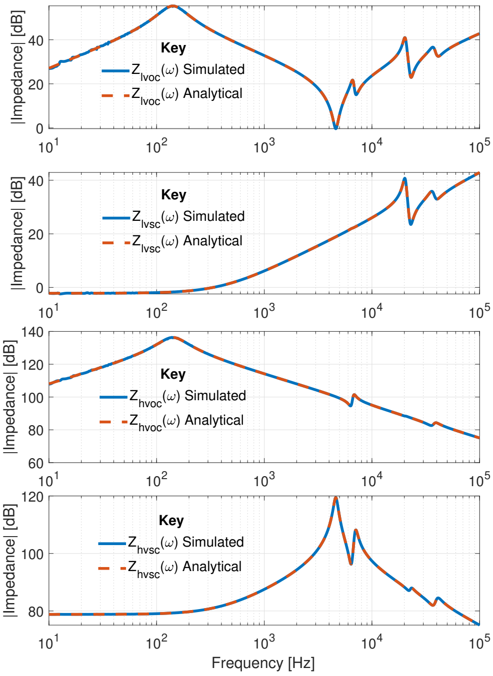

Fig. 3. Analytical and Simulated Frequency Responses of the Model Input Impedances.

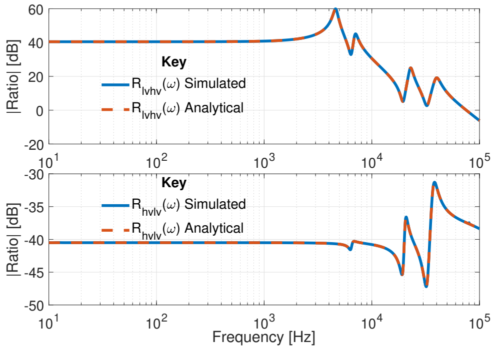

Fig. 4. Analytical and Simulated Frequency Responses of the Model Voltage Transformation Ratios.

III. Parameter Estimation Methodology

A. Overview

Fig. 5 shows a block diagram of the parameter estimation methodology adopted in this investigation. The PRIS perturbation source is applied to the target system model, and the set of frequency responses of the relevant transfer functions, denoted by Γ, is determined. The set of frequency responses for the estimated model, denoted by

$$\tilde{\Gamma} = [\tilde{Z}_{lvoc}(\omega), \tilde{Z}_{lvsc}(\omega), \tilde{Z}_{hvoc}(\omega), \tilde{Z}_{hvsc}(\omega), \tilde{R}_{lvhv}(\omega), \tilde{R}_{hvlv}(\omega)], \tag{9}$$

can be determined through simulated perturbation of the model [12]. However, due to the complexity of the model topology these simulations are time-consuming. The analytical transfer functions are therefore used in the optimisation procedure to improve runtimes.

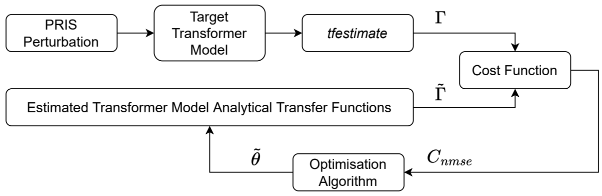

Fig. 5. Parameter Estimation procedure

The Normalised Mean Squared Error (NMSE) cost function, C_{nmse}, is defined by the relationship

$$C_{nmse} = \sum_{r=1}^{N_r=6} \left[\frac{1}{N_k \psi_r} \sum_{k=1}^{N_k} (\epsilon_r(\omega_k))^2 \right], \tag{10}$$

where $\epsilon_r(\omega_k)$ denotes the error between the logarithms of the magnitudes of the frequency responses of the target and estimated models at frequency ω_k. The errors are determined on a point-by-point basis for each frequency response sample ω_k, such that

$$\epsilon_r(\omega_k) = \log_{10} |\gamma_r(\omega_k)| - \log_{10} |\tilde{\gamma_r}(\omega_k)|, \tag{11}$$

where γ_r and $\tilde{\gamma}_r$ represent the r^{th} frequency responses in the target and estimate set, Γ and $\tilde{\Gamma}$, respectively. The sample frequencies ω_k are distributed logarithmically up to N_k samples, such that the contributions from $\epsilon_r(\omega_k)$ to C_{nmse} are distributed equitably across the frequency range of interest. The errors are normalised through a normalisation constant, ψ_r, defined as

$$\psi_r = \max\{\gamma_r(\omega)\} - \min\{\gamma_r(\omega)\} \tag{12}$$

where $\max\{\gamma_r(\omega)\}$ and $\min\{\gamma_r(\omega)\}$ are the maximum and minimum amplitude of the r^{th} target frequency response, respectively. The optimisation algorithm repeatedly adjusts the parameter vector $\tilde{\theta}$ to minimise C_{nmse}.

B. Parameter Vector Constraints and Assumptions

The target circuit presented in Fig. 1 has 36 parameters to be estimated, which translates to a complex multi-dimension optimisation problem. The inductor L_c only serves to couple the core-loss resistance R_c to each winding section. Fixing L_c to a value that places R_c in a numerically convenient range is advised [3]. The parameter L_c is therefore fixed to the target value of $37.5H$. It is assumed that not all flux components that are linked by the lumped winding inductances are confined to the core. Thus, the coupling coefficients $K_{a1c} - K_{b4c}$ are estimated seperately. These assumptions give rise to the following vector of parameters to be estimated:

$$\theta = [R_a,\ \theta_{R_{bc}},\ \theta_{C_{sg}},\ L_a,\ \theta_{L_b},\ \theta_{K_{abc}}] \tag{13}$$

where

$$\theta_{R_{bc}} = [R_{b1},\ R_{b2},\ R_{b3},\ R_{b4},\ R_c], \tag{14}$$

$$\theta_{C_{sg}} = [C_{a10},\ C_{b1},\ C_{b2},\ C_{b3},\ C_{b4},\ C_{b12},\ C_{b34},\ C_{b10},\ C_{ab1}], \tag{15}$$

$$\theta_{L_b} = [L_{b1},\ L_{b2},\ L_{b3},\ L_{b4}], \tag{16}$$

and

$$\theta_{K_{abc}} = [K_{a1b1},\ K_{a1b2},\ K_{a1b3},\ K_{a1b4},\ K_{b1b2},\ K_{b1b3},\ K_{b1b4},\ K_{b2b3},\ K_{b2b4},\ K_{b3b4},\ K_{a1c},\ K_{b1c},\ K_{b2c},\ K_{b3c},\ K_{b4c}]. \tag{17}$$

Table V presents the scaling factors for each model parameter, and the lower and upper bounds set in the optimisation procedure. Wide bounds are set for the procedure to investigate the performance of optimisation algorithms in cases when little *a priori* information is available on the transformer parameters. The parameters are scaled to ensure the optimisation step sizes in all dimensions are similar.

TABLE V
PARAMETER BOUNDARY CONSTRAINTS AND SCALING FACTORS

Parameters	Scaling Factor	Lower Bound	Upper Bound	Units
R_{a1}	10^{-3}	1	1000	$m\Omega$
$\theta_{R_{bc}}$	10^{2}	1	1000	$k\Omega$
$\theta_{C_{sg}}$	10^{-12}	1	1000	pF
L_{a1}	10^{-3}	1	1000	mH
θ_{L_b}	10^{1}	1	1000	H
$\theta_{K_{abc}}$	10^{-2}	99	99.99	

C. Optimisation Procedure

Both Particle-Swarm Optimisation (PSO) [14] and Genetic Algorithm (GA) [15] are used in various case studies to compare the performance of the algorithms. Upon completion of the global optimisation algorithm, the hybrid functionality of the method is enabled, which executes the local *fmincon* solver with the interior-point algorithm to refine the results. The optimisation procedure follows a two-step approach:

1) **Seed iterations:** The global optimisation is executed, and start-points are generated randomly based on the Mersenne Twister pseudo-random number generator with a seed set from 1 to 10. Thus, performing a metaheuristic global optimisation that begins at ten unique sets of start points.
2) **Final seed:** Once all ten parameter estimations are completed the model parameters that obtained the lowest cost function are stored and used as the starting point for a *fmincon* optimisation executing for a maximum of 20 000 function evaluations.

The parameter values that provide the lowest C_{nmse} are adopted as the final parameters.

IV. PARAMETER ESTIMATION RESULTS

The parameter estimation procedure presented in the previous section is applied to PSO and GA using a population size of 300 and a maximum of 200 iterations, as well as a population size of 500 executing for a maximum of 500 iterations. The C_{nmse} values obtained from each of the ten seeds are presented in Table VI. The estimated model parameters that produced the lowest cost function, highlighted in blue, are subsequently used in the *Final seed* step of the optimisation procedure. The particle-swarm optimisation outperforms the genetic algorithm for all seed iterations and case studies, and executes quicker on average compared to the genetic algorithm. Particle-swarm optimisation is therefore better suited for solving multi-dimensional optimisation problems in the context of transformer model parameter estimation. An acceptable result could not be obtained using a population size of 300 running for a maximum of 200 iterations. At the expense of almost double the runtime, the population size of 500 and maximum iterations of 500 obtained the overall best result highlighted in green. The error percentages of the best-estimated model parameters are presented in Table VII, where the n^{th} parameter error is calculated using the relationship

$$\text{Error}(n) = \left| \frac{\theta(n) - \tilde{\theta(n)}}{\theta(n)} \right| \times 100 \quad [\%], \tag{18}$$

where $\tilde{\theta}$ denotes the set of final parameter estimates and θ denote the set of target model parameters in Table I.

TABLE VII
ESTIMATED PARAMETER ERROR PERCENTAGES

Parameter	Error [%]	Parameter	Error [%]	Parameter	Error [%]
R_{a1}	556.08	C_{b3}	36.96	K_{a1b4}	0.17
R_{b1}	74.70	C_{b4}	212.80	K_{b1b2}	0.63
R_{b2}	81.32	C_{ab1}	1517.50	K_{b1b3}	0.11
R_{b3}	85.27	L_{a1}	2.03	K_{b1b4}	0.16
R_{b4}	88.61	L_{b1}	62.39	K_{b2b3}	0.46
R_c	0.94	L_{b2}	580.71	K_{b2b4}	0.16
C_{a10}	97.75	L_{b3}	96.11	K_{b3b4}	0.69
C_{b10}	120.15	L_{b4}	80.60	K_{a1c}	0.43
C_{b12}	89.92	L_c	N/A	K_{b1c}	0.47
C_{b34}	262.12	K_{a1b1}	0.42	K_{b2c}	0.27
C_{b1}	57.73	K_{a1b2}	0.03	K_{b3c}	0.54
C_{b2}	85.05	K_{a1b3}	0.31	K_{b4c}	0.22

The estimated value of C_{ab1} obtained the worst percentage error of 1517.5%, this can be attributed to the inter-winding capacitance only affecting frequencies above 500kHz [16]. The remaining model parameter errors could be a result of the optimisation algorithm converging to a local minima. However, the frequency responses of the estimated model presented in Figures 6 and 7 show close correlation to the target frequency responses. The closely correlated frequency responses suggest that the model parameters are not individually observable, however, the combinations formed by the estimated model parameters are similar to the combinations formed by the target model parameters. The resistive parameters predominantly affect frequency responses at low frequencies as well as the damping of resonant points. As can be seen in Figures 6 and 7 the response at low frequency is estimated correctly with minor errors in the damping of the resonant points. This suggests that the accurate estimation

TABLE VI
COST FUNCTION VALUES FOR PARAMETER ESTIMATION CASE STUDIES

Case Study			Seed Iterations										Final Seed	Avg. Runtime
Alg.	Pop.	Iter.	1	2	3	4	5	6	7	8	9	10		[hrs]
PSO	300	200	0.1498	0.3954	0.3029	0.2868	0.2840	0.0919	0.2059	0.2342	0.1786	0.2016	0.1440	1.147
GA	300	200	0.4765	0.8763	0.6921	0.8341	0.7150	0.8220	0.7227	0.4844	0.4522	0.2191	0.3013	1.272
PSO	500	500	0.2399	0.0873	0.1913	0.1224	0.1821	0.2466	0.1850	0.0778	0.1075	0.0945	0.0035	2.973
GA	500	500	0.5238	0.3048	0.7076	0.4199	0.4973	0.3234	0.6646	0.379	0.4163	0.4644	0.0079	3.655

of the largest resistor R_c causes the frequency responses, and therefore the cost function, to be insensitive to the remaining resistive parameters. The frequency responses are possibly also less sensitive to other model parameters which could cause some of the large errors presented in Table VII. Experimentally, the true transformer model parameters remain unkown. The importance of individual error percentages are, therefore, less significant than reproducing a model that can represent the overall transformer behaviour.

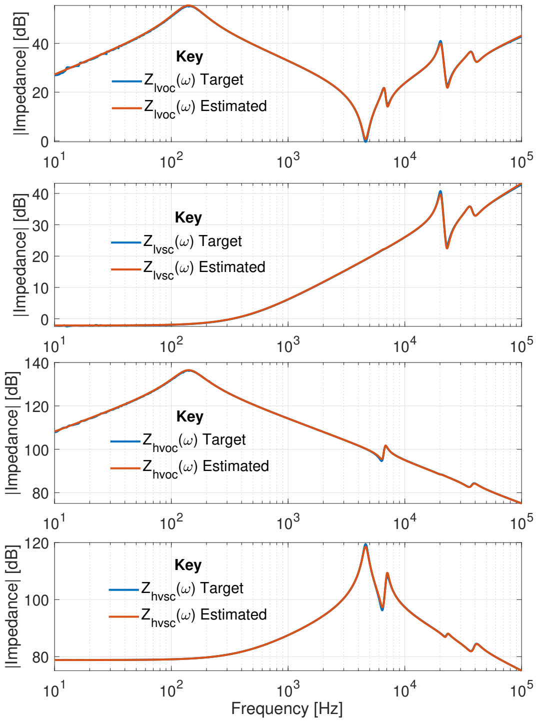

Fig. 6. Target and Estimated Frequency Responses of the Model Input Impedances.

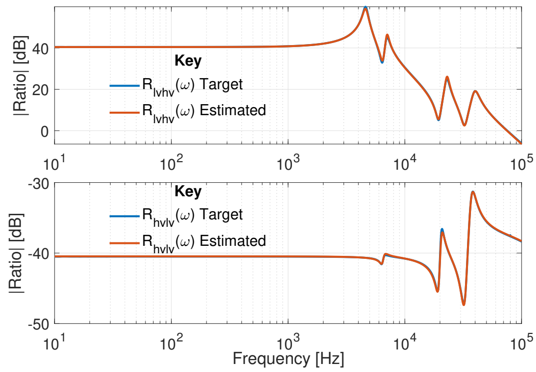

Fig. 7. Target and Estimated Frequency Responses of the Model Voltage Transformation Ratios.

V. Conclusion

This paper investigates the use of a Pseudo-Random Impulse Sequence perturbation signal to perform parameter estimation on a 16kVA, 22kV/240V distribution transformer model using four input impedance frequency response transfer functions and two voltage transformation ratio frequency response transfer functions. The results shows that the proposed PRIS perturbs the transformer model sufficiently up to 100kHz, such that reliable frequency responses can be determined for the transfer functions of interest. PSO shows to provide improved parameter estimation results and quicker runtimes compared to the GA. The research presented in this paper is conducted using simulated data. Further work is required to apply the PRIS perturbation and proposed methodology to a practical distribution transformer. Research into improving the parameter estimation methodology through the weighing of frequency ranges in which resonant points are located and through more advanced optimisation algorithms should be performed.

References

[1] E. Gomez-Luna, G. Aponte Mayor, C. Gonzalez-Garcia, and J. Pleite Guerra, "Current status and future trends in frequency-response analysis with a transformer in service," *IEEE Transactions on Power Delivery*, vol. 28, no. 2, pp. 1024–1031, 2013.

[2] A. Keyhani, S. Chua, and S. Sebo, "Maximum likelihood estimation of transformer high frequency parameters from test data," *IEEE Transactions on Power Delivery*, vol. 6, no. 2, pp. 858–865, 1991.

[3] C. Brozio and H.J.Vermeulen, "Wideband equivalent circuit modelling and parameter estimation methodology for two-winding transformers," *IEEE Proceedings - Generation, Transmission and Distribution*, vol. PAS-150, no. 4, pp. 487–492, 2003.

[4] G. Olivier, R. P. Bouchard, Y. Gervais, and D. Mukhedkar, "Frequency response of HV test transformers and the associated measurement problems," *IEEE Transactions on Power Apparatus and Systems*, vol. PAS-99, no. 1, pp. 141–146, 1980.

[5] D. Douglass, "Potential transformer accuracy at 60Hz voltages above and below rating and at frequencies above 60Hz," *IEEE Transactions on Power Apparatus and Systems*, vol. PAS-100, no. 3, pp. 1370–1375, 1981.

[6] G. R. Slemon, *Magnetoelectric devices: transducers, transformers, and machines*, 2^{nd} ed. Hoboken, New Jersey, USA: John Wiley & Sons, 1966.

[7] H. J. Vermeulen, R. G. Koch, and W. T. Rawlins, "Broadband modelling of magnetic voltage transformers through application of parameter estimation techniques," 6^{th} *International Symposium on High Voltage Engineering*, vol. PAS-6, no. 50.12, 1989.

[8] P. Mukherjee and L. Satish, "Construction of equivalent circuit of a transformer winding from driving-point impedance function – analytical approach," *IET Electric Power Applications*, vol. 6, pp. 172–180(8), March 2012.

[9] A. Abu-Siada, M. I. Mosaad, D. Kim, and M. F. El-Naggar, "Estimating power transformer high frequency model parameters using frequency response analysis," *IEEE Transactions on Power Delivery*, vol. 35, no. 3, pp. 1267–1277, 2020.

[10] F. M. Mwaniki and H. J. Vermeulen, "Characterization and application of a pseudorandom impulse sequence for parameter estimation applications," *IEEE Transactions on Instrumentation and Measurement*, vol. 69, no. 6, pp. 3917–3927, 2020.

[11] C. C. Brozio, "Wideband modelling and parameter estimation of two-winding transformers," Ph.D. dissertation, Department of Electrical and Electronic Engineering, University of Stellenbosch, South Africa, 1999.

[12] D. M. Banks, J. C. Bekker, and H. J. Vermeulen, "Parameter estimation of a two-section transformer winding model using pseudo-random impulse sequence perturbation," in *2021 56th International Universities Power Engineering Conference (UPEC)*, 2021, pp. 1–6.

[13] "Matlab Signal Processing Toolbox," R2020b, the MathWorks, Natick, MA, USA.

[14] J. Kennedy and R. Eberhart, "Particle swarm optimization," in *Proceedings of ICNN'95 - International Conference on Neural Networks*, vol. 4, 1995, pp. 1942–1948 vol.4.

[15] D. Reid, "Genetic algorithms in constrained optimization," *Mathematical and Computer Modelling*, vol. 23, no. 5, pp. 87–111, 1996. [Online]. Available: https://www.sciencedirect.com/science/article/pii/0895717796000143

[16] J. Bak-Jenson, B. Bak-Jenson, S. Mikkelsen, and C. Jensen, "Parametric identification in potential transformer modelling," *IEEE Transactions on Power Delivery*, vol. 7, no. 1, pp. 70–76, 1992.

The Cost Implications of Operating a Coal-Fired Power Plant in a Cycling Mode

Portia T Mzimba
Department of Geography, Environmental Management and Energy Studies
University of Johannesburg
Johannesburg, South Africa
mzimbapt@gmail.com

Kristy E. Langerman
Department of Geography, Environmental Management and Energy Studies
University of Johannesburg
Johannesburg, South Africa
klangerman@uj.ac.za

Joanne Calitz
Enertrag
Enertrag South Africa
Pretoria, South Africa
Calitz@enertrag.com

***Abstract*—High penetration of non-dispatchable wind and solar to the electricity grid forces the base-loading units to cycle on and off or ramp up and down as per electricity demand. This paper analyses the implications of cycling operation, relative to base-load operation, on the resource and maintenance requirements and costs of operating Majuba coal-fired power plant. Majuba power station's extent of cycling within the Eskom generation fleet has been excessive. In 2016, Majuba experienced 69 starts due to cycling operation. The increased boiler tube failures, fuel oil, coal, water and cost were reviewed for 2016. 60% of the boiler tube leaks experienced at Majuba were caused by cycling operation. 61% of fuel oil used was due to cycling operation. Cycling operation also resulted in high forced outage rate, and excessive revenue loss caused by loss of production during forced outages. The cost for cycling incurred by Majuba power station during 2016 was at least R156 919 million, without revenue loss due to the loss of production, when repairing boiler tube leaks caused by cycling operation. When including the revenue loss of R776 314; the total cost for cycling operation was R933 million. The cost of cycling per GWh was R280 676. The plant is also ageing fast due to the consequential damages.**

Keywords—Cycling, base-load, coal-fired power plant, cost, boiler tube leaks, fuel oil, load following

I. Introduction

Fossil fuels were a fundamental driver of the industrial revolution. They have played a strong positive role in technological, social and economic development [1]. The world needs to decarbonise by reducing reliance on fossil fuels and transitioning towards lower-carbon energy sources. Amongst others, wind and solar energy are renewable energy. They are non-dispatchable and produce variable output [2]. High solar and wind penetration to the system results in too much electricity generation during off-peak periods [3] which increases the frequency of the grid and, in the absence of sufficient storage or gas capacity, forces conventional thermal units to be cycled.

Cycling operation is a form of operating conventional power plants in a flexible way by switching them on and off or ramping up and down to meet electricity demand. Coal-fired power plants were not designed to cycle on and off; they were designed to run continuously at stable load and only shut down for maintenance [4]. The change in operation can have implications in a number of areas: it leads to high wear and tear of plant components, resulting in increased maintenance, lower efficiencies and increased primary resource consumption (fuel, coal and water) [5]. Cycling-related failures may not be noted immediately but critical components will eventually start to fail. In some countries where wind and solar energy have advanced, cycling of conventional coal-fired plants has long been a feature of daily operations. In South Africa, not much research has been done on this subject. With the commitment to increase the contribution of intermittent power sources (solar and wind) to the generating system [6], more research studies need to be conducted to find a balance between green energy and sustaining existing coal-fired plants.

Majuba is one of Eskom's coal-fired power stations situated in the southern part of Mpumalanga between Volksrust and Amersfoort towards the boarder of Kwa-Zulu Natal. It is one of the three biggest power stations in South Africa with a total installed capacity of 4 110 MW. There are two types of boilers in coal-fired power plants: once-through boilers and drum-type boilers. In a once-through boiler, all of the water that enters the boiler is turned to steam; the water does not re-circulate. In a drum boiler, a steam-water mixture is generated in the boiler tubes that surround the fire [7]. Majuba plant has the once-through boiler type, characterized by rapid start-up and shutdown. Due to this distinction, Majuba is the most reliable power plant on the Eskom electric system for cycling operation as it can be started and synchronized to the grid within 2 hours. The system operator therefore cycles Majuba on and off and follows the load demand to manage the national electricity grid.

Majuba's operating units have experienced a high number of starts since its commissioning in 1996 due to cycling operation, although it is a base-load thermal plant. The impacts of cycling Majuba have not yet been assessed although the plant is experiencing a high number of boiler tube failures, high fuel oil consumption, and high demineralized water usage and valve components failures. It is important to quantify the impacts and apply mitigation strategies where possible. Hence, the Majuba case study was conducted to better understand and quantify the impacts of cycling on a South African coal-fired power station and the cost thereof.

The study analysed the implications of load-following and cycling operation, relative to base-load operation, on Majuba coal-fired power plant. The following objectives were met: (1) determining the impact of the increased number of starts on boiler tube leaks, (2) quantifying the increased fuel oil usage, water usage and coal usage, (3) evaluating the cycling impact on plant reliability by calculating forced outage rate and (4) estimating Majuba Power Station's revenue loss due to forced outages caused by cycling operation.

II. METHODOLOGY

A. Unit starts and boiler tube failure data

The number of units boiler starts was sourced from the Generation Production and Sales System (GPSS) database. The daily unit-loading regime was sourced from GPSS.

For boiler tube failures, data was sourced from the Initial Notification of Occurrence (INO) database and GPSS. Boiler tube leak repair cost data was sourced from Systems, Applications & Products in Data Processing (SAP) system. The data record for Majuba operating units' yearly number of starts and number of fatigue boiler tube failures from the year 1996 to 2019 has been used. The data covers the commissioning of the plant to present.

Annual number of starts and number of boiler tube failures were determined. Boiler tube failures were classified according to failure mechanism. Thermal fatigue is a failure mechanism caused by cycling operation as a result of temperature and pressure changes. Boiler tube failures due to fatigue were quantified. The data was analysed and compared on a graph to indicate the relationship between number of starts and number of fatigue boiler tube failures. The rate for start per failure was also determined.

The cost incurred for repairing tube leaks since 2014 until 2019 was calculated by using monthly core crew of R2 324 956 which is paid monthly to the contractor. The average cost for repairing a single boiler tube leak was calculated using the tube leak repair register obtained from the contractor.

B. Cycling impact on plant reliability

Cycling affects plant reliability. Reliability of the boiler is affected because of the thermal fatigue and pressure changes that the boiler undergoes when cycling on and off. The thermal fatigue results in boiler tube failures. To determine the impact of cycling on plant reliability, a performance index called Forced Outage Rate was used [8]. For this objective, a comparison was done between Majuba Power Station and Matimba Power Station. Majuba and Matimba power plants are comparable as they were constructed and commissioned at a similar time thus their age is similar. Matimba's construction started in 1981 and Majuba's started in 1983. Commissioning started in 1993 and 1996 respectively. Their designs are similar, both having once-through boilers.

The operating regime (number of starts for each unit) of the two power plants was compared to determine the extent of cycling at each power station from 1996 to 2019. Historic data for both Majuba and Matimba was used to establish the relationship between cycling and plant reliability. A large data population was used for this objective because every start of the unit has consequences for the life span of the plant.

Forced outages due to fatigue boiler tube failures were compared for the two power plants. Data for 2016 was used for calculating forced outages rate for all 6 units of Matimba and Majuba. The equation for FOR from the IEEE -762 Standard [9] was used as follows:

$$FOR = \{(Forced\ Outage\ Hours) \div (Forced\ Outage\ Hours + Service\ hours)\}\ X\ 100 \qquad (1)$$

C. Primary resource usage and manpower utilisation

The year 2016 was selected for the cycling assessment since Majuba units experienced more two-shifting in 2016 than in any other year since 2012. In 2016 and 2017 there was excess capacity on the grid due to the penetration of wind and solar coupled with the (temporary) Eskom plant performance improvement in availability factor (EAF) and additional capacity added to the grid; therefore, Majuba was cycled to manage the national electricity grid. As the generating units de-load at night, the fuel oil used for taking a combustion mill offload and the amount of water and coal used was recorded. In the morning when the system operator (National Control) requests the same generating unit to pick up load, the fuel oil and coal used for starting a combustion mill and additional water used for ramping up load is recorded.

Fuel oil usage was sourced from the Flip logging system. The unit controller for each generating unit allocates the fuel oil used to a specific activity. Fuel oil used due cycling operation was quantified and cost calculated using the fuel oil prices from the supplier. The amount of fuel oil used is in tonnages and the price of fuel per ton was used for determining the total cost of fuel oil used in 2016 for cycling operations.

Water usage data was sourced from Visual Automisation System. Every generating unit is fitted with a flow meter that measures water going into that specific unit. The flow meter readings are sent to the Visual Automisation System instantaneously and stored on the system. The water used for cycling activities for 2016 was summed and cost calculated using the raw water cost data and the cost for chemicals used for treating raw water to demineralized water.

The tonnage of coal used without producing electricity was obtained from Visual Automisation System using the figures of primary air flow into the milling plant.

D. Revenue loss due to forced outages caused by cycling operation

Data for forced outages related to cycling was acquired from GPSS. The duration of unit forced outage and the loss in generation in megawatts was used to calculate revenue lost during downtime in 2016. Lost revenue was quantified using costs from the Majuba Energy Trader as follows:

$$Revenue\ loss\ in\ R' = MWh\ loss\ due\ to\ forced\ outage\ x\ R/MWh \qquad (2)$$

$$MWh\ loss\ due\ to\ forced\ outage = unit\ capacity\ x\ forced\ outage\ hours$$

III. Results

A. Impact of the increased number of starts on the boiler plant

From 1996 to early 2019, Majuba units were started 6833 times (Fig. 1). A total of 577 boiler tube fatigue failures were experienced during the same period and the start per failure rate deteriorated from 67 in 1998 to 3 in 2009. This means that while the station was new in 1998, units could be started 67 times before 1 boiler fatigue failure is experienced however as the plant ages it deteriorated and became prone to failures hence by 2019, a failure is experienced after starting the plant only 3 times.

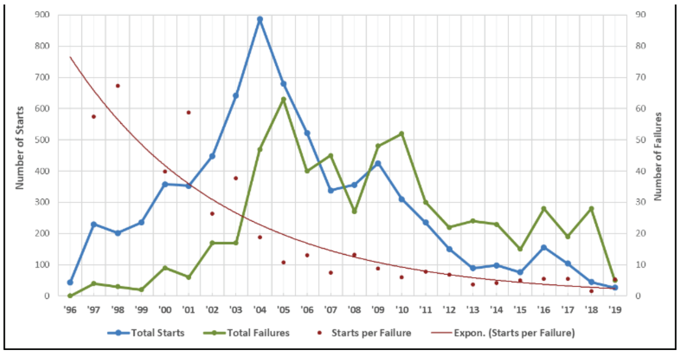

Fig. 1: Cumulative starts versus cycle-related boiler tube failures for all 6 Majuba units

There were a high number of starts between 2002 and 2006, with highest number of starts in 2004 at 886 starts. The number of failures was also the highest in the same period, with highest failures in 2005 at 63 boiler fatigue failures. This clearly indicate that number of starts has an impact on fatigue boiler tube failures. The trend in starts per failure in Figure 1 also clearly indicates a relationship between number of starts and number of failures.

From the year 2014 to 2019, Majuba incurred 228 boiler tube failures, of which 122 were cycle operation induced (Fig. 2). 54% of the tube failures were due to cycling operation. In 2016, 60% of the boiler tube leak failures were caused by cycling operation. The highest number of fatigue boiler tube leaks was experienced in 2016, corresponding to the highest number of starts for the same year (Fig. 1).

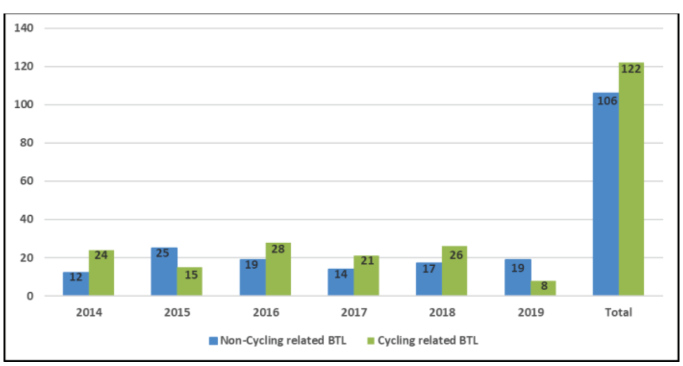

Fig. 2: Number of boiler tube leak failures at Majuba Power Station from 2014 to 2019

Cycling a base-load coal-fired power plant clearly induces boiler tube failure – the higher the number of starts, the more boiler tube failures experienced. The implication of this is that when a high level of wind and solar will be added to the energy mix and coal-fired power plants are cycled, the coal-fired plants will experience more boiler tube leaks. This will affect the performance of the stations due to unplanned unavailability of the plant. The load factor will also be affected by both the cycling regime and the downtime due to boiler tube failure repairs.

The total cost for repairing the boiler tube leaks incurred at Majuba power station from 2014 to 2019 was R103 million, of which R53 million was for cycling induced boiler tube failures. This cost of R103 million excludes the material cost, it is just for manpower and service cost. More than 50% of the money spent for repairing boiler tube leaks at Majuba could have been avoided if the units were not two-shifted. In 2016, boiler tube failures related to cycling operations costed Majuba R34 million (Fig. 3)

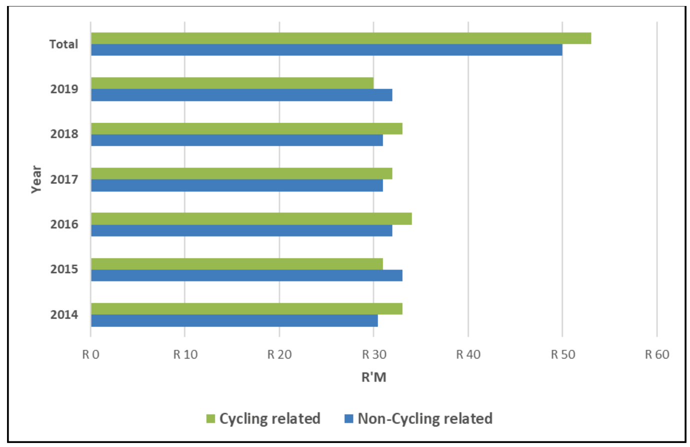

Fig. 3: Cost for boiler tube leak repairs at Majuba Power Station from 2014 to 2019

B. Fuel oil usage, water usage, coal usage and manpower utilisation

Majuba generating units used an excessive amount of fuel oil because of cycling operation. Unit 1 is the highest consumer, and used an additional 3 689 tons of fuel oil in 2016 (Fig. 4) due to cycling operation. This is fuel oil that would not have been consumed if the unit was operating on base-loading. Mill shutdown fuel oil usage was consumed when the units were load-following thus reducing unit load at night by shutting down one out of four mills. Fuel oil used during mill start-up was for ramping up load in the morning. Boiler tube leak related fuel oil usage is when a unit is shut down for tube leak repairs and started-up after the repairs, a total of 2 476 tons of fuel oil was used (Fig. 4). In 2016 Majuba consumed additional 18 926 tons of fuel oil due to cycling operation, which is 61% of total fuel oil used in the year.

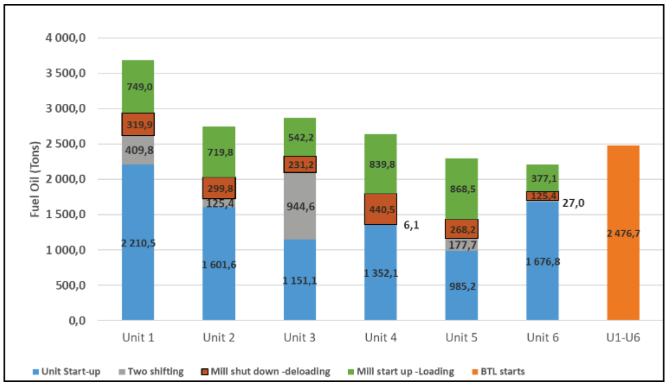

Fig. 4: Fuel oil usage for cycling operation at Majuba Power Station in 2016

Fuel oil used for unit start-ups related to cycling cost at Majuba is R54, 47 million (Fig. 5). Majuba spent R114, 82 million in 2016 on fuel oil used just for cycling the units on and off without producing any megawatts.

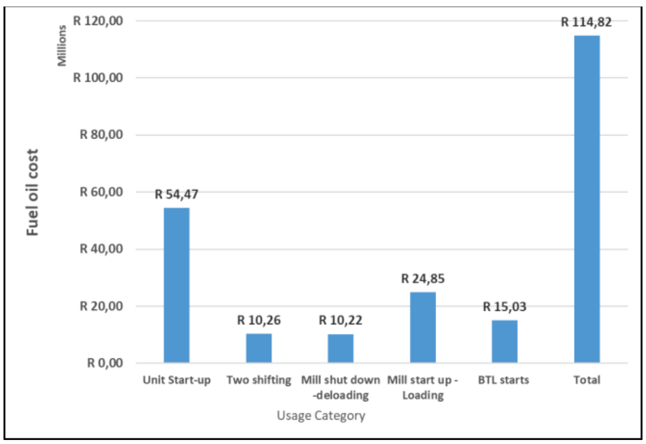

Fig. 5: Cost of fuel oil used for cycling operations at Majuba Power Station in 2016

Cycling operation resulted in excessive use of demineralised water. A total of 70 014 cubic meters of water was used for cycling at Majuba in 2016 (Table 1). This quantity did not contribute in generating megawatts as the water was being dumped during units' shutdown and start-up for two-shifting. When generating units are running on base-load mode, minimal water is used to make up for the losses but when a unit is shutting down, starting up and changing loading, excess demineralised water is used. Demineralised water cost is very high as it includes the cost of raw water and the cost of chemically treating the raw water before it enters the boiler and turbine.

The average annual cost for chemically treating raw water at Majuba is R1 865 424. In 2016, Majuba used a total of 70 014 \cubic meters of demin water (Table 1) which cost R2 250 million due to cycling operation. Similar research papers reviewed for implications of cycling operation never looked at water usage utilisation during cycling [10–19]. Water is a scarce resource for South Africa. The implication of this finding is that water usage for coal-fired power plants will increase drastically when the units operate in cycling regime.

Table 1: Cost of demineralized water used for cycling at Majuba Power Station in 2016

Water Consumption during shutdown & start-up	Unit 1	Unit 2	Unit 3	Unit 4	Unit 5	Unit 6	Total for 2016
Water used after shutdown	2526,06	5 816,97	9 599,88	3 215,62	1 679,88	1 031,35	23869,76
Water used for start-up	4 627,14	11 953,23	10 744,75	12 956,85	4 476,86	1 385,36	46 144,19
Total water used offload	7 153,20	17 770,19	20 344,63	16 172,46	6 156,74	2 416,71	70013,94
Cost of raw water	*R5 494,00*	*R5 494,00*	*R5 494,00*	*R5 494,00*	*R5 494,00*	*R5 494,00*	R384 656,61
2016 cost for water R'	**R39 299,70**	**R97 629,44**	**R111 773,42**	**R88 851,52**	**R33 825,14**	**R13 277,39**	**R2 250 080,61**

In 2016 Majuba used an additional 9 982 tons of coal due to cycling operation which cost R5 839 734. This amount of coal would not have been used without generating megawatts if the units were base-loading. Thermal efficiency is also affected.

C. *Cycling impact on forced outage rate boiler tube failures at Majuba and Matimba Power Stations*

Majuba Power Station's forced outage rate for 2016 is 23% which is about 10 times higher than Matimba's forced outage rate of 2.9% for the same year. Majuba units experienced more forced outages due to boiler tube failures caused by cycling operation.

D. *Majuba Power Station revenue loss due to forced outages caused by cycling operation*

The forced outages experienced at Majuba due to boiler tube leak repairs that were caused by cycling operation cost R 776 million in terms of revenue loss in 2016. This is significantly higher than the revenue loss of R45 million incurred at Matimba Power Station.

E. *Total additional costs incurred by Majuba Power Staion due to cycling operation*

The overall cost incurred by Majuba Power Station in 2016 because of cycling operations is R933 million (Table 2). The total cost includes costs for tube leak repairs (cycling induced), additional water, additional fuel oil usage and coal for cycling related start-ups. Revenue loss due to boiler tube leak repairs was also considered in the total cost of cycling as the business's profit is affected. In 2016 cost of cycling per GWh was R280 676.

Table 2: Total cost of cycling operation at Majuba Power Station in 2016

Cost of Cycling Operation at Majuba Power Station for year 2016	
Revenue loss due to BTL	R776 314 122
Fuel oil usage	R114 823 896
Boiler tube repairs	R34 005 836
Coal usage	R5 839 734
Water usage	R2 250 081
2016 Total	**R933 233 668**

The breakdown of cost components of cycling operation incurred at Majuba in 2016 is displayed on figure 6. For this breakdown, revenue loss cost has been excluded since it is an indirect loss that affects business sales and profit. Fuel oil cost is the highest of the components and the fact that fuel oil prices are continuing to escalate indicate that the cost of cycling coal fires power plants will get significantly high yearly.

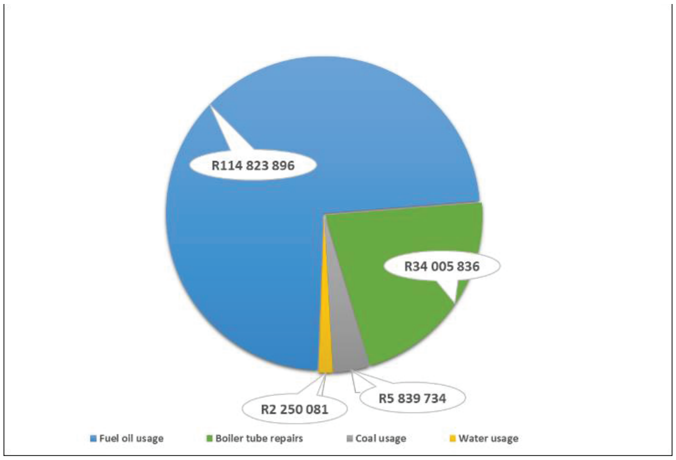

Fig. 6: The breakdown of costs incurred due to cycling operations at Majuba Power Station in 2016

IV. Discussion

This study estimated the cycling cost in 2016 at Majuba Power Station to be R156 919 million. This is the additional amount that was incurred by the station due to cycling operation. This cost exclude the cost for components replacement due to wear and tear as it was outside the research scope. The cost of cycling per GWh was calculated to be R280 676

More fuel oil, coal and water was used due to cycling. Boiler tube failures also result in unplanned unavailability of the units and cause loss of revenue for the power station due to loss in production while repairing boiler tube leaks caused cycling operation. In this case, R776 million was lost due to production loss. Plant managers are experiencing sales and profit losses whereas the system operator reaps the benefits of cycling operation.

60% of the boiler tube leaks experienced at Majuba were caused by cycling operation. 61% of fuel oil used was due to cycling operation. This has huge financial implication with regards to the budget for the power station operational cost. If this cost is not factored in during budgeting, the cycling stations will always overspend and the implication is that it might seem as is if the management is wasting financial resources whereas is the results of cycling operations.

The increased operational costs associated with cycling coal-fired power stations needs to be included in both Eskom's budgets and the Integrated Resource Plan (IRP) modelling. Cycling also affects the availability of units during boiler tube failure repairs. This also needs to be factored into Eskom's energy planning and the IRP assumptions. Majuba units were load following daily for the whole year in 2016. The cost of fuel oil and water used during ramping down at night and ramping up in the morning need to be included in Eskom's budget. It is of note that the price of fuel oil has escalated by 163% since 2016 (6 year period). Therefore the cost of primary energy usage due to cycling will increase significantly yearly thus increasing the total cost of cycling.

V. Conclusion

It is essential to transition from fossil energy to low-carbon energy due to the environmental concerns of greenhouse gas emissions and localised air pollution. Transitioning to a low-carbon economy increases the penetration of non-dispatchable variable wind and solar energy to the electricity grid. System operators have typically relied on conventional power plants to balance demand and supply by ramping them up and down or switching them on and off to accommodate renewable energy in the grid. This is changing the generation output of base-load coal-fired power plants. Coal-fired power plants were not designed to cycle on and off; they were designed to run continuously at stable load and only shut down for maintenance. The change in operation have implications in a number of areas: it leads to high wear and tear of plant components leading to increased maintenance, lower efficiencies and increased primary resource consumption (fuel, coal and water).

The future needs a flexible electricity system. A flexible electricity system that is characterized by a combined set of generators with varying technologies to respond to the variation and uncertainty in net load. A system that is dominated by gas or hydro units will have a higher level of flexibility compared to a system dominated by coal or nuclear generators. At extremely high penetration of renewable energy, a key element of system flexibility is the ability of base-load generators to reduce output to very low levels and cycle on and off following the electricity demand while maintaining system reliability. Until large scale, cost-effective energy storage is available, coal-fired power plants will be cycled.

If the impacts of cycling and the cost can be well understood and the utilities have a process that provide actual operating costs incurred due to cycling, plant management can be able to take proactive operational measures rather than deal with unexpected costs and poor plant performance years after damage to plant systems has been done. The uncertainty surrounding cycling costs lead to these costs being unaccounted for by utilities thus not considered when bidding and trading is done. The costs of cycling coal-fired power stations needs to be compared to other options for balancing variable renewable generation, like energy storage and gas.

VI. Acknowledgments

I would like to express my gratitude to my supervisor Dr. Kristy Langerman. This paper and the research behind it would not have been possible without your exceptional support and guidance. Appreciation to Joanne Calitz for the advices and Andre Rossouw, former Majuba boiler pressure parts engineer and the entire Majuba team. Special appreciation to my husband Christopher, my daughter N'wayitelo and my son Ethan Mzimba

VII. References

[1] H. Ritchie, and M. Roser, "Fossil Fuels". Published online at OurWorldInData.org., 2019. Available from: https://ourworldindata.org/fossil-fuels.

[2] P. de Mars, A. O'Sullivan, and I. Keppo, "Estimating the impact of variable renewable energy on base-load cycling in the GB power system". *Energy*, 2020, 195, p.117041.

[3] J. Lindsay, and K. Dragoon, RNP Summary Report on Coal Plant Dynamic Performance Capability. Renewable Northwest Project, Portland, 2013. Engineering.

[4] N. Troy, E. Denny, and M. O'Malley, "Base-load cycling on a system with significant wind penetration". *IEEE Transactions on Power Systems*, 2010, 25(2):1088-1097. DOI: 10.1109/tpwrs.2009.2037326.

[5] M. Bastaki, "Calculation of generation system reliability index: Loss of Load Probability". *Life Science Journal*, 2020.

[6] IRP. Draft Integrated Resource Plan 2019

[7] J. Kovács, A. Kettunen, and J. Ojala, Modelling and control design of once-through boilers. IFAC Proceedings, 2012, Vol. 45(21), pp.196-200.

[8] P. Rondla, "Analytical Methods for Forced Outage Rate Calculations of Peaking Units". [online] Core.ac.uk, 2012. Available at: <https://core.ac.uk/display/13643059.

[9] Standards.ieee.org. 2020. 762-1987 - IEEE Standard Definitions for Use in Reporting Electric Generating Unit Reliability. Availability, and Productivity. [online] Available at: https://standards.ieee.org/standard/762-1987.html

[10] W. Schill, M. Pahle, and C. Gambardella, "On Start-Up Costs of Thermal Power Plants in Markets with Increasing Shares of Fluctuating Renewables". *SSRN Electronic Journal,* 2016. DOI: 10.2139/ssrn.2723897.

[11] N. Kumar, P.M. Besuner, S.A. Lefton, D.D. Agan, and D.D. Hilleman, Power Plant Cycling Costs, National Renewable Energy Laboratory, 2012. Colorado.

[12] S. Lefton, P. Besuner, and G. Grimsrud, Managing utility power plant assets to economically optimize power plant cycling costs, life, and reliability. Electric Power Research Institute, 1995, 195-208. DOI: 0-7803-2550-8/95$4.00019 95 IEEE.

[13] K. Van den Bergh, and E. Delarue, "Cycling of conventional power plants: Technical limits and actual costs". *Energy Conversion and Management*, 2015, 97:70-77. DOI: 10.1016/j.enconman.2015.03.026.

[14] C.Batlle, and P. Rodilla, "An Enhanced Screening Curves Method for Considering Thermal Cycling Operation Costs in Generation Expansion Planning". *IEEE Transactions on Power Systems*, 2015, 28(4), pp.3683–3691.

[15] K.V.D. Bergh, and E. Delarue, "Cycling of conventional power plants: Technical limits and actual costs". *Energy Conversion and Management*, 2015. 97, pp.70–77.

[16] S. Lefton, P. Besuner, and G. Grimsrud, "Understand what it really costs to cycle fossil-fired units". *Power*, 1997, 141(2):41-42.

[17] V. Bassi, E. Pereira-Bonvallet, M. Abdullah, and R. Palma-Behnke, "Cycling Impact Assessment of Renewable Energy Generation in the Costs of Conventional Generators".*Energies*, 2018, 11(7), pp.1640.

[18] C.Batlle, and P. Rodilla, "An Enhanced Screening Curves Method for Considering Thermal Cycling Operation Costs in Generation Expansion Planning". *IEEE Transactions on Power Systems*, 2013, 28(4), pp.3683–3691.

[19] K.V.D. Bergh, and E. Delarue, "Cycling of conventional power plants: Technical limits and actual costs". *Energy Conversion and Management*, 2015.97, pp.70–77.

[20] M. Bhamjee, "Investigation into reheater drying during boiler shut down", 2015. Available from: http://wiredspace.wits.ac.za/jspui/bitstream/10539/18375/2/submission.pdf.

[21] I. Bird, M. Milligan, and D. Lew, Integrating Variable Renewable Energy: Challenges and Solutions, National Renewable Energy Laboratory, 2013. U.S. Department of Energy.

[22] J.R. Calitz, and I.G. Wright, "Statistics Of Utility-Scale Solar PV, Wind And CSP In South Africa In 2019", 2020. [online] Researchspace.csir.co.za. Available at: <http://researchspace.csir.co.za/dspace/bitstream/handle/10204/10636/Calitz_21959_2019.pdf?sequence=1&isAllowed=y>

[23] I. Cochran, D. Lew, and N. Kumarb, "Flexible Coal: Evolution from Base-load to Peaking Plant". *National Renewable Energy Laboratory*, 2013. DOI: NREL/BR-6A20-60575.

[24] G. Danneman, and S. Lefton, Wind integration and cycling. Paper presented at FOMIS conference 2009, 29 pp. Available from: http://www.ipautah.com/data/upfiles/newsletters/cyclingarticles.pdf

[25] DEA. South Africa's 2 biennial update report, 2017. Available from: https://www4.unfccc.int/sites/ndcstaging/PublishedDocuments/South Africa First/South Africa.pdf

[26] P. Denholm, E. Ela, and M. Milligan, "The Role of Energy Storage with Renewable Electricity Generation". *National Renewable Energy Laboratory*, 2010.

[27] P. Denholm, and M. Hand, "Grid flexibility and storage required to achieve very high penetration of variable renewable electricity".*Energy Policy*, 2011, 39(3):1817-1830. DOI: 10.1016/j.enpol.2011.01.019.

[28] R.S. Dimitrov, "Inside UN Climate Change Negotiations: The Copenhagen Conference". *Review of Policy Research*, 2010, 27(6), pp.795–821.

[29] GE Energy consulting. PJM Renewable Integration Study, 2014. Available: https://www.pjm.com/~/media/committees-groups/subcommittees/irs/postings/pris-executive-summary.ashx.

[30] C. Henderson, Increasing the flexibility of coal-fired power plants. IEA Clean Coal Centre. 2014. DOI: 978–92–9029–564-8.

[31] IEA. Integrating Intermittent Renewable Energy Technologies with Coal-Fired Power Plant. IEA Clean Coal Centre CCC/189, 2011.

[32] IEA. World energy Mix, 2015. Available from: https://www.iea.org/weo/.

[33] Key World Energy Statistics, International Energy Agency, 2019, pp. 6, 36.

[34] D. Khai, R.R. Jackups, I. Feinstein, H.H. Thompson, H.M. Wolf, E.C. Stein, A.D. Gorski, and J.S. Griffith, "Operational aspects of generation cycling". *IEEE Transactions on Power Systems,* 1990, 5(4), pp.1194–1203.

[35] H. Khobai, G. Mugano, and P. Le Roux,."The Impact of Electricity Price on Economic Growth in South Africa". *International Journal of Energy Economics and Policy*, 2017, 7(1), pp.108-116. Available from: http://www.econjournals.com.

[36] M. Kubik, P. Coker, and C. Hunt, "The role of conventional generation in managing variability". *Energy Policy*, 2012, 50, pp.253-261.

[37] D. Lew, G. Brinkman, N. Kumar, S. Lefton, G. Jordan, and S. Venkataraman, "Finding Flexibility: Cycling the Conventional Fleet". IEEE Power and Energy Magazine, 2013, 11(6):20-32. DOI: 10.1109/mpe.2013.2277988.

[38] D. Lew, G. Brinkma, N. Kumar, P. Besuner, D. Agan, and S. Lefton, Impacts of Wind and Solar on Fossil-Fueled Generators. IEEE Power and Energy Society General Meeting, 2012. NREL/CP-5500-53504.

[39] P. Lund, J. Lindgren, J. Mikkola, and J. Salpakari, "Review of energy system flexibility measures to enable high levels of variable renewable electricity". Renewable and Sustainable Energy Reviews, 2015, 45, pp.785-807.

[40] S.J. Mills, Integrating intermittent renewable energy technologies with coal-fired power plant, IEA Clean Coal Centre, 2011.

[41] A. Pegels, "Renewable energy in South Africa: Potentials, barriers and options for support". *Energy Policy*, 2010, 38(9), pp.4945–4954.

[42] I. Pretorius, "Summary of research paper published in Journal of Energy in Southern Africa titled: A perspective of South African coal-fired power station emissions". *Clean Air Journal,* 2016, 26(3), pp.27-40.

[43] Y. Qi, W. Dong, and C. Dong, Fixing Wind Curtailment with Electric Power system reform in China. *CHINA'S ENERGY IN TRANSITION SERIES, 2018.* Available from: https://www.brookings.edu/wp-content/uploads/2018/04/ pdf

2023 SAUPEC Conference, Johannesburg, South Africa, January 24-26, 2023

An IEC 61850 standard-based Edge Computing algorithm to enhance communications in modern power systems

Abdalla Adam
Department of Electrical, Electronics, and Computer Engineering
Cape Peninsula University of Technology
Cape town, South Africa
adama@cput.ac.za

Mkhululi Mnguni
Department of Electrical, Electronics, and Computer Engineering
Cape Peninsula University of Technology
Cape town, South Africa
mngunim@cput.ac.za

Mukovhe Ratshitanga
Department of Electrical, Electronics, and Computer Engineering
Cape Peninsula University of Technology
Cape town, South Africa
ratshitangam@cput.ac.za

Abstract— **Distributed Energy Resources (DERs) are important components of the smart grid architecture. They play a major role in utilizing renewable energy resources and realizing the benefits of decentralized energy production. The IEC 61850 standard has established comprehensive information models and communication services that have solved interoperability issues in substations and DER systems. Moreover, the standard has simplified the design and engineering processes for integrating new equipment, by standardizing the information model for most DER devices. However, several challenges are associated with communications systems of DERs especially in remote sites. These challenges are stemming from the large data volumes that must be transmitted by DERs systems for monitoring and various other applications. Challenges such as the high cost of bandwidth and network traffic overload, cause severely poor communication performance. This paper presents an implementation of the Edge Computing (EC) concept in communication systems of DERs. The EC concept is driving the Internet of Things (IoT) initiative which is based on bringing central intelligence closer to data sources to reduce decision latency and response times. The proposed solution involves utilizing a Real-Time Automation Controller (RTAC) as an intelligent gateway that performs initial analytics on data of DER sites. The gateway model is based on the IEC 61850 standard along with an embedded algorithm for data fusion. A testbed was developed to investigate the impact of EC on communications performance in terms of bandwidth usage.**

Keywords— IEC 61850, Edge Computing, Communication, DERs, Smart Grid

I. Introduction

In recent times, there has been a growing paradigm shift toward renewable energy to replace traditional fossil energy. This global orientation has been largely propelled by the negative environmental impacts of fossil energy on the ecosystem as well as the finite nature of fossil fuel which presents a strategic threat to the future of energy supply. The smart grid initiative is the main driving framework of this orientation as it incorporates renewable energy utilization via dynamic structures such as microgrids and Virtual Power Plants (VPPs). In a microgrid or a VPP, the DERs are controlled coordinatively to enhance the productivity of power generation, minimize losses and ensure efficiency and security of power distribution. Therefore, the successful integration and management of DERs systems depends heavily on the communication system performance [1].

Achieving interoperability is another major issue that presents itself given the proprietary communication protocols and multi-vendor devices that are used in today's DERs systems [2]. The IEC 61850 standard has been a breakthrough in the communications systems of power grids. It has provided solutions for the interoperability issues by adopting object-oriented modelling of devices' information. As well, the standard has enabled communications over the advanced Ethernet technology. However, the growing deployment of DERs has significantly increased the amount of data exchanged across utilities' networks leading to several new challenges. The substantial increase in communication latency is the most critical issue, in addition to cybersecurity, reliability, and the high costs of bandwidth usage [3].

This situation called for the prospect of adopting concepts from the Internet of Things (IoT) initiative into power systems communications. Specifically, the concept of EC that is being extensively implemented within the industrial sector enterprises to address the issues of high data traffic within their networks [4]. In [5], the EC is defined as the distribution of data processing capabilities in a manner that spreads throughout the communication routes from data sources to the cloud. Implementing the EC concept has found large acceptance from various industries and infrastructure sectors especially for monitoring applications.

A major driver to implementing the EC scheme is to reduce the network traffic by distributing data processing capacity throughout the network's edge devices. This feature allows for the reduction of bandwidth usage and minimizes communication and decision-making latencies. The DER sites present a viable use case for EC due to the large volumes of data generated in a single site [6].

This paper presents an implementation of a monitoring scheme of a wind energy DER model utilizing the EC concept. A lab-scale testbed was developed to evaluate the EC gateway's impact on the communication system performance. The wind energy DER model was simulated on a Real Time Digital Simulator (RTDS) and publishes data via the IEC 61850-8-1 Generic Object-Oriented Substation Event (GOOSE) protocol. An RTAC SEL-3555 was utilized as the EC gateway that forwards the data to an Elipse Power SCADA application via IEC 61850-8-1 MMS standard over a local area connection. A data fusion algorithm was developed for the gateway to reduce the data volume before transmission to the SCADA application.

II. METHODOLOGY

A. The wind energy DER model on RTDS

The choice of wind energy in this research work, was mainly motivated by the massive contribution of wind energy being the most utilized renewable source in clean energy production. This fact is mainly driven by the low cost of energy produced from wind. Additionally, wind energy has many other advantages that promote its wide utilization, including the long-life span of system parts, reactive power injection to the grid, minimized costs of installation, operation, and maintenance. [7].

The performance of communication systems is a critical factor in achieving the seamless integration of wind generation systems into smart grids. Wind turbines are built on land or offshore, usually at very distant locations from control centres. Hence, an EC gateway can be utilized to reduce data transmitted from wind turbines' sites to enhance the performance of the communication system. A model consisting of a wind turbine coupled with an electrical generator was developed in RTDS representing a DER site. Several mechanical and electrical measurement data are generated from the simulation model and forwarded to the gateway using IEC 61850-8-1 GOOSE.

The RTDS is a digital computing machine developed to run real-time simulations of power systems to study electromagnetic transients. Real-time simulations need extremely fast computing which is realized via parallel computing technologies implemented in RTDS hardware. Being a digital simulator, the RTDS calculates the state of power system models at discrete time instants with a time-step of 50 microseconds (μs) to satisfy the real-time operation requirements [8]. In RTDS, processors are built into cards which are interconnected using backplane racks contained in cubicles. Each rack may consist of a combination of several types of cards each performs specific functions. The Gigabit Transceiver Network Interface Card (GTNET) enables real-time communications with external devices using various protocols including IEC 61850 (GSE, GOOSE, SV), Modbus, and DNP3 [9].

The model developed by RTDS Inc. simulates the wind generation system at St. Leon windfarm which is integrated with the Manitoba Hydro power system in Manitoba, Canada [10]. The model simulates a wind turbine coupled with an induction generator and connected to the power grid through transformers. A voltage source is configured as voltage behind impedance to simulate a simple load. An overview of the wind generation system model is illustrated in Fig. 1 below. The turbine model in RTDS calculates available wind energy and the turbine's conversion efficiency. The turbine model takes atmospheric parameters as inputs including wind speed, air temperature, barometric pressure, and relative humidity. They are configured to be manually controlled in RSCAD Runtime module. Additionally, the model also includes a simulation of wind gusts which are sudden wind blows. The gust duration and speed are manually set in RSCAD Runtime module.

Following the procedure of RSCAD/RTDS, firstly, a circuit diagram for the model is built in the RSCAD Draft module. Thereafter, the case is compiled, and the simulation is run in RSCAD Runtime module where inputs are controlled by the user and measurements are displayed. The RSCAD Runtime module for the wind generation system is shown in Fig. 2 below. The model allows the user to start/stop the wind turbine. Also, the user can control the grid coupling circuit breaker with two pushbuttons, 'TRIP' and 'RECLS'. Furthermore, the model includes control of coupling the induction generator to the wind turbine. In addition, the model allows for manipulating the setpoints of power demand and turbine speed which consequently drive the pitch angle control module.

The signal names considered for monitoring in the implementation are listed in Table 1 below. These values are from the wind turbine and the induction generator models, in addition to two atmospheric parameters; 'wind speed' and 'air density' which are computed by the wind turbine model.

The IEC 61850-8-1 GOOSE messages are published from RTDS GTNET card. It is configured via the GTNET-GSE v5 component which implements a soft IED with an embedded Substation Configuration Description (SCD) file that specifies a Logical Device (LD) and a GOOSE control block. The SCD Editor tool allows for editing of the GTNET's soft IED parameters. Thereafter, the dataset that will be published via GOOSE can be created and configured by adding data objects (DOs) and setting their data type to "Float32" which is suitable for analog values. Then, the SCD file can be exported as a Configured IED Description file (CID) file. The next step was to configure the RTAC SEL-3555 and develop the intelligent gateway model.

B. The edge computing gateway model

The RTAC SEL-3555 is configured to subscribe to GOOSE messages from RTDS. This is accomplished using the AcSELerator Architect SEL-5032 software [11]. The SCD files of both the GTNET's soft IED and the RTAC SEL-3555 are imported into the software to configure GOOSE subscription.

TABLE I. WIND MODEL DATA TAGS OF THE MONITORING SCHEME

Parameter	Signal name
Generator's busbar phase A voltage	STLWT1a
Generator's busbar phase B voltage	STLWT1b
Generator's busbar phase C voltage	STLWT1c
Wind Gusts value	GUST
Computed Air Density	airdensity
Wind speed in Km/hr	windkph
HubSpeed in rad/sec	HUBSPD
Turbine Power in Mega Watts	pwrturb
Blades Pitch degree	pitchdeg
Rotor Speed in p.u	STLWT1SPD
Stator active power (P) in Mega Watts	STLWT1P
Stator reactive power (Q) in Mega VAR	STLWT1Q

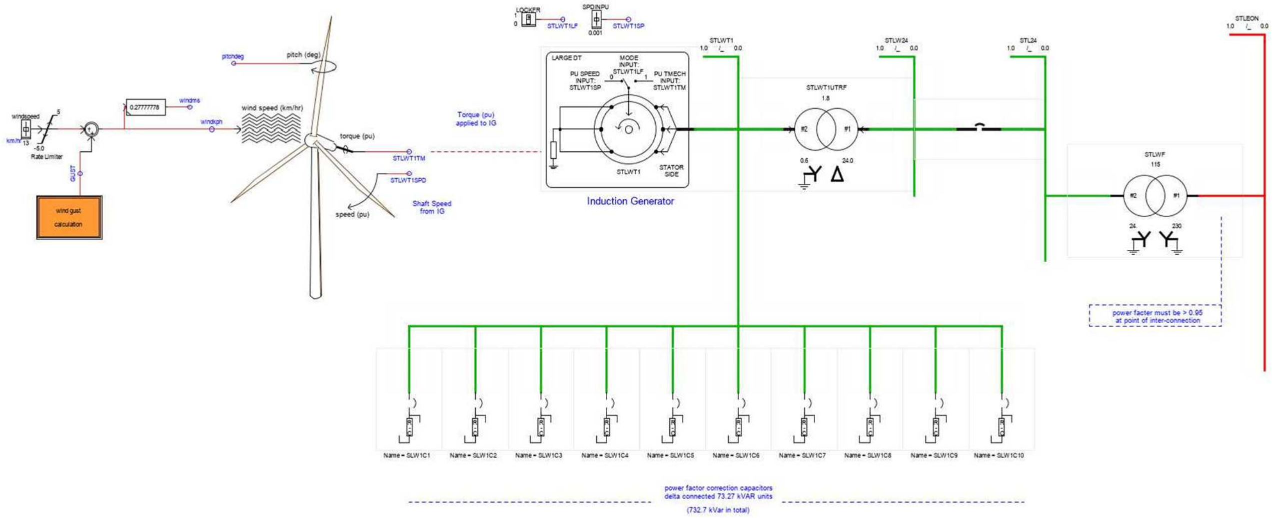

Fig. 1. RSCAD/Draft model of the wind power generation system [10].

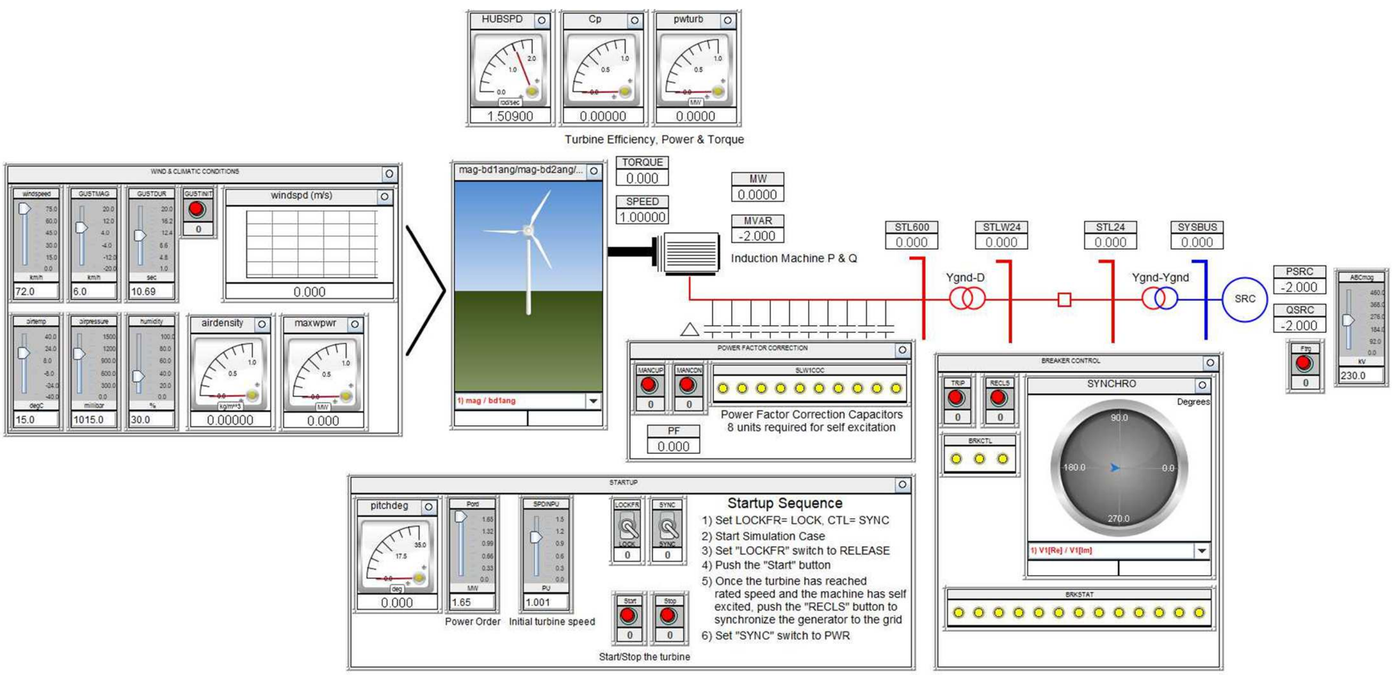

Fig. 2. RSCAD/Runtime model of the wind generation system [10].

The RTAC SEL-3555 gateway acts as an IEC 61850-8-1 MMS server that forwards the received data to the SCADA application. Hence, the received GOOSE messages must be mapped from the GOOSE control block to the server model of RTAC SEL-3555. The server model is modified by adding a new LD and a generic Logical Node (LN) as shown in Fig. 3 below. The created LD 'Wind-Site' and the LN of class 'GGIO' consist 12 analog inputs DOs to match the number of received GOOSE messages. Thereafter, the configured SCD file is imported into AcSELerator RTAC SEL-5033 software to complete the remainder of the configuration.

Mapping of GOOSE messages to the RTAC SEL-3555's server model is accomplished via a customized logic that is developed using the IEC 61131-3 Structured Text (ST) language in a 'Program1' instant that is added to the project as shown in Fig.4 below. The logic simply maps the incoming GOOSE tags to the analog DOs of the RTAC SEL-3555 server model. Finally, the project is saved, compiled, and sent to the RTAC SEL-3555 unit for execution.

C. The EC algorithm

A data fusion algorithm was developed within 'Program1' to evaluate its impact on the communication system performance. The algorithm effectively reduces the number of transmitted data tags to the SCADA application. The monitoring scheme in this implementation involves 12 data tags which are listed in Table. 1 above.

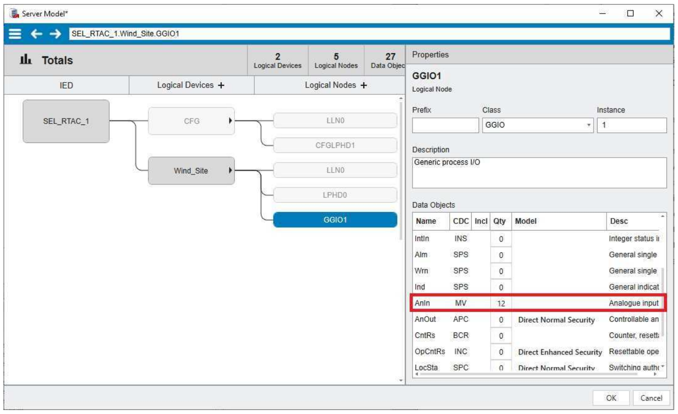

Name	CDC	Incl	Qty	Model	Desc
IntIn	INS		0		Integer status i
Alm	SPS		0		General single
Wrn	SPS		0		General single
Ind	SPS		0		General indicat
AnIn	MV		12		Analogue input
AnOut	APC		0	Direct Normal Security	Controllable an
CntRs	BCR		0		Counter, resetti
OpCntRs	INC		0	Direct Enhanced Security	Resettable ope
LocSta	SPC		0	Direct Normal Security	Switching authi

Fig. 3. Configuration of the RTAC SEL-3555 server model.

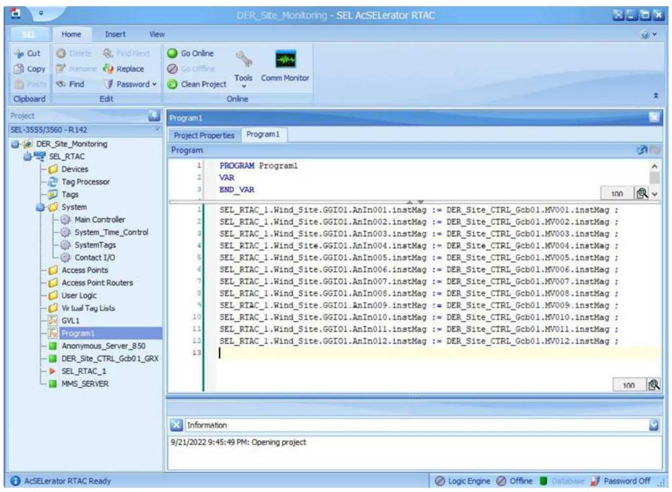

Fig. 4. Mapping GOOSE tags to RTAC SEL-3555's server model DOs.

The data tags, wind gust "GUST", wind speed "windkph", and pitch degree "pitchdeg", are reduced by the algorithm to a single point. This is done by using the gust value as an alarm of high wind speed which can damage the turbines. In the case of gust occurrence, the gateway transmits the pitch degree to inform the control center that the pitch angle control is functional because if it is not, then a manual intervention would be needed to prevent turbine damage during high wind speeds. However, during normal and low wind speeds, the gateway should keep monitoring the wind speed value.

A similar conditional approach is used to perform logical fusion of the tags, turbine power output "pwturb" and generator power output "STLWT1P". During the start-up of the wind turbine and before achieving the rated speed and coupling to the grid, the gateway transmits the turbine power output "pwturb". During this period the generator power output "STLWT1P" would be very small or even a negative value. Thereafter, when the rated speed is achieved and the generator is coupled to the grid, the priority is given to the generator power output to be transmitted to SCADA.

Lastly, the algorithm fuses the tags, rotor speed "STLWT1SPD" and turbine hub speed "HUBSPD" using their correlation via the gear ratio. The algorithm converts the rotor to hub speed, then instead of two tags, the gateway only transmits the difference between the calculated and measured values of the turbine hub speed. Ideally, the difference should be zero and any significant change in its value can be interpreted by SCADA as an indication of mechanical faults in the coupling parts between the turbine hub and the induction machine rotor.

The algorithm compiles all the above-mentioned data fusion processes in a custom logic program. It effectively reduces the received 12 tags from RTDS to only 6 tags that are transmitted via the communication network.

D. The SCADA application

Elipse Power is an advanced SCADA application developed by Elipse software™. The application provides an IEC 61850-8-1 MMS client driver that communicates with compatible MMS server devices over TCP/IP Ethernet connection. This driver is utilized to poll data from the RTAC SEL-3555 gateway. Elipse I/O drivers are implemented as Dynamic Linked Libraries (DLL) files that must be imported into the drivers' objects. Hence, the driver configuration window allows the user to browse the specified DLL file that can be obtained separately from Elipse software™ website [12].

The driver settings window consists of several tabs, the one showed in Fig. 5 below is the 'IEC 61850 Device Config' tab. It allows the user to configure the MMS server device by importing its SCD file using the button 'Browse SCL Files'. Once the file is imported, the IED name, IP address, and the MMS communication parameters are automatically extracted in the designated fields.

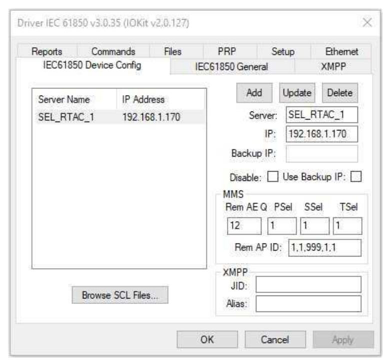

Fig. 5. IEC 61850-8-1 MMS client driver settings.

The 'IEC 61850 General' tab contains the settings for the transport layer where the transport layer protocol is set to MMS. 'Setup' and 'Ethernet' taps allow for configuring the link, and physical layers respectively.

Once all driver settings are complete, a tag browser window is prompted which enables browsing the RTAC SEL-3555's server model in an offline mode. The DOs belonging to the LN 'GGIO' under the functional constraint measurement (MX), which are the DOs to which the GTNET's GOOSE values were mapped, are imported to the driver window. Now, the driver can be activated to establish MMS client-server communication with the RTAC SEL-3555 unit.

III. SIMULATION RESULTS

The simulation was run and the data tags were tracked across the three components of the network path. Firstly, the GOOSE messages published by the DER model on RTDS were captured using GOOSE Inspector software. Secondly, data was monitored using the online mode in RTAC SEL-3555 gateway. Lastly, the IEC 61850-8-1 MMS client driver was activated to poll data and assign a timestamp to each point. The active view of the driver was captured. The above-mentioned captions are demonstrated in Fig. 6 below. Upon implementing the EC algorithm, the data tags transmitted over the network are reduced from 12 to 6 tags as demonstrated in Fig. 7 below. It shows the algorithm taking the 12 data tags received via GOOSE, assigning them to global variables then operating on the variables and the resulting tags are allocated to the RTAC server model DOs which are polled by the IEC 61850-8-1 MMS client driver in the SCADA application.

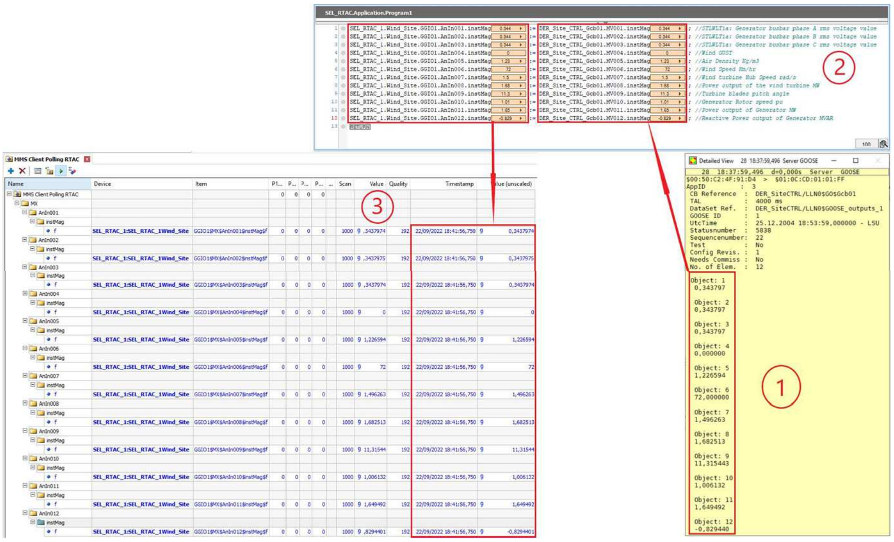

Fig. 6. Data values across the monitoring scheme testbed.

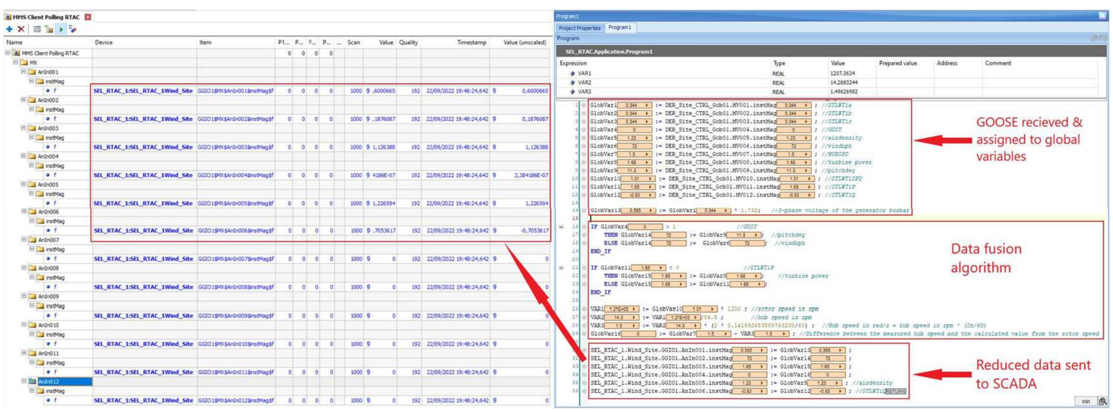

Fig. 7. The monitoring scheme with executing the EC algorithm.

The bandwidth usage was measured as a performance indicator to identify the impact of the EC algorithm. Wireshark software was used to capture the network traffic for a duration of 5 minutes for two test cases. The captured traffic was filtered to get only the traffic between the gateway and the SCADA application.

A. Network traffic without execution of EC algorithm

The bandwidth usage for the scenario with no execution of EC algorithm is shown in Fig. 8 below.

B. Network traffic with execution of EC algorithm

The bandwidth usage for the scenario with execution of EC algorithm is shown in Fig. 9 below.

The obtained results demonstrate the impact of the data fusion algorithm. The capture files were exported to the Comma Separated Values (.csv) format. Thereafter, the average (Arithmetic mean) was calculated for the bandwidth usage of each test case using Microsoft Excel and are listed in Table II. below.

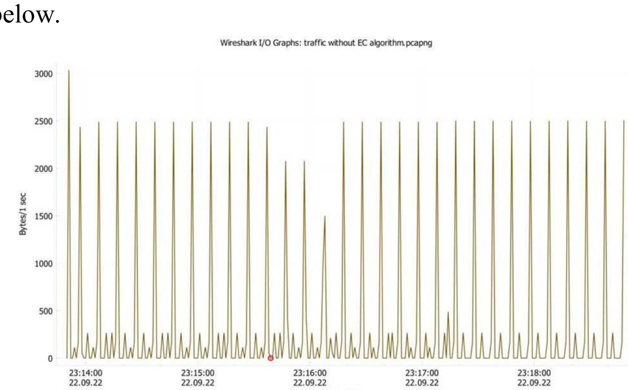

Fig. 8. The bandwidth usage for the scheme without EC algorithm.

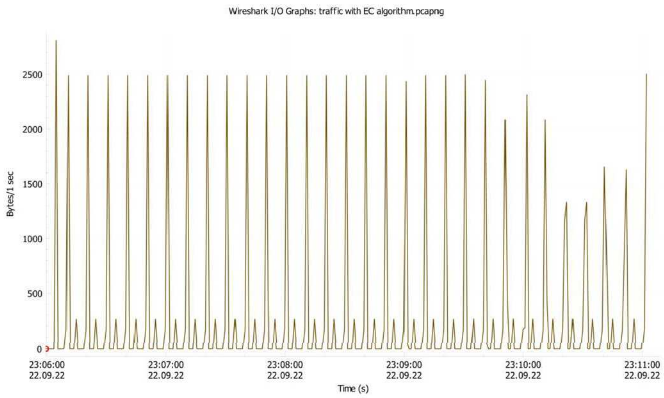

Fig. 9. The bandwidth usage of the scheme with EC algorithm.

TABLE II. BANDWIDTH AVERAGE VALUES FOR THE MONITORING SCHEME TEST CASES.

With EC algorithm	Without EC algorithm	Impact
298.386 Bytes/s	315.481 Bytes/s	17.095 Bytes/s

IV. DISCUSSION

The impact of the EC algorithm in reducing bandwidth usage is noted from the values in Table II above. The difference is relatively small, this is due to the circumstances of the measurement using Wireshark, whereby the capture period was limited to 5 minutes. Furthermore, the lab scale implementation is limited to a small amount of data transmitted over the network. However, the impact of EC can be scaled to real-life applications whereby continuous transmission of large data volumes from remote DER sites takes place. In this case, the impact can be significant on the bandwidth usage which will result in overall enhancement of the communication network performance.

This implementation presents a solid motivation for engineers and system integrators, to consider the significant impact of EC when designing the communication system for any DER site. Moreover, it is observed from the lab-scale implementation works that, adopting the IEC 61850 standard for DER communication systems offers massive potential in terms of achieving interoperability and more importantly simplifying the engineering process.

V. CONCLUSION AND FUTURE RECOMMENDATIONS

In this implementation, a monitoring scheme of a wind power generation model was developed based on IEC 61850 standard. The wind model was simulated in RSCAD/RTDS platform which publishes real-time values via IEC 61850 GOOSE protocol. An edge computing gateway model was developed utilizing the RTAC SEL-3555 unit. The gateway subscribes to GOOSE from the DER model and forwards the data to a SCADA application over the IEC 61850-8-1 MMS protocol. An embedded algorithm was implemented within the gateway to minimize the volume of data transmitted over the network. The impact of the algorithm on the communication performance was evaluated by measuring the bandwidth usage with and without executing the algorithm.

For future research, the impact of EC on communications over wide area networks (WANs) for DER systems can be investigated. Additionally, to implement the IEC 61850 standard for WANs which is specified in part IEC 61850-8-2.

ACKNOWLEDGMENT

This work was funded by the Cape Peninsula University of Technology (CPUT). The testbed and all simulations were conducted in the Centre for Substation Automation and Energy Management Systems (CSAEMS) within the Electrical Engineering department.

REFERENCES

[1] M. Mao, F. Mei, P. Jin, and L. Chang, “Application of IEC61850 in energy management system for microgrids,” 2014, doi: 10.1109/PEDG.2014.6878690.

[2] O. F. A. Sanchez, G. Reina, and M. Mauledoux, “Modeling a microgrid that integrates renewable energies in IEC 61850-7-420 and IEC 61400-25-3,” *J. Eng. Sci. Technol. Rev.*, vol. 11, no. 4, pp. 174–179, 2018, doi: 10.25103/jestr.114.22.

[3] C. H. Liu and J. C. Gu, “Modeling and integrating pv stations into IEC 61850 XMPP intelligent edge computing gateway,” *Energies*, vol. 12, no. 8, 2019, doi: 10.3390/en12081442.

[4] M. Aslett, “Data Analytics at the Edge,” 2019.

[5] M. Tseng, T. Edmunds, and L. Canaran, “Introduction to Edge Computing in IIoT,” 2018. [Online]. Available: www.iiconsortium.org/IISF.

[6] C. S. Cho, W. G. Chen, C. K. C. Liao, J. L. Liao, F. F. Chen, and T. C. Shen, “Building on the distributed energy resources IoT based IEC 61850 XMPP for TPC,” *Proc. - 2019 IEEE Int. Conf. Ind. Cyber Phys. Syst. ICPS 2019*, pp. 61–66, 2019, doi: 10.1109/ICPHYS.2019.8780241.

[7] L. Chang, H. B. Saydaliev, M. S. Meo, and M. Mohsin, “How renewable energy matter for environmental sustainability: Evidence from top-10 wind energy consumer countries of European Union,” *Sustain. Energy, Grids Networks*, vol. 31, Sep. 2022, doi: 10.1016/j.segan.2022.100716.

[8] RTDS, “RSCAD Controls Library Manual,” 2019.

[9] RTDS, “Hardware – RTDS Technologies,” Accessed Jul. 20, 2022. [Online]. Available: https://knowledge.rtds.com/hc/enus/categories/360002176414-Hardware.

[10] RTDS, “Simulating the Manitoba Hydro power system using RTDS, Modelling St. Leon Wind Farm,” 2008.

[11] Schweitzer Engineering Laboratories Inc., “Instruction Manual SEL-3555-2 Instruction Manual 20210720 Real-Time Automation Controller (RTAC),” 2018.

[12] Elipse Software, “Downloads - Elipse Software,” Accessed Sep. 23, 2022. [Online]. Available: https://www.elipse.com.br/en/downloads/?cat=48&key=&language=enus.

Power System Transient Stability Considering Wind Power Generation and System Net-Load

Siyanda Ncwane
Department of Electrical Engineering
University of Cape Town
Cape Town, South Africa
NCWSIY002@myuct.ac.za

Komla A. Folly
Department of Electrical Engineering
University of Cape Town
Cape Town, South Africa
Komla.Folly@uct.ac.za

***Abstract*— Increasing the integration of wind power generators (WPGs) can have a positive or negative impact on the transient stability of power systems. In this study, the transient stability of a power system integrating WPGs is assessed. The power produced by the WPGs is modelled using wind speed measured from three South African sites. The Weibull cumulative distribution function (CDF) is used to convert the wind speed to wind power. Three system loading conditions consisting of low, moderate, and peak demand are assessed. The probabilistic method is used to assess power system transient stability. Five thousand (5000) system operating scenarios are developed by varying the power produced by the WPGs during each of the three loading conditions. Three-phase faults are applied sequentially on power system lines and cleared using a 100 ms fault clearing time. Simulation results show that when the system net-load which is the difference between the total power produced by the WPGs and the system loading is low, the system operates closer to transient instability than when the system net-load is higher.**

Keywords—probabilistic method, system net-load, transient stability, wind power generators, wind speed

I. INTRODUCTION

Due to the adverse impacts of producing energy from fossil fuel-based generation sources, globally, the production of energy from wind power generation has increased. Between 2001 and 2021, wind power generators (WPGs) integrated into power systems increased from 24 GW to 894 GW [1]. The increased integration of WPGs into power systems can have a positive or negative impact on their transient stability depending on wind turbine technology used [2, 3]. Transient stability is the ability of synchronous generators (SGs) within a power system to remain synchronised when faults occur in the system. Transiently stable power systems have adequate capacity to transfer the kinetic energy stored by SGs during system faults. WPGs that integrate fully-rated converter generators or doubly-fed induction generators (DFIGs) result in improved power system transient stability because when there are system faults, they support voltages by injecting reactive power [4]. However, when there are system faults, reactive power is absorbed by WPGs integrating squirrel cage induction generators (SCIGs), resulting in reduced power system transient stability [4].

The transient stability of power systems integrating WPGs has been investigated in multiple studies [2, 3, 5]. Investigations have been performed on power systems integrating WPGs consisting of DFIGs [2, 3, 5, 6] and fully-rated converter based generators [7]. The studies have modelled power system load using a constant power load model [2, 3, 5, 6] and constant impedance load model [7]. The studies performed in [2, 3, 5, 6, 7] investigated the impact of increasing the power produced by WPGs on power system transient stability. The authors in [2, 3, 5, 6, 7] found that keeping the SGs power production constant, while increasing the WPGs penetration level, reduced power system stability. Furthermore, in [3, 7], the authors found that when the SG's power production was reduced while the WPGs penetration level increased, power system stability improved. Reducing the SG's power production results in less kinetic energy stored in the machine's rotor during system faults. This results in less acceleration of the SGs rotors, causing improved transient stability because the SGs have reduced rotor angular deviations during system faults. A limitation of the studies performed in [2, 3, 5, 6, 7] is that they focus solely on whether power system transient stability improves or reduces due to the integration of WPGs. The studies did not consider the impact of the system net-load on transient stability. The system net-load is a portion of the load that cannot be supplied by WPGs due to their low penetration levels, as a result it is supplied by SGs in the power system.

The objective of this study is to investigate the impact of the variable power produced by WPGs on power system transient stability. The power system transient stability is assessed considering the impact of the system's net-load. The power produced by the WPGs is developed using measured wind speed from three South African sites. The developed power is randomly sampled using Monte-Carlo simulations. Three power system loading conditions, namely, low, moderate, and peak demand are considered in this investigation. During each power system loading condition, the power produced by the WPGs is varied. The results show that when the wind power generation penetration level increases, the system net-load reduces causing increased SG maximum rotor angular deviations. This finding suggests that system operating conditions in which the system net-load is low should be considered when assessing the impact of WPGs on power system transient stability.

The remainder of the paper is organised as follows: Section II discusses the methodology used in the investigation, Section III introduces the power system case study, Section IV discusses the simulation results, and Section V is the conclusion.

II. Research Methodology

A. Power System Load

The active and reactive power components of the power system's load have been modelled as a constant power using the polynomial load model shown in (1) and (2), respectively. The constant power load model is used to model the system load by setting the polynomial load model's active power coefficients p_1 and p_2 to 0, and p_3 to 1, and the reactive power coefficients q_1 and q_2 to 0, and q_3 to 1.

$$P = P_o\,[p_1\,\tilde{V}^2 + p_2\tilde{V} + p_3\,] \tag{1}$$

$$Q = Q_o\,[q_1\,\tilde{V}^2 + q_2\tilde{V} + q_3\,] \tag{2}$$

where the load's reactive and active power is Q_o and P_o, respectively, the load bus voltage dependency is $\tilde{V}$, the load's active power coefficients are p_1, p_2 and p_3, and the load's reactive power coefficients are q_1, q_2 and q_3.

B. Wind Power Generation

The power produced by the WPGs is developed using wind speed. The Enercon E-82 E2, 2.05 MW wind turbine power curve is used to convert the wind speed to power [8]. The wind turbine power curve is modelled using a piecewise mathematical model given in (3). The Weibull cumulative distribution function (CDF) is used to model the relationship between the wind speed and the power produced by the wind turbine, as shown in (4) [9]. The total power produced by a WPG consisting of multiple wind turbines is quantified using (5) [10].

$$P_{WG} = \left\{ \begin{matrix} P(v) & 0 \leq v < v_{co} \\ 0 & v \geq v_{co} \end{matrix} \right\} \tag{3}$$

$$P(v) = P_r\left(1 - e^{-\left(\frac{v}{\beta}\right)^{\delta}}\right) \tag{4}$$

$$P_{WPG} = \sum_1^n P_{WG_n} \tag{5}$$

where P_r is a wind turbine's rated power, v is the site wind speed, the wind turbine's cut-out wind speed is v_{co}, n is the number of wind turbines integrated in a WPG, the WPG's n^{th} wind turbine's power production is P_{WG_n}, and the Weibull CDF's shape and scale parameters are δ and β, respectively.

Equation (6) quantifies the WPGs penetration level based on the ratio between the total power produced by the WPGs against the total system load [11]. The integration of WPGs in a power system results in a portion of the system load being supplied by the power they produce. The system net-load given by (7) is a portion of the load that is supplied solely by SGs in a power system integrating WPGs.

$$Penetration\ Level = \frac{\sum P_{WG}}{\sum P_L} \tag{6}$$

$$System\ Net - Load = \sum P_L - \sum P_{WG} \tag{7}$$

where the power produced by the WPGs is P_{WG}, and the power system load is P_L.

C. Probabilistic Power System Transient Stability

1) Power System Transient Stability Analysis

Digsilent PowerFactory 2020 time-domain analysis is used to perform the power system simulations. Time-domain analysis assesses the transient behaviour of the power system. A Python 3 script is used to automate the simulations via the Digsilent PowerFactory application programming interface. Three-phase faults are applied on the power system's transmission lines as was done in [12]. The line onto which the faults are applied is tripped to isolate the faults using a 100 ms fault clearing time [12]. SG rotor angles are monitored during the assessment to determine whether the generator becomes transiently unstable during the studies [12]. When faults are applied in the power system, they cause an imbalance between the SGs mechanical torques and the power system's electromagnetic torques.

In a single machine infinite bus system, the swing equation shown in (8) defines the relationship between an SG's rotor angular acceleration and the balance between its mechanical torque and the power system's electromagnetic torque. An imbalance in which the SG's mechanical torque is larger than the power system's electromagnetic torque causes the machine's rotor to accelerate. The acceleration of the SG's rotor is caused by kinetic energy stored in its rotor during a system fault. The SG's rotor angular acceleration risks the machine becoming transiently unstable should the power system not have adequate capacity to transfer the kinetic energy stored in the SG's rotor.

$$\frac{d^2\delta}{dt^2} = \frac{\omega}{2H}(P_m - P_e) \tag{8}$$

where the SG's inertia constant is H, the SG's rotor angle is δ, the SG's mechanical torque is P_m, and the power system's electromagnetic torque at the SG's terminals is P_e.

In this study, the dynamic performance of the SGs integrated into the power system is modelled using the GENROU model. The dynamic performance of the SGs excitation systems is modelled using the IEEET1 excitation system model. Furthermore, the SGs governor performance is modelled using the BPA_GG governor system model. Also, three fully-rated converter based WPGs are integrated into the test system. The WPGs dynamic performance is modelled using the IEC 61400-27-1 Type 4B generic WPG model.

2) Wind Power Generation Sample Size

Power system transient stability is investigated in this study using the probabilistic method. Monte-Carlo simulations is used to randomly sample power production data from the modelled power produced by the WPGs. The required sample size is quantified using the law of large numbers given by (9). Based on the law of large numbers, increasing the sample size results in the sample mean stabilising as it approaches the population mean [13].

$$\bar{X} = \lim_{n\to\infty} \sum_{i=1}^{n} \frac{X_i}{n} \tag{9}$$

where the i^{th} sampled value is X_i, the population mean is $\bar{X}$, and the sample size is n.

III. Power System Case Study

Fig. 1 shows the IEEE 9-bus test system that is used as a case study. Three WPGs with a capacity of 10.25 MW are integrated into the test system at buses 5, 6 and 8. Each WPG consists of five 2.05 MW fully-rated converter based wind turbines. Each WPG is integrated into the test system using a 40 km, single circuit, 132kV Wolf line templated at 50^0 Celsius, and a 132/230kV step-up transformer.

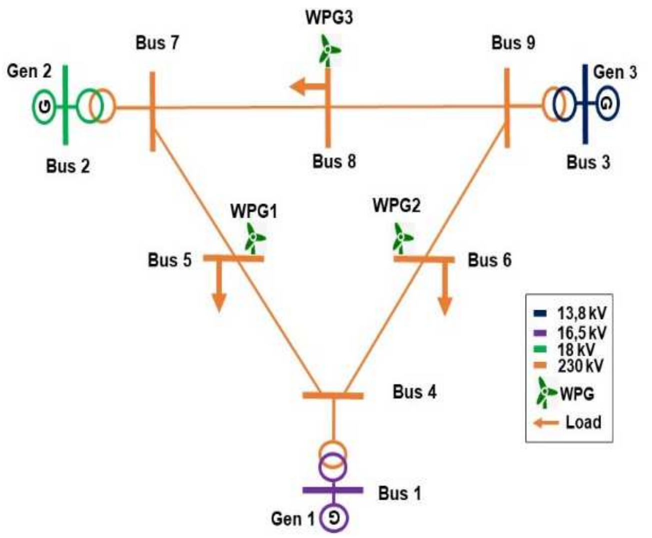

Fig. 1. IEEE 9-bus test system.

The power produced by each of the three WPGs is developed using wind speed measured from three wind speed measurement sites in South Africa. Cup anemometers with a 1% wind speed measurement uncertainty have been used to measure the wind speed at the height of 10 m. The measured wind speed is converted to a wind turbine hub-height of 100 m using the power exponent formula shown in (10).

$$v_2 = v_1 \left(\frac{\mathrm{h}_2}{\mathrm{h}_1}\right)^{\alpha} \tag{10}$$

where v_1 and v_2 are the wind speed at the height h_1 and h_2, respectively, and the site wind speed shear exponent is α.

The shape of the Enercon E-82 E2, 2.05 MW wind turbine power curve modelled using a Weibull CDF with a shape and scale parameter of 4.081 and 9.097, respectively, is shown in Fig. 2. The Weibull CDF selected for modelling the wind turbine power curve is a relevant model as it can be seen that it closely fits the turbine power curve. The Weibull distribution function can be used as a life model to predict the time to failure of equipment. However, in this study, the Weibull distribution function is used to convert the wind speed to power.

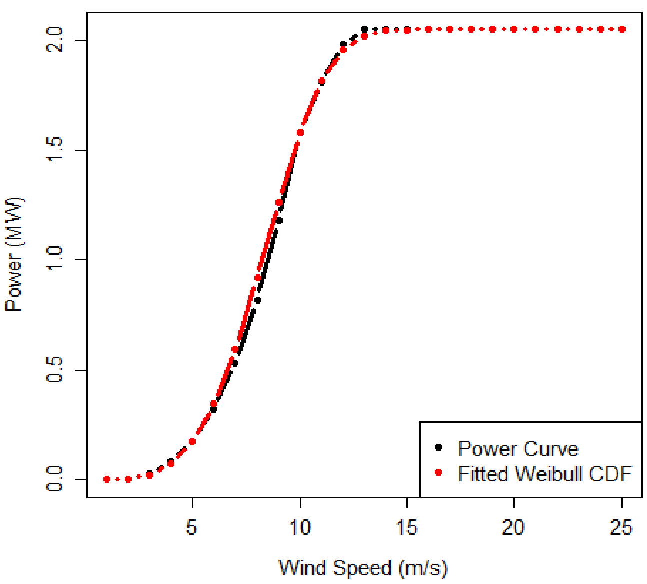

Fig. 2. Power curve.

For each of the three WPGs, Monte-Carlo simulation is used to randomly sample the power developed using the Weibull CDF. The sample moving mean for 5000 samples of the modelled power produced by each of the three WPGs is shown in Fig. 3. Approximately 4180 samples are required for the sample mean of the power produced by the three WPGs to stabilise. In the investigation performed, the required sample size is rounded up to 5000 samples.

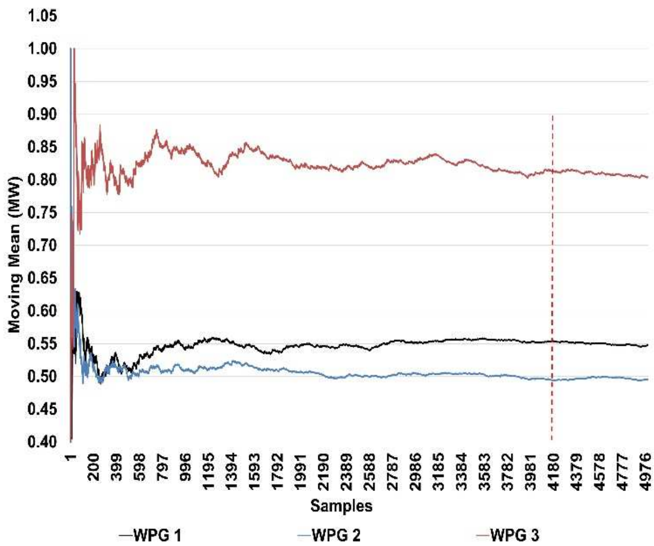

Fig. 3. Normalised moving mean of the WPGs power production.

The impact of the variable power produced by WPGs on power system transient stability is assessed using low, moderate and peak loading conditions representing 20%, 60% and 100%, respectively of peak system load. Table I shows the test system's low, moderate and peak loading quantities. During each of the loading conditions, 5000 samples of power produced by the three WPGs is used to vary the test system's operating conditions. Three-phase faults are applied sequentially on lines 6-9 and 8-9, close to bus 9. A 100 ms fault clearing time is used to isolate the applied faults by tripping the line on which they were applied to. The IEEE 9-bus test system's Gen 3 rotor angle is monitored during the assessment. When the faults are applied close to bus 9, Gen 3's rotor accelerates because the power produced by the machine is stored as kinetic energy in its rotor. The SG's rotor stores the power produced as kinetic energy because it cannot be transferred by the power system to the load due to reduced voltage levels at its terminals during the period the faults are applied.

TABLE I. TEST SYSTEM LOADING.

Loading	Bus 5 (MW)	Bus 6 (MW)	Bus 8 (MW)
Low	25	18	20
Moderate	75	54	60
Peak	125	90	100

IV. SIMULATION RESULTS

A. *Wind Power Generation Penetration Level Impact on Transient Stability*

Fig. 4 and Fig. 5 show scatter plots of the WPGs penetration level versus Gen 3's maximum rotor angle deviations when three-phase faults are applied on lines 6-9 and 8-9 on the IEEE 9-bus test system, respectively. During low, moderate, and peak system loading conditions, the penetration level of WPGs ranges from 0.0% to 48.6%, 0% to 16.2%, and 0% to 9.7%, respectively. When faults are applied on line 6-9 during system low, moderate and peak loading conditions, as the penetration level of WPGs increases, Gen 3's maximum rotor angle deviations range from 86.52^0 to 95.77^0, 41.61^0 to 50.95^0, and 2.82^0 to 9.91^0, respectively. Also, when faults are applied on line 8-9 during system low, moderate and peak loading conditions, as the penetration level of WPGs increases, Gen 3's maximum rotor angle deviations range from 82.61^0 to 90.60^0, 44.27^0 to 51.90^0, and 16.75^0 to 21.30^0, respectively. These results show that the relationship between the penetration level of WPGs and Gen 3's maximum rotor angle deviations is directly proportional. Therefore, an increase in the penetration level of WPGs results in an increase in Gen 3's maximum rotor angle deviations, which causes a reduction in system transient stability. These findings indicate that when assessing power system transient stability with WPGs integrated, system operating conditions in which the WPGs penetration level is high should be considered.

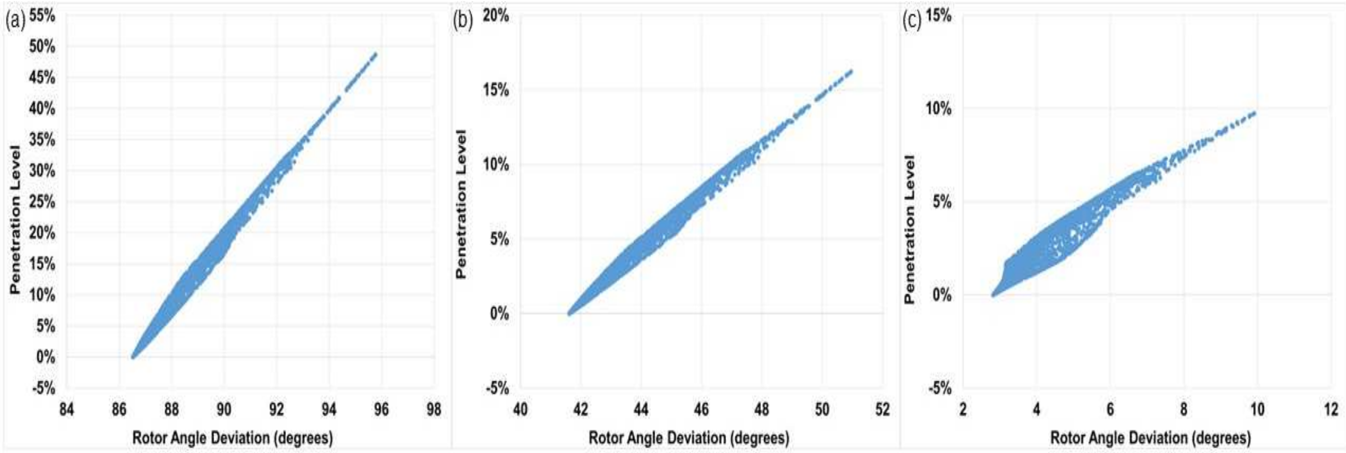

Fig. 4. Scatter plots of WPGs penetration level versus Gen 3's maximum rotor angle deviations when system faults applied on line 6-9 during: (a) low system loading, (b) moderate system loading, (c) peak system loading.

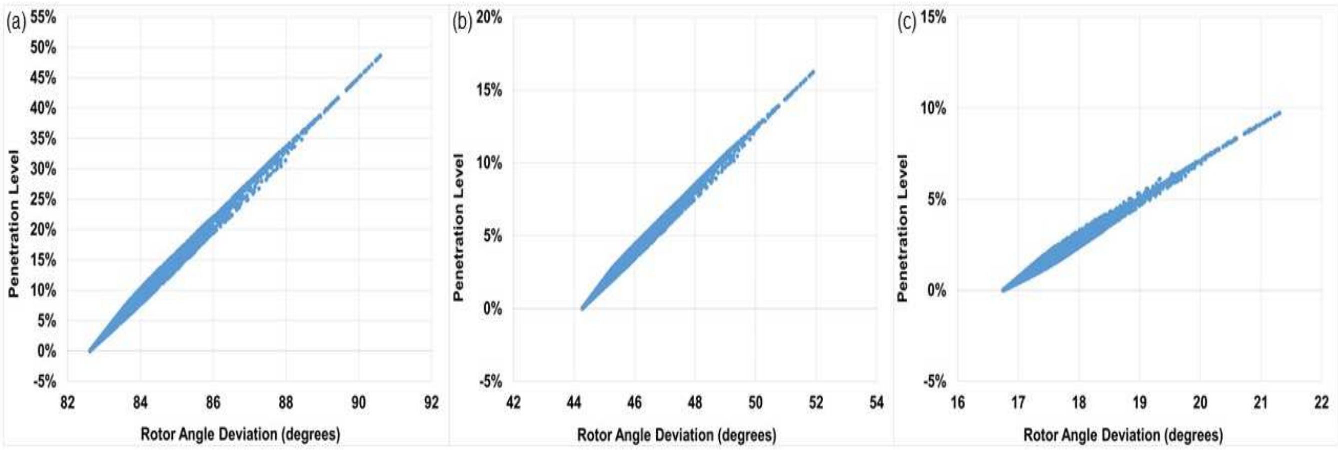

Fig. 5. Scatter plots of WPGs penetration level versus Gen 3's maximum rotor angle deviations when system faults applied on line 8-9 during: (a) low system loading, (b) moderate system loading, (c) peak system loading.

B. System Net-load Impact on Transient Stability

Fig. 6 and Fig. 7 show the scatter plots of the system net-load versus Gen 3's maximum rotor angle deviations when faults are applied on lines 6-9 and 8-9 on the IEEE 9-bus test system, respectively. During low, moderate, and peak system loading conditions, as the penetration level of WPGs increases (see Fig. 4 and Fig. 5), the system net-load reduces from 63MW to 32MW, 189MW to 158MW, and 315MW to 284MW, respectively. When faults are applied on line 6-9 during system low, moderate and peak loading conditions, as the system net-load reduces, Gen 3's maximum rotor angle deviations increase from 86.52^0 to 95.77^0, 41.61^0 to 50.95^0, and 2.82^0 to 9.91^0, respectively. Also, when faults are applied on line 8-9 during system low, moderate and peak loading conditions, as the system net-load reduces, Gen 3's maximum rotor angle deviations increase from 82.61^0 to 90.60^0, 44.27^0 to 51.90^0, and 16.75^0 to 21.30^0, respectively. These results show that the relationship between the system net-load and Gen 3's maximum rotor angle deviations is inversely proportional. This indicates that the power system's transient stability is reduced when the system net-load is low. Therefore, when assessing the transient stability of power systems integrating WPGs, operating conditions in which the system net-load is low should be considered.

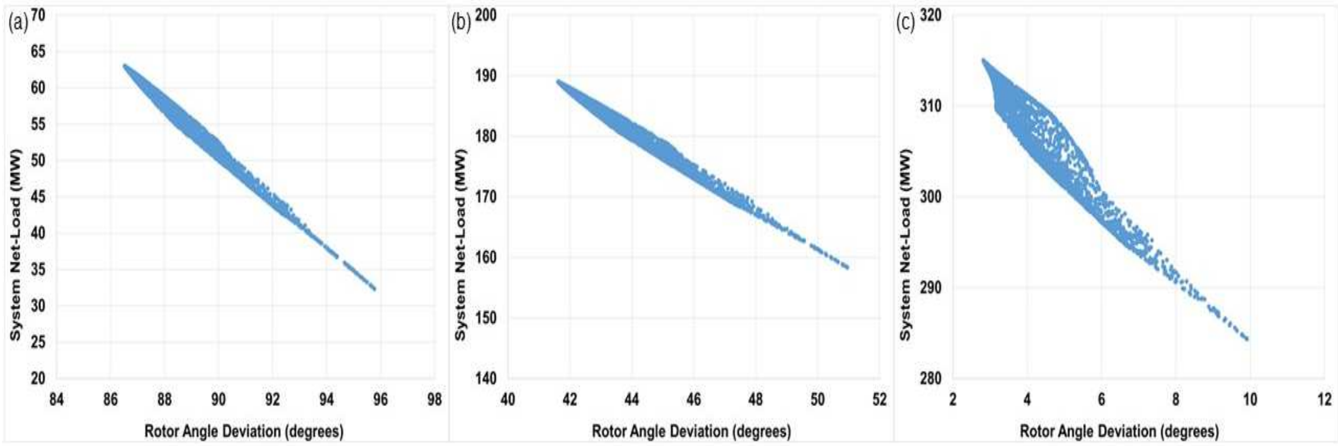

Fig. 6. Scatter plots of system net-load versus Gen 3's maximum rotor angle deviations when faults applied on line 6-9 during: (a) low system loading, (b) moderate system loading, (c) peak system loading.

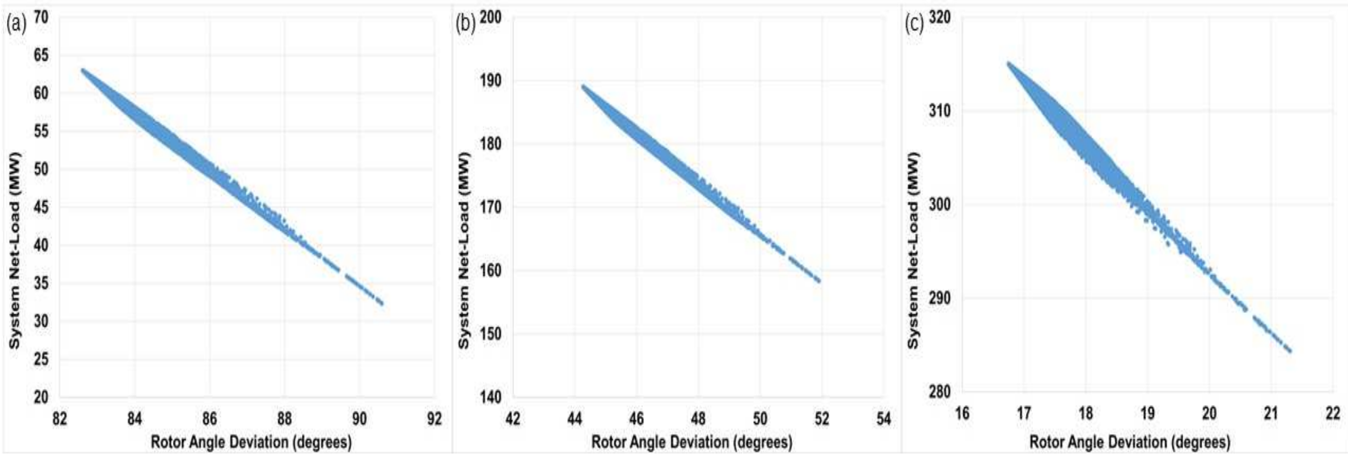

Fig. 7. Scatter plots of system net-load versus Gen 3's maximum rotor angle deviations when faults applied on line 8-9 during: (a) low system loading, (b) moderate system loading, (c) peak system loading.

V. Conclusion

The transient stability of a power system considering the variable power produced by WPGs and the system net-load was investigated in this study. Power system low, moderate and peak loading conditions were investigated. During each of the three system loading conditions, increasing the power produced by the WPGs increases their penetration level, resulting in a reduction in the system net-load. The investigation performed found that in a power system integrating WPGs, when the system net-load reduced due to their increased penetration level, the power system's transient stability also reduced. The implication of the study findings is that operating conditions in which the system net-load is low should be considered when assessing the transient stability of power systems integrating WPGs as they result in the system operating closer to transient instability than when the system net-load is higher.

Acknowledgment

The authors thank the South African Weather Service for giving access to the wind speed measurement data used to model the power produced by wind power generators in this study. Also, the authors thank the National Research Foundation (NRF) for providing financial assistance.

References

[1] J. Lee and F. Zhao, "Global wind report 2022," Global Wind Energy Council, 2022.

[2] B. Wang, L. Zhu and D. Chen, "Mechanism research on the influence of large scale wind power integration on power system angle stability," *Energy Procedia,* vol. 145, no. 1, pp. 295-300, 2018.

[3] C. Lackner, F. Wilches-Bernal and J. H. Chow, "Effects of wind generation integration on power system transient stability," in *IEEE Power & Energy Society General Meeting (PESGM)*, Portland, United States of America, 2018.

[4] S. Ncwane and K. A. Folly, "A review of the impact of integrating wind generation on transient stability," in *2020 International SAUPEC/RobMech/PRASA Conference*, Cape Town, South Africa, 2020.

[5] Z. Yue, Y. Liu, Y. Yu and J. Zhao, "Probabilistic transient stability assessment of power system considering wind power uncertainties and correlations," *Electrical Power and Energy Systems,* vol. 117, no. 2020, pp. 1-11, 2020.

[6] G. M. Tina, M. Giovanni and L. Sebastiano, "Evaluation of technical solutions to improve transient stability in power systems with wind power generation," *Energies,* vol. 15, no. 19, p. 7055, 2022.

[7] R. I. Hamilton, N. P. Panagiotis and B. Keith, "An investigation into spatial and temporal aspects of transient stability in power systems with increasing renewable generation," *International Journal of Electrical Power & Energy Systems,* vol. 115 , no. 2020, p. 105486, 2020.

[8] Enercon, "Enercon product overview," 2015. [Online]. Available: https://wind-

turbine.com/download/101655/enercon_produkt_en_06_2015.pdf. [Accessed 09 March 2020].

[9] N. Bokde, A. Feijóo and D. Villanueva, "Wind turbine power curves based on the Weibull cumulative distribution function," *Applied Sciences,* vol. 8, no. 1757, pp. 1-18, 2018.

[10] O. Sadeghian, A. Oshnoei, M. Kheradmandi, R. Khezri and B. Mohammadi-Ivatloo, "A robust data clustering method for probabilistic load flow in wind integrated radial distribution networks," *International Journal of Electrical Power & Energy Systems,* vol. 115, no. 2020, p. 105392, 2020.

[11] B. Qi, K. N. Hasan and J. V. Milanovic, "Identification of critical parameters affecting voltage and angular stability considering load-renewable generation correlations," *IEEE Transactions on Power Systems,* vol. 34, no. 4, pp. 2859 - 2869, 2019.

[12] S. Ncwane and K. A. Folly, "Impact of load variability modelling on probabilistic power system transient stability," *International Journal of Electrical and Electronic Engineering & Telecommunications ,* vol. 11, no. 5, pp. 344-350, 2022.

[13] H. Silva-Saravia and H. Pulgar-Painemal, "Effect of wind farm spatial correlation on oscillation damping in the WECC system," in *2019 North American Power Symposium (NAPS)*, Wichita, United States of America, 2019.

2023 SAUPEC Conference, Johannesburg, South Africa, January 24-26, 2023

Modeling and Analysis of Multiple Capacitor Coupled Substations at Different Proximities

Sinqobile Wiseman Nene
Department of Electrical Engineering
Tshwane University of Technology
eMalahleni, South Africa
wnene@hailienene.com

Bolanle Tolulope Abe
Department of Electrical Engineering
Tshwane University of Technology
eMalahleni, South Africa
AbeBT@tut.ac.za

Agha Francis Nnachi
Department of Electrical Engineering
Tshwane University of Technology
eMalahleni, South Africa
NnachiAF@tut.ac.za

Abstract—**Electricity plays a critical role in the economy of any country. Access to electricity has become a necessity rather than a luxury over the years. With the modernization and expansion of big cities, the focus for electrification has shifted towards highly concentrated communities. Constructing conventional power distribution networks in sparsely populated rural areas is said to be uneconomical. This gives rise to the need for alternative technologies to supply electricity to these areas, mainly the rural areas. One of the technologies that exists within the un-conventional rural electrification technologies is the Capacitor Coupled Substation (CCS). This technology makes use of the high voltage power transmission lines that normally pass through these communities from town to town. A CCS operates by tapping electrical power from the high voltage lines through the use of capacitors as its key components. As capacitors are known to cause interference on an electrical system, the implementation of a CCS needs to ensure that there is limited interference on the network. This paper modelled and analyzed multiple-CCS focusing on the impact caused by the proximity of each CCS to the nearest one. A three CCS system model was developed through MATLAB/Simulink to simulate the impact on the system when one or more CCS is switched ON or OFF. The results showed that in all the scenarios created, there was minimal disturbance on the supply side and the downstream system except for the reactive power fluctuations on the downstream power network when the CCS were switched. Further analysis was also recommended to understand the impact of each critical component within a CCS.**

Keywords — Capacitor Coupled Substation, Conventional Rural Electrification Technologies, Un-conventional Rural Electrification, System Modeling.

I. INTRODUCTION

Conventional Rural Electrification (CRE) in sparsely populated areas such as rural areas have been considered to be uneconomical due to the perceived low load demand [1]. Un-Conventional Rural Electrification (URE) technologies are thus being explored in order to implement a cost-effective system to supply electrical power to the rural areas [2]. Capacitor Coupled Substation (CCS) is one of the URE technologies that is continuously being explored for rural electrification [3]. CCS is defined as a technology whereby coupling capacitors are used to tap electrical power from a High Voltage (HV) line to distribution levels voltages. The core components of a CCS are the capacitors. Tapping electrical power directly from an HV power transmission line through a CCS can cause transient behaviours on the power network and inevitably affect the main components of a CCS [4].

This paper presents the analysis of a system response when three CCSs, connected to the same power transmission line and located at different proximities from each other, are switched ON and OFF.

The results were achieved through MATLAB/Simulink modeling and simulation and analysing the power transmission line behaviour when multiple CCS are connected to it. The paper also analysed the impact on the power transmission line when the modelled CCS are located at different proximities and are switched ON and OFF at different intervals.

II. BACKGROUND

CCS, as a technology whereby coupling capacitors are used to tap power from the high voltage (HV) lines to distribution level voltages, uses a similar concept as to that of a Capacitive Voltage Transformer (CVT) [5]. A CVT can be defined as “a transformer used in a power system to step down extra-high voltage signals to low voltage signals for metering or operating protective relays” [6]. The structure of a CVT is divided into a capacitive divider and an electromagnetic unit whereby the capacitive divider comprises an insulating cylinder and a series capacitor in it while the electromagnetic unit is comprised of a compensation reactor, a step-down transformer, and a damper [7]. Similar to the CVT which steps down higher voltages to lower measurement voltages, a CCS steps down high voltage from the HV power transmission lines to medium voltage using capacitors. Figure 1 below presents an overly simplified CCS.

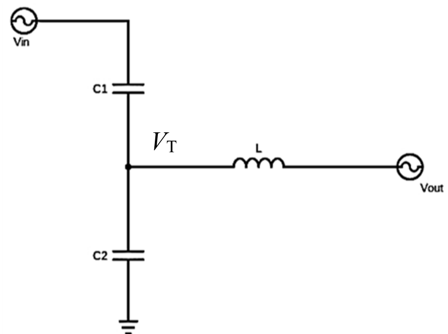

Figure 1: Overly Simplified CCS

Figure 1 above presents a simplified CCS which has a capacitor-divider with capacitors (C_1 and C_2) connected across the incoming voltage (V_{in}) used to supply the desired tap-voltage (V_T) measured from the tapping node between the two capacitors.

The voltage output (V_{out}) is calculated by subtracting the voltage drop across the inductor (L) from V_T. C_1 and C_2 represent capacitor banks rather than individual capacitors where C_1 represents Capacitor Bank 1 and C_2 represents Capacitor Bank 2.

The tap-voltage (V_T) is calculated as follows:

$$V_T = V_{in} \times \frac{C_1}{(C_1 + C_2)} \quad (1)$$

The output voltage is calculated as follows:

$$V_{out} = V_T - V_{L_1} \quad (2)$$

The above formulae, (1) and (2), serve as the basis of the element calculation in a CCS. The objective is to ensure that the V_{out} remains stable as it feeds into a downstream transformer for the power distribution system.

III. Analysis Methodology

Three identical CCS models were developed through MATLAB/Simulink. The CCS were set to be at known equal distances from each other within the same power transmission line. The model was then executed to determine the reference point of the measured parameters. The three CCS were first set at 100km apart, then this distance was increased to 500km, and the system behaviour was analysed. Figure 2 below presents an individual CCS model followed by Figure 3 which presents the multi-CCS model developed.

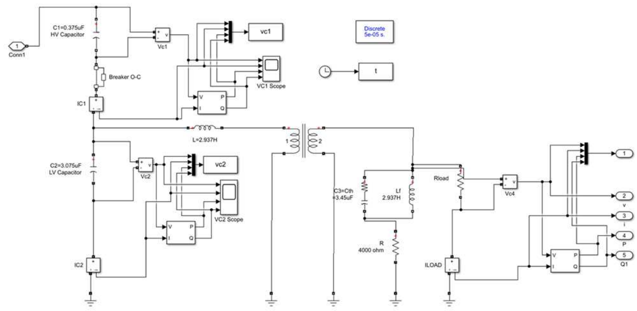

Figure 2: CCS Model (MATLAB/Simulink developed)

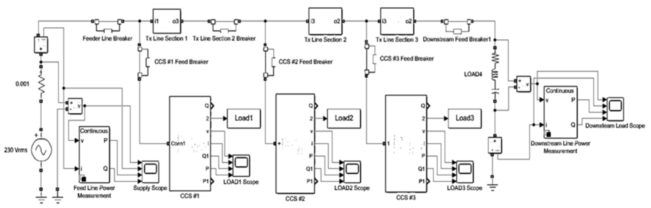

Figure 3: Multi-CCS Model (MATLAB/Simulink developed)

The approach or sequence of the simulation presented in Figure 3 is highlighted below:

A. *Modeling Sequence*

The project followed the following sequence:

1. All breakers were closed (initial state)
2. The main feeder breaker remained closed throughout the simulation.
3. CCS 1 Feed Breaker was set to close at 0.5 seconds
4. CCS 2 Feed Breaker was set to close at 1 second
5. CCS 3 Feed Breaker was set to close at 1.5 seconds

The line distance was first set at 100km between CCS 1 and CCS 2 and between CCS 2 and CCS 3. The line distance between CCS 1 and CCS 2 and between CCS 2 and CCS 3 was then set at 500km and the system analysed accordingly. Furthermore, the system was analysed when any of the CCS is connected and disconnected from the power network.

The main parameters recorded and analysed are the voltage (V), current (A), active power (kW), reactive power (kVAr), the load for all three CCS, and the downstream line and load parameters. The downstream line behaviour analysis is vital as the paper was also intending to establish the overall impact on the network as a whole when a CCS is connected on the line, what happens when it switches ON and OFF, thus identifying the impact that may or may not affect other power consumers connected to the same power network.

IV. Data and Model

The following parameters were used to model and analyse the system behaviour.

A. *Main CCS Parameters*

Table 1 below presents the main parameters that were used during the development of the CCS model.

Table 1: CCS Parameters

Parameter	**Value**
C_1	0.375 µF
C_2	3.075 µF
L	2.937 H
Step-down Transformer	1000 VA, 50 Hz, 230/110 V
Load	Fixed resistive load of 200 Ω

B. *Downstream Laod Parameters*

Table 2 below presents the parameters used for the simulation of the downstream load.

Table 2: Downstream Load Parameters

Parameter	**Value**
Nominal Voltage	230 V_{rms}
Nominal Frequency	50 Hz
Active Power	100 kW
Inductive Reactive Power	100 (+VAR)
Capacitive Reactive Power	100 (-VAR)

C. *Monitored Parameters*

Table 3 below presents the main parameters that were monitored and analysed during the project.

Table 3: Monitored Parameters

Parameter	**Details**
Supply Voltage	Line Voltage
Downstream Parameters	Line Voltage and Current, Load Voltage and Current, Load Active Power and Load Reactive
CCS Parameters	Voltage and Current, Load Active Power and Load Reactive Power.

V. Results and Discussions

The results achieved are presented in this section.

A. *Results*

The simulation was executed with the initial state of all breakers open. The Feed breaker and the line breakers were closed at 0.0167 seconds to power up the network. The individual CCS feed breakers were then closed at 0.5 seconds, 1 second and 1.5 seconds for CCS 1, CCS 2, and CCS 3, respectively. The results are shown below from Figure 4 to Figure 10 when the distance between the CCS was 100km and the simulation run for 2 seconds. Each figure shows the behaviour of the voltage, current, active power, and reactive power within the measured section.

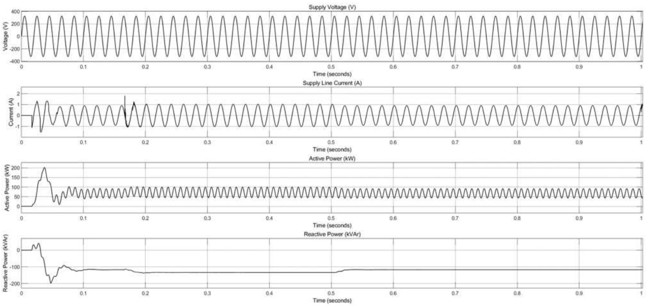

Figure 4: Supply Parameters

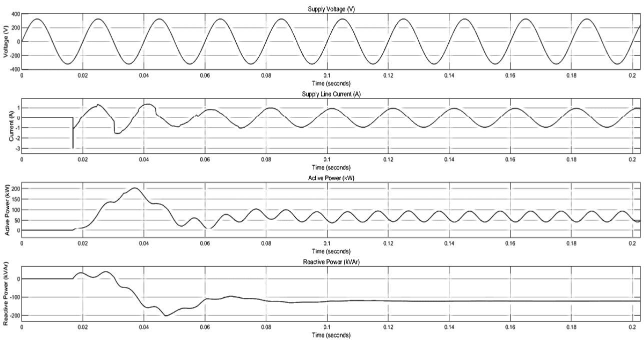

Figure 5: Supply Parameters (expanded view)

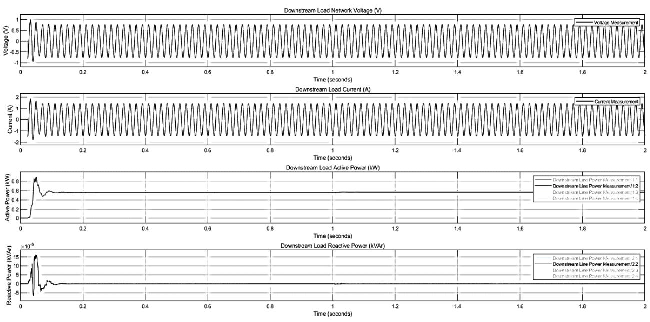

Figure 6: Downstream Load Parameters

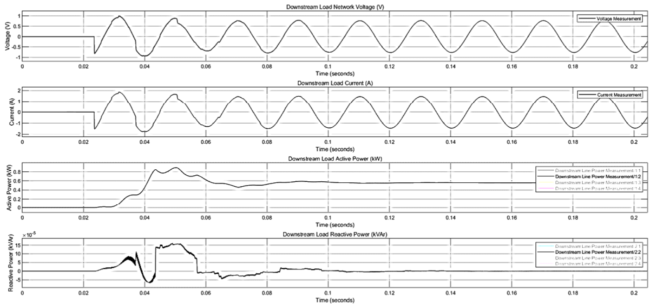

Figure 7: Downstream Load Parameters (expanded view)

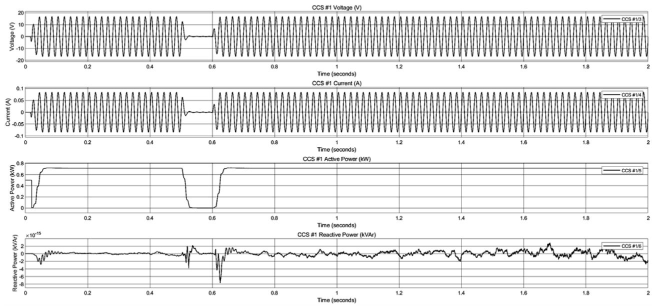

Figure 8: CCS #1 Parameters

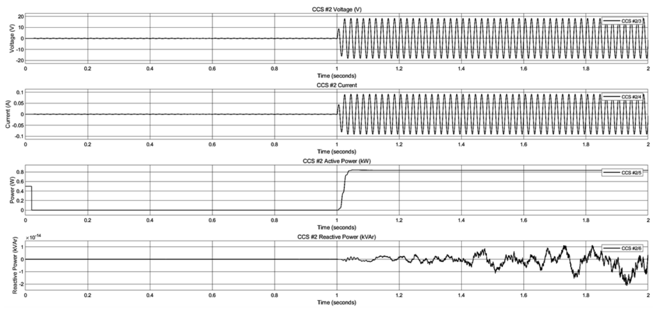

Figure 9: CCS #2 Parameters

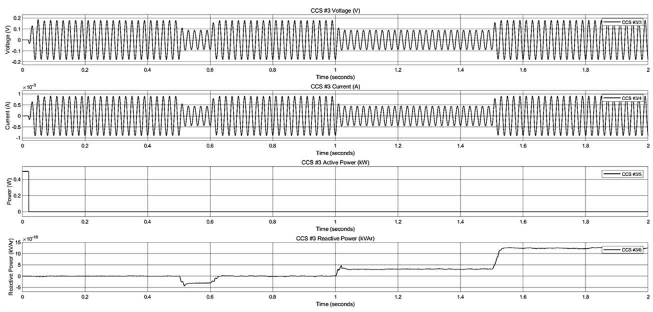

Figure 10: CCS #3 Parameters

The exercise was repeated with a distance set to 500km between the individual CCS and the results are presented on Figure 11 to Figure 17 below:

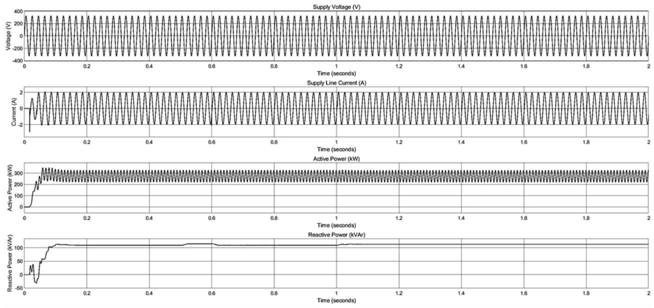

Figure 11: Supply Parameters

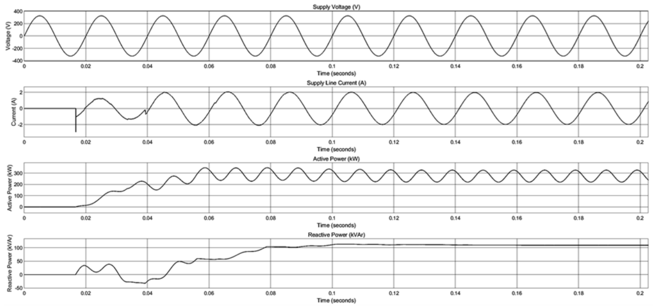

Figure 12: Supply Parameters (expanded view)

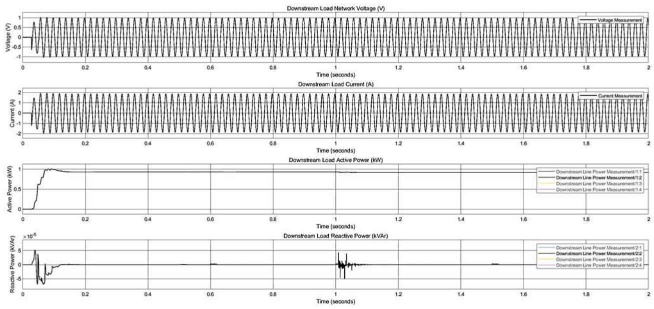

Figure 13: Downstream Load Parameters

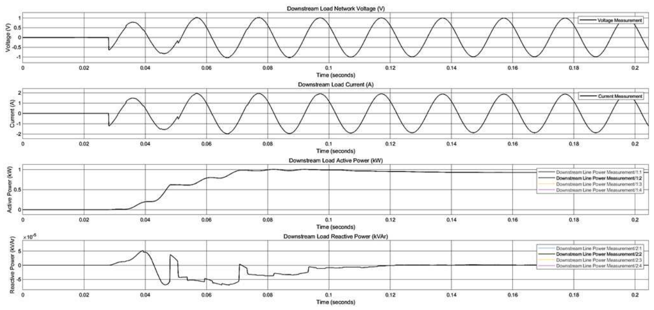

Figure 14: Downstream Load Parameters (expanded)

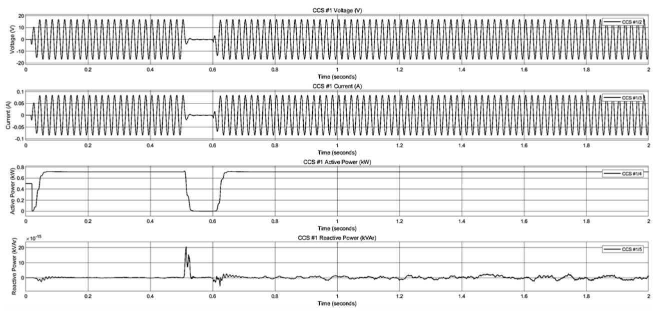

Figure 15: CCS #1 Parameters

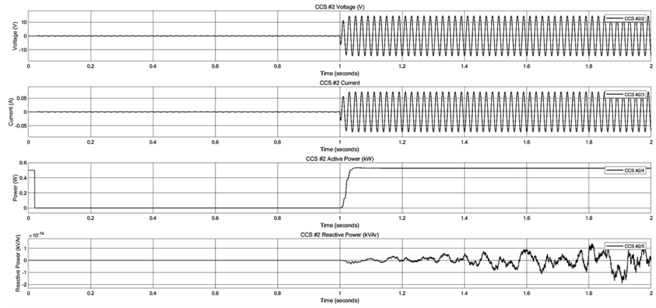

Figure 16: CCS #2 Parameters

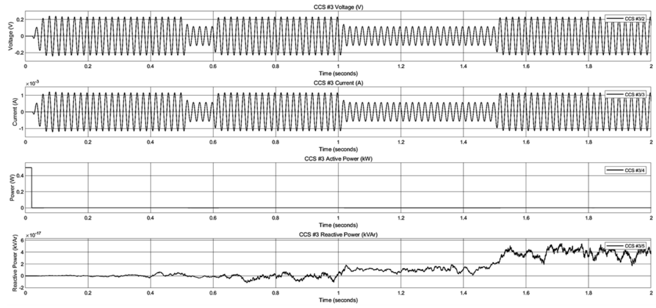

Figure 17: CCS #3 Parameters

Furthermore, the system was simulated with an ON and OFF configuration for CCS 2 closing and opening repeatedly. The results are as follows on Figure 18 to Figure 22:

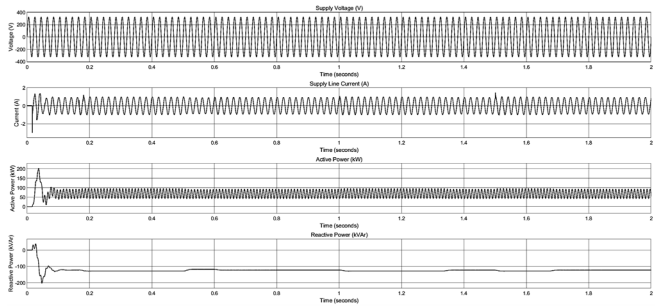

Figure 18: Supply Parameters

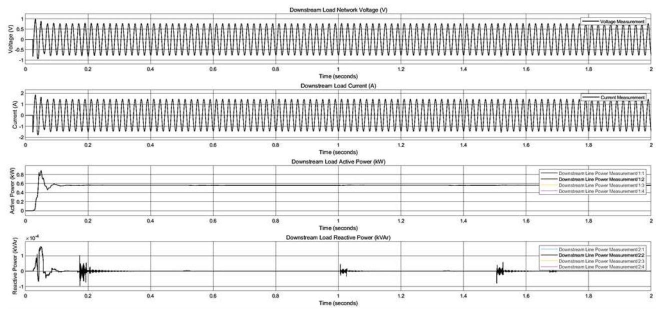

Figure 19: Downstream Load Parameters

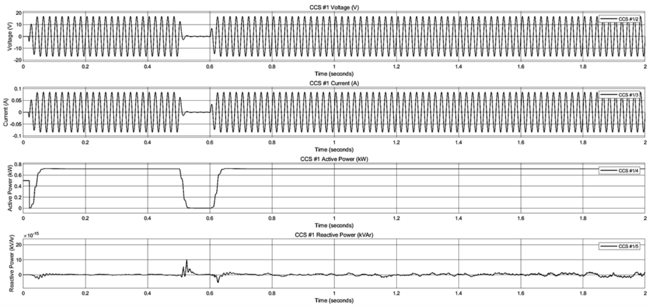

Figure 20: CCS #1 Parameters

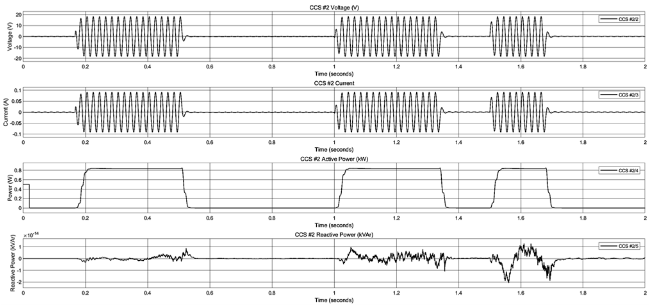

Figure 21: CCS #2 Parameters

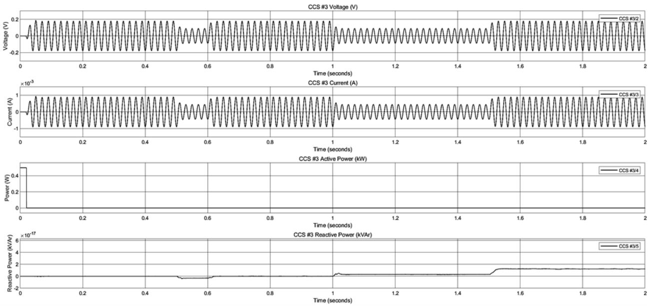

Figure 22: CCS #3 Parameters

The simulation with CCS 2 opening and closing a number of times was repeated but the distance set at 500km. The results are shown on Figure 23 to Figure 27 below:

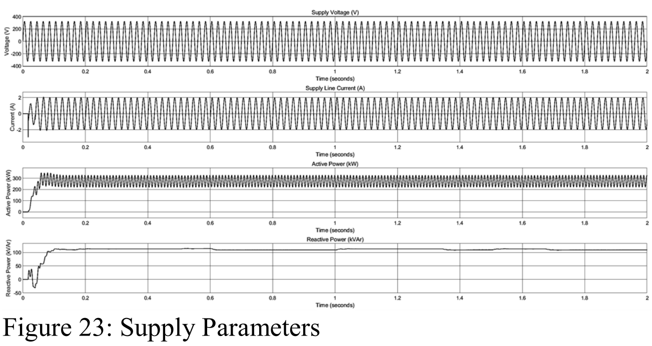

Figure 23: Supply Parameters

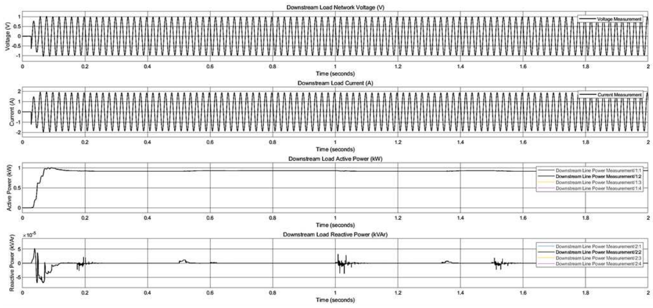

Figure 24: Downstream Load Parameters

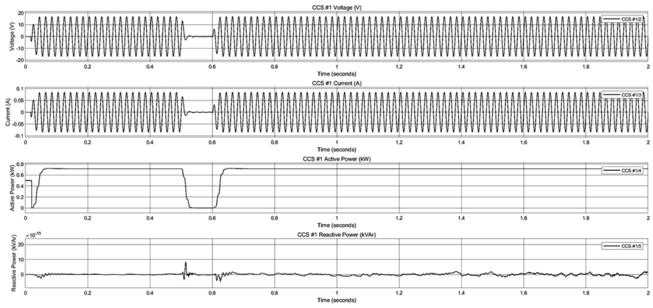

Figure 25: CCS #1 Parameters

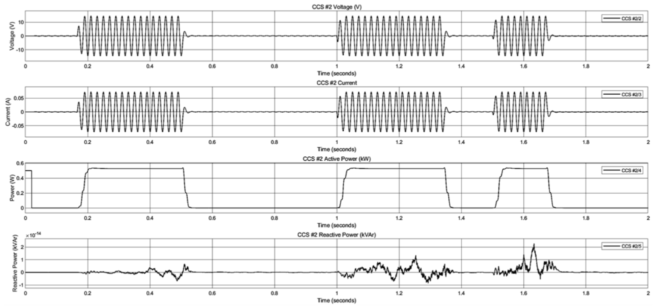

Figure 26: CCS #2 Parameters

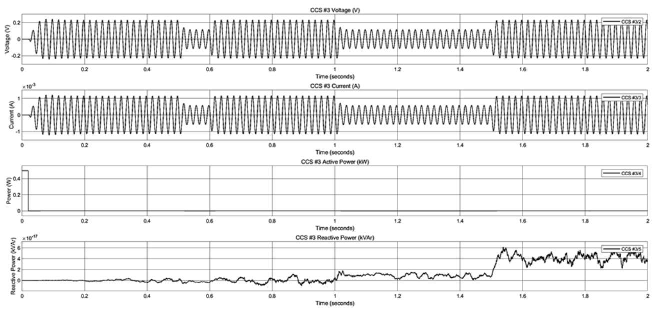

Figure 27: CCS #3 Parameters

B. Discussion

Figures 4 to 10 presents the system when the distance was set at 100km. The notable system response is that the supply voltage was not affected at all during the closing of any of the downstream feeder breakers. The current, active power and reactive power were also only momentarily affected when closing the main supply feed breaker (Tx Line 1 Feed Breaker). The supply system thereafter stabilizes and sees no interference for the remainder of the cycle time when all the downstream system breakers closed.

As seen on the expanded view of the downstream load parameters, in figure 7, the downstream system is also only affected during the initial closing of the Tx Line 1 Feeder Breaker, then stabilizes for the remaining duration of the cycle.

Figure 8 shows that the system affected when closing CCS 1 feeder breaker is CCS 1 itself with the momentary voltage drop resulting in a drop in current and active power and a slight increase in the negative reactive power which only lasts for the duration of the actual state change (switching).

The system appears to respond the same even at longer distances when the distance was set at 500km. The only notable change is the slight delayed system stabilization after the switching and the increased sensitivity of the reactive power which spikes when another section is switched into the system as seen in figure 13.

When CCS 2 feed breaker is switched ON and OFF, the supply side of the power network is still not affected. However, the downstream load system sees some spikes of the reactive power every time any of the feeder breakers upstream either close of open as seen on figure 19 and figure 24.

VI. Conclusion

The analysis conducted on the power transmission line behaviour when multiple CCS are connected to the system showed no notable interference on the supply side of the system and minimal interference on the downstream network from the CCS tap-off node. This, therefore, implies that based on this particular model and analysis, the CCS can be easily adapted into a power transmission network without any notable interference on the overall performance of the power network.

Furthermore, the analysis conducted when the modelled CCS was switched ON and OFF also showed minimal interference on the overall network even at different CCS proximities to each other within the power network.

The author, however, acknowledges that the CCS used on this project did not allow for constant load variations on the CCS system, therefore, it can be concluded that there is no notable interference on the overall network if the CCS connected to it is or are stable.

VII. Recommendations

Recommendations for further studies are as follows:

1. A comprehensive analysis of the CCS based on varying load including switching ON and OFF needs to be conducted in order to identify the limits of the CCS that could be connected to an existing power transmission network without causing notable interferences.

2. An analysis of the downstream system of a CCS should be conducted so as to analyse which has more impact between the varying loads or the switching.

3. A comprehensive analysis of the ferroresonance due to the switching of the CCS and its suppression needs to be conducted.

VIII. References

[1] G. Falchetta, S. Pachauri, E. Byers, O. Danylo and S. C. Parkinson, "Satellite Observations Reveal Inequalities in the Progress and Effectiveness of Recent Electrification in Sub-Saharan Africa," *One Earth,* pp. 364-379, 24 April 2020.

[2] S. Olowosejeje, P. Leahy and A. P. Morrison, " A practical approach for increased electrification, lower emissions and lower energy costs in Africa," *Sustainable Futures,* vol. 2, no. 1, pp. 1-10, 2020.

[3] T. Raphalalani, N. Ijumba and A. Jimon, "Capacitor Divider System for Feeding Distribution Network from an EHV Line," University of Durban Westville, Durban, 2000.

[4] H. Radmanesh, "Ferroresonance Elimination in 275kV Substation," *Electrical and Electronic Engineering,* vol. 2, no. 2, pp. 54-59, 2012.

[5] M. J. Saulo, "Penetration Level of Un-Conventional Rural Electrification Technologies on Power Networks," University of Cape Town, Cape Town, 2014.

[6] V. Mohan, S. Poornima and C. P. Sugumaran, "Mitigation of Ferroresonance in Capacitive Voltage Transformern using Memelements," in *International Conference on HIgh Volatage Engineering and Technology (ICHVET)*, Hyderabad, India, 2019.

[7] B. Chen, L. Du, K. Liu, X. Chen, F. Zhang and F. Yang, "Measurement Error Estimation for Capacitive Voltage Transformer by Insulation Paramters," *Energies,* vol. 10, no. 357, pp. 1-14, 2017.

[8] M. J. Saulo, "Penetration Level of Un-Conventional Rural Electrification Technologies on Power Networks," University of Cape Town, Cape Town, 2014.

2023 SAUPEC Conference, Johannesburg, South Africa, January 24-26, 2023

Distribution network planning practices based on the transition toward active distribution networks

Preshaan Jaglal
Postgraduate School of Engineering Management
Univervisty of Johannesburg
Johannesburg, South Africa
p.jaglal@gmail.com

Annlizé L. Marnewick
Postgraduate School of Engineering Management
Univervisty of Johannesburg
Johannesburg, South Africa
amarnewick@uj.ac.za

Dirk Johan van Vuuren
Engineering Augmented Degree Programme
University of Pretoria
Pretoria, South Africa
dirk.vanvuuren@up.ac.za

***Abstract*— Distribution power system networks in South Africa are transitioning from passive to active which is anticipated to result in several potential impacts concerning traditional practices employed in the planning of the distribution power system network. Through a literature review, several impacts of active distribution networks on traditionally employed passive distribution network planning practices were identified, including practices to manage and support the planning of active distribution power system networks. Risks to the economical and operational planning of the distribution power system network due to the impacts on traditional network planning practices were identified. A research study was therefore required to validate the findings from the literature. The identified impacts and practices were confirmed through a descriptive research study conducted amongst network planners in South Africa. It was determined that the transition to active distribution network planning practices amongst the sample population was to some extent. The risks associated with the employment of passive planning practices to networks transitioning to becoming active are therefore present, however opportunities to readily transition is provided.**

Keywords*— *Distribution network planning, practices, passive network, active network, impacts

I. INTRODUCTION

The culmination of South Africa's climate change endeavours, current electricity generation shortfall and the socio economic conditions of the country, are driving factors of the just energy transition in the electricity sector. This proposed transition is apparent in the country's Integrated Resource Plan (IRP), detailing the favoured energy generation technologies to meet the electricity demand of the country as depicted in Table I. A planned decrease in the share of coal generation and an increase in the share of alternate generation sources, specifically renewable energy generation, is expected by 2030.

TABLE I. INSTALLED GENERATION CAPACITY 2021 – 2030 [1] [2]

Technology	*Total capacity 2021*	*Total capacity 2030*
Coal	74%	43%
Renewables	11%	40%
Gas & diesel	6%	8%
Storage	5%	7%
Nuclear	4%	2%

Renewables, through distributed energy resources (DER), will be integrated on the distribution network of the South African electricity grid. The anticipated increase in renewable energy on the distribution power system network is expected to evolve the distribution network from a traditional passive system into an active system which is depicted in Fig. 1.

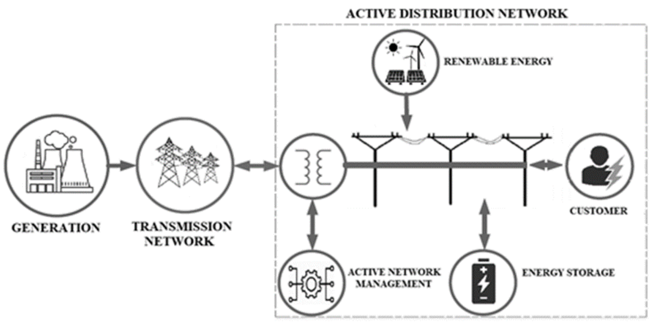

Fig. 1. Active distribution power system network [3]

Active distribution power system networks comprise of typical distribution network infrastructure such as substations, transformers, cabling, metering equipment, and control equipment, with the inclusion of distributed energy resources on both the network and customer connection points resulting in bi-directional power flows [4]. With the anticipated evolution of the distribution power system network, several complexities with respect to the planning of these networks are expected [5]. The changes to the behavior of the network may result in traditional distribution network planning practices employed for passive networks becoming inadequate to perform planning on active networks.

Utilizing unsuitable planning practices for active networks, which may have been suited to passive distribution network systems, has potential economic and operational risks [6][7]. The deficiencies in traditional distribution network planning approaches including the inability to adapt to the changing environment have been of concern for decades [8]. It is therefore mooted that traditional network planning practices employed for passive networks undergo an investigation in reference to active networks [9].

The objectives of this paper was to investigate the potential impacts of active distribution networks on traditional distribution network planning practices in South Africa, and to investigate the practices to support the planning of active distribution networks. The research was performed through a literature review and a descriptive research study across network planning engineers in South Africa.

II. Literature

A. Traditional Passive Distribution Network Planning Practices

Distribution network planning is aimed at conceptually designing the distribution power system to meet demand growth, through timely plans that are the most economical subject to technical and operational constraints [10]. This is performed through several activities with established practices using a structured process. Fig. 2 depicts the conventional distribution network planning process.

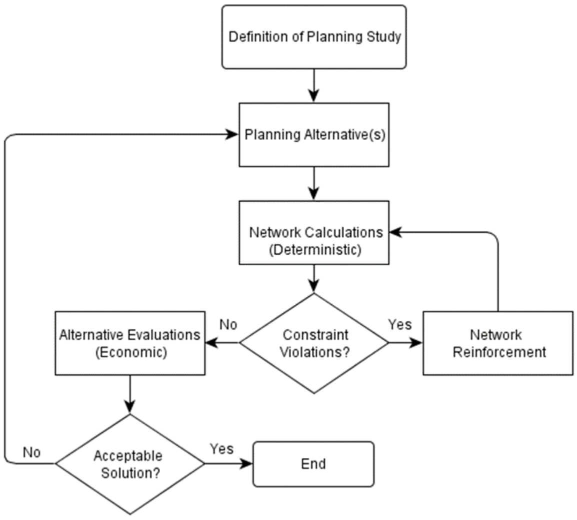

Fig. 2. Conventional distribution network planning process [11]

From the process depicted in Fig. 2, four key stages were identified [12] [13]:

- Definition of the planning study
- Planning alternatives
- Network calculations
- Alternative evaluation

Each of the four key network planning stages consist of various activities under which relevant network planning practices are employed. Network planning activities include data management, load forecasting, alternative development, data modelling and simulation, network assessments and solution selection. Traditionally employed distribution network practices were identified for each of the network planning activities from the literature and are summarized in Table II.

TABLE II. TRADITIONAL DISTRIBUTION NETWORK PLANNING PRACTICES

Stage	***Activity***	***Practice***
Definition of the planning study	Data management	Basic data management [3]
	Load forecasting	Classical forecasting methods and no consideration of active components in forecasts. [11]
Planning alternatives	Alternative development	No consideration of DER optimization and conventional reinforcement solutions. [14]
Network calculations	Data modelling & simulation	Deterministic fit & forget approach with static simulations. [12]
	Network assessments	Conventional network assessments. [6]
Alternative evaluation	Solution selection	Single objective function (minimization of the cost function). [10]

B. Impacts on Traditional Distribution Network Planning Practices

Historically, distribution power system networks were predominantly passive, allowing the simplification of several of the listed practices adopted by distribution network planners in conducting the activities during the conventional network planning process. This was due to the behaviour of the network being majorly influenced by passive components [12].

Distribution power system networks in South Africa are undergoing an evolution from being passive to active, as penetration levels of distributed energy resources and responsive customer loads are becoming increasingly significant. This increases the complexity of the behaviour of the distribution power system network, and therefore the traditional network planning practices previously adopted by distribution network planners [12]. These complexities are a result of the capabilities of distributed energy resources, their introduced randomness and uncertainties, including the involvement of customers in active demand [10].

In reviewing the potential impacts of active distribution networks on traditionally employed distribution network planning practices, several impacts were identified and are summarized in Table III.

TABLE III. IMPACTS ON TRADITIONAL DISTRIBUTION NETWORK PLANNING PRACTICES DUE TO ACTIVE NETWORKS

Activity	***Practice***	***Impacts***
Data management	Basic data management	Significant increase in data and data management requirements. [15]
Load forecasting	Classical forecasting methods and no consideration of active components in forecasts.	Load forecasting accuracy and load shape/ demand levels. [16]
Alternative development	No consideration of DER optimization and conventional reinforcement solutions.	Sub-optimal (i.e., overinvestment) network alternative development. [14]
Data modelling & simulation	Deterministic fit & forget approach with static simulations.	Premature network sterilization & increased planning scenarios. [17] [18]
Network assessments	Conventional network assessments.	Network stability, power quality and safety impacts. [19]
Solution selection	Single objective function.	Multi-objective and complex objective function. [20]

Risks to the economical (i.e., overinvestment) and operational planning (i.e., network stability, power quality) of the distribution power system due to the above listed impacts on traditional distribution network planning practices are evident.

C. Practices to Support the Planning of Active Distribution Networks

It is apparent from the literature that the impacts of active distribution networks on traditional network planning practices are significant enough to consider a transition in the practices employed. This is to ensure the adequate and sustainable planning of the future distribution power system network [21].

In investigating practices to support the planning of active distribution networks, the following summarized practices listed in Table IV were identified.

TABLE IV. ACTIVE DISTRIBUTION NETWORK PLANNING PRACTICES

Stage	***Activity***	***Practice***
Definition of the planning study	Data management	Big data management and data analytics. [15][22]
	Load forecasting	Modern statistical forecasting techniques including the consideration of distributed energy resource and demand side management impacts. [23][16]
Planning alternatives	Alternative development	Optimal distributed energy resource and network flexibility planning. [24][25]
	Active network management	Incorporation of non-network alternatives with information and communication technology needs. [13][14]
Network calculations	Data modelling & simulation	Probabilistic, temporal and co-modelling and simulation. [25] [26]
	Network assessments	System stability, voltage unbalance and reverse power flow assessments. [7]
Alternative evaluation	Solution selection	Automated multi-objective optimization function. [13][20]

It is notable the addition of an active network management activity under the planning alternatives stage is gaining prominence. This refers to the coordination of distributed energy resources as non-network alternatives to provide potential technical and economic benefits for various network issues such as voltage regulation, reliability and power losses [27]. In line with the identified active distribution network planning practices from the literature, Fig. 3 depicts a proposed active distribution network planning process [12].

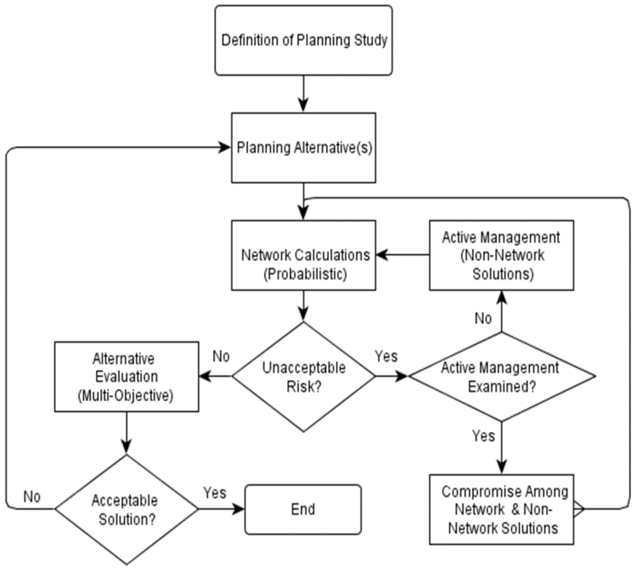

Fig. 3. Active distribution network planning process [12]

The active distribution network planning process consists of key transitions to the conventional distribution network planning process activities and traditional practices employed. There was therefore a need to validate the findings from the literature and to determine the status quo of the transition to active distribution network planning practices in South Africa.

III. RESEARCH METHODOLOGY

Literature has indicated that there are several potential impacts on traditionally employed distribution network planning practices due to active distribution networks, including several employable active distribution network planning practices to manage and support the planning of active networks. A research study was performed amongst distribution network planning engineers in a case organization in South Africa who are responsible for the planning of the distribution power system network.

A quantitative descriptive research design approach was undertaken for the study due to its applicability concerning the research objective. The selected data collection method was a structured self-administered questionnaire which was disseminated amongst network planning engineers in the selected case organization in South Africa.

The selected sampling technique for the sample population was judgement sampling. The judgement sampling approach would allow information to be gathered from well-versed, honest, and knowledgeable cases. The selection of participants in the study was not performed to influence the outcomes (i.e., biased responses), but to rather ensure that experienced and trustworthy responses were received to allow the research objectives to be adequately addressed. This technique is generally utilized for small population samples, which makes probabilistic sampling techniques infeasible [28].

The design of the self-administered questionnaire consisted of structure and unambiguous close-ended questions based on the outcomes of the literature review. This was considered good questionnaire design practice to reduce respondent administration, thereby increasing response accuracy and validity [29]. The questionnaire framework consisted of six categories:

- A – Demographics: To determine the role and experience of participants.
- B – Awareness of active distribution networks: To determine participant awareness levels of the research scope.
- C – Network type: To determine the type of distribution networks being planned by participants (i.e., passive, or active).
- D – Network planning process: To determine the planning stages employed in alignment to the conventional and active distribution network planning processes.
- E – Impacts on distribution planning practices: To validate the findings from literature concerning the impacts on planning practices due to active networks across the various network planning activities.
- F – Employed active distribution planning practices: To validate the findings from literature concerning active network planning practices, and to determine the status quo in South Africa concerning the employment extent of such practices.

IV. Research Findings

The responses from the questionnaire were gathered, processed, and then analysed to derive valuable findings concerning the research objectives.

A. Demographics

Twenty-one responses out of the targeted sampling population of 27 were received indicating a 78% response rate. The demographics of the population sample consisted of network planning engineers, network planning senior engineers and network planning managers, whom form part of distribution network planning departments across the nine provinces in South Africa within the case organization. The diversified roles offer various perspectives with respect to the research categories, as each have varying degrees of responsibility and therefore perception. The majority of participants had more than 10 years of experience in each of their roles, adding to the integrity of the received responses.

B. Awareness of Active Distribution Networks

The majority (53%) of participants to the questionnaire were moderately to extremely aware of active distribution networks. This indicates that the scope of the research is well understood by most of the participants. It was also determined that participants with more than 10 years of experience were the leading category in being moderately to extremely aware. This indicates a potential knowledge gap between experienced and experienced network planners on active distribution networks.

C. Network Type

The network type being managed by network planners in the case organization is currently passive overall, with the majority (64%) of participants indicating null to a small extent of the presence of active control, active management, and demand side management. Distributed energy resource presence is however indicated to be small to some extent. This implies that distribution network planning is still in the fostering stages of active distribution networks, and therefore distribution network planning practices employed may still be mainly geared towards the planning of passive networks.

D. Network Planning Process

The planning process being followed by 81% of participants is a conventional distribution network planning process. The remaining 19% of participants incorporate active network management into their planning process, which is considered to be part of the active distribution network planning process. This indicates that a small portion of network planners in the case organization have transitioned to active network planning.

E. Impacts on Distribution Network Planning Practices

The results from the questionnaire concerning the impacts to the various distribution network planning practices employed under each of the planning activities are summarized in Fig. 4 based on the calculation of the median of the responses through the defined Likert scale. The median is the recommended statistical representation of central tendency for Likert scales [31].

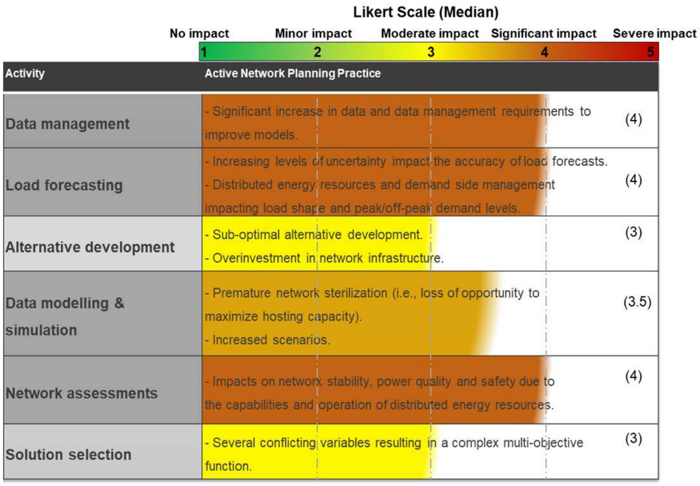

Fig. 4. Impact level per planning activity

It is evident from Fig. 4 that the impact level of active distribution networks on all distribution network planning practices is moderate to significant. This confirms the literature, in which impacts on data management, load forecasting, alternative development, data modelling and simulation, network assessments and solution selection practices were noted.

F. Employed Active Distribution Planning Practices

The outcomes from the data analysis on the results from the questionnaire concerning the employment of active distribution network planning practices are summarized in Fig. 5. Similarly, the results are represented based on the calculation of the median of the responses through the defined Likert scale.

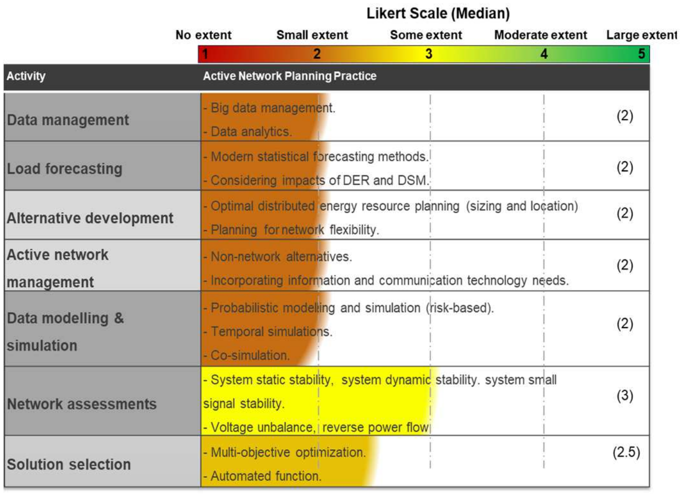

Fig. 5. Employment extent of active distribution network planning practices

The results in Fig. 5 confirm the existence of active distribution network planning practices as identified in literature under the active network planning process. The results also demonstrate that the transition towards active distribution network planning practices amongst the participants across all of the planning activities is small to some extent. This indicates that the transition from passive to active distribution network planning practices in the selected case organization has some way to go, even though the networks being managed are currently still passive.

V. Discussion

Impacts on traditional network planning practices due to active distribution networks were identified by the literature and confirmed by the performed data analysis on the results of quantitative descriptive research study on a case organization in South Africa. The results indicated moderate to significant impacts across all traditional network planning practices. Similarly, several active distribution network planning practices were identified in the literature and confirmed by the quantitative descriptive research study. The results however indicate that distribution network planners in the case organization employ these practices at a small to some extent. This could be attributed to the results of the data analysis indicating that the networks being managed by the distribution network planners in the case organization are still passive. The risks, as revealed by the literature, of employing traditional passive network planning practices to networks transitioning from passive to active are however still present.

VI. Recommendations

It is evident from the literature and data analysis on the results of the descriptive research study that traditionally employed distribution network planning practices would require an adaptation to active distribution network planning practices to mitigate the identified impacts and avoid the potential risks associated with them. Although the results from the research study indicate that the level of extent of employed active distribution network planning practices amongst planners in the case organization is currently small to some extent, there are however opportunities that can be explored to maximize the benefit from some of the practices.

A. *Big Data Management & Data Analytics*

Substantial development and maturity levels of the incorporation and employment of big data management and data analytics in the electric utility space currently exists and can therefore be leveraged [15]. The employment of big data management and data analytics may also improve the employment levels of active distribution network planning practices, such as temporal and probabilistic simulation practices, including the employment of modern forecasting techniques, which are all data-intensive activities. Further potential benefits of the employment of big data management and data analytics could result in better network reliability, customer satisfaction and improved process efficiencies in distribution network planning.

B. *Optimal Distributed Energy Resource Planning*

The optimal planning of distributed energy resources requires a shift from passive to pro-active DER forecasting, modelling, and simulation. The requirements for this approach would be increased manpower or computing power to perform such a function. The benefits that could be attained are however significant. Benefits of the employment of optimal distributed energy resource planning include hosting capacity maximization, increased network health and network security.

C. *Non-network Alternatives*

The results from the data analysis indicate that network planners are aware of the capabilities offered by distributed energy resources. These capabilities include active and re-active power control [32]. The only requirement would therefore be to incorporate non-network alternatives as part of the network planning process. The benefits of non-network alternatives consist of voltage and reactive power support, including network capacity relief, with the potential of significant infrastructure deferment cost savings.

VII. Research Limitation & Future Research

The selected research design approach and the employed research method are not without respective limitations. Limitations include the risk of dishonest responses in utilizing a self-administered online questionnaire [33]. The sample population was also selected from a single case organization, however, there exists several organizations in South Africa with potential network planning departments and practitioners offering different perspectives.

It is recommended that future research consider increasing the research scope and include interviews as a data collection tool to understand why the employment extent of active distribution network planning practices is small to some extent. Understanding the reasons behind the employment extent level of active distribution network planning practices may assist the researcher in investigating and further supporting the transition of practices from passive to active for distribution network planners.

References

[1] J. R. Calitz and J. G. Wright, "Statistics of utility-scale power generation in South Africa," CSIR Energy Centre, Pretoria, 2021.

[2] Department of Mineral Resources and Energy, Integrated Resource Plan (IRP2019), vol. 1, no. 2. South Africa, 2019, p. 100.

[3] A. Ehsan and Q. Yang, "State-of-the-art techniques for modelling of uncertainties in active distribution network planning: A review," Appl. Energy, vol. 239, no. November 2018, pp. 1509–1523, 2019, doi: 10.1016/j.apenergy.2019.01.211.

[4] J. Campillo, From Passive To Active Electric Distribution Networks, no. 202. 2016.
[5] C. D. Iweh, S. Gyamfi, E. Tanyi, and E. Effah-Donyina, "Distributed Generation and Renewable Energy Integration into the Grid: Prerequisites, Push Factors, Practical Options, Issues and Merits," Energies, vol. 14, no. 17, 2021.
[6] F. Pilo, G. Celli, E. Ghiani, and G. G. Soma, "New electricity distribution network planning approaches for integrating renewable," Wiley Interdiscip. Rev. Energy Environ., vol. 2, no. 2, pp. 140–157, 2013, doi: 10.1002/wene.70.
[7] J. Liu, H. Gao, Z. Ma, and Y. Li, "Review and prospect of active distribution system planning," J. Mod. Power Syst. Clean Energy, vol. 3, no. 4, pp. 457–467, 2015, doi: 10.1007/s40565-015-0170-7.
[8] G. W. Ault, C. E. T. Foote, and J. R. Mcdonald, "Distribution System Planning in Focus," IEEE Power Eng. Rev., vol. 21, no. 11, pp. 60–63, 2002, doi: 10.1109/mper.2001.4311127.
[9] J. A. P. Lopes, N. Hatziargyriou, J. Mutale, P. Djapic, and N. Jenkins, "Integrating distributed generation into electric power systems: A review of drivers, challenges and opportunities," Electr. Power Syst. Res., vol. 77, no. 9, pp. 1189–1203, Jul. 2007.
[10] P. S. Georgilakis and N. D. Hatziargyriou, "A review of power distribution planning in the modern power systems era: Models, methods and future research," Electr. Power Syst. Res., vol. 121, pp. 89–100, 2015, doi: 10.1016/j.epsr.2014.12.010.
[11] M. O. W. Grond, J. Morren, and H. J. G. Slootweg, "Requirements for advanced decision support tools in future distribution network planning," IET Conf. Publ., vol. 2013, no. 615 CP, pp. 10–13, 2013, doi: 10.1049/cp.2013.1050.
[12] L. Aleixo et al., "A general framework for active distribution network planning," CIGRE 2013 Lisbon Symp. - Smarts Grids Next Gener. Grids Energy Trends, vol. 2013-April, 2013.
[13] S. You, H. W. Bindner, J. Hu, and P. J. Douglass, "An overview of trends in distribution network planning: A movement towards smart planning," Proc. IEEE Power Eng. Soc. Transm. Distrib. Conf., 2014, doi: 10.1109/tdc.2014.6863446.
[14] G. Celli, F. Pilo, G. G. Soma, and S. A. Rse, "A Comparison of Distribution Network Planning Solutions : Traditional Reinforcement versus Integration of Distributed Energy Storage," 2013 IEEE Grenoble Conf., pp. 1–6, 2013, doi: 10.1109/PTC.2013.6652338.
[15] J. Ausmus, R. S. de Carvalho, A. Chen, Y. N. Velaga, and Y. Zhang, "Big Data Analytics and the Electric Utility Industry," in 2019 International Conference on Smart Grid Synchronized Measurements and Analytics (SGSMA), May 2019, no. 30, pp. 1–7, doi: 10.1109/SGSMA.2019.8784657.
[16] K. B. Lindberg, P. Seljom, H. Madsen, D. Fischer, and M. Korpås, "Long-term electricity load forecasting: Current and future trends," Util. Policy, vol. 58, no. April, pp. 102–119, 2019, doi: 10.1016/j.jup.2019.04.001.
[17] R. Li, W. Wang, Z. Chen, J. Jiang, and W. Zhang, "A review of optimal planning active distribution system: Models, methods, and future researches," Energies, vol. 10, no. 11, pp. 1–27, 2017, doi: 10.3390/en10111715.
[18] A. F. Johnson, "Models to Inform Planning for the Future of Electric Power - Models for Distribution System Planning," in The National Academies of Sciences, Engineering, Medicine, 2020, pp. 41–49.
[19] D. Q. Hung, M. R. Shah, and N. Mithulananthan, "Technical challenges, security and risk in grid integration of renewable energy," Stud. Syst. Decis. Control, vol. 57, pp. 99–118, 2016, doi: 10.1007/978-3-319-30427-4_6.
[20] S. Lakshmi and S. Ganguly, Sustainable Energy Technology and Policies - Transition of Power Distribution System Planning from Passive to Active Networks: A State-of-the-Art Review and a New Proposal, vol. 1. 2018.
[21] M. O. W. Grond, J. Morren, and J. G. Slootweg, "Integrating smart grid solutions into distribution network planning," 2013 IEEE Grenoble Conf. PowerTech, POWERTECH 2013, 2013, doi: 10.1109/PTC.2013.6652346.
[22] M. Kezunovic, P. Pinson, Z. Obradovic, S. Grijalva, T. Hong, and R. Bessa, "Big data analytics for future electricity grids," Electr. Power Syst. Res., vol. 189, no. April, 2020, doi: 10.1016/j.epsr.2020.106788.
[23] Y. Zhang, J. Zhou, and X. Yang, "Research on Development and Upgrade of Distribution Network Planning Technology," iSPEC 2020 - Proc. IEEE Sustain. Power Energy Conf. Energy Transit. Energy Internet, no. 202007300000006, pp. 389–394, 2020, doi: 10.1109/iSPEC50848.2020.9350979.
[24] R. H. A. Zubo, G. Mokryani, H. S. Rajamani, J. Aghaei, T. Niknam, and P. Pillai, "Operation and planning of distribution networks with integration of renewable distributed generators considering uncertainties: A review," Renew. Sustain. Energy Rev., vol. 72, September 2016, pp. 1177–1198, 2017, doi: 10.1016/j.rser.2016.10.036.
[25] A. D. Systems and W. Group, "Planning and Optimization Methods for Active Distribution Systems Working Group C6.19," no. August, 2014.
[26] Y. Xiang et al., "Optimal Active Distribution Network Planning: A Review," Electr. Power Components Syst., vol. 44, no. 10, pp. 1075–1094, 2016, doi: 10.1080/15325008.2016.1156194.
[27] L. Vazquez et al., "Energy System Planning towards Renewable Power System: Energy Matrix Change in Cuba by 2030," IFAC-PapersOnLine, vol. 51, no. 28, pp. 522–527, 2018, doi: 10.1016/j.ifacol.2018.11.756.
[28] A. Maul, "Judgment Sampling," SAGE Encycl. Educ. Res. Meas. Eval., p. 914, 2018.
[29] J. A. Krosnick, "Questionnaire design," Palgrave Handb. Surv. Res., pp. 439–455, 2017, doi: 10.1007/978-3-319-54395-6_53.
[30] H. J Ader; G. J Mellenbergh , Advising on Research Methods - Phases and initial steps in data analysis. Johannes van Kessel, 2008.
[31] M. E. R. Nicholls, "Likert Scales," in The Corsini Encyclopedia of Psychology, Hoboken, NJ, USA: John Wiley & Sons, Inc., 2010.
[32] K. Zou, A. P. Agalgaonkar, K. M. Muttaqi, and S. Perera, "Distribution system planning with incorporating DG reactive capability and system uncertainties," IEEE Trans. Sustain. Energy, vol. 3, no. 1, pp. 112–123, 2012, doi: 10.1109/TSTE.2011.2166281.
[33] S. Sukamolson, "Fundamentals of quantitative research," Lang. Inst. Chulalongkorn Univ., pp. 1–20, 2007.

2023 SAUPEC Conference, Johannesburg, South Africa, January 24-26, 2023

Progress In The Development of the Southern African Regional Grid

Nomihla W. Ndlela
Dept of Electrical Power Engineering
Durban Univesity of Technology
Durban, South Africa
21312861@dut4life.ac.za

Innocent E. Davidson
Dept of Electrical Power Engineering
Durban University of Technology
Durban, South Africa
InnocentD@dut.ac.za

***Abstract*—Southern African countries have the ability to establish a reliable, affordable, and efficient electrical power system; hence, the use of renewable energy is widely recommended. Due to population expansion in Southern Africa, there is an immediate need to expand the electrical supply as well as upgrade electrical power infrastructure in order to improve electricity production. Regional power exchange offers several potential advantages. Indeed, expanding national power markets across international boundaries might reduce supply and demand fluctuations and boost capacity investment. Southern African Power Pool (SAPP) is the regional organization of the Southern African Development Community (SADC) member countries' national utility electricity suppliers in Southern Africa. This review article covers the power electrical difficulties facing the Southern African region, including the available installed capacity, the potential power that may be accumulated, and the expanding population that a peak demand must meet. It also includes the SAPP's aims, vision, and mission to provide power accessibility and reliability in the region.**

Keywords—Grid Reliability, Power Exchange, Power Interconnections, Southern African Power Pool, SAPP challenges

I. INTRODUCTION

Southern Africa is made up of twelve countries: Angola, Botswana, Lesotho, Malawi, Mozambique, Namibia, South Africa, Swaziland, Zambia, Zimbabwe, and Tanzania which is also a member of the Eastern African Power Pool (EAPP), and the Democratic Republic of the Congo (DRC) also known as Central African Power Pool (CAPP) member [1]. Southern Africa is the second of five power pools formed on the African continent under the auspices of the SADC to provide a foundation for regional remedies to electricity generation and supply concerns through coordinated planning and the management of regional power networks [2, 3]. The 1992 Treaty that formed the Southern African Development Community (SADC) resulted in an early concentration on regional resource management. In 1995, SAPP united the national power utilities of the countries involved and the following year, SADC member states ratified the SADC Protocol on Power [4, 5].

In terms of Infrastructure and performance of the energy sector, sub-Saharan African nations have historically struggled behind other parts of the world. Less than 30% percent of the population has access to electricity, compared to around 65% in South Asia and more than ninety percent in East Asia [6]. Furthermore, the average power consumption per capita is only 124 kWh if South Africa is omitted; in comparison, the yearly average consumption per capita in the developing world is 1 155 kWh and in the developed world it is 10, 198 kWh [7].

II. SOUTHERN AFRICAN REGIONAL GRID BACKGROUND

The SAPP is comprised of 12 countries, as shown in Fig.1, with a population of around 350 million and 64GW installed generating capacity, of which 44GW is available to fulfill peak demand of approximately 50GW [8]. Approximately 93% of Africa's coal is produced by South Africa [9, 10]. Mozambique, with 19 GW of hydroelectric potential, 23 TW of solar potential, about 130 Tcf of Natural gas, and 20 billion tons of coal reserves, is one of the most resource-rich countries in the Southern African region [11, 12]. Angola is one of Africa's leading oil producers. [13], lower than 10% of Malawians have access to power [14]. Namibia and Swaziland receive power through South Africa and Mozambique, whereas Zambia produces 95% of its power from hydropower and Zimbabwe relies mostly on fuel

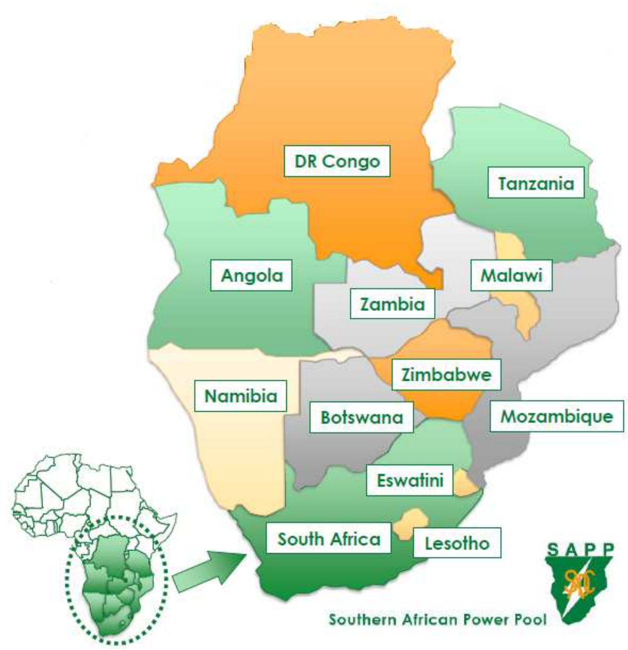

Fig. 1. Southern Africa regional map (2022).

Table I. lists SAPP members and their power utilities, as well as their population for each nation, with the Democratic

Republic of the Congo having the most people and Swaziland having the least [13, 14]. It also highlights the operating members and market participants and categorizes them as Independent Power Producers (IPPs) and Independent Transmission Companies (ITCs) [8].

TABLE I. SOUTHERN AFRICAN POWER POOL UTILITIES AND POPULATION

SAPP Members	Power Utilities	Population (Million)
Angola	Empresa National de Electricidade (ENE)	31.85
Botswana	Botswana Power Corporation (BPC)	2.303
Lesotho	Lesotho Electricity Commission (LEC)	2.125
Malawi	Malawi Electricity Supply Commission (ESCOM)	18.64
Mozambique	Electricidade de Mozambique (EDM)	30.39
Namibia	Namibia power (NAMPOWER)	2.495
South Africa	Electricity Supply Commission (ESKOM)	58.65
Swaziland	Eswatini Electricity Company (EEC)	1.148
Zambia	Zambian Electricity Supply Corporation (ZESCO)	17.87
Zimbabwe	Zimbabwe Electricity Supply Authority (ZESA)	14.65
Angola	Rede Nacional de Transporte de Electricidade (RNT)	31.85
DRC	Societe Nationale d'Electricite (SNEL)	86.841
Tanzania	Tanzania Electricity Supply Company Ltd (TANESCO)	58.043
Operating Members		
Copperbelt Energy Cooperation (CEC)	Zambia (ITC)	
Hidroelectrica de Cahora Bassa (HCB)	Mozambique (IPP)	
Lunsemfwa Hydro Power Company (LHPC)	Zambia (IPP)	
Mozambique Transmission Company (MOTRACO)	Mozambique (ITC)	
Ndola Energy Corporation (INDOLA)	Zambia (IPP)	
Market Participants		
GreenCo Power Services Ltd (GREENCO)	Zambia (IPP)	

Table II. illustrates the South Africa power plant portfolio; it is vital to illustrate the South Africa plant portfolio because it contributes bulk power to both the SAPP grid and the projected Southern African grid [15]. Table III compares installed capacity to power demand to identify which countries require more power access, and then examines current access to electricity to establish the current level of power access [16]. The results were gathered from various sources, as indicated in [13, 14]. South Africa is regarded as having more access to power in the southern African region, whereas Malawi, Zambia, and Mozambique struggle with access to electricity.

TABLE II. PORTFOLIO OF SOUTH AFRICAN POWER PLANTS [13, 14].

Coal – Fired plants	Installed capacity (MW)	Hydroelectricity	Installed capacity (MW)
Arnot	2100	***Conventional hydro stations***	
Camden	1561	Gariep	360
Duvha	3600	Vanderkloof	240
Grootvelei	1200	***Pumped storage schemes***	
Hendrina	2000	Drakensberg	1000
Kendal	4116	Palmiet	400
Komati	1000	Ingula	1332
Kriel	2850	***Other hydropower Stations***	
Lethabo	3708	Colley Wobbles	42
Majuba	4110	Second Falls	11
Matimba	3990	First Falls	6
Matla	3600	Ncora	2.4
Tutuka	3654	***Other renewable energy stations***	
Medupi	4800	Sere Wind Facility	106
Kusile	3200		
Gas/ Liquid turbine stations		***Nuclear***	
Acacia	171	Koeberg	1840
Port Rex	171		
Ankerlig	1327		
Gourikwa	740		
Independent Power Producers (Solar & Wind)			5027
Total Installed Capacity (existing)			58108.4
Eskom Planned capacity additions (Kusile units 5 & 6)			1600

The majority of Namibia and Swaziland's energy comes from South Africa. approximately 60 percent of Namibia's power is exported from South Africa.

TABLE III. SARG COUNTRIES INSTALLED CAPACITY AGAINST THEIR DEMAND & CURRENT ELECTRICITY ACCESS [13, 14].

Country	Installed capacity (MW)	Potential installed (MW)	Power demand (MW)	Current access (%)
South Africa	57777.4	67380	46678	95
Angola	6410.46	8289.26	3378.65	45
Mozambique	3046	9326.9	1650.5	29
Botswana	893.3	2228.3	702	56
Lesotho	73	2161.975	155	44.64
Malawi	406.35	1505.05	470	11
Namibia	661.4	686.4	600	56
Swaziland	78.1	87.1	223	87
Zambia	2762.35	4792.35	2300	31
Zimbabwe	2270	4207	2200	41.9

Fig. 2. represents the available resources in the Southern region, with thermal having the most installed capacity[13], the bulk of which is in South Africa, and oil having the least installed capacity [14, 17]. This data was compiled from a variety of sources, including [13].

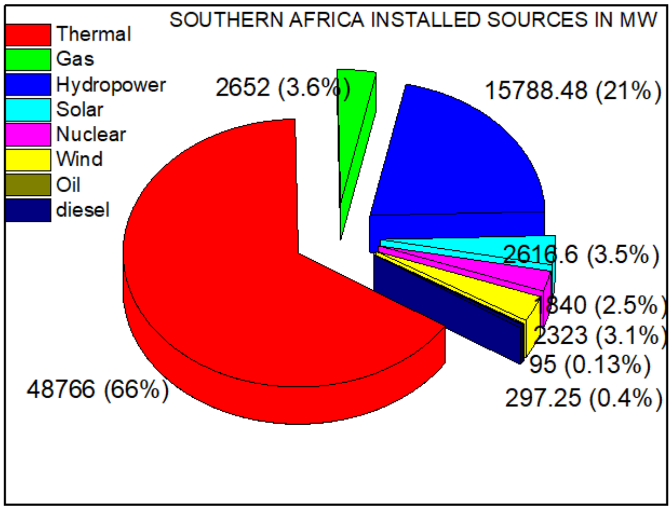

Fig. 2. Installed capacity in the Southern African region.

Fig. 2 shows that thermal resources are the main source of electricity in southern Africa. From Fig. 2, it can be seen that Southern Africa has unevenly distributed sources of electricity, which mandates power interconnections with other Southern African countries that have less access to electricity, such as Malawi, as stated in Table III.

III. SAPP Existing Power Interconnections

The first exchange was among the Democratic Republic of Congo (DRC), Zambia, and Zimbabwe in 1960. Mozambique and South Africa established a power interconnection in 1970. Botswana and South Africa established an interconnection in 1995, while Zimbabwe and South Africa constructed a 400kV link in 1995. Tanzania, Angola, and Malawi currently have no interconnections with other countries, although new electrical lines are planned and are expected soon [18, 19]. Modern transmission and distribution networks are typically categorized as "dumb" systems due to their inability to intelligently respond to the data necessary for the modern grid to function. Again, the present power infrastructure is incapable of delivering appropriate service in terms of electricity efficiency, security, and reliability, or integrating renewable energy on a scale sufficient to fulfill the demand for clean power [20].

Power pools and interconnections were built to ensure network efficiency across increasingly large distances. Participants in the SAPP were given equal rights and duties and committed to acting in cooperation without taking advantage of one another. [4] SAPP controls power trading by interconnecting high-voltage transmission networks in adjacent countries and encouraging a competitive and equal market.[5]. Malawi, Tanzania, and Angola are presently not connected to any SAPP countries [21]. there are however proposed interconnections as shown in Fig. 3.

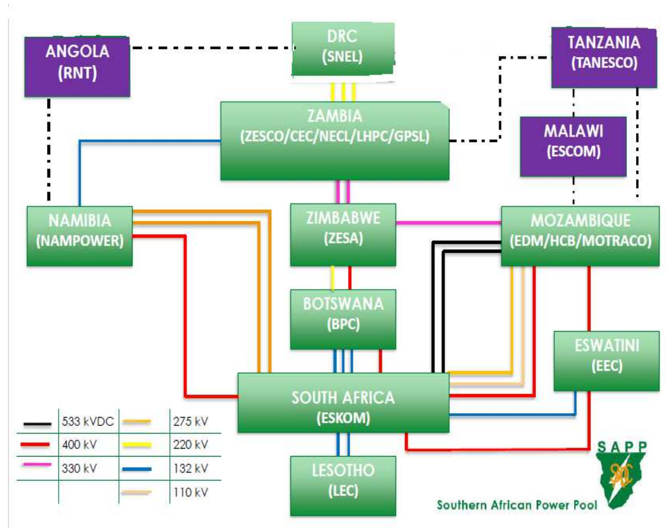

Fig. 3. SAPP existing and future power interconnections (2022).

Fig. 3 displays present and projected power interconnections; it can be noticed from Fig. 3. that South Africa has the highest interconnections due to its large coal-fired generation capacity. Three countries, Malawi, Tanzania, and Angola are not currently connected to any SAPP country. Additionally, the DRC is a member of both SAPP and CAPP. Also, Tanzania is a member of both SAPP and CAPP.

A. *SAPP Objectives*

- For members to organize and collaborate in the planning and management of their power control systems to save expenses whilst preserving the desired levels of reliability, independence, and self-reliance.
- completely recoup their expenditures and participate equally in the subsequent advantages, including reductions in necessary generating capacity, fuel cost savings, and increased utilization of hydroelectric energy.
- Coordinate and collaborate in the planning, implementation, and operations of a regional power market in accordance with the needs of SADC Member States [8].

B. *SAPP Challenges*

The incidence of power shortages in Southern African regions has grown dramatically over the last years due to a variety of issues, including insufficient electrical power supply infrastructure in member countries; Load expansion in poorly planned-for areas; fast population increase, and economic expansion make it difficult for any Southern African country to meet peak demand inside its borders [22]. as stated by [13] In SSA, access to electricity is 43%, with more than half of the countries within the region falling below this level [23]. The other challenge is that there is an inadequate national electrical supply to meet demand. This is mostly because Eskom's older coal-fired power facilities require extensive unplanned maintenance[24]. plus Theft and vandalism of electricity infrastructure cost SAPP participant utilities millions of dollars.

The drop in economic activity in many SAPP countries as a result of COVID-19 restrictions exacerbated the problem [25]

C. SAPP Vision and Mission.

- To be seamless integration, dynamic energy market, and source of sustainable power solutions for SADC and even beyond.
- To offer electricity-related services throughout the region and even above that.

IV. SAPP Future Pespectives & Interconnections.

SAPP envisions achieving a sufficient transmission infrastructure upon completion of the SAPP Regional Transmission Financing Facility Study and enhancements to the transmission pricing methodology [26]. to increase energy market stability by adding members, to allocate transmission capacity more efficiently, and to promote trading portfolios [8]. SAPP is committed to improving system operations through the use of the balancing market to eliminate energy imbalances, the development of a supplementary services market, and the reduction of vandalism and enhanced system performance. Preparation for SAPP-EAPP Integration [27]. to participate in the African continental power integration process, which includes the ongoing Continental Transmission Master Plan study and the African Single Electricity Market study [8].

A 400kV, 101km transmission line interconnecting Hwange and Livingstone through Victoria Falls is part of the ZIZABONA power interconnection through four countries: Zimbabwe, Zambia, Botswana, and Namibia [28]. A 231km long 400kV line between Livingstone and Zambezi, and a 76 km long 400kV line connecting Victoria Falls and Pandamatenga [29]. Eleven priority transmission projects are now being constructed in the SAPP region, as shown in Table IV below. These projects aim to construct new power corridors to stimulate industrial growth and improve the region's food security without overloading the region's present transmission network. One of the most important proposed power interconnection is Zambia–Tanzania–Kenya (ZTK), which aims to connect the EAPP and SAPP [30].

TABLE IV. Power interconnection SAPP projects [30, 31].

Project	Technicaal Parameters	Expected commissioning / Status
Angola-Namibia interconnector (ANNA)	400kV, 360km	2025
Botswana-South Africa Interconnector (BOSA)	400kV	2024
Kolwezi-Solwezi (DRC-Zambia) Interconnector	330kV	Implementation
Malawi-Tanzania Interconnector	400kV	NA
Malawi-Zambia Interconnector	400kV, 286km	2023
Mozambique-Malawi Interconnector (MOMA)	400kV, 218km	2023
Mozambique-Tanzania Interconnector (MOTA)	400kV, 700km	NA
Mozambique-Zambia Interconnector	400kV, 368km	NA
Mozambique-Zimbabwe-South Africa Interconnector (MOZISA)	400kV, 935km	2022
Zambia-Tanzania-Kenya Interconnector (ZTK)	400kV, 2302km 330kV, 373km	implementation
Zimbabwe-Zambia-Botswana-Namibia Interconnector (ZIZABONA)	330kV, 408km	completion
Mozambique – Malawi Interconnector (Tete – Phombeya)	220kV, 200km	N/A

Using power interconnection and considering the present and potential installed capacity demonstrates that the Southern African region has the ability to provide 100% access to electricity. Through the abovementioned SAPP objectives, mission, and vision, it is feasible to achieve sustainable, adequate, and dependable electricity.

V. Conclusion

SAPP is the oldest Power Pool in Africa and it is believed the leading power pool in Africa. Electricity trading on the SAPP competitive market is gaining traction, and EdM is acknowledged for being an active participant; therefore encouraging customers to utilize the market extensively. SAPP is investigating other means of enhancing regional power trade and funding projects. Based on an analysis of the current and proposed connections in southern Africa, as well as the available and potential power, Southern Africa has the ability to power the whole region and provide 100% access to electricity to the growing population through the use of power interconnection.

References

[1] V. R. Nalule, "Regionalism in Addressing Energy Access Challenges," in *Energy Poverty and Access Challenges in Sub-Saharan Africa*. Palgrave Macmillan: cham, 2019, pp. 41-89.

[2] P. Niyimbona, "The challenges of operationalizing power pools in Africa," in *UNDESA Seminar on Electricity Interconnection, Cairo, Egypt, June*, 2005, pp. 19-21.

[3] J. Ngwawi, "Resetting SADC priorities-RISDP review," *Southern Africa. SADC Today,* vol. 16, no. 5, pp. 1-16, 2014.

[4] A. Maupin, "Building a regional electricity market: SAPP challenges," *European Centre for Development Policy MAnagement,* SAIA, p. 6, 2013.

[5] S. Mludi and I. E. Davidson, "Dynamic analysis of Southern Africa power pool (SAPP) network," in *2017 IEEE PES PowerAfrica*, Accra, Ghana, 27-30 June 2017, pp. 1-6, doi: 10.1109/PowerAfrica.2017.7991208.

[6] F. J. Ramos Real and B. Tovar, "Revisiting electric utilities' efficiency in the Southern African Power Pool, 1998-2009," *Journal of Energy in Southern Africa,* vol. 31, no. 1, pp. 1-13, 2020.

[7] O. Rosnes and M. Shkaratan, *Africa's power infrastructure: investment, integration, efficiency*. World Bank Publications, 2011.

[8] SAPP Coordination centre, "Introduction to SAPP," 15 August 2022, 2022.

[9] J. G. Wright and J. Van Coller, "System adequacy in the Southern African Power Pool: A case for capacity mechanisms," *Journal of Energy in Southern Africa,* vol. 29, no. 4, pp. 37-50, 2018, doi: http://dx.doi.org/10.17159/2413-3051/2018/v29i4a5581.

[10] N. W. Ndlela and I. E. Davidson, "Power Planning for a Smart Integrated African Super-Grid," in *2022 30th Southern African Universities Power Engineering Conference (SAUPEC)*, Durban,

South Africa, 25-27 Jan. 2022: IEEE, pp. 1-6, doi: 10.1109/SAUPEC55179.2022.9730631.
[11] M. Procesi *et al.*, "Preliminary Fluid Geochemical Survey in Tete Province and Prospective Development of Geothermics in Mozambique," 2021.
[12] I. El Yaziji, "Analysis of future energy scenarios for Mozambique based on an integrated energy-economy system optimization model," Master of Science – Energy Engineering, Politecnico di Milano, 2021.
[13] U.S Energy Information Administration, " Energy Information Administration" independent statistics and analysis, Washington, DC 20585 1995. Accessed: 06 / 05 / 2020. [Online]. Available: https://www.eia.gov/international/analysis/country/ARE?scr=email
[14] U.S.A Government-Led Partnership, "POWER AFRICA FACT SHEET," United State Agency for International Development (USAID) America, 2013. Accessed: 16/ 04/ 2020. [Online]. Available: https://www.usaid.gov/powerafrica/countries
[15] N. W. Ndlela, "High voltage transmission system planning for a southern African regional grid," MASTER OF ENGINEERING IN ELECTRICAL ENGINEERING, DEPARTMENT of ELECTRICAL POWER ENGINEERING, DURBAN UNIVERSITY of TECHNOLOGY, Durban, 2022.
[16] Eskom. "Generation." https://www.eskom.co.za/eskom-divisions/gx/ (accessed 03-02-2022.
[17] World Bank IEA, "Light up and power Africa," Annual Development Effectiveness Review 2017, 2017 2017. Accessed: 2017.
[18] J. J. Justo, F. Mwasilu, and J.-W. Jung, "Doubly-fed induction generator based wind turbines: A comprehensive review of fault ride-through strategies," *Renewable and sustainable energy reviews,* vol. 45, pp. 447-467, 2015.
[19] S. Busch, M. De Felice, and I. Hidalgo González, "Analysis of the water-power nexus in the Southern African Power Pool," European Union 2020. [Online]. Available: https://ec.europa.eu/jrc
[20] W. Wang and Z. Lu, "Cyber security in the smart grid: Survey and challenges," *Computer networks,* vol. 57, no. 5, pp. 1344-1371, 2013.
[21] N. W. Ndlela and I. E. Davidson, "Reliability and Security Analysis of The Southern Africa Power Pool Regional Grid," in *2022 IEEE PES/IAS PowerAfrica*, Kigali, Rwanda 22-26 August 2022 pp. 1-5, doi: 10.1109/PowerAfrica53997.2022.9905389.
[22] S. Mwale and I. Davidson, "Power deficits and outage planning in South Africa," *Proceedings of the 2nd International Symposium on Energy Challenges and Mechanics,* pp. 19-21, 2014.
[23] P. Valickova and N. Elms, "Potential gains from regional integration to reduce costs of electricity supply and access in Southern Africa," *Energy for Sustainable Development,* vol. 62, pp. 82-100, 2021.
[24] J. Roy-Aikins, "Challenges in meeting the electricity needs of South Africa," in *ASME Power Conference*, Charlotte, North Carolina, USA 2016, vol. 50213: American Society of Mechanical Engineers, p. V001T05A002, doi: https://doi.org/10.1115/POWER2016-59085.
[25] S. A. P. Pool, "Energising the region for economic development," SAPP, Harare, Zimbabwe, 2022.
[26] H. O'BRIEN ALEXANDER, "THE FINANCING OF POWER TRANSMISSION INTERCONNECTOR PROJECTS: ," *A CASE STUDY OF VIABLE FINANCIAL PACKAGING UTILISING PROJECT FINANCE PRINCIPLES FOR THE SOUTHERN AFRICAN POWER POOL (SAPP),* 2010.
[27] A. Oduor, "The Role of Power Pools in the Electrification of the African Continent for Socio economic Development and Transitioning into Clean E nergy," Kigali Rwanda, 2022.
[28] N. W. Ndlela and I. E. Davidson, "A Load Flow Analysis of the Southern African Power Pool Interconnections using High Voltage AC, High Voltage DC, and Flexible AC Transmission System," in *2022 IEEE PES/IAS PowerAfrica*, Kigali, Rwanda 22-26 August 2022, pp. 1-5, doi: 10.1109/PowerAfrica53997.2022.9905074.
[29] A. M. Rose, "Improving the performance of regional electricity markets in developing countries: the case of the Southern African power," Doctor of Philosophy in Engineering Systems, Data, Systems, and Society, Massachusetts Institute of Technology, 2017. [Online]. Available: http://hdl.handle.net/1721.1/112622
[30] Information and analysis on the global electricity transmission industry, "SAPP: Existing Tranmission Network and Planned Interconnections," Washinton, D.C, 05 June 2019. [Online]. Available: www.globaltransmission.info
[31] African Development Bank Group, "Multinational - Zizabona Power Interconnection Project," Data Portal, Multinational, 31 May 2022.

2023 SAUPEC Conference, Johannesburg, South Africa, January 24-26, 2023

Analysis and Compensation of Power Systems with Harmonics and Unbalance

David Oyedokun
Department of Electrical Engineering
University of Cape Town
Cape Town, South Africa
0000-0002-8025-0143

Pitambar Jankee
Department of Electrical Engineering
University of Cape Town
Cape Town, South Africa
0000-0001-8006-2997

Maysam Soltanian
Department of Electrical Engineering
University of Cape Town
Cape Town, South Africa
maysam.soltanian@uct.ac.za

Hilary Chisepo
Department of Electrical Engineering
University of Cape Town
Cape Town, South Africa
hilary.chisepo@uct.ac.za

***Abstract*—Conventional active and reactive power definitions are premised on balanced sinusoidal currents and voltages. In modern power systems with increased converter-driven generation, non-linear loads, harmonics, and source unbalance, inconsistencies in the calculation of reactive power arise. In this paper, we go through the definitions of conventional reactive power, pq theory and the general power theory. A new analytical method based on the hysteresis characteristics of the system is proposed to calculate reactive power (Q) in the presence of unbalance and harmonics. The results showed that under balanced and unbalanced conditions, the proposed method derived from first principles in physics is consistent with pq theory. When harmonics are introduced, however, results for Q differ greatly. This paper shows that the orthogonality assumed by the power triangle may not be valid in practical power systems. The results have implications on the correct compensation in modern power systems with the increasing presence of non-ideal conditions such as those brought about by unbalance and harmonic distortion.**

Keywords—Compensation, harmonics, orthogonality, reactive power

I. Introduction

The transition from fossil fuel-based to converter-driven generation with renewable energy sources (RES) and the increase in non-linear loads such as variable speed drives (VSDs) have increased the level of harmonics in practical power systems. These changes in the nature of power systems present challenges in the validity of assumptions of sinusoidal and balanced system conditions in conventional power theory. Inverter-based generation is increasing in distribution networks which are prone to load unbalance from downstream reticulation. As a result, power calculations in the presence of harmonics and unbalance are of growing concern [1]–[4].

Reactive power (Q) is commonly perceived as an effect of phase displacement between a sinusoidal voltage and a sinusoidal current, where the current is orthogonal to the voltage. Taking a voltage V and a current I with a displacement angle ϕ (phi) between them, the arithmetic function $VIcos\phi$ is the real (active) power in a single-phase system. The physical meaning of this real power is interpreted as a rate of doing work or delivering energy. Voltages and currents are scalar quantities. When represented as a set of scalars, currents and voltages can be treated as vectors in the vector-space. For power system analysis, V and I are represented as phasors (rotating vectors at a specific angular frequency) defined by their magnitude and angle in the complex plane. In phasor analysis, the reference phasor is the voltage phasor which is aligned with the real axis of the complex plane, and the current can be anywhere on the complex plane based on its phase and magnitude. The power phasor (S) is obtained by multiplying the voltage and current phasors. The projection of S onto the real axis is the real power (P) while its projection onto the imaginary axis is the reactive power (Q), as conventionally defined. The decomposition of the apparent power phasor (S) assumes orthogonality between P and Q. This orthogonality is valid for balanced, sinusoidal system conditions. In the presence of unbalance and distortion, the orthogonality may not hold [5], [6].

Conventional power theories treat currents and voltages as vector quantities [7]–[13] even though they are defined as scalars from a physics point of view. If vector algebra is applied to V and I , then the real power P can be calculated by taking the dot product of the two vectors V and I during an interval of time [7]–[13]. This dot product is given by the magnitude of V and the projection of I onto V, represented by a $cos\ \phi$ term.

Power system studies are conducted for network planning, design, post-event analysis and contingency analysis. Therefore, it is important to understand the limitations of existing power theories and explore power theories that do not rely on the orthogonality (or lack of) between P and Q.

In this paper, the derivation of power from first principles of physics is discussed and a new analytical approach to calculate reactive power based on the hysteresis characteristics of the $I-V$ system is proposed. The performance of two other extant power theories, i.e., the new general power theory (GPT) and the pq theory, to reduce network losses are also contrasted.

The rest of the paper is organized as follows. Section II presents the pq theory, the new GPT and the proposed analytical approach of calculating Q. Section III describes the modelling and simulation protocol after which results are presented in section IV. Finally, conclusions are drawn in section V.

II. THEORY DEVELOPMENT

A. Pq theory

The pq theory was introduced by Akagi *et al.* [7], [8] and is readily used nowadays in the control of power-electronic converters, especially for renewable energy applications. The pq theory is based on the concept of reactive power, assuming orthogonality between the active and reactive components of the power. The instantaneous three-phase line to neutral voltages (v_a, v_b, v_c) and currents (i_a, i_b, i_c) vectors measured at the point of connection (PoC) in the *a-b-c* reference frame are transformed to the $0\alpha\beta$ reference frame.

$$\vec{v} = [v_a \quad v_b \quad v_c]^T \tag{1}$$

$$\vec{\imath} = [i_a \quad i_b \quad i_c]^T \tag{2}$$

$$[v_0 \quad v_\alpha \quad v_\beta]^T = [C]\vec{v} \tag{3}$$

$$[i_0 \quad i_\alpha \quad i_\beta]^T = [C]\vec{\imath} \tag{4}$$

$$[C] = \sqrt{\frac{2}{3}}\begin{bmatrix} \frac{1}{\sqrt{2}} & \frac{1}{\sqrt{2}} & \frac{1}{\sqrt{2}} \\ 1 & -\frac{1}{2} & -\frac{1}{2} \\ 0 & \frac{\sqrt{3}}{2} & -\frac{\sqrt{3}}{2} \end{bmatrix} \tag{5}$$

In the $0\alpha\beta$ reference frame, the instantaneous active (real) power $p_{\alpha\beta}$ is calculated by taking the dot product of $[v_0 \quad v_\alpha \quad v_\beta]^T$ and $[i_0 \quad i_\alpha \quad i_\beta]^T$. $p_{\alpha\beta}$ consists of a dc-component ($\bar{p}_{\alpha\beta}$) corresponding to the fundamental frequency positive sequence active power of the load. The oscillating component ($\tilde{p}_{\alpha\beta}$) represent the real power contributed by the harmonic components.

$$p_{\alpha\beta} = u_\alpha i_\alpha + u_\beta i_\beta = \bar{p}_{\alpha\beta} + \tilde{p}_{\alpha\beta} \tag{6}$$

In three-phase four-wire systems, the unbalance component of currents and voltages usually referred to as zero-sequence components of currents and voltages also contribute to the instantaneous active power which becomes:

$$p(t) = u_a i_a + u_b i_b + u_c i_c = u_0 i_0 + u_\alpha i_\alpha + u_\beta i_\beta \tag{7}$$

The reactive power component of power is calculated by multiplying the orthogonal components of current and voltage in the α and β axis as shown below.

$$q_{\alpha\beta} = u_\alpha i_\beta - u_\beta i_\alpha \tag{8}$$

Active power filters inject compensating currents depending on the compensation objective. For harmonic and reactive power compensation, the currents to be injected are determined from $p_c = \tilde{p}_{\alpha\beta} + u_0 i_0 + q_{\alpha\beta}$, where p_c represents the reference compensating power [14]. An inverse Clarke transformation $[C]^{-1}$ is then applied to the compensating currents determined in the $0\alpha\beta$ reference frame to give the compensating currents in the *abc* reference frame.

B. General Power Theory (GPT) [6]

The GPT uses Kirchoff's voltage and current laws, and the law of conservation of energy to propose novel definitions of power quantities including the power factor. No parameter corresponding to reactive power (Q) forms part of the GPT. The inputs to the GPT for determining reference compensating currents to be injected by an active power filter to minimize deliver loss include complex rms (CRMS) values of currents and voltages and the Thévenin equivalent impedance of the network as seen by the PoC. Measurements are made for each wire and each harmonic frequency. It is to be noted that the reference for the voltage measurement is different for each harmonic and therefore needs to be calculated iteratively if network conditions change. An advantage of the GPT is that the same theory applies to a system with any number of wires and harmonic components including dc components.

The GPT identifies an optimal current vector $\overrightarrow{I_A}$ which is a function of the Thévenin voltages measured from the null reference, the Thévenin equivalent resistances of the system and a single real value constant K_A . The compensating currents can be calculated by subtracting the complex source current $I_{S(m,h)}$ (for each wire and at each harmonic) from the complex optimal currents $I_{A(m,h)}$.

C. Derivation of active and reactive powers, p(t) and q(Θ)

Work is defined by the dot product of force (vector, $\vec{F}$) and displacement (vector, $\overrightarrow{dl}$) as shown in (9).

$$w = \int \vec{F}.\overrightarrow{dl} \tag{9}$$

It is known that the electric force from an electric field is equal to $\vec{F}$ which is given by (10).

$$\vec{F} = q_c\vec{E} \tag{10}$$

Where q_c is the electric charge and $\vec{E}$ is the electric field. By combining (9) and (10) we can calculate the electric energy as in (11).

$$w = \int q_c\vec{E}.\overrightarrow{dl} \tag{11}$$

The voltage is defined by (12),

$$v_A = -\int_{ref}^{A} \vec{E}.\overrightarrow{dl} \tag{12}$$

The electric field is conservative, which means that the work done by the electric field is independent of the path, and it depends only on the initial and finals point A and B. In other words, in energy calculations, it is possible to consider displacement between points A and B on a path that is always parallel to the electric field at each point. This means that:

$$v_A = -\int_{ref}^{A} \vec{E}.\overrightarrow{dl} = -\int_{ref}^{A} E\, dl \tag{13}$$

We can conclude the following from (13):

$$dv = -Edl \tag{14}$$

By combining (11), and (14) we can calculate the electric power:

$$w = -\int q_c \, dv \tag{15}$$

$$dw = -q_c dv \tag{16}$$

$$\frac{dw}{dt} = -q_c \frac{dv}{dt} \tag{17}$$

$$p = -q_c \frac{dv}{dt} \tag{18}$$

(18) is the definition of active power which is also equal to the $v\frac{dq_c}{dt}$. This is related to the flow of electric energy in the circuit.

When there is a lag between the input (v) and the output (i) in an electrical system, we have a rate-dependent hysteresis effect which is associated with power loss. The work done on the i(v) system, w_h , is equal to the area under the hysteresis graph and is given by (19) and shown in Fig. 1.

$$w_h = \textit{the area under the } i - v \textit{ graph} = \int idv \tag{19}$$

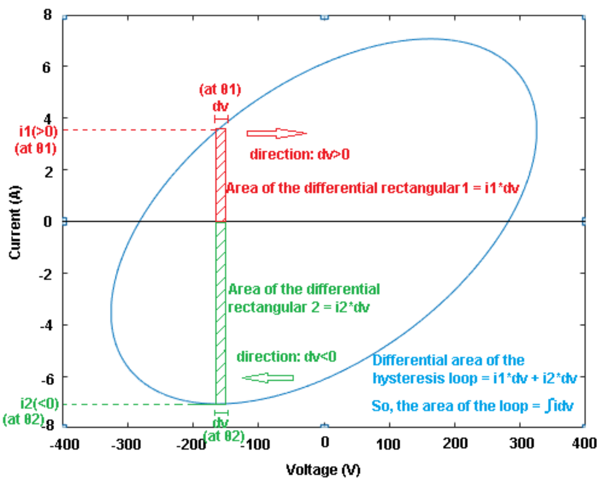

Fig. 1: Calculating the area under the i-v graph

This work done on the system, "$w_h = \int idv$", is equal to what is known as "reactive" energy. This work is due to the lag between the input and output of the system and hence it can be considered to change with phase, "θ".

By using (19), we can calculate the reactive power as the following:

$$w_h = \int idv \tag{20}$$

$$dw_h = idv \tag{21}$$

$$\frac{dw_h}{d\theta} = i\frac{dv}{d\theta} = q(\theta) \tag{22}$$

$$\theta = \frac{2\pi}{T} t \tag{23}$$

where $q(\theta)$ is reactive power which is a function of "θ" and is the rate of change of i(v) hysteresis loss with phase. From (22) we can calculate the average reactive power as the following:

$$Q = \frac{1}{2\pi}\int_0^{2\pi} q(\theta)\, d\theta \tag{24}$$

Q is the average reactive power, and is calculated by averaging the reactive power function, $q(\theta)$, which is a function of θ. Using (23), we can obtain i(θ) and v(θ) from i(t) and v(t). Having i(θ) and by differentiating v(θ) ($\frac{dv(\theta)}{d\theta}$), we can obtain the reactive power function $q(\theta)$ which is equal to $i(\theta)\frac{dv(\theta)}{d\theta}$.

III. Power System Model and Simulation Protocol

Two power systems models were used in this study. The first was a simple model as shown in Fig. 2 with a three-phase supply, a lossless transmission line and a wye-connected load to demonstrate the problems with conventionally defined reactive power. Delivery losses were excluded to make the comparison simple.

Table I shows the test cases used for comparing the calculation of Q using the conventional method and the newly proposed method presented in section II (C).

TABLE I. Test cases (B = Balanced, UB = Unbalanced)

Test case	Load	Source	Harmonics present?
1	B	B	No
2	UB	B	No
3	B	UB	No
4	B	B	Yes
5	UB	B	Yes
6	B	UB	Yes

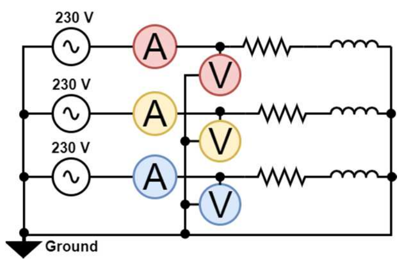

Fig. 2: Power system model for comparing Q calculated from power theories

The second power system model used for this study consisted of three independent single-phase ac-voltage sources modelling a three-phase generator, a resistive and inductive overhead transmission line (typical of an MV or HV) and an unbalanced distorted rectifier load as shown in Fig. 3.

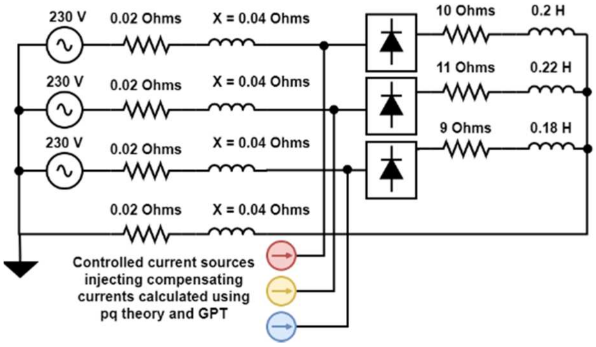

Fig. 3: Power system model for comparing effect of pq compensation and GPT compensation

To distort the system with harmonics, the load was modelled using three single-phase rectifiers with unbalanced resistive and inductive loads. The aim of the simulation was to compare the transmission line losses by injecting compensating currents determined by the pq theory and the GPT. The instantaneous currents and voltages at the PoC were measured. The measurements were post-processed by applying the theory presented in II (A) to calculate the compensating currents using the pq theory. Using the FFT Analysis tool in MATLAB Simulink, the dominant harmonics in the system were identified. Odd harmonics up to the 15th harmonic had the highest magnitudes. Even harmonics were negligible since the distortion was symmetrical. Hence, only odd harmonics up to the 15th harmonic were used to calculate CRMS values of currents and voltages for each wire. The values were then imported onto a spreadsheet that implements the GPT method and calculates compensating currents to be injected to minimize the transmission line losses.

If all the compensating current components determined from p_c are injected, a direct comparison between pq-compensation and GPT compensation will not be reliable. This is because the compensating currents calculated using the pq-theory may include harmonic orders greater than 15th. Hence an FFT of the compensating currents determined by the pq theory was done to only inject odd harmonic components up to the 15th harmonic. The compensating currents were injected at the PoC at time t = 0.5 s using three ideal controlled current sources representing the three phases of an active power filter. The controlled current sources convert the input signal (compensating current signal) to a current. The transmission line losses were calculated by taking the product of the square of the current in each wire and the resistance of the wire. Note that the neutral wire losses were also included.

IV. Results

A. *Comparison of Q-calculation using conventional method and the new proposed method*

Simulation results from the power system models discussed in section III are presented in this section, Fig. 4 shows the electrical quantities for test case 1. Fig.5 shows the electrical quantities for test case 5. The calculation results of apparent power, reactive power from the conventional method and the proposed method under various load and source conditions are presented in table II.

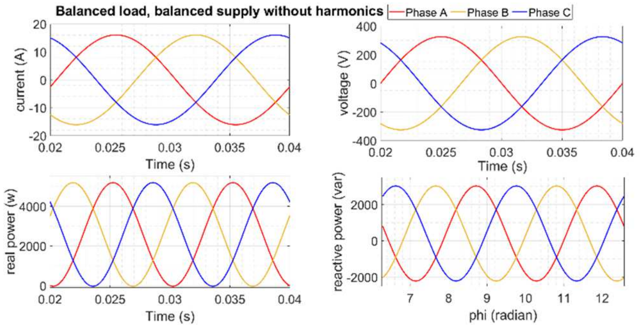

Fig. 4: Currents, voltage, real power and reactive power for balanced load, balanced supply and no harmonics (test case 1)

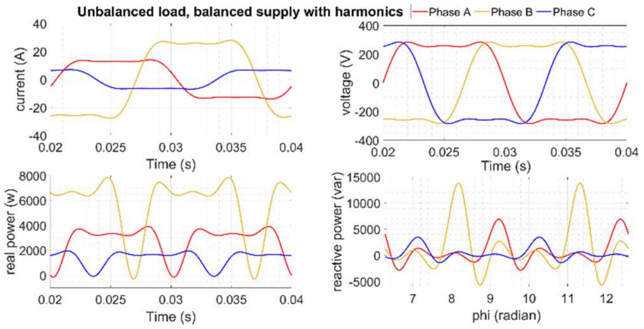

Fig. 5: Currents, voltage, real power and reactive power for unbalanced load, balanced supply and harmonics (test case 5)

TABLE II. SUMAMRY OF CALCULATION RESULTS

Test case	P (W)	S (VA)	Q(Var) from pq theory	Q (Var) from the proposed method
1	7743.93	7838.88	1216.41	1216.41
2	9034.61	9145.39	1419.15	1419.15
3	7987.86	8085.81	1254.74	1254.74
4	8376.92	8550.70	1715.15	2235.28
5	9773.23	9975.97	2000.97	2607.83
6	8640.86	8820.11	1769.17	2305.70

The results from Table II reveal that, in the presence of harmonics, the reactive powers calculated from the proposed method are different from those calculated using the pq theory, but the active powers are the same. One may conclude that when harmonics are present, P and Q are no longer orthogonal. However, when there are harmonics, voltage and current (which are not vectors) can be represented by several phasors with different rotating speeds for each harmonic. So, each harmonic of voltage and current separately can be represented by a phasor and all power phasor analysis including the orthogonality of P and Q are valid for them. It should be noted that there is not one phasor that can represent voltage (with harmonics) and one phasor that can represent current (with harmonics), and we cannot perform phasor analysis here, so the orthogonality of the total P and the total Q is irrelevant based on this method.
This is reflective of modern power systems with increasing non-linear loads and harmonics.

B. *Effect of compensation using pq theory and GPT*

Fig. 6 shows a comparison of the compensating currents calculated by the pq theory and the GPT.

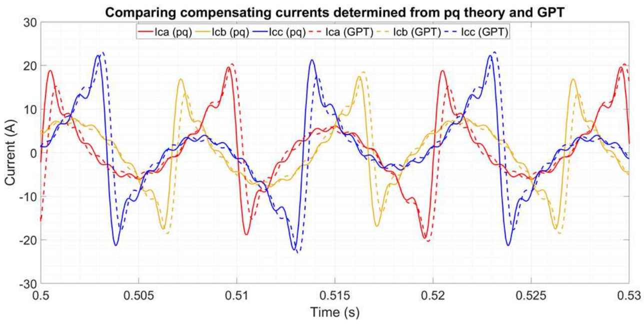

Fig. 6: Compensating currents determined by pq theory and GPT

The active power losses before compensation were 28.89 W. With pq-compensation, the delivery loss after compensation reduced to 19.98 W. GPT compensation caused the losses to drop further to 19.4 W. This highlights a difference between compensation using the pq theory which assumes orthogonality between P and Q, and the GPT whose objective function is to reduce delivery losses to a minimum. The transmission line currents before and after GPT compensation are shown in Fig. 7. Note that the currents were still distorted after compensation because only harmonics up to the 15th were compensated.

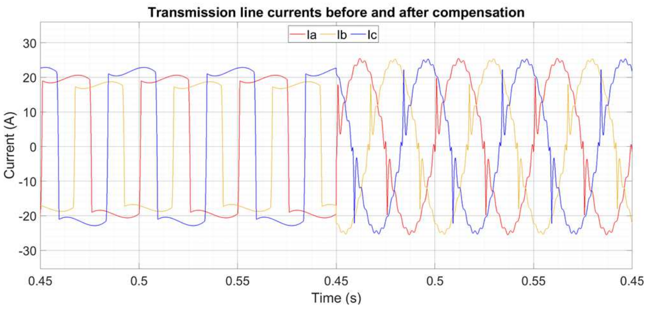

Fig. 7: Transmission line current before and after GPT compensation

V. Conclusion

The authors presented the application of two existing but fundamentally different power theories and proposed an alternative approach based on the hysteresis characteristics of the system. A rigorous approach was also developed to calculate power that is interpreted as conventional Q from the first principles of physics and to compare the values of Q against the pq theory, especially in the presence of distortion and unbalance. With the new approach, the analysis in this paper has demonstrated that in the presence of harmonics, the assumptions of orthogonality between P and Q, as often assumed, might not be valid. Compensation using the GPT revealed that power delivery losses may be reduced when compared to pq-compensation under conditions of harmonics & unbalance. The implications are that three-phase control methods (machine, power-electronic converter, and power systems) that are based on phasor analysis in which one phasor for V and one phase for I are considered in the presence of harmonics, might not offer a realistic interpretation of actual conditions. Further work involves laboratory measurements and comparisons with simulation modeling with the new method.

References

[1] *IEEE Standard Definitions for the Measurement of Electric Power Quantities Under Sinusoidal, Non-sinusoidal, Balanced, or Unbalanced Conditions,* IEEE Standard 1459, 2010.

[2] M. G. Simões, F. Harirchi, and M. Babakmehr, “Survey on time-domain power theories and their applications for renewable energy integration in smart-grids,” *IET Smart Grid*, vol. 2, no. 4, pp. 491–503, 2019, doi: 10.1049/iet-stg.2018.0244.

[3] H. K. M. Paredes, F. P. Marafão, and L. C. P. da Silva, “A comparative analysis of FBD, PQ and CPT current decompositions - Part I: three-phase three-wire systems,” *2009 IEEE Bucharest PowerTech: Innovative Ideas Toward the Electrical Grid of the Future*, pp. 1–8, 2009, doi: 10.1109/PTC.2009.5282173.

[4] H. K. M. Paredes, F. P. Marafão, and L. C. P. da Silva, “A comparative analysis of FBD, PQ and CPT current decompositions - Part II: Three-phase four-wire systems,” *2009 IEEE Bucharest PowerTech: Innovative Ideas Toward the Electrical Grid of the Future*, pp. 1–6, 2009, doi: 10.1109/PTC.2009.5282169.

[5] M. Malengret, “Definition of apparent power in 3-phase 4-wire non-sinusoidal power systems,” Ph.D. dissertation, Dept. Electrical Engineering, University of Cape Town, Cape Town, South Africa 2008.

[6] M. Malengret and C. T. Gaunt, “Active Currents, Power Factor, and Apparent Power for Practical Power Delivery Systems,” *IEEE Access*, vol. 8, pp. 133095–133113, 2020, doi: 10.1109/ACCESS.2020.3010638.

[7] H. Akagi, Y. Kanazawa, K. Fujita, and A. Nabae, “Generalized theory of instantaneous reactive power and its application,” *Electrical Engineering in Japan*, vol. 103, no. 4, pp. 58–66, 1983, doi: 10.1002/eej.4391030409.

[8] H. Akagi, Y. Kanazawa, and A. Nabae, “Instantaneous Reactive Power Compensators Comprising Switching Devices without Energy Storage Components,” *IEEE Trans Ind Appl*, vol. IA-20, no. 3, pp. 625–630, 1984, doi: 10.1109/TIA.1984.4504460.

[9] H. Akagi, S. Ogasawara, and H. Kim, “The Theory of Instantaneous Power in Three-Phase Four-Wire Systems: A comprehensive approach,” *IEEJ Transactions on Industry Applications*, vol. 119, no. 12, pp. 1461–1470, 1999, doi: 10.1541/ieejias.119.1461.

[10] J. L. Willems, “A New Interpretation of the Akagi-Nabae Power Components for Nonsinusoidal Three-Phase Situations,” *IEEE Trans Instrum Meas*, vol. 41, no. 4, pp. 523–527, 1992, doi: 10.1109/19.155919.

[11] F. Z. Peng and J. S. Lai, “Generalized instantaneous reactive power theory for three-phase power systems,” *IEEE Trans Instrum Meas*, vol. 45, no. 1, pp. 293–297, 1996, doi: 10.1109/19.481350.

[12] F. Z. Peng, G. W. Ott, and D. J. Adams, “Harmonic and reactive power compensation based on the generalized instantaneous reactive power theory for three-phase four-wire systems,” *IEEE Trans Power Electron*, vol. 13, no. 6, pp. 1174–1181, 1998, doi: 10.1109/63.728344.

[13] S. Togasawa, T. Murase, H. Nakano. A. Nabae, “Reactive power compensation based on a novel cross vector theory,” *IEEJ Transactions on Industry Applications*, vol. 114, pp. 340–341, 1994.

[14] A. M. Massoud, S. J. Finney, and B. W. Williams, “Review of harmonic current extraction techniques for an active power filter,” in *2004 11th International Conference on Harmonics and Quality of Power*, 2004, pp. 154–159. doi: 10.1109/ichqp.2004.1409345.

Multi-Nodal Energy Systems Modelling Scenarios of South Africa's Power Sector

Ronak Mehta
Department of Electrical Engineering
University of Cape Town
Cape Town, South Africa
mhtron001@myuct.ac.za

David Oyedokun
Department of Electrical Engineering
University of Cape Town
Cape Town, South Africa
davoyedokun@ieee.org

Bruno Merven
Energy Systems Research Group
University of Cape Town
Cape Town, South Africa
brunomerven@gmail.com

Richard Larmour
Department of Electrical Engineering
University of Cape Town
Cape Town, South Africa
richard.larmour@uct.ac.za

***Abstract*— Climate change has brought about a revolution in power sectors worldwide with an urge to increase renewable energy penetration in the generation mix. South Africa, which has conventionally been a coal-dependent power generation country, is transitioning to cleaner resources such as solar and wind, which are abundantly available in the country. This large-scale integration of renewable energy in the national grid brings about the need to increase grid flexibility and strengthening to ensure that the country's power demands are adequately met. This paper thus models South Africa's energy mix in the year 2031 according to their respective supply areas as mentioned in Eskom's Integrated Resource Plan (IRP) 2019 and Generation Connection Capacity Assessment (GCCA) 2023 report, using IRENA's FlexTool software and assesses the transmission bottlenecks that the system might encounter. The results indicate a higher share of renewable energy in the future system, improvements in the unmet demand, reduction of carbon dioxide emissions and reductions in renewable energy curtailment with developments in future plant allocations, battery storage capabilities and transmission line expansions (i.e., investing further in upstream network strengthening to harness a higher yield of renewable generation capacity from the greater Cape areas of South Africa).**

Keywords— Energy systems modelling, FlexTool, load shedding, power sector, renewable energy, South Africa

I. INTRODUCTION

Climate change is becoming a huge threat to humanity and a global emergency [1]. We can already see some of its adverse effects with increasing climate uncertainties, heat waves, draughts, floods and many other such events. These have triggered countries worldwide to pledge to reduce their greenhouse gas (GHG) emissions which are a major contributor to global warming by decarbonizing their major polluting sectors [2].

In South Africa, the power sector is the key contributor to the overall emissions in the country, accounting for around 40% (~225 $MtCO_2e$) of overall emissions [3]. This is because South Africa is and has been a coal-dependent power generation country. Fig. 1 [4] indicates this generation plant mix for the year 2021 under ESKOM (South Africa's public electricity utility which supplies approximately 90% of South Africa's electricity and generates roughly 30% of the electricity used in Africa). Fig. 1 shows that around 85% of the country's installed capacity under ESKOM in 2021 was derived from thermal coal fired power plants.

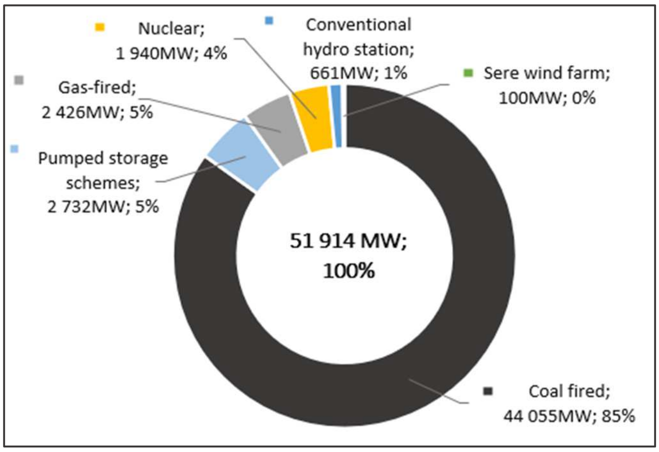

Fig. 1. Eskom's installed generation mix in 2021 (nameplate capacity in MW shown here) [4]

The transition to cleaner, renewable resources will be crucial for the decarbonization of South Africa's power sector. South Africa is abundantly rich in solar and wind resources which can be harnessed to produce electricity in the country. With recent and future improvements in renewable energy penetration and storage capacities, it is likely that the renewable share in the generation mix for South Africa's future power system would increase. This paper thus models South Africa's power system for the year 2031, which is mainly derived from the Integrated Resource Plan (IRP) 2019 [5] and the Transmission Development Plan (TDP) 2022-2031 [6], and analyzes the flexibility and transmission bottlenecks the system might encounter.

II. ENERGY SYSTEMS MODELLING

A. Overview

Energy systems modelling guides the operation of energy systems in conjunction with sector-specific models to provide insights into complex challenges such as climate mitigation responses, ensuring energy security and maintaining grid flexibility [7]. Energy systems modelling of the power sector has been widely used across the globe to assess, simulate, and plan for a future power sector and how it would perform under various energy mix scenarios and different transition pathways [8]-[11].

The study in [9] modelled a 28-node European Union (EU) power network representing 28 EU member states. The PLEXOS framework was used to investigate challenges in the 2030 European power system as the EU transitions towards a low carbon energy system. The study in [10] modelled a 5-node multi-regional model of the Indian power system geared towards energy forecasts of year 2040 to evaluate six different scenarios to assess the effects of battery storage and renewable integration on the Indian power system using the Calliope model framework. The study in [11] modelled a 10-node multi-regional optimization planning model of China's power sector using the linear programming solver of the General Algebraic Modelling System (GAMS) to optimize China's future power sector in meeting demand whilst considering the impact of GHG emissions and carbon mitigation policy scenario. The energy modelling approach in this paper was adapted from [9,10, and 11], based on a widely accepted methodology and used IRENA's FlexTool modelling tool for the implementation, modelling and analyses of South Africa's power sector for the year 2031.

B. Coal-fired plants in South Africa

South Africa's power sector is largely coal-based and has a large fleet of fifteen coal-fired power plants which are mainly located in Mpumalanga. However, a lot of these plants are ageing and are scheduled for decommissioning in the next decade. Table I [12] shows a list of the nominal capacities (also known as sent-out capacity which refers to the difference between the "nameplate" installed capacity and auxiliary power consumption used to operate the plant and its machinery) of coal plants in South Africa according to their location per supply area from 2021 to 2031. This indicates the decommissioning of six coal plants by the year 2031 namely Arnot, Camden, Grootvlei, Hendrina, Komati, and Kriel.

TABLE I. COAL PLANT CAPACITIES FROM 2021 – 2031

		Nominal capacity (MW) in the respective years						
Supply area	**Coal plants**	***2021***	***2022***	***2025***	***2026***	***2027***	***2030***	***2031***
Mpumalanga	Arnot	2100	2100	1860	1116	744	0	0
Mpumalanga	Camden	1481	1481	1111	741	370	0	0
Mpumalanga	Duvha	2875	2875	2875	2875	2875	2875	1917
Mpumalanga	Grootvlei	570	570	0	0	0	0	0
Mpumalanga	Hendrina	1140	1098	185	0	0	0	0
Mpumalanga	Kendal	3840	3840	3840	3840	3840	3840	3840
Mpumalanga	Komati	114	114	0	0	0	0	0
Mpumalanga	Kriel	2850	2640	2850	2375	1900	0	0
Mpumalanga	Kusile	2160	2880	4266	4266	4266	4266	4266
Free State	Lethabo	3558	3558	3558	3558	3558	3558	3558
Mpumalanga	Majuba	3843	3807	3843	3843	3843	3843	3843
Limpopo	Matimba	3690	3690	3690	3690	3690	3690	3690
Mpumalanga	Matla	3450	3450	3450	3450	3450	2875	1725
Limpopo	Medupi	4317	4317	4332	4332	4332	4332	4332
Mpumalanga	Tutuka	3510	3510	3510	3510	3510	3510	3510

C. Renewable energy in South Africa

South Africa has huge untapped solar and wind energy potentials which can be harnessed to generate electricity. In 2021, the country had only 6105 MW of total installed capacity of renewable resources procured from Independent Power Producers (IPPs) of which 500 MW were from Concentrated Solar Power (CSP) plants, 2212 MW from solar photovoltaics, 3343 MW from onshore wind plants, and 50 MW from other resources. Fig. 2 shows these capacities alongside a 2031 case as projected in the Integrated Resource Plan (IRP) 2019, which estimates a total renewable energy (RE) mix of 26630 MW by 2031 [5].

Novel techniques and technology are being developed to reduce power delivery loss from inverter-driven generation. This includes optimal power injection theories. By increasing distribution efficiency, technical losses are reduced and in principle generation availability can be seen as increased [13]–[15].

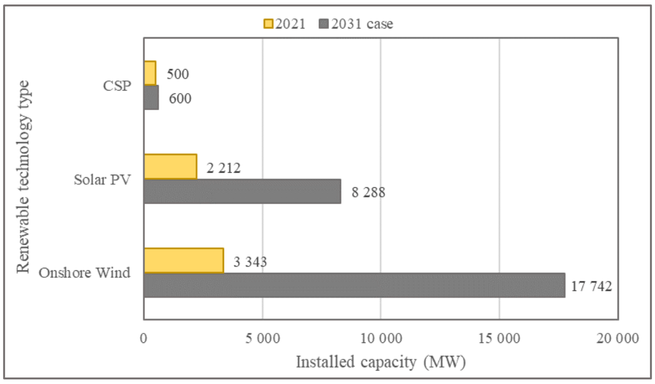

Fig. 2. South Africa's installed renewable capacities in 2021 and 2031 case

D. Electricity demand in South Africa

In 2021, the peak national demand of South Africa was 35004 MW, and it is only set to increase in the future due to rapid increases in economic activity and income, changes in heating, fuel, transportation choices and rising urbanization. The Transmission Development Plan (TDP) 2022-2031 report forecasts a national system peak demand of 42000 MW under the moderate high scenario for the year 2031 [6]. Table II shows the peak demands for each of the supply areas in South Africa for the year 2021 and uses the TDP forecast for 2031.

TABLE II. PEAK SYSTEM DEMAND PER SUPPLY AREA FOR FISCAL YEAR 2021 AND 2031

	Peak demand (MW)	
Supply area	*FY2021*	*FY2031*
Eastern Cape	1584	1900
Free State	1624	1948
Gauteng	10614	12735
Hydra Cluster	205	246
KwaZulu-Natal	6051	7261
Limpopo	2971	3565
Mpumalanga	4223	5067
North West	3280	3935
Northern Cape	685	822
Western Cape	3768	4521
	35004	**42000**

III. MODELLING IN FLEXTOOL

A. Overview

FlexTool is an open-source, node-based energy modelling tool where each node can represent either a region, area or country as seen in Fig. 3 [8].

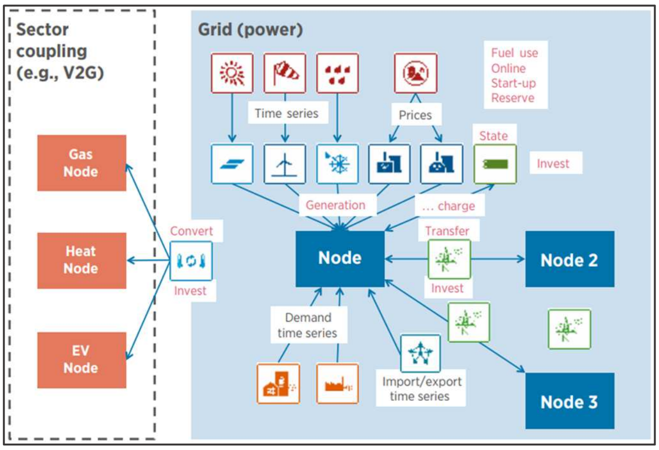

Fig. 3. Overview of energy modelling in FlexTool [8]

The nodes used for modelling and running the simulations in this paper represent South Africa's eleven supply areas as mentioned in the Generation Connection Capacity Assessment (GCCA) 2023 report [16], which included the nine provinces in South Africa, plus the Pelly, and Hydra clusters. However, Pelly was merged with Limpopo (one of the provinces) for this study, due to its proximity to Limpopo and lack of sufficient data to be regarded as a node. Thus, the South African power sector model used for this study comprises a ten-node system (represented by the ten supply areas), with each node having its separate variables such as generation, demand profile and node-to-node transfer connections to name a few.

B. *Useful parameters*

1) *Capacity factor (CF)*

The capacity factor of a generating unit refers to the ratio of the electrical energy produced by this unit for a certain period of time, to the electrical energy that could have been produced at continuous full-power operation during the same period of time [17]. CF is calculated using (1).

$$CF = \frac{Energy\ produced[MWh]}{Capacity[MW] * t[hours]} \tag{1}$$

Where: *Capacity* (in MW) refers to the maximum amount of power that the generating unit can output onto the grid at full capacity and t is the time period in hours for which the CF is calculated, e.g., a month or a year.

As published in [18], the annual capacity factors per supply source in South Africa in 2021 indicated that nuclear plants had the highest capacity factor of 74.6%, followed by coal plants with 54.2%, CSP at 37.8%, wind plants at 35.8% and solar PV plants with a capacity factor of 26.4%.

2) *Surge Impedance Loading (SIL)*

Surge Impedance Loading is defined as the power in which the reactive power of the transmission line becomes zero [21]. i.e., the reactive power generated by the shunt capacitance is consumed by the series inductance of the line. Equation (2) shows how SIL is calculated.

$$SIL = V_0^2 / Z_C \tag{2}$$

$$Z_C = \sqrt{(L / C)} \tag{3}$$

Where: V_0 is the rated line voltage in volts (V), Z_C is the characteristic impedance of the line in ohms (Ω), L is the line inductance in henry (H) and C is line capacitance in farads (F).

IV. Case Studies and Simulation Protocol

A. *Case studies*

The objective was to model different cases which might occur in a South African 2031 power sector scenario and analyze these results to better understand how the interconnected system might behave. Four cases studies were developed and in all the cases, the total renewable energy capacity that was added to the system by 2031 had been kept the same in line with IRP2019 [5]. However, the allocation of these capacities to the supply areas was altered based on either connection capacity constraints or transmission line expansions. Also, the grid was simplified using connectors greater than 110 kV between nodes (supply areas) and by applying the SIL conversion calculation to get the SIL ratings of the high-voltage transmission lines. The four cases studies that were developed are as follows:

1) *Case study I (CS I)*

This case considered the grid connection capacity constraint as documented in the GCCA report [9], which states that the Northern Cape is highly constrained, and no new capacity can be added to this supply area without further grid strengthening. The allocation of renewable capacities in this case study was based on the rank of solar and wind capacity factors per supply area and the connection capacity available within that area. i.e., for solar PV allocation, Northern Cape has the best solar capacity factor of ~30.3%, but does not have any available connection capacity, and thus no new solar PV plant would be allocated to Northern Cape. Instead, the allocation criteria would move to the next best supply area for solar which is North-West with a solar capacity factor of ~30.1% and an available connection capacity of 3470 MW [16]. Thus, from the proposed 6076 MW of new solar capacity by 2031 [5], 3470 MW would be allocated to North-West. This process continued until all of the proposed solar capacity had been allocated and then it moved to allocate the proposed wind capacities with similar criteria. This case also does not include any battery storage capacity for the system. In summary, CS I was a case without transmission line expansion and no battery storage.

2) *Case study II (CS II)*

This case considered the upstream strengthening of transmission lines to unlock more connection capacities in the greater Cape areas. The proposed transmission line expansions included in this study are:

- One 400kV line from Northern Cape to Hydra-cluster.
- One 765kV line from Northern Cape to North-West.
- One 765kV line from Northern Cape to Western Cape
- One 765kV line from Western Cape to Hydra cluster.
- One 765kV line from Eastern Cape to Hydra cluster.
- One 765kV line from Hydra cluster to Free state.
- One 765kV line from Free State to Gauteng.

The allocation criteria of renewable capacities in this case study were similar to that in CS I which was based on the rank of solar and wind capacity factors per supply area and the connection capacity available within that area. However, with these additional connection capacities, more renewable plants would be located in regions with high-capacity factors unlike the trade-offs in CS I due to the connection constraints. i.e., for solar PV allocation, Northern Cape would be allocated first due to its high solar capacity factor of ~30.3%, and availability of additional connection capacity. This process then continued until all of the proposed solar capacity had been allocated and then it moved to allocate the proposed wind capacities with similar criteria. This case also does not include any battery storage capacity for the system. In summary, CS II was a case with transmission line expansion but no battery storage.

3) Case study III (CS III)

This case had similar parameters to CS II in terms of RE allocation and transmission expansion. However, it also included battery storage in the system. Battery storage was allocated to regions that had installed solar PV plants. This study allocated a total of 2000 MW of battery storage capacity as proposed in IRP2019 [5] dividing it according to each supply area's installed solar capacity contribution. In summary, CS III was a case with transmission line expansion and 2000 MW of battery storage capacity.

4) Case study III-Alt (CS III-Alt)

This case was an alternate scenario of CS III in terms of its battery storage capacity. This case allocated a total of 3500 MW of battery storage capacity dividing it according to each supply area's installed solar capacity contribution. In summary, CS III-Alt was a case with transmission line expansion and 3500 MW of battery storage capacity.

Table III illustrates a summary of the dependencies and linkages between cases per category i.e., it shows that CS III and CS III-Alt models use the same parameters for RE allocation and transmission (Tx) expansion as developed in CS II but have different battery storage capacities.

TABLE III. SUMMARY OF CASE DEPENDENCIES PER CATEGORY

	Category modelled in case #		
Cases	*RE allocation*	*Tx expansion*	*Battery storage*
CS I	CS I	✕	✕
CS II	CS II	CS II	✕
CS III	CS II	CS II	CS III (2000MW)
CS III-Alt	CS II	CS II	CS III-Alt (3500MW)

B. Simulation protocol

The hourly generation profiles for each of the cases were obtained as one of the outcomes from the FlexTool simulation. For this study, the analysis of the hourly profiles was done for the worst week in the year of simulation (2031) for each of the cases. The worst week was the one which accounted for the most amount of load shedding.

The other outcomes from the FlexTool simulation that were analyzed in this paper included Variable Renewable Energy (VRE) share, VRE curtailment, load shedding and carbon dioxide (CO_2) emissions. These were analyzed for each of the cases and discussed in the following chapter.

V. RESULTS AND DISCUSSIONS

A. Hourly profiles for the worst week

1) Hourly profile for base case 2021

The worst week in the base case 2021 was week 23 (the first week of June) which accounted for roughly 38% of the total loss of load for the year. In the 2021 base case, we used the monthly availability factors for each of the coal power plants as reported in [19]. The maximum hourly loss of load for the worst week was 3413 MW as seen by the bright red spike in Fig. 4 at hour 3618, and most of it was caused due to lack of enough generation capacity (both from coal and RE plants) especially during the evening peak. It is also seen that a lot more of the peaking Open Cycle Gas Turbine (OCGT) plants are running during this week to compensate for the lack of generation capacity from coal and renewable plants. Week 23 will be the reference week for all the case studies to follow.

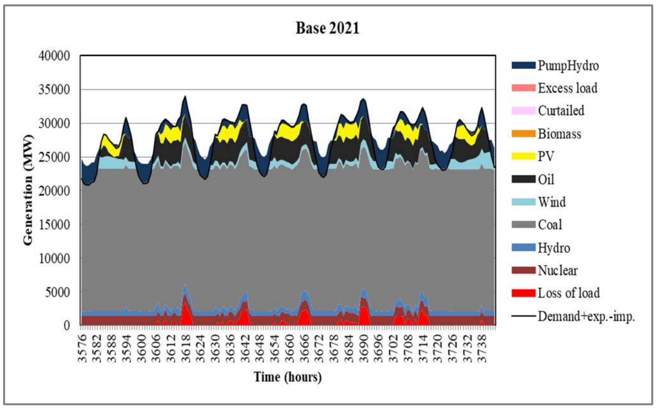

Fig. 4. Hourly profile of the worst week in 2021

2) Hourly profile for CS I

Week 23 in CS I, accounted for roughly 23% of the total loss of load for the year. The maximum hourly loss of load for this week was 1441 MW as seen by the bright red spike in Fig. 5 at hour 3690. It is also seen that due to the increase in generation capacity in 2031, loss of load has significantly reduced. However, due to the lack of transmission expansion and lack of batteries, there is still some unmet demand especially during the evening peaks.

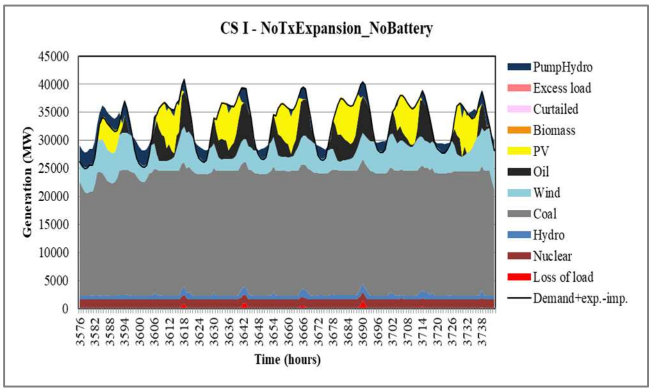

Fig. 5. Hourly profile of week 23 in CS I

3) Hourly profile for CS II

Week 23 (the worst week) in CS II accounted for roughly 43% of the total loss of load for the year. The maximum hourly loss of load for this week was 2841 MW as seen by the bright red spike in Fig. 6 at hour 3618. Week 23 (the first week of June) was seen as the worst week having unmet evening peak demand for most of the cases due to a couple of reasons. Firstly, June to August are winter months in South Africa, and thus, peak demand increases during evening hours due to the increased usage of heaters and geysers. Also, wind and solar capacity factors are at the lowest during these three winter months which add to a lower generation capacity than in summer months, especially without a battery storage option available as is the case for CS II.

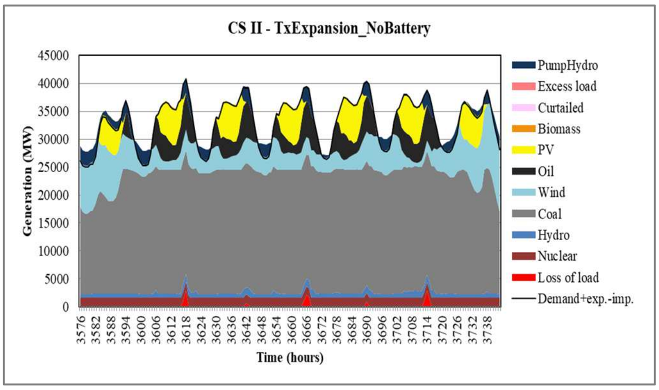

Fig. 6. Hourly profile of week23(worst week) in CS II

4) *Hourly profile for CS III-Alt*

It can be seen from Fig. 7 that for CS III-Alt, there isn't any loss of load during its worst week (week 23). This is because of the addition of battery storage capacity, which can be charged up during the daylight hours and discharged during the evening peak to meet the high winter peak demands of South Africa.

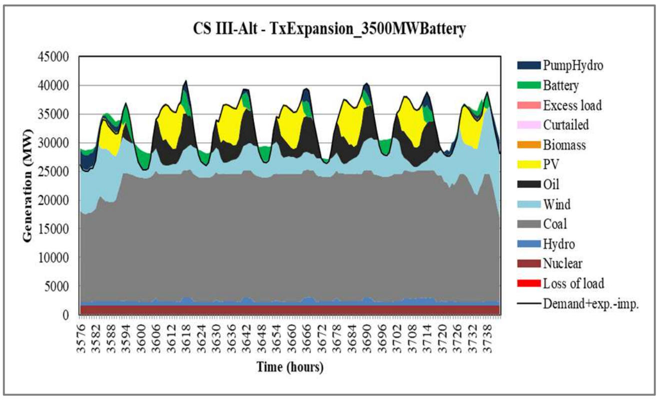

Fig. 7. Hourly profile of week23 in CS III-Alt

Having seen the hourly profiles for the 2031 cases, further comparisons based on various parameters can be conducted. These parameters include but are not limited to the following.

B. *Variable Renewable Energy (VRE) share*

The VRE share refers to the amount of renewable energy contributing to the electricity mix of that system for that particular year. The VRE share for this study takes into account all renewable energies including hydro. Fig. 8 shows that in 2021, the VRE share was just 12% and it is expected to increase to around 30% by 2031. Cases I to III-Alt, all have the same amount of installed RE capacity for 2031, however, Case I differs slightly (less) from the others due to its location of RE plants in lower yield supply areas due to the connection capacity constraint placed on CS I.

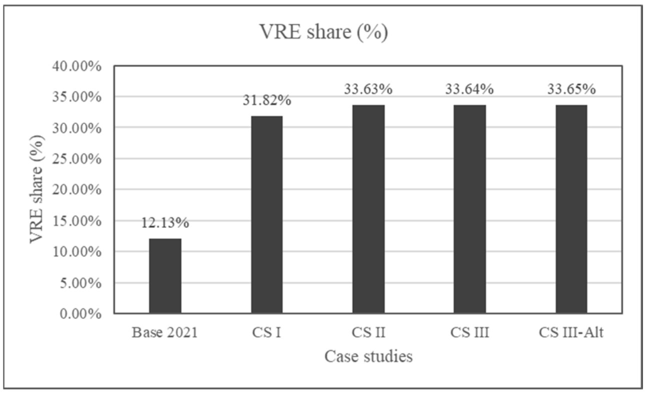

Fig. 8. Comparison of VRE share per case study

C. *VRE curtailment*

VRE curtailment refers to the deliberate reduction of power generation from renewable plants to balance energy demand and supply [20]. Curtailment can also occur due to a transmission constraint. It can be seen from Fig. 9 that base case 2021 and CS I did not have any VRE curtailment. It is also evident that curtailment is significantly reduced with the addition of battery storage as seen from comparing CS II to CS III and CSIII-Alt.

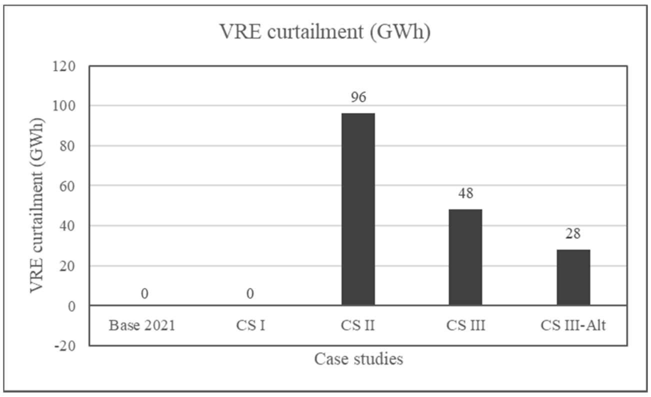

Fig. 9. Comparison of VRE Curtailment per case study

D. *Load shedding*

Load shedding refers to the systematic reduction of system load in order to balance the demand and supply of the system. Whereas loss of load is the unserved/unmet demand of the system. Fig. 10 indicates the comparison of loss of load due to load shedding in all four of the case studies.

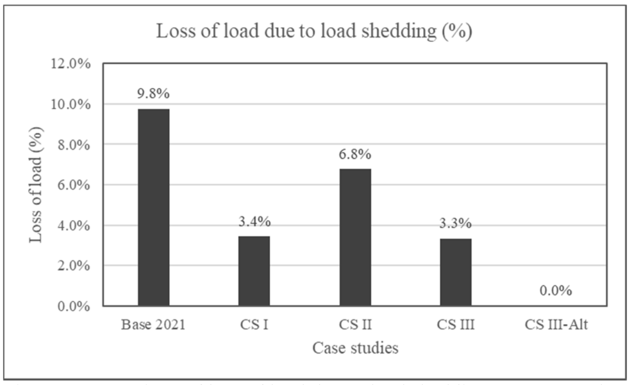

Fig. 10. Comparison of loss of load due to load shedding per case study

E. *Carbon dioxide emissions*

Information about the carbon dioxide emissions of a system is crucial in highlighting how clean a country's generation mix is. Fig. 11 indicates a declining trend of CO_2 emissions with an increase in the renewable energy share for future 2031 scenarios.

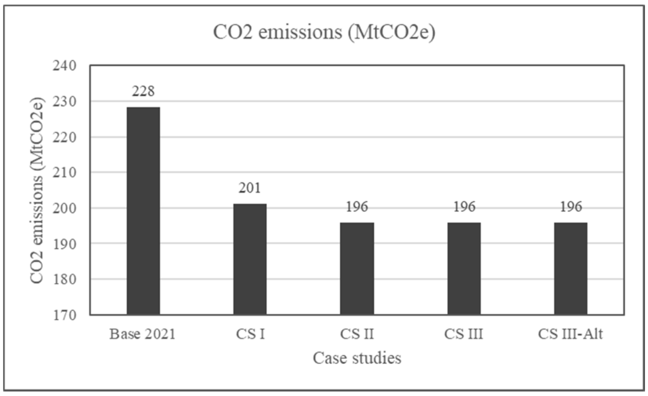

Fig. 11. Comparison of CO_2 emissions per case study

VI. CONCLUSION

In this paper, the authors proposed and analyzed the 2031 South African power system energy mix using energy systems modelling in FlexTool. Simulation of the case studies considered various combinations of RE plant allocations, transmission line expansions and battery storage capabilities which would assist future grid planners to better understand how the load dynamics can be met with a generation mix biased towards renewable energy. The results indicated a higher share of renewable energy in the energy mix for 2031, reduced loss of load due to load shedding (from 6.8% in CS II to no loss of load in CS III-Alt) and reduced carbon dioxide emissions from the power sector from all the cases as compared to the 2021 base case. It also highlighted the importance of battery storage capacities as seen from CS III and CS III-Alt in minimizing VRE curtailment and unlocking additional capacity to meet the country's demand, especially during the evening peaks, which was also aided by strategic RE allocation and transmission expansion to further unlock additional grid capacity especially in the greater Cape areas. Cost-benefit analysis was excluded from this paper, but it remains the subject of ongoing research, and a further work incorporates conducting a power systems analysis in DigSILENT to test for grid stability of the system.

ACKNOWLEDGMENT

The authors are grateful to the Department of Electrical Engineering, University of Cape Town and Energy Systems Research Group for proving the funds and infrastructure to carry out this research.

REFERENCES

[1] "The Paris Agreement," United Nations Climate Change Conference (COP21), 2015. https://www.un.org/en/climatechange/paris-agreement (accessed Sep. 26, 2022).

[2] National Aeronautical and Space Administration, "The Effects of Climate Change," 2022. https://climate.nasa.gov/effects/ (accessed Oct. 13, 2022).

[3] National Business Initiative, "DECARBONISING SOUTH AFRICA'S POWER SYSTEM," *Just Transition and Climate pathways study for South Africa*, Accessed: Oct. 19, 2021. [Online]. Available: https://www.nbi.org.za/wp-content/uploads/2021/08/NBI-Transition-Chapter-Decarbonising-SA-power-11-Aug-2021.pdf.

[4] Eskom Holdings Limited, "GENERATION PLANT MIX," Eskom Fact Sheet, 2021, Accessed: Apr. 07, 2022. [Online]. Available: www.eskom.co.za.

[5] Department of Mineral Resources and Energy, "INTERGRATED RESOURCE PLAN," 2019. Accessed: Oct. 19, 2021. [Online]. Available: http://www.energy.gov.za/IRP/2019/IRP-2019.pdf.

[6] Eskom Holdings Limited, "The Eskom Transmission Development Plan 2022 - 2031," Eskom Transmission: Presentations, 2021. https://www.eskom.co.za/eskom-divisions/tx/transmission-lines/transmission-development-plans/ (accessed May 17, 2022).

[7] M. Ihlemann et al., "SpineOpt: A flexible open-source energy system modelling framework," Energy Strateg. Rev., vol. 43, p. 100902, Sep. 2022, doi: 10.1016/J.ESR.2022.100902.

[8] IRENA FlexTool, "Power system flexibility for the energy transition," IRENA publications, 2018. https://www.irena.org/publications/2018/Nov/Power-system-flexibility-for-the-energy-transition (accessed May 22, 2022).

[9] S. Collins, J. P. Deane, and B. Ó Gallachóir, "Adding value to EU energy policy analysis using a multi-model approach with an EU-28 electricity dispatch model," Energy, vol. 130, pp. 433–447, Jul. 2017, doi: 10.1016/J.ENERGY.2017.05.010.

[10] P. Laha and B. Chakraborty, "Cost optimal combinations of storage technologies for maximizing renewable integration in Indian power system by 2040: Multi-region approach," Renew. Energy, vol. 179, pp. 233–247, Dec. 2021, doi: 10.1016/J.RENENE.2021.07.027.

[11] R. Cheng, Z. Xu, P. Liu, Z. Wang, Z. Li, and I. Jones, "A multi-region optimization planning model for China's power sector," Appl. Energy, vol. 137, pp. 413–426, Jan. 2015, doi: 10.1016/J.APENERGY.2014.10.023.

[12] Eskom Holdings Limited, "Powerplant decommissioning dates," Accessed: Sep. 29, 2022. [Online]. Available: https://cer.org.za/wp-content/uploads/2020/08/Annexure-6.pdf.

[13] G. H. Gabriels, M. O. Windapo, D. T. O. Oyedokun, and S. Ruggeri, "Proposed framework for integration of optimal current injection and multi-agent control of the LV distribution network," 6th IEEE Int. Energy Conf. ENERGYCon 2020, pp. 521–526, Sep. 2020, doi: 10.1109/ENERGYCON48941.2020.9236499.

[14] G. H. Gabriels, D. T. O. Oyedokun, and S. Ruggeri, "Realtime thévenin equivalent impedance at a PCC in the Italian power grid," 2020 Int. SAUPEC/RobMech/PRASA Conf. SAUPEC/RobMech/PRASA 2020, Jan. 2020, doi: 10.1109/SAUPEC/ROBMECH/PRASA48453.2020.9040924.

[15] M. Malengret and C. T. Gaunt, "Active Currents, Power Factor, and Apparent Power for Practical Power Delivery Systems," IEEE Access, vol. 8, pp. 133095–133113, 2020, doi: 10.1109/ACCESS.2020.3010638.

[16] Eskom Holdings Limited, "Transmission Generation connection capacity assessment of the 2023 transmission network (GCCA - 2023) - Phase 2," GCCA 2023: Transmission Network, 2021. https://www.eskom.co.za/Whatweredoing/GCCAReport/Pages/GCCA_2023_Report.aspx (accessed Oct. 27, 2021).

[17] United States Nuclear Regulatory Commission, "Capacity Factor (net)," 2021. https://www.nrc.gov/reading-rm/basic-ref/glossary/capacity-factor-net.html (accessed Sep. 29, 2022).

[18] W. Pierce and B. Ferreira, "Statistics of utility-scale power generation in South Africa in 2021," CSIR Energy Cent., 2022.

[19] S. Comrie, "The collapse of old king coal (part 1)," amaBhungane, 2022. https://amabhungane.org/stories/220928-the-collapse-of-old-king-coal/ (accessed Oct. 15, 2022).

[20] L. Bird, J. Cochran, and X. Wang, "Wind and Solar Energy Curtailment: Experience and Practices in the United States," Natl. Renew. Energy Lab., 2014, Accessed: Oct. 01, 2022. [Online]. Available: www.nrel.gov/publications.

[21] P. Kundur, "Power system stability and control," McGraw-Hill, 1994.

Techno-Economic Analysis of Solar-PV/Battery System for a Foundry Company

Talent Duma
Energy Research Centre
Council for Scientific and Industrial Research
Pretoria, South Africa
tduma@csir.co.za

Bonani Seteni
Energy Research Unit
Voltageon
Pretoria, South Africa
bonaniseteni@gmail.com

Oliver Dzobo
Department of Electrical & Electronic Engineering Science
University of Johannesburg
Johannesburg, South Africa
oliverd@uj.ac.za

***Abstract*—Continuous increase of electricity cost is placing an enormous pressure on the balance sheet of many businesses in South Africa. In the event of load shedding in 2007, about 170 foundry companies had faced difficult times to remain in business and production slowed down by 47%, which was also linked to the instability of Eskom supply and high electricity charges. Now recent support from the South African government for "self-generation" without a license, encourages investments for small-scale embedded generation. However, the issue of solar energy being intermittent is still a concern. Therefore, a battery energy storage system (BESS) is a plausible enabler to be paired with a solar PV system. In this paper, a foundry company located in Johannesburg referred to as "foundry$_{xyz}$" for anonymity is used as a case study to investigate the performance-cost analysis of a solar PV paired with BESS. A System Advisor Model (SAM) was used to design and model two systems (a 547 kWdc solar PV and a 990 kWdc/LiFePO4 battery system). The electricity bill without the solar PV/LiFePO4 battery system for the foundry is R1 746 855 annually. However, the total savings with a 990 kWdc solar PV/LiFePO4 battery system is R 1 228 996 annually reflecting a cost saving of 70.35% for the company's selected load profile.**

Keywords— Solar PV, battery, demand charges, peak shaving, energy cost saving

I. Introduction

The World Bank's energy price index increased to the 26th percentile between January and April of 2022, on top of a 50th percentile increase between January 2020 and December 2021 [1]. This surge is reflected by a sharp price increase in coal as South Africa's primary source of electricity[2]. The high cost of coal supply, operations, and maintenance costs from Eskom results in escalating electricity charges annually, crippling the energy intensive foundry industry. Large industrial consumers such as foundries, are mostly charged on a combination of the fixed charge (Rand/month), demand charge (Rand/kVA), network access charge (Rand/kVA) and energy charge (R/kWh) with Time-of-Use (peak, standard and off-peak) tariff [3]. These charges combined contribute significantly on the foundry's electricity bill. Generally, the monthly bill should consists of basic electricity charges for the total amount of electricity used throughout the billing period and peak demand charges [4]. According to the National Renewable Energy Laboratory (NREL), demand charges alone often account for approximately 30th to 70th percentile of the customer's bill [5]. This means manufacturing and industrial customers such as foundries with seasonal high loads or spikey "demand peak" profiles are hit harder.

Now solar PV system alone can reduce grid dependency whilst reducing the electricity bill. However, pairing solar PV with BESS has additional benefits; not only increases energy/cost savings but also provides a more resilient supply system. BESS can be charged when electricity is cheaper either by the grid or solar PV plant. For prosumers solar PV is best paired with BESS, to store excess energy during the day and supply the load during the night. However, BESS are not only used for storage but as a battery dispatch model. The battery dispatch modes used for behind-the-meter systems; are the peak-shaving and manual dispatch modes. Battery peak shaving dispatch mode is simply used to reduce peak power demand (kW) from the 'Eskom grid' during 24-hours, thus avoiding peak demand penalties [6]. Generally, peak shaving flattens and level off-peak loads, eliminating or reducing the short-term high spikes [7].

When using an on-site battery energy storage system for peak shaving as shown in Fig. 1, you simply discharge during the most expensive periods during the day (indicated by the

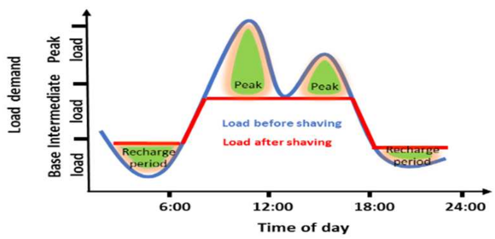

Fig. 1: A load profile before and after peak shaving. [7]

red line in Fig.1) thus eliminating paying peak demand charges. The blue line in Fig.1 indicates the peaks experienced by the load, where the consumer will be penalized by the utility in the monthly electricity bill. Solar PV and lithium ion batteries are a preferred method for peak shaving [8] [9].This is because this battery type is dispatchable and can be strategically configured to charge or discharge during optimal times towards eliminating or reducing the short-term demand charges [10]. The algorithm learns the customer's load profile, forecast peak demand, and alternate from the grid to the LIB system when required. The algorithm assures that no power above a predetermined limit will be drawn from the grid or solar PV system to the battery system until the additional demand is over [11]. The solar PV system combined with a lithium ion battery is silent, clean, requires no human intervention, and does not compel consumers to choose between running important equipment and paying excessive demand costs [11]. This study conducted a performance-cost analysis of a solar PV paired with a lithium iron phosphate battery (LiFePO4) for foundry$_{xyz}$. To offer a viable energy supply system, avoid peak demand penalties and achieve high-cost savings. A System Advisor Model (SAM) was used to design and model two systems (a 547 kWdc solar PV and a 990 kWdc/LiFePO4 battery system).

II. System Overview

A. *Solar-PV/battery storage system design*

This section provides an overview for the design of solar PV paired with a lithium iron phosphate system, outlines mathematical and cost model. Fig.2 shows a line diagram of a grid-tied solar PV/LiFePO4 battery system for a foundry. The system comprises of three energy sources (utility grid, solar PV, and LiFePO4 battery storage system). The sources are set to supply the foundry load using the algorithm shown in Fig.3 Since solar PV/$LiFePO_4$ system supply direct current (DC), an inverter is required to covert DC power to AC power for the foundry load. The system is DC-coupled as shown in Fig.3, because it connects the solar PV/$LiFePO_4$ battery system to a DC bus. DC-coupling is preferred for small-scale systems while alternating current (AC) coupling is best for large-scale systems. This system is designed to supply about 9% of the foundry load and not the entire foundry, because of limited roof space for solar PV installation.

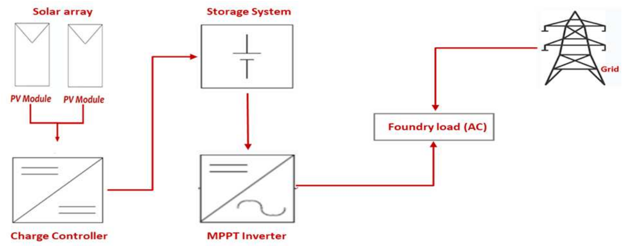

Fig. 2: Single line diagram of a grid-tied solar PV/LiFePO4 battery system.

Although the system is grid-tied, the battery will be charged using excess power from the solar PV system and not from the grid. The grid supplies power to the load, when the solar PV output is below the load demand, ensuring continues supply.

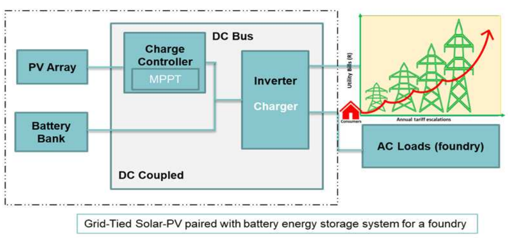

Fig. 3: DC coupled grid-tied solar/LiFePoO4 battery system design.

In this case the battery discharges only when the load exceeds the solar PV system output. The accuracy of designing and modelling a dependable solar-PV system depends on thorough understanding of the load profile. It is therefore important to evaluate the load consumption data to avoid oversizing or under sizing the supply system. The load profile used in this study has an average peak demand of 288 kW and 785 062 kWh of annual energy consumed. Detailed profile of the load is explained in section III. Fig. 5 shows a system flow chart for scheduling the grid-tied solar PV/$LiFePO_4$ system. A system algorithm is important to ensure a constant supply of energy to the load. The load should be supplied continuously as required without any disturbances. The control method will use the available energy source in a cost-effective manner. When the solar-PV system is unavailable the utility grid will supply the load. The night load will be supplied by the excess energy from the battery and grid system. The system is grid-tied, providing a constant supply to the load when solar/battery power is not available. Both the solar-PV/battery system sizing and modelling was done using a mathematical model and SAM.

B. *Mathematical and cost modelling*

In Johannesburg, the average daily solar radiation is approximately 6.5kWh/m^2 per day with a clearness index of about 0,74 as shown in Fig. 3. Clearness index (assess the clearness of the atmosphere) is a number between 0 and 1 and it demonstrate the fraction of the solar radiation hitting through the atmosphere to hit the earth's surface [12].
The following equations “(1)” to can be used to determine the monthly average clearness index for any site when checking ideal location for solar PV installation[12].

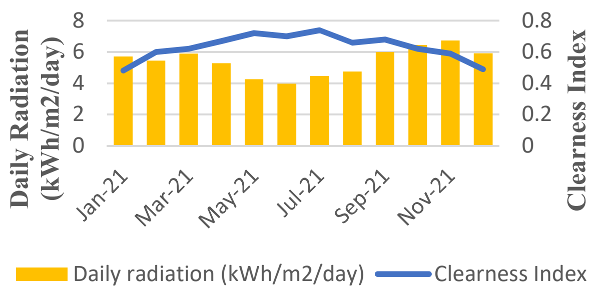

Fig. 4: Average solar radiations vs clearness index for the foundry location.

$$Kt = \frac{\text{Have}}{\text{Ho(ave)}} \tag{1}$$

$$\text{Where,}\ \ \text{Have} = \frac{\text{kWh/m2}}{\text{Day}} \tag{2}$$

That is, H_{ave} is the monthly average radiation on the horizontal surface of the earth [kWh/m^2/day]

$$\text{Ho(ave)} = \frac{\text{kWh/m2}}{\text{Day}} \tag{3}$$

That is, $H_{o(ave)}$ is the horizontal radiation, meaning the radiation on a horizontal surface at the top of the earth's atmosphere [kWh/m^2/day] [12].

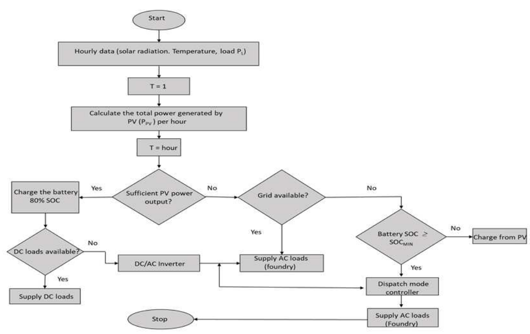

Fig. 5: Flowchart for scheduling the grid-tied solar PV/$LiFePO_4$ battery system.

The interrelations between factors defining PV system sizing are not limited to climate location, capital cost, area available, inverter characteristics, Orientation, and PV/Inverter cost ratio [13]. Sizing a solar PV system accurately is critical when doing financial modelling, to avoid over or under-sizing your system. Oversizing or under-sizing your system greatly impacts the performance of the system inverter [14]. When calculating solar PV kWdc capacity, it must be able to offset the energy consumption or reduce dependency from the grid during the day. In this study calculating the size of the PV array, key variables were considered: daily/monthly load profile (usage), sun-hours and derate factor (considers the system electrical losses during DC/AC conversion) as shown in equation "(4)".

$$\textbf{Solar PVarray size in kWdc} = \frac{\textbf{Usage kWh per Month}}{[\textbf{Sun} - \textbf{hours per month}] * [\textbf{Derate factor of } \mathbf{0,77}]} \quad (4)$$

Where, Monthly usage in kWh is obtained from the historical energy bill. Sun-hours per month is a number of sun-hours per day, according to the location, multiplied by 30 days of the month. Derate factor is considered the electrical losses from the system's DC/AC conversion. [14]

$$\textbf{Electricity usage offset} = \frac{\textbf{Annual Energy produced by solar PV}}{\textbf{Annual energy used}} \quad (5)$$

Now the electrical usage offset in "(5)"does not determine how much is to be paid to the utility company, after the solar PV plant because billing methods used for utility bills depend on the type of consumers (Industrial, commercial, or domestic) and tariff structures. "How you are billed, does affect how much you will pay for electricity" [14]. About 547 kWdc of solar system size was calculated to meet a load with a monthly energy usage averaging at about 60 000 kWh and average annual peak demand of about 288 kW using "(4)". This system's estimated annual energy generated is 924 672 kWh and the load consumed about 785 062 kWh per annum. However, the 547 kWdc rooftop plant does not have enough excess energy to integrate a battery, therefore a 990 kWdc solar PV plant was calculated and modelled to integrate the $LiFePO_4$ battery energy storage for peak shaving dispatch model.

TABLE I shows an overview of the technical specifications of a mono-crystalline module used. The selection of using a monocrystalline solar module instead of a polycrystalline is because mono-c-Si cells are more efficient because they are manufactured from a single source of silicon. Although thin-film technology is less expensive than mono or poly crystalline panels, however it is less efficient [15]. This design and modeling of the solar-PV system focuses on an efficient system whilst reducing energy cost for the foundry. Number of modules was calculated using "(6)"

$$\textbf{No of modules} = \frac{\textbf{Solar PV array rated capacity kW}}{\textbf{Module rated power kW}} \quad (6)$$

Where, Solar PV array rated capacity is calculated at the initial design of the system according to the load using equation "(4)". Module rated capacity is the power rating of the module according to the datasheet from the manufacture.

The optimal yield of a grid-tied solar-PV system depends on the relative size of the solar-PV and inverter rating as shown in TABLE II.

TABLE I: TECHNICAL CRITERIA OF THE MODULE

Mono-crystalline module (mono-c-Si cells)	
Parameter	**Value(s)**
Rated power	500 Wdc
Nominal efficiency	21.38 %
Max power voltage	43.8 Vdc
Max power current	11.7 Adc
Open circuit voltage	51.7 Vdc
Short circuit current	12.3 Adc
Total irradiance, temperature	1000 W/m2, Cell temperature -25° C

TABLE II: TECHNICAL CRITERIA OF AN INVERTER

Parameter	Value
Max. AC power	60033 Wac
Max. DC power	61147 Wac
Nominal AC voltage	480 Vac
Nominal DC voltage	720 Vdc
Max. DC voltage	800 Vdc
Max. DC current	84 Adc
Weighted efficiency	98.2%
MPPT	1

When an inverter is rated at a lower capacity (undersized) than the solar-PV array, the inverter will be overloading. Under sizing can lead to inverter clipping. Clipping occurs when there is more direct current power being supplied into the inverter than it is rated for. The clipped power is lost when there is no battery energy storage. Oversizing the inverter is only recommended when they are plans to add more solar-PV capacity in future, however before than the inverter will underperform. [14]

On the direct current side, an efficiency (Rs) ratio is considered. Rs is the ratio of the PV array capacity at standard test conditions to rated input DC power to the inverter given by equation "(7)".

$$\mathbf{Rs} = \frac{\mathbf{P(pv.rated)}}{\mathbf{P(inv.rated)}} \quad (7)$$

where, P(pv.rated) is for the rated solar-PV capacity and P(inv.rated) is for the DC rated inverter input power. To remain within safe guidelines when designing the solar PV system, the recommended output power should be up to 30% more than the rated inverter. An undersized system has a DC to AC ratio greater than one. The DC to AC ratio is the ratio of DC current produced by the solar-PV panels, against the AC output of the inverter. [14]

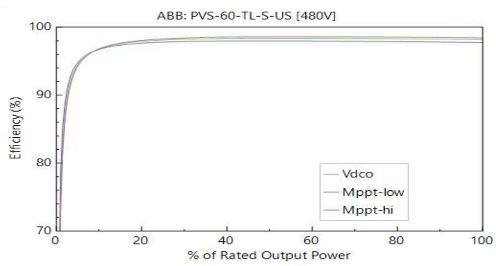

Fig. 6: Inverter efficiency curve.

Fig. 6 shows the performance efficiency of the ABB-PVS-60-TL-S-US [480V] inverter used in this study. Inverter efficiency can range from low, medium, and high, to best represent the ratio of direct current input power to inverter's rated capacity. The selected inverter has a high efficiency of about 98.2%. A high efficiency inverter operates during low insolation levels because of the low self-consumption loss.

TABLE III: BATTERY ENERGY STORAGE SYSTEM SIZING TECHNIQUES

Technical criteria: looks at battery life cycle; operational factors such as charge/discharge rates, temperature, depth of discharge and days of autonomy [18]. Can be defined through dual variables e.g., are the system requirements meet, solar PV curtailment or forecast errors meet by the battery. [19]
Financial criteria: is one of the most used indicators for determining economically, whether a BESS will be coupled with a solar PV system from initial system design. Also assessing the battery's current LCOS and capital cost will determine which battery type is financially viable e.g., Lead acid AGM are more expensive than LiFePO4 battery. Although this is one criterion that often eliminates the coupling of the solar PV/battery systems, it is then important to at least use a combination of the technical and financial indicators for sizing. Financial indicators include but are not limited to capex cost, operation & maintenance (O&M) costs, return on investment (ROI), discount rate, interest rate and net present value (NPV). The levelized cost of storage (LCOS) should be minimized whilst maximizing the NPV to gain a better financial indicator when sizing the battery technology.[18] [19]
Hybrid criteria: current research have been promoting the use of both technical and financial indicators for battery sizing. The approach to combine the two works by optimizing the financial criteria whilst the technical criteria act as a constraint. Basically, the size of the battery system can be determined by minimizing the operating costs and investment cost while restricting the guaranteed reliability. [18] [19]

The maximum efficiency for low, medium, and high efficiency inverters are 84%, 91% and 98%, respectively [16]. Battery energy storage adequate sizing is important when coupling with solar PV system. The size of the battery affects the capital, operations & maintenance costs. Accurate battery sizing can compensate for solar PV forecasting errors. There are three techniques that can be used for battery sizing shown in TABLE III. Three techniques can be used individually or combined to best optimize the system. These are technical, financial and hybrid indicator [17].

Critical functions of battery systems change because of different criteria used for sizing. When using a technical criterion to improve the dynamic characteristic of the solar system, then the battery energy storage system's power capacity plays a crucial role, meaning the rapid speed of delivering power by the battery is important than the total energy the battery can supply. Another way to make the energy capacity less critical is by applying an advanced dispatch modes to gain multiple functions thus the battery system will be used more effectively whilst the overall system uses the battery's energy and power capacity efficiently. This study considered the hybrid criteria for battery sizing to obtain both technical and financial benefits for integrating a BESS in a solar PV plant [18].

TABLE IV shows the overview of the capacity and features of the li-ion phosphate battery used in this study. The battery has an estimated desired bank capacity of 1152 kWh given by equation "(8)". The desired bank power of about 288 kWdc is taken from the max. average peak power of the load. The battery has a nominal voltage of 3.6 V at 2.25 Ah cell capacity. The battery has been set to have 1 day of autonomy (supply without being charged by the solar PV plant). Choosing one-day reduces the battery bank size and cost. The battery in this study is designed to charge only from the solar PV system, not the grid with a minimum state of charge (SOC) of 50% and a maximum state of charge at 100%. This SOC controls the battery not to discharge when at minimum and to stop charging at maximum. The battery is set to peak shave the load to maximize the cost savings for the foundry.

TABLE IV: TECHNICAL CRITERIA FOR THE LIFEPO4 BATTERY

Parameter	Value
Nominal bank capacity	1 152 kWh
Nominal bank power	288 kWdc
Nominal bank voltage	500 Vdc
Cell nominal voltage	3.6Vdc
Cell capacity	2.25 Ah
Total number of cells	142
Days of autonomy	1 day
Cells in series	139

$$\mathbf{Cbattery\ capacity} = \mathbf{EL} * \mathbf{DA} \qquad (8)$$

Where, E_L is the average peak load (kW/month), DA is for days of autonomy (supplying the load independently during outages).

III. METHODOLOGY

A. Modelling Procedure

The modelling of the study was done using System Advisor Model, component selection and sizing calculations for both solar PV/LiFePO4 battery system. The model makes use of key input variables as shown in Fig. 7. When the input variables have been established, a 547 kWdc solar PV rooftop plant was calculated using the monthly load profile. A second plant of 990 kWdc capacity was done to be paired with a $LiFePO_4$ battery. This is because the 547 kWdc plant offsets the energy used by the load but does not have enough excess for battery peak shaving dispatch modelling. If the company decides not to include the battery system, the 547 kWdc solar PV plant is enough to provide energy and cost savings. The expected output from the two models includes both the techno-economic ratio of the system and system reliability. Furthermore, the model is optimized by adding peak shaving dispatch mode using a battery, were it shaves the instantaneous spikes from the load. The battery discharging is set to occur only when the load exceeds the solar PV system output (indicated as peaking).

B. Cost Modelling

In system advisor model (SAM),financial evaluation is key in minimizing overall system cost. The potential or

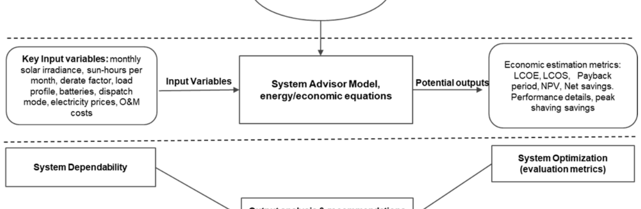

Fig. 7: Procedure for modelling the solar PV/battery system.

expected outputs from the model is shown in Fig. 7 with both technical and cost outputs. The mathematical equations for key output metrics are shown in "(9)" and "(10)" [20].

$$\mathbf{LCOE} = \frac{\mathbf{Total\ lifetime\ cost}}{\mathbf{Total\ lifetime\ output}} \qquad (9)$$

$$= \frac{\sum_{t=1}^{n} \frac{It+Mt+Ft}{(1+r)^t}}{\sum_{t=1}^{n} \frac{Et}{(1+r)^t}}$$

Where, I_t = Investment expenditure in years (Incl. loan); M_t = Operativos & maintenance expeditures; F_t= fuel expenditures in year t; E_t = electricity generation in year t; r = discout rate; n = system life time.

$$\mathbf{NPV} = \frac{\mathbf{Rt}}{\mathbf{(1 + r)^{\wedge}t}} \tag{10}$$

Where, R_t = net cash flow at time t; i = discount rate; t = time of the cash flow.

C. *Load Profile*

Foundry$_{XYZ}$ is a company that was founded in 1991 and expanded in 2001. It is in Boksburg East in Gauteng (South Africa). The company deals with metal casting processes. Its main applications include pumps, railway components, valves, and automotive components. During the energy efficiency audits conducted in 2019, significant energy users identified were the induction furnaces, compressors, fans, and pump motors. The company occupies two sites in one location (site A charged at tariff E and site B is charged at tariff D by Ekurhuleni municipality). This study focused on obtaining energy and cost savings for site A of foundryxyz because of the roof space suitability for solar PV installation. Site A produces automotive parts through metal casting and uses about 785 062 kWh/annum (9% of 9,032,960 kWh total site energy consumption).

Site A is charged at tariff E with a combination of fixed charge (Rand/month), demand charge (Rand/kVA), network access charge (NAC) (Rand/kVA) and energy charge (R/kWh) with Time of Use (TOU: Peak, standard & off-peak charges).

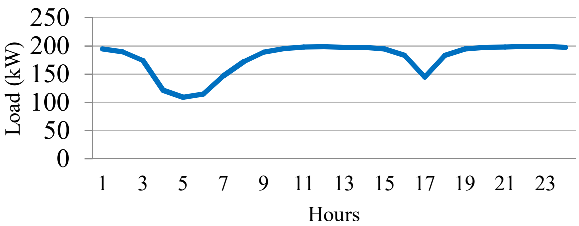

Fig. 8: Daily load profile (kW) for site A.

TABLE V: SUMMARY OF THE LOAD DATA

Average monthly consumption	65 171 kWh
Average monthly peak demand	200 kW
Annual Energy Consumption	782 062 kWh
Annual energy cost	R 1 746 855
Blended energy cost	1.18 R/kWh
Demand charge cost	79.31 R/kVA
Network access charge cost	48.75 R/kVA

Tariff E is for bulk supplies at any voltage with a capacity of > 25kVA and a NAC of < 1 MVA. Foundryxyz is energy intensive with a complex tariff structure, resulting in high electricity bills. Fig. 8 shows the daily load profile for site A of foundryxyz. The profile consists of some of the fans, pumps, and lighting load.

IV. RESULTS AND DISCUSSIONS

This section shows the results of two systems modelled using System Advisor Model (SAM). This was done to identify the optimal system subject to the economic and technical evaluation of the selected foundry site. The 547 kWdc PV system is without a battery bank and the 990 kWdc PV system is paired with the LiFePO4 battery. The objective of this paper is to demonstrate the cost-benefits of installing embedded generation using solar PV and battery peak shaving dispatch mode for foundryxyz.

A. *547 kWdc solar PV system*

The result for a 547 kWdc system is shown in TABLE **VI** with an annual energy yield of about 937 847 kWh. The solar PV system has a reliable performance ratio of 83%. The system will save the foundry (site A) about 46% in energy bill per annum for the first year of operation. The system needs an investment of about R7.2 million with a payback period of only 6.3 years at a LCOE of 77.76 c/kWh. In summer months this system was unable to meet the load demand which could have been due to the increase in ambient temperature in relation to the solar panel output. Therefore, it was than advisable to increase the capacity(990 kWdc) not only for battery pairing but for an energy supply-demand balance.

TABLE VI: RESULTS FOR BOTH SOLAR PV SYSTEMS

Parameters	547 kWdc Values	990 kWdc Values
Annual Energy	937 847 kWh	1 678 756 kWh
Capacity Factor	19.5 %	19.3 %
Energy yield	1712 kWh/kW	1 695 kWh/kW
Performance ratio	83%	83%
Battery roundtrip	-	91.28%
Levelized COE (real)	77.76 c/kWh	89.85 c/kWh
Electricity bill without the	R1 746 855	R 1 746 855
Electricity bill with system	R941 960	R 517 859
Net savings with system	R804 894	R 1 228 996
Percentage energy cost	46%	70.35%
Net present value	R42 584 774	R 58 995 408
Simple payback period	6.3 years	7.5 years
Net capital cost	R7 264 671	R15 507 334

B. *990 kWdc solar-PV paired with $LiFePO_4$ battery*

The result for this system shown in TABLE VI shows an annual energy yield to be about 1 678 756 kWh. The system has a good performance ratio of about 83%. Fig. 9 shows the alternating current (AC) energy from the this system, with excess energy after the load usage. The excess energy is used to charge the battery and be used for peak shaving. The battery roundtrip efficiency is 91.28%, which is the percentage of the energy stored for later use.

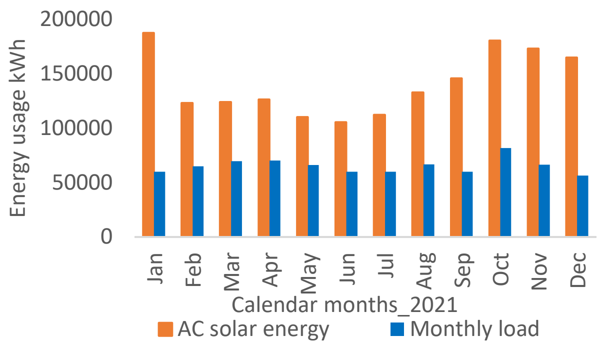

Fig. 9: Energy usage kWh.

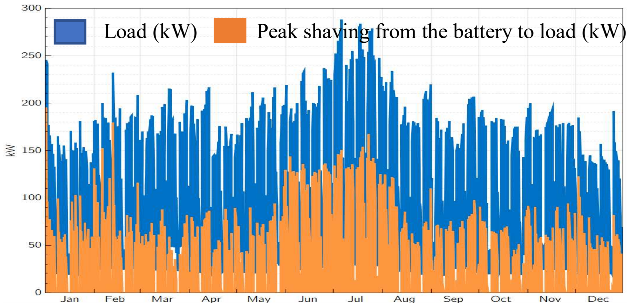

Fig. 10: Battery peak shaving dispatch.

The higher the round-trip efficiency means the less energy loss in the battery storage process [19]. The 990 kWdc solar-PV paired with LiFePO4 battery can save the foundry site A about 70.35% in energy bill per annum. This means the presence of the battery storage system is beneficial when using it for peak shaving. This system needs an investment of about R15 million with a payback period of only 7.5 years at a LCOE of 89.85 c/kWh. The battery system will discharge only when the load exceeds the solar PV system output for peak demand shaving (prolonging the battery lifespan). It uses a one-day look ahead mode (load forecast) as a 'perfect' scenario in attempts to reduce the daily demand peaks using the LiFePO4 battery as indicated in Fig. 10

V. CONCLUSION

In many instances, the battery storage system is excluded from being integrated with solar PV because of its high capital cost or the levelized cost of storage being high. However, they are technical and financial benefits to pairing an intermittent RES like solar PV system with a battery storage system (BESS). This is backed up by the comparisons of the two systems modelled for this business case for the foundry. Solar PV system alone does yield energy-cost savings as shown in TABLE VI but when paired with the LiFePO4 battery, there are increased benefits such as system flexibility, energy security, system stability, and increased electricity bill savings (accurate sizing of the battery for dispatch model reduces the capital, operations & maintenance cost whilst yielding higher bill savings). The pairing of solar PV with BESS (especially lithium ion batteries) should not be hindered by the current high cost associated with it, because such costs are plummeting and policies around feed-in tariffs (selling back to the grid) are improving, making battery energy storage system a good pair with renewables for a more resilient energy system.

ACKNOWLEDGMENT

My gratitude goes to my supervisors Dr B. Seteni and Dr O. Dzobo for their ongoing support and guidance. Thank you to the Council for Scientific and Industrial Research (CSIR) and Foundry$_{XYZ}$ for resource allocation.

REFERENCES

[1] J. G. a. J. Khadan, "The energy shock could sap global growth for years," 2022. [Online]. Available: https://blogs.worldbank .org/developmenttalk/energy-shock-could-sap-global-growth-years.

[2] S. T. Henriques and P. Sharp, "Without coal in the age of steam and dams in the age of electricity: an explanation for the failure of Portugal to industrialize before the Second World War," *European Review of Economic History,* vol. 25, no. 1, pp. 85-105, 2021.

[3] H. Huang, J. T. Fox, F. S. Cannon, S. Komarneni, J. Kulik, and J. Furness, "Binding waste anthracite fines with Si-containing materials as an alternative fuel for foundry cupola furnaces," *Environmental science & technology,* vol. 45, no. 7, pp. 3062-3068, 2011.

[4] K. Jessoe and D. Rapson, "Commercial and industrial demand response under mandatory time-of-use electricity pricing," *The Journal of Industrial Economics,* vol. 63, no. 3, pp. 397-421, 2015.

[5] N. R. Darghouth, R. H. Wiser, G. Barbose, and A. D. Mills, "Net metering and market feedback loops: Exploring the impact of retail rate design on distributed PV deployment," *Applied Energy,* vol. 162, pp. 713-722, 2016.

[6] X. Chen, L. Huang, J. Liu, D. Song, and S. Yang, "Peak shaving benefit assessment considering the joint operation of nuclear and battery energy storage power stations: Hainan case study," *Energy,* vol. 239, p. 121897, 2022.

[7] R. T. de Salis, A. Clarke, Z. Wang, J. Moyne, and D. Tilbury, "Energy storage control for peak shaving in a single building," in *2014 IEEE PES General Meeting| Conference & Exposition*, 2014: IEEE, pp. 1-5.

[8] E. Reihani, M. Motalleb, R. Ghorbani, and L. S. Saoud, "Load peak shaving and power smoothing of a distribution grid with high renewable energy penetration," *Renewable energy,* vol. 86, pp. 1372-1379, 2016.

[9] R. Manojkumar, C. Kumar, S. Ganguly, and J. P. Catalão, "Optimal peak shaving control using dynamic demand and feed-in limits for grid-connected PV sources with batteries," *IEEE Systems Journal,* vol. 15, no. 4, pp. 5560-5570, 2021.

[10] K. H. Chua, H. L. Bong, Y. S. Lim, J. Wong, and L. Wang, "The State-of-the-Arts of Peak Shaving Technologies: A Review," in *2020 International Conference on Smart Grid and Clean Energy Technologies (ICSGCE)*, 2020: IEEE, pp. 162-166.

[11] K. H. Chua, Y. S. Lim, and S. Morris, "Energy storage system for peak shaving," *International Journal of Energy Sector Management,* 2016.

[12] B. A. Aderemi, S. D. Chowdhury, T. O. Olwal, and A. M. Abu-Mahfouz, "Techno-economic feasibility of hybrid solar photovoltaic and battery energy storage power system for a mobile cellular base station in Soshanguve, South Africa," *Energies,* vol. 11, no. 6, p. 1572, 2018.

[13] A. Rahimi, M. Zarghami, M. Vaziri, and S. Vadhva, "A simple and effective approach for peak load shaving using Battery Storage Systems," in *2013 North American Power Symposium (NAPS)*, 2013: IEEE, pp. 1-5.

[14] F. forever, "Lesson 5: Solar inverter oversizing vs. undersizing," 2022. [Online]. Available: https://freedomforever.com/solar-academy/solar-academy-lesson-5-solar-inverter-oversizing-vs-undersizing/.

[15] C. E. C. Nogueira, J. Bedin, R. K. Niedzialkoski, S. N. M. de Souza, and J. C. M. das Neves, "Performance of monocrystalline and polycrystalline solar panels in a water pumping system in Brazil," *Renewable and Sustainable Energy Reviews,* vol. 51, pp. 1610-1616, 2015.

[16] J. D. Mondol, Y. G. Yohanis, and B. Norton, "Optimal sizing of array and inverter for grid-connected photovoltaic systems," *Solar energy,* vol. 80, no. 12, pp. 1517-1539, 2006.

[17] S. X. Chen, H. B. Gooi, and M. Wang, "Sizing of energy storage for microgrids," *IEEE transactions on smart grid,* vol. 3, no. 1, pp. 142-151, 2011.

[18] H. Jia, Y. Mu, and Y. Qi, "A statistical model to determine the capacity of battery–supercapacitor hybrid energy storage system in autonomous microgrid," *International Journal of Electrical Power & Energy Systems,* vol. 54, pp. 516-524, 2014.

[19] D. Agwu, F. Opara, N. Chukwuchekwa, D. Dike, and L. Uzoechi, "Review of Comparative Battery Energy Storage System (BESS) for Energy Storage Applications in Tropical Environment," in *IEEE 3rd International Conference on Electro-Technology for National Development*, 2017.

[20] O. W. o. Energy, "What are LCOE and LACE?," 2022. [Online]. Available: https://www.ourworldofenergy.com/ vignettes.php? type =electrical-power-generation&id=16.

Optimal Placement of a Battery Energy Storage System (BESS) in a Distribution Network

Chukwemeka Emmauel Okafor
Department of Electrical Engineering
University of Cape Town
Cape Town, South Africa

Komla Agbenyo Folly
Department of Electrical Engineering
University of Cape Town
Cape Town, South Africa

Abstract – **This paper focuses on the strategies for the placement of BESS optimally in a power distribution network with both conventional and wind power generations. Battery energy storage systems being flexible and having fast response characteristics could be technically placed in a distribution network for several applications such as peak-shaving, power loss minimization, mitigation of voltage deviations, minimization of congestion, and as an emergency backup for renewable energy generations which are weather dependent for the generation of electricity. For the placement of the BESS, the system costs comprising the costs for the power losses and voltage deviations were used in the formulation of the algorithm for the optimization model. Then, Particle swarm optimization (PSO) and Fmincon MATLAB optimization solver were deployed for the minimization of the objective function. The optimization results from the two methods were used in determining the optimal location of the Battery energy storage system. Moreover, by placing the BESS in the best possible location in the IEEE 33-bus system. Simulation results show that over 50% reduction of the active power losses was achieved, and the magnitude of the voltage at each of the buses of the power distribution network was improved.**
Keywords— Battery energy storage system, Distribution Network, Power losses, Voltage deviations.

I. INTRODUCTION

Over the years, the need for energy security, climate change and sustainability has been the motivating factors responsible for the rise in the quantity of electricity produced by renewable energy sources especially wind and solar photovoltaic. By increasing the penetration level of these energy sources in the power system, the synchronous-based power plants are being reduced. This has led to poor voltage quality, diminished inertia in power system network and significant difference between the peak-loads and the valley loads. The uncertainty together with the intermittent nature of these renewable energy sources (RESs) have driven many researchers into studies and investigations regarding grid level energy storage systems [1]. Many authors have studied the many-sided gains of connecting grid-level energy storage systems in the synchronous and weather-based energy settings [2], [3]. Several research have looked into their roles in the shaving of peak load, regulation of frequency and improvement of transmission and distribution system efficiencies [4]-[7].

However, to maximize the benefits of BESS, it should be economically and efficiently connected to the power system through optimal installation and sizing of the BESS [8]-[11]. For power system frequency and voltage stability, the optimal placement of BESS is of paramount importance [12]. Besides, when BESS is excessively sized, the installation costs are very high [13]. There are several methodologies for finding the optimal location of an energy storage system. These methods could be done analytically, using mathematical programming, exhaustive search (ES), and heuristic techniques (HM) [7].

The best location and capacity of a BESS using the analytical method is determined by solving a set of formulae and algorithms [14]-[17]. During the optimization, predefined constraints both linear and nonlinear are imposed on the process of the optimization and the set of variables and objective function for the best location of the BESS are determined. Using mathematical programming approach, (MP), numerical approaches are adopted in finding the best position optimally for the BESS according to [18]-[22]. MP is also used for solving problems relating to the operation of power systems such as optimal power flow and unit commitment [7]. Some of the methods captured under MP include linear programming, second order cone programming, dynamic programming, and stochastic programming. With the exhaustive search (ES) the best solution could be found in a limited search space with short time frame even for average time problems [7].

Finally, the heuristic method (HM) also known as the artificial intelligence methods could be carried in determining the optimal location without requiring complicating algorithms and much methodological computational processes to know the best location as compared to AM and MP [23]-[25]. Both Genetic algorithm and particle swarm optimization (PSO) being heuristic methods were used to determine the best point for the integration and size of BESS in [12] and [26]. Artificial neural network and PSO were adopted by the authors in the studies in [6] to find the best size and location of a BESS.

This work proposes algorithms for optimal location of BESS in a power distribution network with wind energy generation. The mathematical formulation defined for the best location, minimizes the costs due to active power losses in the transmission lines and the costs of voltage deviations.

The proposed algorithms were tested using modified IEEE 33-bus system. The formulated objective function was solved using particle swarm optimization (PSO) and Fmincon nonlinear MATLAB optimization solver.

This paper is organized as follows: section 2 discusses the problem formulation. Methodology is presented in Section 3, while the simulation results and discussions are provided in section 4 with the conclusion given in section 5.

II. PROBLEM FORMULATION

A. *Objective Function*

The reliability, efficiency, and the power quality of a distribution network (with wind power integration) could be improved by technically placing a BESS in the optimum location.

For optimal placement of the BESS in this paper, the mathematical formulation to be minimized is the distribution system total costs due to active power losses along the lines (C_{PL}), and the voltage regulation costs (C_{VR}). Equation (1) represents the objective function (Fn) while equations (3) and (4) represent the costs due to power losses along the line, the voltage regulation costs.

$$\text{Fn} = \text{Min}\ (C_{sys}) \tag{1}$$

$$C_{sys}= C_{PL} + C_{VR} \tag{2}$$

$$C_{PL}= \sum_{t=1}^{T} \sum_{i=1,j\neq i}^{m}\{(V_i)^2 +(V_j)^2 - 2(V_i)(V_J)(\text{Cos}\ (\delta_i - \delta_j)\}\ \{(G_{ij})\ (\gamma_{loss}) \tag{3}$$

$$C_{VR}= \sum_{t=1}^{T} \sum_{i=1}^{N}(\mid V_i^2 - V_{ref}^2 \mid)^{1/2}\ (\gamma_{VR}) \tag{4}$$

where *Csys* is the distribution system total costs due to active power losses along the lines and voltage regulation costs, C_{PL} is the costs due to active power losses along the lines, C_{VR} is the costs due to voltage regulation, *m*, *N* are the sum of branches and buses, respectively V_i is the per unit voltage at the ith, bus, V_{ref} being the reference voltage is equals 1.0 pu, V_j is the voltage at the jth bus given in pu, G_{ij} is the conductance of the transmission line found between the ith bus and the jth bus, γ_{loss} is the rate of active power loss cost which is 0.284\$/kWh [26] and γ_{VR} is the rate of voltage regulation cost which is 0.142\$/p.u [6].

B. *Constraints*

1) Constraints on the voltage: The constraint equation given in equation (5) is applied to the optimization process. Voltage at each bus is bound to the range which is $\pm 5\%$ of the reference voltage [6], [25].

$$V_{min} \leq V_i \leq V_{max} \tag{5}$$

where V_{min} and V_{max} are the bound limits for the minimum and maximum voltages respectively and V_i is taken as the voltage magnitude at the ith bus.

2) Constraints on the state of charge (SoC): Equation (6) gives the bound charge limits

$$SOC_{min} \leq \text{SOC} \leq SOC_{max} \tag{6}$$

where, SOC_{min} and SOC_{max} are minimum and maximum limits of SOC respectively. These are taken as 20% and 90% for SOC_{min} and SOC_{max} respectively.

3) Constraints imposed on the active and reactive power: The nonlinear active and reactive power constraints are given in equations (7) and (8).

$$\text{P(i) (t)} = V_i\ (t) \sum_{j=1}^{N} V_j(t)(G_{ij}\text{Cos}\theta_{ij}(t) + B_{ij}\text{Sin}\theta_{ij}(t) \tag{7}$$

$$\text{Q(i) (t)} = V_i\ (t) \sum_{j=1}^{N} V_j(t)(G_{ij}Sin\theta_{ij}(t) - B_{ij}\text{Cos}\theta_{ij}(t) \tag{8}$$

where P(i) (t) and Q(i) (t) are the active and the reactive power injected at the ith bus at time (t) respectively. V_i (t) and V_j (t) are the voltages at the ith and jth buses respectively for a time(t). G_{ij} and B_{ij} are the conductance and susceptance between ith and jth bus. θ_{ij}(t) is the power angle between the ith and the jth bus at time (t)

III. METHOLOGY

The best location for placing a BESS in a distribution network with a wind power plant is presented. DIGSILENT Power factory was used for the simulation of the networks and MATLAB for the optimization. Particle Swarm optimization (PSO) technique and Fmincon (nonlinear constraint) MATLAB optimization solver were used in finding the least value of the objective function for the best placement of the battery storage system.

A. Test System

The methodology proposed in this work is tested using an IEEE 33 -bus distribution network (with a wind power plant connected to bus 18). This is shown in Fig 1 and the power plants parameters given in Table 1. The IEEE 33-bus system with the lines and load data is as presented in [26]. The total load on the whole network is 3.715MW.

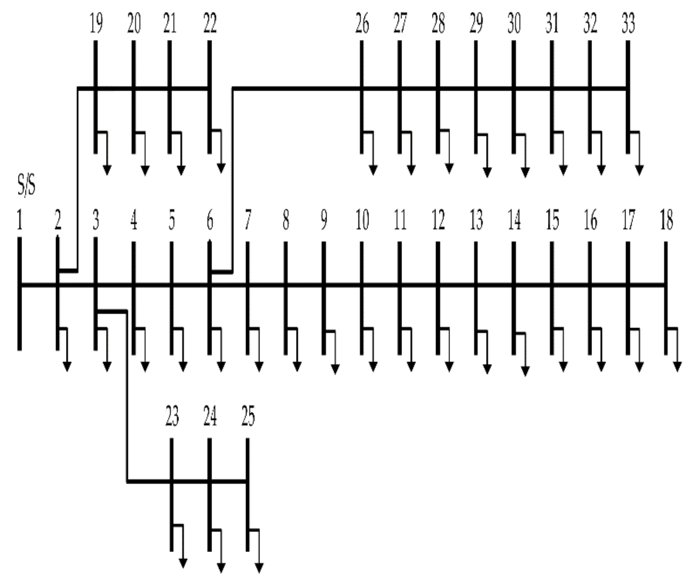

Fig. 1 IEEE 33-bus system [26]

Table 1 Power plants parameters

Type	***Apparent Power (MVA)***	***Real Power (MW)***	***Bus connection***
Synchronous generator	4.37	3.72	1
Wind power plant (WPP)	1.11	1.0	18

B. Particle Swarm Optimization (PSO)

In order to optimize the objective function, particle swarm optimization method is used. Being a population-based search method, it optimizes a problem through computational method [27]. Using he PSO algorithm, its parameters, initial population, initial position, and initial velocity should be initialized. The problem specific bounds are used to find the initial position of the particle which is randomly generated from the uniform distribution. Equations (9) and (10) are deployed to find the position and velocity of particle respectively.

$$p(i)_{new} = \mathrm{p(i)} + V_{p(i)} \quad (9)$$

$$V_{pi} = \mathrm{Wp(i)} + c_1\, r_1(\, p_{best\, i}) \text{ - } \mathrm{p(i)} + c_2 r_2(\, p_{Gbest} \text{- } \mathrm{p(i)}) \quad (10)$$

where V_{pi}, p(i) , $p_{pbest(i)}$, p_{Gbest} are the velocity of the ith particle, the current position of the particle, the personal best position of the particle, the global best position among all particles respectively, w is the inertia weight, c1= c2 = the acceleration factors, and $p(i)_{new}$ being the updated position of the ith particle. The PSO parameters are given in Table 2

Table 2 PSO parameters

PSO parameters	Dimension
Population	200
Inertia weight(maximum)	0.90
Inertia weight (minimum)	0.40
Acceleration factor (c1=c2)	2.05
Lower bound (LB)	0.95
Upper bound (UB)	1.05
Maximum iteration	1000

C. Fmincon MATLAB Optimization Solver

The second method deployed in solving the objective function is the MATLAB optimization solver called Fmincon. Fmincon, is a MATLAB optimization program that finds the minimum of a constrained, nonlinear many-variable function. The conditions (a) to (d) below must be satisfied for the Fmincon solver to give the minimum of the multivariable function.

(a) The constraints in the form of nonlinear inequality constraints must be transformed to C (X) ≤0
(b) The constraints in the form of nonlinear equality constraints must be set as: Ceq (x) = 0
(c) The constraints in the form of linear inequality must be transformed to A(X) ≤ 0
(d) The linear equality constraints of the optimization should be expressed in the form of Aeq(x) = 0

D. Optimization steps for the placement of BESS

The required optimization steps for finding the best location for the BESS for the studied network are summarised in the six steps given below. The corresponding flow chart for the proposed approach is presented in Fig. 2.

(1) Input network data and algorithm parameters.
(2) Choose one candidate location for the 1.55MW BESS (BESS capacity was predetermined)
(3) With BESS placed in any chosen bus carry out a load flow.
(4) Determine the value of the objective function and update the best solution.
(5) Once the last bus is chosen, proceed to step 6, if not go to step 2.
(6) Find the optimal position of the BESS installation, which is the candidate bus providing the minimum value of the objective function.

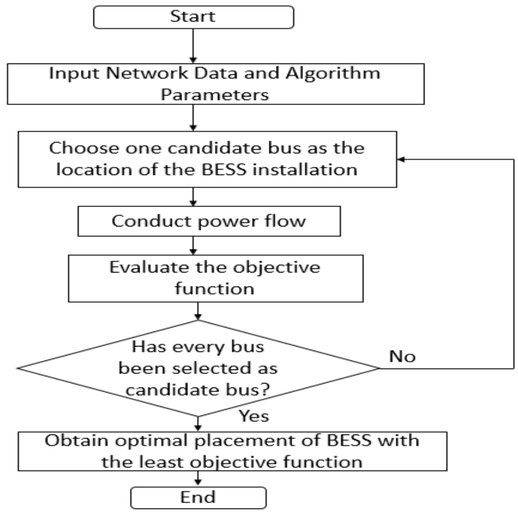

Fig. 2 Flowchart of the proposed approach of optimal placement of BESS

IV SIMULATION RESULTS AND DISCUSSIONS

The determination of the best position for connecting BESS in a distribution network with renewable energy source is the purpose of this work. As discussed earlier, the best location was found based on the minimization of the system costs which comprise the costs of power losses and voltage deviations in the network.

The bus with the least system costs was taken as the best location for the BESS while keeping the distribution system network constraints during the optimization process. MATLAB was used for the optimization and DIgSILENT Power Factory for the simulation. PSO and fmincon MATLAB solver were used for solving the objective functions and their performance was compared.

A. *Priority Analysis*

Priority analysis which determines the best location for BESS based on minimum system costs is proposed. The proposed algorithm which minimizes the system costs based on costs for the active power losses and voltage deviations was deployed to find the best location of the 1.55MW BESS in the distribution network. The algorithm was verified using a modified IEEE 33-bus network. The priority for the placement of BESS is summarized in Table 3. The simulation results showed that the two algorithms used in solving the objective function have approximately the same minimum costs for each candidate bus considered. A total of 32 candidate buses were tested while bus1 was the slack bus. From Table 3 the best location for the BESS is bus 29 which gives a minimum system cost of $247.62 (using PSO for 100 iterations) or $248.66 (using fmincon). The worst location for the BESS is bus 18 which results in a total system cost of $1236.95 (using PSO) and $1239.29 (using fmincon). Also, it is clear from Table 3 that the PSO yields a better optimal value compared to fmincon. This is because PSO is a global optimization algorithm with more search capacity compared to fmincon. Finally, the convergence value of the minimum system costs of $247.62 was validated using PSO to perform 1000 iterations as shown in Fig 4 while Fig3 is the convergence plot for 100 iterations

Table 3. Priority analysis for the placement of BESS

Bus numbers	Minimum system costs ($) using PSO	Minimum system costs ($) using fmincon	Priority
29	247.62	248.66	1
28	258.62	259.08	2
30	265.87	264.23	3
31	272.38	273.13	4
6	288.03	288.79	5
26	290.16	291.91	6
27	296.29	297.04	7
7	308.16	309.04	8
32	313.65	314.03	9
33	326.03	326.41	10
4	370.01	370.88	11
5	374.13	375.07	12
3	410.99	411.27	13
23	452.26	452.54	14
8	460.83	462.08	15
2	493.53	493.81	16
25	530.67	530.95	17
19	534.80	535.08	18
9	545.37	546.75	19
24	576.07	572.22	20
20	617.34	617.62	21
10	627.91	629.26	22
11	659.17	660.68	23
21	699.88	700.16	24
12	709.45	712.07	25
22	741.15	741.43	26
13	824.26	826.13	27
14	865.53	867.40	28
15	948.07	950.04	29
16	1030.60	1032.70	30
17	1154.41	1156.63	31
18	1236.95	1239.29	32

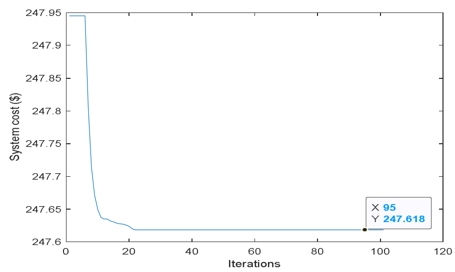

Fig. 3 Convergence plot using PSO 100 Iterations

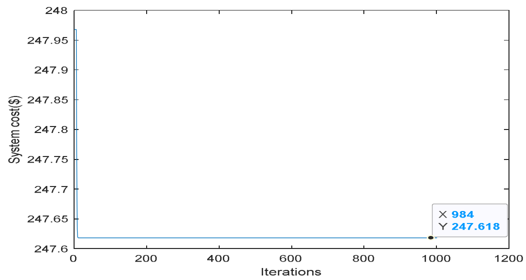

Fig. 4 Convergence plot using PSO 1000 Iterations

B. Comparison of power loses

The power losses in the network were compared based on three scenarios namely power losses before BESS connection to the network, after connection to the optimal location and after connection to some non-optimal locations. The results are as presented in Table 4.

Table 4 Comparison of power losses.

Distribution Network	Power losses (MW)
Without BESS	0.13
With BESS (in optimal location, Bus 29)	0.06
With BESS (non-optimal locations)	
Bus 14	0.21
Bus 17	0.28
Bus 18	0.30

From Table 4, the placement of BESS in the optimal location resulted in the reduction of the total active power losses in the distribution network by over 50% of its value before the placement. However, sitting of BESS in some non-optimal locations increased the total active power losses. Placing the BESS at bus 18, more than doubled the power losses compared to when there was no BESS. This shows that the location of a BESS in a network may lead to an increase/decrease in the Thevenin's equivalent current and resistance of the network which consequently either increase or decrease the power losses of the network.

C. Comparison of voltage profile

The bus voltage profile before the placement of BESS and after in the optimal location was compared and the results presented in Fig 5. From this, it could be easily seen that the optimal placement of the BESS contributed to improving the bus voltage profiles. It should be noted that bus 18 is the location of the wind power plant and bus 29 is the best location of the BESS. The voltage deviations of the system (sum of the voltage deviations expressed in percentage) without the BESS is 94% and with BESS in the optimal location 24%.

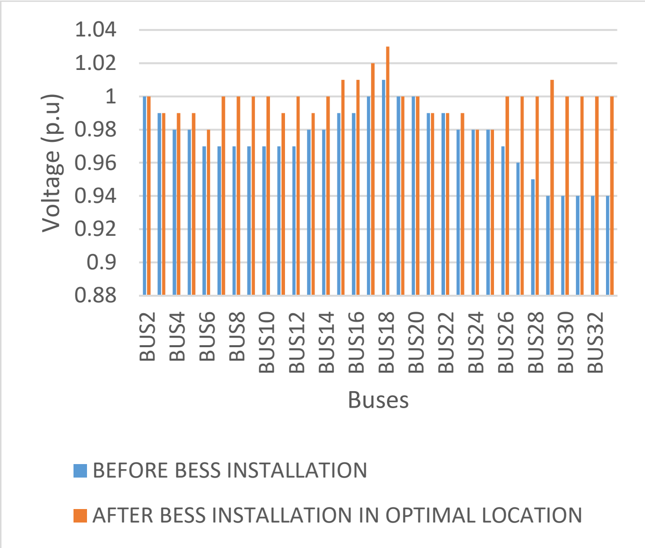

Fig. 5 Voltage profile of the buses

V CONCLUSION

In this work, the algorithm for the placement of BESS in the best location in a distribution network with wind power generation was presented. The objective function for the placement of BESS was formulated to accounts for the costs of the active power losses and voltage deviations. The optimal location of the BESS was determined based on the system costs. The proposed approach helps in the placement of the BESS of 1.55MW capacity at the bus where the costs due to power losses and voltage deviations are minimal. PSO and Fmincon MATLAB optimization solver were used to solve the objective function for the most appropriate position for the BESS in the distribution network. simulations results show that when BESS placed in the best location in a power system, power losses and voltage deviations are reduced, and the system voltage profiles are improved.

REFERENCES

[1] P. Denholm, E. Ela, B. Kirby and M. Milligan "Distribution system voltage performance analysis for high-penetration photovoltaics," National energy laboratory, 2010.

[2] M. Ammer and G. Joos, "A Short term energy storage system for voltage quality improvement in distributed wind power," IEEE Transactions energy converter, vol. 29, pp. 997-1007, 2014.

[3] Z. Ahmed, A.-H. Amer, A. Shaqsi and K. Sopian, "Review of energy storage services,applications,limitations and benefits," Energy reports, vol. 6, pp. 288-306, 2020.

[4] S. Yuanyuan, X. Bolim, W. Di and Z. Baosen, "Using battery storage for peak-shaving and frequency regulation, joint optimization for superlinear gains," IEEE transactions on power systems, vol. 33, no. 3, pp. 2882-2894, 2018.

[5] A. Samir and G.-L. Francisco, "Impact of inertia emulation control of grid-scale BESS on power system frequency response," in International conference for students on applied engineering, Newcastle upon Tyne, UK., 2016.

[6] B. Panyawoot, S. Apirat and F. Pradit, "Optimal siting and sizing of battery energy storage system for distribution network of distribution system operators," Batteries, vol. 6, no. 56, pp. 1-16, 2020.

[7] Z. Matija, G. Pavlos, H. Nikos and C. Tomislav, "Review of energy storage allocation in power distribution network, applications, methods and future research.," IET, Generation, Transmission and Distribution., vol. 10, no. 3, pp. 645-652, 2016.

[8] Y. Wang, H. Xie, X. Teng and Y. Xu, "Optimal energy storage sizing for network micro-grids considering reliability and resilience.," IEEE Access, vol. 7, pp. 86336-86348, 2019.

[9] A. Awad, T. El-Fouly and M. Saloma, "Optimal ESS allocation for benefit maximization in distribution networks," IEEE Transaction on Smart Grid, vol. 8, pp. 1668-1678, 2017.

[10] H. Yang and S. Choi, "Deterministic system analysis to guarantee worst case performance for optimal ESS and PV sizing," IEEE Access, vol. 7, pp. 98875-98892, 2019

[11] L. Wong, V. Ramachandaramorthy, S. Walker and J. Ekanayake, "Optimal placement and sizing of an energy storage system considering the duck curve phenomenon," IEEE Access, vol. 8, pp. 197236-197248, 2020

[12] P. Jung-Wook, K. Dongmin, Y. Kipo and H. Soo, "Optimal placement and sizing of an energy storage system using power sensitivity analysis in a practical stand-alone micro grid," Electronics, vol. 10, pp. 1598-1612, 2021.

[13] A. Satoru, Y. Shinya, I. Masakazu, F. Yu and M. Teru, "Multipurpose control and planning method for battery energy storage systems in distribution network with photovoltaic plant," Electrical power and energy system, vol. 116, pp. 1-13, 2020.

[14] Y. Yang, H. Li, A. Aichorm, J. Zhang and M. Greenleaf, "Sizing strategy of distributed battery storage system with high penetration of photovoltaic for voltage regulation and peak load shaving," IEEE Transaction , smart grid, vol. 5, pp. 982-991, 2014.

[15] Y. Ru, J. Kleissl and S. Martinez, "Storage size determination for grid-connected photovoltaic systems," IEEE Transaction, sustainable energy, vol. 4, pp. 68-81, 2013

[16] Y. Atwa and E. El-Saadany, "Optimal allocation of energy storage system in a distribution system with a high penetration of wind energy," IEEE Transaction, power system, vol. 25, pp. 1815-1822, 2010.

[17] A. Giannitrapani, S. Paoietti, A. Vicino and D. Zarrilli, "Optimal allocation of energy storage system for voltage control in LV distribution networks," IEEE Transaction, smart grid, vol. 8, pp. 2859-2870, 2017.

[18] S. Bahramirad, W. Reder and A. Khodaei, "Reliability-constrained optimal sizing of energy storage systems in a micro grid," IEEE Transaction, smart grid, vol. 3, pp. 2056-2062, 2012.

[19] S. Chen, H. Gooi and M. Wang, "Sizing of energy storage for micro grids.," IEEE Transaction, smart grid, vol. 3, pp. 142-151, 2012.

[20] I. Miranda, N. Silva and H. Leiti, "A holistic approach to the integration of battery energy storage system in island electric grids with high wind penetration," IEEE Transaction, sustainable energy, vol. 7, pp. 775-785, 2015

[21] H. Pandzic, Y. Wang, T. Qiu, Y. Dvorkin, B. Xu, Y. Wang and D. Kirschen, "Near -optimal method for siting and sizing of distributed energy storage in a transmission network," IEEE Transaction, power system, vol. 30, pp. 2288-2300, 2015.

[22] W. Y, R. Fernandez-Bianco, Y. Dvorkin, B. Xu and Y. Wang, "Optimal energy storage siting and sizing. A WECC case study," IEEE Transaction, sustainable energy, vol. 8, pp. 733-743, 2017.

[23] M. Ghofiani, A. Arabali, M. Elezadi-Amoli and M. Fadali, "A frame work for optimal placement of energy storage units within a power system with high wind penetration," IEEE Transaction, sustainable energy, vol. 4, pp. 434-442, 2013.

[24] P. Pilof, G. Carpinelli, G. Celli, S. Mocci and F. Mottola, "Optimal integration of distributed energy storage devices in smart grids," IEEE Transaction, smart grid, vol. 4, pp. 983-995, 2013.

[25] S. Salee and P. Wirasenti, "Optimal siting and sizing of battery energy storage systems for grid suporting in electrical distribution networkork," in 15th international conference on electrical engineering, electronics, computer, telecommunication and information technology., Chiang Rai, Thailand, 2018.

[26] J. Nadeesheni, M. Mohammad and W. Peter, "Optimal operation of distributed energy storage systems to improve distribution network load and generation hosting capability," IEEE Transaction, sustainable energy, vol. 7, no. 1, pp. 250-261, 2016.

[27] Z. Yudong, W. Shuihua and J. Genlin, "A comprehensive survey on particle swarm optimizationalgorithm and its application," Mathematical problems in engineering, vol. 10, pp. 1-38, 2015.

[28] G. Coath and S. Halgamuge, "A comparison of constrained-handling methods for the application of particle swarm optimization to

constrained nonlinear optimization problems," in Congress on evolutionary computations, Canberra, ACT, Australia, 2003.

[29] V. Yamille, K. V. Ganesh, M. Salman and J.-C. Herandez, "Particle swarm optimization: Basic concepts, variants, and applications in power systems.," IEEE Transactions on evolutionary computations, vol. 12, pp. 1-25, 2008.

[30] D. Boeringer and D. Werner, "Particle swarm optimization versus genetic algorithm for phased array synthesis," IEEE Transaction,antenna propagation, vol. 52, pp. 771-779, 2004.

[31] P. Adam, N. Jaroslaw and P. Agnieszka, "Population size in particle swarm optimization," Swarm and evolutionary computation, vol. 58, pp. 1-18, 2020.

A PV-Supplied Cooking Solution using a Hybrid Electric-Thermal Energy Storage System

Learn L. Chiloane [1], Muhammed Aswat [2], Yu-Chieh J. Yen [3] and Willie A. Cronje [4]
School of Electrical & Information Engineering, University of the Witwatersrand, Johannesburg, South Africa
chiloane.learn@gmail.com [1], maswat@pecopower.co.za [2], yu-chieh.yen@wits.ac.za [3] and willie.cronje@wits.ac.za [4]

***Abstract*—This study examines the feasibility of including a thermal energy storage as a supplementary storage method for PV-supplied off-grid application. This approach is done to reduce the cooking energy requirements which enable opportunities for use of smaller battery cell storage, and use of low-powered cooking appliances. The feasibility is evaluated considering a 5 ℓ, 500 W food safe water heater as a thermal energy storage and a 4 ℓ, 200 W slow cooker as a cooking appliance. A thermal analysis using experimental data is employed to validate the effectiveness of the storage water heater under worst-case conditions. Experimental results of the method performed in a laboratory show that the use of pre-heated water between 50 to 97.6 °C to cook rice can reduce electrical cooking energy to a range of 12.36% to 27.79% which translates to the same energy reduction for the battery capacity requirements.**

***Index Terms*—Thermal Energy Storage, Storage Water Heater, Solar PV, Off-Grid Cooking**

I. Introduction

Cooking is the process of combining, mixing and heating food to make it suitable for consumption. This process is an integral part of every human livelihood and it requires a major fraction of household energy to execute. Approximately 2.7 billion people worldwide rely on traditional energy sources for cooking, that can potentially have severe implication for health, economic livelihoods, and the environment [1], [2]. Electric cooking with renewable energy and efficient appliance is a solution for clean and sustainable cooking alternatives [1], [3].

Due to the intermittent nature of renewables (such as wind and solar) and the high energy requirements of cooking, there is a need for large and expensive batteries which make the systems infeasible to use [4], [5]. A proposed alternative method includes the addition of thermal energy storage to be utilised for cooking. This approach includes the storing of surplus renewable energy in the form of water heating, whereby the stored hot water is mixed with food to cook. The method can potentially reduce the cooking period and the electrical energy to cook most staple foods, and hence minimize the battery cell storage requirements. This paper seeks to evaluate the feasibility of utilising the thermal storage in the context of cooking.

The research objectives have been outlined, the rest of the paper is structured as follows: Section II provides the background information of the research, which presents the related previous work on thermal storages and PV cooking systems. Section III details the overall methodology of the research which explains the proposed clean cooking system and the experimental set-up to investigate the influence of adding a thermal storage. Section IV to V discusses the results obtained, and the paper is concluded in Section VI.

II. Background

Many areas in southern Africa experience highest levels of solar energy in the world, with the average solar irradiation ranging from 4.5 to 6.5 kWh/m^2 per day [6]. It is also known that energy cost at the output of solar panels is declining due to their increase in popularity [7]. It has been shown from experimental studies that electric cooking consumes less energy than other energy sources such as gas, paraffin and ethanol gel [5], [8]. These points give a strong argument to consider off-grid electric cooking solutions to be based on solar energy. However, cooking food requires high power and energy, and household cooking demand does not coincide with peak hours of solar energy input.

A. Thermal Energy Storage using Water Heating

Thermal energy storage systems provide an opportunity for a cheaper method of storing energy [7]. Rather than using cell batteries only, it is proposed that thermal storage be added in the systems to store excess energy and later be reclaimed to cook when there is scarce solar input. For most tasks in the household, this method is not feasible as there is no efficient way to return the stored energy back to electrical energy. However, because cooking consumes most of the household energy in the form of heat, this could have a significant impact on the required battery cell capacity to fill household energy needs.

Given that a significant amount of hot water is used to cook, household water heaters are ideal solutions for thermal energy storage as they are capable of heating and storing thermal energy for long hours. If controlled optimally, water heaters with good thermal resistance can service hot water usage for night-time and during days of low solar irradiation. The rest of the remaining cooking process can then be completed by using PV energy during the day or the energy stored in batteries.

B. Solar PV Cooking Systems

In off-grid or on-grid applications, diverting excess renewable energy to heat then storing it has a positive impact on the total electric energy consumption. The following literature

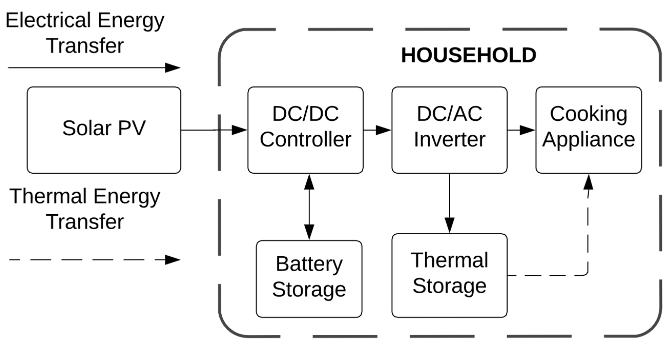

Fig. 1. High-level block diagram of the proposed clean cooking system with thermal storage.

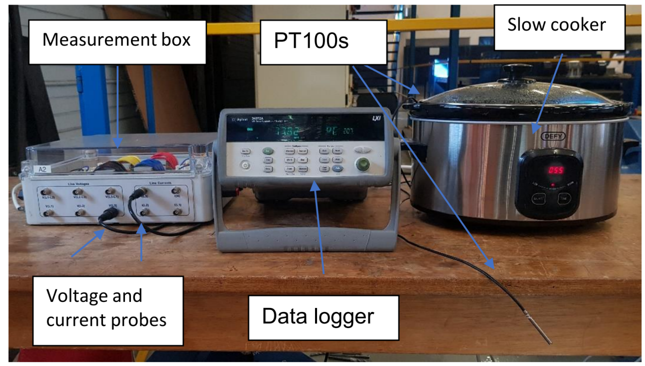

Fig. 2. Cooking experiment set-up with a slow cooker.

focuses on using thermal storage to support PV-supplied systems in the context of cooking.

Authors in [9] developed a system that stores solar PV energy in a phase change material during the day to allow indoor cooking with more power after sun hours. This technique houses a cooking vessel with a phase change material which is heated by a resistive element using a panel. The material, when heated to 180 °C can boil 1 ℓ of water under 1 hour. The core limitations of this work is that the phase change material thermally degrades when heated to higher temperatures, and that low temperature storage is not effective in boiling and cooking food. The authors complete the cooking process using a grid-connected DC source when the temperatures are low. This hybrid compensation is an important aspect of having a battery cell in this study.

In [7] an inverter-less, solar PV cooking system that integrates with the grid for back up power was proposed. The system comprises of a water heater that uses excess solar power and has a 500 W limit for any cooking appliance used. The system performance was evaluated by cooking rice with water stored at 95 °C. This yielded an energy reduction of 18% for a conventional pressure cooker and 30% for an electrical pressure cooker. Using off-grid solar systems to heat water and maintain it at extremely high temperatures is not always guaranteed especially on days with low solar irradiation. Additionally, the study did not objectively validate the texture of the cooked rice in all experiments. This paper focuses on the active electrical energy reduction when food is cooked with pre-heated water at various temperatures in an off-grid cooking system. Moreover, texture measurement methods of staple foods presented in [10], [11] are used to validate the readiness of the food.

III. Methodology

The main objective of the research is to examine the feasibility of adding a thermal storage as a solution for a smaller battery cell storage option in an off-grid cooking system. The approach taken was to first explain the energy transfer of the proposed off-grid cooking system, followed by the analysis of the thermal storage, the experimental set-up of the cooking system and food texture measurement method, and lastly the experimentation to study the influence of cooking with pre-heated water. The following sections detail the overall research approach:

- The proposed off-grid system with thermal storage and a cooking appliance (Section III-A).
- Study of a thermal storage using experimental data (Section III-B).
- Experimental set-up to obtain the relationship between the active energy input and food state (Section III-C).
- Experimentation by cooking with pre-heated water at different temperatures to study the influence of initial thermal energy gain from a thermal storage (Section III-D).

A. Proposed Off-Grid Cooking System

The key functionality of the proposed clean cooking system is to provide a thermal storage necessary to heat-up water using excess solar energy and store it for the cooking process. The system overview is represented by the block diagram in Fig. 1, and it comprises of a solar PV, battery cell storage, thermal energy storage, charging controller, and a cooking appliance. In the system; the solar PV converts solar irradiance to electrical power, the battery storage acts as back-up for days of low solar irradiation and for night time usage, and the thermal energy storage system heats water during the day to be transferred to the cooking appliance.

The focus of the research is on the energy flow balance between the thermal storage and the cooking appliance, accounting for thermal losses and efficiencies involved.

B. Thermal Energy Storage

Storage water heaters are used to heat, store and supply hot water for tasks in a household. To properly analyze their feasibility in the context of cooking, it is important to study their energy storage capabilities. This research considers physical tests of a food safe water heater that is neither piped nor pressurised.

A water urn has the ability to heat and store water. A stainless-steel urn was modified to consume 500 W of power and store 5 ℓ of water in a vertical orientation. Additionally, a thermal blanket was wrapped around the tank to improve its thermal resistance. The power consumption of the urn was measured, including the internal water and ambient temperatures. Once filled with water, the urn was turned on until the water reached 95 °C then turned off for 24 hrs to inspect the cooling profile. The temperature profile of the water inside the tank is discussed in Section IV-A.

C. Cooking Experiment

Experiments are performed to obtain temperature and power profiles which are used for deriving the relation of the energy input (electrical and thermal) and food state.

1) ***Cooking Appliance****:* There is a fair range of cooking appliances that can be used for electric cooking with renewable energy such as slow cookers, pressure-cookers, and induction-cookers. The focus will be on slow cookers due to their low power capabilities and automatic cooking process. Slow cookers consists of a ceramic container which is heated by a resistive element, and a switch for power consumption control. The state of the switch is controlled by a processor, which has three heat settings: low, hot, and warm. The body frame of the slow cooker experience thermal losses to the environment.

The power consumed by the cooker is measured and logged in one second resolution for the entire cooking process. Two temperature sensors are used to measure the temperature profiles; one sensor measures the temperature of the food mixture, positioned about 5 mm above the cooker's container, while the other measures the ambient temperature positioned at least 3 cm away from cooker and their results are also logged. The cooking experimental setup with a 4 ℓ, 200 W slow cooker is presented in Fig. 2.

2) ***Food Texture Measurement****:* Rice is chosen as the cooking medium because it is the staple food for two thirds of the world's population, and it is the fastest growing staple in Africa [10]. Its cooking process can benefit from the use of pre-heated water and therefore ideal for this study. There exists a large variety of rice genes. A single gene is selected based on local availability and to conduct comparable experiments. The rice is cooked at different starting temperatures, periods, and surrounding conditions; hence it is crucial to quantify its readiness in each experiment. Moisture content and hardness are presented as two main factors for determining cooked rice texture [10], [11]. In this study, 50 rice grains are removed from the cooking vessel every 15 mins to track the absorbed moisture content.

3) ***Energy and Food Texture Bench-marking****:* Two operating points to benchmark the state of cooked rice are used and linked to the energy transferred to the cooker. The rice is considered under-cooked if the results are below the lower point, over-cooked if the results are above the higher point, and well-cooked if the results are between the points. The results of cooked rice after each experiment are measured with the developed measurement method and compared to this range.

D. Pre-Heated Water

This subsection focuses on the experiments used to test the effect of starting to cook rice with pre-heated water in a slow cooker on the active energy requirements. The experiments were performed using the set-up presented in Section III-C. Long grain parboiled rice stored at room temperature, with a recommended rice to water ratio of 1:2 is used to obtain the profiles. Dry rice of 300g (1½ cups) that results in 3-4 servings was considered with 600 mℓ of water starting at 25, 50, 75 and 97.6 °C respectively. Experimental studies show that rice can be prepared with energy less than 0.50 kWh when the inside temperature is above 65 °C [7], [8], [12]. The slow cooker was adjusted to consume less than 0.50 kWh of energy in all experiments.

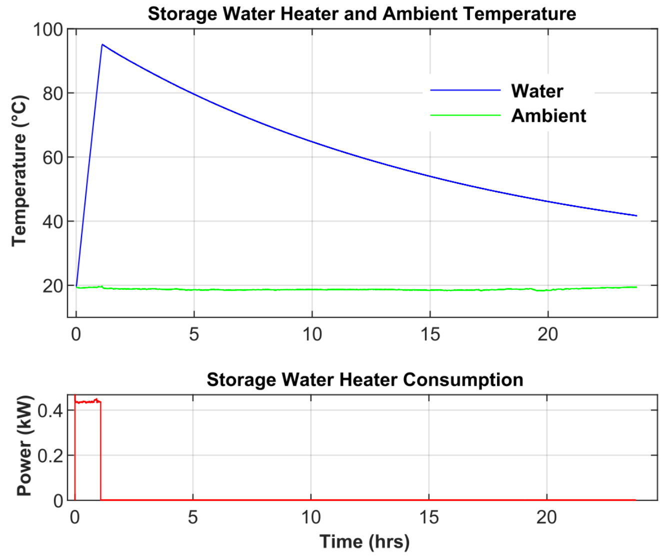

Fig. 3. Experimental profile of a 500 W, 5 ℓ storage water heater showing the temperature and element power consumption response.

IV. Results

The water heater performance and effect of starting to cook with pre-heated water are discussed in the following subsections.

A. Storage Water Heater

The heating of water inside an urn and the cooling profile after reaching a set-point of 95 °C is demonstrated in Fig. 3. The profile shows that the urn takes 1.10 hrs to heat water from 20 to 95 °C, which consumed 0.49 kWh of energy. The ambient temperature was approximately stable with a daily average value of 18.75 °C. The urn takes 5.27 hrs to cool from 95 °C to 75 °C, and 16.21 hrs to cool to 50 °C. Considering the availability of solar energy to maintain the water in the urn at 95 °C until 16:00 pm, the urn will cool down to 75 °C at 21:16 pm, and 50 °C at 08:12 am the following day.

Overall, the heat retention of the urn even at low ambient temperatures is good. Heating up the water takes about an hour and it keeps pre-heated water with enough energy gain for cooking in the following morning. The influence of the energy gain from the pre-heated water is discussed in the following Section IV-B.

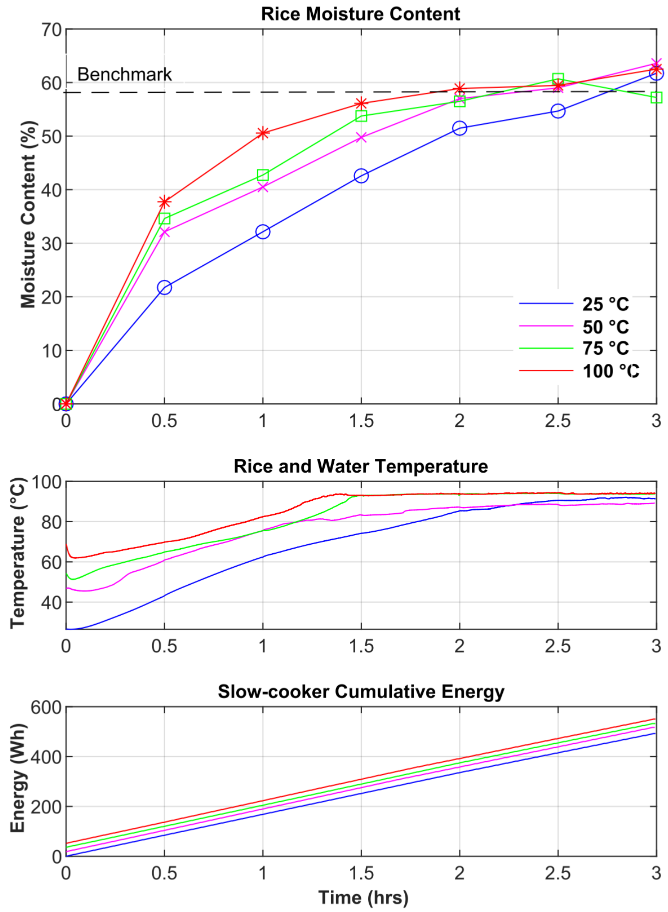

Fig. 4. Resulting rice moisture content, inside temperature, and thermal-electrical energy profiles of cooking rice in a slow cooker. Each grid consists of 4 different profiles of pre-heated water temperature starting at 25, 50, 75 and 97.6 °C. In each experiment 300 g of rice and 600 mℓ of water (1:2 ratio) was cooked for 3 hrs.

B. Pre-Heated Water Influence

The influence of cooking with pre-heated water is demonstrated in Fig. 4. The profiles show the absorbed moisture content of rice, inside temperature dynamics, and the slow cooker's cumulative energy throughout the cooking process. Rice was cooked for 3 hrs with water starting at 25 °C "the experiment baseline", and for the same period with pre-heated water at 50, 75 and 97.6 °C. The profiles show that the rate of moisture absorption is quicker initially with pre-heated water, and that the rice-water mixture reaches steady-state temperature quicker. Between 1.5 and 2.5 hrs, the moisture absorption rate slows down, and starts to decline in some cases. This is because the rice has absorbed all of the available water and it begins to dry due to the heat of the cooker. Ready-to-eat rice is benchmarked between 58.5% - 60.5% moisture content, with the highest being the rice that has absorbed all water.

C. Cooking Energy and Battery Requirement Reduction

From observing the minimum benchmark line in Fig. 4, preparing edible rice with pre-heated water at 25, 50, 75 and 97.6 °C takes 2.76 hrs (455 Wh), 2.37 hrs (399 Wh), 2.23 hrs (376 Wh), and 1.93 hrs (329 Wh), respectively. The pre-heated water temperatures can potentially reduce the electrical energy to cook rice to a range of 12.36 – 27.79% as presented in Table I. The implication on battery capacity is determined using (1). The battery capacity required for a 12 V system is reduced from 99.1 Ah to 86.9 Ah, 81.90 Ah, and 71.7 Ah.

TABLE I
RESULTS OF COOKING RICE IN A SLOW COOKER WITH PRE-HEATED WATER AT DIFFERENT TEMPERATURES.

Parameter	**25 °C**	**50 °C**	**75 °C**	**100 °C**
Initial water temperature [°C]	26.00	52.00	77.00	97.60
Ambient temperature [°C]	23.30	23.60	23.60	23.70
Thermal energy added [Wh]	0.00	18.50	36.00	51.80
Electrical energy [Wh]	455.60	399.30	375.60	329.00
Battery capacity (12V) [Ah]	99.10	86.70	81.90	71.70
Potential battery reduction	-	12.36%	17.56%	27.79%

$$C_b = \frac{E_L}{\eta_{dc/ac} \times \eta_{bat} \times V_B \times DOD} \quad (1)$$

Where C_b is the required battery bank capacity [Ah]; E_L is the cooking energy consumption [Wh]; V_B is the battery bank or system voltage [V]; η_{bat} is the battery bank efficiency (85%); $\eta_{dc/ac}$ is the inverter efficiency (90%); and DOD is the depth of discharge (50%).

V. DISCUSSION

A. Cooking with Pre-Heated Water

The idea of the study is to provide a thermal storage necessary to heat-up water using excess renewable energy and later reclaim it to cook. It was shown from the cooking experiments that rice absorbs water faster when higher water temperatures are initially used, and the time to reach the 58.5% comparison level decreases. This method significantly decreases the total electrical energy consumption required to cook and enable for faster electric cooking with a low-powered cooking appliance.

The idea can be implemented in PV-supplied households by using commercial small storage water heaters with good thermal insulation to ensure minimal heat loss after sun hours. The four experiments performed shows that pre-heated water between 50 – 97.6 °C can reduce electrical cooking energy to a range of 12.36% – 27.79%. This implied that the capacity of the cell batteries required can be reduced by a similar range which carries through to a significant reduction in the financial cost of the battery and the entire system.

B. Future Work

*1) **User Influence**:* One key expansion of the study is the consideration of cooking two meals in a day (i.e., morning and evening meals) to examine the concept even further. This would require analysis of the thermal storage when hot water is removed and replaced with cold water. Replacing hot water with colder water after sun hours would decrease the water temperature and reduce the potential to have higher energy saving before the heater turns on. If the removal is done during the day, this will increase the heating times and retain the energy reduction. Therefore, the hypothesis is that for cooking of two meals, the evening meal would retain the same reduction, but the morning meal would have a lower energy reduction when cold water is inserted.

*2) **Days of Autonomy:*** The main source of power failure in PV-supplied systems is the consecutive low solar irradiation days which require the system to power loads with energy from storage. In this study, the thermal decay curve of the investigated thermal storage shows that it can retain temperatures above 50 °C for 16 hrs. An investment into a small storage heater with better thermal insulation such as thermos flask is required to allow the water to last for 2-3 days while hot.

VI. Conclusion

The high energy requirements of cooking and the intermittent nature of renewable energy sources presents a challenge to offer cheap, clean, and sustainable off-grid cooking alternatives. Rather than sizing the systems with cell batteries only, it was proposed that thermal storage be supplemented to store excess energy and later be reclaimed to cook when there is scarce solar input. Food safe storage water heaters with good thermal insulation are considered suitable thermal storage because they are capable of heating and storing hot water for long hours. An analysis has been employed to study their effectiveness under low ambient conditions with the one under test retaining the water temperature above 50 °C after 16 hrs with no energy input. Rice is used as the cooking medium because its cooking process benefits from the use of pre-heated water. The experimental results demonstrate that rice cooks faster when using pre-heated water of 50 – 97.6 °C, and as a result the active electrical energy required to cook reduced by 12.36 – 27.79%, which translates to a similar battery cell storage reduction.

References

[1] F. Lombardi, F. Riva, M. Sacchi, and E. Colombo. “Enabling combined access to electricity and clean cooking with PV-microgrids: new evidences from a high-resolution model of cooking loads.” *Energy for sustainable development*, vol. 49, pp. 78–88, 2019.

[2] S. Batchelor, E. Brown, N. Scott, and J. Leary. “Two birds, one stone—reframing cooking energy policies in Africa and Asia.” *Energies*, vol. 12, no. 9, p. 1591, 2019.

[3] S. Batchelor. “Is it time for Solar electric cooking for Africa.” *Gamos Concept Note, May, Reading, United Kingdom*, 2013.

[4] M. Leach and R. Oduro. “Preliminary design and analysis of a proposed solar and battery electric cooking concept: costs and pricing.” *Evidence on Demand, UK*, 2015.

[5] S. Batchelor. “Solar Electric Cooking in Africa in 2020: A synthesis of the possibilities.” *London: Evidence on Demand/DFID, DOI*, vol. 10, p. 12774, 2015.

[6] Department of Energy (South Africa). “Renewable energy.” [online]. Available: http://www.energy.gov.za/files/esources/renewables/r_solar.html, Last accessed 26 Oct. 2021.

[7] M. R. Khan and I. Alam. “A Solar PV-Based Inverter-Less Grid-Integrated Cooking Solution for Low-Cost Clean Cooking.” *Energies*, vol. 12, no. 20, p. 5507, 2020.

[8] S. Batchelor. “Africa cooking with electricity (ACE).” *Reading. Gamos Working Paper (Draft as at August 2015). Available at: https://www.researchgate.net/publication/298722923_Africa_cooking_with_electricity_ACE*, 2015.

[9] M. Osei, O. Staveland, S. McGowan, J. B. Unger, N. R. Christler, M. Weeman, M. E. Strutz, M. Walker, M. B. Maun, N. C. Dunning, et al. “Phase change thermal storage: Cooking with more power and versatility.” *Solar Energy*, vol. 220, pp. 1065–1073, 2021.

[10] R. Poritosh, D. Nei, T. Orikasa, H. Okadome, M. Thammawong, N. Nakamura, and T. Shiina. “Cooking properties of different forms of rice cooked with an automatic induction heating system rice cooker.” *Asian Journal of Food and Agro-Industry*, vol. 86, no. 4, pp. 373–388, 2010.

[11] S. Gao, B. Ming, L.-l. Li, R.-z. Xie, K.-r. Wang, and S.-k. Li. “Maize grain moisture content correction: From nonstandard to standard system.” *Biosystems Engineering*, vol. 204, pp. 212–222, 2021.

[12] S. Salehin and A. Sadrul Islam. “Performance Test of Wonder Bag: A Pathway to Reduce Cooking Energy Consumption and CO2 Emission.” *energypedia*, Jul. 2014.

A Distributed Standalone Solar PV and Battery Energy Storage System DC Microgrid

Thandeka Makhanya
Department of Electronic and Computer Engineering. Durban University of Technology. Durban, South Africa
20502104@dut4life.ac.za

Mr. Rathilall Sewsunker
Department of Electronic and Computer Engineering. Durban University of Technology Durban, South Africa
RathilallS@dut.ac.za

Dr. N Pillay
Department of Electronic and Computer Engineering. Durban University of Technology. Durban, South Africa
trevorp@dut.ac.za

Abstract* – The implementation of renewable energy resources has become a demand since it comes with vast benefits. This paper aims to design an optimum distributed standalone 48VDC solar PV microgrid to power a rural village with 30 households. The low voltage microgrid will comprise 3 standalone nano-grids each having a dedicated PV generation point, battery energy storage system, and load. The nano-grids are each interconnected through a global DC bus via a bidirectional DC-DC converter and have the capability to share power amongst each other for optimum operation. Each nano-grid have a local controller which is responsible for local energy management within the nano-grid, while the global energy control is responsible for power sharing management amongst the nano-grids. A hierarchical control strategy based on bus voltage signaling is utilized to control the power flow in the low level and upper level of the microgrid.

***Keywords* – DC microgrid, distributed generation, nano-grid, power sharing.**

I. Introduction

Electricity has become imperative for daily survival, either for domestic, commercial, or industrial consumption. However, electricity generated from renewable energy resources has become a necessity to save the environment by reducing the carbon footprint [1]. Some rural areas in South Africa are partially covered by the utility grid due to certain constraints [2]. The South African solar PV resource map provided by SOLARGIS indicates that the country has the potential to harvest between 4kWh - 5.6kWh of PV-Photovoltaic power per hour daily [3]. Implementation of standalone solar PV microgrids with a low voltage DC distribution network to power these areas can boost social progress and economic growth for these communities while saving the environment. Moreover, microgrids with a DC distribution network are more efficient due to fewer conversions, no reactive power problems, no need to monitor the frequency, and many more benefits. However, there is a shortfall that exists in the process of solar energy harvesting. Solar energy generation depends on certain weather conditions. Nevertheless, poor weather conditions effects can be overcome by proper planning, design, and installation of a microgrid system that will be optimum for the users [4].

II. Literature Review

Distributed renewable energy resources implemented as a standalone microgrid are identified as a potential solution for addressing rural electrification and also have several applications in automotive industries, marine technologies, and communication centers [5]. [6] Covers the design of a low voltage DC microgrid system for rural electrification, the DC microgrid system consists of a PV array as the renewable energy source, a Battery Energy Storage System, a Charge controller, and the energy management system. Furthermore, research shows that DC microgrids are a promising option when integrating distributed renewable energy sources, and energy storage for optimization of reliability and cutting of costs [7]. In [8] a method to control a decentralized Standalone PV based distributed generation DC microgrid composed of multiple PV generation points is proposed. Simulation and experiments were conducted and the results proved the proposed method to be acceptable for power sharing, high efficiency of the system, and decreased losses associated with power distribution. Moreover, a study in [9] compares three topologies for a 20 household rural community. The investigation is conducted to check the impact of different topologies on the efficiency of the solar system. The three topologies are centralized microgrid, distributed standalone home system, and open energy system which is the hybrid approach with interconnected nano-grids. The nano-grids are connected through bidirectional DC-DC converters which allow nano-grids to share power, the Open End System-OES also has a communication system with an algorithm that manages the demand and response between interconnected nano-grids through bidirectional DC-DC converters. The OES topology was more efficient compared to the centralized microgrid and the distributed standalone home system topologies. DC microgrids can be designed based on six different structures *Single-bus, Multi-bus, Multi-terminal, Ring-bus, Ladder-bus, and Zonal* [10, 11]. These structures have their advantages and disadvantages, it is vital to study and understand them to be able to choose the right structure for your design. Moreover, control strategies are vital for an efficient microgrid operation. The control strategies are responsible for the control of power flow, coordinating distributed energy resources and energy storage devices, current control, and voltage control [10-12]. Various control strategies for DC microgrids exist (Hierarchical, Distributed, Centralized and Decentralized) and they can be utilized to achieve an efficient operation of the DC microgrid[10, 13-15].

III. PROPOSED MICROGRID DESIGN.

Most distributed energy resources microgrids are composed of a variety of energy resources which includes the utility grid in some designs. The proposed system will be a standalone design with multiple solar PV generation points and a BES-Battery Energy Storage dedicated to each generation point as illustrated in fig. 2. The proposed topology aims to design a system that will be optimum for the users by allowing the nano-grid with surplus energy to share the energy with the nano-grid in need. For proper planning and design of the microgrid, meteorological data for the location of interest will be collected, load profiles for households will be determined, the sizing of the nano-grids will follow and the control strategy will be designed for load regulation and power sharing. The system will then be simulated on MATLAB/SIMULINK to validate the operation of the microgrid design.

A. Microgrid Location

Noshezi the location of interest for the proposed research is located in the coastal parts of KwaZulu Natal, South Africa, Africa. The location's latitude is -29.6801 and has a longitude of 30.2671. Table 1 shows the meteorological data of Noshezi [16], the location has an average daily Global Horizontal Irradiance of 4.3 *KWh/m²*. This location is good for PV solar installations.

TABLE 1
METEOROLOGICAL DATA OF NOSHEZI.

Month	*Average daily GHI KWh/m²*	*Average monthly GHI KWh/m²*
January	4.72	146.29
February	5.22	146.27
March	4.62	143.13
April	4.23	126.95
May	3.71	114.87
June	3.31	99.36
July	3.65	113.17
August	4.09	126.7
September	4.71	141.31
October	4.81	149.18
November	4.68	140.32
December	4.36	144.38

A. Load Profile forecast

TABLE 2
LOAD PROFILE FORECASTING FOR EACH NANO-GRID.

Appliance	*Quantity.*	*Power rating (W)*	*Number of hours*	*Energy Wh/day*
LED Lamps	80	6	12	5760
Cell Charger	20	5	3	300
Radio	10	10	12	1200
TV/PC	10	30	10	3000
Fan	10	40	12	4800
Fridge	10	90	24	9000
Total				24060

The proposed system is designed to cater to low power applications such as mobile phone charging, lighting, radio, Television, fan, and small refrigerator. All the appliances are assumed to be operating on a 48 VDC rating. The 24-hr consumption for each nano-grid is shown in table 2. The consumption is calculated per 10 households. All 3 nano-grids are equal in terms of design and load profile forecast.

B. PV Array sizing

The PV array size and the number of PV panels required for each nano-grid were calculated with Eq. (1,2). The PV array nominal power at standard test conditions is 7268.9 W. 17 PV panels with a power rating of 430W will be utilized.

$$A_T = \frac{E_T}{S_{Ph}} \tag{1}$$

$$N_{PV} = \frac{A_T}{P_{PV}} \tag{2}$$

A_T – Array total size
E_T – Total daily load demand
N_{PV} – Number of PV panels
S_{Ph} – Average daily sun peak hours
P_{PV} – PV panel peak-watts

D. Battery energy storage sizing

Solar PV panels require the presence of sunlight to produce electrical energy. To overcome the shortfall caused by the absence of sunlight, the BES is required to supplement the solar energy. Furthermore, the BES will be designed to be able to cater to the users for up to 4 consecutive days without being recharged by the PV array. Eq. 3 calculates the global capacity for the BES based on the chosen battery efficiency, depth of discharge, voltage bus, and total daily load demand. Eq. (4-6) calculates the required number of batteries and the number that is connected in parallel and series. The battery energy storage global capacity calculated is 2583.8Ah, number of batteries with a rating of 48 VDC, 200Ah required is 13. Parallel batteries 13, series 1.

$$B_{GC} = \frac{A * E_T}{DOD * \eta_B * V_{Bus}} \tag{3}$$

B_{GC} – Battery global capacity
A – Autonomy.
DOD – Battery depth of discharge.
η_B – Battery efficiency.
V_{Bus} – System bus voltage.

$$N_B = \frac{B_{GC}}{B_C} \tag{4}$$

$$N_{BS} = \frac{V_{Bus}}{B_C} \tag{5}$$

$$N_{BP} = \frac{B_{GC}}{B_C} \tag{6}$$

N_B – Number of batteries
B_C – Chosen Battery capacity.
N_{BS} – Number of Batteries in series
N_{BP} – Number of Batteries in parallel

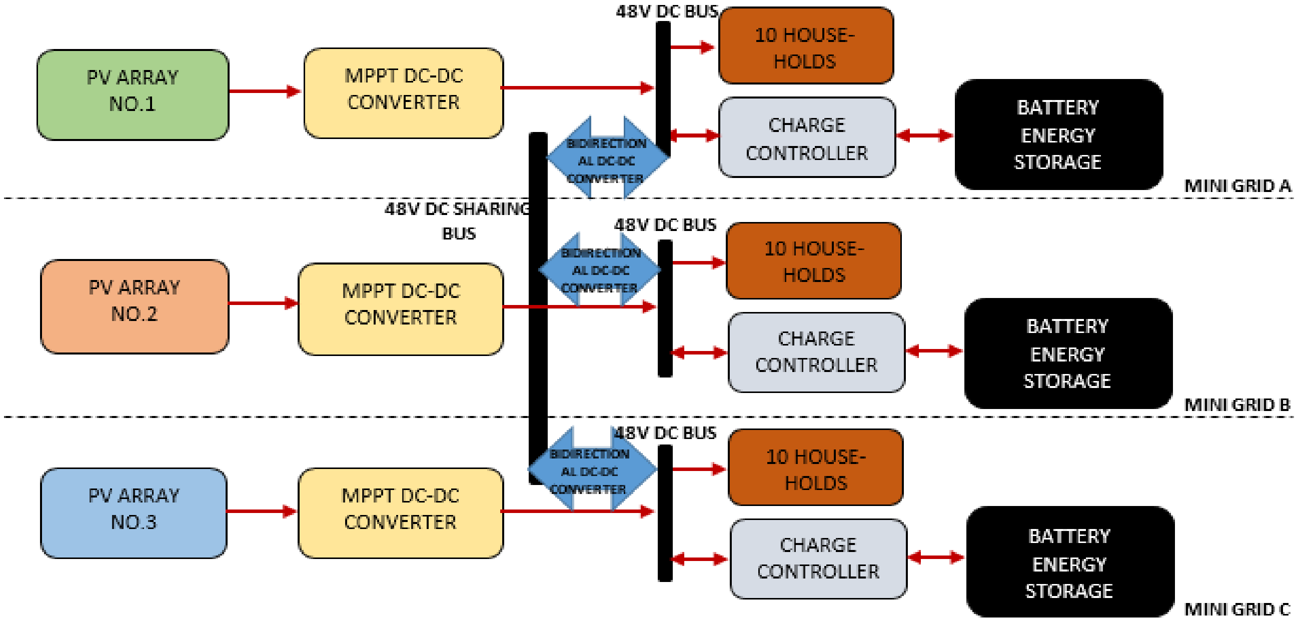

Fig. 1. Proposed system topology block diagram.

E. Microgrid control

The proposed DC microgrid structure as shown in fig. 2 was designed based on the zonal structure[10, 11]. Hierarchical control with two levels (Low Level and Upper Level) will be utilized for DC bus voltage regulation and power sharing [10]. The DC microgrid has 3 independent nano-grids, and each nano-grid has a low level controller for local control. The nano-grids are interconnected by a sharing DC bus through bidirectional dc-dc converters, sharing power among the nano-grids will be controlled by the upper level controller for global control. Both low level and upper level controllers will utilize a DC bus signaling method to regulate the local DC bus voltage by switching between the PV array and BES, and to control power sharing among nano-grids.

F. Controller design

a)Low level controller

This controller is responsible for maintaining the 48V DC local bus voltage. The controller will continuously sense local bus voltage and alternate between energy sources accordingly. The PV array is the primary source, BES secondary source, and sharing DC bus the third source. The low level controller comprises the battery energy storage control and the PV array controller.

b)PV Array control

The energy required to meet the demand for each nano-grid is sourced from separate PV arrays. Due to weather change and impedance mismatch between the PV array and the load which causes inefficient energy transfer an MPPT-Maximum Power Point tracker can be utilized to harvest the maximum power from the PV arrays [17]. The P&O-Perturbation and Observation MPPT was implemented on SIMULINK as illustrated in fig. 2. The MPPT will be coupled with a non-isolated Buck-Boost converter. The MPPT generate a duty cycle to control the switching of the Buck-Boost converter. The non-isolated Buck-Boost converter will buck the PV array output voltage greater than 48V and will boost the PV array output voltage less than 48V to maintain the bus voltage of 48V.

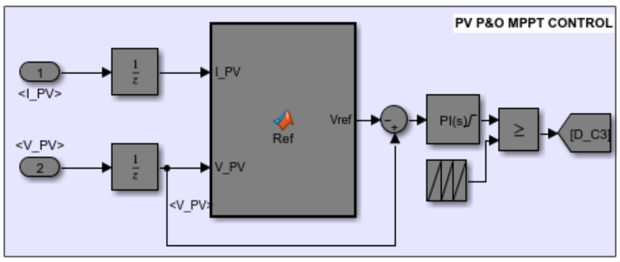

Fig. 2. P&O MPPT controller

c)Battery control

The BES controller will monitor the local bus voltage and select charging or discharging mode depending on the status of the local bus voltage. When the local bus voltage is 48V the controller will select charging mode if the SOC- State of Charge is less than 100%, and when the bus voltage is less than 48V the controller will select discharging mode if the SOC is greater than 10%. Fig. 3 illustrates the battery controller implemented on MATLAB/SIMULINK. Fig. 4s illustrates the operation of a breaker switch between the local bus and the BES, the BSC-Breaker Switch Controller works in conjunction with the battery controller. The BSC operates by checking the SOC of the battery and the state of the local bus voltage. The BSC generates a state signal of 0 to open the breaker switch if these two conditions are true SOC is 100% and the bus voltage is 48V, or when SOC < 10% and the local bus voltage is < 48. If the SOC is < 100% and the local bus voltage is 48V, the BSC generate a state signal of 1 to close the switch and allow the BES to charge. If the SOC >10% and the local bus voltage is < 48V the controller will generate a state signal of 1 to close the switch to allow the BES to regulate the local bus voltage.

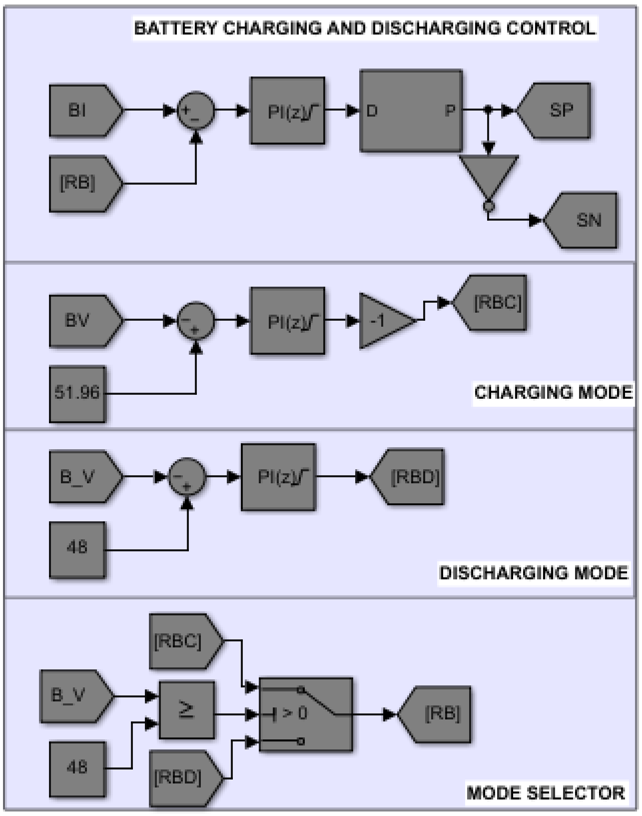

Fig. 3. Battery charge and discharge controller

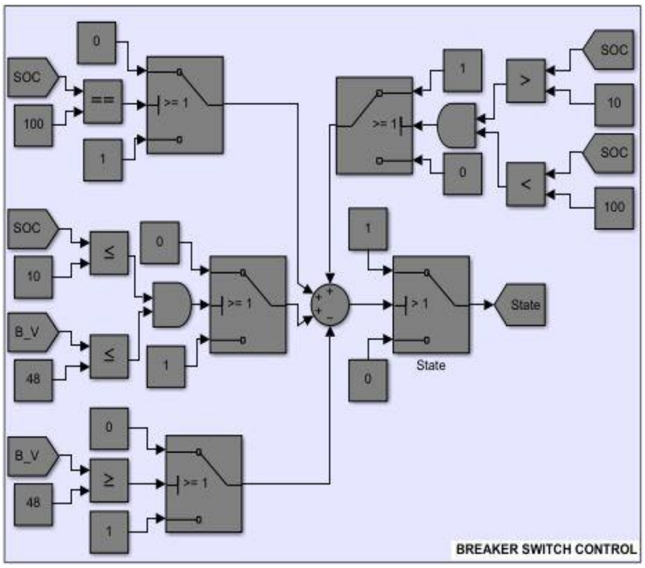

Fig. 4. Beaker Switch Controller

d)Upper level controller

A bus signaling control strategy will be applied to control power sharing in this level. The upper level controller will sense, and monitor local bus voltages and the BES SOC to enable the nano-grids to share power or utilize power available in the sharing bus. The power will be shared to and from the nano-grids via a bidirectional dc-dc converter. Fig. 6 illustrates the power sharing control algorithm implemented on MATLAB/SIMULINK for the upper level controller. The nano-grid will only share the power when the BES is fully charged. Fig. 6 illustrates how the upper controller will execute the control of allowing the nano-grids to share surplus power via a sharing bus. The upper controller will monitor the local bus voltage, the SOC of the BES and will enable a nano-grid with surplus power to share to the global bus. The upper level controller work in conjunction with the priority selector. The priority selector illustrated in fig. 5 ensure one nano-grid is catered for by the global bus at a time when the voltage is >=48 and also ensures that the power is shared only when the there is a nano-greed in need.

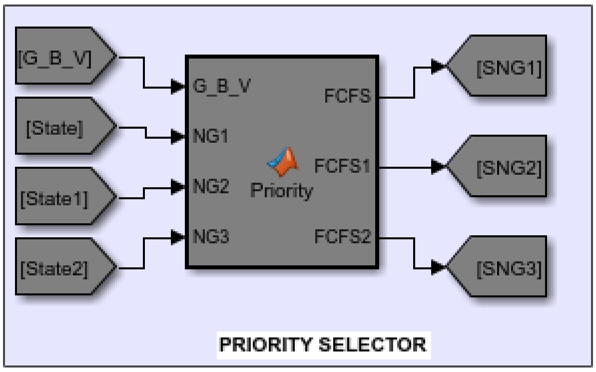

Fig. 5. Priority selector

IV. RESULTS

The local controller algorithm was implemented and simulated with MATLAB/SIMULINK. Fig. 7 & 8 illustrates the local bus voltage regulation by the PV arrays and the BES responding to the change in solar radiation which is directly proportional to the PV array output voltage. To test the local control algorithm solar radiation input was varied from 0-1000 W/m^2. The local control algorithm managed to monitor and regulate the local bus voltage by changing between two distributed sources (PV and BES). A small percentage of undershoot and overshoot occurs during the transition and can be noticed on the bus voltage signal. When the BES is fully charged and enough energy is harvested from the primary source the Buck-Boost converter regulate the local bus voltage to 48V. However, when the energy harvested from the primary source is not enough to meet the demand, BES is enabled to cater for the load demand and regulate the bus voltage to 48V. Moreover, it can be observed in fig. 8 that nano-grid 1 during the first 4 seconds had surplus power with a full BES but was not able to share the power to nano-grid 3 which was in need due to the absence of upper level controller.

The upper level controller algorithm was implemented and simulated, the results are illustrated in fig. 9. To test the algorithm nano-grid 3 solar radiation input was set to zero and the BES was discharged to zero SOC. Nano-grid 1 had surplus power during the first 2 seconds and the surplus power was shared to nano-grid 3. The sharing was halted by the drop in solar radiation in nano-grid 1 causing the power harvested by nano-grid 1 to be only enough for it local load demand. Furthermore, nano-grids incapability to meet the load demand can be caused by different factors which can be technical or environmental.

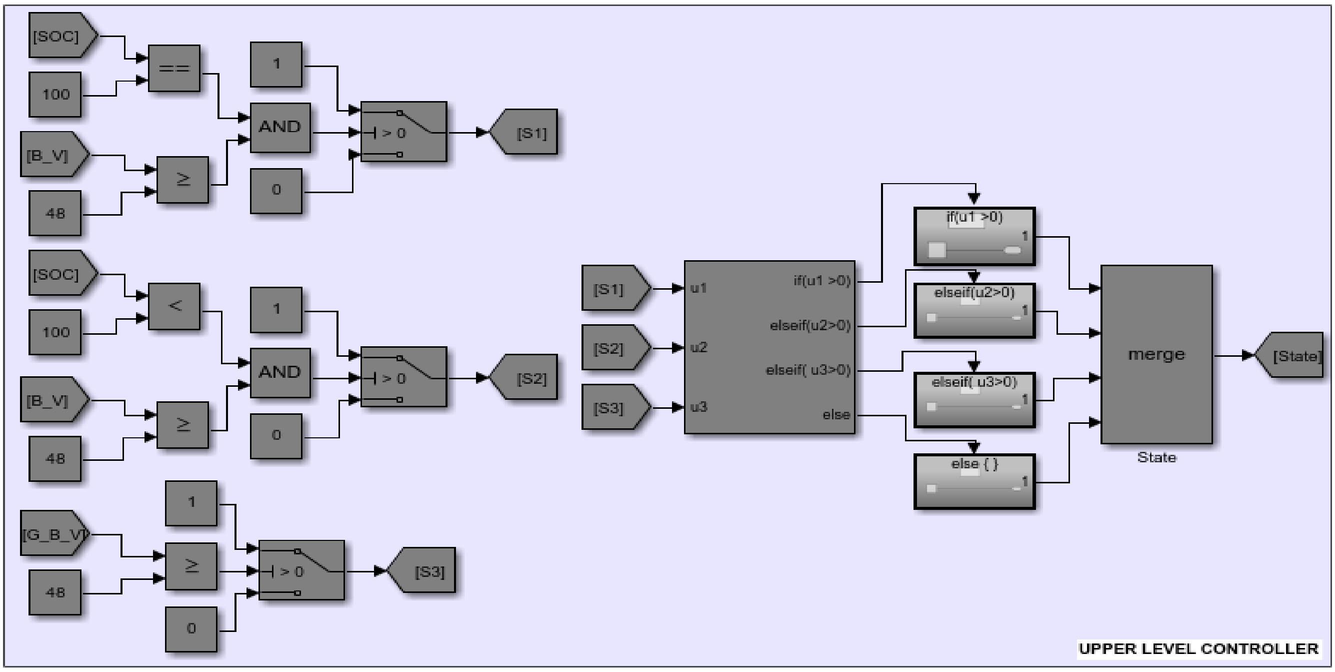

Fig. 6. Upper level controller SIMULINK algorithm.

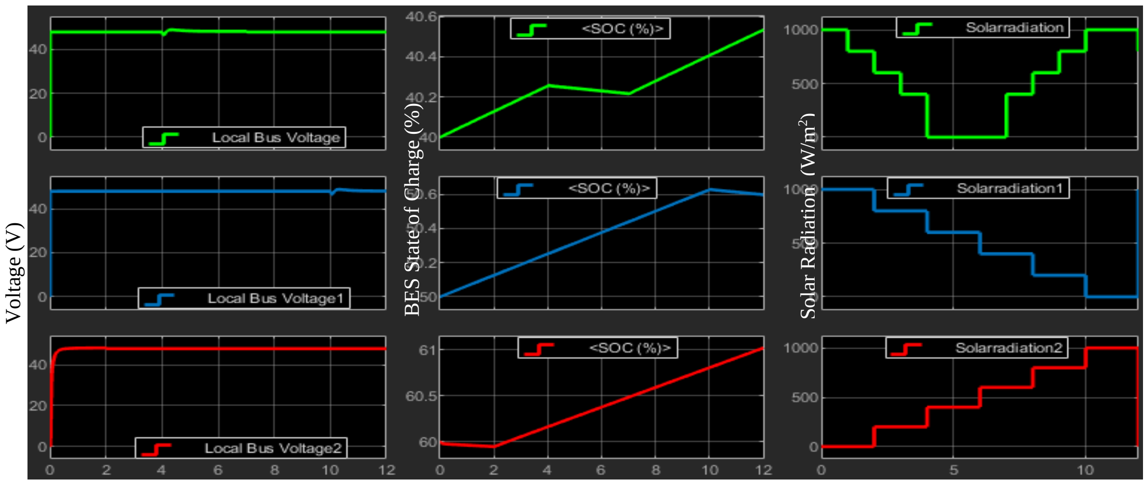

Time (s)

Fig. 7. Local controller SIMULINK simulation results.

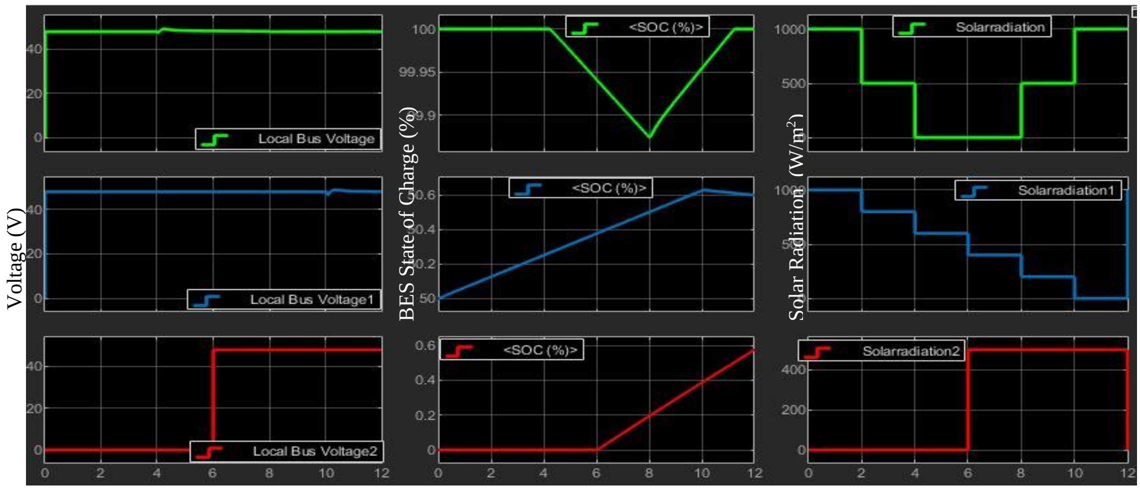

Time (s)

Fig. 8. Local controller SIMULINK simulation results 2

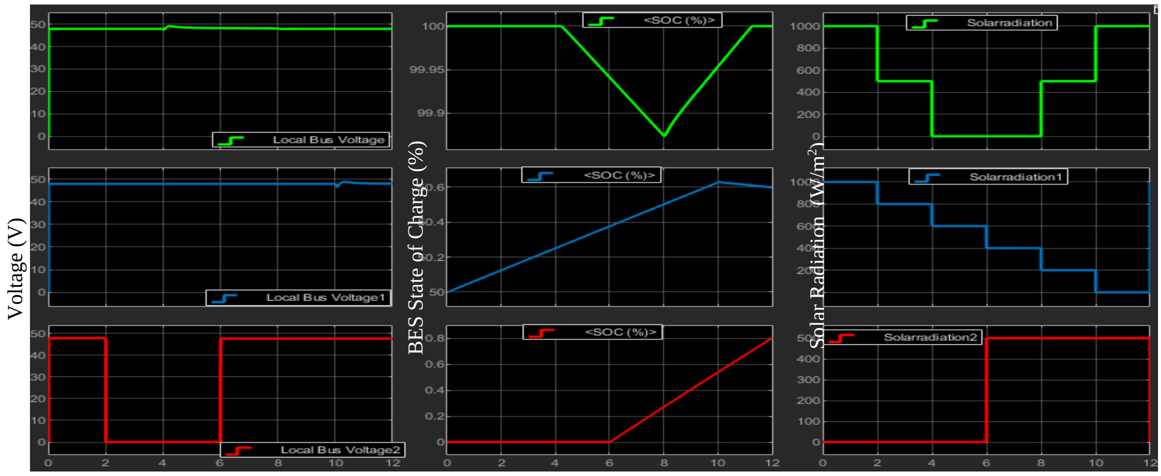

Fig. 9. Upper level controller algorithm SIMULINK simulation results.

V. Conclusion

This paper proposes a distributed solar PV and battery energy storage DC microgrid with multiple nano-grids interconnected to share power. This microgrid structure aims to design a microgrid that allows a nano-grid with surplus power to share the power with the load shedding nano-grid. The upper controller ensures that the power shared is the surplus power to avoid driving the sharing nano-grid to load shedding. Both the low level and upper level controllers utilize the dc bus signaling strategy to monitor and regulate local bus voltage and control power sharing. The proposed design was simulated and verified to be a microgrid structure that allows excess power to be shared to avoid load shedding to nano-grids when there is surplus power available from one of the nano-grids.

References

[1]M. Elshimy and K. M. El-Aasar, "Carbon footprint, renewable energy, non-renewable energy, and livestock: testing the environmental Kuznets curve hypothesis for the Arab world," *Environment, Development and Sustainability,* vol. 22, no. 7, pp. 6985-7012, 2020/10/01 2020, doi: 10.1007/s10668-019-00523-0 Accessed:10-10-2021.
[2]S. SA. "Statistics BY Place." Department: Statistics South Africa, 2011. [Online]. Available: http://www.statssa.gov.za/?page_id=4286&id=8542. Accessed:25-10-2020
[3]SOLARGIS. "Solar resource maps of South Africa." 2020. [Online]. Available: https://solargis.com/maps-and-gis-data/download/south-africa Accessed:10-10-2020
[4]A. R. Jordehi, "Allocation of distributed generation units in electric power systems: A review," *Renewable and Sustainable Energy Reviews,* vol. 56, pp. 893-905, 2016. [Online]. Available: https://doi.org/10.1016/j.rser.2015.11.086 Accessed:29-12-2020.
[5]M. Hamza, M. Shehroz, S. Fazal, M. Nasir, and H. A. Khan, "Design and analysis of solar PV based low-power low-voltage DC microgrid architectures for rural electrification," *2017 IEEE Power & Energy Society General Meeting, Chicago,IL,* 2017. [Online]. Available: http://ieeexplore.ieee.org/stamp/stamp.jsp?tp=&arnumber=8274134&isnumber=8273724 Accessed:25-10-2019.
[6]G. M. Bokanga, A. Raji, and M. T. Kahn, "Design of a low voltage DC microgrid system for rural electrification in South Africa," *Journal of Energy in Southern Africa,* vol. 25, no. 2, pp. 9-14, 2014. [Online]. Available: http://www.scielo.org.za/scielo.php?pid=S1021-447X2014000200002&script=sci_arttext&tlng=es Accessed:10-10-2020.
[7]K. Palaniappan, S. Veerapeneni, R. Cuzner, and Y. Zhao, "Assessment of the feasibility of interconnected smart DC homes in a DC microgrid to reduce utility costs of low income households," in *2017 IEEE Second International Conference on DC Microgrids (ICDCM)*, 2017: IEEE, pp. 467-473. [Online]. Available: https://ieeexplore.ieee.org/stamp/stamp.jsp?tp=&arnumber=8001087 Accessed:25-09-2020.
[8]M. Nasir, Z. Jin, H. A. Khan, N. A. Zaffar, J. C. Vasquez, and J. M. Guerrero, "A Decentralized Control Architecture Applied to DC Nanogrid Clusters for Rural Electrification in Developing Regions," *IEEE Transactions on Power Electronics,* vol. 34, no. 2, pp. 1773-1785, 2019, doi: 10.1109/TPEL.2018.2828538 Accessed:20-01-2021.
[9]A. Werth, N. Kitamura, I. Matsumoto, and K. Tanaka, "Evaluation of centralized and distributed microgrid topologies and comparison to Open Energy Systems (OES)," in *2015 IEEE 15th International Conference on Environment and Electrical Engineering (EEEIC)*, 2015: IEEE, pp. 492-497. [Online]. Available: https://ieeexplore.ieee.org/stamp/stamp.jsp?tp=&arnumber=7165211 Accessed:19-08-2021.
[10]J. Kumar, A. Agarwal, and V. Agarwal, "A review on overall control of DC microgrids," *Journal of energy storage,* vol. 21, pp. 113-138, 2019. [Online]. Available: https://www.sciencedirect.com/science/article/pii/S2352152X18302019 Accessed:12-02-2021.
[11]P. P. Padhi and K. Deepa, "Dc microgrids: architecture and challenges," in *IOP Conference Series: Materials Science and Engineering*, 2021, vol. 1070, no. 1: IOP Publishing, p. 012098. [Online]. Available: https://iopscience.iop.org/article/10.1088/1757-899X/1070/1/012098/meta Accessed:10-03-2022.
[12]M. Lonkar and S. Ponnaluri, "An overview of DC microgrid operation and control," in *IREC2015 The Sixth International Renewable Energy Congress*, 24-26 March 2015 2015, pp. 1-6. [Online]. Available: https://ieeexplore.ieee.org/abstract/document/7110892 Accessed:15-01-2021.
[13]Y. Yao, N. Ertugrul, and S. A. Pourmousavi, "Power Sharing and Voltage Regulation in Islanded DC Microgrids with Centralized Double-Layer Hierarchical Control," in *2021 31st Australasian Universities Power Engineering Conference (AUPEC)*, 2021: IEEE, pp. 1-6. [Online]. Available: https://ieeexplore.ieee.org/abstract/document/9597804 Accessed:12-01-2022.
[14] L. Zhang, T. Wu, Y. Xing, K. Sun, and J. M. Gurrero, "Power control of DC microgrid using DC bus signaling," in *2011 Twenty-Sixth Annual IEEE Applied Power Electronics Conference and Exposition (APEC)*, 2011: IEEE, pp. 1926-1932. [Online]. Available: https://ieeexplore.ieee.org/abstract/document/5744859 Accessed:24-11-2020.
[15]F. Li, Z. Lin, Z. Qian, and J. Wu, "Active DC bus signaling control method for coordinating multiple energy storage devices in DC microgrid," in *2017 IEEE Second International Conference on DC Microgrids (ICDCM)*, 2017: IEEE, pp. 221-226. [Online]. Available: https://ieeexplore.ieee.org/abstract/document/8001048 Accessed:15-05-2021.
[16]Solcast. "Solar Irradiance Data." Solcast, 2020. [Online]. Available: https://solcast.com. Accessed:10-06-2020
[17]M. A. Eltawil and Z. Zhao, "MPPT techniques for photovoltaic applications," *Renewable and Sustainable Energy Reviews,* vol. 25, pp. 793-813, 2013/09/01/ 2013, doi: https://doi.org/10.1016/j.rser.2013.05.022 Accessed:25-02-2021.

Satellite to Ground Communication Energy Storage Selection

Simphiwe A Ntlela
Department of Electrical Power Engineering
Durban University of Technology,
Durban, South Africa
21219472@dut4life.ac.za

Innocent E. Davidson
Department of Electrical Power Engineering
Durban University of Technology,
Durban, South Africa
innocentD@dut.ac.za

***Abstract*— LEO power requirements have significantly increased as a result of the rising demand for broadband services from Low Earth Orbit Communication Satellites (LEO), as well as the high power needs of high-definition digital broadcasts and rising communication spectrum demands. In this study, three energy storage technologies are shown using flywheels and chemical batteries as the source of energy for LEO satellites during the eclipse. Every structure is created and adjusted with the energy needs of an example LEO satellite and several important satellite characteristics are talked about. The electronic storage device and interfaces are displayed to provide a sufficient view for comparing them in various ways. Following that, an assessment between. These energy storage systems (ESSs) are utilized by taking into consideration weight, operational temperature, effectiveness, dependability, and Self-discharge fading. Lastly, the Conclusion lists the top systems that are advised they are capable.**

Keywords*— *Leo satellite power supply, flywheel, storage of power system, chemical battery

I. INTRODUCTION

In satellite communication, energy management has always been a significant problem. Geostationary orbit (GEO), Low Earth orbit (LEO), and Medium Earth orbit (MEO) satellites are the three categories into which satellites can be divided [1]. LEO satellites orbit the earth at distances between 300 and 1000 kilometres [1-2]. LEO satellites only need a little amount of power because they are so close to the sun. Therefore, sunlight typically provides them with all of their energy needs. However, the majority of these satellites experience eclipses for a portion of their rotating period. Therefore, an energy storage system (ESS) is required to keep them alive throughout the eclipse. The satellite that is being examined in this article is a standard microsatellite, which is located approximately 700 kilometres from the planet. Therefore, the time span will last for roughly 90 minutes, which will include 30 minutes of the eclipse and 60 minutes of daylight. Its typical power usage is 40W, and the DC bus voltage is 28 volts. The ESS should be charged and stored with enough energy when the satellite is exposed to the sun (in a charging condition) to provide the satellite with the necessary power during an eclipse (discharge state). The most popular technologies for short-term energy storage, in general, are superconducting magnetic energy storage systems (SMESS), flywheel Energy storage systems (FESS), and chemical cell energy storage systems (CBESS) [3-4]. Efficiency, longevity, dependability, operative temperature, weight, volume, and system cost are the most crucial factors in an ESS for satellite applications. Up until the late 1990s, when (National Aeronautics and Space Administration) NASA began using flywheel energy storage systems in the international space station, the only energy storage devices for LEO satellites were chemical cells [5-6]. The limiting of their charge and discharge cycles, which reduces their performance and lifespan, is the most significant issue with cells [7]. Because the period of LEO satellites is 1.5 to 1.74 hours in relation to their orbit, the rate of charge/discharge is quite high, which limits battery capacity to 3-5 years [7].

Flywheels were first proposed for use as energy storage systems in satellites by Dr Kirk of Maryland University and NASA in 1976 [8-9]. Instead of being heavy, they should be created with a large radius and operate quickly to store more power. Therefore, flywheels are an alternative to chemical batteries in certain applications. For LEO satellite communication, two ESSs based on chemical batteries and flywheels are constructed and optimized as a source of energy when the satellite is in an eclipse and the light's radiation is blocked. The optimal ESS for this application is then determined by comparing these several ESS types in terms of efficiency, dependability, weight, temperature, and self-discharge. The remainder of this article is structured as follows: A flywheel energy storage system is constructed and optimized in Section III. A chemical battery-based energy storage system is designed in Section II Then, in Section IV, an assessment of different energy storage devices is provided, taking into account factors like their effectiveness, dependability, temperature, weight, and self-discharging. The final section, the conclusion, shows which power storage solution, when viewed from several angles, is the best.

II. GROUND POWER STORAGE FOR FLYWHEEL

In FESS, when the satellite is in sunlight, the surplus of provided energy by solar cells is stored into rotational kinetic energy using an electrical machine. During eclipse duration, stored kinetic energy is converted into electrical energy. The advantages of FESSs for satellite applications are presented in [10-11], and [12-15] and some are lower power demand, unlike flywheels, which require a continuous energy supply, Li-ion batteries do not need a source for ongoing charging. Less expensive to maintain: Li-ion modules feature an integrated battery management system that enables remote cell monitoring. However, flywheels have moving parts that require routine maintenance and replacement by trained workers. Broad autonomy range: Flywheels can enable autonomies of just over 30 seconds whereas Li-ion cells can provide autonomies of several hours.

A few of these benefits include their use in satellite attitude control, unlimited charge/discharge cycles, lifespan, higher efficiency, higher energy density, larger discharge depths, and thermal independency. In [16-17], instructions for designing and optimizing flywheel energy storage systems are provided in order to reduce stress and weight for space applications.

A. *Design of Flywheel and Electrical Machines*

A flywheel and an electrical machine connected are two important components of the (Flywheel Energy Storage System) FESS. A typical FESS is depicted in several portions in Fig. 1.

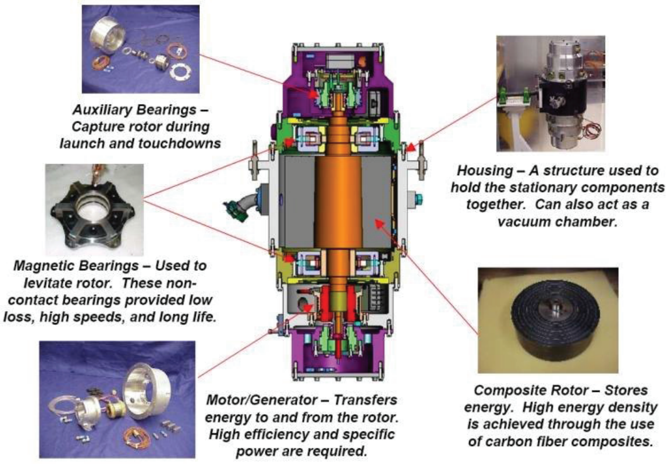

Fig. 1. The various parts of a FESS [1]..

During the charge period, electricity energy transforms into kinetic power, and flywheel speeds rise until they reach their maximum permissible speed, which is limited by mechanical factors. E_n calculates the flywheel's energy stored using Equation (1).

$$E_n = \frac{1}{2} I_{total}(\omega_{22} - \omega_{12}) \quad (1)$$

Flywheels can rotate at a speed between 20000 and 60000 rpm [15], [17]. When the machine is charged, it functions as a motor, converting energy into a mechanical energy form, and when it is discharged, it functions as a generator, converting electric power back into electrical form. Typically, this machine has three phases. So an inverter with three phases and different speeds is required. The outcome of designing and optimizing a FESS for the mentioned spacecraft is presented in **Table I** [17].

B. *FESS Power Electronics*

The power electronic block diagram for FESS power management is shown in Fig. 3. This circuit differs significantly from the CBESS power electronic circuit in several key ways. An additional inverter is included in the FESS energy electronic circuit to accommodate the three-phase electrical device. This inverter ought to be able to provide a changeable frequency field inversely proportional to the flywheel's speed [9].

TABLE I. DESIGN AND OPTIMIZATION OF FESS RESULT

Charge/ Discharge Time (s)	**Min. Speed (rpm)**	**Max. Speed (rpm)**	**Min. Line Voltage(V)**	**Max. Voltage (V)**
3600/1800	20000	60000	24	72
Energy Efficiency	**Mass (kg)**	**Volume (cm^3)**	**Average self-discharge (iron losses) (w)**	
97%	1.2	832	0.8	

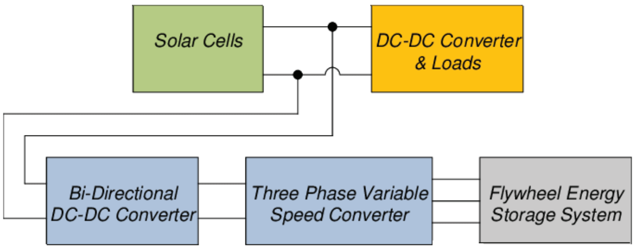

Fig. 2. Block diagram of power electronic

This extra inverter has a potential of 95% efficiency. Therefore, the FESS power electronics' high capacity is 90.25%. The charge and discharge control algorithm of FESS is comparable to CBESS.

III. BATTERY-BASED CHEMICAL POWER STORAGE SYSTEM

Chemical battery-based ESSs are the first to be described because they are the most common ESSs. Chemical battery technology recently underwent significant advancements in a variety of applications. Compared to many other storage solutions, this kind of energy storage system is very affordable and easily accessible. Additionally, cells are static devices, which is advantageous compared to dynamic storage solutions like flywheels.

A. *Arrangement of a battery*

Ni-Cd, Ni-H2, and Li-Ion batteries are the three most popular battery types used in space programs. The characteristics of these batteries are shown in Table II.

TABLE II. LI-ION, NI-H2, AND NI-CD BATTERY PROPERTIES

Battery Properties	**Ni-Cd**	**Ni-H2**	**Li-Ion**
Specific Energy (Wh/kg)	30	60	100-265
Energy Efficiency (%)	72	70	99%or higher
Self-discharge (%/day)	0.5	5	5
Temperature Range (°C)	0 to 40	-20 to 30	-20 to 45
Cell Voltage (V)	1.2	1.2	4.2
Memory Effect	Yes	Yes	No

Ni-Cd, which has a lighter weight. Although Ni-H2 and Li-ion have higher self-discharge rates than Ni-Cd, LEO satellites have relatively short charge and discharge times, therefore this parameter has very little impact. Additionally, Li-Ion has a wider operating temperature range than Ni-H2 and Ni-Cd. Li-Ion is therefore a better choice for CBESS in this application.

15% is the maximum depth of drain allowed for chemical batteries in low earth orbits [11], and the sample satellite uses 40W for 30 minutes (20Wh) during the eclipse. Therefore, the energy capacity for batteries should be:

The capacity of batteries = 20/0.15 Wh =133.33Wh.

TABLE III. BATTERY DESIGN RESULT

Battery Type	**Weight includes box (kg)**	**Energy efficiency**	**Self-discharge dissipation (W)**
No memory effect	7.8	99%	0.27

B. Model-Based Satellite Power Network Approach Satellite Power System of CBESS

Typically, parallel and series topologies are used to connect load energy storage systems. Overall efficiency is higher with parallel structure. In addition, multiple topologies are utilized in the satellite power transmission system as DC-DC converters. Each topology offers unique benefits and drawbacks. In earlier investigations, the bidirectional push-buck topology has been most frequently mentioned. About 95% of the CBESS power electronics built on this chassis are efficient.

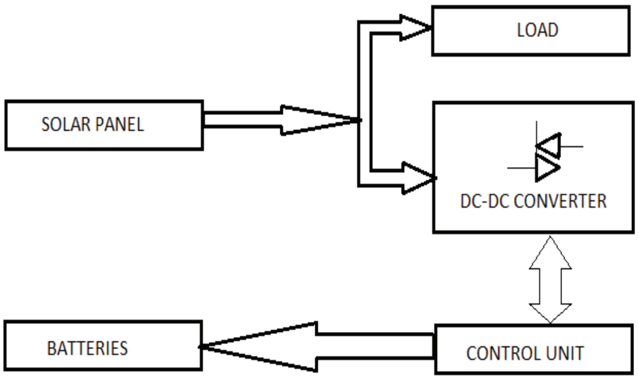

Fig. 3. A bidirectional boost-buck converter for a CBESS for satellite applications that is a parallel-connected diagram of power electronic

Fig. 3 depicts the parallel design of a DC-DC bi-directional converter for CBESS, and the batteries are linked to the DC bus by a parallel DC-DC converter. As depicted in Fig. 4, there are three modes of functioning for satellites in relation to sunlight. A brief explanation of the three modes according to sunlight will be followed by a demonstration.

- **First mode:** When the satellite is exposed to sunshine, it should regulate the DC bus voltage to ensure that the solar panels are working at their maximum power point tracking (MPPT). Additionally, the batteries should be charged in accordance with their charging characteristics and temperature.
- **Second mode:** The batteries can only provide lean charging and standby to the discharge state when they are charging.
- **Third mode:** When the batteries are draining, they are unable to supply the satellite with the necessary energy during the eclipse.

IV. COMPARISON

This section discussed an entire analysis of these ESSs in order of significance. Efficiency, dependability, operational temperature, weight, and self-discharge dissipation are the five categories into which the assessment is divided.

A. Efficiency

Efficiency is the most crucial satellite design factor. Applications; Since a system with greater efficiency yields fewer heat issues and a smaller area of solar panels. then this aspect is regarded as the initial comparison subject. The efficiency of flywheels is around 2% lower than that of chemical batteries, as seen in Tables II and III. A three-phase power inverter using FWESS has a maximum efficiency of 95%. Due to the FWESS's identical efficiency in the charge and discharge states, the overall energy efficiency of this ESS is 76.63% ([95%, 95%, 97%]**2**). Battery energy efficiency is 99%, making the overall CBESS efficiency ([99%95%]**2**) 88.45%. Therefore, from this perspective, CBESS is the best option.

B. Reliability

Mead Time Between Failure (MTBF) is equivalent to satellite lifetime because there are no access options for space-based repairs of LEO satellites. Reliability is therefore the second most crucial factor in the design of a satellite. More reliability, in accordance with MIL-HDBK-217, is produced by fewer used components, as well as lower losses and temperatures [17]. The least reliable of these ESSs drive circuits is the FESS drive circuit since it features an extra inverter, which increases heating and losses while also using more components. In contrast, chemical batteries have a short lifespan compared to flywheels, which means they are less reliable. Because of their rapid rotation, flywheels experience severe mechanical stresses. Flywheels operate at extremely high speeds and are subject to several mechanical stresses. Consequently, they are less reliable than chemical batteries as a result of these mechanical stresses and their drive circuit. In conclusion, CBESS is the most dependable ESS.

C. Temperature

The satellite's temperature and distance from the sun are both rapidly changing as it rotates around the planet. The selected chemical battery has a restricted functioning temperature range between -20 ^{0}C and 45 ^{0}C, as shown in Table I [10]. Temperature changes in FESSs cause a 2.5% error rate every 10 ^{0}C when permanent magnets are utilized in electrical machines [17-18]. CBESS is the most adaptable choice in this strategy, and FWESS is ranked second.

D. Weight

The weight of a satellite determines how expensive its launch will be. Weight is a crucial design parameter, then. The results of the optimum design approach and Tables II and III show that CBESS weighs 6.6 kg more than FWESS. FWESSs are thus great from this perspective.

E. Self-discharge

Each ESS dissipates internally. In order to fix them in fully charged condition (Trickle charge), a very low current is required. Tables 1 and 3 show that FWESS has 0.53W more self-discharge dissipation than CBESS. As a result, FWESS requires more trickle charge than CBESS.

V. CONCLUSION

The primary characteristics of a conventional LEO satellite are discussed in this study. We examine, design, and optimize various energy storage technologies for energy supplements. Then, within each of them, a comparison is made in terms of effectiveness, dependability, operational temperature, weight, and self-discharge dissipation to determine which is the best option for an energy storage system in satellite applications. When all of the ESS's advantages and disadvantages are taken into account, the CBESS is the most highly recommended flywheel-based ESS because of its superior efficiency, reliability, and temperature range of operation.

ACKNOWLEDGEMENT

The authors acknowledge the assistance from Prof IE Davidson and Dr Abayomi A. Adebiyi and the DUT staff for their support and encouragement in the preparation of this paper.

REFERENCES

[1] P.E. Kascak, B. H. Kenny, T. P. Dever, W. Santiago, and R. H. Jansen "International space station bus regulation with NASA Glenn research center flywheel energy storage system development unit." In *proceeding of the 36th Intersociety Energy Conversion Engineering Conference*, pp.1-15, 2001.

[2] E. Lee, "A micro HTS renewable energy/attitude control system for micro/nano satellites," *IEEE Transaction on Applied Superconductivity,* vol. 13, no. 2, pp. pp. 2263-2266, 2003.

[3] J. A. Kirk and P. A. Studer, "Mechanical Capacitor," NASA TND-8185, 1976.

[4] G. E. Rodriguez, P. A. Studer, and D. A. Baer, "Assessment of flywheel energy storage for spacecraft power systems," *NASA Technical Memorandum*, pp. 70, 1983.

[5] Saftabatteris. [Online]. Available: http://www.saftbatteris.com

[6] C. D. Brown, "Elements of spacecraft design," AIAA Education Series, Parallel Structure, 2002.

[7] R. Gules, J. P. Pacheco, H. L. Hey, and J. Imhoff, "A maximum power point tracking system with parallel connection for PV stand-alone applications," *IEEE Transaction on Industrial Electronics*, vol. 55, no. 7, pp. 2674-2683, 2008.

[8] W. Xiao, N. Ozog, and W. G. Dunford, "Topology study of photovoltaic interface for maximum power point tracking," *IEEE Transaction on Industrial Electronics*, vol. 54, no. 3, pp. 1696-1704, 2007.

[9] M. A. Arslan, "Flywheel geometry design for improved energy storage using finite element analysis," *Material and Design*, vol.29, no. 2, pp.514-518, 2007.

[10] W. Wang, "Design of high-speed flywheel motor/generator for aerospace applications," PhD dissertation, The Pennsylvania State University, pp. 128, 2003.

[11] B. Abdi, J. Milimonfared, J. S. Moghani, and A. K. Kaviani, "Simplified design and optimization of slotless halbach machine for micro-satellite's electro-mechanical batteries." *International Review of Electrical Engineering* (I.R.E.E.), vol. 4, no. 2, pp.305-311, 2009.

[12] United States. Dept. of Defense, "Reliability prediction of electronic equipment," Military handbook; MIL-HDBK-217F, Jan. 1992.

[13] NASA Langley Research Center. [Online]. Available: http://www.larc.nasa.gov

[14] The Tech Museum of Innovation. [Online]. Available: http://www.thetech.org

[15] C. S. Wang and M. H. Nehrir, "Power management of a stand-alone wind/Photovoltaic/Fuel cell energy system," *IEEE Transaction on Energy Conversion*, vol. 23, no. 3, pp. 957–967. 2008.

[16] C. Abbey and G. Joos, "Supercapacitor energy storage for wind energy applications," *IEEE Transaction on Industry Applications*, vol. 43, no. 3, pp. 769–776, 2007.

[17] D. Christopher, R. F. Beach, and J. R. Barton, "A flywheel energy storage system test on the International Space Station," In IEEE *Proceedings of the Thirty-Second Intersociety Energy Conversion Engineering Conference* (Cat. No. 97CH6203), vol. 3, pp. 1762-1766, 1997.

The Green Hydrogen as a Renewable Energy Source and Storage in the Transportation Sector of Germany

Adimchinobi Asiegbu
EECE Department
Cape Peninsula University of Technology
Cape Town, South Africa
221599061@cput.ac.za

Tariq Kahn
EECE Department
Cape Peninsula University of Technology
Cape Town, South Africa
khant@cput.ac.za

Ali Almaktoof
EECE Department
Cape Peninsula University of Technology
Cape Town, South Africa
almaktoofa@cput.ac.za

Abstract— The need for sustainable and environmentally friendly energy sources is very crucial if future generations are to be spared of the misdoings of past generations. Climate change, environmental pollution, radiation pollution, and the altering of the balanced ecology of the green planet earth is now a significant challenge, because if not mitigated, some island nations will disappear in the future, due to human activities energized by unsustainable fossil fuels. Based on these facts, Germany has taken concrete and important steps to stem the tide of this ill wind by embracing the Green Hydrogen system. This is more obvious in the transport system that produces more than 40% of Green House Gases in Europe. Because Germany is an industrialized European nation, the government has introduced Green Hydrogen for transportation in accordance with European Union energy policy.

Therefore, this paper provides a clear, concise analysis and implementation of Green Hydrogen energy in the smart energy system. The paper presents Green Hydrogen in transportation in four sections, namely, Geographical, Chemical, social, and economic aspects, respectively. The last section of this paper is the discussion of results from cost/feasibility analysis, with an erudite conclusion and recommendations made at the end of this research.

Key words— hydrogen, renewable energy, energy storage, fossil, fuel, hybrid, energy mix, generation.

I. INTRODUCTION

The need for reducing Green House Gases (GHGs), mitigating climate change, environmental pollution, and the rise in sea level, necessitates the need for alternative energy supply and a shift from conventional generation of energy from fossil fuel sources to hybrid renewable energy. In a hybrid renewable energy generation mix, Green Hydrogen (GH) plays the critical role of energy storage and energy source. It also serves as an important chemical in the manufacturing of chemical substances and products like the industrial hydrogenation process. The transport sector in Germany is a significant energy consumer and GHGs emitter. To reduce these GHGs, hydrogen energy access and use in the transport sector is imperative. This objective is achieved by analysis of hydrogen as an energy source and storage in the transport sector, using Germany as a model. This model can serve as a standard for other countries to implement hydrogen as an important player in their energy and power generation mix. GH in transportation is analyzed in four sections, namely, Geographical, Chemical, social, and economic aspects, respectively. A conclusion is drawn from these aspects at the end of this paper.

II. GEOGRAPHICAL FEATURES OF GERMANY

The Federal Republic of Germany (FRG) has a well-structured democratic federal republic form of government with its capital in the metropolitan city of Berlin as the national capital. The official language is German, the national currency is the (continental) Euro, the total geographical area is 349,223 square kilometers, and the major rivers are Danube, Rhine, Main, and Elbe. The population projected growth rate is 200,000 per year starting from 1985, and currently, the population is 80,457,737 [1]. Germany has various landscapes and many primary energy sources, like wind energy, hydropower, biomass, solar energy, and other renewable, environmentally friendly, and sustainable primary energy sources [2]. Because of the rise in demand or consumption of energy with respect to time from fossil fuel energy sources, which results in climate change, ozone layer depletion, environmental pollution, and the increase of Green House Gases (GHGs) like Carbon (IV) Oxide (CO_2), Sulphur (IV) Oxide (SO_2), Carbon (II) Oxide (CO), Nitrogen (IV) Oxide (N_2O), Hydrofluorocarbons, Perfluorocarbons, Sulphur hexafluoride (SF_6) [3], the government of Germany seeks to discourage generation of energy from fossil fuel sources like coal, crude oil, natural gas, and fuel wood. But supports renewable energy sources which are environmentally and economically sustainable, especially the green hydrogen energy sources [4].

Transportation activities produce an average of 28% of CO_2 emissions in the European union (EU) [5]. Germany being the largest economy, the wealthiest and a post-industrial nation in continental Europe, respectively, produces more CO_2 than the average value in Europe. Thus, the need for change in primary energy sources that will positively change the geographic, social, economic, and salient features of the world, and the German nation, is very crucial. To reduce the exploration and exploitation of land, atmosphere, and the earth's biosphere for fossil energy primary sources, the geography and geology of green planet earth need to be balanced and maintained by switching to renewable energy sources like hydro or hydrokinetics energy, solar energy, and wind energy. This primary sustainable energy sources are seasonal and fluctuates, making a reliable energy storage inevitable. one of such long lasting and reliable energy storage and energy mix, especially in the distributed generation is the green hydrogen energy. The ArcGIS® simulation software produced by Environmental Systems Research Institute (ESRI) is a Geographic Information System (GIS) used to analyze, organize, and map spatial data in the modelling of hydrogen supply chain network. The Model for Optimization of Regional Hydrogen Supply (MOREHyS) is used to design the hydrogen infrastructure to serve the energy storage and source role [6].

III. CHEMICAL ASPECTS OF HYDROGEN

Hydrogen can be produced from electrolysis of (acidified) water (with few drops of Tetraoxosulphate (VI) acid (H_2SO_4)). The input electrical energy is converted to chemical energy stored in the liberated hydrogen gas (the lightest gas) through an upward delivery channel, with highest thermal combustion energy of all the fossil fuel per kilogram equal to 141.80 MJ/kg according to Table 1. This is the highest heating value per kilogram and more than twice the heating value of methane.

Table 1: Higher Heating Value (HHV) and Lower Heating Value (LHV) of some common fuels at 25 °C [7].

Fuel	HHV	LHV
	MJ/kg	MJ/kg
Hydrogen	141.80	119.96
Methane	55.50	50.00
Ethane	51.90	47.62
Propane	50.35	46.35
Butane	49.50	45.75
Pentane	48.60	45.35
Paraffin wax	46.00	41.50
Kerosene	46.20	43.00
Diesel	44.80	43.4
Coal (anthracite)	32.50	
Coal (lignite - USA)	15.00	
Wood (MAF)	21.70	
Wood fuel	21.20	17.0
Peat (dry)	15.00	
Peat (damp)	6.00	

Fuel	MJ/kg	kJ/mol
Methanol	22.7	726
Hydrazine	19.4	622.0
Hexamine	30.0	4,200.0
Ethanol	29.7	1,367
Carbon	32.8	393.5
Benzene	41.8	3,268
Ammonia	22.5	382.6
Acetylene	49.9	1,300
1-Propanol	33.6	2,020

Oxygen, being the other liberated chemical element, which is particularly useful in the hospital, is evolved through the downward delivery channel (heavy gas). The stored energy in the hydrogen gas can be controlled and used as a fuel for Internal Combustion Engine (ICU) for locomotives, mechanical machines, aircraft engine, industrial manufacturing of various chemical products, and fuel cell for powering electrical machines and devices. In a fuel cell the hydrogen gas chemical energy is converted to electrical energy, producing water as the product of the electrochemical reaction between hydrogen and oxygen in the fuel cell. The energy density of hydrogen is 120 MJ/kg or 33.6 kWh/kg [8]. Thus, hydrogen serves as an energy source and storage. A prototype fuel cell system delivers a nominal output power of 31.5 W at 12 V for 38 h with only one recharging cycle, and twice the energy density of conventional storage systems [9]. Hydrogen produced from electrolysis of water, using electrical energy from renewable sources like hydro, wind, solar etc. is called Green Hydrogen (GH) [10].

Transportation being a significant energy consumer is considered as a standard for implementation of the green hydrogen energy, and this is referred to as the Green Hydrogen (GH) for transportation, using Germany as a case study or template. Green Hydrogen is the splitting of a water molecule to yield one molecule of hydrogen (two atoms of hydrogen) and one atom of oxygen, when a direct current electricity is passed through water. the GH produced can be stored as Liquid Hydrogen (LH) or Compressed Hydrogen (CH), transported (in pipelines or in tanks using trucks), and used as a primary energy source (for direct heating, electrical energy, industrial or commercial purpose) when the wind energy, solar energy, and other renewable sources are not available or in short supply [11]. Oxygen atom is very reactive, solely responsible for combustion (an example of oxidation reaction) and must be paired to form diatomic (O_2) gas in nature, yielding heavy oxygen molecules that descends through the downward delivery displacement. Hydrogen atom is also reactive and the only atom that loses electron to forms proton (an example of reduction reaction) that must be paired to form the lightest chemical element ($H_{2(g)}$), ascending through the upward delivery displacement. The two half (electron) reactions are collectively known as redox reaction, with water as the product. $O_{2(g)}$ is abundant in the atmosphere but $H_{2(g)}$ is not, making it a limited chemical reagent and renewable green energy source and storage.

IV. SOCIAL ASPECTS OF GREEN HYDROGEN

The GH produced should be acceptable, socially and economically appealing, strategically located, and must pass through some market and economic routes before getting to the energy consumer (Households, Industries, commercial users, Building energy users) in the society. The cost of GH transportation using truck is reduced using four different strategies, and at high compressed pressure of 250 Bars and 350 bars in the year 2030 according to [12]. Thus, modern infrastructure must be in place, or the old infrastructure must be upgraded to accommodate the peculiar needs of GH storage, transportation, and end device direct use as a clean energy source. The hydrogen transportation infrastructure in Germany, projected/modelled for year 2030 is shown in Figure 1. The parameters that can improve hydrogen access include the hydrogen storage facilities, hydrogen production plants in place, number of connecting networks for hydrogen transportation and the flow rate of hydrogen gas or liquified hydrogen.

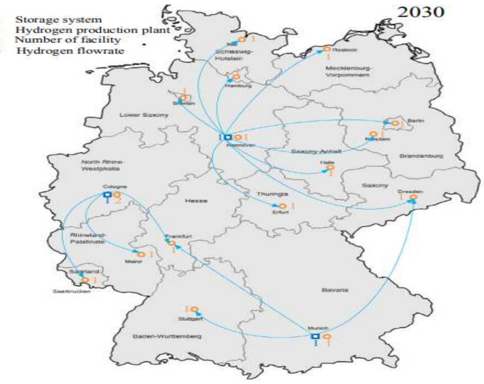

Figure 1: The GH transportation infrastructure for 2030 [13].

V. ECONOMIC ASPECTS OF GREEN HYDROGEN ENERGY SOURCE

To encourage the use GH, the Germany government introduced a pilot program for the use of Fuel Cell Electric Vehicles (FCEV) and Hydrogen Supply Chain (HSC) [14]. Based on the current trend in energy demand and savings from using high energy equipment or energy system, cost savings from avoiding health issues resulting from GHGs, and environmental pollutions, implementation of distributed energy system, advancement in technology, and future research breakthroughs, the cost of generating GH will decrease and GH/energy access will increase. The global need and demand for hydrogen from refining, ammonia, and other sources is shown in Figure 2.

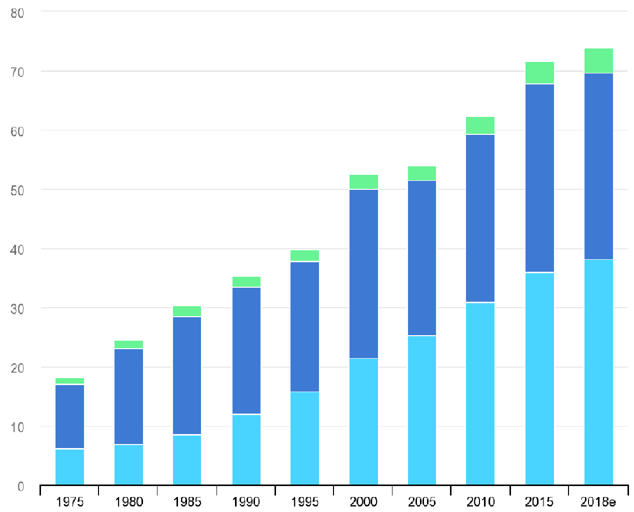

Key: Refining, Ammonia, Other

Figure 2: World Hydrogen needs and demand [15].

The hydrogen supply chain depicted in figure 3, shows the renewable energy sources that is used to produce hydrogen. The hydrogen is liquified and transported through a tanker truck to conditioning and storage facilities. Finally, the hydrogen is supplied to the fueling and refueling stations for easy access to the public and industrial users.

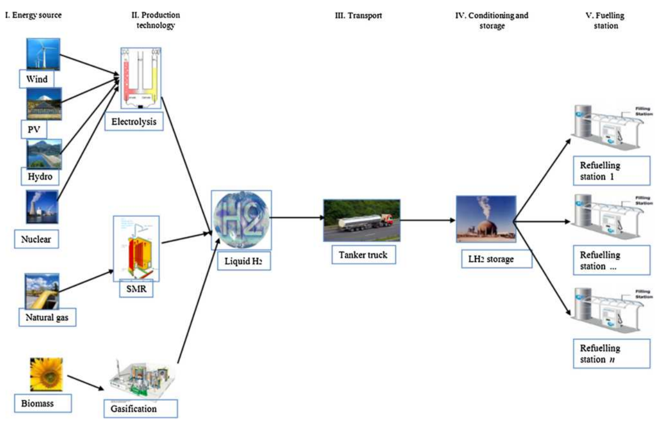

Figure 3: Hydrogen Supply Chain (HDC) [16].

Geographic tool, like the geographic information system (GIS) can be used to model the supply chain managements systems like the Hydrogen Supply Chain (HDC) systems. Model for Optimization of Regional Hydrogen Supply is used to do geographic analysis (and economic feasibility) of the German HDC [6]. FCEVs will be sustainable, since it is an example of hydrogen to renewable energy technology, which is reliable (it can travel long distances without the need to recharge or refuel car batteries), can be integrated into the distributed generation system, and can capture wind energy, hydro energy, nuclear energy, and solar energy directly from a natural energy rich environment.

The new cost of using hydrogen energy will change according to the equation: the **New Cost = the reference Cost X (New Capacity / Reference Capacity)**$^{\textbf{Power Low Factor}}$ [17]**.** Where the power low factor is assumed to be 0.6 for Green Hydrogen (GH), transported through pipelines. The capacity of GH in Germany is 960 Tons/day, capital cost of production is 1910 million $USD, and production unit cost is 6.40 $USD [18]. Due to increase in demand of GH in Germany, the new expansion cost of the current capacity that will double the original capacity (1920 Tons/day at a power factor of 0.6, is calculated as **New Cost = 1910 * 10^6 * $(1920 / 960)^{0.6}$ = 2895 * 10^6** $USD, up to $USD 3820 million (double of the cost at power low factor of 1), and a new unit cost of $USD 12.8. This shows that if the demand is doubled, the cost tend to double, if the present infrastructure is not modernized in future. The pipeline transportation of GH becomes viable when the GH market share value of Fuel Cell Electric Vehicle (FCEV) is at least 10%, and if more than 30% of GH is to be transported, national centralized network should be implemented instead of regional networks [19].

GH produced needs to generate less than 9.5 kg $CO_{2(g)}$ per kg of $H_{2(g)}$ produced, to offer an advantage, with a reduction of tank-to-well emissions by 2020 to 95 g/km, equivalent to 113 g CO_2/km in a well-to-wheel scenario [20]. GH should cost < 5.3 US$/kg between 2020 and 2030 [6], and < US$7.11per kg in 2050 [21] to be economically viable. The European Union (EU) commission directive on the alternative fuels infrastructural deployment, recommend a H_2 refueling station at an interval of 300 km on the motorways and high ways to mitigate the energy access issues [22][23].

VI. RESULT AND DISCUSSION

GH implementation is currently expensive, and it may not be within the reach of low income and developing nations, since it will take Germany about $USD 3820 million and a new unit cost of $USD 12.8 to double its current capacity, even though Germany has significant hydrogen transportation infrastructure. If 30% or more of GH is to be transported through the pipeline, then national centralized pipeline network should be implemented instead of a regional network. This will ensure lower cost, broader reach of the GH, higher use and penetration of GH, and increased access of GH. GH will cost between 5.3 US$/kg and

US$7.11per kg from 2020 to 2050. The refueling stations should be spaced 300km apart from each other. Despite this prohibitive cost of integrating hydrogen in the energy mix, GH is a game changer, because it will be an efficient storage of energy in the chemical energy form, which can be easily converted to heat and electrical energy using modern technologies. Because of the high heat value of hydrogen, it will be difficult to use it as fuel in the ICE of cars, as cooking fuel or in some mechanical machineries. However, hydrogen is used in fuel cells, which makes it suitable for future Electric Vehicles (EVs). It can replace electric furnace in future, and it will be useful in chemical and metal refining industries. GH has the least carbon footprint and GHGs emissions.

VII. CONCLUSION AND RECOMMENDATIONS

Renewable energy in Germany is growing and receiving attention from the Germans and the EU. The German government and the EU commission have incentivized and prioritized decarbonization of the environment, prevention of emission of pollutant, elimination of biological toxins (Mercury, Lead etc.), and GHGs into atmosphere and biosphere. Through constant research in energy, modern and efficient energy equipment should be used, as a compliance to energy standards and policy by energy users or consumers. Green Hydrogen (GH) is embraced in Germany, as a way of energy storage from variable energy input from various renewable energy sources like wind and solar energy, respectively. This GH electrolysis technology provides fluidity and reliability to the distributed generation in German Smart Grid (SG) and future Smart Energy system. The GH primary energy source can function as a battery, direct heater, direct boiler, and other residential, commercial, and industrial purposes. From the results retrieved from this research paper, the cost of GH production will reduce with respect to time provided efficient energy equipment is used, modern and reliable energy transmission system is in place, like efficient pipelines, and smart grid.

Finally, the hydrogen infrastructure for the transportation sector in Germany, can serve as a model for other countries to use and further develop to suit their peculiar needs and Sustainable Development Goals (SDGs) with regards to energy access, energy storage and energy savings.

Considering the study done in this work, the following recommendations are made:

- ❖ The spatial variations in hydrogen demand can be improved by demand modelling using any of the software mentioned in this study.
- ❖ Due to constrains associated with harvesting GH from renewable sources, other sources with less carbon footprint like biogas (through Steam Methane Reforming (SMR) Hydrogen Production technology route shown in figure 3) can be considered in the generation of GH in energy and power generation mix.
- ❖ Using Carbon capture and storage innovative technologies, natural gas pipelines for supplying GH (30% or more) will improve energy access and energy storage.
- ❖ The possibility of integrating GH in the industries should be investigated and implemented to lower overall cost of GH and increase GH demand.
- ❖ Optimization of GH production should be accelerated using Dynamic Programming (DP).

VIII. ACKNOWLEDGMENT

We thank the Electrical, Electronics, and Computer Engineering (EECE) Department of Cape Peninsular University of Technology, for their support and contribution to this research. Also, we thank our families for their unquantifiable support and understanding throughout this academic exercise.

REFERENCES

[1] "GERMANY (Federal Republic of)," in *1977*, 2020.
[2] K. Hansen, B. V. Mathiesen, and I. R. Skov, "Full energy system transition towards 100% renewable energy in Germany in 2050," *Renew. Sustain. Energy Rev.*, vol. 102, 2019, doi: 10.1016/j.rser.2018.11.038.
[3] R. Tuckett, "Greenhouse gases," in *Encyclopedia of Analytical Science*, 2019.
[4] W. P. Schill, "Residual load, renewable surplus generation and storage requirements in Germany," *Energy Policy*, vol. 73, 2014, doi: 10.1016/j.enpol.2014.05.032.
[5] P. Thalmann and M. Vielle, "Lowering CO2 emissions in the Swiss transport sector," *Swiss J. Econ. Stat.*, vol. 155, no. 1, 2019, doi: 10.1186/s41937-019-0037-3.
[6] M. Ball, M. Wietschel, and O. Rentz, "Integration of a hydrogen economy into the German energy system: an optimising modelling approach," *Int. J. Hydrogen Energy*, vol. 32, no. 10–11, 2007, doi: 10.1016/j.ijhydene.2006.10.016.
[7] S. G. Lias *et al.*, "Ionization Energetics data, NIST Chemistry WebBook, NIST Standard Reference Database Number 69," *Natl. Inst. Stand. Technol. Gaithersbg. MD*, vol. 20899, 2011.
[8] K. K. Gangu, S. Maddila, S. B. Mukkamala, and S. B. Jonnalagadda, "Characteristics of MOF, MWCNT and graphene containing materials for hydrogen storage: A review," *Journal of Energy Chemistry*. 2019, doi: 10.1016/j.jechem.2018.04.012.
[9] G. Han *et al.*, "Development of a high-energy-density portable/mobile hydrogen energy storage system incorporating an electrolyzer, a metal hydride and a fuel cell," *Appl. Energy*, vol. 259, 2020, doi: 10.1016/j.apenergy.2019.114175.
[10] B. S. Thapa and B. Thapa, "Green Hydrogen as a Future Multi-disciplinary Research at Kathmandu University," in *Journal of Physics: Conference Series*, 2020, vol. 1608, no. 1, doi: 10.1088/1742-6596/1608/1/012020.
[11] J. F. Hake, J. Linssen, and M. Walbeck, "Prospects for hydrogen in the German energy system," *Energy Policy*, vol. 34, no. 11, 2006, doi: 10.1016/j.enpol.2005.12.015.
[12] A. Lahnaoui, C. Wulf, H. Heinrichs, and D. Dalmazzone, "Optimizing hydrogen transportation system for mobility by minimizing the cost of transportation via compressed gas truck in North Rhine-Westphalia," *Appl. Energy*, vol. 223, no. February, pp. 317–328, 2018, doi: 10.1016/j.apenergy.2018.03.099.
[13] A. Ochoa Bique and E. Zondervan, "An outlook towards hydrogen supply chain networks in 2050 — Design of novel fuel infrastructures in Germany," *Chem. Eng. Res. Des.*, vol. 134, 2018, doi: 10.1016/j.cherd.2018.03.037.
[14] S. De-León Almaraz, C. Azzaro-Pantel, L. Montastruc, and M. Boix, "Deployment of a hydrogen supply chain by multi-objective/multi-period optimisation at regional and national scales," *Chem. Eng. Res. Des.*, vol. 104, pp. 11–31, 2015, doi: 10.1016/j.cherd.2015.07.005.
[15] G. S. Ogumerem, C. Kim, I. Kesisoglou, N. A. Diangelakis, and E. N. Pistikopoulos, "A multi-objective optimization for the

design and operation of a hydrogen network for transportation fuel," *Chem. Eng. Res. Des.*, vol. 131, pp. 279–292, 2018, doi: 10.1016/j.cherd.2017.12.032.

[16] S. De-León Almaraz, M. Boix, C. Azzaro-Pantel, L. Montastruc, and S. Domenech, "Spatial-based Approach of the Hydrogen Supply Chain in the Midi-Pyrénées Region, France," in *Computer Aided Chemical Engineering*, vol. 33, 2014.

[17] M. Kim and J. Kim, "Optimization model for the design and analysis of an integrated renewable hydrogen supply (IRHS) system: Application to Korea's hydrogen economy," *Int. J. Hydrogen Energy*, vol. 41, no. 38, pp. 16613–16626, 2016, doi: 10.1016/j.ijhydene.2016.07.079.

[18] A. Lahnaoui, C. Wulf, and D. Dalmazzone, "Optimization of hydrogen cost and transport technology in france and germany for various production and demand scenarios," *Energies*, vol. 14, no. 3, 2021, doi: 10.3390/en14030744.

[19] J. André, S. Auray, D. De Wolf, M. M. Memmah, and A. Simonnet, "Time development of new hydrogen transmission pipeline networks for France," *Int. J. Hydrogen Energy*, vol. 39, no. 20, 2014, doi: 10.1016/j.ijhydene.2014.04.190.

[20] A. Boretti, "Fuel cycle CO2-e targets of renewable hydrogen as a realistic transportation fuel in Australia," *Int. J. Hydrogen Energy*, vol. 36, no. 5, 2011, doi: 10.1016/j.ijhydene.2010.12.071.

[21] European Commission, "HyWays - The European Hydrogen Roadmap," *Dir. Res. Inf. Commun. Unit*, vol. Directorat, no. Contract SES6-502596, 2008.

[22] N. Gürbilek, "DIRECTIVE OF THE EUROPEAN PARLIAMENT AND OF THE COUNCIL on the deployment of alternative fuels infrastructure," *J. Chem. Inf. Model.*, vol. 53, no. 9, 2013.

[23] C. De Cauwer, A. Guillemot, G. Cragues, J. Van Mierlo, T. Coosemans, and M. Messagie, "Towards EU-wide Interoperability of charging infrastructure for electric vehicles - The Belgian Case," 2018.

Potential of Abandoned Mine Infrastructure for Pumped Hydropower Energy Storage Implementation in South Africa

Uwem Okon Ikitde
Dept. of Electrical Power Engineering
Durban University of Technology
Durban, South Africa
22175913@dut4life.ac.za

Innocent E. Davidson
Dept. of Electrical Power Engineering
Durban University of Technology
Durban, South Africa
innocentD@dut.ac.za

Abayomi A. Adebiyi
Dept. of Electrical Power Engineering
Durban University of Technology
Durban, South Africa
abayomia@dut.ac.za

Abstract— **Electricity is found to be the most vital factor in a country's growth and economic development. Hydropower holds a prime position in terms of electricity generation among separate sites of sustainable power. Its potential to boost the global economy and lessen the reliance on petroleum-based fuels cannot be overstated. Yet, one of the obstacles to the effective deployment of the Pumped Hydroelectric Power Energy Storage (PHES) facility is the geographical restriction. The deployment of abandoned mines voids as existing infrastructure is one of the possible means of overcoming this hindrance. This study investigates the availability of abandoned mine voids for the implementation of PHES. The design guidelines, cost estimates for PHS installation in South Africa, site availability and cost of PHS future plans as well as the potential of developing PHS with other renewable energy and benefits to South Africa's electricity network are discussed. The study contributes to innovative ways of generating bulk electricity storage for local community users in South Africa.**

Keywords— ***abandoned mines, energy storage, hydropower, renewable energy, underground water, mining.***

1 INTRODUCTION

Societal growth and development have been proved over the past centuries to be intertwined around a reliable energy supply system [1]. Fossil fuels have generally been recognized as the primary energy source of bulk electric power generation Power generation like solar, wind, hydro, and biomass have emerged as the foundations of sustainable power expansion to lessen reliance on fossil and nuclear fuels [2]. The most widely used technique in the world for massive energy backups is PHES. Currently, the global PHES plant has 161 GW and it's expected to increase by 78 GW before 2030. Fig. 1 and 2 depicts the global yearly increase of PHES plant installations and the annual plant capacity increment by regions [3]. Energy storage systems enhance energy infrastructure through the use of generating technologies which significantly contributes to electric power network reliability and security [4]. The fundamental principle of PHES is the storage of electrical power in the form of hydro energy potential. Typically, pump-storage systems have an upper and lower aquifer. At times of low power consumption, water is pumped from the upper aquifer to the lower aquifer. Turbines release water into the aquifer during times of high power consumption to generate electricity. The typical cycle duration is one to several hours.

The amount of power generated is determined by the difference in elevation of the two reservoirs and the volume of water involved. This technology requires very large water reservoirs. Recently, the idea of using numerous abandoned or underground mines as storage reservoirs has been studied in different countries [5]–[7]. South Africa has lots of potential abandoned underground mines for hydropower installations more than the EU. Fig. 1, shows the potential of underground mines for energy storage in South Africa in comparison with other countries [7].

The power distribution sector in South Africa is evolving to accommodate the humongous ongoing changes. The major drivers of these evolving changes consist of system security, and reduced power distribution losses are the primary goals, along with economic concerns. Although there is a huge electric power generation capacity in South Africa, however, they are mostly fossil-fueled power plants that are incompatible with the global push for renewable or clean energy technology. Along with the geographical location, South Africa has access to hydropower potentials aside from other sustainable energy sources like coastal wind and sunlight. Because of the RES's intermittent nature, an energy storage system must be used; pumped hydropower energy storage (PHES) is among the most popular options PHES is a typical energy storage system with an efficiency of 85% [8] It contributes about 3% of total generating capacity globally. The Drakensberg 1,000 MW pumped storage system and the Ingula 1,332 MW pumped storage facility are both located in South Africa [6]. However, the height difference between two constructed reservoirs or natural bodies of water is used by PHES, which has proven to be highly restrictive in the past. an innovative modification of PHES, which minimizes environmental impacts and eliminates the need for surface topology [9]. Because of geographical, environmental, and social and economic limitations, PHES development is only permitted in select places [10]. The utilization of abandoned mines for underground energy storage facilities, however, has recently gained attention as an effective infrastructure for the installation of PHES plants for power generation with low environmental impact [6], [7], [10]. Around a million mines are assumed to remain abandoned globally [11]. According to [12], the global overall pumped storage capacity in China is focusing on the development of 165,000 Megawatts. Huge storage spaces are needed for the PHES reservoir, which could not be present in highly populated or urbanized locations. The two reservoirs of the PHES must be significantly elevated to enhance sufficient head difference for effective electricity generation, which completely roll out the use of flat areas. Using closed quarries or mines for lower reservoir construction is considered an attractive asset for energy generation and the provision of new resources with significant environmental benefits [13]. However, a brief overview of the use of underground cavities and their potential for PHES plants have been reviewed and summarised by [2], [11]. Mining is a lucrative venture in South Africa and there are lots of available mine voids which are abandoned for years without any active economic involvement. This study investigates the prospect and availability of abandoned mines for PHES implementation in South Africa to enhance bulk electricity generation for rural community users in South Africa. Its cost estimation for past and future installations is also investigated as well as the benefits over economics and social energy security are also discussed.

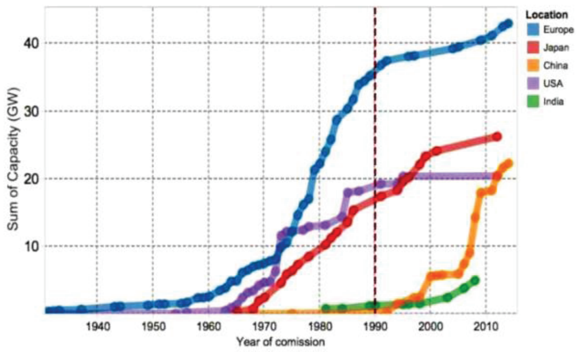

Fig. 1: Global PHES yearly capacity increase

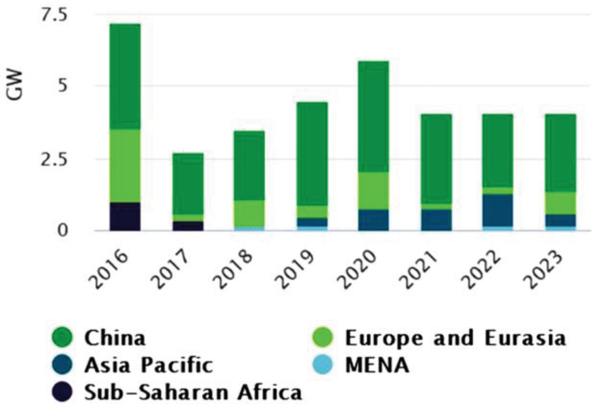

Fig. 2: Annual PHES capacity increase by regions

Table 1: Underground mines that could be used for power storage applications [11]

City	No. of mines	State	Depth range (m)	Water outflow (Mm^3/yr)
France	81	Flooded	500-1200	120
Germany	23 4	Flooded Non-flooded	200-1800 200-1300	48-54
Poland	28 26	Active Non-active	300-800 300-800	209
Spain	36 12	Flooded Non-Flooded	200-700 300-600	37
UK	64	Flooded	300-1200	Nill
South Africa	6000	Flooded	2998-3900	-

I. ABANDONED MINES IN SOUTH AFRICA

South Africa is endowed with important minerals and metals such as coal, diamond, gold, platinum, chromium, cadmium and so on. Mining is a lucrative venture in South Africa, which emerged as the major employment industry in recent years and contributed immensely to the economic development of the country. Mining in South Africa started as early as 1840 with coal exploitation in Natal. Later in 1867 came the discovery of alluvial diamonds where the source was discovered to be a kimberlite igneous tunnel [14]. This was also followed by the discovery of gold in 1887 in Johannesburg. The city of Johannesburg has rapidly grown because of this and developed into the Saharan region of Africa's industrialization hub. Since then, gold has been discovered. has birthed more mines in the country. In 2004, about 59 different minerals were produced till 2010, and new mining and prospective applications have been lodged all over South Africa [15].

South Africa has become the leading world supplier of assorted minerals and mineral products of constant high quality. Fig. 3 and 4 indicate the mining prospect and the positions of active mines in South Africa. However, due to the competitiveness in price and depreciation of most minerals mines have been abandoned. According to the department of minerals and energy, there are over 6,000 abandoned mines across South Africa especially along Golden Arc – elliptical basin in Johannesburg, Free State and Northwest provinces. Fig. 5, shows the abandoned mines within the vicinity of South Africa [16]. However, with this large number of abandoned mines, the implementation of Switching from conventional sources of energy with high emissions to renewable energies with low emissions is possible with the PHES plan

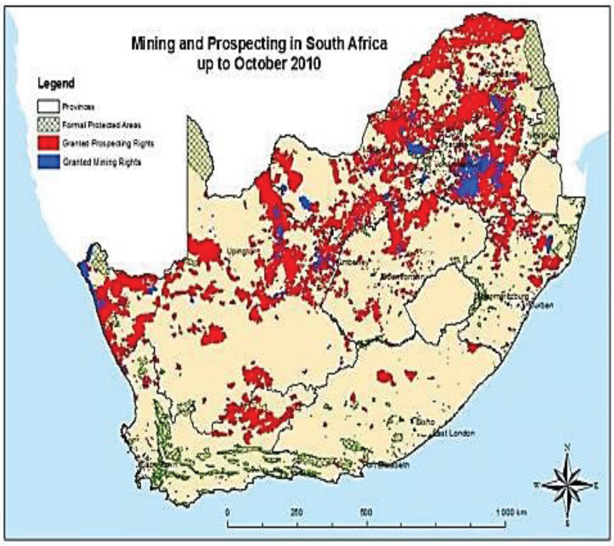

Fig 3: Mining Prospect in South Africa up to 2010

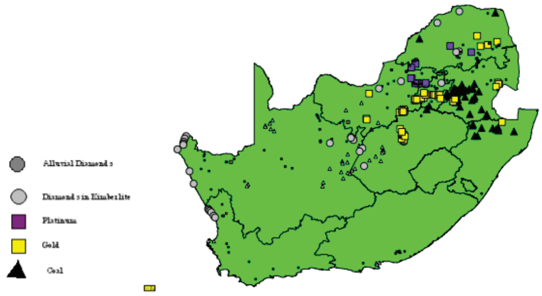

Fig. 5. Abandoned and active mines [16]

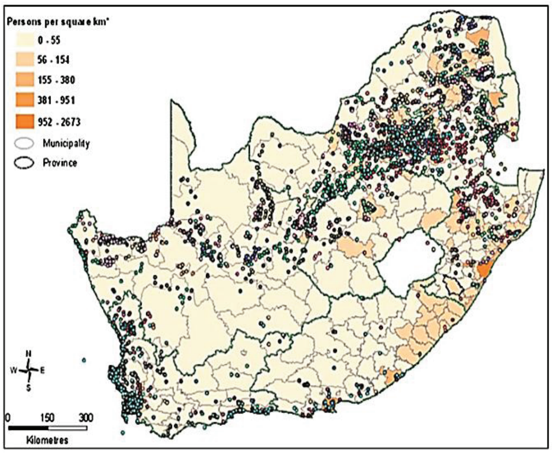

Fig. 5: Abandoned mines within the vicinity of South African settlement areas [17]

A. *Advantages of Mine caverns for UPHES installation*

There are lots of potentials in the use of abandoned mines for the UPHES system installation. Mine drainage generates large sources of differential heads suitable for the installation of PHES systems. With already excavated caverns extending to hundreds or thousands of feet underground, they can accumulate substantial volume of water throughout the post-decommission years, which can relief the burden of initial extensive water fill. The existing infrastructure common among mine features such as shaft and gallery size could facilitate the implementation and standardization of PHES across multiple areas, serving initial cost of procurement and construction. Also, it can reduce environmental concerns as most of the abandoned mines have no immediate purposeful usage.

II. PHES Implementation and Design Guidelines in South Africa

Hydropower potential is not very abundant in South Africa. The infrastructure for primary water supply and inter-basin transfers have historically been linked to the development of hydropower (Drakensberg PHES scheme, Palmiet PHES, and Ingula PHES scheme). Currently, South Africa has around 2912 MW of PHES, which is made up of the plants shown in the table below.

Table 2: PHES scheme in SOUTH AFRICA [12]

Name of PHES	Capacity (MW)	Ave. gen head (m)	Pump/turbine flowrates (m^3/s)	Types of turbines pumped	Commissioned year
Steenbras (CTCC)	180	286	15/19	Francis	1979
Drakensberg (Eskom)	1000	430	55/78	Francis	1982
Palmiet (Eskom)	400	265	45/70	Francis (Single stage)	1987
Ingula (Eskom)	1332	450	67/85	Francis	2017

Presently, according to the energy generation sector in South Africa represented by the department of energy (DoE), hydropower storage is recognised as an efficient energy provision, a stand-by and peaking generation facility to some 40,000 MW base-load thermal plants. Hydro-pumped storage plant uses 2 to 3 seconds of hydraulic starting time and 15s to get into full load production [12]. The general planning/design principles used by the planners and designers, as well as the characteristics analysis of the as-built parameters of the South African PHES, mainly conformed to the following.

i. The static head for a large PHES site should be between 100 and 700 m.
ii. Use a typical gradient between the upper and lower reservoirs of at least 1:10 wherever possible.
iii. It's crucial to establish the water availability evaluation at the chosen site, which takes water losses and evaporation into account.
iv. The pump/turbine unit needs to be located at least 25 m below the lower reservoir level in order to prevent cavitation.
v. The upper and lower reservoirs' development costs and land configuration are crucial for ensuring the installed PHES's feasibility.
vi. The use of abandoned mines caverns for the lower reservoir construction should be prioritized to reduce the overall costs of investment of the PHES
vii. The installed PHES are for the peaking loads and used as the stand-by facilities to the coal-fired base load power plants.
viii. In three of the four PHES sites that were examined, water is transferred between basins while also producing hydropower.

The existing PHES are were design for weekly operational cycle but due to high demand and apparent daily outstripping,
Eskom's pumped storage facilities are compelled to switch from weekly to daily basis [12]. The production of South African power plants from 2010 to 2017 is displayed in Table 3 below.

Table 3: The South African's power station output between 2010 to 2017

Year	Coal fired station	Nuclear station	Hydro-electric station	Diesel & gas turbine	RE sources (W+IPPs)	Pumped storage stations	PSS capacity in SA
2010/11	220219	12099	1960	197	2+1833*	2953	Palmiet (400 MW)
2011/12	218212	13502	1904	709	2+4107*	2962**	
2012/13	214807	11954	1077	1904	1+3516*	3006**	
2013/14	209483	14106	1036	3621	2+3671*	2881**	
2014/15	204838	13794	851	3709	1+6022*	3107**	
2015/16	199888	12237	688	3936	311+9033*	2919**	Ingula unit(1332mw)
2016/17	200893	15026	579	29	345+11529*	3294**	

N/B: *The amount of GWh generated from the IPPs, **The amount of GWh required for pumping is typically about 1000 GWh over output (about 30% on average)., PSS is a net energy consumer

III. Cost Estimate for PHS scheme in South Africa

The PHES installation cost estimate in South Africa could be based on the most recently completed project in 2017, Ingula 1332 MW. The project was initially estimated at $ 1 billion in 2005 and was completed at the cost of $2.24 billion in 2017, which translates to approximately $1682 KW [18]. The project started in 2005 and it encounters several challenges including delays and cost overruns. The average construction period of PHS is approximately 7 to 8 years but due to the challenges the construction period was extended to 12 years which drives high the project cost significantly. Other factors which have also contributed to the delay and increase cost overruns of the Ingula PHS scheme [3] include. The delay was caused by an underground incident when the steel inclined shaft was being grouted. Without this occurrence, the cost was projected to be $1140/kW and the project was delayed by nearly 1.5 years.

- Costs associated with contract acceleration.
- A decline in the exchange rate for the Rand, etc.
- Unanticipated scope of civil works, primarily as a result of geotechnical conditions, accounting for 10% to 20% of civil costs.
- Overspending on turbines by $36 million budget

IV. Site availability and costs estimate for future proposed PHS schemes

After the completion of the Ingula peaking capacity (1333 MW) project in 2017, further development of another PSS project seems to be postponed to 2030 (Barta & Water Resources Engineering, 2017). Meanwhile, several PHS schemes have been identified by Eskom's integrated strategic Electricity plan for future implementation (van Dongen et al., 2021). A comprehensive survey has been conducted between the 1980s and 1990s, and about ninety-nine feasible sites were highlighted and scrutinized based on technical, economic, environmental, and legal requirements [12]. The next huge PHS projects are Lima (Tubatse) and Mutale. Fig. 6 shows the potential PHS scheme locations in South Africa.

In the province of Limpopo, Eskom intends to carry out this substantial pump storage facility (Lima) along the escarpment between the Nebo Plateau and Steelpoort River valley. Eskom developed and finished a feasibility study for a 1000-megawatt capacity-rated plant in 2000. Yet a thorough design analysis carried out in 2007 suggested a capacity concept of 1500 MW, made up of four 375 MW variable speed turbine units running with a net head of 629 m each [18]. According to the 2008 feasibility study report, the cost of construction would be $1,28 billion, or $1023 per kW and $67,4 per megawatt hour. The plan seemed to have some potential because the upper reservoir would already be built and the water source would come from the De Hoop Dam, which was completed in 2014 [12]. The lower dam (De hoop dam in Fig. 7) was built with a high and short penstock in good rock with granites. The Olifants River Water Resource Development Project was designed to provide water to 400 000 people, as agreed upon by Eskom. The 2008 financial crisis, high development costs, and uncertainties around projected future energy peak demands, however, have all delayed the site's development [3], [12].

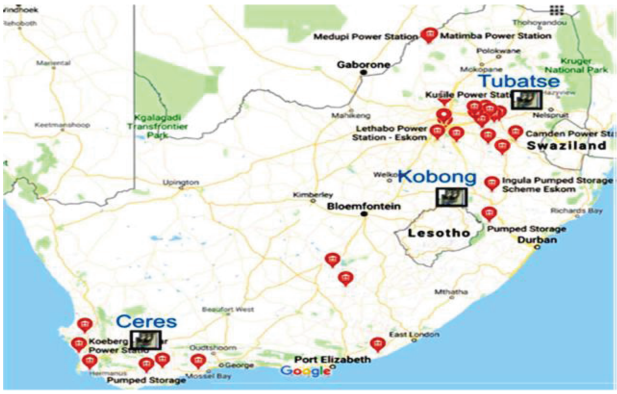

Fig. 6: Potential PHES location scheme in South Africa [3], [12], where the red spots indicate the current power plants.

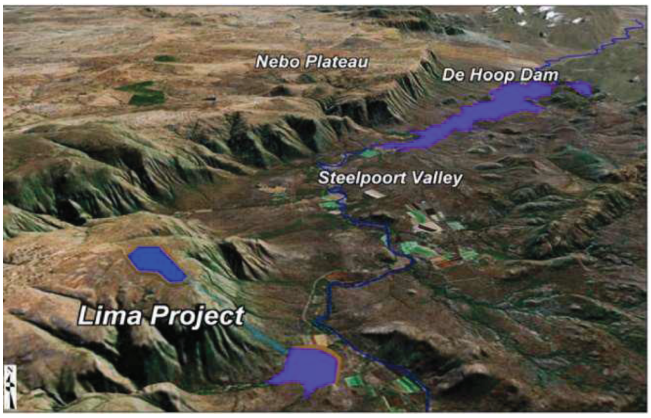

Fig. 7: Lima (Tubatse) PS scheme project layout [18]

Another project that was supposed to be included in the Lesotho Highland Water project agreement's Phase II is the Kobong PHS scheme. The Katse Dam, which had already been built during phase I, was intended to be a lower dam. A \$0.78 billion building cost estimate was made [18]. A seven-year building period was envisaged, with a capacity of 1200 MW. The lower reservoir will be located in the impoundment created by the existing Katse Dam, and only the higher dam storage will need to be erected [12]. The feasibility study conducted in 2014, indicated the technical feasibility of the project but economic feasibility was subject to a series of assumptions which include variation in market price rates, project capital cost, funding availability, and integration of the PHS scheme into Lesotho and South Africa grid.

V. The Prospect of development of small-scale PHES with other renewable resources

Both urban and rural areas in South Africa have access to significant water supply infrastructure. As shown in Fig. 8, there are several prospects for building small-scale pumped storage systems in conjunction with other renewable energy sources and technologies, such as wind. This could make the market price of electricity affordable. Such a project will be promising in an already existing elevated concrete reservoir where only one reservoir needs to be constructed. The research has been done in other parts of the world. Table 4 given below represents a theoretical sizing for small, pumped storages of 2, 5 and 10 MW.

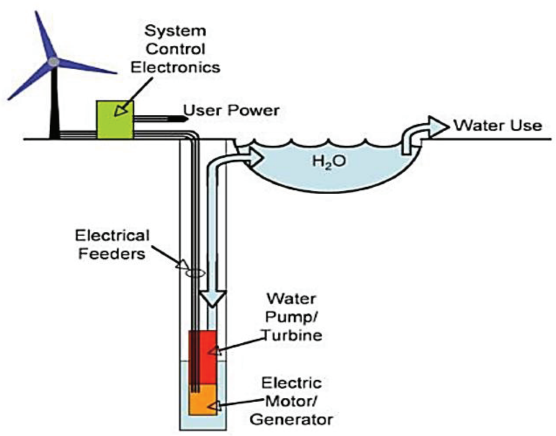

Fig. 8 UPHS system with wind storage [19]

Table 4: Example of small-scale pump storage with abandoned mine infrastructure

PHS Scheme Items	Turbine pump size		
	2 MW	5 MW	10 MW
Flowrates in PaT (M^3/s)	0.809	2,023	4046
Size of pipeline (mm)	700	1000	1200
Pump head, type: steel material	7.2 m	9.5 m	144 m
Pipeline friction head (fibre glass option with 1200 m length)	4.0 m	5.3 m	8.0 m
Upper Reservoir capacity (m^3)	20 000	40 000	80 000

VI. Benefits of UPHS System in South Africa Electricity Network

Electricity network benefits can include chances for lucrative investments, reduced system operating costs, and the introduction of new projects. South Africa should be commended for both its reliable and safe electricity supply and its reasonable electricity prices. In fact, switching to pumped-storage plants instead of antiquated grid-connected oil-fired units, whose reliability periodically falls below 50%, could help to tackle many societal problems brought on by frequent system disruptions and load shedding. In some circumstances, this swap could aid in reducing the estimated 31% of energy losses along transmission and distribution lines [20]. Moreover, pumped-reduced storage operation and maintenance costs compared to those of thermal facilities should lower power rates, which are currently relatively high for most customers.

VII. Conclusion

An effective substitute for the use of fossil fuels is hydropower. To achieve the energy-related Sustainable Development Goals on climate change, it is anticipated that 800 GW of hydropower would be needed over the next 20 years. The International Hydropower Association (IHA) estimates that the total amount of hydropower installed in 2019 was 1308 gigawatts (GW), an increase of almost 15 GW from 2018. This suggests that additional efforts are required to increase hydropower generation on a yearly basis in order to reach the goal in the following few decades. Based on this analysis, it is clear that South Africa still has the capacity to develop valuable technologies to support large-scale power system plans in the future. However, more research is needed to accurately understand the inputs, assumptions, and methodology employed in the model of this current study in order to actualize the future expansion planning of the new projects. In general, both nationally and internationally, a deeper understanding of the expenses, benefits, and flexible PHS technologies for future power systems is needed.

VIII. Acknowledgement

The authors gratefully acknowledge the Durban University of Technology for their financial support

IX. References

[1] S. Y. Khan, "a Comparative Study and Analysis of Phes and Ugphes Systems," UKZN, 1-121, 2015.

[2] R. Madlener and J. M. Specht, "An exploratory economic analysis of underground pumped-storage hydro power plants in abandoned deep coal mines," *Energies*, vol. 13, no. 21, 2020, doi: 10.3390/en13215634.

[3] C. van Dongen, B. Bekker, and A. Dalton, "Valuation of pumped storage in capacity expansion planning—a south african case study," *Energies*, vol. 14, no. 21, 2021, doi: 10.3390/en14216999.

[4] A. Poulain, J. R. de Dreuzy, and P. Goderniaux, "Pump Hydro Energy Storage systems (PHES) in groundwater flooded quarries," *J. Hydrol.*, vol. 559, pp. 1002–1012, 2018, doi: 10.1016/j.jhydrol.2018.02.025.

[5] P. J. Schubert, "Abandoned Mine Voids for Pumped Storage Hydro," *Insights Min. Sci. Technol.*, vol. 01, no. 3, pp. 3–8, 2019, doi: 10.19080/imst.2019.01.555563.

[6] D. Jiang, S. Chen, W. Liu, Y. Ren, P. Guo, and Z. Li, "Underground Hydro-Pumped Energy Storage Using Coal Mine Goafs: System Performance Analysis and a Case Study for China,"

Front. Earth Sci., vol. 9, no. November, pp. 1–15, 2021, doi: 10.3389/feart.2021.760464.

[7] J. Menéndez, A. Ordóñez, R. Álvarez, and J. Loredo, “Energy from closed mines: Underground energy storage and geothermal applications,” *Renew. Sustain. Energy Rev.*, vol. 108, no. December 2018, pp. 498–512, 2019, doi: 10.1016/j.rser.2019.04.007.

[8] K. Shirinda, K. Kusakana, and S. P. Koko, “Techno-economic analysis of a standalone solar PV with groundwater pumped-hydro-storage system,” *Proc. 27th Int. Conf. Domest. Use Energy, DUE 2019*, no. 1, pp. 90–95, 2019.

[9] N. Mousavi, “Edith Cowan University,” *Grants Regist. 2022*, pp. 376–377, 2021, doi: 10.1057/978-1-349-96042-2_425.

[10] V. Kitsikoudis *et al.*, “Underground pumped-storage hydropower (UPSH) at the martelange mine (belgium): Underground reservoir hydraulics,” *Energies*, vol. 13, no. 14, 2020, doi: 10.3390/en13143512.

[11] J. Menéndez, J. M. Fernández-Oro, M. Galdo, and J. Loredo, “Pumped-storage hydropower plants with underground reservoir: Influence of air pressure on the efficiency of the Francis turbine and energy production,” *Renew. Energy*, vol. 143, no. December, pp. 1427–1438, 2019, doi: 10.1016/j.renene.2019.05.099.

[12] Barta and Water Resources Engineering, “The contribution of pumped storage schemes to energy generation in South Africa,” 2017.

[13] E. Pujades, P. Orban, P. Archambeau, V. Kitsikoudis, S. Erpicum, and A. Dassargues, “Underground pumped-storage hydropower (UPSH) at the Martelange mine (Belgium): Interactions with groundwater flow,” *Energies*, vol. 13, no. 9, pp. 1–21, 2020, doi: 10.3390/en13092353.

[14] G. G. Martin, “Underground pumped hydroelectric energy storage,” *Large Energy Storage Syst. Handb.*, pp. 77–109, 2011, doi: 10.1201/b10778-9.

[15] H. Álvarez, G. Domínguez, A. Ordóñez, J. Menéndez, R. Álvarez, and J. Loredo, “Mine water for the generation and storage of renewable energy: A hybrid hydro–wind system,” *Int. J. Environ. Res. Public Health*, vol. 18, no. 13, 2021, doi: 10.3390/ijerph18136758.

[16] C. Didier *et al.*, “Mine Closure and Post-Mining Management International State-of-the-Art International Commission on Mine Closure International Society for Rock Mechanics,” no. November 2008, 2008, doi: 10.13140/2.1.3267.8407.

[17] S. E. Mhlongo and F. Amponsah-dacosta, “International Journal of Mining , A review of problems and solutions of abandoned mines in South Africa,” no. October, 2018, doi: 10.1080/17480930.2015.1044046.

[18] C. Van Dongen, “Potential for New Pumped Storage Schemes in South Africa,” pp. 266–271, 2020.

[19] S. Y. Khan and I. E. Davidson, “Underground Pumped Hydroelectric Energy Storage in South Africa using Aquifers and Existing Infrastructure,” *NEIS Conf. 2016*, no. September, pp. 119–122, 2017, doi: 10.1007/978-3-658-15029-7_19.

[20] S. Ekoh, I. Unsal, and A. Maheri, “Optimal sizing of wind-PV-pumped hydro energy storage systems,” *4th Int. Symp. Environ. Friendly Energies Appl. EFEA 2016*, pp. 5–10, 2016, doi: 10.1109/EFEA.2016.7748776.

Investigating the Effect of Convection on the Rating of Buried Cables Using the Finite Element Method

J.S Balla Mballa
Power Engineering
Vaal University of Technology
Vanderbiljpark, South Africa
212063286@edu.vut.ac.za

J.J Walker
Walmet Consultancy (Pty) Ltd.
Vereeniging, South Africa
jerry@walmetconsultancy.co.za

I.K Kyere
Power Engineering
Vaal University of Technology
Vanderbiljpark, South Africa
isaack@vut.ac.za

***Abstract*—This paper presents the effect of convection heat flow across the ground surface on the thermal rating of three single-core, 132kV, XLPE cables buried underground. The cable was modelled for thermal analysis using the Finite Element Method (FEM). This study demonstrates the use of FEM to investigate the effect of convection on the rating of buried cables in flat formations using QuickField Finite Element Simulation software under steady-state heat transfer analysis. As a result, developing a model to simulate this type of situation necessitates important considerations such as the following boundary conditions: burial depth, soil thermal resistivity, and soil temperature, which play an important role in the simulation's accuracy and reliability. The results show that when the ground surface is taken as a convection interface, the conductor temperature rises and may exceed the maximum permissible temperature when rated current flows. This is because the ground surface acts as a convection interface between the soil and the air (fluid). This result correlates when compared with the results obtained using the IEC60287 analytical method, which is based on the condition that the ground surface is an isotherm.**

Keywords*—*finite element method, convection, buried cables, steady-state rating.

I. Introduction

Convection and radiation are important heat transfer mechanisms from the cable's surface to the surrounding air, for cables installed in the air. Convection heat transfer is classified according to the nature of the flow, which in this case is natural, and induced by buoyancy forces because natural convection is assumed to only occur at the cable's outside surface [1]. The equations in the IEC60287 standard [2] are typically used to determine the continuous or steady-state rating of underground cables. The assumption used in these computations is that the earth's surface is an isotherm. As a result, it ignores convection heat loss, radiation heat loss, and surface heating from solar radiation. Due to the ability to incorporate a variety of conditions, such as non-uniform soil conditions and extra heat sources around the cable, computer simulations using the Finite Element Method (FEM) were facilitated in determining the temperature rise in the buried cable. This is quite difficult to accomplish using the analytical calculation method. It has been proved that by modelling the cable in great detail, FEM can get the same results as traditional computed methods for the temperature rise in a cable [3].

In calculating underground cable ampacity, the heat transfer coefficient at the soil–air contact is critical when convection occurs. Calculating the heat transfer coefficient accurately is complex because of the temperature variations at the earth's surface. When convection heat flow is applied at the ground's surface, the cable's current rating shows that the temperature of the cable is higher at a constant load than obtained using the conventional approach mentioned in [4].

The results in [5] show that when the boundary is defined as an isotherm, the computed cable temperature is less than the actual steady-state temperature when convection is applied at the surface. The coefficient of convection heat transfer is proportional to the amount of fluid (air) passing through the surface [6].

This paper investigates the effect of convection heat flow over a boundary (ground surface) on the rating of underground cables in relation to temperature distribution.

II. FINITE ELEMENT ANALYSIS

A. Basis of FEM models

Three 132 kV aluminium conductor cables with XLPE insulation, 1000 mm^2, corrugated seamless aluminium sheath (CSA) encased, laid in flat formation with a 2xD separation spacing, and buried at a depth of 1000mm were selected for this study. The steady-state rating of the cables using the analytical technique is 840A at 90°C conductor temperature, 30°C soil temperature, and 1.2K.m/W thermal resistivity of the soil.

B. Quickfield simulation model

The geometry was created using QuickField Finite Element Software and modelled in 2D as a square with a 10m side each. It was assumed that the medium's left, right, and bottom edges were fully insulated due to their distance from the cable's heat source. At a maximum air temperature of 30°C, convective heat flow was considered for the upper boundary (ground surface). The first simulation was conducted with the ground surface treated as an isotherm (constant temperature), and the findings were compared to those of the second simulation, which included convectional heat flow effects on the ground surface. Figure 1 and figure 2 shows the geometry model with the mesh and the dimensions of the geometry model respectively.

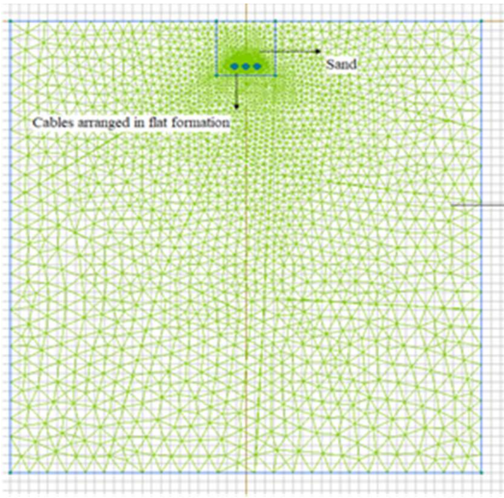

Fig. 1. Quickfield Geometry model with mesh.

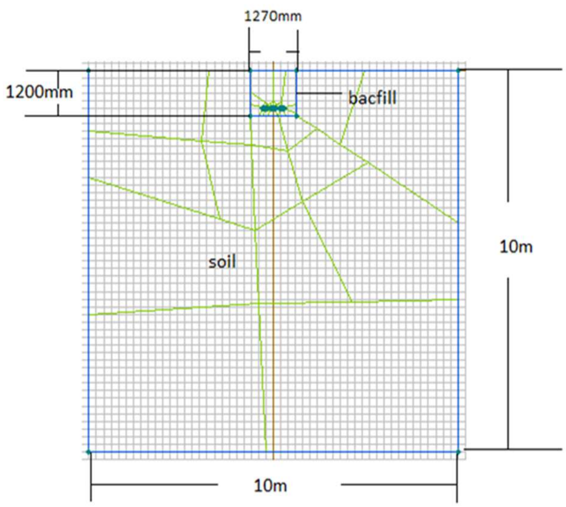

Fig. 2. QuickField set-up view of simulation model.

Table 1 shows the values for the properties of the materials used in the simulation.

TABLE I. MATERIAL PROPERTIES

Material	Cable layer	Volumetric heat sources (W /m^3)	Thermal conductivity (W/K.m)	Temperature (°C)
Aluminium	Conductor	27518.4	205	–
PVC	Jacket	0	0.1667	–
XLPE	Insulation	706.398	0.2857	–
PE	Semiconductor screen	0	0.4	–
Corrugated Aluminium	Sheath	0	205	–
Soil/ Air	–	0	0.83	30

a. TABLE I. MATERIAL PROPERTIES.

C. Thermal analysis when the ground surface is an isotherm

At this point, it is critical to consider the position of boundaries while using finite element simulations. The field for the prior model is a square of 10m on each side. The cable was buried 1000mm below the surface of the ground. QuickField^{TM} computed the conductors' steady-state temperature (thermal rating) which resulted in 91.60°C under this condition using a conductor with a current carrying capacity of 840A. This resulted in a heat loss of 27518.4kW/m^3 using manual calculation [8], as shown in Table 1. Figure 3 below illustrates the isothermal impact on the ground surface.

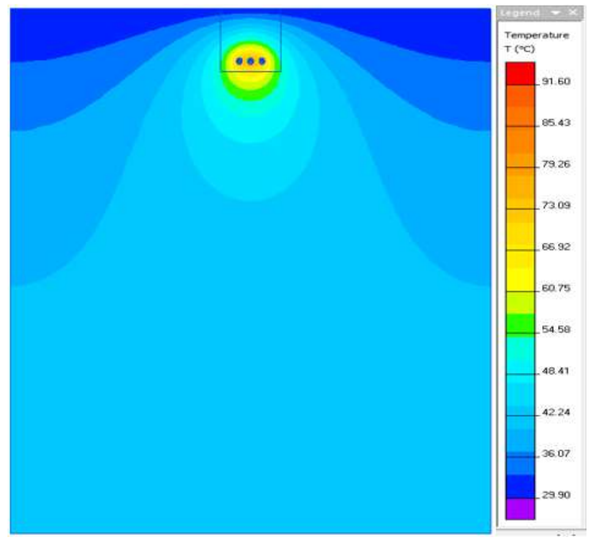

Fig. 3. Ground surface as an isotherm at 30°C

D. Thermal analysis when the ground surface is non-isothermal

According to [2], the rating is based on the assumption that the ground directly above the cable is not in direct contact with sunlight. As a result, the radiation heat from direct sunlight is disregarded. However, this effect heats the soil directly above the cable, and heat transfer between the soil and the air occurs via convection. The ground surface cannot be considered an isotherm in this scenario due to the temperature difference between the soil directly above the cable and the soil some distance away.

In this simulation, natural convection was taken into account, which occurs when an object emits energy into its surroundings. Natural convectional flow can be laminar or turbulent [7]. The coefficient of convection heat transmission is proportional to the flow of the fluid (air) in contact with the surface. For horizontal surfaces, buoyancy forces are largely parallel to the surface, and fluid flow is severely restricted and highly dependent on the arrangement of the surface and fluid. When the ambient air temperature is greater than the soil temperature, the surface prevents vertical movement and restricts the fluid's convection circulation. The fluid flow will be assumed to be turbulent for this investigation, given that the wind speed cannot be predicted. The following formula is used to calculate the convection heat transfer coefficient with air as the fluid (cold, facing downwards) and a horizontal surface [7].

$$h = 0.00152 \times \theta^{0.33} \ W/m^2.K \qquad (1)$$

Where h is the convection heat transfer coefficient, θ is the difference in temperature between the fluid and the surface. Using equation (1), and assuming that the fluid temperature is ignored, the difference in temperature between the fluid and the surface is increased in 5°C increments. The thermal current rating will be calculated at different temperatures of 5, 10, 15, 20, 25, and 30 degrees Celsius, which will yield different convection heat transfer coefficients. Table 2 displays the results obtained after the simulation, while figure 4 depicts one of the results showing the isotherms obtained at 5°C when the heat convection transfer coefficient of 2.59 was used.

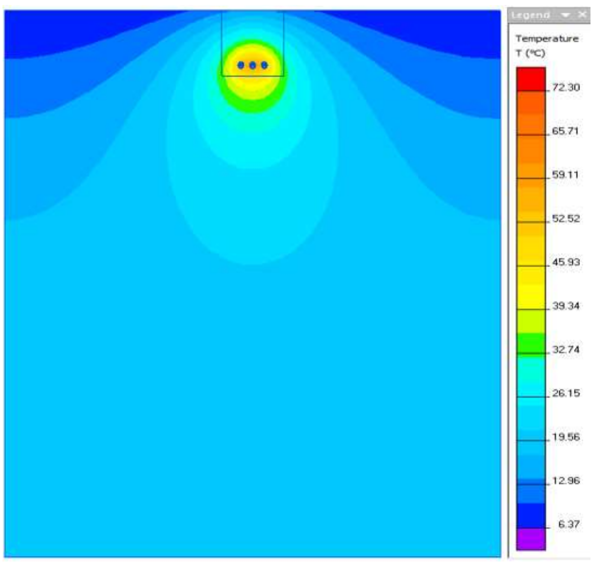

Fig. 4. Isotherms with convection heat transfer coefficient of 2.59.

Figure 4 clearly shows that at a heat convection coefficient of 2.59, the ground surface is not an isotherm because the temperature directly above the surface where the cables are located is higher and gradually decreases as it moves away from the cables.

III. RESULTS

The thermal rating of the cable for different convection heat transfer coefficients was calculated at different designated surface temperatures during the simulation. Figure 4 depicts the effect of convection on the ground surface. We can observe from the results that when the surface temperature is increased there is an increase in temperature in the cables across the boundary, which is shown by an increase in the peak shown in figure 5 that occurs in the middle of the graph. Figure 6 below shows the relationship between the conductor temperature and the surface temperature, as the surface temperature increases the conductor temperature increases as well. This is the case because the fluid temperature is ignored and only the surface temperature is considered.

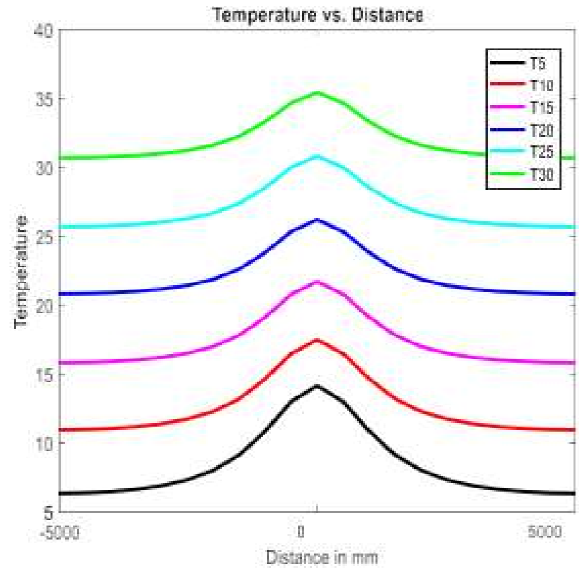

Fig 5. Temperature distribution on the ground surface when affected by convection.

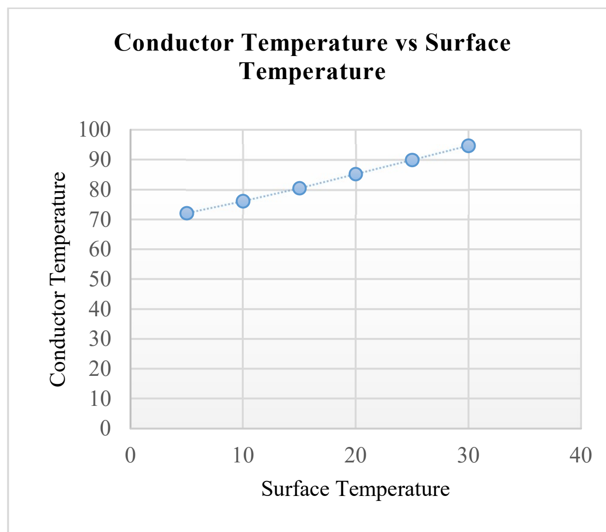

Fig. 6. Conductor temperature Vs surface temperature when affected by convection

The conductor temperature values for the different convection heat transfer coefficients were calculated with QuickField when the ground surface is affected by convection heat flow, which is shown in table 2. Table 2 also shows that when the convection heat coefficient is applied at the same temperature (30°C) as when the ground surface is an isotherm [8], the conductor temperature exceeds the maximum permissible temperature of 90°C as stated in the studies of [4] and [9].

TABLE II. CONDUCTOR TEMPERATURE WITH CONVECTION EXPERIENCED AT THE GROUND SURFACE WITH CHANGE IN SURFACE TEMPERATURE.

Temperature (°C)	Convection heat transfer coefficient (W/m². K)	Conductor Temperature (°C)
30	4.67	94.70
25	4.39	89.90
20	4.08	85.20
15	3.72	80.50
10	3.25	76.10
5	2.59	72.30

b. TABLE II. CONDUCTOR TEMPERATURE WITH CONVECTION EXPERIENCED AT THE GROUND SURFACE WITH CHANGE IN SURFACE TEMPERATURE.

Figure 7 below shows the temperature distribution in the middle conductor when convection is experienced at the ground surface when the surface temperature is 30°C.

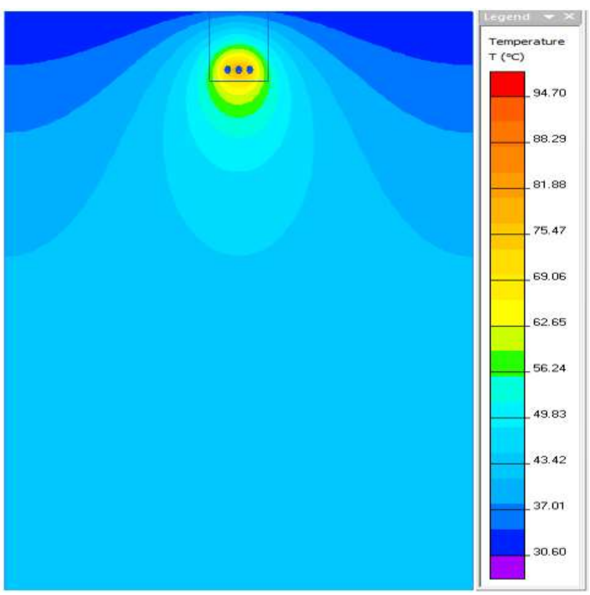

Fig. 7. Isotherms with convection heat transfer coefficient of 4.67.

IV. CONCLUSION

The simulations using QuickField show that convection affects the rating of cables buried underground, as the procedures described in the IEC60287 Standard considers the ground surface as an isotherm and the steady-state temperature of the cables is a function of the surface temperature, as well as the temperature of the conductor being 90°C. From the change in conductor temperature (thermal rating) observed in the middle cable shown in table 2, considering a steady state, applying the convection coefficient is not the correct procedure according to IEC60287 Standard, as it will result in a much higher predicted cable conductor temperature. The simulation indicates a conductor temperature of up to 94.70°C as shown in figure 7. With the results observed, convection effects can be confirmed. Additionally, as indicated in Table 2, when the ground surface is under the effect of convection and is lower than 30°C, the conductor temperature is lower than expected by the IEC60287 Standard. As a result of these findings, it may be concluded that the surface temperature difference along boundaries also impacts the thermal rating of underground cables. This finding will be advantageous in South Africa, as the country is in a subtropical zone where the air temperature is higher than the ground temperature.

ACKNOWLEDGMENT

The first author wishes to express gratitude for the financial support obtained throughout this research from the Vaal University of Technology.

REFERENCES

[1] G.J. Anders, "Rating of electric power cables in unfavorable thermal environment". New Jersey: John Wiley & Sons, Inc, 2005.

[2] IEC 60287-1-1 Edition 1.2, Calculation of current rating – Part 1-1: Current rating equations (100% load factor) and calculation of losses – General, 2006.

[3] IEC 60287-2-1: Electric cables – Calculation of current rating. Part 2-1: Thermal resistance – Calculation of thermal resistance, 2006.

[4] S. Purushothaman, F. de León, M. Terracciano, "Calculation of cable thermal rating considering non-isothermal earth surface", IET Generation. Transmission. Distribution., 2014, Vol. 8, Issue. 7, pp. 1354–1361. ISSN 1751-8687.

[5] J. J, Walker, "Finite element modelling to determine the rating of buried power cables", 2020. Accessed: Feb 9, 2022. DOI:978-1-7281-5511-1.

[6] T., Joubert, J.J, Walker, "Modelling a buried cable with finite element software" SAUPEC proceedings, 2003.

[7] J.R., Simonson, Engineering heat transfer, Macmillan Education, 1988.

[8] J. S, Balla Mballa, J.J, Walker & K.I, Kyere, "Application of finite element method to compare the installation requirements in a buried cable according to IEC60287", International Symposium on High Voltage Engineering and Application, ISH conference, China, 21-25 November 2021.

[9] J. J, Walker & T.R. Becker, "Investigating the effect of convection, radiation and solar radiation heat loss on the rating of buried power cables using Finite Element Simulations" International Conference on High Voltage Engineering and Application (ICHVE), Athens: Greece 10-13 September 2018.

Power Quality Classification Scheme For A Grid-Integrated Power Distribution System

K. Moloi and H. M. Langa
Department of Electrical Engineering
Vaal University of Technology
Vanderbijlpark, South Africa
moloikt023@gmail.com, hendrickl@vut.ac.za

***Abstract*— The energy trajectory has evolved over the years with the inclusion of distributed generation based on renewable energy (RE) technologies on the power system grid. The inclusion of RE technologies improves the power availability and security. However, there are serious technical concern which include voltage and frequency variation. In this paper, a power quality (PQ) classification scheme for a power distribution grid-integrated system with (RE) technologies is proposed. The proposed scheme uses the wavelet packet transform (WPT) for signal processing and feature extraction, and support vector machine (SVM) is used for PQ events classification. The proposed scheme was implemented using the WEKA machine learning platform. Furthermore, the neural network (NN) and naïve bayes (NB) classification techniques ware also tested to validate the proposed technique.**

Keywords—Classification, Distributed generation, Power quality, Support vector machine

I. Introduction

The evolution of the traditional power generating system has gained acceleration over the past years with the inclusion of distributed generation (DG) being integrated into the existing power grid. The change in power generation trajectory was ignited by environmental impact that fossil fuels emit during power generation. The integration of DGs into the power grid particularly the photovoltaic (PV) and wind energy (WE) systems have been widely used to improve the system reliability and power security. However, the integration of these DG technologies introduces technical constrains such as voltage and frequency variations, which ultimately impacts on the power quality (PQ) of the system [1, 2]. Also, the dependency of the PV and WE technologies on the weather conditions further impacts the energy forecasting techniques, resulting in improper energy management system.

The PQ diagnostic issue is an important aspect within the power engineering fraternity. A significant contribution has been made by different researchers to develop technique for PQ disturbance detection. The general logic design consists of a signal processing technique, feature extraction segment and a classification scheme. It is essential to classify the type of PQ disturbance correctly, as this gives indication to the operational problem in the system. To improve the PQ of the system, any disturbance impacting the systems PQ must be known prior in order to build a mitigation strategy [3]. Hybrid classification techniques based on signal processing and patten recognition have been widely used to classify PQ disturbance correctly [4, 5]. The authors in [6], proposed a technique based on Stockwell's transform (S-Transform) for statistical feature extraction and fuzzy-C clustering technique for PQ pattern recognition. The proposed scheme was tested on a power grid integrated with large PV solar system. The scheme produced good results. In [7], a technique based on discrete wavelet transform (DWT) and neural network (NN) was proposed for PQ disturbance classification. Intelligent systems such as NN [8], fuzzy logic and particle swarm optimization (PSO) [9], support vector machine (SVM) [10], and probabilistic neural network (PNN) [11] are reported to have been used for PQ disturbance classification.

In this paper, a hybrid PQ disturbance classification scheme based on stationary wavelet transform (WPT) and SVM is proposed. The scheme uses the WPT segment to decompose the signal into narrow bands and subsequently statistical features are extracted from the bands. A feature matrix is then formulated. The matrix is used as input to SVM for PQ disturbance classification. The remaining sections of the paper are categorized as follow. The theoretical overview of wavelet packet transform (WPT) and feature extraction implementation is discussed in section II, in section III, the SVM overview and classification is discussed. In section IV, the architecture of the proposed classification scheme is discussed, in section V a case study is discussed to test the validity of the proposed scheme. In section VI, the results observed are discussed and lastly section VII discusses the conclusion of the work.

II. Theoretical Overview of Wavelet Packet Transform

Signal tracking and analysis forms an integral part of power system condition monitoring. The wavelet transform (WT) technique has been widely used to solve engineering problems. Wavelet packet transform (WPT) and DWT are powerful tools which have been used in several field such as signal tracking, data compression and feature extraction. The DWT and WPT are orthogonal wavelet decomposition analysis, where the measured signal is passed through several filters, though the number of filters in WPT is greater than that of DWT. As depicted in Fig. 1, when using DWT, the signal is passed through both the low and high filters corresponding to the approximation and detail coefficient. At each level of decomposition, the detail coefficient is abundant, and the approximation coefficient signal is further passed through both the low and high filters. The process results in less data accumulated at each decomposition level. On the contrary, when WPT is employed as depicted in Fig. 2, the signal is passed through both the low and high filters. At each level of decomposition both the approximation and detail functions are further passed through the low and high filters, resulting in greater data output.

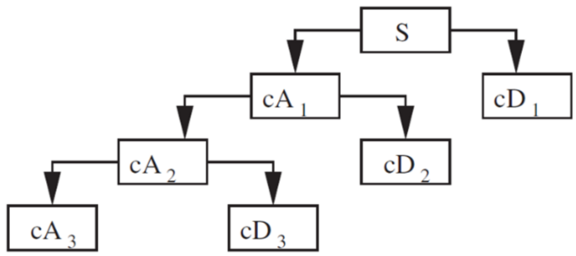

Fig. 1: DWT decomposition tree

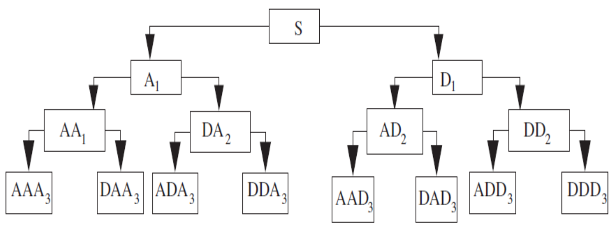

Fig. 2: WPT decomposition tree

Using both the low filter $h(k)$ and high filter $g(k)$ the recursive functions are defined mathematically as:

$$W_{2n}(x) = \sqrt{2}\sum_{k=0}^{2N-1} h(k)W_n\,(2x-k) \quad (1)$$

$$W_{2n+1}(x) = \sqrt{2}\sum_{k=0}^{2N-1} g(k)W_n\,(2x-k) \quad (2)$$

where, the scaling factor $W_O = \phi(x)$, and $W_1 = \psi(x)$ is the wavelet function. The WPT function can be represented mathematically as:

$$W_{j,n,k}(x) = 2^{j/2}W^n(2^{-j}x-k) \quad (3)$$

The specific time-frequency data of a signal can be measured as the inner product of the signal and the basis function of the same signal. The WPT coefficients of a function (f) can be computed as:

$$W_{j,n,k} =< f, W_{j,n.k} >= \int f(x)\,W_{j,n.k}(x)dt \quad (4)$$

Feature extraction is a mathematical technique used to transform high data dimension into small data dimension without losing the data significance. In the present work the WPT decomposition is performed until the fourth level $(AAA_3 \cdots DDD_3)$. Statistical features which include the standard deviation (*Std*), energy (*En*), skewness (*Sk*), kurtosis (*Ku*), entropy (*Et*) and mean (*Mn*) are extracted from the decomposed signal. For simplicity application, the features are extracted at ¼ scale of the whole data spectrum. For instance, if there are 1000 data samples in a cycle, 250 samples will be analyzed, and features extracted. The extraction of the data will be recursive until the whole data spectrum is covered.

III. Theoretical Overview of Support Vector Machine

The initial development of support vector machines (SVMs) was aimed at solving statistical problems using structural risk minimization analogy [12, 13]. Over the past decades, SVMs have widely used in various fields for pattern recognition and classification. The application of SVM requires the mapping of input vector data into a high dimensional space to determine the hyperplane. The hyperplane is the margin that separates the data classes accordingly. The hyperplane is set to optimal if the separation margin between two different data classes is maximum. Mathematically the hyperplane can be calculated equivalently as determining the quadratic optimization problem as:

$$min\frac{1}{2}|w|^2 + C\left(\sum_{I=1}^{L}\zeta_I\right) \quad (5)$$

Subject to $y_i(w.x_i + b) \geq 1 - \zeta_i, \qquad \zeta_i \geq 0\forall i$

Where, x_i is the ith instance and the class label which can either be +1 or -1 is defined as y_i. Solving equation (5) using the dual form results in:

$$\max L_D = \sum_I \alpha_i - \frac{1}{2}\sum_{i,j}\alpha_i\alpha_j y_i y_j\left(x_i^T x_j\right) \quad (6)$$

Subject to $0 \leq \alpha_i \leq C \quad \forall I, \qquad \sum_I \alpha_I y_I = 0$

In most PQ disturbances the data is not linearly separable. For such cases the kernel function is used to compute the hyperplane. The most used kernel functions are the linear, quadratic, radial bias function, and polynomial.

IV. Architecture of the Proposed Method

The design of the logic sequence for PQ disturbance classification is depicted in Fig. 3. The process begins with the measurement of voltage signals at the terminal source, The measured voltage is passed through the WPT for signal decomposition. Subsequently, the statical features are extracted from the decomposed signal, the features are used then use to train SVM for PQ disturbance classification.

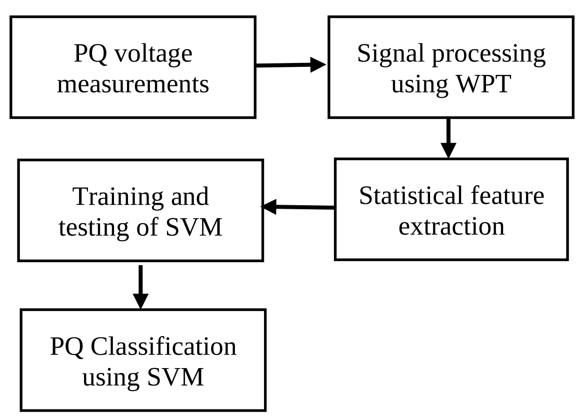

Fig. 3: PQ disturbance classification logic sequence

V. Case study

In order to evaluate our scheme, a 14 bus IEEE system is used. The network is modelled at distribution level of 22 kV. The power system is modified with the connection of both the PV and WE technology. In this work, the PV and WE technologies are modelled based on their electrical characteristics. The PV technology can be modelled as an asynchronous generator with the real power generated P_{ASG} and reactive power Q_{ASG} mathematically defined as:

$$Q_{ASG} = \sqrt{P_{ASG}{}^{2}\left(\frac{1}{cos^2\phi} - 1\right)}, \qquad (7)$$

where, the operating power factor of the PV technology system is given by $\cos\phi$. Furthermore, the WE technology can be modelled as an induction generator with the real power P_{IG} and the reactive power required to magnetize the induction generator computed as:

$$Q_{IG} \approx V^2 \frac{X_c - X_m}{X_c X_m} + \frac{X}{V^2} P_{IG}{}^{2}, \qquad (8)$$

Where, V, X_c and X_m are the system voltage, capacitive reactance and magnetizing inductance respectively. The modified power distribution network is depicted in Fig. 4.

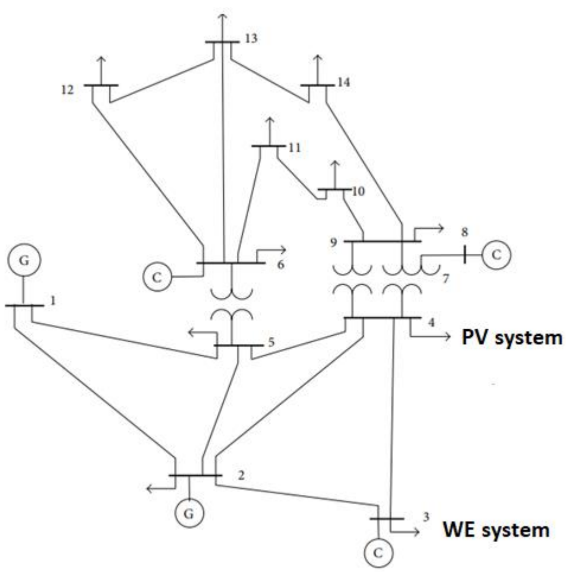

Fig. 4: IEEE 14 bus modified system under study

VI. Results and discussion

This section discusses the simulation results obtained from the proposed PQ disturbance scheme. In order to evaluate the efficiency of the proposed scheme, different PQ events must be evaluated. The PQ events classes and description are represented in Table I. One important aspect of using WPT is the selection of a mother wavelet. In this work, the symlet4 mother wavelet is selected. The selection is based on the statistical comparison of different mother wavelet. The statistical comparison of different mother wavelet is depicted in Table II. Various PQ disturbance events are depicted in Fig. 5. The results show how different PQ disturbances impact on the quality of the voltage of the system.

TABLE I. PQ SIGNAL CLASSES AND DESCRIPTION

Signal class	Description
S1	Voltage sag due to PV and WE technologies
S2	Voltage swell due to PV and WE technologies
S3	Voltage spike due to PV and WE technologies
S4	Voltage notch due to PV and WE technologies
S5	Harmonics due to WE and PV technology
S6	Sag with Harmonics due to PV and WE technology
S7	Swell with Harmonics due to PV and WE technology

TABLE II. PQ SIGNAL CLASSES AND DESCRIPTION

Mother wavelet	Standard dev.	Absolute mean
Db4	1.755	1.880
Db14	1.571	1.955
Sym4	1.320	1.052
Sym14	1.455	1.250

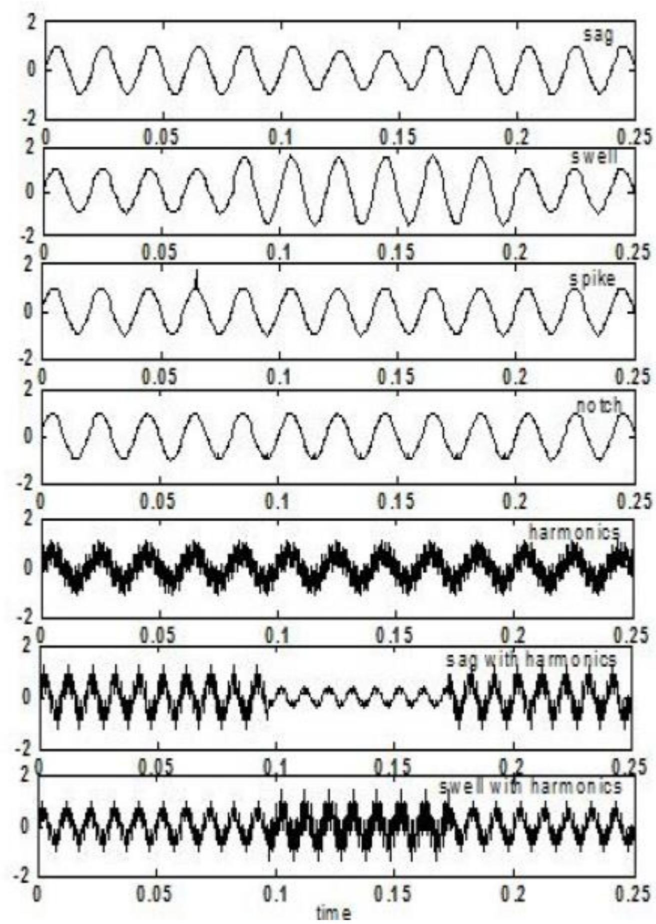

Fig. 5: Numerous PQ disturbances under study

Pattern recognition and classification is an essential engineering segment. This segment enables engineers to identify and locate problematic sections withing the power system and develop technical strategies to mitigate them. In the present work SVM is used to classify different PQ disturbances. The classification matrix using WPT-SVM is depicted in Table III. The results observed indicate an average accuracy of 98%. In order to evaluate the importance of signal decomposition using WPT, 1000 cases of each PQ disturbance events were evaluated to test the validity of the proposed scheme. From the presented results in Table IV, it is observed that there is a significant increase of accuracy from 74.3% to 97.8% when using WPT decomposition segment. To further validate the proposed scheme, the naïve bayes (NB) and neural network (NN) classifiers were also tested. The comparison results of the are presented in Table V. The results indicate a high accuracy for the proposed WPT-SVM PQ disturbance scheme.

TABLE III. PQ SIGNAL CLASSES AND DESCRIPTION

Signal class	S1	S2	S3	S4	S5	S6	S7
S1	100	0	0	0	0	0	0
S2	2	95	0	2	0	0	1
S3	0	1	99	0	0	0	0
S4	0	0	0	97	1	1	0
S5	1	0	0	0	99	0	0
S6	0	0	0	0	0	100	0
S7	0	0	1	1	2	0	96
Accuracy = 98%							

TABLE IV. PQ SIGNAL CLASSES WITH AND WITHOUT WPT

Signal class	No. of cases	Without WPT		With WPT	
		Correctly classified	Incorrectly classified	Correctly classified	Incorrectly classified
S1	1000	810	190	950	50
S2	1000	890	110	955	45
S3	1000	778	222	1000	0
S4	1000	920	80	1000	0
S5	1000	433	567	995	5
S6	1000	585	415	950	50
S7	1000	791	209	1000	0
Total	7000	5207	1793	6850	522
% Accuracy		74.3		97.8	

TABLE V. CLASSIFICATION COMPARIOSN WITH OTHER SCHEMES

Scheme	Accuracy (%)
WPT-NB	88
WPT-NN	91
WPT-SVM	98

VII. CONCLUSION

The continuous assessment of PQ of the power system network is an important exercise, which must be undertaken with critical care. Protection engineer often uses the PQ disturbances to evaluate the integrity and security of the system. In this paper, a hybrid WPT-SVM scheme is proposed to classify the PQ disturbances in a hybrid integrated power system with the PV and WE technologies. The proposed scheme uses the WPT for signal decomposition and feature extraction. The extracted statistical features are subsequently fed into the SVM classifier for training and testing purposes. The scheme produced an accuracy level of 98%, signifying its robust ability to distinguish different PQ events correctly. Future work will entail the analysis of PQ events with a hybrid network comprising of a battery storage system.

REFERENCES

[1] S. K. Kim, J. H. Jeon, C. H. Cho, J. B. Ahn and S. H. Kwon, "Dynamic modeling and control of a grid-connected hybrid generation system with versatile power transfer," IEEE Transaction on Industrial Electronics, vol. 55, no. 4, p. 1677–1688, 2008.

[2] O. O. Osaloni and A. K. Saha, "Distributed Generation Interconnection with Improved Unified Power Quality Conditioner for Power Quality Mitigation," in International SAUPEC/RobMech/PRASA, Cape Town, South Africa, 2020.

[3] G. K. Budumuru and P. Ray, "An Intelligent Approach for Power Quality Event Classification," in IEEE 1st International Conference on Energy, Systems and Information Processing (ICESIP), Chennai, India, 2019.

[4] M. B. I. Reaz, F. Choong, M. S. Sulaiman, F. Mohd-Yasin and M. Kamada, "Expert system for power quality disturbance classifier," IEEE Transaction on Power Delivery, vol. 22, no. 3, p. 1979–1988, 2007.

[5] K. Moloi and J. A. Jordaan, "Power Quality Assessment of A Wind Power-Integrated System into the Power Grid," in 5th International Conference on Renewable Energies for Developing Countries (REDEC), Marrakech, Morocco, 2020.

[6] O. P. Mahela and A. G. Shaik, "Power quality recognition in distribution system with solar energy penetration using S-transform and Fuzzy C-means clustering," Renewable Energy, vol. 106, pp. 37-51, 2017.

[7] M. Masoum, S. Jamali and N. Ghaffarzadeh, "Detection and classification of power quality disturbances using discrete wavelet transform and wavelet networks," IET Science, Measurements and Technology, vol. 4, no. 4, pp. 193-205, 2010.

[8] S. Mishra, C. Bhende and K. Panigrahi, "Detection and classification of power quality disturbances using s-transform and probabilistic neural network," IEEE Transaction on Power Delivery, vol. 23, no. 1, pp. 280-287, 2008.

[9] B. Biswal, P. K. Dash and K. B. Panigrahi, "Power quality disturbance classification using fuzzy c-means algorithm and adaptive particle swarm optimization," IEEE Transaction on Industrial Electronics, vol. 56, no. 1, pp. 212-220, 2009.

[10] E. Güney and O. Ç. Ç. Kocaman, "Classification of Stockwell Transform Based Power Quality Disturbance with Support Vector Machine and Artificial Neural Networks," ournal of Intelligent Systems: Theory and Applications, vol. 5, no. 1, pp. 75-84, 2022.

[11] I. S. Samanta, P. K. Rout, K. S. S. Mishra and M. Cherukuri, "Fast TT transform and optimized probabilistic neural network-based power quality event detection and classification," Electrical Engineering, vol. 104, p. 2757–2774, 2022.

[12] V. Vapnik, The nature of statistical Learning Theory, New York: Springer-Verlag, 1995.

[13] M. A. Hearst, S. T. Dumais, E. Osman, J. Pltt and B. Scholkopf, "Support vector machines," IEEE Intelligent Systems and Applications, vol. 13, pp. 18-28, 1998.

Speed Function MPPT Control of Self-Magnetised DC-Connected Wound Rotor Synchronous Wind Generator – An Equivalent DC System Study

Maarten J. Kamper, Graham C. Garner and Xiangyiming Kong
Department of Electrical and Electronic Engineering
Stellenbosch University, Stellenbosch, South Africa
email: kamper@sun.ac.za

***Abstract*—In this paper, a simple but effective maximum power point tracking control method is proposed for DC-grid-connected wound rotor synchronous wind generators. However, to investigate and prove the method through theory and practical demonstration, an equivalent DC system was first studied. Per-unit analysis was used to explain the control method, which required only turbine speed information for maximum power point operation. Practical demonstration of a 2-kW system confirmed the simplicity and ability of the control method to operate the turbine always at or close to maximum power point.**

***Keywords*—maximum power point, DC grid, wound rotor, synchronous wind generator.**

I. Introduction

In small-scale (< 100 kW) wind turbine generator systems, rare-earth permanent magnet (PM) generators are used almost exclusively. These generators have high efficiency and power density, but suffer from the environmental, production and cost issues of the rare-earth PM materials. The latter aspects force industry to also look at so-called non-PM wind generator options for small-scale wind energy applications.

Among the non-PM wind generators are the cage, reluctance and wound-rotor generators, of which the former two need active synchronous rectifiers, while the latter can be operated with active-synchronous or passive diode bridge rectifiers. As the use of active-rectifier converters in the top tower of small-scale systems is difficult and costly, these converters must be installed at ground level, which is not ideal from a long supply-cable and electromagnetic interference point of view. Furthermore, the reliability of active rectifiers relative to passive diode rectifiers is very bad. This all makes the use of wound-rotor synchronous generators (WRSGs) with top tower-installed passive diode rectifiers a very attractive non-PM option.

Connecting the rectified DC-voltage wind generator system to a DC system is quite common in very small (< 5 kW) wind energy systems, such as for battery charging [1]. But the advantages of having a DC grid system to interface with the renewable energy and electrical loads are also realised in large-scale wind energy systems [2]-[9]. In these systems, the wind energy system is connected to the DC system by either active rectifiers [3], [5], [9], diode rectifiers in series with DC-DC converters [6], [10], or else by only diode rectifiers [1], [8]. The viability and control of using WRSGs in DC-connected systems are considered by [4], [7] and [11], amongst others.

In this paper, we consider the small-scale DC wind energy system shown in Fig. 1. It consists of a geared wind turbine drive train with a WRSG connected to a DC-DC converter via a full-bridge diode rectifier. The DC-DC converter, which is under duty cycle control, supplies the load with DC power. The DC load can either be a water-heating element, a hydrogen electrolyser, or a storage battery or fixed DC-grid voltage source. The WRSG is self-magnetised by using a permanent magnet brushless exciter (PMBE), which is powered mechanically from the wind turbine, as shown in Fig. 1. In [11], a similar WRSG wind turbine system is considered connected to a fixed DC grid, but here the field voltage and thus flux of the WRSG is controlled by a DC-DC converter. It is shown that this system has its advantages, but with the disadvantage of an oversized wind generator

The heart of the paper is the proposed function generator, shown in Fig. 1. The function generator controls the duty cycle of the DC-DC converter in such a way that maximum power point tracking (MPPT) is always obtained. This is done by only measuring the frequency or the mechanical speed of the generator. Such a MPPT control method was first proposed and evaluated by [10] for a small-scale PM wind generator. The method distinguishes itself from the classical perturb and proportional-integral-derivative (PID) MPPT control methods [12], [13]. The method can be considered as continuous variable as perturb and PID control actions are absent.

In this paper, we determine the speed function of the function generator in Fig. 1 for different types of DC loads. Also, the sensitivity to load parameter changes, as well as the dynamic stability of the proposed control system, are investigated. To confirm the method with measured results, the study in this paper is done using an equivalent DC system. The analysis is done in per-unit at a base power level of 2.1 kW.

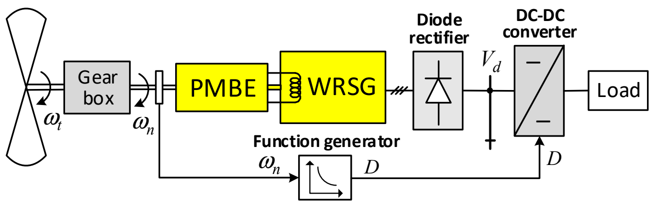

Fig. 1. DC-connected geared WRSG wind turbine system.

II. System Description

In this section, the turbine characteristics and equivalent DC generator system are described briefly.

A. Turbine power characteristics

The per-unit turbine power curves of the WRSG system are shown in Fig. 2. At a maximum turbine power point of P_t = 1.0 pu (2.1 kW), the turbine speed is ω_t = 1.0 pu (320 rpm) at a wind speed of 12 m/s. At ω_t = 0.313 pu turbine speed, the turbine is at its cut-in speed (100 rpm) at 3 m/s wind speed. Hence, the per-unit maximum power-point (MPP) power of the turbine (dotted line in Fig. 2) is expressed by

$$P_{t(\mathrm{MPP})} = \omega_t^3 \text{ (pu).} \tag{1}$$

With a gear ratio of 4.688, the per-unit speed of the WRSG in Fig. 1 is 1 500 rpm (ω_n = 1.0 pu), with ω_n = 0.313 pu the cut-in speed of the WRSG at 469 r/min.

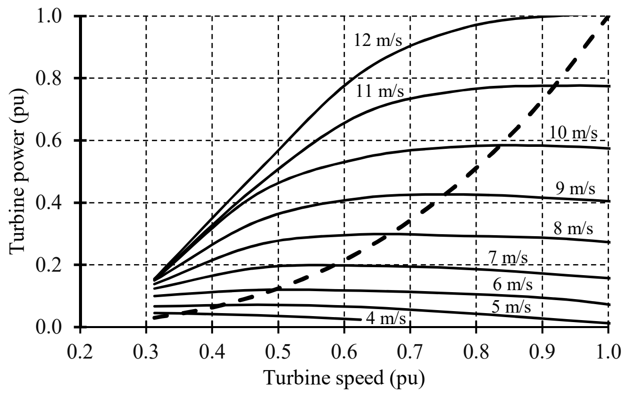

Fig. 2. Turbine power versus turbine speed, with wind speed a parameter; the dotted curve shows $P_{t\,(\mathrm{MPP})}$.

B. Equivalent DC system

The equivalent DC system is shown in Fig. 3. In the place of the PMBE in Fig. 1, we use a fixed field-current DC machine as DC exciter (DC-E), as shown in Fig. 3. The DC-E is mechanically connected to the DC generator (DC-G), which replaces the WRSG and diode rectifier in Fig. 1. The generated armature voltage of the DC-E is used to supply the field circuit of the DC-G, as shown in Fig. 3.

Table I gives all the system parameters of the equivalent DC system based on the laboratory test system. Parameters E_a, I_a and R_a in Table I are the induced voltage, current and resistance of the armature circuit of the DC-G respectively.

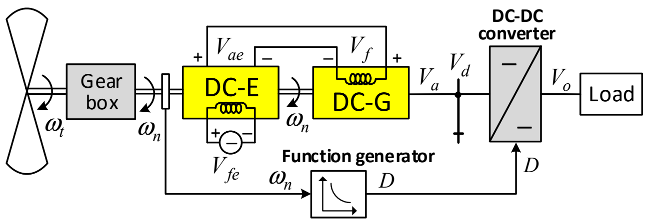

Fig. 3. Equivalent DC generator wind turbine system.

TABLE I: System parameters of equivalent DC system.

Parameter	Base value
P_{base}	2.1 kW
$E_{a(\mathrm{base})}$	190 V
$I_{a(\mathrm{base})}$	11.05 A
$R_{a(\mathrm{base})}$	17.19 Ω
$\omega_{\mathrm{base(low\ speed)}}$	33.57 rad/s (320 rpm)
$\omega_{\mathrm{base(high\ speed)}}$	157.1 rad/s (1 500 rpm)
R_a	2.56 Ω
L_a	12.2 mH
R_a	0.149 pu
J	21 kg.m^2
Gear ratio	4.688

C. DC-DC converter

In the system in Figs. 1 and 3, we consider a buck–boost DC-DC converter. This is to allow for extreme volt-current load specifications, namely high-voltage low-current loads or low-voltage high-current loads. Considering the converter as lossless, and in the continuous conducting mode, the relationships between the output and input voltages and currents of the buck–boost converter are determined by the duty cycle, D, in Fig. 3 as

$$\frac{V_d}{V_o} = \frac{1-D}{D} = a\ ; \quad \frac{I_d}{I_o} = \frac{D}{1-D} = \frac{1}{a}\,. \tag{2}$$

D. DC loads

Three types of DC loads for the small-scale wind energy DC system are possible, as shown in Fig. 4. These are constant DC voltage source loads with a very small internal resistance, such as batteries and constant DC-voltage grids, loads modelled as voltage sources in series with a relatively large internal resistance, such as hydrogen-electrolyser loads and, lastly, pure resistor loads, such as water-heating elements. In this study and analysis, we consider only the extreme of these loads, namely the constant voltage source load in Fig. 4(a), and the pure resistor load in Fig. 4(c).

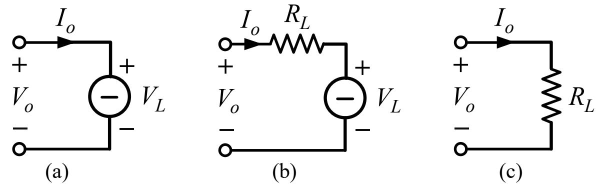

Fig. 4. DC load models of (a) ideal battery or DC grid, (b) hydrogen electrolyser, and (c) water-heating element.

III. Per-Unit Modelling

In this section, we consider the steady state per unit description of the DC-equivalent system in Fig. 3. This is in an attempt to derive a mathematical expression of the duty cycle versus speed of the function generator in Fig. 3, with the turbine always at MPP according to (1).

A. Turbine and generator modelling

Referring to the high-speed side of the gearbox in Fig. 3, the per-unit turbine power is described on the basis of (1) as

$$P_{t(\mathrm{MPP})} = \omega_n^3\,, \tag{3}$$

where ω_n is the per-unit speed of the DC-G in Fig. 3. The rotational losses of the system, which include the windage and friction losses of the drive train, as well as the core losses of both the DC-E and DC-G, can be determined experimentally for the system as a function of speed. From this, the per-unit value of the rotational losses as a function of speed can be obtained, which is typically a function of the form

$$P_{rot} = k\omega_n^y\ , \tag{4}$$

and where k and y are determined experimentally. The per-unit developed armature power of the DC-G can now be determined from (3) and (4), as

$$P_a = E_a I_a = P_t - P_{rot}\,, \tag{5}$$

where E_a and I_a are the induced armature voltage and armature current of the DC-G. E_a is a function of the speed, ω_n, and the field flux of the DC-G. The field flux is a function of the induced armature voltage of the DC-E, as shown in Fig. 3, which in turn is again a function of the speed of the system, ω_n. If we linearise the flux change with speed (through a per-unit point of speed and flux), and ignore the small armature voltage drop in the DC-E, then the per-unit induced armature voltage of the generator can simply be modelled by

$$E_a = \omega_n^2\,. \tag{6}$$

The per-unit armature voltage of the DC-G, which is also the DC supply voltage to the DC-DC converter, as shown in Fig. 3, is given by

$$V_d = V_a = E_a - I_a R_a\,. \tag{7}$$

B. Per-unit load modelling

The circuit parameters of the general load model in Fig. 4(b) can be referred to the generator side of the converter in Fig. 3 using (2), as

$$V_L' = aV_L\,; \quad I_o' = \frac{1}{a} I_o\,; \quad R_L' = a^2 R_L\,. \tag{8}$$

Note that (8) is valid in per unit based on the base values of the equivalent DC system in Table I. Thus, the V_L, I_o and R_L in (8) are per-unit values based on the base values of the voltage, current and resistance in Table I.

C. Duty cycle versus speed

With the referred load model of (8), we can rewrite (7) as

$$E_a = V_d + I_a R_a = V_L' + I_a R_L' + I_a R_a\,. \tag{9}$$

With $I_a = P_a / E_a$ from (5), and E_a given by (6), (9) can be rewritten using (8) as

$$\begin{aligned} \omega_n^2 &= aV_L + \frac{P_a}{\omega_n^2} a^2 R_L + \frac{P_a}{\omega_n^2} R_a \\ \Rightarrow & \left(P_a R_L\right) a^2 + \left(V_L \omega_n^2\right) a + \left(P_a R_a - \omega_n^2\right) = 0. \end{aligned} \tag{10}$$

From (10), a can be solved as

$$a = \frac{-V_L \omega_n^2 + \sqrt{V_L^2 \omega_n^4 - 4 P_a R_L (P_a R_a - \omega_n^4)}}{2 P_a R_L}\,, \tag{11}$$

and hence the duty cycle D from (2) as

$$D = \frac{1}{1+a}\,. \tag{12}$$

Given per-unit load parameters V_L and R_L, and with R_a known, we can determine $D = f(\omega_n)$ numerically by choosing a series of values for ω_n and calculate P_t, P_{rot} and P_a accordingly from (3) to (5), and then a and D from (11) and (12) (see further Section IV(*C*) in this regard).

IV. System Duty Cycle Versus Speed Function

In this section, we consider the unique duty cycle versus speed function of the wind energy system in Fig. 3 using the per-unit analysis in the previous section. The calculations are based on the system parameters of Table I. For the per-unit P_{rot} calculation of (4), we took $k = 0.08$ and $y = 1$ in the analysis. Only two of the types of DC loads are considered, namely the voltage source in Fig. 4(a) and the resistor in Fig. 4(c).

A. Power, voltage and current variation with system speed

In Fig. 5, the power and DC link voltage and current variation versus turbine speed of the wind energy system are shown, with the wind turbine always at maximum power. Note that these performance curves stay the same, independent of the type of DC load.

It is shown in Fig. 5 that the efficiency of the system at $\omega_n = 1.0$ pu speed is almost 83%. The highly linear variation in the DC link current, $I_d = I_a$ with ω_n in Fig. 5, can be understood from (3), (5) and (6), namely that, with P_a following P_t very closely, we have $P_a = E_a I_a = \omega_n^2 I_a \approx \omega_n^3$, which implies that $I_a \approx \omega_n$ in per-unit values. The quadratic function of V_d versus ω_n in Fig. 5 stems from the fact that R_a is relatively small, which implies that $V_d = V_a \approx E_a = \omega_n^2$.

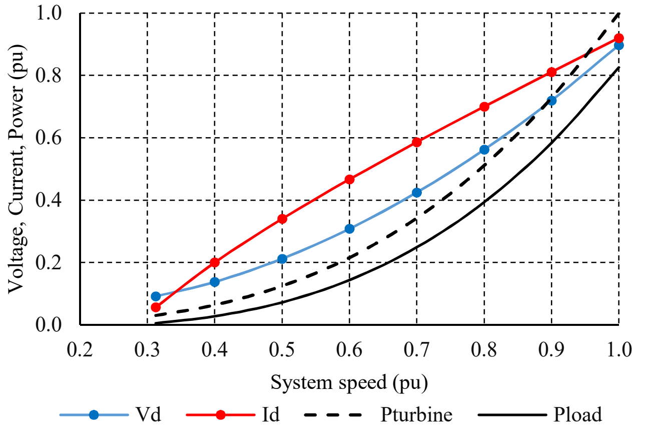

Fig. 5. DC-link voltage and current versus per-unit system speed with the turbine at maximum power point.

B. Duty cycle with voltage source and resistor as loads

In Fig. 6, the MPP duty cycle versus the system speed calculated according to (12) is shown for two voltage source loads. The decreasing duty cycle is from (2), due to the increase in V_d with system speed (see Fig. 5) and the constant load voltage.

In Fig. 7, the MPP duty cycle versus system speed is shown for two resistor loads. Here, the very flat duty-cycle curves are because of the load resistor voltage and current that follow to a certain extent the voltage and current on the generator side as power increases, with only a slight change in the referred resistor load. The duty cycle hence varies little.

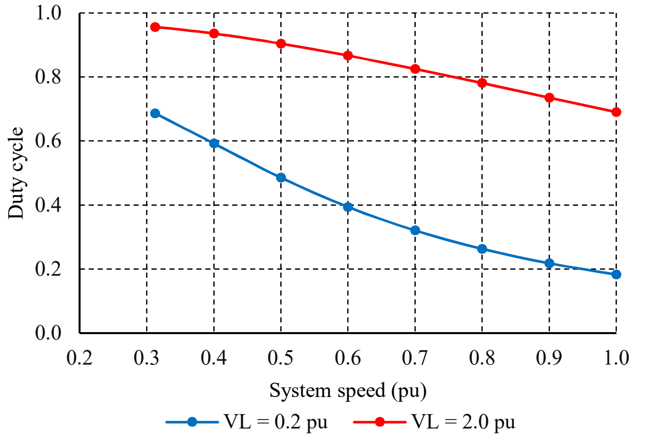

Fig. 6. Duty cycle versus per-unit system speed for 0.2 pu (38 V) and 2.0 pu (380 V) DC voltage source loads.

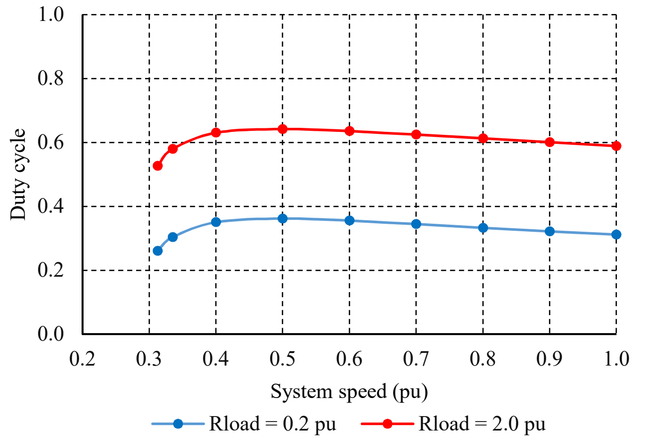

Fig. 7. Duty cycle versus per-unit system speed for 0.2 pu (3.44 Ω) and 2.0 pu (34.4 Ω) resistor loads.

C. Duty cycle versus speed function

An objective of the study was to determine the function of the function generator in Fig. 3 to have the wind energy system always at maximum power-point operation. This function has system speed as input and duty cycle as output, i.e.

$$\omega_n \rightarrow \boxed{f(\omega_n)} \rightarrow D\,. \tag{13}$$

From Figs. 6 and 7 it can be seen that these functions are very smooth and can easily and accurately be expressed by a second-degree interpolating polynomial of the form

$$D_{\mathrm{MPPT}} = f(\omega_n) = c_1\omega_n^2 + c_2\omega_n + c_3\,, \tag{14}$$

where c_1, c_2 and c_3 are determined from the data of three points on the duty-cycle curve.

The method to determine (14) for a specific load is to key into a microprocessor the parameters of the load, do the data calculations at a number of speeds according to (12), and then determine the coefficients of (14) from this data. Of course, the load parameters can also be measured to determine (14) in real time, or the coefficients c_1 to c_3 can be determined over time by machine learning algorithms to maximise the energy harvesting.

V. Sensitivity To Load Parameters

It is always important to determine the sensitivity of the MPPT wind energy system to load parameter changes. To determine this for the proposed MPP control system, we investigated the change in load parameters on the MPPT. In the case of the voltage source load in Fig. 4(a), it means a variation in the load voltage, V_L, and in the case of the resistor load in Fig. 4(c), a variation in the load resistance, R_L.

Fig. 8 shows the effect of a change in the constant voltage of the voltage source in Fig. 4(a) on the MPPT of the turbine. The zero-percentage curve is of the duty cycle function determined according to the given voltage, as in Fig. 6. The +5% and -5% curves are the MPPTs of the turbine, using the same duty cycle function as in Fig. 6, but now with a +5% and -5% change in the constant voltage of the voltage source. The system speed is clearly very sensitive to such small changes in voltage. This is due to the relatively small armature resistance, R_a, between the referred load voltage, V_L', and the armature-induced voltage E_a; the incorrect duty cycle, thus with a changed V_L', forces a change in E_a, and consequently in the speed. The energy harvest, however, is shown in Fig. 8 to be almost insensitive to ±5% load voltage changes due to the flat turbine power characteristics.

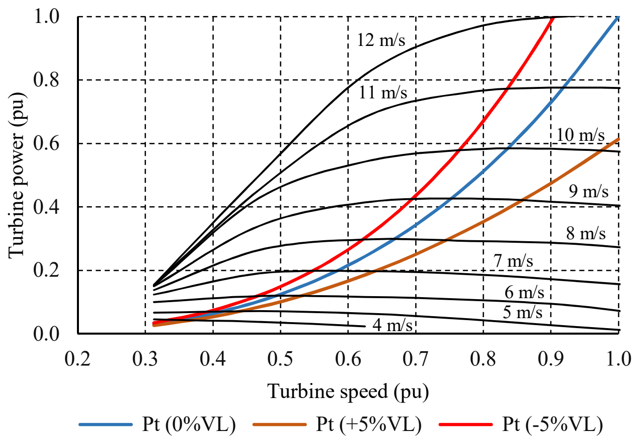

Fig. 8. Effect of percentage load voltage variations on the MPPT.

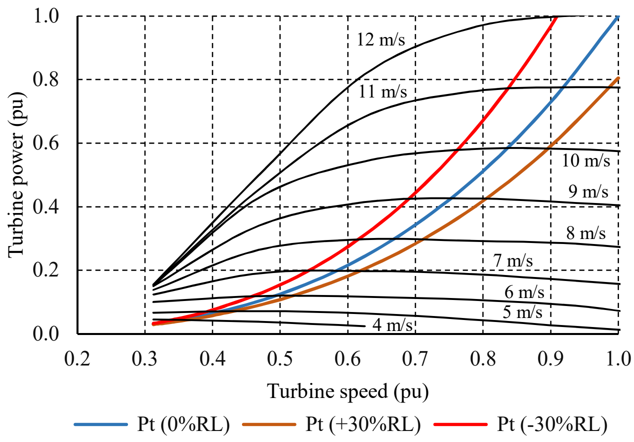

Fig. 9. Effect of percentage load resistance variation on the MPPT.

The same process as just described for the voltage source load is followed in Fig. 9, but in this case with the resistor load [Fig. 4(c)] connected to the wind energy system and with the effect of percentage changes in resistance value on the MPPT. The ± 30% curves in Fig. 9 are the MPPTs of the turbine using the duty cycle functions as in Fig. 7, but with a ± 30% change in resistance value. It is shown in Fig. 9 that the MPPTs are very insensitive for relatively large percentage changes in load resistance. Also, this result can be explained on the basis of the analytical model that was developed.

VI. System Stability

An important aspect of any wind energy system, and hence the proposed system in Fig. 3, is its stability under dynamic conditions. This is important, as wind speeds can vary rapidly, as in the case of wind gusts. What therefore is in question is whether the proposed control system using (14) is stable under dynamic wind speed conditions.

In a study of a similar PM generator system [10], it was found that the system is stable and has the properties of a low-pass filter. It therefore was expected that the proposed system in Fig. 3 would also be stable. However, to confirm this, MATLAB Simulink simulations were done of the system in Fig. 3, using the system parameters of Table I.

The response of the duty cycle of (14) for a step plus sinusoidal wind-speed input to the wind energy system of Fig. 3 is shown in Fig. 10. The frequency of the sinusoidal input is varied in three cases, as shown in Fig. 10(a) to (c). These results confirm the stability of the system against step wind-speed inputs and the behaviour of the system as a low-pass filter at high wind-speed frequencies.

VII. Practical System and Results

To test the proposed MPPT wind energy system in Fig. 3 practically, use was made of two mechanically connected DC machines, as shown in Fig. 11(a). One of the DC machines was used as DC-E and the other as DC-G. The machine in the middle of the two DC machines is an induction machine that was used with a variable speed drive (VSD) to drive the system; the induction machine VSD therefore emulates the wind turbine in Fig. 3.

To implement the proposed control, a microprocessor and a step-down DC-DC converter were used, as shown in Fig. 11(b). The microprocessor measures the speed of the system and outputs the pulse-width modulation (PWM) duty cycle to the DC-DC converter according to (14).

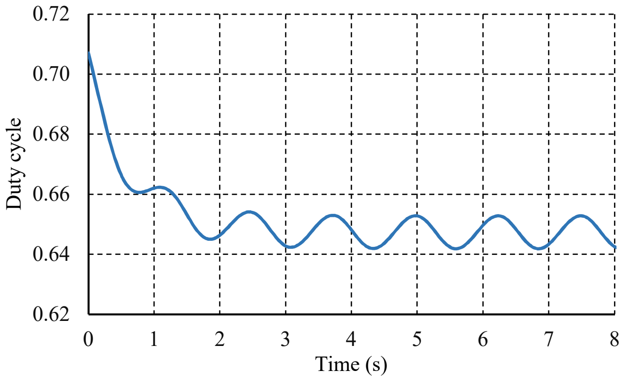

(a) Step plus 0.8 Hz wind speed input.

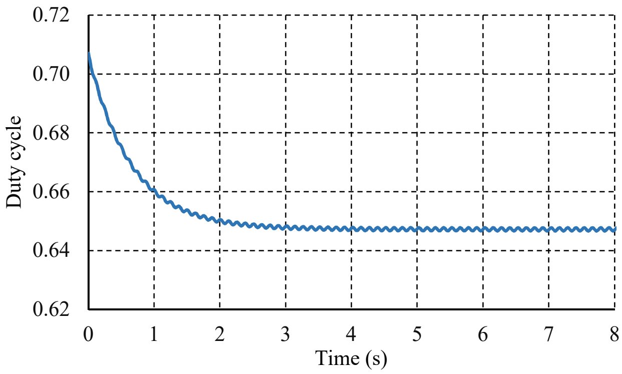

(b) Step plus 8 Hz wind speed input.

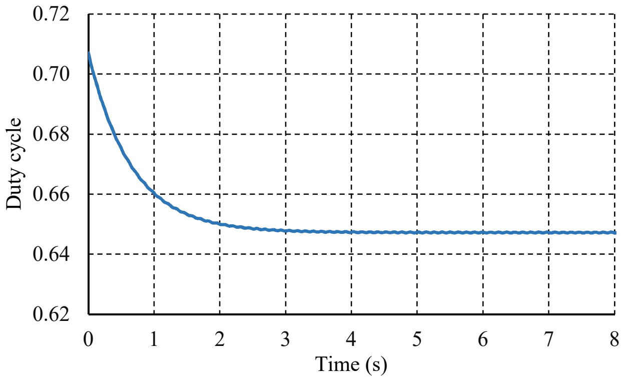

(c) Step plus 32 Hz wind speed input.

Fig. 10. Duty cycle step and frequency response versus time of the proposed MPP-control wind energy system.

For the tests, the speed of the system was adjusted using the VSD. In the first test, the open circuit characteristics of the DC-E and DC-G in Fig. 3 were measured. These results are shown in Fig. 12. As shown, the field current versus speed of the DC-G is linear, as expected. However, the induced voltage E_a versus speed is not completely quadratic, as assumed by (6); $E_a = \omega_n^{1.5}$ gives a good fit instead. The reason for this deviation is the non-linear magnetisation relationship between the field current and generated flux of the DC-G.

For the load tests, the output power of the DC-G was measured and compared with the estimated power output under MPP control. For the estimated power, we used the measured relationship of E_a versus speed in Fig. 9 from the cut-in speed. The measured and estimated results are shown in Figs. 13 and 14, for a resistor and battery load respectively. For the resistor load, the comparison between the measured and estimated powers is almost perfect, as shown in Fig. 13. For the battery load, however, the comparison was not as good, as shown in Fig. 14. The reason for the latter is the high sensitivity of the


(a)

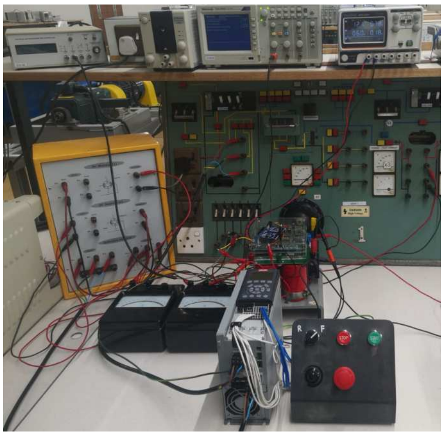
(b)

Fig. 11. Practical test system, (a) DC-E, DC-G and induction machine (middle), and (b) DC-DC converter, VSD and micro-controller.

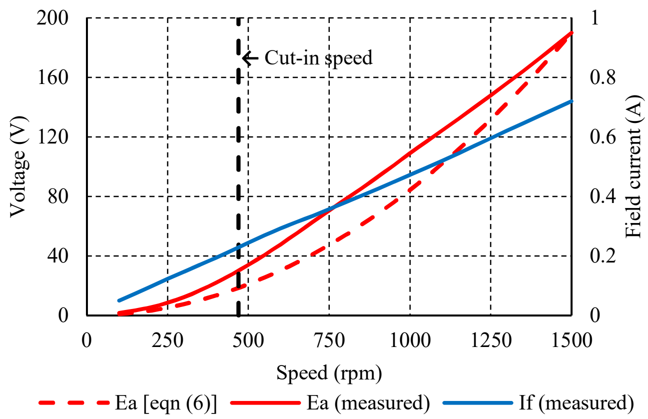

Fig. 12. Measured induced field current and voltage versus speed of the DC generator.

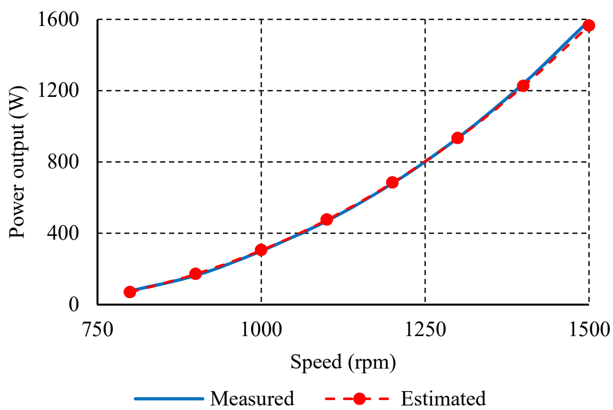

Fig. 13. Measured and estimated MPP generator output power versus speed for a 28-Ω resistor load.

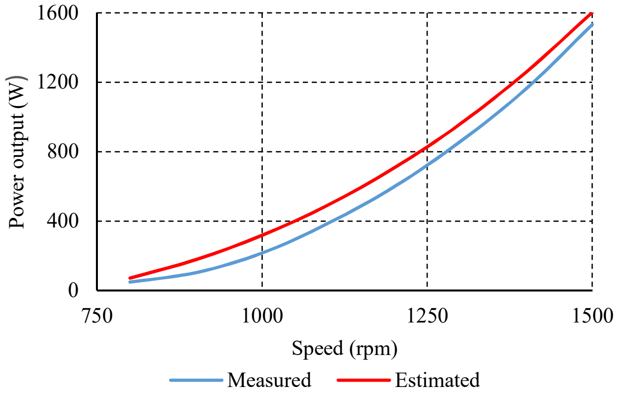

Fig. 14. Measured and estimated MPP generator output power versus speed for a 72 V, 30 mΩ internal resistance battery load.

system to the duty cycle; this is because of the very small internal battery and generator resistances. The comparison in Fig. 14 is nevertheless deemed sufficient.

VIII. Conclusion

In this paper, a proposed MPP control of a WRSG connected to a DC load via a diode rectifier and DC-DC converter is investigated by means of an equivalent DC system study. In this method, the DC-DC converter is optimally controlled according to a MPP determined duty cycle speed function. From the analysis and results, the following conclusions are drawn.

The MPPT duty cycle speed function gives a simple relationship and can be represented accurately with a second-degree interpolating polynomial. The implementation on a microprocessor is thus very simple.

The MPPT duty cycle speed function is shown to be very load specific; it varies greatly between types of DC loads. However, the V_L and R_L parameters of the DC load can easily be keyed into the controller, and the duty cycle speed function quickly determined by the microprocessor.

The sensitivity of the proposed MPP control method to load parameter variation is shown to depend on the type of DC load. For resistive loads, the sensitivity is very low. For DC voltage source loads, however, the system is very sensitive due to the very small armature resistance, R_a, of the DC-G. In this regard, it should be noted that, for a WRSG system, the sensitivity to changes in the DC voltage source will be much less due to the relatively high internal synchronous reactance, X_s, of the WRSG ($X_s >> R_a$).

Simulations of the proposed MPP-controlled wind energy system show that the system is absolutely stable against changes in wind speed and that it behaves as a typical low-pass filter.

Experimental results from an equivalent DC system confirm the proposed MPP control method. The simplicity of the control system was shown in the practical setup, using a microcontroller with a simple speed function to determine the MPP duty cycle.

To compensate for large variations in DC load parameters, these parameters can be measured and the MPPT duty cycle speed function can be adjusted in real time. Also, the three coefficients of the MPPT speed function of (14) can be optimised over time by machine-learning algorithms to maximise the harvesting of wind energy.

References

[1] C.J.J. Labuschagne and M.J. Kamper, "Evaluation of PM rotor topologies for impedance matching of small-scale passive DC-connected wind generator systems," 24th International Conference on Electrical Machines (ICEM), Gothenburg, Sweden, pp. 1896-1902, Aug 23-26, 2020.

[2] K. Musasa, N. I. Nwulu, M. N. Gitau and R. C. Bansal, "Review on DC collection grids for offshore wind farms with high-voltage DC transmission system," IET Power Electron., vol. 10, no. 15, pp. 2104–2115, Dec 2017.

[3] P. Huynh, P. Wang and A. Banerjee, "An integrated permanent-magnet-synchronous-generator-rectifier architecture for limited-speed-range applications," IEEE Energy Conversion Congress and Exposition (ECCE), Portland, OG (USA), pp 3413–3420, Sep. 2018.

[4] M. S. U. Khan, A. I. Maswood, K. Satpathi, M. T. Iqbal and A. Tripathi, "Analysis of brushless wound rotor synchronous generator with unity power factor rectifier for series offshore DC wind power collection," 44th Annual Conference of the IEEE Industrial Electronics Society (IECON), Washington, DC (USA), pp 1693–1698, 2018.

[5] M. Pape and M. Kazerani, "On the efficiency of series-connected offshore DC wind farm configurations", IEEE Energy Conversion Congress and Exposition (ECCE), Baltimore, MD (USA), pp 921–926, Oct. 2019.

[6] O. Beik and A.S. Al-Adsani, "Parallel nine-phase generator control in a medium-voltage DC wind system, " IEEE Trans. on Industrial Electronics, vol. 67, no. 10, Oct. 2020.

[7] O. Beik 1 and A.S. Al-Adsani, "Active and passive control of a dual rotor wind turbine generator for DC grids," IEEE Access, Volume 9, pp. 1987-1995, 2021.

[8] M. Gholamian and O. Beik, "Coordinate control of wind turbines in a medium voltage DC grid," IEEE Energy Conversion Congress and Exposition (ECCE), Detroit (USA), Oct 2022.

[9] H.A. Hussain K.A. Nour Al-Deen, "Design and control of series-DC wind farms based on three-phase dual active bridge converter," IEEE Energy Conversion Congress and Exposition (ECCE), Detroit (USA), Oct 2022.

[10] L.P. Mdakane and M.J. Kamper, "Simple robust MPPT control for wind energy DC-grid connected systems", IEEE 45th Annual Conference of the Industrial Electronics Society (IECON), Lisbon (Portugal), pp. 2498-2500, 14-17 Oct. 2019.

[11] J.H. Giliomee and M.J. Kamper, "Maximum power point field control of direct DC grid-connected wound rotor synchronous wind generator system," IEEE 30th Southern African Universities Power Engineering Conference (SAUPEC), Durban, South Africa, 25-27 Jan 2022.

[12] R. Rathi and K.S. Sandhu, "Comparative analysis of MPPT algorithms using wind turbines with different dimensions & ratings," 1st IEEE International Conference on Power Electronics, Intelligent Control and Energy Systems (ICPEICES-2016), Jul 4–6, 2016.

[13] L. Aleksandr, G. Demidova, O. Alassaf, D. Lukichev, A. Rassõlkin and T. Vaimann, "MPPT algorithms for wind turbines: review and comparison," 29th International Workshop on Electric Drives: Advances in Power Electronics for Electric Drives (IWED), Moscow, Russia. Jan 26–29, 2022.

2023 SAUPEC Conference, Johannesburg, South Africa, January 24-26, 2023

Analysis of a Hoist Motor Regenerated Energy System

Chrispin Namponya
Department of Electrical Power Engineering
Durban University of Technology
Durban, South Africa
21856070@dut4life.ac.za

Innocent E. Davidson
Department of Electrical Power Engineering
Durban University of Technology
Durban, South Africa
innocentD@dut.ac.za

Abayomi A. Adebiyi
Department of Electrical Power Engineering
Durban University of Technology
Durban, South Africa
abayomia@dut.ac.za

***Abstract*—High demand in industrial processes has resulted in technological advancements, particularly where materials need to be handled efficiently to realize profits. The overhead crane is a versatile machinery that diversely achieves movements of heavy objects that other material handling methods cannot manage in complex environments. The application of variable frequency drives (VFDs) on cranes achieves smooth and precise handling of heavy objects and consequently eliminates mechanical shock, thus prolonging machinery lifespan. To manoeuvre a load at the desired speed, the motors are often operated at a fraction of their rated speeds. At low speeds, the motor rotation opposes the generated torque. During this phase, the motor is electrically braking and behaving as a generator. The motor is feeding energy towards the VFD in what is known as regeneration. To mitigate the effects of the rising energy in the VFD, external resistors are connected to dissipate the energy as heat. The project aims to study VFD energy flow and design a system that recycles energy based on the findings. A VFD hoist has been constructed in laboratory conditions to investigate the compatibility of existing renewable energy storage technology to replace the resistors for crane-safe requirements.**

Keywords—variable frequency drives (VFDs), supercapacitor, DC bus, bidirectional DC-DC converter, regenerated energy, dynamic braking

I. INTRODUCTION

In modern processes, overhead crane motions are required to be very precise for safe operations. The application of Variable Frequency Drives (VFDs) [1-3] for crane motor control achieves smooth and precise handling of heavy objects and consequently safeguards the crane from the effects of mechanical shock thus prolonging machinery lifespan. In rotating types of machinery such as cranes, torque and motor rotation oppose each other when the machine has to slow down and stop. When hoisting machinery lowers a heavy load, the motor rotation and the generated torque oppose each other. In hoists designed with a counterweight system, the opposition of generated torque and motor direction occurs when a hook is raised with no load attached. In these cases, the hoist motor operates in a generator mode which develops energy in the crane's electrical system. This process is referred to as regeneration. Cranes produce huge amounts of regeneration in every operational cycle. Regeneration energy rises to dangerous levels in the VFD system if it is not discarded appropriately. Currently, the most common solution employed on crane systems to mitigate the rising regenerated energy is by redirecting it to resistors where it is converted to thermal energy. This process is referred to as dynamic braking. In dynamic braking, the VFD is protected but the resistors lose valuable energy from the crane as heat to the environment. Active Front Ends (AFE) that convert the regenerated energy to be directed back to the grid may be employed to save energy. However, the converted currents from the AFEs are not exactly sinusoidal as they contain some ripple of the switching frequency. This creates harmonics that need to be actively filtered to avoid distortions to the grid, it is a very costly exercise.

This paper proposes an implementation of recycling regenerated energy in a VFD machinery system. The research aims to formulate a practical technique for conserving regenerated energy by studying a typical industrial overhead VFD hoist under controlled laboratory conditions. The technique will investigate the overall energy and financial benefits of the implementation. Using a bidirectional DC-DC converter, it is possible to direct regenerated energy from the machinery to a power storage package and return it to the machinery on demand. A bidirectional DC-DC converter operates in buck mode where electrical power is absorbed from the VFD to the storage pack and operates in boost mode to supply power from the storage pack. This implementation is aimed at reducing machinery operational energy losses by containing system-regenerated energy as opposed to dissipating it as heat to the environment. The objective of the research is to design a practical energy-saving solution that can be implemented easily and safely into existing machinery. The research is designed to pioneer further study of other similar electrical machinery and applications. The research aims at developing a model for industrial electrical types of machinery to operate at optimal conditions as efficiently as possible [4-6]. The research will demonstrate the best options to achieve the reliability of industrial plants that will pay back financial dividends by eliminating unplanned production stoppages and by reducing energy demands. By conducting a performance analysis of industrial machinery, we are able to detect shortcomings of the running system and develop appropriate solutions.

II. LITERATURE REVIEW

A standard variable frequency drive (VFD) consists of a diode/thyristor six-step unidirectional rectifier on the power supply input and an insulated gate bipolar transistor (IGBT) bidirectional inverter on the induction motor end. The rectifier and the inverter are connected through a DC link (DC bus) as shown in Fig. 1. A typical overhead crane consists of several VFDs operating different motors for functions such as hoisting, cross travel and long travel motions. To achieve instantaneous torque control during acceleration and deceleration, crane VFDs are operated in a vector mode control. A motor operates in a motoring and a braking mode.

In a motoring mode it converts electrical energy to mechanical energy, which supports its motion. In a braking mode, it works as a generator converting mechanical energy to electrical energy, thereby opposing the motion. A motor can provide motoring and braking operations for both forward and reverse directions. In loads involving up-and-down motions such as the hoisting application, the speed of the motor which causes upward motion is considered forward motion and is given a positive sign. The downward motion is considered the reverse direction and it is assigned the negative sign.

When an induction motor is braking or overhauling under loaded conditions, it acts as a generator causing energy to flow back into the VFD through the bidirectional IGBT inverter. The unidirectional rectifier prevents the energy from flowing back to the mains supply line thereby raising the DC bus voltage to harmful levels. To control the DC bus voltage in hoisting machines, a chopper circuit in the VFD directs the regenerated energy to a set of resistors to convert it into thermal energy [7-9]. This energy is lost from the crane system and contributes negatively to the problem of global warming.

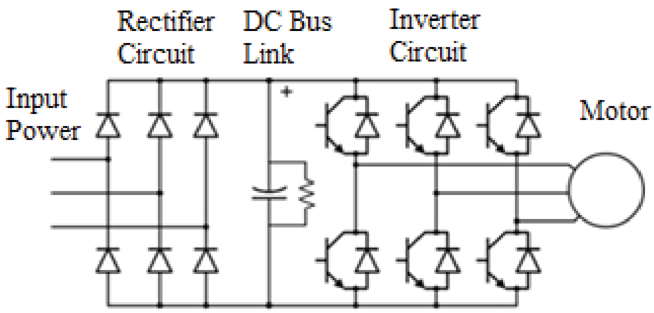

Fig. 1. The basic layout of a typical six-diode VFD

Other methods of saving the regenerated energy are achieved by adding AFE technology to the VFD to convert the DC energy to AC power and redirect it to the grid. The AFE technology has proven to be very costly as extra filters are required to mitigate harmonics that are developed during the conversion phase. AFEs are further disadvantaged by the fact that the maximum output voltage is typically limited to around 87% of the AC supply to achieve acceptable harmonic distortion levels. This results in higher motor losses and lowers operational efficiency. AFEs generate significant levels of ground leakage current which can cause inadvertent ground fault trips and failure of sensitive equipment in a plant. The objective of the research is to store the regenerated energy by employing Renewable Energy Technology (RET) thereby minimising energy losses from the system.

III. METHODOLOGY

A. Case study

A case study survey of an industrial line overhead crane is carried out during real-time production runs. The crane has a 25-ton 50 kW three-phase 400 V hoisting unit. Monitoring software is incorporated on the crane hoist VFD for a continuous period of 6 eight-hour shifts. The data is downloaded for analysis. The results collected are displayed in Fig. 2 and explained in tables II and III. The results show that there are considerable energy losses in the resistors during the regenerative dynamic braking of the crane. The plant has four such cranes operating at the same time resulting in total annual losses of over 38 500 kWh of electrical energy equal to R100 000, due to hoist dynamic braking alone. This amount is equivalent to the average energy consumption of ten households per year. This serves as the motivation for the study.

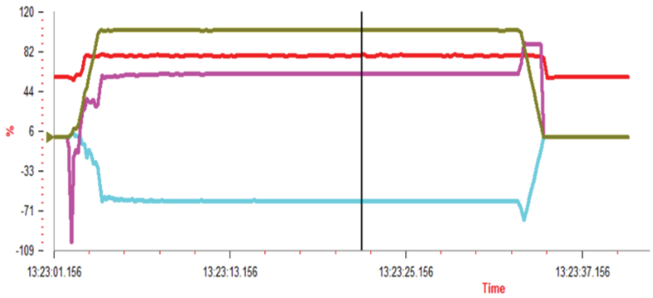

Fig. 2. Dynamic Braking of a 50kW crane hoist

TABLE I. DYNAMIC BRAKING OF 50KW CRANE HOIST

Trend Signals	Min	Max	Signal Scaling
(1) DC Bus Voltage	563 VDC	789 VDC	1000 (VDC/100%)
(2) Torque Reference	-129.4 %	90.0 %	100.0 (%/100%)
(3) Motor Speed	0.00 Hz	51.23 Hz	50.00 (Hz/100%)
(4) Output Power	-30.8 kW	2.4 kW	50.0 (kW/100%)

TABLE II. DYNAMIC BRAKING OF 50KW CRANE HOIST

Dynamic Braking (DB) results of a 50kW production crane hoist			
DB Power	30.8kW		
DB duration	30s/cycle	304h/year	
Energy losses due to DB			9636kWh/year
Tariff			R2.77769/kWh
Financial losses due to DB			R26 000.00/year

B. Experimental model

Extreme safety industrial requirements and the possibility of dropping heavy loads during experimental implementations for the study resulted in the construction of a laboratory model of a crane hoist. A 1000 kg hoisting capacity unit presented in Fig. 3 has been designed and constructed for analyzing the regenerative energy under controlled conditions. The hoisting unit is operated with a 1.5 kW three-phase 380 VAC, 40% duty cycle induction motor with an electromechanical brake. A 3 kW three-phase 360 – 400VAC VFD with a real-time monitor display is used to operate the motor. The VFD has an internal chopper circuit connected to the DC bus and an external dynamic braking resistor. The aim of the study is to conduct a complete analysis of the DC bus voltage and output power on a typical industrial hoisting application during the regeneration phase. The hoist will be subjected to various loads as in a typical industrial operational setting. From the findings, calculations will be carried out to develop a circuit that will replace the external dynamic braking resistor with RET. The proposed RET will include a suitable DC-DC bidirectional converter and a supercapacitor based on the findings. In the motoring mode, energy will be drawn from the supercapacitor via the DC bus to operate the motor. The VFD will only draw energy from the grid when the supercapacitor voltage drops below the minimum DC bus operational voltage level.

The DC bus voltage is designed to operate below an upper limit *Vmax* and above a lower limit *Vmin* to control the VFD. *Vmax* is set to protect the VFD hardware from over-voltage damage and the *Vmin* voltage is set to maintain sufficient voltage to operate the motor efficiently. When the voltage is out of the minimum and maximum range, the VFD protection circuit will trip. The values differ with various VFD designs depending on the manufacturer. In this study, Equations (1) and (2) were used for the parameter settings of the VFD.

$$V_{max} = K_a\sqrt{2}(400)V_{DC} \tag{1}$$

Where K_a is the volt-drop coefficient of the VFD three-phase bridge rectifier circuit as provided by the manufacturer.

$$V_{min} = \sqrt{2}(360)V_{DC} \tag{2}$$

TABLE III. MACHINE PARAMETERS

Machines Parameters	**Value**
Motor power Voltage	380 V
Motor Rated Current (FLA)	3,70 A
Motor Rated Slip	3,020 Hz
Motor No-Load Current	1,67 A
Motor Pole Count	4
Motor Line-to-Line Resistance	11,846 Ω
Motor Leakage Inductance	24,2 %
Motor Saturation Coefficient 1	0,50
Motor Saturation Coefficient 2	0,75
Motor Rated Power	1,50 kW
Motor speed N	1400 rpm
Gearbox ratio GR	96:1
Gearbox output speed	15 rpm
Gearbox efficiency η_G	80%
Rope drum diameter D	600mm

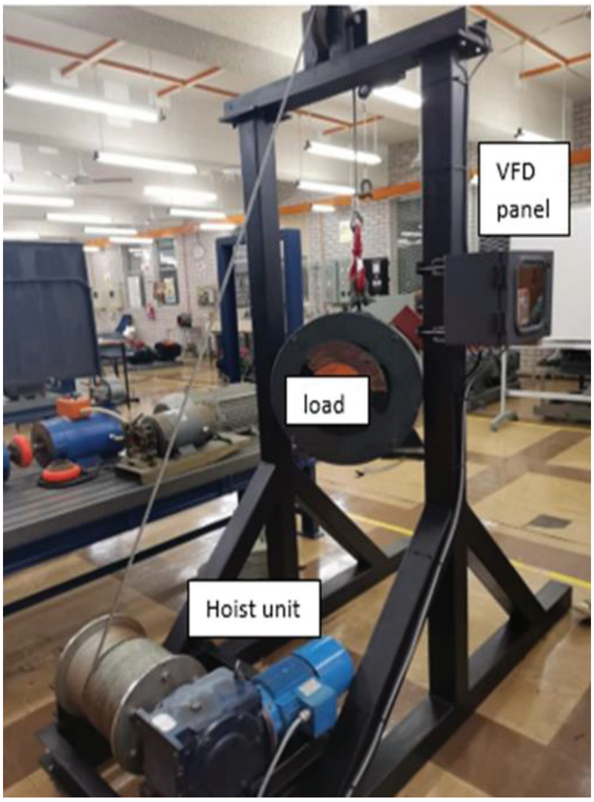

Fig. 3. Laboratory hoisting assembly two-fall rope system set up

The dynamic Equation of the hoist machinery is given by

$$T_m = T_L \pm (d\,/\,dt)(J\omega_m) \tag{3}$$

Where T_m is the motor torque, T_L is the load torque and J is the moment of inertia of the machinery. For constant inertia traction machines $dJ/dt = 0$ therefore

$$T_m = T_L \pm J(d\omega_m\,/\,dt) \tag{4}$$

The component $J(d\omega_m/dt)$ is the dynamic torque of the machinery. When $T_m > T_L$ then $(d\omega\,/\,dt > 0)$ the system accelerates and decelerates when $T_m < T_L$. Steady-state operation is reached when $T_m = T_L$, then $\omega = constant.$ When fully loaded at steady state condition, the load m is equally distributed on a two-fall rope hoist system shown in Fig. 2. The load torque (T_L) at the rope drum is determined with Equation (5).

$$T_L = \left({}^{m}\!/_{2}\right) \times g \times \left({}^{D}\!/_{2}\right) \tag{5}$$

The load torque at the motor end is calculated by a factor of the gear ratio (GR) and the gearbox efficiency (η_G) from Table III. The maximum motor torque (T_{mmax}), peak motor power (P_P), and dynamic braking resistance (R_b) are determined with Equations (6), (7) and (8) respectively.

$$T_{mmax} = {}^{T_L}\!/_{(GR \times \eta_G)} \tag{6}$$

$$P_p = T_{mmax} N \frac{2\pi}{60} \tag{7}$$

$$R_b = \frac{V_{max}^2}{P_P} \tag{8}$$

C. Common DC bus

An overhead crane system consists of hoisting, cross-movement and bridge travelling units which are operated independently of each other. A crane system may consist of several VFDs and induction motors performing various functions. Installing a set of the energy-storing device for each VFD is costly. The research proposes installing a single storage pack connected to all the crane VFDS via a common DC bus as shown in Fig 4. The advantage of a common bus is that VFDs can share and balance power when some motors are in motoring mode while others are in generation mode. During this condition, the motoring VFDs utilise power from the regenerating VFDs thereby conserving energy and reducing demand from the grid. Excess energy that is not utilised by the VFDs is absorbed into the storage pack via a bidirectional DC-DC converter connected to the common DC bus. The stored energy is drawn by the crane system during demand instead of drawing from the grid [10-13]. Due to the fast power changes and high peak values that will be experienced on the common DC bus, supercapacitors have been selected for the energy storage design due to the high-power density and fast response time that will be required. Supercapacitors have proven to be reliable for similar applications in smart grid systems such as uninterruptable power supplies and fuel cell renewable energy systems [14-15].

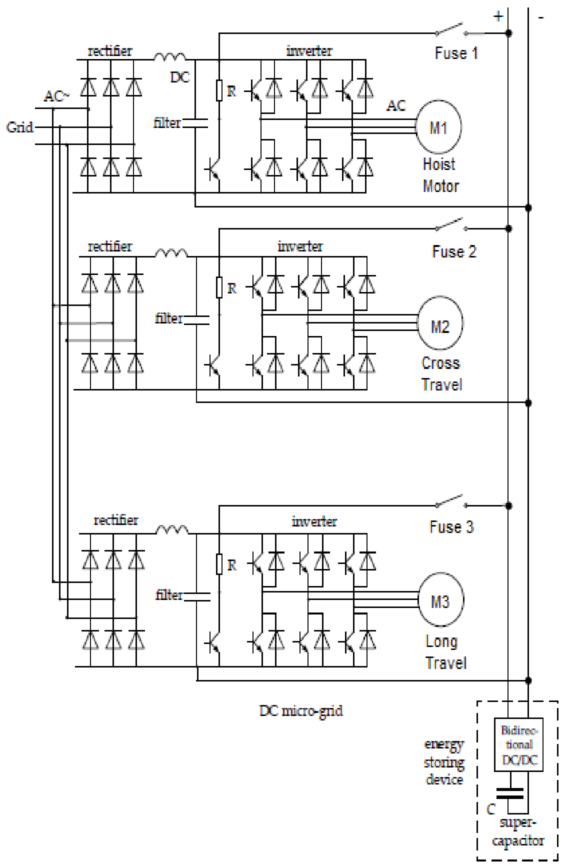

Fig. 4. Overhead crane multiple VFD system with a common DC bus

IV. Experimental Results

Tables IV and V present the regenerative braking experimental measurements of the variance between DC bus voltages, motor torque, and output power at different operational speeds. Figures 4 and 5 depict the recorded readings of the system. Table V provides the regenerative power measurements that are required for the sizing of the storage unit and the bidirectional DC-DC converter [16-18]. The DC-DC converter is set to charge and discharge the storage unit to maintain the VFD bus voltage operational range.

TABLE IV. Measurements During the Hoisting-Up Full Load

Trend Signals	Min	Max	Signal Scaling
(1) DC Bus Voltage	522 VDC	540 VDC	1000 (VDC/100%)
(2) Torque Reference	0.0 %	146.5 %	100.0 (%/100%)
(3) Motor Speed	0.00 Hz	48.90 Hz	50.00 (Hz/100%)
(4) Output Power	0.0 kW	0.95 kW	1.5 (kW/100%)

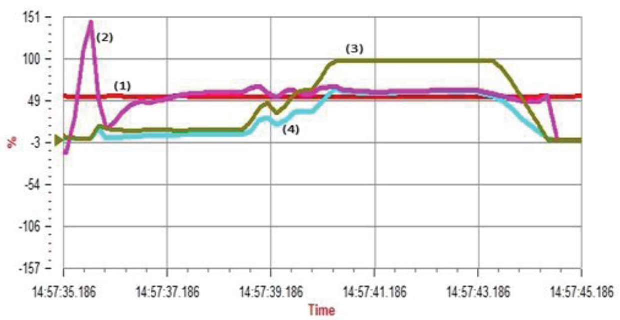

Fig. 5. Experimental results during hoisting-up full load

TABLE V. Measurements During the Descent of Full Load

Trend Signals	Min	Max	Signal Scaling
(1) DC Bus Voltage	531 VDC	787 VDC	1000 (VDC/100%)
(2) Torque Reference	-142.1 %	15.5 %	100.0 (%/100%)
(3) Motor Speed	0.00 Hz	50.58 Hz	50.00 (Hz/100%)
(4) Output Power	-0.17 kW	0.11 kW	1.5 (kW/100%)

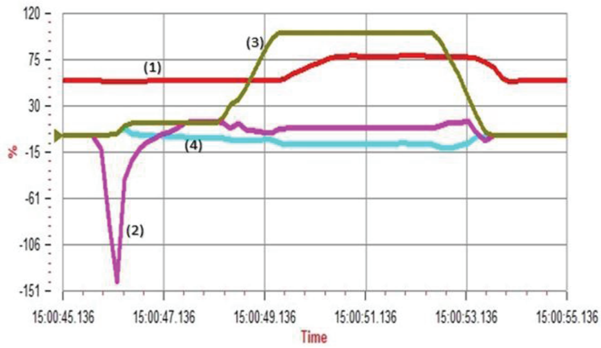

Fig. 6. The experimental result during the descent of the full load

Equations (9) and (10) were considered in calculating the maximum potential energy (Ep) of the full load m at the height of lift (h) and capacitance (C) of the storage unit.

$$E_p = mgh \tag{9}$$

$$C = \frac{2a(E_p)}{(V_{max}^2 - V_{min}^2)} \tag{10}$$

Where a is the design safety factor for this application.

The duration of an operational cycle t_d is 4.5s. The power P_c of the storage unit and the DC-DC converter is given by

$$P_c = {}^{E_p}/_{t_d} \tag{11}$$

$$\text{Maximum current } I_{max} = {}^{P_c}/_{V_{min}} \tag{12}$$

$$\text{Minimum current } I_{min} = {}^{P_c}/_{V_{max}} \tag{13}$$

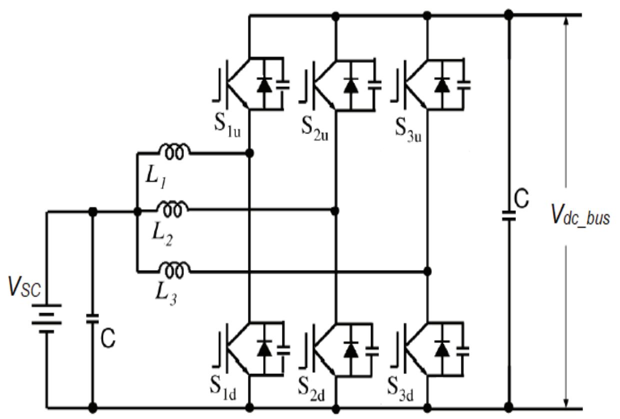

Fig. 7. High-power density DC-DC converter connected between DC bus and supercapacitor (SC)

In the crane application, the regeneration power is not continuous. This creates very high current ripples every time the current is directed to the DC-DC converter thus compromising the lifespan of the converter as well as the supercapacitor. To solve this problem, a three-phase converter is used. The current in the three-phase application is divided equally between a set of inductors resulting in reduced current stresses and consequently reducing the size and the rating of the components. The result is a high-power density DC-DC converter as shown in Fig 7.

When the drive is initially powered up, the standby voltage on the DC bus is supplied from the mains through the VFD rectifiers. The DC-DC converter control is set to prevent the charging of the supercapacitor at the standby voltage. Maximum safe operational voltage based on Equation (1) $V_{Cmax} \approx 730\ V_{DC}$ and the minimum voltage for the operation $V_{Cmin} \approx 510\ V_{DC}$ based on Equation (2). When the motor is braking, the power to the DC bus is negative thereby charging the DC bus capacitor until it reaches the value V_{max}. At V_{max}, the DC-DC converter maintains the DC voltage by controlling the current to the supercapacitor. This is the normal operational mode where the supercapacitor current is positive, and it is subsequently charged. At this stage, the braking energy is stored in the supercapacitor. While the DC bus voltage is maintained by the DC-DC converter, there is no current flow from the grid power supply. The VFD bus controller monitors the DC-DC converter to maintain a constant DC bus voltage. When the supercapacitor is discharged to a voltage below the standby level, the VFD rectifiers draw current from the supply to maintain the voltage and thereby charging the supercapacitor. When the DC bus voltage has dropped below the standby level, the supercapacitor continues to supply the DC bus even if the grid is interrupted. This is called the ride-through mode whereby the supercapacitor will operate the motor until the grid power is returned or until it reaches its V_{Cmin} setting [19-20].

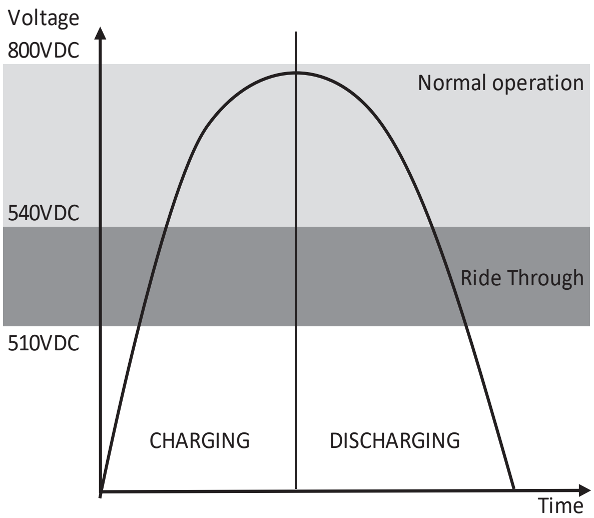

Fig. 8. Voltage-Time characteristics of a supercapacitor

V. Conclusions

DC-DC converters are applied as the effective interface between the power system and the energy storage units in renewable energy systems. Using MATLAB and PowerWorld simulator, it is possible to carry out precise DC-DC converter sizing, supercapacitor (ultracapacitor) sizing and energy flow calculations to validate the design analysis findings. The research confirms that it is possible to convert wasteful regenerative machinery into a conservative system that saves considerable energy without compromising performance and safety. The research has provided a cost-effective approach to finding a system conservation or an upgrade solution that would otherwise be complex. By studying regenerated voltages on the DC bus of a particular machine, a suitable conservative energy system can be implemented. With recent advancements in supercapacitor technology, the existing dynamic resistors on the machinery can now be replaced safely with suitable storage package units without affecting performance. The research provides a more positive energy-saving solution for the environment by significantly reducing the thermal impact that is generated in the dynamic braking resistors. The future of the research can be specialised in designing and modelling control systems of bidirectional converters, especially for advanced topologies with different modes of operations. The investigation is in progress.

Acknowledgement

The authors acknowledge the Durban University of Technology Smart Grid Research Centre for providing research facilities for this study.

References

[1] Bocker, Joachim, and Shashidhar Mathapati. "State of the art of induction motor control." *2007 IEEE International Electric Machines & Drives Conference*. Vol. 2. IEEE, 2007.

[2] Mitrovic, N., Kostic, V., Petronijevic, M. and Jeftenic, B., 2009. "Multi-motor drives for crane application," *Advances in Electrical and Computer Engineering*, *9*(3), pp.57-62.

[3] Inoue, Kaoru, Kenji Ogata, and Toshiji Kato. "A study on an optimal torque for power regeneration of an induction motor." *2007 IEEE Power Electronics Specialists Conference*. IEEE, 2007.

[4] J. Kammermann, I. Bolvashenkov, S. Schwimmbeck and H. -. Herzog, "Techniques for comparative analysis and its application to electric traction machines," *2016 19th International Conference on Electrical Machines and Systems (ICEMS),* Chiba, 2016, pp. 1-5.

[5] A. D. Chernyshev, T. A. Lisovskaya and R. A. Lisovskiy, "Comparative analysis of different electrical motor types as a traction drive part in electrical transmission," *2017 International Conference on Industrial Engineering, Applications and Manufacturing (ICIEAM),* St. Petersburg, 2017, pp. 1-5.

[6] D. Yellamati, E. Arthur, S. James, G. Morris, T. Heydt and E. Graf, "Predictive Reliability Models for variable frequency drives based on application profiles," *2013 Proceedings Annual Reliability and Maintainability Symposium (RAMS)*, Orlando, FL, 2013, pp. 1-6.

[7] Beldjajev, V., T. Lehtla, and H. Molder. "Influence of regenerative braking to power characteristics of a gantry crane." *Proceedings of the 2010 Electric Power Quality and Supply Reliability Conference*. IEEE, 2010.

[8] Saha, S., Kosaka, T., Matsui, N. and Sundarsingh, V.P., 1998, December. "Regenerative braking in a low power lift drive system." In *1998 International Conference on Power Electronic Drives and Energy Systems for Industrial Growth, 1998. Proceedings.* IEEE.

[9] Agrawal, S.K., Kumar, V., Alam, A. and Thakura, P., 2014, December. "Regenerative braking for induction motor drive." In *2014 6th IEEE Power India International Conference (PIICON)* (pp. 1-6).

[10] M. Irfan, N. Saad, R. Ibrahim and V. S. Asirvadam, "An intelligent diagnostic system for the condition monitoring of AC motors," *2013 IEEE 8th Conference on Industrial Electronics and Applications (ICIEA)*, Melbourne, VIC, 2013, pp. 1248-1253.

[11] Sivakumar, S., M. Jagabar Sathik, P. S. Manoj, and G. Sundararajan. "An assessment on performance of DC–DC converters for renewable energy applications." *Renewable and Sustainable Energy Reviews* 58 (2016): 1475-1485.

[12] Padhee, Subhransu, Umesh Chandra Pati, and Kamalakanta Mahapatra. "Overview of high-step-up DC–DC converters for renewable energy sources." *IETE Technical Review* 35, no. 1 (2018): 99-115.

[13] Adak, M.F.; Duru, N.; Duru, H.T. "Elevator simulator design and estimating energy consumption of an elevator system". *Energy Build*. 2013, 65, 272–280.

[14] Bako, Z.N.; Tankari, M.A.; Lefebvre, G.; Maiga, A.S. "Experiment-based methodology of kinetic battery modeling for energy storage,". *IEEE Trans. Ind*. Appl. 2019, 55, 593–599

[15] Abbey, Chad, and Gza Joos. "Supercapacitor energy storage for wind energy applications." *IEEE transactions on Industry applications* 43, no. 3 (2007): 769-776.

[16] D. K. Chaturvedi, M. S. Iqbal and M. P. Singh, "Condition monitoring of induction motor," *2015 International Conference on Recent Developments in Control, Automation and Power Engineering (RDCAPE)*, Noida, 2015, pp. 135-140.

[17] Fossati, J.P., Galarza, A., Martín-Villate, A. and Fontan, L., 2015. A method for optimal sizing energy storage systems for microgrids. *Renewable Energy*, *77*, pp.539-549.

[18] P. Zhang, Y. Du, T. G. Habetler and B. Lu, "A survey of condition monitoring and protection methods for medium voltage induction motors," *2009 IEEE Energy Conversion Congress and Exposition*, San Jose, CA, 2009, pp. 3165-3174.

[19] Yang, Y.; Bremner, S.; Menictas, C.; Kay, M. "Battery energy storage system size determination in renewable energy systems," *A review. Renew. Sustain. Energy Rev.* 2018, 91, 109–125.

[20] Duran-Gomez, Jose Luis, Prasad N. Enjeti, and Annette von Jouanne. "An approach to achieve ride-through of an adjustable-speed drive with flyback converter modules powered by super capacitors." *IEEE Transactions on Industry Applications* 38.2 (2002): 514-522.

Analysis of Large-scale Non-Overlap Winding Wound Rotor Synchronous Machine with Stator Slitting

U Coetzee
Electrical and Electronic Engineering
Stellenbosch University
Stellenbosch, South Africa
22615180@sun.ac.za

K. S. Garner
Electrical and Electronic Engineering
Stellenbosch University
Stellenbosch, South Africa
garnerks@sun.ac.za

***Abstract*— Non-overlap windings have a downfall in that they result in a high quantity of magnetomotive force, sub- and higher-order harmonics, leading to core saturation, increased losses and vibration. Wound rotor machines with non-overlap windings and especially large yokes, result in massive core losses due to the high amount of flux generated in the machine. Stator slitting is proposed as a simple method to mitigate the core losses in the machine, while maintaining the desired electrical performance of the machine. It is shown that stator slitting increases the working harmonic and reduces the other sub-harmonics, evidenced by the increased average output torque and reduced torque ripple and core losses. The study is completed on a 5 MW 16/18 pole/slot wound rotor synchronous machine using finite-element analysis.**

Keywords—generator, harmonics, losses, stator slitting, wind.

I. INTRODUCTION

The advancement of renewable energy technologies for power generation continues to be a focus are while electricity shortages threaten global economies. The developments in wind energy remain one of the fastest growing technologies. Synchronous generators (SGs) are used widely in wind turbines to achieve full variable speed control with the generator connected to the electric grid through a full-scale power converter via a step-up transformer as depicted in Fig. 1.

Machines operating at low speeds (LS) of below 100 r/min are effective at converting subsequent low-speed winds into electrical power. Additionally, machines operating at these lower speeds are cheaper to make, weigh less, and require less maintenance as they do not go through intensive mechanical stress [1]. Unfortunately high-speed winds, which are present at top priority areas for wind turbine placement due to their high amounts of power potential, are not effectively converted into electricity by these LS generators [2]. Increasing the speed of an electrical machine is one of the most effective ways to increase its efficiency, yet this seemingly simple solution comes with numerous engineering challenges. A machine operating at high speeds (HS), classified as above 500 r/min, experiences not only increased centrifugal stresses on the rotor, which increase the possibility of mechanical failure, but electrical phenomena such as high-frequency losses. The high power density of such machines results in increased heating, making effective cooling of critical importance [1]-[2]. Medium speed (MS) machines in the 100-500 r/min range provide a good balance between the benefits and drawbacks of both LS and HS operation. A MS machine has a relatively simple gearbox design which results in lower costs as well as less maintenance, and does not suffer to the same extent as HS machines from mechanical stress.

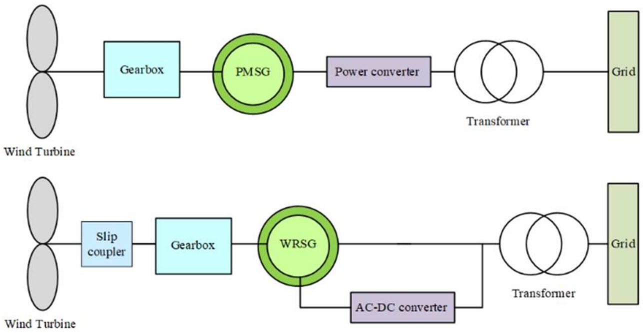

Fig. 1. Wind turbine connection configurations for synchronous generators.

MS machines also operate at relatively effective efficiencies at wind speeds typical to wind farm sites [1]. The wind energy industry is thus becoming more interested in adopting wind generators connected to single or two-staged gearboxes and operating at medium-speed. SGs can be manufactured with high pole numbers, which create a balance between efficiency, cost, reliability, and generator size. Although permanent magnet SGs (PMSGs) are popular, the need for environmentally friendly, rare-earth-free technologies is growing. The wound rotor SG (WRSG) is still the best option to comply accurately with the grid codes for direct grid connection. To minimize costs, applying non-overlapping stator windings in these generators is very attractive [3].

Overlapping stator windings in a single- or double-layer arrangement are generally used in generators. The magnetomotive force (MMF) distribution of such windings is closely sinusoidal for high values of the slots per pole per phase, q, resulting in low MMF harmonic content [4][4]. High q values also equate to high numbers of coils required, increasing the copper needed and the necessary manufacturing time and cost. In contrast, non-overlap windings are more affordable and easier to manufacture, with shorter end windings and a higher torque-to-weight ratio of the machine. The lower slot number of a non-overlap winding means that a low number of coils is required and thus a reduction of manufacturing costs of the winding. Unfortunately, non-overlap windings generate a high number of MMF sub- and higher-order harmonics due to the low q value [5]-[7]. This generally translates to increased core losses and torque ripple. The increased core losses are especially true for large-scale machine with large rotor yokes like the WRSG. For wind generators, low torque ripples are required to minimize vibration in the drive train. Various ways to reduce MMF harmonic content exist, but in many cases these methods are complex, reduce the torque density of the machine and are unable to reduce the core losses effectively [8]-[10]. This study explores the concept of stator slitting to reduce MMF harmonic content and subsequently the core losses of a 5 MW 16/18 pole/slot WRSG. The conceptual machine is displayed in Fig. 2. It has been shown in [11] that the application of flux barriers in a stator yoke can decrease MMF sub-harmonics while increasing the main harmonic. The study in [12] places flux barriers in the middle of stator teeth without windings to create a modular stator structure. The study concludes that the sub-harmonics are reduced, and the working harmonic of a 14/12 pole/slot machine is strengthened. Stator slits are placed in wound or unwound teeth of a small 10/12 pole/slot machine in [13] and similar results are recorded.

In this paper, stator slits are placed in a large 16/18 pole/slot machine. The 16-pole machine is an attractive medium-speed option to further reduce the required gearbox ratio in comparison with the popular 10- and 12-pole machine. The MMF harmonic analysis is investigated, and the placement, shape and size of the stator slits is determined. The machine performance is analyzed using finite-element analysis (FEA) in ANSYS Maxwell using transient analysis. The results are verified with SEMFEM, an in-house FEA tool.

II. Methodology and Conceptual Design

The concept of stator slitting requires that barriers of air are placed in the stator teeth and through the stator yoke. The stator is subsequently segregated into several modular parts. The aim of the slits is to limit the magnetic flux of sub-harmonics in the stator core. This means that the required pitch of the slits must be longer than the machine's pole pitch. The placement of the slits is thus dependent on the stator arrangement in terms of number of slots and winding layers. Limiting the magnetic flux of sub-harmonics has the possible effect of reducing the core losses of the machine. It is well-known that core losses are dependent on the material type, the quantity of magnetic flux travelling through the section of material and the frequency of the varying flux. In core loss analysis the machine is segregated into n sections according to the flux density. The core loss for a particular section at a certain frequency can be described by [14]

$$P_{Fe,n} = P_{15}\left(\frac{B_n}{1.5}\right)^2 m_{Fe,n}\,, \qquad (1)$$

where P_{15} is the manufacturer-specified loss rating of the material for a peak flux density of 1.5 T, B_n is the peak flux density of the area and $m_{Fe,n}$ is the mass of the particular section. It stands to reason that if the magnitude of the peak flux variation can be lowered, the core loss of a section can be reduced.

The 5 MW 16/18 pole/slot WRSG has a double layer winding, and the working harmonic is the fourth harmonic. The specifications and key parameters of a conceptual 5 MW model used in this investigation are given in Table I. The results are obtained from ANSYS Maxwell. The FEA-simulated output torque of the machine at rated q-axis current is depicted in Fig. 3. The stator slits are inserted down the center of wound stator teeth to maintain a symmetrical design and to not induce additional space harmonics [13]. Furthermore, in [13] the method describes the insertion of the stator slits into wound teeth specifically, which results in alternating teeth being slit for a single-layer stator winding configurations, and every tooth being slit for double-layer stator winding configurations, as is the case in this study. It is thus deemed as sufficient to place the slits in each stator tooth, making the slit pitch equal to the stator slot pitch and therefor larger than the pole pitch. The stator is therefore segregated into 18 sections as shown in Fig. 4 and a close-up of the modelled stator slits in displayed in Fig. 5.

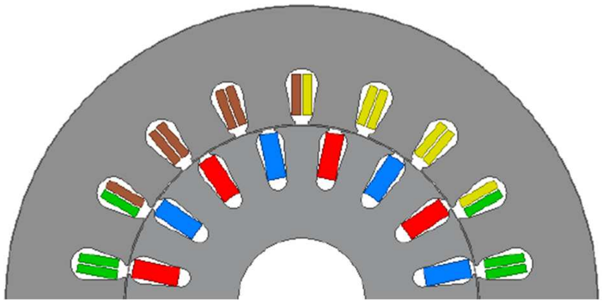

Fig. 2. Half cross-section and winding layout of the 5 MW non-overlap 16/18 pole/slot WRSG.

TABLE I: SPECIFICATIONS OF THE 5 MW GENERATOR.

Specifications	Numerical value
Rated power (MW)	5
Rated torque (kNm)	127
Rated speed (r/min)	375
Rated frequency (Hz)	50
Number of poles	16
Number of stator slots	18
Stator outer diameter (mm)	2134
Rotor outer diameter (mm)	1270
Rotor inner diameter (mm)	460
Stack length (mm)	1500
Air gap thickness (mm)	5.25
Phase current [A]	4000
Field current [A]	200

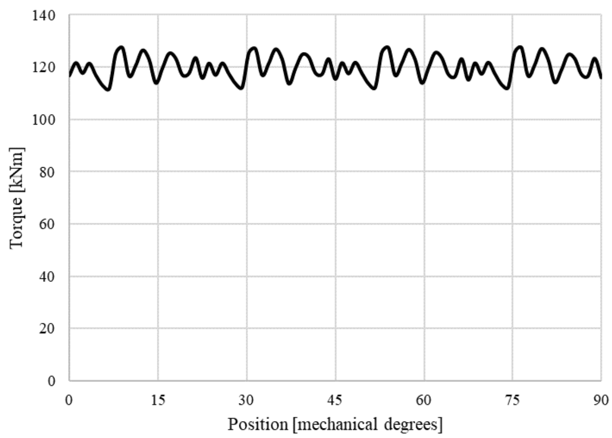

Fig. 3. Calculated torque and torque ripple of the 5 MW 16/18 WRSG with rated q-axis current.

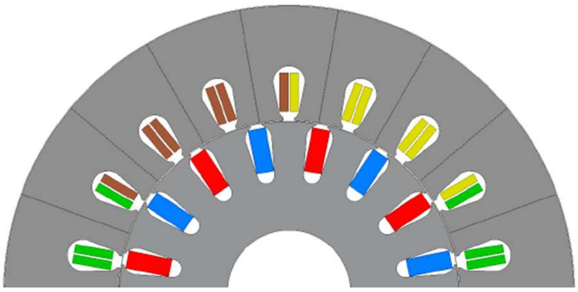

Fig. 4. Slitted stator of the 5MW 16/18 pole/slot WRSG model.

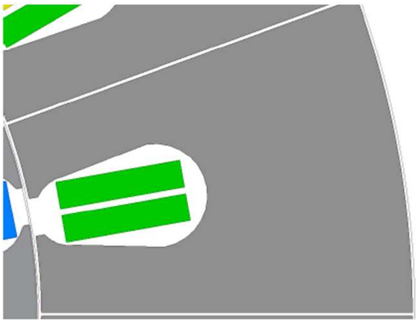

Fig. 5. Close-up of arbitrarily modelled stator slits.

III. Stator Slit Design

The width of the inserted stator slits must be determined to reduce the core losses without reducing the average torque of the machine or increasing the torque ripple. If the slit is too thin, the effect on the flux path of the sub-harmonics will be minimal. However, if the slit is too wide, the flux path of the working harmonic can also be interrupted. The width of the slit is swept from 0.5-8 mm in steps of 0.1 mm and the torque, torque ripple and core losses are recorded for each iteration. The process flow of the investigation is shown in Fig. 6.

The FEA performance results for key widths of the stator slits are listed in Table II. The efficiencies displayed exclude the mechanical losses. The average output torque tends to decrease as the slit width increases due to the disturbance of the main flux path as the width becomes too large. However, even the largest width has a higher average output torque compared to the conventional model. This indicates the improvement of the working harmonic because it is the torque-producing harmonic.

Fig. 7 displays the torque ripple versus the slit width. The reduction of some sub-harmonic MMF content is evidenced by the decreasing torque ripple as the slit width increases. The trend of the rotor core loss for various slit widths is depicted in Fig. 8, while the stator core loss trend is displayed in Fig. 9. There is a large initial reduction in the rotor core losses but then reaches a steady state. Although the slit inhibits some sub-harmonic magnetic flux, it cannot reduce the amount of flux penetrating the rotor core due to its location in the stator. On the other hand, the stator core losses start to increase as the slit width increase, although the value is still lower than the initial stator core losses. The increasing core losses can be attributed to an increased variation of the flux density around the slit as the width increases, relating to (1).

The output torque curves for the conventional model and the model with the 0.5 mm slits are displayed in Fig. 9. In general, the model with the 0.5 mm slit provides the better overall machine performance in comparison with the conventional model and the larger slits.

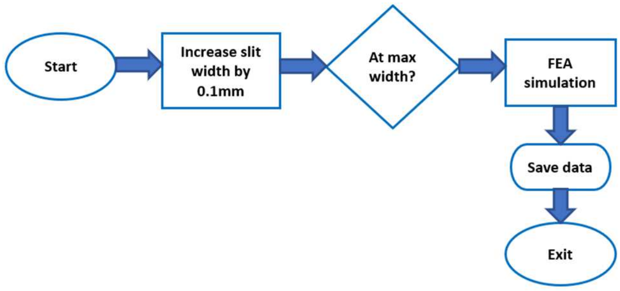

Fig. 6. Process flow of the design variation of the stator slit width.

TABLE II: FEA PERFORMANCE RESULTS OF KEY STATOR SLIT WIDTHS.

Performance parameter	No slit	0.5 mm	1 mm	4 mm	8 mm
Rated power [MW]	4.67	4.83	4.8	4.77	4.74
Average torque [kNm]	119	123	122.3	121.4	120.8
Torque ripple [%]	13.4	8.5	7.3	6.7	5.6
Rotor core loss [kW]	15	10.7	10.65	10.5	10.6
Stator core loss [kW]	39	34	35.2	36.4	37.1
Copper loss [kW]	71.3	71.3	71.3	71.3	71.3
Efficiency [%]	97.3	98.2	98.15	98.12	98.09

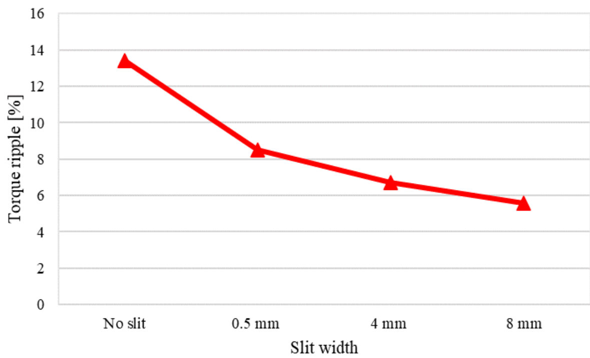

Fig. 7. Torque ripple versus slit width.

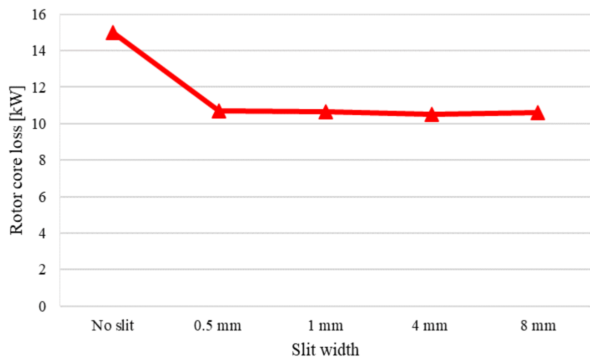

Fig. 8. Rotor core loss versus slit width.

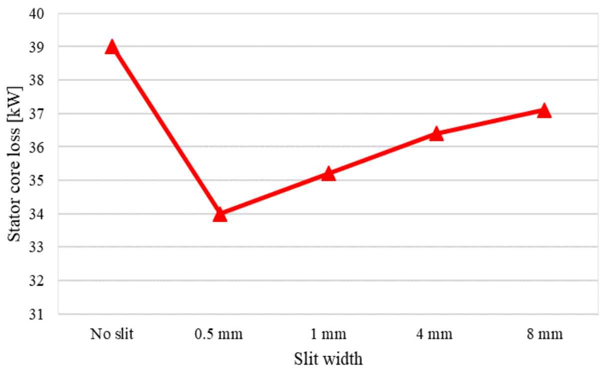

Fig. 9. Stator core loss versus slit width.

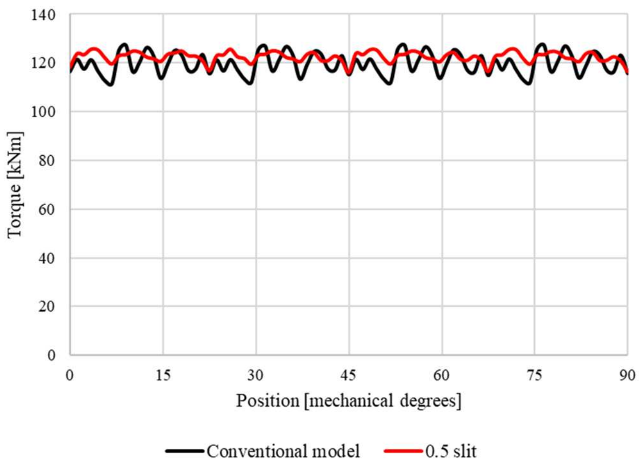

Fig. 10. Calculated torque and torque ripple of the 5 MW 16/18 WRSG conventional model and the model with the 0.5 mm slits with rated q-axis current.

IV. Flux Distribution Analysis

Fig. 11 shows the flux density at rated q-axis current of the conventional model while Fig. 12 shows the flux density of the model with the 0.5 mm slits. The change in flux density is obvious around the location of the slits and between the rotor poles. Figs. 13 and 14 depict the flux lines of the conventional and slitted model respectively. It is seen that the slits modify the path of the flux lines and helps concentrate the flux around the stator slots.

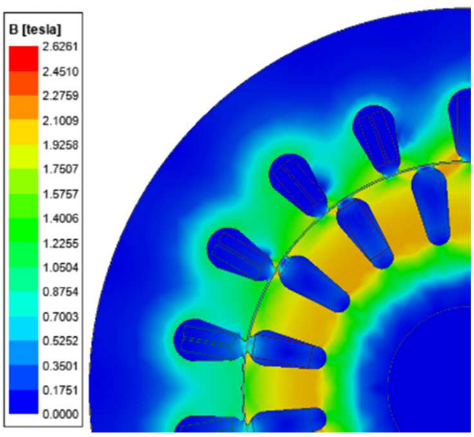

Fig. 11. Simulated FEA flux density of the 5 MW 16/18 WRSG conventional model with rated q-axis current.

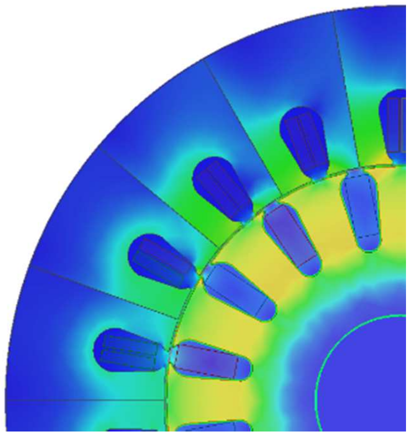

Fig. 12. Simulated FEA flux density of the 5 MW 16/18 WRSG model with the 0.5 mm slits with rated q-axis current.

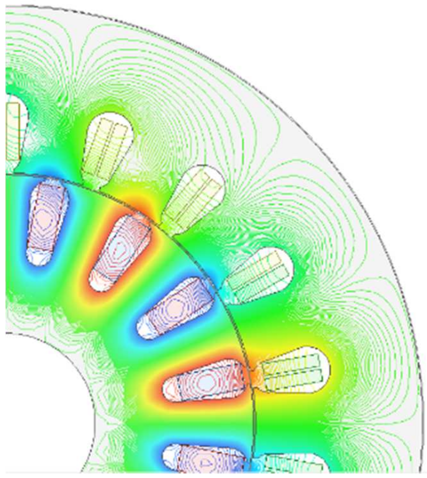

Fig. 13. Simulated FEA flux lines of the 5 MW 16/18 WRSG conventional model with rated q-axis current.

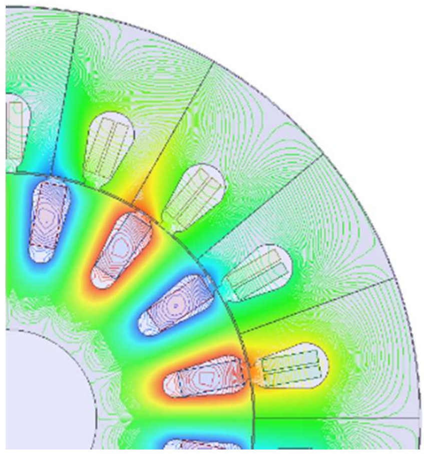

Fig. 14. Simulated FEA flux lines of the 5 MW 16/18 WRSG model with the 0.5 mm slits with rated q-axis current.

V. Conclusion

In this paper, the effect of placing slits in the stator on specifically the core losses, but also on the torque ripple and average torque of the machine, is investigated in a large non-overlap winding WRSG. The investigation shows that placing these slits in the wound stator teeth of a machine with a double-layer stator winding can largely reduce the rotor core losses and torque ripple while improving the average output torque. This is true for an optimum width of the slit where the flux path of the MMF sub-harmonics is modified. An analysis of the flux density and flux lines shows the change in the flux around the area of the slits and between the rotor poles which supports this finding. The original method in [11] of applying stator slitting to a machine with a single-layer stator coil configuration resulted in alternating stator teeth being slit. The adaptation of this method for machines with double-layer stator coil configurations whereby each stator tooth is slit proved to not provide the same level of increased efficiency as initially expected, though the method still improved the machine performance in comparison with the conventional model.

REFERENCES

[1] H. Gitano-Briggs, “Low speed wind turbine design,” in Advances in WindPower, R. Carriveau, Ed. Rijeka: IntechOpen, 2012, ch. 11. [Online]. Available: https://doi.org/10.5772/53141.

[2] U. B. Akuru and M. J. Kamper, “Contemporary wind generators,” Journal of Energy South Africa, vol. 26, no. 3, Aug 2015.

[3] G. Dajaku, S. Spas, X. Dajaku, D. Gerling, “An Improved Fractional Slot Concentrated Winding for Low-Poles Induction Machines”, 19th International Conference for Electrical Machines, September 2016, pp. 116-121, Germany.

[4] J. Jürgens, A. Brune and B. Ponick, “Electromagnetic design and analysis of a salient-pole synchronous machine with tooth-coil windings for use as a wheel hub motor in an electric vehicle”, 2014 International Conference on Electrical Machines (ICEM), pp. 744-750, 2-5 Sept. 2014.

[5] N. Bianchi, S. Bolognani, M. D. Pre and G. Grezzani, “Design considerations for fractional-slot winding configurations of synchronous machines”, in IEEE Trans. on Industry Applications, vol. 42, no. 4, pp. 997-1006, 2006.

[6] M. Nakano and H. Kometani, “A study on eddy-current losses in rotors of surface permanent magnet synchronous machines”. IEEE Transactions on Industry Application, vol. 42, No. 2, March/April 2006.

[7] Z. Q. Zhu, Z. P. Xia, L. J. Wu and G. W. Jewell, “Analytical modelling and finite element computation of radial vibration force in fractional slot permanent magnet brushless machines”. IEEE International Electric Machines and Drives Conference, IEMDC2009, Florida USA, May 3-6, 2009, pp.157-164.

[8] M. V. Cistelecan, F. J. T. E. Ferreira, M. Popescu, “Three phase tooth-concentrated multiple-layer fractional windings with low space harmonic content,” 2010 IEEE Energy Conversion Congress and Exposition (ECCE), pp. 1399–1405, Atlanta, GA 2010.

[9] H.-J. Kim, D.-J. Kim, J.-P. Hong, “Characteristic analysis for concentrated multiple-layer winding machine with optimum turn ratio,” IEEE Trans. Magn., Vol. 50, No. 2, pp. 789–792, February 2014.

[10] G. Dajaku, D. Gerling, “A novel 24-slots/10-poles winding topology for electric machines,” 2011 IEEE International Electric Machines Drives Conference (IEMDC), pp. 65–70, Niagara Falls, ON, 15–18 May 2011.

[11] G. Dajaku, W. Xie, and D. Gerling, “Reduction of low space harmonics for the fractional slot concentrated windings using a novel stator design”, IEEE Trans. Magn., vol. 50, no. 5, 8201012, May 2014.

[12] G. J. Li, et al., “Comparative studies of modular and unequal tooth PM machines either with or without tooth tips,” IEEE Trans. Magn., vol. 50, no. 7, 8101610, July 2014.

[13] Y. Yokoi and T. Higuchi, "Stator Slitting of 12-Slot 10-Pole Concentrated Winding Motors," in IEEE Transactions on Industry Applications, vol. 54, no. 5, pp. 4377-4385, Sept.-Oct. 2018, doi: 10.1109/TIA.2018.2846591.

[14] J. Pyrhönen, T. Jokinen and V. Hrabovcová, *Design of Rotating Electric Machines*, Second edition, Wiley (United Kingdom), p. 201, 2014.

Comparison Between A Three Level Inverter Synchronous Reluctance Machine and A Permanent Magnet Assisted Synchronous Reluctance Machine Drives

Lesedi Masisi, *Senior Member, IEEE*
School of Electrical and Information Engineering
University of the Witwatersrand
Johannesburg, South Africa, 2000

***Abstract*—This paper is concerned with the use of a three level neutral point clamped (3L-NPC) inverter for a permanent magnet assisted synchronous reluctance machine (PMaSynRM). A comparison is conducted between a 3L-NPC inverter SynRM and PMaSynRM drives. The SynRM suffers from a poor power factor. Poor power factor translates to the need for a bigger inverter, moreover increases the challenge of balacing the two dc link capacitors of the three level 3L-NPC inverter. Using permanent magnets to assist the SynRM improves the power factor of the electric machine. This results in reduced burden of the 3L-NPC inverter dc link capacitors balancing algorithm. The inverter size can also be reduced to suit the size of the electrical machine. The three level inverter SynRM drive produced lower torque ripple of 0.7% as compared to the PMaSynRM drive. However the three level inverter PMaSynRM drive had a higher Root Mean Square (RMS) voltage for the same dc link voltage as compared to that of the SynRM drive. This would result in higher machine speed achieved as compared to the SynRM drive and ultimately higher constant power speed range which is desirable for traction applications. The neutral point voltage ripple between two drives was relatively the same with only a difference of 0.3%.**

***Index Terms*—Three level inverter, neutral point (NP) voltage ripple, neutral-point-clamped (NPC), synchronous reluctance machine (SynRM), saliency, permanent magnet-assisted synchronous reluctance machine (PMaSynRM).**

I. Introduction

The SynRM has shown great interest for traction and industrial applications. The rotor of the machine is easier to manufacture and unlike the induction machine it has less cooling demand. The machine does not make use of permanent magnets which tend to have fluctuating prices. The machine operates on the principle of reluctance and as such does not have any rotor bars or copper inside the rotor. Though electric and hybrid vehicles are reliant on the permanent magnet machines there is a growing design work for SynRM for traction applications [1], [2]. However, the machine suffers from high demand of reactive power. This results in a bigger inverter because of high reactive power demand. The parameter used to indicate power factor perfromance is the saliency. Saliency is the ratio between the d-axis and q-axis inductance, the higher the d-axis inductance as compared to q-axis inductance the higher the saliency. The higher the saliency the higher the power factor [3].

Improving the SynRM power factor and performance by addition PMs has been a growing research area [4]–[7]. [7] conducted a modification of the PMaSynRM motor design for improved torque performance. The use of PMaSynRM for traction application has also grain interest [4]. In [4] a sensitivity analysis and design of a high performance machine for traction applications is conducted. The work showed that change in air gap length had little effect on the d-axis inductance. However, the q-axis inductance decreases rapidly as the air gap length increased. In [8] a PMaSyRM that uses ferrite magnet that does not use rare earth materials is proposed. It was shown that the proposed machine had competitive power density and efficiency as the conventional rare-earth permanent magnet based machines for traction applications. [9] conducted a design and analysis of a novel PM assisted SynRM using non rare earth magnets (AlNiCo). There was a gained power density, reduced torque ripple and manufacturing costs. A PMaSynRM using variable flux PMs was designed in [10], the PMs are non-rare earth based. Because the magnets could be demagnetized on the fly, the machine could be operated as a pure SynRM. It was not clear how a variable flux based PMaSynRM would have benefits for both industrial and traction applications.

There is a high demand for more dc bus voltage in traction applications and the three level inverter has gained much interest over the traditional two level inverter. The three level inverter provides better power quality for the electric machines as compared to the two level inverter. Unlike the two level inverter the switches of a three level inverter switch across half the dc bus voltage and this results in a lower dv/dt. A further benefit of this is that lower voltage rated switches can be used. The drawback is that four switches are used in a leg as compared to two switches as is the case for the two level inverter. The three level inverter makes use of two dc bus capacitors. These two capacitors should be balanced at all times in order for the superior benefits of the three level inverter to be enjoyed [11]. In [3] it was shown that the poor power factor of the SynRM causes the three level inverter to lose its natural dc bus capacitor balancing effect. A sizing method for the two dc link capacitor was developed that incorporated the parameters of the SynRM.

[12] used a three level inverter for an induction machine drive operating under direct torque and flux control. Both torque and current ripple could be reduced with an improved speed transients. In [13] a 3L-NPC inverter drive for traction applications is compared to a two level inverter drive. Power quality of the motor was improved which translated into reduced losses. [14] focused on torque ripple minimization using a 3L-NPC inverter operated at low switching frequency. The work proposed an optimal pulse width modulated (PWM) which minimized the combined root mean square value of the torque harmonics. A 3L-NPC inverter was used to drive a dual three phase permanent magnet synchronous motor (PMSM) at low switching frequencies [15]. To the knowledge of the authors there is no existing work on the use of a 3L-NPC inverter for a PMaSynRM drive application. This paper will explore the performance of a 3L-NPC inverter PMaSynRM drive. An existing dc bus capacitor balancing algorithm will be used [3].

The paper is arranged as follows, section II, the operation of the 3L-NPC inverter and the balancing algorithm used. Section III the machine model and control. Section IV describes the simulation work and summary of the results. Section V concludes the paper and the appendix shows the parameters of the machine.

II. Three Level Inverter

The diagram of the three level inverter is shown in Fig. 1. The inverter is comprised of 12 power switches, which is an additional of six switches when compared to the traditional two level inverter. Space vector modulation scheme will be adopted for the control of the switches. The space vectors for the inverter switching are depicted in Fig. 2. There is a maximum of 27 voltage vectors. Active vectors are 19 whereas 8 vectors are redundant. ZV, SV, MV, and LV are the

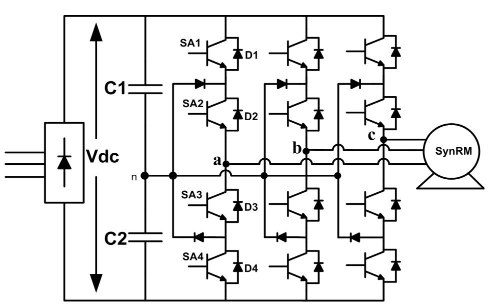

Fig. 1. 3L-NPC inverter

zero, small, medium and large vectors respectively. Table I shows the switching states of Fig. 2. When measuring the pole voltages there are three different switching states, a positive (P), negative (N) and zero (0) voltage state, described as 1,0, and -1 respectively.

A. Three Level Inverter Modulation Scheme

This paper makes use of a switching scheme that was developed by [3]. The scheme forms part of the nearest

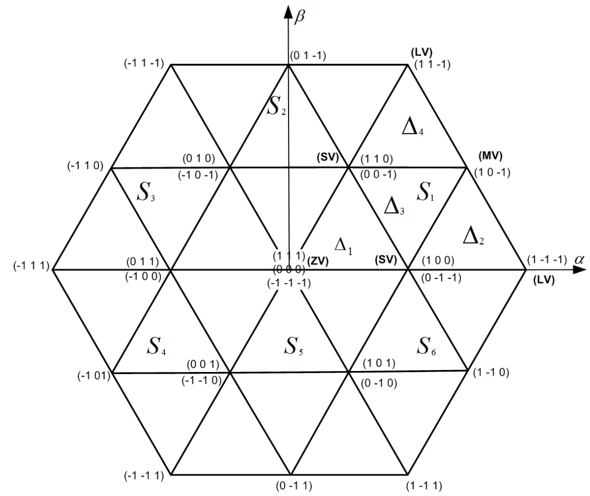

Fig. 2. Space vector modulation scheme of the 3L-NPC inverter

TABLE I
Pole voltage states of phase A

States	S_{A1}	S_{A2}	S_{A3}	S_{A4}	V_{ao}
P (Positive)	1	1	0	0	$\frac{1}{2}V_{dc}$
O (Zero)	0	1	1	0	0
N (Negative)	0	0	1	1	$-\frac{1}{2}V_{dc}$

three vector (NTV) modulation scheme family. Based on the hexagon shown in Fig. 2, the closest three vector in the triangle is chosen as the reference voltage vector moves around the Hexagon. These vectors (11-1,1-1-1,-111,-11-1, 1-11 and -1-11) and (000, 111 and -1-1-1) referred to as large vectors and the zero vectors respectively have no impact on the neutral point voltage imbalance. This is because when they are active the neutral point current is zero. Whereas in order to manage the neutral point voltage imbalance the small vectors need to be utilized. These vectors need to be managed well in order to arrest the neutral point voltage ripple even to zero. As the modulation index increases as a result of increased demand for the rms voltage, the medium vectors will become activated.

The medium vectors are 10-1, 01-1, -110, -101, 0-11 and 1-10, as shown in Fig. 2. They are less effective in managing the imbalance between the two dc link capacitors. For example in the regions of triangle 2 (Δ_2) and 4 (Δ_4), a single small vector is usable. This means that there will be a great challenge to improve voltage imbalance of the two dc link capacitors. Whereas in the region with at least two small vectors balancing of the two dc link capacitor voltage is highly improved.

The primary challenge of this inverter is voltage balancing of the the dc link capacitors referred to as the neutral point voltage ripple. This neutral point voltage ripple is a measure of the voltage imbalance across the two dc bus capacitors. The two dc link capacitors are used for creating a neutral point voltage. This is where the zero pole voltage state is obtained in order for the benefits of this inverter to be enjoyed. The development of capacitor voltage balancing algorithms has generated significant interest. [16]–[18]. Therefore, the NTV utilized in this paper selects three vectors with the objective of mitigating the ripple of the neutral point voltage. Only sector

I of the balancing algorithm used is presented in Table II, whereas Table III displays the corresponding computation of the dwell times of the vector states.

TABLE II
PHASE A SWITCHING SCHEME

NP Voltage	Triangle	Sequences	Steps
$V_{c1} > V_{c2}$	1	000,100,110 // 110-100-000	2
$V_{c1} < V_{c2}$	1	-1-1-1,0-1-1,00-1 // 00-1,0-1-1,-1-1-1	2
$V_{c1} > V_{c2}$	2	100,1-1-1,10-1 // 10-1,1-1-1,100	3
$V_{c1} < V_{c2}$	2	0-1-1,1-1-1,10-1 // 10-1,1-1-1,0-1-1	2
$V_{c1} > V_{c2}$	3	110,100,10-1 // 10-1,100,110	2
$V_{c1} < V_{c2}$	3	00-1,0-1-1,10-1 // 10-1,0-1-1,00-1	3
$V_{c1} > V_{c2}$	4	110,10-1,11-1 // 00-1,10-1,110	3
$V_{c1} < V_{c2}$	4	00-1,10-1,11-1 // 11-1,10-1,00-1	3

TABLE III
PHASE A SWITCHING VECTORS AND SWITCHING PERIOD FORMULATIONS

Triangles	Vectors	Dwell times
1	000,-1-1-1,111	$t_0 = T\left[1 - 2ksin(\gamma + \pi/3)\right]$
	100,0-1-1	$t_1 = 2kTsin(\pi/3 - \gamma)$
	110,00-1	$t_2 = 2kTsin(\gamma)$
2	100,0-1-1	$t_1 = 2T\left[1 - ksin(\gamma + \pi/3)\right]$
	10-1	$t_3 = 2kTsin(\gamma)$
	1-1-1,	$t_4 = T\left[2ksin(\pi/3 - \gamma) - 1\right]$
3	100,0-1-1	$t_1 = T\left[1 - 2ksin(\gamma)\right]$
	110,00-1	$t_2 = T\left[1 - 2ksin(\pi/3 - \gamma)\right]$
	10-1	$t_3 = T\left[2ksin(\pi/3 + \gamma) - 1\right]$
4	110,00-1	$t_2 = 2T\left[1 - ksin(\gamma + \pi/3)\right]$
	10-1	$t_3 = 2kTsin(\pi/3 - \gamma)$
	11-1	$t_4 = T\left[2ksin(\gamma) - 1\right]$

The graphical representation of Table II is illustrated in Figs.3 and4. Selecting vector ”100” would cause a negative NP current that discharges the upper capacitor (C_1), while vector ”0-1-1” produces a positive NP current that discharges the lower capacitor (C_2). It is worth noting that although both switching states 100 and 0-1-1 produce the same voltage, the direction of the neutral point current is different. Equations

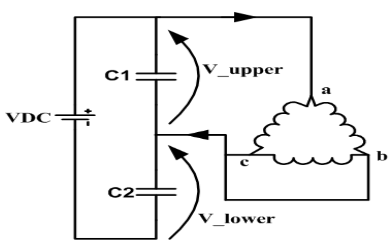

Fig. 3. The small vector (100) is employed to discharge the upper capacitor.

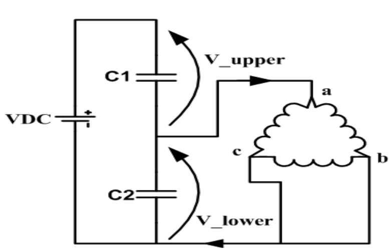

Fig. 4. To discharge the lower capacitor, the small vector (0-1-1) is employed

(1) and (2) demonstrate how the reference vector is computed.

$$V_{ref} = d_s V_s + d_M V_M + d_L V_L \quad (1)$$

$$d_s + d_M + d_L = 1 \quad (2)$$

The duty cycles of the small, medium, and large switching state vectors are denoted as d_s, d_M, and d_L respectively. In [19], it is demonstrated that two types of voltage imbalance occur during converter operation. The first is in the form of a voltage deviation, which usually happens during transients. The second is a low-frequency voltage oscillation during steady-state operation of the converter. The percentage of the voltage NP ripple can be computed from Eq. (3). It will be used as one of the parameters for the comparison between the 3L-NPC inverter SynRM and PMaSynRM drives.

$$v_{NP\%} = \frac{(V_{C1} - V_{C2})}{(V_{C1} + V_{C2})} * 100 \quad (3)$$

III. MACHINE MODEL AND CONTROL

Fig. 5 shows the rotor design of the unoptimized SynRM. The the SynRM and the PMaSynRM can have the same stator. The major difference is on their rotor designs. The PMaSynRM has permanent magnets in the flux briers, whereas the SynRM has only air in the flux barriers as shown in Fig. 5. A vector control policy was implemented in order

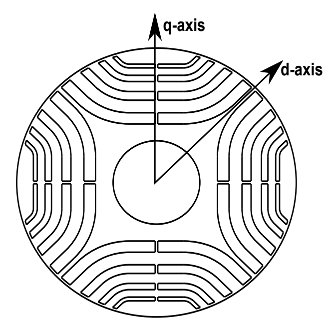

Fig. 5. Unoptimized SynRM rotor design

to control the speed of the machine and achieve maximum torque with the least current. The use of vector control on the machine is a well known application [20], [21]. The three-level NPC inverter drive for a SynRM is illustrated in Fig. 6, which employs constant angle control to maintain specific d-q-axis currents at an appropriate load. The machine model can

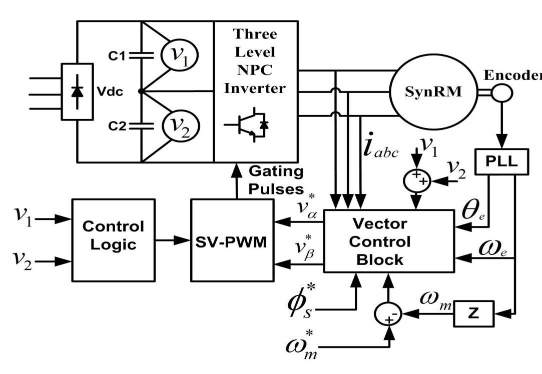

Fig. 6. Electric drive using SynRM with a three-level NPC inverter

be described from Eq. (4)-(14). Eq. (6) is the phase voltage the inverter needs to supply in order to achieve the required machine performance. That needs to be the same as the voltage described in Eq. 1.

$$v_q = Ri_q + \frac{d\lambda_q}{dt} + \omega_e \lambda_d \tag{4}$$

$$v_d = Ri_d + \frac{d\lambda_d}{dt} - \omega_e \lambda_q \tag{5}$$

$$v_{ref} = \sqrt{v^2{}_d + v^2{}_q} R \tag{6}$$

$$\lambda_d = L_d i_d \tag{7}$$

$$\lambda_q = L_q i_q \tag{8}$$

$$I_s = \sqrt{i^2{}_q + i^2{}_d} \tag{9}$$

Eq. (10 to (13) are different representations of the torque generated within the reluctance machine.

$$T_e = \frac{3}{2} P(|\lambda_s||i_s| \cdot sin(\theta_s) \tag{10}$$

$$T_e = \frac{3}{2} P(\lambda_{md} i_q - \lambda_{mq} i_d) \tag{11}$$

$$T_e = \frac{3}{2} P(L_d - L_q) \frac{i_s^2 sin(2\theta_s)}{2} \tag{12}$$

$$T_e = \frac{3}{2} P((L_d - L_q) i_d i_q) \tag{13}$$

$$Jp\omega_r = T_e - T_L - B\omega_r \tag{14}$$

where i_d, i_q, v_d, v_q, L_d, L_q, λ_d and λ_q represent the d and q axis currents, voltages, inductance and the flux linkages respectively. ω_e, I_s and R denotes the inverter frequency, current vector and the stator resistance respectively. Due to the dependence of the machine's inductance on the current and magnetic material, the SynRM represents a non-linear load. It is designed such that the d-axis inductance is always higher than the q-axis inductance. The relationship between the saliency ratio and power factor is shown in Eq. (15), detailed derivations can be found in [22]. Generally the SynRM has poor saliency ratio which inherently means a poor power factor.

$$cos(\varphi)_{max} = \frac{k-1}{k+1} \tag{15}$$

The saliency of the SynRM machine and the load power factor angle, represented by k (L_d/L_q) and φ, respectively. The maximum power factor versus the saliency ratio of the SynRM is presented in Fig.7, which is based on Eq.(15) and is a reproduction of the corresponding relationship in [22]. The experimentally measured d-q inductance used in this paper is shown in Fig. 8. Improving the saliency ratio of the SynRM has been an area of active research. This has led to the use of PMs to assist the performance of the SynRM. Though the use of PMs does not improve the saliency ratio, it brings an improvement on the power factor of the machine. In the PMaSynRM the PMs assist in reducing the q-axis flux linkage and improves torque performance as described in Eqs. (16) and (17).

$$\lambda_q = L_q i_q - \lambda_{PM} \tag{16}$$

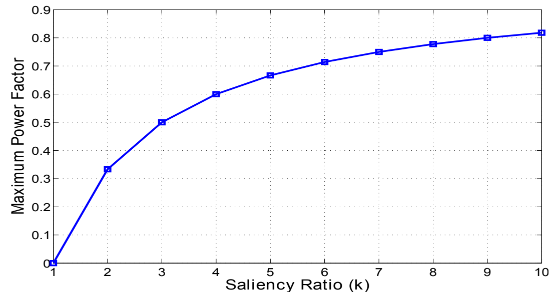

Fig. 7. Power factor at maximum Vs. the saliency ratio

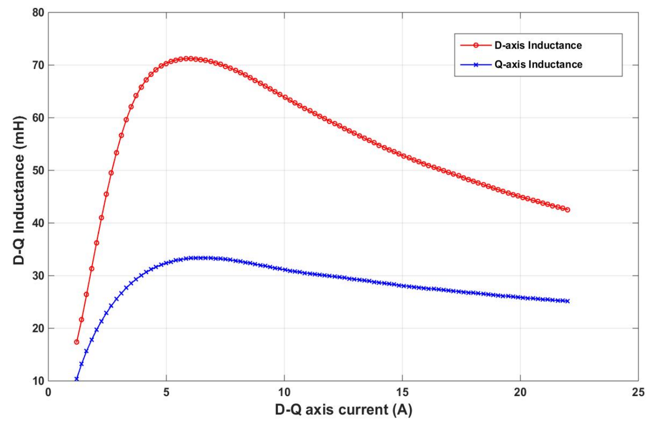

Fig. 8. D-Q inductance of the SynRM

$$T_e = \frac{3}{2} P((L_d - L_q) i_d i_q) + \lambda_{PM} i_d \tag{17}$$

Figs. 9 and 10 show the simplified phasor diagram of the SynRM and the PMaSynRM respectively. The angle between voltage phasor (V_s) and the current phasor (I_s) is reduced for the PMaSynRM. This is because of the magnetic flux of the PMs acting against the magnetic flux present in the q-axis as shown in Fig. 10. This is also described in Eq. (16). In the

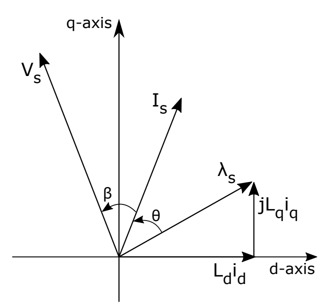

Fig. 9. Simplified phasor diagram of SynRM

PMaSynRM the difference between L_d and L_q is dominant, the PMs serve as additional torque. This is in agreement with literature as the improved torque and power factor would improve the constant power speed range [23]. Fig. 11 shows the torque improvement on the machine when PMs are used. At a particular current angle maximum torque higher than that of the SynRM can be achieved. A control method was used in order to operate the machine at appropriate current angle.

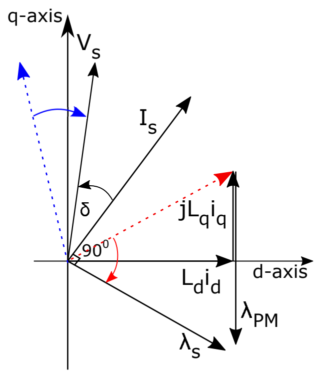

Fig. 10. Simplified phasor diagram of PMaSynRM

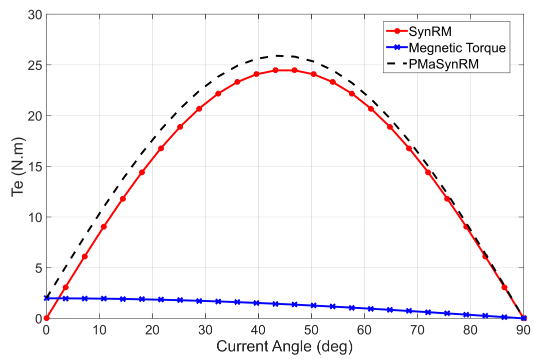

Fig. 11. SynRM Vs the PMaSynRM

IV. Simulation Results

Matlab Simulink was used for the simulation studies. Figs. 12 and 13 show the simulation results of the 3L-NPC inverter SynRM and the PMaSynRM drive respectively. The NP voltage ripple is higher on the SynRM as compared to the PMaSynRM. During transients stage at the start of the operation of the motor, the PMaSynRM produced less NP voltage ripple as compared to the SynRM. It can also be observed that the large vectors are less active during low torque loading for the PMaSynRM drive as compared to the SynRM drive. This means that the modulation index was lower for the PMaSynRM as compared to the SynRM drive. Whereas they both achieved same load torque and speed. This means that higher speed ranges can be achieved on the PMaSynRM as compared to the SynRM drive for the same dc link voltage. This is valuable for the electric vehicle applications. It further supports what has been reported in literature that the use of PMs on the SynRM extends it constant power speed range [23]. Table IV shows the summarized comparison between the three level inverter SynRM and PMaSynRM drives. There was not much significant difference on the neutral point voltage and the RMS phase current between the two drives. The torque ripple was also lower by 0.7% for the SynRM drive.

TABLE IV
Comparison between a three level inverter SynRM and PMaSynRM drive @ 15 N.m load torque

Parameters	SynRM Drive	PMaSynRM Drive
Torque ripple (%)	4.3	5.0
V_{NP} (%)	1.7	1.4
I_{phase} (RMS)	12.1	11.9

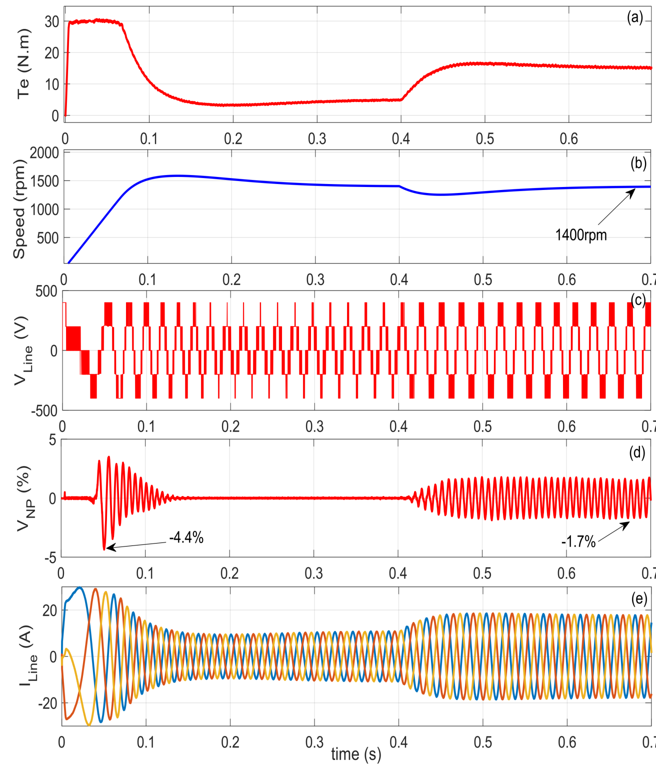

Fig. 12. Three level inverter SynRM drive

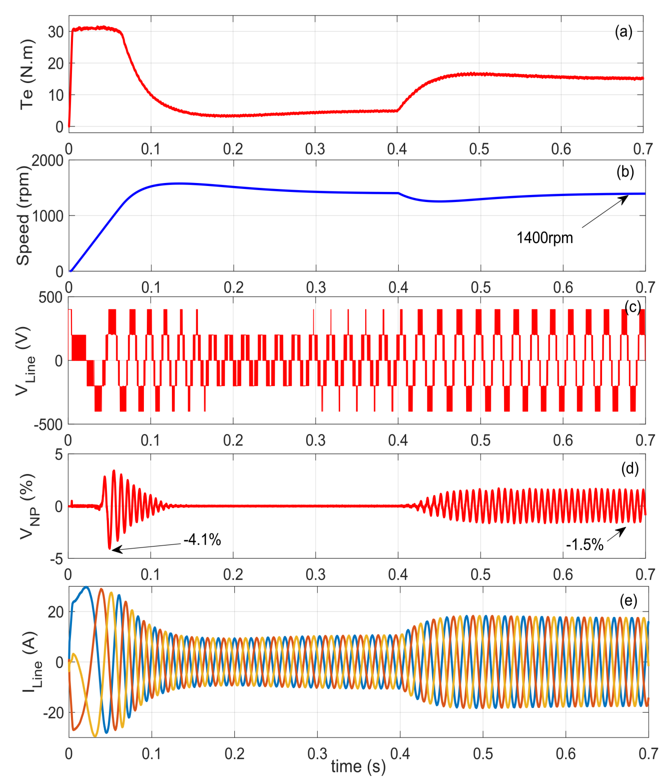

Fig. 13. Three level inverter PMaSynRM drive

V. Conclusion

This paper presented a comparison between a 3L-NPC inverter SynRM and a PMaSynRM drives. This work can be summarized as follows:

- The PMs used to assist the SynRM improve the machine power factor and constant power speed range.
- The 3L-NPC inverter PMaSynRM drive produced lower NP voltage ripple during transients and during steady state operation. Even the difference was only approximately 0.3% and 0.2% during transients and steady state operation respectively.
- The 3L-NPC inveretr PMaSynRM drive had more rms voltage available as compared to the SynRM drive for the same dc bus voltage.
- The torque ripple of the PMaSynRM drive were higher as compared those of the SynRM drive by 0.7%.
- The use of PMs on the SynRM brings about good benefits that could be enjoyed for traction applications. One trade off is the cost of the PMs that tend to be unstable. There was not much significant difference

Appendix

TABLE V
Machine parameters

Line voltage V_{L-L}	220 V
Stator line current at rated I_{L-L}	16.5 A
Induction machine stator	5 hp
Number of poles P	4
Phase resistance R_s	0.9 Ω
Magnet Flux (λ_{PM})	0.02 V.s

Acknowledgment

The research for this work was entirely supported by the National Research Foundation of South Africa, with funding provided under Grant Number 137771.

References

[1] C. P. Riley, N. P. Sawant, D. Ilea, A. Venskus, A. M. Bedford, A. M. Michaelides, X. Vinamata, P. J. Topping, J. M. Soler-Vizan, E. Odvarka, J. D. Wale, D. J. Hawke, and J. M. Reeve, “Simulation based design of reluctance motors for traction applications in hybrid and electric vehicles,” in *7th IET International Conference on Power Electronics, Machines and Drives (PEMD 2014)*, 2014, pp. 1–6.

[2] N. Bianchi, S. Bolognani, E. Carraro, M. Castiello, and E. Fornasiero, “Electric vehicle traction based on synchronous reluctance motors,” *IEEE Transactions on Industry Applications*, vol. 52, no. 6, pp. 4762–4769, 2016.

[3] L. Masisi, P. Pillay, and S. S. Williamson, “A three-level neutral-point-clamped inverter synchronous reluctance machine drive,” *IEEE Transactions on Industry Applications*, vol. 51, no. 6, pp. 4531–4540, 2015.

[4] P. Li, W. Ding, and G. Liu, “Sensitivity analysis and design of a high performance permanent-magnet-assisted synchronous reluctance motor for ev application,” in *2018 IEEE Transportation Electrification Conference and Expo (ITEC)*, 2018, pp. 406–411.

[5] S. S. Maroufian and P. Pillay, “Pm assisted synchronous reluctance machine design using alnico magnets,” in *2017 IEEE International Electric Machines and Drives Conference (IEMDC)*, 2017, pp. 1–6.

[6] A. Mohammadi and S. M. Mirimani, “Design and analysis of a novel permanent magnet assisted synchronous reluctance machine using finite-element-method,” in *2020 11th Power Electronics, Drive Systems, and Technologies Conference (PEDSTC)*, 2020, pp. 1–5.

[7] A. Nobahari, A. Vahedi, and R. Nasiri-Zarandi, “A modified permanent magnet-assisted synchronous reluctance motor design for torque characteristics improvement,” *IEEE Transactions on Energy Conversion*, vol. 37, no. 2, pp. 989–998, 2022.

[8] M. Obata, S. Morimoto, M. Sanada, and Y. Inoue, “Characteristic of pmasynrm with ferrite magnets for ev/hev applications,” in *2012 15th International Conference on Electrical Machines and Systems (ICEMS)*, 2012, pp. 1–6.

[9] S. S. Maroufian and P. Pillay, “Design and analysis of a novel pm-assisted synchronous reluctance machine topology with alnico magnets,” *IEEE Transactions on Industry Applications*, vol. 55, no. 5, pp. 4733–4742, 2019.

[10] I. Manolas, A. Kladas, D. Svechkarenko, and R. Chin, “Demagnetization under normal operation in variable flux pm-assisted synchronous reluctance machines,” in *2018 IEEE International Magnetics Conference (INTERMAG)*, 2018, pp. 1–2.

[11] J. Pou, R. Pindado, D. Boroyevich, and P. Rodriguez, “Evaluation of the low-frequency neutral-point voltage oscillations in the three-level inverter,” *IEEE Transactions on Industrial Electronics*, vol. 52, no. 6, pp. 1582–1588, 2005.

[12] R. K. Behera, T. V. Dixit, G. Kiran, and S. P. Das, “Three-level inverter fed high performance induction motor drive system for high power application,” in *2006 India International Conference on Power Electronics*, 2006, pp. 17–21.

[13] P. S. Jamwal, S. Singh, and S. Jain, “Three-level inverters for induction motor driven electric vehicles,” in *2020 3rd International Conference on Energy, Power and Environment: Towards Clean Energy Technologies*, 2021, pp. 1–6.

[14] A. Tripathi and G. Narayanan, “Torque ripple minimization in neutral-point-clamped three-level inverter fed induction motor drives operated at low-switching-frequency,” *IEEE Transactions on Industry Applications*, vol. 54, no. 3, pp. 2370–2380, 2018.

[15] M. Gu, Z. Wang, K. Yu, X. Wang, and M. Cheng, “Interleaved model predictive control for three-level neutral-point-clamped dual three-phase pmsm drives with low switching frequencies,” *IEEE Transactions on Power Electronics*, vol. 36, no. 10, pp. 11 618–11 630, 2021.

[16] H. Liu, N. Choi, and G. Cho, “Dsp based space vector pwm for three-level inverter with dc-link voltage balancing,” in *Industrial Electronics, Control and Instrumentation, 1991. Proceedings. IECON '91., 1991 International Conference on*, oct-1 nov 1991, pp. 197 –203 vol.1.

[17] J. Zhang, “High performance control of a three-level igbt inverter fed ac drive,” in *Industry Applications Conference, 1995. Thirtieth IAS Annual Meeting, IAS '95., Conference Record of the 1995 IEEE*, vol. 1, oct 1995, pp. 22 –28 vol.1.

[18] K. Yamanaka, A. Hava, H. Kirino, Y. Tanaka, N. Koga, and T. Kume, “A novel neutral point potential stabilization technique using the information of output current polarities and voltage vector,” *Industry Applications, IEEE Transactions on*, vol. 38, no. 6, pp. 1572–1580, 2002.

[19] G. Orfanoudakis, M. Yuratich, and S. Sharkh, “Nearest-vector modulation strategies with minimum amplitude of low-frequency neutral-point voltage oscillations for the neutral-point-clamped converter,” *Power Electronics, IEEE Transactions on*, vol. 28, no. 10, pp. 4485–4499, 2013.

[20] R. Trubenbach, A. Mackay, and M. Kamper, “Performance of a reluctance synchronous machine under vector control,” in *Power Electronics Specialists Conference, 1993. PESC '93 Record., 24th Annual IEEE*, 1993, pp. 803–808.

[21] I. Boldea, *Reluctance Synchronous Machines and Drives, 1996 :Clarendon Press, Oxford*, 1996.

[22] T. Matsuo and T. Lipo, “Rotor design optimization of synchronous reluctance machine,” *Energy Conversion, IEEE Transactions on*, vol. 9, no. 2, pp. 359–365, 1994.

[23] M. Hofer and M. Schrodl, “An analysis of ferrite magnet assisted synchronous reluctance machines for low power drives including flux weakening,” in *2019 IEEE International Electric Machines & Drives Conference (IEMDC)*, 2019, pp. 650–655.

Design and Optimization of a Large Scale Grid Connected Wound Rotor Synchronous Machine

Nosimilo N Siphepho
Department of Electrical Engineering
Stellenbosch University
Stellenbosch, South Africa
24668621@sun.ac.za

Karen S Garner
Department of Electrical Engineering
Stellenbosch University
Stellenbosch, South Africa
garnerks@sun.ac.za

***Abstract*—The integration of renewable energy to the utility grid is a steadily rising process. The growth of the renewable energy sector is of great importance in the era of carbon emission reduction and so governments' energy regulatory authorities have set standards known as 'grid codes' to assist this process and limit negative impacts of these unpredictable energy sources on the quality of electricity produced. This paper looks at the design and optimization of a 3MW, 18 slot, 16 pole, double layer wound rotor synchronous machine designed for a grid connected wind energy application.**

***Index Terms*—design, grid-connected, load currents, multi-objective optimization, non-gradient, non-overlapping, wind energy.**

I. Introduction

Wind energy applications are largely dominated by induction machines and permanent magnet machines [1]. Induction machines (IMs) are preferred for their compactness, durability which makes them perfect for offshore applications [2]. Permanent magnets (PMs) also are attractive because of their high power and torque densities, and because they are brushless maintenance time is reduced [3]. However both these topologies are a little unsuited for grid connected applications. IMs require reactive volt-amperes compensations [4] and PMs lack the flux variation required by the utility grid [5] and in this aspect wound rotor synchronous machines (WRSMs) surpass these two prevalent wind energy generators. WRSMs are excited by direct current in their field, fed by either brushes or brush-less means and the variation of this field current is enough to meet the necessary flux variation required by the grid code without a need for extra equipment [6].

The breakthrough in power electronics came at an opportune time, when electric machine designers were looking for cost effective solutions to make renewable energy integration to the grid economically feasible. This brought forth what is known as 'converter fed machines'. The technology allowed for designers to rethink the traditional methods of design, allowing for flexibility in the number of stator slots, number of phases etc. Traditionally machines were wound with an integral slot overlapping winding (ISOW) which was preferred because of the sinusoidal air gap magneto motive force (mmf) waveform. It came with disadvantages like long end windings which increased the losses, frequent cross phase faults because of the overlapping windings, complexity in machining slots as the number of slots required had to be a multiple of the poles. This implied that in low speed application with many poles even a higher number of slots was required thus greatly reducing the fill factor and strongly compromising the structural integrity of the machine. To counteract all these negative properties a fractional slot non overlapping winding (FSNOW) is used. This type of winding is characterised by a number of slots per pole per phase q that is not an integer but a fraction [7]. The main drawback of the FSNOW is the high harmonic content in the mmf waveform. In literature this is one of the most studied topics, especially in wind generator applications as most topologies has adopted the FSNOW. Large scale generation is becoming more favoured over low scale generation especially for offshore wind sites. This is because efficiency increases as the megawatt (MW) rating increase and so decreasing the levelized cost of energy (LCOE). In fact, the price of wind power decreased by 40% as the power rating increased from 95 KW in the 80s to about 2000 KW in 2006 [8]. This makes wind energy integration to the utility an economically feasible idea. In grid connected wind applications certain standards need to be met in regards to machine performance, on the grid side these are known as the grid codes. There are expectations of reactive power control, power factor control and frequency control and many more placed on the wind energy system. This paper seeks to optimize a 3MW, 400V fractional slot non overlapping wound rotor synchronous machine to make it grid compliant. The optimization function seeks to reduce the torque ripple, the active mass while increasing the efficiency and making sure that the heating limit for air cooled machines is not exceeded.

II. Preliminary Design

The preliminary design of a machine is a complicated science that requires knowledge of electromagnetic fields behaviour. Over the years scientist have gathered and compressed equations that describe the characteristics of a machine. The set of estimations given by [9] helps shorten the design process. Using the analytical equations together with Finite Element Method (FEM) the working model can be designed.

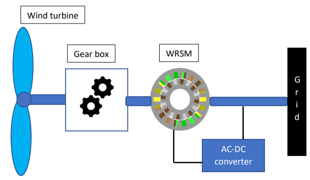

Fig. 1. grid tied Wound rotor synchronous machine wind energy system.

The first step in machine design is the formulation of main dimensions, that is the length L and the air gap density D. These are derived from the torque equation of the machine. The torque is a function of the rated output power, such that

$$T = \frac{P_{out}}{2\pi n}, \tag{1}$$

where P_{out} is the power output, n is the rated speed in rpm. This torque can also be expressed as:

$$T = \sigma_{Ftan} \frac{\pi D^2 L}{2}, \tag{2}$$

where σ_{Ftan} is the tangential stress and the term $\frac{\pi D^2 L}{2}$ defines the volume of the rotor for the rated torque. The values of tangential stress for an air cooled machine are estimated between 17 KPa to 59.5 KPa . From equation (2) we can solve for the term D^2L and depending on the application we can set the length of the machine. For our application it is advisable to opt for a longer stack length and as a result in the work of a stack length of 1.5m was chosen for the preliminary design. Therefore the main dimensions are solved.

After solving for main dimensions the next step is to solve for slot dimensions for both stator and rotor. These are based on the magnetic and current loading of the machine, that is the rating of the machine. Table 2 summarizes the machine specifications. According to design specifications, the parameters are fed into a python based, time stepped FEM and the performance of the machine is computed. The preliminary design process can be summarised in the flowchart shown in figure 2.

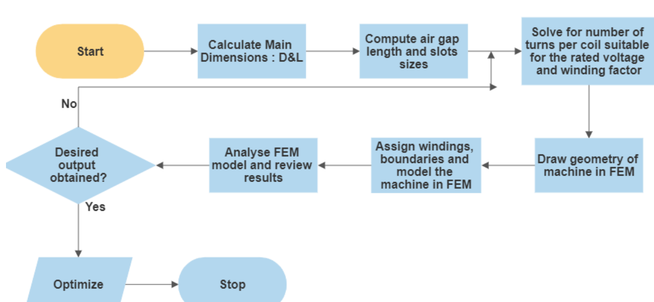

Fig. 2. Preliminary design process.

TABLE I
SPECIFICATIONS OF THE 3 MW 16/18 SYNCHRONOUS WOUND ROTOR MACHINE

Parameter	Value
Rated Power (MW)	3
Rated Torque (KNm)	76
Rated speed(r/min)	375
Rated Frequency(Hz)	50
Tangential stress (Pa)	33 500
Number of Stator slots	18
Number of Rotor slots	16
Air gap length (mm)	4.6
Stack length(mm)	1500
Stator outer diameter(mm)	1600
Stator inner diameter(mm)	989
Rotor shaft diameter(mm)	460

III. GRID CODES

Grid codes can be defined as stipulations set to ensure the smooth operation of the grid. That is stability, quality of electricity and safe operation has to be ensured. Renewable energy plants integrated to the utility grid must not disturb the operation of the grid, so in South Africa the National Energy Regulator (NERSA) gives grid codes for renewable energy plants.

TABLE II
RENEWABLE PLANT CATEGORIES.

Category	Rated Power Range	Voltage Connection	Voltage Limits
A1	$0 < A1 \leq 13.8KVA$	LV	$\pm15\%to\pm10\%$
A2	$13.8KVA \leq A2 \leq 100KVA$	LV	$\pm15\%to\pm10\%$
A3	$100KVA \leq A3 < 1MVA$	LV	$\pm15\%to\pm10\%$
B	$1MVA \leq B < 20MVA$	LV & MV	$\pm10\%$
C	$\geq 20MVA$	HV	$\pm10\%$

In this work we are focusing on grid codes specifically for category B, as the desired optimum WRSM lies within this range. For machines in this category there are set of standards regarding : reactive power capabilities, requirement of voltage regulation , frequency control requirements, low voltage ride through (LVRT) and many more. Fig.3 shows the expected reactive power capabilities. It is therefore imperative to come up with design constraints that satisfy all these conditions. Some of the grid connection specifications are highlighted in table II, furthermore the following stipulations should be observed :

- From 0.2 p.u generator load the power factor should be between 0.975 leading or lagging as illustrated in fig 3
- Reactive power and voltage control should be within a tolerance of 0.5 % of rated power
- The system should stay connect to the grid during short transient faults.
- Frequency should vary between 47 Hz and 52 Hz at a rate of change of 1.5 Hz/s [10]

A significant part of the grid regulations are incorporated in the control side of the machine, but part of it has to be dealt with in the design stage of the generator. Therefore the grid code is considered when the optimisation of the machine is undertaken.

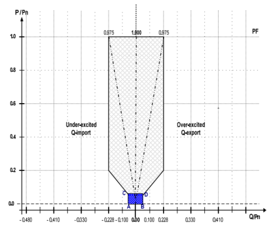

Fig. 3. Reactive Power capabilities grid requirement for category B [11]

IV. Optimization overview

Lei $et.al$ in [12] defines optimization as an art of searching for the best solution among many feasible solutions. It is an essential part of machine design, and is implemented to improve performance of pre-existing FEM models. Bramerderfer $et.al$ in [13] explore design optimization techniques and trends, they explain that there is never one optimum solution in machine design. The best machine is defined according to optimization objectives, which in our case is to make the WRSM grid compliant.

To efficiently complete this task, a group of output variables known as objectives are compiled. These are the desired outcomes, then we come up with boundaries for other performance parameters according to standards. These are known as constraints and they ensure that the obtained solutions are practically feasible.

It is known that machine parameters are interdependent, which makes single-objective optimizations time consuming tasks that may never lead to a practical solution. In this regard the ideal machines does not exist, that is to say if one of the objective is met there will be a deficit in another [14]. A practical example will be the increase in air gap may positively reduce the torque ripple but adversely reduce the power and torque density. For this reason we employ multiple objective optimization. To solve for the optimal solution to our design problem constraints are put in place to make sure that the stability, thermal condition and practicality of the machine is not compromised.

We can therefore define the optimization function $F(\mathbf{x})$ where,

$$\mathbf{x} = [I, \theta, sG, rG, Nt, Idc, L]. \tag{3}$$

Subject to

$$\mathbf{x} = [x_1, x_2, x_3, ..., x_n]\epsilon X \tag{4}$$

$$\mathbf{y} = [y_1, y_2, y_3, ..., y_n]\epsilon Y \tag{5}$$

Where $\mathbf{x}$ is the decision vector, X is the parameter space, $\mathbf{y}$ is the objective vector and Y is the objective space.

The decision vector defines the machine geometry and the electric and magnetic loading, where I is the peak value of stator current θ is the current angle, sG defines the stator slot shape and stator outer diameter parameters, rG defines rotor slot shape and rotor shaft parameters, Nt is the number of rotor turns, Idc is the excitation current and L is the stack length. The compilation of all elements in the decision vectors within the constraints which satisfy the the objectives is known as the Pareto optimal. From all these solution the best machine is chosen based on optimization purpose.

V. Optimization considerations

Before setting up the optimization platform, a lot of factors have to be considered. This is to make sure the solution satisfy the requirements of the optimization whilst still within practicality, thermal and synchronisation stability bounds. For grid connected WRSMs wind applications, these factors should be carefully considered :

1) The torque ripple should be less than 6 % for wind energy generators.
2) The efficiency should be high for large scale machines.
3) The overall active mass should be as low as possible.
4) The terminal voltage should be around 230 V , giving allowance for permissible voltage variation according to the grid code.
5) The power factor of the machine must lie within 0.975 lagging and 0.975 leading.
6) The current densities of the machine should lie within bounds of an air cooled machine, considering the AJ constant defined in [9]

After all these factors have been considered the following step is to find a suitable optimization algorithm to employ in order to find the best solution. There is an option to either use gradient based or non gradient based methods. Gradient based methods are advantageous in that they are fast because they work incrementally eliminating invalid points within the given range and population. The main disadvantage is that there is a possibility of missing the optimal solution because of how the algorithms operate.

On the other hand , non-gradient based methods are adaptive which make them slow. In the given boundary conditions and population they iterate over a wide range of values in random directions. They cover a lot of combinations of the decision vector elements to produce numerous solutions to the design problem.

One of the most popular non-gradient based algorithm is the non-dominated sorting generic algorithm (NSGA), it was first presented by Srinivas and Deb in 1994 [15]. It is one of the most efficient and well known multi-objective evolutionary algorithms. NSGA posses three unique characteristics : fast non-dominated sorting approach , fast crowded distance estimation procedure , and simple crowded comparison operator [16]. For this work NSGA is chosen as the optimization algorithm. The flowchart in fig 4 sums up the functionality of the NSGA.

Particle Swarm Optimization (PSO) is another non-gradient based algorithms and examples of gradient algorithms include the: Modified Method of Feasible Direction (MMFD), Sequential Quadratic Programming (SQP), Sequential Linear

Programming (SLP) and the Sequential Unconstrained Optimization (BIGDOT).

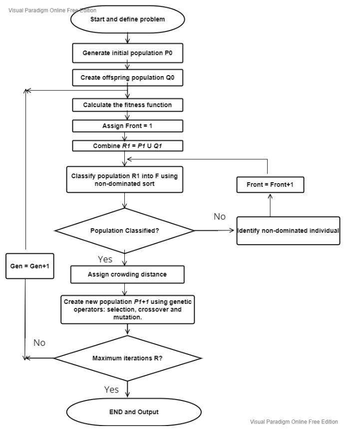

Fig. 4. Flowchart of NSGA [14].

VI. Optimization environment and process

The two dimensional preliminary design is simulated in the python based in house software called SEMFEM. From the analytical design a geometry is composed and from calculated rated values and the corresponding electrical and magnetic loading conditions specified , an estimation of limits can be developed. The advantage of running the python script is its versatility and ease to modify all parameters. An efficiently set mesh and optimum time steps makes each evaluation fast, and shortens the design time. For the optimization SEMFEM is interfaced with the optimization software Visual-Doc. With a specified input and output file, Visual-Doc runs the python script and varies the inputs within the set range to achieve the optimization objectives.

Visual-Doc is a robust software consisting of a various optimization methods to choose from. It provides options for both gradient and non-gradient based optimization. In this work all the optimizations were non gradient based, particularly employing the non-dominated sorting generic algorithm II (NSGA II).

The process of setting the non-gradient based optimization using NSGA in Visual-Doc can be summed up in the following steps:

1) First, SEMFEM is interfaced with Visual-Doc by setting the input file, output file, python script and python executable program file locations in Visual-Doc.
2) Then the initial values of inputs are set and a pre-run test is performed.
3) If the test is void of errors, then data can be linked for optimization.
4) Upper and lower limits as well as objectives are set for both input and output variables.
5) The choice of optimization method is made, choosing the preferred algorithm and setting population.
6) To monitor patterns of the optimization, simulation monitors are calibrated according to users interest.

The setup in table III shows the variables, divided into inputs and output with the boundaries for each defined. Table IV gives the objectives of the optimization.

A. Solving for load currents

The primary software used to simulate the machine takes load current or current densities as inputs. This however is contradictory to how the utility grid works. In grid connected machines the voltage of the grid is known and fixed and to correctly simulate grid connection, the load current must be solved. Potgier and Kamper in [17] propose a method that estimates the load current I_s using the rated copper losses of the machine. The value of the current obtained from solving the rated copper losses is used as an initial guess in an iterative process solving for the d-q currents I_d and I_q of the machine. Using this method, after only three iterations the solution converges towards true value. The drawback of this method is the need for an accurate initial estimate.

To avoid solutions that do not converge, Mabhula and Kamper in [18] propose two methods that use the impedance information of the machine to compute the load currents. The first method is the frozen permeability only method. They use frozen permeability to compute the impedance matrix of the machine at the working point. After the impedance is obtained, the voltage matrix and impedance matrix are used to compute the load currents. This method can be used together with an iterative loop , allowing for the user to start with inaccurate first guesses. The whole iterative process is:

1) Firstly, make an initial guess of I_d and I_q .
2) For that machine geometry , run a non linear solution. Solve for all machine performance parameters as modelled.
3) Freeze the permeabilities. Then with only I_d given and both I_q and excitation current zero, solve for the inductances using a linear solution. Such that :

$$L_{md} = \frac{\lambda_d - \lambda_f}{I_d} \tag{6}$$

$$M_{mdq} = \frac{\lambda_q}{I_d} \tag{7}$$

when,

$$I_q = I_{dc} = 0 \tag{8}$$

4) Perform another linear solution with only I_q given and both I_d and I_f are zero. Such that :

$$L_{mq} = \frac{\lambda_q}{I_q}. \tag{9}$$

$$M_{mqd} = \frac{\lambda_d}{I_q} \tag{10}$$

when ,

$$I_d = I_{dc} = 0 \tag{11}$$

5) A final linear solution is done with field current only and both I_d and I_q equivalent to zero. Then three inductances can be defined :

$$L_{mdf} = \frac{\lambda_d}{I_f} \tag{12}$$

$$L_{mqf} = \frac{\lambda_q}{I_f} \tag{13}$$

$$L_{mff} = \frac{\lambda_f}{I_f} \tag{14}$$

when,

$$I_d = I_q = 0 \tag{15}$$

6) Use the voltage solved for in the nonlinear solution for the first estimate of voltage angle Δ_s. Use the fixed grid voltage to formulate a new voltage matrix, such that:

$$V_d = V_g sin(\Delta_s.) \tag{16}$$

$$V_q = V_g cos(\Delta_s.) \tag{17}$$

Where V_g is the fixed grid rms voltage .

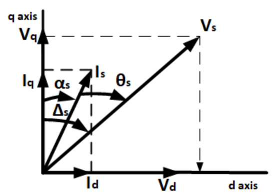

Fig. 5. Phasor diagram show load currents of WRSM

7) With the new voltage matrix together with the impedance matrix the load currents can be found. The current matrix can be expressed as :

$$I = Z^-1 * V. \tag{18}$$

The new values of I_d and I_q from the solved current matrix become the new estimate in the following iteration. The whole process is repeated again until the value of $V_t - V_g$ approaches zero.

VII. Results of Optimization

The criteria in choosing the best machine is based on power density, that is a solution lying within all the constraints but with the highest power density. After optimization the highest power density obtained was 0.42 kW/kg. It can be seen that as the algorithm adapts for a higher power density the slot opening of the rotor slots become more wider to accommodate the low torque ripple requirement. The stator bore diameter is reduced to decrease the weight of the machine. It is evident that as the mass is reduced so is the efficiency of the machine, Fig 8 shows how the efficiency gradually increase as the mass is increased. As the multi-objective optimization is employed the optimum point in terms of efficiency is a compromise that allow all the other conditions to be true. Fig 10 shows the relationship between load currents, excitation current and power density. Power is a function of torque, and torque is directly proportional to load current. As the load current increases , so does the torque and the power. The field current is responsible for keeping the voltage at the required 230 V rms. The main dimensions are closely related to the torque capacity of the machine, Fig 9 shows this relationship from obtained solutions of the optimization.

TABLE III
Optimization Variables

Parameter	Type	Lower limit	Upper Limit
δ (mm)	input	2.5	5
sHs0 (mm)	input	5	20
sHs1 (mm)	input	80	120
sBs0 (mm)	input	50	120
rHs0 (mm)	input	5	15
rHs1(mm)	input	10	15
rHs2 (mm)	input	80	125
rBs0 (mm)	input	50	120
rBs1 (mm)	input	60	120
rBs2 (mm)	input	40	120
I (kA)	input	2	7
I_{dc} (A)	input	10	200
N_t	input	10	500
$r_{ostator}$ (mm)	input	750	1000
r_{shaft} (mm)	input	230	330
L (mm)	input	600	2000
θ (degrees)	input	0	90
T_{ripple} (%)	output	0	6
V_t	output	230	240
T_{avg} (kNm)	output	76	77
$J_s(A/mm^2)$	output	1	5
$J_r(A/mm^2)$	output	1	5
PF	output	0.975	1

TABLE IV
Optimization Objectives

Parameter	Objective
Active mass	minimize
Power density	maximize
Efficiency	maximize

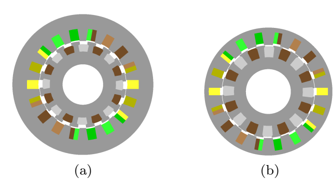

Fig. 6. 2D FEM models of (a) Preliminary WRSM (b) Optimized WRSM.

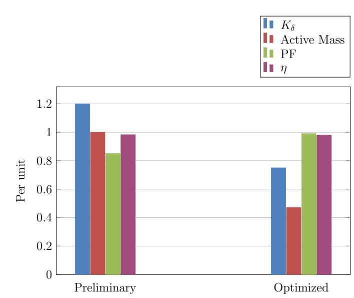

Fig. 7. Comparison of properties between preliminary design and the optimized machine.

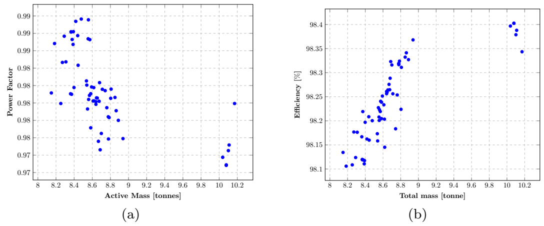

Fig. 8. Active mass against power (a)factor and (b) efficiency .

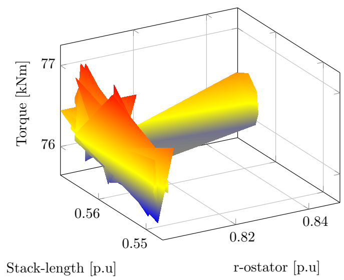

Fig. 9. Main dimensions versus torque.

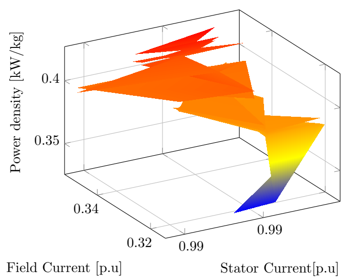

Fig. 10. Relationship between stator and field current versus power density.

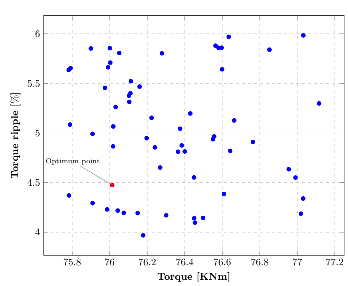

Fig. 11. Pareto front of torque and torque ripple of the WRSM..

VIII. Conclusions

The aim of this work was to optimize a large scale wound rotor synchronous machine, to improve its performance and make it grid complaint. It could be seen that the objectives were met, the torque ripple was reduced to an acceptable 4.4% and the active mass of the WRSM was decreased by more than 40% to increase the power density of the machine. Using the iterative process to solve for load current and simulate grid conditions, it was seen that the power factor is within the acceptable grid requirement which is between 0.975 leading and lagging. By setting the limits on the current densities, the heating limit was set to be appropriate for air cooling and thus the thermal limit was not exceeded. It can therefore be concluded that an optimum solution that is also grid complaint was obtained.

References

[1] O. Anaya-Lara,D. Campos-Gaona, E. Moreno-Goytia, and G.Adam, Offshore wind energy generation: control, protection, and integration to electrical systems. (John Wiley & Sons,2014)

[2] M.Paez, M.Salles, and C. Rahmann, "Large induction motors in distributed wind power generation." *2013 International Conference On Clean Electrical Power (ICCEP)*. pp. 399-406 (2013)

[3] J.Pyrhönen, J. Nerg, J.Puranen, M. Haavisto, & Others, "Permanent magnet technology in wind power generators." *The XIX International Conference On Electrical Machines-ICEM 2010*. pp. 1-6 (2010)

[4] A.Trzynadlowski, Control of induction motors. (Elsevier,2000)

[5] A.Jain, S. Shankar, and V. Vanitha, "Power generation using permanent magnet synchronous generator (PMSG) based variable speed wind energy conversion system (WECS): An overview." *Journal Of Green Engineering*. **7**, 477-504 (2017)

[6] Q. Ali, T. Lipo, and B. Kwon, "Design and analysis of a novel brushless wound rotor synchronous machine." *IEEE Transactions On Magnetics*. **51**, 1-4 (2015)

[7] G.Dajaku, S. Spas, and D. Gerling, "Advanced optimization methods for fractional slot concentrated windings." *Electrical Engineering*. **101**, 103-120 (2019)

[8] M. Blanco, "The economics of wind energy." *Renewable And Sustainable Energy Reviews*. **13**, 1372-1382 (2009)

[9] T. Jokinen, V. Hrabovcova, and J. Pyrhonen, "Design of rotating electrical machines." (John Wiley & Sons,2013)

[10] S.A Government, GRID CONNECTION CODE FOR RENEWABLE POWER PLANTS (RPPs) CONNECTED TO THE ELECTRICITY TRANSMISSION SYSTEM (TS) OR THE DISTRIBUTION SYSTEM (DS) IN SOUTH AFRICA. (https://www.sseg.org.za/wp-content/uploads/2019/03/South-African-Grid-Code-Requirements-for-Renewable-Power-Plants-Version-2-8.pdf,2014), Accessed: 2022-07-26

[11] S. Sewchurran, and I. Davidson, "Guiding principles for grid code compliance of large utility scale renewable power plant intergration onto South Africa's transmission/distribution networks." *2016 IEEE International Conference On Renewable Energy Research And Applications (ICRERA)*. pp. 528-537 (2016)

[12] Y. Lei, Z. Zhao, S. Wang, D. Dorrell, and W. Xu, "Design and analysis of star–delta hybrid windings for high-voltage induction motors." *IEEE Transactions On Industrial Electronics*. **58**, 3758-3767 (2010)

[13] G.Bramerdorfer, J. Tapia,, J. Pyrhönen, and A. Cavagnino, "Modern electrical machine design optimization: Techniques, trends, and best practices." *IEEE Transactions On Industrial Electronics*. **65**, 7672-7684 (2018)

[14] G. Lei, X. Chen, J. Zhu,Y. Guo, W. Xu, and K. Shao, "Multiobjective sequential optimization method for the design of industrial electromagnetic devices." *IEEE Transactions On Magnetics*. **48**, 4538-4541 (2012)

[15] N. Srinivas, and K. Deb, "Muiltiobjective optimization using nondominated sorting in genetic algorithms." *Evolutionary Computation*. **2**, 221-248 (1994)

[16] Y. Yusoff, M. Ngadiman, and A. Zain, "Overview of NSGA-II for optimizing machining process parameters." *Procedia Engineering*. **15** pp. 3978-3983 (2011)

[17] J. Potgieter, and V Kamper, "Design specifications and optimisation of a directly grid-connected PM wind generator." *2013 IEEE Energy Conversion Congress And Exposition*. pp. 882-889 (2013)

[18] M. Mabhula, and M. Kamper, "Gradient-based Multi-objective Design Optimisation Formulation of Grid-connected Wound-rotor Induction Motors." *2020 International Conference On Electrical Machines (ICEM)*. **1** pp. 163-169 (2020)

2023 SAUPEC Conference, Johannesburg, South Africa, January 24-26, 2023

On the Study of Induction Motor Fault Identification using Support Vector Machine Algorithms

Pamela Zitha & Bonginkosi A. Thango
Dept. of Electrical and Electronic Engineering Technology
University of Johannesburg
Johannesburg, South Africa
217043937@student.uj.ac.za; bonginkosit@uj.ac.za

Abstract—**Induction motors are ever-present in various commercial and industrial processes owing to their high-power capacity, dependability, and low manufacturing costs. However, during their operation their susceptible to heat, mechanical stress, electrical stress, and corrosion. These stresses do not affect the operation of induction motor, however, in a long run it may develop into a major fault which can cause additional maintenance costs and unscheduled downtime, resulting in overall production loss, high financial loss, and sometimes serious human injuries. This work investigates the performance of an induction motor based on various faults conditions. A MATLAB/Simulink platform is used to develop an induction motor model. The performance of induction motor is evaluated on the three-phase line connected to it since implementing a fault in a line affects the performance induction motor. The faults that were tested were no fault condition and faults between AB, AC, BC, AG, CG, BG as well as ABCG. Training dataset was extracted from the sinusoidal waveforms of this various fault conditions. The data is given to the classification learner app in MATLAB for learning. Furthermore, this data set imported to workspace for the training purposes in the classification learner app. Different SVM learning algorithms are trained to deduce the highest learning algorithm in prediction time. The highest SVM learning algorithm according to the results is cubic and Fine Gaussian SVM learning algorithms which shows 100% accuracy on prediction time. The confusion matrix is then used to compare the true predicted and the false predicted classes.**

Keywords— Induction motors, faults, support vector Machine (SVM)

I. INTRODUCTION

Induction machines are rapidly gaining popularity in renewable energy applications, necessitating ongoing research into the machines' performance. Failure to regulate faults in the processes may cause considerable economic losses, degrade the quality of the process performance, or even cause serious damage to human life or health, as well as the environment [1]. Most rotor failures are confluence by multiple factors such as when the rotor is under stress. This stressor could be classified as electromagnetic, dynamic, residual, environmental, thermal, and mechanical in general. In an IM the distance between the internal diameter of the rotor and the outside diameter of a rotor is known as the air gap. This can be avoided if the air gap length is kept to a minimum [1]. SVMs are learning models that have been supervised by accompanying Learning techniques for data classification and regression analysis. SVM analysis method is well-known as a classification and regression artificial intelligence approach. SVMs are used in a variety of fields, including digital advertising, text summarization, and genomics. The type of SVM that is frequently used for linear regression and classification tasks is called Simple SVM. Classification is a type of supervised machine learning, where the response is discrete. Supervised learning algorithm takes known response and train a model to generate predicted response on new data [2].

The industry has endorsed motor detection of faults as a means of ensuring the consistent and dependable operation of modern industrial systems. Motors are put through their paces in a variety of circumstances and environments. Any motor failure means undesired downtime, expensive repairs, and possibly human casualties [3]. It accounts for a wide range of load levels by combining the current signals of two phases. Electrical or mechanical failure can be used to classify the many problems associated with induction motors. Bearing problems account for Stator-related problems account for 38% of all IM faults in the rotor account for miscellaneous faults account for ten percent of the total. Bearing troubles, winding of stator shortages, shaft unbalance, damaged rotor bars, and air gap eccentricity are all common squirrel-cage motor faults. The motor would create an imbalanced increased heat, induced current, fluctuating torque, and lower torque magnitude because of these faults [4]. Rotor failures are among the most prevalent electrical IM problems, accounting for roughly 10% of all failures. Rotor windings, rotor bars in wound rotor machines, and end rings in squirrel cage induction motors are all susceptible to these faults. Casted rotors are utilized largely for small motors, while manufactured rotors are used for larger motors. During operation, thermal, electromagnetic, and mechanical stressors can all affect the rotor, resulting in rotor defects. Broken rotor bars can be caused by pulsing loads, frequent direct online starts, and manufacturing faults [5].

The most prevalent causes are winding problems and insulation failure. It causes 30–40percent of the overall reported IM failures. The failure the in insulation of the stator is caused by discharge in electrical, cooling system leakage, winding heating causing a temperature rise, and winding bracing with loose ends [6].

II. MATERIALS AND METHODS

A. Fundamental principle of SVM learning algorithm

SVMs are learning models that have been supervised by accompanying Learning techniques for data classification and regression analysis. They were first designed for data with exactly two classes, suggesting that the relating problem was a two-class problem with only two values for the class labels [7]. The operation of a linear classifier occurs when there is a straight line between two classes. In this way each data point in every two different categories will be grouped. This shows the number of lines to the choose from the endless. When compared with other algorithm such as k-nearest neighbours, the linear SVM algorithm is superior, because the data point is classified by best. It selects the line that slits the data and is the farthest distance from the nearest data point [7].

SVM quadratic is used when data sets are not linearly separable, to find an interval between two groups. Can get around this, the data is shifted to a greater space and then classified with a classification algorithm. Data sets can be learned more efficiently as the nth degree expansion increases [8]. The function that allows the non-linear model to be learned is called the polynomial kernel. In a feature space, this allows vectors (training samples) to be equal over the original variables' polynomials. To capture the data, the modification of implicit features utilizing kernels of non-linear cubic polynomials has a 3D non-linear aspect is required [8].

Advantages of SVM

- They've long been known to be excellent at text classification and to scale well for rich attributes, which is critical in GUI-based datasets.
- SVMs can offer better classification results with less training data.
- The data of other users do not affect the learning of one user.
- To put it another way, a user's profile can be built purely from his own data, with no help from other users [3].

B. *Proposed Induction motor model*

The induction motor model in Fig. 1, was developed using a MATLAB Simulink. The stator and rotor's windings are joined by a wye to an internal neutral point. The model is connected to 3 phases namely: phase A, phase B and phase C. The fault was implemented between any phase and ground in the three-phase fault (short-circuit). A Simulink logical signal controls the fault operation when the external switching time mode is selected. The phase-locked loop (PLL) system can be used to synchronize on set of three-phase sinusoidal signals of variable frequency. A bridge of selected power electronic devices is implemented by the voltage measurement block. Each switch device is connected in series with RC snubber circuits. The output signal parameter is disabled when the block is not utilized in a phasor simulation and a POWERGUI block is added to the model. Receive signals from the 'Goto' block with the specified tag in the block parameter. The voltage and current output in volts and amperes or in per unit values. The fault is implemented on the difference because a fault is implemented on a line it affects the induction motor's operation. In a three-phase fault block the different fault condition can be measured which are the no-fault condition, the fault voltage, fault current, fault voltage, and current. The results are measured in the scope.

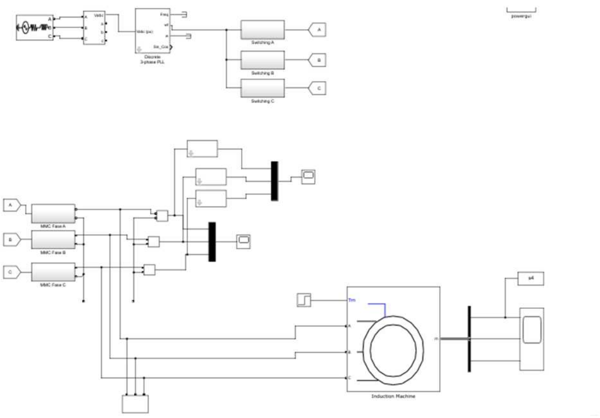

Fig. 1. Induction motor model

The performance parameters of the induction motor together with the types of faults that are simulated in this work are given in TABLE I.

TABLE I. PERFORMANCE PARAMETER AND FAULTS TYPE.

Performance parameter	Type of faults
Torque Rotor current Stator current	No fault
	Phase (A to B)
	Phase (A to C)
	Phase (A to Ground)
	Phase (B to C)
	Phase (B to Ground)
	Phase (C to Ground)
	Phase A, B, C and ground

After simulating various faults in the MATLAB Simulink, the fault current profiles will be used as data for training in the SVM learning algorithm. The SVM learns better with the known output, therefore, since it has the prior knowledge about the dataset it can train without human help. The SVM will classify whether the outcome is a no-fault condition or a fault condition. SVM will classify the outcome according to the fault conditions. The flowchart in Fig. 2 illustrates this process.

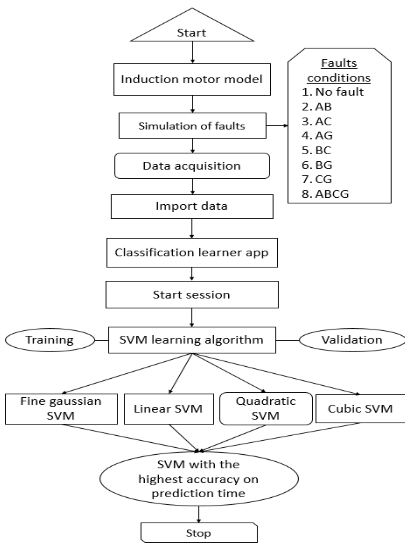

Fig. 2. Process flow chart.

C. *Classification learner app*

Fig. 3 demonstrate the process of classification learning workforce. Where the data is imported into classification learner app. From training to validation.

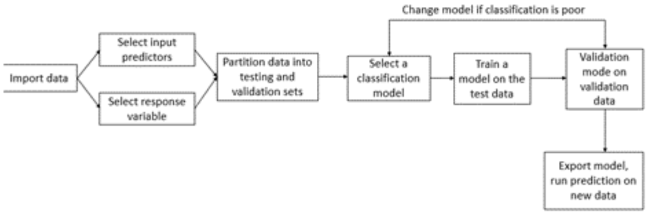

Fig. 3. Classification learner App process flowchart.

In Fig. 4 illustrates the process of classification model a model that is designed to perform a task of classification is called a classification mode. In this model the data are divided into desired output labes.

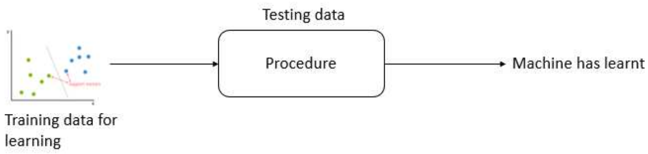

Fig. 4. SVM learning algorithm.

The data is given to computer for learning. The computer will know about different fault condition. The process that the computer will follow to learn about the different faults data called machine learning. After computer learn about the featured of faults data then we can give the test data. Since the data has the prior knowledge about the data it can train the data without human help. Therefore, it will automatically classify the training without the human help.

III. Results and Discussion

Since implementing a fault in a line affect the operation of induction motor, the faults were implemented between any phase and ground. The faults that were tested in this work were no fault condition and faults between AB, AC, BC, AG, CG, BG as well as ABCG. The performance parameters are stator current, electromagnetic torque and rotor current. The simulated sinusoidal waveformsl on the model is extracted as dataset for training in a classification learner app. The dataset was gathered based on the results obtained from the simulation of the induction model.

In Fig. 5, the electromagnetic torque, stator current and rotor current of the no-fault of the induction motor is demonstrated. It can be observed that the induction motor is operating without faults from 0 sec to 0.5 sec.

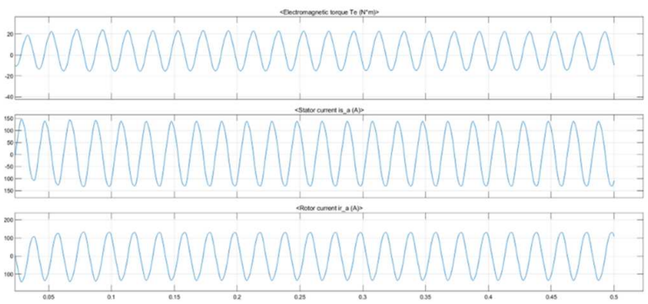

Fig. 5. No fault condition.

The fault implemented between phase A and phase B is shown in Fig. 6 below and the electromagnetic torque, stator current and rotor current are shown. Initially, the motor is operating without fault from 0 to 0.1 seconds, the faults starts occurring from 0.1 to 0.3.

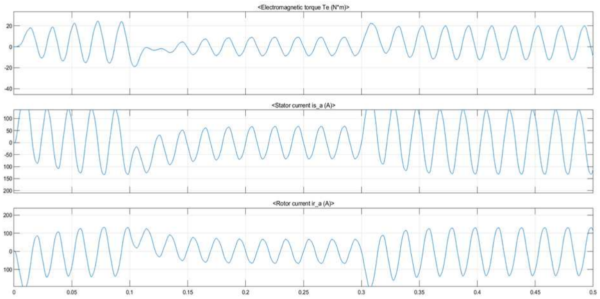

Fig. 6. Fault between phase A and B

In Fig. 7 shows the simulated fault condition between phase A and phase C demonstrating the performance parameters.

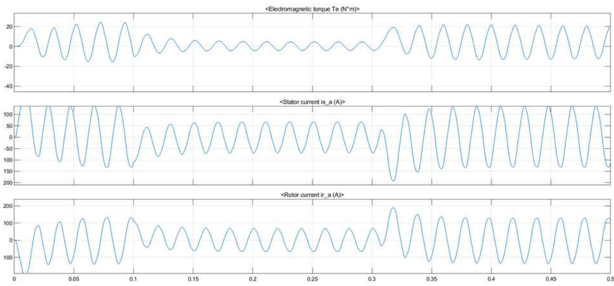

Fig. 7. Fault between phase A and C

Fault between phase A and ground is shown in Fig. 8 below, where electromagnetic torque was operating at a normal state until a fault occurs at 0.1 seconds later. The torque kept increasing which caused the speed of the IM to decrease and it affects the performance of stator current and rotor current.

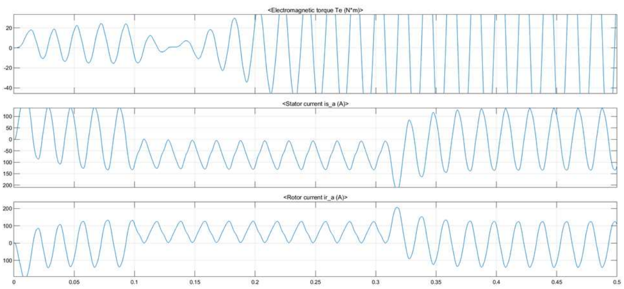

Fig. 8. Fault between phase A and G

Fig. 9 Shows the faults between phase B and phase C. This fault condition is similar to the fault simulated in Fig. 8.

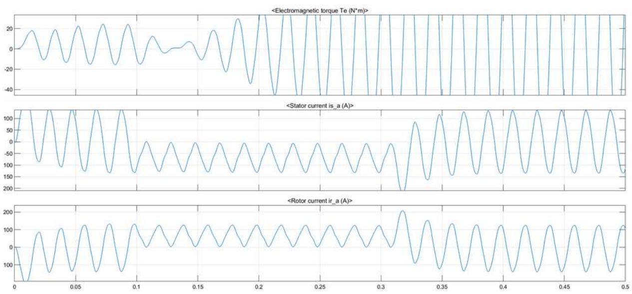

Fig. 9. Fault between phase B and C

Fig. 10 demonstrate fault between phase B to ground. Where the electromagnetic torque is rapidly increasing causing the motor speed to decrease while affecting the stator current and rotor current.

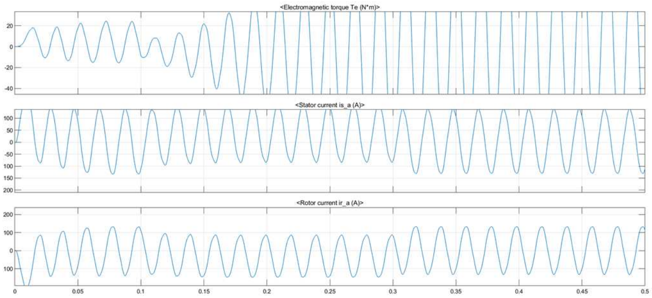

Fig. 10. Fault between phase B and G

In Fig. 11 is the fault implemented between phase C and ground from which the electromagnetic torque is rising as discussed previously causing the induction motor to function slowly.

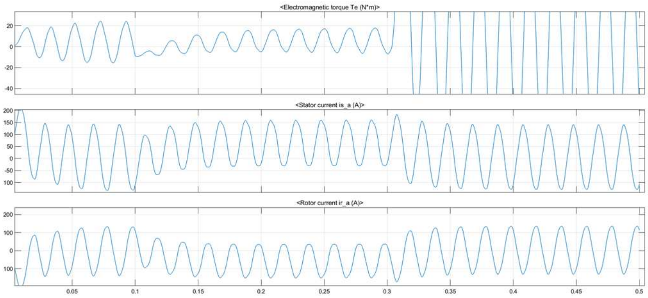

Fig. 11. Fault between phase C and G

Fig. 12 shows all the simulated faults combined together.

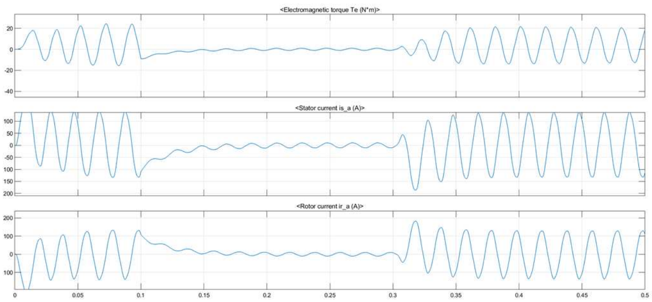

Fig. 12. Fault between ABCG

The simulated result from the developed induction motor model on MATLAB Simulink. The three-phase fault measures different fault conditions using current fault in this work. The performance parameters that were tested in order to obtain different fault signals were electromagnetic torque, stator current, and rotor current. The time is one of the common parameters in all the conditions. The model is trained for 0.5 seconds in each case.

Fig. 5 shows a no-fault condition where the sinusoidal waveforms are constant. Different fault conditions start from Fig. 6 to Fig. 12, where in most cases the motor operates in a normal state for 0.1 seconds and then the fault occurs in the waveform signals. The fault in all the fault conditions is mainly caused by the increase in torque, which decreases the motor's performance below normal. The electromagnetic torque, stator current, and rotor current signals drop below normal, and at about 0.35 seconds, the motor goes back to normal again.

A training data is data that already has data classified into different categories which are no fault, AB,AC, AG, BC,BG,CG and ABCG. The data is given to the classification learner app for learning. This classification learner app will know about no fault, AB,AC,AG,BC,BG,CG and ABCG and its features. The process that the computer will follow to learn about the different faults data called machine learning. After computer learn about the featured of faults data then we can give the test data. Since the data has the prior knowledge about the data it can train the data without human help. Therefore, it will automatically classify the training without the human help.

In Fig. 13, Fig. 14 and Fig. 15 shows the confusion matrix of the results.

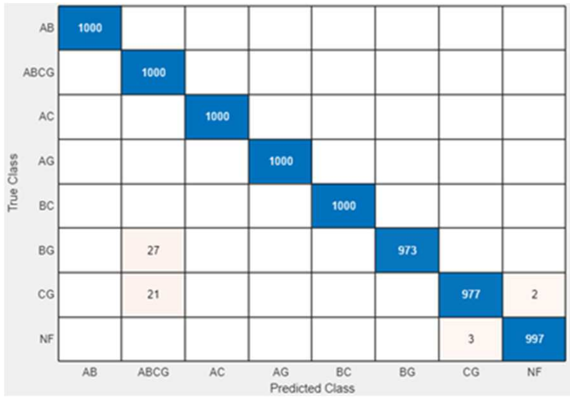

Fig. 13. Number of observations

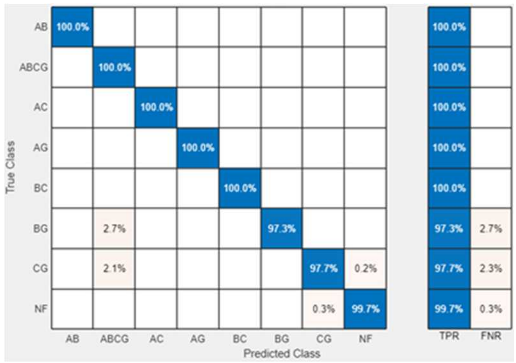

Fig. 14. True Positive Rates (TPR) False Negative Rates (FNR)

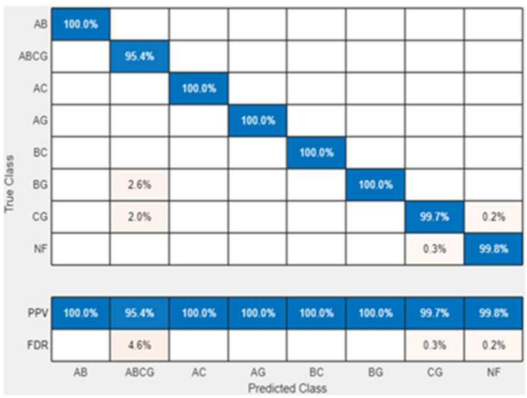

Fig. 15. Positive predictive Values (PPV) False Discovery Rates (FDR)

The class response is the various fault conditions whereas the predictor in this work is the electromagnetic torque, stator current and rotor current. After loading the dataset in classification learner apply and stated session, then started training data based on all SVM learning algorithm. The results shows that the learning algorithm with the highest accuracy in prediction time is Cubic SVM and Gaussian SVN as shown in Fig. 16.

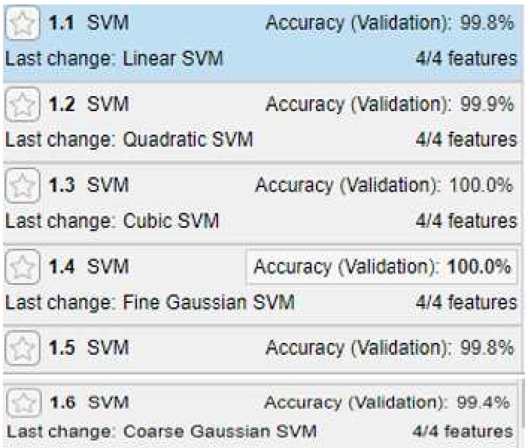

Fig. 16. SVM Learning algorithm

The rows on the confusion matrix plot in Fig. 15 represent the output class, or anticipated class, while the columns represent the actual class (Target Class). The diagonal cells relate to accurately categorized observations. The off-diagonal cells are associated with observations that were misclassified. In each cell, the number of observations and the proportion of all observations are displayed. The percentages of all the defects that are correctly and wrongly assigned to each class are displayed in the column on the far right of the plot. The accuracy (or positive predictive value) and false discovery rate are common names for these measurements. The percentages of all fault conditions belonging to each class that are correctly and wrongly classified are displayed in the row at the bottom of the plot. These measurements are frequently referred to as the false negative rate and recall, respectively. The overall accuracy is displayed in the cell in the plot's lower right corner. In Fig. 16, the first two diagonal cells show the number and percentage of correct classifications by the trained network. Faults AB, AC,AG,BC,BG were classified correctly by 100%. NF was classified 99.7% and 0.3% was incorrectly classified. ABCG was 95.4 correctly classified and 4.6% incorrectly classified. Both fault CG and BG were correctly classified by 97.3% and incorrectly classified by 2.7%.

IV. Conclusion

In this work, an induction motor model was designed and developed using MATLAB Simulink. This model was simulated under the following conditions: normal conditions and by implementing different fault between any phase and ground. The proposed model was able to display different faults characteristic curves of the electromagnetic torque, stator current and rotor current under various fault conditions. The simulated faults are viz. AB, AC, AG, BC, BG, CG, and ABCG. The dataset comprises of 8000 different fault conditions. The simulated signal was then used to extract the dataset from the wave signals. The dataset was used for training in the classification learner app using the SVM learning algorithm, and the SVM with the highest training at prediction with time was found to be the Cubic and Fine Gaussian SVM with an accuracy validation of 100%.

References

[1] X. Liang, M. Z. Ali and H. Zhang, "Induction Motors Fault Diagnosis Using Finite Element Method: A Review," in *IEEE Transactions on Industry Applications*, vol. 56, no. 2, pp. 1205-1217, March-April 2020, doi: 10.1109/TIA.2019.2958908.

[2] R. Jigyasu, A. Sharma, L. Mathew and S. Chatterji, "A Review of Condition Monitoring and Fault," *Second International Conference on Intelligent Computing and Control Systems (ICICCS) IEEE*, pp. 1713-1721, 2018.

[3] P. Kumar and A. S. Hati, "Review on Machine Learning Algorithm Based Fault Detection in Induction Motors," *Archives of Computational Methods in Engineering* 28(3), pp. 1929-1940, 2020.

[4] K. N. Gyftakis and A. J. M. Cardoso, "Reliable Detection of Stator Interturn Faults of Very Low Severity Level in Induction Motors," in *IEEE Transactions on Industrial Electronics*, vol. 68, no. 4, pp. 3475-3484, April 2021, doi: 10.1109/TIE.2020.2978710.

[5] H. Guo and M.-K. Liu, "Induction motor faults diagnosis using support vector machine to the motor current signature," *In 2018 IEEE Industrial Cyber-Physical Systems (ICPS)*, pp. 417-421, May 2018.

[6] M. Z. Ali, M. N. S. K. Shabbir, X. Liang, Y. Zhang and T. Hu, "Machine Learning-Based Fault Diagnosis for Single- and Multi-Faults in Induction Motors Using Measured Stator Currents and Vibration Signals," in *IEEE Transactions on Industry Applications*, vol. 55, no. 3, pp. 2378-2391, May-June 2019, doi: 10.1109/TIA.2019.2895797.

[7] Thango, B.A. On the Application of Artificial Neural Network for Classification of Incipient Faults in Dissolved Gas Analysis of Power Transformers. *Mach. Learn. Knowl. Extr. 2022*, 4, 839-851. https://doi.org/10.3390/make4040042.

[8] Targets (no date) Plot classification confusion matrix - MATLAB. Available at: https://www.mathworks.com/help/deeplearning/ref/plotconfusion.html;jsessionid=d591f54688f2f9b2267aa79ec794 (Accessed: October 31, 2022

Determining an Induction Machine's Torque-Speed Curve from an Audio Spectrogram Recorded During Run-Up

James Braid
School of Electrical and Information Engineering
University of the Witwatersrand
Johannesburg, South Africa
james.braid@wits.ac.za

***Abstract*—This paper presents an alternative technique for the determination of an induction motor's torque-speed curve. Normally done using a handheld tachometer, a storage oscilloscope and associated paraphernalia, an audio recording (in the form of a spectrogram) of the machine running across its full speed range, was instead taken on-site using a smart phone. Since the sound components of the machine are directly proportional to its speed, one clear audio harmonic was chosen, isolated and processed into an equivalent speed-vs-time trace. The method worked surprisingly well whilst the machine was producing sound at speed, however the audio levels close to zero-speed dropped away and proved problematic, being drowned out by the environmental background noise. It was therefore necessary to employ a curve-fitting technique to interpolate the zero-speed point, critical for the scaling of the torque-speed curve by the locked-rotor torque. Although this was successfully done by trial-and-error, it is postulated that in future, by knowing the number of parallel branches in the rotor equivalent circuit (i.e. single-cage or double-cage) and hence the anticipated shape of the torque-speed curve, the order of the curve-fitting polynomial can be constrained, greatly simplifying the curve-fitting procedure.**

***Index Terms*—induction motor, torque-speed curve, spectrogram, curve-fitting**

I. Introduction

The work presented here stemmed from the need to verify the torque-speed curve of a 0.5 MW, 2-pole squirrel cage induction machine, on site, for Actom Large Machines (Benoni), as part of the battery of commissioning tests, in line with IEEE 112 standards [1]. The measurement technique employed in this instance differed from the one traditionally used in that, instead of a handheld tachometer being used to record a speed-vs-time trace, a spectrogram of the machine's sound, showing both the frequency components (related directly to shaft speed) and their intensities, plotted versus time, was recorded instead. This was achieved using a suitable smart phone application combined with the superior computational ability of the smart phone. The motivation for doing this was three-fold: 1.) the equipment traditionally used required assistants and was cumbersome to transport to site; 2.) the said equipment had been paced in long-term storage at the university and was unavailable; 3.) as an interesting academic exercise.

II. Description of Testing

To determine the torque-speed curve of the machine, three parameters are required: speed, acceleration and supply voltage, over its full speed range. Under no-load conditions and therefore only accelerating its own inertia, the machine is first run up to full-speed in one direction. The phase rotation of the supply voltage is then reversed so that the machine decelerates through the braking-region (i.e. "plugging" [2]), crosses the zero-speed point, and accelerates through the motoring-region to full speed in the opposite direction. The testing is done at a reduced voltage to prevent saturation effects from distorting the unsaturated performance measurements, and to allow a long enough testing period (over time) to record sufficient data points for post processing.

Traditionally, a speed-vs-time trace is produced by a handheld tachometer, held against the conical centre of the rotor's shaft. A simple opamp-based electronic differentiating circuit is used to produce an acceleration-vs-time trace, and both traces are fed into a digital storage oscilloscope. Plotting the two traces against each other results in an acceleration-vs-speed curve, not too unlike the actual torque-speed curve, assuming that the friction and windage losses are negligible (an acceptable assumption if the machine is mechanically uncoupled from its load). Since the torque produced by an induction machine is proportional to the square of the supply voltage (and hence is very sensitive to it) [1], a voltage-vs-time trace is simultaneously recorded using the oscilloscope. This signal is normally provided directly from the instrumentation transformer installed in the manufacturer's test-bed control room. By scaling the acceleration-vs-speed trace appropriately with the supply voltage trace, and then by the locked-rotor torque (at zero-speed), the machine's torque-speed curve is derived.

In this instance, a spectrogram (a plot of frequency and intensity versus time) was recorded from which a speed-vs-time trace was extracted. Since the vibration and hence sound emitted by the machine is inherently related to the rotational speed of the rotor, there is direct correlation between the spectrogram plot and the speed-vs-time function. The largest source of the machine's sound, due to windage, comprises (integer multiple) harmonics related to the number of impeller blades, and hence the shaft's speed, providing several "speed traces" from which to choose from. During pre-testing, it was found that the location of the recording device plays an important role in the success of this method: any position located within the forced-cooling airflow results in white noise drowning out the audio signals of interest - it was found that the surface of the cooling fan shroud acts as a good transmitter of sound and hence provides the ideal location. Fig. 1 shows the author recording the spectrogram at this location.

Fig. 1. Recording the machine's sound in close proximity to the fan's shroud, but out of the axially-directed airflow.

Although the principal advantage to this method is the simplicity of the equipment required and lack of physical coupling to the machine, the major disadvantages of recording an audio trace are the lack of any sound near to the zero-speed point (from literature, a common problem with all techniques yet critically important for applying the locked-rotor scaling value), and the large amount of background noise within the factory environment that significantly reduces the amount of usable data points in this region. A lesser disadvantage of this method is the increased post-processing required, to derive an acceleration-vs-time trace, which now needs to be derived mathematically, by computing the derivative of the speed-vs-time trace - this was traditionally done in real-time by an opamp differentiator circuit.

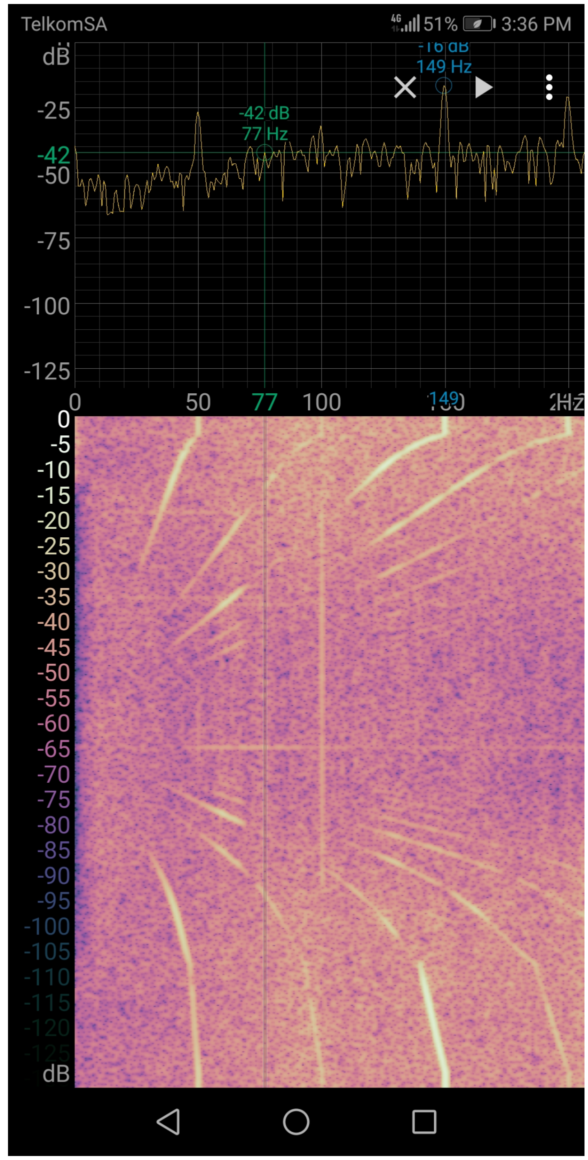

Fig. 2. An example of the recorded output showing the real-time FFT analysis at the top, and the recorded spectrogram (over time) below that.

III. Contextualisation

A brief review of literature suggests that the problem in question has been of interest for decades; Cormack's work undertaken in the mid-1950s, provides a valuable summary of emerging techniques of that era, citing two papers (the earlier one from the 1930s) in which the "traditional method" of using a shaft-connected tachometer, as presented above, was described [3]. He also cites a paper in which an early form of "digital" process was experimented with: using high- and low-speed cameras to capture a reference point on the rotor's shaft, and hence deduce the angular speed (and subsequently the acceleration) from the period between photographs. In his own work, he develops a "deflection transducer" that measures the torque produced by the machine, mounted in a rocking cradle, reacting against a restoring spring. Although this setup is inappropriate for on-site testing of a machine, his signal analysis method is fundamental: the x-axis of a CRT is supplied with a speed-vs-time signal provided by a shaft-coupled permanent magnet generator, and the y-axis of the CRT is the measured deflection due to the torque reaction i.e. effectively a plot of acceleration-vs-speed. This method skips the noise-prone differentiation function, reducing the processing to a simple and robust single-step function. In his conclusion, as well as of those cited, all are in agreement that their methods of measuring the torque at and about zero-speed prove to be inaccurate and hence problematic, since the not-insignificant harmonic torques, as a consequence of the stator-rotor slot combinations, are most profound at low speeds. The work presented here shares this same short-coming and merely presents an alternative but more convenient method of deriving a speed-vs-time trace.

Moving forwards in time, Yamey and Robinson in the mid-1970s, present an early version of a true digital acceleration sensor, to derive the torque, using a rudimentary pulse counter to encode the rotor's position [4]. During a fixed period of one second, the number of pulses counted was used to determine the angular speed, and hence acceleration. Once again, they concluded that low speed measurements proved inaccurate (particularly the period containing the direction reversal of rotation at zero-speed) and that to gain accurate results over the full speed range, the acceleration time needed to be in the order of tens-of-seconds, achieved by conducting the experiment at reduced voltage.

The focus of more current-day research is into the sensorless measurement of the speed and torque, and similarly, the estimation of various machine parameters, whilst in operation. As an example, Ahmed and Toliyat present a sensorless speed transducer that relies on induced harmonics in the motor's line current, due to saliency effects in the machine's assembly, to provide a suitable speed signal [5]; the work presented here is in principle very similar, but relies on the audio harmonics produced by the machine as the source of the speed signal. As another example, Kliman et al demonstrate a sensorless torque transducer, which estimates the airgap torque from the measured line currents and known machine parameters [6]. Although reasonably accurate (to within say 5%), they highlight the issues of relying on assumptions, particularly regarding the magnetic symmetry of the machine, crucial to the calculation of the airgap torque; additionally, saturation effects and core losses are entirely ignored. This supports the case of taking a practical measurement, particularly for unique, hand-built machines, where the impacts of manufacturing tolerances and minor defects need to be included. The foundation for the technique presented here is therefore laid.

IV. Measurements Recorded

The "Spectroid" application was downloaded and installed onto a smart phone; Fig. 2 shows an example of the output screen, taken after a recording had been completed. The graph at the top shows the real-time Fast Fourier Transform (FFT), plotting the sound intensity (in dB) on the y-axis and frequency on the x-axis. From initial testing on site, the first four audio harmonics showed the most promise and hence the upper frequency limit was set to 200 Hz. The sampling frequency of the device was set to 96 kHz and an appropriate FFT algorithm was selected. The recording took place over about 80 seconds and approximately 1250 sample points were recorded within this duration. This gives a sampling average over about 60ms per sample.

The plot in the lower half of Fig. 2 is the recorded spectrogram. The x-axis shows the frequency scale (low frequencies to the left, high frequencies to the right); intensity (dB) is indicated by the colour scale (on left hand side: soft is dark, loud is white), and the y-axis is the time scale: the plot scrolls from bottom to top, with the latest recorded data appearing at the bottom (i.e. rotated by 90°when imagining a time-scrolling recording device).

Immediately apparent from the plot in Fig. 2 is the large amount of background noise, indicated by the pink / purple coloured areas. Despite this, the machine's harmonics are still clearly audible (louder, brighter) above the background noise, except when the machine operates close to zero-speed, where the traces fade into the noise floor (approximately half way up). The distinct vertical line at 100 Hz is the dominant component of the background noise, generated by the loud electromagnetic hum from the nearby generating set, being supplied with 50 Hz AC. The feint horizontal line, about half way up, was an impulse created by the author (by tapping the device), to indicate more or less where the direction cross-over point is located i.e. zero-speed point.

Since the machine under test was relatively small in power rating and the test requires it to be conducted at reduced voltage, it was not crucial to record the supply voltage for this particular machine, as this could be well controlled by the test-bed operator. Several pre-test runs were done to experiment with the settings above and to choose an appropriate voltage, sufficiently high so as to cover the full-speed range over the 80-second period, and sufficiently low so as to avoid saturation effects. In discussions with the test-bed operator, this was typically about 25% of the machine's rated value, and remained relatively constant over the full speed range.

V. Data Analysis

After the testing session, the spectrogram plot was exported from the device and imported into a mathematical processing package. To make the spectrogram more interpretable and resemble a more traditional speed-vs-time plot, the image was first rotated by 90°counter clockwise such that frequency (read "speed") was on the y-axis and time was on the x-axis, and secondly, split into two parts: reverse- and forward- rotation, with the reversed portion being inverted to show a negative speed. Fig. 3 shows the re-mapped spectrogram.

The four lowest harmonics (fundamental: 50 Hz, second: 100 Hz, third: 150 Hz and fourth: 200 Hz) are clearly evident in both Fig. 2 and Fig. 3. Since all the harmonics are related by an integer multiple to one another, and all are directly related to the shaft speed, the data points (white "X"s) from all the

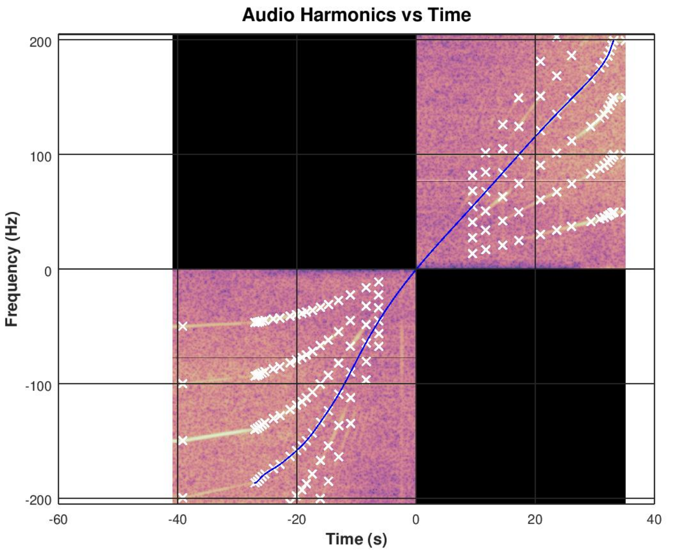

Fig. 3. Spectrogram of machine's sound, running from full-speed in the reverse direction (left-portion), to full-speed in the forwards direction (right-portion). Extracted data points are marked with white "X"s; the blue curve shows the best-fit polynomial through the 4th-harmonic data points.

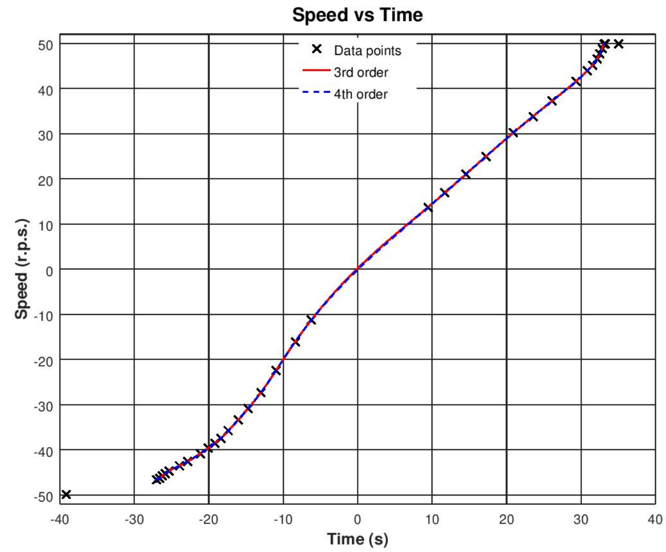

Fig. 4. Extracted speed-vs-time curve showing a 3rd and 4th order best-fit spline (red 3rd order curve almost perfectly overlaid by blue 4th order curve, except about the zero-speed point).

traces were used to determine a best-fit spline (blue curve) through the data.

There are four distinct areas of operation evident: firstly, the machine is run at full-speed in the reverse direction (at time t = -40s). Then, whilst the phase rotation was being reversed, the machine coasts, slowing down slightly towards t = -27s. Upon re-energisation, the machine produces a braking torque (slip = 2) and the machine rapidly decelerates towards zero-speed (t = 0s, slip = 1) where it crosses over from reverse rotation to forward rotation. It then accelerates in the forward direction, reaching full speed (t = 33s, slip = 0), whereafter it continues to run at no-load (t = 35s). The substantial pull-out torque is clearly evident by the very steep climb in speed, towards the end of the trace (t = 32s). Since the torque characteristics are of interest, the coasting and free-running periods are ignored, and the spline fit (blue curve) is constrained to the period between these two transition points as shown.

Fig. 4 shows the extracted speed-vs-time plot; the corresponding data points (from Fig. 3) are shown with the black "X"s and the blue curve shows the best-fit spline curve through the data points of interest - the point at the extreme left is coasting and the point at the extreme right is free-running. Clearly evident in this figure is the lack of data points about the zero-speed point (t = 0s); this required a substantial amount of post-processing to determine the best-fit curve. Not clearly shown in the figure is a second (red) best-fit curve, overlaid by the blue curve; the two curves (3rd and 4th order polynomials respectively) both fit the data points very well and converge well on the anticipated curve through zero-speed, offering confidence in the solution.

With an algebraic function for speed-vs-time now explicitly known, the derivative (acceleration) is very straightforward to compute and is completely noise-free (unlike the result of doing this electronically as in the past).

Finally, ignoring friction and windage losses, the resultant torque-speed curve is determined by scaling the acceleration function by the measured locked-rotor torque (at zero speed); with the voltage assumed to remain constant, there was no need for any further scaling, other than up to rated voltage.

VI. Results

A. Torque-vs-Speed Curve

An unsaturated locked-rotor torque value was provided by the manufacturer from previous tests; the resultant torque-speed curve for the machine is therefore shown in Fig. 5 below.

From the figure, the 3rd and 4th order polynomials fit the data points (black "X"s) tightly and correlate well with one another, except on either side of the zero-speed point, where slight differences are evident. However, good correlation exists at zero-speed itself, which is critical for the scaling by the locked-rotor torque. The red and blue circles indicate the nodes where the corresponding polynomial segments have been spliced together. The graph shows a very high pull-out torque and compares well with the manufacturer's design data.

B. Critical Analysis of Experimental Technique Used

Once a basic testing methodology had been decided upon, the testing itself was quick and straightforward. A fair amount of prior experimentation was done in the university's laboratory, testing the methodology on the small machines there. Unfortunately, this did not prove valuable as the laboratory environment (very quiet) and small machines tested (only a few kW) differed significantly from the one in this testing instance.

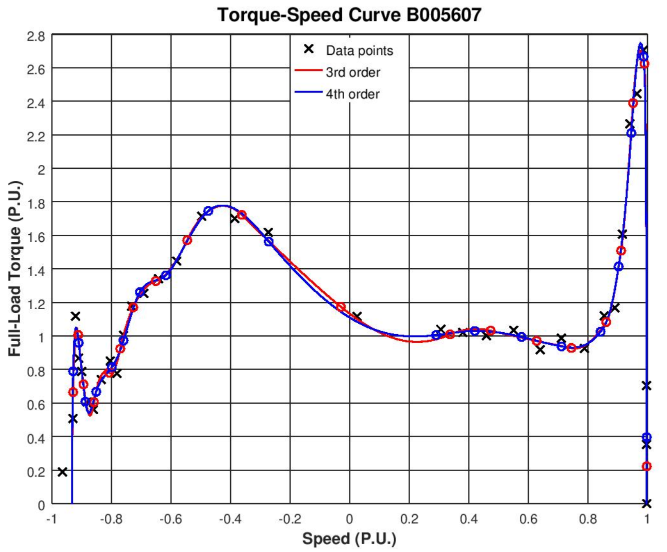

Fig. 5. Resultant torque-speed curve for the machine under test, across the full speed range.

The background noise in the laboratory was very low, resulting in the Signal-to-Noise Ratio (SNR) of the small machine's sound to be very good. This provided usable data virtually right up to the moment of zero-speed. In contrast, the on-site location within the factory environment was very challenging and the SNR was poor. This is evident in Fig. 3 (and consequently Fig. 4) where, due to the overwhelming background noise, no usable data points could be extraced from about t = -6s to t = 9s i.e. approximately 15s of "silence" during, arugably, the most critical range of speed. This gave rise to the need for the intensive curve-fitting process since trendlines through the other data points shown in Fig. 3, would clearly converge through a single point (at zero speed).

In an attempt to indicate where the zero-speed point was reached during the recording, the feint vertical line at t = -3s indicates where the author tapped the smart phone when the shaft appeared stationary. However, from Fig. 3, the mismatch between the apparent zero-speed point and the actual one (at t = 0s), is obvious. Two reasons for the error are postulated: Firstly, the very slow deceleration results in the (very large diameter) shaft rotating extremely slowly prior to the zero-speed point and therefore the exact stationary position is hard to accurately verify by eye - in contrast, the smaller machines tested decelerated much quicker and it was quite easy to see when the (small diameter) shaft had stopped. Perhaps the assistance of a stroboscope here would be beneficial. Secondly, a moment of stiction in the large machine would have slightly delayed the start of the acceleration stage, resulting in the shaft remaining stationary for a pause, and hence contributing to the error.

Nonetheless, despite the challenges above, the pre-testing provided the necessary expertise in the use and setting up of the spectrogram application, which was beneficial.

It can be argued that the convenience in the simplification of the equipment and ease of testing came at the expense of the extra time and effort in the post-processing required. The major benefit of deriving a well-fitting polynomial is that the (troublesome) differentiation process results in an explicit and noise-free algebraic function, making the exercise worthwhile. To reduce the complexity of the post-processing, it is proposed that a "grey box" modelling approach be implemented in that, one already knows the expected shape of the torque-speed curve (primarily dependent on known functions of slip and rotor resistance) and therefore the number of possible polynomial best-fit curves, and their order, can be immediately constrained - in this instance, this was experimentally determined by trial-and-error to be 3^{rd} or 4^{th} order. It is speculated that this order is dependent upon the number of parallel branches in the rotor circuit; and could be an interesting academic exercise.

Although the technique worked well in this application, for machines exhibiting synchronous- or harmonic- torques, it is doubtful that the number of data points would be sufficient to accurately detect these. Certainly, polynomials of a much higher order (or an increased number of spliced lower-order polynomials) would be required to plot these. This requires further investigation and experimentation in the university's laboratory and would be interesting future research.

For larger machines or machines with less simple torque-speed curves, maintaining (and hence assuming) a constant voltage during testing, may prove problematic and therefore a voltage trace really should be recorded. With the method postulated here, this is not possible at the moment and some form of synchronised voltage recording method would need to be investigated.

Since an induction machine's torque is dependent upon its speed (due to the slip), the work presented here in deriving a torque-speed curve is limited to induction motors only. However, similar methods could be used to empirically model the responses of other types of motors, combined with their drives and control schemes, for use in greater system models.

VII. Conclusion

A novel technique was used to determine the machine's speed-vs-time plot, and hence acceleration, based on an audio spectrogram recording of the machine's sound, whilst running across its full speed range. Although this simplified the on-site test equipment required and made the testing very straightforward, it came at the expense of a large post-processing exercise. Nonetheless, the advantages and disadvantages are discussed here and the exercise proved very interesting from an academic point of view. It is proposed that, by knowing some details of the machine's rotor equivalent circuit, and hence the shape of the anticipated torque-speed curve, a "grey-box" modelling approach can be adopted and the curve-fitting process greatly simplified.

Acknowledgment

I would like to extend my sincere gratitude to Mr Derek Wood at Actom Large Machines for allowing this work, and the data herein, to be used and published here.

References

[1] IEEE Standard Test Procedure for Polyphase Induction Motors and Generators, in IEEE Std 112-2017, pp. 1-115, 14 Feb 2018.

[2] P.C. Sen, Principles of Rotating Machines and Power Electronics. John Wiley & Sons, 1989.

[3] W. Cormack, "The measurement of the torque slip curves of induction motors", in Transactions of the South African Institute of Electrical Engineers, vol. 46, no. 5, pp. 127-142, May 1955.

[4] C. G. Yamey and P. B. Robinson, "A digital accelerometer for torque-speed studies", in Transactions of the South African Institute of Electrical Engineers, vol. 65, no. 9, pp. 207-209, Sep 1974.

[5] S. Ahmed and H. A. Toliyat, "A novel speed sensorless technique for obtaining the speed-torque characteristics of induction motors for commissioning", IEEE International Electric Machines and Drives Conference (IEMDC), 2001, pp. 905-910.

[6] G. B. Kliman, R. A. Koegl, W. J. Premerlani and T. B. Breen, "A demonstration of a sensorless torque meter for AC motors," IAS '96. Conference Record of the 1996 IEEE Industry Applications Conference Thirty-First IAS Annual Meeting, 1996, vol. 1, pp. 633-637.

The Analytical Study of the Controlled Switching of an AC Vacuum Circuit Breaker for Fault Interruption

Nadeem Goolam Hoosen
Department of Electrical Power Engineering, Faculty of Engineering and the Built Environment
Durban University of Technology
Durban, South Africa
20502637@dut4life.ac.za

Evans Eshiemogie Ojo
Department of Electrical Power Engineering, Faculty of Engineering and the Built Environment
Durban University of Technology
Durban, South Africa
evanso@dut.ac.za

Nelson Mutatina. Ijumba
School of Electrical Engineering
Faculty of Engineering
Univeristy of KwaZulu-Natal
Durban, South Africa
mutatinak@gmail.com

Abstract - This paper presents the findings from the analysis of an indoor Alternating Current (AC) Medium Voltage (MV) Vacuum Circuit Breaker (VCB) during fault interruption when connected to a MV power line. The circuit breaker fault interruption phenomenon was investigated during Phase-to-Earth faults. This concept was simulated using an electromagnetic transient program (EMTP). An analysis was conducted when advanced controlled switching (ACS) technology was applied to the circuit breaker to achieve current zero (CZ) tripping. CZ tripping during fault interruption was successfully achieved, with the simulation results indicating a reduced arcing current, voltage and a reduction in transient recovery voltage (TRV). The results demonstrated an improved lifecycle of the circuit breaker when compared to a non-controlled conventional circuit breaker.

Keywords—arcing, controlled switching, current zero, interruption phenomena, medium voltage, vacuum breaker.

I. Introduction

In high voltage applications, the technology called controlled breaker switching was initially developed to control the circuit breakers connected to unloaded systems. For this application the breaker closed at the earliest CZ point to prevent inrush currents. This technology was further developed into an ACS which factors in its environmental conditions. This includes the idle time and temperature when energising the circuit breaker. The implementation of controlled switching technologies ensured that the circuit breaker was energised at a time with the least effects of arcing and inrush currents which is caused by residual flux [1]. The controlled switching technologies was also accomplished in high voltage fault interruption, where CZ tripping was implemented to reduce the effects of arcing currents. This possess an adverse effect on the circuit breaker arcing contacts which results in a reduced equipment lifespan [2].

The use of air blast and Sulphur hexafluoride (Sf6) gas interruption mediums for outdoor circuit breakers is primarily used in the implementation of controlled switching technology [3]. However, the implementation of ACS using an indoor vacuum circuit breaker has not been established. The AC Medium Voltage VCB using ACS technology was implemented in this study. The approach was prompted by the fact that majority of faults occur on the distribution power system, which consequently contribute to a typical analysis of more than 46 % of circuit breakers on a power system [4, 5]. These findings have led to an analysis on the lifecycle of a MV circuit breaker for fault interruption by adopting ACS to interrupt faults. The purpose was to produce results that:

- Make a significant impact on the majority of a power system rather than just the 46% which is attributed to the high voltage zone of the power system.
- Effectively improve the circuit breaker useful life (UL) hence reducing costs on power utilities.

This paper investigates the lifecycle improvements of the 11 kV indoor VCB using ACS. The VCB is connected to its load via a 11 kV power line which is represented by the power circuit shown in Fig. 1. A Phase-to-Earth short circuit fault was applied to this power circuit. The EMTP was used for the simulation and the results obtained for the VCB fault interruption phenomena. This was in terms of the interruption time, arcing current, arcing voltage, transient recovery voltage and current chopping for both the ACS and the non-controlled VCB switching.

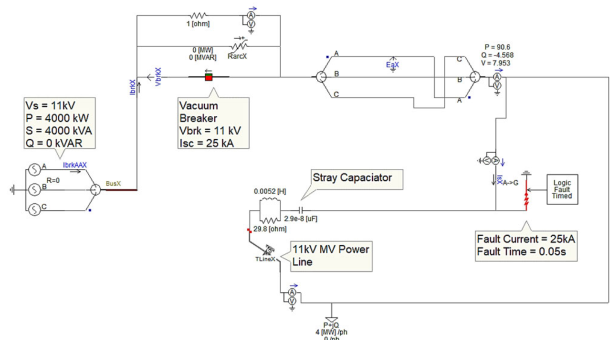

Fig.1. Controlled Switching Power Circuit Diagram

The analysis and comparison of results obtained aided the understanding of the impact that the controlled switching technology has on the VCB during fault interruption when compared to a non-controlled VCB. This was relevant to the lifecycle improvement [6, 7].

II. Methodlogy

ACS integrated logic was created within the EMTP. This program uses the principles of summation and comparator logic to provide swift fault clearing times coupled with reduction in arcing effects and inrush currents [8, 9]. The model comprises of several black box models. One of these black box models is the predicted controlled trip time logic module which extrapolates the fault current instant time results using the logic derived from (1).

$$T_{If}\left(t\right) = I_F \cdot \left[sin(\omega \cdot t + \alpha - \varphi) - sin\left(\alpha - \varphi\right) \cdot e^{(-t/\tau)}\right] \quad (1)$$

Where, T_{If} is the fault current logic instantaneous time, I_F is the fault current time, t is the time, ω is the power system frequency, α is the phase angle of the phase voltage when the fault is initiated, L is the source to fault inductance, R is the source to fault resistance and τ is the time constant of the symmetrical transient component of fault current.

The fault time results from (1) are used as an input in (2) to obtain the overall predicted CZ trip time (T_{co}) that was derived from a hypothesis which forms part of the ACS logic.

$$T_{co} = \left[\left(T_{If}\right)\right) + \left(\Delta T_{temp} + \Delta T_{Idle} + T_{std}\right)\Big]\Big|\Big[\left(T_{If}\right)\Big) + \left(\Delta T_{temp} + \Delta T_{Idle} + T_{std}\right)\Big]\Big| + 0.01 \quad (2)$$

Where, T_{If} is the fault current logic instantaneous time, ΔT_{temp} is the compensation time based on temperature times, ΔT_{Idle} is the compensation time based on idle time, T_{std} is the standard VCB opening time.

The predicted CZ controller is the core black box module which determines the future CZ trip time considering the fault current time as a reference point. This coupled with the ACS summation black box model which summates the idle, temperature and standard time delays is shown in Fig. 2.

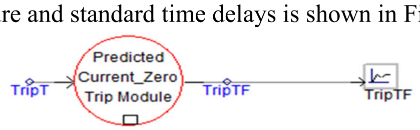

(a)

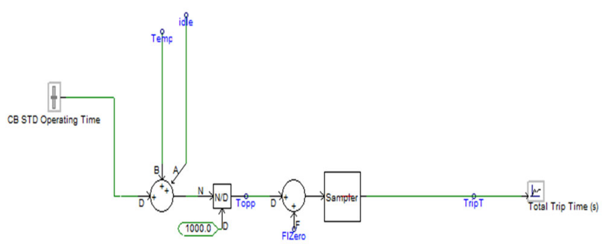

(b)

Fig 2. Black box Models: Predicted CZ Trip (a), Advanced Controlled Summation Black Box Module (b)

The VCB delays in conjunction with the fault time instant is processed to ascertain the earliest CZ trip time. The trip time results use the logic to facilitate only CZ tripping. The predicted CZ controlled logic from a hypothesis was implemented on a Phase-to-Earth fault with earth connection by synchronizing it to the trip commands of phase A of the 3-phase 11 kV indoor VCB using EMTP. The remaining breaker poles operate at no more than half a cycle apart in a RYB/ABC sequence.

The VCB interruption phenomena results was compared and analysed using the EMTP. The thermal and energy results were transposed into the Arrhenius equation (3) to measure the rate of change relevant to the VCB lifespan with reference to the temperature and energy of the arc [6, 7].

$$k = e\frac{E_A}{RT} \quad (3)$$

Where E_A is the energy produced by the arc in kJ mol^{-1}, R is the gas constant at 8.31 $JK^{-1}mol^{-1}$, T is the Temperature of the Arc in ℃, e is the base of natural logarithm and K is the Kinetic Rate constant in M^{-1}. S^{-1}.

III. SIMULATION RESULTS

The simulation for the ACS was conducted at current angles namely 30°, 60° and 90° to produce results that was used for analysis of the VCB interruption phenomena to determine the impact on the VCBs lifecycle. The simulated results for the fault interruption phenomena are as follows:

A. *Interruption time*

In Fig. 3 to Fig. 5, the IspX represents the conventional VCB curve while the Isp represents the ACS graph results. The advanced controlled VCB interruption time deviates from the conventional VCB at current interruption. The ACS interruption time as shown in Fig. 3 to Fig. 5, achieved CZ interruption. However, the conventional VCB trips at any current instant that is dependent on its interruption time.

The fault current angles between simulations have proven to have an impact on the current interruption angle and current interruption trip time for non-controlled switching. However, for the controlled VCB, the current interruption time is the only parameter impacted due to the fault trip angle with all the simulated interruptions occurring at CZ [3]. The interruption time in Fig. 3 for IspX and Isp is 0.057 s and 0.071 s at a 30° fault angle. From Fig.4, the interruption time for IspX and Isp is 0.049 s and 0.06 s at a 60° fault angle. Lastly, in Fig. 5 the interruption time for IspX and Isp is 0.039 s and 0.05 s at a 90° fault angle

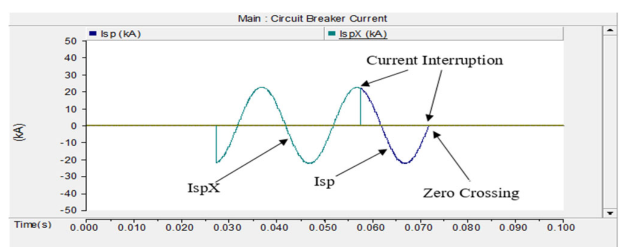

Fig.3. SN1 Controlled Switching Vs Conventional Interruption time.

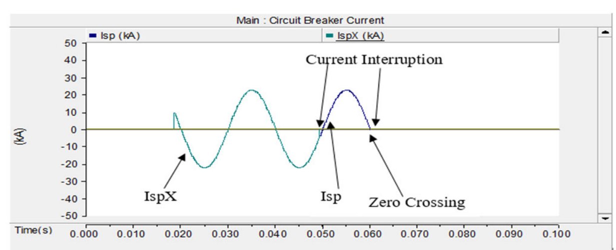

Fig.4. SN2 Controlled Switching Vs Conventional Interruption time.

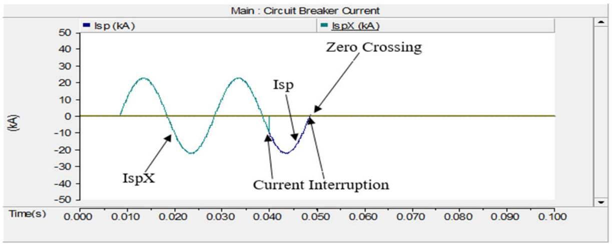

Fig.5. SN3 Controlled Switching Vs Conventional Interruption time.

B. *Arcing Voltage and Current*

The arc voltage and arc fault current compared between the conventional and ACS VCB operations for all simulations are shown in Fig. 6 to Fig. 8. VaX and IspX represents the conventional graphs while Va and Isp represents the ACS graph results for the arc voltage and arc current. Fig. 6 illustrates the arc voltage VaX and Va of 9.95 kV and 8.82 kV respectively while the arc current for IspX and Isp are 24.76 kA and 22.34 kA. Fig. 7 illustrates the arc voltages for VaX and Va are 9.97 kV and 8.89 kV while the arc current for IspX and Isp are 24.64 kA and 22.11 kA. Lastly in Fig. 8, the arc voltages for VaX and Va are 9.93 kV and 8.95 kV while the arc current for IspX and Isp are 24.89 kA and 22.28 kA.

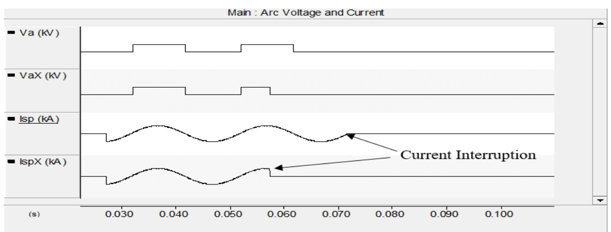

Fig.6. SN1 Controlled switching vs Conventional Arc Voltage and Current.

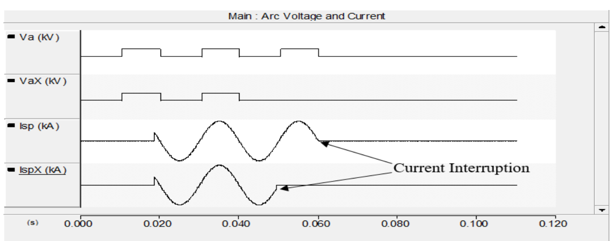

Fig.7. SN2 Controlled switching vs Conventional Arc Voltage and Current.

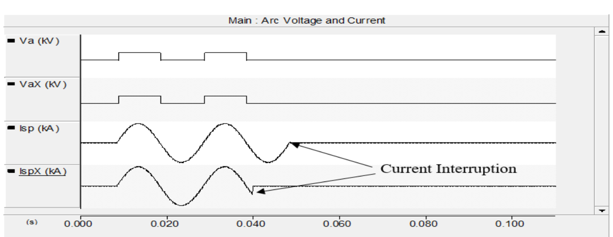

Fig.8. SN3 Controlled switching vs Conventional Arc Voltage and Current.

When the arc fault current results of SN1 to SN3 for ACS are compared to the conventional results in Fig. 6 to Fig. 8, the arc current output produced had decreased by an average of 10 % in the ACS. The major influence on the lower arc fault current output is the ability of the ACS to interrupt the VCB at CZ [8].

The arc quenching capabilities of the conventionally operated VCB was found to be 10 % higher when compared to the ACS vacuum circuit breaker. This is proportional to the arc fault current produced. The withstand fault current capabilities for both the ACS and conventional switching VCB was below the withstand capabilities of 600 A/µs of the selected VCB rating.

The simulated output VCB arc voltage for SN1 reduced by 11% while the percentage decrease for SN2 was 12% and for SN3 was 10 % when ACS was implemented. A significant improvement is present in reduction of VCB arc voltage when CZ tripping is implemented. The regulated arc voltage results between simulations are within a tolerance range of 1% for ACS. The CZ interruption increased the VCB resistance within the contact's arc gap therefore increased its ability to trip swiftly while reducing the heat losses produced from high arc voltages [10]. Overall the ACS vacuum circuit breaker produced lower arc voltage and current results when compared to a conventional switching VCB.

C. *Current Chopping*

The chopping current comparison between the conventional and ACS VCB operations for all simulations are shown in Fig. 9 to Fig. 11. IflaX represents the conventional graphs while Ifla represents the ACS graph results. In Fig. 9, the peak chopping current for IflaX is 0.15A whereas Ifla is -0.03 nA. The duration of the current chopping for IflaX is 0.002 s while Ifla is 0.001 s. In Fig. 10, the peak chopping current for IflaX and Ifla are 0.5 A and 0.065 nA. The duration of the current chopping for IflaX is 0.0034 s and for Ifla it is 0.001 s. Lastly in Fig. 11, the peak chopping current for IflaX is indicated as 0.6 A whereas Ifla is 0.01 nA. The duration of the current chopping for both IflaX and Ifla are 0.0024 s and 0.001 s respectively.

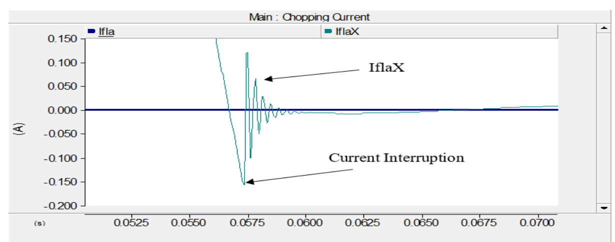

Fig.9. SN1 Controlled switching vs Conventional Chopping Current.

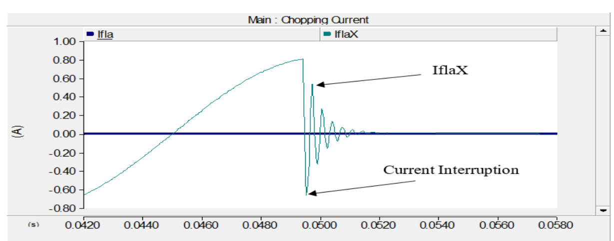

Fig.10. SN2 Controlled switching vs Conventional Chopping Current.

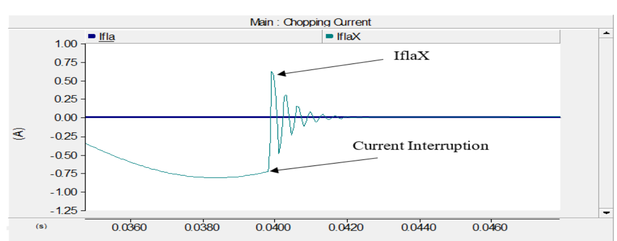

Fig.11. SN3 Controlled switching vs Conventional Chopping Current.

The controlled VCB chopping current is much smaller than the conventional chopping current results for Fig. 9 to Fig. 11 with values not exceeding 0.065 *nA*. Hence it's not visible on the simulated graphs and shown as 0 A when compared to the conventional VCB chopping current results. The yields for ACS chopping current indicates a decrease in chopping current when using ACS. Effectively, the chopping current values when ACS was implemented reduced the duration and magnitude of the chopping current. This was due to the interruption occurring at a lower current [11].

D. Transient recovery voltage

The TRV compared between the conventional and ACS VCB operations for all simulations are shown in Fig. 12 to Fig.14. EaX represents the conventional graphs of the TRV while Ea represents the ACS graph results. In Fig. 12, the TRV for EaX and Ea are 29.95 kV and 23.53 kV for a duration of 0.003 s and 0.001 s, respectively. The Rate of Rise of Recovery Voltage (RRRV) for EaX is 5.19e^{-4} whereas for Ea it is 4.71e^{-4}. In Fig. 13, the TRV EaX = 29.75 kV and Ea = 22.23 kV. The duration of the TRV for EaX = 0.004 s and Ea = 0.001 s. The RRRV for EaX = 5.35e^{-4} and Ea = 4.45e^{-4}. Lastly in Fig. 14, the TRV EaX = 23.37 kV and Ea = 13.73 kV. The duration of the TRV for EaX = 0.004 s and Ea = 0.001 s. The RRRV for EaX = 4.67e^{-4} and Ea = 2.75e^{-4}.

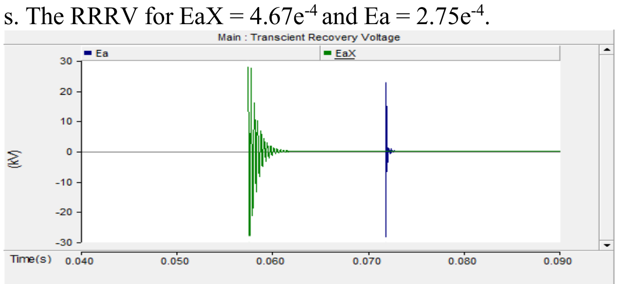

Fig.12. SN1 Controlled switching vs Conventional TRV

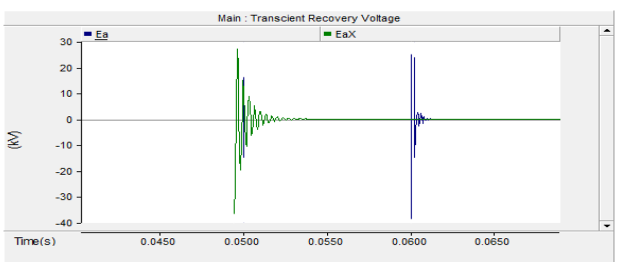

Fig.13. SN2 Controlled switching vs Conventional TRV

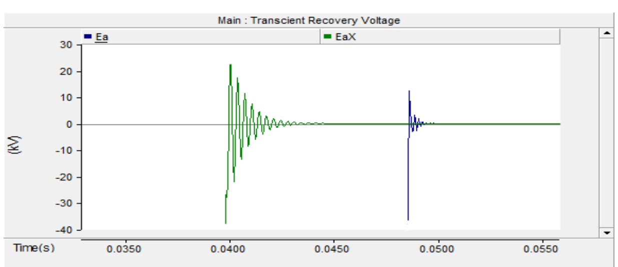

Fig.14. SN3 Controlled switching vs Conventional TRV

The magnitude of the TRV for ACS was decreased by an average of 12% for Fig. 12 to Fig. 14 when compared to the conventional VCB interruption. This is due to fault interruption occurring near CZ for conventional VCB switching rather than at CZ. The change in magnitude of the TRV for EaX for the conventional switching for Fig. 12 to Fig. 14 are no more than 3% when the fault current angle changes. These results indicate the fault current angle also has an influence on the TRV magnitude. The RRRV for the conventional VCB is 12% higher on average when compared to the ACS results. The RRRV is proportional to the TRV [12]. Hence, the percentage difference between the RRRV and the TRV remain the same for ACS and conventional switching. The VCB probability of gaining restrike voltage is reduced when the RRRV is reduced thus an improvement of 12% is favourable when using ACS. It was also observed that when the TRV peak increased, the time to peak is reduced as the short circuit fault was reduced. This also caused the RRRV requirements to increase in order to provide swift VCB trip times. Overall, ACS TRV is lower due to CZ interruption[13]

E. Temperature, Energy and Power of Arc

The simulated arcing temperature, energy and calculated power output results obtained are shown in Table I for conventional switching and in Table II for ACS.

TABLE I. CONVENTIONAL TEMPERATURE, ENERGY AND POWER OUTPUT RESULTS

Temperature, Energy and Power Output Results			
Simulation No. (SN)	***(P) - Arc Active Power (W)***	***Energy of Arc (J)***	***Peak Arc Temperature (°C)***
SN 1	3245	138834.18	7287.64
SN 2	3351	138541.57	7272.28
SN 3	3339	138635.71	7277.23

TABLE II. ADVANCED CONTROLLED TEMPERATURE, ENERGY AND POWER OUTPUT RESULTS

Temperature, Energy and Power Output Results			
Simulation No. (SN)	***(P) - Arc Active Power (W)***	***Energy of Arc Power (J)***	***Peak Arc Temperature (°C)***
SN 1	2303.00	98390.77	5164.70
SN 2	2245.00	92815.82	4872.06
SN 3	2233.00	92847.18	4873.71

The arc temperature results in Table I and Table II are within the expected VCB withstand capabilities rated for a period of 1s [14].Temperature rise for ACS was on average 32% lower than when conventional VCB switching was implemented. The arc energy produced was found to be the major influence on the temperature of the arc due to its proportionality [15]. This power of the arc relative to the energy of the arc during the VCB operation was calculated using equation (4) to produce the results obtained in Table I and Table II.

$$E = R.\ I^2.t \tag{4}$$

Where, t is the time period of current, R is the resistance and I is the current. The energy produced in relation to the temperature is represented in equation (5)

$$E = \lambda.\ T \tag{5}$$

Where, λ is a function of heat dissipation rate I_2t also known as hysteresis losses, T= the temperature. The above equations (4) – (5) demonstrates that for a constant current, an increased arc contact resistance will produce more arc energy therefore increasing the arc temperature [16]. The arc time duration for SN1 to SN3 in both conventional and ACS simulations decreased as the fault current angle increased.The lower temperature magnitude on the ACS together with the regulated rise to Peak Arc Time Instant (τ) effectively reduced the thermal rise of the arc within the VCB.

F. Circuit Breaker lifespan impact diagnosis

The Kinetic rate constant (k) results for conventional switching and ACS together with the lifespan expectancy in years of the ACS are shown in Table III.

TABLE III. KINETIC RATE CHANGE AND LIFESPAN RESULTS

Efficiency Output Results				
Simulation No. (SN)	***Conventional Rate Constant (k)***	***ACS Rate Constant (k)***	***% Rate Contact Change***	***Lifespan in Years***
SN 1	0.109744	0.113336	3.28%	0.7
SN 2	0.109750	0.100134	8.69%	1.7
SN 3	0.109732	0.100208	8.76%	1.8

The energy of the arc and peak arc temperature results obtained from Table I and Table II are used as a basis for transposition of values into the Arrhenius equation (3) to determine the circuit breaker kinetic rate contact results. The results in Table III are for breakers that operate at an average of 4 to 40 times a year with an average lifespans of 20 years [15].

The results produced for SN1 to SN3 shows an increase in lifespan expectancy of the VCB relevant to the decrease in energy and temperature for ACS. The lifespan expectancy was found to be dependent on the effects of the energy produced by the thermal rise which is impacted by the fault current angle and the magnitude of the current interruption. The best yields were at 90° which increased the lifespan by 1.8 years.

IV. DISCUSSION

Presented in the paper are the simulated results of the conventional VCB under fault operations when compared to the VCB using an ACS logic. Based on the simulations, the ACS, successfully tripped the VCB at CZ for fault interruption for all simulations. The average arc current had reduced by 10% and average arc voltage had reduced by 11% upon implementation of ACS. The change in chopping currents was found to be almost negligible when compared to the non-controlled conventional VCB. The reduction of the chopping currents for ACS had triggered the reduction of the TRV to an average of 12%. The overall power of the arc for ACS had reduced by an average of 32% due to the reduction in arc current at interruption and restrike voltage.

The results were subsequently transposed using the Arrhenius method for both conventional and ACS circuit breakers and the findings have indicated an average VCB UL improvement of 7% for the ACS VCB. However, the UL of the VCB over and above the implementation of advance controlled switching, was still dependent on the fault current angle and the environmental conditions of the VCB. Overall, the application of the ACS method was successful in increasing the UL of the breaker by a short duration . The average UL of a VCB is 20 years and by extending the lifecycle of the VCB by an average of the simulations completed, that being 1.4 years. The cost of replacement may be differed by 1.4 years which will have a significant impact on the annual capital expenditure budget for power utilities.

REFERENCES

[1] Smitha. K. S. and Abhilash. G. R, "Reduction of transformer inrush current by controlled switching method," 2019.

[2] Z. Huang, X. Duan, H. Wan, and J. Zou, "Improvement of breaking capability of vacuum circuit breaker using controlled fault interruption," in *2013 2nd International Conference on Electric Power Equipment - Switching Technology (ICEPE-ST)*, 2013, pp. 1-4.

[3] R. Thomas, "Controlled Switching of High Voltage SF6 Circuit Breakers for Fault Interruption," Bachelors Degree, Department of Electric Power Engineering, Chalmers University of Technology, Goteborg Sweden, 514L, 2004.

[4] C. E. Solver, B. Bergman, A. Carvalho, S. Dessanti, and H. Furuta, "First results from on-going CIGRÉ enquiry on reliability of high voltage equipment," in *Conference Present and future of high voltage equipment and substation technologies*, 2005.

[5] A. Mercier, M. Lacroix, and P. TaiIlefer, "Benefits of controlled switching of MV circuit breakers,"in *Raportti.CIRED: 23rd International Conference on Electricity Distribution. Lyon* 2015.

[6] T. Olsen, "Electrical equipment lifespan: watt in the world? | T&D Guardian Articles | USA," (in English), 2019.

[7] J. Clark. (2013). *rate constants and the arrhenius equation*.Accessed:Oct.20,2020.[Online].Available :https://www.chemguide.co.uk/physical/basicrates/

[8] K. M. Dantas, W. L. Neves, D. Fernandes Jr, G. A. Cardoso, and L. C. Fonseca, "On applying controlled switching to transmission lines: Case studies," in *International Conference on Power Systems Transients (IPST)*, 2009, p. 6.

[9] H. Ito, "Current status and future trend of controlled switching system," in Journal *Mitsubishi Electric ADVANCE,* vol. 117, pp. 2-5, 2007.

[10] Z. Zhang, Y. Nie, and W. Lee, "Arc Voltage Characteristics of Medium-Low Voltage Arc Fault in Short Gaps," in *2018 IEEE Industry Applications Society Annual Meeting (IAS)*, 2018, pp. 1-8.

[11] B. K. Rao and G. Gajjar, "Development and application of vacuum circuit breaker model in electromagnetic transient simulation," in *Power India Conference, 2006 IEEE*, 2006, p. 7 pp.: IEEE.

[12] H. Bahirat, M. Ali, and K. Praveen, "Effects of transient recovery voltages on circuit breaker ratings," *Internal Journal of Spring,*Vol 2, no.2, pp. 94-101, 2008.

[13] A. Sepehri. (2019). *Transient Recovery Voltage | Interruption of Small Inductive Currents*. Accessed:Oct.10,2020.[Online].Available:https://www.powerandcables.com/transient-recovery

[14] P. Kumar, A. Kale, A. K. Singh, and M. Ranade, "Internal Arc Fault Simulation in MV Panel for Thermal and Structural Withstand," in *2018 IEEE Holm Conference on Electrical Contacts*, 2018, pp. 405-411: IEEE

[15] F. Ledbetter, "Medium-Voltage Vacuum Circuit Breaker Life Extension,*in CBS Conference*" , 2017, pp. 1-9.

[16] E. Nasrallah. (2019).*Electrical contacts in MV & HV Power Circuit Breakers.* Accessed:Aug.19,2020.[Online].Available:https://electricenergyonline.com/energy/magazine/306

Analytical Approach Towards Low Power Device (Differential Amplifier) Using DG MOSFET

Thabiso Tekisi and Viranjay M. Srivastava
Department of Electronic Engineering,
Howard College, University of KwaZulu-Natal,
Durban - 4041, South Africa.
thabisotekisi@gmail.com, viranjay@ieee.org

Abstract **- A Double-Gate (DG) MOSFET-based differential amplifier has been designed in this research work. This DG MOSFET has the capacity to reduce Short-Channel Effect (SCE) in low-power devices. In this differential amplifier, the differential input–differential output mode of operation has been analyzed for following parameters: (i) differential gain, (ii) common-mode gain, (iii) common mode rejection ratio, and (iv) frequency response. The results achieved are *22.64 dB*, *-224.22 dB*, *246.86 dB*, and *65 MHz*, respectively. Based on these results, the designed differential amplifier is justified for the use in operational amplifiers as input stage, RF, and other low-power electrical/electronic devices.**

Keywords— Double-gate MOSFET; Differential amplifier; Device; Energy efficiency; Low power electronics, Microelectronics.

I. INTRODUCTION

Gordon Moore predicted that the transistor (BJT/MOSFET) counts doubled after every eighteen months, on-chip for electrical/electronic devices. Process scaling benefits modern electronics. The goal of faster scaling is to build a separate transistor that consumes less power and is compact [1, 2]. *Tian et. al.* [3] have designed a Silicon carbide fully differential amplifier up to *500 °C*. The base-current compensation technique was applied to overcome the low input resistance of the amplifier. The open and closed loop gains were *58 dB* and *53 dB*, respectively. *Hashem* [4] has designed and analyzed a BJT-based differential amplifier. *Yang and Andreou* [5] designed a multiple-input floating gate MOSFET differential amplifier: analog computational building block. The open-loop gain was *72 dB* with one differential input pair grounded. A unit gain and CMRR were *360 kHz* and *52 dB*, respectively. *Tripathy and Bhadra* [6] designed a high-speed two-stage operational amplifier with high CMRR and it was implemented using single-gate MOSFET. The gain, slew rate, and gain bandwidth were measured to be 70 dB, *119 V/μs*, and *30 MHz*, respectively. *Coe et. al.* [7] designed a model of a MEMS sensor using a common gate MOSFET differential amplifier. The sensor was used to integrate transduction and amplification while the MEMS gate modulated the relative gate capacitance and drain current. The sensitivity and responsivity of the sensor were measured to *68 μA* and *2.2 mV/degree*, respectively. *Takao et. al.* [8] designed a monolithically integrated three-axial accelerometer using stress sensitive CMOS differential amplifier. Chopper stabilization was used to improve the signal-to-noise ratio. The sensitivity in X, Y, and Z was measured to be *23 mV/G*, *23 mV/G*, and *192 mV/G*, respectively. The resonant frequency for X, Y, and Z was obtained as *1250 Hz*, *1250 Hz*, and *1500 Hz*, respectively. *Bangadkar et. al.* [9] performed a study of differential amplifiers using CMOS. The N-channel and P-channel MOSFETs were used to design differential pair and current mirrors. *Pakaree and Srivastava* [10] have designed a Double-Gate (DG) MOSFET-based differential amplifier. Differential gain, common-mode gain, CMRR, and frequency response were realized as *-8.69 V/V*, *0.40 V/V, 19.06,* and *32 MHz*, respectively. *Pillay and Srivastava* [11] designed an active-loaded differential amplifier using a double-gate MOSFET. Differential gain and frequency responses were *1.7 V/V – 1.8 V/V* and *42 MHz*, respectively.

A differential amplifier is a device that amplifies the voltage difference between two input signals and is a crucial building block in analog integrated circuits. It is commonly used to build the input stages of operational amplifiers. The gain, common-mode rejection ratio, and frequency response are some of the parameters used to measure or analyze the amplifier's performance. Previously, BJTs and single-gate MOSFETs were used to construct the differential amplifier; however, the gain could not be improved further, and in MOS amplifiers, short-channel effects and leakage gate current were higher. To solve the mentioned challenges, a double-gate MOSFET-based differential amplifier has been designed in this research work. It has the capability to reject common signals on the input signals. The primary focus is on lower-power and high-frequency applications with common parameters, i.e., differential gain, common mode gain, CMRR, and amplifier gain bandwidth. This research paper has been organized as follows. Section II discusses the proposed solution of the differential amplifier. Section III presents the parametric analysis to evaluate the performance of the designed amplifier. Finally, Section IV concludes the work and recommends the future aspects.

II. PROPOSED DESIGN OF DIFFERENTIAL AMPLIFIER

The MOSFET is the most widely used transistor in digital and analog circuits and is the core of modern electrical/electronic devices. In addition, a new version is the Double-Gate (DG) MOSFET as shown in Fig. 1(a). On the other hand, the differential amplifier is an electrical circuit that amplifies the differences between two input signals. One of the most common applications of MOSFETs in analog circuits is the construction of differential amplifiers. Because they possess a high input impedance, MOSFET-based differential amplifiers utilized in Integrated Circuits (IC) include operational amplifiers [7].

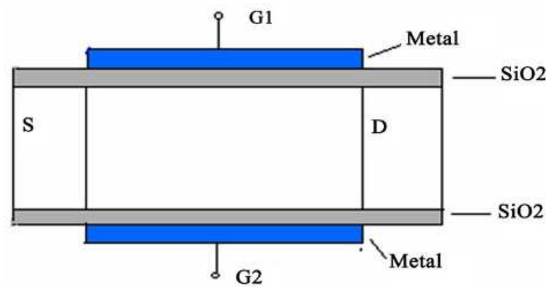

(a)

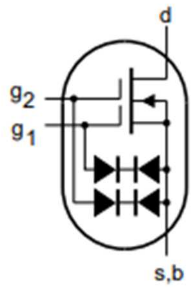

(b) (c)

Fig. 1. (a) Basics of DG MOSFET, (b) Pin diagram, and (c) internal configuration of BF998 MOSFET.

The authors of this work have presented a differential amplifier that uses BF998 DG MOSFETs because of its ability to decrease Short-Channel Effects (SCEs) and gate current leakage. The MOSFET (BF998) has two gates and can be used in two ways: (i) symmetrical: both gates are controlled by the same input; (ii) asymmetrical: both gates are powered separately, as shown in Fig. 1(b) and Fig. 1(c) [11-13]. These characteristics distinguish this DG MOSFET from regular MOSFETs. The designed differential amplifier consists of two N-channel matched DG MOSFETs (M_1 and M_2), a constant current source (developed by R_SS and V_SS), and the same drain resistances (RD_1 and RD_2). The capacitors, C_1 and C_2 are used to filter out any DC voltage that might be available from the source. It uses a dual supply voltage of $\pm$ *12 V*. Asymmetrical mode of operation is used on this design because it gives more control such that gate-2 is responsible for transconductance, threshold voltage, and drain current characteristics.

When an AC signal is applied on M_1 (through V_{G1-1}) that has 0^0 phases, the second AC signal that is 180^o out of phase is applied on V_{G1-2} (of transistor M_2). According to the BF998 datasheet, gate-2 is biased with 4 V to turn-ON the MOSFET and to make it in the saturation region. When both signals are applied, the first input signal on V_{G1-1}, the same signal is realized on the source terminal of M_1. The same happens when the 180^o out of phase signal (on V_{G1-2}) is applied on M_2, the input signal is realized on the source terminal of M_2. When these two input signals meet at the middle at point X as depicted in Fig. 2(b), point X becomes a fixed point. This results in a constant current at that point, X. Regardless of what happens with the input voltages, the current will always be the same at point X. When the input signal on V_{G1-1} rises, the input signal on V_{G1-2} falls, this creates the gain of this amplifier.

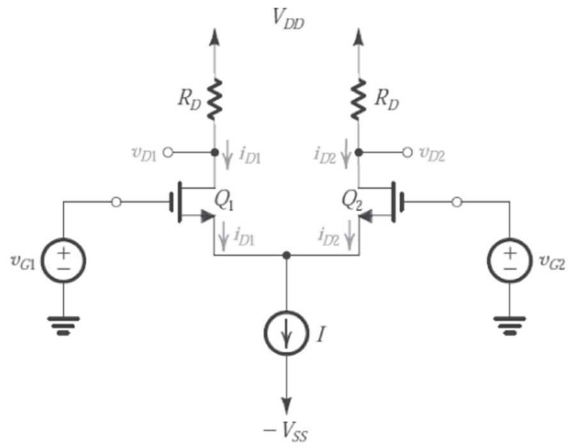

(a)

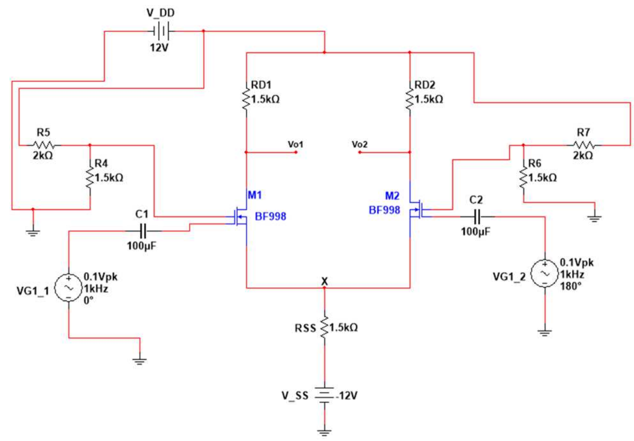

(b)

Fig. 2. (a) Basic differential amplifier [12], and (b) Designed differential input–differential output circuit diagram.

III. PARAMETRIC ANALYSIS

The performance of the designed Double-Gate MOSFET-based differential amplifier is evaluated with parameters: (i) differential voltage gain, (ii) common-mode gain, (iii) common mode rejection ratio (CMRR), and (iv) frequency response for differential input – differential output mode.

A. Differential Input with Differential Output

The full capacity of the circuit is utilized when a differential amplifier is connected with a differential input and a differential output. This particular arrangement is demonstrated in Fig. 2(b).

Typically, two input signals that are *180^o* out of phase are used in this topology. Due to this, the difference (differential) signal is doubled as large as each input. This is similar to the two-input single-output differential amplifier having *180°* out of phase input signals. The first output is a signal in phase with the second input and the second output is a signal in phase with the first input signal. The amplitude of each output signal is equal to the input signal scaled by the amplifier's gain. With *180^o* out of phase input signals, each output signal has an amplitude multiplier of the amplifier's gain larger than both input signals. When an output signal is measured between the amplifier's two output terminals, as indicated by V_{o1} and V_{o2} in Fig. 2(a). The resultant output signal has double the amplitude of either signal at V_{o1} or signal at V_{o2}. This is because V_{o1} and V_{o2} are 180° out of phase with each other. When the input signals are 180° out of phase, the combined output signal has an amplitude equal to the amplitude of one input signal multiplied by two times the amplifier's gain.

B. *Differential Gain*

The differential gain could be determined by considering the differential half-circuit of the MOSFET differential amplifier. A MOSFET differential amplifier's output voltage signal can also be obtained differentially, i.e., between two drains:

$$V_{od} = V_{o1} - V_{o2} \tag{1}$$

as shown in Fig. 2. The differential gain of the differential amplifier will be [5]:

$$A_d = \frac{V_{od}}{V_{id}} = g_m R_{D1} \tag{2}$$

where V_{id} is the differential input voltage signal, this proves that the differential gain (using Eq. (1) and Eq. (2)) only depends on the MOSFET's transconductance and drain resistance. Fig. 3 depicts the differential input–differential output signal at *1 kHz.*

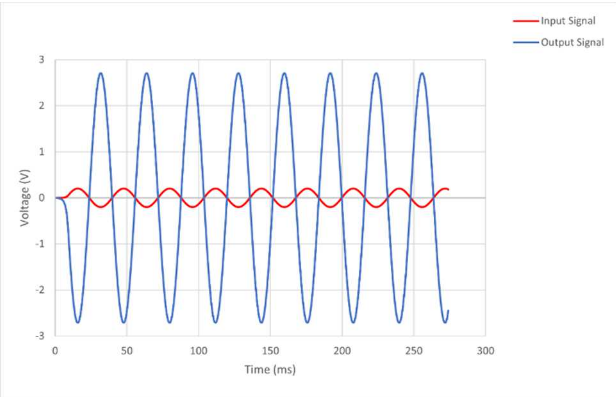

Fig. 3. Differential input – differential output signal of a designed differential amplifier.

The differential input signal has been used on the designed DG MOSFET-based differential amplifier. Both signals had an amplitude of $0.1\ V_{pk}$, generated at *1 kHz*. The second input was 180° out of phase. The differential voltage has been obtained to be $5.42\ V_{pk-pk}$, while the differential input is $0.4\ V_{pk-pk}$.

TABLE I. SUMMARY OF DIFFERENTIAL GAIN WITH VARIED INPUT SIGNAL, V_{G1_2}

VG1_1 (V_{pk})	VG1_2 (V_{pk})	Differential input voltage (V_{pk-pk})	Differential output voltage (V_{pk-pk})	Differential Gain (V/V)
0.1	0.1	0.4	5.42	-13.55
0.1	0.3	0.8	10.7	-13.38
0.1	0.5	1.20	15.7	-13.08
0.1	0.8	1.80	21.4	-11.89

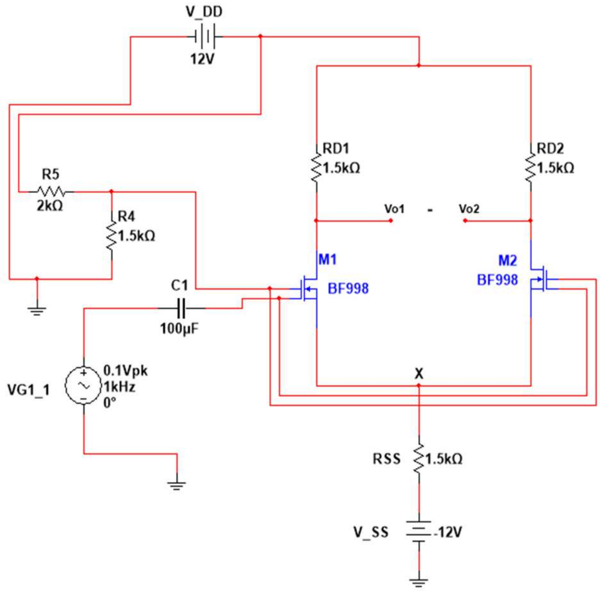

Fig. 4. Common-mode input voltage circuit diagram.

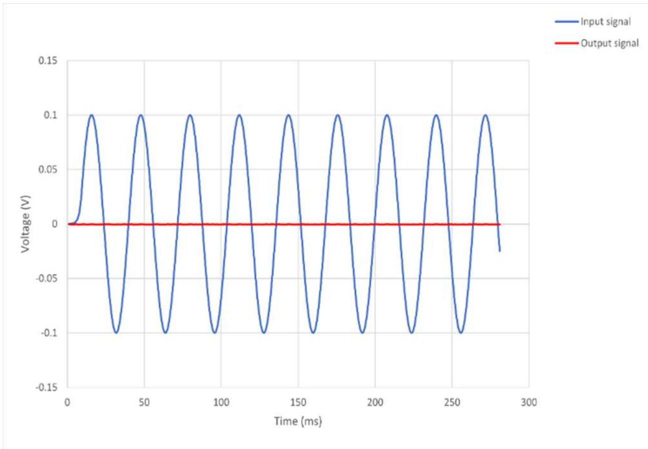

Fig. 5. Common mode input voltage–output voltage signal.

This result in a differential voltage gain of *-13.55 V/V.* Further investigation has been done by varying the amplitude of one input signal, V_{G1_2}. Table 1 summarizes this analysis. Table I shows that the maximum differential voltage gain is achieved when both signals have *0.1* V_{pk} amplitude. Increasing V_{G1-2} results in reduced gain, and beyond *0.5* V_{pk}, the differential gain has exponentially decreased, which proves that the MOSFETs are no longer in the saturation region.

C. *Common Mode Voltage Gain*

Consider applying identical voltage signals, V_G, to the two gate terminals. As depicted in Fig. 4, $V_{G1\_1} = V_{G1-2} = V_G$. Because the two inputs share V_G, it is referred to as common-mode voltage [10, 14, 15].

In ref. [10], it has been proved that if both MOSFETs remain in the saturation region, drain current will divide equally amongst M_1 and M_2 and drain voltage will not change. As a result, the differential amplifier rejects common-mode input signals, as shown in Fig. 5. The output voltage is *1.23 pV* ≈ 0 V. This is ideally zero; in real life, the output voltage is not 0 V because of a mismatch in transistors and resistors. Common mode voltage gain is achieved as *6.15 pV V/V.*

D. Common Mode Rejection Ratio

The CMRR of a differential amplifier assesses the device's ability to discard input signals similar to both inputs. A high *CMRR* is significant in applications where the signal of importance is represented by a small voltage fluctuation superimposed (potentially substantial) voltage offset or when the voltage difference between two signals comprises pertinent information. The CMRR of a differential amplifier defines the offset attenuation [7] can be used as:

$$CMRR = \frac{|A_d|}{|A_{cm}|} \tag{3}$$

Using Eq. (3) to calculate the common mode rejection ratio of the amplifier, it has been realized as:

$$CMRR = \frac{|A_d|}{|A_{cm}|} = \frac{13.55}{6.15\times10^{-12}} = 2203\times10^{9}\,V/V$$

CMRR = 246.86 *dB*.

E. Frequency Response

The degree to which an amplifier will function properly with respect to a particular frequency range is measured by its frequency response. The differential amplifier will not work properly above a specific cut-off frequency [16-18]. With reference, the frequency response can be determined as [19, 20]:

$$f = \frac{1}{2\pi\tau} \tag{4}$$

The frequency response of the designed differential amplifier, using Eq. (4), has been realized as *65 MHz,* as shown in Fig. 6.

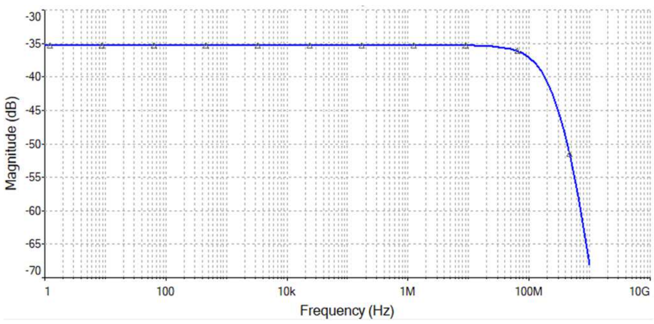

Fig. 6. Frequency response of a differential input – differential output amplifier.

IV. Conclusions and Future Recommendations

Parametric analysis has been performed on the designed DG MOSFET-based differential amplifier using BF998 device. The obtained results show that the performance of the designed amplifier is better compared to existing models. Differential gain, common mode gain, CMRR, and frequency response have been analyzed. The results were *-13.55 V/V*, *6.15 pV*, *246.86 dB*, and *65 MHz*, respectively.

Future improvements can be made by using active devices such as current mirrors instead of restive loads. A constant current source can also be utilized. Also, a specific application in the area of low-power electrical devices in line with 4IR, smart grids, nanomaterials, mechatronics, etc. [21, 22] will be designed and discussed.

Acknowledgment

Authors are thankful to Mr. Logan Pillay, Chairperson of TESP, Mr. Cecil Ramonotsi, CEO, Eskom Development Foundation, South Africa and Mr. Tshidi Ramaboa, Eskom Academy of learning, Human Resources, Midrand. The authors are also thankful to Ms. Leena Rajpal, Public Relation officer, University of KwaZulu-Natal, Durban, South Africa for providing various support to carry on this research work.

References

[1] Ralph K. Cavin, Paolo Lugli, and Victor V. Zhirnov, “Science and engineering beyond Moore's law,” *Proceedings of the IEEE*, vol. 100, pp. 1720 – 1749, April 2012.

[2] International Roadmap for Devices and Systems (IRDS™), May 2021, https://irds.ieee.org.

[3] Ye Tian, Luigia Lanni, Ana Rusu, and C. M. Zetterling, “Silicon Carbide fully differential amplifier characterized up to 500 ºC,” *IEEE Transactions on Electron Devices*, vol. 63, no. 6, pp. 2242 – 2247, June 2016.

[4] M. A. Hashem, "Analysis and design of BJT differential amplifier," *5th International Conference on Engineering Technology and its Applications (IICETA)*, Iraq, 31 May - 1 June 2022, pp. 227-232.

[5] Kewei Yang and Andreas G. Andreou, "The multiple input floating gate MOS differential amplifier: an analog computational building-block," *IEEE International Symposium on Circuits and Systems (ISCAS)*, London, UK, 30 May - 2 June 1994, pp. 37-40.

[6] Dhananjaya Tripathy and Pritam Bhadra, "A high speed two stage operational amplifier with high CMRR," *3rd IEEE International Conference on Recent Trends in Electronics, Information & Communication Technology (RTEICT)*, Bangalore, India, 18-19 May 2018, pp. 255-259.

[7] D. J. Coe, J. M. English, R. G. Lindquist, and T. J. Kaiser, “Model of a MEMS sensor using a common gate MOSFET differential amplifier,” *Journal of Physics D: Applied Physics,* vol. 39, no. 20, pp. 4353 – 4358, Sep 2006.

[8] H. Takao, Y. Matsumoto, and M. Ishida, "A monolithically integrated three axial accelerometer using stress sensitive CMOS differential amplifiers," *International Solid-State Sensors and Actuators Conference (Transducers '97)*, Chicago, USA, 19 June 1997, pp. 1173-1176.

[9] B. Bangadkar, A. Lamba, V. Bhure, “Study of Differential amplifier using CMOS,” *International Journal of Engineering Research and General Science,* vol. 3, no. 2, pp. 2091 – 2730, March-April 2015.

[10] Japheth E. Pakaree, and Viranjay M. Srivastava, "Realization with fabrication of double-gate MOSFET based differential amplifier," *Microelectronics Journal,* no. 91, pp 70-83, July 2019.

[11] Suvashan Pillay and Viranjay M. Srivastava, “Design and comparative analysis of active-loaded differential amplifier using double-gate MOSFET,” *SN Applied Sciences*, vol. 4, no. 8, article 204, pp. 1-15, Aug. 2022.

[12] BF998; BF998R Silicon N-channel dual gate MOSFET datasheet," NXP Semiconductors, August 1996.

[13] BF909; BF909R N-channel dual gate MOS-FETs datasheet.

[14] Adel S. Sedra and Kenneth C. Smith, *Microelectronic circuits*, 7th Ed., Oxford University Press, USA, 2015.

[15] Juan Pablo M. Brito, and Sergio Bampi, "A DC offset and CMRR analysis in a CMOS 0.35μm operational transconductance amplifier using Pelgrom’s area/accuracy tradeoff,” *Microelectronics Journal,* no. 40, pp 1281-1292, June 2008.

[16] Naveenbalaji Gowthaman and Viranjay M. Srivastava, "Arbitrary alloy semiconductor material based DG MOSFET for high-frequency industrial and hybrid consumer applications," *14th IEEE Int. Conf. on AFRICON*, Arusha, Tanzania, 13-15 Sept. 2021, pp. 583-587.

[17] M. Saqib Akhoon, Abdullah G. Alharbi, Majid A. Bhat, Shahrel A. Suandi, Javed Ashraf, and Sajad A Loan, "Design and simulation of carbon nanotube based current source load differential amplifier," *International Conference on Microelectronics (ICM)*, New Cairo City, Egypt, 19-22 Dec. 2021, pp. 140-143.

[18] J. K. Kasthuri Bha and P. Aruna Priya "Low power & high gain differential amplifier using 16 nm FinFET," *Microprocessors and Microsystems*, vol. 71, Nov. 2019.

[19] Robert L. Boylestad and Louis Nashelsky, *Electronic devices and circuit theory,* 7th Ed, Prentice Hall, USA, 2012

[20] Bob Cordell, *Designing audio power amplifiers,* McGraw Hill, New York, USA, 2012.

[21] Efe F. Orumwense, Thomas J. Afullo, and Viranjay M. Srivastava, "Improving energy efficiency in cognitive radio networks using a 2-step cooperative spectrum sensing approach," *Southern Africa Telecommunication Networks and Applications Conference (SATNAC)*, George, South Africa, 4 - 7 Sept. 2016, pp. 332-336.

[22] Bolagun O. Emmanuel, Pius A. Owolawi, and Viranjay M. Srivastava, "Hybrid power systems for GSM and 4G base stations in South Africa," *13th IEEE Int. Conf. on AFRICON*, Cape Town, South Africa, 18-20 Sept. 2017, pp. 1003-1008.

Cryptocurrency Mining Powered by Renewable Energy Using a DC-DC Connection

P. Rorich, K. Moloi, T. F. Mazibuko and I. E. Davidson
Department of Electrical Power Engineering
Faculty of Engineering and Built Environment
Durban University of Technology, Durban, South Africa
22063813@dut4life.ac.za, KatlehoM@dut.ac.za, ThokozileM1@dut.ac.za, InnocentD@dut.ac.za

Abstract — **Cryptocurrency mining is energy-intensive and large operations could put pressure on an already failing national grid in South Africa. Therefore, this report will discuss a way to alleviate some energy pressure from cryptocurrency mining using solar energy. This is relevant since cryptocurrency is gaining adoption and is increasingly being used and relied upon. Cryptocurrency is also an investment vehicle, and many use cases for blockchain technology have been and are being developed. By using MATLAB Simulink software, the DC-DC connection was designed and simulated. The output voltage results of the system were compared to the required voltages that a Graphics-Processing-Unit (GPU) mining rig requires, and the financial feasibility was determined by calculating how many cryptocurrency coins were mined per day and compared against fiat value. The results of the design show that it is theoretically possible to have a DC-DC connection directly from solar panel system to the mining rigs without the need to convert to AC first. It was also determined that such a system is financially viable as the return on investment was estimated to be around 2 years.**

Keywords* — *Buck converters, cryptocurrency mining, DC-DC connection, Graphics Processing Unit, solar power.

I. Introduction

Cryptocurrency is a digital or virtual currency that is secured by cryptography and is becoming increasingly more popular and being adopted at an incredible rate due to its utility and non-manipulable nature [1]. Cryptography refers to secure information and communication techniques derived from mathematical concepts and a set of rule-based calculations called algorithms, to transform messages in ways that are hard to decipher [2]. Its inception is in the form of the most popular cryptocurrency today, Bitcoin, which was created by a person under the pseudonym Satoshi Nakamoto in 2009 . The key concept behind this technology is the decentralization of the blockchain information, which involves the infallible distribution of the complete history of records on several machines, called nodes, that are not under the control of a single entity [3]. Cryptocurrency is believed to be the next wave of technology due to the invention of the blockchain. Decentralized monetary value can be exchanged permissionlessly on a global scale. Cryptocurrency mining can only be done when the algorithm has a Proof-of-Work consensus mechanism and is the process where a computer or Application-Specific-Integrated-Circuit (ASIC) solves algorithmic equations to earn a reward by using only electricity and an internet connection. Therefore, for a mining operation to be profitable electricity cost must be cheaper than the amount made by mining coins and the machines must be kept cool.

Cryptocurrency mining powered by solar energy has been done before but most of the time the solar energy is sold to the grid and uses the grid's electricity. Studies on this topic have also been done but very few have gone into the component-level design, and none have done a DC-DC connection. Addressing these missing links is important to fully understand the operational viability of the proposed design. The hypothesis of the study is that a DC-DC connection from PV arrays to mining rigs is possible.

Cryptocurrency mining uses an enormous amount of electricity globally. Bitcoin mining uses an enormous amount of power globally, roughly around 91 Terawatt hours (TWh) of electricity annually, for comparison, this is more electricity usage than Finland's consumption with a population of 5.5 million people [4]. Another issue is a local one, load-shedding is a frequent occurrence and disrupts the economy of South Africa in a huge way in terms of finance and productivity. Due to cryptocurrency mining being energy-intensive, the ideal situation is if energy is abundant and cheaply available as well as load shedding is non-existent. The reality of the situation is that the South African National power grid is often under pressure and cannot comfortably sustain a large-scale cryptocurrency mining operation without some sort of supplementation or alternative energy source. When observing already established mining operations internationally, it is seen that some of these operations can have capacities well over 100MW and run continuously 24 hours a day. The consequence of adding such a mining operation to the grid in South Africa is that it can put a huge load on local and national grids. This pressure could result in the loss of time, money and productivity since all a mining operation needs is electricity and the hardware.

To avoid placing more pressure on an already suffering national grid, the proposal of this project is to fully power a cryptocurrency mining rig with renewable energy, specifically solar energy using a direct DC-DC connection. By researching existing solar energy technology, the overall viability in serving a crypto mining operation with solar energy in South Africa will be determined. Most solar renewable resources will convert their outgoing DC voltage to AC by use of inverters. Since mining machines use DC power to operate, the viability of a DC-to-DC connection from a renewable source to mining machines will also be determined as this can possibly save on overall costs due to lower losses.

The aim of this project is to design a DC-DC connection between solar panels and a mining rig so that no conversion to AC is required. The objectives of this research report are as follows:

- Design a solar system that can support a 1kW mining rig.
- Design a system in which solar panels can directly power a mining rig
- Evaluate the financial feasibility of the design.

II. Buck Converter

The buck converter is a form of DC-to-DC converter that can take input directly from a DC source. The buck converter acts as a step-down circuit. However, the DC applied to the Buck Converter is then converted to a high-frequency AC, using a switching transistor, driven by a pulse width modulated square wave. This results in a high-frequency AC wave, which can then be re-converted to DC [5]. A buck converter consists of a switching transistor, diode, inductor and capacitor. Initially, when the transistor is ON the current to the load is restricted because energy is also being stored in the inductor. Over time, the current in the load and charge in the capacitor will gradually increase. In this state, the diode has no effect on the circuit as it is in reverse bias mode [5]. When the transistor is switched off, the energy stored in the magnetic field around the inductor is released back into the circuit in the form of back emf. The back emf from the inductor causes current to flow via the load and the diode which is in forward bias mode. Once the inductor has returned a large part of its stored energy to the circuit and the load voltage begins to fall, the charge stored in C1 becomes the main source of current, keeping current flowing through the load until the next "ON" period begins [5].

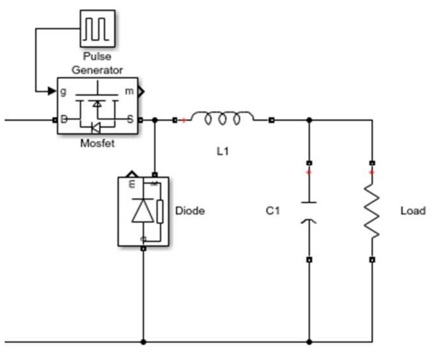

Fig 2.1: Buck Converter

A. Buck Converter Design

$$D = \frac{V_O}{V_S} \quad (1)$$

Where D= Duty cycle, Vo= Output Voltage, Vs= Supply Voltage

$$Lmin = \frac{(1-D)R}{2fs} \quad (2)$$

Where $Lmin$ = Minimum inductor value, R= Resistance, fs= switching frequency

Assuming the inductance to be 25% larger for inductor current to be continuous and assuming switching frequency to be 40kHz.

$$L = Lmin \cdot 0.25 + Lmin \quad (3)$$

$$C = \frac{1-D}{8L(\frac{\Delta V_o}{V_o}) \cdot fs^2} \quad (4)$$

Where $\frac{\Delta V_o}{V_o}$ = Ripple Voltage

Assuming ripple voltage to be 5% [6].

III. Standard GPU Miners and PC Connectors

Since ASIC miner circuit diagrams aren't freely available, and thus no way to know what DC voltages are needed and where, the DC-to-DC design cannot be implemented, hence a GPU miner will be used in the design process because the information is freely available. In a traditional GPU miner set-up, normal computer components are used. Such components are CPU (Central Processing Unit), motherboard, hard drive, power supply and graphics card. The CPU is the machine's "brain" and is placed in its slot on the motherboard. The hard drive is a storage and boot-up device and is where the operating system of the miner is stored. The GPUs are the components that do the mining, and all of this is powered by a power supply that converts 230V mains AC voltage to DC voltages that the components require. However, in the design, the need for the power supply is bypassed because the solar panels produce DC voltages but will need to be stepped down to meet the miner's requirements. This information can be obtained by observing what voltages are delivered via the connectors coming from a power supply since computer components are standardized. The 24-pin motherboard connector is the main connector and is plugged straight onto the motherboard. This connector delivers a variety of different voltages to the motherboard. The next connector is the CPU 8-pin connector, it consists of 12V and common pins and is plugged into the motherboard. The last connector is the 6-pin, it consists of 12V and common pins as well as a sensor pin, these plug into the GPUs and is how they get their power. The pin layout of a 6-pin GPU connector can be seen below. Knowing the connector information is important for this project because the design will need to supply these specific voltages to the relevant pins in the connectors.

Table 3.1: 6 Pin GPU Connector layout [7]

6 Pin GPU Connector					
Colour	**Signal**	**Pin**	**Pin**	**Signal**	**Colour**
Yellow	12V	4	1	GND	Black
Yellow	12V	5	2	Sense	Green
Yellow	12V	6	3	GND	Black

IV. Factors that Influence Solar Energy in South Africa

Solar radiation is the electromagnetic radiation emitted by the sun. Solar radiation measurement is important because its data is the foundation of research for the development of solar energy technologies. Accurate knowledge of the strength of the sun is important for the technical and economic evaluation of solar energy technologies, therefore, obtaining true solar measurements is important in assessing the available solar resource at a particular location. Reliable solar measurements are also important in the development of empirical models to predict and forecast the availability of solar energy at any location [8]. The equations below are used to calculate the solar irradiation at any location at any time of the day for ideal conditions [9].

$$\delta = 23.45\sin[(\tfrac{360}{365}(n-81)] \tag{5}$$

Where δ= Solar declination, n= number of days.

$$\sin\beta = \cos L \cos H + \sin L \sin\delta \tag{6}$$

Where β= Altitude angle, L= Latitude, H= Hour angle.

$$m = \sqrt{(708\sin\beta)^2 + 1417} - 708\sin\beta \tag{7}$$

Where m= air mass ratio.

$$\sin\emptyset_S = \frac{cos\delta sinH}{cos\beta} \tag{8}$$

Where $\emptyset_S$= Solar azimuth.

$$I_B = Ae^{-Km} \tag{9}$$

Where I_B= Beam irradiation, A= Apparent flux radiation, k= atmospheric optical depth.

$$A = 1160 + 75\sin\left[\frac{360}{365}(n-275)\right] \tag{10}$$

$$k = 0.174 + 0.035\sin\left[\frac{360}{365}(n-100)\right] \tag{11}$$

$$I_{BC} = I_B cos\theta \tag{12}$$

Where I_{BC}=Beam irradiation on the PV panel, θ=incidence angle.

$$I_C = I_{BC} + I_{DC} + I_{RC} \tag{13}$$

Where I_C=, I_{DC}=, Diffuse insolation on PV panel I_{RC}=Reflected insolation on the PV panel.

For fixed solar panel orientation:

$$cos\theta = cos\beta\cos(\emptyset_S - \emptyset_C)\sin\Sigma + \sin\beta\cos\Sigma \tag{14}$$

Where $\emptyset_C$=PV azimuth.

$$C = 0.095 + 0.04\sin\left[\frac{360}{365}(n-100)\right] \tag{15}$$

Where C= Sky diffuse factor.

$$I_{DC} = I_B C\left(\frac{1+cos\Sigma}{2}\right) \tag{16}$$

$$I_{RC} = I_B\rho(C + sin\beta)\left(\frac{1+cos\Sigma}{2}\right) \tag{17}$$

Where ρ= reflectance factor

By observing Figure 4.1 below, the results from the study confirm that Arid Interior climates are superior in terms of solar potential in South Africa while the subtropical coastal areas are inferior. A factor that coincides with GHI is the number of hours of sunlight per day. The longer the sun is

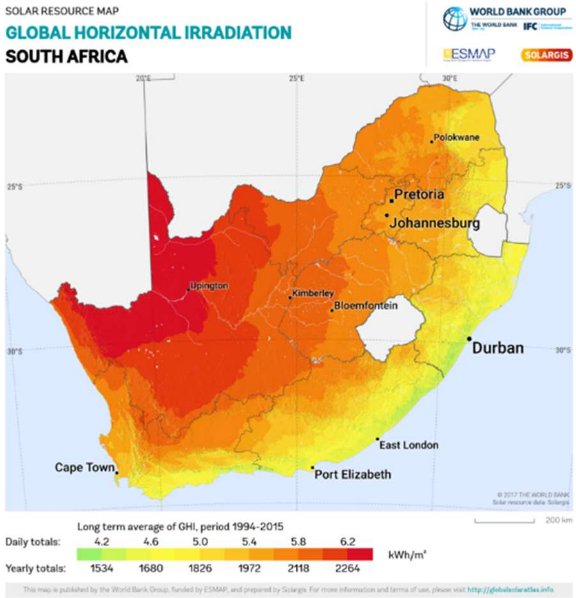

out, the more energy it can produce in a day. This factor is seasonal as summer months have longer days while winter days have shorter days. By referring to the graph below, Figure 4.2, it is seen that Solar energy is directly proportional to hours in a day.

Fig 4.1: GHI in South Africa

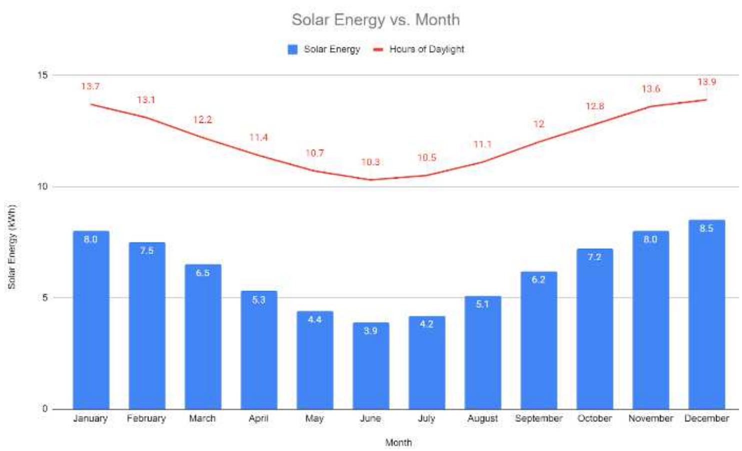

Fig 4.2: Solar energy compared to hours of sunlight per day [10]

Ambient and solar panel temperatures need to be considered as well since as temperatures increase the power output and thus the efficiency decreases. Photovoltaic modules are tested at a temperature of 25°C, which is Standard Test Conditions (STC) and depending on their installed location, heat can reduce output efficiency by 10-25%. As the temperature of the solar panel increases, its output current increases exponentially, while the voltage output is reduced linearly [11]. To determine the effect of temperature on a solar panel's performance, the equations below may be used [9].

$$T_{Cell} = T_{amb} + (\frac{NOCT - 20°}{0.8}) \cdot S \quad (18)$$

Where T_{Cell} = Cell temperature, T_{amb} = Ambient temperature, NOCT= Nominal operating cell temperature & S= solar insolation

$$Voc = V[(1 - Temp\ coefficient)(T_{cell} - T_{STC})] \quad (19)$$

Where Voc= Open circuit voltage new & V= Open circuit voltage from data sheet

$$P_{max} = P[(1 - Temp\ coefficient)(T_{cell} - T_{STC})] \quad (20)$$

Where P_{max}= Max power due to temperature

Shading is another factor that can hinder the performance of a PV system that needs to be considered. There are two types of shading, Static and Dynamic [12]. Static Shading occurs when obstructions like trees or buildings shade and Dynamic Shading occurs when clouds, dust and bird droppings obstruct the PV panel with direct sunlight. The reason why shading is an important factor to consider is that if one panel is covered by shade then all the connected panels within the string will also lose power. Every cell in the cell string must operate at the current set by the shaded cell [12]. This can cause a significant loss of output power but can be reduced by grouping cells that are frequently shaded into a parallel string or by using bypass diodes [13]. Bypass diodes are used within a module that allows current to bypass shaded regions of a module [13]. Therefore, by utilizing bypass diodes, the higher current of the unshaded cell strings can flow around the shaded cell string.

V. Profitability and Return on Investment

The daily energy consumed by any mining hardware depends upon its power requirements and its operating time, which is recommended as 24 hours:

$$E_{req} = P_{miner} \cdot 24hrs \quad (21)$$

Where E_{req}= Power Consumed per day& P_{miner}= Power required by miner

A PV system must be designed to provide not only this energy, but also to compensate for the losses incurred by the electrical system (cables and batteries), the installation setup (orientation angle, shadowing, and manufacturing tolerance of panels) and operating conditions (efficiency drop due to high temperatures and yield reduction due to dirt accumulation). All these losses generally escalate the requirements by 50% [3].

$$E_{sup} = E_{req} \cdot 1.5 \quad (22)$$

Where E_{sup}= Power supplied by PV system.

$$W_{peak} = {E_{sup}}/{PSH} \quad (23)$$

Where W_{peak}= Peak power by PV system & PSH= Peak sun hours.

The total cost of the PV system would incorporate the cost of PV panels and the cost of the mechanical mountings, cables and batteries.

$$C_{PV} = W_{peak} \cdot C_{SP} \quad (24)$$

Where C_{PV}= Cost of PV system & C_{SP}= Cost of solar panels.

For the BOS, a general rule of thumb is that its cost is around 50% of the panels' cost [3].

$$C_{BOS} = C_{PV} \cdot 0.5 \quad (25)$$

Where C_{BOS}= Cost of other PV system materials

$$C_{total} = C_{PV} + C_{BOS} + C_{miner} \quad (26)$$

Where C_{total} =Total cost of system & C_{miner}= Cost of mining hardware

The number of coins mined in a day depends on factors such as the hash rate of the hardware, the net hash-rate of the whole network, the time required to mine a single block and the block reward to the successful miner. This is given by:

$$N = \frac{H}{H_{net}} \cdot \frac{3600sec/hr \cdot 24hr/day}{t} \cdot r \quad (27)$$

Where N = Number of coins mined per day, H = Hash rate of hardware, H_{net} = Total network hash rate, t = Time required to mine a block & r = Miner reward

The revenue from running the mining hardware will depend upon the number of coins mined in a
day and their market price.

$$R = N \cdot P \quad (28)$$

Where R= Revenue per day, N= Number of coins mined per day & P= Market price of coins

Finally, the payback period (M), in months, for this system can be calculated as:

$$M = \frac{C_{total}}{R} \cdot \frac{12\ months}{365\ days} \quad (29)$$

Table 5.1: Mining hardware characteristics of GPUs [14]

GPU Model Type	Hash rate (MHs)	Price (R)	Power Consumption (W)	Efficiency (MHs/W)
MSI GeForce RTX 3060	48.2	8799	107	0.450467289
MSI GeForce RTX 3070	62.34		115	0.542086956
GAINWARD GeForce RTX 3080	102	18199	223	0.457399103

Table 5.2: Solar panel comparison

Solar Panel Model	Cost
Poly PV system 250w solar panel with cable	R1310
275W Solar Panel (Poly)	R1795
CNBM 330W Polycrystalline Solar Panel	R2250

VI. DESIGN METHODOLOGY

PV systems typically output DC voltage, then are converted by use of inverters. The AC is then used by consumers that require AC. Mining rigs typically have power supplies that convert AC to DC to be used by the machine. For this design, the idea is to remove the conversion to AC and have the DC power from the solar panels' power the mining rig directly. The mining machines require certain types of connections and voltages, being 12V, 5V and 3.3V. In order to accomplish this, Buck Converters are used to step-down the output voltage from the PV array to the required voltage. Referring to the section II, by use of the equations for the Buck Converter the values for the circuit components and duty cycles are found as seen in Table 6.1 below. After calculating for the values of the circuit components, the next step is to build the Buck Converter circuit with the use of MATLAB Simulink and use the calculated values. The circuit diagram for the buck converters can be seen below in Figure 6.1. After configuring the buck converters, the next design is for the PV system. The PV system design followed that of [15] to get the base of the design. Trial-and-error was then used to get the right output power which is 1kW or above at STC temperature and at 1000W/m^2. The trial-and-error results can be seen below in Table 6.2. Finally, all subsystems are placed together as seen in Figure 6.3.

Table 6.1: Buck Converters' calculated values

	Duty Cycle	**Lmin (μH)**	**L (μH)**	**C (μF)**	**R (Ω)**	**fs (kHz)**	**Vripple**
Buck Converter 75V-12V	0.15989	84.011	105.014	125	8	40	5%
Buck Converter 75V-5V	0.06662	93.338	116.68	125	8	40	5%
Buck Converter 75V-3.3V	0.04397	95.603	119.5	74.87	8	40	5%

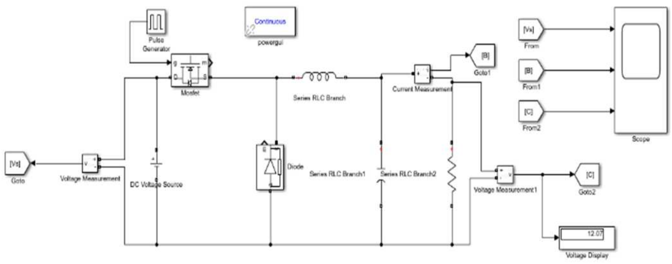

Fig 6.1: Buck converter design (75V-12V)

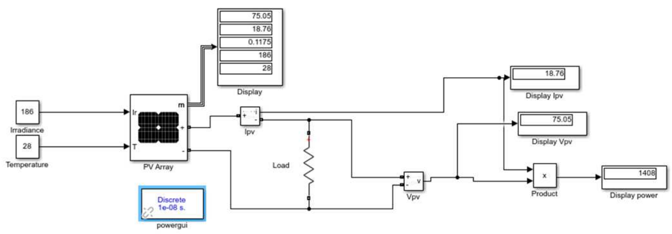

Fig 6.2: PV system design [15]

Table 6.2: PV system simulation data

Trial Number	**Parallel**	**Series**	**T (°C)**	**Irradiance (W/m^2)**	**Vo (V)**	**Io (A)**	**Po (W)**
1	3	2	25	1000	64.75	16.19	1048
2	2	3	25	1000	62.3	15.57	970.3

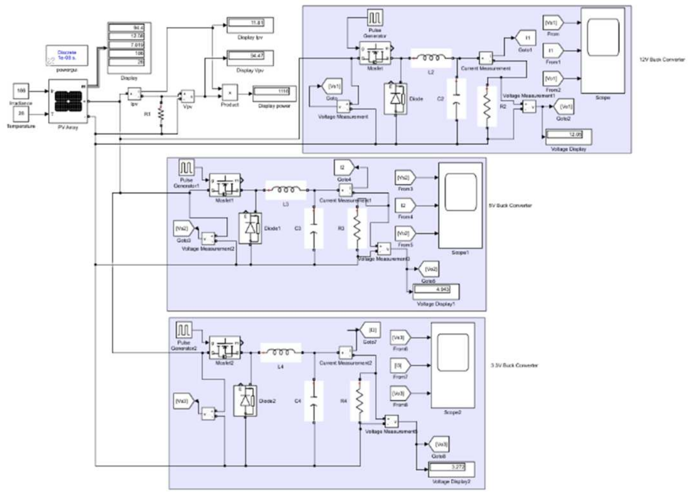

Fig 6.3: PV and Buck Converter system

VII. RESULT, ANALYSIS AND DISCUSSION

By referring to Table 7.1 below, it is observed that the output voltage values were not equal to or close to the required values of 12V, 5V and 3.3V respectively. By changing the duty cycle of each buck converter slightly, the right output voltages were achieved as seen in table 7.2.

Table 7.1: Output results of the full system with calculated Duty Cycle Values.

Subsystem	**Duty Cycle**	**Vo (V)**	**Io (A)**	**Po (W)**
PV System	-	100.4	12.55	1261
Buck Converter 75V-12V	0.15989	13.58	1.706	-
Buck Converter 75V-5V	0.06662	5.03	0.628	-
Buck Converter 75V-3.3V	0.04397	3.094	0.387	-

Table 7.2: Output results of full system with optimized Duty Cycle Values.

Subsystem	**Duty Cycle**	**Vo (V)**	**Io (A)**	**Po (W)**
PV System	-	100.4	12.55	1261
Buck Converter 75V-12V	0.143	12.1	1.51	-
Buck Converter 75V-5V	0. 06662	5.033	0.628	-
Buck Converter 75V-3.3V	0. 0463	3.281	0.4103	-

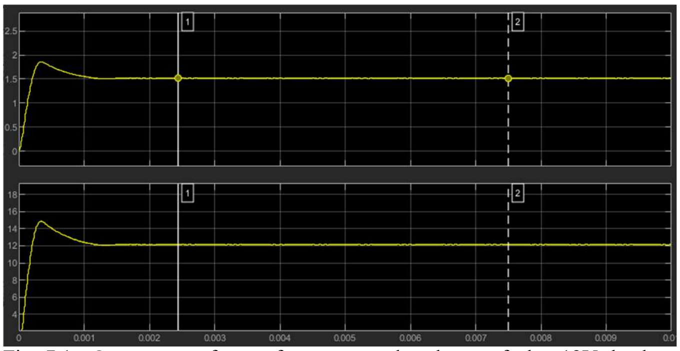

Fig 7.1: Output waveform of current and voltage of the 12V buck converter.

By referring to Table 7.2 above, it is observed that the designed DC-DC system successfully outputs the required values to their respective loads which are R2 in the 12V system, R3 in the 5V system and R4 in the 3.3V system thus the system is viable to directly power a mining rig.

To calculate for profitability and return on investment of the project, the equations in the literature review were used. Since the miner is GPU based the “MSI GeForce RTX 3070 Gaming Z Trio 8G LHR 8GB” was selected because it has the best efficiency in terms of hash rate per watt as per Table 5.1. Thus 8 of these GPUs can be used in a miner which will use around 920W while mining, the other components on the rig will use around 80W thus 1000W in total for the miner. This also means that the miner will cost R124 632. As seen in Table 5.1, 6 panels are needed and the panel model selected is “Poly PV system 250w solar panel with cable” as seen in Table 5.2, thus the cost of the solar panels is R7 860. The cost of the other equipment for the PV system will be around half of the cost of the panels which is R3 930 [3]. This brings the total cost of the system to R136 422. The most profitable cryptocurrency to mine on GPU miners is Ethereum. The miner will have a hash rate of around 498.72Mhs thus the Ethereum earned per day is 0.006 ETH. Thus, if one Ethereum coin is taken as being worth R30 600 ($1800) then the miner will make R183.6($10.80) per day. Thus, the return on investment of the whole project will be 743 days which is just over 2 years if the rig were to run 24 hours per day.

VIII. CONCLUSION AND RECOMMENDATIONS

In this report, a DC-DC direct connection from a PV array to a cryptocurrency mining rig is developed and designed. By utilizing information from previous studies, from resources on the internet and from my own personal knowledge and experience in cryptocurrency mining - information that is relevant to the project is presented in Section I. In Section II, III, IV and V the buck converter, standard GPU miners and pc connectors, factors that influence solar energy in South Africa, and profitability and return on investment was discussed respectively. The design and simulations will be found in Section VI and the analysis and results in Section VII. The results show that the direct connection from the solar panels to the mining rig is possible since the design was able to output 12V, 5V and 3.3V. Finally, the return on investment is then calculated, which could come in just under 2 years. This report also builds upon existing knowledge and adds knowledge in a way that is new and relevant because a DC-DC connection to a mining rig has not been done before. The limitation of the design in its current state is that it can also only be powered by solar energy during the day since there is no battery pack or connection to the grid for mining when solar energy isn’t available. However, this limitation is planned on being solved in future research.

In addition to adding a secondary power supply like a battery pack or connection to mains, it is recommended that automatic control like a MPPT system as well as electrical protection is added to the system to prevent over-volting and over-current damage to the system.

IX. REFERENCES

[1] J. Frankenfield, "“Cryptocurrency”," Investopedia, 11 Jan 2022. [Online]. Available: https://www.investopedia.com/terms/c/cryptocurrency.asp. [Accessed 20 March 2022].

[2] UPE, "Cryptography," Spark, [Online]. Available: https://upe.cs.fiu.edu/cybersecurity_03_05_2019/. [Accessed 11 May 2022].

[3] N. u. Rehman, "Feasibility Model For Solar-Powered Cryptocurrency Mining," October 2021. [Online]. Available: : (PDF) Feasibility Model For Solar-Powered Cryptocurrency Mining. [Accessed 2022 April 2022].

[4] E. Kim, "Bitcoin mining consumes 0.5% of all electricity used globally and," Business Insider South Africa, 7 September 2021. [Online]. Available: https://www.businessinsider.co.za/bitcoin-mining-electricity-usage-more-than-google-2021-9?r=US&IR=T. [Accessed 11 May 2022].

[5] Anon, "Buck Converters," PC Power Supply Voltage Data and Connector Types, [Online]. Available: https://learnabout-electronics.org/PSU/psu31.php. [Accessed 22 May 2022].

[6] M. C. Engineering, 19 February 2020. [Online]. Available: https://www.youtube.com/watch?v=ZWs2HJZTWAA&t=2s. [Accessed 27 May 2022].

[7] F. Wempen, "F. Wempen," 26 June 2001. [Online]. Available: https://www.techrepublic.com/article/untangling-the-wires-getting-to-know-your-power-supply/. [Accessed 21 May 2022].

[8] B. Mabasa, "B. Mabasa," Nov 2019. [Online]. Available: : (PDF) Assessment of Global Horizontal Irradiance in South Africa. [Accessed 22 May 2022].

[9] G. M. Masters., Renewable and Efficient Electric Power Systems, John Wiley & Sons, Inc., 2013.

[10] W. Spark, "Climate and Average Weather Year Round in Kimberley South Africa," [Online]. Available: https://weatherspark.com/y/90479/Average-Weather-in-Kimberley-South-Africa-Year-Round. [Accessed 22 May 2022].

[11] S. Fox, "How Does Heat Affect Solar Panel Efficiencies?," 6 December 2018. [Online]. Available: https://www.cedgreentech.com/article/how-does-heat-affect-solar-panel-efficiencies#:~:text=Pho. [Accessed 21 May 2022].

[12] D. Solar, "THE EFFECTS OF SHADING ON SOLAR PANELS," 1 March 2022. [Online]. Available: https://www.deegesolar.co.uk/solar_panels_shading/#:~:text=The%20Effects%20of%20Shading. [Accessed 22 May 2022].

[13] C. Brown, "Shading losses in PV systems, and techniques to mitigate them," 3 June 2022. [Online]. Available: https://www.aurorasolar.com/blog/shading-losses-for-pv-systems-and-techniques-to-mitigate-the. [Accessed 4 June 2022].

[14] S. F. Channel, "“100% LHR unlock WITHOUT Nicehash in NBminer! ETH hashrate for 3060,3060 Ti,3070,3070 Ti,3080,3080 Ti," 9 May 2022. [Online]. Available: https://www.youtube.com/watch?v=iXSoEW_5AHY. [Accessed 27 May 2022].

[15] P. a. E. Channel, "How to use PV array in," 29 March 2021. [Online]. Available: https://www.youtube.com/watch?v=2FPIUGZ_agg&t=2s. [Accessed 27 May 2022].

Improvement of a Three-Phase Z-Source Inverter Performance

Mbulelo Siyabonga Perfect Ngongoma
Durban University of Technology
Department of Electrical Power Engineering
Durban, South Africa
22290726@dut4life.ac.za

Innocent E Davidson
Department of Electrical Power Engineering
Durban University of Technology line
Durban 4001, South Africa
InnocentD@dut.ac.za

John T. Agee
Department of Electrical, Electronic and Computer Engineering
University of KwaZulu-Natal
Durban 4001, South Africa
ageej@ukzn.ac.za

***Abstract*—In this paper a mathematical design and simulation model of a Z-source inverter (ZSI) is presented. Three pulse width modulation (PWM) techniques viz. simple boost control (SBC), constant boost control (CBC) and the maximum boost control (MBC), are developed and applied to the designed ZSI and the critical performance parameters are analyzed under each of these PWM switching techniques. These critical performance parameters include the boost factor (B), DC-link voltage ($V_{dc\text{-}link}$), percentage of total harmonics distortion (%THD), modulation index (m) and the voltage stress across the IGBT/MOSFET switching components ($V_{stress\text{-}ratio}$). A different topology, the Capacitor-Boosted Z-Source Inverter (CB-ZSI) is then proposed. This different architecture is formed by addition of two parallel capacitors C_{p1} and C_{p2} across inductors L_1 and L_2 respectively on a classical ZSI topology and has proven an improved performance when comparing the critical performance parameters of a CB-ZSI to those of a classical ZSI. The boost factor of CB-ZSI is increased by more than 56% at SBC technique, more than 25% at CBC technique and more than 14% at MBC technique on average. The voltage stress ratio across the switching devices of a CB-ZSI is reduced by more than 40% at MBC technique, more than 5% at CBC control and increased by 1.7% for MBC PWM control technique on average. %THD for CB-ZSI is reduced by more than 112% for SBC technique, more than 16.8% for CBC and increased by more than 24% for MBC technique on average.**

Keywords — % total harmonics distortion, boost factor, capacitor-boosted-Z-Source Inverter, current-source inverter, DC-link voltage, modulation index, switching components switching stress, voltage-source inverter, Z-source inverter.

I. Introduction

This article examines a Z-source inverter, a type of power converter (ZSI). Professor F.Z. Peng created a unique topology for a DC-AC converter called a ZSI in 2002 [1], and it has been shown to successfully address most of the performance problems associated with the more often used traditional topologies [1], [2]. Voltage-source and current-source inverters, abbreviated as VSI and CSI, respectively, were the conventional topologies used for inverting related applications like connecting PV electricity to the utility grid before the invention of the ZSI [1], [2], [3], [4], [5].

A. *A Voltage-Source Inverter*

The fundamental circuit of a conventional three-phase voltage-source inverter is shown in Figure 1. A DC voltage source that feeds the primary inverting stage is created by connecting a DC power source in parallel with a large capacitor [1], [2]. A DC power source can be a battery, fuel cell stack, diode rectifier, and/or capacitor depending on the use of a VSI [1], [3]. A PV cell or an array of PV cells serves as a DC power supply in a PV system application [1], [2]. Six electrically controlled switching devices (IGBTs/MOSFETs) make up a bridge, each of which consists of a power transistor and an anti-parallel or freewheeling diode. This diode has the capacity to block voltage in one direction and allow bidirectional current flow. VSIs are popular for converting applications, but they have theoretical and conceptual constraints [4], [5].

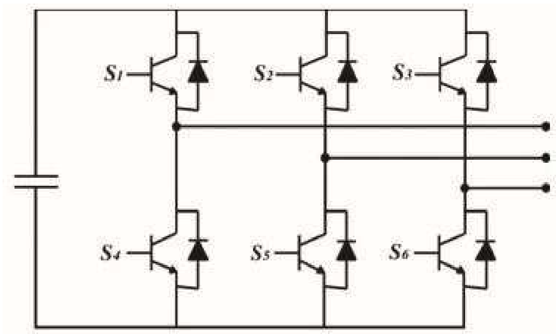

Fig. 1. A voltage-source inverter

A VSI can only produce voltages either below or above the DC-link voltage as its output voltage [1], [2], [3]. This means that the VSI either boosts or buck-boosts the input voltage [1], [4]. Whenever in inverter state (DC-AC converter), the VSI reduces input voltage and increases it in rectifier state (AC-DC converter) [1], [2], [3], [4]. The intended AC output requires an additional CD-DC boost converter stage in instances where overdrive is wanted but the available DC voltage is constrained [1], [4]. The total system's efficiency is negatively impacted, and the VSI's costs are increased because of this extra stage [1], [3], [4].

A shoot-through condition (shorted single-phase leg, any two-phase legs, or all three phase legs) [1], would result from concurrently turning on the upper and lower switching devices of the same phase leg, which would damage a VSI [1], [3], [5]. The dependability of VSI is seriously compromised in some instances when electromagnetic interference (EMI) noise inadvertently gates on switching devices, resulting in a shoot through event [1], [4], [5]. Engineers have implemented "dead time" to prevent upper and lower switching devices from turning on at the same time, hence avoiding a shoot-through circumstance, in response to this problem with VSIs [1], [5]. But "dead legs" lead to increased waveform distortion, etc., which lowers the output power's quality [1], [3], [4], [5], [6].

B. *A Current-Source Inverter*

The fundamental circuit of a conventional three-phase current-source inverter is shown in Figure 2. A DC power source and a sizable inductor are connected in series to create a DC source [1], [6],. The power switching components of the switching devices (IGBTs/MOSFETs) typically include gate turn-off thyristors (GTOs), silicon-controlled switches (SCRs), or power transistors with series diodes [1], [3], [6], [7]. These series diodes are capable of blocking voltage in both directions and providing unidirectional current flow. A CSI also has theoretical and conceptual limits [1], [7], [8].

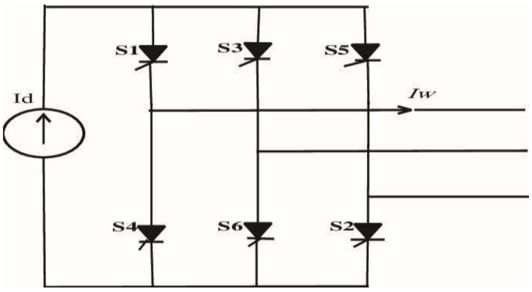

Fig. 2. A current-source inverter

Like the VSIs, the CSI's output voltage is constrained to levels that either buck or boost the DC-link voltage [1], [7], [9]. The CSI lowers the input voltage when in the rectifier mode and raises it when in the inverter mode [1], [9]. To get the desired AC output in applications where overdrive is desired, but the available dc voltage is constrained, a second DC-DC boost converter stage is required [1], [9], [10]. The system's efficiency is impaired, and its overall expenses are increased by this additional stage [1], [6], [10].

At all times, at least one lower switching device and one upper switching device shall be gated on. If not, a DC inductor would experience an open circuit, which would kill the inverter [1], [10]. A significant flaw in the reliability of CSI is the occurrence of Electromagnetic Interference (EMI) noise, which may accidentally gate-off the switching devices and cause the DC inductor to open circuit [1], [11]. Engineers have introduced "overlap time" for safe current commutation to address this CSIs issue and stop the open circuit of a DC inductor state from happening [1], [10], [11]. However, "overlap time" causes greater waveform distortion, etc., which lowers the output power's quality [1], [12].

A series diode must be used in conjunction with highspeed and high-performance transistors such insulated gate bipolar transistors to block reverse voltage on the main switching components of a current source inverter (IGBT) [1], [11]. This inhibits the direct use of intelligent power modules (IPMs) and low-cost, high-performance IGBT modules [1], [13].

C. *Why is a ZSI Most Preferred Than VSI and CSI*

VSIs and CSIs have several topological issues. The input voltage can only be boosted or buck-boosted by the VSIs and CSIs; it cannot be both [1]. This suggests that the range of possible output voltages is restricted to those that are either higher than or lower than the input voltage [1], [13]. VSI and CSI main circuits are not interchangeable. It is not possible to use the VSI's main circuit for the CSI application, and the reverse is also true [13]. Because EMI noise can affect both VSIs and CSIs, their dependability is jeopardized. Most of the weaknesses of VSIs and CSIs have been demonstrated to be overcome by Z-source inverters [1], [12], [13]. ZSIs can buck-boost and are resistant to a shoot-through which is catastrophic in the case of the VSIs and CSIs [1]. This is the motive behind the increased focus of researchers on the Z-source inverters [1], [13]. Figure 3 shows a basic diagram of a ZSI which has a DC input (battery/fuel cell/PV array), a Z-impedance network (L1, L2 and C1, C2) and a three-phase universal bridge made of switching devices (S1, S2, S3, S4, S5 and S6).

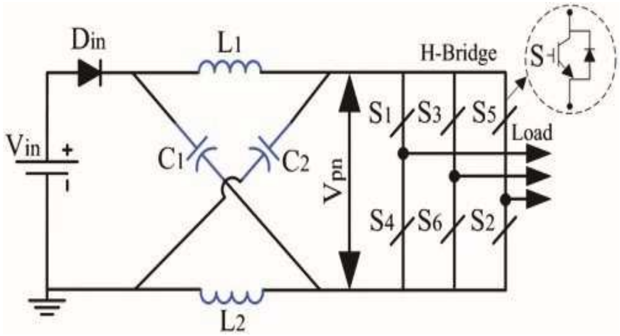

Fig. 3. A z-source inverter

II. DESIGN AND MODELLING OF A Z-SOURCE INVERTER

This section designs a z-source inverter (ZSI) circuit and then develops and applies several PWM control strategies to it. The outcomes for each PWM control method are thereafter provided and thoroughly explained. The voltage stress (V_{stress}), modulation index (m), and boost factor (B) are among the crucial performance factors examined. The design of a ZSI circuit must meet the following requirements: a total power rating of 2000 W, an input DC voltage range of 200 V to 500 V, and a switching frequency of 10.05 kHz [1].

Capacitor design, inductor design, filter design, power diode design, and the choice of power electronic switching devices are the four main categories under which a ZSI circuit is designed [1]. The four ZSI design sections are presented in the subsections that follow. The designed values indicate the lowest value that designed components can be [1], but it is frequently difficult to obtain the exact component rating that is determined by the design calculations in a real-world setting where components have standard values [1], [13]. An example of this case is resistor series, E3, E6, E12, etc [1]. 13]. The selected values ought to be higher than and as near to the intended value as possible [1], [12], [13].

A. *The Inductor Design*

A Z-impedance network's L_{1min} and L_{2min} minimum inductance requirements are determined through the inductor design procedure [1]. The average inductor current $I_{L(AVG)}$, the current ripple ΔI, and a DC-link voltage $V_{DC\text{-}LINK}$ should first be computed to archive the minimal inductance design. (1) and (2) are used to archive a ripple current [1], [7], [13].

$$I_{L(AVG)} = P/V_{IN} \tag{1}$$

The ripple current can be estimated by calculating the highest and minimum currents [1]. Using (2) [1], [13], [14], it is possible to determine the maximum peak-to-peak current as follows:

$$I_{MAX} = I_{L(AVG)} + 30\% \text{ and}$$

$$I_{MIN} = I_{L(AVG)} - 30\%$$

$$\therefore \Delta I = I_{MAX} - I_{MIN} \tag{2}$$

It is crucial to plan for the worst-case situation when designing an electrical circuit because doing so increases the design's stability and reliability [1], [14]. The highest limit is set at a boost factor B of 5, for this reason [1], [13], [14]. Therefore, theoretically, the capacitor an inductor, and the switching devices, which were calculated using the assumption (max. B at 5) will successfully survive the pressures placed on them if the ZSI works at boost factor range of 1 to 5 [1]. As a result, the minimal inductance need L_{min} can now be computed using (3), where T is the switching period and $V_{DC\text{-}LINK}$ is the maximum DC-link voltage. [1], [8], [4].

$$1/[1-2(T_0/T)] \leq B \quad (3)$$

$$L_{MIN} = (V_{DC\text{-}LINK(MAX)}\ T_0)/\ \Delta I \quad (4)$$

B. *The Capacitor Design*

Calculating the minimum capacitance requirements for a Z-impedance network, C_{1MIN} and C_{2MIN}, is the process of capacitor design. An average inductor current, shoot-through time, and capacitor ripple voltage must first be computed to archive the minimal capacitance design [1]. These calculations may be found in (1) and (3). The required minimum capacitance is obtained using equations (5) and (6) to determine voltage ripple [1], [14].

$$\Delta V_C = V_{DC\text{-}LINK} \times 3\% \quad (5)$$

$$C_{MIN} = (I_{L(AVG)}\ T_0)/\ \Delta V_C \quad (6)$$

C. *The Filter Design*

Over LC and L-filters, LCL-filters are the most popular option [1], [5], [13], [14]. This decision was made based on the weight, cost, and size of LCL relative to those of LC and L-filters [1]. Although the values of the inductors and capacitors used in LCL filters are low compared to the values needed for LC and L-filters [1], [2]; they nonetheless produce outstanding results in the region of 100 kilovolt-amperes [1], [12], [14]. Compared to LC and L-filters, LCL-filters have excellent switching frequency attenuation of -60 Db/decade [1], [14]. It is possible to design an LCL-filter by using (7) to (11) [1]. Z_B, C_B, V_φ, and P stand for the inverter's base impedance, base capacitance, output phase voltage, and rated power, respectively [1]. First, second, and filter capacitor are designated by the letters L_{F1}, L_{F2}, and C_F, respectively [1], [15].

$$Z_B = V_\varphi/P \text{ therefore,} \quad (7)$$

$$C_B = 1/(2\pi f\ Z_B) \text{ where f is the switching frequency} \quad (8)$$

$$\square\ C_F = C_B \times 20\% \quad (9)$$

$$L_{F1} = V_{IN}/(6f\Delta I_{MAX}) \text{ where } \Delta I_{MAX} = 0.1\ I_{MAX} \quad (10)$$

$$L_{F2} = [(1/k_a^2)-1]/\ C_F 2\pi f \text{ where } k_a \text{ is an attenuation factor of 20\%} \quad (11)$$

D. *Selection of a Diode and Switching Devices*

Maximum line-to-line voltage $V_{L\text{-}L}$ and load current I_{LOAD} are calculated using the formulas in (12) and (13) below because the maximum voltage across the diode and through the power electronic switches equals the peak DC-link voltage and the maximum current through the diode equals the maximum inductor current [1]. So, when the power transfer is at its highest, the maximum current via the switches, $I_{SWITCH(MAX)}$ is defined by (14) [1], [13].

$$V_{L\text{-}L} = V_{ABC(\varphi)}\ (2)_{1/2} \quad (12)$$

$$\square\ I_{LOAD} = P/[(3)^{1/2}\ V_{L\text{-}L}], \text{ at unity power factor} \quad (13)$$

$$\square\ I_{SWITCH(MAX)} = 1/2\ I_{LOAD} + 2/3\ I_{F1} \quad (14)$$

The switching devices and a diode to be selected generally have current and voltage ratings exceeding the above calculated values by at-least 25% as a safe working margin [1], [5].

III. Simulation Results of a ZSI

The MATLAB Simulink software was used for the ZSI modelling. This section covers the simulation results of a ZSI driven by the simple boost control (SBC), continuous boost (CBC), and maximum boost control (MBC) pulse width modulation signal generators [1].

A. *The Simple Boost Modulation Technique Results*

As a safe operating margin, the switching devices, and a diode to be used typically have current and voltage ratings that are at least 25% higher than the previously computed values [1].

$$V_{ABC(\varphi)} = [(3)_{1/2} m\ B_{SBC} V_{IN}]/2 \quad (15)$$

$$\text{where } B_{SBC} = 1\ /\ (2m - 1);\ 0.5 < m < 1 \quad (16)$$

Figure 4 shows the unfiltered three-phase output voltage for the SBC PWM technique sampled when V_{in} was 200V and m at 0.65. The rest of the results are presented at table 1 [1].

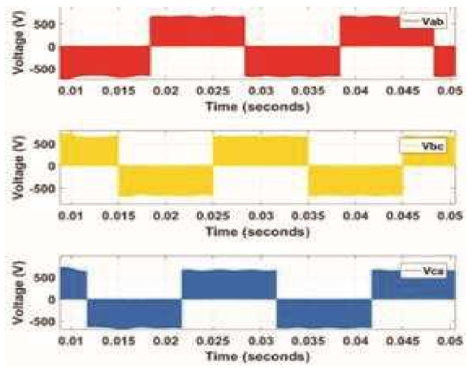

Fig. 4. SBC Unfiltered line voltages [1]

Unfiltered line voltages for the SBC PWM approach are shown in Figure 4. According to SANS 10142 standard documents, the South African national grid specification for percentage of total harmonics distortion is below 5% as presented in table 1 [1], 14]; the amplitude of phase and line waveforms, as well as a DC-link voltage, comply with (15) and (16). On table 1, a few theoretical relationships can be verified such as the (15) and (16). The modulation index is the only component that influences the voltage stress across

TABLE I. Table Showing Results of Critical Performance Parameters of a ZSI Under the SBC Technique

Varying V_{in} and m								
m	0.65	0.65	0.65	0.65	0.75	0.75	0.75	0.75
V_{in}	200	300	400	500	200	300	400	500
B	3.22	3.22	3.23	3.23	1.94	1.94	1.95	1.95
V_{stress}	2.98	2.98	2.98	2.98	2.59	2.59	2.59	2.60
%TH	3.75	3.75	3.75	3.75	1.14	1.14	1.14	1.14
G	2.09	2.09	2.10	2.10	1.46	1.46	1.46	1.46

Table 3 continues								
m	0.85	0.85	0.85	0.85	0.95	0.95	0.95	0.95
V_{in}	200	300	400	500	200	300	400	500.
B	1.42	1.42	1.42	1.42	1.10	1.10	1.10	1.10
V_{stress}	2.33	2.34	2.33	2.34	2.09	2.09	2.09	2.10
%TH	1.14	1.14	1.14	1.14	1.14	1.14	1.14	1.14
G	1.20	1.21	1.21	1.21	1.05	1.05	1.05	1.05

the switching devices, the boost factor (and consequently the gain factor), and the proportion of overall harmonic distortion [1]. As the modulation index rises, all these measures indicate a reduction. Both the input voltage and the modulation index affect both the output voltage and the DC-link voltage [1]. With an increase in either the input voltage or the modulation index, both the output voltage and the DC-link voltage rise; the contrary is likewise true [1], [13].

B. *The Constant Boost Modulation Technique Results*

For the CBC modulation technique, the output phase voltage of a ZSI is defined by (17) where B_{CBC} is the boost factor of the constant boost modulation technique defined by (18) [1].

$$V_{ABC(\varphi)} = [(3)^{1/2} m B_{CBC} V_{IN}]/2 \quad (17)$$

$$\text{where } B_{CBC} = 1 / [(3)^{1/2} 2m - 1];\ 0.577 < m < 1.155 \quad (18)$$

Figure shows the unfiltered three-phase output voltage for the CBC PWM technique sampled when V_{in} was 200V and m at 0.65 [1]. The rest of the results are presented at table 2.

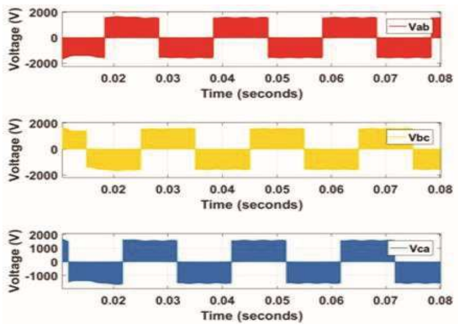

Fig. 5. CBC Unfiltered line voltages [1]

Figure 5 shows unfiltered line voltages for the CBC PWM technique. The amplitude of phase and line waveforms, as well as a DC-link voltage, conform to (17) and (18), and the %THD is also below 5% [1].

TABLE II. TABLE SHOWING RESULTS OF CRITICAL PERFORMANCE PARAMETERS OF A ZSI UNDER THE CBC TECHNIQUE [1]

Varying V_{in} and m								
m	0.65	0.65	0.65	0.65	0.75	0.75	0.75	0.75
V_{in}	200	300	400	500.	200.	300.	400	500.
B	7.95	8.00	8.00	8.00	3.35	3.33	3.37	3.36
V_{stress}	1.79	1.79	1.79	1.79	1.52	1.52	1.54	1.53
%TH	4.00	4.00	4.00	4.00	3.72	3.72	3.72	3.72
G	5.16	5.20	5.20	5.20	2.51	2.50	2.53	2.52
Table 3 continues								
m	0.85	0.85	0.85	0.85	0.95	0.95	0.95	0.95
V_{in}	200	300	400	500	200	300	400	500
B	2.11	2.13	2.12	2.10	1.55	1.55	1.55	1.56
V_{stress}	1.27	1.30	1.30	1.30	1.19	1.18	1.18	1.20
%TH	2.68	2.68	2.68	2.68	3.95	3.95	3.95	3.95
G	1.79	1.81	1.80	1.78	1.47	1.47	1.47	1.48

same as in the case of SBC technique, table 2 contains a set of results that validates the theoretical definitions (17) and (18) [1].

C. *The Maximum Boost Modulation Technique*

For the MBC modulation technique, the output phase voltage of a ZSI is defined by (19) where B_{MBC} is the boost factor of the constant boost modulation technique defined by (20) [1].

$$V_{ABC(\varphi)} = [(3)^{1/2} m B_{MBC} V_{IN}]/2 \quad (19)$$

$$\text{where } B_{CBC} = 1 / [3(3)^{1/2} m - \pi];\ 0.605 < m < 1 \quad (20)$$

Figure 6 shows the unfiltered three-phase output voltage for the MBC PWM technique sampled when V_{in} was 200V and m at 0.65 [1]. The rest of the results are presented at table 3.

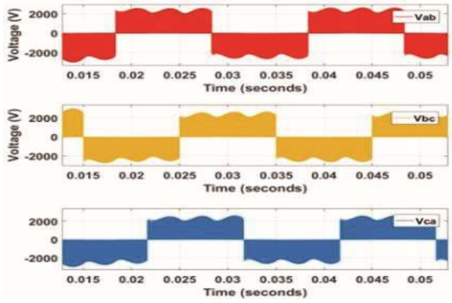

Fig. 6. MBC Unfiltered line voltages [1]

Figure 6 shows unfiltered line voltages for the MBC PWM technique. The amplitude of phase and line waveforms, as well as a DC-link voltage, conform to (19) and (20), and the %THD is also below 9.63%. Same as in the case of SBC and MBC technique, table 3 contains a set of results that validates the theoretical definitions (19) and (20) [1].

TABLE III. TABLE SHOWING RESULTS OF CRITICAL PERFORMANCE PARAMETERS OF A ZSI UNDER THE MBC TECHNIQUE [1]

Varying V_{in} and m								
m	0.65	0.65	0.65	0.65	0.75	0.75	0.75	0.75
V_{in}	200	300	400	500	200	300	400	500
B	13.0	13.0	12.2	12.1	4.05	4.08	4.06	4.10
V_{stress}	1.77	1.77	1.65	1.65	1.36	1.36	1.36	1.37
%TH	10.3	10.3	10.3	10.3	9.26	9.26	9.26	9.26
G	8.45	8.45	7.96	7.80	3.03	3.06	3.04	3.07
Table 3 continues								
m	0.85	0.85	0.85	0.85	0.95	0.95	0.95	0.95
V_{in}	200	300	400	500	200	300	400	500
B	2.50	2.51	2.51	2.50	1.87	1.74	1.80	1.80
V_{stress}	1.31	1.33	1.33	1.34	1.23	1.22	1.21	1.21
%TH	15.0	15.0	15.0	15.0	15.0	15.0	15.0	15.0
G	2.12	1.81	1.80	1.78	1.78	1.47	1.71	1.71

IV. PROPOSING A CAPACITOR-BOOSTED-Z-SOURCE INVERTER

This section's goal is to suggest a new type of Z-source inverter called a capacitor-boosted-Z-Source Inverter (CB-ZSI) [1]. The naming of this proposed inverter is driven by the

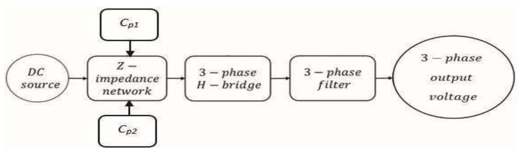

Fig. 7. The CB-ZSI block diagram [1]

fact that the typical inverter's z-impedance is modified by connecting two capacitors in series with the original impedance inductors (Fig.7), enhancing the inverter's boosting capability [1]. When the previously developed PWM control techniques in the previous (SBC, CBC, and MBC) are applied to a CB-ZSI, it has been demonstrated that the response of the conventional Z-source inverter is altered by the addition of two shunt capacitors C_{p1} and C_{p2} to the corresponding inductors L_1 and L_2 (topological amendment) [1]. This chapter develops a CB-ZSI and compares its performance to a ZSI.

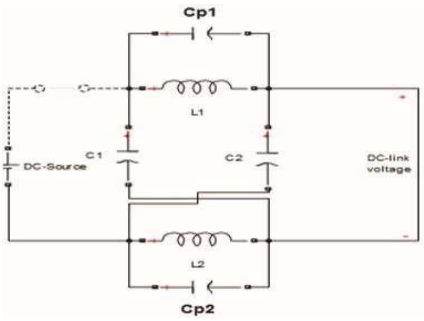

(a)

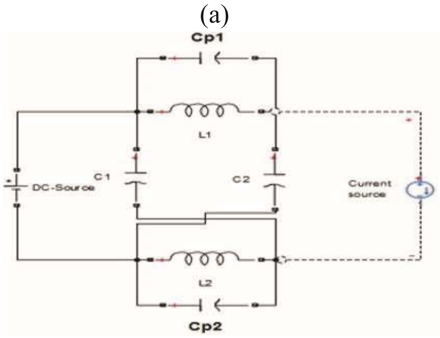

(b)

Fig. 8. (a) Equivalent shoot-through CB-ZSI circuit [1]; (b) Equivalent non-shoot-through CB-ZSI circuit [1]

A. *Circuit Analysis*

At steady state, the average inductor voltage across inductors L_1 and L_2 for a conventional ZSI is zero [1], 12], [14]. The average inductor voltage across inductors L_1 and L_2 is no longer zero for the CB-ZSI, though [1]. Shunt capacitors C_{p1} and C_{p2} in parallel with the respective inductors L_1 and L_2 make this straightforward. Referring to figure 8, these capacitors maintain a potential difference across the inductors that tends to be negative relative to V_{in} [1]. A typical inductor voltage-time product ($T = T_1 + T_0$ interval where T_1 is non-shoot-through and T_0 is shoot-through time) is therefore as follows:

$$V_L T = V_C T_0 + (V_{IN} - V_C)\, T_1 = V_{Cp} T \qquad (21)$$

$$\text{And let } V_{Cp} = V_a T_0 + V_b T_1 \qquad (22)$$

$$\text{where } V_a = k_a V_C,\ V_b = k_b V_C,\ k_a, k_b - \text{proportional factors (\%)} \qquad (23)$$

$$\therefore V_C T_0 + (V_{IN} - V_C)\, T_1 = V_a T_0 + V_b T_1 \qquad (24)$$

$$B = V_{DC\text{-}LINK}/V_{IN} = 1/\,(1\text{-}2(1+k_a)\, D_0, \quad k_a \neq (2D_0 - 1)/2\, D_0 \qquad (25)$$

B. *CB-ZSI vs. ZSI results*

The same set of results was harvested on the CB-ZSI as in the previous section for the ZSI [1]. However, only a summary of the CB-ZSI results will be presented here and be compared to those of a ZSI [1]. Table 4 below shows the comparison of the CB-ZSI and ZSI on some critical performance parameters over the same input conditions.

TABLE IV. ZSI VS CB-ZSI (CP = 1 AND 2%) AT SBC, CBC, AND MBC [1]

Parameter	ZSI, SBC	CB-ZSI, SBC, C_p=1%	CB-ZSI, SBC, C_p=2%	ZSI, CBC	CB-ZSI, CBC, C_p=1%	CB-ZSI, CBC, C_p=2%	ZSI, MBC	CB-ZSI, MBC, C_p=1%	CB-ZSI, MBC, C_p=2%
V_{DClink}(V)	644.8	1009	1210	1590	2000	2398	2601	2701	2779
$V_{AC(3\varphi)}$ (V)	216.5	573.6	586.4	888.0	1118	1143	1465	1480	1491
%THD	3.750	3.120	2.760	4.000	2.070	1.87	10.37	31.41	37.32

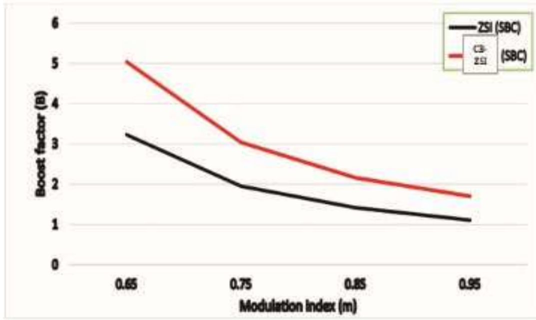

(a)

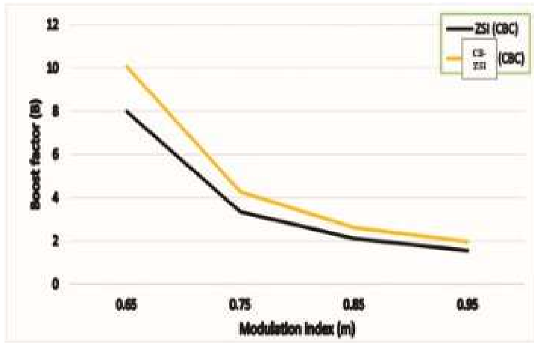

(b)

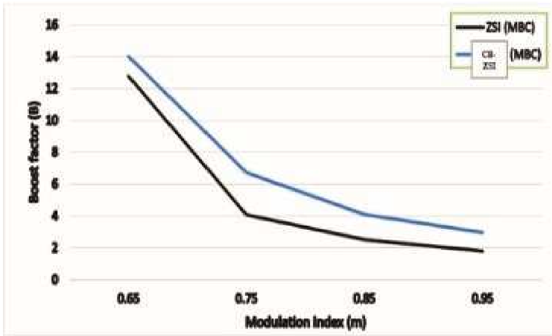

(c)

Fig. 9. m vs B for (a) SBC control technique [1]; (b) CBC control technique [1]; (c) MBC control technique [1]

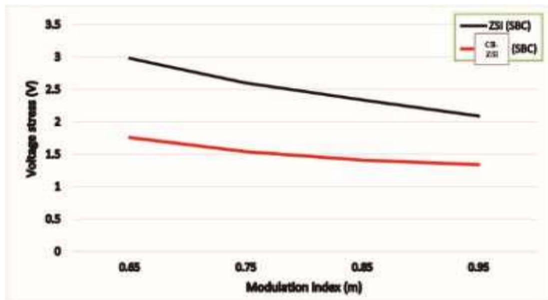

(a)

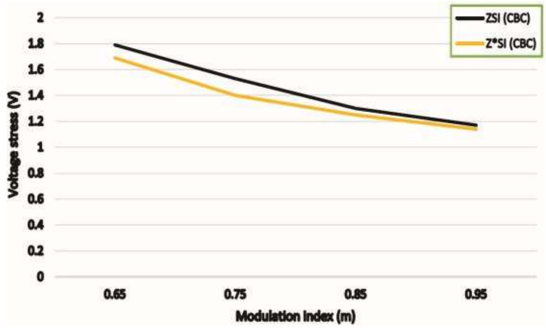

(b)

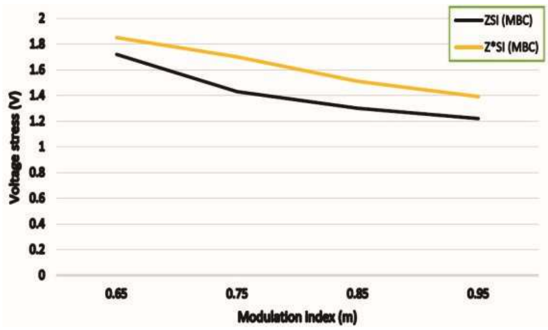

(c)

Fig. 10. V_{stress} vs B for for (a) SBC control technique [1]; (b) CBC control technique [1]; (c) MBC control technique [1]

Two main facts can be concluded from table 4 relating to the comparison of CB-ZSI and th ZSI. Firstly, a CB-ZSI shows an increase in the boost factor with increase in shunt capacitance (because of increase in DC-link voltage) compared to a ZSI for the same input voltage and modulation index [1]; secondly, increasing the shunt capacitance increases a gain factor of a CB-ZSI compared to a ZSI for the same input voltage and modulation index [1]. The above stated facts hold across all three PWM control techniques, viz. SBC, CBC, and MBC [1].

Figure 9 show that inclusion of a shunt capacitance C_p that is 1% of C_1 improves the boost factor of CB-ZSI by more 56% at SBC technique, more than 25% at CBC technique and more than 14% at MBC technique on average [1]. Since the gain factor is a linear function of a boost factor with the proportionality constant being the modulation index, the percentage of improvement of gain factors from ZSI to CBZSI remains the same as that of boost factors across SBC, CBC, and MBC techniques [1].

Figure 10 shows that the voltage stress ratio across the switching devices is reduced by more than 40% at MBC technique, more than 5% at CBC control and increased by 1.7% for MBC PWM control technique on average [1]. CB-ZSI also shows improved performance on the %THD for SBC and CBC while it worsens for MBC technique. %THD is reduced by more than 112% for SBC technique, 16.8% for CBC and increased by more than 24% for MBC technique on average [1].

V. Conclusion and Future Work

More insight is required on the operation of a CB-ZSI. To build on top of the work of this research study, a formula that define the shunt capacitance Cp and correlate it to a specified amount of boost it incurs in a CB-ZSI still needs to be established. The limits of C_p also need to be established. As C_p approaches zero, a CB-ZSI converges to an ZSI; What happens C_p approaches infinity? The proportional factors k_a and k_b still need to be unpacked. A formula for these factors to form a characteristic table which shows k_a and k_b values for different values of C_p still need to be established to aid easy circuit design of a CB-ZSI.

VI. References

[1] Ngongoma, Mbulelo Siyabonga Perfect. *Impact of different pulse width modulation (PWM) techniques on the performance of a three phase Z-Source inverter (ZSI)*. Diss. 2019.

[2] R. R. Kumar, S. Kumar, and A. Yadav, “comparison of PWM techniques and inverter performance,” *IOSR Journal of Electrical and Electronics Engineering (IOSR-JEEE),* vol. 4, no. 1, pp. 1822, 2013.

[3] R. Mali, N. Adam, A. Satpaise, and A. Vaidya, "Performance comparison of two-level inverter with classical multilevel inverter topologies." pp. 1-7.

[4] A. A. Usmani, M. Shahrukh, and A. Mustafa, "Comparison of different three phase inverter topologies: A review." pp. 19-24.

[5] S. Sonar, “A new configuration of three-level ZSI using transistor clamped topology,” *Energies,* vol. 13, no. 6, pp. 1469, 2020.

[6] N. Kshirsagar, P. Debre, A. Kadu, and R. Juneja, "Design of three phase Z-source inverter for solar photovoltaic application." pp. 16.

[7] M. Abbasi, M. Mardaneh, A. H. Eslahchi, and Z. Hashemi, “Extended boost switched-embedded-capacitor-inductor Zsi with low voltage stress on capacitors and soft-start capability,” *IETE Journal of Research*, pp. 1-10, 2021.

[8] S. Kumaravel, V. Thomas, S. K. Tripathy, and S. Ashok, "Performance Analysis of a Z-Source Inverter with Controller for Autonomous System Application." pp. 355-359.

[9] A. J. Viji, R. Balamanigandan, and B. Manimaran, “Power Quality Improvement of Grid Connected PV System Fed ZSIDVR with Advanced Control Strategy,” *Journal of Green Engineering,* vol. 10, pp. 9574-9586, 2020.

[10] N. Saeed, A. Ibrar, and A. Saeed, “A review on industrial applications of Z-source inverter,” *Journal of Power and Energy Engineering,* vol. 5, no. 9, pp. 14-31, 2017.

[11] G. Prakash, C. Subramani, K. Dhineshkumar, and P. Rayavel, "Analysis of Extended Z-source Inverter for Photovoltaic System." p. 012071.

[12] Y. Xu, and H. Xiao, “Combinative Voltage Vector-Based Model Predictive Control for Performance Improvement of Quasi Z-Source Inverter,” *IEEE Access,* vol. 9, pp. 143013-143025, 2021.

[13] A. Alam, M. K. Mukul, and P. R. Thakura, “Stability analysis and reliability evaluation of a Z-source inverter,” *International Journal of Power Electronics,* vol. 7, no. 1-2, pp. 1-15, 2015.

[14] M. Gobi, and P. Selvan, “Photovoltaic Power injected to the Grid with Quasi Impedence Source Inverter,” *International Journal of Engineering Research and General Science,* vol. 2, no. 3, pp. 421-426, 2014.

Comparative Analysis Of Simple Boost, Constant Boost And Maximum Boost Pulse Width Modulation Schemes On A Three-Phase Z-Source Inverter

Mbulelo S. P. Ngongoma
Department of Electrical Power Engineering
Durban University of Technology
Durban 4001, South Africa
mbulelo26644@gmail.com

Innocent E Davidson
Department of Electrical Power Engineering
Durban University of Technology line
Durban 4001, South Africa
InnocentD@dut.ac.za

John T. Agee
Department of Electrical, Electronic and Computer Engineering
University of KwaZulu-Natal
Durban 4001, South Africa
ageej@ukzn.ac.za

***Abstract*—This paper aims to compare the switching capabilities of the three most cited Pulse Width Modulation (PWM) control techniques in the application of three-phase Z-Source Inverters (ZSI). The Simple, Constant and Maximum Boost PWM control techniques are mathematically designed and applied to a 2 k-W ZSI and the critical performance metrics of the inverter, viz. the boost factor (B), voltage stress ratio across the switching components (V_{stress}) and the percentage of total harmonic distortion (%THD), are analyzed and compared for each of PWM control techniques. The Maximum boost control technique yield the highest boost factor however at a cost of increased %THD in the output power signals. The simple Boost PWM control incurs the highest V_{stress} across the switching components. The constant boost control is intermediate while the simple and maximum boost controls are the extremes for all three performance metrics. It is best to understand the performance characteristics associated with each PWM control technique to make an appropriate selection of the best-suited PWM control scheme for a particular application.**

Keywords—% total harmonics distortion, boost factor, modulation index, switching components switching stress, Z-source inverter Introduction

I. INTRODUCTION

This paper aims to comparatively analyse the three most popular pulse width modulation (PWM) schemes on the application of a three-phase Z-source inverter (ZSI), namely, the simple boost control (SBC), constant boost control (CBC) and maximum boost control (MBC) techniques. The critical performance parameters of a ZSI are carefully observed under the influence of each of the PWM switching techniques and compared to identify the strengths and weaknesses of each switching technique. This paper is intended to be a quick guide for other researchers or designers to determine the appropriateness of a PWM control technique of choice for a particular inverter application. Therefore, in the coming sections, a detailed mathematical design and software simulation results of three pulse-width-modulation (PWM) control schemes for a three-phase Z-source inverter (ZSI) will be presented and analysed.

II. BACKGROUND

. A ZSI is a recent topology of a DC-AC converter proposed by Prof. F.Z. Peng in 2002 and it has since attracted the attention of many researchers due to its capability to overcome the majority of conceptual and practical limitations faced with the traditional topologies of the DC-AC converters [1], [2], [3]. Figure 1 shows a topological circuit of the first ZSI inverter generation. However, several different topologies have been proposed by different scholars to improve the performance of ZSI's and their suitability for different applications.

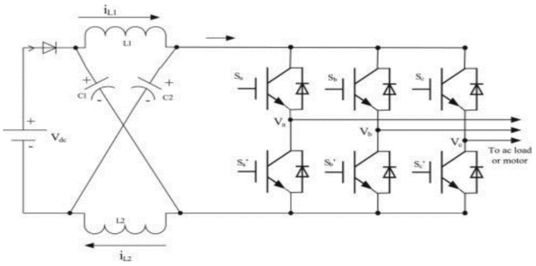

Fig. 1. A classical ZSI topologica6l circuit

Abbasi [4] proposed a switched inductor Z-source inverter (SL-ZSI). This topology has two additional inductors and six diodes in the 'SL-impedance network' compared to a 'Z-impedance network' of a classical ZSI as shown in figure 2. This topology has a superb voltage boost and is stable across a range of input voltages [5]. The great voltage boost is caused by a low shoot-through time (T_0) requirement to achieve a particular boosting level of an SL-ZSI compared to a classical ZSI [6]. This inverter can be controlled with several PWM switching schemes including SBC, CBC, and MBC.

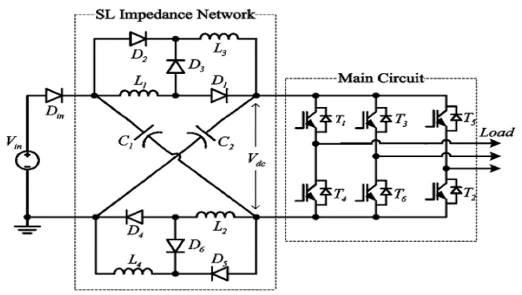

Fig. 2. An SL-ZSI topological circuit

Jokar Kouhanjani [7] proposed two trans-Z-source inverters, the first being an inductor-capacitor-capacitor-transformer-Z-source inverter (LCCT-ZSI) and, secondly, an inductor-capacitor-capacitor-transformer-quasi Z-source inverter (LCCT-qZSI) as shown in figure 3. Both these trans-ZSI's improved the voltage-boosting capabilities even though LCCT-ZSI supersedes LCCT-qZSI [7]. LCCT-qZSI, however, has a greater power conversion efficiency compared to LCCT-ZSI [7]. Both these inverters can be controlled with several PWM switching schemes including SBC, CBC and MBC [7].

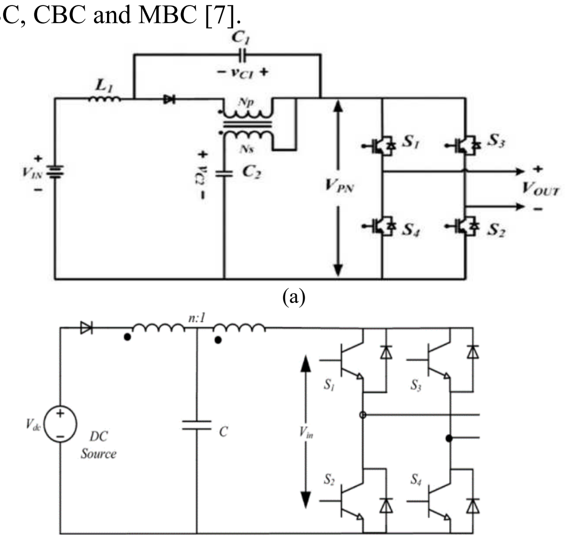

Fig. 3. (a) An LCCT-ZSI topological circuit; (b) An LCCT-qZSI topological circuit

Mbulelo SP {Ngongoma, 2019 #162}proposed a capacitor-boosted-Z-source inverter (CB-ZSI), a topology achieved via the addition of two shunt capacitors to inductors L_1 and L_2 of a classical ZSI as shown in figure 4. This topology has a greater voltage boost and hence gain factor relative to a classical ZSI for SBC, CBC and MBC techniques. This enhanced voltage-boosting capability is caused by the shunt capacitors which charge up and maintain a potential difference during the non-shoot-through time in every switching cycle and transfer their stored energy together with the Z-impedance network to the output during a shoot-through state. The voltage stress across the switching devices SW1-SW6 was greatly reduced thus improving the output power signals (Less %THD).

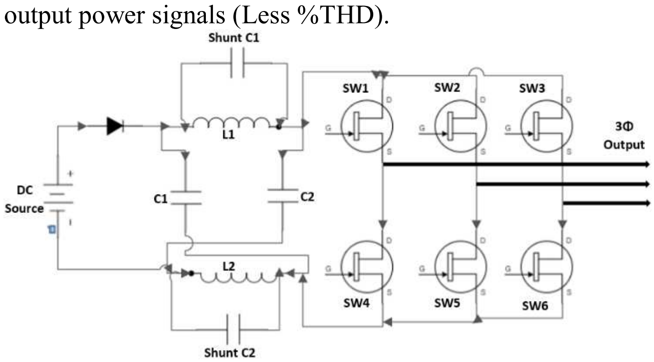

Fig. 4. A CB-ZSI inverter.

In the coming sections, each PWM control technique (SBC, CBC and MBC) will be mathematically designed and applied to the switching devices of a pre-designed 2 k-W Z-source inverter whose components' ratings are listed in table 1 below. The performance results of the inverter under the influence of each switching scheme will be presented and analysed comparatively.

TABLE I. COMPONENTS' RATINGS FOR THE ZSI

Components rating for the Z-source inverter	
Component	***Rating (units)***
Inductors (L_1, L_2)	6.63 m-H, 6.63 m-H
Capacitors (C_1, C_2)	7.96 µ-C, 7.96 µ-C
Maximum diode voltage	707.1 V
Maximum switching device current	7.48 A
Filter (L_{f1}, L_{f2}, C_f)	55 m-H, 41m-H, 2.98 µ-C

III. DESIGN AND IMPLEMENTATION OF THE PWM CONTROL TECHNIQUES

A. Simple boost PWM control technique

Defined are the three functions $V_{ac(3\varphi)}$, $V_{carrier}$ and $V_{constant}$. (1) is a three-phase fundamental waveform which is the objective that all the three-phase inverters seek to achieve, where V_m and ω are the maximum voltage and the angular frequency of the sinusoidal phase waves respectively. (2) is a high-frequency triangular carrier wave where A and T are constants. (3) is a function of two constant lines enveloping and/or intersection (1) and (2) on the maximums (crests) and minimums (troughs) [3], [4].

$$V_{ac(3\varphi)}(t) \begin{cases} V_{a(\varphi)}(t) & V_m \sin(\omega t) \\ V_{b(\varphi)}(t) & V_m \sin(\omega t - 120) \\ V_{c(\varphi)}(t) & V_m \sin(\omega t - 240) \end{cases} \quad (1)$$

$$V_{carrier}(t) \begin{cases} 4A/T\ [\ t - (n\text{-}1/4)\ T] \\ -4A/T\ [\ t - (n\text{-}1/4)\ T] \\ \text{where } n \in \mathbb{Z} \end{cases} \quad (2)$$

$$V_{constant}(t) \begin{cases} L \\ -L \\ \text{where } V_m \le L \le 1\ \&\ -1 \le -L \le -V_m \end{cases} \quad (3)$$

The simple boost-based controller is a digital circuit which applies six digital switching signals to the gates of the power switching components of a three-phase inverter. Therefore, to fully define all the switching states of this controller, 5 secondary functions of Boolean type are formed from the three primary functions of time $V_{ac(3\varphi)}$, $V_{carrier}$ and $V_{constant}$. These Boolean functions are A, B, C, D as well as E and they can each yield either 0 (when the actual yield is negative) or 1 (when the actual yield is positive).

$$A = \text{Boolean}\ [V_{a(\varphi)}(t) - V_{carrier}(t)] \quad (4)$$

$$B = \text{Boolean}\ [V_{b(\varphi)}(t) - V_{carrier}(t)] \quad (5)$$

$$C = \text{Boolean}\ [V_{c(\varphi)}(t) - V_{carrier}(t)] \quad (6)$$

$$D = L - V_{carrier}(t) \quad (7)$$

$$E = V_{carrier}(t) - (-L) \tag{8}$$

where Boolean[] is the Boolean operator

The truth table below defines the switch states of all six switching devices in a three-phase H-bridge of a ZSI using the above secondary Boolean functions where $SW_{1(SBC)}$ to $SW_{6(SBC)}$ are the first to the sixth switching device respectively.

TABLE II. TRUTH TABLE FOR AN SBC PWM GENERATOR

+ve peak shoot-through			-ve peak shoot-through		
Phase leg A: $SW_{1(SBC)}$ and $SW_{4(SBC)}$					
A	D	$SW_{1(SBC)}$	$\bar{A}$	E	$SW_{4(SBC)}$
0	0	1	0	0	1
0	1	0	0	1	0
1	0	N/A	1	0	N/A
1	1	1	1	1	1
Phase leg B: $SW_{2(SBC)}$ and $SW_{5(SBC)}$					
B	D	$SW_{2(SBC)}$	$\bar{B}$	E	$SW_{5(SBC)}$
0	0	1	0	0	1
0	1	0	0	1	0
1	0	N/A	1	0	N/A
1	1	1	1	1	1
Phase leg C: $SW_{3(SBC)}$ and $SW_{6(SBC)}$					
C	D	$SW_{3(SBC)}$	$\bar{C}$	E	$SW_{6(SBC)}$
0	0	1	0	0	1
0	1	0	0	1	0
1	0	N/A	1	0	N/A
1	1	1	1	1	1

The six Boolean equations for $SW_{1(SBC)}$ to $SW_{6(SBC)}$ can be derived from table 2 using the Sum of Products (SOP) method and figure 1 is the resultant block diagram for a simple boost PWM controller for phase leg A. The same controllers apply for phase legs B and C with only the 120˚and 240˚ phase shift respectively.

$$SW_{1(SBC)} = \bar{A}\cdot\bar{D} + A\cdot D \tag{9}$$

$$SW_{2(SBC)} = \bar{B}\cdot\bar{D} + B\cdot D \tag{10}$$

$$SW_{3(SBC)} = \bar{C}\cdot\bar{D} + C\cdot D \tag{11}$$

$$SW_{4(SBC)} = A\cdot\bar{E} + \bar{A}\cdot E \tag{12}$$

$$SW_{5(SBC)} = B\cdot\bar{E} + \bar{B}\cdot E \tag{13}$$

$$SW_{6(SBC)} = C\cdot\bar{E} + \bar{C}\cdot E \tag{14}$$

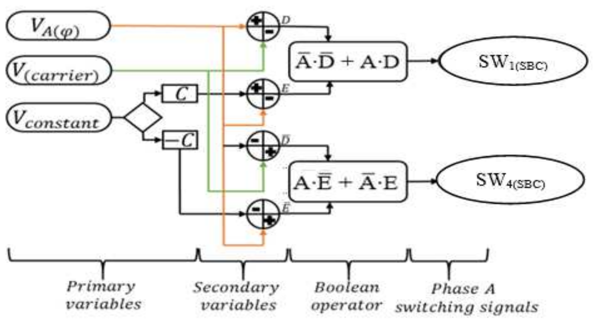

Fig. 5. Simple boost control signal generator for phase leg A

The above-designed SBC signal generator was implemented on the MATLAB Simulink environment and applied to a 2 k-W ZSI (refer to table 1) while varying the input variables input voltage V_{in} and modulation index m independently. V_{in} was varied between 200 to 500V in increments of 100V while m was varied between 0.65 to 0.95 in increments of 0.10. B is the boost factor, V_{stress} is the voltage stress across the switching components, %THD is the percentage of total harmonic distortion and G is the voltage gain ratio. Figure 6 shows the unfiltered output line voltages when the input voltage was 200V and the modulation index was 0.65, the rest of the results are presented in table 3.

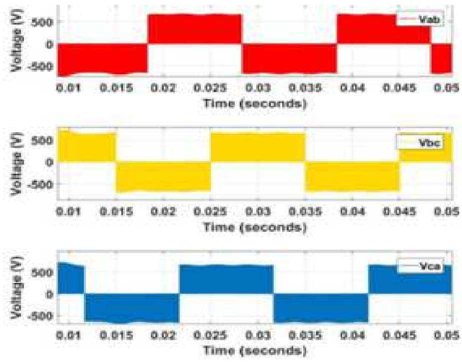

Fig. 6. SBC unfiltered output line voltages (Vin = 200, m=0.65)

TABLE III. RESULTS FOR SBC SIGNAL GENERATOR

Varying V_{in} and m								
m	0.65	0.65	0.65	0.65	0.75	0.75	0.75	0.75
V_{in}	200	300	400	500	200	300	400	500
B	3.22	3.22	3.23	3.23	1.94	1.94	1.95	1.95
V_{stress}	2.98	2.98	2.98	2.98	2.59	2.59	2.59	2.60
%THD	3.75	3.75	3.75	3.75	1.14	1.14	1.14	1.14
G	2.09	2.09	2.10	2.10	1.46	1.46	1.46	1.46
Table 3 continues								
m	0.85	0.85	0.85	0.85	0.95	0.95	0.95	0.95
V_{in}	200	300	400	500	200	300	400	500.
B	1.42	1.42	1.42	1.42	1.10	1.10	1.10	1.10
V_{stress}	2.33	2.34	2.33	2.34	2.09	2.09	2.09	2.10
%THD	1.14	1.14	1.14	1.14	1.14	1.14	1.14	1.14
G	1.20	1.21	1.21	1.21	1.05	1.05	1.05	1.05

B. *Constant boost PWM control technique*

The constant boost control technique is similar in all respect to the previously developed simple boost control technique with the only difference being the injection of a 16% amplitude third harmonic to the fundamental reference waveform (1) which consequently alters the boost factor of the CBC control technique thus differentiating it from that of an SBC control technique[5], [6]. Therefore, defined below is the new reference waveform of the CBC control technique:

$$V_{ac(3\varphi)}(t) \begin{cases} V_{a(\varphi)}(t) + V_{(3rd\ harmonic)} \\ V_{b(\varphi)}(t) + V_{(3rd\ harmonic)} \\ V_{c(\varphi)}(t) + V_{(3rd\ harmonic)} \end{cases}$$

$$V_{ac(3\varphi)}(t) \begin{cases} 1.156\sin(\omega t) + 0.167\sin(3\omega t) \\ 1.156\sin(\omega t - 120) + 0.167\sin(3\omega t) \\ 1.156\sin(\omega t - 240) + 0.167\sin(3\omega t) \end{cases} \tag{15}$$

The definition of secondary Boolean variables, formation of the truth table, derivation of the six Boolean equations for gating the six switching devices of the H-bridge and hence the modelling of the control circuit on MATLAB Simulink remains the same. Therefore, below is table 4 showing the sample of results of a 2 k-W ZSI under the switching influence of a CBC PWM generator. Figure 7 shows the unfiltered output line voltages when the input voltage was 200V and the modulation index was 0.65, the rest of the results are presented in table 4.

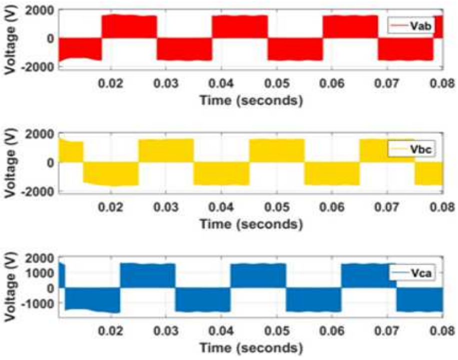

Fig. 7. CBC unfiltered output line voltages (Vin = 200, m=0.65)

TABLE IV. RESULTS FOR CBC SIGNAL GENERATOR

Varying V_{in} and m								
m	0.65	0.65	0.65	0.65	0.75	0.75	0.75	0.75
V_{in}	200	300	400	500.	200.	300.	400	500.
B	7.95	8.00	8.00	8.00	3.35	3.33	3.37	3.36
V_{stress}	1.79	1.79	1.79	1.79	1.52	1.52	1.54	1.53
%THD	4.00	4.00	4.00	4.00	3.72	3.72	3.72	3.72
G	5.16	5.20	5.20	5.20	2.51	2.50	2.53	2.52
Table 4 continues								
m	0.85	0.85	0.85	0.85	0.95	0.95	0.95	0.95
V_{in}	200	300	400	500	200	300	400	500
B	2.11	2.13	2.12	2.10	1.55	1.55	1.55	1.56
V_{stress}	1.27	1.30	1.30	1.30	1.19	1.18	1.18	1.20
%THD	2.68	2.68	2.68	2.68	3.95	3.95	3.95	3.95
G	1.79	1.81	1.80	1.78	1.47	1.47	1.47	1.48

C. *Maximum boost PWM control technique*

The maximum boost control technique is developed using the fundamental reference wave (1) and the carrier wave (2) only. In this technique, all the zero states are converted into shoot-through states to achieve maximum boost [1], [4]. I-M are the six Boolean secondary functions that are used to define all the possible switching states of the six switching devices $SW_{1(MBC)}$ to $SW_{6(MBC)}$ in truth table 5.

$$I = \text{Boolean}\,[V_{a(\varphi)}(t) - V_{b(\varphi)}] \tag{16}$$

$$J = \text{Boolean}\,[V_{b(\varphi)}(t) - V_{c(\varphi)}] \tag{17}$$

$$K = \text{Boolean}\,[V_{c(\varphi)} - V_{a(\varphi)}(t)] \tag{18}$$

$$L = \text{Boolean}\,[V_{a(\varphi)}(t) - V_{carrier}(t)] \tag{19}$$

$$M = \text{Boolean}\,[V_{b(\varphi)}(t) - V_{carrier}(t)] \tag{20}$$

$$N = \text{Boolean}\,[V_{c(\varphi)}(t) - V_{carrier}(t)] \tag{21}$$

Truth table 5 defines the switching states of only the upper switches per phase leg. The lower corresponding switch has an equal but opposite (negate all the variables) equation to that of the upper switch. Table 5 is a long truth table, therefore, deriving the gating equations directly from it would lead to unnecessarily long equations with sums of more than 20 products (more than 100 AND, OR, etc. gates).

TABLE V. TRUTH TABLE FOR AN MBC PWM GENERATOR

State	I	J	K	L	M	N	$SW_{1(MBC)}$	$SW_{1(MBC)}$	$SW_{1(MBC)}$
0	0	0	0	0	0	0	N/A	N/A	N/A
1	0	0	0	0	0	1	N/A	N/A	N/A
2	0	0	0	0	1	0	N/A	N/A	N/A
3	0	0	0	0	1	1	N/A	N/A	N/A
4	0	0	0	1	0	0	N/A	N/A	N/A
5	0	0	0	1	0	1	N/A	N/A	N/A
6	0	0	0	1	1	0	N/A	N/A	N/A
7	0	0	0	1	1	1	N/A	N/A	N/A
8	0	0	1	0	0	0	N/A	N/A	1
9	0	0	1	0	0	1	N/A	N/A	1
10	0	0	1	0	1	0	N/A	N/A	1
11	0	0	1	0	1	1	N/A	N/A	1
12	0	0	1	1	0	0	0	1	1
13	0	0	1	1	0	1	N/A	N/A	1
14	0	0	1	1	1	0	0	0	1
15	0	0	1	1	1	1	1	1	1
16	0	1	0	0	0	0	N/A	1	N/A
17	0	1	0	0	0	1	1	1	0
18	0	1	0	0	1	0	N/A	1	N/A
19	0	1	0	0	1	1	N/A	1	N/A
20	0	1	0	1	0	0	N/A	1	N/A
21	0	1	0	1	0	1	0	1	0
22	0	1	0	1	1	0	N/A	1	N/A
23	0	1	0	1	1	1	1	1	1
24	0	1	1	0	0	0	N/A	1	N/A
25	0	1	1	0	0	1	N/A	1	N/A
26	0	1	1	0	1	0	N/A	1	N/A
27	0	1	1	0	1	1	N/A	1	N/A
28	0	1	1	1	0	0	0	1	1
29	0	1	1	1	0	1	0	1	0
30	0	1	1	1	1	0	N/A	1	N/A
31	0	1	1	1	1	1	1	1	1
32	1	0	0	0	0	0	1	N/A	N/A
33	1	0	0	0	0	1	1	N/A	N/A
34	1	0	0	0	1	0	1	0	1
35	1	0	0	0	1	1	1	0	0
36	1	0	0	1	0	0	1	N/A	N/A
37	1	0	0	1	0	1	1	N/A	N/A
38	1	0	0	1	1	0	1	N/A	N/A
39	1	0	0	1	1	1	1	1	1
40	1	0	1	0	0	0	N/A	N/A	1
41	1	0	1	0	0	1	N/A	N/A	1
42	1	0	1	0	1	0	1	0	1
43	1	0	1	0	1	1	N/A	N/A	1
44	1	0	1	1	0	0	N/A	N/A	N/A
45	1	0	1	1	0	1	N/A	N/A	1
46	1	0	1	1	1	0	0	0	1
47	1	0	1	1	1	1	1	1	1
48	1	1	0	0	0	0	1	N/A	N/A
49	1	1	0	0	0	1	1	1	0
50	1	1	0	0	1	0	1	N/A	N/A
51	1	1	0	0	1	1	1	0	0
52	1	1	0	1	0	0	1	N/A	N/A
53	1	1	0	1	0	1	1	N/A	N/A
54	1	1	0	1	1	0	1	N/A	N/A
55	1	1	0	1	1	1	1	1	1
56	1	1	1	0	0	0	N/A	N/A	N/A
57	1	1	1	0	0	1	N/A	N/A	N/A
58	1	1	1	0	1	0	N/A	N/A	N/A
59	1	1	1	0	1	1	N/A	N/A	N/A
60	1	1	1	1	0	0	N/A	N/A	N/A
61	1	1	1	1	0	1	N/A	N/A	N/A
62	1	1	1	1	1	0	N/A	N/A	N/A
63	1	1	1	1	1	1	N/A	N/A	N/A

In practical prototypes, this would lead to an extremely messy control circuit with excessive noise due to numerous components and hence diminished performance. Therefore, the Karnaugh maps (k-maps) were used to optimise the switch gating equations from the excess of 20 to about 7 products. Figures 8-10 show the k-maps and hence the optimisation of the switching equations (22) to (27) for the switching devices of each phase leg A, B and C.

NOTE: N/A = d = don't care or impossible states

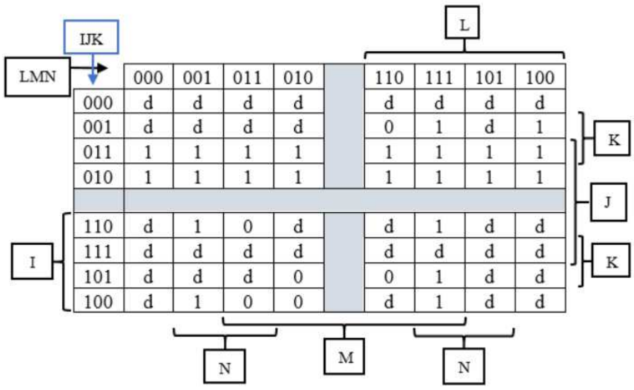

Fig. 8. K-map for phase leg A (SW1(MBC) and SW4(MBC))

$$SW_{1(MBC)} = I\bar{J}\bar{K} + IJ\bar{K} + I\bar{J}LMN + J\bar{K}\bar{L}\bar{M}N + \bar{I}KLMN \quad (22)$$

$$SW_{4(MBC)} = \bar{I}JK + \bar{I}\bar{J}K + \bar{I}J\bar{L}\bar{M}\bar{N} + \bar{J}KLM\bar{N} + I\bar{K}\bar{L}\bar{M}\bar{N} \quad (23)$$

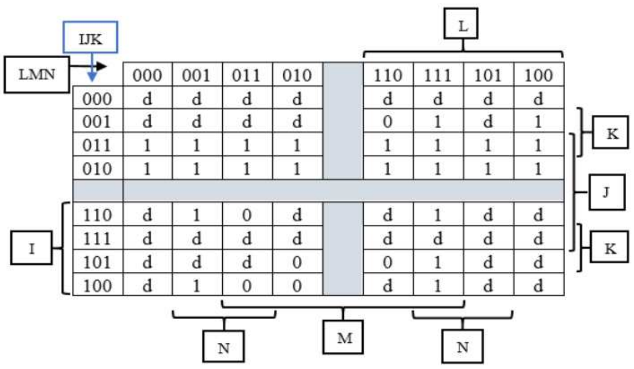

Fig. 9. K-map for phase leg B (SW2(MBC) and SW5(MBC))

$$SW_{2(MBC)} = \bar{I}J + I\bar{J}LMN + \bar{I}KLMN + \bar{I}KL\bar{M}\bar{N} + J\bar{K}LMN + J\bar{K}\bar{L}\bar{M}N \quad (24)$$

$$SW_{5(MBC)} = I\bar{J} + \bar{I}J\bar{L}\bar{M}\bar{N} + I\bar{K}\bar{L}\bar{M}\bar{N} + I\bar{K}\bar{L}MN + \bar{J}K\bar{L}\bar{M}\bar{N} + \bar{J}KLM\bar{N} \quad (25)$$

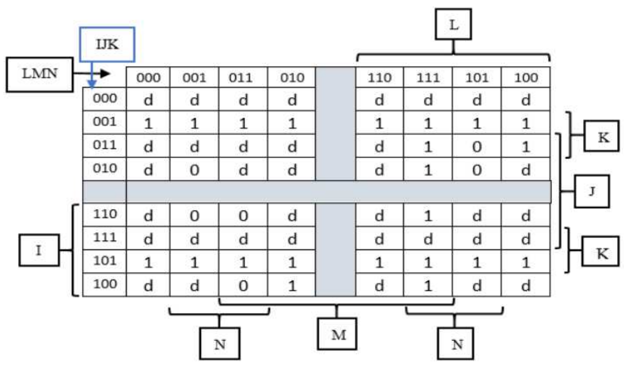

Fig. 10. K-map for phase leg C ($SW_{3(MBC)}$ and $SW_{6(MBC)}$)

$$SW_{3(MBC)} = I\bar{J}K + \bar{I}\bar{J}K + \bar{I}KLMN + I\bar{J}\bar{L}M\bar{N} + I\bar{J}LMN + J\bar{K}LMN + \bar{I}KL\bar{M}\bar{N} \quad (26)$$

$$SW_{6(MBC)} = \bar{I}J\bar{K} + IJ\bar{K} + I\bar{K}\bar{L}\bar{M}\bar{N} + \bar{I}JL\bar{M}N + \bar{I}J\bar{L}\bar{M}\bar{N} + \bar{J}K\bar{L}\bar{M}\bar{N} + I\bar{K}\bar{L}MN \quad (27)$$

Figure 11 below shows a block diagram of a maximum boost control PWM signal generator for all three phase legs.

Table 6 shows the sample of results of a 2 k-W ZSI under

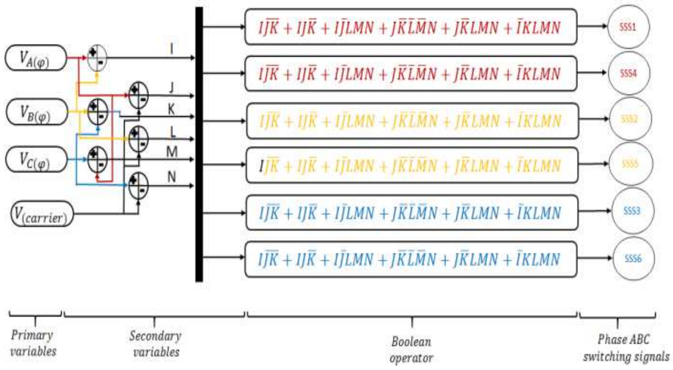

Fig. 11. Maximum boost control signal generator for phase legs A, B and C

the switching influence of an MBC PWM generator. Figure 12 shows the unfiltered output line voltages when the input voltage was 200V and the modulation index was 0.65, the rest of the results are presented in table 6.

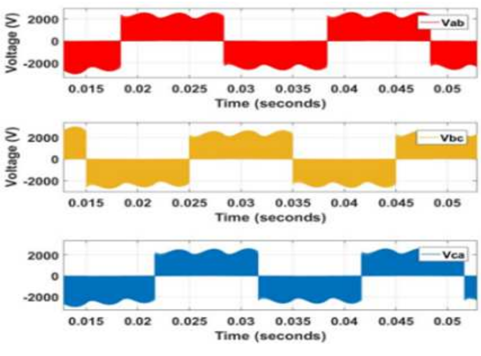

Fig. 12. MBC unfiltered output line voltages (Vin = 200, m=0.65)

TABLE VI. RESULTS FOR MBC SIGNAL GENERATOR

Varying V_{in} and m								
m	0.65	0.65	0.65	0.65	0.75	0.75	0.75	0.75
V_{in}	200	300	400	500	200	300	400	500
B	13.0	13.0	12.2	12	4.05	4.08	4.06	4.10
V_{stress}	1.77	1.77	1.65	1.65	1.36	1.36	1.36	1.37
%THD	10.3	10.3	10.3	10.3	9.26	9.26	9.26	9.26
G	8.45	8.45	7.96	7.80	3.03	3.06	3.04	3.07
Table 3 continues								
m	0.85	0.85	0.85	0.85	0.95	0.95	0.95	0.95
V_{in}	200	300	400	500	200	300	400	500
B	2.50	2.51	2.51	2.50	1.87	1.74	1.80	1.80
V_{stress}	1.316	1.339	1.339	1.349	1.237	1.223	1.212	1.216
%THD	15.0	15.0	15.0	15.0	15.0	15.0	15.0	15.0
G	2.12	1.81	1.80	1.78	1.78	1.47	1.71	1.71

IV. DISCUSSION OF THE RESULTS

Below is a list of the observations made on the above study in section II. For all the simple boost, constant and maximum boost PWM control schemes:

- The boost factor is dependent on the modulation index and independent of the input voltage.
- The switching device voltage stress ratio is dependent on the modulation index and independent of the input voltage.
- The percentage of total harmonics distortion is dependent on the modulation index and independent of the input voltage.
- The gain factor is dependent on the modulation index and independent of the input voltage.
- The output voltage is dependent on both the input voltage and the modulation index.

On top of the above-stated observations, the simple boost PWM control technique has:

- Lowest output voltage gain factor, for the same modulation index, amongst all the three presented switching techniques (Cons).
- Highest switching device voltage stress ratio, for the same modulation index, amongst the three presented switching techniques (Cons)
- Lowest % total harmonics distortion, for the same modulation index, amongst the three presented switching techniques (Pros)

The Constant boost PWM control technique has:

- The output voltage gain factor which is higher than that of the simple boost but lower than that of the maximum boost control technique for the same modulation index.
- The switching device voltage stress ratio which is lower than that of the simple boost but slightly higher than that of the maximum boost control technique for the same modulation index.
- The % total harmonics distortion which is higher than that of the simple boost but lower than that of the maximum boost control technique for the same modulation index.

The maximum boost PWM control technique has:

- The highest output voltage gain factor, for the same modulation index, amongst all the three presented switching techniques (Pros).
- Lowest switching device voltage stress ratio, for the same modulation index, amongst the three presented switching techniques (Pros)
- Highest % total harmonics distortion, for the same modulation index, amongst the three presented switching techniques (Cons)

Figure 6 below is a graph showing the gain factors for different modulation index values for the simple boost, constant boost, and maximum boost control techniques.

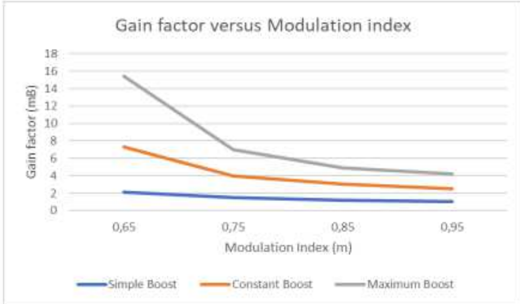

Fig. 13. Graph showing gain factor for different modulation index settings for SBC, CBC, and MBC PWM techniques

V. CONCLUSION

The study in this paper aimed to highlight the pros and cons of each of the investigated PWM switching techniques viz., the simple boost, constant boost, and maximum boost control techniques. Therefore, using this paper as a guide, one can select the best-suited PWM control scheme based on the needs and constraints of their application.

For future considerations and as an expansion of the scope of this paper, the Space Vector Pulse Width Modulation (SVPWM) technique will be investigated.

VI. REFERENCES

[1] R. R. Kumar, S. Kumar, and A. Yadav, “comparison of PWM techniques and inverter performance,” IOSR Journal of Electrical and Electronics Engineering (IOSR-JEEE), vol. 4, no. 1, pp. 18-22, 2013.

[2] K. V. Kumar, P. A. Michael, J. P. John, and S. S. Kumar, “Simulation and comparison of SPWM and SVPWM control for three-phase inverters,” ARPN journal of engineering and applied sciences, vol. 5, no. 7, pp. 61-74, 2010.

[3] R. Mali, N. Adam, A. Satpaise, and A. Vaidya, "Performance comparison of two-level inverter with classical multilevel inverter topologies." pp. 1-7.

[4] M. Abbasi, M. Mardaneh, A. H. Eslahchi, and Z. Hashemi, “Extended boost switched-embedded-capacitor-inductor Zsi with low voltage stress on capacitors and soft-start capability,” IETE Journal of Research, pp. 1-10, 2021.

[5] A. J. Viji, R. Balamanigandan, and B. Manimaran, “Power Quality Improvement of Grid Connected PV System Fed ZSI-DVR with Advanced Control Strategy,” Journal of Green Engineering, vol. 10, pp. 9574-9586, 2020.

[6] P. Jamuna, G. Ramani, and K. Suresh, “Performance validation of PV system incorporated ZSI-dynamic voltage restorer for long-lasting power quality improvement,” Journal of Testing and Evaluation, vol. 49, no. 5, pp. 3602-3619, 2020.

[7] M. Jokar Kouhanjani, A. Seifi, and M. Mehrtash, “Dynamic model and small signal analysis of Z-source inverter,” IETE Journal of Research, vol. 65, no. 3, pp. 342-350, 2019.

Experimental Identification of the Output Impedance Frequency Response of an Open-Loop Half-Bridge Inverter

Ian Paul Gerber
Dept. of Electrical and Electronic Engineering
Stellenbosch University
Stellenbosch, South Africa
Email: 21011788@sun.ac.za

Fredrick Mukundi Mwaniki
Dept. of Electrical and Electronic Engineering
Stellenbosch University
Stellenbosch, South Africa
https://orcid.org/0000-0003-1466-4484

Hendrik Johannes Vermeulen
Dept. of Electrical and Electronic Engineering
Stellenbosch University
Stellenbosch, South Africa
https://orcid.org/0000-0003-4356-4044

***Abstract*—DC-AC inverters are used extensively in renewable energy applications in modern power systems. Characterization of the output impedance of an inverter is important for the design and analysis of inverter systems, especially for grid-tied applications. In this paper, a half-bridge inverter is perturbed using pseudo-random impulse sequence perturbations, and the output impedance of the inverter is subsequently estimated from experimental measurements. It is shown that the output impedance of the open-loop half-bridge inverter can be characterized by using small-signal perturbations. The effects of deadtime, carrier frequency, modulation index and DC voltage magnitude on the output impedance of a practical standalone half-bridge inverter are also investigated. It is shown that some of these parameters have a non-linear influence on the frequency response of the inverter output impedance.**

***Index Terms*—inverter, half-bridge, wideband, output impedance, frequency response, perturbation**

I. Introduction

Power electronic devices, including DC-AC inverters, have a vast range of applications in the mining industry, variable speed drive systems, distributed generation, electric vehicles and renewable energy conversion [1]. Half-bridge inverters are, amongst others, utilized for induction heating [2], integrating renewable energy sources with the grid [3] and avionics [4]. Half-bridge inverters are, furthermore, sometimes preferred to full-bridge inverters in low- and medium-voltage applications, as they are constructed using fewer circuit components [5].

Obtaining the output impedance of inverters is vital for the design and analysis of inverters in interconnected systems. The output impedance of inverters can be used to investigate the stability of grid-connected inverters [6], as well as the source of dominant harmonic emissions [7]. Power sharing between parallel connected inverters is for instance determined by the output impedance of the inverters [8], [9]. The implementation and performance of voltage and frequency droop control methods can, furthermore, be dependent on the output impedance of the inverter [10].

The output impedance of an inverter can be derived analytically using average modelling techniques [11]. In practice, however, important parameters such as filter and controller parameters are often unknown. This complicates the use of the average modelling technique. Various system identification methods have been proposed in the literature for determining the output impedance of practical inverters. Valdivia *et al.* [12] made use of current and voltage step responses to determine the output impedance of an inverter as part of a black-box modelling approach. Cespedes made use of wideband perturbation methods [13] to excite an inverter over a wide frequency band and subsequently estimate its impedance frequency response.

Wideband excitation signals are commonly used to perturb power system equipment in system identification applications. The Pseudo-Random Impulse Sequence (PRIS) signal is a wideband excitation signal that is suitable for use in high-power, high-voltage environments, such as inverter systems [14]. The PRIS source has been applied to characterize grid impedances [15], transformers [16], [17] and capacitive voltage transformers [18], [19]. It has also been applied to inverters through simulation [20].

In this paper, a single-phase, standalone, open-loop, half-bridge inverter is investigated. The inverter topology under investigation purposefully neglects connection to the grid and a control-loop. The practical half-bridge inverter is perturbed using a PRIS source to allow characterization of the output impedance. The effect of the deadtime, carrier frequency, DC input voltage and modulation index on the output impedance are investigated.

II. Practical Half-Bridge Inverter Arrangement

A half-bridge inverter converts DC power to AC power by making use of two complementary switches. These switches are controlled by Pulse Width Modulation (PWM) gating signals to produce an AC voltage that varies between half the DC input voltage and the negative thereof. This AC voltage is filtered by a low-pass filter to produce a single sinusoidal output voltage.

Fig. 1 shows the circuit diagram of the practical open-loop half-bridge inverter under investigation. Two 1MBH60D-090A IGBTs, Q_1 and Q_2, are used to construct a half-bridge switching leg. The half-bridge inverter has a fundamental frequency of $f_1 = 50Hz$. An inductor, L_f, of $2mH$ and a capacitor, C_f, of $1000\mu F$ are used as an LC filter. The cut-off frequency of the LC filter, f_{cut}, is $f_{cut} = 112.54Hz$.

Sinusoidal Pulse-Width Modulation (SPWM) is implemented using an Altera DE0 FPGA. The modulation index is $m_a = 0.8$. A unity triangular carrier wave with a carrier frequency, f_c, of $1kHz$ is used, while deadtime is added. A DC power supply, V_d, of 30 V is used as input to the inverter. Two $2200\mu F$ DC-link capacitors, both labelled C_i, are used to equally split the DC voltage. A resistive load of 100Ω, R, is connected across the output of the inverter. A 16-bit NI 9223 Data Acquisition (DAQ) module is used to measure the time-domain signals at a sampling frequency of $f_s = 1MHz$.

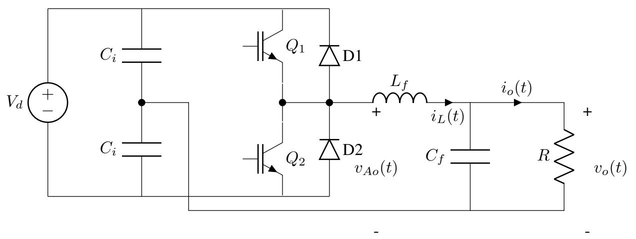

Fig. 1: Half-bridge inverter circuit diagram.

Fig. 2 shows the measured time-domain output voltage and output current, denoted by $v_o(t)$ and $i_o(t)$ respectively, of the practical half-bridge inverter arrangement while it is operated without perturbation. The amplitude of the modulated voltage at the fundamental frequency, V_{Ao}^1, is given by the relationship

$$V_{Ao}^1 = V_d \times \frac{m_a}{2} = 30 \times \frac{0.8}{2} = 12V. \quad (1)$$

The amplitude of the output voltage, $v_o(t)$, is slightly lower compared to the voltage V_{Ao}^1 due to the voltage drop across the LC filter. The output voltage and current, $v_o(t)$ and $i_o(t)$, are nearly sinusoidal with some switching ripple.

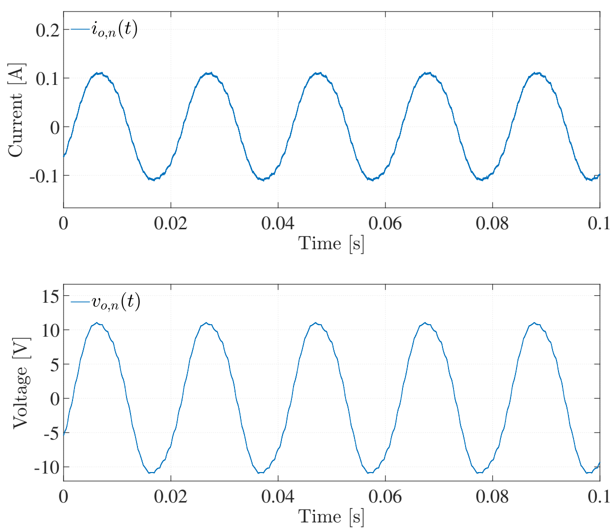

Fig. 2: Measured time-domain output current and voltage waveforms, $i_{o,n}(t)$ and $v_{o,n}(t)$ respectively, of the half-bridge inverter under normal operating conditions.

III. Output Impedance Frequency Response of the Half-Bridge Inverter

A. Analytical Half-Bridge Inverter Impedance Transfer Function

Fig. 3 shows the half-bridge inverter circuit while the top switch, Q_1, is conducting and the bottom switch, Q_2, is open. The switches are assumed to be ideal, with negligible resistance. The freewheeling diodes, D_1 and D_2, of the IGBTs are neglected in this mathematical analysis. The DC voltage source used to supply the half-bridge inverter has an internal resistance, R_{dc}, measured as 1.94Ω. The filter inductor, L_f, has a series resistance, r_L, of 0.745Ω. These resistances are included in the circuit shown in Fig. 3, to obtain a more accurate representation of the practical half-bridge inverter.

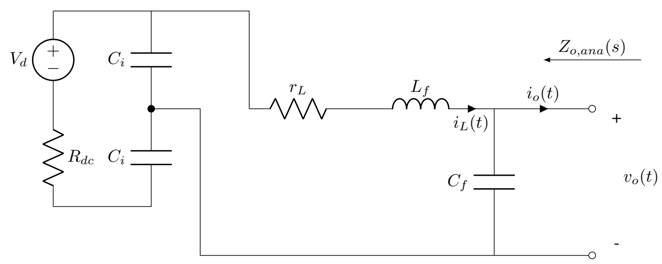

Fig. 3: Circuit configuration of a half-bridge inverter.

The analytical output impedance, $Z_{o,ana}(s)$, of the circuit shown in Fig. 3 is derived as

$$Z_{o,ana}(s) = \left(\frac{1}{\left(\frac{1}{R_{dc}+\frac{1}{sC_i}} + sC_i\right)^{-1} + r_L + sL_f} + sC_f\right)^{-1} \quad (2)$$

Equation (2) can be simplified to yield:

$$Z_{o,ana}(s) = \frac{s^3 R_{dc}{C_i}^2 L_f + s^2 R_{dc}{C_i}^2 r_L + 2s^2 C_i L_f + 2sC_i r_L + 1}{s^4 R_{dc}{C_i}^2 L_f C_f + s^3 R_{dc}{C_i}^2 r_L C_f + 2s^3 C_i L_f C_f ... \\ ... + 2s^2 C_i r_L C_f + sC_f + s^2 R_{dc}{C_i}^2 + 2sC_i} \quad (3)$$

When the bottom switch, Q_2, is conducting and the top switch, Q_1, is open, the output impedance of the resultant circuit would be equal to $Z_{o,ana}(s)$. It is important to note that (3) does not represent the output impedance of the inverter, but merely the output impedance of the circuit in Fig. 3. Fig. 4 shows the frequency response of the analytical output impedance, $Z_{o,ana}(s)$. For the frequency range considered in this investigation, i.e. between $0.1Hz$ and $100kHz$, the impedance response exhibits series and parallel resonances at approximately $48Hz$ and $125Hz$ respectively. The series resonant point is attributed to a series combination of the DC link capacitors and the filter inductor, while the parallel resonance point is attributed to the LC filter.

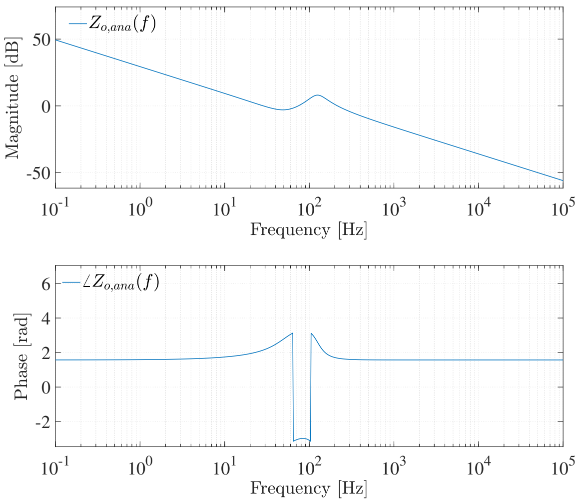

Fig. 4: Magnitude and phase response of the analytical transfer function, $Z_{o,ana}(f)$, of the output impedance of the circuit of the half-bridge inverter while Q_1 is conducting and Q_2 is open.

B. Perturbation of the Half-Bridge Inverter

During perturbation of the open-loop half-bridge inverter, the PRIS source is connected in parallel with the load as shown in Fig. 5. This allows for the injection of a perturbation current, rather than causing voltage perturbation. The PRIS source consists of a DC voltage source connected through an H-bridge and a series RLC impedance. The H-bridge switches are controlled using a Pseudo-Random Binary Sequence (PRBS) gating signal [14].

In this investigation, the PRIS source is tuned such that a suitable PRIS perturbation signal is produced for the frequency range of interest. This is done by using a PRBS10 with a clock frequency, f_{clk}, of $500Hz$ to control the H-bridge. To obtain appropriate time-constants at the selected clock frequency, the RLC impedance values are chosen as $1k\Omega$, $47\mu H$ and $4\mu F$ respectively. The values of the RLC circuit are also chosen to limit the current through the PRIS source. The perturbed output voltage and current waveforms are recorded over a time interval.

Fig. 6 compares the measured output voltage and currents of the perturbed arrangement, i.e. $i_{o,p}(t)$ and $v_{o,p}(t)$ respectively, with the measured output voltage and currents obtained under normal operating conditions, i.e $i_{o,n}(t)$ and $v_{o,n}(t)$ respectively. The superimposed perturbations are clearly evident on the current waveform, $i_{o,p}(t)$.

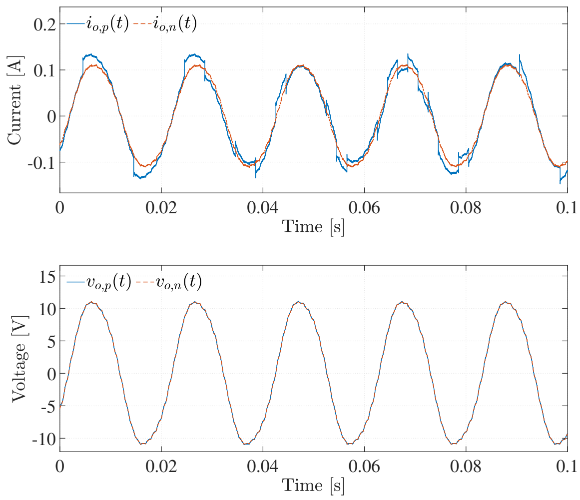

Fig. 6: Measured time-domain $i_{o,n}(t)$ and $v_{o,n}(t)$, as well as $i_{o,p}(t)$ and $v_{o,p}(t)$.

C. Determining the Output Impedance of the Half-Bridge Inverter

The output impedance of the half-bridge inverter is determined using a two-measurement approach [20]. The frequency responses of the measured voltage and current under perturbed conditions, i.e. $I_{o,p}(f)$ and $V_{o,p}(f)$, and normal operating conditions, i.e. $I_{o,n}(f)$ and $V_{o,n}(f)$, are used in (4) to obtain the output impedance [20]:

$$Z_o(f) = \frac{V_{o,p}(f) - V_{o,n}(f)}{I_{o,p}(f) - I_{o,n}(f)} \tag{4}$$

The two-measurement approach represented by (4) assumes that the perturbed and normal measurements are referenced to the same angle. This is, however, not always the case in practice, in which case the perturbed and normal measurements need to be synchronised. In this investigation, the synchronisation of the two sets of measurements is performed by aligning the PWM signals. This is motivated by the fact that the inverter switches, Q_1 and Q_2, are controlled by the PWM signals. The PWM gating signals under normal and perturbed conditions are aligned by fixing the PWM signal that is recorded while the inverter is operating under normal conditions and shifting the PWM signal that is measured while the inverter is perturbed in increments of the sampling time, $T_s = 1/f_s$. While shifting the perturbed PWM signal over one fundamental period, $T_1 = 1/f_1$, in increments of T_s, the Mean Squared Error (MSE) value is determined between

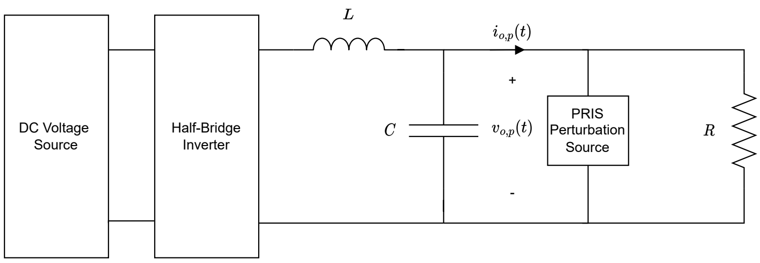

Fig. 5: Perturbation arrangement of the half-bridge inverter. The PRIS source is connected in parallel with the load.

each shifted perturbed PWM signal and the PWM signal under normal conditions. The time shift that produces the smallest MSE value is adopted as the shift with which to align the normal and perturbed voltage and current signals.

Fig. 7 shows the aligned PWM signals under normal and perturbed conditions. It can be seen that although the measured PWM signals contain random noise, the alignment of the PWM signals is not influenced by the random noise, as the time-domain signals lie on top of each other. The perturbed output current and voltage waveforms, $i_{o,p}(t)$ and $v_{o,p}(t)$, are shifted with the same number of sampling periods as the perturbed PWM signal to synchronize with the current and voltage waveforms obtained for normal operating conditions, i.e. $i_{o,n}(t)$ and $v_{o,n}(t)$.

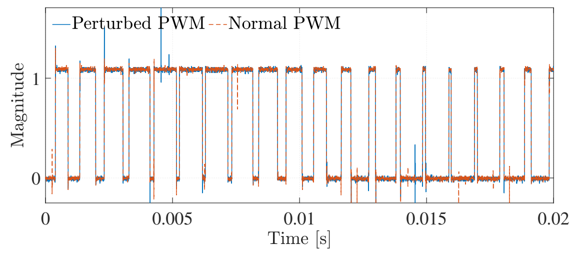

Fig. 7: Measured PWM signals under normal and perturbed operating conditions after alignment.

The small-signal perturbations can be observed by subtracting the aligned perturbed and normal output voltage and current waveforms as indicated in the numerator and denominator of (4). Fig. 8 shows these small-signal perturbations. As expected, the current waveform exhibits random impulse characteristics due to the applied PRIS perturbation.

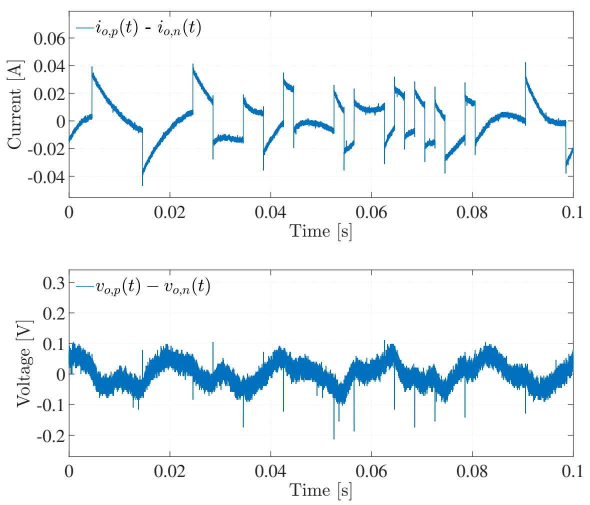

Fig. 8: PRIS perturbations on $i_{o,p}(t)$ - $i_{o,n}(t)$ and $v_{o,p}(t)$ - $v_{o,n}(t)$ respectively.

Fig. 9 compares the frequency response of the output impedance of the practical half-bridge inverter, $Z_o(f)$, obtained using the two-measurement approach described by (4) with the analytical transfer function, $Z_{o,ana}(f)$ defined by (3). For the frequency range considered in the investigation, i.e. $10Hz$ to $400Hz$, both frequency responses have a series and parallel resonance pair and similar shapes. The practical results thereby confirm that the DC capacitors, denoted by C_i, influence the output impedance $Z_o(f)$ of the open-loop half-bridge inverter, and the DC voltage source cannot be assumed as stiff. The output impedance frequency response of the inverter is a linear approximation of a non-linear system, hence the non-smooth nature of the frequency response.

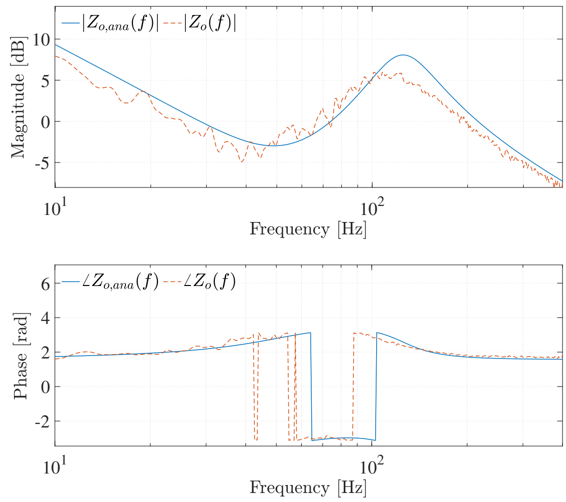

Fig. 9: Magnitude and phase response of the estimated output impedance, $Z_o(f)$, of the practical half-bridge inverter compared to $Z_{o,ana}(f)$.

Fig. 10 shows the practical arrangement used to perturb the half-bridge inverter.

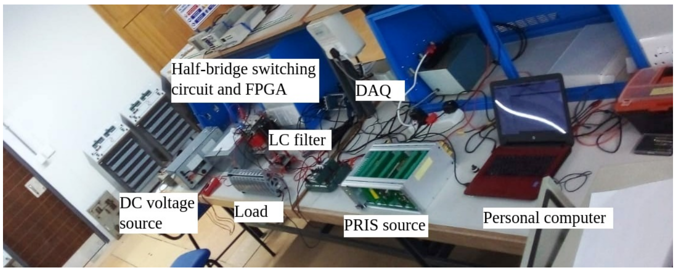

Fig. 10: The practical arrangement used during this investigation.

D. Effects of deadtime, carrier frequency, modulation index and DC voltage

The effect of the deadtime, carrier frequency, magnitude of the modulation index and the DC voltage magnitude on the output impedance can be investigated, as complete control of the operation of the half-bridge under investigation operation allows for easy manipulation of these parameters.

1) Effect of the Deadtime: Deadtime is typically added to the PWM gating signals to prevent a short-circuit across the two IGBTs in the half-bridge inverter. To investigate the effect of deadtime on the output impedance of the inverter, the deadtime added to the PWM signals is varied across $10\mu s$, $20\mu s$ and $30\mu s$. Fig. 11 shows the estimated output impedance of the half-bridge inverter as a function of the deadtime. The results show that the damping and locations of the resonant points in the frequency response of the output impedance are not influenced significantly by the deadtime. The half-bridge inverter is a non-linear system. Therefore, the linear frequency-domain approximation of the output impedance inevitably exhibits non-linear behaviour. Therefore, the phase is affected by the ripple present on the estimated frequency response of $Z_o(f)$ and varies inconsistently.

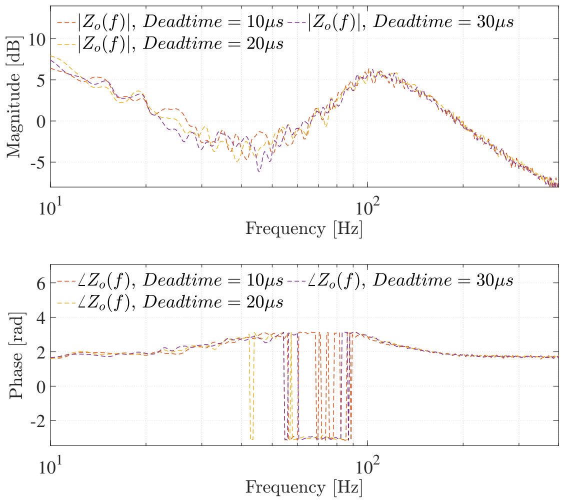

Fig. 11: Magnitude and phase response of the output impedance, $Z_o(f)$, of the half-bridge inverter as a function of the deadtime.

2) Effect of the Carrier Frequency: The frequency f_c of the triangular carrier waveform used in the SPWM is varied to investigate its impact on the inverter output impedance frequency response. The frequency f_c is varied from 500 Hz with increments of 500 Hz. Fig. 12 shows the estimated output impedance of the half-bridge inverter as a function of f_c. The second resonant point is slightly more damped when $f_c = 1kHz$, as compared to other values of f_c.

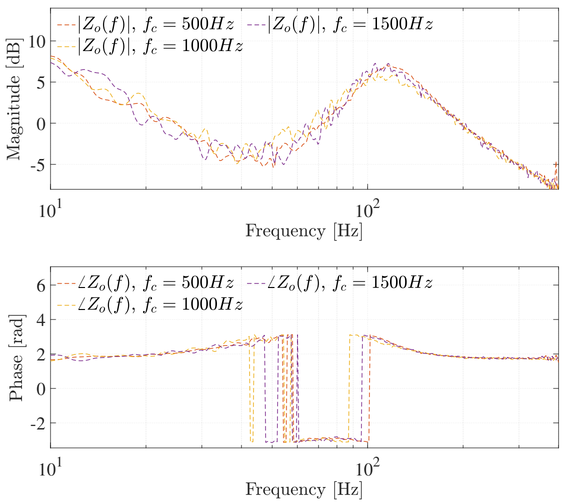

Fig. 12: Magnitude and phase response of the output impedance, $Z_o(f)$, of the half-bridge inverter as a function of the carrier frequency f_c.

3) Effect of the Modulation Index: The effect of the modulation index, m_a, on the output impedance, $Z_o(f)$, is investigated by varying m_a across 0.1, 0.25, 0.5, 0.75 and 1. Fig. 12 shows the estimated output impedance of the half-bridge inverter as a function of the modulation index. Changing the modulation index has a non-linear effect on the damping of the resonant points of the output impedance of the half-bridge inverter, especially at the lower resonant frequency. These results show that the modulation index can significantly influence the output impedance. Therefore, the value of the modulation index should be carefully considered in the operation of an inverter. Varying the modulation index can change the output impedance of the inverter and subsequently influence the inverter stability, harmonic emissions and power sharing within an interconnected inverter system.

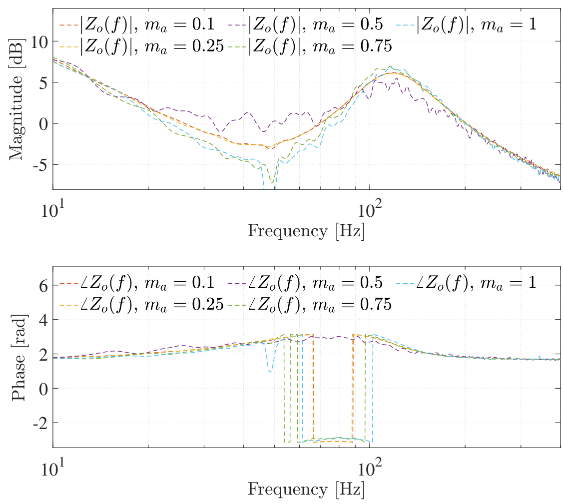

Fig. 13: Magnitude and phase response of the output impedance, $Z_o(f)$, of the half-bridge inverter as a function of the modulation index m_a.

4) Effect of the DC Voltage Magnitude: The DC input voltage magnitude, V_d is varied across $20V$, $30V$, $40V$ and $50V$ to determine the effect of V_d on $Z_o(f)$. Fig. 12 shows the estimated output impedance of the half-bridge inverter as a function of the DC voltage magnitude. The frequency band between the two resonant points is affected when changing the DC voltage magnitude. When the DC voltage magnitude is increased, the magnitude of the output impedance frequency response decreases in this region.

As the DC voltage magnitude influences the output impedance, variances in the DC voltage and, thus, power supplied by renewable energy sources can cause the interconnected inverter system to behave differently as compared to nominal operation. Therefore, the use of a two-stage inverter topology to ensure a constant DC voltage supply to the inverter is preferable [21].

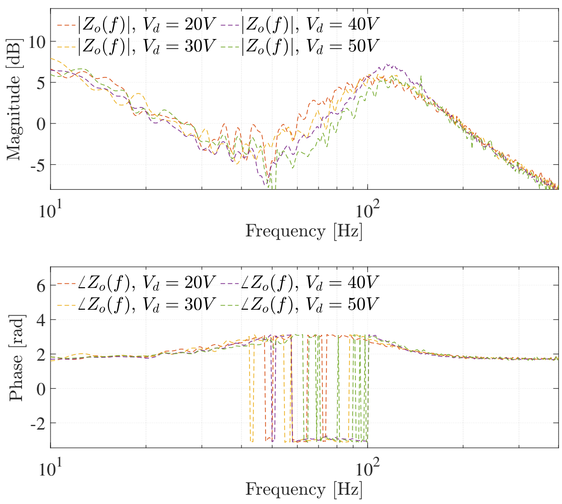

Fig. 14: Magnitude and phase response of the output impedance, $Z_o(f)$, of the half-bridge inverter as a function of V_d.

IV. Conclusion

In this paper, the output impedance of a practical open-loop half-bridge inverter is investigated. The half-bridge inverter is perturbed with a PRIS source and a small-signal analysis is conducted to obtain the frequency response of the output impedance. The results suggest that the PRIS is a suitable perturbation signal for characterising the frequency response of the output impedance of a practical open-loop half-bridge inverter experimentally.

The effects of the deadtime, carrier frequency, modulation index and DC voltage magnitude on the output impedance of the inverter are investigated. It is shown that the modulation index affects the output impedance frequency of an open-loop half-bridge inverter response non-linearly. The DC voltage magnitude also affects the magnitude response of the output impedance. Therefore, the DC voltage and modulation index of an interconnected inverter system should be designed appropriately to ensure stability, ideal power sharing and control of the source of dominant harmonic emissions.

References

[1] H. Vahedi and K. Al-Haddad, "Half-bridge based multilevel inverter generating higher voltage and power," in *2013 IEEE Electrical Power Energy Conference*, 2013, pp. 1–6.

[2] S. Yachiangkam, C. Karnjanapiboon, S. Janjornmanit, A. Namin, E. Chaidee, T. Sriprom, W. Tammawan, S. Srita, U. Kamnarn, N. Takorabet, and P. Thounthong, "Implementation of half-bridge class d voltage-source inverter for domestic medical applications," in *2022 19th International Conference on Electrical Engineering/Electronics, Computer, Telecommunications and Information Technology (ECTI-CON)*, 2022, pp. 1–4.

[3] C.-L. Shen and J.-C. Su, "Grid-connection half-bridge pv inverter system for power flow controlling and active power filtering," *Int. J. Photoenergy*, vol. 2012, Jun. 2012.

[4] E. Şener and G. Ertasgin, "Design of a half-bridge current-source inverter topology for avionic systems," *Aerospace*, vol. 9, Jul. 2022.

[5] T. Khemkhaeng, S. Nutwong, E. Mujjalinvimut, S. Maiket, and N. Wiraphonsawan, "Design of a current source half-bridge inverter used in wpt system," in *2022 19th International Conference on Electrical Engineering/Electronics, Computer, Telecommunications and Information Technology (ECTI-CON)*, 2022, pp. 1–5.

[6] L. Jessen and F. W. Fuchs, "Modeling of inverter output impedance for stability analysis in combination with measured grid impedances," in *2015 IEEE 6th International Symposium on Power Electronics for Distributed Generation Systems (PEDG)*, 2015, pp. 1–7.

[7] B. Peterson, J. Rens, M. G. Botha, and J. Desmet, "On harmonic emission assessment: A discriminative approach," *SAIEE Afr. Res. J.*, vol. 108, Dec. 2017.

[8] L. Xinchun, L. Fangrui, D. shanxu, and K. Yong, "The analysis of inverter output impedance and its influence on circulating power for inverters paralleling," in *2008 3rd IEEE Conference on Industrial Electronics and Applications*, 2008, pp. 568–570.

[9] J. Guerrero, L. G. de Vicuna, J. Matas, M. Castilla, and J. Miret, "Output impedance design of parallel-connected ups inverters with wireless load-sharing control," *IEEE Trans. Ind. Electron.*, vol. 52, no. 4, pp. 1126–1135, 2005.

[10] K. De Brabandere, B. Bolsens, J. Van den Keybus, A. Woyte, J. Driesen, and R. Belmans, "A voltage and frequency droop control method for parallel inverters," *IEEE Trans. Power Electron.*, vol. 22, no. 4, pp. 1107–1115, 2007.

[11] C. Yoon, H. Bai, R. N. Beres, X. Wang, C. L. Bak, and F. Blaabjerg, "Harmonic stability assessment for multiparalleled, grid-connected inverters," *IEEE Trans. Sustain. Energy.*, vol. 7, no. 4, pp. 1388–1397, 2016.

[12] V. Valdivia, A. Lazaro, A. Barrado, P. Zumel, C. Fernandez, and M. Sanz, "Black-box modeling of three-phase voltage source inverters for system-level analysis," *IEEE Trans. Ind. Electron.*, vol. 59, no. 9, pp. 3648–3662, 2012.

[13] M. Cespedes and J. Sun, "Three-phase impedance measurement for system stability analysis," in *2013 IEEE 14th Workshop on Control and Modeling for Power Electronics (COMPEL)*, 2013, pp. 1–6.

[14] F. Mwaniki and H. Vermeulen, "Characterization and application of a pseudo-random impulse sequence for parameter estimation applications," *IEEE Trans. Instrum. Meas.*, vol. PP, pp. 1–1, Aug. 2019.

[15] F. M. Mwaniki and H. J. Vermeulen, "Grid impedance frequency response measurements using pseudo-random impulse sequence perturbation," in *2019 9th International Conference on Power and Energy Systems (ICPES)*, 2019, pp. 1–6.

[16] F. Mwaniki and A. Sayyid, "Characterizing power transformer frequency responses using bipolar pseudo-random current impulses," *Int. J. Power Electron. Drive Syst.*, vol. 12, p. 2423, Dec. 2021.

[17] D. M. Banks, J. Cornelius Bekker, and H. J. Vermeulen, "Parameter estimation of a two-section transformer winding model using pseudo-random impulse sequence perturbation," in *2021 56th International Universities Power Engineering Conference (UPEC)*, 2021, pp. 1–6.

[18] I. P. Gerber, F. M. Mwaniki, and H. J. Vermeulen, "Parameter estimation of a ferro-resonance damping circuit using pseudo-random impulse sequence perturbations," in *2021 56th International Universities Power Engineering Conference (UPEC)*, 2021, pp. 1–6.

[19] A. Solomon, F. Mwaniki, and H. Vermeulen, "Application of pseudo-random impulse perturbation for characterizing capacitor voltage transformer frequency responses," in *2020 6th IEEE International Energy Conference (ENERGYCon)*, 2020, pp. 744–748.

[20] I. P. Gerber, F. M. Mwaniki, and H. J. Vermeulen, "Parameter estimation of a single-phase voltage source inverter using pseudo-random impulse sequence perturbation," in *2022 IEEE International Conference on Environment and Electrical Engineering and 2022 IEEE Industrial and Commercial Power Systems Europe (EEEIC / ICPS Europe)*, 2022, pp. 1–6.

[21] D. Meneses, F. Blaabjerg, García, and J. A. Cobos, "Review and comparison of step-up transformerless topologies for photovoltaic ac-module application," *IEEE Trans. Power Electron.*, vol. 28, no. 6, pp. 2649–2663, 2013.

2023 SAUPEC Conference, Johannesburg, South Africa, January 24-26, 2023

An Assessment of some Power Converter Topology Evaluation Metrics

Future Letsoalo
School of Electrical and Information Engineering
Witwatersrand
Johannesburg, South Africa
letsoalo.future@gmail.com

Ivan Hofsajer
School of Electrical and Information Engineering
Witwatersrand
Johannesburg, South Africa
ivan.hofsajer@wits.co.za

***Abstract*— Many different power electronics topologies can fulfil the same conversion function. However, there are no systematic topology evaluation methods. Compared to competing topologies, assessment metrics supplied with new topologies are normally chosen to show the new ones in the best light. This paper assesses several different topology performance metrics to establish a systematic approach to topology evaluation. Four different single-switch DC-DC buck topologies are used to illustrate their use. Comparative plots are presented and discussed to help interpret the metrics. A new unified metric is proposed for simplified topology evaluation.**

Keywords—DC-DC conversion, Processed power, Component stress factors, Topology, performance metric, RMS

I. Introduction

Most papers proposing a new topology will offer the circuit diagram level description, a mathematical analysis of the ideal switching waveforms from which the power transfer function is derived as well as some of the main voltage and current stresses. The converter is then demonstrated experimentally and the main waveforms are shown to agree with the ideal converter waveforms within parasitic constraints. There's often a section that places the converter in the context of other converters with a similar function. The new converter is compared to existing ones and the poor aspects of the existing ones are compared to the positive properties of the proposed one. The conclusion is most often that the new topology works very well and performs better than other topologies for the application.

The problem with this approach is that it is difficult to objectively see if the new topology is better than the previous ones, as the new topology may be complex and unfamiliar.

The strategies used to compare several topologies often consist of compiling a table of properties of the converters and using that data to make an argument. While this approach is certainly useful it can be quite subjective as to which properties are chosen and how they are weighted. A multi-objective approach such as the Pareto-front is applied in these cases, however, these can be tedious for a quick evaluation.

Most new topology papers include experimental results including an efficiency measurement. Sometimes different topologies are assessed via a meta-analysis of previously presented experimental results. For example, the efficiency of a new step-down converter may be compared with the reported efficiencies of several previous step-down converters with roughly similar power levels. The problem with this approach is that the exact conditions of the different experimental investigations are not known. Most efficiencies are in the mid 90% and small changes in the design choices and construction layout can easily swing the efficiencies by a few percentage points and change the rankings of the converters. The level to which the experimentally constructed converters were refined is also not known.

One solution to this problem is to have a single designer construct and measure multiple different topologies under the same conditions. While this is possible it is not feasible if there is a large number of topologies. For this to take place it would be beneficial to have some form of pre-filtering before the experimental work.

In this paper, we consider two main existing approaches to systematic assessment and compare them with each other. The first approach centres on the amount of power the converter processes and can be thought of as an energy-based method [1]. The second approach centres on the component stress and can be thought of as a loss-based method [2], [3]. The paper also introduces a modification that tries to unify the two methods.

Each method is described and then applied to several buck converters to illustrate the utility of the method. This also helps in the interpretation of the meaning of the output of the two methods. The conventional buck will be employed as a baseline and then compared to the buck-boost, a switched inductor topology and a hybrid switched inductor topology. The buck-boost is included as it is well known that the buck-boost is an indirect topology and processes all the output power. This should make it reflect poorly in any assessment method. The topologies were chosen as single switch non-isolated topologies to reduce the complexity of the interpretation of the metrics. The methods described here can be applied to other converters as well.

The main contributions of this paper are 1) a systematic approach to topology selection; 2) a critical assessment of two existing metrics, illustrated using four topologies and showing their performance relative to the fundamental limit of power conversion; 3) a summary of utility of metrics, and 4) proposed a unifying metric which combines multiple metrics.

II. Foundational Assumptions

A. Zero loss

It is routine to first consider a topology from a zero-loss perspective with ideal components. The two methods described here both make that assumption. There is zero power loss in the switches and reactive components. The consequence of this is that the input power equals the output power and over a complete switching cycle there is zero net energy gain or delivery from reactive components.

B. Zero ripple

A zero ripple assumption implies that the inductors and capacitors are large enough that their currents and voltages respectively have no ripple and can be considered DC values.

The simplest way to achieve this in the analysis is to replace the inductors with a current source with a value equal to the average value of the inductor current. The capacitors are replaced with a voltage source at the average value of the capacitor voltage. This assumption is normally used when a topology's large signal transfer function is determined.

The two methods described here both make the zero ripple assumption in their underlying analysis. Normally the size of the inductor ripple has an impact on the performance of the converter. The zero ripple assumption leads to the best possible performance metrics for topology and also makes the comparison between topologies slightly fairer as the amount of ripple is not included as a parameter.

C. Continuous Conduction Mode

As a consequence of the zero ripple approximation, the converters will be analysed in the continuous conduction mode. This leads to the best possible utilization of the components and leads to the best possible performance metrics.

III. Fundamental Conversion Limits

A. Processed power

The task of a DC-DC converter is to convert the input DC voltage to a different output DC voltage. This requires switching action. This switching action and the power exchanged by the inductors and capacitors in the topology were studied and fundamental limits on the minimum required amount of switching and power exchange between the reactive components were derived in several seminal papers [5]–[7]. This work has not found much utility until recently when it has been used with success by [1], [4], [8] who have used it to analyse and derive new power conversion architectures and the topologies that process the least amount of power. This has led to new novel power conversion architectures and a better understanding of the power conversion process.

In this paper, the foundational work of Wolaver [5] is used to assess the internal operations of a power converter and assess how close a topology comes to achieving the minimum required processed power. The minimum processed power for a converter depends on its function. For the step-down dc-dc converter the minimum processed power as determined by Wolaver is

$$P_{processed} = P_{in}(1 - \frac{V_{out}}{V_{in}}) \quad (1)$$

From this equation, it can be seen that if the output voltage is not stepped down and the output equals the input then zero power needs to be processed. As the output voltage drops the conversion burden becomes larger and the amount of the total input power that needs to be processed increases.

The power processed by a single reactive component is given by equation *(2)* [8].

$$P_{component} = \frac{1}{2T}\int_0^T |v(t)i(t)|dt \quad (2)$$

Under the assumption of zero ripple, the voltages and currents in equation *(2)* have constant values during the on and off times of the switch. Furthermore, during the on time of the switch the component will be releasing energy and in the off time of the switch, the energy will be received back to the component. With these two simplifications equation *(2)* can be written as equation *(3)*, deliberately dropping the absolute value operation.

$$P_{component} = D(V_{onstate} I_{onstate}) \quad (3)$$

Where D is the duty cycle and $V_{onstate}$ and $I_{onstate}$ are the voltages and currents of the reactive component during the on-state of the switch.

The conventional buck converter will be analysed here to show the utility of this equation and the typical analysis method. The buck converter circuit is shown in Fig. 1. The input capacitor is included as the buck converter has a fluctuating input current and the capacitor will be used to carry the fluctuation current.

The buck converter is redrawn in Fig. 1 showing the zero ripple modeling. The capacitors have been replaced a with voltage source with the average value of the capacitor voltage and the inductor replaced with a current source with the average value of the current in the inductor. The load resistor has been replaced by a voltage source at the output voltage.

The converter's input and output are modelled as two voltage sources in parallel. For analysis purposes, the current is split into a constant DC part and a fluctuating AC part with no average value. In Fig.1, $V_{in}I_{in}$ is the constant input power which equals the constant output power $V_{out}I_{out}$. The voltage source V_{Cin} carries the fluctuating power and will have a zero average over one switching cycle. Splitting the input and output sources in this way is useful as it allows the reactive power processed by the source to be split apart from the average power delivered by the source. The authors in [9] and [10] show that the reactive contribution from the source is vital to describe all the power processed by the converter.

Under zero ripple conditions, the output capacitor does not carry any current and its contribution to the processed power will be zero. The only reactive components remaining are the input capacitor (represented by the source V_{Cin}) and the inductor current (represented by the source I_L). The waveforms of these components in the time domain are shown in Fig. 2.

Applying equation *(3)* to the data in Fig. 2 the processed powers of the input capacitor and inductor can be found as:

$$P_L = DI_{out}(V_{in} - V_{out}) = V_{in}I_{in}(1 - D) \quad (4)$$

$$P_{Cin} = DV_{in}(I_{in} - I_{out}) = -V_{in}I_{in}(1 - D) \quad (5)$$

The processed powers of the different components determined in this way will always add to zero no matter the topology of the converter. The original definition of the processed powers includes the absolute value operator which hides this balance. For this reason, the definition of the processed power has been modified and is valid as long as the original assumption of zero ripple is maintained.

Equations *(4)* and *(5)* are normalised to the input power $V_{in}I_{in}$ and plotted as a function of the converter gain V_{out}/V_{in}, which for the buck converter is equal to the duty cycle D. This is shown in Fig. 3 along with the Wolaver limit(dotted red lines) showing the minimum amount of processed power required, as shown, the conventional buck converter is at the Wolaver limit.

For any conversion effort, reactive power is exchanged between the inductor and the input capacitor. For any converter the total exchanged power for any conversion effort will add to zero. However, the exchanged power will not necessarily meet the limit for minimum processed power. More examples will be shown in section V.

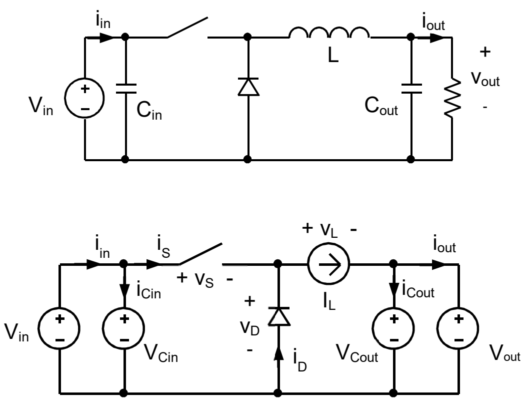

Fig. 1. Buck converter topology with input Capacitor(Cin)(TOP), (BOTTOM) Buck zero ripple modelling

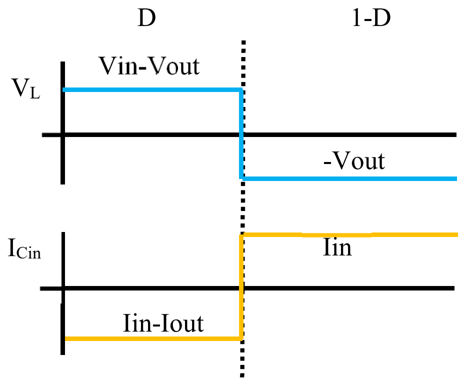

Fig. 2. Buck inductor voltage(vL) and Capacitor Current ($ICin$)

B. VA rating

Additionally, the Wolaver foundational limits describe that to perform the conversion, the switches that generate the fluctuating AC power need to meet a minimum requirement in terms of their VA ratings. Moore et al [6] state that to generate this AC power the VA rating of a switch needs to be at least 4x the AC power. Furthermore, the generated AC power needs to be rectified again in the converter and therefore there need to be diodes or synchronous rectifiers with an equal VA rating.

Where there are multiple switches and diodes the linear sum of the VA ratings of all switches and the linear sum of the VA ratings of all the diodes should be used [8], [11].

As the minimum required processed power is known from equation *(1)* it is possible to write an equation for the minimum required VA rating of all the switches and diodes for any step-down conversion effort.

$$VA_{min} = 8\left(P_{processed}\right) = 8P_{in}\left(1 - \frac{V_{out}}{V_{in}}\right) = 8V_{in}I_{in}(1 - D) \quad (6)$$

The VA rating of a switch or diode is determined in the usual way as the product of the blocking voltage in the "off" state and the conduction current in the "on" state. For the buck converter of Fig. 1 and using the waveforms of Fig. 2:

$$VA_{total} = VA_{switch} + VA_{diode} = V_{in}\frac{I_{in}}{D} + V_{in}\frac{I_{in}}{D} \quad (7)$$

The fundamental limit on the VA rating and the combined VA rating of the switch and diode are plotted with a normalised input power in Fig. 4. It can be seen that the buck converter

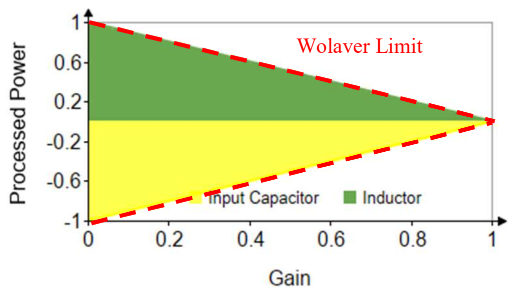

Fig. 3. Buck Converter Processed Power, input capacitor ,and Inductor, at the Wolaver limit

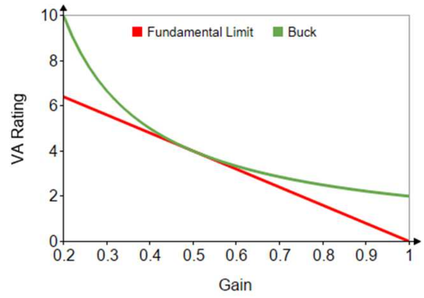

Fig. 4. VA rating of buck (switch and diode) in relation to Wolaver minimum VA rating

meets the fundamental VA rating at a gain of 0.5 and for different gains does not perform as well.

IV. Component Stress Factors

The second systematic assessment strategy is the use of the component stress factors. These are metrics attached to the semiconductors, capacitors and inductors that attempt to quantify the amount of resources needed to implement them. As the metrics are technology independent it is possible to obtain a relative indication of the resources needed between different topologies.

The approach was originally suggested by [3] and refined by [2]. It has been used with various modifications with some success by [12], [13]. However, the method itself has not been subjected to scrutiny.

A core assumption in using this method is the zero ripple approximation. This again removes the dependence of the inductor current ripple and gives a best-case set of metrics. However, there is no fundamental reason why the assumption cannot be relaxed.

A. Semiconductor stress factor

Each type of component has a slightly different definition of the stress factor. The semiconductor stress factor is defined as the maximum voltage squared multiplied by the RMS current squared.

$$SF_{semi} = \frac{{I_{RMS}}^2 {V_{max}}^2}{{P_{in}}^2} \quad (8)$$

This attempts to find a device-independent loss term. The resistance of the channel of a MOSFET is somewhat proportional to the square of the voltage, which multiplied by the RMS current can give a metric of the approximate comparative loss. Using this metric exclusively assumes that all switches are MOSFET based, which while correct for synchronous rectifiers will not be accurate when using normal diodes. This metric also does not capture switching loss effects. In the examples given later in this paper, the assumption of synchronous rectifiers will be used.

B. Capacitor stress factor

The capacitor stress factor is defined similarly with the square of the voltage being related to the volume (energy storage) and the RMS current related to the loss.

$$SF_{cap} = \frac{{I_{RMS}}^2 {V_{max}}^2}{{P_{in}}^2} \tag{9}$$

C. Inductor stress factor

The inductor stress factor is related to the RMS current as this gives the winding loss and the resistance is proportional to the number of turns (the applied voltage) and inversely proportional to the winding window area. The absolute value of the winding voltage average is defined as shown.

$$\begin{gathered} SF_{ind} = \frac{{I_{RMS}}^2 {V_{avg}}^2}{{P_{in}}^2} \\ V_{avg} = |Dv_{Lon}| + \left|(1-D)v_{Loff}\right| \end{gathered} \tag{10}$$

To illustrate the utility of this approach the same buck example is considered. It is a simple matter to find the maximum voltages and the RMS currents under zero ripple conditions using the waveforms of Fig. 2.

$$\begin{gathered} SF_{semi} = \frac{1}{D} + \frac{1-D}{D^2} \\ SF_{cap} = 4(D-1)^2 \\ SF_{ind} = \frac{1}{D} - 1 \end{gathered} \tag{11}$$

The stress factors can be determined as a function of the converter gain as in equation *(11)* and are plotted in Fig. 5. From the figure, it is clear that for low gains where the duty cycle becomes small there is a large stress on the switches. This points to the known difficulties of very small duty cycles. The capacitor and inductor stresses also tend to not favour low gains.

While there have been cases where the three stress factors have been added to produce a single figure of merit [12], [13], they will not be added in this paper. The different stress factors describe different things and their weightings are not necessarily equal.

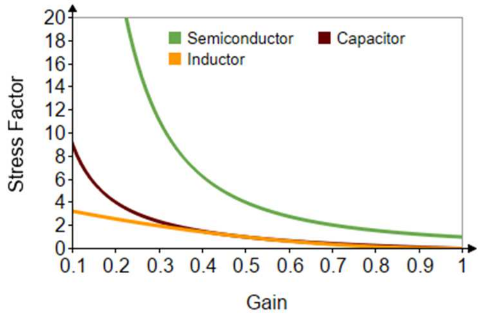

Fig. 5. Buck component stress factors

V. Use of the Metrics

To illustrate the use of the metrics four different topologies will be compared to each other. The standard buck will be used as the baseline. The conventional buck-boost in Fig. 6 (a), the basic switched inductor buck in Fig. 6 (b), and the switched inductor hybrid in Fig. 6 (c) will also be used.

It is not immediately obvious as to which of the two switched inductor topologies will perform better or if indeed the standard buck will perform better. These three topologies are assessed using the zero ripple analysis described in the previous two sections. For all three topologies, the input and output capacitors contribute to the processed power and both capacitors are treated as voltage sources carrying the input and output current ripples respectively.

The contribution of each of the converter's components to the processed power can easily be seen in Fig. 7. Along with the Wolaver limit shown in red. It is also clear that the hybrid switched inductor converter meets the Wolaver limit, while the switched inductor processes slightly more. The buck-boost always processes the total amount of power. It is also clear that for the switched inductor converters the input capacitors process much more power than the output capacitors. The utility of these plots is that they allow a quick visual comparison of the different converters in terms of the power fluctuating inside the converter.

It is also easy to see if a converter is a minimum conversion topology or not. However, the problems due to extreme duty cycles are not visible. If there is a large difference between the power processed by two different topologies for the same gain, then it is unlikely that the topology with the higher processed power will be the preferred one. This will be expanded on in section VII.

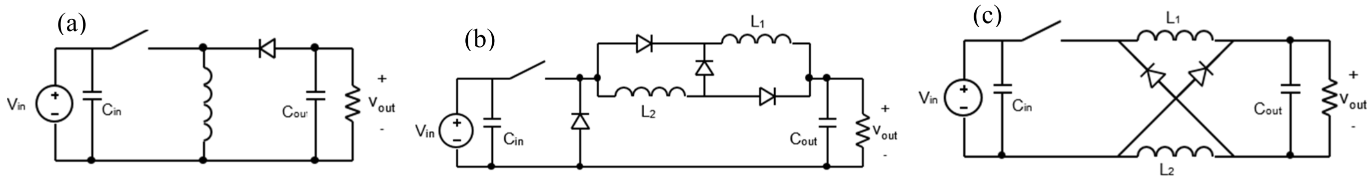

Fig. 6. (a) Buck-Boost, (b) Switched Inductor, (c) Hybrid switched Inductor

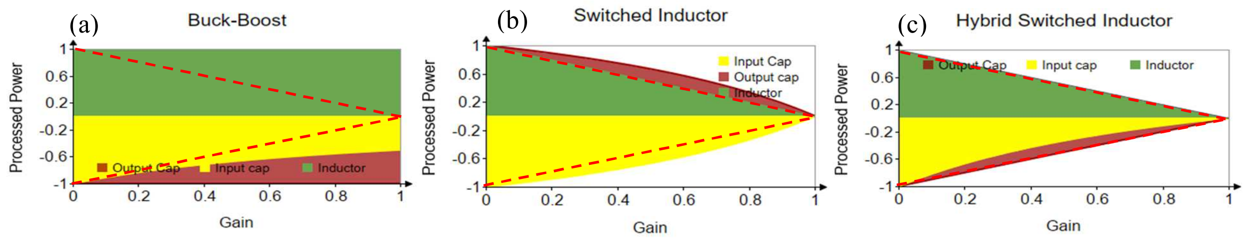

Fig. 7. Processed Power plots, (a) Buck-Boost, (b) Switched Inductor, (c) Hybrid Switched Inductor

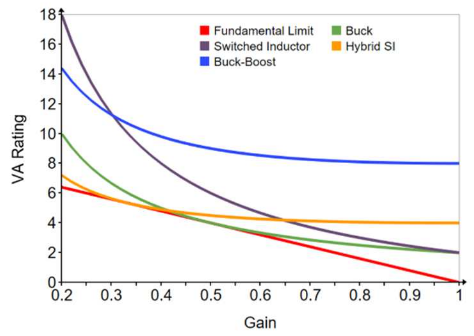

Fig. 8. VA Rating comparison of the topologies

The total VA rating of the topologies as well as the fundamental limit is shown in Fig. 8. This shows the extent to which the topologies are utilizing the switches effectively. From the figure, it is clear that the hybrid switched inductor utilizes the switches almost as well as the buck. Except at gains close to unity the basic switched inductor converter does not perform well.

The component stress factors for the different topologies are shown in Fig. 9. The relative performances of the different topologies can be seen. The hybrid switched inductor converter generally performs well, especially when the output becomes low. The stress factors take directly into account the effects of extreme duty cycles and conduction loss mechanisms. For gains below about 0.5, the hybrid switched inductor is the most preferred. The results are in line with the literature [14]. The series inductors make it able to achieve high step-down gains with less switching stress.

VI. METRIC COMPARISON AND RMS POWER METRIC

From the similarities above an argument can thus be made on a potential of a single metric that holistically characterises converter topologies. The properties captured are "lenses" for looking at individual aspects of the same waveform. It is proposed that a metric that captures characteristic change over time and the peak has the potential as a unifying metric. An approximation such as zero ripple, reduces the waveforms into a constant magnitude, hiding the effects of variation and the peak.

RMS quantifies how far the instantaneous power in the component varies from its average power. Thus the RMS of a waveform is related to ripple and peaks, which are directly linked to losses and high VA-rated components. The stress factors use the RMS of current only and actually capture some of these variations but only in the current waveform. Such information is hidden by the absolute value definition of the processed power metric in equation (2). Thus the processed power metric is rewritten in equation (12) to define the RMS metric. A similar argument to that of processed power is made, that a good converter is one with a smaller RMS.

$$RMS\ metric = \frac{1}{T}\sqrt{\int_0^T v(t)^2 i(t)^2 dt} \qquad (12)$$

The results of the RMS of power for all four topologies are given in Fig. 10. The RMS plots for the buck (Fig. 10 (a)) and hybrid (Fig. 10 (b)) are similar to the processed power plots in Fig. 3 and Fig. 7(c). The RMS metric further captures the high stresses on the inductor and capacitor at low gains, only previously captured by the inductor and capacitor stress factors in Fig. 9 (a) and (b). The total RMS power in Fig. 10(c) also provides similar curves to the semiconductor stress factor plots in Fig. 9. The RMS metric also paints the hybrid switched inductor in better light to the buck converter for gains below 0.5.

VII. DISCUSSION

The two assessment methods have been previously described in literature, but not critically analysed as shown in this paper. From the analysis, the metrics were shown to mostly paint the same picture of the topologies although defined differently. From these results, a single RMS metric was proposed to unify multiple metrics and thus simplify topology selection.

The key aspect of the processed power metric is its alignment with the fundamental DC-DC power conversion limits by Wolaver and Moore. However, the metric is limited as it hides the stress on passives at low-duty cycles due to the absolute value definition. The VA rating compliments the processed power metric, highlighting the differences in switch utilization between the two topologies, but also doesn't show the characteristic difference between the hybrid and buck converter at 0.5 gain. The stress factor captures these characteristics (in Fig. 9(c)) and reveals the high stresses expected at low gains on the passives and switches. These results are attributed to the RMS definition of the stress factors, which tends to amplify outliers due to the square, especially at low gains.

An interesting output from the critical analysis is the similarities between the metrics, they all seem to paint the same picture of the topologies considered. The slight differences in the metric numeric values are attributed to their different definitions, the use of absolute value versus RMS.

The metrics are common in that they quantify fluctuations (or AC) components in a converter due to switches and passives, which link to size, losses, and cost of the topologies. Thus a bad topology is taken as one with high processed power, component stress factor, or RMS value. The metrics paint the buck-boost converter as a bad performer at all duty cycles, particularly for single gain applications, compared to other converters. This is valid since the buck-boost is well-known as an indirect topology, meaning there is no direct transfer of power from the input to the output. All the input power is processed by the inductor and capacitors, meaning it has a 100% "AC" component or fluctuations. Whilst other topologies transfer some of the power directly from the input to the output, resulting in a smaller "AC" component, thus lower overall size, losses, and overall cost.

The outcome of this paper is further validated by an agreement in results between the VA rating metric and semiconductor stress factors and total RMS metric. The comparative results obtained between the buck and hybrid SI are in line with results in literature[14].

Another major outcome of this paper is the symmetry observed along the x-axis for all topologies, signifying the balance in the exchange of processed power between the inductor and input and output capacitors. The balance is further proof of the importance of splitting the source into reactive power, modelled by the input capacitance of the source, and its average power in the analysis. This balance was also observed for the non-linear RMS metric. This is unexpected and thus assumed to be a special case for zero-ripple approximation.

The utility of the existing metrics(processed power and stress factors) is undoubtedly in comparing topologies though each one seems to provide a limited perspective. The proposed RMS metric was shown to combine multiple perspectives in a single metric. The plots presented provide a designer with a visual comparison from which suitable topologies can be selected, based on their requirements for size, power dissipation(losses), component cost, and so forth.

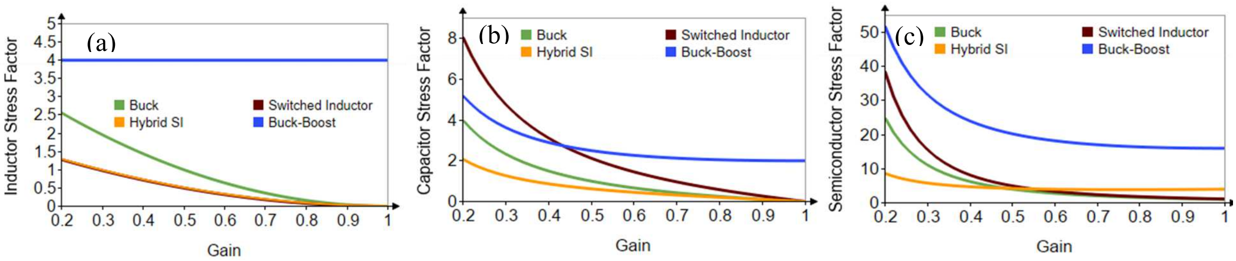

Fig. 9. Comparative stress factors for four topologies, a) inductor, b) capacitor, and c) Semiconductor stress factor.

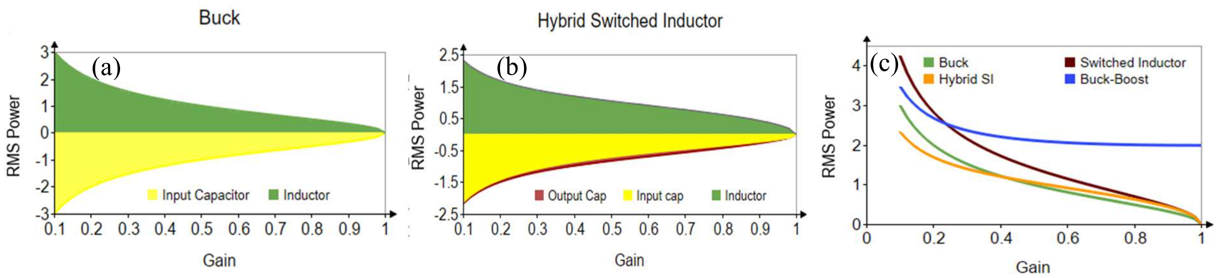

Fig. 10. RMS of power plots, a) Buck, b) Hybrid SI inductor and capacitor, and c) comparative RMS Power

A designer with a volume constraint as an example, can select a converter with a higher capacitor RMS compared to the inductor at the desired gain, and take advantage of the capacitor's high energy density, resulting in an overall lower converter volume. Converters with high VA ratings or high semiconductor stress factors or a single total RMS will require costly switches, thus these metrics can be used to minimize the overall converter cost, provided this is a constraint.

The metrics considered only capture the core power processing topology and other potentially important factors such as ease of control, the complexity of gate drivers, component count, and so on, will also need to be considered for a holistic topology design.

VIII. Conclusion

A systematic approach to topology selection has been presented. A processed power-centred approach and stress factors-based approach were critically assessed, comparing four different topologies relative to fundamental power conversion limits. The metrics were shown to paint the same but limited picture of the topologies though defined differently. The component stress factors were found to provide more information on the topology, due to their RMS definition. An RMS metric was introduced as a potentially simplified and holistic metric for topology selection.

References

[1] J. A. Cobos, H. Cristobal, D. Serrano, R. Ramos, J. A. Oliver, and P. Alou, "Differential power as a metric to optimize power converters and architecture," *2017 IEEE Energy Convers. Congr. Expo.*, 2017, doi: 10.1109/ECCE.2017.8096427.

[2] E. Wittenbreder, "Topology selection by the numbers - Part one," pp. 32–36, 2006.

[3] B. Carsten, "Converter Component Load Factors: A Performance Limitation of Various Topologies," *Pci*. pp. 31–49, 1988.

[4] Z. Ye, S. R. Sanders, and R. C. N. Pilawa-Podgurski, "Modeling and Comparison of Passive Component Volume of Hybrid Resonant Switched-Capacitor Converters," *2019 IEEE 20th Work. Control Model. Power Electron. COMPEL 2019*, vol. 37, no. 9, pp. 10903–10919, 2019, doi: 10.1109/COMPEL.2019.8769707.

[5] D. H. Wolaver, "Fundamental study of dc to dc conversion systems.," Massachusetts Institute of Technology, 1969.

[6] E. T. Moore and T. G. Wilson, "Basic considerations for DC to DC conversion networks.," *IEEE Trans. Magn. 2*, no. 2, pp. 620–624, 1966, doi: 10.1109/TMAG.1966.1065901.

[7] Dan H. Wolaver, "Requirements on switching devices in DC-to-DC converters," *IEEE Power Electron. Spec. Conf.*, pp. 111–117, 1973, doi: 10.1109/PESC.1973.7065177.

[8] C. Li and J. A. Cobos, "Classification of Differential Power Processing Architectures Based on VA Area Modeling," *IEEE J. Emerg. Sel. Top. Power Electron.*, vol. 6777, no. c, pp. 1–1, 2021, doi: 10.1109/JESTPE.2021.3093654.

[9] M. L. da S. M. and H. L. H. J. R. Rakoski Zientarski, J. R. Pinheiro, "'Understanding the partial power processing concept: A case-study of buck-boost dc/dc series regulator,'" *2015 IEEE 13th Brazilian Power Electron. Conf. 1st South. Power Electron. Conf. (COBEP/SPEC)*, pp. 1–6, 2015, doi: 10.1109/COBEP.2015.7420092.

[10] Z. Shi, K. W. E. Cheng, S. L. Ho, and W. Xu, "More general definition of energy factor and its application in isolated converters," *2009 3rd Int. Conf. Power Electron. Syst. Appl. PESA 2009*, 2009.

[11] R. W. Erickson and D. Maksimović, *Fundamentals of Power Electronics Third Edition*. 2014.

[12] R. Panigrahi, S. K. Mishra, A. Joshi, and K. D. T. Ngo, "Synthesis of DC-DC Converters from the voltage conversion ratio and prescribed requirements." .

[13] A. M. S. S. Andrade, L. Schuch, and M. L. Da Silva Martins, "Analysis and design of high-efficiency hybrid high step-Up DC-DC converter for distributed PV generation systems," *IEEE Trans. Ind. Electron.*, vol. 66, no. 5, pp. 3860–3868, 2019, doi: 10.1109/TIE.2018.2840496.

[14] O. Cornea, O. Pelan, and N. Muntean, "Comparative study of buck and hybrid buck switched-inductor DC-DC converters," *Proc. Int. Conf. Optim. Electr. Electron. Equipment, OPTIM*, no. April, pp. 853–858, 2012, doi: 10.1109/OPTIM.2012.6231912.

Optimization of Hybrid Power System for Cost Minimization: Case Study of a University Library

Kayode Timothy Akindeji
Department of Electrical Power Engineering
Durban University of Technology
Durban, South Africa
kayodea@dut.ac.za

Abstract— **The unprecedented increase in electricity consumption around the globe continues to place an enormous burden on national power grids, particularly during peak demand periods. The frequent load shedding in South Africa is a major concern for universities; hence, there is a need to find alternative sources in form of renewable energy sources (RES) or hybrid systems. Outages on campuses could lead to loss of revenues and quality time; which may include the cost of sustaining teaching, learning, and research. This study aims to ensure continuous supply to critical loads such as a university library using a hybrid system of diesel generator, solar PV, and battery storage at minimum cost. A non-linear objective function is formulated such that the library load is met by RES when available with the battery otherwise the diesel generator (DG) is switched on. A MATLAB function called "quadprog" is used to solve the optimization problem. The results show that the hybrid system performs better than the DG only with fuel cost reductions of 31% and 22.3% for summer weekdays and weekends respectively and 29.3% and 40.7% for winter weekdays and weekends respectively.**

Keywords—campus, HRES, PV, library, optimal

I. INTRODUCTION

Load shedding has become a regular experience in South Africa recently, necessitating the need to consider the viability of off-grid or hybrid systems for university campuses. Mbomvu et al [1], defines load shedding "as a measure which is executed to diminish the strain placed on an electricity grid, by means of provisionally cutting the supply of electricity (deliberately) to limiting the utilization of energy supply, as caused by an over-demand thereof". During load shedding that could last for two hours at a time, lectures, practical experiments are disrupted, and the entire university internet network (IP phones off) might be down if there is no alternative energy source.

Several application of hybrid renewable energy system (HRES) on university campuses have been reported in literature. In some instances, the microgrid concept was used as the platform to integrate renewable sources such as wind, small hydro, solar PV with different objectives. A microgrid in this context can be defined as an integrated energy system that operates either in an off grid (standalone) mode or grid tied (connected) mode. A microgrid was used as an active learning tools at the College of Engineering at McNeese State University (MSU), Lake Charles, Louisiana for electrical power engineering students in partnership with ABB Inc. USA supplying the campus microgrid with digital automation, protection and monitoring technology [2]. The authors of [3] proposed hybrid firefly lion algorithm to optimize the energy management system of a university campus microgrid. The main objective was to reduce the cost of energy on the campus this was achieved by dividing all the appliances into shiftable and non-shiftable categories. An evaluation of a hybrid off grid RES system was done in [4] to supply the university campus load with low cost and reduced CO_2. The assessment was performed during load shedding periods or when the grid was not available. Another application of HRES on a university campus was reported in [5]. The objective of the study was to evaluate the cost and reliability of an off grid HRES for a three-storey lecture building which consists of laboratories and faculty offices. A review of the use of RES in university campus microgrid was carried out in [6] with a conclusion that solar PV is the most used RES on university campuses followed by other hybrid systems. A methodology to implement a campus microgrid was proposed in [7] at the University of Puerto Rico, Mayagüez campus. Simulations were performed using OpalRT by considering the available resource and system capacity to meet critical loads of the university. The results showed that the proposed microgrid was able to satisfy the demand with better reliability when compared with the conventional electrical network. The optimization of RES is not limited to electrical loads in buildings but extends to electric vehicle for transportation within and outside the university. In [8], solar energy system was optimized for electric vehicle at a university campus in Dhaka, Bangladesh. The objective was focused on maximizing solar PV usage for electric vehicles and minimized CO_2 emission (environmental impact) on campus.

Therefore, the main aim of this study is to investigate the feasibility of an off-grid HRES to satisfy the electrical loads of a university library at a minimum cost. The remaining part of the paper is organized as follows: Section II gives a brief details of the hybrid system and its sub models, section III presents the mathematical formulation of the non-linear objective function with the constraints. The analysis and discussion of the results are captures in section IV and section V concludes the paper

II. THE HYBRID SYSTEM CONFIGURATION

The proposed HRES considered in this work consists of solar PV, diesel generator, battery, and library load, as shown in Fig.1. The communication (control) for the entire system is not included but assumed to operate at 100% efficiency.

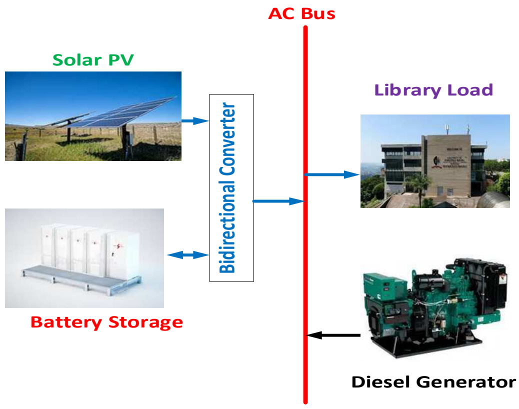

Fig. 1. Proposed HRES Configuration

A. Photovoltaic(PV) System Model

Many models have been used to describe the behavior of photovoltaic cells as well as to predict the energy produced by these cells. The common model used comprises a current that depends on cell temperature and solar radiation, a diode, a series resistance and a shunt resistance [9]. Scientifically, PV (solar) cells convert solar radiations from sunlight into direct current proportional to the intensity of the radiation and cell temperature. Equation (1) is used to determine the power in kW produced by the solar PV array. In this work, the estimated area for the solar PV is 1000 square meter.

$$P_{pv} = A \times \eta_p \times \eta_{pc} \times P_f \times I_d \quad (1)$$

A represents the area of the solar panel (m^2), η_p is the efficiency of the solar PV panel, η_{pc} represents the efficiency of the inverter, P_f is the packing factor of the solar PV panel, while the daily irradiance is represented by I_d [5].

B. Battery Energy System

Energy storage such as battery plays a important role in a off grid hybrid system by increasing the reliability of the power supply acting as the storage medium when there is excess generation and discharging stored energy during peak load demand when RESs are not sufficient to meet the load demand [10]**.** A major status indicator of the battery is the state-of-charge (SOC), which shows its remaining energy. The battery's SOC limit is formulated as an inequality constraint to ensure that battery is charged and dis-charged under specified limits in (2) as follows [11]**:**

$$B_{soc,max} \geq B_{soc}(t) \geq B_{soc,min} \quad (2)$$

B_{soc} represents the battery state of charge, while $B_{soc,min}$ and $B_{soc,max}$ are minimum and maximum state of charge of the battery bank. $B_{soc,min}$ is set to be 0,5 $B_{soc,max}$, the charge efficiency is 85% and the discharge efficiency is 100%.

C. Diesel Generator (DG) Model

Due to the intermittent nature of renewable energy sources, diesel generators are deployed in hybrid systems to serve as backup. However, the operation of DG must be within the limit specified by the manufacturer at any instance. Equation (3) represents a constraint that must be consider for maximum efficiency of the DG [12].

$$P_{dg}^{\min} \leq P_{dg}(t) \leq P_{dg}^{\max} \quad (3)$$

The fuel consumption of the DG is directly proportional to the fuel cost and is modelled according to (4).

$$FC(t) = \alpha P_{dg}(t) + \beta P_{dg,rated}(t) \quad (4)$$

Where, FC(t) represents the fuel consumption rate(l/h), $P_{dg}(t)$ is the output of DG in kW and $P_{dg,rated}$ is the rated capacity (kW) of the DG. α and β represents the fuel curve intercept coefficient (l/h/kW) and the diesel curve intercept coefficient (l/h/kW) respectively.

D. Load Model and Data

The main energy consuming equipment in the library is the chiller unit which is used for air conditioning. Other electrical loads include computers, photocopying machines, audio visual equipment etc. In other words, cooling constitutes major part of the electricity bill of the library and the university by extension [13].

TABLE 1. LOAD DATA FOR UNIVERSITY LIBRARY

Time	**13 March 2019 Summer Weekday (kW)**	**16 March 2019 Summer Weekend (kW)**	**13 August 2019 Winter Weekday (kW)**	**17 August 2019 Winter Weekend (kW)**
00:30	216	207	172	175
01:30	216	208	173	173
02:30	215	208	170	172
03:30	216	206	170	170
04:30	215	205	168	170
05:30	213	205	169	170
06:30	214	204	169	168
07:30	213	199	173	165
08:30	242	200	220	173
09:30	271	220	244	173
10:30	274	258	236	188
11:30	289	250	255	202
12:30	290	248	255	209
13:30	304	248	260	192
14:30	278	240	259	195
15:30	279	236	251	184
16:30	277	234	242	172
17:30	254	225	211	171
18:30	234	217	188	172
19:30	227	219	179	174
20:30	234	220	181	174
21:30	223	220	181	174
22:30	223	218	177	173
23:30	221	215	173	171

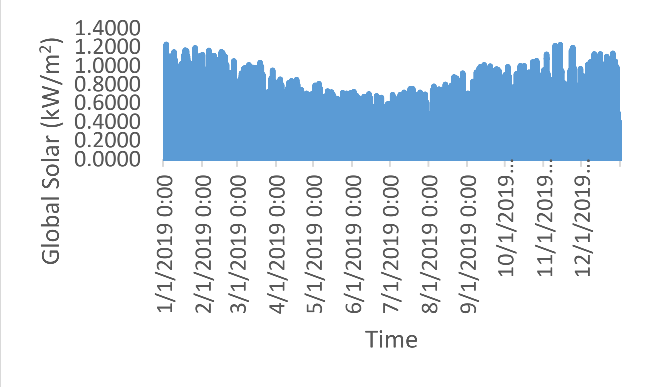

Fig. 2. Monthly Solar Radiation

III. Optimization Model and Objective Function

The main aim of this work is to minimize cost of fuel during load shedding or off-grid operation and maximize the benefits of RES when available. In other words, the optimization problem seeks to find the optimal scheduling of generation at every hour of day that reduces the fuel cost and maximizes the use of the RES while completely meeting the library load demand and others operating limits. As such, the hybrid power system is configured to give priority solar PV in satisfying the load, however, if the PV output is not enough to meet the load, the battery will discharge provided that it does not violate its operating limits. The diesel generator will be switched on the condition that both solar PV and battery are not able to satisfy the load demand that is the DG is kept at minimal use. In a situation where the total load demand is met by solar PV only, the excess energy generated by the RES is stored in the battery. To achieve the above, the optimization problem is formulated to minimize the diesel generator fuel cost during the operating time. Therefore, the objective function is shown in (5) below [12]:

$$\min\ C_f\ \sum_{t=1}^{N}\left(aP_{dg}^2(t)+bP_{dg}(t)\right) \tag{5}$$

Subject to the following constraints:

$$P_{pv}(t)+P_{bd}(t)-P_{bc}(t)+P_{dg}(t)=P_d(t) \tag{6}$$

$$P_{pv}(t)\geq 0, P_{bc}(t)\geq 0, P_{bd}(t)\geq 0, P_{dg}(t)\geq 0 \tag{7}$$

$$P_i^{min}\leq P_i(t)\leq P_i^{max} \tag{8}$$

$$B_{soc}^{min}\leq B_{soc}(o)+\eta_c\sum_{t=1}^{N}P_{bc}(t)-\eta_d\sum_{t=1}^{N}P_{bd}(t)\leq B_{soc}^{max} \tag{9}$$

The first constraint (6) above is to ensure that the total power supplied by the solar PV, battery, diesel generator and the power to charge the battery at any hour equals to the load demand at the same hour. The second constraint (7) ensures that power supplied by the solar PV (P_{pv}) directly to the load, the power charging the battery (P_{bc}), power discharged by the battery (P_{bd}) to the load and power from the diesel generator (P_{dg}) are all greater than or equal to zero. Equation (8) ensures that each energy source i is constrained to operate within its minimum and maximum values.

Equation (5) is a nonlinear objective function with linear constraints that can be solved using different methods. The *quadprog* function in MATLAB R2022b Optimization Toolbox was used to solve the objective function.

Four different load models were used for this case study; these were hourly load data for typical days during summer weekday and weekend and winter weekday and weekend all during the 2019 academic session. The simulation parameters for the solar PV, diesel generator and battery were taken from [12].

IV. Results and Discussion

This section presents and discusses the MATLAB simulation results as shown in Figs. 3-6. In these figures, the power flow to and from the battery are represented as '*BC'* and '*BD'* respectively, '*PV*' and '*DG'* denote the power from the solar PV and the diesel generator respectively while the library load is denoted by '*Demand'*. As observed for the figures, in all the four scenarios, the DG and battery were both used to meet the load in the early and late hours of the days considered. The period of availability of the PV during summer was longer (07h00 – 19h00) than winter (08h00 – 18h00) and the highest peak power generated by the PV was

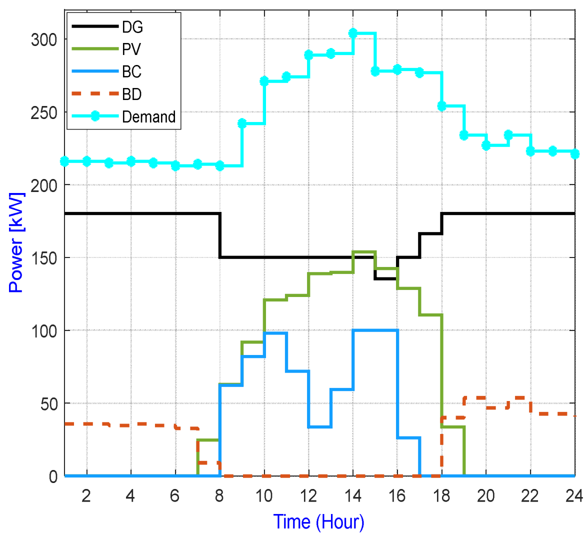

Fig. 3. Summer weekday power flow

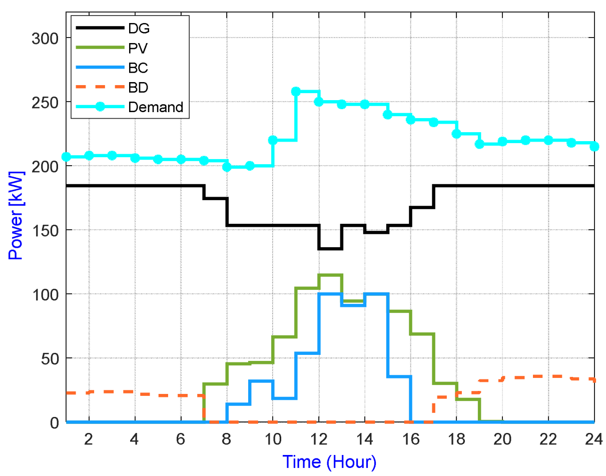

Fig. 4. Summer weekend power flow

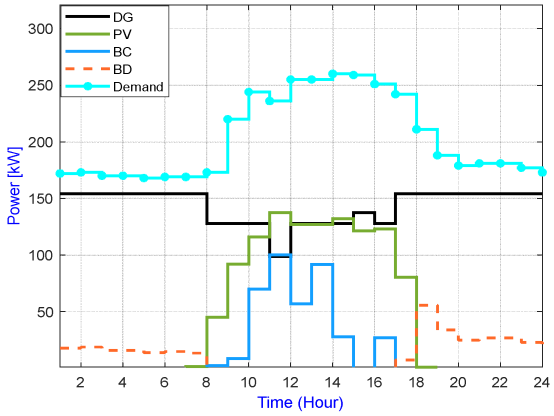

Fig. 5. Winter weekday power flow

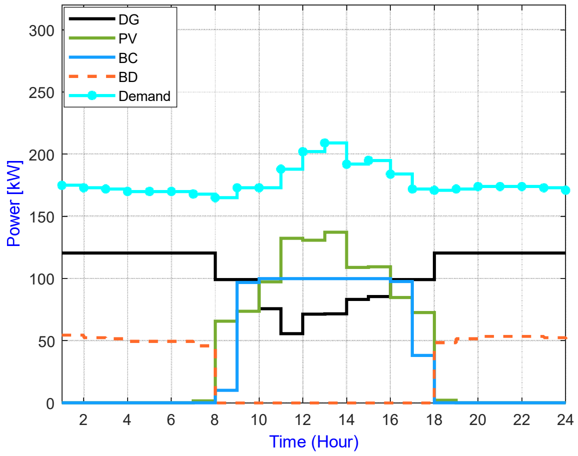

Fig. 6. Winter weekend power flow

during summer (153.89 kW at 14h00). In all the four scenarios, there was no time during a day that the PV output only satisfied the load, this was as a result of limited number of PV panel as the PV system was not sized to meet the entire load of the library. The good thing was that, there was no time of the day that the diesel generator alone was used to meet the load, whenever the PV was not available, the battery discharged having being charged during the day. Fig. 3 shows the summer weekend power flow, one interesting thing was that the peak load (304 kW) coincided with peak PV output (153.89 kW) at 14h00, this pattern was observed on winter weekend (Fig. 6) with both peaks occurring at 13h00.
In ideal situation, the demand in winter should be higher than summer, but for the library, the demand in summer was higher than demand in winter due to higher temperature making the reading rooms hot and uncomfortable without air-condition. Also, the weekday demand was more than the weekend demand showing that students used the library more on weekdays. The implication of higher demand is more fuel consumption translating to more fuel cost without alternative energy source. Table 2 shows the fuel costs for the four scenarios, comparing the fuel cost values for the hybrid system with diesel only option. The results show that the hybrid system attains 31% and 22.3% savings in summer, and 29.3% and 40.7% savings in winter on weekdays and weekends respectively in comparison with the diesel generator only system. The total fuel saving in winter was more than that of summer, this was because the demand for winter was lower, and however, the average PV output for winter was more thereby reducing the fuel consumption of the diesel generator during this period.

TABLE 2. FUEL COST SAVING

System	**Summer ($/hour)**		**Winter ($/hour)**	
	Weekday	***Weekend***	***Weekday***	***Weekend***
DG Only	58.38	53.10	48.76	42.60
Hybrid	40.27	41.28	34.46	25.27
Saving	**18.11**	**11.82**	**14.30**	**17.33**

V. CONCLUSION

An optimized hybrid renewable energy system is presented and analyzed. The results demonstrate how the use of renewable energy source could minimize fuel cost and reduce emission of greenhouse gases on campus. In order to increase the savings, the sizes of the solar PV array and battery storage can be increased. This application can be extended to other major building facilities on campus or better still, a campus microgrid that is made up of RES, battery, fuel cell etc. could be implemented. In conclusion, apart from the monetary benefit, there are other remarkable benefits that cannot be numerically quantified in optimizing HRES.

ACKNOWLEDGMENT

The author appreciates the University of KwaZulu Natal for access to the load data and Durban University of Technology for the grant received to complete the program.

REFERENCES

[1] L. Mbomvu, I. T. Hlongwane, N. P. Nxazonke, Z. Qayi, and J.-P. Bruwer, "Load Shedding and its Influence on South African Small, Medium and Micro Enterprise Profitability, Liquidity, Efficiency and Solvency," 21 April 2021, Available: http://www.businessresolution.co.za/.

[2] K. R. Khan, M. M. Haque, D. Sachdeva, and M. B. K. Morgan, "A campus microgrid used as an active learning tool for new generation of electrical power engineers," *International Journal of Electrical Engineering & Education,* 59(4). pp. 307-328,2022.

[3] H. Ullah, M. Khan, I. Hussain, I. Ullah, P. Uthansakul, and N. Khan, "An Optimal Energy Management System for University Campus Using the Hybrid Firefly Lion Algorithm (FLA)," *Energies,* vol. 14, no. 19. pp. 6028, 2021.

[4] K. S. Khan, Z. Ullah, B. Khan, I. Sami, S. M. Ali, and C. A. Mehmood, "Assessment of Hybrid Off Grid Wind Photovoltaic system:A Case Study of University Campus," presented at the International Conference on Energy Conservation and Efficiency (ICECE), Lahore, Pakistan, 22-23 November 2017,.

[5] S. Gangwar, D. Bhanja, and A. Biswas, "Cost, reliability, and sensitivity of a stand-alone hybrid renewable energy system—A case study on a lecture building with low load factor," *Journal of Renewable and Sustainable Energy,* vol. 7, no. 1. pp. 013109, 2015.

[6] K. T. Akindeji, R. Tiako, and I. E. Davidson, "Use of Renewable Energy Sources in University Campus Microgrid - A Review," 2019 International Conference on the Domestic Use of Energy (DUE), 2019, pp. 76-83.

[7] Y. V. Garcia, O. Garzon, F. Andrade, A. Irizarry, and O. F. Rodriguez-Martinez, "Methodology to Implement a Microgrid in a University Campus," *Applied Sciences,* vol. 12, no. 9. pp. 4563, 2022.

[8] N. Chowdhury, C. Hossain, M. Longo, and W. Yaïci, "Optimization of Solar Energy System for the Electric Vehicle at University Campus in Dhaka, Bangladesh," *Energies,* vol. 11, no. 9. pp. 2433, 2018.

[9] Vinod, R. Kumar, and S. K. Singh, "Solar photovoltaic modeling and simulation: As a renewable energy solution," *Energy Reports,* vol. 4, pp. 701-712, 2018.

[10] M. Kaur, S. Dhundhara, Y. P. Verma, and S. Chauhan, "Techno - economic analysis of photovoltaic - biomass - based microgrid system for reliable rural electrification," *International Transactions on Electrical Energy Systems,* vol. 30, no. 5. e12347, 2020.

[11] H. U. R. Habib *et al.*, "Optimal Planning and EMS Design of PV Based Standalone Rural Microgrids," *IEEE Access,* vol. 9, pp. 32908-32930, 2021.

[12] K. T. Akindeji, R. Tiako, and I. Davidson, "Optimization of University Campus Microgrid for Cost Reduction: A Case Study," *Advanced Engineering Forum,* vol. 45, pp. 77-96, 2022.

[13] J. Liyanagama, W. Seneviratne, and A. H. K. Balasooriya, "Green Library Project (GLP) : a strategic energy saving solution for the library, Open University of Sri Lanka using solar power," presented at the International Conference on Knowledge Collaboration in Engineering., India, January, 2014.

Calculating the Aerodynamic Drag Coefficient of a Toyota Avanza Car CAD Model using CFD Analysis

Nicholas Xavier
Department of Mechanical Engineering Science
University of Johannesburg
Johannesburg, South Africa
Nicholasixavier317@gmail.com

***Abstract*—Computational Fluid Dynamics (CFD) is paramount for the design development and optimization of vehicles; it is an integral element in vehicle performance analysis. This paper studies the aerodynamic properties of a Toyota Avanza car using CFD analysis to calculate the aerodynamic drag coefficient of the car, this will be used in the design of the conversion of the Internal Combustion Engine (ICE) Toyota vehicle to an electrically powered one (EV).**

The study entails the vehicle's model that was designed using Autodesk Fusion 360 and was simulated for CFD using Autodesk CFD Ultimate. The results were used to calculate the aerodynamic drag coefficient of the car and were found to be slightly above the stipulated range in the car's specification books. It was established that more accurate results could be achieved if the CAD model was more refined. Future work is focused on access to open-road simulation tools to aid the conversion process of the car to an EV, this will help in the design phase where the motor sizing could use a more accurate drag coefficient for its calculation.

Keywords—CFD, CAD, Aerodynamic Drag, Aerodynamic Drag Coefficient, ICE, EV

I. Introduction

As the automobility industry shifts to the electrification of automobiles, developing countries are hindered. Due to their economic status explored via the broad lens of demographics, odds of a successful transition to an Electric Vehicle (EV) dominated society are slim [1], unless automobile conversions are the heart of that transition.

The Faculty of Engineering and the Built Environment (FEBE) at the University of Johannesburg has undertaken the task of converting an internal combustion engine (ICE) Toyota Avanza 2009 car model to one that will be electrically powered (EV). To better understand the vehicle dynamics for an effective conversion, the car is modelled using Autodesk Fusion 360 then simulated for the drag coefficient using Autodesk CFD. The drag coefficient will be essential for the motor sizing calculations. The CFD models are pivotal to better understand the interaction of air particles and the car, this is crucial for the optimization studies that will be undertaken in the latter phases of the project.

II. Literature Review

A. *Electric Car Conversions*

Automobile conversions are effortless, timely and costly effective. They specialise in the process of transforming Internal Combustion Engine Vehicles (ICEVs) to ones that are electrically powered (EVs) [2]. Although vast improvements have been developed and adopted in recent years, the conversion industry, though with an embraced business model, has not been gaining momentum as should. This is true because of the prevailing marketing strategies of prevalent EV automobility manufacturing companies. These strategies have altered the paradigms of automobile owners, today the idea consumers have of electric cars is one centred around the idea of the future in terms of aesthetics.

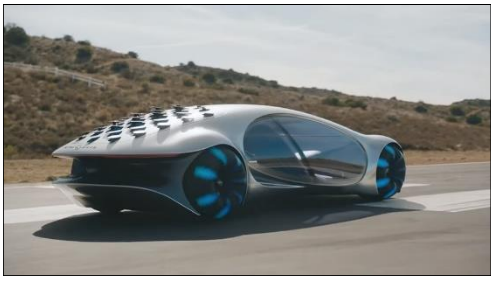

Figure 1: An example of a figure showing the deceiving idea of EVs. Photo licensed under CC BY-NC-ND [3]

The adoption of the conversion business model among other reasons will help restore the idea of automobility electrification, save money, because of the cost-effective nature of the conversion, and reduce waste, as car owners will not have to lose their preciously adored cars for EVs. Special attention will have to be paid to technical specifications when it comes to these conversions to ensure successful conversions that will be approved of quality and safety. Lessons learned in the conversion space are focal to the customization of conversion kits to meeting specific requirements tailored for range per charge and acceleration performance.

The evident demand for technical expertise requires the involvement of engineering professionals to make effective decisions in relation to battery capacity, motor sizing specific for that automobile, to eliminate the conversion process without the knowledge of critical parameters that often lead to the failure of the design [4]. Furthermore, poor vehicle performance and reliability is possible when the electric motor and other relative design factors do not match with the characteristics of the replaced internal combustion engine shared with the same car body and chassis [5].

The conversion process is well-timed following the worldwide fuel crisis and the adoption model of the green and sustainable culture hitting the world like a wave. Furthermore, the process is now well-backed following the current technological breakthroughs and milestones in the Electric Vehicle field.

B. *Computational Fluid Dynamics (CFD)*

1) *CFD*

Computational Fluid Dynamics (CFD) is one of the branches of mechanics of fluids, it specialises in the engineering art of analysing and solving problems that involve fluid flows using numerical methods and mathematical algorithms that simulate physical phenomena during design phases [6]. It is a key tool that helps engineering experts and automobile designers to optimise their design models to ensure effective decision making on the designs as means to improve their vehicle performance analysis.

CFD is therefore ideal for the following reasons:

- It is key to providing flexibility to alter design parameters without the expense of hardware changes, giving engineers the freedom to explore alternative designs that would be ideally feasible than otherwise.
- It provides faster turnaround time than the conventional route of experimenting.
- Pivotal for the identification of root problems, which is more logically suited for troubleshooting.
- It provides comprehensive information relating to flow field, especially in regions where conventional experimentation measurements are either complex or impossible to obtain.

Even with simplified equations and high speed modern supercomputing abilities, there is a limit of cases employed to configure certain real-world cases.

a) Aerodynamic Drag

Aerodynamic Drag is the resistance force caused by the motion of a body through air. A drag force acts opposite to the direction of the oncoming flow velocity. This is the relative velocity between the body and the fluid.

The drag force exerted on a body traveling through a fluid is given by:

$$Aerodynamic\ Drag = \frac{1}{2}\rho v^2 A C_d, \quad (1)$$

Where:

ρ is the air density, equating to 1.225 kg/m

v^2 is the square of the speed of the body relative to the fluid

A is the projected cross-sectional area of the body perpendicular to the flow direction

C_d is the drag coefficient, that varies along the speed of the body

b) Governing Fundamental Principles

The physical aspects of any fluid flow are governed by three fundamental principles:

- Conservation of Mass (Continuity Equation)
- Newton's Second Law relating force and the rate of change in momentum
- Conservation of Energy (Energy Equation)

All these principles are expressed in terms of basic calculus equations which are generally either integration or partial differential equations. In essence, CFD is simply the engineering art of replacing integrals or partial derivatives in the fundamental equations with discretized algebraic forms, which in turn are mathematically solved in iterations to obtain numerical values for the flow field at discrete points in a space and/or time.

The following are the discretisation methods in CFD:

- Finite Difference Method (FDM)
- Finite Volume Method (FVM)
- Finite Element Method (FEM)

CFD codes are structured around numerical algorithms that are capacitated with the ability of practically solving fluid problems, these codes use sophisticated yet simplified user interfaces to input the problem parameters to iterate results. The codes consist of three main elements that specialise in pre-processing of the model and data inputs, solving section, and the post-processing of the data outputs.

2) Governing Equations

The computational flow model is based on the finite volume formulation of unsteady incompressible Navier-Stokes equations [7]. Certain assumptions govern the output of this equation and configure thereon, the cases in investigations.

This paper focuses on fluid flow that is said to be turbulent. Turbulent flows examined in all lines of transport quantities (mass, momentum, and energy), tend to exhibit perioding, irregular fluctuations in time and space, such conditions enhance the mixing of these transport variables to efficiently model the physical world.

For the purpose of this investigation, the standard k̲ - Ɛ turbulence model is utilised in the process of analysing the two- and three-dimensional models entailed in this paper. The model was chosen because it is popular, it is a semi-empirical model, with two extra transport equations to represent the turbulent properties of the flow. This model helps us determine the turbulent kinetic energy (*k̲*) and the dissipation of the turbulence (Ɛ).

$$\frac{\partial u}{\partial x} + \frac{\partial v}{\partial y} + \frac{\partial w}{\partial z} = 0\,, \quad (2)$$

$$u\frac{\partial u}{\partial x} + v\frac{\partial u}{\partial y} + w\frac{\partial u}{\partial z} = -\frac{1}{\rho}\frac{\partial p}{\partial x} + \frac{1}{\rho}\left(\frac{\partial \tau_{xy}}{\partial y} + \frac{\partial \tau_{xz}}{\partial z}\right) + B_x\,, \quad (3)$$

$$u\frac{\partial v}{\partial x} + v\frac{\partial v}{\partial y} + w\frac{\partial v}{\partial z} = -\frac{1}{\rho}\frac{\partial p}{\partial y} + \frac{1}{\rho}\left(\frac{\partial \tau_{xy}}{\partial x} + \frac{\partial \tau_{yz}}{\partial z}\right) + B_y\,, \quad (4)$$

$$u\frac{\partial w}{\partial x} + v\frac{\partial w}{\partial y} + w\frac{\partial w}{\partial z} = -\frac{1}{\rho}\frac{\partial p}{\partial z} + \frac{1}{\rho}\left(\frac{\partial \tau_{xz}}{\partial x} + \frac{\partial \tau_{yz}}{\partial y}\right) + B_z, \quad (5)$$

Where u is the x – component of the velocity vector, v is the y – component, and w is the z – component. The symbol, ρ, stands for air density, p, standing for static pressure, τ, standing for shear stress, and B_x, B_y, and B_z, standing for body forces [7].

3) Transport Equations for standard k̲ - Ɛ turbulent models

The Navier – Stokes Equations were used to analyse the airflow investigated in this paper under the model of turbulence.

For Turbulent Kinetic Energy k̲:

$$\frac{\partial}{\partial t}(\rho k) + \frac{\partial}{\partial x_i}(\rho k u_i) = \frac{\partial}{\partial x_j}\left[\left(\mu + \frac{\mu_t}{\sigma_k}\right)\frac{\partial k}{\partial x_j}\right] + G_k + G_b - \rho\varepsilon - Y_M + S_k, \quad (6)$$

For Turbulent Energy Dissipation ε:

$$\frac{\partial}{\partial t}(\rho\varepsilon) + \frac{\partial}{\partial x_i}(\rho\varepsilon u_i) = \frac{\partial}{\partial x_j}\left[\left(\mu + \frac{\mu_t}{\sigma_\varepsilon}\right)\frac{\partial \varepsilon}{\partial x_j}\right] + C_{1\varepsilon}\frac{\varepsilon}{k}(G_k + C_{3\varepsilon}G_b) - C_{2\varepsilon}\rho\frac{\varepsilon^2}{k} + S_\varepsilon, \quad (7)$$

Where: G_k – represents the generation of turbulence kinetic energy due to the mean velocity gradients,

G_b – represents the generation of turbulence kinetic energy due to buoyancy,

Y_M – represents the contribution of the fluctuating dilatation in compressible turbulence to the overall rate of dissipation,

$C_{1\varepsilon}$, $C_{3\varepsilon}$, and $C_{2\varepsilon}$ – represent constants,

σ_k and σ_ε – represent turbulent Prandtl numbers for the k̲ and Ɛ, respectively,

S_k and S_ε represent user-defined sources terms [7].

4) Turbulent Viscosity

$$\mu_t = \rho C_\mu \frac{k^2}{\varepsilon}, \quad (8)$$

Where: C_μ is a constant.

5) Production of Turbulent Kinetic Energy

From the exact equation for the transport of k, this term may follow this definition:

$$G_k = -\rho u_i' u_j' \frac{\partial u_j}{\partial x_i}, \quad (9)$$

G_k evaluated in a manner consistent with the Boussinesq hypothesis:

$$G_k = \mu_t S^2, \quad (10)$$

Where: S - represents the modulus of the mean rate-of-strain, in the manner of the following definition:

$$S \equiv \sqrt{2S_{ij}S_{ij}}, \quad (11)$$

$$S_{ij} = \frac{1}{2}\left(\frac{\partial u_i}{\partial u_j} + \frac{\partial u_j}{\partial u_i}\right) \quad (12)$$

6) The Generation of Turbulence due to Buoyancy

$$G_b = \beta g_i \frac{\mu_t}{Pr_t} \frac{\partial T}{\partial x_i}, \quad (13)$$

Where: Pr_t - represents the turbulent Prandtl number for energy,

g_i – representing the component of the gravitational vector in the i-th direction,

β – represents the coefficient of thermal expansion, defined in the following manner:

$$\beta = -\frac{1}{\rho}\left(\frac{\partial p}{\partial T}\right)_p, \quad (14)$$

7) The Dilatation Dissipation

The dilatation dissipation term Y_M in equation (6), is modelled in accordance with:

$$Y_M = 2\rho\varepsilon {M_t}^2, \quad (15)$$

Where: ${M_t}^2$ – represents the turbulent Mach number, simply defined as follows:

$$M_t = \sqrt{\frac{k}{a^2}}, \quad (16)$$

Where: a – represents the speed of sound, defined as follows:

$$a \equiv \sqrt{\gamma RT}, \quad (17)$$

8) Model Constants

All the constants of the model were determined as default values in the simulation tool. These default values are entrusted for fundamental turbulent shear flows. They have also been proven effective for a wide range of wall-bounded and free shear flows.

III. The Toyota Avanza and CAD Model

A. The car

The following is one of the cars under conversion and were procured via the institution's finance department that offered them as cadavers for the conversion process. Credits to the project team, and other stakeholding units for the image.

Figure 2: Figure of the Toyota Avanza Car that will be converted to a fully Electric Vehicle.

B. The Modelling Tool

The Autodesk Fusion 360 tool was used to model the External Structure of the Toyota Avanza car.

C. The CAD Model

The CAD model was modelled with the aid of a drawing of the vehicle, and it was sourced from Pinterest with the stated credits.

1) The Drawing

The drawing was modified into front, side, and back pictures that were used as canvases in the process of modelling the Toyota Avanza car.

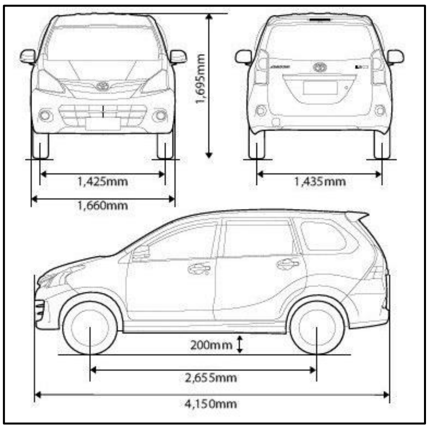

Figure 3: The figure of the drawing used to model the Toyota Avanza [8]

2) The CAD Model

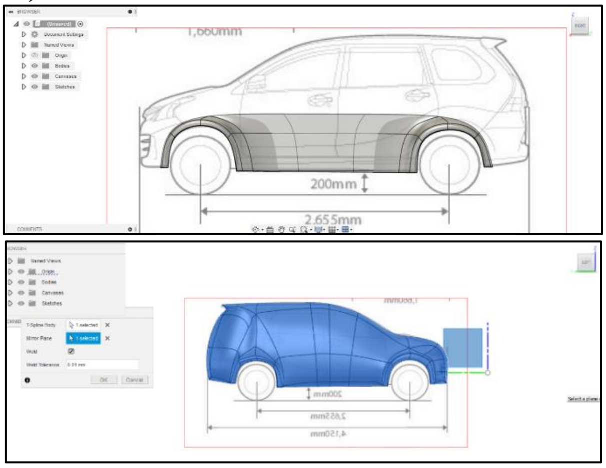

Figure 4: CAD model figures during design with the aid of a side cavass.

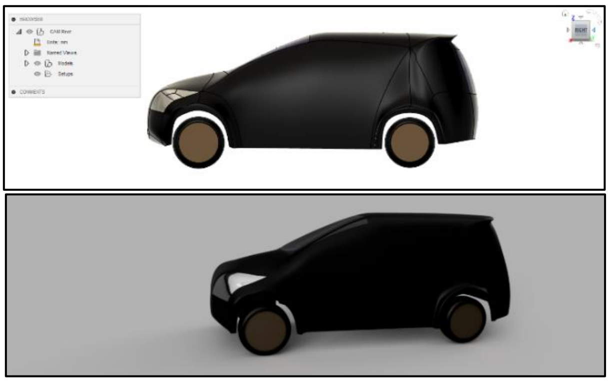

Figure 5: The images of the rendered model prior CFD Analysis

IV. CFD ANALYSIS

A. *Simulation Tool*

The Autodesk CFD Ultimate simulation tool was used to help us perform the CFD analysis of the car, and as a result, help us calculate the aerodynamic drag coefficient of the car.

1) *Geometric Tools*

The model analysis when transferred to the CFD analysis tool was found with no body misconfigurations or complex shape, this allowed for no merging of body parameters. The next step was to create an external volume.

a) *External Volume*

The external volume is paramount for the CFD modelling of the car, it serves a region that bounds the model in a wind tunnel sort of a configuration space, effective for standard CFD simulation.

B. *Assigning of Materials*

1) *The Car Body*

The car body was assigned aluminum as a material for testing.

2) *The External Volume*

The external volume was assigned air because this is an aerodynamic simulation.

C. *Boundary Conditions*

1) *Simulation Velocity*

The boundary velocity was set to *35m/s*.

2) *Simulation Pressure*

The pressure was set to *0kPa* at gage pressure.

3) *Slip Symmetry*

The top, side, and front sides were applied a slip symmetry.

D. *Generation of the Mesh*

Generating the mesh is an integral step in the process of CFD analysis, this is because the partial differential equations that govern fluid flow and heat transfer are not usually amenable to analytical solutions, except for very simple cases. This simplified model is called the mesh model.

1) *Mesh Setting*

a) *Surface Refinement*

Auto refining was set for the mesh setting.

b) *Gap Refinement*

Gap refinement was set for the mesh setting.

c) *Length Scale*

Length scale was left at default, for intelligent analysis.

2) *Mesh Sizing*

Mesh Sizing was set to automatic size.

E. *CFD Solution Settings*

1) *Heat Transfer*

The investigation was set to investigate flows than thermal analysis.

2) *Flows*

a) *Compressibility*

The flow was set to incompressible flow

b) *Turbulence*

Turbulence followed the k̲ - Ɛ model, this model in Autodesk CFD Ultimate is called the k-epsilon model.

F. *Solution Iterations to Run*

The simulation was run at 350 iterations.

V. CFD SOLUTION

A. *Results*

The following plot was generated from the CFD analysis, it shows the k̲ - Ɛ model as per progression in iterations.

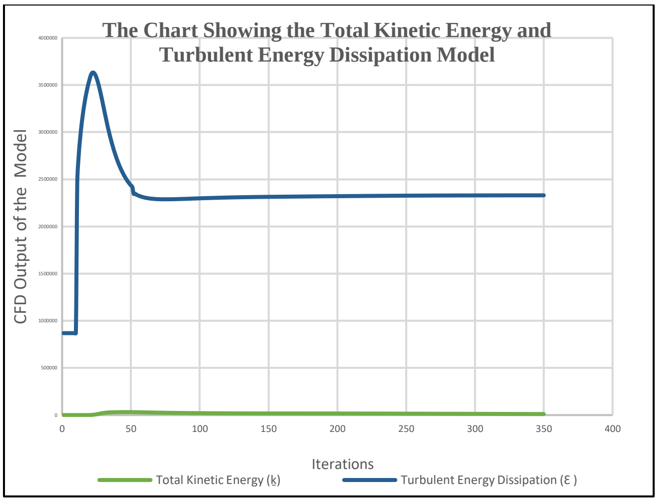

Figure 6: Showing the k̲ - ε model with the progression of the iterations

B. *CFD Models*

1) *Two-Dimensional CFD Analysis of the Car*

The car's 2D CFD results were achieved using planar cutting, the wind tracing technique was employed to demonstrate the movement of the air particles relative to the car model. The following figure explicitly demonstrates that.

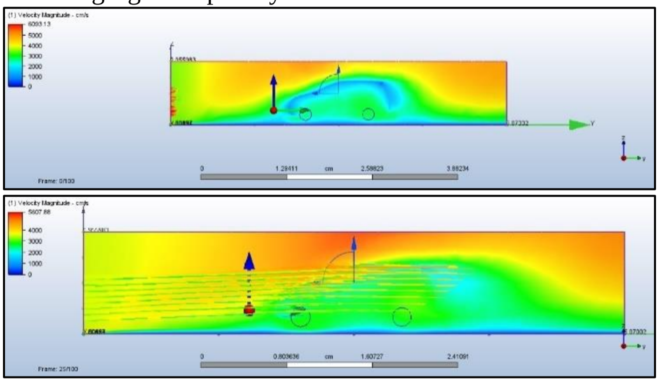

Figure 7: Plane model of the CFD, the turbulence is also observed under the car because the car model was originally not closed.

2) *Three-Dimensional CFD Analysis of the Car*

The car's 3D CFD Analysis was explored in one way, using CFD results display using ISO Volumes. The display also employs the wind tracing technique to aid our idea of the wind particle movement relative to the modelled car.

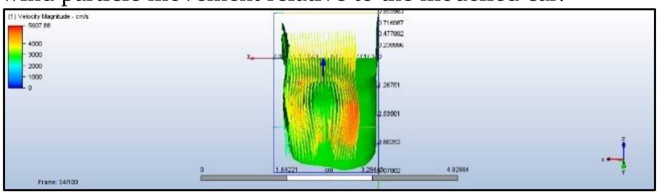

Figure 8: The CFD Model of the ISO Volume and the flow around the car using wind particle traces from the top view.

VI. THE AERODYNAMIC DRAG COEFFICIENT CALCULATION

A. *CFD Analysis Results*

Table 1: Table Showing the CFD Wall Calculation Results

CFD RESULTS		
From CFD Model	Aerodynamic Drag in kN (F_x)	0.584417313
	Area in cm^2 (Frontal)	22308.6
From Formula	Air Density in kg/m^3 (ρ)	1.225
	Drag Coefficient (C_d)	?

B. Aerodynamic Drag Calculation

Using equation (1), the following drag coefficient was calculated.

$$C_d = \frac{2Drag}{\rho v^2 A}$$

$$C_d = \frac{2 * (0.584417313x10^3)}{1.225 * (35)^2 * (22308.6x10^{-4})}$$

$$C_d = 0.3491472091$$

C. Interpretation of Results

The normal range of the drag coefficient of the Toyota Avanza car ranges from 0.2 - 0.3 [9], a drag coefficient of 0.35 is above this range. This might be because of the turbulence resulting from the opened base of the car. It is also likely that the CFD model was ran from an unrefined model, the more unrefined, the less streamlined it is, this results to more drag, thus the resulting drag coefficient slightly higher. This can be modified for more accurate results in the future. The CFD model may also be ran with more than 350 iterations in the future for more accurate results and multiple CFD tools can be used to verify the results.

VII. Conclusions and Recommendations

The study was successful in the investigation and calculation of the aerodynamic drag coefficient. The CAD model assisted in the running of the CFD simulation, and the drag coefficient was found to be 0.35. This value is slightly out of the drag coefficient range of a typical Toyota Avanza car (0.2 – 0.3). The deviation might have been caused by unrefined regions of the model and the limited number of iterations employed.
It is therefore recommended that more time be taken to refine the CAD model, or even to explore more efficient modelling tools, like Autodesk 3ds Max. The base of the car should also be closed to limit the unnecessary turbulence observed in the CFD model. More tools can also be employed for the CFD simulation to help verify and improve the nature of the output CFD results, and as a result, improve the aerodynamic drag coefficient of the car.

VIII. Future Work

Future work is focal to the betterment of the CFD analysis model as a means to determine a more realistic aerodynamic drag coefficient. This refined drag coefficient will be used to initiate the design process of sizing the motor for the conversion of the car to an EV. More refined simulation tools offering open-road access simulations, that mimic a more real-world analysis must be integrated for ideal solutions. Latter phases of the project must also consider employing the live wind tunnel testing to validate the vehicle performance model.
Successful conversion of the Toyota Avanza car to an EV will be instrumental to taking the conversion model to a fully commercial space. Commercializing the model in a country like South Africa, where Toyota Avanza cars are dominating the roads for the sole purpose of public transportation and fleet [10], may result into a viable business model that is guaranteed sustainability.

IX. Acknowledgments

Special thanks to Prof P. Naidoo for the support in the form of motivation and guidance towards the compilation of the journal article. Endless gratitude for also reviewing my work and assistance with final editing.

X. References

[1] S. Z. Rajper and J. Albrecht, "Prospects of Electric Vehicles in the Developing Countries: A Literature Review," *Sustainability,* vol. 12, 2020.

[2] G. Mirko, D. Stamenković, V. M. Popovic, S. R. Muzdeka and A. Micovic, "Electric Vehicle Conversion: Optimisation of Parameters in the Design Process," *Tehnicki Vjesnik*, vol. 24, no. 4, pp. 1213-1219, January 2017.

[3] UJ VILAGTUDAT, "Mercedes-Benz has unveiled an Avatar-like electric car prototype that almost looks like it's alive," Blogspot, September 2020. [Online]. Available: https://ujvilagtudat.blogspot.com/2020/09/a-mercedes-benz-egy-avatarszeru.html.

[4] T. Porselvi, M. K. Srihariharan, J. Ashok and K. S. Ajith, "Selection of Power Rating of an Electric Motor for Electric Vehicles," *International Journal of Engineering Science and Computing,* vol. 7, no. 4, pp. 6469-6472, 2017.

[5] J. A. Sanguesa, V. Torres-Sanz, P. Garrido, F. J. Martinez and J. M. Marquez-Barja, "A Review on Electric Vehicles: Technologies and Challenges," *Smart Cities,* vol. 4, pp. 372-404, 2021.

[6] I. Nishant, P. Jignesh, P. Rajan, S. Raikaan and S. Satyam, "CFD analysis of car body aerodynamics and Design modification for drag reduction," Academia.edu, 2019.

[7] D. Damjanović, D. Kozak, . M. Živić, Ž. Ivandić and T. Baškarić, "CFD analysis of concept car in order to improve aerodynamics," *A jövő járműve,* pp. 108-115, 2011.

[8] Blueprints, "Toyota Avanza Vector Drawing," [Online]. Available: https://za.pinterest.com/pin/317574211210628321/.

[9] Toyota Avanza Hatfield, *Toyota Avanza 1.5 Technical Specification and Dimensions,* Pretoria: 2022 Ultimate Specs - The Most Comprehensive Car Specifications Database, 2006.

[10] News24, "#SaferCarsforAfrica: Here's how safe Toyota's Avanza really is in SA," News24, 29 May 2019. [Online]. Available: https://www.news24.com/wheels/news/guides_and_lists/safercarsforafrica-heres-how-safe-toyotas-avanza-really-is-in-sa-20190529.

The impact of GPS cleaning techniques on vehicle dynamics calculations

Timothy James McBride*, Kenneth John Nixon*

*School of Electrical & Information Engineering
University of the Witwatersrand, Johannesburg, South Africa
Email: Timothy.McBride@students.wits.ac.za, Ken.Nixon@wits.ac.za

***Abstract*—An investigation was performed to determine the impact of GPS cleaning techniques on vehicle dynamics calculations. GPS data is commonly used in vehicle dynamics problems and investigations however this data is not always accurate and a preprocessing or cleaning of the data will usually be performed to identify and remove erroneous points. Logical, statistical and elevation cleaning were used on the data and the results were compared to a truthful data source obtained from an on-board diagnostics device and a barometer. The results show the cleaning techniques used with the GPS speed data had a marginal benefit and are not necessary with some cases causing the cleaned data to be less accurate than the raw GPS data. The elevation cleaning had a significant impact on the final vehicle dynamics results and caused improvement to both the power and energy calculations. Future recommendations are to look at the impact of cleaning techniques with less accurate GPS data.**

***Index Terms*—Vehicle Dynamics, On-Board Diagnostics, GPS Cleaning, Elevation Cleaning, Road Grade**

I. Introduction

Global Positioning System (GPS) is a widely adopted technology that has revolutionised location tracking. It is a technology that is used in multiple industries and has many applications. One of these applications is the use of vehicle tracking and simulations. GPS is used to identify the position of a vehicle as it travels along a route. A vehicles velocity, engine load and acceleration can be extracted from this data however it can have a number of incorrect values which results in the errors being compounded into these calculations. GPS cleaning techniques are applied to the data to identify and correct the errors present. This research investigates the impact of the cleaning techniques on the vehicle dynamics calculated.

GPS cleaning methodologies can be classified into two main categories: statistical and logical based approaches [1]. The statistical approach makes use of mathematical methodologies to identify outliers from the data while the logical approach considers physical constraints present within the system. The process for GPS cleaning for both methodologies is broken into two processes: error detection and repairing [1, 2].

A test vehicle is fitted with a barometer, an On-Board Diagnostics (OBD) and a GPS device to track the vehicle as it travels along three different routes, city, freeway and residential. The GPS data and the vehicles velocity is recorded directly through the vehicles OBD port. The barometer is used to track the relative altitude of the vehicle as it travels. The OBD and barometer data are used as ground truth for the vehicles data. The GPS data is cleaned and then compared to the truthful data to determine the effectiveness of the cleaning techniques performed. Both a logical and statistical approach are used to identify any erroneous points within the GPS data. The erroneous points are removed accordingly and a Piecewise Cubic Hermite Interpolating Polynomial (PCHIP) interpolation algorithm is applied to the data to fill any missing points.

II. Background

A. Literature Review

GPS cleaning is a common practice when performing data processing, Schuessler and Axhausen [3] use raw GPS data to survey the travel patterns of individuals in Swiss cities. The raw GPS data is cleaned and smoothed before post processing techniques are applied to the data to determine various individual travel behaviours. The techniques used to clean the data include erroneous point elimination and Gaussian kernel smoothing. Multiple criterion are used to determine point removal. Anomalous point detection becomes an important criterion for identifying erroneous spatial points. Patal et al [4] present a novel method for cleaning GPS data without revealing any information about the user's actual location. The method makes use of the physical quantities present within the GPS data to identify anomalous points within the data. Each physical property is calculated and a statistical z test is applied to determine which of the points are anomalies.

Prabha and Kabadi [1] provide a comprehensive analysis on the various methods of GPS cleaning and look at both the standard GPS cleaning methods as well as the diversified research based approaches. Critical loopholes within the existing methods of GPS cleaning are identified and it is concluded that there is still a need to investigate cleaning method focusing on using erroneous data as the methodologies presented made use of error free data obtained from a controlled research environment.

Yu et al [5] provide a unique approach to vehicle simulations. An investigation is done to identify the impact on fuel consumption and vehicle emissions caused by online ride hailing DiDi taxis. The data preprocessing follows a logical based approach and makes use of system constraints to filter out unnecessary data.

Abbruzzo et al [6] proposes a GPS preprocessing algorithm with a focus on the mobility of cruise passengers in urban contexts. The algorithm proposed is a statistical method and makes use of change point analysis to discover multiple segments within the GPS data. Each segment is analysed separately and statistical method is applied, any points that fall outside the defined thresholds are removed.

B. GPS Fundamentals

GPS is a positioning system that works by calculating the position of a receiver in relation to 4 or more orbiting satellites. The receiver determines the time of flight for the signals transmitted between the receiver and the orbiting satellites. Since the speed of the transmission is constant and the time of flight is directly proportional to the distance travelled, the distance to each satellite can be calculated. A process of trilateration is used to determine the latitude, longitude and elevation of the receiver [7, 8].

C. User Equivalent Range Errors

User Equivalent Range Errors (UERE) are errors that are caused during the transmission of GPS data from the transmitter to the receiver. These errors are caused by anomalies in the hardware or interference that occurs during the transmission of the signal [9].

1) Hardware Errors: GPS hardware consists of two major components, transmitters and receivers. Since GPS is highly dependent on the travel time of the signals between the transmitter and receiver one of the main errors that can occur is when the time is inaccurate. The GPS satellites' time can drift up to a millisecond, which will result in a significant error. The receiver's time can also drift however this can be corrected by comparing the time arrival of two GPS signals whose transmission times are accurately known [9].

2) Physical Errors: GPS is highly dependent on the location of the satellites and the receiver, the signal has to travel through the atmosphere to reach the receiver. The atmosphere delays signals and has varying density around the globe resulting in varying delays. The location of satellite in relation to the receiver can also impact the delay caused, if the satellite is directly overhead it will result in a smaller delay. Models of the atmosphere can be used to reduce the impact of these errors however they cannot be eliminated entirely [3, 9, 10].

Multipath errors are caused by reflection of signals on surrounding objects such as buildings or trees. The GPS receiver needs to discriminate between these signals and the ones directly transmitted from the satellites. Multipath errors are very common in forests or urban environments due the size and quantity of surrounding objects [3, 9, 11].

D. GPS Cleaning Techniques

GPS cleaning is the preprocessing of GPS data to identify and remove any erroneous points within the collection of data, it also includes the process of filling any missing points within the data [1].

1) Logic Based: Logic based techniques define set boundaries for which the system can operate within, these boundaries are usually defined by the physical constraints within the system and will include setting boundaries on the physical characteristic of object being tracked [1, 3].

2) Statistical Based: A statistical based approach will look at the data as a series of data points and apply statistical methods, like the interquartile range method, to identify outliers within the context of the data. A general approach for GPS speed data is to pair the outlier detection with change point analysis so that subsections of the data analysed. Statistical techniques do not consider the physical properties of the system and only account for the numerical context of the data [6, 12].

3) Elevation Cleaning: In vehicle dynamics energy and power calculations are sensitive to road grade. A larger road grade will require more power from the vehicle to overcome the forces of gravity. Road grade is the vertical distance over the horizontal distance usually expressed in percentage. In modern GPS receivers it is possible to obtain the elevation values at the different points of longitude and latitude however these values are highly sensitive to UERE. Cleaning techniques need to be applied to rectify the errors present within the data [13, 14].

III. Methodology

The vehicle and altitude data was recorded along different routes travelled by the test vehicle. The data consists of inner city, freeway and residential routes to get a representation of the different travel types that can occur. Each data set is loaded into MATLAB where different cleaning techniques are applied to the data. The OBD and barometer data is treated as truthful data to compare the effect of the cleaning techniques applied to the GPS data. The speed and elevation data is used to calculate the road grade and the power output of the vehicle at discrete time intervals using Equation 1 and Equation 2 [15].

$$ma[n] = F_t[n] - (F_a[n] + F_r[n] + F_g[n] + F_d[n]) \quad (1)$$

$$P[n] = F_t[n] * v[n] \quad (2)$$

Where:

F_t = Traction Force
F_a = Aerodynamic Drag
F_r = Rolling Resistance
F_g = Gravitational Force
F_d = Additional Disturbance Forces
F_n = Traction Force
v = Vehicle Velocity

The total energy for the system as the vehicle travels along the route can be determined by taking the sum of the power over the course of the route travelled. The total energy of the system is determined for the truthful data, raw GPS data and cleaned GPS data. The error between the truthful data and the GPS data is calculated.

A. Logical Cleaning

Logical cleaning was applied to the data in an attempt to remove the erroneous points in the data set. Three main assumptions are made based off of the physical characteristics of the system as shown in Table I, these assumptions are used to define boundaries for the system. Any points that occur outside of the boundaries are either discarded or replaced with an appropriate value. PCHIP interpolation is used to fill any missing points after the thresholding techniques are applied to the data.

TABLE I
LOGIC BASED ASSUMPTIONS AND BOUNDARIES USED TO CLEAN GPS DATA

Assumption	Boundary Equation
Speed is zero while vehicle is stationary	$Speed \leq 0.3m.s^{-1} = 0m.s^{-1}$
Speed shouldn't be greater than 140km per hour	$Speed \geq 40m.s^{-1} = NaN$
Acceleration shouldn't be greater than $3m.s^{-2}$	$Accel \geq 3m.s^{-2} = NaN$

B. Statistical Cleaning

To perform statistical cleaning the data is first separated into sub arrays by using change point analysis, each sub array is analysed in isolation and the interquartile range method (IQRM) is used to test for outliers within the data. Detected outliers are discarded as they are assumed to be erroneous.

$$\begin{aligned} L_{upper} &= Q_3 + \lambda * IQR \\ L_{lower} &= Q_1 - \lambda * IQR \end{aligned} \tag{3}$$

The boundaries $(L_{upper}, Llower)$ show in Equation 3 are calcualted for each sub array obtained from the change point analysis. The tuning parameter $\lambda > 0$ is multiplied by the interquartile range (IQR) and is added or subtracted from the upper and lower quartiles (Q_3, Q_1). It is used to detect the outliers within the data. A value of 1.5 used for the tuning parameter indicates that any points outside the defined boundaries are outliers [6].

C. Road Grade Calculations

Before Road grade can be calculated the GPS elevation data is cleaned and smoothed. The GPS elevation data obtained contains a high number of discrete steps between elevation values caused by UERE. A third order low pass Butterworth filter is applied to the data to remove the discrete high frequency components present.

The slope is calculated by taking the difference in the relative altitude (h) and dividing it by the difference in distance travelled. To calculate the distance travelled the cumulative integral of the velocity data is determined and the unique values are mapped to the relative altitude. The data is re-sampled into constant distance increments of size d. The angle of inclination is calculated using Equation 4.

$$\alpha = \tan^{-1}\left(\frac{h[n] - h[n-1]}{d}\right) \tag{4}$$

The angle of inclination (α) is sampled at each time step accordingly and the corresponding gravitational forces acting on the vehicle are calculated.

IV. RESULTS

This section presents the results obtained from the investigation done, initially the velocity data is analysed and presented followed by the elevation and lastly the vehicle dynamics.

A. GPS Speed Cleaning

The speed obtained from each route before cleaning is shown and compared to the OBD speed in Figure 1. For each route it can be seen that the GPS speed closely resembles the values obtained from the OBD data however there is some error between the data sets.

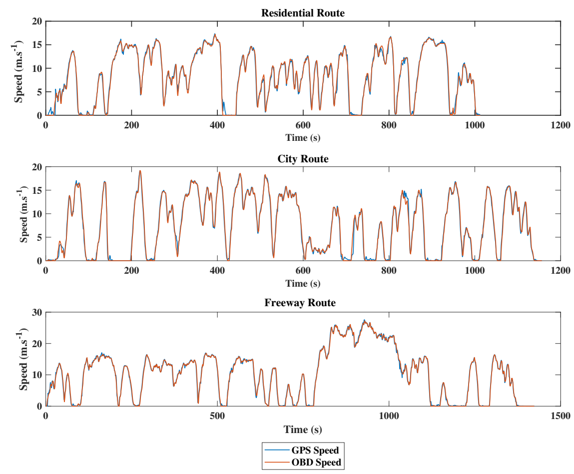

Fig. 1. The speed measured for each route using a GPS and OBD device without cleaning

B. Logical Cleaning

After applying logical cleaning the GPS speed more closely matches the OBD speed as the logical cleaning checks for a stationary threshold of $0.3m.s^{-1}$ and sets it to zero. There is an increased acceleration whenever the vehicle moves to or from a stationary position. Figure 2 shows the cleaned results for the city route, the effect of stationary periods is most clear from this route.

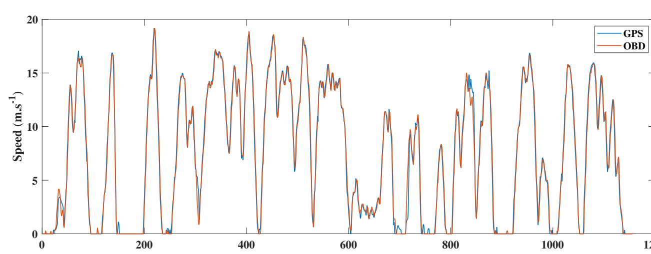

Fig. 2. The GPS and OBD vehicle speed for a city route with data cleaning

The logical cleaning does improve the match between the OBD and GPS speed across each of the routes. Table II shows the mean and standard deviation of the difference between the GPS and OBD speed for each of the routes after logical cleaning is performed. The cleaning method reduced the mean for each route however the standard deviation is increased as the cleaning method does introduce its own errors. The benefit of the cleaning technique is minimal with the most impact occurring in the city route with an improvement to the mean difference of $0.017 m.s^{-1}$.

TABLE II
MEAN AND STANDARD DEVIATION OF THE DIFFERENCE BETWEEN GPS AND OBD SPEED WITH LOGICAL CLEANING

Route travelled	Mean $m.s^{-1}$)		Standard deviation $m.s^{-1}$)	
GPS Data Used	Raw	Cleaned	Raw	Cleaned
City Route	0.449	0.432	0.426	0.484
Freeway Route	0.376	0.361	0.365	0.373
Residential Route	0.413	0.409	0.426	0.438

C. Statistical Cleaning

The statistical method for detecting outliers is dependent on the number change points within the data. If an incorrect change point analysis is performed then the IQRM will falsely identify accurate data points as outliers. Additionally the IQRM has lower probability of detecting outliers. Figure 3 shows the effect of an incorrect change point analysis on the statistical cleaning methodology.

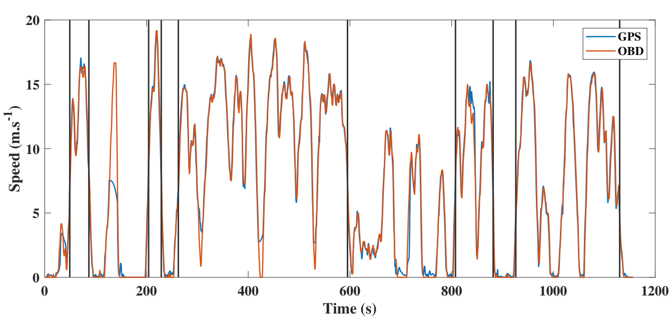

Fig. 3. Statistical cleaning performed on GPS data when there is a small number of change points

Once there are sufficient change points used within the cleaning method the algorithm is able to successfully remove outliers from the data. Table III shows the mean difference when statistical cleaning is applied for the city route with different quantities of change points.

The number of change points has a relationship to the difference between the test and truthful data. The difference decreases as the changes points are increased with the largest decrease occurring at 25 change points. The optimal number of change points is route dependent as some routes will have more relevant changes than others. For the purposes of this investigation a value of 25 change points is used. The mean

TABLE III
THE MEAN DIFFERENCE OBTAINED FROM STATISTICAL CLEANING WITH VARYING QUANTITY OF CHANGE POINTS

Change Points	mean $(m.s^{-1})$
5	0.471
10	0.544
15	0.458
20	0.463
25	0.439
30	0.440

and standard deviations of the difference in OBD and GPS is calculated for each route and shown in Table IV.

TABLE IV
MEAN AND STANDARD DEVIATION OF THE DIFFERENCE BETWEEN GPS AND OBD SPEED WITH STATISTICAL CLEANING AND 25 CHANGE POINTS

Route travelled	Mean $m.s^{-1}$)		Standard deviation $m.s^{-1}$)	
GPS Data Used	Raw	Cleaned	Raw	Cleaned
City Route	0.449	0.439	0.426	0.464
Freeway Route	0.376	0.399	0.365	0.439
Residential Route	0.413	0.414	0.426	0.428

The city route sees a reduction in the mean while the residential and freeway route see an increase. The standard deviation increases for each of the routes which indicates that the statistical cleaning method used has a negative impact on the data and actually causes a loss in accuracy. The change is minimal and it would be more beneficial to use the raw GPS speed data.

D. Elevation Cleaning

The elevation data obtained from the GPS receiver is different to the results obtained from the barometer as shown in Figure 4. The GPS results are a combination of step functions with discrete intervals for the change in altitude, this is not accurate to geographical elevation. The cleaning method applied to the elevation is a 3rd order low pass filter to remove the high frequency components within the signal.

Figure 5 shows the results for the city route after cleaning has been performed, the result is a closer match to the barometer data. The inclines and declines in the cleaned result are still steeper than the barometer data and will have an impact on the final energy calculation.

The cleaning has the most impact on the city and residential routes with the least impact on the freeway route. Figure 6 shows the results for the freeway route, there is a long period where the GPS data remains approximately $-120m$ before it steps up to $-10m$. In the barometer data this change in altitude occurs over a longer period of time. The cleaning method is not able to fix such a large change.

E. Vehicle Dynamics

The different cleaning methods each have an impact on the vehicle dynamics as the properties cleaned are used in the

TABLE V
TOTAL VEHICLE ENERGY CALCULATED FOR EACH ROUTE WITH DIFFERENT CLEANING METHODS APPLIED

Speed Data	OBD	GPS		Logical Cleaning GPS				Statistical Cleaning GPS			
Altitude Data	Barometer	GPS		Barometer		Cleaned GPS		Barometer		Cleaned GPS	
Result Type	Energy (MJ)	Energy (MJ)	Error (%)	Energy (MJ)	Error (%)	Energy (MJ)	Error (%)	Energy (MJ)	Error (%)	Energy (MJ)	Error (%)
City Route	4.945	6.343	28.28	4.924	0.42	4.734	4.26	4.933	0.24	4.750	3.94
Freeway Route	6.217	7.16	15.09	6.367	2.41	5.572	10.38	6.370	2.46	5.645	9.21
Residential Route	4.477	5.423	21.14	4.535	1.31	4.467	0.23	4.542	1.46	4.49	0.32

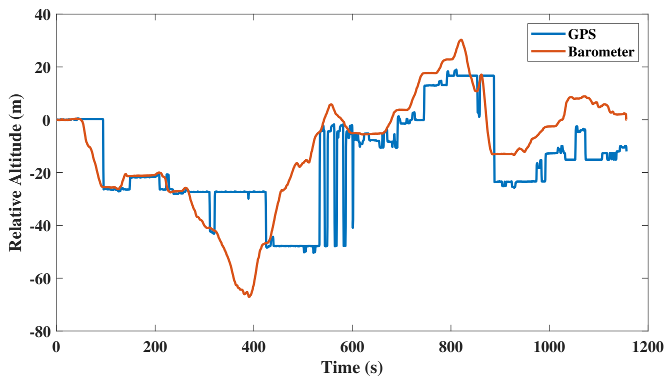

Fig. 4. The gps and barometer relative altitude detected while travelling along the city route

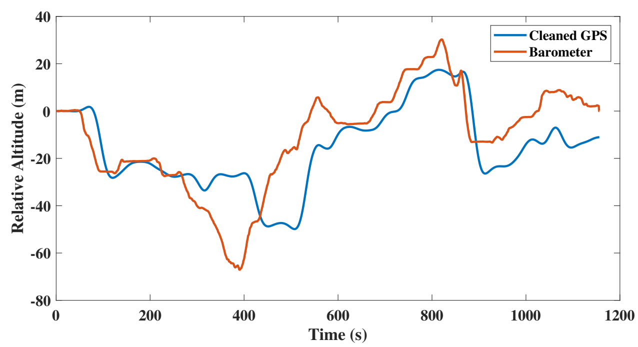

Fig. 5. The gps and barometer relative altitude detected while travelling along the city route after cleaning

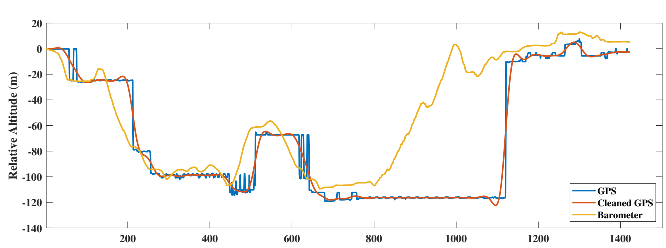

Fig. 6. The GPS, cleaned GPS and barometer relative altitude over the freeway route

calculations. The elevation cleaning has the largest impact on the final energy result while the speed cleaning has a minor impact. Table V shows the energy values calculated with the error for each of the techniques. Each of the cleaning methods reduces the error obtained and produces a value for the energy that more closely matches the values determined from the OBD data.

Figure 7 shows the instantaneous power for the residential route with each of the cleaning methods applied. There is a high number of spikes in the data caused by the high inclines present with in the elevation data. The logical cleaning technique more accurately matches the instantaneous power obtained from the OBD data compared to the statistical cleaning method which can been seen in the impulses present in Figure 7. The impulses correspond to periods of high acceleration from the speed data.

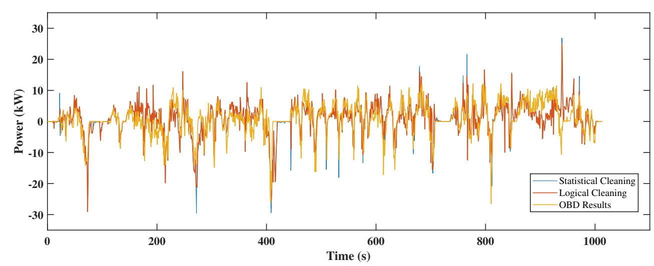

Fig. 7. Instantaneous power for different cleaning methods and OBD data

V. DISCUSSION

From the results obtained it is clear that each of the cleaning techniques is able to reduce the error between the truthful OBD data and the test GPS data however the sample size of routes covered is limited and could be improved by recording more routes travelled in different areas. The logical and statistical speed cleaning methods provided marginal improvements to the final result and the impact on the total energy was minimal.

The logical cleaning method performed better for the instantaneous power calculation. This is caused by the acceleration boundary applied during cleaning process. When the total energy is calculated the difference in these high power impulses will be averaged out resulting in the statistical cleaning performing better for the total energy calculations. There are additional issues with the statistical cleaning method primarily the requirement for a defined number of change points. If the number of change points is too few or too great then the cleaning technique will have a negative impact on the output.

Overall the logical cleaning approach proves to be a better option as the result is not limited by the number of change points in the route and it performed better when comparing the mean difference between the cleaned GPS speed and the OBD speed. The improvement from the cleaning is very marginal and is not sufficient enough to warrant the use of the cleaning techniques. In some cases the implementation of the cleaning technique resulted in a negative effect on the speed data. A future recommendation would be to look at the impact of cleaning techniques on GPS data with missing sections or with lower accuracy data.

The elevation data had the most significant impact on the final energy and power calculations. The GPS elevation data is largely inaccurate and for an optimal result a barometer or an alternative road grade sensor should be used to obtain the elevation of the route however if only the GPS elevation data is available then cleaning methods should be used to improve the accuracy of the vehicle dynamic calculations.

VI. Conclusion

Cleaning techniques and methods are an important preprocessing technique for vehicle dynamics calculations. They are able to improve the accuracy of GPS data obtained from a vehicle as it travels to more closely match the speed obtained from an OBD device. The speed data form the GPS receiver is sufficiently accurate without performing cleaning and in certain cases the cleaning methods will actually reduce the accuracy of the result. This result is largely due to the use of high accuracy GPS data. The main benefit of the cleaning can be seen in the elevation data which has a significant impact on the power and energy requirements for the vehicle however even after cleaning the GPS elevation data there are still inaccuracies with the results and it would be more beneficial to make use of a secondary sensor, such as a barometer or alternative device, to obtain the elevation data.

References

[1] R. Prabha and M. G. Kabadi, "A comprehensive insight towards Pre-processing Methodologies applied on GPS data," *International Journal of Electrical and Computer Engineering (IJECE)*, vol. 10, no. 3, p. 2742, Jun. 2020. [Online]. Available: http://ijece.iaescore.com/index.php/IJECE/article/view/19930

[2] X. Chu, I. Ilyas, S. Krishnan, and J. Wang, "Data Cleaning: Overview and Emerging Challenges," Jun. 2016, pp. 2201–2206.

[3] N. Schuessler and K. W. Axhausen, "Processing Raw Data from Global Positioning Systems without Additional Information," *Transportation Research Record*, vol. 2105, no. 1, pp. 28–36, Jan. 2009, publisher: SAGE Publications Inc. [Online]. Available: https://doi.org/10.3141/2105-04

[4] V. Patil, P. Singh, S. Parikh, and P. K. Atrey, "GeoSClean: Secure Cleaning of GPS Trajectory Data Using Anomaly Detection," in *2018 IEEE Conference on Multimedia Information Processing and Retrieval (MIPR)*, Apr. 2018, pp. 166–169.

[5] Y. Sui, H. Zhang, X. Song, F. Shao, X. Yu, R. Shibasaki, R. Sun, M. Yuan, C. Wang, S. Li, and Y. Li, "GPS data in urban online ride-hailing: A comparative analysis on fuel consumption and emissions," *Journal of Cleaner Production*, vol. 227, pp. 495–505, Aug. 2019. [Online]. Available: https://www.sciencedirect.com/science/article/pii/S0959652619312387

[6] A. Abbruzzo, M. Ferrante, and S. De Cantis, "A pre-processing and network analysis of GPS tracking data," *Spatial Economic Analysis*, vol. 16, no. 2, pp. 217–240, Apr. 2021, publisher: Routledge _eprint: https://doi.org/10.1080/17421772.2020.1769170. [Online]. Available: https://doi.org/10.1080/17421772.2020.1769170

[7] R. L. M. Ragu, "Fundamentals of GPS," in *Satellite Remote Sensing and GIS Applications in Agricultural Meteorology*. Indian Institute of Remote Sensing, Dehra Dun, pp. 126 – 150.

[8] G. Xu and Y. Xu, *GPS: Theory, Algorithms and Applications*. Berlin, Heidelberg: Springer Berlin Heidelberg, 2016. [Online]. Available: http://link.springer.com/10.1007/978-3-662-50367-6

[9] J. Stevens, J. M. Smith, and R. A. Bianchetti, "5.3 GPS Error Sources," in *Mapping our Changing World*. [Online]. Available: https://www.e-education.psu.edu/geog160/node/1924

[10] J. Hao and S. Guo, "The study of dual frequency ionospheric error correction method and accuracy analysis based on GPS," Sep. 2011, pp. 1–4.

[11] T. Kos, I. Markezic, and J. Pokrajcic, Sep. 2010, pp. 399–402, iSSN: 1334-2630.

[12] G. Barbato, E. M. Barini, G. Genta, and R. Levi, "Features and performance of some outlier detection methods," *Journal of Applied Statistics*, vol. 38, no. 10, pp. 2133–2149, Oct. 2011.

[13] B. Yazdani Boroujeni, H. Frey, and G. Sandhu, "Road Grade Measurement Using In-Vehicle, Stand-Alone GPS with Barometric Altimeter," *Journal of Transportation Engineering*, vol. 139, pp. 605–611, Jun. 2013.

[14] J. Wang and D. Xie, "GPS elevation fitting study based on ternary polynomial regression," *Earth Sciences Research Journal*, vol. 24, pp. 201–205, Apr. 2020.

[15] C. Fiori, K. Ahn, and H. A. Rakha, "Power-based electric vehicle energy consumption model: Model development and validation," *Applied Energy*, vol. 168, pp. 257–268, Apr. 2016.

High Speed Photography of Streamer Breakdown in Air Gaps Less than 15 cm Using HVDC

Keshlan Moodley
Discipline of Electrical, Electronic and Computer Engineering
University of KwaZulu-Natal
Durban, South Africa
keshlanm7@gmail.com
0000-0003-4784-3374

Andrew Swanson
Discipline of Electrical, Electronic and Computer Engineering
University of KwaZulu-Natal
Durban, South Africa
swanson@ukzn.ac.za
0000-0002-9965-4746

Abstract **— As atmospheric air is used as electrical insulation for high voltage equipment and power apparatus, it is important that research is conducted on the insulation to ensure reliability and continuity of the electrical network. It is imperative to investigate the streamer development in air with differing environmental characteristics as it determines the breakdown strength of multiple electrode arrangements. The paper presents the results obtained from the high-speed photography of streamer breakdown under DC voltage in air. The results are used to elaborate on the initiation and propagation of a cathode directed streamer and indicate the influence of gap length as well as atmospheric pressure on the appearance of streamers. The secondary streamer mechanism was present for all the discharges that occurred, and it was seen noted that single streamers occurred for these gap lengths. It was observed that as the gap length increased there was a resulting increase in the length of the stem and streamers would take a bent path for gap lengths greater than 10 cm. The branching of streamers at the anode tip occurred at pressures greater than 994,0 hPa and a streamer would take a bent path when propagating towards the cathode because of the presence of space charge along the path.**

Keywords — High Speed Photography, Streamer Breakdown, Air, HVDC

I. INTRODUCTION

A significant amount of high voltage equipment and power apparatus implement atmospheric air as electrical insulation and most of this equipment play an important role in the electrical power system [1, 2, 3]. Therefore, it is essential that the insulation be of an acceptable standard whilst maintaining its high electrical insulation properties to ensure continuity and reliability of the electrical network [1, 3].

Electrical streamers are fast moving ionization fronts and are recognized as being the precursor of sparks as they create the first ionized path for heat-dominated spark discharges. It also performs the same function in the inception and propagation of lightning leaders [4]. The investigation of streamer development is important as it determines the breakdown characteristics of multiple electrode arrangements especially when a lightning impulse voltage or direct voltage is applied [4]. As indicated by Luque et al. [5], a positive streamer emerges from an electrode with a pointed tip at voltages lower in magnitude when compared to negative voltages. This makes it an important component to consider for electrical system design hence investigations performed in the past focused on positive streamers.

Tarasenko et al. [6], conducted an experiment that investigated the breakdown of atmospheric air in a non-uniform electric field using an ICCD camera. The use of the camera allowed for the research into the dynamics that are involved in the formation of a streamer. It was observed from the results that the streamer elongates and reduces in diameter after it crossed half the distance of the gap when approaching the plane electrode. The results also concluded that single streamers develop from needle electrodes as it causes a maximum local electric-field enhancement.

Seeger et al. [7] investigated both streamer and leader breakdown mechanisms for air gaps less than a metre. The experiment involved observing pre-breakdown discharges and breakdown paths using a high-speed camera and an image intensifier. Results showed that there was a formation of high luminosity stems which occurred when the voltage applied to the electrode was for a short period of time. This indicated that the leader inception occurred by the stem mechanism.

The paper presents the experimental results obtained from the investigation of streamer breakdown using high speed photography. The results from the experiment indicate that

- The secondary streamer mechanism was present for all the gap lengths investigated
- Single streamers occurred for the gaps investigated.
- As the gap length increased there was a resulting increase in the length of the stem.
- Streamers would take a bent path for gap lengths that were greater than 10 cm.
- It was observed that the branching of streamers at the anode tip occurred at pressures greater than 994.0 hPa.
- A streamer would take a bent path when propagating towards the cathode due to the presence of space charge along the path.

The experimental setup used for the investigation is discussed in Section II whilst Section III indicates the experimental results and provides a discussion on the results obtained.

II. EXPERIMENTAL PROCEDURE

A. Experimental Procedure Layout

The experimental setup consisted of a 2 stage Cockcroft-Walton DC generator that is rated at 500 kV. Fig 1 is an illustration of the setup that was implemented for the photography of the streamer breakdown for various air gaps.

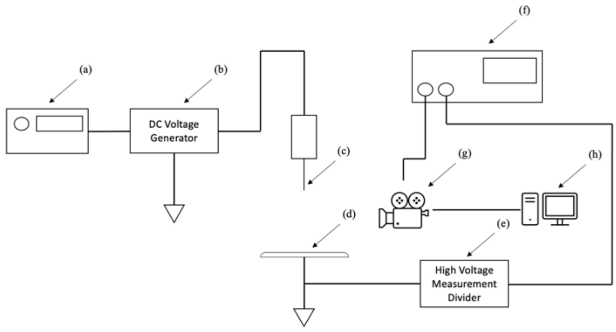

Fig. 1. The layout for the experimental procedure: (a) – HVDC control unit, (b) – HVDC generator, (c) – High voltage needle electrode, (d) – Grounded plane electrode, (e) – High voltage measurement system, (f) – Oscilloscope, (g) – High speed camera (h) – Computer

B. *Electrode Configuration for Streamer Initiation*

An investigation that was performed by Luque et al. [5] on both positive and negative streamers in ambient air implemented a needle-plane geometry. This was done as the use of a needle-plane electrode configuration resulted in streamers emerging from the pointed electrode. It should be noted that needle-plane electrode configurations are used in laboratory experiments and engineering applications as it creates an inhomogeneous field. A needle-plane electrode configuration was used in the experiment conducted in this paper. The high voltage needle was made of iron and had a cylindrical body that was 12 cm in length whilst the diameter of the body was 1 mm. The plane electrode had a diameter of 16 cm and is connected to ground.

C. *Phantom Miro M110 High Speed Camera*

Streamers were observed using a Phantom Miro M110 high speed monochrome camera which had a Nikon AF NIKKOR 50 mm 1:1.8 D lens attached. The camera was positioned 1 m away from the electrodes in a direction that allowed it to be perpendicular to the axis of the air gap. The camera was set to record at 300 000 frames per second with an exposure time of 2.94 ms using a resolution of 64x8 pixels. It was required to set the aperture on the lens to f/1.8 to allow for maximum light to pass through when recording the experiment.

D. *Oscilloscope*

A Yokogawa DL9140 digital oscilloscope was used in the experimental procedure to trigger the high-speed camera to stop recording the instant electrical breakdown of the air gap occurred.

III. Experiment Results and Discussion

A. *The Formation of a Positive Streamer Using High Speed Photography*

The images captured by the high-speed camera depicting the progress of the streamer in an air gap of length 12 cm is seen by referring to Fig 2. A voltage of 58.74 kV was applied to the needle electrode. The anode is located at the top of the frame and is represented by (a) whilst the cathode is located at the bottom of the frame and is represented by (c).

Electrons that are present in a gas at any radial distance from the avalanche axis performs the function of creating more avalanches when in the presence of an externally applied electric field. The avalanches that are created can either be short or long. Photoelectrons are created in the vicinity of the positive ion space charge channel. These positive ions were left behind by the initial avalanche. The electrons located at the anode end are in the presence of an enhanced field that exerts a directive action drawing the electrons into the anode [8]. A conducting plasma that originates from the anode is formed due to the electrons that were created, from the ionization process, being drawn into the positive space charge feed. Positive ions that are left behind perform the function of extending the space charge towards the cathode [8]. The creation of streamer corona is seen at (b) in (1) with the streamer stem extending slightly at point (d) in (2). The electrons that are present are also responsible for the creation of photons that continue this process. This results in the positive space charge developing towards the cathode as a positive space charge streamer. This is represented at (e) in (3) and (f) in (4) as the stem is seen extending towards the cathode [8].

The propagation of the streamer towards the cathode results in the production of a filamentary region of intense space charge that is distorted along a line that is parallel to the field. A very steep gradient is produced at the cathode end of the streamer tip by the plasma. The photoelectron avalanches that are produced by radiation occurs at the cathode and it produces an intense ionization near it. The positive ions that are created by this process can influence secondary emission by increasing it. This results in branching from the stem as seen clearly in (h). The fifth frame (5) indicates that the streamer has crossed the gap as seen at (g). A source of visible light occurs because of a cathode spot that was formed by the space charge streamer when it approached the cathode. A conducting filament bridges the gap when the streamer reaches the cathode. Once an efficient cathode spot has occurred, a return electron current proceeds up the streamer channel resulting in electrical breakdown [8]. This is seen in (6) and is represented at point (i) as a bright source of visible light can be seen and electrical breakdown has occurred in the gap.

B. *The Influence of Gap Length on the Appearance of Streamers in Air*

High-speed photography was conducted for gap lengths greater than 5 cm when the experiment was performed. It was attempted to record the initiation and propagation of the streamer for a 2 cm gap length, but it was not possible as the streamer did not give off enough light that could be recorded

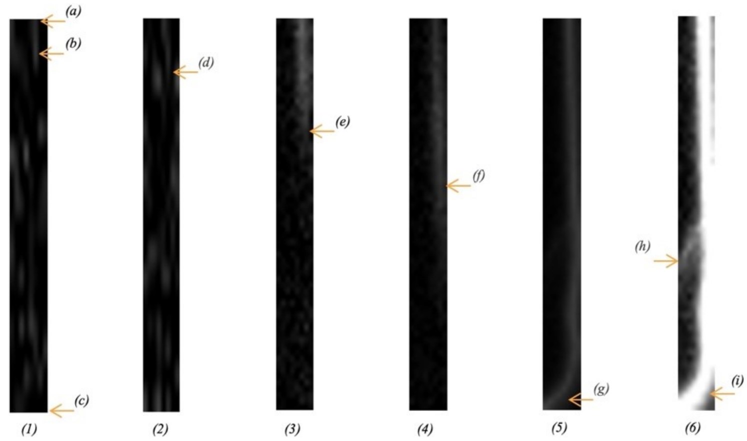

Fig. 2. The initiation and propagation of a cathode directed streamer for a gap length of 12 cm when a voltage of 58.74 kV was applied to the anode. Note that a single streamer occurred. (1) – The initiation of the streamer is seen. (2) – The extension of streamer. (3) – A further extension of the streamer from the anode. (4) – The streamer has extended halfway across the gap. (5) – The primary streamer has progressed and completely crossed the gap. (6) – Electrical breakdown of the gap had occurred as a bright light had been emitted. A branch from the streamer is seen.

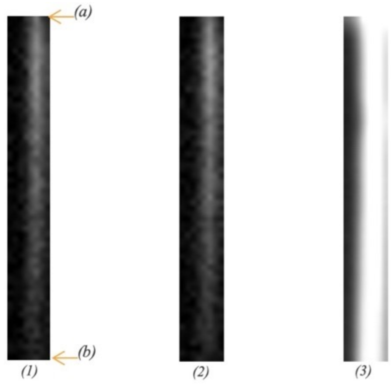

Fig. 3. The propagation of the streamer for a gap length of 5 cm. (1) – The streamer has propagated from the anode towards the cathode. (2) – The streamer has extended further towards the cathode. (3) – Electrical breakdown of the air gap.

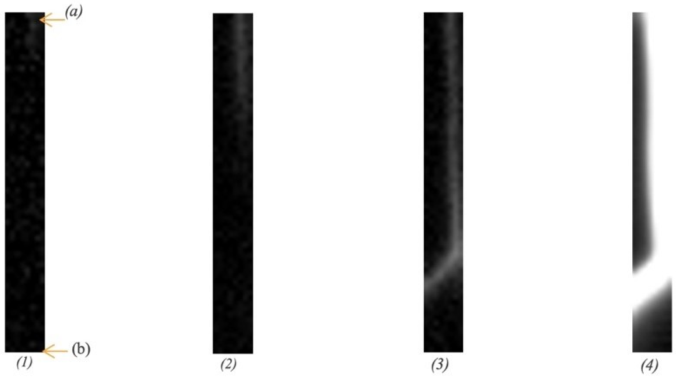

Fig. 4. The propagation of the streamer for a gap length of 10 cm (1) – The initiation of the streamer is seen. (2) – The extension of streamer from the anode. (3) – The primary streamer has progressed and completely crossed the gap. (4) – Electrical breakdown of the gap has occurred as a bright light has been emitted.

by the camera. This also occurred when the electrode distance was set to 5 cm as the initiation of the streamer from the anode tip could not be seen but streamers that crossed the gap and emitted enough light was able to be recorded by the camera as seen in Fig 3.

Referring to Figs 3, 4, and 5, the anode and cathode are represented by (a) and (b) respectively in these figures. Fig 3 represents the frames that could be captured for a 5 cm gap length. A voltage of 30.94 kV was applied to the anode. The streamer had already crossed the gap and breakdown occurred in frame (3).

Fig 4 represents frames that depict the initiation and propagation of a streamer for a 10 cm gap length. The voltage applied to the anode was 55.03 kV. It is seen in frame (3) that the stem of the streamer had elongated when compared to Fig 3. It was also observed that the streamer bent its path when it approached the cathode. Frame (4) depicts the electrical breakdown of the air gap.

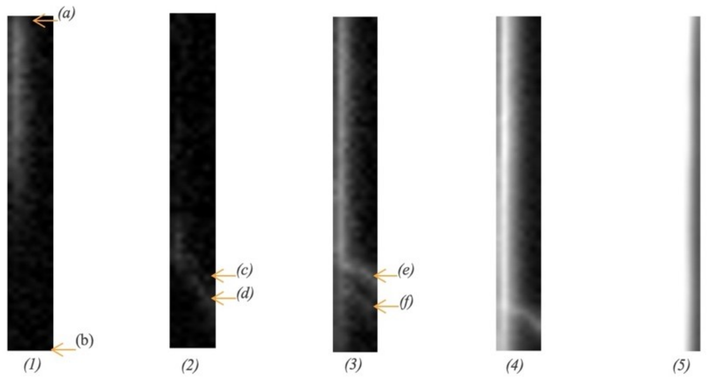

Fig. 5. The initiation and the propagation of a streamer for a gap length of 15 cm. (1) – The extension of the streamer from the anode is seen. (2) – A further extension of the streamer as well as branches is seen from the streamer. (3) – The primary streamer has crossed the gap as well as multiple branches is seen. (4) – An increase in the amount of light emitted by the streamer and the presence of a single branch near the cathode. (5) Electrical breakdown of the gap has occurred as a bright light has been emitted.

Referring to Fig 2, the streamer initiation and progression of it for a 12 cm gap length can be seen. When comparing Fig 2 to Fig 3 and 4, it is seen that as the gap length increased there was an increase in the elongation of the stem. A single branch also appeared at point (h) in the sixth frame of Fig 2 and these branches were not present for the smaller gaps.

Fig 5 represents the propagation of the streamer and the electrical breakdown of an air gap that has a length of 15 cm. The voltage that was applied to the anode was 88.95 kV. Apart from the increase in the elongation of the stem when the gap length increased, it was also observed that the number of branches that were present had also increased. These branches are seen at points (c) and (d) in frame (2) as well as in points (e) and (f) in frame (3).

The secondary streamer mechanism was the breakdown mechanism that was present for all the discharges that occurred in the experiment as seen in [7]. The primary streamer crossing the gap is seen in Figs 2, 3, 4, and 5.

For all the gap lengths investigated, it was seen that single streamers occurred, and this is due to the quasiuniform electric field that was created by the needle-plane electrode configuration. This type of electric field results in narrower and direct streamer structures being formed [6, 9]. This type of streamer was expected as indicated by the results obtained by Tarasenko et al. [6]. It was seen that as the gap length increased there was a resulting increase in the length of the stem.

Branches appeared for gap lengths that were equal to or greater than 12 cm in length with the number of branches increasing as the gap length increased. The appearance of branches in longer air gaps was expected as seen in the results obtained by Zhao et al. [10]. When analysing the high-speed photographs of air gaps greater than 10 cm, it was observed that streamers would occasionally take a bent path when propagating towards the cathode.

C. *The Influence of Pressure on Streamers*

Fig 6 below displays the initiation of a cathode directed streamer from the anode when the atmospheric pressure was 994.0 hPa. The distance between the electrodes in the frame below was 15 cm.

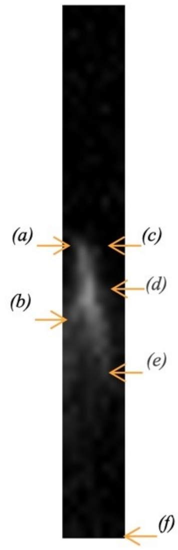

Fig. 6. The initiation of a streamer from the anode when the atmospheric pressure was 994.0 hPa in the laboratory. A voltage of 77.50 kV is applied to the anode and the resulting branches is seen at the anode tip.

Points (a) and (f) in Fig 6 represent the tip of the anode and cathode respectively. A voltage of 77.50 kV is applied to the anode. Referring to points (b), (c), (d) and (e) in the frame, it is seen that a branching structure is observed at the anode tip.

It was observed by Pancheshnyi et al. [11], that the branching of streamers at the anode tip was only observed at pressures greater than 906.59 hPa (680 torr). This was also observed in Fig 6, as branching occurred at the streamer tip at a pressure that was greater than 906.59 hPa.

D. *The Bent Path a Cathode Directed Streamer Takes*

It was observed that streamers would take a bent path when propagating towards the cathode for electrode distances greater or equal to 10 cm. This is seen in Fig 7 below where the electrodes are separated by 15 cm. The high-speed video camera recorded the frame in Fig 7 at a rate of 140 000 frames per second with an exposure time of 6.6 ms.

The bent path a positive streamer takes, when propagating, could be a result of the electron density being increased non simultaneously with different rates in different regions of the discharge volume when it is formed. As a result of this, an electron density gradient at the ionization wavefront is created. This causes the direction of the electric field component to be different from the background electric field resulting in the positive streamer bending when propagating towards the streamer [12].

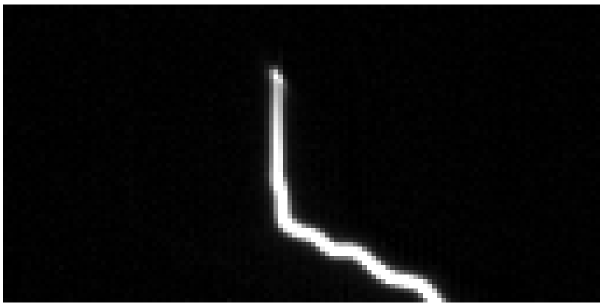

Fig. 7. The bent path a streamer takes for a gap length of 15 cm when approaching the cathode.

Streamers choose to follow paths that have increased levels of electron density when propagating but they are also unable to propagate through regions that consist of very high amounts of space charge [12]. It is seen in Fig 8 at point (b) that the streamer is bending its path when approaching the cathode at point (d). This could be a result of excess space charge being present at point (c).

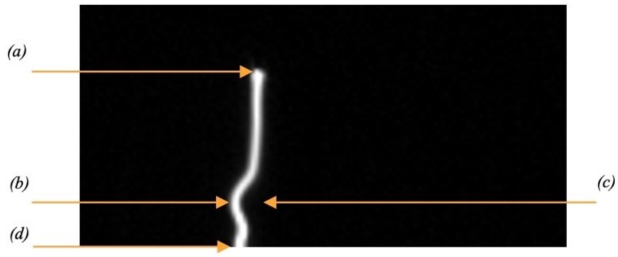

Fig. 8. The bent path a streamer takes when approaching the cathode for a 15 cm gap length. The location of an increased region of space charge is assumed in the frame.

This was apparent in an investigation performed by West [13], as the experiment consisted of applying an impulse voltage (1.2/50 ms) to a Rogowski profile spark gap. A laser beam that entered the spark gap at 90° was included in the experiment which supplied space charge at a specific point in the gap. It was observed that the HV arc produced bent around the laser-induced plasma when approaching the cathode.

E. The Analysis of the Electric Field of a Streamer that takes a Bent Path

Fig 9 represents the results obtained from a FEMM simulation showing the electric field distribution of an air gap. A high voltage was applied to the needle electrode and excess space charge was present in the form of spheres in the air gap. The cathode was grounded in the simulation.

As seen in Fig 9, the application of a voltage that is near the breakdown magnitude results in the positive ions that are left behind by previous streamer discharges to be distributed [14]. This is found at points where there are positive space charge spheres present in the figure. It is seen from the FEMM model created that the electric field around the positive space charge sphere is much higher when compared to the magnitude of the electric field that is present at the tip of the anode. Electrons that are present in the gap attach to these positive space charge spheres. Thus, resulting in the positively charged spheres becoming negatively charged.

If there is an initial electron and a high electric field region present near the anode, then a streamer would be initiated, and it would begin to propagate. As seen in the figure, the streamer takes a path that goes around the now negatively charged sphere as it is not able to propagate through regions that have a high concentration of electrons. The streamer is then obligated to propagate through areas that consist of an electric field that is strong enough to continue the collisional ionization and attachment processes. Therefore, it was seen that the presence of space charge influences the path a streamer takes when propagating by bending around it [15].

IV. Conclusion

It is essential that research is conducted on electrical insulation that is used in high voltage apparatus and power equipment to ensure the continuity and reliability of the electrical network. Investigating streamer development in air is important as it determines the breakdown characteristics of multiple electrode arrangements. High speed photography was implemented to investigate the streamer breakdown of air gaps that were less than 15 cm using HVDC in this paper. The results were used to elaborate on the initiation and propagation of a cathode directed streamer and explain the influence gap length and atmospheric pressure has on the appearance of streamers. It was seen that secondary streamer mechanism was present for all the gap lengths investigated and it was noted that single streamers occurred throughout the investigations. It was also seen that as the gap length increased there was a resulting increase in the length of the stem and streamers would take a bent path for gap lengths that were greater than 10 cm. The bent path taken by the streamers when propagating could be a result of the electron density being increased non simultaneously with different rates in different regions of the discharge volume when it is formed or the streamer not being able to propagate through regions that consist of very high amounts of space charge. It was also observed that the branching of streamers at the anode tip occurred at pressures greater than 994.0 hPa.

Acknowledgment

The authors would like to thank Eskom for funding the research through the Tertiary Education Support Programme.

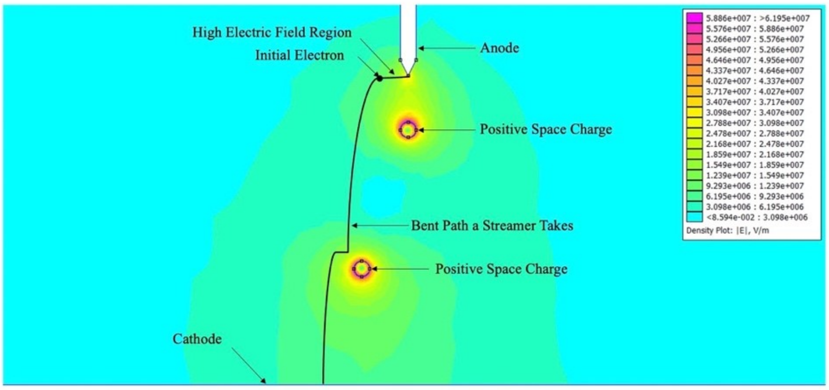

Fig. 9. A FEMM model showing the electric field distribution in an air gap when there is a presence of excess space charge in the form of spheres. The path a streamer may take because of space charge being present in the air gap is seen.

REFERENCES

[1] T. Iwata, H. Okubo, H. Kojima, N. Hayakawa and F. Endo, "Positive Streamer Propagation and Breakdown Characteristics in Non-uniform Air Gap," in *2010 International Conference on High Voltage Engineering and Application*, New Orleans, 2010.

[2] M. Radmilovic´-Radjenovic´, B. Radjenovic´ , Z. Nikitovic´ , Š. Matejcik and M. Klas, "The Humidity Effect on the Breakdown Voltage Characteristics and the Transport Parameters of Air," *Nuclear Instruments and Methods in Physics Research B,* vol. 279, pp. 103-105, 2012.

[3] A. S. Menesy, X. Jiang, M. A. Ali, H. M. Sultan, N. M. Alfakih and S. Kamel, "Partial Discharge and Breakdown Characteristics in Small Air Gap Lengths Under DC Voltage in Needle-Plane Electrode Configuration," in *IEEE IAS Industrial and Commercial Power System Asia Technical Conference*, Weihai, 2020.

[4] P. N. Mikropoulos, B. C. Sarigiannidou, C. A. Stassinopoulos and C. Tsakiridis, "Influence Of Humidity On Positive Streamer Propagation and Breakdown in a Uniform Field in Air," *IEEE Transactions on Dielectrics and Electrical Insulation,* vol. 15, no. 2, pp. 416-425, 2008.

[5] A. Luque, V. Ratushnaya and U. Ebert, "Positive and Negative Streamers in Ambient Air: Modeling Evolution and Velocities," *Journal of Physics D Applied Physics,* vol. 41, no. 23, 2008.

[6] V. F. Tarasenko, G. V. Naidis, D. V. Beloplotov, M. I. Lomaev, D. A. Sorokin and N. Y. Babaeva, "Streamer Breakdown of Atmospheric-Pressure Air in a Non-Uniform Electric Field at High Overvoltages," *Russian Physics Journal,* vol. 61, no. 6, pp. 1135-1142, 2018.

[7] M. Seeger, T. Votteler, J. Ekeberg, S. Pancheshnyi and L. Sánchez, "Streamer and Leader Breakdown in Air at Atmospheric Pressure in Strongly Non-Uniform Fields in Gaps Less than One Metre," *IEEE Transactions on Dielectrics and Electrical Insulation,* vol. 25, no. 6, pp. 2147-2156, 2018.

[8] L. B. Loeb and J. M. Meek, "The Mechanism of Spark Discharge in Air at Atmospheric Pressure. I," *Journal of Applied Physics,* vol. 11, pp. 438-447, 1940.

[9] D. Mitchard, P. Widger and A. Haddad, "Analysis of Light Emission and Schlieren from Short Gap High Voltage Streamer Impulses Representing Lightning," 13 May 2021. [Online]. Available: https://www.researchsquare.com/article/rs-310823/v2. [Accessed 8 November 2021].

[10] X. Zhao, M. Becerra, Y. Yang and J. He, "Elongation and branching of stem channels produced by positive streamers in long air gaps," *Scientific Reports,* vol. 11, no. 1, 2021.

[11] S. Pancheshnyi, M. Nudnova and A. Starikovskii, "Development of a Cathode-Directed Streamer Discharge in Air at Different Pressures: Experiment and Comparison with Direct Numerical Simulation," *Physical Review E,* vol. 71, pp. 016407-1 - 016407-12, 2005.

[12] C. Zhang , V. F. Tarasenko, . T. Shao, D. V. Beloplotov, M. I. Lomaev, R. Wang, D. A. Sorokin and P. Yan, "Bent Paths of a Positive Streamer and a Cathode-Directed Spark Leader in Diffuse Discharges Preionized by Runaway Electrons," *Physics of Plasmas,* vol. 22, no. 3, pp. 033511-1 - 033511-8, 2015.

[13] N. J. West, "Investigation into Phenomena Observed During the Interaction of a Focused High-Energy Laser Beam with High Voltage Electric Fields," Johannesburg, 2008.

[14] N. Hayakawa, K. Hatta, S. Okabe and H. Okubo, "Streamer and Leader Discharge Propagation Characteristics Leading to Breakdown in Electronegative Gases," *IEEE Transactions on Dielectrics and Electrical Insulation,* vol. 13, no. 4, pp. 842-849, 2006.

[15] K. Moodley and A. Swanson, "Modelling of Streamer Breakdown Under Positive Polarity HVDC in Subtropical Conditions," Durban, 2021.

2023 SAUPEC Conference, Johannesburg, South Africa, January 24-26, 2023

Practical Study on the Lifetime Prediction of High Voltage Cross-Linked Polyethylene Cable (XLPE) using Thermal Aging

R.M Mutepe, B.A Thango, P.N Bokoro
Dept. of Electrical and Electronic Engineering Technology
University of Johannesburg
Johannesburg, South Africa
222251942@student.uj.ac.za; bonginkosit@uj.ac.za; pitshoub@uj.ac.za

***Abstract*—A high-voltage and medium-voltage cable distribution network is an extensive section of the distribution route. The electrical cable system remains the most important channel or brain connection that allow all other dynamic section to function. Since the electrical cables system is entrenched often it is challenging and costly to install new ones. When the cable ages, a degradation of the electrical and mechanical properties of the insulating material occurs triggering irreversible changes in the chemical construction and hence reducing the service life of the cable. When the conductor operating temperature increases, there is a subsequent speeding up of the XLPE aging process, and consequently a reduction in the life of the cable. The key objective of this paper is to present a model for determining the thermal aging of XLPE HV cables. In addition, this paper examines the thermal aging of high voltage XLPE cable for HV distribution network, using consistent load. Based on the cable properties such as the insulation temperature, thermal aging is determined using the Thermal Aging model and Arrhenius law. In this work, the model is developed based on this premise to predict the lifetime of a 132kV, single core, 1000mm^2 Cross-linked polyethene (XLPE) cable. This paper specifically implements the lifetime model of a high-voltage cable using thermal aging. The results show that when an XLPE cable is operated at a lower temperature of 70°C is likely to survive many years (+50 years) in service, than when it is operating at a normal cable operating temperature of 90°C.**

***Keywords*— cross-linked polyethene cable (XLPE), thermal aging, lifetime, degradation**

I. INTRODUCTION

High voltage and medium voltage cables are as unreceptive electrical apparatuses, nonetheless, not all is far from the truth. In the initiation phase, voltage and current flow through the electrical cable system over a range of frequencies [1]. Because of the essential boundaries of cable properties such as conductor and insulation, other influences such as temperature, capacitance and impedance all form undesirable challenges, which must all take into account and constructed out nor be possibly lessened as far as feasible. Electrical apparatus that are connected can also contribute to unfavourable effects in electrical cable systems but then again the most crucial battle be it characteristic or persuaded is how conductor resistance impacts current flow as heat is produced through this. In addition, speedy degradation can be caused by voids and poor workmanship, and high temperature in the existence of air is the key adversary of entirely polymer insulation but light, some alkaline, acids and gases can speed up degradation [2]. Degradation due to heat comes in the form of a molecule that has deteriorated activated by a lengthy chain of molecules breaking and countering with each other to bring changes to the cable properties. These variations characteristically comprise minimized flexibility, cracking, changes in colour and abridged elongation. Many cables insulation consists of stabilizers which are used to sluggish the course by mopping up free radicals, then again the acknowledged standard internationally to investigate aging performance for medium voltage cable insulations is well-defined by IEC60216 which forms part of accelerated heat aging on cables sample. For example, comparing the un-aged cable sample elongation at break performance against aged cable samples, formulating the outcomes on an Arrhenius plot and inferring to predict lengthy life performance.

In this work, a model is developed to predict the lifetime of the newly manufactured high-voltage XLPE cable, which will furnish insight to the customer on the planned lifespan of the operational service. It was found that at a cable operating temperature, the cable will likely survive up to 40 years in service, as high temperatures play a crucial role in degrading the cable insulation.

II. CROSS-LINKED POLYETHYLENE CABLE (XLPE) AND THERMAL AGING

The useful life of a cable system is mainly determined by the rate of deterioration of both mechanical and electrical properties of its XLPE insulating components through thermal ageing [3]. An increase in the conductor's continuous operating temperature will accelerate ageing and reduce the expected life. In general, cross-linked polyethene cable (XLPE) cable is rated at 90 °C and the expected returns from the insulation life are around 40 years [4]. Nevertheless, by reducing the conductor temperature to 70°C the life of a cross-linked polyethene cable (XLPE) cable can increase to more than 40 years.

- Polyvinyl chloride material (PVC) = 70°C
- Cross-linked polyethene cable (XLPE) = 90°C
- Propylene rubber (EPR) = 90°C

A. Cable Failure Mechanisms

Cable aging is likely to focus on the sites of inadequacies, such as contaminants, protrusions, voids, and roughness of semi-conducting screen, all of which, in the presence of water, might make it possible for the growth of creations known as water trees. These inadequacies invariably form regions of high electric stress, which accelerate contained aging. Such regions ultimately become the sites of electrical trees producing partial discharge, which, in the end, lead to a complete dielectric failure. Even though water treeing may primarily assist the beginning of electrical trees, at the later stage they might delay the growth [5]. Once the location of inadequacies with electrical trees has been noticed, situated and detached, the remaining length of cable develops much more reliable and significantly less prone to an upcoming service outage.

As a result, a failure can occur due to hyperthermia, without damaging the specimen, and for these reasons the predictive value is developed as per the criteria, as such, this must be taken into consideration that the material is then projected to reach its life span. With an increase in temperature, the level of deterioration grows quickly, which results in a speeding up of the chemical reactions taking place in cable materials, as a result, it is essential to minimize the temperature to safeguard the lengthy life of electrical systems [6]. Since the heat behaviour of materials, is substantially vicissitudes from one-cable material to another, there is a classification as per the high temperature they can withstand for a sensibly extensive period.

Polyvinylchloride (PVC) and polyethene (PE) are the main cable material that is utilized in the cable manufacturing industry. They offer conductors and sheaths for more than thousands of different types of conductors and cable material. In South Africa, for example, PVC makes up 55% of the market; polyethene 39% and several other resins include the remaining, 6%. In some other countries, however, polyethene and its copolymers are the main resin, followed by PVC, nylons, fluoropolymers and others [7]. Different types of polyethene are used in the cable industry such as cross-linkable polyethene (XLPE) and high density etc. Fig. 1 shows the summary of the process flow for predictive cable life based on the individual failure model.

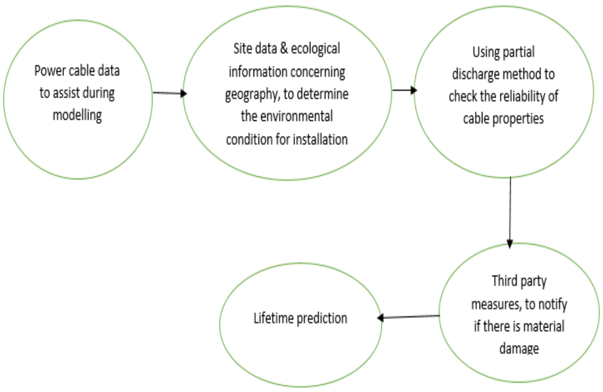

Fig. 1. Predictive cable life based on individual failure model.

The general prediction of the thermal life aging of XLPE cable under thermal conditions can be expressed as follows in Equation (1).

$$In(t) = e^{\left(\left(\frac{A}{T}\right)+A^1\right)} \quad (1)$$

Where,
t – Time in hours
T – Absolute temperature K (273 + ^{0}C)
A – Constant 14500 for XLPE
A^1 – Constant of -27.19 for XLPE

B. Temperature influence on the aging of XLPE cable

The Arrhenius model of dielectric aging state that the impact of high-temperature rise is to accelerate the rate of degradation of a cables XLPE cable insulation in such a way that the logarithm of time to end is inversely proportional to the absolute temperature (T) [9]. This equation can be expressed as follows in Equation (2).

$$Z(t) = De^{(-BcT)}\ ;\ cT = \frac{1}{T_0} - \frac{1}{T} \quad (2)$$

Where,
$Z(t)$ – Expected Life at Subjected Temperature (T)
D – Design Life
B – Constant for XLPE
T_0 – Ambient temperature
T – Specified temperature

C. Electric Field Stress around the conductor core Screen and Insulation

The calculation of electric field stress at the surface of the conductor core/screen, as per the IEC guideline is generally designed to be less than 8 kV/mm and can be expressed as follows in Equation (3).

$$E = \frac{V}{\left(r \times \ln\left(\frac{R}{r}\right)\right)} \quad (3)$$

Where,
V – Applied voltage
r – Conductor/conductor Screen external radius
R – Insulation external radius

The electric field stress at the surface of the insulation core of the cable is calculated using equation (4) below, and as per IEC standards, it is designed to be less than 4 kV/mm [10].

$$E = \frac{V}{\left(R \times \ln\left(\frac{R}{r}\right)\right)} \quad (4)$$

III. Lifetime Valuation of XLPE Cable for Thermal Aging

In this section, the results for predicting the lifetime of an XLPE cable using thermal aging have been presented. It is crucial during the design stage to understand the ageing features of insulations when choosing cables for use in systems where long life is required. Table I shows the cable ratings that are designed to ensure the long lifetime of the cable.

TABLE I. CABLE RATING

Description	Ratings
Cable Design Temperature	90 °C
Cable Project Temperature	72 °C
Cable Rated Voltage	132 kV
Cable Maximum Voltage	145 kV

The dimensions and voltages of the cable are recorded in Table II. The latter assist in understanding the construction of the cable as a whole and gives insight when developing a fitting model.

TABLE II. CABLE PARAMETERS

Cable parameters	Values
Outer Radius of the XLPE Insulation Screen (Rio)	36.8mm
Outer Radius of the XLPE Insulation (Rio)	35.8mm
Outer Diameter of Core Screen (Rii)	17.8mm
The thickness of XLPE Insulation (ti)	18.01mm
Operating Temperature of the Cable (Tm)	90°C
Phase Voltage (Vph)	76.2kV
Peak Voltage of (Vp-ph)	108kV
Nominal Line Voltage (VL)	132kV
Phase Voltage (Vph)	83.7kV
Phase Voltage (Vph)	118.4kV
Maximum Line Voltage (VML)	145kV

These parameters are attained by considering a cable sample in which the corresponding electrical parameters and dimensions are measured as illustrated above.

A. *Thermal Life Aging – a predictive model*

When the cable insulation, specifically materials that are organic, are exposed to 76ºC raised temperatures they are subject to weakening. Weakening forms variations in the bodily properties of cable materials so that they turn out to be incapable to meet their functions after a certain time, this means failure.

The thermal characteristics of XLPE as defined by the Institution of Electrical Engineers (IEE) and highlighted in "Commentary on IEE Wiring Regulations 16th Edition and BS 7671:2001," published in 2002 (ISBN 085 296 237 1). The discussion around the predictive life of XLPE (PRC) until the deterioration phase at 90 °C operating temperature; for insulated electric cables, the estimated predictive life is 40 years (Permanent rating = load/temperature maintained for 24 hours per day). The general equation was used to calcite thermal aging. In TABLE III, the thermal aging results for the sample cable considered in TABLE I and TABLE II are presented.

TABLE III. RESULTS OF THERMAL AGING

Description	Parameters
Time in Hours to Failure of the Cable due to thermal Aging at Maximum Design Temperature (t)	346 245.5835 hrs
Time in Hours to Failure of the Cable due to thermal Aging at Specified Temperature (t)	2 782 848.238 hrs
Maximum Design Temperature (Tk)	90ºC
Specified Project Temperature (Tk)	70ºC
Constant for XLPE (A)	14 500
Constant for XLPE (A 1)	-27.19
IEEE Expected Thermal Age of the Cable in Years (Design Life) - At Maximum Design Temperature (tE)	40 years
IEEE Expected Thermal Age of the Cable in Years (Design Life) - At Specified Project Temperature (tE)	318 years

These results constitute proof that the level of increase in the design life of cross-linked polyethene is inversely proportional to the temperature. When there is a decrease in 5°C, the level of an upsurge in the period maximised nearly double. Scientifically, such a level has an adverse exponential factor yielding from the exponential association of the theoretical Arrhenius equation. However, from a practical viewpoint, it can be viewed by the presence of everlasting variations in the molecules assembly of the cable insulation properties that directed to chemical reactions of cross-linking between chains, hydrolysis and oxidation that eventually results in a degradation of electrical properties and mechanical materials. As stated above, it is well understood that there are certain factors such as temperature, radiation and the presence of water vapour, which play a crucial role in the accelerated ageing of the electrical system. An investigation of the XLPE predictive model under thermal ageing showed that an increase in the ageing temperature of XLPE results in accelerated chemical reactions and therefore increases the material thermal degradation. Which then results in an eminent decrease in its mechanical properties and henceforth a decrease in its life span.

The studied cable aging results due to electric stress and temperature using Equation (2) are tabulated in Table IV.

TABLE IV. ELECTRIC STRESS & TEMPERATURE AT NOMINAL SYSTEM VOLTAGE

Description	Aging States
B	12 430 K
T0	90ºC
T - Maximum Design Temperature	90ºC
T - Specified Temperature	70ºC
(cT)1	0
(cT)2	-0.00014373
L - Maximum Design Temperature	40 years
L - Specified Project Temperature	239 years

The results of the electric field stress at the surface of the insulation core of the cable are tabulated in TABLE V.

TABLE V. ELECTRIC FIELD STRESS

Cable properties	Voltage/mm
Reference Electrical Stress Voltage at the Conductor Screen as per IEC Specification	8kV/mm
Reference Electrical Stress Voltage at the Insulation/Core Screen as per IEC Specification	4kV/mm
Design Electrical Stress Voltage at the Surface of the Conductor Screen (Emax) at U0	6.1kV/mm
Design Electrical Stress Voltage at the Surface of the Insulation/Core Screen (Emin) at U0	3kV/mm
Electrical Stress Voltage at the Surface of the Conductor Screen (Emax) at Um	6.7kV/mm

IV. CONCLUSION

A profound study of the mathematical model was deliberated, and the lifetime model was used as a predictive model for XLPE power cables. A sample of 132kV, single core, 1000mm^2 power cable was used to calculate its life span in the industry, and a number factor was taken into account throughout the calculations:

- Firstly, a mathematical model that takes into account the cable properties and its dimensions
- An anticipated predictive model of power cables centred on real physical sensations as stated by the above models
- The capability of the model to predict the number of years the customer must expect the cable life span due to environmental conditions such as temperature
- The established predictive model assessment can offer valuable competence in prognostics and proper guidance in choosing the correct parameter during the design stage of the cable.

REFERENCES

[1] Yi Zhang, Zaijun Wu, Jiajie Xu, Xiao Tan, Dongdong Zhang, Yuanjing Zeng, Gang Liu, Remaining lifespan prediction of cross-linked polyethylene material based on GM(1, N) grey models, *IET Generation, Transmission & Distribution,* 10.1049/gtd2.12312, 16, 2, (376-384), (2021).

[2] P. Hahn and R. Polansky, "Estimation of the service lifetime of cable sheath materials designed for working in harsh operating environment," *2015 16th International Scientific Conference on Electric Power Engineering (EPE)*, 2015, pp. 307-310, doi: 10.1109/EPE.2015.7161074.

[3] Hongkun Lv, Tianhao Lu, Lingqi Xiong, Xianggao Zheng, Yuyan Huang, Mingliang Ying, Jiecong Cai, Zhuo Li,Assessment of thermally aged XLPE insulation material under extreme operating temperatures, *Polymer Testing*,Volume 88,2020,106569,ISSN 0142-9418,doi:https://doi.org/10.1016/j.polymertesting.2020.106569.

[4] L. Boukezzi and A. Boubakeur, "Prediction of mechanical properties of XLPE cable insulation under thermal aging: neural network approach," *in IEEE Transactions on Dielectrics and Electrical Insulation*, vol. 20, no. 6, pp. 2125-2134, December 2013, doi: 10.1109/TDEI.2013.6678861.

[5] Mecheri, Yacine, et al. "Effect of thermal ageing on the properties of XLPE as an insulating material for HV cables." *International Electrical Insulation Conference*, IET Centre, Birmingham, UK. 2013.

[6] Mecheri, Yacine, et al. "Dielectric and mechanical behavior of cross-linked polyethylene under thermal aging." *2000 Annual report conference on electrical insulation and dielectric phenomena* (Cat. No. 00CH37132). Vol. 2. IEEE, 2000.

[7] M. Qatan, M. E. Farrag, B. Alkali and C. Zhou, "Modeling and Analysis of the Remaining Useful Life of MV XLPE Cable: Case study of Oman Oil and Gas Power Grid," *2018 53rd International Universities Power Engineering Conference (UPEC)*, 2018, pp. 1-6, doi: 10.1109/UPEC.2018.8541946.

[8] L. Boukezzi, A. Boubakeur, S. Rondot, O. Jbara and C. Laurent, "Characterization Tests and analysis of cross-linked polyethylene (XLPE) used in high voltage cables insulation under thermal constraint," *2014 International Conference on Electrical Sciences and Technologies in Maghreb (CISTEM)*, Tunis, Tunisia, 2014, pp. 1-8, doi: 10.1109/CISTEM.2014.7076969.

[9] Boukezzi L, Boubakeur A. Effect of thermal aging on the electrical characteristics of XLPE for HV cables. *Transactions on Electrical and Electronic Materials*. 2018 Oct;19(5):344-51.

[10] IEC 60840:2020, “60840:2020 - Power cables with extruded insulation and their accessories for rated voltages above 30 kV (Um= 36 kV) up to 150 kV (Um = 170 kV) - Test methods and requirements”, *European standards*, Europe, 2020. doi: https://www.en-standard.eu/iec-60840-2020-power-cables-with-extruded-insulation-and-their-accessories-for-rated-voltages-above-30-kv-um-36-kv-up-to-150-kv-um-170-kv-test-methods-and-requirements/.

Testing of different materials for composite aircraft lightning protection

Sihle Simelane
School of Electrical and Information Engineering
University of the Witwatersrand
Johannesburg, South Africa
1974997@students.wits.ac.za

Thandi Magoro
School of Electrical and Information Engineering
University of the Witwatersrand
Johannesburg, South Africa
1707061@students.wits.ac.za

Hugh Hunt
School of Electrical and Information Engineering
University of the Witwatersrand
Johannesburg, South Africa
Hugh.Hunt@wits.ac.za

Wisani Hlungwana
School of Mechanical, Industrial and Aeronautical Engineering
University of the Witwatersrand
Johannesburg, South Africa
1830038@students.wits.ac.za

Lebogang Moloisane
School of Mechanical, Industrial and Aeronautical Engineering
University of the Witwatersrand
Johannesburg, South Africa
Lebogang.Moloisane@wits.ac.za

***Abstract*—In this paper, the testing and investigation of the mesh layer on composite materials as well as the effectiveness of the coating made using the cold spray process for the purpose of aircraft lightning protection are conducted. The results from the coated composite material samples are compared to those without coating. The investigation is carried out by quantifying the damage on the composite material radially when struck by lightning and comparing the temperature profiles of the materials. The 8/20 generator is used to generate the lightning current impulse. The results are summarized as follows: for an increase in the current, there is a significant increase in the damage on the composite material for both coated and uncoated samples. For an increase in current, there is a slight increase in the maximum measured temperature for both samples. Furthermore, the temperature profile of coated samples showed slightly higher temperature when compared to the uncoated samples. Overall, the coated samples have less radial damage for the same lightning currents when compared to samples which were not coated. This confirms that the cold spray coating process can indeed be used for protection, restoration and possibly manufacturing of aircraft composite materials.**

Keywords—Composite Material, Lightning, Copper Mesh, Cold Spray, Coating

I. INTRODUCTION

Lightning strikes on commercial airplanes are common with a likelihood of occurring more than once for every 3000 flight hours every year [1]. This necessitates the development of lightning protection for aircraft. Before the development of composite materials which started in the 1960s [2], lightning protection was not a major concern since copper and aluminium metals were used to shield the aircraft and with their high conductivity, they provided good protection [7]. However, with the introduction of composite materials for aircraft bodies, the problem of lightning protection was born because the composite materials have less conductivity. Lightning protection in composite materials for aircraft bodies is provided by a copper mesh layer within the composite materials. Composite materials are chosen for aircraft manufacture for their great properties which include corrosion resistance, strength and lightweight [4-5]. There are three widely commercially used composite material reinforcements namely: carbon fibre, fibreglass and amid fibre [6]. The carbon fibre reinforced composite material is the commonly used and it is the one under investigation in this paper. Lightning attaches to an airplane at one spot and exits from another [7], these are called the entry or in points and the exit or out points in this paper.

The aim of this paper is twofold. Firstly, it is to present the testing and investigation of the mesh layer on composite materials for aircraft lightning protection. Secondly, it is to investigate the effectiveness of the coating made using the cold spray process for lightning protection. The lightning damage results from composite material samples with coating are compared to those of samples without coating. The composite material under test has a copper-based mesh layer. The purpose of the mesh layer is to provide a conductive path for the lightning current to spread reducing the current density per unit area which in turn reduces the damage [8].

The structure of this paper is as follows: section II outlines the literature review, section III focuses on the background, section IV outlines the methodology, section V presents the results and related discussions, section VI outlines the safety measures taken to ensure the experiment is ran successfully, section VII presents the recommendations and lastly section VIII concludes the findings of this paper.

II. LITERATURE REVIEW

Lightning tests are passed or failed depending on whether the damage compromises safety. The lightning institute was established in 1946 where studies centred on lightning and relevant protection methods were discussed [9]. A lightning experimental study conducted by Firaboli et al. revealed that the mesh layer provides good lightning protection when laid on the surface of composite laminates [10]. A study done by Rajesh et al. on damage response of carbon fiber-reinforced panels coated with conducting material showed that metallic coating performed better at lightning protection compared to coating consisting of different materials [11]. Composite materials have poor conductivity implying that they have low lightning protection capabilities on their own hence they are coupled with an aluminium or copper mesh layer which is highly conductive [12]. Temperature generated during a lightning strike plays a significant role in mechanical and chemical damages. The high temperatures are commonly due to high resistivity of the material and these high temperatures can be mitigated by improving the conductivity of the material [9-13]. The matrix resin on the composite material acts as an insulator which leads to resistive heating during a lightning strike resulting in a tremendous rise in temperature which causes fiber damage and resin pyrolysis [13]. In a case where the composite material has been damaged the cold spray process can be used for restoration of the mesh [14].

From the literature review it is evident that the conductivity of the composite material, coating and the temperature during a lightning strike play a significant role in the amount of observed damage. In this paper some of the studies above have been used as a reference point for some aspects of the presented work below.

III. BACKGROUND

A. *Apparatus*

- 8/20 impulse generator setup
- Oscilloscope
- Multi-meter
- Testo thermal camera
- Laptop

B. *Assumptions*

- The composite material samples given are assumed to be identical i.e., the samples have the same type of material, copper mesh, resistance per unit area and geometric dimensions.

- The coated samples were coated with the same parameters i.e., the pressure, temperature and number of coating layers. Any minor difference in these parameters is taken to not have a significant effect on the results.

C. *Constraints*

- The allowed charging voltage is 20 kV for the provided 8/20 generator. This limit in charging voltage limits the lightning current. The maximum measured current was 24.3 kA for the coated sample at 20.1 kV charging voltage.

- Unavailability of the copper cold spray powder in large quantities. The available copper powders are the C5003 and C0075. The C0075 is tailored for the cold spray process with applications in copper-based component repair [3]. The C5003 is tailored for cold spray applications that require high electrical conductivity, an antimicrobial surface and thermal management [16].

- Ten identical composite material samples. Comparing different composite materials cannot be done for this investigation since all the samples available are identical.

IV. METHODOLOGY

A. *Laboratory experiment*

The experiment is performed using the 8/20 generator. The generator can be operated in current or combination mode. For this experiment it is operated in current mode. The equivalent circuit diagram is depicted in Figure 1 below.

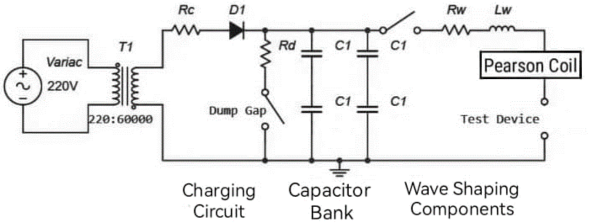

Figure 1: 8/20 generator current mode circuit.

The 8/20 impulse generator above is used to imitate lightning currents with a rise time of $8\mu s$ and a fall time of $20\ \mu s$.The generator parameters are: $C1 = 30$ µf, $R_w = 0.367\Omega$ *and* $L_w = 1.56$ µH. The maximum peak current measured using this generator is 24.3 kA. The setup is readily available to use at the High Voltage Lab at the University of the Witwatersrand.

B. *Resistance of a 3D conductor*

For simplicity, the copper mesh layer is modelled as a sheet to understand its resistive properties. This copper mesh layer makes the airplane to be a faraday cage. A faraday cage is a conductive metal container that blocks electric fields [14].

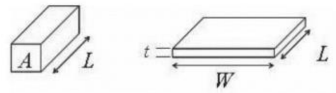

(a) (b)

Figure 2: Copper mesh layer layout with diagrams where (a) shows the labelling of the 3D mesh for cross section area *A* and length *L* and (b) shows the labelling of a 3D mesh with thickness *t*, width *W* and length *L* [15].

$$R = \rho \frac{L}{A} \tag{1}$$

$$R = \rho \frac{L}{Wt} \tag{2}$$

$$R = \frac{\rho}{t}\frac{L}{A} \tag{3}$$

$$R = R_s \frac{L}{W} \tag{4}$$

Where ρ is the resistivity of the copper conductor used, σ is the conductivity, t is the thickness of the sheet, W is the width of the sheet and L is the length of the sheet.

The thickness of the sheet layer is constant since all samples used are identical. The length and the width are kept constant for all samples by ensuring that the distance between the lightning entry and exit points is the same for all samples being tested. The distance between all points is 17cm. This ensures that the variations in resistance are very small such that a good relationship between current and radial damage can be derived. The entry and exit points are drilled on the sample and current is forced to enter at one end and exit on the other end.

C. *Lightning strike procedure*

The sample being tested is placed in the space named test device on Figure 1. It is connected to the test gap using conductors which are connected to the to the 8/20 generator. The charging voltage is observed live on the multi-meter, and it is stepped up with steps of approximately 2 kV from 6.3 kV till 20.1 kV for both coated and uncoated samples. This ensures that current, i , is proportional to the charging voltage, V, by Ohm's law described by (5) below.

$$i = \frac{V}{R} \tag{5}$$

The peak value of the lightning current is measured using the oscilloscope. For a 2 kV increase in charging voltage an increase of 2 kA with minor variations is observed for the uncoated samples and this attributed to (5) since the resistance is kept constant. For the coated samples, a 2 kV increase in charging voltage results in a current increase that is far greater than 2 kA.

D. *Measurements*

The three measurements taken after every lightning strike are listed below.

Current

The charging voltage is increased in steps of about 2 kV as described on section (IV)(C). This in turn increases the current as described by (5) where the resistance is kept constant, and the voltage is the only varying parameter. The peak value of the current magnitude across the sample is measured and obtained using the oscilloscope. Before every strike, the oscilloscope is made ready to measure the peak value of the current, the rising and falling time.

Radial damage

The samples are closely inspected after the lightning strike and the furthest point of damage from the centre of the drilled hole is marked. Using a ruler, the distance from that point to the centre is measured and it is recorded as the radial damage in cm. This process is done for all samples.

Thermal measurements

The testo thermal camera is used to take thermal images of the samples. The first thermal image taken is the entry point one, followed by the exit point and lastly, the picture of the whole sample showing the entry and exit points of the lightning current. The camera allows visualization of the different temperatures across the sample. Using a timer, the images are taken in less than 5 seconds between successive measurements. The thermal camera is placed 15 cm above the entry and exit point on top of a ruler when taking the thermal images. The image showing the entry and exit points is taken at about 30 cm above the surface of the sample. Taking images from a controlled distance ensured that the resolution of the images across the samples is the same, hence different samples can be fairly compared.

V. RESULTS AND DISCUSSIONS

A. *Conductance of the composite material*

Figure 3 below presents the plot of charging voltage and the lightning current measured on the coated and uncoated samples.

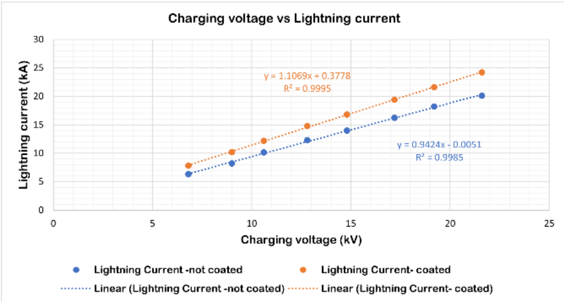

Figure 3: Charging voltage vs lightning current.

The R-squared values (which are 1.000 when rounded-off to 3 decimal places) indicate a high linear correlation between the charging voltage and the current. The gradient of a straight-line, m, can be obtained using (6) which is equal to 1 divided by the resistance of the material. The strong correlation and the fit of the linear regression validate the proposed methodology in section (IV)(B).

$$m = \frac{\Delta y}{\Delta x} = \frac{\Delta i}{\Delta V} = \frac{1}{R} \tag{6}$$

$$R = \frac{1}{m} \tag{7}$$

$$R_{uncoated} = \frac{1}{m_{uncoated}}\Omega = \frac{1}{0.9424} = 1.061\Omega \tag{8}$$

$$R_{uncoated} = \frac{1}{m_{coated}}\Omega = \frac{1}{1.1069} = 0.903\Omega \tag{9}$$

$$R \propto \frac{1}{\sigma} \tag{10}$$

The resistance values are obtained using (7)(8) and (9). The resistance for the uncoated sample is $R_{uncoated} = 1.061\ \Omega$ and the resistance of the coated sample is $R_{coated} = 0.903\ \Omega$. Equations (1) and (10) suggests that resistance is inversely proportional to conductivity. With all geometric parameters kept constant, $R_{uncoated} > R_{coated}$.This implies that the conductivity of the coated material is higher than that of the uncoated material. These results suggest that the coating of the composite material introduced a more conductive layer compared to the conductivity of the composite material with no coating.

B. *Radial Damage Analysis*

The results presented in Figure 4 and Figure 5 show the lightning current vs radial damage for the sample without coating and the one with coating, respectively. For both coated and uncoated samples it is observed that an increase in current is accompanied by an increase in radial damage. Furthermore, it is observed that for low currents the exit or ground point experiences more damage compared to the point of strike. As the current becomes higher there is a switch i.e., the point of strike experiences more radial damage compared to the exit point.

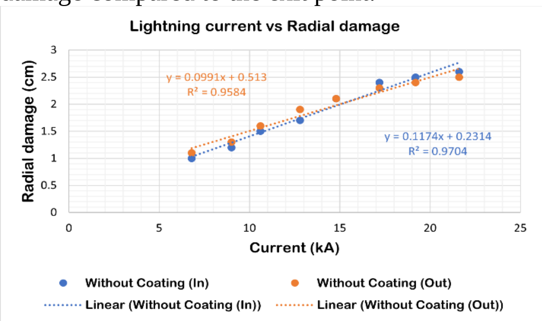

Figure 4: Current vs radial damage on uncoated material

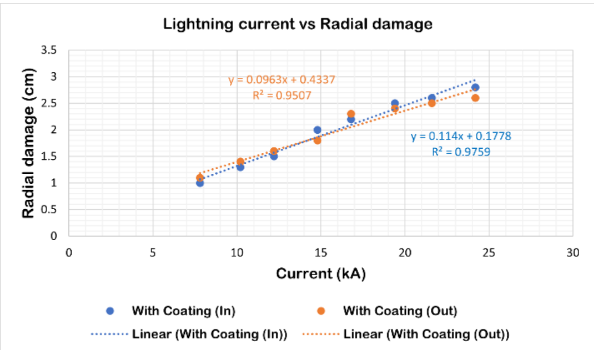

Figure 5: Current vs radial damage on coated material

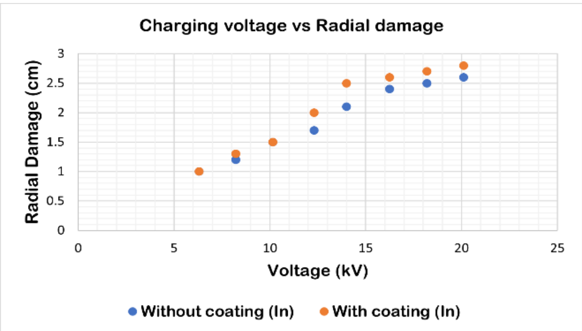

Figure 6: Charging voltage vs radial damage on coated and uncoated material.

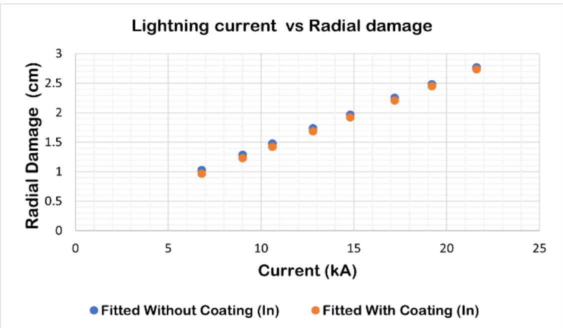

Figure 7: Fitted lightning current vs radial damage on uncoated and coated material.

(a) (b)

Figure 8:(a) Before lightning strike and (b) after lightning strike

From Figures 4 and 5, it is observed that the coated and uncoated samples show the same current and radial damage trend. The coated samples have another layer of conductivity. The coating changes the conductivity and hence the resistance where it is applied as observed in section (V)(A). For the same charging voltage, different current values are measured for the coated and uncoated samples. The change in current measurements for the same charging voltage implies there is a change in resistance when coating is applied to the materials.

The comparison of the radial damage for the coated and uncoated samples is done with the focus on the point of the lightning strike (In). A similar analysis was done for the ground point (Out) and the same conclusion was reached.

The entry points (In) on Figures 4 and 5 should be plotted on the same axis in order to compare the radial damage. Although the points appear like they can be combined on one axis, it must be noted that the currents are not the same for the same charging voltages on Figures 4 and 5 because the coated and uncoated samples have difference resistance (see section (V)(A)). Figure 6 is adopted to plot the damage on entry points for the coated and uncoated samples vs the charging voltage since it was kept the same for both samples. The results presented on Figure 6 seem to imply that the coated samples experienced more radial damage for the same charging voltage. While this might appear like a compelling and accurate conclusion, it should be rigorously evaluated since it is in contradiction with the presented literature. For lightning tests, it is the current which plays a significant role in causing damage rather than the voltage. Therefore, the conclusion presented by Figure 6 where the damage is compared to the charging voltage is not final.

As seen in Figures 4 and 5, the data is fitted to a linear regression model. The blue lines on both figures fit the data for the entry (In) points. The obtained R-squared values for the coated and uncoated samples are 0.9704 and 0.9759 respectively. The logarithmic, exponential and moving average trends were fitted to the data and gave less R-squared values compared to the ones obtained from the linear regression estimate, and therefore a linear model was chosen. The obtained R-squared values indicate a strong correlation hence the linear model is acceptable for modelling the distribution of these points.

Using the trendline equations for the entry points (In) from Figures 4 and 5, Figure 7 is generated. The equations are used to estimate the radial damage at every instant for the same current value for the coated and uncoated sample. The results on Figure 7 indicated that for the same current values the coated samples incur less damage compared to the uncoated sample. This is expected since we have already deduced from section (V)(A) that the coating is highly conductive when compared to an uncoated sample. This new finding from Figure 7 is acceptable since it corroborates the presented literature. Figures 8 (a) and (b) show a sample before and after the lightning strike. It is evident that the copper layer is destroyed and worn away. As seen this damage does not go in depth on the composite material. The internals of the airplanes will be safe.

C. *Thermal Profile of samples*

This section presents the analysis of the temperature profiles for the coated and uncoated samples which are exposed to currents of 19.4 kA and 19.2 kA respectively. Figures 9 and 10 both have two peaks labelled entry and exit point which are 17 cm apart.

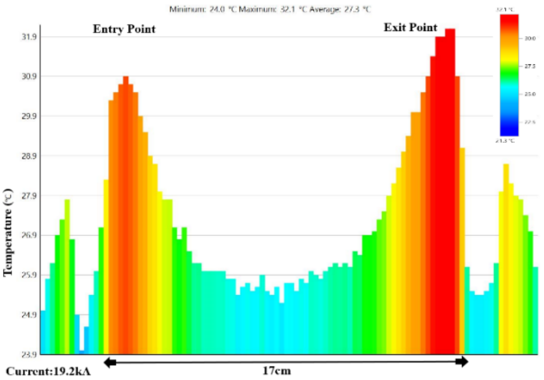

Figure 9: Temperature profile of uncoated sample

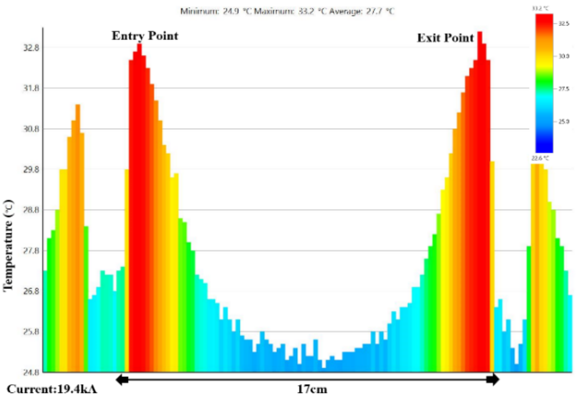

Figure 10: Temperature profile of coated sample

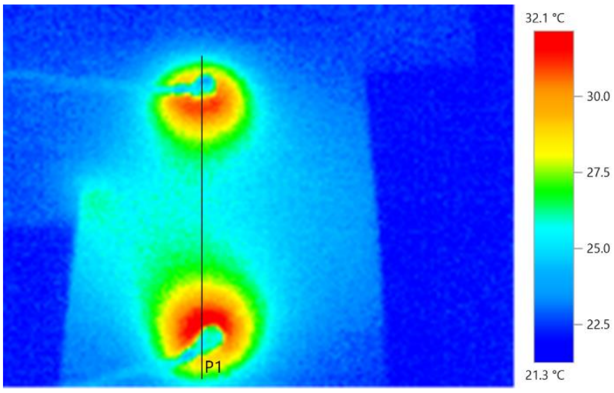

Figure 11: Thermal picture of a composite sample.

Lightning strikes transmit high currents in a short time period which is accompanied by severe heating which causes evaporation of the composite layer [9]. The two peaks on both samples are attributed to current density [9]. There is high current density at the entry and exit points which causes high temperature at those points. The rest of the composite material is at lower temperatures because the current is distributed throughout as shown in Figure 11. The entry point is observed to have lower temperatures compared to the exit point for both coated and uncoated samples.

The coated material recorded a maximum temperature of 33.2℃ while the uncoated material recorded a maximum temperature of 32.1℃. Similarly, the minimum recorded temperatures for the coated and uncoated are 24.9℃ and 24.0℃ respectively. The higher temperatures for the coated samples can be attributed to the following reasons. There was a difference in the room temperature between the times when the lightning strike was performed for the coated and uncoated samples. There was also a current difference between the samples where the coated sample was subjected to 19.4 kA while the uncoated sample was subjected to 19.2 kA, and this can be attributed to the fact that the current was not a controllable variable since the materials have different resistances (see section (V)(A)).

VI. Future Recommendations

Similar experiments aimed at evaluating the damage with increasing currents should follow the proposed method in section (IV)(C). A trial experiment was done with points placed at unknown varying distances from one another. The results obtained showed no trend since three variables were changing at the same time at any point i.e., charging voltage, resistance caused by the change in the distance between the two points and the current. Different currents were measured for the same charging voltage when the entry and exit points are at a different distance compared to the previous test. The current vs radial damage plot before keeping the resistance showed no trend, all points appeared random. Furthermore, the experiment should be done in a controlled environment. This is done to avoid temperature differences that can be mistaken for reasons other than the actual reasons.

Controlling current is difficult. For future experiments a trial experiment should be done aimed at approximating the resistance of the samples as done in this investigation. Knowing the resistance will enable current to be directly controlled using ohm’s law.

The pressure and area of contact between the conductors from the impulse generator and the composite material surface should be maintained the same. Failure to ensure the cable is well attached affects the temperature profile as seen on Figure 8. The huge difference between the temperature at the entry and exit point is attributed to the contact of the conductor with the composite material. The conductor was not fully in contact compared to the exit point.

Different composite materials should be tested using different industry available cold spray repairing powders in order to understand the behaviour of different coatings on the same material. The thickness of the coating can be further investigated by examining different coating layers for the same charging voltage. Finding the resistance, as done in this paper, of materials of different thicknesses will aid in knowing if the conductivity is increasing or decreasing, hence conclusions which are in line with existing literature can be made.

Although the tested composite material has displayed an increase in lightning protection with the C0075 coating, the conclusion of this investigation cannot be generalized for very large currents for the C0075 copper powder. For this experiment and within the limit of the available generator, the C0075 copper power has proven to have protection capabilities. For high lightning current tests and protection, the C5003 copper power should be used because of its high conductivity as explained in section (III)(C).

VII. CONCLUSION

It can be concluded from this investigation that the composite material put under test has protection capabilities. The cold spray coating process has the potential to repair, as observed coated samples showed less radial damage under the same lightning current compared to samples which were not coated. The coating increased the conductivity of the composite material and hence reduced the damage. For the range of current values that can be attained with the generator, there is no significant difference in the temperature of a coated and uncoated sample.

ACKNOWLEDGMENT

This Work is based on the research supported in part by the National Research Foundation of South Africa and their support of the Johannesburg Lightning Research Laboratory through the Thuthuka programme (Unique Grant No:122038) and by DEHNAFRICA and their support of the Johannesburg Lightning Research Laboratory.

REFERENCES

[1] W. Golding, "Lightning strikes on commercial aircraft: How the airlines are coping," *Journal of Aviation/Aerospace Education & Research*, 2005.

[2] B. Alemour, O. Badran, and M. R. Hassan, "A review of using conductive composite materials in solving lightning strike and ice accumulation problems in aviation," *Journal of Aerospace Technology and Management*, 2019.

[3] "Commercial powder - supersonic spray," *CenterLine Supersonic SprayTechnology*,Jan-2020.[Online].Available: https://www.supersonicspray.com/uploads/documents/SST-TDS-C0075-PR-2_0-0120.pdf. [Accessed: 10-Oct-2022].

[4] Nedelcu, Roxana, and Pierrick Redon. "Composites materials for aviation industry." In *International Conference of Scientific Papers "Scientific Research And Education In The Air Force" AFASES*. 2012.P. Vas. "Simulation and monitoring of induction motors with rotor asymmetry", *Proceeding of the 6th International Conference on Electrical Machines*, Manchester, pp. 435-439, May 1992.

[5] K. Sharma and G. Srinivas, "Flying smart: Smart materials used in aviation industry," *Materials Today: Proceedings*, vol. 27, pp. 244–250, 2020.

[6] M Mrazova, "Advanced composite materials of the future in aerospace industry," *INCAS BULLETIN*, vol. 5, no. 3, pp. 139–150, 2013.

[7] Sweers, Greg, Bruce Birch, and John Gokcen. "Lightning strikes: protection, inspection, and repair." *Aero Magazine* 4, no. 2012 (2012): 19-28.

[8] K. Sharma and G. Srinivas, "Flying smart: Smart materials used in aviation industry," *Materials Today: Proceedings*, vol. 27, pp. 244–250, 2020.

[9] T. Hu and X. Yu, "Lightning performance of copper-mesh clad composite panels: Test and Simulation," *Coatings*, vol. 9, no. 11, pp. 1–14, Nov. 2019.

[10] P. Feraboli and H. Kawakami, "Damage of carbon/epoxy composite plates subjected to mechanical impact and simulated lightning," *Journal of Aircraft*, vol. 47, no. 3, pp. 999–1012, 2010.

[11] P. S. M. Rajesh, F. Sirois, and D. Therriault, "Damage response of composites coated with conducting materials subjected to emulated lightning strikes," *Materials & Design*, vol. 139, pp. 45–55, Feb. 2018

[12] C. Soutis, "Fibre reinforced composites in aircraft construction," *Progress in Aerospace Sciences*, vol. 41, no. 2, pp. 143–151, Feb. 2005.

[13] T. M. Dhanya and C. S. Yerramalli, "Lightning strike effect on carbon fiber reinforced composites – effect of copper mesh protection," *Materials Today Communications*, vol. 16, pp. 124–134, May 2018.

[14] A. Smorgonskiy, F. Rachidi, M. Rubinstein, N. V. Korovkin, and A. P. Vassilopoulos, "Are standardized lightning current waveforms suitable for aircraft and wind turbine blades made of composite materials?" *IEEE Transactions on Electromagnetic Compatibility*, vol. 59, no. 4, pp. 1320–1328, Aug. 2017.

[15] M. Ryazanov, *Sheet Resistance*. 2016.

[16] Commercial powder - supersonic spray, Jan-2020. [Online]. Available:https://www.supersonicspray.com/uploads/documents/SST-TDS-C5003-PR-2-0

2023 SAUPEC Conference, Johannesburg, South Africa, January 24-26, 2023

Characterization of Cavity PD Under Impulse Voltage in Polyethylene Insulation

Tibello Vincent Mphuti
School of Electrical & Information Engineering
University of the Witwatersrand
Johannesburg, South Africa
1501593@students.wits.ac.za

Cuthbert Nyamupangedengu
School of Electrical & Information Engineering
University of the Witwatersrand
Johannesburg, South Africa
cuthbert.nyamupangedengu@wits.ac.za

***Abstract*— Understanding PD (Partial Discharge) phenomena under impulse voltage is important knowledge for the improvement of reliability of HV (High Voltage) equipment. PD in HV equipment can cause severe insulation deterioration resulting in breakdown, production loss and high cost of repairs. HV equipment insulation can fail due to PD activities which are initiated by impulse voltages such as lightning and switching. The latter has been exacerbated by load shedding switching operations in South Africa. PD detection under AC (Alternating Current) frequency voltage conditions is well developed, however there is inadequate knowledge in PD detection and diagnosis under non-power frequencies. The challenge is to enable PD detection during impulse voltage, due to the overlaps between the impulse voltage and the PD frequencies. In the present work, balanced PD detection circuit is implemented to suppress impulse voltage interference for the purpose of detecting cavity PD under impulse voltage. The measurement results show that PD pulses occur on specific locations of the impulse test voltage waveform and is consistent with similar results in the literature.**

Keywords — Cavity PD, Impulse voltage, Balanced PD detection circuit

I. INTRODUCTION

PD is localized electrical discharge activity that partly span punctured insulation between conductors. PD occurs if the dielectric strength of an insulation material is exceeded under normal voltage application and abnormal voltages due to the intensity of the localized ionization, which can lead to insulation breakdown [1].

A PD detection system is an important tool for diagnosis and analysis of the dielectric condition of insulation material in HV power systems. Typical partial discharges are corona (air ionization) due to non-uniform field on sharp end of insulation or connection, surface discharges due to interfacing of different insulation material, cavity discharges due to voids formed in solid or liquid insulation material and treeing as a result of electrical stress and moisture in insulation material. PD can continuously degrade the insulation material [2]. Power plant equipment do not only experience operating voltages, but also encounter lightning impulse and switching impulses [1]. PD detection under AC frequency voltage is well developed, however there is limited information on the efficacy of PD detection and characteristics under impulse voltages [1, 3]. PD measurement system that can effectively detect and measure PD’s on incipient defects under impulse voltage is of benefit in the understanding of PD phenomena. The knowledge is necessary to make informative decision with regards to HV equipment insulation diagnosis. Catastrophic failure in power plant can be mitigated in that regard [4].

It’s evident that HV equipment in operation, are not only subjected to AC operating voltage, but also transient voltages such as lightning and switching impulse. The transient voltages can superimpose on the normal AC voltage supply to HV equipment in-service. This phenomenon can result in hidden PD activity which may continue under normal AC operating voltage due to the degradation of stressed insulation caused by nature of PD process initiated by transient voltages [5].

PD measurements under impulse voltage can provide useful information about incipient defects in HV equipment. Therefore, it is considered important to diagnose insulation condition of HV equipment under impulse voltages [6]. The present paper represents a balanced PD detection system for cavity PD detection under impulse voltage.

II. THE EXPERIMENTAL MEASUREMENTS

A. PD defect model

The test specimen is a parallel plate electrode set-up for creating cavity PD, which consists of copper electrodes and sandwiching polyethylene sheets with one sheet having a cavity as shown in Fig 1. One of the common dielectric materials used to fabricate voids is High Density Polyethylene (HDPE) due to its high dielectric strength [7], and is of interest in this study as it simulates the power cable insulation system [8]. The complex relative permittivity is 2.3 on frequency band 1.0 kHz to 30 MHz for HDPE [9]. HDPE has advantages in that is sufficiently flexible and has high impact strength [10]. Fig 2 shows the schematic of the test cell. The test cell is immersed in oil to avoid unwanted surface discharges and flashovers.

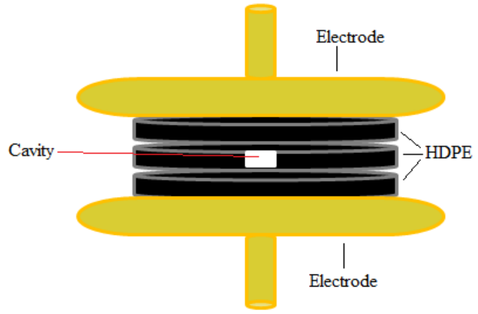

Fig 1: Parallel plate electrode set-up with cavity

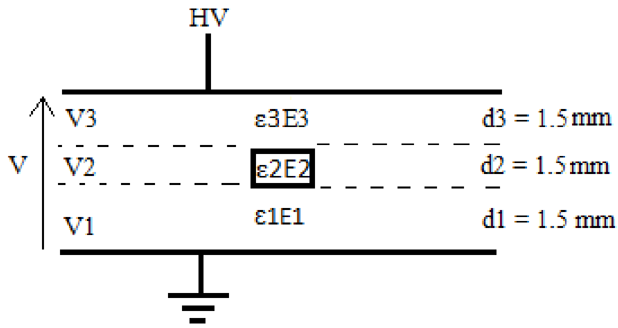

Fig 2: Schematic of test cell

The cavity thickness is 1.5 mm (thickness of a single sheet) with a diameter of 3 mm. At 0.8 bar air pressure, from Paschen curve minimum breakdown voltage is 4.5 kV. With reference to the 3-layer model in Fig 2, and (1) together with the cavity sparkover voltage from the Paschen curve, the voltage across the test object that would initiate PD in the cavity can be determined.

$$E_2 = \frac{V}{\frac{\varepsilon_2}{\varepsilon_1} d1 + \frac{\varepsilon_2}{\varepsilon_2} d2 + \frac{\varepsilon_2}{\varepsilon_3} d3} \qquad (1)$$

Where:

E_2: Magnitude of field intensity in air cavity

d_1: Polyethylene thickness

d_2: Air cavity thickness

d3: Polyethylene thickness

ε_1: Polyethylene relative permittivity = 2.3

ε_2: Air relative permittivity = 1

ε_3: Polyethylene relative permittivity = 2.3

V: Applied voltage to the test specimen

The minimum required externally applied voltage to initiate PD in the cavity is therefore calculated using (1) as 8,4 kV

B. *The balanced PD detection circuit*

PD detection through measurement of the energy emitted by the PD event can give information about its location and source. PD detection circuits are based on the principles of processing energies emitted by PD events. Various PD detection techniques have been exploited with their ability to detect PD activity under impulse voltage. However, PD detection under impulse voltage is relatively challenging. In various ultrawideband PD detection methods such as inductive probe, electromagnetic radiation detection using antenna, capacitive probe and acoustic sensors, the efficacy of the measurements is limited.

Wu et al. [5, 6] investigated the effects of transient voltages on HV cable with an artificial defect using two High Frequency Current Transformer (HFCT) under AC, impulse voltages of different polarity and superimposed voltages. PD activities are reported under longer impulse front time and switching impulse.

Mitra et al. [3] and Densley et al. [11] reported smallest discharges detected, using a bridge PD detection circuit. PD activity behaviour on artificial air-filled cavities of different dimensions in solid insulation under lightning and switching impulse voltage was detected. Kreuger and Shihab [12] investigated PD measurement on a three-core belted power cable using balanced bridge method and reported that different PD results are obtained due to the sensitivity limitations of the measuring circuit.

Hayakawa et al. [13] investigated electrical insulation characteristics of a High Temperature Superconducting cable insulation model. The test object was subjected to AC voltages superimposed with lightning impulse voltage. PD signal was not detectable under ac voltage before the impulse voltage application. PD signal was detected under the subsequent AC voltage after the application of impulse voltage.

Balanced PD detection circuit is adopted in the present research paper for characterization of cavity PD under impulse voltage. The setup to investigate PD detection under impulse is shown in Fig 3. Table I below shows various PD detection methods and each methods advantage and disadvantages

TABLE I. PD detection methods

PD detection methods		
Technique	***Pros***	***Cons***
PD current detection through coupling capacitor	Suitable for conventional narrow band PD detection	Not suitable for ultrawideband PD detection
PD current magnetic field through inductive probe	Suitable for ultrawideband PD detection	-Susceptible to impulse voltage interference -Require a filter (suppress PD)
PD transient electric field using capacitive probe	Suitable for ultrawideband PD detection	-Susceptible to impulse voltage interference -Require a filter (suppress PD)
PD event acoustic energy through acoustic sensor	Suitable for ultrawideband PD detection	-Susceptible to impulse voltage interference and external noise -Require an amplifier (PD not origin)

PD detection methods		
Technique	***Pros***	***Cons***
PD electromagnetic radiation through antenna	Suitable for ultrawideband PD detection	-Susceptible to impulse voltage interference and external noise -Require an amplifier (PD not origin)
Balanced bridge	-Suitable for ultrawideband PD detection -Noise cancelation	Need to be balanced to allow cancelation

Generally, the balanced bridge method for PD detection consists of resistors and identical adjustable capacitors [14]. The noise can only be suppressed when the electric bridge is in the balanced state, however the distributed stray parameters can cause the bridge not to be balanced [14]. An RLC filtering circuit in the form of a toroidal core for PD detection can be used. The concept of a balanced bridge method is used in this paper. The proposed balanced PD detection circuit is made of a high permeability ferrite toroid which is for high frequency application. The toroid core comprises of common primary windings on which the test specimen is connected to. PD test specimen and PD free specimen are used. The toroid core consists of an optimized secondary winding on which PD signal is measured using a Tektronix 6 GHz digital scope and displaying both PD magnitudes and applied lightning impulse voltage which is measured via the voltage probe. Fig 3 presents the equivalent circuit and the picture of the balanced PD detection setup.

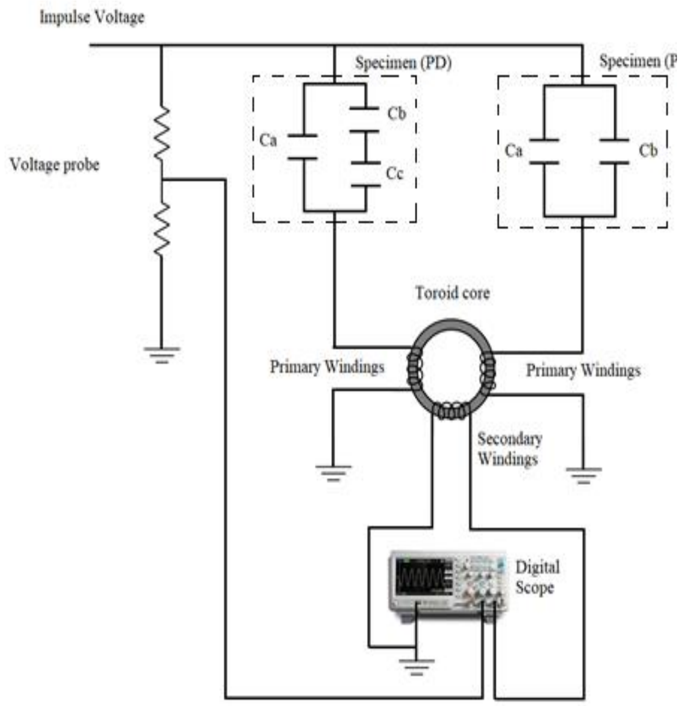

(a)

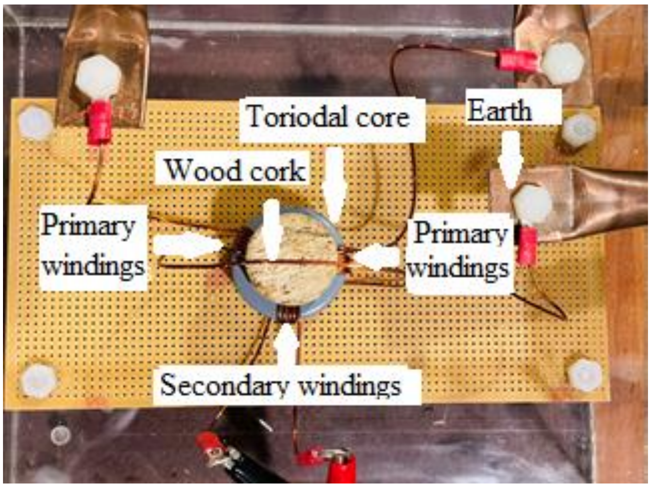

(b)

Fig 3: (a) Balanced PD detection equivalent circuit and (b) Balanced PD detection circuit picture.

C. *Experimental Procedure*

A single stage lightning impulse voltage source used in this research experiment is as shown in Fig 4. The components of the impulse generator are adjustable to produce the desired standard waveforms in accordance with the IEC 60060-1 [15].

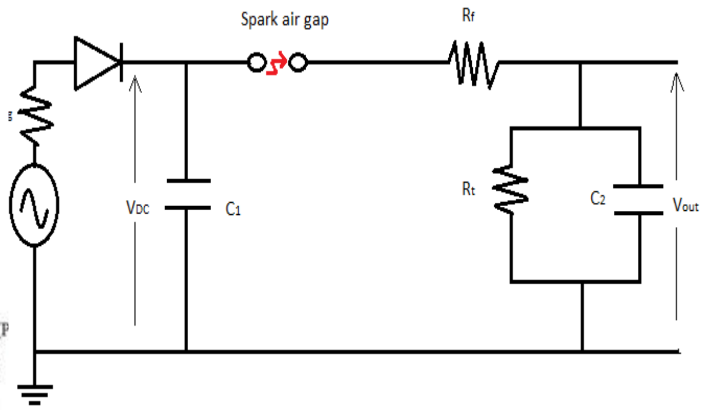

(a)

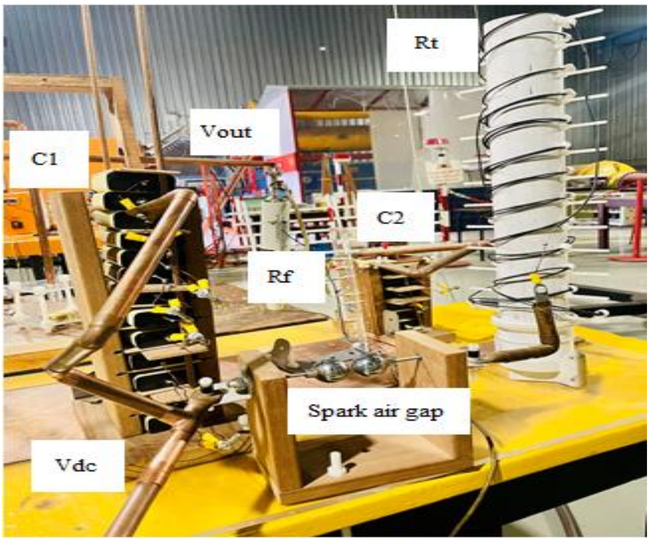

(b)

Fig 4: (a) Single stage impulse voltage generator equivalent circuit diagram, (b) Single stage impulse voltage generator picture.

Impulse voltage shots of incremental peak magnitude are applied on the test specimen until the PD activity is observed. The same impulse voltage magnitude is repeated in applying stress shots to the specimen, while recording PD signals in every event. There are considerable wait period intervals between shots to allow for space charge dispersion in the cavity that would influence the next PD activity. To ensure that the obtained signals are indeed from the defected test specimen, a control experiment was conducted where two defect-free specimens were tested in a balanced mode. The obtained measurement results are presented in Fig 5, where there is no evidence of PD in the defect free setup. The test impulse voltage is sufficiently cancelled out in the balanced bridge.

III. RESULTS AND DISCUSSION

The lightning impulse voltage shown in Fig 5 was measured using a voltage probe connected to a digital oscilloscope. PD detection circuit integrity and efficiency is proved as shown by the balanced PD (free) detection circuit output signal in Fig 5 below. Fig 5 is the background noise benchmark for cavity-free test specimen.

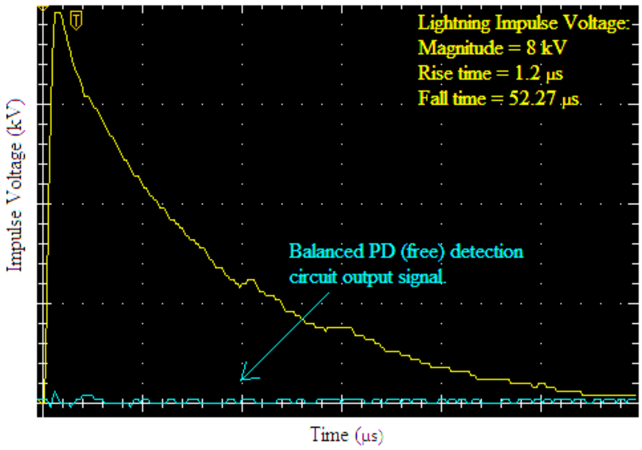

Fig 5: Measured lightning impulse voltage and Balanced PD free detection circuit output signal

A. *PD detection and extraction*

PD detection and extraction under lightning impulse voltage is achieved using the balanced PD detection circuit and the results are presented below.

Under the same condition of the lightning impulse voltage specification as shown in Fig 5, parallel plate electrode set-up with cavity as shown in Fig 1, was introduced on one leg on the balanced PD detection circuit and the other leg with PD free specimen (HDPE sheets with no cavity). As shown in Fig 6, 7, 8 and 9, PD pulses are detected and recorded using a digital oscilloscope during the application of lighting impulse voltage stress.

Fig 7 also presents typical measured PD relative to the test impulse voltage. Observed are the main discharges during the rise time of the lightning impulse voltage and reverse discharges during the fall time of the lightning impulse voltage. It is evident that the reverse discharges obtained in Fig 7, 8 and 9 during the fall time are influenced by the residual charge because of the space charge developed on the cavity wall due to PD activity during the rising edge of the impulse voltage [16].

From Niemeyer's [17] generalised PD model and the theory of cavity discharge mechanisms, space charges are in the opposite polarity to the initial field, however with the fall time of the lightning impulse voltage being significantly shorter than the dispersion time of the space charge, the resultant voltage established by the space charge can exceed the cavity sparkover voltage and therefore, initiate the reverse PD [16]. Reverse discharges are dependent on the cavity surface conductivity which change with aging condition [16]. The obtained results shown in Figs 6, 7, 8 and 9 are representative of typical measurements obtained. Because of the stochastic nature of PD measurement, event may give slightly different results but within the statistical insignificant variations.

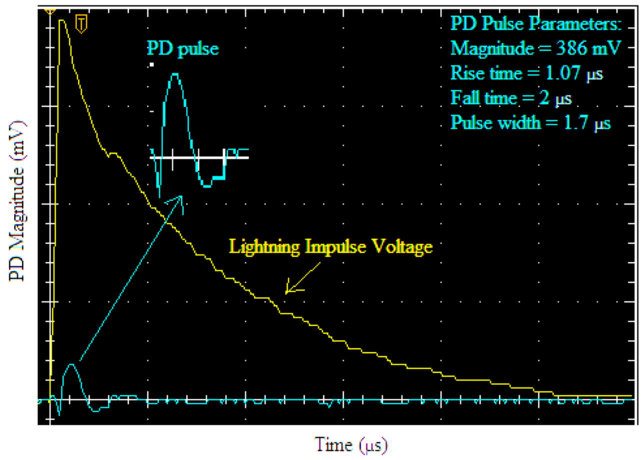

Fig 6: Measured PD pulse obtained during lightning impulse voltage shots

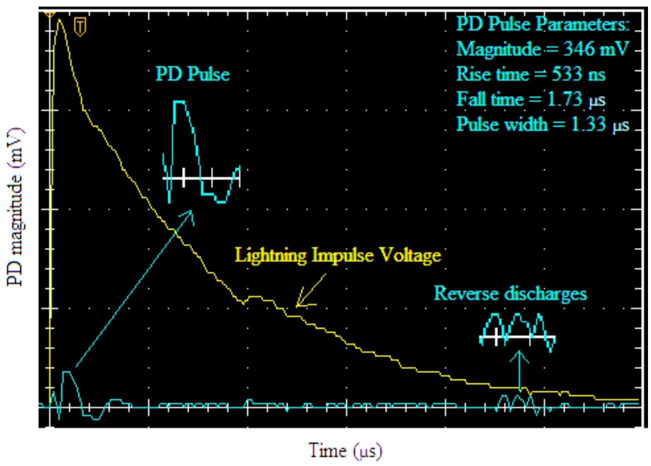

Fig 7: Measured PD pulse and positive reverse discharges because of polarity inversion under lightning impulse voltage

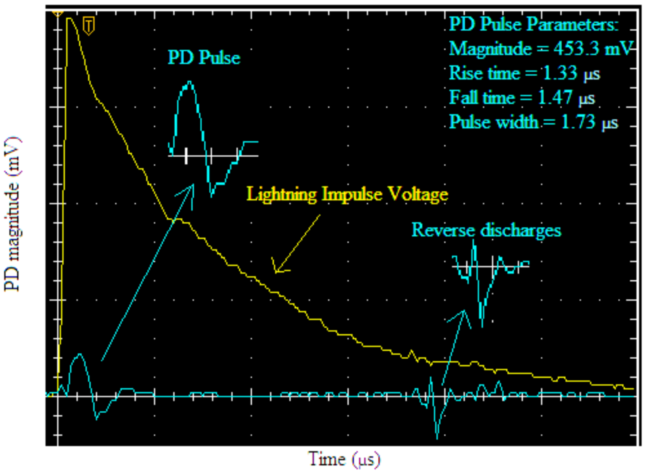

Fig 8: Measured PD pulse and negative reverse discharges because of polarity inversion under lightning impulse voltage

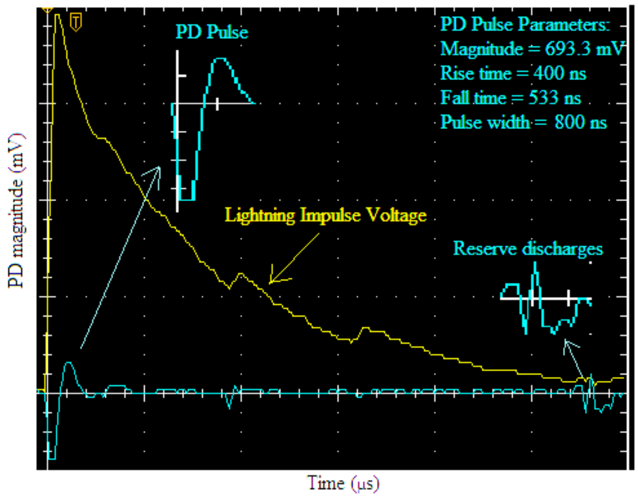

Fig 9: Space charge effect on measured PD pulse and reverse discharge after multiple lightning impulse voltage shots

IV. CONCLUSION

The measurements result for cavity PD under lightning impulse voltage are presented in this paper. Balanced PD detection circuit enabled measurement of PD pulses on the front and tail of the impulse voltage. The observed main discharges and reverse discharges are consistent with similar results in the literature. The role of PD generated space charge in the cavity in influencing discharges, subsequent discharges on the tail of the impulse voltage is evident in the obtained results.

Balanced PD detection circuit is viable for characterization of cavity PD under impulse voltage. Future work will entail comparing of cavities and corona under impulse test voltage.

REFERENCES

[1] Z. Sun, X. Zhao, J. L, Yanming L.I. Experiment Investigation of Partial Discharges under Impulse Voltage. IEEE 9th International Conference on the Properties and Applications of Dielectric Materials, 19-23 July 2009, pp 525-529.

[2] Wadhwa C.L. High Voltage Engineering. New Age International (P) Ltd., Publishers, New Techno Press, third edition, 2010.

[3] G. Mitra., M.M. Sakr, B. Salvage. Detection and measurement of discharges in gaseous cavities in solid dielectrics under impulse voltage conditions. Proc. IEE, Conference on Dielectric and Insulating Materials, Vol 112, No 5, May 1965, pp 1056-1060.

[4] V.R. Garcia-Colon. Partial Discharge Measurement During Impulse Testing. IEEE Conference on Electrical Insulation & Dielectric Phenomena, October 2014

[5] J. Wu, P.V.M. Van Nes, A.R. Mor, J.J. Smit. Partial Discharges in XLPE Insulated Cable under Superimposed Transient Voltages. Electrical Insulation Conference (EIC), 16-19 June 2019, pp 221-225.

[6] J. Wu, A. Rodrigo Mor, P. Van Nes, J.J. Smit. Measuring method for partial discharge in a high voltage cable system subjected to impulse and superimposed voltage under laboratory. Electrical Power and Energy Systems 115 (2020) 105489.2019.

[7] P. H. F. Morshuis. Partial discharges mechanisms. PhD thesis, Delft University of Technology, 1993.

[8] G. Callender, P. L. Lewin. Modeling Partial Discharge Phenomena. IEEE Electrical Insulation Magazine, University of Southampton, Vol 36, No 2, March/April, pp 29-36.

[9] Y. Hasegawa, Y. Ohki, K. Fukunaga, M. Mizuno, K. Sasaki. Complex Permittivity Spectra of Various Insulating Polymers at Ultrawide-Band Frequencies. Electrical Engineering in Japan, Vol 198, No 3, 2017 Translated from Denki Gakkai Ronbunshi, Vol. 135-A, No 2, February 2015, pp. 63–68.

[10] S. Ziad, A. Dabbak, H. A. Illias, B. C. Ang, N. A. A. Latiff, M. Z. H. Makmud. Electrical Properties of Polyethylene/Polypropylene Compounds for High-Voltage Insulation. Energies 2018, pp 1-13, www.mdpi.com/journal/energies. Accessed on 2020/08/22

[11] R.J. Densley, B. Salvage. Partial Discharges in Gaseous Cavities in Solid Dielectric Under Impulse Voltage Conditions. IEEE Transaction on Electrical Insulation, Vol EI-6, No 2, June 1971, pp 54-62.

[12] F.H. Kreuger, S Shihab. Partial discharge measurement on three-core belted power cables. IEEE Transaction on power delivery, Vol 4, No 2, April 1989, pp 927-931.

[13] N. Hayakawa, R. Yamaguchi, Y. Ukai, H. Kojima1, F. Endo, H. Okubo. Partial Discharge Activities under AC/Impulse Superimposed Voltage in LN2/Polypropylene Laminated Paper Insulation System for HTS Cables. 9th European Conference on Applied Superconductivity (EUCAS 09), Journal of Physics: Conference Series 234, 2010.

[14] L. Gang, W. Guangning, T. Demin. The System Architecture of Selective Frequency Balance Measurement for PD. Conference Record of the 2006 IEEE International Symposium on Electrical Insulation, pp 151- 154.

[15] IEC 60060-1. High-voltage test techniques Part 1: General Definitions and Test Requirements. 2010

[16] L. Gui, Y. Mi, S. Deng, L. Liu, X. Ge, W. Ouyang. Partial Discharge Characteristics of an Air Gap Defect in the EpoxyResin of a Saturable Reactor under an Exponential Decay Pulse Voltage. IET Review Copy Only, pp 1-18.

[17] L. Niemeyer. A Generalized Appraoch to Partial Discharge Modeling. IEEE Transaction on Dielectric and Electrical Insulation, Vol. 2, No. 4, August 1995.

2023 SAUPEC Conference, Johannesburg, South Africa, January 24-26, 2023

Simulation of PD Characteristics of Closely Coupled Air Cavities Using MATLAB/SIMULINK

Mathew Thekiso
Electrical Engineering, Vaal University of Technology
Vanderbijlpark, South Africa
mthekiso@vut.ac.za

Cuthbert Nyamupangedengu
Electrical Engineering, Vaal University of Technology
Vanderbijlpark, South Africa
cuthbertn@vut.ac.za

Isaac Kwabena Kyere
Electrical Engineering, Vaal University of Technology
Vanderbijlpark, South Africa
isaack@vut.ac.za

***Abstract*— Air cavities are among the common sources of partial discharge (PD) activities in insulation. PD may lead to electrical insulation degradation and breakdown. The present study is carried out to investigate PD characteristics in closely coupled double cavities compared to single cavities in solid insulation. A modified three-capacitor PD simulation model is built in MATLAB SIMULINK. The coupling of the two 1.5 mm diameter identical cavities varied between 0.01 mm and 3.5 mm and the resultant PD characteristics captured. For comparison, simulations of PD activity of a single cavity of same dimensions were also conducted under the same voltage conditions. The findings are that the double cavity partial discharge magnitudes are greater when the separation distance between the cavities gets smaller compared to a single cavity. As the coupling distance increases, the PD magnitude becomes like that of a single cavity. The total PD pulses in one cycle of the closely coupled cavities is less than double the number of pulses in a single cavity of same dimensions. These findings are interesting as they give new perspectives on understanding PD characteristics in multiple cavities.**

***Keywords*— Partial discharge, Double cavity PD**

I. Introduction

In manufacturing processes of underground power cables, it is vital that the cable is subjected to stringent tests such as dielectric strength and partial discharge (PD). Air-filled cavities in insulation material are one of the potential sources of PD activity and ultimately may cause degradation and breakdown of the insulation and complete failure of the electrical equipment [1]. A partial discharge is defined as localized electrical discharge that partially bridges the gap between conductors at different voltage and separated by insulation material [2], [3]. In most cases, such discharges appear as electrical pulses of short duration in the order of nanoseconds. There are standard physical PD measurement methods for laboratory environments and for field environments. In the study of PD phenomena, computer-based simulations are useful in validating measurements as well as further understanding the nature of PD mechanisms.

In the literature, most PD studies have been conducted ether through physical measurements or simulations using single cavities. However, PD cavity defects often occur as multiple cavities. There is therefore need for further studies to understand to what extent PD characteristics in single cavities compare with those of double and multiple cavities. In the present study, the focus is on understanding double cavities PDs focusing on how the degree of cavity coupling influences PD characteristics and how that compares with single cavity of same dimensions and under same voltage conditions.

The study is conducted through simulations using the three-capacitor PD model implemented in MATLAB SIMULINK™. The studied PD characteristics are PD magnitude, repetition rate and PD phase resolved patterns.

II. Selection of PD Cavity Parameters

In modelling PD activity, cavity (void) parameters are important [3]. PD characteristics change accordingly with the size of the void. Voids in insulation materials can be shaped cylindrical, cubical, or any other. The test object used in the simulation, illustrated in Fig. 1, comprises of polyethylene material. According to the common sizes of voids in insulation material, a spherical void with a diameter (d_1 and d_2) as in Table 1 was used in a cylindrical sample (40 mm×5 mm) in the simulation. The void is in the middle of the sample, in which the air pressure (P) is 100 kPa. The AC voltage source was applied to each sample with an amplitude of 21 kV and frequency of 50 Hz. Two plane electrodes were used to sandwich the insulation. The structure of the sample is shown in Fig. 1.

The Paschen curve is used to determine the void spark-over voltage. The values were determined to be in the range of 5 kV to 6 kV for a 1.5 mm cavity, taking the pressure in the cavity into consideration, these values can increase [4]. The simulation voltage of 5 kV across the cavity for 1.5 mm is used. The voltage greater than the simulated value would become the PD inception voltage (PDIV).

For PD to occur, the voltage needs to be equal to or greater than the PDIV and there is a need for a seed electron to be available, the latter is a stochastic time lag process [4] and is simulated as a random function in Fig. 2. A time lag occurs after the inception voltage is reached before a PD is initiated. Therefore, the PD inception voltage in practical measurements may not be exactly equal to the simulated calculated inception voltage due to the randomness of seed electrons availability.

III. Simulation Model Construction

There are various methods for simulating PD which include the three-capacitor equivalent circuit model, dipole model, Niemeyer's model, and Finite Element Analysis (FEA) model. Among the options, the three-capacitor model is the simplest and commonly used. One of the strengths in this PD modelling technique is that it requires minimum computational power. In the present study, the three-capacitor equivalent circuit is therefore adopted.

The three-capacitor equivalent circuit of the PD Model in represented in Fig. 1. C_c is the capacitance of the cavity. The capacitance of the healthy insulation above and below the cavity is (C_b). The parallel capacitor (C_a) is the capacitance of the remaining parts of the insulation. The dimensions of the test object used are as indicated in Fig. 2 and the values of the equivalent circuit elements are in Table 1.

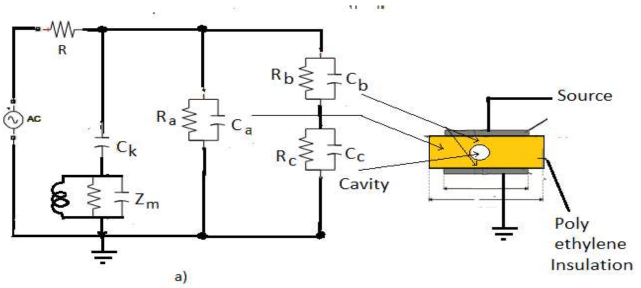

Fig. 1. Simulation model of three-capacitor for single air cavity

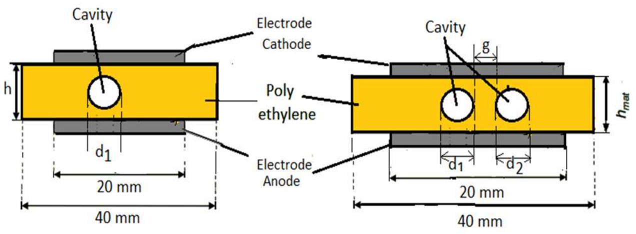

Fig. 2. Test samples material for single and double voids

The simulation of the cavity is implemented in SIMULINK™. Models in Simulink can be processed by both discrete-time and continuous-time signals in the powergui block. The discrete-time signals are a sequence of values that correspond to a particular instant in time. Sample times are defined as the time instant at which a signal occurs.

When the step solver is set for continuous-time inputs, it generates continuous-time outputs. The values vary continuously with time. Powergui is the first block to load on the simulation model page. The circuit represents the state-space equations of the model. The powergui block displays and can generate reports of steady-state voltages and currents. Other measurement parameters can be analyzed in the powergui.

In this study, the solver is ordinary differential (ODE23tb) set to use the step solver and variable-step type. The simulation time is set to stop at 1/50 with the number of minimum consecutive steps at 1. The number of consecutive zero crossings for simulation is set at 1000. The three-capacitor PD model as implemented in SIMULINK™ is presented in Fig. 3. Table 1 presents more details of the circuit components.

IV. THE SIMULATED IEC 60270 PARTIAL DISCHARGE MEASUREMENT SYSTEM

In Fig. 3 the PD measurement system is in accordance with the IEC 60270 standard. The major components in the system are the coupling capacitor (C_k), a high voltage source, wide

Table 1. Components and their settings

Component	Settings	Function
Breaker	Initial status: 0 Switching times (s): External checked Breaker resistance R_{on}(Ω): 0.01 Snubber resistance R_s (Ω): 10^{16} Other values use the default	To simulate the discharge in the cavity No discharge is 0 and discharge is 1. The switch is triggered by an external signal
AC Voltage Source	Parameters Peak amplitude (V): $21x10^3$ Phase (deg): 0 Frequency (Hz): 50 Other values use the default	To simulate the source voltage of the system with no background noise.
Parallel RLC measurement	Branch type: RLC Resistance R (Ω): 130 $x10^{-3}$ Inductance L (H): 17.60 $x10^{-3}$ Capacitance C (F): 100 $x10^{-12}$ Other values use the default	It is used for measuring the pulses that are generated by closing and opening the switch. It is a wide band filter to filter only the discharges.
Series RL Source	Branch type: RL Resistance R (Ω): 200 Inductance L (H): 0.11 $x10^{-3}$ Other values use the default	It is used to block any background noise from the source to feed into the measurement of specific partial discharge.
Series C_k	Branch type: C Capacitance C (F): 1 $x10^{-9}$ Other values use the default	A coupling capacitor to allow measurement of specific partial discharge
Single: Parallel RC $_a$	Branch type: RC Resistance R (Ω): 1831 $x10^6$ Capacitance C (F): 3.646 $x10^{-12}$ Other values use the default	To simulate the healthy part of the insulation
Single: Parallel RC $_{b1}$	Branch type: RC Resistance R (Ω): 572 $x10^6$ Capacitance C (F): 0.1139 $x10^{-12}$ Other values use the default	To simulate the insulation above and below the cavity
Single: Parallel RC $_{c1}$	Branch type: RC Resistance R (Ω): 471 $x10^6$ Capacitance C (F): 0.00417 x 10^{-12} Other values use the default	To simulate the cavity in the simulation
Single: Parallel RC $_{res1}$	Branch type: RC Resistance R (Ω): 1000 $x10^6$ Capacitance C (F): 1000 $x10^{-12}$ Other values use the default	To simulate the surface residual charge and the surface internal discharge of the cavity

band measuring impedance (Z_m), the test object, and the PD measuring instrument [5]. The gap distance between the cavities varied from 0.01 mm to 3.5 mm. Therefore, any change in the distance between the cavities results in a slight change in the value of C_a and R_a because of the slight change in insulation thickness. The cavity equivalent circuit values of C_c and R_c the insulation values of C_b and R_b are not affected by variations in the distance between the two identical cavities.

In the model, equivalent capacitances are determined using (1) to (4). Equivalent resistances are determined using (5) to (8).

$$C_a = \frac{\varepsilon_0\, \varepsilon_r\, (A_{ins} - A_{cav})}{h} \tag{1}$$

$$C_b = \frac{\varepsilon_0\, \varepsilon_r\, A_{cav}}{h-d} \tag{2}$$

$$C_c = \frac{\varepsilon_0\, A_{cav}}{d} \tag{3}$$

$$C_{gap} = \frac{\varepsilon_0\, \varepsilon_r\, A_{cav}}{l_{gap}} \tag{4}$$

$$R_a = \frac{\rho_m\, h}{A_{ins} - A_{cav}} \tag{5}$$

$$R_b = \frac{\rho_m\, (h-d)}{A_{cav}} \tag{6}$$

$$R_c = \frac{\rho_0\, d}{A_{cav}} \tag{7}$$

$$R_{gap} = \frac{\rho_m\, l_{gap}}{A_{cav}} \tag{8}$$

Where;

$$A_{cav} = \pi d^2 \tag{9}$$

and

$$A_{ins} = \frac{1}{4}\pi d^2 \tag{10}$$

V. THE SIMULATED RESULTS OF PD CHARACTERISTICS IN DOUBLE CAVITIES

A lot of work has been done by research on PD simulation of single void for various parameters. Other researchers in [6]-[8] have conducted some studies on multiple voids but with limited simulations [9], [10].

A PD Finite Element Analysis model has been previously used to compare PD characteristics in 1 mm diameter single and double cavities in polyethylene [11]. In the study, the influence of the coupling distance versus the electric field magnitude was investigated.

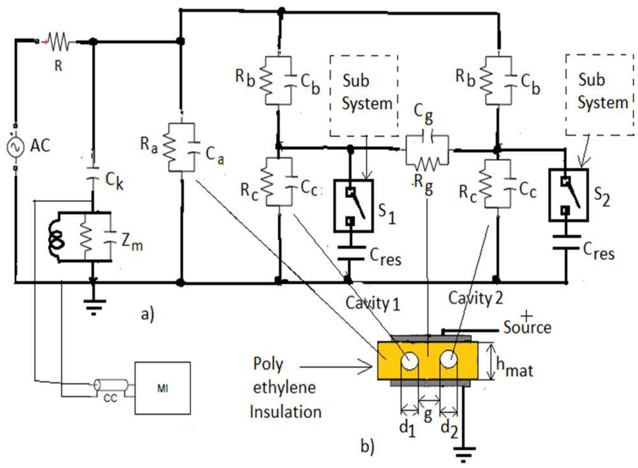

Fig. 3. A simulation model of three-capacitor circuit for double cavities

TABLE 2. CALCULATION OF VALUES

Void	Gap length (mm)	C_a (pC)	C_b (pC)	C_c (pC)	R_a (Ω)	R_b(Ω)	R_c(Ω)	C_{gap} (pC)	R_{gap}(Ω)
Single		1.237	0.02	0.041	1.610×10^{13}	9.903×10^{14}	2.122×10^{13}		
Double	0.01	1.222	0.02	0.041	1.628×10^{13}	9.903×10^{14}	2.122×10^{13}	7.038	2.829×10^{13}
	0.10	1.222	0.02	0.041	1.628×10^{13}	9.903×10^{14}	2.122×10^{13}	0.704	2.829×10^{14}
	0.70	1.222	0.02	0.041	1.628×10^{13}	9.903×10^{14}	2.122×10^{13}	0.101	1.981×10^{15}
	1.50	1.222	0.02	0.041	1.628×10^{13}	9.903×10^{14}	2.122×10^{13}	0.047	4.244×10^{15}
	3.00	1.222	0.02	0.041	1.628×10^{13}	9.903×10^{14}	2.122×10^{13}	0.024	8.488×10^{15}
	3.50	1.222	0.02	0.041	1.628×10^{13}	9.903×10^{14}	2.122×10^{13}	0.021	9.903×10^{15}

The resistivity, ρ_o, of air is take as 10^{10}, resistivity, ρ_m, of polyethylene to be approximately 10^{12}, permittivity of free space, ε_0, is 8.85x 10^{-12} F/m, permittivity of polyethylene, ε_r, is 2.25, the thickness of the insulation, h, is 5 mm, and the diameter of the insulation between the electrodes is 20 mm. The area of the insulation between the electrodes, A_{ins} = 3.142 x 10^{-4} mm^2, which stays the same for single cavity and double cavities. The diameter of the single cavity is d_1 =1.5 mm and for double cavities d_1 =d_2 = 1.5 mm, where the spherical area is A_{cav} =7.069 x 10^{-6} mm^2. The calculated values using (1) to (8) are in Table 2.

The 50 Hz high voltage supply with a peak value of 21 kV is used in the model in Fig 3. The switch (S_1) simulates the spark-over of the air gap at the set time. The switch is set to close and open simulating cavity spark-over.

When a high voltage supply is applied to the circuit model, the cavity gets charged and when seed electron appears in the cavity, breakdown occurs and that is partial discharge.

It was concluded that the electric field strength within the cavity is inversely proportional to the gap between cavities. For cavity separation of less than 3.5 mm, the electric field magnitudes within cavities influence each other and in turn the PD characteristics. In that regard, the PD magnitudes and repetition rates were found to be higher in the double cavity than in the single cavity [11]. This phenomenon was explained using the effect of the enhanced electric field on PD mechanisms [11]. However, the said study did not include the dynamics of the electric field in the two cavities during a PD event.

Using the simulation of single void, the authors modified the single void model to study the discharge characteristics of double voids. Fig 3 shows the inclusion of the second void in the simulation model.

The resultant PD pulses in double cavities is shown in Fig. 5. The PD pattern indicates that the PD pulses are more frequent in the double cavity as compared to a single cavity as indicated in Fig. 4 and Fig. 5. Fig. 6 indicates that double cavity has higher PD magnitude than single cavity. In Fig. 8, as the cavity separation distance increases, the PD magnitude reduces and becomes of the same order of magnitude. Beyond 3 mm, the PD magnitude in double cavities become like that in single cavity.

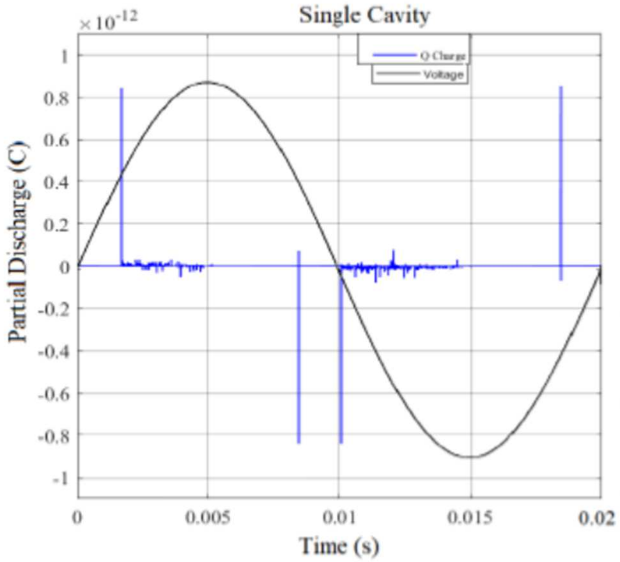

Fig. 4. Simulated PD pulses in a single cavity

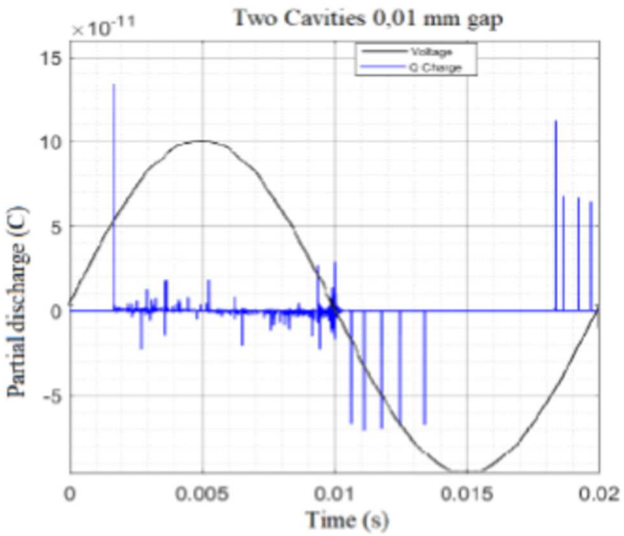

Fig. 5. Simulated PD pulses in double closely coupled cavities.

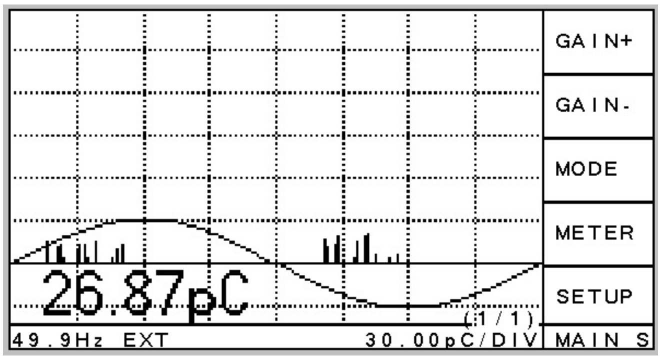

Fig. 6. Physically measured PD pulses in a single cavity

To validate the PD simulation results, a physical measurement setup was implemented for a single cavity like the simulated setup. Each sample of practical experiment is calibrated at 20 pC to suppress the background noise level. The pulse pattern in Fig. 6 is as measured at PD inception voltage. For the closely coupled double cavities (at 0.01 mm separation), the obtained physical measurement results are as shown in Fig. 7. The simulation results are like the physical measurement results, and this gives confidence in the efficacy of the model in simulating the behavior of partial discharges.

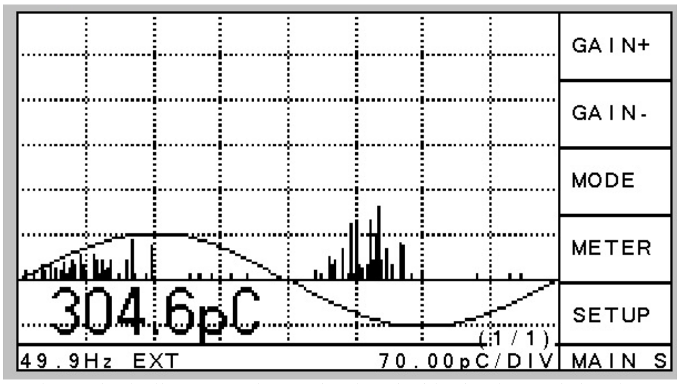

Fig. 7. Physically measured PD pulses in a double closely coupled cavity

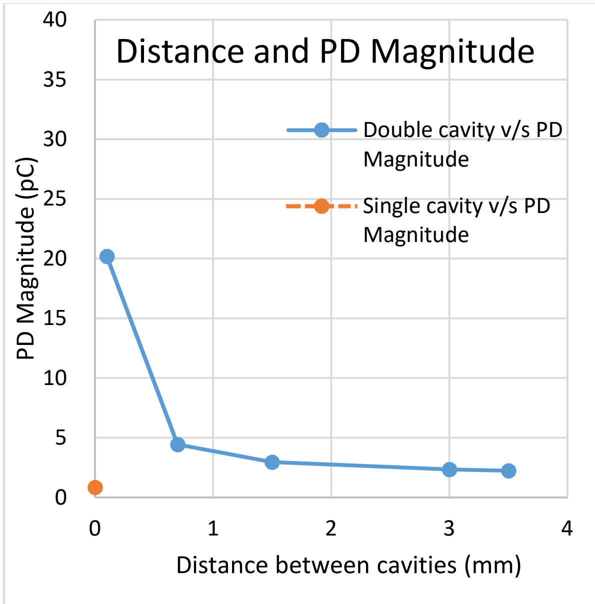

Fig. 8. PD magnitude simulation for double cavities and a single cavity.

VI. EFFECT OF COUPLING DISTANCE ON PD MAGNITUDE IN DOUBLE CAVITIES

With reference to Fig. 8, the closer the cavities are, the bigger the PD magnitude becomes. As the distance between the two cavities increases, the resultant PD pulse magnitude becomes like those of a single cavity. This behaviour can be explained by monitoring the changes in the capacitor that represents the coupling between two cavities and how the voltage across this capacitor influences the voltage in the cavity as the neighbouring cavity is discharging. With reference to the modified three-capacitor equivalent circuit model of the double cavity test setup, the following occurs during the sequence of PD events:

a) Before any of the two cavities discharge, the electric fields inside the two cavities are equal.

b) Due to statistical time-lag differences of seed electron availability in the cavities one cavity discharges first. Let be this be cavity 1.

c) As the cavity discharges in the model, this is represented by the closing of the switch S_1.

d) C_{ref} charge up thereby establishing V_{ins} across the cavity 1.

e) The resultant voltage in undischarged cavity 2 becomes the same as that of the series-connected capacitor C_{res} (1) and C_k. In other words, the voltage across the second cavity increases by V_{res} resulting in an increased electric field in cavity 2.

f) When the seed electron becomes available in cavity 2, the discharge occurs under a higher electric field than if it was a single cavity. The resultant charge magnitude is bigger than in a single cavity. Meanwhile cavity 1 extinguishes and sequence repeat.

g) As the cavities get more closer, C_g increases with increased charge and voltage thereby further increasing the resultant PD magnitude and this explains the trend in Fig. 8.

VII. CONCLUSION

Characterization of PD in a single cavity and closely coupled double cavities were analysed. The analysis of the circuit was done using SIMULINK™. The simulation and practical values correlate in that the closer the double cavities are, the bigger the discharge. As the distance between the two cavities increases, the resultant PD pulse magnitude becomes like those of a single cavity. The PD repetitive rate for closely coupled cavities is higher being the results of simulation and validated through physical measurements. Future work includes monitoring the time to failure and PD characteristics evolution as a function of time from inception to complete failure for closely coupled double cavity defects in comparison with single cavities.

REFERENCES

[1] C. Pan, G. Chen, J. Tang and K. Wu, "Numerical modeling of partial discharge in a solid dielectric-bounded cavity: A review," *IEEE Transactions on Dielectric and Electrical Insulation*, vol. 26, no 3 pp. 981 -1000, 2019.

[2] I Kyere, C. Nyamupangedengu and J. Walker, "Partial Discharge Magnitude with Voltage in Single and Double Cavity," in *2020 International SAUPEC/RobMech/PRASA Conference*, Cape Town, South Africa, 2020.

[3] SANS, "SANS 60270: High voltage test techniques - partial discharge measurement," South African National Standards, Pretoria, 2000.

[4] E. Kuffel, W. Zaengl and J. Kuffel, "Non-destructive insulation test: Partial-discharge measurements," in *High Voltage Engineering Fundamental: Second Edition*, Oxford: Butterworth-Heinemann, 2000, pp. 421-422.

[5] T. Venge and C. Nyamupangedengu, "Influence of Supply Voltage Frequency on Cavity Partial Discharge Parameters: Simulation Results," *2020 Southern African Universities Power Engineering Conference/Robotics and Mechatronics/Pattern Recognition Association of South Africa (International SAUPEC/RobMech/PRASA)*, Cape Town, South Africa, 2020.

[6] S.I. Jeon, D.S Shin, D.H. Yun, K. M. Han and M. Han, "A study on the partial discharge characteristics according to the distribution pattern of voids within insulation" in *Proceedings of 1995 IEEE 5th International Conference on Conduction and Breakdown in Solid Dielectrics, Leicester*, UK,1995.

[7] G.C. Crichton, P.W. Kalsson and A. Pederson. "Partial Discharge in Ellipsoidal and Spheroidal Voids". *IEEE Transactions on Electrical Insulation,* Vol.24, No.2, pp.335-340, 1989.

[8] P.Y. Chia, A.C. Liew. "Novel approach to partial discharge signals modeling in dielectric insulation void using extension of lumped capacitance model" in *Proceedings of PowerCon 2000, International Conference on Power System Technology*, Perth, Australia, 2000.

[9] C. Forssen and H. Edin, "Modeling of a discharging cavity in a dielectric material exposed to high electric fields," in *Proceeding of COMSOL, Multiphysics User's Conference*, Stockholm, Sweden, 2005.

[10] C. Y.Ren, Y.H. Cheng, P Yan, Y.H. Sun and T. Shao. "Simulation of Partial Discharges in Single and Double Voids Using SIMULINK" in *Proceedings of the 2006 Twenty-Seventh International Power Modulator Symposium, Arlington*, USA, May 2006.

[11] M. Hlongwane, R.K Links and C Nyamupangedengu, "Characterising Double Cavity Partial Discharges", in *2021 Southern African Universities Power Engineering Conference/Robotics and Mechatronics/Pattern Recognition Association of South Africa (SAUPEC/RobMech/PRASA)*, Potchefstroom, South Africa, 2021.

Test Voltage Frequency Effects on Electric Field Profiles in MV Cable Joints

Bishen Sukdev
School of Electrical and Information Engineering
University of Witwatersrand
Johannesburg, South Africa
bishensukdev@gmail.com

Cuthbert Nyamupangedengu
School of Electrical and Information Engineering
University of Witwatersrand
Johannesburg, South Africa
cuthbert.nyamupangedengu@wits.ac.za

***Abstract*— On-site testing of cable systems is performed to verify the components' integrity and the installation work's quality. Although power cable systems operate at 50 Hz power frequency, they are commonly tested using 0.1 Hz Very Low Frequency (VLF) during on-site commissioning. In that regard, there is a knowledge gap in understanding how electric field stress distribution behaviour within Medium Voltage (MV) power cable systems varies under these 0.1 Hz VLF test conditions. This knowledge gap compromises the reliability of power cable accessories tests. Thus, this study aimed to identify the extent electric stress distribution is affected by variations in test voltage frequency. Finite Element Method (FEM) simulation models of an MV Joint were developed and analysed to compare 50 Hz power frequency to the 0.1 Hz VLF test condition. An equivalent resistance and capacitance (RC) circuit model was developed to validate and interpret the obtained simulation results within the cable joint. It has been confirmed that a change in voltage frequency from 50 Hz to 0.1 Hz causes changes in the electric field profile in the accessories. Questions arise on the efficacy of VLF tests on shielded power cables in comparison with 50 Hz tests.**

***Keywords*— 0.1 Hz VLF, Electric Field Stress, MV XLPE, Power Cable Joint, FEM, Modelling, Permittivity, Conductivity**

I. INTRODUCTION

Electrical distribution systems form part of the electric power grid network and are generally comprised of overhead lines and shielded electrical cable systems. Due to space limitations and environmental imperatives, shielded electrical cable systems are the preferred technology in urban areas [1].

The critical components of these cable systems are the insulated power cables and cable accessories, which are cable joints and cable terminations. Most faults in power cables occur in the cable accessories such that the latter is often referred to as the weakest link in a power cable system. Although some of the problems are attributed to poor workmanship, flaws in the stress control design are a possible source of reliability problems of power cable accessories.

It is now standard practice to perform on-site testing of the cable system to verify the integrity of components and the quality of installation work performed by the installers. Power cable systems are predominantly capacitive and are commonly tested using 0.1 Hz Very Low Frequency (VLF) test voltage waveforms during on-site commissioning. This is as VLF testing benefits from a reduced reactive power requirement, resulting in the reduced size and weight of the test equipment on-site [2] [3]. The effect of this 0.1 Hz VLF test frequency on the electric field stress distribution within the Medium Voltage (MV) cable and accessories compared to the normal operating conditions of 50 Hz power frequency is an area that still needs to be understood.

It is essential to understand this behaviour as, during testing, improperly controlled stress can lead to premature failure mechanisms such as Partial Discharge (PD) and early system failure in the case of high peak stresses, reducing the reliability of distribution systems. On the other hand, in the case of low stresses during testing, it could be the case that cable systems are not stressed sufficiently to detect manufacturing and installation defects.

In that regard, there is a problem with understanding how electric field stress distribution behaviour within MV power cable systems varies under VLF test conditions versus operating conditions. Therefore the contribution of this paper is to identify the extent the electric field stress distribution is affected by variations in the test voltage frequency within power cable joint structures.

The study's findings show that the change of test voltage frequency from 50 Hz to 0.1 Hz causes corresponding changes in the electric field profile in the accessories. The changes are such that the stress at 0.1 Hz is less than at 50 Hz. Therefore, the implication of testing cable systems at 0.1 Hz is that it does not subject the cable accessory to normal operating conditions.

II. FACTORS INFLUENCING ELECTRIC FIELD DISTRIBUTION IN MV CABLE JOINTS

Electrical Field Stress Distribution (EFSD) within MV AC cables and accessories depends on the permittivity and conductivity of the insulation material, the geometry structure, and the applied voltage [4], among other factors.

Electric field distribution in AC cables and accessories highly depends on the material's permittivity (ε_r). For AC voltage, at a bound of two adjacent materials of different permittivities (ε_1 & ε_2), the electric field strength lines (E_1 & E_2) experience refraction as governed by the relationship $\varepsilon_1 E_1 = \varepsilon_2 E_2$. The stress will be more significant in the lower permittivity material [5].

On the other hand, the electrical field distribution under DC conditions is mainly governed by the material's electrical conductivity (σ). Electrical conductivity strongly depends on temperature and electric field strength [6], resulting in the strong temperature dependence of electric field within DC cable systems. The above relationships are confirmed by Walker & Wolmarans [7] [8]; in the context of using VLF test voltage, the electric field distribution shows a dependence on both permittivity and conductivity. Thus, both permittivity and conductivity variances within the dielectrics of the cable accessories impact the electric field distribution. Consequently, that which affects permittivity and conductivity, in turn, affects the stress distribution, which can be the case with the test voltage frequency.

III. SIMULATION METHODOLOGY

The procedure in executing this work comprised of Finite Element Method (FEM) model development of the MV cable joint and simulation was performed to compare the electric field behaviour results of 50 Hz power frequency to 0.1 Hz test voltage frequency. A simplified equivalent circuit model was developed to validate the FEM results and identify the general principle for the manifested response. The model analysed the voltage response behaviour and corresponding electric stress across the cable joint material components.

A. Model Development

The simulated cable joint is a heat shrinkable single core cross-linked polyethylene (XLPE) straight joint, suited to a single core 300 mm^2 aluminium conductor, XLPE insulated, copper tape screened, PVC sheathed Type B 19/33 kV MV power cable compliant with SANS 1339. The components of the joint accessory are described in Fig. 1.

The model geometry was drafted to scale using AutoCAD® design software and was imported into the FEM simulation platform COMSOL Multiphysics®. The AC/DC module is well suited to perform the electrostatics analysis using the Electric Currents (EC) physics interface to perform frequency-domain studies.

B. Simulation Model Material Properties

The material properties used for the FEM model are summarised in Table I. The data was collected from a wide range of literature and manufacturer data sheets [10]-[17]. Where exact material specifications were not obtainable, reasonable approximations were made in line with these past studies [18]-[23].

The data in Table I shows an increase in permittivity in the semi-conductive and accessory dielectric materials when the frequency is reduced from 50 Hz to 0.1 Hz. This increase is due to polarization mechanisms such as dipole effects which contribute to dielectric losses at lower frequencies. It is noted that the cable XLPE insulation properties are not significantly affected by the changes in frequency. The accessory materials that make up the joint's layered interfaces are more susceptible to changes in frequency.

C. Simulation Parameters

The model is simulated with adjusted material properties for the respective frequencies at the same voltage U_0 = 19 kV (RMS)/ 26.87 kV (peak). The material properties of the relative permittivity are frequency adjusted and applied as defined in columns 4 and 5 of Table I.

IV. SIMULATION RESULTS: JOINT ACCESSORY STRESS PROFILES AT 50 HZ AND 0.1 HZ (VLF)

The electrical stress magnitude and distribution characteristics are essential to understanding the cable system interface and failure mechanism behaviour [13]. The stress magnitude influence failure mechanisms such as the inception of partial discharges. Stress distribution affects the interface electrical treeing behaviour. The results of the FEM simulation identified a peak electric field of 4.35 kV/mm that occurs in the XLPE insulation adjacent to the conductor in the cable region for both 50 Hz and 0.1 Hz VLF. Regarding the electric field intensity maps of Fig. 2, there is a noticeable difference in the field patterns for 50 Hz compared to 0.1 Hz VLF. The field map shows a decrease in field stress in the cable XLPE insulation and an increase in field stress in the

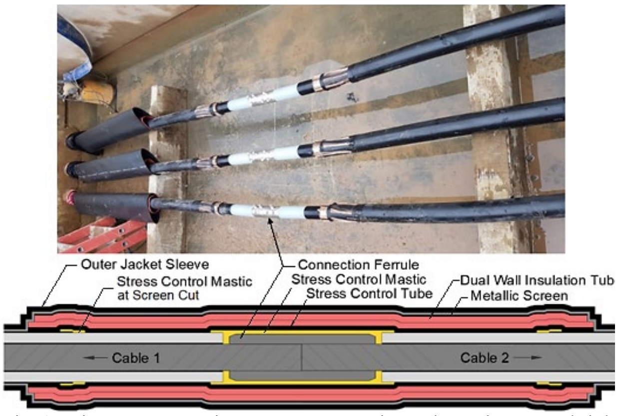

Fig. 1. Joint Accessory Picture & Cross Section Schematic, Heat-Shrink Single Core Straight Joint [9]

joint material components for the 50 Hz condition. The 0.1 Hz condition shows a greater magnitude of field stress contained within the cable XLPE insulation leading to the connection ferrule.

With reference to Fig. 3, it is noted that the electric field stress profile following the edge of the XLPE/Stress Control Tube (SCT)/mastic surface is uniform along the shielded co-axial cable length. There is, however, a spike at the screen cut position at 280 mm. The peak electric field at the 50 Hz power frequency test condition is 55 % greater than the 0.1 Hz VLF electric field peak. The 0.1 Hz VLF waveform along the SCT region is reasonably uniform and maintains a magnitude similar to that of the screened XLPE/SCT cable region. At the central connection ferrule/mastic region, the field drops significantly for the 0.1 Hz condition to 0.2 kV/mm, while the field at 50 Hz is 160 % greater within this region. Therefore, for the same voltage magnitude, the electric field profiles in the joint are different for 50 Hz and 0.1 Hz.

Fig. 4 (a) Position 2 shows the electric field at the screen cut position. The 0.1 Hz VLF condition has a reduced peak at the XLPE-mastic interface compared to the 50 Hz condition. Also noticeable is the greater electric field strength in the mastic, SCT, and joint insulation regions for the 50 Hz waveform. Fig. 4 (b) shows the field profile at Position 3, located at the overlap of the joint on the cable insulation. The electric field within the XLPE region at 0.1 Hz VLF is 27 %

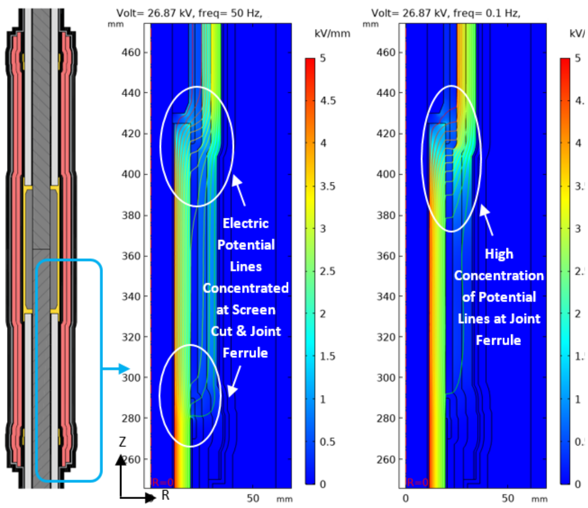

Fig. 2. Joint Electric Field Intensity Map at 50 Hz Frequency (left) and 0.1 Hz VLF (right) with the conductor at U_0 = 26.87 kV

TABLE I: MATERIAL PROPERTIES USED WITHIN FEM JOINT MODEL [10] - [23]

Component	Material	Permittivity ε_r @ 50 Hz	Permittivity ε_r @ 0.1 Hz	Conductivity σ [S/m]
Air	Air	1	1	1.0×10^{-14}
Cable Conductor	Aluminium EC1350	1	1	3.57×10^{7}
Conductor Screen	XLPE with Carbon Black	$5 \times 10^{3} + i3 \times 10^{8}$	$2 \times 10^{5} + i1 \times 10^{10}$	<1
Cable Insulation	XLPE	$2.3 + i1 \times 10^{-3}$	$2.3 + i1 \times 10^{-2}$	1.0×10^{-15}
Core Screen	XLPE with Carbon Black	$1 \times 10^{5} + i1 \times 10^{9}$	$1 \times 10^{7} + i5 \times 10^{10}$	<1
Cable Metallic Screen	Copper	1	1	5.80×10^{7}
Cable Outer Jacket	PVC	6	6	7.58×10^{-12}
Connection Ferrule	Aluminium Alloy, Tin Plated	1	1	2.95×10^{7}
Stress Control Tube (SCT)	Cross Linked Polyolefin	25	30	1.0×10^{-9}
Stress Control Mastic	Polyolefin with chemical additives	25	30	1.0×10^{-9}
Heat-shrink Insulation Tube	Cross Linked Polyolefin	$5.5 + i0.13$	$10 + i1.5$	1.0×10^{-14}
Dual wall Ins. Tube	Cross Linked Polyolefin	$3 + i0.13$	$10 + i1.5$	1.0×10^{-14}
Dual wall Ins. Tube Screen	XLPO with Carbon Black	$1 \times 10^{5} + i1 \times 10^{9}$	$1 \times 10^{7} + i5 \times 10^{10}$	<1
Outer Jacket Heat-shrink Sleeve	Cross Linked Polyolefin	$< 5 + i0.13$	$10 + i1.5$	1.0×10^{-13}

greater than that of the 50 Hz conditions. However, the peak electric field magnitude within the joint insulation is 230 % greater in the 50 Hz power frequency condition. Fig. 4 (c) shows the field at Position 4 at the centre of the joint, where it is noted once more that the electric field in the mastic, SCT, and joint insulation regions is more significant for the 50 Hz waveform than the 0.1 Hz condition.

To summarise the results from the FEM simulations, the change of voltage frequency from 50 Hz to 0.1 Hz causes changes in the electric field profile in the accessories. These notable differences in behaviour are apparent and are likely due to the increased layered interfaces in the form of stress control and dielectric material used in the joint design. In order to stress to the same level at the joint's critical parts, the VLF's applied voltage magnitude must be increased. This increased stress level on VLF is required to reach breakdown conditions equivalent to the 50 Hz power frequency test condition [24]. This concept relates well with the literature in which, from experience described in work done by CIGRE [25], testing breakdown at VLF conditions typically occurs at 1 to 4 times higher voltage than 50 Hz. The cause of the differences in the electric stress profile at 50 Hz compared to 0.1 Hz can be explained in terms of the equivalent circuit model of the joint, as presented in the next section.

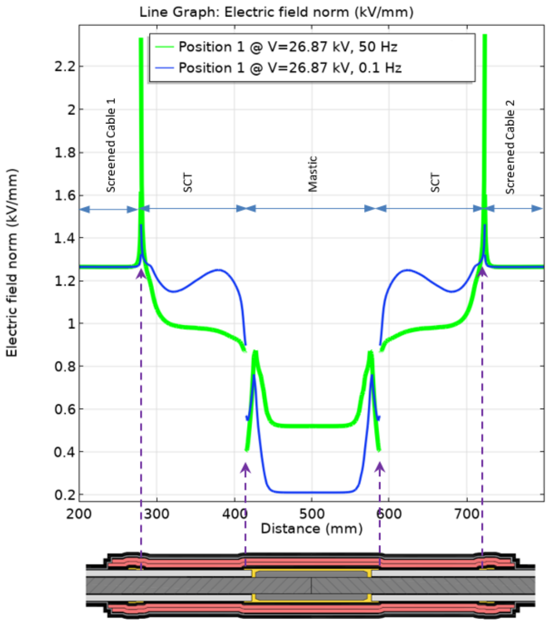

Fig. 3. Electric Field longitudinally along the XLPE/SCT/mastic surface for 50 Hz vs 0.1 Hz with the conductor at $U_0 = 26.87$ kV

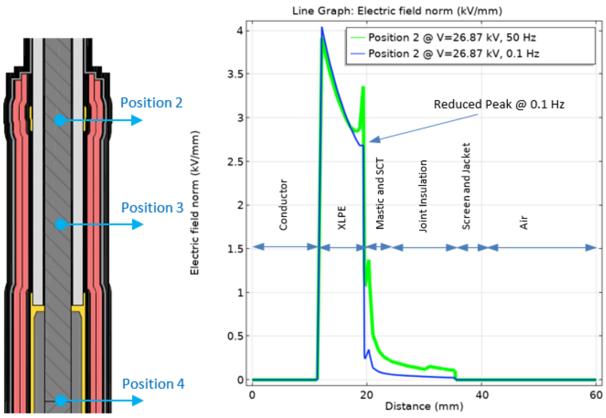

(a) Electric Field at Position 2

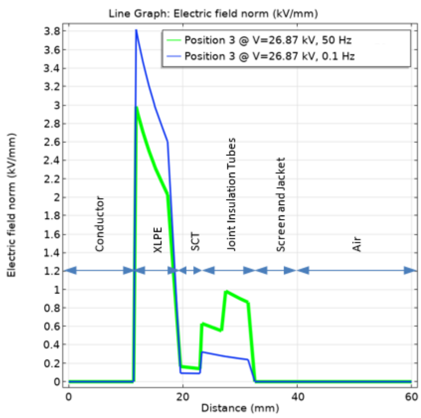

(b) Electric Field at Position 3

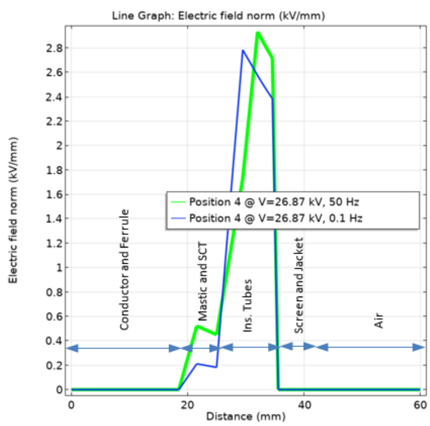

(c) Electric Field at Position 4

Fig. 4. Electric Field at Positions 2 - 4 radially outward from conductor centre for 50 Hz vs 0.1 Hz Conditions with the conductor at $U_0 = 26.87$ kV

V. Frequency-Dependent Equivalent Resistance & Capacitance (RC) Circuit Model of the MV Joint

The model proposed in this section is developed to analyse the theoretical behaviour expected within the elemental components of the screened cable joint. The model is developed to validate the results obtained from the FEM simulation by assessing the behaviour of the equivalent model at 50 Hz and 0.1 Hz.

A. Electric Field Distribution Theory

At DC voltage, electric field distribution within dielectrics is determined primarily by the conduction current J_c, given in (1) [26]:

$$J_c = \sigma \cdot E \tag{1}$$

Where σ is the electric conductivity and E is the electric field. This conduction field is time-invariant; thus, DC electric fields are classified as stationary or steady-state stress. Power frequency and very low frequency AC voltage electric fields may be classified as quasi-stationary/quasi-static fields as these vary slowly with time. The components of conduction current J_c and displacement (polarization) current J_d influence the resultant electric field distribution [26]. J_d is given in (2):

$$J_d = dD/dt \tag{2}$$

A simplified equivalent circuit model may be approximated by combining the capacitance and resistance, as illustrated in Fig. 5, to cater to J_d and J_c [26]. Multiple equivalent circuits may be combined for systems made up of numerous dielectric layers (such as in a cable joint) in the form of Maxwell's Two-layer model, with a series connection of the parallel equivalent circuits.

The bulk/leakage resistance R_0 and geometric capacitance C_0 parameters of the cable joint dielectrics are calculated using (3) & (4) for simple screened coaxial constructions [27]:

$$R_0 = \frac{\ln(\frac{b}{a})}{2\pi\sigma l} \tag{3}$$

$$C_0 = \frac{2\pi\varepsilon_0\varepsilon_r l}{\ln(\frac{b}{a})} \tag{4}$$

Where σ is conductivity, ε_r is the relative permittivity, ε_0 is the permittivity of free space, l is the length, and a and b are the inner and outer radii of the dielectric.

B. Equivalent RC Circuit Model of the MV Cable Joint Accessory Implementation in MATLAB® Simulink

The cable joint circuit model is presented in Fig. 6. The RC circuit components were calculated using (3) & (4). Table II presents data for conditions considered at 50 Hz power frequency and 0.1 Hz VLF. This data is used to configure the MATLAB® Simulink models.

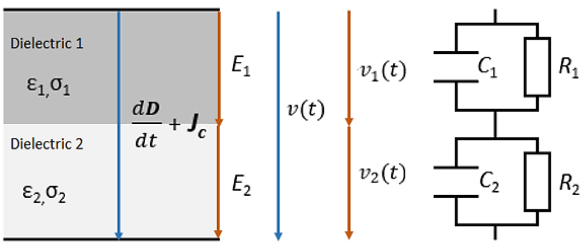

Fig. 5. Displacement & Conduction Field Equivalent Network Model [26]

TABLE II: Cable Joint Accessory RC Circuit Elements

Component	@ 50 Hz	@ 0,1 Hz
C_{isc} [F/m]	3.81×10^{-6}	1.53×10^{-4}
R_{isc} [Ω/m]	1.16×10^{-2}	1.16×10^{-2}
C_{ins} [F/m]	2.36×10^{-10}	2.36×10^{-10}
R_{ins} [Ω/m]	8.64×10^{13}	8.64×10^{13}
C_{sct} [F/m]	8.68×10^{-9}	1.04×10^{-8}
R_{sct} [Ω/m]	2.55×10^{7}	2.55×10^{7}
C_{dwt} [F/m]	8.76×10^{-10}	1.59×10^{-9}
R_{dwt} [Ω/m]	5.56×10^{12}	5.56×10^{12}
C_{tsc} [F/m]	1.84×10^{-4}	1.84×10^{-2}
R_{tsc} [Ω/m]	4.81×10^{-3}	4.81×10^{-3}

The MATLAB® Simulink model for the MV cable joint equivalent circuit is presented in Fig. 7. Source V_s is an AC voltage supply configured to match the FEM supply source of 26.87 kV at 50 Hz power frequency condition and 26.87 kV at 0.1 Hz frequency for the VLF condition.

C. Modelling Results

The voltage response over the dielectrics of the cable and joint accessory is presented in Fig. 8 for 50 Hz power frequency compared to the voltage response at 0.1 Hz VLF test voltage frequency. Voltage sensors V1 to V5 are placed across each dielectric as set up in the Simulink model, shown in Fig. 7. Voltage V1 is measured across the conductor screen, V2 across the XLPE Insulation, V3 across the stress control tube, V4 across the dual wall insulation tube, and V5 across the insulation tube screen.

The peak voltage differential V1 across the conductor screen dielectric is 17.8 µV for 50 Hz and has decreased by 99.8 % to 40.2 nV for the 0.1 Hz condition. A similar response occurred with the peak voltage differential V5 across the insulation tube screen dielectric decreasing from 7.4 µV at 50 Hz to 16.7 nV at 0.1 Hz. The potential differences across these semiconductor components are much smaller than the supply voltage of 26.87 kV and may be considered negligible.

The insulation materials had the most significant influence, with a dominant impact measured across V2 for the XLPE insulation, as indicated by Fig. 8 (a). A peak voltage differential of 20.7 kV was experienced at 50 Hz. This increased to 23.4 kV at 0.1 Hz VLF, an increase of 13 %. The graphs in Fig. 8 (b) show the stress control tube measured an 84 % decrease from 557.9 V to 87.2 V across V3, and from Fig. 8 (c), V4 also experienced a reduction of 38 % from 5.59 kV to 3.47 kV at 0.1 Hz test frequency.

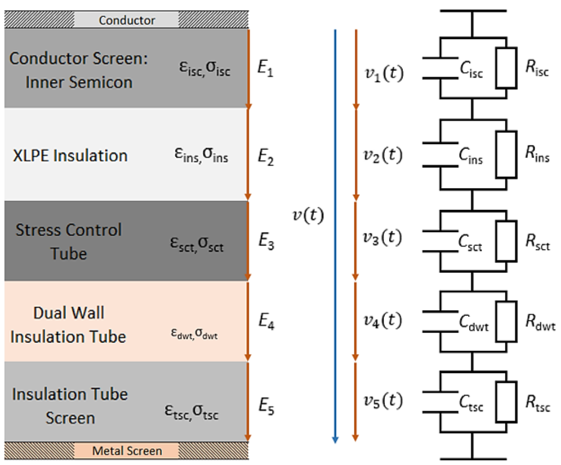

Fig. 6. Circuit Model of Cable Joint Accessory region

D. Voltage Profile across Accessory Layers Using the RC Circuit Model

The electric potential was plotted for each dielectric component in the accessory using the data drawn from the equivalent circuit implemented in MATLAB® Simulink, shown in Fig. 9. This was compared to the electric potential plot obtained from the COMSOL Multiphysics® FEM model, shown in Fig. 10. There is good agreement in the behaviour of the two models, which compare the potential across the dielectrics for 50 Hz frequency versus 0.1 Hz test voltage frequency. Comparing the electrical potential over the XLPE insulation region, there is a more significant potential difference for the 0.1 Hz condition, which corresponds to a greater electric field within this region. In the joint insulation tube region, a more significant potential difference is observed for the 50 Hz condition, resulting in a greater electric field. The difference in the graphs can be attributed to the greater accuracy of the FEM simulation solution.

VI. Results and Discussion

The results show notable differences in the magnitude of electric potential and electric field stress for the varied frequency conditions within the MV cable joint model. As was presented in the FEM study, these differences in behaviour are very apparent and are likely due to the increased layered interfaces in the form of stress control and dielectric material used in the design of the cable joint.

The XLPE insulation, SCT, and dual wall insulation tube materials are similar in magnitude of permittivity and hence capacitance, as well as in having high levels of resistivity, as presented in Table II. For this reason, the model responds with a shared effect over these three components.

Within this multi-dielectric arrangement, it is observed that field displacement takes place, whereby the lower permittivity dielectrics experience a higher electric field compared to the higher permittivity dielectrics [26]. This corresponds well with the RC behaviour model, as the capacitance is more significant for higher permittivity materials, such as the stress control tube and the dual wall insulation tube. The capacitance is smaller for lower permittivity materials, such as XLPE insulation. Thus, the smaller capacitance leads to a greater reactance that results in a more significant volt drop over the region, which results in more significant electric field stress over this component section.

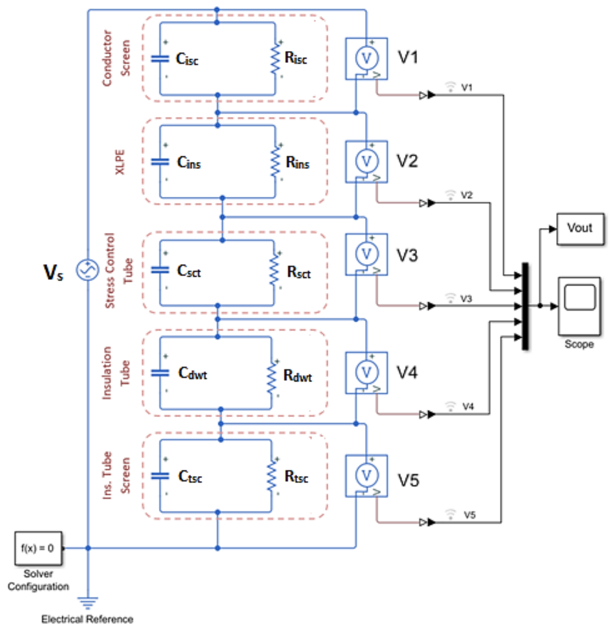

Fig. 7. MV Cable Joint Accessory modelled in MATLAB® Simulink

When investigating the frequency effects on the accessory model in Fig. 8, it was found that the potential difference measured across V2 in the XLPE insulation region increased by 13 % when the test frequency was changed from 50 Hz to 0.1 Hz. Accordingly, there was an 84 % decrease in potential difference measured across V3 in the stress control tube and a 38 % decrease across the dual wall insulation tube measured by V4. This behaviour can be attributed to the changes in permittivity of the dual wall insulation tube and stress control tube that were found to increase in magnitude under the influence of the reduced test voltage frequency. This resulted in increased capacitance components and hence a reduced reactance contribution. The XLPE insulation capacitance was unchanged, resulting in the same reactance contribution. Additionally, the reactance of all components was increased proportionally with the reduction in frequency. Thus, with this increase in impedance over the XLPE region, a more significant voltage drop occurs.

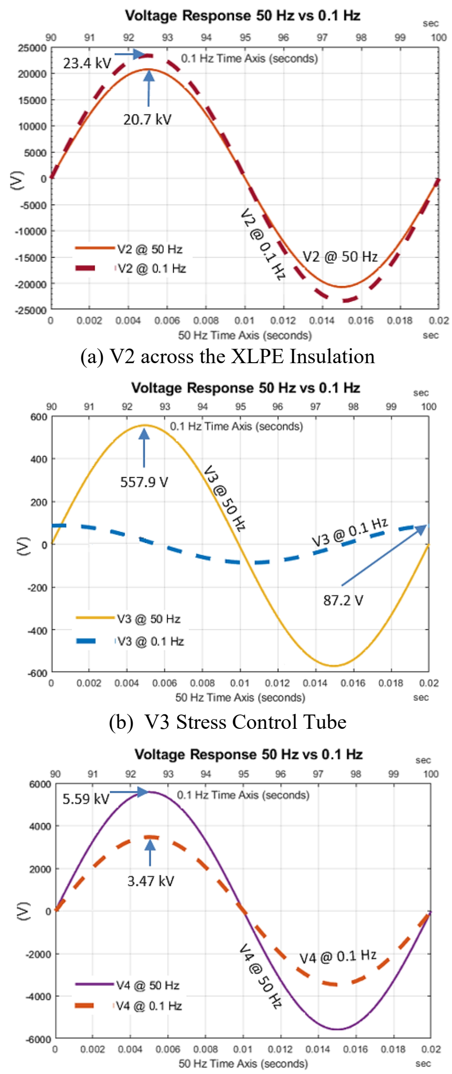

(a) V2 across the XLPE Insulation

(b) V3 Stress Control Tube

(c) V4 Insulation Tube

Fig. 8. Voltage response of dielectric components under test conditions of 50 Hz versus 0.1 Hz VLF, voltage across a) the XLPE insulation layer, b) the stress control tube, and c) the joint insulation tube layer

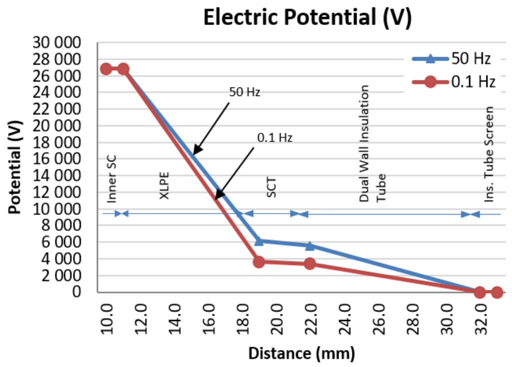

Fig. 9. Simulink Model results for Electric Potential calculated at Dielectric Components of the Joint model simulated for 50 Hz power frequency and 0.1 Hz VLF Conditions

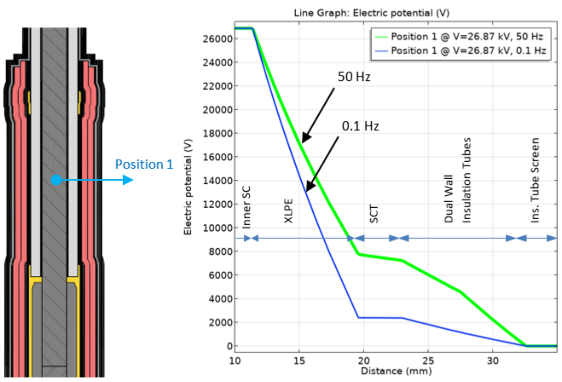

Fig. 10. COMSOL Multiphysics® Model - Electric Potential at Position 1 radially outward from conductor centre for 50 Hz and 0.1 Hz

VII. Conclusion

From this study, it can be concluded that electric stress within the accessory materials decreases with test voltage frequency. The behaviour is attributed to the changes in permittivity and conductivity of the accessory components as a function of frequency. At the same time, the electric stress within the cable insulation region is burdened with an equivalent increase in field stress, as the permittivity remains constant under these operating conditions. Thus it is justified that, in practice, a scaling factor is used when testing cable systems at VLF test voltage. The question still stands, however, whether upscaling the voltage will perfectly match the stress profiles at the two test voltage frequencies.

References

[1] BICC Cables, Electric Cables Handbook, Third Edition, G. F. Moore, Ed., Oxford: Blackwell Science Ltd., 1999.

[2] T. Venge and C. Nyamupangedengu, “Influence of Variable Frequency of the Applied Voltage on Cavity Partial Discharge Parameters: A Critical Review,” in 2019 Southern African Universities Power Engineering Conference/Robotics and Mechatronics/Pattern Recognition Association of South Africa (SAUPEC/RobMech/PRASA), Bloemfontein, South Africa, 2019.

[3] H. T. Putter, D. Götz, F. Petzold and H. Oetjen, “The evolution of VLF testing technologies over the past two decades,” in PES T&D 2012, Orlando, FL, USA, 2012.

[4] N. Raicevic, S. Ilic, S. Aleksic and R. Dimitrijevic, “Improving safety of cable networks by modeling deflectors of cable accessories,” in 4th International Conference on Power Engineering, Energy and Electrical Drives, Istanbul, Turkey, 2013.

[5] M. S. Naidu and V. Kamaraju, High Voltage Engineering Second Edition, 2nd ed., Montréal, Québec: McGraw-Hill, 1996.

[6] Y. Qin, N. Shang, M. Chi and X. Wang, “Impacts of temperature on the distribution of electric-field in HVDC cable joint,” in 2015 IEEE 11th International Conference on the Properties and Applications of Dielectric Materials (ICPADM), Sydney, NSW, Australia, 2015.

[7] J. Walker and A. Wolmarans, “Electrical stress distribution in cable accessories when testing at different frequencies,” in 2010 International Conference on High Voltage Engineering and Application, New Orleans, LA, USA, 2010.

[8] T. Joubert and J. Walker, “Influence of heat-shrink joints and terminations on Tan δ values of a medium voltage cable installation at very low frequency,” in Jicable'15 9th International Conference on Insulated Power Cables, Versailles, France, 2015.

[9] Kiltealy Electrical Services Ltd., “MV and HV Cable Jointing,” 2014. [Online]. Available: http://kiltealyelectrical.ie/services/mv-cable-jointing/. [Accessed 10 02 2022].

[10] B. S. Mitchell, “Electrical Conductivity of Selected Materials,” in An Introduction to Materials Engineering and Science: For Chemical and Materials Engineers, John Wiley & Sons, Inc., 2004, pp. 893 - 899.

[11] Leader Universal Aluminium Sdn. Bhd., “Product Specification Aluminium Rods Grade EC 1350,” Leader Universal Aluminium Sdn Bhd, Johor, Malaysia, 2015.

[12] Borealis Compounds Inc., “Product Data Sheet: Polyethylene Borlink™ LE4212, LE0595, LE0520,” Borealis group, New Jersey, United States of America, 2017.

[13] Alpha Plast (PTY)LTD, “Product Data Sheet: F2050B7 E,” ALPHA PLAST (PTY)LTD, Randhart, 2018.

[14] Nexans, “Data Sheets: Stress Grading Mastic, Heat-Shrinkable Medium Wall Insulating Tube, Heat-Shrinkable Anti-Tracking Rain Sheds,” Nexans, Paris, France, 2021.

[15] IKEBANA Engineering Limited, “Brochure: Stress Grading Mastic (SGM) Yellow Mastic, Heat Shrinkable Stress Control Tubes SCT, Semi-Conductive Tubes, Heat Shrink Insulating Tubes,” KNILL GRUPPE, Ratchaburi, Thailand, 2021.

[16] PCA Technologies, “Data Sheet: Insulation Tubing, Semi-Conductive / Insulation Double Layer Screened Insulating Composite Tubing, Stress Control Tubing, Yellow Stress Control /Void Filler Mastic,” PCA Technologies, Gujarat, 2021.

[17] WOER, “LV & MV Power cable accessories,” Shenzhen WOER Heat-Shrinkable Material CO.,LTD, Shenzhen P.R.CHINA, 2021.

[18] H. Zhou, W. Hanafusa, K. Udo, N. Hirai and Y. Ohki, “Degradation of Flame-retardant Cross-linked Polyolefin Aged by Heat and Radiation,” in 2020 IEEE International Conference on High Voltage Engineering and Application (ICHVE), Beijing, China, 2020.

[19] P. Geng, J. Song, M. Tian, Z. Lei and Y. Du, “Influence of thermal aging on AC leakage current in XLPE insulation,” AIP Advances, vol. 8, no. 2, pp. 025115: 1-16, 2018.

[20] T. Maier, K. Schmehl and T. Leibfried, “Dielectric Frequency Measurement of Semiconductive Layers in Xlpe Cables,” in 2018 IEEE Conference on Electrical Insulation and Dielectric Phenomena, Cancun, Mexico, 2018.

[21] A. Gorji, S. Banerjee and S. Jayaram, “Dielectric Characterization Study on Medium-Voltage Ethylene Propylene Rubber (EPR) and Tree-Retardant Cross-Linked Polyethylene (TR-XLPE) Cables under Varying Thermal Conditions,” in 2020 IEEE Electrical Insulation Conference (EIC), Knoxville, TN, USA, 2020.

[22] K. Zhang, L. Li, L. Zhong, L. Cao, M. Xu, G. Chen and M. Fu, “DC dielectric properties of thermo-plastic polyolefin materials,” in IEEE Conference on Electrical Insulation and Dielectric Phenomena (CEIDP), Toronto, ON, Canada, 2016.

[23] G. Lupo, C. Petrarca, L. Egiziano, V. Tucci and M. Vitelli, “Numerical evaluation of the electric field in cable terminations equipped with nonlinear grading materials,” in 998 Annual Report Conference on Electrical Insulation and Dielectric Phenomena (Cat. No.98CH36257), Atlanta, GA, USA, 1998.

[24] CIGRE Working Group B1.38, Technical Brochure 841 - After laying tests on AC and DC cable systems with new technologies, Paris, France: CIGRE, 2021.

[25] CIGRE Working Group D1.48, Technical Brochure 751 - Electrical properties of insulating materials under VLF voltage, Paris, France: CIGRE, 2018.

[26] A. Küchler, High Voltage Engineering: Fundamentals - Technology - Applications, Berlin, Germany: Springer Vieweg, 2018.

[27] S. Sulaiman, A. M. Ariffin and D. T. Kien, “Determining the Number of Parallel RC Branches in Polarization/Depolarization Current Modeling for XLPE Cable Insulation,” International Journal on Advanced Science Engineering Information Technology, vol. 7, no. 3, pp. 971-979, 2017.

Country-Wide Evaluation of the South African Lightning Detection Network Location Accuracy

Nkululeko Tanase
School of Electrical and Information Engineering
University of the Witwatersrand
Johannesburg, South Africa
2041512@students.wits.ac.za

Tumelo Manape
School of Electrical and Information Engineering
University of the Witwatersrand
Johannesburg, South Africa
2128069@students.wits.ac.za

Hugh GP Hunt
School of Eelctrical and Information Engineering
University of the Witwatersrand
Johannesburg, South Africa
hugh.hunt@wits.ac.za

***Abstract*— This paper evaluates the country-wide location accuracy of the South African lightning detection network (SALDN)between 2007 and 2019. The authors used the suggested method by Zhu et al to evaluate the South African Lightning Detection Network through a set of lightning events for a period of 12 years. For the towers used, the SALDN location accuracy median location error decreased from 304.14 m to 236.80 m after the 2010 upgrade and it decreased from 236.80 m to 158.11 m after the 2015 upgrade.**

***Keywords*— Density-bar, Elevated-density area, Location accuracy, SALDN**

I. Introduction

The South African Weather Services installed a Lightning Detection Network (LDN) in 2005 across the country and it became operational in 2006. Originally the LDN had 19 sensors to detect lightning strokes, throughout the years there have been upgrades on the LDN leading to 26 sensors as of 2021 [1]. The upgrades on the LDN include adding more sensors to the network, rearrangement of sensors, and updating the sensor software. These upgrades affect the location accuracy of the SALDN and were investigated in this paper.

This paper aims to evaluate the location accuracy of the SALDN for the period 2007 and 2019. The approach used for this evaluation is based on the algorithm suggested by Zhu et al. [2]. The fundamental theoretical assumption that underpins this algorithm is provided in the background, and further detailed in the method section.

II. Background

South Africa has the high number of cases of injuries and deaths related to lightning, therefore an LDN is important for implementing lightning protection [3]. Another application of the LDN is to check regions with a high lightning density, thus ensuring that human activities are limited or avoided in that region.

A. Assumptions

- All the lightning events in the SALDN data are cloud-to-ground events.
- The method by Zhu et al finds an elevated-density area around the towers and the lightning events on the elevated-density area are assumed to be events terminated on the tower.

III. Literature review

The SALDN uses Magnetic Direction Finding and Time of Arrival sensors which are incorporated in a method known as the Improved Accuracy from Combined Technology (IMPACT). When lightning strikes, electromagnetic radiation is generated, and the Magnetic Detection Finding sensors detect the electromagnetic radiation produced. While the Time of Arrival method compares the difference in time of arrival of the reported lightning events from individual sensors [4].

Sensors in the SALDN report lightning events with errors due to sensor calibration, electromagnetic signal propagation loss factor, placement of sensors, and inconsistent topography [2], [4], this leads to different errors in different regions. Therefore, the performance of the LDN is assessed by confirming if reported lightning events are correctly located.

Studies done by Hunt et al. [5] evaluate the performance of the network using high-speed camera photographic images relating to time stamped on the images to the SALDN data, this method is known as Time Correlating method [5], [6]. From this method, the location accuracy was determined by calculating the median distance of the location of the SALDN-reported lightning event and the location of the area which was struck by lightning. This study was only done in Johannesburg for the two towers Brixton Tower and Hillbrow tower.

Another existing solution for evaluating the LDN comprises the use of median confidence ellipses of the reported strokes. This method checks whether the location of the reported stroke is within the region of its reported confidence ellipse [5], [7]. The confidence ellipse is described as the region where there is a high chance of lightning occurrence.

The SALDN has a median location error of 500 m across the country [6]. According to [5], [6], the location accuracy of the SALDN improves as the upgrades are performed on the LDN.

IV. Method

To evaluate the country-wide location accuracy of the SALDN, the steps below are followed.

A. *Identify a sufficient number of tall structures in each province in South Africa.*

It is known that tall structures attract lightning because they create a short path for lighting to travel from the clouds to the ground by initiating Cloud to Ground lightning discharges which may be upward or downward strikes.

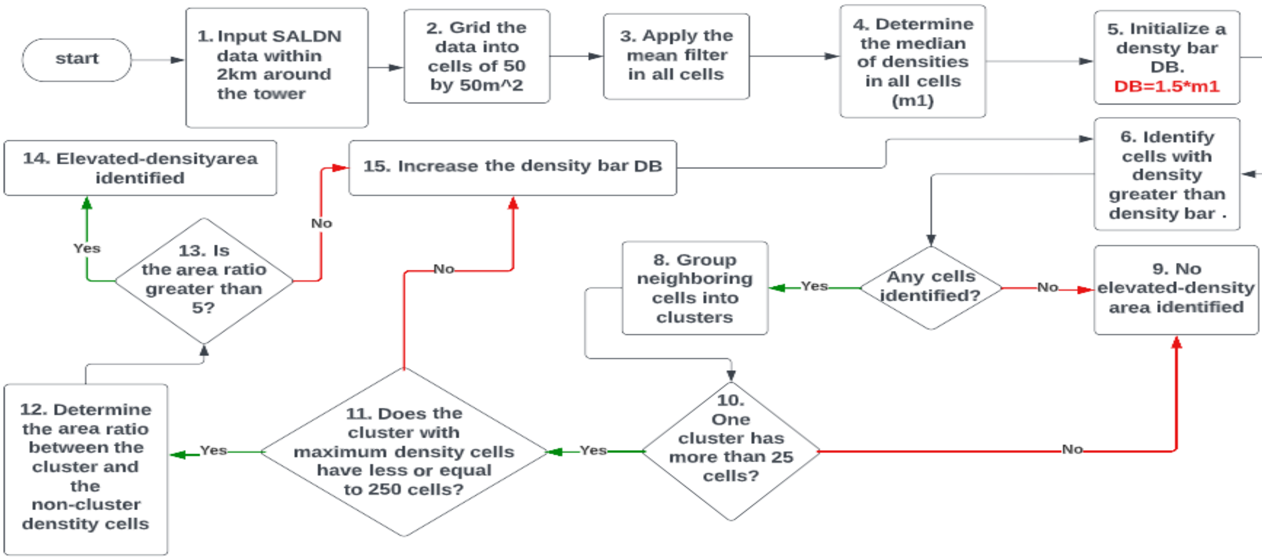

Fig. 1. Algorithm used to identify the elevated-density area [2].

The criteria used to identify tall structures are that they must be taller than any other structures within their 2 km radial distance and they must have existed between 2007-2019 period.

A total number of 33 towers were identified across South Africa and most of them are TV and radio towers. Figure 2 shows the location of the identified tall structures and SALDN sensors. The identified towers have heights above ground ranging from 140 m to 300 m.

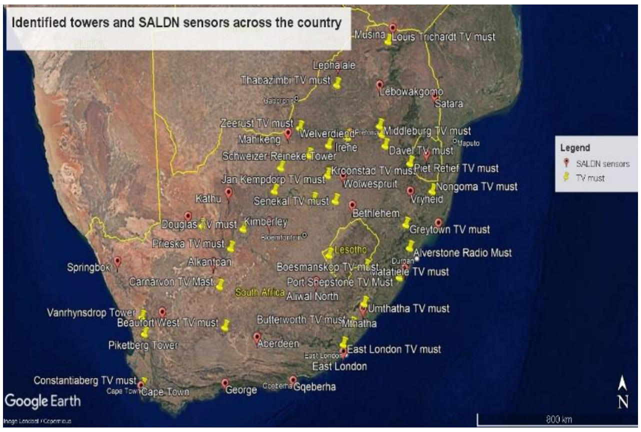

Fig. 2. Location of SALDN sensors and identified towers in South Africa.

B. Apply the methods of Zhu et al. [2] to SALDN data over a range of years to estimate the location accuracy.

The SALDN data from 2007 to 2009 was divided into three periods according to the upgrades done to the SALDN. The periods are 2007-2009, 2010-2014, and 2015-2019.

The following section describes the algorithm in figure 1 below. The step 1 is to input the SALDN data within 2 km of the tower, this step was done for each identified tower shown in figure 2.

Figure 3 shows the SALDN lightning events within 2 km of the Hillbrow tower during the 2015-2019 period.

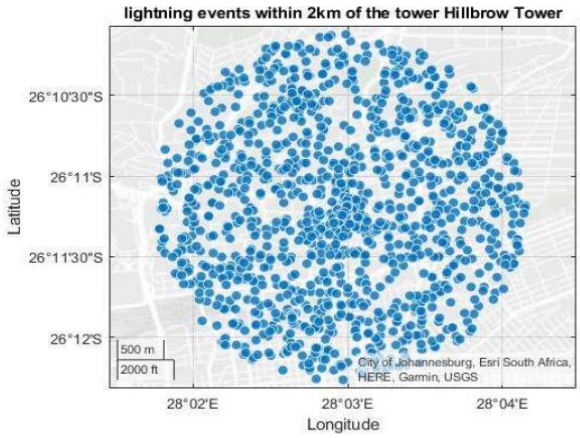

Fig. 3. Lightning events within 2km of the Hillbrow tower (26^0 11’ 32’’ S, 28^0 0’ 24’’E).

The second step is to grid the data around the tower into cells of 50x50 m^2 and count the number of lightning events in each cell. To reduce the variations in the number of lightning events in each cell, the mean filter values in each cell then become the densities in each cell. From the densities in each cell, a median value is determined (median cell density).

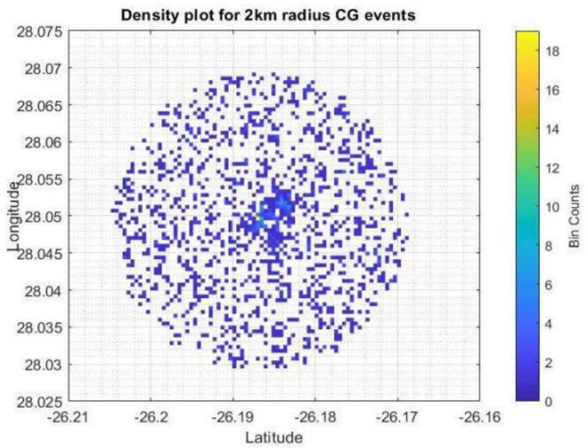

Fig. 4. Corresponding density plot of the lightning events around the Hillbrow tower.

Figure 4 shows the density plot of the Hillbrow tower after steps 1-4 of the algorithm in figure 1 have been applied. Step 5, multiply the median cell density by 1.5 to create an initial density bar.

The density bar is a threshold that filters cells with a high lightning density within 2 km of the tower.

The density bar is then subtracted from each cell density. If their difference is greater than zero, it means that the cells are greater than the density bar and are grouped into clusters, and if their difference is equal to or less than zero, then there is no elevated-density area, and these density cells become a non-cluster area [2].

In the step of grouping cells greater than the density bar into clusters, two clustering methods were investigated. The first method is K-means clustering and the second method is Hierarchical clustering.

K-means clustering

K-means cluster is a centroid-based technique that uses a looping process. Using the number of clusters known as k, this number also determines the required number of centroids. Initially, k number of centroids are selected, and objects are grouped based on the nearest centroids. Then, within each group, the Euclidean distances between the centroids and samples are calculated. Then after, new centroids are assigned and new groups are formed, the Euclidean distance is calculated again. This process repeats until there is the convergence of samples and there is no reassigning of clusters. K is determined by using the Elbow method which is determined by the data set. It is a graph that takes the shape of a human elbow, the point where its slope is no longer steep is referred to as optimal k [8], [9].

Hierarchical clustering

Hierarchical clustering is a technique that initially assumes individual objects or data sets are clusters, then the closest clusters are grouped distance between two clusters. The number of clusters is determined by a dendrogram which depends on the data set variation. A dendrogram is a representation of nested grouping links of different levels [8].

In comparing the two cluster algorithms, the median location error they produced for Sentech tower during 2015-2019 was compared with the median location error of 80.5 m obtained after the 2014 upgrade in the SALDN [1], [6]. The one with the lowest difference was used for the rest of the towers. Table 1 below shows that the K-means clustering algorithm has the lowest difference, yet close to 80.5 m, and was used.

Table 1. Comparison between the clustering algorithms' median location error for Sentech tower.

LEGEND		HIGH	LOW
Algorithm	Median location error (m)	Median location error (m) [6]	Difference
K-means clustering	70.7107	80.5	9.7893
Hierarchical clustering	111.8034	80.5	31.303

The clusters developed from the K-means clustering algorithm were checked if they contain cells greater than 25, step 10. If not, there is no elevated area in the SALDN data around the tower used. If yes, the cluster/s were further checked if the cluster containing the maximum density cell has cells less than or equal to 250. If no, the density bar was increased, and the algorithm is repeated from step 6. If yes, the area of the non-cluster area was divided by the area of the cluster area, and it was checked if it was greater than five. If no, the density bar was increased, and the algorithm was repeated from step 6. If yes, the cluster is identified as the elevated-density area [2]. Steps 10-13 from the algorithm in figure 2 ensure that enough cells are clearly shown, not less and not more.

Elevated-density area is a group of cells that are greater than the density bar and the lightning events on the cells are assumed to be terminated on the tower [2].

Figure 5 shows the clustering of the cells greater than the density bar and greater than 25 but less than 250. The position of the tower is at (40,40). The purpose of the density bar is to ensure that cells with high density stand out and that cells with low density are filtered out [2].

The other two clusters away from (40,40) in figure 5 have cells greater than the density bar but are less than 25 as a result do not qualify to be elevated-density areas.

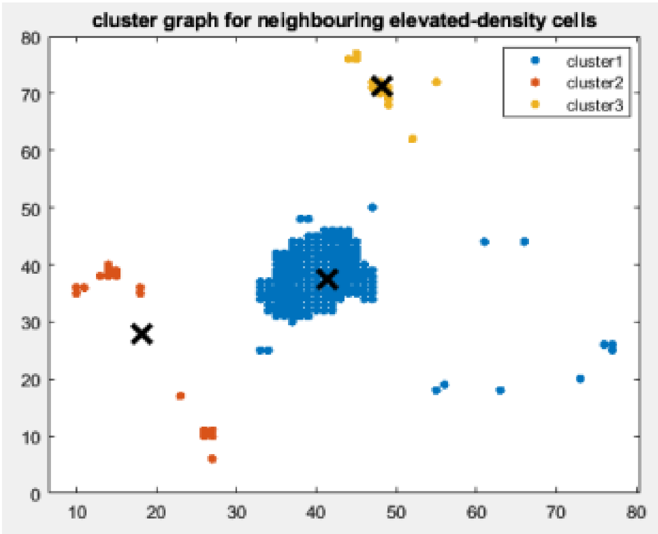

Fig. 5. Clusters of the Hillbrow tower using k-means.

Having identified the elevated-density area, the distances between the coordinates of the towers, and the coordinates of the lightning events from the SALDN data in the elevated-density area are determined. From the distance values, the median of the distance is then the median location error of the location accuracy in each tower [2], [6].

The arithmetic mean for the median location error location accuracy for the towers in each province is determined [2]. To find the national location accuracy, the arithmetic median for all the provinces is determined.

The final step is comparing the results with the self-evaluation of the SALDN median location error performance for location accuracy which is 500 m [6].

V. Results and Analysis

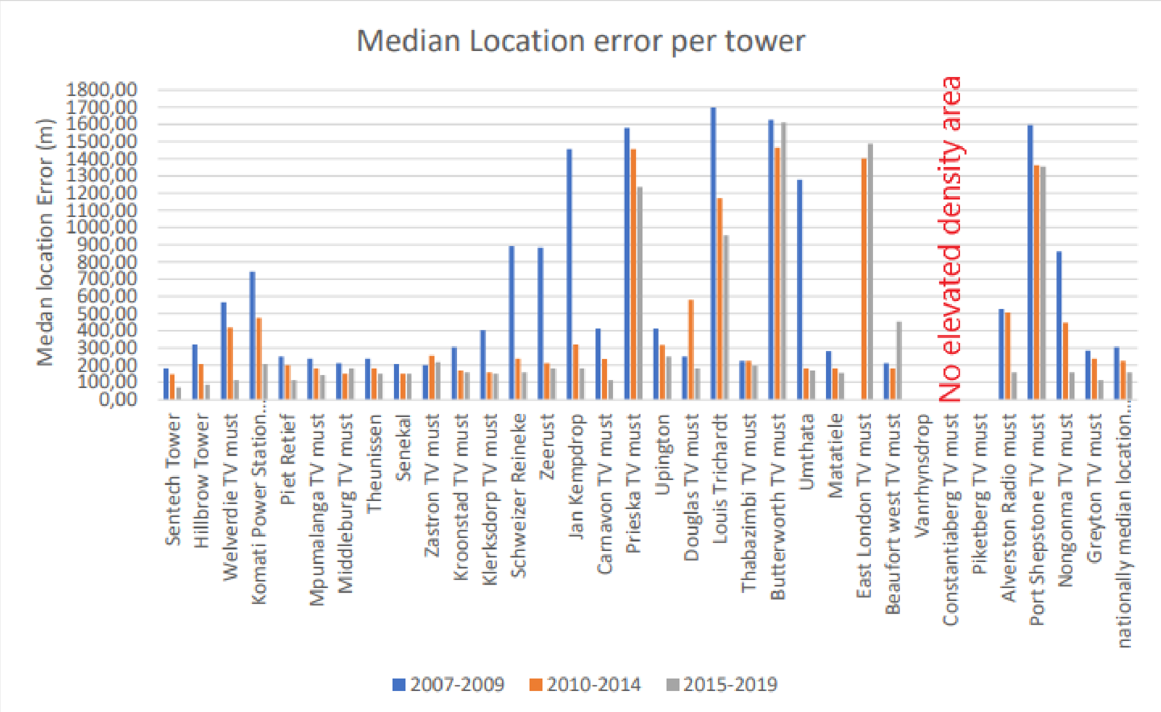

Fig. 6. Median location error for each tower per period

Table 2. Tower median location error per period.

Year period	2007-2009	2010-2014	2015-2019	Year period	2007-2009	2010-2014	2015-2019
Name of tower	**Median location error (m)**	**Median location error (m)**	**Median location error (m)**	**Name of tower**	**Median location error (m)**	**Median location error (m)**	**Median location error (m)**
Gauteng				**Limpopo**			
Sentech Tower	180.27	145.71	70.71	**Louis Trichardt**	1690	1170	955.24
Hillbrow Tower	320.15	206.15	154.05	**Thabazimbi TV mast**	223.60	223.60	169.20
Welverdiend	565.68	419.75	111.80				
Mpumalanga				**Eastern Cape**			
Komati PS	743.30	474.34	206.15	**Butterworth TV mast**	1620	1460	1610
Piet Retief TV mast	250.00	200.00	118.80	**Mthatha**	1270	180.19	169.27
Mpumalanga TV mast	236.80	180.27	141.42	**Matatiele TV mast**	280.40	180.27	154.05
Middleburg TV mast	212.13	150.00	141.42	**East London TV mast**	No elevated-density area	1400	1480
Free State				**Western Cape**			
Theunissen TV mast	236.80	180.27	150.00	**Beaufort West TV mast**	212.13	No elevated-density area	452.76
Senekal TV mast	206.15	154.06	150.00	**Vanrhynsdrop**	No elevated-density area	No elevated-density area	No elevated-density area
Boesmanskop TV mast	200.00	254.95	217.86	**Constantiaberg TV mast**	No elevated-density area	No elevated-density area	No elevated-density area
Kroonstad TV mast	304.13	169.19	150.00	**Piketberg**	No elevated-	No elevated-	No elevated-

					density area	density area	density area
Northwest				**Kwa-Zulu Natal**			
Hartbeesfontein	403.11	158.11	150.00	**Alverstone Radio mast**	525.72	507.08	158.11
Schweizer-Reineke	890.22	412.31	236.80	**Port Shepstone TV mast**	1590	1360	1350
Zeerust TV mast	884.59	212.13	180.27	**Nongoma TV mast**	860.23	447.21	158.11
Jan Kempdorp	1200	320.15	180.27	**Greytown TV mast**	284.62	236.80	111.80
Northern Cape							
Carnarvon TV mast	413.08	235.91	111.80				
Prieska TV mast	1570	1450	1230				
Upington TV mast	413.68	316.22	250.00				
Douglas TV mast	250.00	580.54	180.27				

The data in table 2 shows the median location errors for all the identified towers. The median location errors decrease for all towers as the periods increase except for the Boesmanskop TV mast and the Douglas TV mast in 2010-2014. This may be caused by the rearrangement of the sensor locations in 2011 [1].

Also, the reason for having no elevated density in 2010-2014 for the Beaufort West TV mast may be due to the arrangement of the sensors in 2011. However, the rearrangement of sensors in 2011 worked for the East London TV mast as there was an identified elevated density cell in 2010-2014 as compared to 2007-2009.

For the following towers Vanrhynsdrop, Constantiaberg TV mast, and Piketberg there are no elevated-density cells identified for all the periods 2007-2009, 2010-2014, and 2019. This means that all the density cells around these towers are less than the initial density bar. Another reason may be that the upgrades done on the LDN by adding more sensors, rearranging the sensors, and upgrading the software of sensors did not improve the performance of the SALDN in that region.

For towers that report higher median location errors greater than 500 m, there are fewer lightning events recorded around and far apart from the tower during that period. This in turn will cause the identified elevated-density area to be far away from the tower. The reason for the few recorded lightning events that are far from the tower might be that there are fewer sensors in that region, that the sensors are far from the tower. Most towers identified in the Western Cape region had fewer reported strokes for all the seasons within its 2 km radial distance. This was not surprising considering that the towers are situated in a region having less than one Lightning flash per square kilometer per annum as documented [10].

Figure 6 above shows the median location errors for each tower per period. The median location error for all towers was estimated as 304.14 m for the 2007-2009 period. During this period, the network consisted of 19 sensors. During the 2010-2014 period three more sensors were added and the median location error for all towers was reduced to 236.80 m. A similar observation was seen for the 2015-2019 period with the median location error reduced further to 158.11 m, as that three more sensors were added to the network again and the Vaisala software went for upgrades [9]. On the other hand, eight of them indicated a reduced error for both the 2010-2014 and 2015-2019 seasons [11].

Table 3. Arithmetic mean for median location error for each province.

Year period		2007-2009	2010-2014	2015-2019
Province	**Number of towers**	**Arithmetic mean for median location error (m)**	**Arithmetic mean for median location error (m)**	**Arithmetic mean for median location error (m)**
Gauteng	**3**	355.36	257.20	112.18
Mpumalanga	**4**	360.55	251.15	150.19
Free State	**4**	236.77	189.61	166.96
Northwest	**4**	844.48	275.67	186.83
Northern Cape	**2**	661.69	645.66	443.01
Limpopo	**4**	956.80	696.80	575.72
Eastern Cape	**4**	1056.8	805.11	858.33
Western Cape	**4**	212.13	No elevated-density area	454.76
Kwa-Zulu Natal	**4**	815.214	637.77	444.50

Table 3 shows the arithmetic mean for median location error for each province using the identified towers. The arithmetic mean for Western Cape is not identified during 2010-2014 because every tower had no elevated-density area.

It is also worth noting that there is a bias in the arithmetic mean for median location error as the number of towers identified in Gauteng and Limpopo is not four as the rest of the provinces, this means that the division in the arithmetic means of Gauteng is 3 and in Limpopo is 2 instead of 4.

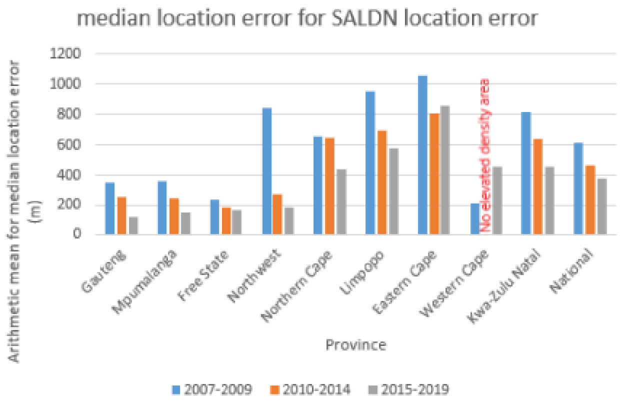

Fig. 7. Bar graph for arithmetic median location errors.

From the graphical representation of table 3 shown in figure 7 above, the arithmetic means for the median location error decrease with the increase in years as more upgrades are done on the SALDN, however, for provinces with towers that have no identified elevated density areas (Eastern Cape and Western Cape) affect the trend seen for other provinces. The reason for the low arithmetic mean for median location error and high arithmetic mean for median location error in 2007-2009 and 2015-2019 respectively for Western Cape is that there is only one tower that had an elevated area hence finding the mean makes no difference.

The performance of the SALDN improves as more upgrades are done to it (adding more sensors and upgrading the sensor software) by having lesser and lesser median location errors per upgrade for most provinces.

In this section, the results in table 3 will be compared with the SALDN self-evaluation of 500 m.

The arithmetic mean for median location errors for Gauteng, Mpumalanga, Free State, and Western Cape were lesser than the self-evaluation in all periods. While Northwest had an arithmetic mean for median location error that is lesser than the self-evaluation for the 2010-2014 and 2015-2019 periods. On the other hand, Kwa-Zulu Natal had an arithmetic mean for median location error that is lesser than the self-evaluation for the 2015-2019 periods.

The rest of the provinces had an arithmetic mean for median location error that is greater than the self-evaluation in all periods. However, the error decreased as the periods increased.

VI. Recommendations

The median location error of lightning events around Louis Trichardt tower was quite higher, though the area has more sensors covering the tower region, it is suggested that the terrain loss propagation factors must be corrected. However, a time correlation is advised. As for coastal and less reported flashes regions, it is recommended that increasing intervals for more than four years is passed to the algorithm since there are very low flashes per square kilometer per annum.

To reduce the bias in the arithmetic mean for median location errors, the number of towers should be the same in each province. Adjustments in the algorithm shown in figure 2 may be made by making the area in step 13 to be greater than ten as standard, this affects the density bar by ensuring that is high, which in turn will make sure that the elevated-density area is decreased and cells with a very high density are only considered.

The effect of clusters also impacts the median error especially when clusters include elevated density cells which are outliers and this was noticed when analyzing the Port Shepstone tower for all periods. Hence, large errors were reported, and this was observed for both clustering methods. The problem with these clusters is that they group objects unsupervised. A supervised clustering method in which clustered data set based on regions is recommended.

To make sure that more lightning events are captured, more sensors must be added as planned by the South African Weather Services to add more sensors, especially on the edge [1]. Most provinces had an arithmetic mean for median location error that is greater than the self-evaluation, therefore the SALDN self-evaluation value of 500 m should be changed to be province specific.

VII. Conclusion

The Zhu et al. [2] algorithm was presented and estimated the median location error for identified towers. The median location error for identified towers was compared with the SALDN self-evaluation error of 500 m. The median location error was found to be 304.14 m during 2007-2009, 236.80 m during 2010-2014, and 158.11 m during 2015-2019.

Acknowledgment

This work is based on the research supported in part by the National Research Foundation of South Africa and their support of the Johannesburg Lightning Research Laboratory through the Thuthuka programme (Unique Grant No.: 122038) and by DEHNAFRICA and their support of the Johannesburg Lightning Research Laboratory. the authors would like to thank the South African Weather Service (SAWS) for their support and for providing the SALDN data used in this paper, specifically Morné Gijben and Rydall Jardine.

References

[1] M. Gijben, "The South African Lightning Detection Network," in *MTG LI Mission Advisory Group Meeting*, 2021.

[2] Y. Zhu, W. Lyu, J. Cramer, V. Rakov, P. Bitzer, and Z. Ding, "Analysis of location errors of the U.S National Lightning Detection Network using lightning strikes to towers," *Journal of Geophysical Research: Atmospheres,* vol. 125, no. 9, 2020.

[3] M. Mahomed, A. D. Clulow, S. Strydom and M. J. Savage, "Lightning monitoring and detection techniques: Progress and challenges in South Africa," *South African Journal of Science,* vol. 117, no. 1-2, pp. 1-7, 2021.

[4] H. G. Hunt, "A Methodology for matching lightning detection network data with ground-truth records," University of the Witwatersrand, Johannesburg, 2012.

[5] H. Hunt, Y. Liu, and K. J. Nixon, "Evaluation of the South African Lightning Detection Network using Photographed Tall Tower Lightning Events from 2009 - 2013," *2014 International conference on lightning protection (ICLP),* pp. 1746-1751, 2014.

[6] H. Fensham, C. Schumann, H. Hunt, J. Tasman, K. Nixon, T. Warner, and M. Gijben, "Performance evaluation of the SALDN using highspeed camera footage of ground truth lightning events over Johannesburg, South Africa," *2018 34th International Conference on Lightning Protection (ICLP),* pp. 1-5, September 2018.

[7] J. Lopez, M. Murphy, J. A. Aranda, S. Gaztelumendi, M. Maruri, and D. de la Vega, "Analysis of the geographical configuration of a lightning detection network and its influence in the Accuracy of Lighting Location," in *2010 International Lightning Detection Conference*, Orlando, Florida, 2010.

[8] A. Nirmala and S. Saravanan, "A Study on Clustering Techniques on Matlab," *International Journal of Science and Research,* vol. 3, no. 11, pp. 1497-1502, 2014.

[9] S. Yildirim, "K-Means Clustering-Explained," Towards Data Science, 3 March 2020. [Online]. Available: https://towardsdatascience.com/k-means-clustering-explained-4528df86a120. [Accessed 20 September 2022].

[10] B. Bhavika, The influence of terrain elevation on lightning density in South Africa, Johannesburg: University of Johannesburg, 2007.

[11] M. Gijben, "The lightning climatology of South Africa," *South African Journal of Science,* vol. 108, no. 3, pp. 1-10, 2012.

Breakdown Voltage of Natural Ester-Based Nanofluid: A comparison between anatase-TiO_2 and rutile-TiO_2 nanoparticles

Mabontsi Miya* Cuthbert Nyamupangedengu* Ken Nixon* Nosipho Moloto†
*School of Electrical and Information Engineering
†School of Chemistry
University of the Witwatersrand, Johannesburg, South Africa
mabontsi@gmail.com, cuthbert.nyamupangedengu@wits.ac.za, ken.nixon@wits.ac.za, nosipho.moloto@wits.ac.za

***Abstract*—Nanoparticles have been found to improve the dielectric properties of insulation fluids. Existing literature has shown that the improvement given by these nanoparticles is dependent on the different properties of the nanoparticles, including the type and the amount of nanoparticles used. This work presents a study on the effects of TiO_2 nanoparticles on the breakdown strength of natural ester oil. A uniform field AC breakdown voltage test was used to compare anatase and rutile TiO_2 polymorphs' effects on a natural ester liquid. The nanofluid containing anatase-TiO_2 was found to provide the highest breakdown voltage for different concentrations. A maximum improvement of 85% was obtained with a sample containing 0.05 vol% of anatase-TiO_2. Rutile-TiO_2 had a 61% improvement at the same volume concentration. The improvement is attributed to the electron-trapping ability of the nanoparticles. The possible related electron transfer mechanisms are discussed.**

Keywords—Nanofluids, TiO_2, anatase, rutile, natural ester, AC breakdown voltage

I. Introduction

Transformer oil is an integral part of the electrical network. Its health is critical to the efficiency of the entire network. Insulation oil provides the dielectric and cooling functions of the transformers. Over the years, mineral oil has successfully provided this. However, it is prone to explosions during fault and high load conditions due to its lower fire point. The oil is also harmful to the environment given that it has a very low biodegradability rate. Additionally, mineral oil has a risk of running out due to the scarcity of petroleum fuel on which mineral oil is based [1]–[6].

In recent years, many researchers have focused on natural ester oils as alternative insulating liquids for large power transformers due to better sustainability. Natural ester oils have a higher fire point of 300 ˚C, which is double that of mineral oil [6]. They are also biodegradable as they are vegetable based, and are therefore renewable.

Although natural ester oil possesses superior properties, its application has limitations due to the characteristics of having higher viscosity and therefore lower cooling effects, higher oxidation rate, and inconsistent breakdown voltage behaviour especially at higher temperatures [1], [6].

Nanoparticles have been employed by researchers to address the shortfalls associated with natural esters. The integration of nanoparticles in insulation oils forms a nanofluid with improved dielectric properties. Rafiq *et al.* [2], and Suhaimi *et al.* [4], conducted reviews on nanofluids for power transformer applications, confirming the improvement of the resultant nanofluids' dielectric properties. They also concluded that the resultant properties of nanofluids depend on the type of particles, size, and percentage loading. Among the nanoparticles commonly used in nanofluids are Fe_3O_4, ZnO, Al_2O_3, SiO_2, and TiO_2. However, TiO_2-based nanofluids exhibit better dielectric properties as compared to other nanofluids. In the literature, Olmo *et al.* [7] modified natural ester oil with TiO_2 nanoparticles. The breakdown voltage of the resultant nanofluid was reported to have improved by 33%. Muangpratoom [5], compared nanofluids modified with TiO_2, ZnO, and $BaTiO_3$. It was concluded that at 0.01 vol%, TiO_2 had the most breakdown voltage improvement. Koutras *et al.* [8], also studied an ester-based nanofluid with TiO_2 nanoparticles and found a 22% improvement in the breakdown voltage with the nanofluid containing 0.02% of TiO_2.

It is notable from the literature that TiO_2 nanoparticles in natural ester oil enhance the breakdown strength of the resultant nanofluid. However, TiO_2 exists in two common stable polymorphs, namely, rutile and anatase [9], [10]. The phases have different properties and industrial uses. According to Stamate *et al.* [11], the electrical properties of anatase and rutile TiO_2 differ significantly. Their study on TiO_2 film suggests that the rutile dielectric constant is higher than that of anatase. This indicates that the polymorphs may have significantly different effects on the dielectric strength of nanofluids.

Currently, there is limited literature that specifies the phase of TiO_2 that results in the most improved nanofluid. In this regard, this work compares the effects of rutile-TiO_2 and anatase-TiO_2 nanoparticles on the uniform breakdown voltage of natural ester oil. The following sections present the materials, experimental methods, and the breakdown voltage test results.

II. Materials and Methods

A. Material Characterisation

Midel eN 1204 canola-based ester oil and the SkySpring nanomaterials Inc. sourced TiO_2 nanoparticles were used in the preparation of the nanofluids. Table I and Table II present the supplier specifications of the oil and nanoparticles respectively. Similar nanoparticles were used to ensure optimal comparability.

TABLE I: NATURAL ESTER OIL SUPPLIER SPECIFICATIONS

Midel 1204 Properties		
Property	***IEC 62770 Limit***	***Actual***
Dielectric Breakdown (kV)	≥ 35	66.3
Moisture Content	≤ 200	15.09
Dissipation Factor @90°C	≤ 0.05	0.004
Density @20°C (g/cm^3)	≤ 1.0	0.92
Viscosity @40°C (mm^2/sec)	≤ 50	37

TABLE II: TiO_2 NANOPARTICLES SUPPLIER SPECIFICATIONS

TiO_2 Nanoparticles Properties		
Property	**Rutile-TiO_2**	**Anatase-TiO_2**
Purity (%)	99.5	99.5
Average diameter (nm)	10 - 30	10 - 30
Specific Surface area (m^2/g)	~50	> 50

The physical properties of the nanoparticles were further confirmed with the use of Raman spectroscopy and Transmission Electron Microscopy (TEM).

A pure rutile-TiO_2 phase is characterized by four Raman shifts at 143±1 cm^{-1}, 235±5 cm^{-1}, 448±2 cm^{-1}, and 609±2 cm^{-1}. While pure anatase-TiO_2 has a sharp peak at 144±1 cm^{-1}, followed by four more at 196±1 cm^{-1},395±1 cm^{-1}, 518±2 cm^{-1}, and 639±1 cm^{-1} [10]. Fig. 1 shows the standard Raman Spectra signatures of the pure nanoparticles' phases, while Fig. 2 and Fig. 3 show the experimented rutile and anatase nanoparticles, respectively. Eleven samples of data were taken at different spots of a grid spread with each of the nanoparticles. It is notable from the figures that the spectra are almost identical for all sample iterations of the Raman. This coincides with a purity of 99.5% as per specifications.

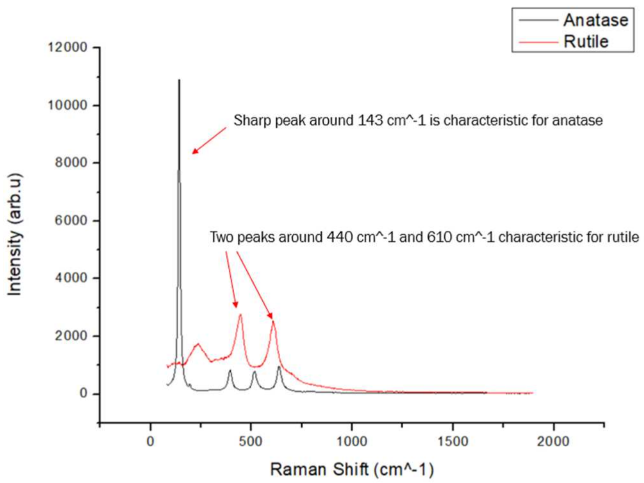

Fig. 1: Standard Raman Spectra of Phase-Pure TiO_2 Polymorphs

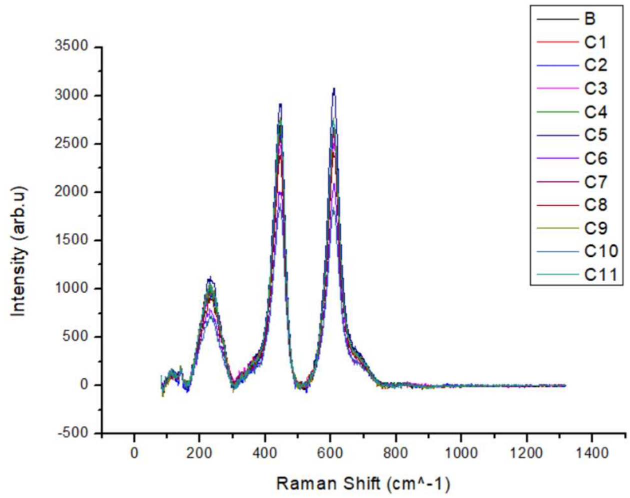

Fig. 2: Raman Spectra for Rutile TiO_2

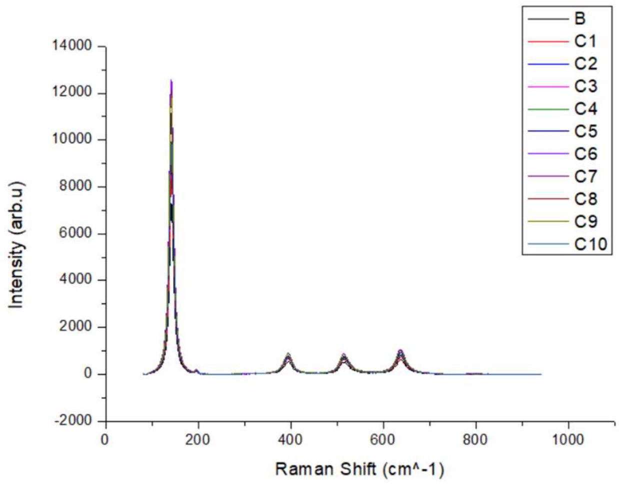

Fig. 3: Raman Spectra for Anatase TiO_2

TEM analysis also confirmed the sizes and morphology of the nanoparticles. Fig. 4 and Fig. 5 show the TEM images of the rutile and anatase TiO_2 respectively, confirming the particles' diameter range of 10-30 nm with quasi-spherical shapes as per the materials' specifications in Table I. In addition, the rutile sample is more agglomerated compared to the anatase TiO_2.

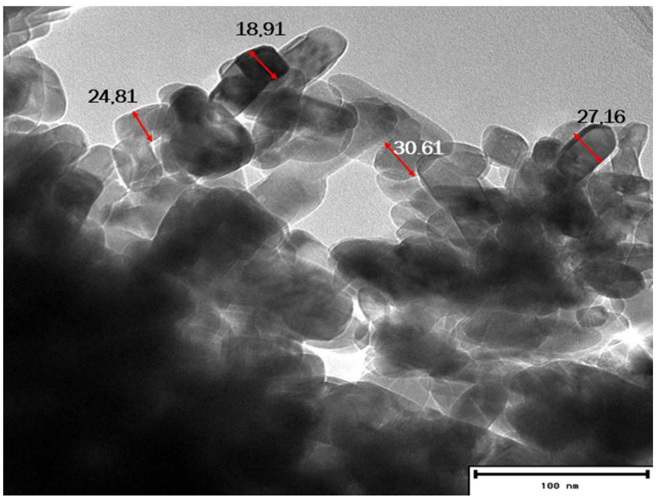

Fig 4: TEM Image of rutile TiO_2 nanoparticles

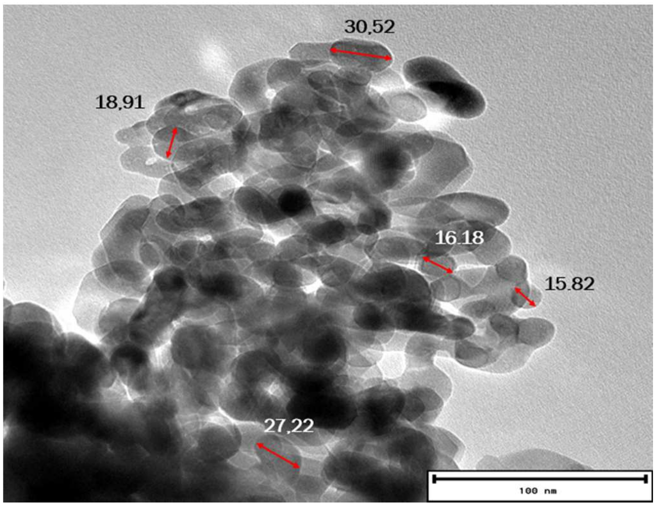

Fig 5: TEM image of anatase TiO_2 nanoparticles

B. *Nanofluid Synthesis*

Uniform dispersion of nanoparticles is critical for an optimal enhancement of the base oil's properties. To ascertain this, a two-step method of synthesis was adopted for the preparation of the nanofluids. Three samples of each polymorph nanoparticles in different concentrations were added to the natural ester to form the nanofluids. The composite was stirred with a magnetic stirrer at 60˚C for 30 minutes, followed by ultrasonication for 1 hour to form a homogeneously dispersed nanofluid. Lastly, the samples were oven dried for 24 hours to eliminate excess moisture. Fig. 6 illustrates the synthesis process.

A total of 6 nanofluid samples were conducted at 0.01 vol%, 0.03 vol%, and 0.05 vol% for each phase of the nanoparticles. The rutile-TiO_2 nanofluids will be referred to as R1, R2, and R3 for concentrations 0.01%, 0.03%, and 0.05% respectively. The anatase-TiO_2 nanofluids will be referred to as A1, A2, and A3 for concentrations 0.01%, 0.03%, and 0.05% respectively.

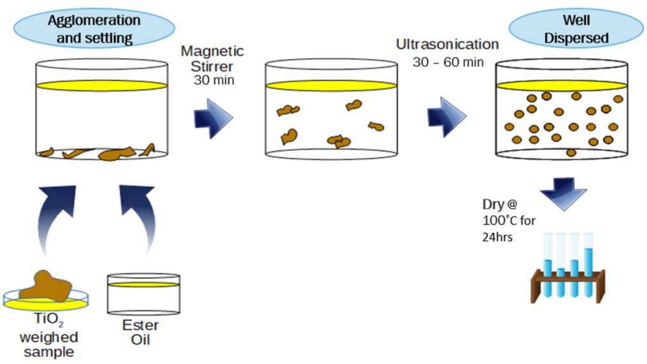

Fig. 6: 2-Step Nanofluid Synthesis Process

C. *Breakdown Voltage Experimental Procedure*

Uniform electric field breakdown tests were conducted following the IEC60156 standard. Due to the higher viscosity of ester fluids, the rest time before experiments and in-between shots was extended to 15 min and 5 min respectively to ensure bubbles are depleted in the oil. The test cell used comprised of sphere-sphere brass electrodes spaced 2.5 mm apart. The experimental set-up was as per Fig. 7, comprising of a variable AC supply, a Step-up transformer, a current limiting resistor, a voltage divider, and the test cell. A voltmeter was used to record the breakdown voltages. As per the standard, 6 breakdown shots were recorded per sample.

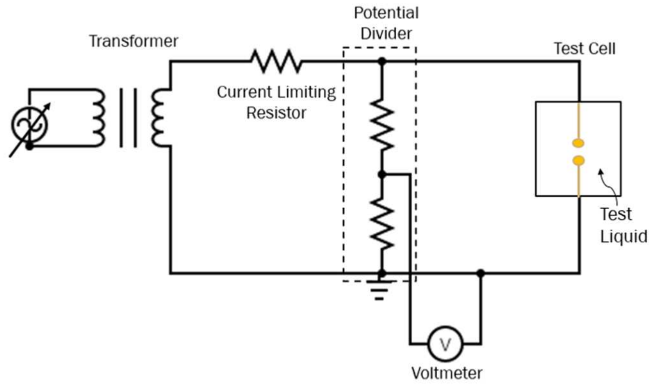

Fig. 7: AC Uniform Breakdown Test Circuit Diagram

III. Results and Discussion

Fig. 8 and Fig. 9 present the breakdown results of rutile-TiO_2 and anatase-TiO_2 nanofluids, respectively.

It is evident from the figures that the use of TiO_2 nanoparticles in both polymorphs yields an improved breakdown voltage. The trend increases with the increase in nanoparticle concentration. It is notable in both graphs that the results of the nanofluids lie well above the distribution of the pure ester fluid breakdown voltage. This shows a clear enhancement of the breakdown voltage in the nanofluids.

A. *Rutile-TiO_2 Nanofluid Breakdown Voltage*

Rutile-TiO_2 had the highest average breakdown voltage of 49.3 kV from sample R3, which is over 60% enhancement compared to the 30.6 kV recorded for pure oil. It is however notable that sample R2 exhibited the most optimal results based on the repeatability of results. A narrow interquartile range is observed, indicating less scattering of plots compared to those of R1 and R3.

B. *Anatase-TiO_2 Nanofluid Breakdown Voltage*

Similar to the rutile-based nanofluid, the anatase-based nanofluid exhibited an increase in the breakdown voltage as the concentration of anatase-TiO_2 nanoparticles was increased. 56.6 kV was recorded as the highest average breakdown voltage from sample A3. Based on the compact distribution of the results, this sample gave the most optimal resultant nanofluid.

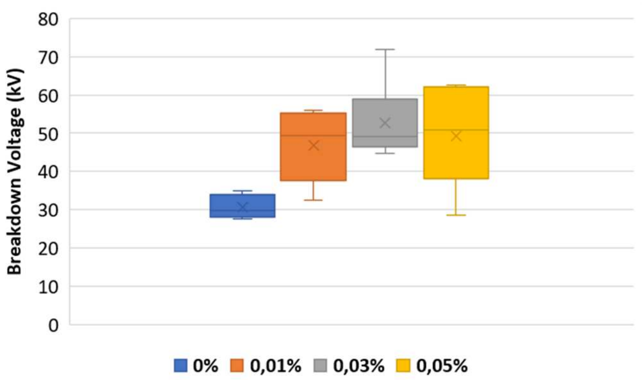

Fig. 8: Effects of rutile-TiO_2 loading on the breakdown voltage of an ester-based nanofluid

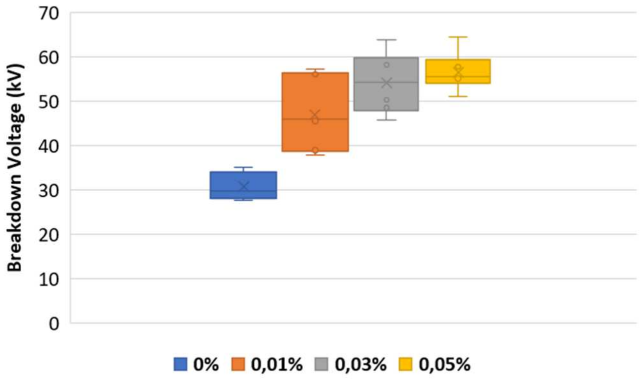

Fig. 9: Effects of anatase-TiO_2 loading on the breakdown voltage of an ester-based nanofluid

C. *Rutile vs Anatase TiO_2 Breakdown Voltage Enhancement*

A further comparison of the influence of the two morphologies on natural ester oil gives distinct differences in the amount of the resultant breakdown voltage enhancement. The anatase polymorph is found to have the most prominent effect on the breakdown strength of the oil. In Fig. 10, a clear comparison of the percentage improvement of breakdown voltage is presented. The two profiles follow a similar trend of enhancement, although the anatase-based nanofluids resulted in a much higher enhancement, a maximum of 85% improvement. However, samples R1 and A1 resulted in the same extent of improvement. This indicates that the superiority of the anatase polymorph is more evident at higher concentrations.

D. *Possible Mechanisms*

The results obtained are contrary to the common belief that rutile TiO_2 has better dielectric properties due to its higher thermal stability as compared to anatase [11], [12]. However, anatase nanoparticles have been reported to have superior effects over rutile in other applications, particularly in photocatalysis processes. These are relatable to nanodielectrics because of the electron activity attributed to the polymorphs' effects.

According to most literature, the enhancement of the breakdown voltage in nanofluids is attributed to the electron scavenger nature of nanoparticles. In a nanofluid, the interface between the nanoparticles and the oil forms an electrical double layer around the nanoparticles. In this layer are free ions on the outer-most diffuse layer, which have the ability to attract and trap free electrons. Fig. 11 shows a representation of the interface. During breakdown, the nanoparticles tend to attract and trap the electrons from the streamer [13]–[15]. This phenomenon results in a reduction in the electric field strength, and the energy of the streamer. Hence, a much higher voltage is required for a complete breakdown.

In photocatalysis studies, researchers have studied the electron trapping of TiO_2 polymorphs. It was reported that anatase has a larger band gap than rutile. According to the electron band theory, semiconductive solid particles have a narrow gap between the valency band and conduction band as seen in Fig. 12, which electrons may cross given the right energy. The conduction band has shallow traps and free reactive electrons, while the valency band is occupied by deeper trapped electrons which may move to the conduction band and reduce the shallow trap holes. Thus, reducing the shallow trapping ability. When a smaller band gap exists, trapped electrons can easily move to the conduction band, causing the conduction band to repel electrons [16]–[18]. It is evident from the literature that anatase-TiO_2 has a larger electron band gap than rutile. The band gap is 3.2 eV and 3.0 eV for anatase and rutile respectively [17], [18]. This entails that, for the same size and concentration of nanoparticles, anatase crystals will require higher energy to facilitate electron transfer. It follows that the shallow-trap mechanism associated with nanofluids may be having a much higher effect on anatase nanoparticles, hence the resultant breakdown voltage is higher than that of the rutile nanoparticles.

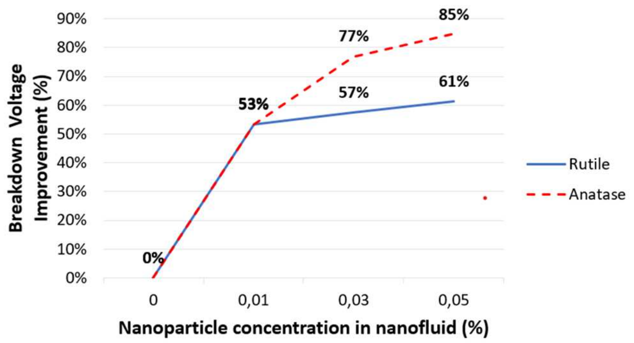

Fig. 10: Improvement of the Breakdown Voltage of Natural Ester oil based on rutile and anatase TiO_2 nanoparticles loading

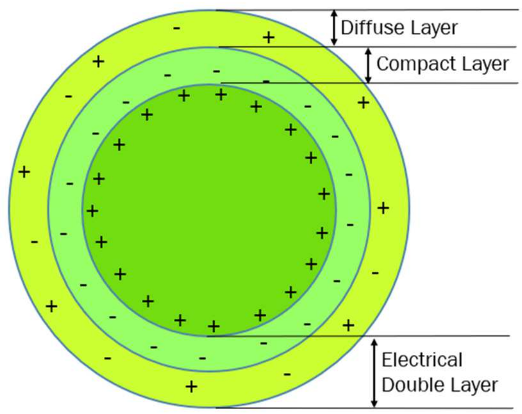

Fig. 11: Model of a nanoparticle in insulating fluid

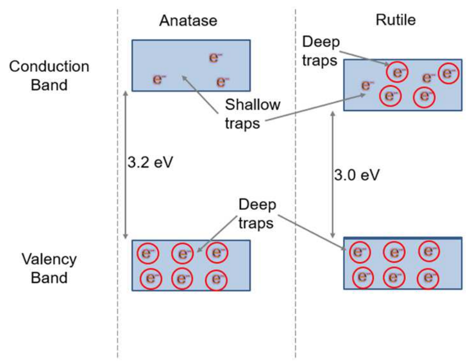

Fig 12: TiO_2 rutile and anatase solid state band gap

IV. Conclusion

The integration of nanoparticles into ester oil results in a nanofluid with enhanced dielectric properties. The use of TiO_2 nanoparticles in natural ester oil has proven to significantly improve the breakdown voltage of the resultant nanofluid. Both the anatase and rutile TiO_2 polymorphs exhibit this enhancement. The composite containing 0,05 vol% of anatase-TiO_2 resulted in the highest improvement at 85% of the base fluid's breakdown voltage. The rutile-TiO_2 nanofluid also had a maximum improvement at 0.05 vol% of the base fluid. The breakdown voltage improved by 61%, which is significantly lower than that of anatase-TiO_2.

The improvement of the breakdown voltage is attributed to the electron-trapping ability of nanoparticles. The electron band theory and the differences in anatase and rutile band gaps are likely responsible for the differences in rutile and anatase breakdown voltage enhancements.

The experimental results from this work indicate that the anatase polymorph of TiO_2 nanoparticles is more prominent in providing improved dielectric properties to natural ester oil. This is inconsistent with the literature that suggests that rutile-TiO_2 has better dielectric properties than anatase. Rutile-TiO_2 is also more stable than anatase, which gives rise to an inquisition about the extent of improvement that anatase-TiO_2 has under different conditions. It is thus, prudent to pursue more studies on the effects of the polymorphs on the dielectric properties of the nanofluids.

Acknowledgment

The authors would like to acknowledge Dr. Russell Martins of M&I Materials for his support in this work. Further acknowledgment goes to M&I Materials for funding the work, and the Wits MMU for the analysis of nanoparticles.

References

[1] D. M. Mehta, P. Kundu, A. Chowdhury, V. K. Lakhiani, and A. S. Jhala, 'A review on critical evaluation of natural ester vis-a-vis mineral oil insulating liquid for use in transformers: Part 1', *IEEE Trans. Dielectr. Electr. Insul.*, vol. 23, no. 2, pp. 873–880, Apr. 2016, doi: 10.1109/TDEI.2015.005370.

[2] M. Rafiq, M. Shafique, A. Azam, and M. Ateeq, 'Transformer oil-based nanofluid: The application of nanomaterials on thermal, electrical and physicochemical properties of liquid insulation-A review', *Ain Shams Eng. J.*, vol. 12, no. 1, pp. 555–576, Mar. 2021, doi: 10.1016/j.asej.2020.08.010.

[3] I. Fofana, V. Wasserberg, H. Borsi, and E. Gockenbach, 'Challenge of mixed insulating liquids for use in high-voltage transformers.1. Investigation of mixed liquids', *IEEE Electr. Insul. Mag.*, vol. 18, no. 3, pp. 18–31, May 2002, doi: 10.1109/MEI.2002.1014964.

[4] S. N. Suhaimi, A. R. A. Rahman, M. F. Md. Din, M. Z. Hassan, M. T. Ishak, and M. T. bin Jusoh, 'A Review on Oil-Based Nanofluid as Next-Generation Insulation for Transformer Application', *J. Nanomater.*, vol. 2020, pp. 1–17, Feb. 2020, doi: 10.1155/2020/2061343.

[5] P. Muangpratoom, 'The Effect of Temperature on the Electrical Characteristics of Nanofluids Based on Palm Oil', J. Eng. Technol. Sci., vol. 53, no. 3, Jul. 2021, Art. no. 210312, doi: 10.5614/j.eng.technol.sci.2021.53.3.12.

[6] B. A. Tlhabologo, R. Samikannu, and M. Mosalaosi, 'Alternative liquid dielectrics in power transformer insulation: a review', *Indones. J. Electr. Eng. Comput. Sci.*, vol. 23, no. 3, p. 1761, Sep. 2021, doi: 10.11591/ijeecs.v23.i3.pp1761-1777.

[7] C. Olmo, C. Méndez, F. Ortiz, F. Delgado, and A. Ortiz, 'Titania Nanofluids Based on Natural Ester: Cooling and Insulation Properties Assessment', *Nanomaterials*, vol. 10, no. 4, p. 603, Mar. 2020, doi: 10.3390/nano10040603.

[8] K. N. Koutras, I. A. Naxakis, A. E. Antonelou, V. P. Charalampakos, E. C. Pyrgioti, and S. N. Yannopoulos, 'Dielectric strength and stability of natural ester oil based TiO_2 nanofluids', *J. Mol. Liq.*, vol. 316, p. 113901, Oct. 2020, doi: 10.1016/j.molliq.2020.113901.

[9] G. Cao and N. Yi, 'Quantitative Analysis of Anatase-Rutile Mixtures by Raman Spectroscopy', p. 4, 2020.

[10] A. R. Zanatta, 'A fast-reliable methodology to estimate the concentration of rutile or anatase phases of TiO2', *AIP Adv.*, p. 8, 2017.

[11] M. Stamate, G. Lazar, and I. Lazar, 'Anatase-rutil TiO_2 thin films deposited in a D.C. magnetron sputtering system', *Romanian Journal of Physics*, vol 53, no. 1, p. 217-221.

[12] F. Liang, L. Zhang, and W.-Z. Lu, 'Dielectric performance of polymer-based composites containing core-shell Ag@TiO_2 nanoparticle fillers', *Appl Phys Lett*, p. 5, 2016.

[13] J. Fal, O. Mahian, and G. Żyła, 'Nanofluids in the Service of High Voltage Transformers: Breakdown Properties of Transformer Oils with Nanoparticles, a Review', *Energies*, vol. 11, no. 11, p. 2942, Oct. 2018, doi: 10.3390/en11112942.

[14] D.-E. A. Mansour, A. M. Elsaeed, and M. A. Izzularab, 'The role of interfacial zone in dielectric properties of transformer oil-based nanofluids', *IEEE Trans. Dielectr. Electr. Insul.*, vol. 23, no. 6, pp. 3364–3372, Dec. 2016, doi: 10.1109/TDEI.2016.005697.

[15] Y. Zhong *et al.*, 'Insulating properties and charge characteristics of natural ester fluid modified by TiO_2 semiconductive nanoparticles', *IEEE Trans. Dielectr. Electr. Insul.*, vol. 20, no. 1, pp. 135–140, Feb. 2013, doi: 10.1109/TDEI.2013.6451351.

[16] H. Ijadpanah-Saravy, M. Safari, A. Khodadadi-Darban, and A. Rezaei, 'Synthesis of Titanium Dioxide Nanoparticles for Photocatalytic Degradation of Cyanide in Wastewater', *Anal. Lett.*, vol. 47, no. 10, pp. 1772–1782, Jul. 2014, doi: 10.1080/00032719.2014.880170.

[17] T. Luttrell, S. Halpegamage, J. Tao, A. Kramer, E. Sutter, and M. Batzill, 'Why is anatase a better photocatalyst than rutile? - Model studies on epitaxial TiO2 films', *Sci. Rep.*, vol. 4, no. 1, p. 4043, May 2015, doi: 10.1038/srep04043.

[18] J. J. M. Vequizo, H. Matsunaga, T. Ishiku, S. Kamimura, T. Ohno, and A. Yamakata, 'Trapping-Induced Enhancement of Photocatalytic Activity on Brookite TiO_2 Powders: Comparison with Anatase and Rutile TiO_2 Powders', *ACS Catal.*, vol. 7, no. 4, pp. 2644–2651, Apr. 2017, doi: 10.1021/acscatal.7b00131.

Johannesburg Lightning Nowcasting From Meteorological Data and Electric Field Using Machine Learning

Oratile Marope
Electrical and Information Engineering
University of the Witwatersrand
Johannesburg, South Africa
1057107@students.wits.ac.za

Bhekumuzi G. Tshabalala
Electrical and Information Engineering
University of the Witwatersrand
Johannesburg, South Africa
1706880@students.wits.ac.za

Carina Schumann
Electrical and Information Engineering
University of the Witwatersrand
Johannesburg, South Africa
carina.schumann@wits.ac.za

Hugh.G.P. Hunt
Electrical and Information Engineering
University of the Witwatersrand
Johannesburg, South Africa
hugh.hunt@wits.ac.za

***Abstract*—This paper presents the work and findings of using machine learning algorithms namely, logistic regression (LR), random forest (RF), and long short-term memory (LSTM) network, to nowcast Johannesburg's cloud-to-ground lightning events within a 30 km radius of the city center between the period of 1 November 2021 to 27 February 2022. The investigation evaluated each model's ability to nowcast lightning strokes over the city from recorded historical values of the electric field, air temperature, dew point, and relative humidity for a forecast horizon of 15 minutes. Performance metrics indicate that the recall score for the LSTM is the lowest at 53% while that of the RF and LR are 80% and 93% respectively. The RF and LSTM models achieved lower recall scores but demonstrated less sensitivity to making false predictions, while the logistic regression made a relatively higher number of false positive misclassifications. A precision score of 41% for the LSTM indicates that the model is able to predict non-lightning occurrence more precisely than the LR and RF models which reported precision scores of 9% and 11% respectively. The models' prediction performance over the Sentech and Hillbrow towers has also been assessed and analyzed, and results indicate that a model's predictive ability is heavily influenced by cloud-to-cloud lightning.**

***Index Terms*—Recall, Precision, Random Forest, Logistic Regression, LSTM, Cloud-to-ground lightning, cloud-to-cloud lightning**

I. Introduction

Lightning may be defined as an uncontrolled, unanticipated, and rapid release of electrical energy from thunderstorms when the air reaches dielectric breakdown due to negative charges in the clouds being attracted to positive charges on the ground [1]. Lightning is known to cause fatalities and damage to infrastructure (homes, wind turbines, and power lines) [2]. In South Africa, it is reported that lightning strikes cost around R500 million in insurance claims every year for lightning-related damages [2]. The accurate and reliable prediction of lightning events all over the country, therefore, provides a suitable means of mitigating the adverse effects of lightning by issuing warnings to the general public and businesses.

For many years, South Africa had no detection or observation technology for lightning events [3]. This was until early 2000 when the South African Weather Service (SAWS) installed and operated a country-wide lightning detection network (SALDN) that had 19 sensors in the year 2005 [3]. The number of sensors has since increased to 25 up to date in an attempt to improve the accuracy and reliability of the network [3]. This initiative allowed the weather service to provide lightning forecast information to the public with a with 90 % prediction efficiency and 0.5 km location accuracy [3]. However, despite these developments, large parts of rural South Africa (and Africa at large) still remain vulnerable to lightning due to not receiving any lightning forecast and warnings at a local level. Machine learning-based warning systems have the advantage of being relatively cheaper to commission and maintain than country-wide sensors and have been shown to achieve excellent results in literature [4].

II. Problem Definition

This investigation seeks to make use of commonly available meteorological parameters such as air temperature, relative humidity, dew point, and the electric field to develop and compare three different machine learning models' ability to forecast if a cloud-to-ground lightning stroke will occur within a 30 km radius of Johannesburg city center in the next 15 minutes. The investigation also aims to examine how well the best-performing model identified during the investigation can accurately predict lightning events over the two city towers namely, the Sentech and Hillbrow towers.

Input meteorological data is obtained from the Johannesburg Lightning Research Laboratory (JLRL) while real lightning event data is obtained from the South African Lightning Detection Network (SALDN). The number of strokes that occur within a single 15 minutes window is not considered; the focus is instead placed on whether a lightning stroke will occur or not.

III. LITERATURE REVIEW

A fair amount of research about the use of machine learning techniques to predict lightning for the South African context exists in literature with each author exploring the usage of a different model with different input data to analyze results. S. Mzila [5] trains a standard deep neural network (developed from first principles) to predict lightning from meteorological data provided by SAWS using python and the Keras library for all nine provinces in South Africa and compares the results against true SALDN lightning data. The performance of the standard neural network is further compared against the performance of a radial basis network for the same data. Results indicated the developed neural network achieved an accuracy of 79% on both low-density and high-density areas.

A. La Fata *et al.* [6] provides the results of using a random forest classifier to predict cloud-to-ground lightning events from eighteen geo-environmental parameters (air temperature, wind speed, rainfall, etc) for 1- hour forecast horizon. It was found that the model achieved a recall score of 95%, a precision score of 8%, and an accuracy score of 93%. N. Makgatho *et al.* [7] presents the results of comparing a logistic regression model against a deep neural network for lightning prediction from meteorological data provided by SAWS. The deep neural network achieved a ROC- AUC score of 98% while the logistic regression model achieved a ROC- AUC score of 87%. Y. Essa *et al.* [8] investigates four machine learning algorithms- Auto-Regressive (AR), Auto Regressive Integrated Moving Average (ARIMA), and the LSTM model, that use univariate historical lightning-flash data (from SALDN) to predict the number of cloud-to-ground lightning flashes in South Africa for three hours ahead. This paper argues the strength of non-parametric models for lightning prediction and reports that the AR and ARIMA models performed similarly with a MAPE of 15312 and 15080 respectively, while the LSTM outperforms both of these with a MAPE of 3705. This paper is one of the first to deploy an LSTM model for lightning predictions.

IV. METHODOLOGY

To develop each of the three models listed, the system flow diagram depicted in Fig. 1 was followed. First, the input data is pre-processed by filling in missing data and organizing the date-time stamps of the data in chronological order. The next step is to model the time series problem as a supervised learning technique where values of a previous time (*t-1*) were to be used to predict the output (lightning event or no lightning event) at the present time *t*. Once this is done, statistical analysis of the data is performed to explore data characteristics, and input parameter relationships (correlation and probability density graphs) are conducted to ascertain if the data quality is sufficient to answer the investigation question as well as make informed guesses of which parameters are important and which are not. In addition, feature engineering which involved taking absolute values of the electric field, normalizing the values of input parameters, and taking time-lagged versions of input features (as far back as *t- 12* or three hours ago)- by sliding window technique, and taking a different combination of independent variables to predict the dependent outcome was explored.

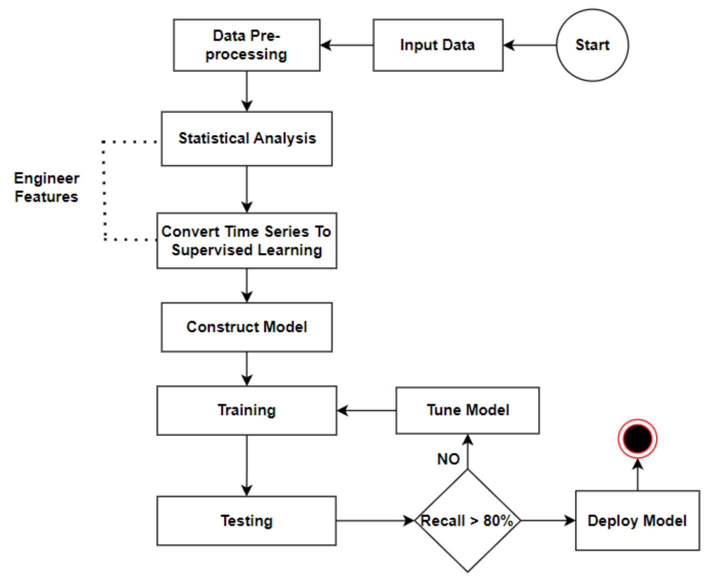

Fig. 1. Model Construction Flow Diagram

The model construction step involved splitting the input data into training, validation and testing set such that the model is tested on input data it has not seen to ensure reliable results. The data split followed a 65%: 15%: 20% split ratio respectively for the logistic regression model, while the random forest and LSTM were spit according to a 70% training and 30% testing ratio.

A. The Imbalanced Dataset Problem

Most machine learning problems adopt maximizing accuracy as the ultimate goal to achieve because the classifier (model) is expected to operate on data with an equal or normal distribution [9]. This approach breaks down when training on an imbalanced dataset. In particular, for many machine learning algorithms, the assumptions of equal data distribution are embodied by the placement of a 0.5 threshold on a continuous output of probabilities [9]. This default threshold implies that for every probability outcome $y_{probability}$ produced by each of the three models, values of probability where $y_{probability} \geq 0.5$ are considered as lightning stroke occurred, while probabilities where $y_{probability} < 0.5$ are considered as no stroke occurred. However, this threshold can be manually manipulated to be anything else between 0 and 1, instead of the given 0.5 default by a technique known as threshold sweeping.

Statistical analysis of the input data revealed that the data contained a total of 11 424 entries of which, 98% belonged to the class where there was no lightning stroke while only 2% contained lightning stroke cases. This immediately indicates that the dataset is largely imbalanced and so accuracy cannot be used as a reliable performance metric due to a phenomenon known as the accuracy paradox [10]. N. Japkowicz *et al.* [9] suggests strategies such as threshold sweeping, change of performance metrics, cost-sensitive learning, and evaluating different classification models to resolve this problem. These methods retain the integrity of the input data without introducing foreign characteristics and have been explored in this investigation.

V. Logistic Regression Model

Logistic regression is often the go-to parametric classifier for binary classification problems. This model applies an activation function known as the sigmoid function to estimate the probability of an event occurring based on single or multivariate data. The model then attempts to fit a line of best fit determined using a technique known as gradient descent to determine the intercept and coefficients to model the line. The logistic regression model's performance was trained on the following conditions:

1) Time lagged version of electric field up to 3 hours ago (with positive and negative values). This model is labelled as 'Lagged EField (*t-12*)'.
2) On all four input parameters (air temperature, relative humidity, dew point, and electric field). This model is labelled as 'All Four Features'.
3) On just the electric field (both positive and negative values). This model is labelled as 'EField (+/-)'.
4) On absolute values of the electric field. This model is labelled as 'Abs. EField'.

The results presented are after the model's hyper-parameters have been tuned so that the model is 'conscious' of the imbalance in the dataset and is capable of heavily penalizing the model's incorrect predictions for the minority class more than it penalizes incorrect predictions for the majority class. This is known as cost-sensitive learning [11]. The model's threshold was also optimized (by threshold sweeping using the ROC curve) such that a different threshold to the default value of 0.5 is applied to the results.

A. Results

The recall score represents the model's ability to detect positive cases (lightning stroke events), precision refers to the model's ability to detect negative cases (no lightning event), the F-1 score indicates the balance between recall and precision, while the ROC- AUC score represents the area under the curve of a ROC curve which is a plot of the relationship between true predictions and false predictions. The accuracy scores of each model have also been indicated but will not be used to critically evaluate the models' performance. Table I below shows that the logistic regression model with absolute values of electric field as the single input feature has the best overall performance with a recall score of 93% and a ROC- AUC score of 90%, albeit a lower F-1 (17%) score than 2 other models ('EField(+/-)' and 'All Four Features' models). The low F-1 score indicates that this model has a higher prediction power for detecting lightning events but a reduced ability to detect no lightning conditions due to a misclassification problem that occurs when the conditions for a lightning event are present, but no cloud-to-ground lightning stroke occurs. This misclassification is a result of what is known as a recall and precision trade-off where high recall has an associated low precision value [12]. This problem often occurs in imbalanced datasets and is highlighted by the confusion matrix representations of all four model variations in table II. The red highlighted cells indicate misclassifications and the green highlighted cells represent correct predictions.

TABLE I
PERFORMANCE METRICS EVALUATION OF LOGISTIC REGRESSION MODEL VARIATIONS

	Lagged EField (t-12)	All Four Features	EField (+/-)	Abs. EField
Accuracy (%)	90	91.90	94.23	85
Recall (%)	60	73	70	93
Precision (%)	7.8	12	15	9
F-1 Score (%)	14	23	25	17
ROC- AUC (%)	81	83	82	90
Cost- Sensitive	*No*	*No*	*Yes*	*Yes*
Optimal Threshold	0.013	0.021	0.48	0.35

TABLE II
LOGISTIC REGRESSION VARIATIONS CONFUSION MATRIX PARAMETERS

	Lagged EField (t-12)	All Four Features	EField (+/-)	Abs. EField
True Positive (TP)	22	22	21	28
False Positive (FP)	200	159	115	298
False Negative (FN)	8	8	9	2
True Negative (TN)	1959	1997	2044	1861

Table II lists the confusion matrix values of true positive (correctly predicted lightning events), false positive (false lightning stroke predictions), false negative (actual lightning strokes not predicted), and true negative (correctly predicted non-lightning events) for each developed model. This table indicates that the 'Abs. EField' model has the lowest number of false negative predictions (2), but the highest number of false positives (298) of all models, indicating that the model falsely misclassified no lightning events as lightning strokes 298 times. All other three models have comparative values of true positive and true negative predictions. The recorded values under each model, are out of 2 189 data entries that formed part of the testing set. Only 30 entries from this testing set had cloud-to-ground lightning strokes. Hence the sum of true positive and false positive predictions sums up to 30 for each model.

It can be seen from Table I that accuracy decreases with increasing ROC- AUC and recall scores; this further proves the point that accuracy is not a reliable metric to use when working with imbalanced data. Table I further demonstrates that models which had cost-sensitive learning generally outperformed models that utilized the threshold sweeping technique as the only approach to fine-tune the models and improve performance. This table also indicates that the time-lagged versions of the electric field model '(Lagged EField *t- 12*') performed the worst as input features to predicting lightning events with the model scoring the lowest recall, precision, F-1, and ROC- AUC scores. This result is attributed to the fact that lightning is a very fast-forming and disappearing phenomenon that usually lasts for 0.2- 1 second [1]. Therefore adding later versions of the electric field to the model is seen to reduce the model's performance instead of improving it because the data granularity of 15 minutes is too large a window for a lot of physical parameters to change and not resemble the likelihood of lightning anymore.

The 'All Four Features' model demonstrates that the air temperature, relative humidity, and dew point features add little to no significance to the predictive power of the model as it performed lower than the uni-variate 'EField (+/-)' model. The 'All Four Features' model is an extension of the 'EField (+/-)' model where temperature, humidity, and dew point parameters were added as additional features. The 'Abs. EField' model outperforms the model with positive and negative values of the electric field because the logistic regression model is a uni-directional model with an inability to learn data patterns in both a forward and reverse direction. The 'Abs. EField' model will be referred to as the logistic regression model from this point on as it is the best-performing variation developed.

VI. Random Forest and LSTM Models

The random forest classifier is a non-parametric classification model that uses an ensemble of decision trees that operate on each input feature to decide whether some input data will produce a lightning stroke or not. This classifier is powerful to use because it combines the output of each decision tree (of which there might be hundreds) to make this decision by aggregating the output of the tress.

The long short-term memory (LSTM) network is a deep learning algorithm commonly used for natural language processing (NLP) tasks and handwriting recognition. This model has however found application in common classification problems due to its ability to learn and memorize both long and short-term dependencies and data patterns that produce a certain outcome [13]. The LSTM network also has feedback connections that allow the model to use the previous inputs in conjunction with input at the present time to determine an outcome [13]. The results of the random forest and LSTM models are provided and analyzed below. Both these models were tested on all four parameters as input features.

A. Results

Table III shows that the random forest outperformed the LSTM model with higher recall and ROC- AUC scores. The LSTM however, recorded the highest precision and F- scores of all models built. Previously analyzed models (including the random forest) demonstrated high recall scores but low precision, and subsequently low F-1 scores. The LSTM reported a significantly higher precision score (almost double that of the random forest and logistic regression models). Table IV also shows that this model recorded the lowest numbers of false positive misclassified predictions than the rest of the models. The LSTM, however, recorded the highest number of false negatives- actual lightning cases not detected, than other models due to there not being a 'sufficient' sample size representation of the minority (lightning stroke) class in the dataset for the model to adequately learn the data patterns that produce lightning conditions. "Most of the existing deep learning algorithms do not take the data imbalance problem into consideration. As a result, these algorithms can perform well on balanced data sets while their performance cannot be guaranteed on imbalanced data sets" [14]. S. Wang *et al.* [14] proposes a custom loss function, *mean squared false error*, to introduce the principle of cost-sensitive learning to imbalanced LSTM classification problems, while D. Devi *et al.* [15] proposes a cost sensitive random forest model to handle data imbalances. However, due to time constraints, the cost-sensitive LSTM and Random Forest models with the proposed loss functions could not be implemented in time for investigation.

TABLE III
PERFORMANCE METRIC SCORES OF LOGISTIC REGRESSION, RANDOM FOREST AND LSTM

	Logistic Regression	Random Forest	LSTM
Recall(%)	93	80	53
Precision (%)	9	11	41
F-1 Score (%)	17	19	46
ROC- AUC (%)	90	85	76

TABLE IV
CONFUSION MATRIX PARAMETERS OF ALL THREE MODELS

	Logistic Regression	Random Forest	LSTM
True Positive (TP)	28	24	16
False Positive (FP)	298	199	23
False Negative (FN)	2	6	14
True Negative (TN)	1861	1960	2136

VII. Johannesburg Lightning Prediction

This section presents the graphical results of how well the three developed models predict the cloud-to-ground lightning activity in Johannesburg. Fig. 2 shows the recorded actual cloud-to-ground lightning events in the city for the period: 03 Feb 2022 - 25 Feb 2022, while Fig. 3 shows each model's prediction ability for detecting each recorded stroke in Fig. 2. It can be seen from the presented figures that the random forest and logistic regression models have a similar prediction pattern and both make a higher number of erroneous classifications (false positives), while the LSTM model makes fewer error predictions. The LSTM however, can be seen failing to predict lightning events that actually happened more than the other two models, as is the case for the third true stroke from the right in Fig. 2. The LSTM did not successfully predict this stroke in Fig. 3 and can be seen to remain flat while the random forest and logistic regression models spike to report that they were able to successfully detect it. Due to its high percentage recall of 93%, the logistic regression model is still recognized as the best-performing model out of the three. This model will now be used to predict lightning events over the two inner city towers (Sentech and Hillbrow tower) for the month of November.

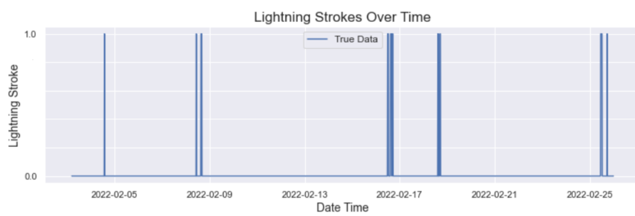

Fig. 2. Johannesburg actual lightning strokes

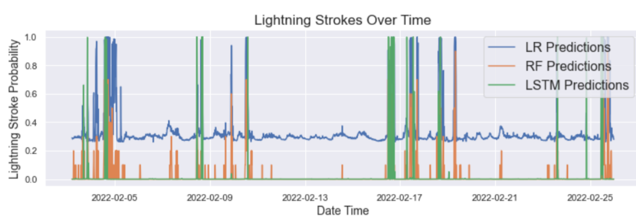

Fig. 3. Johannesburg lightning stroke prediction

VIII. Sentech and Hillbrow Tower Predictions

Fig. 4 shows the actual cloud-to-ground lightning strokes recorded over the towers, with the Sentech tower shown in blue and the Hillbrow tower shown in orange. Only one stroke can be seen over each tower for the whole month (November 2021). Fig. 5 shows the corresponding cloud-to-cloud lightning events over the towers for the same time period. Fig. 6 shows the prediction probabilities of the logistic regression model for lightning events over both the Sentech and Hillbrow towers.

As seen from Fig. 4 and Fig. 5, most lightning activity that occurred over the towers was cloud-to-cloud lightning and this influenced the logistic regression's predictions in Fig. 6 to report possible cloud- to ground strokes (as this is what is being investigated) multiple times when in reality only one cloud- to ground stroke occurred over each tower but

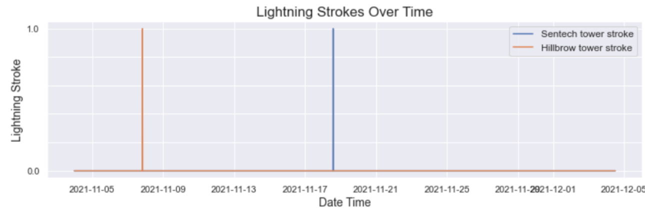

Fig. 4. Cloud to ground lightning over the towers

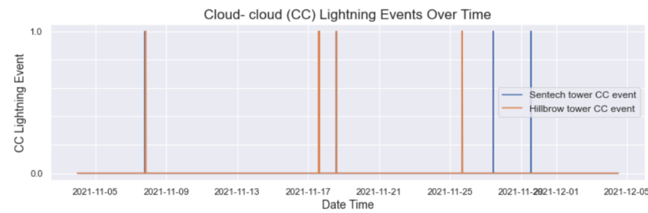

Fig. 5. Cloud to cloud lightning over the towers

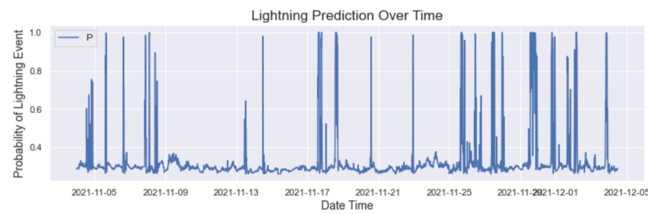

Fig. 6. Lightning prediction over the towers

at different times. Reference [1] states that only 25% of all lightning events involve the ground. Therefore, all other types of lightning activity that occur do not involve the ground and instead dissipate in the air. The meteorological and physical parameter conditions that produce the other 75% of lightning events are however similar to the lightning that makes contact with the ground. By this reason, it can be inferred that all other types of lightning activity- such as intra-cloud, cloud-to-air, and cloud-to-cloud, all bear an influence on the logistic regression's predictive performance for the towers. This thus explains the large number of false spike predictions seen in Fig. 6.

IX. Discussion

Results indicated that the LSTM deep learning model achieved the best F-1 and precision scores, but required a larger data sets to perform comparatively in ROC- AUC and recall scores to the logistic regression model. This model is thus considered to have the worst performance among all three models in terms of predicting lightning occurrences. The non-parametric random forest model achieved similar results to the logistic regression model, achieving recall and precision scores of 80% and 85% respectively; however, it was noticed that the model required techniques of cost-sensitive learning to increase its precision and recall scores. This is also true for the LSTM model whose recall and ROC- AUC scores require cost-sensitive learning so the model learns to concentrate attention of learning data dependencies towards predicting the minority class more than it does the majority class.

An undesired trade-off between recall and precision was discovered in the models and it is hereby concluded that it is impossible to increase both these performance metrics at the same time when tuning the models. It was found that lightning events such as cloud-to-cloud, intra-cloud, and cloud-to-air influence machine learning algorithms to make a high number of false positive predictions for cloud-to-ground lightning.

X. FUTURE RECOMMENDATIONS

To improve the performance of all three models for every evaluation metric, it is hereby recommended that a larger dataset to the four month's worth of data used in this investigation be used to train and test the models. Ideally, a dataset set with more than 2 years' worth of data is deemed suitable. Having a bigger dataset would allow the models to have more samples of the minority class to better learn dependencies and feature relationships that produce lightning. Oversampling and undersampling dataset pre-processing techniques should also be explored to reduce the imbalance of the dataset as recommended by [16]. This will help to increase the efficiency of cost-sensitive learning techniques when applied to each model.

Cloud-to-cloud lightning has been proven to be more common than cloud-to-ground lightning, and this form of lightning is also said to occur before cloud-to-ground lightning strokes events by [1]. Due to this, it is further recommended that cloud-to-cloud lightning should be included during model construction as an input feature or a third output class so that it is not entirely ignored as it has been seen that this form of lighting greatly influences the prediction results of models. Data granularity of fewer than 15 minutes is recommended so that meteorological and physical parameters that govern the occurrence of lightning events, e.g. electric field, are sampled at higher frequencies as lightning is a fast occurring and disappearing event. Techniques of multi-step forecasting can then be explored to provide forecasts at much larger horizon times to warn the public.

XI. CONCLUSION

All types of lightning discharges in the air owe their existence to the relationship of complex, dynamic, and measurable physical parameters in the air. This investigation found that the electric field is the single most dominant predictive parameter in forecasting lightning. It is therefore proposed that electric field values have good potential to accurately predict lightning and achieve recall and precision scores close to 90% when cost-sensitive learning approaches are adopted. This paper concludes that machine learning is indeed a suitable alternative for lightning prediction.

ACKNOWLEDGMENT

This work is based on the research supported in part by the National Research Foundation of South Africa and their support of the Johannesburg Lightning Research Laboratory through the Thuthuka programme (Unique Grant No.: 122038) and by DEHNAFRICA and their support of the Johannesburg Lightning Research Laboratory. The authors would like to thank the South African Weather Service (SAWS) for their support and for providing the SALDN data used in this paper, specifically Morné Gijben and Rydall Jardine

REFERENCES

[1] J. R. Dwyer and M. A. Uman, "The physics of lightning," *Physics Reports*, vol. 534, no. 4, pp. 147–241, 2014.

[2] N. McCain, "Sa sees 100 deaths from lightning strikes a year - now scientists are lobbying for more awareness," Jun 2022.

[3] M. Mahomed, A. D. Clulow, S. Strydom, M. J. Savage, and T. Mabhaudhi, "Lightning monitoring and detection techniques: Progress and challenges in south africa," *South African Journal of Science*, vol. 117, no. 1-2, pp. 1–7, 2021.

[4] A. Mostajabi, D. L. Finney, M. Rubinstein, and F. Rachidi, "Nowcasting lightning occurrence from commonly available meteorological parameters using machine learning techniques," *Npj Climate and Atmospheric Science*, vol. 2, no. 1, pp. 1–15, 2019.

[5] S. Mzila, *Using Neural Networks to Predict Lightning*. PhD thesis, University of the Witwatersrand, Johannesburg, 2021.

[6] A. La Fata, F. Amato, M. Bernardi, and D'Andrea, "Cloud-to-ground lightning nowcasting using machine learning," in *2021 35th International Conference on Lightning Protection (ICLP) and XVI International Symposium on Lightning Protection (SIPDA)*, vol. 1, pp. 1–6, IEEE, 2021.

[7] N. Makgatho, R. Ajoodha, and H. G. Hunt, "Using traditional machine learning algorithms to classify lightning occurrence,"

[8] Y. Essa, H. G. Hunt, and R. Ajoodha, "Short-term prediction of lightning in southern africa using autoregressive machine learning techniques," in *2021 IEEE International IOT, Electronics and Mechatronics Conference (IEMTRONICS)*, pp. 1–5, IEEE, 2021.

[9] N. Japkowicz *et al.*, "Learning from imbalanced data sets: a comparison of various strategies," in *AAAI workshop on learning from imbalanced data sets*, vol. 68, pp. 10–15, AAAI Press Menlo Park, CA, 2000.

[10] M. F. Uddin, "Addressing accuracy paradox using enhanched weighted performance metric in machine learning," in *2019 Sixth HCT Information Technology Trends (ITT)*, pp. 319–324, IEEE, 2019.

[11] C. X. Ling and V. S. Sheng, "Cost-sensitive learning and the class imbalance problem," *Encyclopedia of machine learning*, vol. 2011, pp. 231–235, 2008.

[12] S. A. Alvarez, "An exact analytical relation among recall, precision, and classification accuracy in information retrieval," *Boston College, Boston, Technical Report BCCS-02-01*, pp. 1–22, 2002.

[13] S. Siami-Namini, N. Tavakoli, and A. S. Namin, "The performance of lstm and bilstm in forecasting time series," in *2019 IEEE International Conference on Big Data (Big Data)*, pp. 3285–3292, IEEE, 2019.

[14] S. Wang, W. Liu, J. Wu, L. Cao, Q. Meng, and P. J. Kennedy, "Training deep neural networks on imbalanced data sets," in *2016 international joint conference on neural networks (IJCNN)*, pp. 4368–4374, IEEE, 2016.

[15] D. Devi, S. K. Biswas, and B. Purkayastha, "A cost-sensitive weighted random forest technique for credit card fraud detection," in *2019 10th international conference on computing, communication and networking technologies (ICCCNT)*, pp. 1–6, IEEE, 2019.

[16] T. Zhu, C. Luo, Z. Zhang, J. Li, S. Ren, and Y. Zeng, "Minority oversampling for imbalanced time series classification," *Knowledge-Based Systems*, vol. 247, p. 108764, 2022.

Significance of Nanoparticles on Electrical Breakdown Strength of Oil-Impregnated Paper Reinforced with Rutile-TiO_2

Mohammed Mahmood Katun
School of Electrical and Information EngineeringUniversity of the Witwatersrand
Johannesburg, South Africa
gimmohmk483@gmail.com

Chandima Gomes
School of Electrical and Information EngineeringUniversity of the Witwatersrand
Johannesburg, South Africa
chandima.gomes@wits.ac.za

Cuthbert Nynamupangedengu
School of Electrical and Information EngineeringUniversity of the Witwatersrand
Johannesburg, South Africa
cuthbert.nyamupangedengu@wits.ac.za

***Abstract*—One of the essential characteristics of kraft paper insulating material used in a power transformer is its ability to withstand electric field stress without breaking down easily. Kraft paper insulation reinforced with nanoparticles produces a nanodielectric with improved breakdown strength. However, the mechanics that results to increase in breakdown strength are seldom mentioned in the literature. In this work, the electrical breakdown voltage of a fabricated nanocomposite kraft paper is presented. The impact of the nanoparticles on fibre length and breakdown voltage was studied. From the results, the nanoparticle has no influence on the fibre length. The breakdown voltage of the nanocomposite kraft paper improved by 15% as compared to the unfilled kraft paper. The improvement is associated with charge carriers trapped within the interaction zone of the fabricated nanocomposite kraft paper.**

Keywords—Transformer, oil-impregnated paper, nanocomposite kraft paper, kraft paper, fibre length, interaction zone, nanotechnology, nanoparticles, nanofiller

I. INTRODUCTION

The electrical field stress induced by lightning and switching affects the transformer winding insulation. These stresses are referred to as transient overvoltage. They contribute to about 10% of transformer failures [1].

Meanwhile, the operational reliability of the transmission and distribution network is directly affected by the condition of the power transformer. In a power transformer, the winding insulation is designed based on its capacity to withstand the rated electric field stress before breaking down [2], [3].

Oil and kraft paper are the insulation used in the transformer [4], [5]. The micro-cell voids of cellulose fibre (kraft paper) are filled with the oil during impregnation. Before the breakdown of the oil-immersed paper, the oil is first stressed beyond its limit and discharge will occur, which eventually breakdown the kraft paper. With the continuous increase in demand for electricity and voltage levels, it is important to design winding insulation that can withstand electrical-induced stress and guarantee service reliability [6].

In this regard, many researchers have in recent times been working towards improving the dielectric properties of both the oil and kraft paper insulation using nanotechnology [7]. Nanoparticles (nanofiller) made from MgO, SiO_2, Al_2O_3, ZnO, and TiO_2 are used to modify the transformer insulations. The electrical, thermal, and mechanical properties of the nanocomposite dielectrics were reported to have improved [2], [8], [9]. However, this paper is focused on presenting the improvement recorded in the breakdown strength of a fabricated nanocomposite kraft paper using nanoparticles, and understanding the interaction between the nanofiller and cellulose fibre which results in the suppression of the electric field stress. The significance of nanoparticles on the electrical breakdown strength of modified oil-impregnated paper are rarely discussed in the literature. In this present work, rutile-TiO_2 nanoparticles were chosen because of their superior stability in reaction and thermal resilience as compared to other nano-metal oxides [2], [8]. The preceding sections present the experimental procedures of fabricating the handsheet, a test on the fibre length and the breakdown examination of the fabricated nanocomposite kraft paper.

II. EXPERIMENTAL PROCEDURE

A. *Materials*

Rutile-TiO_2 NPs (surface modified and unmodified with surfactants), Electrical unbleached kraft pulp, filler retention aid donated by from Sappi™ Technology Centre (Innovation Hub, Pretoria). All chemicals were used as received.

B. *Fabrication of the handsheets*

The procedure involved two experiments: the fabrication of the control (reference/unfilled kraft paper) sample and the fabrication of samples filled with nanoparticles (with rutile-TiO_2 NPs). The procedure of the handsheet-making complied with procedures in TAPPI T 205 [10]. The rutile-TiO_2 nanocomposite kraft paper was fabricated following the process illustrated in Figure 1. The same procedure was followed for the control (reference) sample but without adding the nanofillers and retention aid. The fibre length and breakdown strength on the handsheet were then studied.

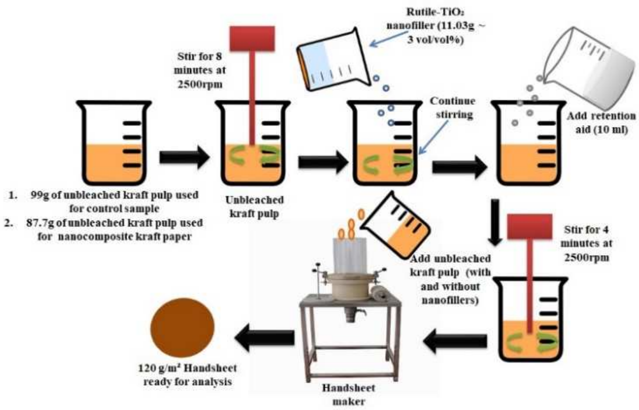

Fig. 1: Fabrication procedure of the kraft paper specimens.

C. *Fibre length Characterization*

The L&W FT+ tester was used to determine the influence of nanoparticles on the fibre length of the fabricated nanocomposite kraft paper. Figure 2 shows a graph presenting the fibre length of the fabricated handsheets. The Alkyl ketene dimer (AKD) and Alkenyl Succinic anhydride (ASA) are the surfactants used to modify the rutile-TiO_2 NPs surface in different percentage volumes.

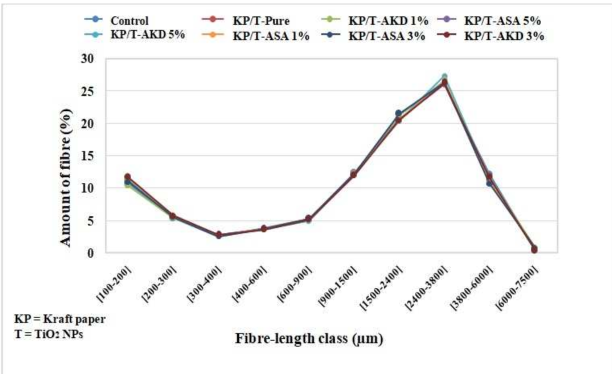

Fig. 2: Graphical representation of the fibre length constituents in the various specimens.

From the graph of the fibre length distribution, the fibre length of all the sampled specimens falls within the fibre length class of softwood. The fibre length analysis also shows that the nanofiller does not influence the fibre length. Unbleached softwood cellulose fibres have a length measured between 1.8 to 4 millimetres. These woods are more robust and have a longer length compared to hardwood. This makes it a preferred raw material for fabricating kraft paper insulation for power transformers [11]–[17].

III. BREAKDOWN STRENGTH TEST OF THE FABRICATED KRAFT PAPER SPECIMENS

To determine the effect of modification on the new material, the dielectric breakdown strength of each sample paper was studied. Before the breakdown tests were carried out, the samples were oil-impregnated. This was done by drying the kraft paper at 90 °C for 48 hours. Transformer oil (mineral) was added, and the oven temperature was controlled at 40 °C for another 24 hours. The breakdown test was set up with homemade equipment as in Figure 3 and was done in accordance with IEC 60243 standard [18]. Three replicates of each sample were tested on seven different spots

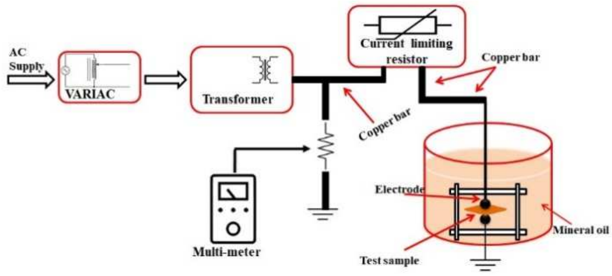

Fig. 3: Breakdown test setup.

From Figure 4, the breakdown strength of all the fibres containing either modified or unmodified rutile-TiO_2 NPs increased while the control sample had a lower value. The highest breakdown strength was 43.4 kV/mm. About 15% increase in breakdown strength was recorded as compared to the reference sample. It was however notable that the specimen that gave the best result was kraft paper filled surface-modifed rutile-TiO_2 NPs (KP/T-AKD3%).

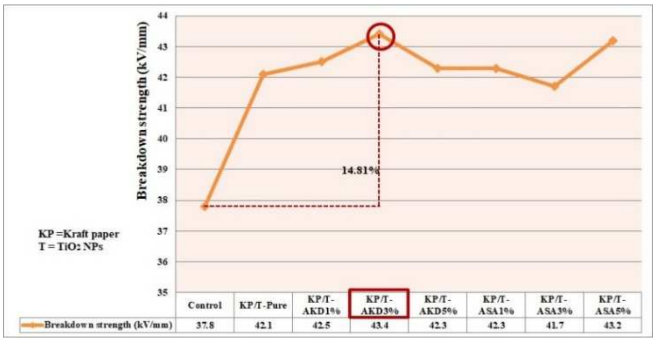

Fig. 4: Breakdown voltage of the fabricated kraft paper.

Compared with other literature, kraft paper modified with nanoparticles has shown significant improvement in its breakdown strength. Liao *et al.* [19] reinforced kraft paper insulation with TiO_2 NPs, and the breakdown voltage of the modified kraft increased by 21%. Yuan and Ruijin [20] modified kraft paper insulation with montmorillonite (MMT), and the breakdown voltage of the oil-impregnated paper increased by 13% . Tang *et al.* [21] used Al_2O_3 NPs to modify kraft paper insulation; it was reported that adding Al_2O_3 NPs greatly improved the AC breakdown strength of the kraft paper insulation. In a similar effort, Tang *et al.* [22] used SiO_2 NPs to modify kraft paper insulation, and from the experimental results, the breakdown voltage of the modified insulation increased by 14%. The breakdown voltage of modified kraft paper insulation was reported to have improved when TiO_2-NPs were optimized for power transformer application [23]. The next subsection explains the chemistry within the nanocomposite kraft paper that produce the 15% increase in breakdown strength.

A. Impact of the nanoparticles on the resultant breakdown strength of the fabricated nanocomposite kraft paper

To understand the interaction between the nanofiller (rutile-TiO_2 NPs) and cellulose fibre which results in the suppression of the electric field stress and increases the breakdown strength of the composite kraft paper, this section describes the fabricated nanocomposite kraft paper in relation to the proposed model by Tanaka *et al.* and Li *et al.*.

The interactive mechanisms between the rutile-TiO_2 NPs and the cellulose fibre were view from areas of physics, quantum mechanics and electromagnetic principle [24]–[29].

Tanaka [27], [29] 2005 proposed a model to explain the interaction around the polymer and nanoparticles. In his work, a multi-layered core model for polymer nanocomposites interface was presented for electrical insulation. His model including the New Potential Barrier model of Li *et al.* [25] could be used to explain the interaction that results in improved electrical field withstand of the fabricated nanocomposite kraft paper.

Since the interface (in the nanocomposite kraft paper) is the channel that bonds the rutile-TiO_2 NPs with the cellulose fibre, from Tanaka model, the interface of the fabricated nanocomposite kraft paper is made of three layers with the first corresponding to the layer that is bonded to both rutile-TiO_2 NPs and cellulose fibre (kraft pulp). This connection is facilitated by the unsaturated bond and organic groups (surfactants) on the surface of the rutile-TiO_2 NPs. The rutile-TiO_2 NPs then connect with the cellulose fibre by hydrogen, ionic and covalent bonds. The second layer (transitional region) is a region within the model that consists of the cellulose chain which bound with the surface of the rutile-TiO_2 NPs and the first layer. Because of the arrangement of the cellulose chain and its cohesive energy density (CED), large energy is needed to break this bond [6]. The third layer (loose layer) interacts with the second layer. This layer comprises of various chain structure/shape, chain mobility and free crystallinity from cellulose chain (polymer matrix). The bonded and transition region (interaction zone) together define the electrical field strength of the fabricate nanocomposite kraft paper as illustrated in Figure 5.

Based on the interaction zone, Li *et al.* proposed a new potential barrier model in 2011. The proposed model considered the interaction zone (with in the nanocomposite kraft paper) as an independent region and the thickness of the transition region to be smaller than the mean free path of the carriers. According to the model, charge carriers are trapped in the interaction zone when the rutile-TiO_2 nanoparticle is in scattered dispersion of the fabricated nanocomposite kraft paper. This result to a decrease in mobility and density of carriers which cause an increase in breakdown strength of the fabricated nanocomposite kraft paper by 15%.

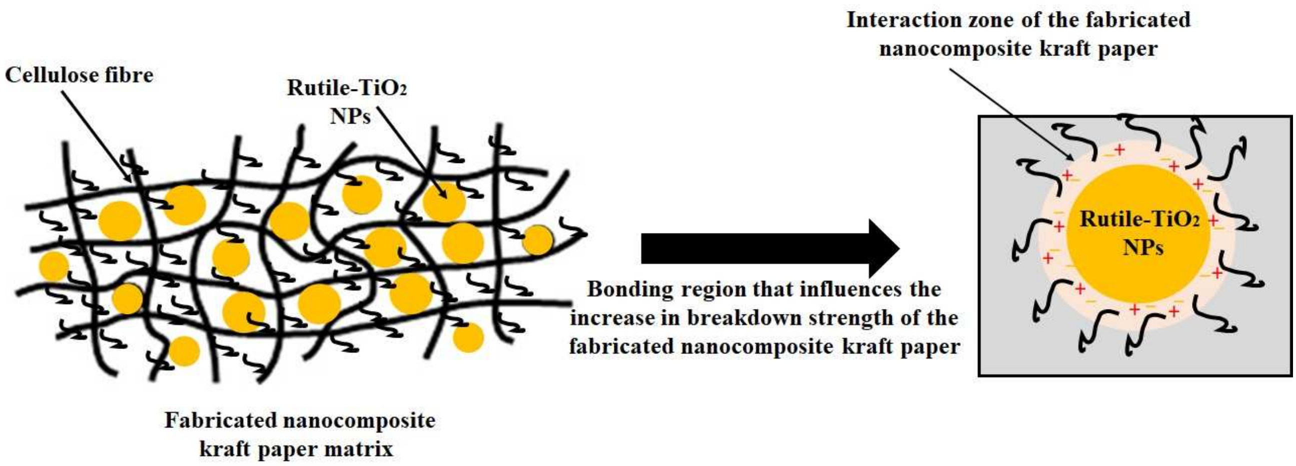

Fig. 5: Interaction zone in nanocomposite kraft paper.

In summary, the 15% increase in breakdown strength of the nanocomposite kraft paper can be translated into decrease in winding insulation failure due to transient overvoltage caused by lightning. With this nanocomposite kraft paper, smaller power transformer can be deigned to withstand more electric field stress.

IV CONCLUSION

This work presents the application of nanoparticles to improve the electrical property of nanocomposite kraft paper for power transformer application. The reinforcement of the nanoparticles (rutile-TiO_2 NPs) in kraft pulp to fabricate the nanocomposite insulation paper were described in this work. The impact of the reinforced rutile-TiO_2 NPs on the fibre length and the electrical breakdown strength were examined. The presence of the rutile-TiO_2 NPs does not affect the fibre length of the fabricated nanocomposite kraft paper. The improvement recorded in the breakdown strength is associated with the characteristic mechanism of the bonding within the structure of the fabricated nanodielectric and the behavior of the interaction zone to the electric field stress. In polymer nanocomposite, the resultant dielectric properties are influenced by nanoparticles size, percentage loading, uniformity of filler distribution, agglomeration as well as surfactant used. These parameters need more research attention to unravel some ambiguities regarding their impact on the final properties of polymer nanocomposite insulation.

ACKNOWLEDGMENT

The authors thank Sappi™ Technology Centre (Innovation Hub, Pretoria) for their invaluable support. The Tertiary Education Trust Fund (TETFund) is also greatly acknowledged for supporting Mahmood MK in the research work.

REFERENCES

[1] J. Singh and S. Singh, "Transformer failure analysis: reasons and methods," *International Journal of Engineering Research*, vol. 4, no. 15, p. 5, 2016.

[2] M. K. Mahmood, C. Nyamupangedengu, C. Gomes, and A. Smith, "Reducing Hydrophilic Characteristics of Kraft Paper Insulation by Reinforcing With Surface Modified Rutile-TiO2 Nanoparticles," *IEEE Access*, vol. 10, pp. 102237–102246, 2022, doi: 10.1109/ACCESS.2022.3208596.

[3] M. Zhang, J. Liu, M. Yin, H. Jia, and J. Lv, "Assessment on Oil-Paper Insulation Aging of Transformer Based on Dielectric Response Model," *Electric Power Components and Systems*, vol. 47, no. 13, pp. 1145–1155, Aug. 2019, doi: 10.1080/15325008.2019.1663454.

[4] V. A. Thiviyanathan, P. J. Ker, Y. S. Leong, F. Abdullah, A. Ismail, and Md. Zaini Jamaludin, "Power transformer insulation system: A review on the reactions, fault detection, challenges and future prospects," *Alexandria Engineering Journal*, vol. 61, no. 10, pp. 7697–7713, Oct. 2022, doi: 10.1016/j.aej.2022.01.026.

[5] T. A. Prevost and T. V. Oommen, "Cellulose insulation in oil-filled power transformers: Part I - history and development," *IEEE Electrical Insulation Magazine*, vol. 22, no. 1, pp. 28–35, Jan. 2006, doi: 10.1109/MEI.2006.1618969.

[6] S. Li *et al.*, "Short-term breakdown and long-term failure in nanodielectrics: a review," *IEEE Trans. Dielect. Electr. Insul.*, vol. 17, no. 5, pp. 1523–1535, Oct. 2010, doi: 10.1109/TDEI.2010.5595554.

[7] J. E. Contreras, E. A. Rodriguez, and J. Taha-Tijerina, "Nanotechnology applications for electrical transformers—A review," *Electric Power Systems Research*, vol. 143, pp. 573–584, Feb. 2017, doi: 10.1016/j.epsr.2016.10.058.

[8] M. Mahmood, R. Kadzutu-Sithole, N. Moloto, C. Nyamupangedengu, and C. Gomes, "Improving thermal stability and hydrophobicity of rutile-TiO2 nanoparticles for oil-impregnated paper application," *Energies*, vol. 14, p. 7964, Nov. 2021, doi: 10.3390/en14237964.

[9] M. M. Katun, A. Smith, R. Kadzutu-Sithole, C. Gomes, C. Nynamupangedengu, and N. Moloto, "Impact of fibres and reinforced nanoparticles on tensile strength of transformer oil-impregnated paper," in *2022 30th Southern African Universities Power Engineering Conference (SAUPEC)*, Jan. 2022, pp. 1–6. doi: 10.1109/SAUPEC55179.2022.9730720.

[10] "TAPPI T 205:Forming handsheets for physical tests of pulp." Technical Association of the Pulp & Paper Industry, Revision 2012.

[11] P. Jusner, E. Schwaiger, A. Potthast, and T. Rosenau, "Thermal stability of cellulose insulation in electrical power transformers – A review," *Carbohydrate Polymers*, vol. 252, p. 117196, Jan. 2021, doi: 10.1016/j.carbpol.2020.117196.

[12] N. Španić, I. Plazonić, V. Jambreković, and Ž. Barbarić-Mikočević, "Wood and nonwood fibres length as main factor affecting their suitabillity as raw materials for papermaking industry," 2018.

[13] G. Chinga-Carrasco, A. Miettinen, C. L. Luengo Hendriks, E. Kristofer, and M. Kataj, "Structural Characterisation of Kraft Pulp Fibres and Their Nanofibrillated Materials for Biodegradable Composite Applications," in *Nanocomposites and Polymers with Analytical Methods*, J. Cuppoletti, Ed. InTech, 2011.

[14] M. Fiserova, J. Gigac, and J. Balberčák, "Relationship between fibre characteristics and tensile strength of hardwood and softwood kraft pulps," *Cellulose Chemistry and Technology*, vol. 44, pp. 249–253, Jul. 2010.

[15] A. Johansson, "Correlations between fibre properties and paper properties," KTH Royal Institute of Technology, Stockholm, Sweden, 2011.

[16] H. Karlsson, "Strength Properties of Paper produced from Softwood Kraft Pulp," Karlstad University Studies, Karlstad, Sweden, 2010.

[17] R. P. Kibblewhite and D. Brookes, "Fibre, beating and papermaking properties of kraft pulps from New Zealand beech species," *New Zealand Journal of Forestry Science*, vol. 7 (3), pp. 425–444, 1977.

[18] "IEC 60243, 'Electric strength of insulating materials'."

[19] R. Liao, C. Lv, L. Yang, Y. Zhang, W. Wu, and C. Tang, "The insulation properties of oil-impregnated insulation paper reinforced with nano-TiO2," *J. Nanomaterials*, vol. 2013, p. 1:1-1:1, Jan. 2013, doi: 10.1155/2013/373959.

[20] Y. Yuan and R. Liao, "A Novel Nanomodified Cellulose Insulation Paper for Power Transformer," *Journal of Nanomaterials*, vol. 2014, pp. 1–6, 2014, doi: 10.1155/2014/510864.

[21] C. Tang, S. Zhang, J. Xie, and C. Lv, "Molecular simulation and experimental analysis of Al2O3-nanoparticle-modified insulation paper cellulose," *IEEE Transactions on Dielectrics and Electrical Insulation*, vol. 24, no. 2, pp. 1018–1026, Apr. 2017, doi: 10.1109/TDEI.2017.006315.

[22] C. Tang, X. Li, F. Yin, and J. Hao, "The performance improvement of aramid insulation paper by nano-SiO2 modification," *IEEE Transactions on Dielectrics and Electrical Insulation*, vol. 24, no. 4, pp. 2400–2409, 2017, doi: 10.1109/TDEI.2017.006560.

[23] D. Liu, J. Ye, X. Xu, C. G. Deng, and X. Li, "Optimization of mass fraction and particle size of TiO2 additives in application of HVDC transformer insulation," in *2019 IEEE 20th International Conference on Dielectric Liquids (ICDL)*, Jun. 2019, pp. 1–4. doi: 10.1109/ICDL.2019.8796662.

[24] I. A. Tsekmes, R. Kochetov, P. H. F. Morshuis, and J. J. Smit, "A unified model for the permittivity and thermal conductivity of epoxy based composites," *J. Phys. D: Appl. Phys.*, vol. 47, no. 41, p. 415502, Sep. 2014, doi: 10.1088/0022-3727/47/41/415502.

[25] S. Li, G. Yin, S. Bai, and J. Li, "A new potential barrier model in epoxy resin nanodielectrics," *IEEE Transactions on Dielectrics and Electrical Insulation*, vol. 18, no. 5, pp. 1535–1543, Oct. 2011, doi: 10.1109/TDEI.2011.6032822.

[26] S. Raetzke and J. Kindersberger, "Role of interphase on the resistance to high-voltage arcing, on tracking and erosion of silicone/SiO2 nanocomposites," *IEEE Transactions on Dielectrics and Electrical Insulation*, vol. 17, no. 2, pp. 607–614, Apr. 2010, doi: 10.1109/TDEI.2010.5448118.

[27] T. Tanaka, M. Kozako, N. Fuse, and Y. Ohki, "Proposal of a multi-core model for polymer nanocomposite dielectrics," *IEEE Transactions on Dielectrics and Electrical Insulation*, vol. 12, no. 4, pp. 669–681, Aug. 2005, doi: 10.1109/TDEI.2005.1511092.

[28] T. Andritsch, R. Kochetov, P. H. F. Morshuis, and J. J. Smit, "Proposal of the polymer chain alignment model," in *2011 Annual Report Conference on Electrical Insulation and Dielectric Phenomena*, Oct. 2011, pp. 624–627. doi: 10.1109/CEIDP.2011.6232734.

[29] T. Tanaka, "Dielectric nanocomposites with insulating properties," *IEEE Trans. Dielect. Electr. Insul.*, vol. 12, no. 5, pp. 914–928, Oct. 2005, doi: 10.1109/TDEI.2005.1522186.

Analysis of Solar Irradiation Impact on Grid-tied Photovoltaic Systems' Power Quality Characteristics

Abayomi A. Adebiyi
Department of Electrical Power Engineering
Durban University of Technology, South Africa
abayomia@dut.ac.za

Innocent E. Davidson
Department of Electrical Power Engineering
Durban University of Technology, South Africa
innocentD@dut.ac.za

Abstract **- The usage of photovoltaic systems in the production of electrical energy has increased, either as a way to provide electricity in places where there is no grid connection (stand-alone systems) or by feeding electricity into the grid (grid-tied systems). As the price of energy produced from fossil fuels rises, solar energy emerges as a feasible alternative source in a liberated energy market. However, it continues to have issues that must be fixed for it to be universally acknowledged as a viable replacement for fossil fuels. It is necessary to solve the underlying issue of the quality of the power generated by photovoltaic technology. In this study, power quality experiments were run with a grid-tied PV system to ascertain how solar irradiation variation impacts power quality quantities, results for low and average irradiance situations are measured and analyzed. The investigation showed that low solar irradiation significantly increases current total harmonic distortion, which frequently pushes power factor outside of acceptable limit and injects reactive power into the grid.**

Keywords— PV system, power quality, solar irradiation, and harmonics distortion.

I. Introduction

The objectives of green and sustainable energy are met by photovoltaic (PV) technology, which also offers an alluring technique of power generation [1]–[4]. Extensive studies are still being conducted to improve the PV cell efficiency and maximize energy output by minimizing power losses and better-utilizing incident solar irradiation [5]. PV systems' performance and efficient operation depend on several variables. One of the most essential components in the operation of PV systems is the atmospheric conditions, this has a major impact on the effectiveness and reaction of the entire system in terms of power quality [6]–[8]. Some of the factors that affect the power quality of PV systems include the variable power flow caused by solar irradiation variations, temperature, and the selection of power electronics equipment. To prevent harmonics, inter-harmonics, and voltage variation, the PV system must produce a sinusoidal voltage and current output. With the high penetration level of PV systems in the distribution grid, low solar irradiation could cause undesirable distortions in supply quality (current and voltage) and power at the point of common coupling possibly exceeding allowable grid code thresholds. The inverter, a component of a PV system that converts DC power to AC, has several characteristics that relate to the quality of the electricity it generates. The performance and power characteristics of an inverter during input and output variations can be influenced by its circuit design. Even when inverters adhere to standards, a high number of PV inverters on a low-voltage distribution system might result in power quality issues [9]. Such performance, which is characterized by low power quality, is frequently problematic since it limits the proper functionality of equipment and results in complex electronic device collapse [10-11]. The performance of an 8 kW grid-connected PV system's power quality has been studied in this paper. The test PV installation in Pietermaritzburg, South Africa's KwaZulu-Natal province, has 30 fixed-mounted PV panels installed at a small complex. This installation has the Cadmium telluride (CdTe) solar cell technology used. The PV system is connected to the grid and is distributed over three phases. The objective of this study is to provide and analyze the power quality data gathered from the PV site and to give pertinent technical data for the PV industry. For four weeks, different power quality quantities were measured for the study among which the current harmonics, voltage harmonics, power factor, and real and reactive power were measured. The current and voltage total harmonic distortion (THD) was also monitored. High current total harmonic distortion was found during the low solar irradiation scenario after the measurement analysis. It has also been discovered that the power factor occasionally violates the permissible limit, resulting in considerable reactive power being injected into the distribution grid.

II. Test System Configuration

An 8 kW PV system with 30 fixed-mounted PV panels has been investigated in this study. The power generated was distributed via a three-phase system. The data collection system was installed in accordance with IEC 61724 standard. For the PV system yield performance, weather parameters including global horizontal irradiance (GHI), direct normal irradiance (DNI), ambient and panel temperature, and real and reactive power generated were measured in real-time every five minutes throughout the day. Figure 1 depicts the configuration of the grid-connected PV system.

A. Grid-tied PV System Standard

While designing and integrating a PV system into a distribution grid, certain considerations are to be factored. The IEEE standard 2030.11-2021, "IEEE Standard Distributed Energy Resources Management Systems (DERMS) Functional Specification," provide guidelines on how to operate and ensure compatibility of the PV system and distribution grids operation. The IEEE Standard 519, which outlined the requirements for harmonic control and power quality enhancement in electrical power systems and recommended best practices, was also taken into account when installing this grid-connected PV system. It establishes the limitations on harmonic voltage and current. This standard necessitates the involvement of both utilities and end users and set the voltage and current total harmonic distortion (THD) limits for the utilities and energy consumer. The THD_V and THD_I limits were set to 5% and 3% respectively. Likewise, the maximum individual harmonic component for voltages below 69 kV is set to 3% [12]-[14].

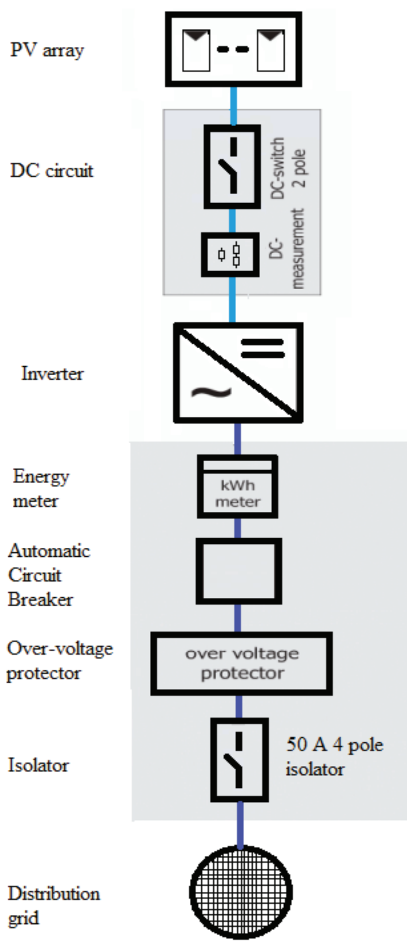

Fig.1. The experimental PV system configuration

III. Results and Discussion

Use At the PV site's point of common coupling, power performance indicators have been collected and compared with data on solar irradiation recorded from the same location. The real and reactive power, voltage, and current for each harmonic frequency are the power quality characteristics that were measured for a period of four weeks. The power factor and total harmonic distortion of the voltage and current have also been monitored for the test period. The solar irradiation incident on the Pv array was also measured. From the measured data, two scenarios of low and average solar irradiation have been evaluated and presented in this section. Figure 2(a) depicts the sun irradiation data on a typical day in August in Pietermaritzburg. The PV system's active power output, which is highly reliant on irradiation is presented in Figure 2(b). It is observed that the intermittent nature of solar irradiation impacts the amount of active power the PV system injected into the distribution grid. With a high-level penetration of the PV system on the distribution grid, the system's unpredictable response may cause problems for the power utility who would have previously scheduled for peak demand load. The reactive power, as depicted in Figure 2(c), changes randomly throughout the day. The operation of the distribution grid, which is based on the idea of the unity power factor, is sustained by the intelligent inverter installed to properly controlled the VAR demand. As shown in Figure 2(d), the power factor values are found to be within the standard desirable limit of 0.9 for a significant portion of the day, however, the power factor deviates from this limit during low solar irradiation periods though the power factor at other times of the day dropped below the limit, the reactive power demand is lower.

However, assuming a very high penetration level, consistent reactive power variation in PV systems could cause capacitor switching as a result, the amplitude and duration of voltage transients and oscillations can vary. If a transient's amplitude exceeds predetermined thresholds, it may cause sensitive electronic equipment to malfunction or reduce the life span of grid components. Reducing the occurrence of such transients is thus ideal and intelligent PV system inverters are now designed to regulate the issue of reactive power by offering superior compensation based on the requirements of the distribution utility and system power factor [15]. It is known that the level of voltage harmonics inherent in the grid and the instantaneous power supplied by the PV inverter are two factors that influence the current harmonic generated by the inverter [16]. The total harmonic distortion of the output voltage and current of the inverter measured at the PCC between the inverter and the grid coupling impedance, are shown in Figures 2(e) and 2(f), respectively. Due to its inverse relationship with the fundamental current, the current THD increased significantly to 42% early in the morning and late in the evening, well above the IEEE limit of 5%, during the average solar irradiation condition. In contrast, the voltage THD remained fairly constant throughout the day ranging between 1.5% – 2.4% well within the acceptable limit.

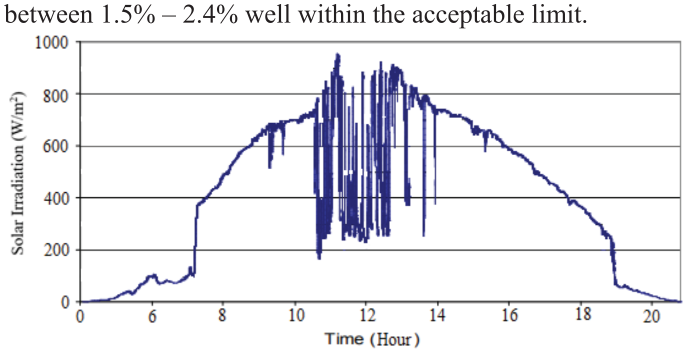

Fig.2(a). The measured average solar irradiation on a typical day

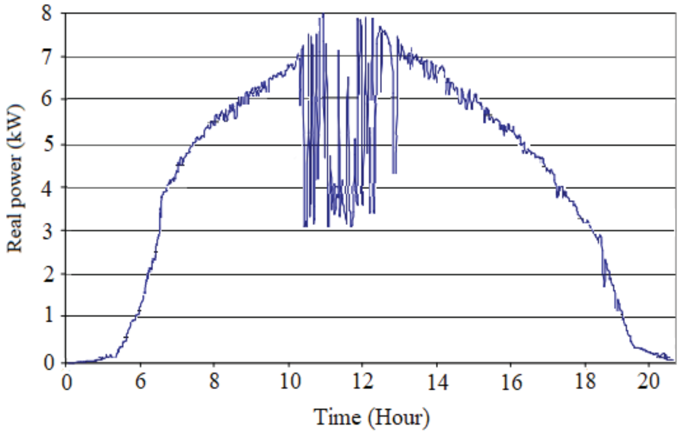

Fig.2(b). Real power measured during average solar irradiation

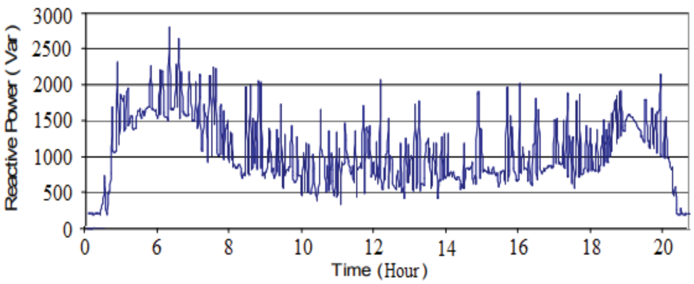

Fig.2(c). Reactive power measured during average solar irradiation

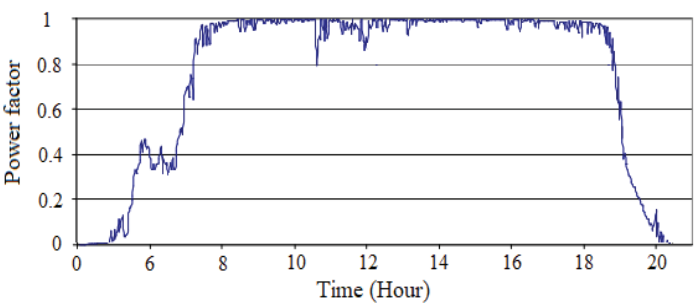

Fig.2(d). Power factor measured during average solar irradiation

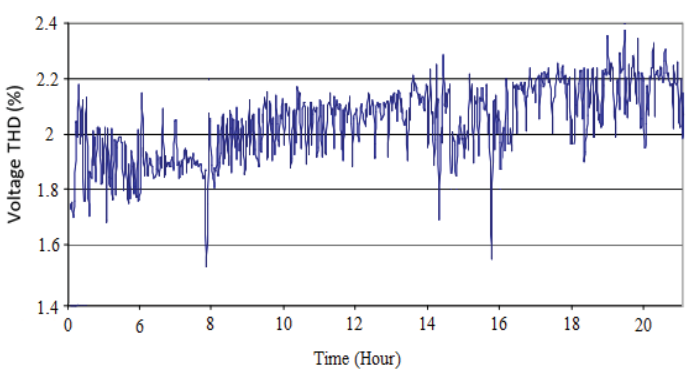

Fig.2(e). Measured voltage THD during average solar irradiation

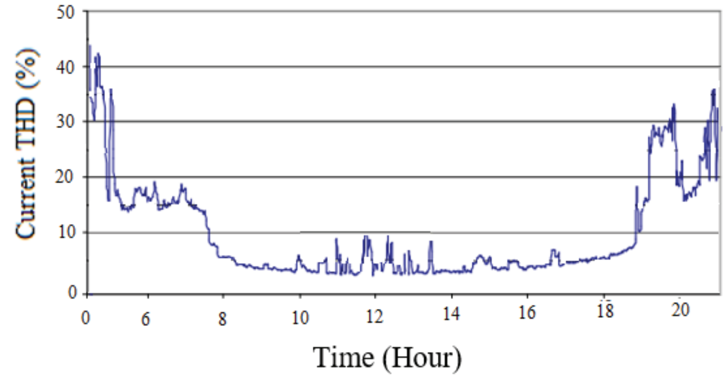

Fig.2(f). Measured current THD during average solar irradiation

The second scenario investigated how low solar irradiation affected the power quality of the PV system. Figure 3(a) to 3(f) depicts the findings of the power quality parameters measured. Low solar irradiation, as shown in Figure 3(a), has a significant impact on the output power generated by the PV system as shown in Figure 3(b). The power factor fluctuated below 1 between 0.6 and 0.9 between early morning and late evening when solar irradiation was low, which caused a spike in reactive power. Since the current THD has an inverse relationship with the fundamental current, the current THD increased significantly to 93% early in the morning, well above the IEEE limit of 5%, during the low solar irradiation condition, however, the calculated total demand distortion (TDD), which is the calculated harmonic current distortion against the full load demand, remained fairly constant. While the voltage THD fluctuated during the day, it generally stayed within the permissible range of 1.9% to 2.6% as depicted in Figure 3(e).

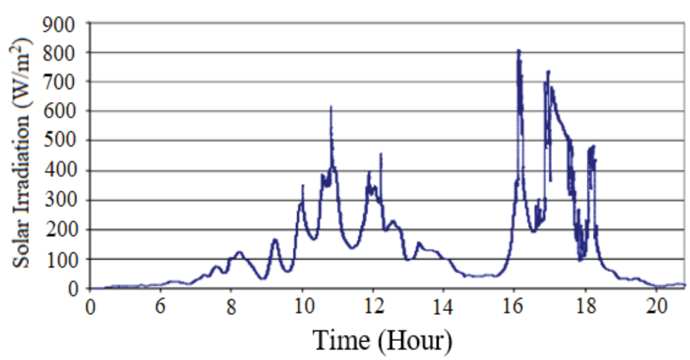

Fig.3(a). Solar irradiation measured on a low irradiation day

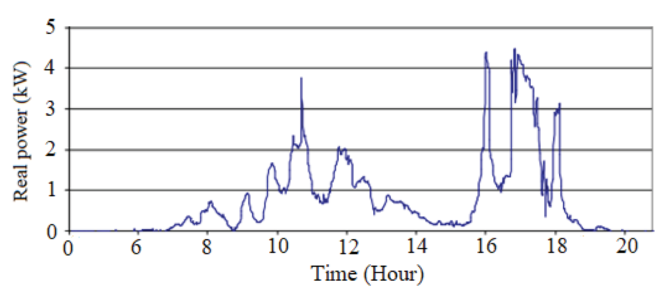

Fig.3(b). Real power measured during low solar irradiation

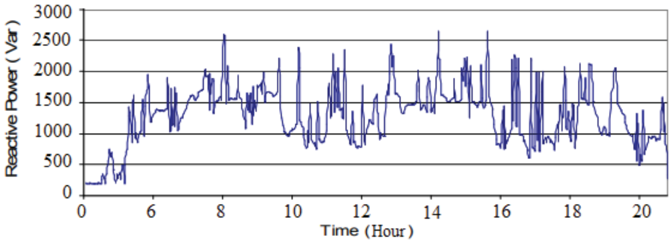

Fig.3(c). Reactive power measured during low solar irradiation

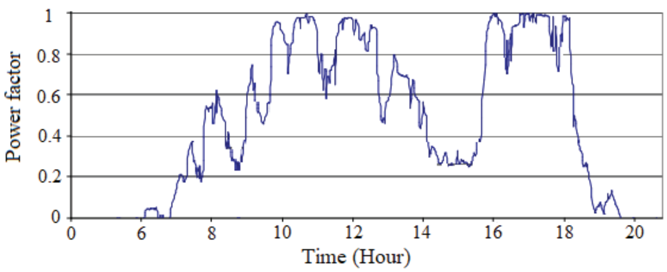

Fig.3(d). Power factor measured during low solar irradiation

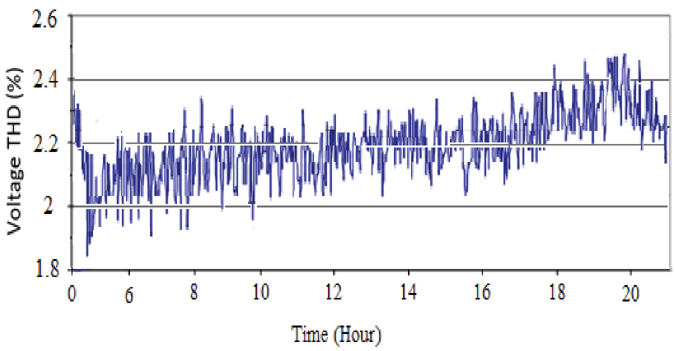

Fig.3(e). Measured voltage THD during low solar irradiation

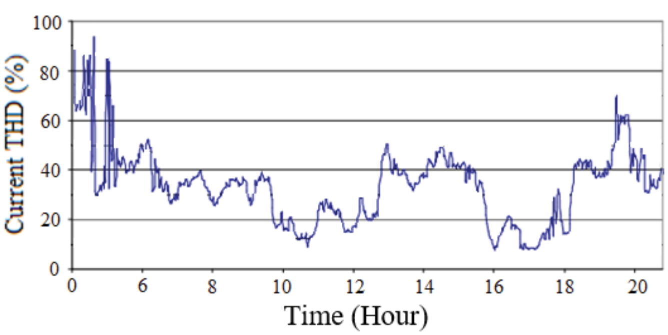

Fig.3(f). Measured current THD during low solar irradiation

Figure 3(e) illustrates the data measured for the voltage THD during low solar irradiation, which peaks at 2.6%. it is observed that the voltage of the system is not significantly affected by low solar irradiation since the p-n junction voltage in PV cells is temperature-dependent. In contrast to the influence of solar irradiation on voltage THD, this study demonstrates that solar irradiation level has a very substantial impact on the level of current THD. The current THD increases beyond the tolerable limit under low solar irradiation.

CONCLUSION

Results from power quality observations made at a grid-tied PV installation are reported in this study. The operation of the grid-tied PV systems has been observed in relation to the general impact of solar irradiation using measurements from an 8kW PV system. Results for two distinct scenarios, notably average and low solar irradiation, have been taken into consideration, and the solar irradiation impact on the power quality measures has been evaluated. Low solar irradiation has been discovered to have a substantial effect on the output power quality of the PV system. Future research on harmonic distortion should focus on establishing the precise harmonic order concerned and implementing effective THD mitigation techniques. Similarly, the simulation output results from a mathematical model of a suitable PV system utilizing the experimental average and low solar irradiation data may be compared to the experimental results.

ACKNOWLEDGEMENT

The Durban University of Technology Smart Grid Research Center's facility support for the authors is acknowledged.

REFERENCES

[1] Adebiyi AA, Ojo EE, Davidson IE. "Performance Evaluation of a Grid-tied PV System in the East Coast of South Africa." In the proceedings of IEEE PES/IAS PowerAfrica, 2020, pp. 1-5.

[2] Gan CK, Tan PH, Khalid S. "System performance comparison between crystalline and thin-film technologies under different installation conditions." In the proceedings of IEEE Conference on Clean Energy and Technology, 2013, pp. 362-367.

[3] Adebiyi AA, Lazarus IJ, Saha AK, Ojo EE. "An Experimental Analysis of the Impact of a Grid-Tied Photovoltaic System on Harmonic Distortion." In the proceedings of International Conference on Power Electronics and Renewable Energy Systems 2022, pp. 431-444. Springer, Singapore.

[4] Dartawan K, Hui L, Austria R, Suehiro M. "Harmonics issues that limit solar photovoltaic generation on distribution circuits." In the proceedings of the World Renewable Energy Forum, 2012, pp. 13-17.

[5] Elkholy A. "Harmonics assessment and mathematical modeling of power quality parameters for low voltage grid connected photovoltaic systems." Solar Energy. 2019, pp. 1-26.

[6] Pinto RJ, Pinto Simões Mariano SJ, Calado MD. "Power quality experimental analysis on rural home grid-connected PV systems." International Journal of Photoenergy, vol. 24, 2015, pp. 1-16.

[7] Mahela OP, Khan B, Alhelou HH, Tanwar S, Padmanaban S. Harmonic mitigation and power quality improvement in utility grid with solar energy penetration using distribution static compensator. IET Power Electronics, vol. 14(5), 2021, pp. 1-22.

[8] Saidi AS. "Impact of grid-tied photovoltaic systems on voltage stability of Tunisian distribution networks using dynamic reactive power control." Ain Shams Engineering Journal, vol. 13(2), 2022, pp. 1-8.

[9] Sharew EA, Kefale HA, Werkie YG. "Power Quality and Performance Analysis of Grid-Connected Solar PV System Based on Recent Grid Integration Requirements." International Journal of Photoenergy. 2021, pp.1-14. https://doi.org/10.1155/2021/4281768

[10] Irfan MM, S. Rangarajan S, Collins ER, Senjyu T. "Enhancing the Power Quality of the Grid Interactive Solar Photovoltaic-Electric Vehicle System." World Electric Vehicle Journal, vol. 12(3):, 2021, pp. 1-19.

[11] Ahsan SM, Khan HA, Hussain A, Tariq S, Zaffar NA. "Harmonic analysis of grid-connected solar PV systems with nonlinear household

loads in low-voltage distribution networks." Sustainability, vol. 13(7), 2021, pp. 1-23.
[12] Sabin D, Norwalk M, Kittredge K, Johnston S. IEEE Power Quality Standards. In the proceedings of 20th International Conference on Harmonics & Quality of Power (ICHQP) 2022, pp. 1-6.
[13] Mahela OP, Khan B, Alhelou HH, Tanwar S, Padmanaban S. "Harmonic mitigation and power quality improvement in utility grid with solar energy penetration using distribution static compensator." IET Power Electronics, vol. 14(5), 2021, pp. 1-22.
[14] Arranz-Gimon A, Zorita-Lamadrid A, Morinigo-Sotelo D, Duque-Perez O. A review of total harmonic distortion factors for the measurement of harmonic and interharmonic pollution in modern power systems. Energies. 2021, vol. 14(20), pp.1-38.
[15] Alabri W, Jayaweera D. "Voltage regulation in unbalanced power distribution systems with residential PV systems." International Journal of Electrical Power & Energy Systems. 2021, pp.1-12.
[16] Salem WA, Gabr Ibrahim W, Abdelsadek AM, Nafeh AA. "Grid connected photovoltaic system impression on power quality of low voltage distribution system." Cogent Engineering, vol. 9(1), 2022, pp. 1-12.

Design and Application of the Passive Filters for Improved Power Quality in Stand-alone PV Systems

Sandile Dlamini
Department of Electrical Power Engineering
Durban University of Technology
Durban, South Africa
21434128@dut4life.ac.za

Innocent E. Davidson
Department of Electrical Power Engineering
Durban University of Technology
Durban, South Africa
innocentD@dut.ac.za

Abayomi A. Adebiyi
Department of Electrical Power Engineering
Durban University of Technology
Durban, South Africa
abayomia@dut.ac.za

Abstract— **Harmonic components have developed in power systems due to the nonlinear properties of the circuit components utilized in power electronics-based products and their rapid application. Power systems rely on fundamental quantities like sinusoidally varying voltage and current, which oscillate at a frequency of 50 Hz. The standard restrictions of IEEE-519-1992 are utilized as a benchmark in this study. To generate the best output, the total harmonic distortion (THD) should be decreased below the limit even for certain individual harmonic numbers, and reflect the power factor output. Using the results of the simulation and projections for each mitigation strategy, by using this methodology, the THD_I can be reduced below the IEEE-519 standard while also providing cost and electrical advantages. Analyzed and modelled is the PV system, which comprises solar panels, a DC-DC converter, a DC-AC inverter, and a nonlinear load. This paper discusses the fundamentals of filter design and PV system components. It also discusses harmonics' causes and effects, as well as ways to the improvement of power factor (PF), and power quality (PQ) and to make sure that our power systems, do protect all the equipment connected to the PV system. A proposed standalone PV system and a Passive LLCL filter were designed to reduce current total harmonic distortion (THD_I) and voltage total harmonic distortion (THD_V). The non-linear loads and the secondary side of the inverter are separated by an LLCL passive filtration, and simulation results obtained with MATLAB/Simulink software are consistent with the theoretical study. The values of THD_V and THD_I decreased from 90.88% to 1.967% and 74.24% to 1.95%, respectively.**

Keywords— PV System, passive filter, DC–AC converter, harmonic mitigation, total harmonic distortion (THD),

I. INTRODUCTION

The South Africa Governments are becoming more interested in the value of integrating renewable energy sources like wind and solar to evaluate the performance of power systems due to the decline in the use of fossil fuels. Solar energy, which has recently surpassed all other renewable energy sources in popularity, is one of the most intriguing modern technologies. By using photovoltaic (PV) modules for a stand-alone system, solar energy is directly harnessed from the sun. Nonlinear components utilized in electric circuits are the primary cause of harmonic generation. By injecting harmonic elements into the waveforms, these components distort the sinusoidal waveform of the voltage and current signals. These harmonic components appear as multiples of the primary components by integers [1]. Harmonic currents produced by power electronics circuit components like transistors, diodes, thyristors, IGBT and MOSFET switches, commonly cause harmonic distortion and power system quality degradation in electrical power systems [2]. The output current quality of a PV inverter is driven by a variety of factors. The amount of solar irradiation is a significant component that raises the levels of current THD and reactive power. Low irradiance levels, such as at sunrise, sunset, and on cloudy days, cause an increase in the THD_I of the output current, but this effect is severely reduced once the PV inverter's output active power reaches its nominal value. The output signal is distorted harmonically because of the power converters that are used to connect PV systems to the power load. To establish a distributed renewable energy generating system, Any other renewable energy sources can be integrated into a solar generation system, linked with the grid, or operated independently (a stand-alone system). Home lighting and water pumps are examples of medium-power applications that use contemporary standalone PV-powered medium-power systems [3, 4]. Figure 1 depicts the single-phase stand-alone photovoltaic system.

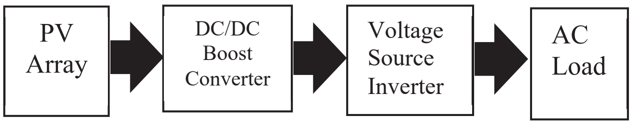

Fig. 1. Configuration of a stand-alone photovoltaic system(single-phase)

This system is made up of a Photovoltaic array that produces the necessary dc voltage by connecting several Solar cells in parallel and series. A dc-dc boost converter is required to produce a controlled higher dc voltage since the voltage collected from a Photovoltaic is low and it is preferred to achieve a constant voltage from the system. Without the need for a transformer, an inverter that connects the Photovoltaic to the standalone application can provide an ac output voltage [5]. Due to its straightforward and convenient control mechanism, the traditional pulse width modulated inverter (PWM) was frequently employed for small PV systems. PWM inverters typically use quick semiconductor switch switching, which produces high-frequency noise [6]. Additionally, all PWM schemes automatically generate harmonics because of the high dv/dt and di/dt semiconductor switching transients. When an off-grid non-linear load or a connection to the grid is involved, these defects outcome in a distorted inverter secondary side, that affects (PQ) power quality. Harmonics in the line current and line voltage are often eliminated using passive filters. Additionally, such filtration of passive increase the realiabilty and (PF)Power Factor of the system [7][8].

The principal focus of this research is the design and analysis of several passive filter designs for a single-phase standalone PV system for medium power applications. LLCL filtration topologies are used for the passive filter design [9]. Each passive filter used in this study is evaluated for total harmonic distortion (THD), and a comparison is made regarding power quality (PQ) perfection/improvement. The paper is segmented as follows: Section I introduced the study. In Section II, there is a brief explanation of the modelling single-phase PV system. The harmonic analysis of the Photovoltaic system, section III. The LLCL designs analysis for the standalone PV system is covered in Section IV. Section VI completes the assignment after Section V has examined the simulation results of an off-grid PV system modelling.

A. PV Array Modeling

The simplest form of a solar cell is designed using a current source, a diode, a shunt resistor R_{sh}, and a resistor R_S.

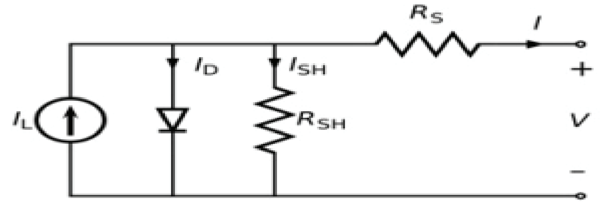

Fig. 2. A PV Cell model

The fundamental PV cell model has been developed. There are three inputs, but only two of them are essential for determining how the system will function and generating more output power [10]. The output voltage for the photovoltaic cells is designed using Equation (1) below.

$$V_C = \frac{cKT_O}{e} In \frac{I_{ph} + I_d - I_c}{I_c} \qquad (1)$$

where **e** = charged electrons; **K** = Boltzmann's constant; $\boldsymbol{I_C}$= current drawn from a PV cell; $\boldsymbol{I_{ph}/I_L}$= photovoltaic current dependent on temperature and sun irradiation; $\boldsymbol{I_d}$= diode's reverse saturation current and $\boldsymbol{T_o}$= operating temperature.

The temperature along with sun irradiation affects how much power a PV array generates. Using a known temperature and known solar irradiation level, a PV array model is created [11]. The model has been improved and adjusted to take temperature and solar radiation fluctuations into account. Output voltage and photocurrent of a PV cell change when the surrounding temperature T_α varies. Similarly, variations in the sun's S_C solar irradiation have an impact on the photovoltaic current and operating temperature of PV cells [11, 12].

B. DC-DC Step-up Boost Converter Modelling

The output voltage from the PV module is modified using a step-up boost converter according to the application. A boost converter in step-up mode is shown in Figure 4. It is made up of a controlled switch S, a diode D, a boost inductor L, a filter capacitor C, and a load resistance R. The boost converter's output voltage V_O is given by Equation. (2)

$$\frac{V_O}{V_{IN}} = \frac{1}{1-D} \qquad (2)$$

where: D is the duty cycle of the converter switch.

An inductor value is selected to ensure continuous current flow through the inductor. Current ripple I is often engineered to be 5% of a current output I_0, whereas the voltage ripple V is frequently chosen to be 3% of the output voltage V_O [13, 14].

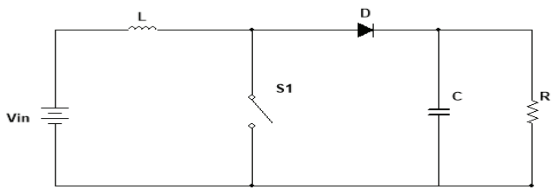

Fig. 3. DC-DC boost converter design

Using Equations (3) and (4), the values of Capacitor C and then Inductor L was selected.

$$L = \frac{V_{in}d}{8f_{sw}\Delta V} \qquad (3)$$

$$C = \frac{I_O d}{f_{sw}\Delta V} \qquad (4)$$

Where f_{SW} is the dc/dc converter switch's switching frequency. The switches are controlled by pulse width modulation technology, and the DC link voltage produced by the dc-dc converter is transformed into an AC output by a single-phase bridge inverter circuit [15]. The inverter output is linked to the load.

C. DC–AC inverter

DC electricity produced by renewable energy sources (RES) like solar power plants needs to be converted into AC electricity [16]. A key part in satisfying this requirement is played by inverters, which stand out for having qualities such as dependability, economy, simplicity, and efficiency [17]. Inverters are also used in wind power facilities for power conversion. DC/AC converter (inverters) are widely used along with many advantages, their major disadvantages are that they produce undesired harmonics. The electricity produced by these harmonics is unfavourable. Due to their resemblance to the system frequency, the low-order harmonics which are produced by the inverter are dangerous to the PV system. These harmonics might have large amplitude levels in comparison to the system's fundamental component. In RES, these system harmonics have an effect that greatly reduces system efficiency [16].

II. Harmonics

The current and voltage distortions known as harmonics are caused by the system's nonlinear loads. Harmonic distortions are a major challenge in circuits with power electronics components as well as other electrical loads with non-linear characteristics. Harmonics is one of the most significant problems with RESs. Harmonic distortions are worse when control circuits are used with power electronics [18]. IEEE standard 519-2014/1992 states that a low voltage system must undergo a harmonic analysis if the THD at the point of common connection (PCC) is greater than 8% [19].

TABLE I. Current Limitations On Distribution Systems' Distortion (IEEE519-1992)

Current limitations (IEEE519-1992)						
$V_n < 69kV$						
I_{SC}/I_L	h<11	11<h<17	17<h<23	23<h<35	H>35	%TDD
<20	4.0	2.0	1.5	0.6	0.3	5.0
20-50	7.0	3.5	2.5	1.0	0.5	8.0

Current limitations (IEEE519-1992)						
$V_n < 69kV$						
50-100	10.0	4.5	4.0	1.5	0.7	12.0
100-1000	12.0	5.5	5.0	2.0	1.0	15.0
1000 >	15	7.0	6.0	2.5	1.4	20.0
69<V_{in} $\leq 161\ kV$						
I_{SC}/I_L	h< 11	11<h<17	17<h<23	23<h<35	H> 35	%TDD
<20	2.0	1.0	0.75	0.3	0.15	2.5
20-50	3.5	1.75	1.25	0.5	0.25	4.0
50-100	5.0	2.25	2.0	0.75	0.35	6.0
100-1000	6.0	2.75	2.5	1.0	0.5	7.5
1000>	7.5	3.5	3.0	1.25	0.7	10.0
$V_{in} > 161kV$						
I_{SC}/I_L	h< 11	11<h<17	17<h<23	23<h<35	H> 35	%TDD
<50	2.0	1.0	0.25	0.3	0.15	2.5
50>	3.0	1.5	1.15	0.5	0.22	4.0

According to the IEEE 519-1992 standard, nonlinear loads are those that happen in electric grid users or off-grid systems when main source measurements of harmonic currents are present (Recommended Practices and Requirements for Harmonic Control in Electric Power Systems) [20]. Limits for triple harmonic emissions from single-phase equipment have been established under the IEC 1000 3-2 standard (Limits for Harmonic Current Emissions). These standards are not difficult to meet in many applications, and the most cost-effective options are currently being developed. Three categories of IEEE and international harmonic standards can be thought of:

- Measuring harmonics: IEC 1000-4-7
- Consumer/System boundaries: IEEE 519-1992, IEC 1000-2-2, IEC 1000-3-6.
- Equipment boundaries: IEC 1000-3-2 (up to 16), IEC 1000-3-4 (16-75 A).

The two standards, IEC 1000-3-2 and 1000-3-4, are thought to have the biggest influence on power electronics design since they place explicit restrictions on certain harmonic content. Additionally, IEEE 519 places restrictions on a few unique harmonics to reduce the harmonics at the common junction. IEEE 519-1992 is the most frequently mentioned harmonic standard. IEEE 519 aimed to define reasonable harmonic targets for nonlinear load electrical systems. It analyzes and outlines fairly constant harmonic restrictions for both consumers and electrical companies or electrical systems [21, 22].

When the short-circuit power is largely due to voltage distortion high-amplitude harmonic currents are an inevitable effect of non-sinusoidal currents. While voltage harmonics are useless in these circumstances, current harmonics seriously impair communication links. The restrictions on harmonic voltage and current are laid forth in the IEEE 519 Standard. This standard's goal is to stop harmonic currents from negatively impacting other consumers and the power grid by travelling backwards. Table 1 the traditional distribution system distortion of the current limitations (IEEE-519- 1992) [23]. The short-circuit rate (SCR = IKD/IL), to which the maximum short-circuit current IKD and the average of the maximum monthly demand load current IL currents are applied, determines the specific constraints in this table. 25 per cent of the limits on odd harmonics are placed on even harmonics [24]. The ratio of THD is created by subtracting the fundamental component's effectiveness derived from the harmonic effective voltage or current values. The thermal phenomenon associated with all the harmonics is referred to as total harmonic distortion. It is the most crucial factor considered when figuring out how high the harmonic components should be in relation to the fundamental component. This applies to both voltage and current. For voltage, total harmonic distortion is expressed as

$$THD_V = 100\ \times \frac{\sqrt{{V^2}_2 + {V^2}_3 + ..{V^2}_n}}{{V^2}_1} \tag{5}$$

$$THD_I = 100 \times \frac{\sqrt{\sum_{n=2}^{\infty} I_n}}{I_1} = 100 \times \frac{\sqrt{I^2 - {I^2}_I}}{I_1} \tag{6}$$

Sinusoidal waveform distortions in voltage and current can be produced by non-linear loads, even ones with low power. Just a few of the negative effects of harmonic components on the PV system off-grid are increased element losses. Increased voltage drops in off-grid PV systems, fluctuating voltage levels, erroneous measurements produced with measuring devices, and issues with control circuits are some of the issues that might affect the operation of a power system. These harmonic waveforms are represented in Figure 4 below.

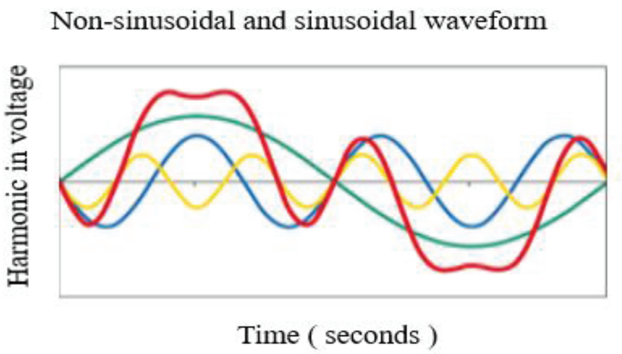

Fig. 4. The harmonic components in a single-phase PV system

The green waveform in Figure 4 indicates the first harmonic (fundamental) in the single phase system, Blue indicate the third harmonics waveform, and yellow indicates the fifth harmonic waveform. The red-coloured waveform indicates the non-sinusoidal waveform.

III. LLCL Passive Filter Design and Analysis

The passive filters improve the quality of the power in Photovoltaic stand-alone structures. Over the past ten years, the LLCL filter was already extensively used in a range of renewable energy applications due to the significant global increase of renewable energy sources (RESs). Power electronic components such as thyristors, diodes, MOSFETs, and IGBTs generate harmonic currents that cause critical power quality issues in PV systems [25, 26]. When the THD is at its peak during low solar irradiation, a PV system operator may be obliged to use larger, more costly filters or even disconnect the PV system from the grid to avoid paying the utility operator's significant THD penalty. By using these nonlinear components, the system's harmonic performance is increased. Moreover, the most important harmonic sources in an off-grid power system are rectifiers, inverters, and DC/DC converters. This issue manifests itself near the resonance frequency [27]. Harmonic levels by altering the current or voltage at one or more frequencies. Designs are generally created to maximize the effectiveness of harmonic components. The use of filters is motivated by both technical and economic factors. Its goal is to reduce the economic and technological costs associated with the damaging effects of harmonics on filters.

The LLCL Passive filters are circuits composed of capacitors C_f, inductors L_1, inductors L_2, and inductors L_f that are installed between the loads and the solar converter. As a result, they are intended to reduce harmonic components that exist outside of the fundamental frequency. In comparison to an active filter, a passive LLCL filter has many benefits, including guaranteed stability, zero power consumption, and low cost, with a traditional design. The primary voltage of a DC-AC converter is shown in Figure 5.

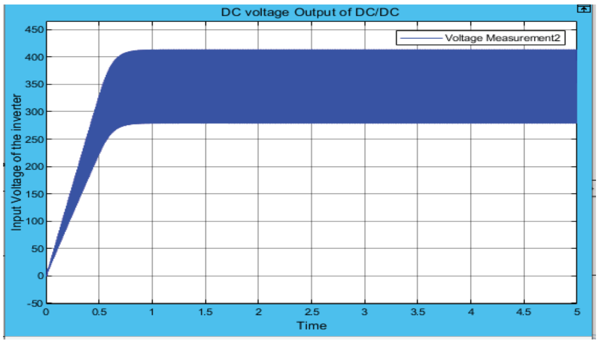

Fig. 5. The primary voltage of a DC-AC CONVERTER

Figure 5 is the output DC voltage of the step-up boost converter which becomes the primary voltage of the DC-AC converter. where the input voltage of the step-up boost converter comes from the PV array output DC voltage. Equation 1 defines the information regarding the parameters and how the voltage step-up boost is configured from the PV array inverter. The parameters are as follows: 5 parallel strings, series connected modules per string 9.5, maximum power 213.15 W, 50 cells per module (N_{cell}), open circuit voltage V_{OC} = 36.3 V, shot circuit current I_{SC} = 7.35 A, temperature coefficient of V_{OC} = -0.36099 (%/^{0}C) and I_{OC} 0.102, solar irradiation = 1000 W/m^2 and PV cell temperatures 25 ^{0}C. Model parameters: I_L = 7.8516 A, I_O = 2.925e^{-10}A, Diode ideality factor 1.1773, R_{sh} = 400.71 Ω, R_S = 0.3941 Ω, The LLCL filter's schematic diagram as designed is depicted in Figure 6.

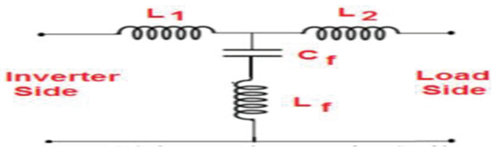

Fig. 6. LLCL filter schematic illustration [9]

For standalone PV systems, a passive LLCL harmonic filter should be properly designed. When designing a passive LLCL filter, one must take into account the solar system's regulated total harmonic distortion, the amount of reactive power (R_P) required in the system, the volume of THD produced from outside sources, and non-linear loads within the system. The LLCL filter is located between the secondary side of the inverter and the non-linear load. The filter makes sure that the system is protected from harmonic distortions [28]. The impedance considers changing for effective harmonics, as well as the filtration's working values, can all be considered (frequency, temperature, voltage). The fundamental frequency on the filters or band-pass, also known as the reactive power (R_P), determines its value. The amount of basic reactive power supplied by the capacitors is the same [29]. The harmonic current and voltage rise to exceptionally high levels if the resonance event occurs in or close to one of these harmonic components. As a result, changing the filter alters the frequency of resonance. It is a useful method for improving the quality of power generated to an inductive RLC load by an off-grid PV system. An inductance L_1 on the inverter output, an inductance L_2 is linked with an AC load, and a capacitor C_f comprising a passive LLCL filtration circuit. Equation (7) defines the transfer-function, for the LLCL filter.

$$G_{LOAD}(jw) = \frac{L_f C_f S^2 + 1}{[L_1 L_2 C_f + (L_1 + L_2) C_f] S^3 + (L_1 + L_2) S} \qquad (7)$$

IV. Modelling and Result

A full wave bridge rectifier with RL load connected to a standalone PV system with a passive filter is proposed and simulated using Matlab/Simulink as shown in figure 8 in this paper. The simulation is performed as a series AC reactor with a tuned filter to the fifth harmonics and a high pass filter to compensate for higher-order harmonics.

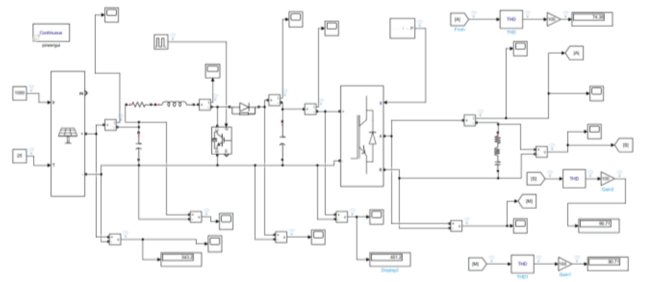

Fig. 7. A stand-alone PV system without an LLCL filter

The analyses investigated the compliance of the standalone PV system to the IEEE standard limit for current total harmonic distortion (THD_I) and voltage total harmonic distortion (THD_V) and mitigate the poor THD_V to less than 5% from the unfiltered current and voltage THD of 74.24% and 90.88% respectively to mitigate the negative impact of the high-order harmonics on the entire PV system.

A. *Equations of LLCL Filter*

The LLCL filter's frequency response should be selected from the range described in Equation (8). Whenever this range is selected, within the off-grid solar system, there is no resonance.

$$10 f_L < f_{res} < 0.5 f_{sw} \qquad (8)$$

Where f_L is the load frequency, f_{sw} is the switching frequency and f_{res} is the resonance frequency

The resonance frequency of the LLCL filter is defined in Equation (9)

$$f_{res} = \frac{1}{2\pi \times \sqrt{(\frac{L_1 L_2}{L_1 + L_2} + L_f)C_f}} \tag{9}$$

We could perhaps mitigate more harmonics by increasing C_f but This lowers the efficiency of the entire filter system by increasing the reactive power and increasing the current demand for L_1. Equation (10) defines the reactive power absorbed by the capacitor.

$$Q_C = \frac{3{V_{rated}}^2}{X_C} = \frac{3{V_{rated}}^2}{\frac{1}{\omega C}} = 3(2\pi f)C{V_{rated}}^2 \leq \beta P_{rated} \tag{10}$$

Under which Qc denotes the reactive power consumed with the capacitor. V_{RATE} remains the effective phase voltage value. is the rate of reactive power accumulation. It is usually chosen as shown below.

$$\beta < 5\% \tag{11}$$

By looking at reactive power consumed within the system the conditions rated for filtration are considered and used to calculate the C_f value for the LLCL filter (11). The C_f valuation for the LLCL filter is determined by Equation (12).

$$L_1 = \frac{V_{in}}{8 I_H f_{res}} \tag{12}$$

$$L_2 = \frac{L_1}{\beta} \tag{13}$$

$$L_f = \frac{1}{C_f {f^2}_{sw}} \tag{14}$$

In this Equation (13), β is the ratio factor of the inductor. For medium and low-power devices, the coefficient is set to be bigger than 1. Where I_H is the amount of ripple current, that is rated <5% of the current, and V_{in} is the DC voltage or output of the DC TO DC boost to the DC to AC converter (inverter).

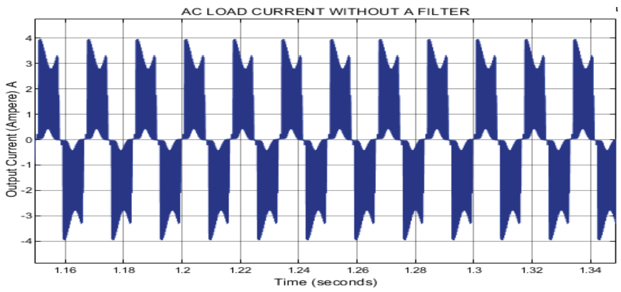

(a)

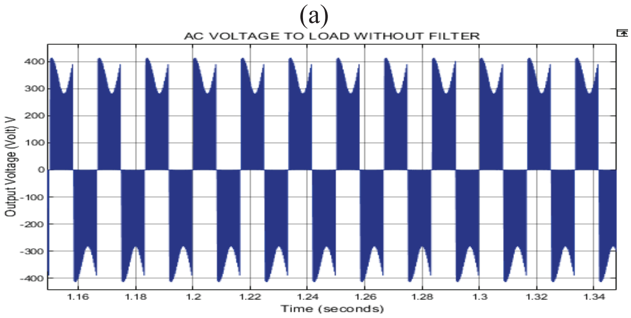

(b)

Fig. 8. (a) the output current waveform of the PV system without a filter, (b) the output waveform of voltage without a filter

B. *Designed PV System with an LLCL Filter*

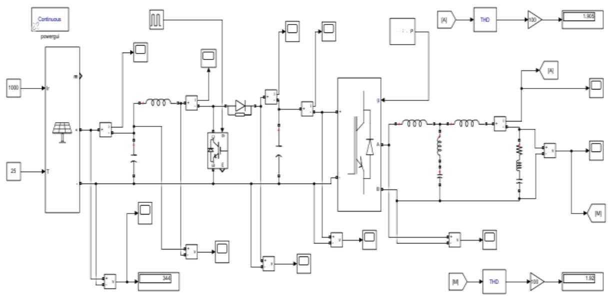

Fig. 9. A stand-alone Photovoltaic with LLCL filtration

TABLE II. LLCL FILTER PARAMETERS

Parameter of Passive LLCL Filter	**Principles components sizing**
L1	883.9 mH
Lf	590 uH
Cf	169.8 uF
L2	17618 mH

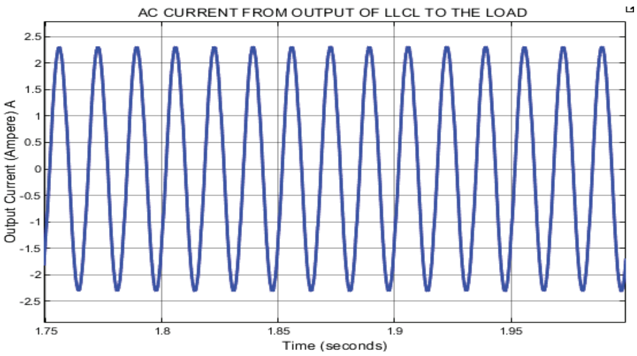

(a)

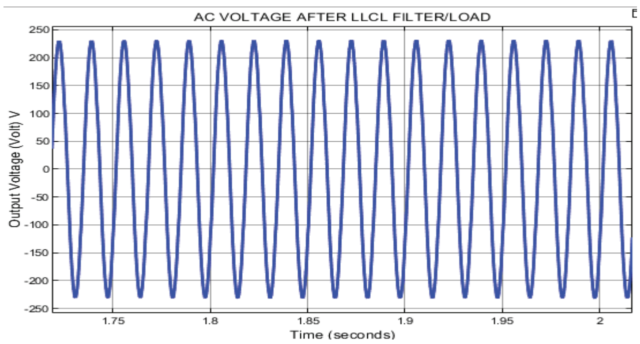

(b)

Fig. 10. (a) current waveform with LLCL filter on a PV system. (b) voltage waveform with LLCL filter

V. RESULTS AND DISCUSSION

The entire standalone system may be affected by higher-order harmonics. These effects reduce the efficiency of the power system and other equipment. Off-grid PV systems have both odd and even harmonics. The amount of radiation present affects THD values. At lower radiation levels, the THD value has been observed to increase. According to the simulation results, odd harmonics components make up more harmonics than even harmonics. correspondingly demonstrates, the THD_I and THD_V value has decreased towards 1.95%, and 1.961% respectively. In Figure 10 the results show a shootout on waveform which could damage the equipment connected to the system. With the IEEE standard to reduce harmonic components. Figure 12 shows the effect of the LLCL filter, where harmonic components are reduced into significant values and with such total harmonic distortion mitigation, it means improved power quality, Power Factor, and protection of equipment within the system.

VI. CONCLUSION

This paper compares the filter designs on the current THDi, THDv stand-alone PV system with and without the passive LLCL filter. The outcome of the MATLAB simulation demonstrates that the passive LLCL filter successfully lower voltage and current total harmonic distortions. THDv and THDi values were reduced from 90.88% to 1.967% and 74.24% to 1.95%, respectively. The analyzed results conclude that the proposed passive filter design for a stand-alone PV system improves power quality, and power factor and protects the system. In the future, the LLCL filter can be compared with other passive filters and active filters to analyze total harmonic distortion within the stand-alone PV system.

ACKNOWLEDGEMENT

The Smart Grid Research Centre, Durban University of Technology provided facility support for this study and is hereby acknowledged.

REFERENCES

[1] S. Adak, "Harmonics Mitigation of Stand-Alone Photovoltaic System Using LC Passive Filter," Journal of Electrical Engineering & Technology, vol. 16, no. 5, pp. 2389-2396, 2021.

[2] H. Bai, X. Wang, P. C. Loh, and F. Blaabjerg, "Harmonic analysis and mitigation of low-frequency switching voltage source inverter with series LC filtered VSI," in 2017 IEEE Applied Power Electronics Conference and Exposition (APEC), 2017: IEEE, pp. 3299-3306.

[3] S. Khomfoi and L. M. Tolbert, "Power electronics handbook," University of Tennessee, p. 2, 2007.

[4] S. Weixiang, "Design of standalone photovoltaic system at minimum cost in Malaysia," in 2008 3rd IEEE Conference on Industrial Electronics and Applications, 2008: IEEE, pp. 702-707.

[5] S. Jain and V. Agarwal, "A single-stage grid connected inverter topology for solar PV systems with maximum power point tracking," IEEE transactions on power electronics, vol. 22, no. 5, pp. 1928-1940, 2007.

[6] M. Jayaraman, V. Sreedevi, and R. Balakrishnan, "Analysis and design of passive filters for power quality improvement in standalone PV systems," in 2013 Nirma University International Conference on Engineering (NUiCONE), 2013: IEEE, pp. 1-6.

[7] G. Brando, L. Di Noia, R. Rizzo, D. Lauria, and C. Pisani, "An advanced system for power supply and power quality improvement of isolated AC passive network," in 2015 International Conference on Renewable Energy Research and Applications (ICRERA), 2015: IEEE, pp. 1446-1450.

[8] O. Deveci and C. Kasnakoğlu, "Performance improvement of a photovoltaic system using a controller redesign based on numerical modeling," International Journal of Hydrogen Energy, vol. 41, no. 29, pp. 12634-12649, 2016.

[9] A. Suleyman, H. Cangi, and A. S. Yilmaz, "Design of an LLCL type filter for stand-alone PV systems' harmonics," Journal of Energy Systems, vol. 3, no. 1, pp. 36-50, 2019.

[10] S. Lyden, M. Haque, A. Gargoom, and M. Negnevitsky, "Modelling photovoltaic cell: Issues and operational constraints," in 2012 IEEE International Conference on Power System Technology (POWERCON), 2012: IEEE, pp. 1-6.

[11] X. Bao, F. Zhuo, Y. Tian, and P. Tan, "Simplified feedback linearization control of three-phase photovoltaic inverter with an LCL filter," IEEE Transactions on Power Electronics, vol. 28, no. 6, pp. 2739-2752, 2012.

[12] I. Altas and A. Sharaf, "A photovoltaic array simulation model for Matlab-Simulink GUI environment," in 2007 International Conference on Clean Electrical Power, 2007: IEEE, pp. 341-345.

[13] A. R. Jordehi, "Maximum power point tracking in photovoltaic (PV) systems: A review of different approaches," Renewable and Sustainable Energy Reviews, vol. 65, pp. 1127-1138, 2016.

[14] C. W. Lander, Power electronics. McGraw-Hill, Inc., 1987.

[15] N. H. Baharudin, T. Mansur, F. A. Hamid, R. Ali, and M. I. Misrun, "Topologies of DC-DC converter in solar PV applications," Indonesian Journal of Electrical Engineering and Computer Science, vol. 8, no. 2, pp. 368-374, 2017.

[16] M. A. Memon, S. Mekhilef, M. Mubin, and M. Aamir, "Selective harmonic elimination in inverters using bio-inspired intelligent algorithms for renewable energy conversion applications: A review," Renewable and Sustainable Energy Reviews, vol. 82, pp. 2235-2253, 2018.

[17] M. H. Etesami, N. Farokhnia, and S. H. Fathi, "Colonial competitive algorithm development toward harmonic minimization in multilevel inverters," IEEE Transactions on Industrial Informatics, vol. 11, no. 2, pp. 459-466, 2015.

[18] M. M. Elkholy, M. El-Hameed, and A. El-Fergany, "Harmonic analysis of hybrid renewable microgrids comprising optimal design of passive filters and uncertainties," Electric Power Systems Research, vol. 163, pp. 491-501, 2018.

[19] Y.-S. Cho and H. Cha, "Single-tuned passive harmonic filter design considering variances of tuning and quality factor," Journal of International Council on Electrical Engineering, vol. 1, no. 1, pp. 7-13, 2011.

[20] M. Bajaj and A. K. Singh, "Hosting capacity enhancement of renewable-based distributed generation in harmonically polluted distribution systems using passive harmonic filtering," Sustainable Energy Technologies and Assessments, vol. 44, p. 101030, 2021.

[21] M. A. E. Alali, Z. Sabiri, Y. B. Shtessel, and J.-P. Barbot, "Study of a common control strategy for grid-connected shunt active photovoltaic filter without DC/DC converter," Sustainable Energy Technologies and Assessments, vol. 45, p. 101149, 2021.

[22] B. Sahoo, S. K. Routray, and P. K. Rout, "Execution of robust dynamic sliding mode control for smart photovoltaic application," Sustainable Energy Technologies and Assessments, vol. 45, p. 101150, 2021.

[23] IEEE 519-1992 - IEEE Recommended Practices and Requirements for Harmonic Control in Electrical Power Systems n.d, 1992 IEEE.

[24] A. Casaleiro, R. A. e Silva, B. Teixeira, and J. M. Serra, "Experimental assessment and model validation of power quality parameters for vehicle-to-grid systems," Electric Power Systems Research, vol. 191, p. 106891, 2021.

[25] M. Tali, A. Obbadi, A. Elfajri, and Y. Errami, "Passive filter for harmonics mitigation in standalone PV system for non linear load," in 2014 International Renewable and Sustainable Energy Conference (IRSEC), 2014: IEEE, pp. 499-504.

[26] W. Wu, Y. He, T. Tang, and F. Blaabjerg, "A new design method for the passive damped LCL and LLCL filter-based single-phase grid-tied inverter," IEEE transactions on industrial electronics, vol. 60, no. 10, pp. 4339-4350, 2012.

[27] Y. Liu, W. Wu, Y. He, Z. Lin, F. Blaabjerg, and H. S.-H. Chung, "An efficient and robust hybrid damper for $ LCL $-or $ LLCL $-based grid-tied inverter with strong grid-side harmonic voltage effect rejection," IEEE Transactions on Industrial Electronics, vol. 63, no. 2, pp. 926-936, 2015.

[28] K. Prabha, T. Malathi, and M. Muruganandam, "Power Quality Features Improvement In Single-Phase Grid-Connected Inverter With Non-Linear Loads."

[29] A. H. Patel, "Power quality of stand-alone “Photovoltaic (PV) and Wind” energy-based system

Maximum Power Point Tracking Algorithms Performance Comparison for a Grid-Tied Photovoltaic System

Louis Nicaise Nguefack
Department of Electrical Power Engineering
Durban University of Technology, South Africa
ngueflouis@gmail.com

Innocent E. Davidson
Department of Electrical Power Engineering
Durban University of Technology, South Africa
innocentD@dut.ac.za

Abayomi A. Adebiyi
Department of Electrical Power Engineering
Durban University of Technology, South Africa
abayomia@dut.ac.za

***Abstract* – Since the photovoltaic (PV) system output power is dependent on solar irradiation and operating temperature, the maximum power point tracking (MPPT) algorithm is required to track the maximum power point (MPP) of the PV system regardless of climatic conditions. The perturbation and observation (P&O) algorithm is the conventional solution for the MPPT controller, but it has oscillation issues around the MPP operating point; enhancing the MPP tracked by this algorithm has been a major focus for academics. This paper presents the design and modelling of a Type-1 and Type-2 Fuzzy Logic Controller (FLC) for tracking the maximum power point of a PV system in Matlab/Simulink for a 150 W PV system. A comparative analysis of the P&O, Type-1 and Type-2 Fuzzy Logic Controllers was conducted under steady and varied solar irradiation conditions. The simulation results demonstrated the superiority of the Type-2 FLC algorithm in terms of power loss reduction and minimization of oscillations at the maximum power point.**

Index Terms - Photovoltaic (PV) system, MPPT controller, Fuzzy Logic Controller, Power loss reduction.

I. INTRODUCTION

The world's energy demands are rapidly increasing, resulting in excessive fossil fuel usage, which has had significant environmental implications such as global warming and the depletion of the ozone layer. Diversification of energy supplies is critical for mitigating the adverse effects of fossil fuel energy technologies, which threaten global ecological sustainability. Also, rising fuel prices and increasing fossil resource scarcity may have significant economic and political consequences for countries that depend on fossil fuels for energy generation. As a result, increasing energy efficiency and installing optimal renewable energy sources are critical for long-term development [1-2]. Different studies have shown that renewable energy technologies are cost-competitive compared with conventional power generation [3-5]. As a result, some countries have implemented new energy policies to stimulate investment in alternative energy sources such as solar PV systems, wind, biomass, and small-scale hydropower. The solar PV system is one of the most important renewable energy sources, and its market share is expected to expand in the future. According to the International Renewable Energy Agency (IRENA) research, solar PV systems and wind power will make up a significant portion of electrical output by 2050 with 14.5 terawatts of installed capacity. Renewables are estimated to have a combined power output capacity of approximately 20 terawatts [6]. The challenge with PV systems is the uncertainty of how much solar irradiation they will receive as weather conditions changes suddenly, causing the peak solar irradiation availability to differ from peak electricity demand. MPPT, a technique for effective energy tracking, is required for efficient load power delivery and energy storage to provide a continuous power output [7]. Figure 1 illustrates the application of solar PV systems as both stand-alone and grid-connected systems. A grid-connected PV system has been considered for this study.

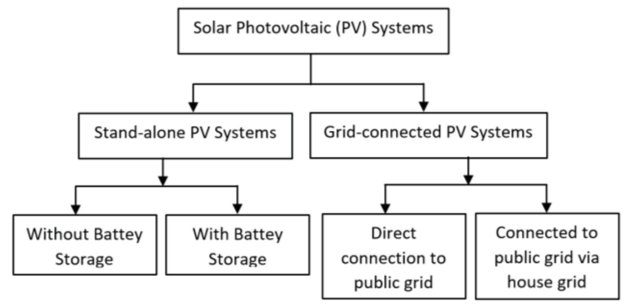

Fig. 1 Applications of PV Systems [8]

In the research of solar PV systems, two methodologies are possible: experimental and numerical simulation. This study engages the numerical simulation to determine an efficient MPPT algorithm suitable for a grid-tied PV system to extract the maximum power from the PV array. Likewise, provide an optimized MPPT algorithm with low power losses and quick maximum power point tracking during changing environmental operating conditions.

A DC-DC boost converter was designed for the PV system to implement the different MPPT control to compare the performance indices of MPPT algorithms which include the convergence rate and computational complexity. Apart from the conventional Perturbation and Observation (P&O), Incremental Conductance (IC), and Hill Climbing MPPT methods, several new MPPT methodologies have been developed in recent years. However, artificial intelligence-based MPPTs such as Artificial Neural Networks (ANN) and Fuzzy Logic Control (FLC) for PV systems are becoming more popular to circumvent the limitations of conventional MPPT algorithms. Fuzzy Logic Control (FLC) is one of the artificial intelligence techniques used widely to improve the results of conventional methods of MPPT. The FLC works basically in three main stages, i.e., fuzzification, rule base inference system, and defuzzification. In fuzzification, the input is converted from crispy numeral value to linguistic variable based on the degree of membership assigned. Then, the rule-based inference is used to find out the output of the fuzzy logic controller. The Mamdani, Sugeno, and Tsukamoto method of the FLC inference system has been studied [9]. The Mamdani inference system was utilized to convert the precision output per the rule base [10-11]. Defuzzification is the process of converting output linguistic variables into numerical values. The paper is organized as follows: a brief overview of the considered PV model, description of the proposed MPPT method, a detailed analysis of the MPPT technique, the results discussion, and conclusions.

II. DESIGN AND MODELLING OF A PHOTOVOLTAIC SYSTEM

A. *Moddelling of PV Cell*

A PV panel is expressed analytically by its current against voltage (I-V) characteristics obtained by arranging the solar cells in series and parallel. However, due to the PV cell operational characteristic, the current against the voltage curve is nonlinear. Therefore, a single diode model representation of solar cells has been considered for this study analysis among the different analytical models of the PV system that have been proposed in the literature [13-14]. The dependence of the model on solar irradiation and temperature conditions is vividly presented in equations (1) to (3). Considering the PV panels' series and parallel connections, the PV array power curve derived from the mathematical model in equations (1) to (3) is depicted in Fig. 2.

$$I_{PV} = n_p\left(I_{ph} - I_0\left[e^{\frac{q(V_{PV}+R_S I_{PV})}{AkTn_S}} - 1\right] - \frac{(V_{PV} + R_S I_{PV})}{n_S R_{sh}}\right) \tag{1}$$

$$I_{ph} = I_{ph\_STC} + K_I(T - T_{STC})\frac{G}{G_{STC}} \tag{2}$$

$$I_0 = \frac{I_{SC\_STC} + K_I(T - T_{STC})}{e^{(V_{OC_{STC}}+K_V(T-T_{STC}))/V_T - 1}} \tag{3}$$

The typical power against voltage (P-V) curve of the PV array during uniform solar irradiation includes a single peak, as presented in Fig. 2.

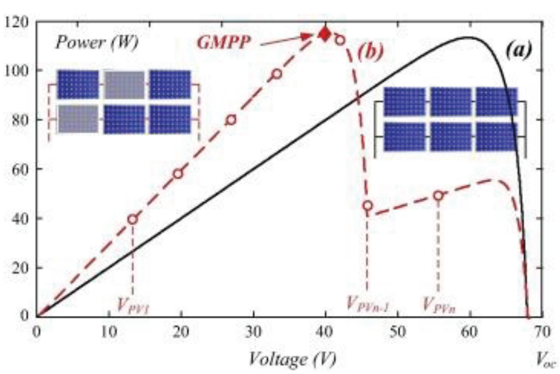

Fig. 2 PV panel P–V characteristic under (a) uniform solar irradiation and (b) shading condition [13].

When a portion of a PV panel is partially shaded, the current flowing through the unshaded cells decreases, resulting in hot-spot heating that causes the shaded cell crack [13]. Therefore, an external bypass diode is connected to allow the current from the unshaded cells to flow to the shaded cells, preventing the hot-spot phenomenon that damages PV cells. A similar approach is used at the PV array level. Despite the mitigation of the partial shading by the bypass diode, the power generated by the PV system reduces due to two factors: the amplitude and position of the global MPP shift when the shading condition varies, and the P–V curve has several peaks. PV array's P–V characteristic during uniform and partial shaded operating conditions depicted in Fig. 2 emphasize these two factors. The MPPT implementations presented in the following sections are designed to extract the maximum power from the PV array during rapid and repeated shade condition variations. Table I shows the electrical specification of the 150 W Microtek PV panel (MTK150W/12V) used.

TABLE I
ELECTRICAL PARAMETER OF THE PV PANEL MTK150W/12V

Parameter	Value
Panel Watts	150 Watt
Voltage at Maximum Power (V_{MPP}) [V]	17.72
Current at Maximum Power (I_{MPP}) [A]	8.47
Open Circuit Voltage (V_{OC}) [V]	22.47
Short Circuit Current (I_{SC}) [A]	8.90
Module Efficiency (%)	14.91%

B. *DC-DC Boost Converter*

The DC-DC converter is generally utilized in regulated switch-mode DC power supplies. The input of this converter is an unregulated DC voltage obtained from the PV array, and it fluctuates due to variations of solar irradiation and temperature. The average DC output voltage is controlled for this converter to obtain the desired value, notwithstanding the input voltage variation. Output voltage regulation in the DC-DC converter is achieved by consistent adjustment of the amount of energy absorbed from the source and injected into the load, controlled by the relative durations of the absorption and injection intervals. The converter operates in two different modes depending upon its energy storage capacity and the relative length of the switching period. These two modes are the discontinues conduction mode (DCM) and continuous conduction mode (CCM). The input-output voltage relationship for a DC-DC boost converter in continuous conduction mode can be calculated using the averaging principle presented in Equation (4).

$$\frac{V_o}{V_{in}} = \frac{1}{1-D} \tag{4}$$

A graphical representation of the boost converter is presented in Fig. 3. Only four external components are required for the DC-DC boost converter: an inductor, an electronic switch, a diode, and an output capacitor. The detail of the boost converter topology and operation has been discussed in [14,15].

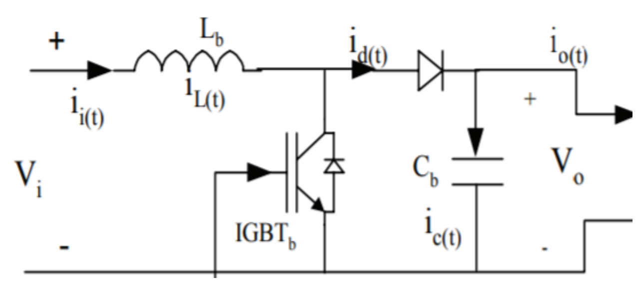

Fig. 3 Circuit diagram of a DC-DC Boost Converter

III. MPPT CONTROL ALGORITHMS

A. *Perturbation and Observation (P&O) based MPPT*

It is one of the simplest MPPT algorithms to implement and only requires a voltage and current sensor to calculate the power and compare it to the previous cycle power. The algorithm's method of operation is presented in Fig. 4. This conventional MPPT technique depends on the change in the PV-generated power as the voltage changes. As $\Delta P/\Delta V > 0$, the conventional controller shifts the PV voltage in the same direction. Otherwise, the MPPT controller reverses the voltage step variation in the direction of the MPP. Therefore, the amplitude of involved oscillations around the MPP relies on the applied voltage step size.

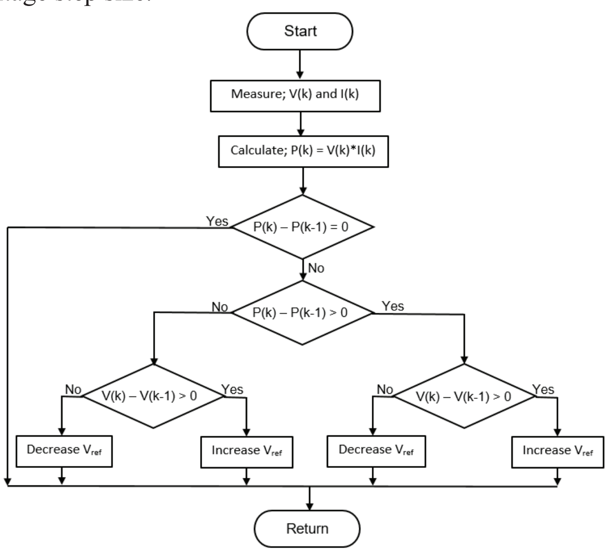

Fig. 4 P&O MPPT algorithm flowchart

B. *Fuzzy Logic Control based MPPT*

Fuzzy logic control is a technique for designing nonlinear controllers using heuristic data. The block diagram of a fuzzy logic controller is presented in Fig. 5.

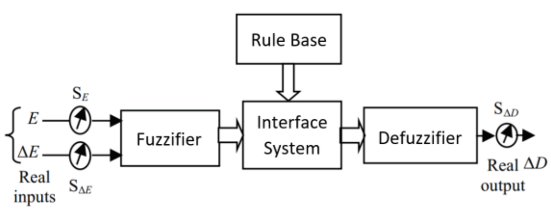

Fig. 5 The fuzzy logic controller structure

The FLC designed for this study has two input variables (error, *E,* and change in error, *ΔE,* and one output control signal, *ΔD).* The input and output at sampling time, k, are computed as follows:

$$E(k) = \frac{[P(k) - P(k-1)]}{[V(k) - V(k-1)]} \tag{5}$$

$$\Delta E(k) = E(k) - D(k-1) \tag{6}$$

$$D(k) = D(k-1) + \Delta D(k) \tag{7}$$

Where: P(k) and V(k) are the PV panel output power and voltage at the sampling k. D(k) is the change in the duty ratio, which is used as the control output of FLC to compute the actual duty ratio D(k) of the DC-DC boost converter at sampling k. E(k) denotes the slope of the P-V curve. As a result, the sign of E(k) indicates the location of the operational point at sample k on the PV panel's power against voltage (P-V) curve, either to the left or to the right of MPP, while the input E(k) defines the movement direction of this point. Fig. 6 presents the MATLAB/Simulink simulation model of FLC. The three main components of the FLC are fuzzification, fuzzy inference system, and defuzzification.

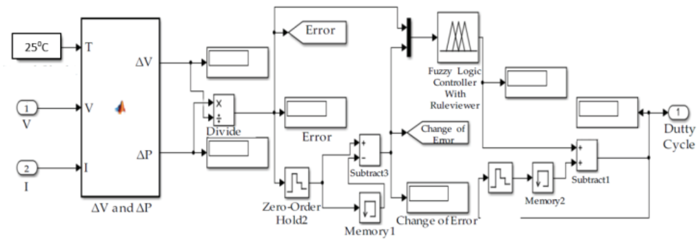

Fig. 6 Model of Fuzzy Logic Controller.

1) *Fuzzification*

As illustrated in Fig. 5, the two inputs (E(k) and ΔE(k)) are normalized using scaling factors (S_E) and ($S_{\Delta E}$) and then transformed to the degree of fuzzy variables using linguistic sets. The membership grades of the input and output variables utilized in this investigation are shown in Figures 7 to 9, with five fuzzy subsets for each membership function: Negative Medium (NM), Negative Small (NS), Zero (Z), Positive Small (PS), and Positive Medium (PM) (PM).

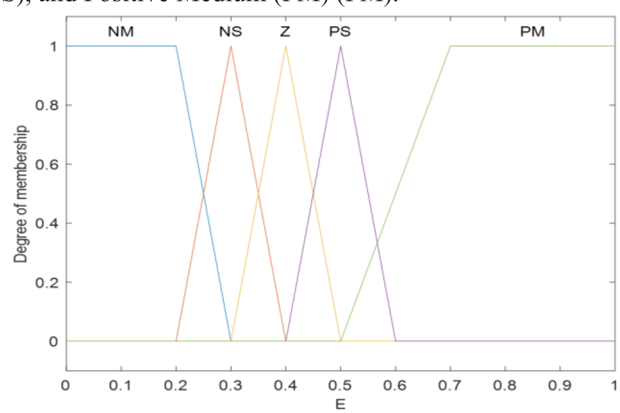

Fig. 7 Membership functions for input variable (E)

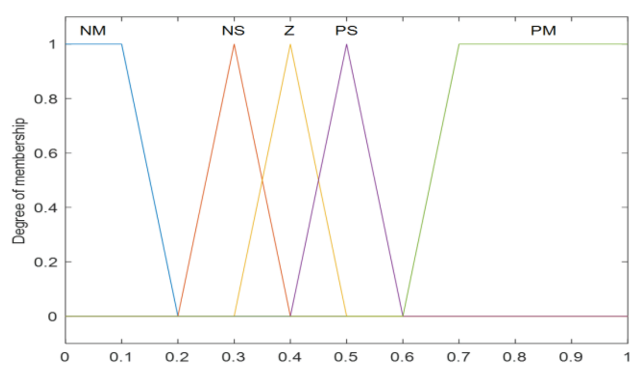

Fig. 8 Membership functions for input variable (ΔE)

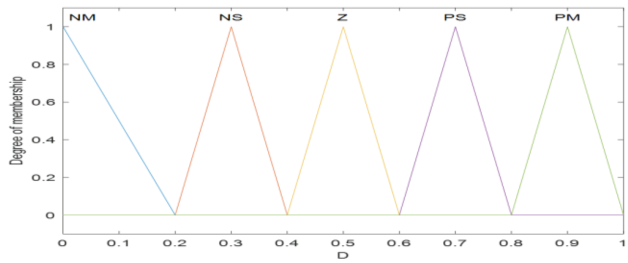

Fig. 9 *Functions for output variable (D)*

2) Fuzzy Rules and Interference System

The inference system uses the fuzzy IF-THEN rules to the fuzzy inputs and produces the aggregated fuzzy output. Table II presents the twenty-five fuzzy IF-THEN rules considered in this study to generate the suitable control signal (D). The MPP's operating point position determines the rules. For example, the duty ratio (D) is altered if the operating point shifts away from the MPP or converges toward the MPP. This means that if the operating point is distant on the left of the MPP and the change in the P-V slope is zero, then the duty ratio is decreased mainly to attain the MPP.

TABLE II
FLC RULE BASE

E \ ΔE	NM	NS	Z	PS	PM
NM	PS	PM	NM	NM	NS
NS	PS	PS	NS	NS	NS
Z	Z	Z	Z	Z	Z
PS	NS	NS	PS	PS	PS
PM	NS	NM	PM	PM	PS

3) Defuzzification

Defuzzification is a process of interpreting the fuzzy set resulting from the base rule inference system and converting them to a single output value to track the ΔV. This process may be performed by any one of several defuzzification methods. This study used the center of gravity (CoG) method generally computed with Equation (8) to control the DC-DC boost converter.

$$\Delta D = \frac{\sum_{i=1}^{n}[\Delta D_i \times \mu(\Delta D_i)]}{\sum_{i=1}^{n}\mu(\Delta D_i)} \qquad (8)$$

4) Type-1 Fuzzy Logic Control based MPPT

The Type-1 Fuzzy Logic Control (T1-FLC) examines the output PV power at each sample (time-k) and determines the change in power relative to voltage (Δ_P/Δ_V). If this value is greater than zero, the controller alters the duty cycle for switching the DC-DC boost converter to increase the voltage until the power is maximum or the value (Δ_P/Δ_V) = 0. If this value is less than zero, the controller changes the duty cycle for switching the boost converter to decrease the voltage until maximum power is obtained [16-17].

5) Type-2 Fuzzy Logic Control based MPPT

Type-2 Fuzzy Logic Control (T2-FLC), a better alternative to type-1 FLC that functions effectively with modeling uncertainty, has been considered to track the PV system MPPT. Figure 9 depicts the structure of a type-2 FLC. It's related to the type-1 FLC, except that at least one of the rule base's fuzzy sets is type-2. As a result, the inference system's output is type-2 sets, which require a type reducer to convert to type-1 sets before defuzzification is performed. A typical interval Type-2 FLC consists of two membership functions – primary and secondary. The primary membership grade of a type-2 FLC is a normal fuzzy set in [0, 1], while the secondary membership is a crisp number in [0, 1] [20]. The secondary membership function and range of uncertainty are decided by the third dimension of type-2 fuzzy sets and footprint-of-uncertainty (FOU), respectively. These type-2 FLC features extend an additional degree of freedom to handle various uncertainties, such as highly uncertain PV systems, to boost their operational efficiency during grid interaction.

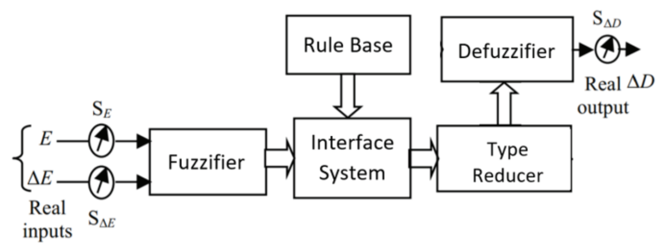

Fig. 10 Type-2 Fuzzy Logic Controller structure

IV. SIMULATION RESULTS AND DISCUSSION

The grid-tied PV system modelled in MATLAB/Simulink implements three maximum power point tracking methods (P&O, Type-1 FLC, and Type-2 FLC algorithms) for a comparative analysis of the dynamic performance of the three optimized MPP. In addition, two scenarios of constant and variable operating atmospheric conditions have been simulated for the PV system. Firstly, the simulation was performed at Standard Test Condition (STC). For the STC scenario (1000 W/m^2 solar irradiance and 25^{0}C temperature), the three MPPT controllers' performance was analyzed. Figure 11 presents the results obtained for the power delivered to the load with a simulation time of 10 seconds. It is observed that the Type-2 FLC extract a maximum power of 149.68 Watt with a good steadiness time of 0.75 seconds.

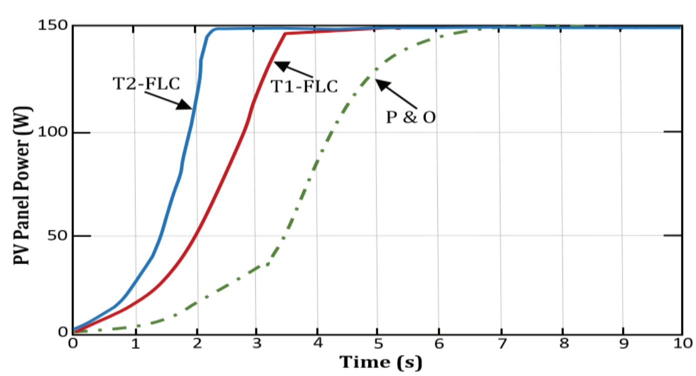

Fig. 11 MPPT performance comparison at Standard Test Condition

Figure 12 depict the different duty cycle of tested MPPT algorithms. The result shows that the P&O controller has large oscillations between 0.1 and 0.57, while the Type-1 FLC and Type-2 FLC stabilized at 0.67 and 0.78 for the duty cycle, respectively.

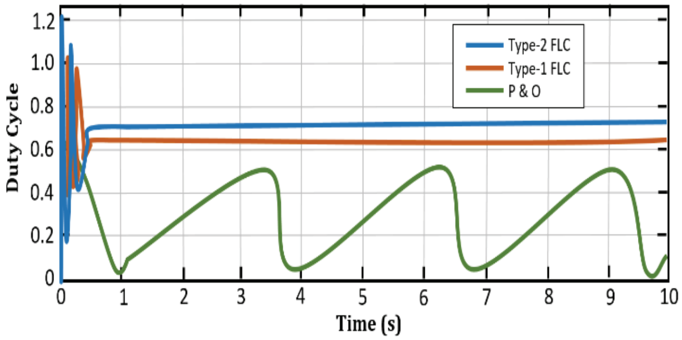

Fig. 12 Comparison of the duty cycle control at STC

During variable operating atmospheric conditions, intermittent cloud movement causes the PV array's output power to fluctuate drastically. As a result, the three maximum power point tracking algorithms were tested under different solar irradiation levels to verify the dynamic performance of the MPPT controllers. Fig. 13 presents the variable solar irradiation rising from 200 W/m^2 to 1000 W/m^2, assuming the PV system temperature is constant at 25^{0}C.

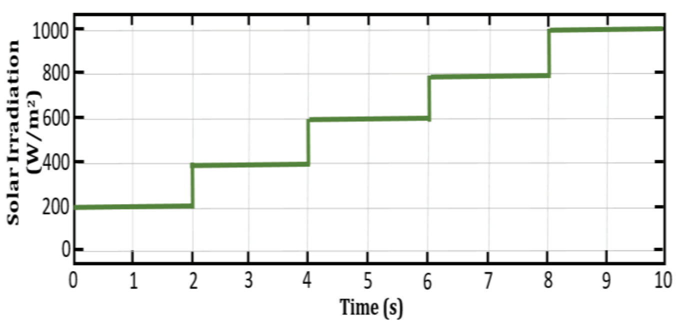

Fig. 13 Varied solar irradiation from 200 W/m^2 to 1000 W/m^2

There are five periods of operation (2 seconds each), corresponding to the solar irradiation values of 200 W/m^2, 400 W/m^2, 600 W/m^2, 800 W/m^2, and 1000 W/m^2, respectively. The controller regulates the converter duty cycle during each period to track the maximum power consistent with the solar irradiation. Figures 14, 15, and 16 depict the power generated by the PV system using the three different tracking algorithms at varied atmospheric conditions.

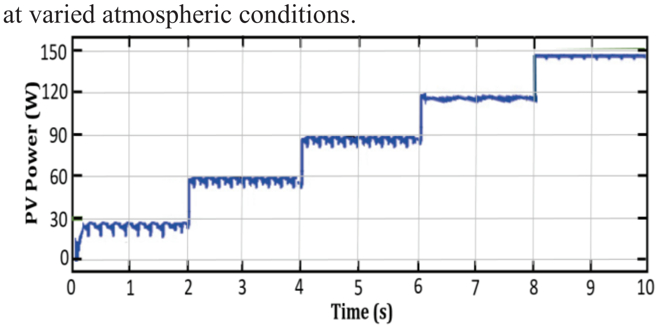

Fig. 14 Output power based on a P&O MPPT algorithm

Tables II to IV presents the results of the PV system mathematical model, which used variable solar irradiation and a 25°C operating temperature. The simulated PV system results indicate that all the MPPT algorithms tracked the electrical specification of the PV panel presented in Table 1 at G = 1000 W/m^2 and T = 25 °C, with the Type-2 FLC producing the best result.

TABLE II

RESULTS OF THE PV SYSTEM WITH P&O MPPT ALGORITHM

Parameter	**200 W/m²**	**400 W/m²**	**600 W/m²**	**800 W/m²**	**1000 W/m²**
Voltage (V_{MPP}) V	4.84	8.69	12.53	14.90	17.69
Current (I_{MPP}) A	5.53	6.57	6.81	7.85	8.26
MPP (W)	26.77	57.09	85.33	116.97	146.12

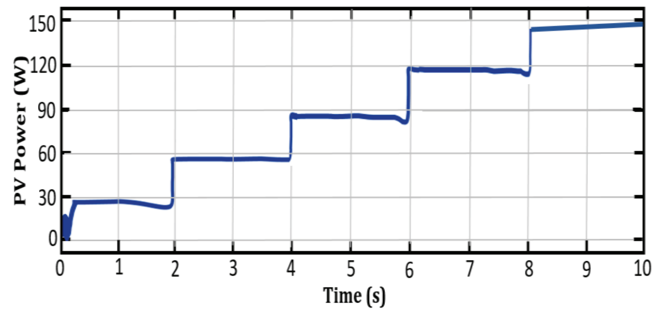

Fig. 15 Output power based on a Type-1 FLC MPPT algorithm

TABLE III

RESULTS OF THE PV SYSTEM WITH TYPE-1 FLC MPPT ALGORITHM

Parameter	**200 W/m²**	**400 W/m²**	**600 W/m²**	**800 W/m²**	**1000 W/m²**
Voltage (V_{MPP}) V	5.39	10.71	12.67	14.93	17.67
Current (I_{MPP}) A	5.19	5.48	6.98	7.87	8.32
MPP (W)	27.97	58.69	88.43	117.50	147.01

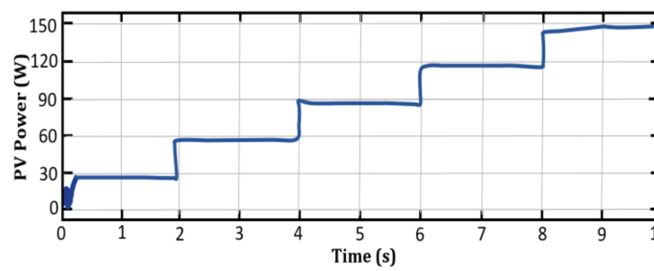

Fig. 16 Output power based on a Type-2 FLC MPPT algorithm

TABLE IV

RESULTS OF THE PV SYSTEM WITH TYPE-2 FLC MPPT ALGORITHM

Parameter	**200 W/m²**	**400 W/m²**	**600 W/m²**	**800 W/m²**	**1000 W/m²**
Voltage (V_{MPP}) V	4.63	8.61	11.38	14.32	17.70
Current (I_{MPP}) A	6.47	6.91	7.86	8.34	8.45
MPP (W)	29.96	59.50	89.46	119.43	149.56

It is evident from the results presented in Figures. 14, 15, and 16 that the Type-2 FLC-based MPPT algorithm has a better transient response. It tracked the MPP with fast response compared to the other MPPT algorithms; thus, the power losses due to the MPP tracking process are reduced at the different solar irradiation levels. For each simulation interval, the P&O MPPT algorithm resulted in average power losses of 3.19 W, 2.41 W, 4.13 W, 2.46 W, and 3.44 W for the five different solar irradiation operating levels. The losses were computed using power obtained with the Type-2 FLC algorithm as a reference.

V. Conclusion

A comparative analysis of the dynamic performance of three different MPPT algorithms was conducted in this study based on steady and transient operating conditions of PV systems. The simulation results obtained verify the capacity of the Type-2 FLC MPPT algorithm in tracking the PV system generated power at the maximum point than the P&O and Type-1 FLC MPPT techniques. Under standard test conditions, the Type-2 FLC MPPT algorithm outperforms the P&O and Type-1 FLC MPPT algorithms in steady-state responsiveness and oscillation. During the solar irradiation variations condition, the three algorithms presented a good performance and extracted the maximum power according to the electrical specification of the PV panel. However, the P&O control algorithm had oscillations due to the sudden changes in irradiation. The performance of the MPPT algorithms is arranged from best to worst as follows: Type-2 FLC, Type-1 FLC, and P&O.

Acknowledgement

The authors acknowledge the Durban University of Technology (DUT) Research and Postgraduate Support for the Green Engineering and Process Sustainability scholarship.

References

[1] C.L Nkashama, "Maximum power point tracking algorithm for photovoltaic home power supply." Master dissertation, Faculty of Engineering, University of Kwa-Zulu Natal, 2011.

[2] A.Y. Appiah, X. Zhang, B.B.K. Ayawli, and F. Kyeremeh, "Long short-term memory networks based automatic feature extraction for photovoltaic array fault diagnosis." *IEEE Access*, *7*, pp.30089-30101, 2019.

[3] S. Dahlke, J. Sterling, and C. Meehan, "Policy and market drivers for advancing clean energy." *Advances in Clean Energy Technologies*, pp.451-485, 2021.

[4] A. Shahrouz, and A. Jrn, "A review of renewable energy supply and energy efficiency technologies." *IEEE Transactions on Power Electronics*, *8145*(1), pp.998-1009, 2014.

[5] P.A Owusu, and S. Asumadu-Sarkodie, "A review of renewable energy sources, sustainability issues and climate change mitigation." *Cogent Engineering*, *3*(1), pp.1-14, 2016.

[6] D. Gielen, R. Gorini, N, Wagner, R. Leme, L. Gutierrez, G. Prakash, E. Asmelash, L. Janeiro, G. Gallina, G. Vale, and L. Sani, "Global energy transformation: a roadmap to 2050," 2019.

[7] A. Adebiyi, I. Lazarus, A. Saha, and E. Ojo, "Performance analysis of PV panels connected in various orientations under different climate conditions" in *Proceedings of the 5th Southern African Solar Energy Conference (SASEC 2018)*, pp. 46-51, 2018.

[8] J.A. Nelson, "*The physics of solar cells*." World Scientific Publishing Company, 2003.

[9] A. Saepullah, and R.S. Wahono, "Comparative analysis of mamdani, sugeno and tsukamoto method of fuzzy inference system for air conditioner energy saving." *Journal of Intelligent Systems*, *1*(2), pp.143-147, 2015.

[10] DN Luta, and AK Raji, "Comparing fuzzy rule-based MPPT techniques for fuel cell stack applications." *Energy Procedia*, *156*, pp.177-182, 2019.

[11] S.P. Singh, A.K. Gautam, S.P.Tripathi, and B. Kumar, "Performance comparison of MPPT techniques using Cuk converter for photovoltaic energy conversion system." IEEE *3rd International Conference on Computational Intelligence & Communication Technology (CICT)*, pp. 1-6, 2017.

[12] A.A. Adebiyi, A.K. Saha, I.J. Lazarus, I.J. and EE Ojo, "Investigation to Determine the Impacts of SPV Penetration on an Unbalanced Distribution Grid" in *Proceedings of IEEE PES/IAS PowerAfrica* pp. 116-120, *2019*.

[13] S.A. Rizzo, and G. Scelba, "ANN-based MPPT method for rapidly variable shading conditions." *Applied Energy*, *145*, pp.124-132, 2015.

[14] A.A. Adebiyi, I.J. Lazarus, A.K. Saha, and EE Ojo, "Performance analysis of grid-tied photovoltaic system under varying weather condition and load." *International Journal of Electrical & Computer Engineering pp. 94-106*, *11*(1), 2021.

[15] BM. Hasaneen, and A.A.E. Mohammed, "Design and simulation of DC/DC boost converter." In proceeding of IEEE *12th International Middle-East Power System Conference* pp. 335-340, *2008*.

[16] C.B. Salah, and M. Ouali, "Comparison of fuzzy logic and neural network in maximum power point tracker for PV systems." *Electric Power Systems Research*, *81*(1), pp.43-50, 2011.

[17] M.A.A.M. Zainuri, M.A.M. Radzi, A. Che Soh, and N.A. Rahim, "Development of adaptive perturb and observe-fuzzy control maximum power point tracking for photovoltaic boost dc–dc converter." *IET Renewable Power Generation*, *8*(2), pp.183-194, 2014.

2023 SAUPEC Conference, Johannesburg, South Africa, January 24-26, 2023

Analytical and Experimental Determination of Panel Generation Factor for Witbank Area

K. P. Phukubje, A. F. Nnachi, A. O Akumu
Dept. of Electrical Engineering
Tshwane University of Technology
Emalahleni, South Africa
bje@webmail.co.za; nnachiaf@tut.ac.za; akumuao@tut.ac.za

***Abstract*— In recent years, there has been growing interest in a transition to green energy, particularly Photovoltaic systems. This interest has been and will continue to create a need for accurate Photovoltaic system design, installation and maintenance. A panel generation factor (PGF) is critical in calculating the energy output of photovoltaic panels. An inaccurate panel generation factor may lead to an under-design or over-design of a photovoltaic system. This may lead to failure to meet energy capacity requirements, premature failure of system components and over-expenditure on the capital of a photovoltaic system installation. PGF is dependent on the climate of the area. The climate of Witbank in South Africa is classified as warm and temperate. In this study, an analytical method was used to determine the PGF of the Witbank area to be 3.46. In order to validate the analytical value, an experiment was conducted using 200 Wp and 15 Wp panels. The experimental value obtained was 3.61, which gives a deviation of 4.2% compared to the analytical value.**

Keywords*— Panel generation factor, PGF, Photovoltaic, solar design.

I. INTRODUCTION

Over the years, there has been growing activism and concerns about global warming that is caused by air, land and water pollution. This pollution is especially exacerbated by heavy industrial sectors such as coal-fired power generation and every other industry that plays a role in carbon emissions. The UN climate change conference of 2021 in Glasgow are a typical example of mounting pressure on global governments to reduce their carbon footprint on the earth [1].

There has been a growing interest in renewable energy in recent years. The most interest has been in Solar, Bioenergy, Wind and Hydro energy. Solar energy has been the preferred source of renewable energy over all these others due to the fact that it is not exhaustible; it is the cleanest and currently is far more available than it can be utilized [2]. According to [2]solar energy demand has been increasing over the years due to the modular nature of PV panels. The main disadvantage of this renewable energy is the initial start-up/installation cost. The costs have decreased significantly recently due to increased demand and subsequent large-scale production.

One of the critical factors in designing an efficient PV system is assessing the solar energy in the location where the system will operate. This is crucial as it will affect the sizing of the PV panels. A panel generation factor of an area can be described as a climate-based factor/constant that determines the maximum output energy of a solar PV panel for a particular region or location of a specific climate. The factor is dependent on the climate of the area.

The insolation or irradiation value that directly affects the calculation of the panel generation factor may be obtained from meteorological institutions [2].

A panel generation factor is critical in calculating the energy output of photovoltaic panels. Therefore, it is crucial in accurately designing photovoltaic systems [2] [3]. Accurate design of a PV system will ensure that the system functions at its optimal design capacity and will further ensure the system's longevity, resulting in a good return on investment sooner. When the panel generation factor is not accurately known, the calculations to design the required energy output will be inaccurate. This may result in the over-design or under-design of the system. This may create a false perception that the PV panels cannot produce the rated energy output per the manufacturer's specifications. Over-design would result in unnecessary capital being spent on the PV system. It would take longer to realize a return on investment. Under-design would result in an insufficient power supply and subsequent rework, which would cost more capital investment.

PGF can be determined experimentally or through meteorological data [3]. In [3] PGFs for climate class 1 (tropical coastal climate with many days of clear skies and few cloudy), climate class 2 (tropical coastal climate with most days partly cloudy), climate class 3 (Cloudy periods of five to seven days occur regularly) and climate class 4 (cloudy periods of ten or more days occur regularly) were recommended to be 3.86, 3.43, 3.0 and 2.57, respectively recommended as guidelines. Jessica et al. [4], experimentally obtained a PGF of 3.625 for the Apo area of the federal capital territory in Niger, a tropical country classified as having a typical tropical climate.

The panel generation factor for the Witbank area is currently unknown with precision. It has not yet been experimentally determined and published in reputable academic literature for practical use in designing PV solar systems for the Witbank area. It can be estimated from online solar databases such as the Global Solar Atlas [5]. It provides a map-based summary of the global natural solar resources. The absence of a credible experimentally-determined panel generation factor for the Witbank area affects designers and installers of PV systems, clients or end-users of PV systems and businesses that sell PV panels to be installed in the Witbank area. The problem is mostly observed when PV systems have to be designed and installed to the required output as per the client's requirements. This research work presents an analytical and experimental determination of the panel generation factor for the eMalalheni (Witbank) area.

II. DETERMINATION OF PANEL GENERATION FACTOR

The panel generation factor (PGF) is the maximum energy per day that 1 Wp panel can produce. PGF is used for fast approximate and simplified sizing of off-grid solar-PV arrays. It is a varying factor depending on the climate or global geographical location of the site. Every climate has a different PGF. The sunnier the climate, the larger the factor. In tropical coastal climates, a 35Wp panel can produce average daily energy of 120Wh/day; hence a 1Wp panel would produce 3.43Wh/day (120/35 Wh/day), which is the PGF for that climate. So to get how many Wh/day a panel can produce, just multiply PGF by peak-watt (Wp) rating of the panel [3].

PGF can be determined analytically or experimentally. This section covers the application of both methods used for the determination of PGF for the eMalahleni (Witbank) area.

A. *Analytical determination of eMalahleni PGF*

PGF can be analytically determined using equation (1) [4]:

$$PGF = \frac{\bar{G}_T f_{PV}}{\bar{G}_{T,STC}} \qquad (1)$$

where

$\bar{G}_T$ is the solar radiation incident on the panel (kWh/m^2 per day)

f_{PV} is the correction factor of PV

$\bar{G}_{T,STC}$ is the incident radiation at standard test condition (1 kW/m^2).

The correction factor f_{PV} is calculated using the equation

$$f_{PV} = f_1 \times f_2 \times f_3 \times f_4 \times f_5 \qquad (2)$$

Where

f_1 is the correction factor for loss due to temperature above 25°C (15%)

f_2 is correction factor sunlight not striking the panel directly (5%)

f_3 is the correction factor for PV system not operating at maximum power point (10%)

f_4 is the correction factor for dust/dirt on the panel (5%)

f_5 is the correction factor due to the ageing of the PV panel (10%)

Hence $f_{PV} = 0.85 \times 0.95 \times 0.9 \times 0.95 \times 0.9 = 0.6214$

From the Global Solar Atlas shown in figure (1), the horizontal irradiance for the Witbank area used as a case study is 2029.7 kWh/m2 per year, which equals 5.56 kWh/m^2 per day. Substituting these values in equation 1, the PGF = 5.56 x 0.6214 = 3.46

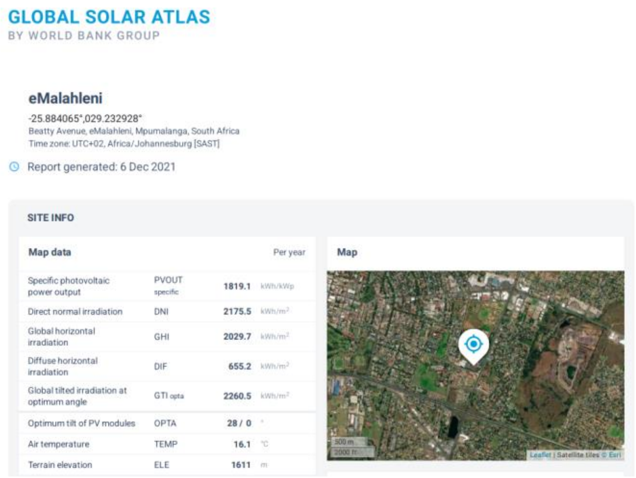

Fig. 1. Solar map report for Witbank (monthly) from Solargis solar map [5]

B. *Experimental determination of eMalahleni PGF*

This section covers the setup used to determine the panel generation factor of the Witbank area experimentally.
Figure 2 shows the block diagram of the experiment. Figure 3 the PV system experimental setup, which consists of:

- A white wooden board (1000mm x 800mm) on which the components were mounted
- 200 W monocrystalline PV panel and 15 W monocrystalline PV panel,
- A 12/24V MPPT charge controller by Epever,
- Charge controller Software by Epever
- An RS-232 data logger with communication cables by Epever,
- Data logger software by Epever
- A 12V 100Ah rechargeable deep cycle battery,
- A 1000 W inverter and
- A DC load consisting of a 150W variable resistor and a 10W DC LED light.

Figure 4 shows the angle measuring tools used to set up the tilt angle for the 200 W and 15 W panels shown in figure 5.

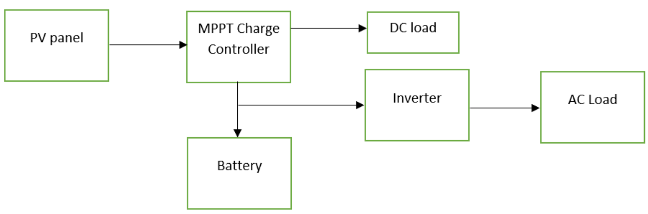

Fig. 2. Block diagram of experimental PV system [6].

Fig. 3. The experimental setup

Fig. 4. 200 W panel tilted at an angle with respect to Witbank latitude of 26°

Fig. 5. 200 W and 15 W panels tilted at an angle with respect to Witbank latitude of 26°

The main aim of the experiment for the panel generation factor was to use a PV panel of a particular rating to capture as much solar radiation as possible from morning until late afternoon and record the current and voltage readings of the PV panel. The data collected over some time would be used to compare the average energy produced by the PV panel and the peak Watt rating of the PV panel to determine the panel generation factor of Witbank.

In the initial stages of the experiment, a 200W PV panel and a variable resistor were utilized to capture solar radiation throughout the day. A 15W PV panel was used to verify the results obtained through the 200W PV panel. The voltage and current readings were measured at 15-minute intervals using a Fluke digital multimeter. The need for a charge controller soon became necessary as it provided the advantage of a built-in voltage measurement, current calculation of power and data logging. This eliminated the need for manual measurements with a multimeter and manual logging of data. The charge controller required a 12V or 24V rechargeable battery for it to switch on. This is why a battery was added to the system. The PV panels were tilted at the latitude angle of 26° (GPS co-ordinates of the experiment 25.8843°S, 29.2321°E on Mandela Street, Witbank, Mpumalanga, South Africa). This is the angle at which most of the average solar radiation per day is captured.

Six experiments were carried out. On 11/12/2021 from 09h30 to 16h30 the first experiment was conducted on a 15 Wp and a 200Wp PV panel. It was a sunny day with clear a sky. Measurements of voltage and current were taken at 15 minute intervals for both panels. These 15 minute averages were used to calculate the energy. The table for the measurement in December is shown Table 1 and 2. The 15Wp panel yielded 50.69 Wh and the 200Wp PV panel yielded energy of 782.37 Wh. The experiments continued on the other dates as shown in the tables 3 and 4.

Table 1 – Current and Voltage measurement from 15 Wp PV panel

Date & Time	Array Current(A)	Array Voltage(V)	Array Power(W)	Energy (Wh) 15min average
2021/12/11 09h00	0,2	20	4	1
2021/12/11 09h15	0,1	19	1,9	0,475
2021/12/11 09h30	0,2	19,4	3,88	0,97
2021/12/11 09h45	0,4	20,6	8,24	2,06
2021/12/11 10h00	0,56	20,79	11,6424	2,9106
2021/12/11 10h15	0,6	20	12	3
2021/12/11 10h30	0,612	20,2	12,3624	3,0906
2021/12/11 10h45	0,628	20,02	12,57256	3,14314
2021/12/11 11h00	0,165	19,62	3,2373	0,809325
2021/12/11 11h15	0,656	20,22	13,26432	3,31608
2021/12/11 11h30	0,621	20,9	12,9789	3,244725
2021/12/11 11h45	0,65	20,05	13,0325	3,258125
2021/12/11 12h00	0,666	19,58	13,04028	3,26007
2021/12/11 12h15	0,164	19,5	3,198	0,7995
2021/12/11 12h30	0,667	20,19	13,46673	3,3666825
2021/12/11 12h45	0,589	19,84	11,68576	2,92144
2021/12/11 13h00	0,176	19,43	3,41968	0,85492
2021/12/11 13h15	0,168	19,47	3,27096	0,81774
2021/12/11 13h30	0,484	20,55	9,9462	2,48655
2021/12/11 13h45	0,155	19,51	3,02405	0,7560125
2021/12/11 14h00	0,45	20,68	9,306	2,3265
2021/12/11 14h15	0,145	19,86	2,8797	0,719925
2021/12/11 14h30	0,11	19,55	2,1505	0,537625
2021/12/11 14h45	0,086	19,41	1,66926	0,417315
2021/12/11 15h00	0,094	19,66	1,84804	0,46201
2021/12/11 15h15	0,12	19,57	2,3484	0,5871
2021/12/11 15h30	0,135	19,28	2,6028	0,6507
2021/12/11 15h45	0,277	20,34	5,63418	1,408545
2021/12/11 16h00	0,094	18,4	1,7296	0,4324
2021/12/11 16h15	0,06	19,85	1,191	0,29775
2021/12/11 16h30	0,064	19,3	1,2352	0,3088
Total			202,75672	50,68918

Table 2 - Current and Voltage measurements from 200 Wp panel

Date & Time	Array Current(A)	Array Voltage(V)	Array Power(W)	Energy (Wh) 15min average
2021/12/11 09h00	2,66	20	53,2	13,3
2021/12/11 09h15	1,3	19	24,7	6,175
2021/12/11 09h30	2,66	20,05	53,333	13,33325
2021/12/11 09h45	5,32	20,6	109,592	27,398
2021/12/11 10h00	7,45	20,79	154,8855	38,721375
2021/12/11 10h15	7,98	20	159,6	39,9
2021/12/11 10h30	8,14	20,2	164,428	41,107
2021/12/11 10h45	8,71	22,41	195,1911	48,797775
2021/12/11 11h00	5,46	19,94	108,8724	27,2181
2021/12/11 11h15	8,73	20,22	176,5206	44,13015
2021/12/11 11h30	2,7	20,25	54,675	13,66875
2021/12/11 11h45	2,5	19,41	48,525	12,13125
2021/12/11 12h00	11,03	20	220,6	55,15
2021/12/11 12h15	10,8	20,44	220,752	55,188
2021/12/11 12h30	8,87	21,2	188,044	47,011
2021/12/11 12h45	7,83	20,05	156,9915	39,247875
2021/12/11 13h00	2,34	21,5	50,31	12,5775
2021/12/11 13h15	9,2	20,76	190,992	47,748
2021/12/11 13h30	2,58	20,36	52,5288	13,1322
2021/12/11 13h45	8,41	21,21	178,3761	44,594025
2021/12/11 14h00	2,8	20,45	57,26	14,315
2021/12/11 14h15	1,982	20,42	40,47244	10,11811
2021/12/11 14h30	1,59	20,8	33,072	8,268
2021/12/11 14h45	1,5	20,58	30,87	7,7175
2021/12/11 15h00	3,5	21	73,5	18,375
2021/12/11 15h15	6,04	21,28	128,5312	32,1328
2021/12/11 15h30	4,46	21	93,66	23,415
2021/12/11 15h45	1,8	19,7	35,46	8,865
2021/12/11 16h00	1,622	20,02	32,47244	8,11811
2021/12/11 16h15	1,022	20,05	20,4911	5,122775
2021/12/11 16h30	1,069	20,17	21,56173	5,3904325
Total			3129,46791	782,3669775

The six experiments conducted using a 15Wp PV panel yielded an average energy generation of 46.63Wh generated by the 15Wp PV panel. Therefore from [3] and [7], the Panel Generation Factor can be calculated as: 46.63 Wh / 15Wp = 3.11 PGF.

The six experiments were also conducted using a 200 Wp PV panel, which yielded an average energy generation of 722.17 Wh generated, as shown in table 4. The PGF was calculated as: 722.17 Wh / 200Wp = 3.61 PGF for Witbank.

Table 3 – Energy generation of 15Wp PV panel

15W PV Panel Weekly Measurements	
Date	Total Energy (Wh) 15 min average
Saturday, December 11, 2021	50.69
Saturday, March 5, 2022	55.5
Saturday, April 2, 2022	56.5
Saturday, April 23, 2022	41.7
Saturday, April 30, 2022	33.6
Saturday, May 14, 2022	42.27
Total Energy	280.26
Average Energy	46.71
15W panel generation factor calculation	**3.114**

Table 4 – Energy generation of 200 Wp PV panel

200W PV Panel Weekly Measurements	
Date	Total Energy (Wh) 15 min average
Saturday, December 11, 2021	782.37
Saturday, March 5, 2022	858.4
Saturday, April 2, 2022	873.87
Saturday, April 23, 2022	644.96
Saturday, April 30, 2022	519.68
Saturday, May 14, 2022	653.776
Total Energy	4333.056
Average Energy	722.176
200W panel generation factor calculation	**3.61088**

The difference in PGF between the 15 Wp and 200 Wp panels is suspected to be due to the difference in the construction quality of the two PV panels. Each panel was from a different manufacturer. Another 200 Wp PV panel (from the same manufacturer as the 200 Wp test panel) gave similar performance results of PGF of 3.61.

Comparing the analytical and experimental PGF, the percentage deviation of the experimental from the analytical is 4.2% (i.e. (3.61-3.46)/3.46 x 100). The most probable cause is that apart from one experiment conducted in December, the rest started in March (early autumn) until May (late autumn). The experiments missed out on the year's warmest months (October – February) and therefore failed to capture the high solar radiation.

In South Africa, the summer season is between December and the end of February; the autumn season is between March and the end of May, and the spring season is between September and end of November [8].

According to its manual, PV Watts makes several assumptions about the type and configuration of the system it attempts to model for a particular area. Errors may be as high as 10% for annual energy generation and 30% for monthly values. These are errors based on long-term historical data.

In a particular year, actual PV system performance may deviate by as much as 0% on monthly values [9].

According to [10], Solargis has been improving the accuracy of its high-resolution solar maps for South Africa, Lesotho and Swaziland. This improvement was done by taking ground solar measurements at 14 high-standard solar-measuring stations and adapting the Solaris solar model with this data. The ground measurements were sourced by Eskom, SASOL, GeoSUN Africa, SAURAN, STERG and Ripasso Energy. The authors report that uncertainty for Direct Normal Irradiance was reduced from the 8% - 9.5% range to the 5%-6% range. The reduction in uncertainty for Global Horizontal Irradiation was from the 3%-4% range to the 3% - 3.5% range.

It is recommended that sampling or experimentation be done for the months covering the four seasons of the year to have a clearer picture of the year's average solar radiation and, therefore, a more accurate PGF for Witbank. Permanent installation on a roof would be the best approach to recording all the solar data for a year.

III. Conclusion

For the accurate design of an off-grid PV system, a panel generation factor is critical in calculating the energy output of the photovoltaic panels. Knowing PGF, which is climate based will aid in avoiding the over or under-design of V systems.

Witbank in South Africa has a temperate highland tropical climate with dry winters. This study presents an analytical and experimental determination of the panel generation factor for the Witbank area. The PGF of Witbank was experimentally determined as 3.61 and was validated analytically with a percentage deviation of 4.2%.

IV. References

[1] UKcorp26, "UN Climate Change Conference UK 2021," 05 November 2021. [Online]. Available: https://ukcop26.org/.

[2] A. Waqas, F. Haroon, U. R. Ata, A. Qasim, J. Mohsin and N. Ali, "Design considerations of stand-alone solar photovoltaic system," in *2018 International conference on computing, electronic and electrical engineering (ICE Cube)*, Quetta, Pakistan, 2018.

[3] H. A. Wade, "Chapter 9 System Sizing," in *Solar photovoltaic sytems technical training manual*, Paris, UNESCO Publishers, 2003, pp. 83-95.

[4] J. A. Onwuzuruike and A. A. Maruf, "Experimental Determination of Panel Generation Factor for Apo Area of Federal Capital Territory in Nigeria," *Journal of Scientific Research & Reports*, vol. 24, no. 3, pp. 1-5, 2019.

[5] ESMAP, "Global Solar Atlas," ESMAP, 29 November 2019. [Online]. Available: https://globalsolaratlas.info/support/getting-started. [Accessed 05 November 2021].

[6] Epever, "EPEVER," 02 January 2022. [Online]. Available: https://www.epever.com/wp-content/uploads/2021/05/Tracer-AN-SMS-EL-V1.0.pdf. [Accessed 01 February 2022].

[7] N. Abrams, "State University of New York, College of Environmental Science and Forestry," State University of New York, 20 November 2019. [Online]. Available: http://www.esf.edu. [Accessed 21 November 2021].

[8] C. Cronje and J. Maritz, "South Africa's weather and seasons: What you need to know," Expat Explore, 1 March 2005. [Online]. Available: https://expatexplore.com/. [Accessed 18 May 2022].

[9] A. P. Dobos, "PV Watts Calculator," 01 September 2014. [Online]. Available: https://www.nrel.gov/docs/fy14osti/62641.pdf. [Accessed 08 April 2022].

[10] M. Suri, T. Cebecauer, A. J. Meyer and J. L. van Niekerk, "ACCURACY-ENHANCED SOLAR RESOURCE MAPS OF SOUTH AFRICA," in *Third South African Solar Energy Conference*, Skukuza, 2015.

Architecture of Renewable Energy System via Non–Terrestrial Communication Nodes

A.A Periola
Electrical, Electronic and Computer Engineering
Cape Peninsula University of Technology
periolaa@cput.ac.za

Abstract— The transition from non–renewable energy sources to green (renewable) energy sources result in challenges that lead to the occurrence of energy gaps at several epochs. Energy gaps occur when the power output from renewable energy sources is insufficient to meet the load demand of retiring non–renewable energy sources. This results in undesirable load-shedding events. The presented research addresses this challenge by proposing new renewable energy sources that have not received sufficient consideration. Two energy sources have been motivated by advances in communication and computing networks in the aspects of underwater data centers and stratosphere-based data centers. The research presents an architecture and mechanism enabling these communication nodes to enable electricity contribution to the grid. Performance evaluation shows that the use of the proposed mechanism reduces the energy gap by at least 1.97% and at most 36.6% on average.

Keywords – Cloud Data Centers, Multi-disciplinary Perspective, Renewable Energy, Future Grid

I. INTRODUCTION

The increasing population coupled with a rising digital appetite profile makes it important to design more computing platforms to host the content being accessed by subscribers. The design, launch, and use of more computing platforms result in the increased consumption of electrical energy [1–2]. The projected increase in energy consumption has been recognized to constitute a constraint on the operation of computing platforms in the future [3–4]. In addition, there is an increasing consideration on the use of renewable energy in data center systems [6–7]. The use of renewable energy is also receiving consideration within a broader context [8–10]. This has arisen due to the need to reduce the environmental degradation associated with the use of existing fossil fuels for energy generation [11]. Currently, there is an increasing drive to transition to the full use of renewable energy sources [12–13].

The execution of this transition requires harnessing all (or a significant number) renewable energy sources. This is important to prevent or limit the occurrence of energy shortfalls which may lead to load-shedding. This has been observed in cases of executing a transition to the full use of renewable energy sources [14–16]. The occurrence of this limitation can be addressed by making use of more renewable energy sources. Currently, the renewable energy sources being considered are: (1) Solar, (2) Wind (offshore), (3) Wind (onshore) ,and (4) Wave (tidal) [17–18].

However, there are other forms of renewable energy sources that have arisen due to technological advances. For example, the emergence of underwater computing systems and platforms provides another channel to utilize renewable ocean energy sources. The discussion in [19] notes that Microsoft Natick (an underwater data center) utilizes electricity from the grid. However, the feasibility of utilizing electricity arising from the underwater data center (such as one arising from Microsoft Natick) has not been considered. In addition, there is a limited use of aerial wind energy. However, it is important to consider the design of systems that harness aerial wind energy.

The use of renewable energy sources that are previously harnessed on a significant scale is important. This is deemed necessary to ensure that renewable energy sources can meet the power demand currently being served by existing non-renewable use contexts.

The main contribution of this paper is the presentation of an intelligent system that enables renewable energy sources to meet their full potential. The full potential in this context is the use of only renewable energy sources to meet the emerging electricity demand. In the considered context, green energy i.e., renewable energy sources alone are used. The use of only green energy sources enables a full transition to the use of renewable energy sources. The research being presented recognizes that the realization of the intended transition can lead to the occurrence of energy gaps (epochs where there is load-shedding). The energy gaps arise when the power supply from renewable energy power sources falls short of the load being driven by non–renewable energy sources. The research also describes the architecture of the intelligent system.

In the presented research, underwater renewable energy sources are accessible via the deployment of underwater data center systems. This puts underwater data center systems in a position where they can enable the transfer of renewable energy from the submarine environment to the terrestrial grid. However, the suitability of underwater data center systems (UDCSs) as a power node instead of the roles of a communications node or computing node is yet to receive significant research attention. This is being done in this paper to increase the contribution of underwater renewable energy sources to the renewable energy sources that contribute to the grid via the incorporation of blue renewable energy sources. The research presents an intelligent architecture enabling the integration of UDCSs. UDCSs have received consideration to function only as communication and computing nodes. They have not received consideration as power nodes in renewable energy systems.

The rest of the research is organized as follows. Section II discusses background work. Section III describes the problem being addressed. Section IV presents the proposed architecture. Section V formulates the performance model. Section VI presents the results of performance evaluation and benefits of the proposed intelligent architecture. Section VII concludes the presented research.

II. EXISTING AND BACKGROUND WORK

Advances in realizing efficient computing platforms have enabled the realization of computing platforms that utilize free cooling. These computing platforms are in the non–terrestrial environment such as the underwater environment [19, 20–21], stratosphere [22–23] and outer space [24]. These computing platforms are in regions with abundant supply of renewable energy sources. The discussion in [20] proposes an underwater smart grid towards realizing the provisioning of electrical power to underwater data centers (UDCs). The discussion in [20] advances [19] because the underwater data center system uses wave and tidal energy in [20] instead of increasing the load on the grid as occurring in [19]. The discussion in [21] describes the adoption of the initiative of underwater computing platforms by other entities. In this case, it is seen that the focus is mainly on identifying free cooling benefits instead of discussing the provisioning of power to the grid.

The existing consideration of UDCs focuses on their role solely as computing platforms. In this context, the UDC comprises hundreds of servers that require energy for operation. The UDC incorporates an onboard power subsystem that enables the functioning of servers in executing data storage, processing, and algorithm execution. In a UDC, the servers can experience underutilization or maximum usage. During the occurrence of underutilization, some servers in the UDC are not being utilized giving rise to excess energy. The use of the resulting excess energy in meeting power demands in external systems have not been sufficiently considered in research literature.

In [22], Microsoft considers the notion that the data center can also be a battery that can make energy contributions to the grid. This consideration has largely focused on the use of batteries that are associated with the future grid. This new perspective raises the notions that data centers can be considered as active entities in power networks as well as communication systems. However, a mechanism enabling this transition without impairing server functionality has not been sufficiently considered. In addition, the discussion in [22] presenting this innovation from Microsoft has not considered the data center location.

Another non–terrestrial environment suitable for hosting data centers is the stratosphere. The stratosphere presents a cold environment that is suitable for hosting future data centers. The stratosphere-based data center can intercept solar radiation in the stratosphere. The context of [23] and [24] is that stratosphere-based data centers are powered using solar energy. The use of stratosphere-based data centers has not considered the stratosphere from the perspective of being an excellent solar radiation collection location.

The siting of data centers in space as seen in [25] is deemed necessary to reduce the latency for executing data transfer in space-based internet of things related applications and networks. However, the realization of energy transfer from space-based data centers is challenging. This is because of the challenges of achieving high efficiency wireless power transfer due to the large distance. The use of a transmission line is also challenging as satellites in the low earth orbit are mobile. Furthermore, the high altitude of the geostationary orbit and potential collision with low earth orbiting satellites makes the use of a power line challenging.

The discussion in this aspect has noted that the emergence of non–terrestrial data center systems has led to a case where renewable energy sources are being used in previously unconsidered contexts and locations. However, the use of renewable energy sources in these contexts has only been considered within the scope of powering non–terrestrial computing platforms. Their role in enabling the realization of transitioning to a green energy future has not been considered.

III. PROBLEM DESCRIPTION

The scenario being considered comprises a scenario making use of non–renewable energy sources (NRESs) and renewable energy sources (RESs). Let α_1 and α_2 denote the set of NRESs and RESs, respectively.

$$\alpha_1 = \{\alpha_1^1, \alpha_1^2, \dots, \alpha_1^M\} \quad (1)$$
$$\alpha_2 = \{\alpha_2^1, \alpha_2^2, \dots, \alpha_2^N\} \quad (2)$$

Let the power capacity of the m^{th} non–renewable energy source (NRES) at the epoch $t_y, t_y \epsilon\, t, t = \{t_1, \dots, t_Y\}$ be denoted as $P_1(\alpha_1^m, t_y), \alpha_1^m \epsilon\, \alpha_1$. In addition, the power capacity of the n^{th} renewable energy source (RES) at the epoch t_y, is denoted as $P_1(\alpha_2^n, t_y), \alpha_2^n \epsilon\, \alpha_2$. The desired transition to use renewable energy occurs seamlessly when:

$$\sum_{m=1}^{M}\sum_{y=1}^{Y} P_1(\alpha_1^m, t_y) \leq \sum_{n=1}^{N}\sum_{y=1}^{Y} P_1(\alpha_2^n, t_y) \quad (3)$$

The case in (3) is one in which the power capacity associated with RESs exceeds or is equal to that of the NRESs in the duration comprise the considered epochs. In the case where RESs capacity exceeds NRESs capacity, this is beneficial as additional load can be supported. The scenario in (3) arises when a significant number of power plants that utilize NRESs are de-commissioned. This arises due to the need to limit carbon emissions and realize environmental protection. However, there is a transition challenge in the scenario:

$$\sum_{m=1}^{M}\sum_{y=1}^{Y} P_1(\alpha_1^m, t_y) > \sum_{n=1}^{N}\sum_{y=1}^{Y} P_1(\alpha_2^n, t_y) \quad (4)$$

In (4), the NRES capacity exceeds the RESs capacity. Hence, a full transition to RES results in energy gaps or load shedding epochs. In this case, a solution is needed to address the resulting load-shedding. This is the role of the propose mechanism.

The non–occurrence and occurrence of energy gaps as implied are shown in Figure 1 and Figure 2, respectively.

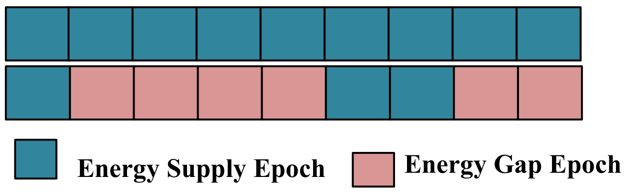

Top: Figure 1–Power supply in the desired case showing non–occurrence of energy gaps. Bottom: Figure 2–Power supply showing the occurrence of energy gaps.

IV. PROPOSED SOLUTION

The proposed solution opines that the use of previously unconsidered RESs enables the realization of a scenario described in (3).

The rest of the discussion in this section is divided into two aspects. The first aspect describes how UDCs can serve as a bridge to provide electricity to the grid. The second aspect focuses on how the stratosphere data center can be used in a role to provide electricity to the grid.

A. Role of Underwater Data Centers

UDCs present a system that provides an interface between terrestrial entities (cloud computing organization) and the ocean environment. In this interface, the terrestrial entity is not strictly limited to the identity of a cloud computing organization. Rather, the terrestrial entity can be generic.

The existing consideration of UDCs focuses only on their role as computing platforms and communication nodes. The discussion in the presented research considers that UDCs can act as nodes in power systems. This arises when UDCs donate excess power arising from long term server underutilization to a generic entity.

In this case, the generic entity is a terrestrial entity. The terrestrial entity is an energy utility organization operating a smart grid system. In the consideration here, the terrestrial entity is hybrid. It functions as a cloud computing organization and as an energy utility. As an energy utility, the power subsystem (with its storage) aboard the UDC donates its excess energy to the terrestrial grid. Excess energy arises when the servers experience long term underutilization.

The UDC comprises the computing payload and the power payload. The power payload comprises wave and tidal generators that access marine renewable energy sources and generate electricity. The generated electricity is primarily used to ensure continuity in UDC operation when desired.

The proposed power payload is contributed by an organization seeking to derive marine renewable energy driven electricity. This organization also provides a connection to the grid. The cloud computing organization provides the UDC computing payload, provides intelligent mechanism and software for power payload monitoring and management. The proposed hybrid consideration is presented in Figure 1.

In Figure 1, the UDC power payload hosts multiple mini–marine tidal generators. The cloud computing organization in Figure 1 hosts the UDC's computing payload and its related power management entities. The power organization hosts entities related to the power payload and power payload to grid connection.

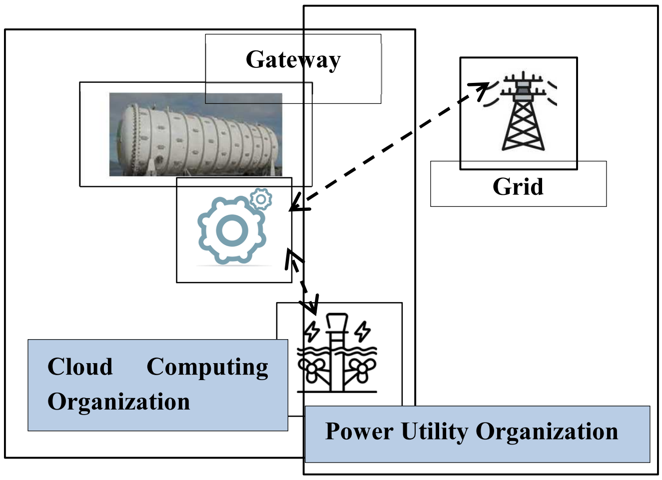

Figure 1: UDC Integration into the conventional grid.

B. Role of Stratosphere Based Data Centers

The stratosphere is a near space region with higher magnitude of incident solar radiation than obtainable on the earth's surface. This is due to the reduction of light intensity with increasing separation distance from a given light source (in this context, the source is the sun). In addition, the stratosphere has less obstacles that absorb sunlight in comparison to the earth's surface i.e., the terrestrial context. This makes the stratosphere a feasible and an attractive region for intercepting solar radiation. In this case, the attractiveness of the stratosphere has driven the use of electricity derived from solar energy in high altitude platforms. Data centers located in the stratosphere are unable to utilize the full capacity of the accessible solar energy derivable from the solar radiation being intercepted. In addition, the consideration of stratosphere-based data centers in the capacity of contributing to RES usage has not received sufficient research consideration.

However, tapping solar radiation from the stratosphere presents a new dimension that differs from the sole use of solar radiation intercepted only in the terrestrial plane. From a wave analytics perspective, the use of only solar radiation intercepted at the terrestrial plane limits the usefulness of solar radiation that is utilized in the generation of energy to the use of solar radiation with wave relations only occurring at the terrestrial plane. The inclusion of the stratosphere enables the inclusion of radiation wave dynamics occurring at the level of the stratosphere as well for electricity generation.

The use of the stratosphere in this case can be realized via the use of the proposed hybrid stratosphere-based data center (HSDC). The HSDC increases the utilization of the stratosphere as an atmospheric region. The HSDC has three sub–entities. These are: (1) Computing sub–entity (CSE), (2) Data and Management sub–entity (DMSE), and (3) Power sub–entity (PSE). The CSE comprises servers and the associated cooling gear. It executes the functions of data storage, algorithm execution and data communications. The PSE hosts the solar to electrical energy conversion payload. It provides power to the CSE's payload. The CSE and the PSE can be owned by a cloud computing organization. Alternatively, the CSE and PSE can be owned by the cloud computing organization and power utility organization, respectively. The DMSE hosts mechanisms enabling power management and supply of electrical power to the CSE or external power networks.

Solar energy arising from the proposed HSDC is received in an exclusive region. In this region, the derived electricity is transmitted to a terrestrial power utility solution. The transmission is realized via an inter–connecting cable. The inter–connecting cable passes through unmanned aerial vehicles (UAVs) deployed at varying altitudes.

The relations between the CSE, DMSE and PSE in the HSDC showing the role of UAVs is shown in Figure 2. The scenario in Figure 2 shows bi–directional communications between the terrestrial power station and the PSE. In this case, there are two UAVs i.e., UAV 1 and UAV 2. The mobility of UAV 1 and UAV 2 enables the cable to avoid aerial obstacles. In this case, the cable path is in an aerial location that is not used by commercial aviation applications. The use of a cable has been motivated by the use and feasibility of a space elevator [26]. In the proposed solution and in Figure 2, the use of a cable hosted within a space elevator system is feasible due to the low mass and weight of a cable in comparison to space bound payloads.

Advances that have been made as regards the realization of a space elevator are useful in the realization of a cable from the stratosphere to the terrestrial power utility. Furthermore, an increasing demand for electricity access given an increasing global population necessitates tapping this renewable energy source. The cable being used in this case is not exposed to a significant radiation that necessitates hardening or the execution of cable resistant procedures. Hence, existing cables that are used in high voltage power systems can be utilized. An estimate using the information in [27] shows that such a cabling can be realized at an amount of up to $6.0m.

In addition, Figure 2 shows how the DMSE enables the exchange of control related information between the CSE and the PSE. Furthermore, the CSE has a line directly connected to the PSE that enables CSE operation. Figure 2 shows that the terrestrial power station also receives the electrical power derived from the UDC and the associated tidal wave generators in the underwater environment. The terrestrial power station (TPS) receives the electrical power output arising from the HSDC and the UDC (alongside its associated components). The received power serves as an input to the grid. The grid also receives inputs from existing RESs. An integration of renewable power sources of the proposed solar energy (from stratosphere-based data centers) and renewable energy (from UDC is shown in Figure 3.

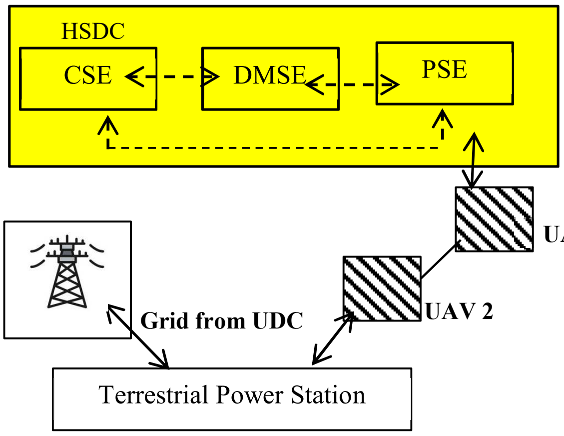

Figure 2: Relations between entities associated with the HSDC being used to access renewable solar energy.

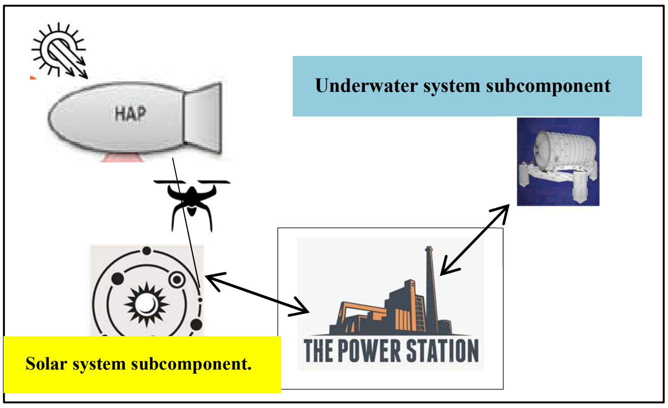

Figure 3: Integration of renewable energy sources from the solar and underwater subcomponent into the power station.

V. PERFORMANCE FORMULATION

The performance metric of interest is the energy gap arising before and after the use of the proposed architecture. The energy gap is formulated considering the existing RESs and proposed RESs (UDC associated system and HSDC). In the performance formulation, the existing RESs are: (1) Terrestrial Solar, (2) Onshore wind, and (3) Offshore wind. In formulating the energy gap, the set of existing and utilized RESs is distinct from the set of possible RESs that can be utilized which is given as α_2. Let the set of existing and utilized RESs be denoted α_3:

$$\alpha_3 = \{\alpha_3^1, \alpha_3^2, \ldots, \alpha_3^B\} \tag{5}$$

The energy gap before and after the incorporation of the proposed mechanism are denoted ς_1 and ς_2, respectively. In this case, the energy gap is the differential between the existing and utilized energy sources and proposed RESs. A difference in this case implies that RESs have a significant power output.

$$\varsigma_1 = \sum_{y=1}^{Y}\big(A(m,y) - A(b,y)\big) \tag{6}$$

$$A(m,y) = \sum_{m=1}^{M} P_1(\alpha_1^m, t_y) I(\alpha_1^m, t_y) \tag{7}$$

$$A(b,y) = \sum_{b=1}^{B} P_1(\alpha_3^b, t_y) I(\alpha_3^b, t_y), \alpha_3^b \epsilon\, \alpha_3 \tag{8}$$

In the case where the proposed approach is incorporated, the energy gap is the differential between utilized energy sources and all renewable energy sources (existing and proposed renewable energy sources).

$$\varsigma_2 = \sum_{y=1}^{Y}\sum_{m=1}^{M}\sum_{b=1}^{B}\sum_{n=1}^{N} A_1(m,y) - \big(A_2(n,y) + A_3(b,y)\big) \tag{9}$$

$$A_1(m,y) = P_1(\alpha_1^m, t_y) I(\alpha_1^m, t_y) \tag{10}$$

$$A_2(n,y) = P_1(\alpha_2^n, t_y) I(\alpha_2^n, t_y) \tag{11}$$

$$A_3(b,y) = P_1(\alpha_3^b, t_y) I(\alpha_3^b, t_y) \tag{12}$$

$I(u, t_y)\, \epsilon\, \{0,1\}, u\, \epsilon\, \{\alpha_1^m, \alpha_2^n, \alpha_3^b\}$ denotes the activity status of the power source entity u. An active power source and inactive power source contributes and does not contribute electricity to the grid, respectively. The power source entity u is inactive and active at the epoch t_y when $I(u, t_y) = 0$ and $I(u, t_y) = 1$, respectively.

VI. PERFORMANCE EVALUATION

The performance evaluation is done and presented in this section. The energy gap is investigated considering the use of NRESs from existing multiple sources i.e., diesel, hydropower and nuclear. The existing RESs being considered are terrestrial solar, onshore wind and offshore wind. The newly introduced RESs are underwater wave energy and stratosphere based solar energy. The performance parameters are presented in Table 1. The simulation results for the existing case and proposed case are presented in Figure 4 and Figure 5, respectively.

In this case, the use of the proposed energy sources reduces the energy gap by an average of 1.93%. In this case, the performance benefit is small because of the high amount of energy realized from coal, nuclear and diesel NRESs. Hence, the contributions from RESs (existing and proposed) are small in comparison in the existing and proposed mechanisms. In the simulation, the existing case is described by (7). This does not consider the role of the UDC or stratosphere-based data centers as being capable of making contributions to the grid.

The proposed case is formulated in (10). In this case, the role of the UDC or stratosphere-based data centers in making contributions to the grid is considered.

The performance benefit is also investigated for a scenario where the power output from the NRESs (coal, nuclear and diesel) are significantly reduced. Such a case models a scenario where the use of RESs is being gradually incorporated with increasing contribution. In this case, the simulation parameters are presented in Table 2. Simulation results for the existing case and proposed case are in Figure 6 and Figure 7, respectively.

The inclusion of the proposed energy sources results in a reduction of the energy gap. A reduction of the energy gap is beneficial as it implies that RESs meet the load demand previously satisfied by RESs being retired from use. Analysis shows that the energy gap is reduced by 36.6% on average.

Table1: Simulation Parameters for high-RES contribution

Parameter	Value
Minimum power from coal	2.67 MW
Maximum power from coal [28]	544.8 MW
Mean power realized from coal	243 MW
Minimum power from nuclear	8.21 MW
Maximum power from nuclear [29]	268.1 MW
Mean power from nuclear	158.6 MW
Minimum power from diesel plant	1.97 MW
Maximum power from diesel plant [30]	239.2 MW
Mean power from diesel plant	118 MW

Minimum power from coal	2.67 MW
Maximum power from coal [28]	544.8 MW
Mean power realized from coal	243 MW
Minimum power from nuclear	8.21 MW
Maximum power from nuclear [29]	268.1 MW
Mean power from nuclear	158.6 MW
Minimum power from diesel plant	1.97 MW
Maximum power from diesel plant [30]	239.2 MW
Mean power from diesel plant	118 MW
Maximum power from terrestrial solar [31]	2.4 MW
Minimum power from terrestrial solar	0.02 MW
Mean power realized from terrestrial solar	0.98 MW
Maximum power from onshore wind [32]	2.3 MW
Minimum power realized from onshore wind	0.005 MW
Mean power realized from onshore wind	1.12 MW
Maximum power from offshore wind [33]	14.4 MW
Minimum power from offshore wind	0.034 MW
Mean power realized from offshore wind	7.88 MW
Maximum power realized from underwater	7.4 MW
Minimum power realized from underwater	0.2 MW
Mean power realized from underwater	3.87 MW
Maximum power realized from stratosphere	7.5 MW
Minimum power realized from stratosphere	0.005 MW
Mean power realized from stratosphere	3.45 MW

Table 2: Simulation Parameters for low-RES contribution

Parameter	Value
Minimum power realized from coal	1.95 MW
Maximum power realized from coal	50.1 MW
Mean power realized from coal	26.4 MW
Minimum power realized from nuclear	0.097 MW
Maximum power realized from nuclear	28.3 MW
Mean power realized from nuclear	15.9 MW
Minimum power realized from diesel plant	1.46 MW
Maximum power realized from diesel plant	249.8 MW
Mean power realized from diesel plant	127.9 MW
Maximum power from terrestrial solar	2.48 MW
Minimum power from terrestrial solar	0.22 MW
Mean power realized from terrestrial solar	1.42 MW
Maximum power realized from onshore wind	2.49 MW
Minimum power realized from onshore wind	0.09 MW
Mean power realized from onshore wind	1.49 MW
Maximum power realized from offshore wind	14.1 MW
Minimum power realized from offshore wind	0.44 MW
Mean power realized from offshore wind	6.72 MW
Maximum power realized from underwater	7.2 MW
Minimum power realized from underwater	0.4 MW
Mean power realized from underwater	4.04 MW
Maximum power realized from stratosphere	7.5 MW
Minimum power realized from stratosphere	0.11 MW
Mean power realized from stratosphere	3.91 MW

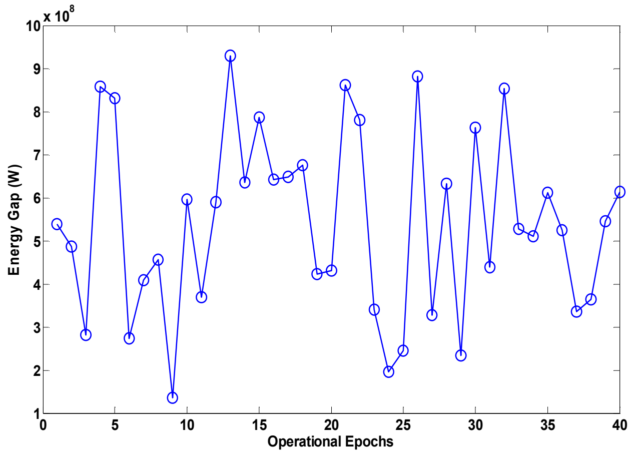

Figure 4: Energy Gap in the existing case considering high NRESs contribution.

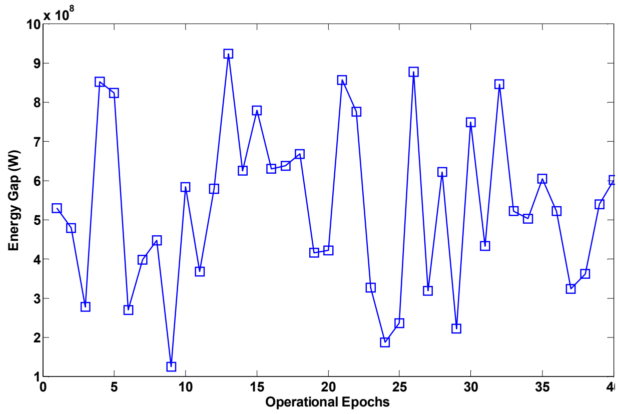

Figure 5: Energy Gap in the proposed case considering high NRESs contribution.

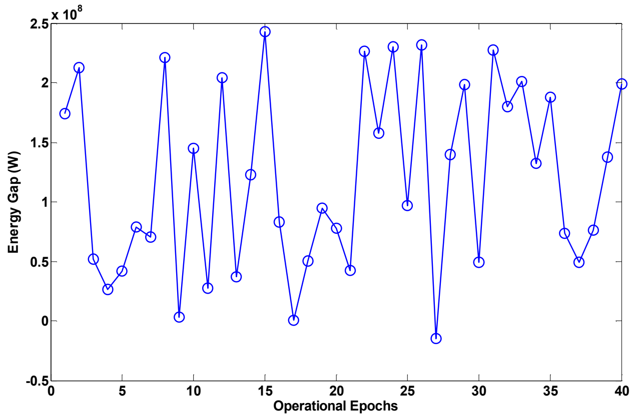

Figure 6: Energy Gap in existing case considering reduced contribution of RESs.

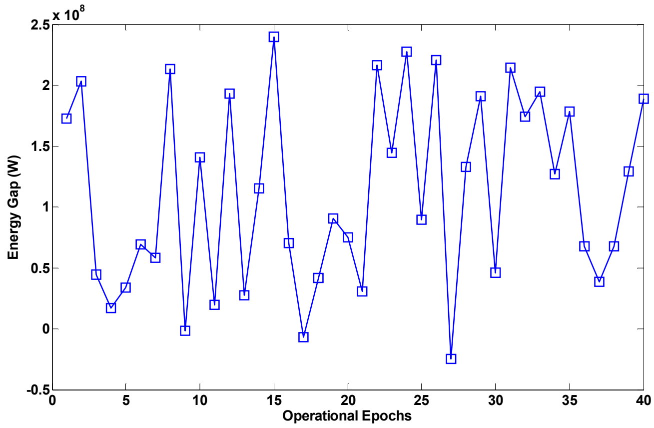

Figure 7: Energy Gap considering reduced RES contribution.

VII. CONCLUSION

The discussion in the paper addresses the challenge of the occurrence of energy gap that occurs while transitioning to the full use and adoption of renewable energy sources. The non–inclusion of a significant number of renewable energy sources is identified to be capable of resulting in the occurrence of energy gaps leading to the occurrences of load shedding. The presented research proposes the use and integration of underwater tidal energy and stratosphere derived solar energy into the grid. The integration of underwater tidal energy is recognized to benefit from advances in communication and computing networks that has led to the design and use of underwater data centers. In addition, the new solar source being recognized is from the stratosphere. This option is also arising due to the advances as regards stratosphere-based data centers and their role in communications and computing networks. Future work will focus on the techno-economic analysis of the design of a cable that enables the transmission of solar energy from the stratosphere to a terrestrial power station. This is deemed necessary to consider the perspective of a power utility organization.

ACKNOWLEDGMENT

The support of the Department of Electrical, Electronic and Computer Engineering of the Cape Peninsula University of Technology is highly acknowledged by the author.

REFERENCES

[1] J.Sutton-Parker, “Can analytics software measure end user computing electricity consumption?,” Clean Technologies and Environmental Policy, May 2022, doi: 10.1007/s10098-022-02325-x.

[2] A. Tarafdar, M. Debnath, S. Khatua, and R. K. Das, “Energy and Makespan Aware Scheduling of Deadline Sensitive Tasks in the Cloud Environment,” Journal of Grid Computing, vol. 19, no. 2, Apr. 2021, doi: 10.1007/s10723-021-09548-0.

[3] J.Shuja, K. Bilal, S. A. Madani, and S. U. Khan, “Data center energy efficient resource scheduling,” Cluster Computing, vol. 17, no. 4, pp. 1265–1277, Mar. 2014, doi: 10.1007/s10586-014-0365-0

[4] J. Rhodes, T. Deetjen, and C. Smith, “Impacts of Large, Flexible Data Center Operations on the Future of ERCOT,” 2021. Accessed: Aug. 22, 2022. [Online]. Available: https://www.ideasmiths.net/wp-content/uploads/2022/02/LANCIUM_IS_ERCOT_flexDC_FINAL_2021.pdf

[5] M. S. Hoosain, B. S. Paul, S. Kass, and S. Ramakrishna, “Tools Towards the Sustainability and Circularity of Data Centers,” Circular Economy and Sustainability, Jul. 2022, doi: 10.1007/s43615-022-00191-

[6] B.Whitehead, D. Andrews, A. Shah, and G. Maidment, “Assessing the environmental impact of data centres part 1: Background, energy use and metrics,” Building and Environment, vol. 82, pp. 151–159, Dec. 2014, doi: 10.1016/j.buildenv.2014.08.021.

[7] M. Shamimul Islam, A. Jahid, A. S. M. Tanvir Islam, Sharif, M. Anwar Sadath and M. Kamrul Hasan Monju, "Energy Sustainable Provisioning for Green Data Centers," 2018 International Conference on Innovations in Science, Engineering and Technology (ICISET), 2018, pp. 378-383, doi: 10.1109/ICISET.2018.8745652.

[8] A. Thiaw and S. Toure, “Innovation for the Better: How Renewable Energy Technologies Improve Living Standards,” Sustainable Energy Access for Communities, pp. 119–125, 2022, doi: 10.1007/978-3-030-68410-5_11.

[9] A. A. Masoud, “Renewable energy and water sustainability: lessons learnt from TUISR19,” Environmental Science and Pollution Research, Mar. 2020, doi: 10.1007/s11356-020-08504-x.

[10]M. Hafner, S. Tagliapietra, and L. de Strasser, “Prospects for Renewable Energy in Africa,” Energy in Africa, pp. 47–75, 2018, doi: 10.1007/978-3-319-92219-5_3

[11] M. T. Kartal, S. Kılıç Depren, F. Ayhan, and Ö. Depren, “Impact of renewable and fossil fuel energy consumption on environmental degradation: evidence from USA by nonlinear approaches,” International Journal of Sustainable Development & World Ecology, pp. 1–18, Jun. 2022, doi: 10.1080/13504509.2022.2087115

[12] M. F. Bashir, M. Sadiq, B. Talbi, L. Shahzad, and M. Adnan Bashir, “An outlook on the development of renewable energy, policy measures to reshape the current energy mix, and how to achieve sustainable economic growth in the post COVID-19 era,” Environmental Science and Pollution Research, Apr. 2022, doi: 10.1007/s11356-022-20010-w

[13] I. Todd and D. McCauley, “An inter-disciplinary approach to the energy transition in South Africa,” Discover Sustainability, vol. 2, no. 1, Jul. 2021, doi: 10.1007/s43621-021-00043-w

[14] L. Baker and J. Phillips, “Tensions in the transition: The politics of electricity distribution in South Africa,” Environment and Planning C: Politics and Space, vol. 37, no. 1, pp. 177–196, Jun. 2018, doi: 10.1177/2399654418778590

[15] O. O. Babayomi, D. A. Dahoro, and Z. Zhang, “Affordable Clean Energy Transition in Developing Countries: Pathways and Technologies,” iScience, p. 104178, Mar. 2022, doi: 10.1016/j.isci.2022.104178

[16] S. E. Uhunamure and K. Shale, “A SWOT Analysis Approach for a Sustainable Transition to Renewable Energy in South Africa,” Sustainability, vol. 13, no. 7, p. 3933, Apr. 2021, doi: 10.3390/su13073933

[17] D. Zhang and C. Ma, “Utilization of tidal current and wave energy help the implement of the carbon emissions peak and carbon neutrality strategy in China,” IOP Conference Series: Earth and Environmental Science, vol. 983, no. 1, p. 012055, Feb. 2022, doi: 10.1088/1755-1315/983/1/012055

[18] D.Bhatnagar, D. Preziuso, and R. O’Neil, “Power Generation from Tides and Waves,” The Palgrave Handbook of International Energy Economics, pp. 195–212, 2022, doi: 10.1007/978-3-030-86884-0_12

[19] “Under the sea, Microsoft tests a datacenter that’s quick to deploy, could provide internet connectivity for years,” Stories, Jun. 06, 2018. https://news.microsoft.com/features/under-the-sea-microsoft-tests-a-datacenter-thats-quick-to-deploy-could-provide-internet-connectivity-for-years/

[20] AA Periola, AA Alonge and KA Ogudo, Underwater Computing Systems and Astronomy–Multi-Disciplinary Research Potential and Benefits’, ASTES Journal, Vol. 6, No. 1, 2021, pp 1000 – 1011.

[21] Z.-H. Hu, Y.-X. Zheng, and Y.-G. Wang, “Packing computing servers into the vessel of an underwater data center considering cooling efficiency,” Applied Energy, vol. 314, p. 118986, May 2022, doi: 10.1016/j.apenergy.2022.118986

[22] J.Roach, ‘Microsoft datacenter batteries to support growth of renewavbles on the power grid’, [Online] Available: https://news.microsoft.com/innovation-stories/ireland-wind-farm-datacenter-ups/ , July 7, 2022.

[23] S. C. Arum, D. Grace, P. D. Mitchell, M. D. Zakaria, and N. Morozs, “Energy Management of Solar-Powered Aircraft-Based High Altitude Platform for Wireless Communications,” Electronics, vol. 9, no. 1, p. 179, Jan. 2020, doi: 10.3390/electronics9010179

[24] O. Anicho, P. B. Charlesworth, G. Baicher and A. Nagar, "Autonomous Unmanned Solar Powered HAPS: Impact of Latitudes and Seasons on Power and Communications Coverage," 2018 IEEE International Conference on Communication, Networks and Satellite (Comnetsat), 2018, pp. 7-12, doi: 10.1109/COMNETSAT.2018.8684145.

[25] J. Kua, S. W. Loke, C. Arora, N. Fernando, and C. Ranaweera, “Internet of Things in Space: A Review of Opportunities and Challenges from Satellite-Aided Computing to Digitally-Enhanced Space Living,” Sensors, vol. 21, no. 23, p. 8117, Dec. 2021, doi: 10.3390/s21238117

[26] D.M. Popescu and S.X. Sun, ‘Building the space elevator: lessons from biological design.’ J. R. Soc. Interface 15: 20180086. http://dx.doi.org/10.1098/rsif.2018.0086

[27] https://www.dacepricebooklet.com/table-costs/high-and-low-voltage-underground-electrical-power-cables-0

[28] Kumar, R., Sharma, A.K. & Tewari, P.C. Cost analysis of a coal-fired power plant using the NPV method. J Ind Eng Int 11, 495–504 (2015). https://doi.org/10.1007/s40092-015-0116-8

[29] Di Maio, F.; Bani, L.; Zio, E. The Contribution of Small Modular Reactors to the Resilience of Power Supply. J. Nucl. Eng. 2022, 3, 152–162. https://doi.org/10.3390/jne3020009.

[30] https://www.engineeringchoice.com/what-is-diesel-power-plant/

[31] Iakovleva, E.; Guerra, D.; Tcvetkov, P.; Shklyarskiy, Y. Technical and Economic Analysis of Modernization of Solar Power Plant: A Case Study from the Republic of Cuba. Sustainability 2022, 14, 822. https://doi.org/10.3390/ su14020822.

[32] https://www.renewablesfirst.co.uk/windpower/windpower-learning-centre/much-power-generate-wind-turbine/ onshore wind

[33] https://www.nationalgrid.com/stories/energy-explained/onshore-vs-offshore-wind-energy 3.6 MW.

2023 SAUPEC Conference, Johannesburg, South Africa, January 24-26, 2023

Optimum Reliability Integrated WEF Renewable Technology into the Eskom Distribution Grid, in the Eastern Cape Operating Unit

Siyamthanda Luthando Matondolo
Department of Electrical Engineering
Cape Peninsula University of Technology,
Bellville South Industrial, Cape Town, RSA
profcya@gmail.com and MatondSL@eskom.co.za

Mohammed Tariq Kahn
Department of Electrical Engineering
Cape Peninsula University of Technology,
Director: Centre for Distributed Power and Electronic System, Consultant and Reseacher in Energy Technology
Bellville South Industrial, Cape Town, RSA
khant@cput.ac.za

Abstract **– This research paper is to look at integrated optimum reliability WEF renewable technology into the Eskom Distribution grid, in the ECOU. Republic of South Africa has the abundant of the coal assets valued at 53 billion tonnes in which current production equates to 200 years of coal reserve of supply left. Currently the country is moving away from fossil such as coal energy source to more environmentally friendly energy source which is renewable technology which have far low carbon emission compared to current coal source. The energy crisis in the country has seen more renewable energy (WEF) integrated to the Eskom utility network grid to address energy crisis or loadshedding, hence therefore research question are these WEF integrated renewable technology optimum and reliable in the utility distribution network grid in the ECOU.**

Keywords – Renewable Energy (WEF), Load Forecast, Loadshedding/Energy Crisis, Pollution/Carbon Emissions, Cost v Sustainability (Just Transition).

I. Introduction

Republic of South Africa has been an enormous increase in demand for electricity energy most after fall of apartheid ere and as result of rapid industrial development, rapid immigration growth around urban areas and massive rural electrification led to severe energy crisis today. South Africa has been facing energy crisis or loadshedding which affect country economy and the country has also facing serious climate change effects hence therefore as a country renewable energy is a fundamental necessity and access to the right renewable energy services provides opportunities to reduce carbon emissions and play role in the current 15 years loadshedding energy crisis [1]. Defining loadshedding for ordinary citizen to understand we can say that "loadshedding is planned schedule process whereby the electricity demand or power consumption has exceeded its installed supply capacity which leads or results to the power utility implementing power supply cuts or blackouts to reserve the total national power supply blackout [2]. From all sectors such as mining, automobile, restaurants, financial banking centres, large/small factories to tourism sector (guesthouse, hotel, lodge etc.), hospitals and were many citizens ended up having long power outages [3]. Electricity or power supply it has not just change our lives, but it has become part of our daily lives and now is the main backbone of our everyday modern world, daily life, and economy [4]. Coal traditionally dominates the energy supply sector in the Republic South Africa. Eskom produces 77% of the South Africa's electricity maily from the coal power stations. South Africa is gifted with the coal reserved, with resever coal for nearly 200 years. The coal is still projected to provide its segment of the total electricity generation flea market for years to come. There are 5 large main users of coal energy source which are RSA, USA, India, Japan and China which combine makeup 82% of total global usage of coal [5]. This vast rapid development in severely damaging coal energy usage is compared with fairly small impact from renewable sources. The renewable energy technology is intensely linked with numerous features of sustainable development but traditionally procedures have not chosen renewable energy technologies led to a propagation of private and public sector capital for more lucrative deals, seriously polluting energy generation technologies [6].

Republic South African government then realised that environment shift is a serious peril to Republic South Africa (RSA) as country and a main problem to continued impoverishment decline and alleviation throughout its various scopes. That created a huge concerned that consequently to demands for a change over in approach to bring about the concern of environment changes a main importance in the country. Having this awareness, the Republic of South Africa (RSA) is commencement to proactively connect its intentions with environment change main concern within a sustainable improvement structure of renewable energy as alternative power supply [7]. The remnant fuels such as liquid fuels (crude oil), uranium, coal, biomass and gas these remain the main central role in the socio-economic growth in the Republic of South Africa (RSA), although concurrently delivering the needed infrastructural economic which end up the country becoming an attractive host for foreign investments in the energy sector [8]. The Republic of South African government also recognised lasting goal to develop an energy industry that will power a completely non-subsidised replacement to fossil fuels. The strategic methodology has been concretised out of considerable fiscal sustenance for renewable energy study and growth [9]. In recently year wind energy facility generation are currently more and more prevalent option of technology for new capacity adding up in power systems global. Various considerations have added to this trend such as environmental concerns and a constant increase in fossil fuel prices are central to these factors [10]. The wind energy facility (WEF) technology has demonstrated to be one of the greatest effective cheapest alternative obtainable source of renewable energy presenting comparatively with orthodox fossil energy source [11].

II. WIND ENERGY FACILITY IN SOUTH AFRICA

Wind Energy Facility (WEF), or wind farms as at occasionally named, are groups of wind devices utilised to generate electricity via natural wind. Most of WEF are privatedly own and their operation by businesspeople who then persuade utility such Eskom and Municipality to buy electricity produced on the WEF for those utilities to sell it to public citizens. These WEF are also known as Independent Power Producers (IPPs) [12]. These Wind Energy Facilities (WEFs) are the product of the wind air which is moving. The wind energy facility is a unrestricted renewable energy source, and it is the world’s fastest developing electricity resource [13].
Around the globe most utility and electricity developers use wind turbine to catch the wind energy. This wind turbine catches wind through rotor blades that wind flows through the rotor blades then cause rotation of rotor blades and spin main shaft powering a rotor inside a generator and result to production of electricity please see Figure 1.

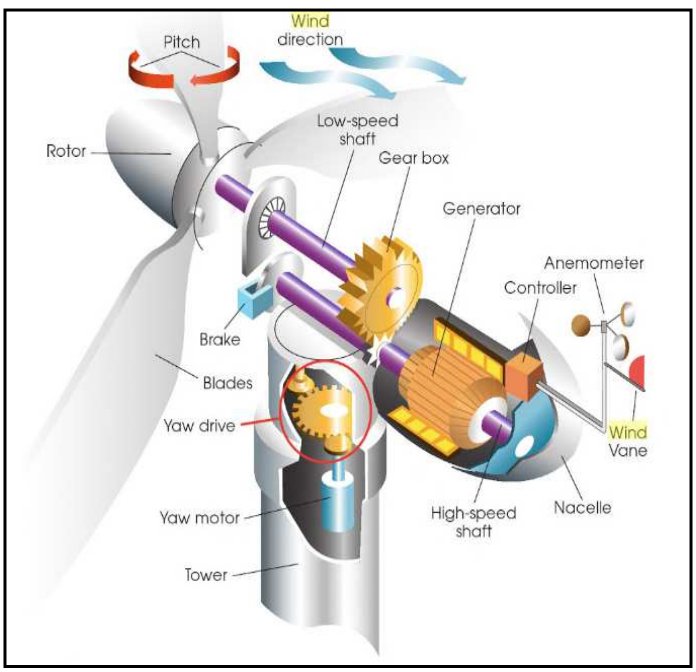

Fig. 1 Main components of a typical modern high-power WEF turbine [14].

The operation of this WEF the generated electricity moves into the cables that are connect to the turbine, then moves downstream the turbine tower and collectively combine after that with the wind energy facility (WEF) from the other wind turbines before entering local electricity network or the national grid such as Eskom grid in the case of South Africa which provide power to South Africans [13]. WEF may comprise of numerous wind turbines and cover a stretched area of hundreds of square kilometres. They can be offshore or onshore WEF and in RSA main is the land were they normal get to be installed or established may be used for agriculture or other purposes. WEF and Solar from the Sun, are a unrestricted free renewable energy sources that are traditional from natural source and will forever generate electricity. The energy which is obtained from the wind energy facilities normally rely on the natural wind velocity. The higher the velocity wind, the great the energy that can be produced to generate electricity on a substantial amount. Nevertheless, this necessitates substantial areas of territory to connect sufficient wind turbines or generators, which might results to noise and that affect environment. The Republic of South Africa has reasonable wind capability, particularly adjacent to the coastal areas of Eastern Cape (EC) and Western Cape (WC), see Figure 2 below:

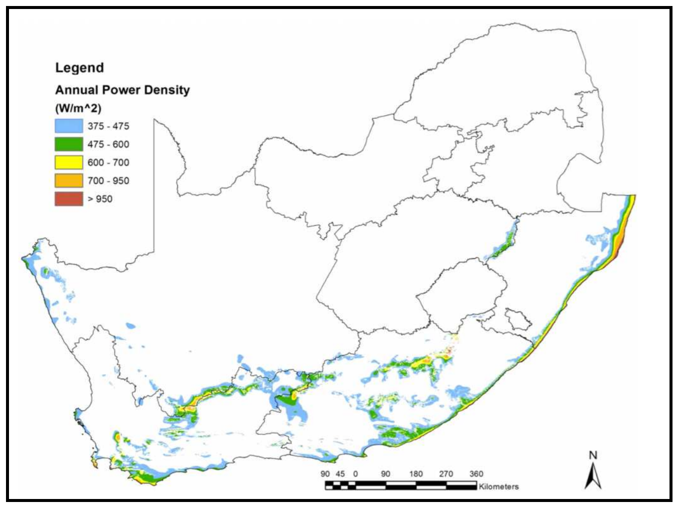

Fig. 2 Best WEF resource quality areas in South Africa [19].

The Republic of South Africa has an extraordinary echolon of Renewable Energy probabilities and aligned with the state or government pledge to changeover to a low-slung carbon emission of 17 800MW by 2030 which is the government target for now and that’s according to the IRP 2010. The newly generated energy power to be produced are expected to to be from mainly renewable energy suppliers as per Figure 2. According to IRP 2010 the plan was by end October 2016, 2800MW was meant to be secured from 53 Independent Power Producers (IPPs) which most have been complete and some final stage of completion. Most of IPPs from Bid Window one (BW1) and BW2 which were expensive contracts most of these are complete and are delivering power to the

Eskom grid. Bid Window three (BW3), this one most are final stage of completion but varying on the different project's building phase [15]. The Republic of South Africa's reliance on hydrocarbons power station, mostly coal, has made the (RSA) as the country, the world's 13th largest CO^2 producer [16]. The preservation of the current existing coal power stations fleet has remained problematic, and energy available factors (EAF) capacity went down currently to nearly 50% in 2022. The foremost to frequent electricity deficiencies, which may possibly be alleviated by quick implementation of renewable energy, particularly wind energy facilities (WEF). As of 2021 South Africa is rank number one in Africa and Middle East region in terms of wind energy renewable technology installation with 2 956MW which is 0.4% of globally and 46.1% in Africa and Middle East region in terms of wind energy facilities [17]. South Africa has excellent wind resources, which are yet to be fully utilised. The rapid growth of the renewables energy expansions in the RSA has grow into a requirement, as renewable energy which is alleged to be the lonely energy supplier of new energy power that can be implemented rapidly sufficient to help South Africa's electricity shortages crisis [18]. The Republic of South Africa's new WEF renewable energy power programme is the rapid or quickest increasing progamme of the new energy alternative in the world for the past seven (7) years. This has enticed roughly about \$15 billion of venture capital into wind and solar renewable energy projects encompassing a constellation of new Independent Power Producers (IPPs) provide finance backing by overseas venture capital or investers. The Republic of South Africa (RSA) is currently poignant in the direction of a sizeable wind energy industry with a local connected capacity in additional of 6,000 MW by 2021, if not more quickly, and an earmarked one of as a minimum 37,000 MW by 2050 if the draft IRP is made policy [20].

III. LOAD FORECAST AND DEMAND SUPPLY

The effective and economic investment of the electrical power distribution structure is a network planner's responsibility. To do this, the network planner has to look forward to how much power should be distributed also where and when it will be required. The fundamental to supply development is a well planned and coordinated medium-to-long span load forecast. This gives the future estimate forecast demand electrical in terms of the location, magnitude and temporal (time) features. The planners ought to continuously be looking forward as conceivable in an effort to integrate the planning of generation, transmission, sub-transmission, distribution, embedded/distributed generation and demand side options, to ensure that the development of grid networks and the usage of resources are optimum. "The intention of supply development is to offer a systematic and efficient extension of apparatus and amenities to meet the functionality's future potential electricity requirement with an appropriate echolon of reliability."

In recent years as mentioned earlier there has been an enormous upsurge in need for energy in the Republic of South Africa in recent years as a result of rapid industrial development, rapid immigration growth around urban areas and massive rural electrification led to severe energy crisis today. South Africa is gifted with coal and relies heavily on coal to meet its energy needs. The RSA utility (Eskom) at present generates just over 90% of the country's requered and consequently of this it has monopolised distribution as the primary generator and distributor. The Eskom is accountable for expanding and preserving the country's generation power power stations, the transmission lines and distribution line. Eskom also connect to interconnections with the Southern African Energy Power grid network. The RSA, national demand load forecast at System peak is delivered on all three scenarios, and from there onwards the Provincial and Main Transmission Substation (MTS) forecasts is delivered on only the recommended forecast scenario to equilibrium the topmost conjecture forecast with that of each generates and tranmit throught transmission and distribution lines to (MTS) [21]. The Eskom load demand evaluated through tramission and distribution low scenario which are founded on expectations that there will be a prolonged subdued growth rate in the RSA as country. Most of the industries sector had not have large rapid growth due to global current crisises. Then there is local negative view in line with the slege economic growth due to persisting loadshedding, the reduce status to junk status The figure 3 below shows scenarios presumes association with a low general local economic growth average of nearly 0.5%, lower than the projected GDP of 1%. A summary of these 3 scenarios is showed in Figure 3:

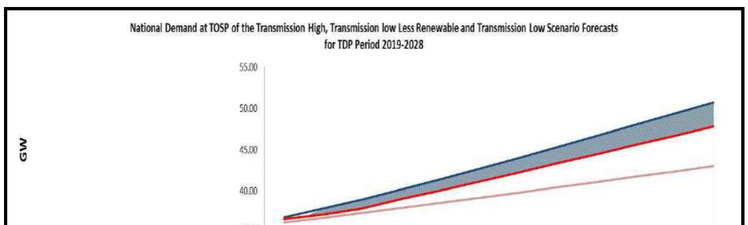

	2017	2018	2019	2020	2021	2022	2023	2024	2025	2026	2027	2028
Capacity absorbed by Off Grid RE	35.60	37.84	38.97	40.16	41.40	42.67	43.98	45.31	46.66	48.02	49.38	50.73
Tx High Less RE	36.57	37.12	37.87	38.99	40.04	41.11	42.21	43.32	44.45	45.57	46.69	47.80
Maximum System Demand(MSD) Tx High (65GW @2040)	36.76	37.84	38.97	40.16	41.40	42.67	43.98	45.31	46.66	48.02	49.38	50.73
Maximum System Demand(MSD) Tx High Less RE (58GW @2040)	36.57	37.12	37.87	38.99	40.04	41.11	42.21	43.32	44.45	45.57	46.69	47.80
Maximum System Demand(MSD) Tx Low (Junk Status 50GW @2040)	36.16	36.73	37.31	37.91	38.52	39.14	39.76	40.40	41.04	41.69	42.34	42.99

Fig. 3: Transmission Forecast Scenario's for TDP period 2019-2028 [21].

There where a number of generations plans in place to bring equilibrium in the supply and demand imbalance South Africa which is currently experiencing. Ingula, Kusile and Medupi coal fire-stations were all planned to be completely in service or commissioned by 2022 but unfortunately Kusile still under construction some unit/s. Additionally, there is commitment program from the RSA government to complete connect as much as they can of (IPPs) to the national electricity grid network as part of the implementation of the Integrated Resource Plan (IRP) 2010-2030 to ease up current energy crisis. The Transmission High forecast assumes return of industries which would have a significant effect in specifically Northern Cape Province with the mining of Fe-Mg and Iron Ore, mining of coal in Limpopo Province, as well as increased industrial and export activities in the Eastern Cape. The Eastern Cape region as province has a substantial amount of renewable capacity especially in wind technology which assists in the supply even at time of system peak. The Eastern Cape has two main manufacturing city centre, East London and Port Elizabeth, with fairly technologically advanced manufacturing companies such as Volkwagen (VW), Isuzu, Mercedes Benz just naming few automobile manufactures. A new harbour has been built at Coega, just north of Port Elizabeth, which is linked to an Industrial Development Zone (Coega IDZ) to attract new investment. The figure 4 below clearly indicates which of the sectors has the greatest influence on the economy of the province, next to that in the upper right half of the figure is a correlation between the load and the GVA growth in the region. An R2 value close to 1 shows good correlation. The Eastern Cape had a province peak load demand of 1,532 MW in 2016 and the load demand at the TOSP was 1462 MW. The province peak load demand is predictable to grow or expand to around 2 136 MW by 2028 with a TOSP contribution of 2 136 MW.

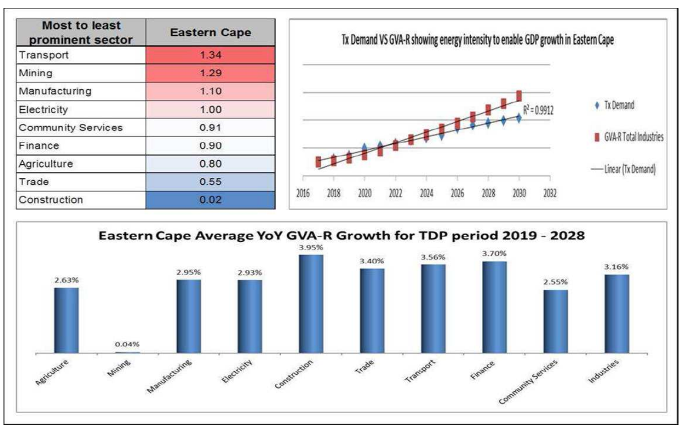

Fig. 4: Economic Summary for Eastern Cape 2019-2028 [21].

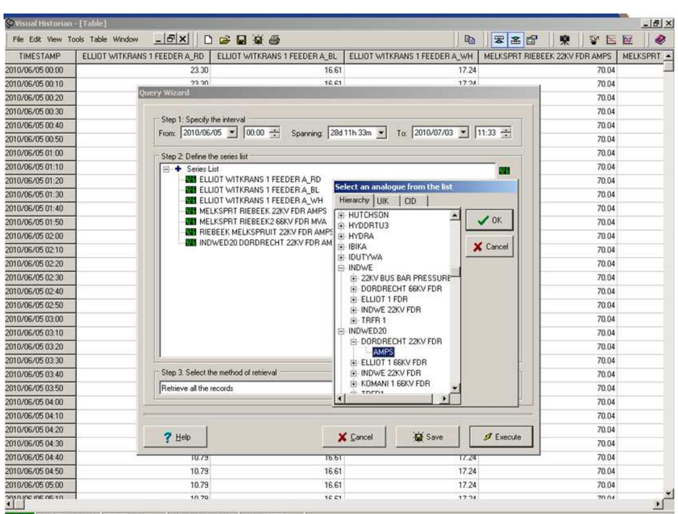

Fig. 5: Virtual History Systsem].

MV90 data is system were customer usage or customer load records that are measured using devices apparatus for the intention of charging or billing them. We have added statistical meters to MV90, using the same system, for the load forecast purposes. The only data in the structural system which correlates to KVAr and KW. SCADA used primarily to evaluate monitoring of load apparatus and control the network through optimisation. Information system data in the system includes everything that is measured such as follow: (current, power, frequency, tap change postion, voltage, oil temperature, breaker status, protection status etc. The SCADA data and MV90 data follow very different paths. The previous SCADA system used was a system called 8501. The problem with 8501 was that the software could only run-on hardware that was out of warrantee. The components were also difficult to source when they fail.

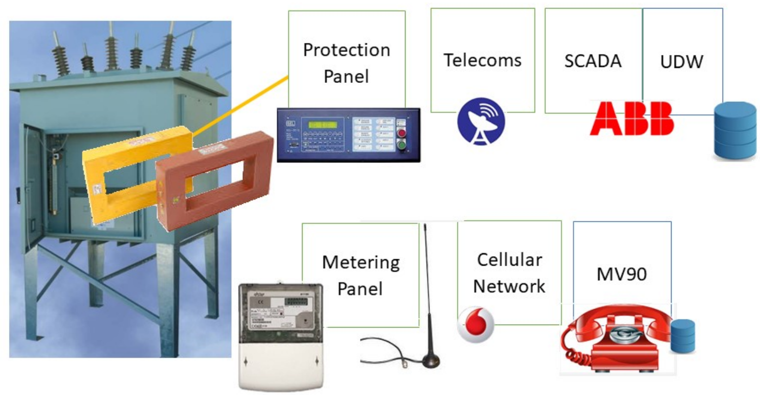

Fig. 6: M90 v SCADA].

In summary load forecasting is the first task to be performed before commencing with the planning of new networks to supply future demand. By performing a geo-based load forecast based on socio economic principals the forecaster gains insight into the factors which ultimately drives the load behaviour. Using domain specialists improves the assumptions which the forecast is based on and adds credibility to the forecast which makes it more defendable.

IV. LOADSHEDDING CRISIS WITH INTEGRADED WEF

Republic of South Africa since 2006 it has experience loadshedding till today. Electricity is the major and main key drivers for the country economic development growth and economic stability. This fact that the newest technology of the twentieth (20th) century is electricality or power supply which has completely changed our world profoundly for the better since the discovery of it. Electricity or power supply it has not just change our lives, but it has become part of our daily lives and now is the main backbone of our everyday modern world, daily life, and economy. Electricity is number one from all household essential services such as wated and sewerage because without electricity all other household services such as water need electricity, sewerage need electricity because both utilising pumps to pump such service to relevant site such as water station pump and sewerage stations [22]. With no doubt or contradicting electricity remain the most significant 20th Century evented or discovered modern technology. It has changed our lives and the whole global community overwhelmingly since the discovery till to date and change our livelihood completely. Electricity remains the backbone of nearly most if not all the global community as the modern industrial technology to imporve country's economy and livelihood of its citizens.

The impact of loadshedding to millions of South African citizens, businesses, industrial sectors such financial sector like banks and ATMs, Mining, agriculture like milk, vegetable and fruit farmers to count just few sectors; and it has negative impact to millions of households where it has damaged their appliances, their frigerated medication and food. The Republic of South Africa (RSA) still remain with high rate of Human Immunodeficiency Virus (HIV) and Tuberculosis (TB) which most of these medications need refrigeration which get affect by loadshedding is implemented [23]. South African utility (Eskom) stated that it implements loadshedding to avoid total national blackouts which can devasted the country and they state that the loadshedding stages implementation development is based on the risk and consumption electricity demands to ensure that loadshedding is applied in a fair equitable manner that does not disadvantage certain areas; and to ensure fifteen percent (15%) reserve margins [24]. The utility (Eskom) consignments the country by a further 1 000MW of loadshedding. Eskom has 1 to 8 loadshedding stages and depends on Eskom role out of loadshedding but in the jurisdiction of municipality then municipality will have their own loadshedding approach but will be influence by Eskom loadshedding as example villages, townships and suburbs are pretentious by all Eskom stages differs on a range of factors. This includes time of day the loadshedding when it is acknowledged by Eskom or by municipality jurisdiction [25]. Reality according to Eskom if there do not implement these loadshedding stages then utility network grid will suffer catastrophic failure. As said fortunately we have not yet experience stage 7 or 8 loadshedding as the country this will be catastrophic not only to the economy. It will plunge the country into dangerous chaos which will affect critical institution such as Hospitals, airports, harbours, retail industry, agriculture, mines, and critical infrastructure will struggle to function and to back to normality [26].

Recently the country experience worst week loadshedding stage 6 for a number of consecutive days which was the second time South Africa experiencing loadshedding stage 6, first time South Africa's worst loadshedding was in December 2019 and last just for just a day [27]. In summary, the impact of loadshedding not only Eskom customers but whole country including the rand verse US dollar due to this loadshedding in July 2022 so rand getting weaker against the US dollar that's according to Johannesburg Stock Exchange (JSE). According to different economist the economic impact of loadshedding is estimated around R1.5 billion to R4 billion per day depending what loadshedding stage the country is experiencing. As already been indicated that this situation it has been existence now for fifteen (15) years and unfortunately unabated.

V. INTEGRATED WEF RENEWABLE ENERGY

As we already indicated in our literature review that the Republic of South Africa is projected to have a high level of Renewal Energy potential commitment programs which are aligned with the government commitment to just transition to a low carbon economy, 17 800MW of the 2030 target according to the IRP 2010. The newly produced energy power to be created as expected from mainly WEF and Solar renewable energy sources, with 5 000 MW to be in operational since 2019 and further 2 000MW (i.e., combined 7 000MW) operational by 2024 [27]. IPPs BW1, BW2, BW3 and BW4 are completed and surely connected to the network grid then BW5, and BW6 mostly pending [28]. Eastern Cape province has been alluded in the table below account for about 1441MW in different status which in operations, in construction and some in planning stages which actual mean (approval planning and financing) have been complete. Eastern Cape as province is the leading South Africa with Wind Energy Facilities. Eastern Cape province has excellent wind resources, which are yet to be fully utilised.

TABLE I: Generation capacity WEF Technology installed, in construction and in planning in the ECOU Eskom network grid.

Technology	Mega Watts (MW)	REIPPP	Onshore	Status
Droper Wind Farm	97MW	1	Yes	In Operation
Cookhouse Wind Farm	135MW	1	Yes	In Operation
MetroWind Van Stadens Wind Farm	27MW	1	Yes	In Operation
Jeffrey Bay Wind Farm	138MW	1	Yes	In Operation
Red Cap Kouga Wind Farm – Oyster Bay	80MW	1	Yes	In Operation
Chaba Wind Farm	20.6MW	2	Yes	In Operation
Grassridge Wind Farm	59.8MW	2	Yes	In Operation
TOTAL	**557.MW**			
Amakhala Emoyeni (Phase1)	134MW	2	Yes	In Construction
Waainek Wind Farm	23.4MW	2	Yes	In Construction
Tsitsikama Community Wind Farm	94.8MW	2	Yes	In Construction
Nojoli Wind Farm	87MW	3	Yes	In Construction
Red Cap – Gibson Bay	111MW	3	Yes	In Construction
TOTAL	**450.6MW**			
Nxuba Wind Farm	140MW	4	Yes	In Planning
Golden Valley Wind Farm	120MW	4	Yes	In Planning
Wesley – Ciskei Wind Farm	33MW	4	Yes	In Planning
Oyster Bay Wind Farm	140MW	4	Yes	In Planning

Technology	Mega Watts (MW)	REIPP P	Onshor e	Status
TOTAL	**433MW**			
FINAL TOTAL	**1 441MW**			

Global Wind Energy Council (GWEC) 2017 report the Republic of South Africa is rank number one and projected number one in Africa and Middle East region in terms of wind energy renewable technology installation with 2 094 MW which is 0.4% of global and 46.1% in Africa and Middle East region in terms of wind energy facilities. Therefore, this means Eastern Cape province with 557.4MW wind power already in operation or commissioned it account for 26.62% of wind energy facilities which mean a quarter of installed WEF in South Africa [29].

VI. RECOMMENDATION, CONCLUSION AND FUTURE RESEARCH

Republic of South Africa since 2006 it has experience energy crisis or loadshedding till today. Electricity is and will remain the one of the key main drivers for economic development and growth and with country economic stability. The Republic of South Africa (RSA) has high level of potential in the WEF and Solar renewable energy technology look at RSA government commitment to just transition to a low carbon, with a target of 17 800 MW in 2030. But review of IRP needs to be done to include Nuclear Power station which also clean energy and have base load. Future research can include whole country and solar system as another potential renewable energy in South Africa.

ACKNOWLEDGMENT

God, the Holy Spirit and my family always give me strenght not to give up on my schoolwork. Furthermore, I owe special thanks to my supervisor, Prof. Mohamed Tariq Kahn for his guidance, patience, gentle manner and understanding.

REFERENCES

[1] Niselow, T., 2019. Sunday Read: Load shedding through the years and how Eskom has struggled to keep the lights on, Cape Town: News24.
[2] Oxford Dicitionary, 2022, Loadshedding definition, https://www.dictionary.com/browse/load-shedding.
[3] Joel Krupa & Sarah Burch, 2021. A new energy future for South Africa: The political ecology of South African renewable energy. Energy Policy, Volume 39, pp. 6254-6261.
[4] Kenny, A., 2018. Eskom Laid low by corruption, mismanagement and renewables, Johannesburg: Politicsweb.
[5] Eskom, 2021, 'Fact Sheet: Coal in South Africa", page 1, https://www.eskom.co.za/wp-content/uploads/2021/08/CO-0007-Coal-in-SA-Rev-16.pdf
[6] Jefferson, M., 2018. Accelerating the transition to sustain energy systems. Energy Policy, Volume 36, pp. 4115-4125.
[7] UNEP, 2017. Intergovernmental Panel on Climate Change. [Online] Available at: https://www.ipcc.ch/pdf/assessment-report/ar4/syr/ar4_syr_full_report.pdf [Accessed 18 Febrauary 2017].
[8] Department of Energy, 2019. State of Renewable Energy in South Africa, Pretoria: Department of Energy.
[9] Department of Mineral and Energy RSA, 2019. White Paper on Renewable Energy, Cape Town: South African Government.
[10] Barberis Negra N. & Holmstrom O., 2017. Aspects of revelance in offshore wind farm reliability assessment., IEEE Trans Energy Convers, 22(1), pp. 156-166.
[11] Dimitrovski A. & Tomsovic K., 2018. Impact of Wind generation uncertainty on generating capacity adequancy. In 9th International conference on probabilistic methods applied to power systems, pp. 1-6.
[12] Energy Information, 2018. Wind Energy - - Energy from Moving Air. [Online] Available at: http://www.ei.lehigh.edu/learners/energy/readings/wind.pdf [Accessed 23 June 2016].
[13] Genesis Energy, 2021. WIND, Martinborough: ElectroCity.
[14] Paul A. Lynn, 2019. Onshore and Offshore Wind Energy: An Introduction. In: J. W. &. S. Ltd, ed. Onshore and Offshore Wind Energy: An Introduction. West Sussex: Wiley
[15] Department of Energy, 2018. Independent Power Producer Procurement Programme. [Online] Available at: https://www.ipp-renewables.co.za/ [Accessed 04 May 2018].
[16] GWEC, 2018. Global Wind Energy Council (Uniting the global wind industry. [Online] Available at: http://gwec.net/wp-content/uploads/2012/06/Global-Wind-2008-Report.pdf [Accessed 20 March 2018].
[17] GWEC, 2021. Global Wind 2006 Report, s.l.: Global Wind Energy Council.
[18] GWEC, 2022. Global Wind Energy Council (Uniting the global wind industry. [Online] Available at: http://gwec.net/wp-content/uploads/2012/06/Global-Wind-2008-Report.pdf [Accessed 20 November 2022].
[19] Walwyn Brent, David Richard, & Alan Colin, 2018. Renewable energy gathers steam in South Africa. Renewable and Sustainable Energy Reviews, Volume 41, p. 390.
[20] GWEC, 2020. Global Wind Energy COUNCIL. [Online] Available at: http://gwec.net/wp-content/uploads/vip/GWEC_PRstats2017_EN-003_FINAL.pdf [Accessed 21 November 2022].
[21] Jana Breedt and Danie Payne, 2017. Transmission Demand Forecast Report for Planning Purposes of the TDP Period 2019 to 2028, Johannesburg: Eskom.
[22] Kenny, A., 2015. The rise and fall of Eskom - IRR. [Online] Available at: https://www.politicsweb.co.za/documents/the-rise-and-fall-of-eskom--irr [Accessed 23rd September 2022].
[23] Wilson, L., 2020. 5 Ways that Load shedding impacts health in South Africa, Cape Town: Borgenproject.
[24] Swart, M., 2020. Understanding the different stages of loadshedding, Roodepoort: Roodeport Records.
[25] Eskom, 2022. Loadshedding Stages Explained in Detail, Tshwane: Show-me.
[26] Kahla, C., 2021. Load shedding stages explained: Here's what you need to know, Durban: The Citizen.
[27] Pieters, B., 2022. The cost of Eskom load shdding, Johannesburg: Pieters Associates Business Accounting Practitioners.
[28] Department of Energy, 2018. Independent Power Producer Procurement Programme, Pretoria: Department of Energy.
[29] GWEC, 2019. Global Wind Report. [Online] Available at: http://www.gwec.net/wp-content/uploads/vip/GWEC-Global-Wind-2015-Report_April-2016_22_04.pdf [Accessed 02 09 2017].

2023 SAUPEC Conference, Johannesburg, South Africa, January 24-26, 2023.

An Economic Feasibility Study for Off-Grid Hybrid Renewable Energy Resources

Emmanuel Idowu Ogunwole and Senthil Krishnamurthy
Department of Electrical, Electronic, and Computer Engineering,
Center for Substation Automation and Energy Management Systems
Cape Peninsula University of Technology,
PO BOX 1906, Symphonyway, Bellville, Cape Town, South Africa - 7535
[1]emmanuelidowu18@gmail.com
[2]KrishnamurthyS@cput.ac.za

***Abstract*—Renewable energy resources (RES) are gaining popularity worldwide. As a result, renewable energy sources (RES) are now considered an alternative source of electric power generation in many communities. Furthermore, using renewable energy sources reduces pollution caused by coal and the release of carbon into the atmosphere by power plants. This article focuses on the economic feasibility of renewable energy resources since it is one of the obstacles in building and executing effective and efficient power generation with RES. An optimizer function of HOMER Pro software was employed in this study to develop a cost-effective power-generating RES configuration. The system uses an IEEE 14-Bus load demand of 259 MW supplied by five generators tested the design system in an IEEE 14-Bus test system with a total load demand of 259 MW supplied by five generators. The loads were classified as critical or non-critical. Three case studies were considered: 1. a case in which all five generators supplied the loads, 2. a case in which one generator was replaced by solar PV with the same generating capacity, and 3. a case in which two generators were replaced by both solar PV and wind turbine respectively. The decrease in net present cost (NPC), Levelized cost (COE), and operating cost (OC) demonstrate the efficacy of the proposed system topologies with various forms of RES.**

Keywords*—Economic feasibility study, sensitivity analysis, Renewable energy resources, solar PV, wind turbine, batteries, converters, cost optimization, grid-connected and islanded mode.

I. INTRODUCTION

Due to global warming, population growth, and industrialization, resulting in increased power demand, renewable energy resources (RES) have attracted much attention worldwide. As a result, renewable energy resources are now being evaluated as an alternative source of electricity generation in several communities. With the crucial function of electric energy (electricity) in our modern rural and urban environments, electricity has contributed significantly and substantially to social, economic, and environmental growth [1].

Over the years, renewable energy investment has grown in popularity, significantly increasing billions of dollars in many industrialized nations such as Japan, the United States of America, and China, with African countries not far behind. South Africa is one of the African countries that has accepted and invested heavily in a renewable energy mix. The mixed energy consumption situation in South Africa in 2020 is depicted in Fig. 1. Many research projects are still in the works by academics to create more energy from existing resources to fulfill societal demand and to determine which one is more cost-effective and does not contribute to climate change or have any negative impact.

With a desperate need for more energy generation capacity in South Africa due to the epileptic generation capacity of electricity that the country is currently experiencing, which leads to frequent load-shedding in the country. The South African government has concluded a deal of three projects and 420 MW of wind power in the Renewable Energy Independent Power Producer Procurement Programme (REIPPPP). The projects will offer onshore wind energy technologies and will be able to sell power to ESKOM (a South African Utility company) for 20 years.

Integrating renewable energy sources (IRES) has been widely employed for clean/consistent energy supply and cost reduction in energy consumption tariffs. Furthermore, IRES contribute significantly to social amenities and rural development since many rural regions, particularly in Africa, suffer from insufficient electricity supply [2], [3].

Due to the inevitable causal link between electric energy and social and economic growth and carbon emission reduction, the government and several commercial parastatals are concentrating increasing attention on integrating renewable energy for a continuous and uninterrupted supply of electric power [4]. Thus, renewable energy (RE) participates in various factors that provide an economical, efficient, and long-term source of energy in the environment. Furthermore, using renewable energy reduces pollution caused by coal and the release of carbon into the atmosphere by power plants. Solar Home Systems (SHSs) provide abundant RES in remote areas. However, the real downside of SHSs is that the power generated by SHSs, combined with their short supply duration, prevents customers from realizing the rewards of modern electricity [5].

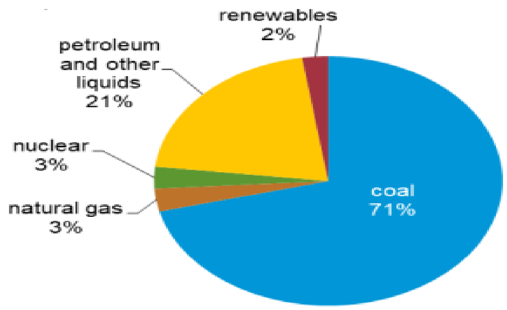

Fig. 1. Sum of Primary Energy consumption in South Africa, 2020 [6].

This research provides an efficient economic feasibility assessment to address the problem of power deficiency and cost, one of the primary problems that hybrid renewable energy designers confront. The approach known as Loss of Power Supply Probability was developed to address the issue of power shortfall and expense (LPSP). The LPSP technique, which is the ratio of all unmet loads to total electric load demand, is a worldwide used statistic to quantify the stability of HRES on an annual basis. The proposed solution was implemented in HOMER Pro software utilizing the HOMER cost optimization function.

II. RESEARCH METHODOLOGY

A. *Proposed system mathematical formulation*

In this study, the research approach covers three scenarios of sensitivity optimization on fuel costs. Under each scenario, we have three options based on system configuration and fuel cost sensitivity analysis. Fig. 2 and 3 below depicts the proposed system architecture and method used under consideration.

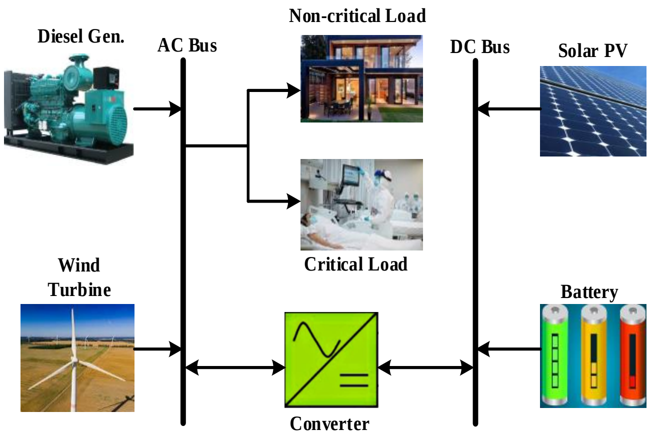

Fig. 2. Proposed system architecture

The chosen system design is optimized for sensitivity analysis depending on the three fuel costs. Furthermore, each sensitivity optimization scenario is further subdivided into three options, each consisting of a mix of energy-generating sources with different fuel costs. Equations (1)–(3) are the proposed equations for the sensitivity optimization for scenario 1 for each option.

$$SOC_{1-option1} = GEN_1 + GEN_2 + GEN_3 + GEN_4 + GEN_5 \quad @\ 0.5\ (\$/L) \tag{1}$$

$$SOC_{1-option2} = GEN_1 + GEN_2 + GEN_3 + GEN_4 + GEN_5 \quad @\ 1.0\ (\$/L) \tag{2}$$

$$SOC_{1-option3} = GEN_1 + GEN_2 + GEN_3 + GEN_4 + GEN_5 \quad @\ 1.5\ (\$/L) \tag{3}$$

SOC: Sensitivity Optimization Case

In scenario 2, one of the five generators has been replaced with solar PV and a storage system of the same capacity (battery). The solar PV and battery are the system's backup in the event of a false outage or the need for repair on any of the generators. Different fuel costs are often utilized to do sensitivity analysis on the specified system. Each sensitivity optimization scenario is further subdivided into three options, each consisting of mixed energy resources with different fuel costs. Equations (4)–(6) are the proposed equations for the sensitivity optimization examined in this scenario for each option.

$$SOC_{2-option1} = GEN_1 + GEN_2 + GEN_3 + GEN_4 + PV_5 + Battery \quad @\ 0.5\ (\$/L) \tag{4}$$

$$SOC_{2-option2} = GEN_1 + GEN_2 + GEN_3 + GEN_4 + PV_5 + Battery \quad @\ 1.0\ (\$/L) \tag{5}$$

$$SOC_{2-option3} = GEN_1 + GEN_2 + GEN_3 + GEN_4 + PV_5 + Battery \quad @\ 1.5\ (\$/L) \tag{6}$$

In scenario 3, two generators were replaced with a wind turbine system and solar PV, integrating two renewable energy resources (PV and wind) into the system design. Both fuel prices and wind speed are employed in this scenario to do sensitivity optimization analysis on the system. Furthermore, each instance of sensitivity optimization analysis is separated into three options. Equations (7)–(9) are the recommended equations for optimizing system sensitivity in this scenario.

$$SOC_{3-option1} = GEN_1 + GEN_2 + GEN_3 + WT_4 + PV_5 + Battery \quad @\ 0.5\ (\$/L) \tag{7}$$

$$SOC_{3-option2} = GEN_1 + GEN_2 + GEN_3 + WT_4 + PV_5 + Battery \quad @\ 1.0\ (\$/L) \tag{8}$$

$$SOC_{3-option3} = GEN_1 + GEN_2 + GEN_3 + WT_4 + PV_5 + Battery \quad @\ 1.5\ (\$/L) \tag{9}$$

B. *Cost optimization function*

In HOMER, all system architectures are rated based on their Net Present Cost (NPC), which is the fundamental metric for determining system optimization and computing the system's Cost of Energy (COE). The NPC in HOMER is equal to the sum of all component costs, including sales and purchasing power to and from the grid (P-grid), salvage value (SV), and air pollution fines. Therefore, the total NPC may be calculated mathematically as [9]:

$$T_{NPC} = CC + RC + O\&M + SV + P_{grid} \tag{10}$$

Where,
CC, RC, and O&M are the capital, replacement, operation, and maintenance costs.

Because the fundamental goal of optimization is to decrease and maintain acceptable levels of system dependability. As a result, reducing COE and maintaining system dependability at an appropriate level is critical. COE may therefore be determined analytically using (11) [10]:

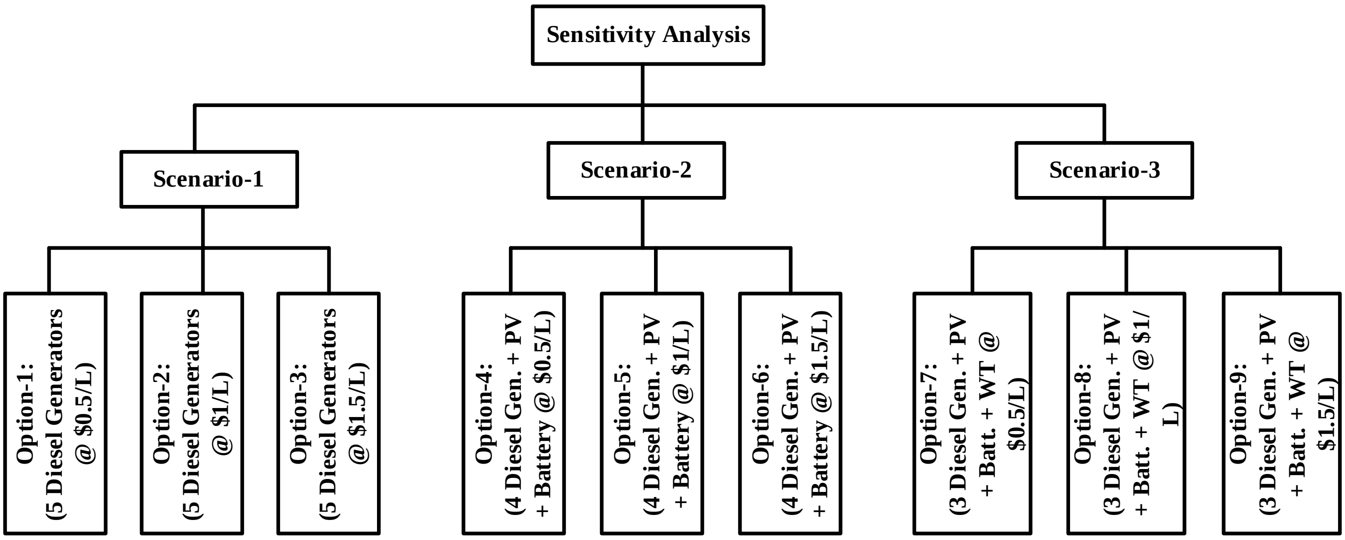

Fig. 3: Diagrammatic representation of the proposed method

$$COE\ (kWh) = \frac{T_{NPC} * C_{RF}}{P_d} \tag{11}$$

Where,

C_{RF} and P_d are the capital recovery factor and the electric load demand, respectively. The capital recovery factor's principal role is to transform the present value into the same yearly cash flows, and it can be stated as (12) [11]:

$$C_{RF} = \frac{n(1+n)^y}{n(1+n)^y - 1} \tag{12}$$

Where,

n, y are the interest rate and project lifespan in years.

Power deficit is one of the primary issues of hybrid renewable energy source (HRES) design. It often happens when the total energy supply is insufficient to satisfy the total energy demand. The strategy known as Loss of Power Supply Probability can help alleviate the power shortage problem (LPSP). The LPSP technique, which is the ratio of all unmet loads to total electric load demand, is a worldwide used statistic to quantify the stability of HRES on an annual basis. LPSP may be expressed mathematically as (13) [12]:

$$LPSP = \frac{\sum_1^T P_{unmet}(t)}{P_d} \tag{13}$$

Where,

$P_{unmet}(t)$ is the unmet load in an hour (h) and can be expressed as (14):

$$P_{unmet}(t) = \begin{cases} 0 & E_l(t) < E_{tot}(t) \\ E_l(t) - E_{tot}(t) & E_l(t) > E_{tot}(t) \end{cases} \tag{14}$$

Where,

E_l and E_{tot} are the load demand and total available power generated at time t.

The two states of LPSP are either zero (0) or one (1). The zero (0) state means no unmet load available ($P_{unmet}(t) = 0$), while the one (1) state indicates that there exists an unmet load during the period of simulation ($P_{unmet}(t) > 0$). Furthermore, for a given hybrid renewable energy system, HOMER reduces both T_{NPC} and LPSP [13].

$$P_{tot} \leq \left(P_{PV} + P_{WT} + P_{grid}\right) \tag{15}$$

$$\left(RF = \frac{P_r}{P_d}\right) > 80\% \tag{16}$$

III. SIMULATION RESULTS AND DISCUSSION

The recommended system is optimized utilizing a total energy demand of 259 MW from an IEEE 14-bus test system powered by five (5) generators. The loads in this investigation were classified into two categories: non-critical and critical loads. The loads were split in half to avoid a total blackout in the event of an unanticipated event and to make scheduling easier.

The proposed system uses an annual discount rate of 8%, an inflation rate of 2%, a project duration of 25 years, and a capacity shortfall fraction of 0%. HOMER synthesizes hourly solar radiation over twelve months using Graham's technique. Graham's technique is used in data production to generate hourly variability and spontaneous correlation. Fig. 4 depicts the proposed system's daily load profile. It can be seen that there is an early morning (between the hours of 06:00 am) and evening rise (between the hours of 5:00 pm to 9:00 pm) in electricity use. This is expected as people generally wake up early to prepare for work and come back in the evening to prepare supper, possibly take showers, and watch television.

Fig. 5 depicts the daily solar irradiation profile. The monthly average solar radiation values ranged from 2.850 to 8.180 kWh/m2/day, with an annual average of 5.43 kWh/m2/day. It can also be seen from the GHI (Global Horizontal Irradiation) profile that the solar radiations are very high at the beginning and the end of the year and very low at the middle of the year. Therefore, May until August represented the months of the rainy season, and there are likely to be more cloudy days during these months. Finally, fig. 6 shows the monthly average wind speed profile. Here the reference wind speed is measured at the reference height.

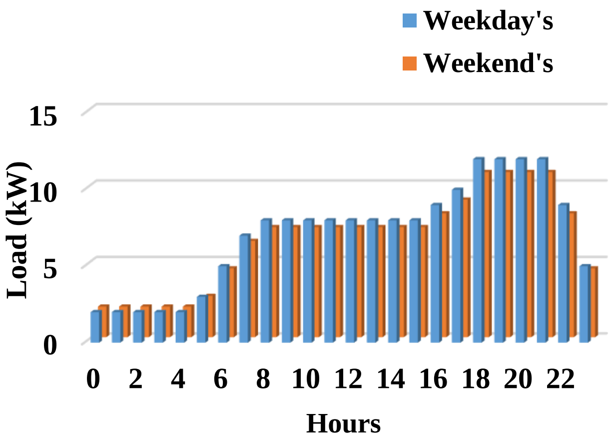

Fig. 4. Daily hourly load profile

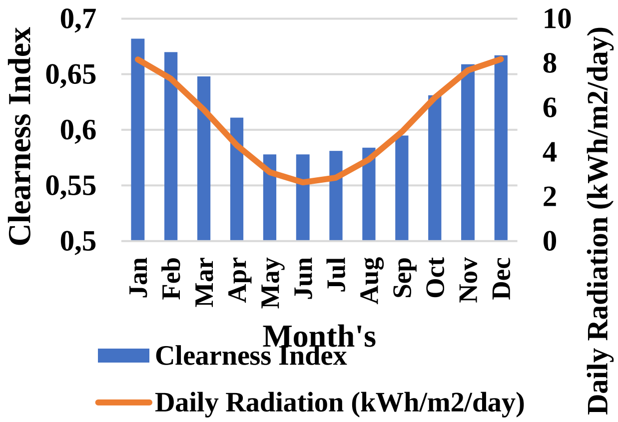

Fig. 5. Monthly solar irradiation and clearness index for a year

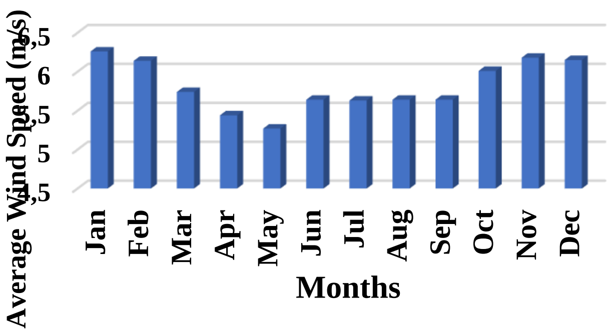

Fig. 6. Monthly average wind speed for a year

To achieve the goal of this study, the following three scenarios were considered:

A. CASE 1: Sensitivity optimization investigation with all the five diesel generators

Table 1 below details the total energy production by each component in this case. Fig. 7 and 8 show the monthly energy production of each generator as well as an overview of the system costs. The extra power generated is 132 kWh/year, equal to 0.139 percent, with no unmet load or capacity shortfall.

TABLE 1. TOTAL ELECTRIC POWER PRODUCTION BY EACH COMPONENT.

Fuel price ($/L)	**Sensitivity cases**	**Sensitivity options**	**Energy resources**	**Total energy generation (kWh/year)**	**The ratio of total generation (%)**
0.5, 1.0, 1.5	SOC_1	Options _1,2,3	Diesel Gen_1	91.906	60.1
			Diesel Gen_2	67.170	71.0
			Diesel Gen_3	24.751	26.1
			Diesel Gen_4	2.673	2.82
			Diesel Gen_5	72.5	0.0766
			Excess electricity	30	23.139
			Renewable fraction	0	%
			Unmet electric load	0	0
			Capacity shortage	0	0

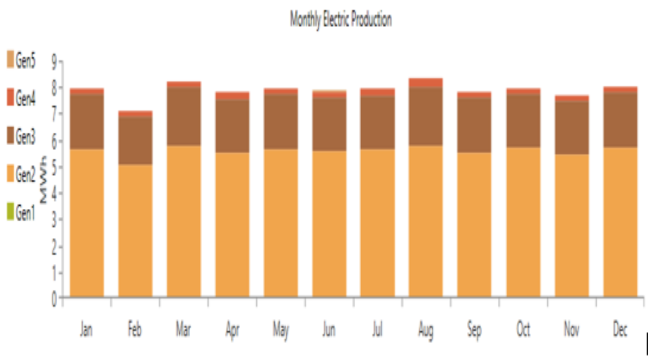

Fig. 7. The monthly energy production of the power system with diesel generators

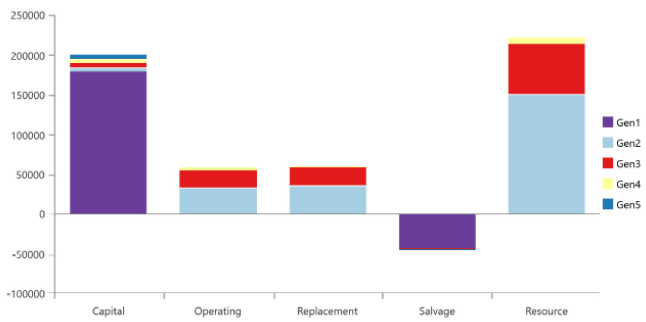

Fig. 8. The base case power system cost summary with five diesel generators

B. *CASE 2: Sensitivity optimization investigation with one generator replaced with solar PV*

To satisfy the needed load requirement, one of the generators was replaced with a renewable energy source (solar PV) of the same capacity. In addition, a storage system (battery) with a capacity of 1 kW was also attached to store surplus produced energy when generation exceeds consumption. The converter transforms the solar PV and battery's DC output power to the needed AC input power for the loads. Table 2 below gives comprehensive details of total energy production by each component in this case. Fig. 9 and 10 show the monthly energy production of each element as well as a breakdown of the system costs.

TABLE 2. TOTAL ELECTRIC POWER PRODUCTION BY EACH COMPONENT AND RENEWABLE PENETRATION

Fuel price ($/L)	Sensitivity cases	Sensitivity Options	Energy resources	Total energy generation (kWh/year)	The ratio of total generation (%)
0.5	SOC_2	Option_1	Diesel Gen_1	8.32	0.636
			Diesel Gen_2	2.235	1.17
			Diesel Gen_3	44.613	34.1
			Diesel Gen_4	16.813	12.9
			Solar_PV_5	66.237	50.7
			Excess electricity	34.608	26.5
			Renewable fraction	31.8	%
			Unmet electric load	0	0
			Capacity shortage	0	0
1.0	SOC_2	Option_2	Diesel Gen_1	41.25	31.1
			Diesel Gen_2	17.065	0.732
			Diesel Gen_3	38.862	26.7
			Diesel Gen_4	12.228	8.40
			Solar _PV_5	93.349	64.2
			Excess electricity	48.206	33.1
			Renewable fraction	44.8	%
			Unmet electric load	0	0
			Capacity shortage	0	0
1.5	SOC_2	Option_3	Diesel Gen_1	72.0	0.0409
			Diesel Gen_2	15.90	0.335
			Diesel Gen_3	26.727	15.2
			Diesel Gen_4	17.609	4.33
			Solar_PV_5	40.924	80.1
			Excess electricity	72.781	41.4
			Renewable fraction	63.0	%
			Unmet electric load	0	0
			Capacity shortage	0	0

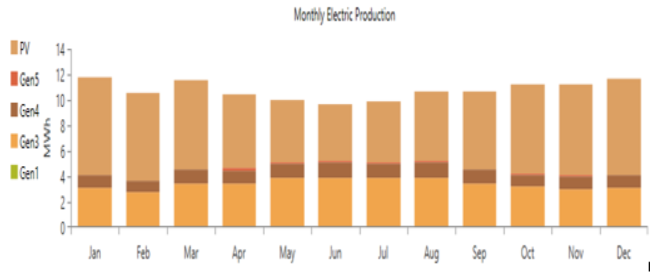

Fig. 9. The monthly energy production of the power systems with diesel generation and PV system.

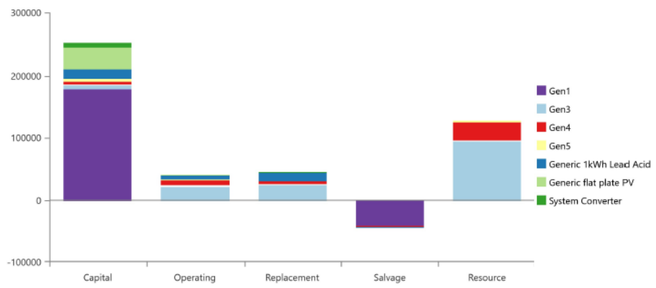

Fig. 10. The system cost summary with diesel generation and PV system

C. *CASE 3: Sensitivity optimization investigation with two generators been replaced with solar PV and wind turbine*

This system layout combines hybrid renewable energy sources (solar PV and wind turbine) with a series of generators to satisfy the energy demands of the loads. The fifth generator has been replaced with a wind turbine of the same capacity in this scenario. Table 3 below gives a detailed description of total energy production by each component in this case.

Fig. 11 and 12 show the monthly energy production of each component as well as an overview of the system costs.

TABLE 3. TOTAL ELECTRIC POWER PRODUCTION BY EACH COMPONENT AND RENEWABLE PENETRATION

Fuel price ($/L)	Sensitivity cases	Sensitivity Options	Energy resources	Total energy generation (kWh/year)	The ratio of total generation (%)
0.5	SOC_3	Option _1	Diesel Gen_1	15.17	0.394
			Diesel Gen_2	10.348	7.89
			Diesel Gen_3	36.648	27.9
			Wind_Turbine_4	46.329	12.5
			Solar_PV_5	67.291	51.3
			Excess electricity	34.285	26.1
			Renewable	49.7	%

			fraction		
			Unmet electric load	0	0
			Capacity shortage	0	0
1.0	SOC_3	Option _2	Diesel Gen_1	12.66	0.189
			Diesel Gen_2	7.671	5.45
			Diesel Gen_3	30.123	21.4
			Wind_Turbine_4	33.419	23.7
			Solar_PV_5	69.399	49.3
			Excess electricity	43.901	31.2
			Renewable fraction	59.7	%
			Unmet electric load	0	0
			Capacity shortage	0	0
1.5	SOC_3	Option _3	Diesel Gen_1	14.92	0.307
			Diesel Gen_2	5.092	3.17
			Diesel Gen_3	20.951	13.1
			Wind_Turbine_4	66.837	41.7
			Solar_PV_5	67.066	41.8
			Excess electricity	62.530	39.0
			Renewable fraction	71.9	%
			Unmet electric load	0	0
			Capacity shortage	0	0

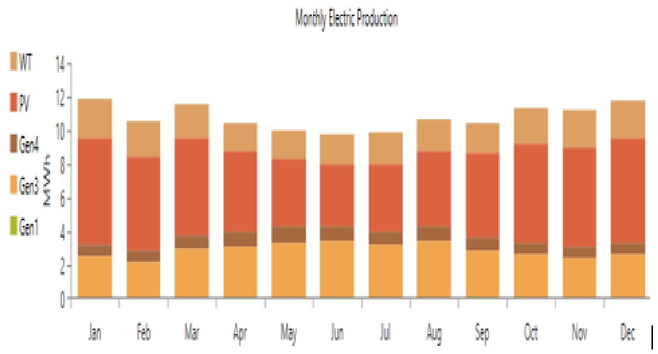

Fig. 11. The monthly energy production for the power systems with coal generators, PV, and wind turbines

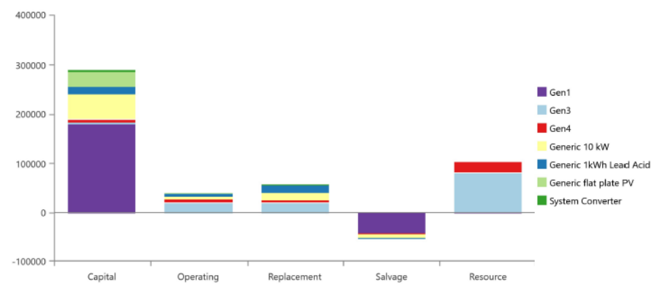

Fig. 12. The system cost summary for the power systems with diesel generators, PV, and wind turbines

Table 4 provides a detailed description of the system's net present costs (NPC), Levelized cost of Energy (COE), and operating and maintenance expenses (O&C). Table 4 shows that the winning system design is the system configuration in scenario 3 (Option 1), with an NPC of $445,976.50, a COE of $ 0.3649, and an O & C of $ 11,897.10. According to the simulation findings, the system architecture in example 3 (Option 1) meets all of the system's required load demand while generating a surplus of 34.285 kWh/year with no unmet electric load or capacity shortfall.

TABLE 4. TOTAL SYSTEM COST SUMMARY FOR ALL THE PROPOSED CASES

Sensitivity cases	Sensitivity options	NPC	COE	O & C
CASE 1	Option_1	361,117.70	0.2955	26,000.18
	Option_2	582,952.40	0.477.	43,160.06
	Option_3	804,787.10	0.6585	60,319.95
CASE 2	Option_1	417,919.20	0.3420	12,941.73
	Option_2	537,077.80	0.4395	21,330.14
	Option_3	632,770.40	0.5178	24,785.00
CASE 3	**Option_1**	**445,976.50**	**0.3649**	**11,897.10**
	Option_2	495,577.70	0.4055	15,566.32
	Option_3	566,550.80	0.4636	17,112.08

IV. CONCLUSION

This project aims to build and simulate a community energy system that will assist significant electricity and natural gas customers lower operational costs. Economic feasibility analysis on a hybrid (solar PV-Wind turbine-diesel generators) stand-alone system design was performed in the cost optimizer function in HOMER Pro software. Based on the system's net present value, energy cost, and operating cost numbers. The suggested system demonstrates that the proposed system architectures 2 and 3, which feature the integration of solar PV and wind turbines, are more cost-effective than Case 1, which is the base Case. Furthermore, the suggested system design in Case 3 was chosen as the most inexpensive and efficient to deploy with lower operational costs.

ACKNOWLEDGMENT

The authors greatly appreciate the management of Cape Peninsula University of Technology (CPUT) and the Center for Substation Automation and Energy Management System of the Department of Electrical, Electronic, and Computer Engineering, Bellville Campus, CPUT. South Africa. For providing a well conducive research environment to carry out this study. This work is supported partly by the National Research Foundation (NRF) under Grant NRF Thuthuka Grant Number 138177 (TTK210329591306). Also, the authors acknowledge the research grant support from the Eskom Tertiary Education Support Programme (TESP) and the Eskom Power Plant Engineering Institute (EPPEI) in carrying out this research work.

REFERENCES

[1] K. A. Kavadias and P. Triantafyllou, “Hybrid renewable energy systems’ optimization. A review and extended comparison of the most-used software tools,” *Energies (Basel)*, vol. 14, no. 24, Dec. 2021, doi: 10.3390/en14248268.

[2] H. al Garni and A. Awasthi, “Techno-economic feasibility analysis of a solar PV grid-connected system with different tracking using HOMER software,” *2017 5th IEEE International Conference on Smart Energy Grid Engineering, SEGE 2017*, pp. 217–222, 2017, doi: 10.1109/SEGE.2017.8052801.

[3] B. K. Das, N. Hoque, S. Mandal, T. K. Pal, and M. A. Raihan, “A techno-economic feasibility of a stand-alone hybrid power generation for remote area application in Bangladesh,” *energy*, vol. 134, pp. 775–788, 2017, doi: 10.1016/j.energy.2017.06.024.

[4] L. M. Halabi, S. Mekhilef, L. Olatomiwa, and J. Hazelton, “Performance analysis of hybrid PV/diesel/battery system using HOMER: A case study Sabah, Malaysia,” *Energy Convers Manag*, vol. 144, pp. 322–339, 2017, doi: 10.1016/j.enconman.2017.04.070.

[5] M. Qolipour, A. Mostafaeipour, and O. M. Tousi, “Techno-economic feasibility of a photovoltaic-wind power plant construction for electric and hydrogen production: A case study,” *Renewable and Sustainable Energy Reviews*, vol. 78, no. March, pp. 113–123, 2017, doi: 10.1016/j.rser.2017.04.088.
[6] K. E. Adetunji, O. A. Akinlabi, and M. K. Joseph, “Developing a Microgrid for Tafelkop Using HOMER,” Sep. 2018. doi: 10.1109/ICABCD.2018.8465442.
[7] A. Fayaz Ahamed, R. Rakesh Vibahar, S. Purusothaman, M. Gurudevan, P. Ravivarma, and A. Professor, “Optimization of Hybrid Microgrid of Renewable Energy Efficiency Using Homer Software,” 2021.
[8] L. H. S. Santos, J. A. A. Silva, J. C. Lopez, N. B. Arias, M. J. Rider, and L. C. P. da Silva, “Integrated optimal sizing and dispatch strategy for microgrids using HOMER Pro,” Sep. 2021. doi: 10.1109/ISGTLatinAmerica52371.2021.9543015.
[9] Z. W. Geem and J. H. Kim, “Optimal energy mix with renewable portfolio standards in Korea,” *Sustainability (Switzerland)*, vol. 8, no. 5, 2016, doi: 10.3390/su8050423.
[10] H. Liu, D. Azuatalam, A. C. Chapman, and G. Verbič, “Techno-economic feasibility assessment of grid-defection,” *International Journal of Electrical Power and Energy Systems*, vol. 109, no. January, pp. 403–412, 2019, doi: 10.1016/j.ijepes.2019.01.045.
[11] A. Yasin and M. Alsayed, “Optimization with excess electricity management of a PV, energy storage and diesel generator hybrid system using HOMER Pro software,” *International Journal of Applied Power Engineering (IJAPE)*, vol. 9, no. 3, p. 267, Dec. 2020, doi: 10.11591/ijape.v9.i3.pp267-283.
[12] A. A. Imam, Y. A. Al-Turki, and R. Sreerama Kumar, “Techno-economic feasibility assessment of grid-connected PV systems for residential buildings in Saudi Arabia-A case study,” *Sustainability (Switzerland)*, vol. 12, no. 1, 2020, doi: 10.3390/su12010262.
[13] T. Lambert, P. Gilman, and P. Lilienthal, “MICROPOWER SYSTEM MODELING WITH HOMER.”

2023 SAUPEC Conference, Johannesburg, South Africa, January 24-26, 2023

Transient Operation of a Hybrid Wind Farm With FSIG and PMSG

O. Apata
Department of Electrical Engineering
University of Johannesburg
Johannesburg, South Africa
g.apata@ieee.org

D.T.O. Oyedokun
Department of Electrical Engineering
University of Cape Town
Cape Town, South Africa
davoyedokun@ieee.org

P.N. Bokoro
Department of Electrical Engineering
University of Johannesburg
Johannesburg, South Africa
pitshoub@uj.ac.za

Abstract— **A novel control strategy for a hybrid wind farm comprising of both the permanent magnet synchronous generator (PMSG) and fixed speed induction generator (FSIG) under a symmetrical grid fault is proposed in this research work. With a coordinated control of the hybrid wind farm, the proposed strategy seeks to provide maximum reactive power support to the FSIG and improve the recovery of the grid during the symmetrical grid fault by utilizing the operational characteristics of the PMSG. This invariably improves the output power quality and performance of the FSIG without the need for extra communication equipment between the different wind power generators.**

Keywords— ***Fixed speed induction generator (FSIG), doubly fed induction generator (DFIG), hybrid wind farm, permanent magnet synchronous generator (PMSG), wind turbine (WT)***

I. Introduction

The co-location of wind generators to form a hybrid wind farm can improve the efficiency of such wind farms and increase their total power production [1]. As observed in [2], under non-ideal grid conditions, wind farms can be installed side by side for optimal performance. This is applicable to the fixed speed inductor generator (FSIG) based wind turbine (WT) system and the variable speed generator based WT system. The variable speed WT system can either be a doubly fed induction generator wind system (DFIG) or the permanent magnet synchronous generator (PMSG) wind system. The combination of such individual wind systems connected in parallel at point of common coupling (PCC) and connected to the grid by a transmission line is referred to as a hybrid wind farm, as shown in Fig. 1. Such hybrid wind farms could play a pivotal role in power power-sharing agreements in decentralized or centralized microgrid structures, fulfilling policy requirements to balance power system reliability, adequate return on investment and prioritizing the needs of communities local to renewable energy based power generation sites [3].

The research conducted in [2] shows that a hybrid wind farm can be configured as a PMSG-FSIG, DFIG-FSIG and DFIG-PMSG wind conversion system. As seen in Fig. 1 which shows a schematic representation of the PMSG-FSIG hybrid wind farm system, the individual wind farms which make up the hybrid wind farm are connected in parallel at PCC and grid connected by a transmission line.

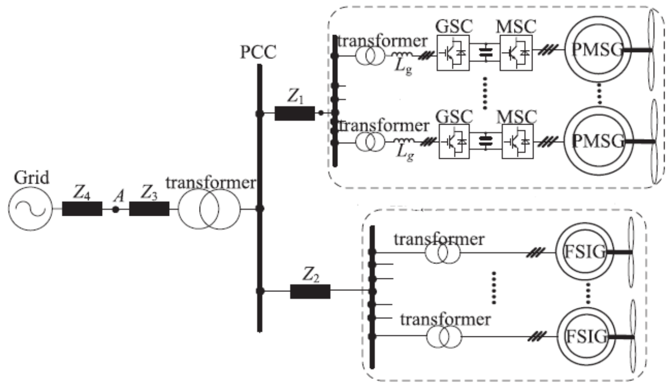

Fig. 1. PMSG-FSIG hybrid wind system

The various researches carried out in [4], [5], [6] and [7] showed that the DFIG wind system and FSIG wind system can be installed together side by side. Though the various researches have shown that voltage support can be provided to the grid and reactive power support provided to the FSIG wind system by a coordinated control of the DFIG-FSIG hybrid wind system, however, during a grid fault condition the reactive power support provided to the FSIG wind system from the DFIG is restricted because of the partially rated converters of the DFIG. This implies that the DFIG has limited capacity to improve the operational performance of the hybrid DFIG-FSIG wind system during a transient condition. The ability of the DFIG to provide compensation is also impacted by its output power, the impedance of the transmission network and the generator speed.

Unlike the DFIG with partially rated converters, the PMSG has more efficient fully rated power converters that gives it a better advantage of terminal voltage and strong reactive power support ability during a transient grid condition. The PMSG also has the unique ability to control a wider operating region for various control targets. By effectively controlling the PMSG, the operational performance of a nearby FSIG or DFIG based wind system can be improved during a grid fault condition. This characteristic of the PMSG gives it an advantage over the DFIG in a hybrid wind farm configuration with the FSIG wind system. The focus of this research, therefore, is the hybrid wind system consisting of the FSIG and PMSG WT systems.

In this paper, the behaviour of the FSIG-WT system is studied under a transient condition. A control strategy is developed that enables the PMSG provide the required reactive power support needed by the FSIG based wind system during a grid fault condition .

The rest of the paper is divided as follows. The hybrid wind farm topology is presented in section II while Section III presents the hybrid wind farm control strategy. Section IV shows the results of extensive simulations carried out and the paper is concluded in section V.

II. Hybrid Wind Farm Topology

The aggregate modelling approach is used in modelling the wind system in the Simulink environment of MATLAB. It is important to note that the hybrid wind farm can consist of multiple wind turbines depending on the requirement of the hybrid wind farm. The number of wind turbines shown in Fig. 1 is therefore for illustration purposes only. For the purpose of this research, the hybrid wind farm modelled consists of a 10 MW PMSG and 20 MW FSIG wind farm connected in parallel at the PCC and connected to the grid by a 35-kV short transmission line while the hybrid wind farm is connected to the grid by a 110 kV transmission line. By means of simple pitch control method modelled into the control system, and at rated power, the mechanical torque output of the PMSG wind system is effectively reduced. The relationship between the generator speed for different wind speeds and the output power of the turbine is shown in Fig. 2. Since extensivie research has been carried out on modelling the FSIG and PMSG wind systems in [8], [9], [10], the modelling process of the hybrid wind farm will not be discussed in this research work. However, it is important to note that all variables and electrical parameters are referred to the stator while the rotor and stator quantities are represented in the direct (d)-quadrature (q) axis reference frame.

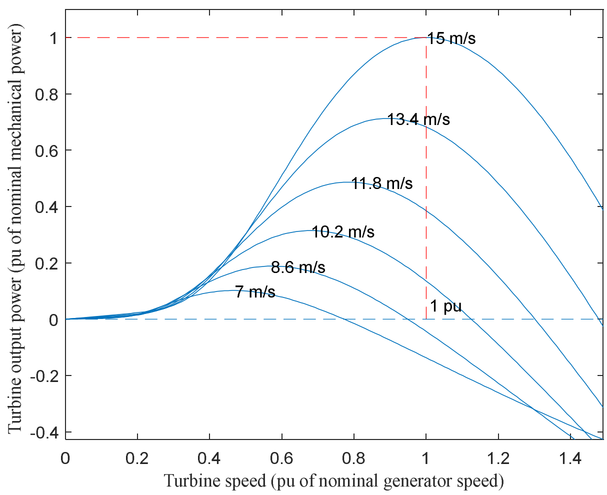

Fig. 2. Turbine output power vs generator speed

III. Control Strategy Of the Hybrid Wind Farm

The control strategy developed for the hybrid wind farm is dependent on a current allocation strategy developed by the in the grid side converter (GSC) of the PMSG as shown in [11]. The GSC is controlled to provide the maximum required reactive power required for voltage support of the hybrid wind farm under a grid fault condition. A coordinated control of the hybrid wind farm is achieved based on the developed current allocaiton strategy in [11] that allows the GSC of the PMSG to efficiently support the FSIG wind system during a fault condition bearing in mind the requirements of the grid code. According to the grid code requirements, it is expected that a grid-connected wind farm must be able to provide the required reactive currents I_Q needed by the wind farm when a grid fault occurs and the per-unit value of I_Q is expected to fulfill the conditions

$$I_Q \geq 1.5\,(0.9 - \mathrm{V_G})I_r,\ 0.2 \text{ pu } \leq V_G \leq 0.9\text{pu} \qquad (1)$$

The terminal voltage of the grid-connected wind farm is given as V_G and the rated current of the wind farm is given as I_r. It can be inferred from (1) that $1.5\,(0.9 - V_G)I_r$ is the minimum reactive current needed by the wind farm during a grid fault condition. Based on the requirement of the grid code, it can be deduced that the maximum allowable current i_{gmax} should be greater than the maximum reactive current, i_{gqmax} of the GSC hence $i_{gqmax} \leq i_{gmax}$. In order to maintain voltage control of the dc-link and prevent the possibility of the the GSC exceeding rated current, the current on the d-axis is kept unchanged and the q-axis current i_{dq} is changed to fulfill the reactive power requirement of the wind system. The output reactive current limit of the GSC can be determined by considering the current capacity of the GSC and calculated as:

$$i_{gqmax} = \sqrt{(i_{gmax})^2 - (i_{gd})^2} \qquad (2)$$

Taking the requirement of the grid code into consideration as expressed in (1), the current limit of the GSC shown in (2) is modified and expressed as

$$i_{gqmax} = \sqrt{I_{gmax}^2 - (\frac{\mathrm{P_P}}{\mathrm{V_g}})^2} \geq 1.5\,(0.9 - V_G)I_r \qquad (3)$$

This implies that the real and reactive power priority of the GSC controller changes when there is a drop in the terminal voltage below 0.9 p.u. However in steady state conditions, DC-link voltage regulation is given high priority while during a transient condition, voltage control is given a higher priority. Fig. 3 describes the current allocation strategy proposed in this paper while Fig. 4 describes the detailed control process required to fulfil the conditions in (2). The actual and reference values of the active power output of the PMSG is given as P_g, and P^* respectively, while the actual and reference values of the reactive power output of the PMSG is given as Q_g and Q^* respectively. Based on the maximum current rating of the converter, the amplitudes of i_{gd}^* and i_{gq}^* are limited. It is important to point out that while the fault condition lasts, the PMSG will have its output power momentarily reduced while the DC voltage also rises momentarily during the control of i_{gd}^* to provide more reactive current reference i_{gq}^* in the GSC for the required reactive power support in the FSIG-based wind system.

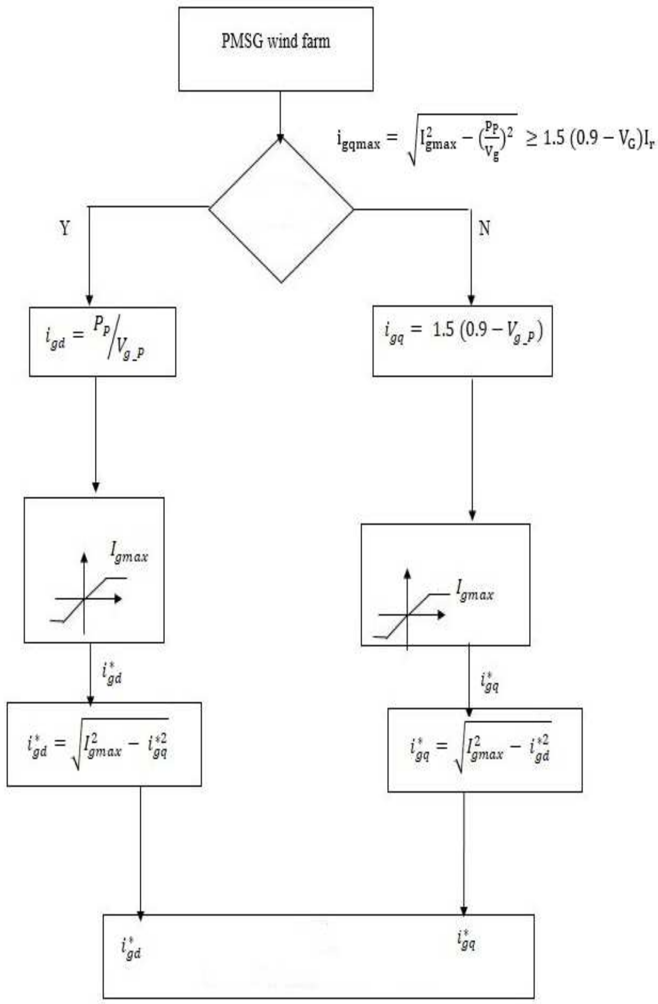

Fig. 3. Proposed current allocation strategy

During the grid fault condition on the hybrid wind farm system, a network parameter check of the FSIG wind system is carried out by the proposed control mechanism developed in [11] to determine if there is a provision to fulfill the grid code requirement and to determine the minimal reactive power needed by the FSIG wind system. Depending on the severity of the fault condition and the associated voltage sag, an over voltage and overcurrent may occur in the FSIG wind system as a result of the transient components in the stator flux of the FSIG .

In order to meet the requirements of the grid code during the low voltage period, the reactive current i_{gq}^* reference value is set as the required minimum reactive current of the low voltage condition. When the fault condition occurs, the proposed control strategy developed in [11] is deployed immediately taking into consideration the maximum allowable current of the GSC of the PMSG and independently sets both active and reactive current reference values. The converters of the PMSG are then regulated by the PI controllers based on the available current reference values. The maximum allowable current i_{gmax} is then determined by passing the current components i_{gd} and i_{gq} through the current limiter which is a set point that determines the maximum allowable current references that can pass through. The main reason for limiting the reference currents is to protect the switching power electronic components of the power converter. The resulting current references, i_{gd}^* and i_{gq}^*, are then transformed into the respective d-q reference frame to provide the required reactive and active power needed during the transient condition.

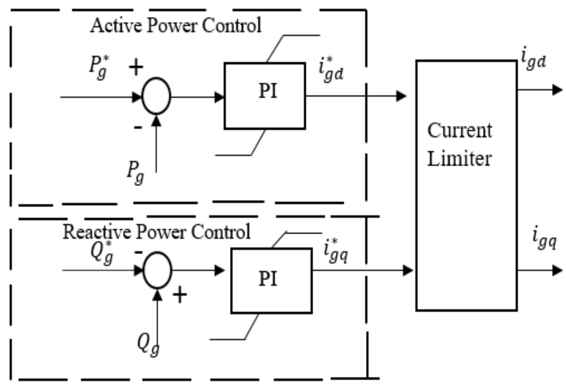

Fig. 4. Current limiter control process

IV. Simulation Protocol And Results

The simulation results of the modelled hybrid wind farm are presented in this section. Both the grid voltage of the hybrid wind farm and the behaviour of the FISG wind system are observed with and without the proposed strategy in steady state and under a transient grid fault condition.

A. Steady-state operation

The individual wind farms are controlled to operate normal in steady state because of the absence of voltage sag on the grid and are therefore are controlled to supply maximum active power. As seen in Fig. 5, 6 and 7, the active power output of the respective PMSG and FSIG-based wind farms and the corresponding grid voltage of the hybrid wind farm is normal. Fig. 8 and 9 represents the reactive power profile of the FSIG wind system in steady state while Fig. 9 shows the dc link voltage of the PMSG converter.

B. Transient state operation

At t = 20 seconds, a balanced three-phase line-to-line-to-line fault is introduced into the wind power system which lasts for 0.2 seconds, taking into consideration the grid code requirements. To protect the rotor circuit of the FSIG wind system from overcurrent, its protection system is triggered during the initial stage of the fault condition. As seen in Fig. 10, a dip of 0.32 pu occurs on the grid voltage as a result of the fault condition introduced into the power system. Fig. 11 and 12 respectively shows the effect of this grid condition on the FSIG wind system. It is observed that the FSIG based wind system absorbs reactive power from the grid to remain connected while its output power drops to 0.2 pu. The reference control variables are altered to provide the required reactive power support during the fault condition by a coordinated control of both reactive and active current references of the GSC and the proposed current allocation strategy. The reactive current reference i_{gq}^* is then controlled to provide the needed reactive current during the grid fault condition. The reactive current of the GSC is assigned a higher priority than the injected active power during the grid voltage sag.

As shown in Fig. 13 and 14 repectively, 0.38 pu of reactive power is generated by the PMSG during the grid fault condition to improve the grid voltage of the hybrid wind farm to 0.39. As mentioned in section III, the PMSG based wind system experiences a temporary decrease in its output power to 0.75 p.u as shown in Fig. 15 before returning to its rated output power. Fig. 16 shows an improvement in the reactive power profile of the FSIG based wind system as it absorbs a lesser amount of reactive power from the grid with the support provided from the PMSG and Fig. 17 shows an improvement in the active power profile of the the FSIG-based wind system by returning to its rated operating point.

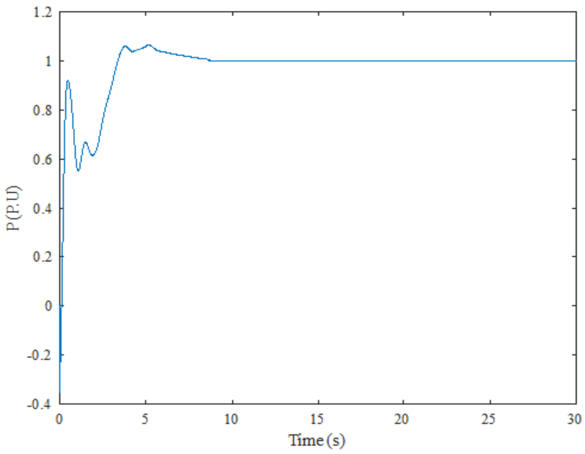

Fig. 5. Output active power of PMSG wind farm

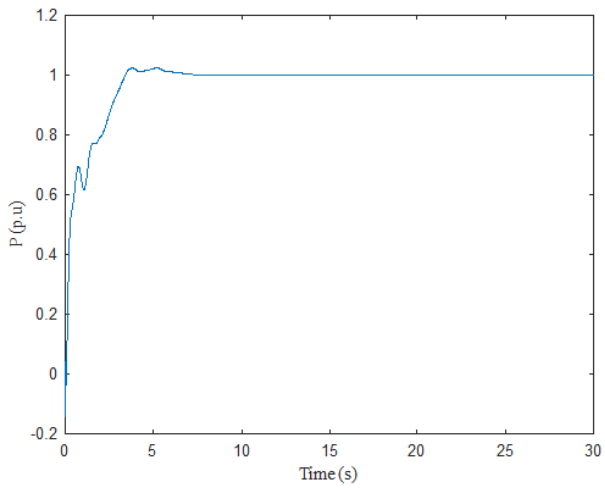

Fig. 6. The output power of FSIG wind farm

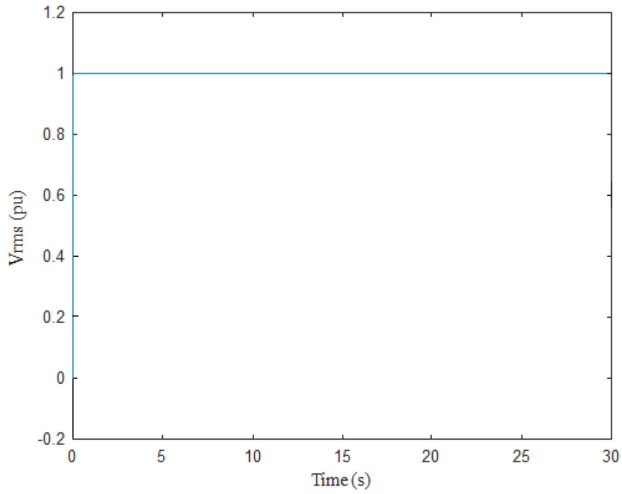

Fig. 7. Grid voltage of the hybrid wind farm

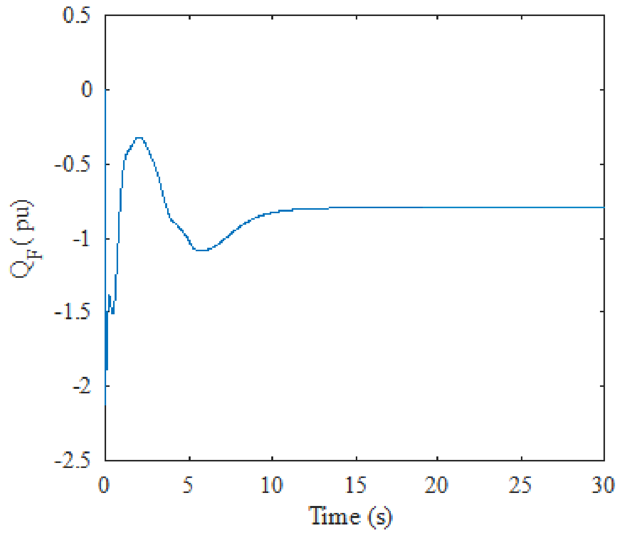

Fig. 8. Reactive power output of the FSIG wind farm

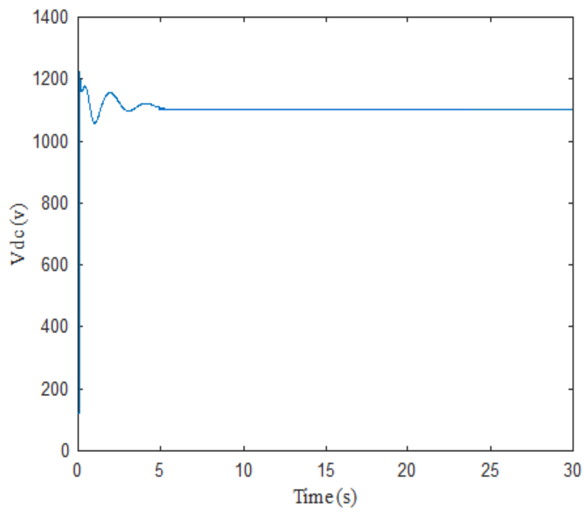

Fig. 9. DC link voltage

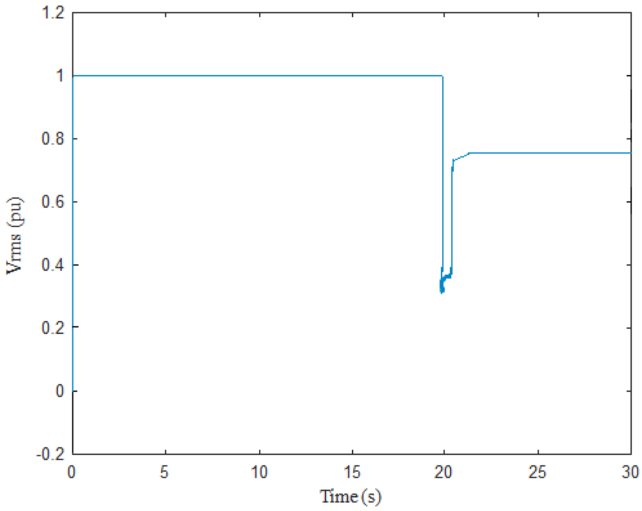

Fig. 10. Grid voltage of the hybrid wind farm

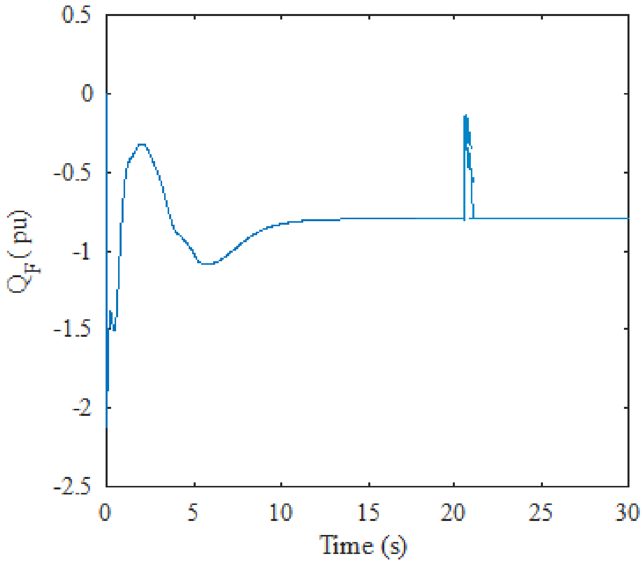

Fig. 11. Reactive power output of the FSIG wind farm

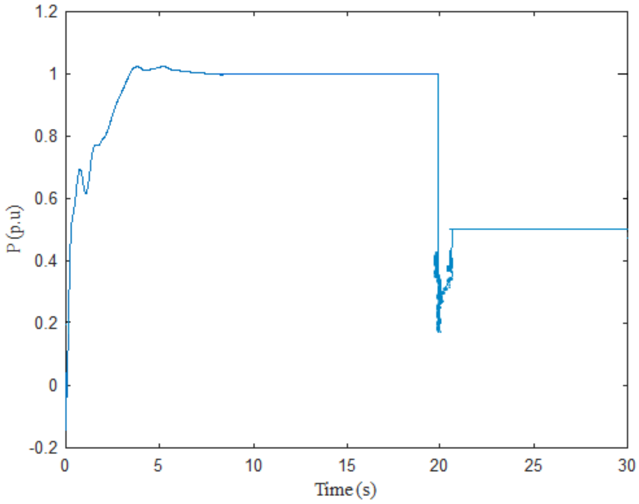

Fig. 12. Output active power of FSIG-based wind farm

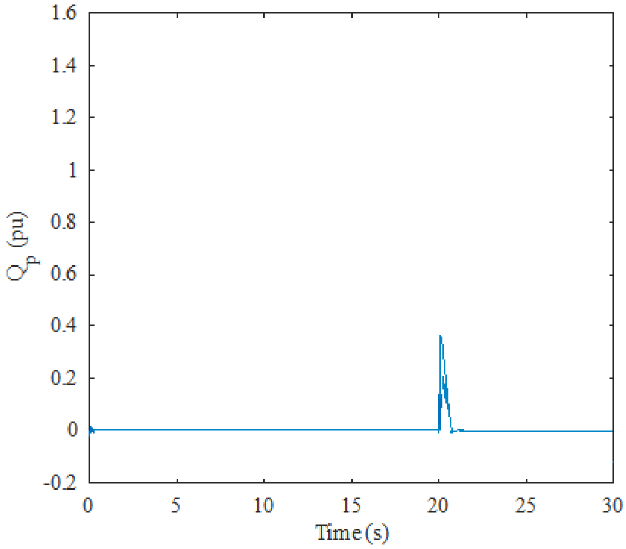

Fig. 13. Reactive power output of PMSG wind farm.

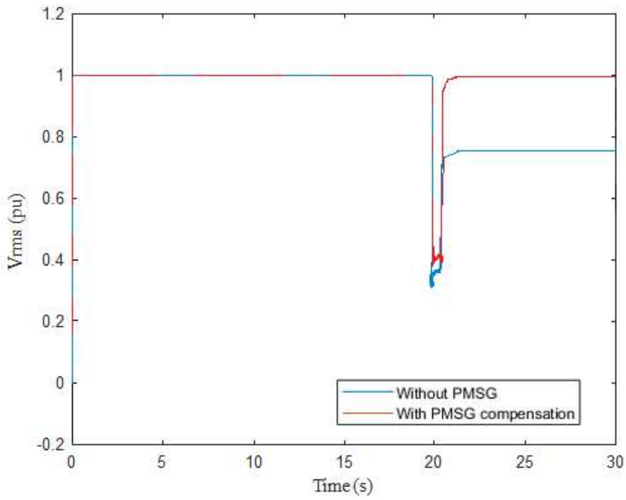

Fig. 14. Grid voltage of hybrid wind farm

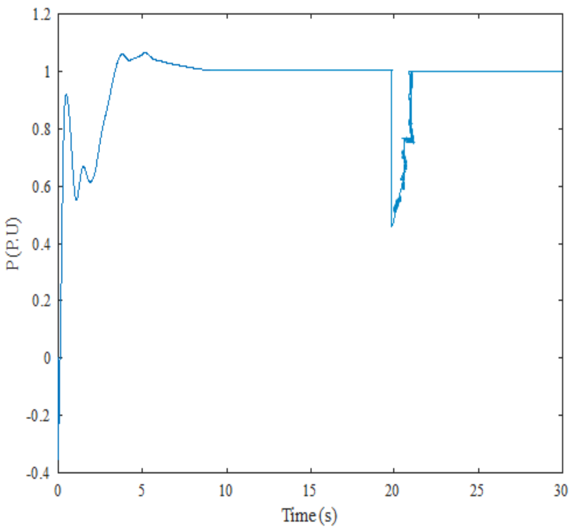

Fig. 15. Output of PMSG based wind farm

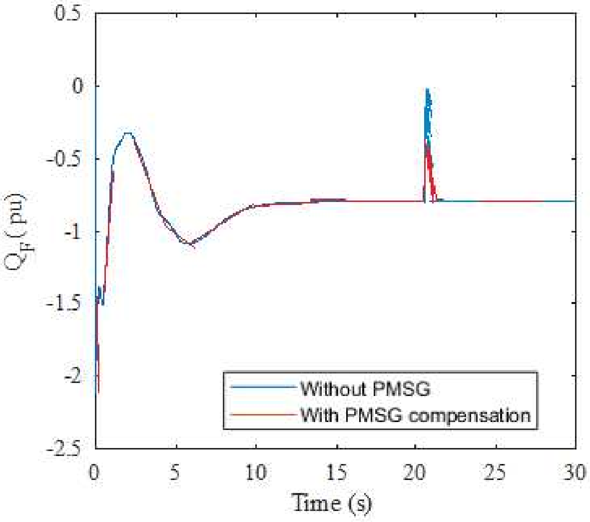

Fig. 16. Reactive power output of FSIG wind farm

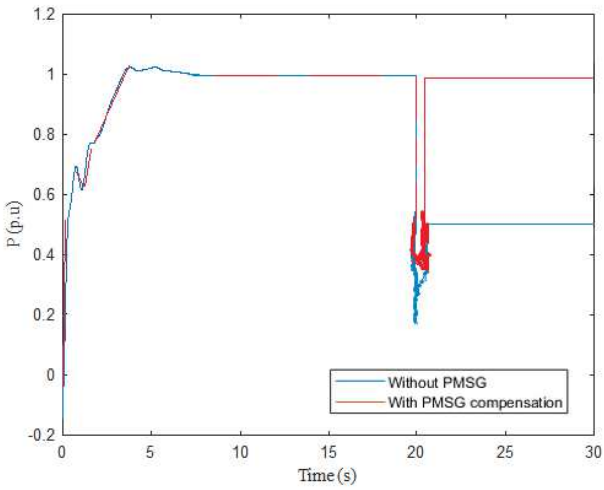

Fig. 17. Output of FSIG wind farm

V. Conclusions

The validity of the proposed control strategy has been tested by rigorous simulations on the modelled hybrid wind farm. The proposed control strategy was tested on the modelled hybrid wind farm under a balanced three phase grid condition and the results presented have shown that during the transient condition on the hybrid wind farm. The FSIG wind system showed significant improvements in its performance without the need for extra communication devices between the various wind power generators. There is also an improvement in the grid voltage of the hybrid wind farm.

References

[1] J. Lu et al, "DG control strategies for grid voltage unbalance compensation," in Energy Conversion Congress and Exposition (ECCE), 2014 IEEE, 2014, pp. 2932-2939.

[2] O. Apata and D. T. O. Oyedokun, "Improving The Dynamic Performance Of Grid Connected Fixed Speed Wind Farm Using Variable Speed Wind Turbines," 2020 IEEE PES/IAS Power Africa, Nairobi, Kenya, 2020, pp. 1-5

[3] Motjoadi, Vinny, Pitshou N. Bokoro, and Moses O. Onibonoje. "A review of microgrid-based approach to rural electrification in South Africa: Architecture and policy framework." *Energies* 13.9 (2020): 2193.

[4] Foster, Sarah, Lie Xu, and Brendan Fox. "Coordinated control and operation of DFIG and FSIG based Wind Farms." 2007 IEEE Lausanne Power Tech. IEEE, 2007

[5] Foster, Sarah, Lie Xu, and Brendan Fox. "Coordinated reactive power control for facilitating fault ride through of doubly fed induction generator-and fixed speed induction generator-based wind farms." IET Renewable Power Generation 4.2 (2010): 128-138.

[6] Sulla, Francesco, Jörgen Svensson, and Olof Samuelsson. "Fault behavior of wind farms with fixed-speed and Doubly-Fed Induction Generators." 2011 IEEE Trondheim PowerTech. IEEE, 2011

[7] Wang, Yi, and Lie Xu. "Coordinated control of DFIG and FSIG-based wind farms under unbalanced grid conditions." IEEE Transactions on Power Delivery 25.1 (2009): 367-377

[8] Kim, Hong-Woo, Sung-Soo Kim, and Hee-Sang Ko. "Modeling and control of PMSG-based variable-speed wind turbine." *Electric Power Systems Research* 80.1 (2010): 46-52.

[9] Errami, Y., M. Maaroufi, and M. Ouassaid. "Modelling and control strategy of PMSG based variable speed wind energy conversion system." *2011 International Conference on Multimedia Computing and Systems*. IEEE, 2011.

[10] Anaya-Lara, Olimpo, et al. *Wind energy generation: modelling and control*. John Wiley & Sons, 2011.

[11] Apata, O. “Reactive power compensation of fixed speed wind turbines using a hybrid wind turbine technology.” 2022 ,Faculty of Engineering and the Built Environment ,Department of Electrical Engineering. http://hdl.handle.net/11427/36671

Optimal Positioning and Sizing of Distributed Generation to Reconfigure Power Network Using Wind Power DG

Mlungisi Ntombela
Faculty of engineering and built environment, Department of electrical power engineering
Durban university of technology
Durban, South Africa
mlungisi390@gmail.com

Kabeya Musasa
Faculty of engineering and built environment, Department of electrical power engineering
Durban university of technology
Durban, South Africa
MusasaK@dut.ac.za

Moketjema Clarence Leoaneka
Faculty of engineering and built environment, Department of electrical power engineering
Durban university of technology
Durban, South Africa
Moketjemal@dut.ac.za

Abstract: --- **Power loss and voltage instability are two main issues with distribution systems. However, by appropriately reconfiguring the network, which entails including distributed generation (DG) units in the distribution network, these issues are typically minimized. The appropriate sizing and placement of DGs are essential in this regard. The optimal location and size of the DGs are determined by artificial intelligence (AI), which is a hybrid genetic algorithm and particle swarm optimization, both before and after the radial network is reconfigured (HGAPSO). When DG units were introduced to the test system, the simulation results revealed a noticeably better increase in the % power loss reduction. Similar improvements are made to the system's minimal bus voltage. The comparison study's findings demonstrated that the proposed approach is successful in lowering voltage variance and power loss in the distribution system. Using MATLAB software, the suggested technique is assessed on the IEEE-33 bus radial distribution system.**

Keywords: *voltage deviation, power loss minimization, distributed generation, particle swarm optimization, and network reconfiguration.*

1. INTRODUCTION

For all energy utilities, supplying the increased demand for electricity presents a considerable challenge. Most of the world's energy needs are mostly satisfied by fossil fuels. Future energy plans must take into account renewable resources due to the rise in greenhouse gas emissions, the effects of global warming, the depletion of fossil fuels, and the rising cost of fuel. Over the past ten years, many nations have given the advancement of renewable energy technology top priority. The power losses and voltage instability brought on by their multiple networks present a significant challenge for electrical distribution firms [1]. Due to these issues, their operating expenses are on the rise and their profits are falling.

There are many difficulties facing the current distribution networks. Customers place a high value on voltage profiles since they are required for premium voltage-controlled electrical equipment. DGs can boost the voltage at the end of a feeder by offering voltage assistance. Due to the existence of DGs, distribution grids may experience significant changes in network dependability, power flow, relay safety, voltage profile, and stability. Better distribution network reliability and power stability, as well as a number of operational and cost-effective benefits, are some of the main benefits of DG integration in power systems. Better voltage profiles, less power loss, peak load shaving, fewer transmissions, and network expansion are a few of the advantages for both utilities and customers. [2]

To determine the position and size of several DG units, limit branch current, and improve voltage stability both before and after the distribution network was reconfigured, this research used a multi-objective PSO-based technique. The integration of multiple DGs slightly improves network performance in terms of bus voltage magnitude, line current limitation, reducing voltage volatility, and energy losses. By making additional modifications to the distribution system, one can increase a self-contained micro-performance grid. When examining their effects, DG units' main drawbacks are taken into account: voltage profile, voltage volatility, current, and power losses. [3].

2. TYPE OF ELECTRICAL DISTRIBUTION NETWORKS

To provide low voltage electric current to consumer loads, the electrical power distribution system was introduced. radial and ring distribution networks are among the two types of distribution networks. The ring distribution system, showed in Figure 2.3, has feeders arranged in a ring shape that terminates back at the supply sub-station. The radial distribution system shown in figure 1, which has separated feeders that each come from a single sub-station [12]. This network reconfiguration is carried out at the radial distribution network as one of the requirements. A PSO approach is recommended in order to address the multi-objective optimization problem. When radial distribution networks are compared to transmission systems, the distribution network often has a much higher R/X ratio. Our suggested solutions addressed DG sizing and placement in order to raise voltage profile and reduce loss in the base and updated distribution system. [4].

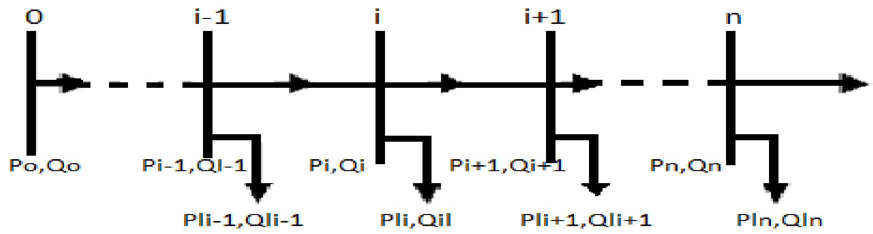

Figure 1: Load flow distribution system

2.1 Test system Description

This study analyzes the IEEE-33 bus radial system with 33 nodes, 37 total lines, 32 loads, 32 PQ buses, 1 feeder, and 1 slack bus. There are 32 closed switches and 5 open switches that are often used. The main power source in the network is Substation Bus 1, which maintains a constant voltage of 12.66 kV. Line and load information for the 33-bus test system is obtained from [6]. Figures 2a and 2b, which represent the previous and succeeding configurations of the IEEE-33 bus network, respectively. Each load is regarded as a continuous load, requiring 2300 kVAr of reactive power and 3715 kW of active power. Considerations like voltage profile and power losses are made in order to examine the consequences of the DGs.

2.2 System Reconfiguration

The switches that make up the distribution system can be divided into different groups. Given the loading situation, this uses the network resources that are available the best. By locating and sizing DGs through reorganizing the feeder, we proposed minimizing active and reactive power loss in the rebuilt network. Whether to keep the switch state open or closed is determined by the feeder. NR is a method for changing the distribution network's topology using switches placed throughout different states. To move a network from its existing configuration to an ideal state, its switching states are altered. As a result, NR aims to lessen the distribution system's overall power losses and voltage fluctuation. [5].

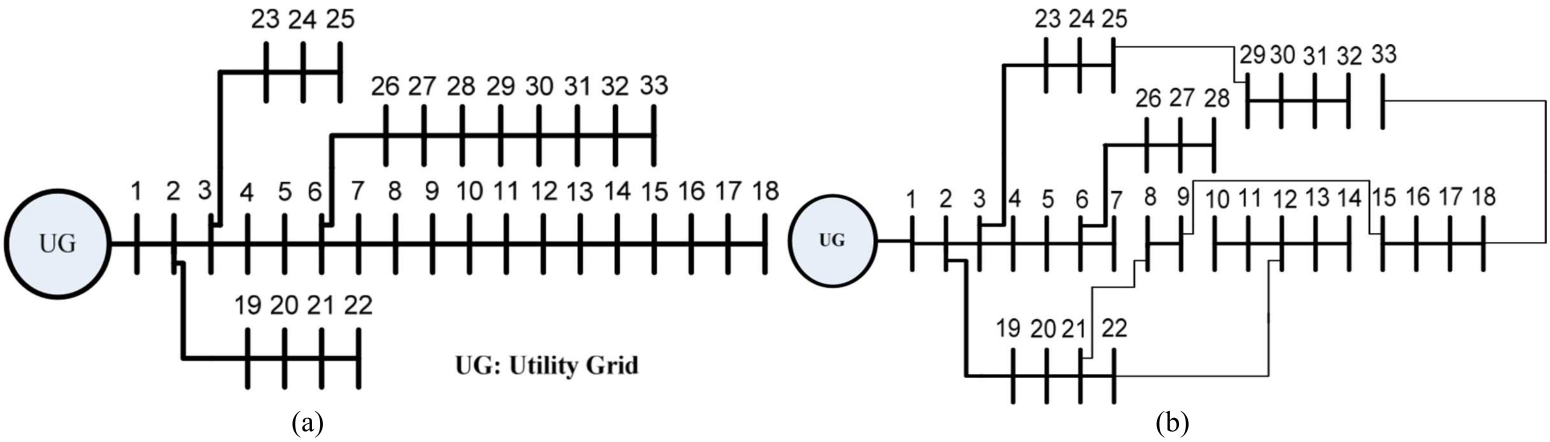

Figure 2 (a, b): IEEE-33 bus test system before and after reconfiguration respectively

3. DG Placement of the Distribution System

The main driving forces behind the integration of DGs into distribution networks are the depletion of energy resource assets, increases in load demand, and the requirement for clean power generation. DGs may be a significant help in converting passive distribution networks into active distribution networks [7]. The most precise DG sizing and placement are needed to convert a conventional radial distribution network into an independent micro-grid network. The feeder's current capacity, the system's voltage profile, and operating restrictions must all be met at once in order to reduce network power loss and regulate voltage changes in each bus (within predetermined limits). [8].

3.1. Implementation of Genetic Algorithm

By simulating the biological processes that take place in an ecosystem, successive generations of the population in GA adjust to their surroundings. Using genetic algorithms and unrestricted optimization techniques, the evolutionary adaptation principle was modeled.GA is when the population represents candidate solutions due to n chromosomes. Each chromosome represents a real value vector with m dimensions, where m is the quantity of variables that were optimized.

3.2. PSO Algorithm

PSO is artificial intelligent optimization technique that draws its initial inspiration from the social behavior of fish schools and flocks of birds. The PSO algorithm creates a population of particles that positioned randomly throughout the search space. Particles represent solutions to the problem and have fitness values. It optimized based on its fitness [10]. Eventually, particles will move towards the optimal position as they will have experienced their best position and the best solution. An updated velocity of particles was based on three factors, namely its past velocity; its best position to date and the best position the entire swarm has reached in the past [11]

3.3. Power Generation Limit

This upper and lower real and reactive power generation limits also apply to generators and other reactive sources [12].

$$P_{gi}^{min} \leq P_{gi} \leq P_{gi}^{max}, i = 1,2, \dots Ng \quad (1)$$

$$Q_{gi}^{min} \leq Q_{gi} \leq Q_{gi}^{max}, i = 1,2, \dots Ng \quad (2)$$

P_{gi}^{min} and P_{gi}^{max} are the real power generation limits, both minimum and maximum; and

Q_{gi}^{min} and Q_{gi}^{max} are the reactive power generation's minimum and maximum limitations.

3.4. Voltage Limit

The magnitude limits for upper and lower voltages, as well as at bus-i, are included. In actual practice, the generator voltage will be equal to the load or bus voltage and some values related to the line impedance and the power flowing along the line. It is important to maintain a standard voltage on each line [13,14].

$$V_i^{min} \leq V_i \leq V_i^{max}, i = 1,2, \dots Ng \quad (3)$$

Where: V_i^{min} and V_i^{max} are the minimum and maximum voltage limits.

3.5. DG Power Generation Limit

Upper and lower limits on their real and reactive power production must be satisfied by distribution generators (DGs) linked at bus-i [15].

$$P_{DGi}^{min} \leq P_{DGi} \leq P_{DGi}^{min}, i = 1,2, \dots Ng \quad (4)$$

$$Q_{DGi}^{min} \leq Q_{DGi} \leq Q_{DGi}^{min}, i = 1,2, \dots Ng \quad (5)$$

P_{DGi}^{min} and P_{DGi}^{min} are the minimum and maximum real power generation limits of the distributed generators.

Q_{DGi}^{min} and P_{DGi}^{min} are the minimum and maximum reactive power generation limits of the distributed generators.

3.6. Type of DG used

A DG that injects active power and absorbs reactive power, which is Hydro Power. The number of DGs to be used will be determined by the proposed algorithm and one will be placed per selected bus.

4. RESULTS AND DISCUSSION

4.1. Power Loss Reduction

Based on the columns in Table 4.5 that represent fitness and DG size, four optimal locations for the DGs of Type B and their corresponding optimal sizes were selected. The minimal fitness values and corresponding DG sizes were allocated at these locations. The four most effective locations, together with their optimum DG sizes, are as follows:

- Bus numbers 19 and 30 each have a DG generating 12.0010MW and absorbing 0.4882MVar, respectively.
- Bus numbers 24 and 21 each have a DG generating 11.9470MW and absorbing 0.5042MVar. Bus number 30 also has a DG generating 11.3651MW and absorbing 0.5807MVar, respectively.

Table 1: Comparison of Bus Voltage using wind power DG

Method	Bus Number	DG Size	Power Losses		Power Loss Reduction		%Power Loss Reduction	
		MW	MW	MVar	MW	MVar	%MW	%MVar
Power Loss without DG			17.8798					
GA	10	9.0384-j0.0882	11.5265	-	6.3533	-	35.6967	-
	18	11.1120-j0.7150						
	22	11.7480-j0.5891						
	30	10.0081-j0.4870						
PSO	10	11.885-j0.7970	11.1056	-	6.7742	-	37.8874	-
	18	10.8811-j0.3215						
	20	11.5631-j0.8990						
	30	11.5310-j0.3831						
IPSO	10	12.0215-j0.5260	11.2099	-	6.6699	-	37.3041	-
	19	10.8610-j0.3002						
	22	11.9170-j0.8370						
	30	11.9560-j0.5260						
HGAIPSO	19	12.0010-j0.4882	10.2021		7.6777	-	42.9406	22.36547
	21	11.9470-j0.5042						
	24	11.9179-j0.0692						
	30	11.3651-j0.5807						

Table 1 shows the comparison of the results of the power losses as a function of the different methods. When compared to GA, PSO and IPSO, the HGAIPSO method shows the greatest reduction in power loss, which is 42.9406. The proposed method performed better than GA which is 35.6967%; PSO which is 37.8874%; and IPSO which is 37.3041%.

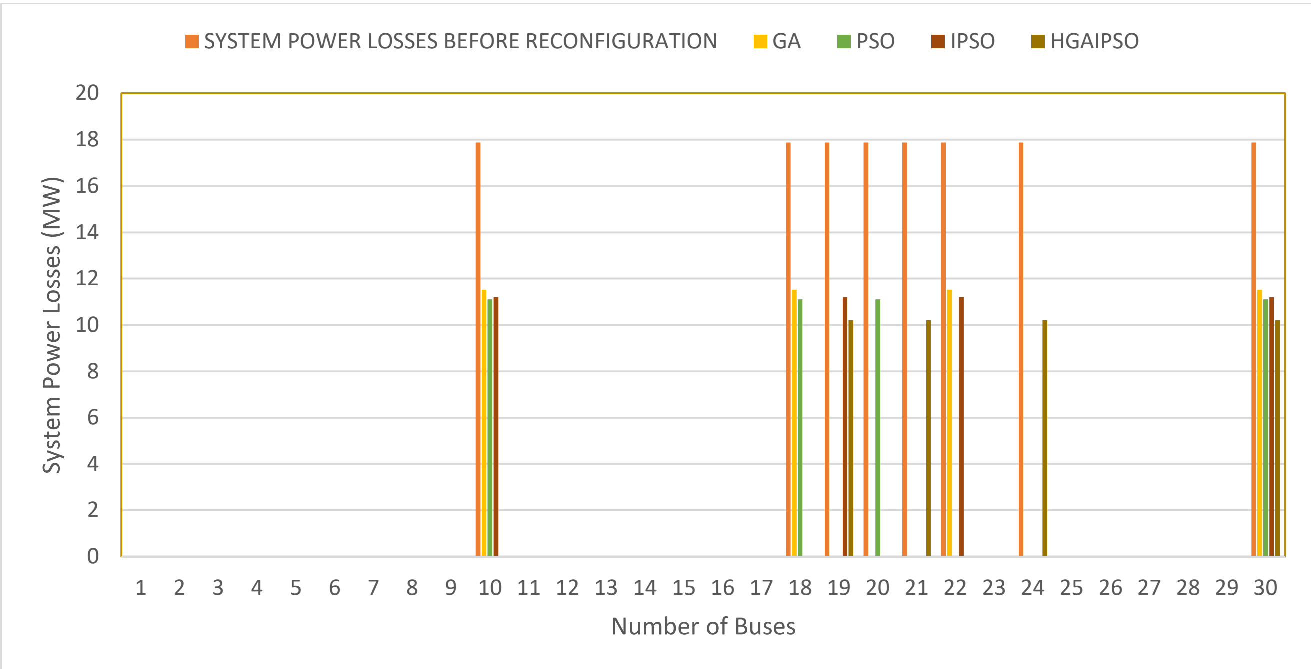

Figure 5: A comparison of Results for power loss obtained from Wind Power DG

4.2. Voltage Profile

The results from figure 6 clearly show that the use of the HGAIPSO method significantly lowers the bus voltage, which means the inclusion of the DGs by optimizing their placement and sizing. Based on the optimization of the wind power DG location and size, it was possible to achieve a lower bus voltage level of 1.01pu from 0.973pu. This means that the highest value was maintained at 1.095pu. Therefore, based on these data, the bus voltage profile has improved.

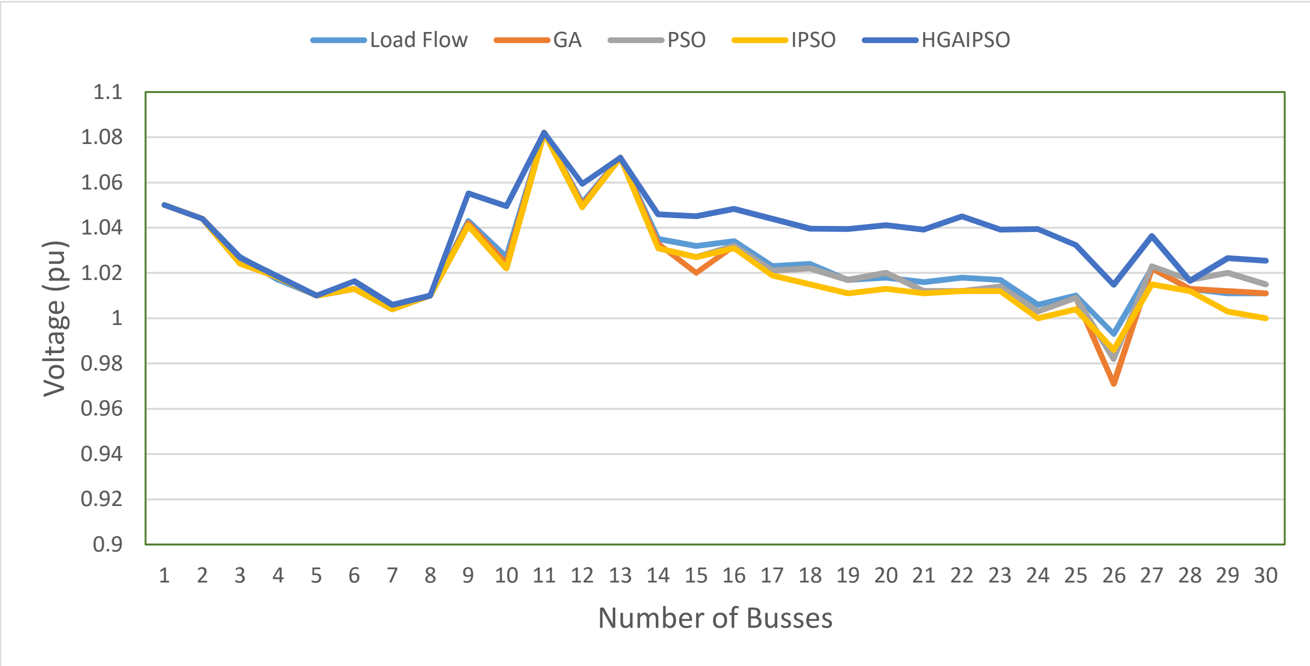

Figure 6: Bus voltage profile comparison using Wind Power DG

5. CONCLUSION

The IEEE-30 bus test system's losses are decreased and the voltage profile can be improved as a result of HGAIPSO, proving that this method is more effective at optimizing this parameter than GA, PSO, and IPSO. In studying the impact of distribution generation on power loss and voltage profile using the HGAIPSO algorithm, it clearly demonstrated that there was a reduction in system power losses as distributed generators were introduced to the power system up to an optimal number. In addition, it was also observed that the voltage profile would be having a different way that would result in the worsening of bus voltages within the acceptable range upon further DG introduction from the optimal number. The research objectives were met successfully and the HGAIPSO optimization algorithm implemented in this study was demonstrated to be more effective than GA, PSO and IPSO for optimum locating and sizing of DGs in the power distribution system to minimize losses.

6. REFERENCES

[1] Minnan Wang and Jin Zhong, “A Novel Method for Distributed Generation and Capacitor Optimal Placement considering Voltage Profiles”, 978-1-4577-1002-5/11/©2019 IEEE, Vol. 7, pp. 47-55, 2019.

[2] Satish Kansal, B.B.R. Sai, Barjeev Tyagi, Vishal Kumar “Optimal placement of distributed generation in distribution networks”, International Journal of Engineering, Science and Technology,Vol. 3, pp. 47-55, 2011.

[3] Ackermann, T., Anderson, G. and Soder, L., “Distributed Generation: A Definition”, Electric Power System Research, Vol. 8, pp.195-204, 2018.

[4] Soroudi. A and M.Ehsan.: "Multi objective distributed generation planning in liberized electricity market", in IEEE Proc., Vol.9 ,pp.1-7, 2011.

[5] S. Chandrashekhar Reddy, P. V. N. Prasad and A. Jaya Laxmi, “Power Quality Improvement of Distribution System by Optimal Placement and Power Generation of DGs using GA and NN”, European Journal of Scientific Research ISSN 1450-216X, Vol.69, pp. 326-336, 2012.

[6] An D.T. L et al. “Maximising Voltage Support in Distribution Systems by Distributed Generation”, Australian Research Council and Aurora Energy, Tasmania, Vol.12, 2015.

[7] Andrew Keane, Member, Luis (Nando) F. Ochoa, Eknath Vittal, Chris J. Dent and Gareth P. Harrison, "Enhanced Utilization of Voltage Control Resources with Distributed Generation", ©2011 IEEE, Vol.15, pp.456-564, 2011.

[8] W. El-Khattam, K. Bhattacharya, Y. H. Hegazy, et al.: "Optimal investment planning for distributed generation in a competitive electricity market" (Abstract), IEEE Trans. Power Syst., Vol.5, pp. 1674-1684, 2018.

[9] Ault, G.W. and J.R. McDonald, "Planning for distribution generation within distribution networks in restructuted electricity markets". IEEE Power Eng. Rev., Vol.20, pp.52-54, 2016.

[10] Caisheng, W. and M.H. Nehrir. "Analytical approaches for optimal placement of distributed generation sources in power systems." IEEE Trans. Power Sys. Vol.19(4): pp.27-34, 2013.

[11] Rahmat-Allah Hooshmand — Mohammad Ataei, "Optimal capacitor placement in actual configuration and operational conditions of distribution systems using RCGA", Journal of Electrical Engineering, Vol. 58, pp.189–199, 2019.

[12] Yustra, Mochamad Ashari and Adi Soeprijanto, "Optimal Distributed Generation (DG) Allocation for Losses Reduction Using Improved Particle Swarm Optimization (IPSO) Method", J. Basic. Appl. Sci. Res., Vol.2(7), pp 7016-7023, 2012.

[13] M. Vatankhah and S.M. Hosseini, "PSO based voltage profile improvement by optimizing the size and location of DGs", IJTPE, issue 11, Vol.4, pages 135-139, February 2012.

[14] M. M. Aman, G. B. Jasmon, K. H. Solangi, A. H. A. Bakar, and H. Mokhlis, "Optimum Simultaneous DG and Capacitor Placement on the Basis of Minimization of Power Losses", International Journal of Computer and Electrical Engineering, Vol.5, No.5, October 2013.

[15] Nasim Ali Khan, S. Ghosh, S. P. Ghoshal, "Optimal siting and sizing of shunt capacitors in radial distribution systems using Novel BPSO algorithm", International Journal of Emerging Technology and Advanced Engineering, Vol.3, Issue 2, February 2013.

Network Integrated Power Architecture for Terrestrial and Modular Data Center Contexts

A.A Periola
Electrical, Electronic and Computer Engineering
Cape Peninsula University of Technology
periolaa@cput.ac.za

***Abstract*—** The transition to renewable energy is a strategy that has been recognized for future data centers seeking to limit environmental emissions. In addition, innovation has led data center operators to install high-capacity renewable energy farms. However, the energy outputs from these farms are not totally utilized during the epochs of low server utilization. The surplus energy can be used to operate modular data center systems experiencing a power deficit. The presented research proposes an architecture to use surplus power in terrestrial data centers is used to meet the power deficit in modular data center systems. Performance evaluation shows that the proposed mechanism increases the power available to the modular data center by 78.3%. In addition, the proposed mechanism increases the number of communication epochs for modular data centers by 49.7% on average.

Keywords – Cloud Data Centers, Cyberphysical Networks, Renewable Energy, Future Grid

I. INTRODUCTION

The need to realize low carbon emissions has necessitated the transition to using renewable energy sources [1–3]. This has led to rapid innovation in the design and use of renewable energy technologies [4–6]. The need to design a robust and responsive system for utilizing renewable energy sources and technologies has necessitated the design of the smart grid. The smart grid fuses the technologies of intelligent systems and communication networks thereby enhancing future power systems [7–8].

It is also recognized that there is an inherent asymmetricity in the distribution of renewable energy sources. This has led to the consideration of a supergrid [9 – 13]. The super grid enables multiple, different, and connected regions to benefit from renewable energy sources in distant locations and regions. The establishment of a supergrid requires the interconnection of multiple grids across diverse locations. Such an initiative has been recognized to be capable of enhancing power security. Besides enabling power access, a supergrid should be able to provide information on the suitability of different energy sources across multiple locations to meet the energy demand across other locations.

Renewable energy sources (RESs) can arise from different locations and in different forms. The use of RESs has been considered to replace non–renewable energy sources for the benefit of environment friendly operation, and preservation. However, the use of RESs is being reduced due to the ongoing Russia–Ukraine conflict. This has led to a temporal increase in the use of Coal for electricity generation. Nevertheless, this temporal spike in Europe or in other similar contexts (due to insufficient RES driven electricity) should not lead to a jettison of the realization of low carbon emission obtainable via the use of advancing RESs and associated technology.

The need to transition to renewable energy has motivated cloud computing service providers to adopt RESs and associated systems [14–16]. These systems can be integrated into the super grid. This integration into the supergrid has two benefits to future computing service providers with large systems of terrestrial data centers. In the first case, the supergrid enables renewable energy systems associated with large-scale terrestrial data centers to provide excess power to newly deployed multiple modular data centers. The second case is one in which the super grid enables large-scale terrestrial data centers to meet their energy deficit via other renewable energy systems comprising the supergrid system. These benefits necessitate the need to design a super grid that meets the energy deficit for provisioning power required to operate computing entities in communication networks i.e., terrestrial data centers and modular data centers. The focus of the discussion here is the design of a framework for a super grid that meets these performance requirements. The contributions of this paper are:

1. First, the paper proposes an intelligent energy system comprising communication and computing networks with an interface between a terrestrial data center (TDC), modular data center (MDC), and the super grid system. The proposed network comprises a network gateway (N–GW) that enables the processing of power surplus and deficit-related requests from TDCs, MDCs, and the supergrid system. In the proposed network, the N- GW executes data communications and decision-making in the cyber–physical system comprising TDCs, MDCs, and the super–grid.
2. Secondly, the paper formulates and investigates the ability of the proposed network to meet the energy deficit for MDCs considering the case where the TDCs with renewable energy capacity have a surplus. In addition, the paper considers how the improvement of the energy deficit of MDCs enhances their data communications by increasing the number of communication epochs. Furthermore, the paper evaluates the performance benefits considering the MDC energy gap and the number of communication epochs.

The rest of the research is organized as follows. Section II discusses the background work regarding the relations between the cloud and the super grid. Section III describes the problem. Section IV presents the proposed solution. Section V formulates the performance model. Section VI evaluates the performance benefits. Section VII is the conclusion.

II. EXISTING AND BACKGROUND WORK

Mishra *et al.* [17] note that cloud computing systems can be used to execute the computational demands of power systems. This is realized by providing a platform that enables the hosting of power system related software. The use of the results from this software requires that power systems be closely linked to cloud computing systems. Examples of areas influenced in this manner are protection, distribution, marketing, scheduling, and marketing. The discussion in [18] has a similar perspective and proposes a software defined power system (in this case for a microgrid). The discussion in [17] has not explicitly recognized the role of the cloud in a power system operational context. The case in [18] also focuses on the micro–grid which is on a smaller scale in comparison to the large supergrid or mega–grid. The case of a super–grid requires the inter–operation of multiple software defined micro–grid systems, a challenge that has not been addressed in [18].

Gurav *et al.* [19] identify that the incorporation of cloud computing platforms is required to realize the decentralization of the power grid. This enables making information about consumer behavior and performance in one grid available to another grid. In addition, the discussion in [19] recognizes the cloud computing model as being suitable for power grid management with the benefits of autonomic operation, low response time, high data reliability, high scalability, and high level of security. However, the description of a cloud information and data management architecture in a manner that enables inter–operability between multiple power grid with different scale is not presented and requires further research.

The study in [20] presents a power grid that integrates multiple RESs using communication networks. This is done for RESs that are distributed over a wide area. Two power sources have been considered. These are: (1) battery and (2) photovoltaic solar power system. However, a wide area network can comprise multiple RESs such as offshore wind, onshore wind, and aerial wind. This context of heterogeneous renewable sources (HRSs) has not been considered in [20].

Reichenberg *et al.* [11] present the discussion on the supergrid considering an HRS model. However, the focus in [11] is on the HRS's decarbonization potential. In addition, a sensitivity analysis based on the different percentage distribution of varying RESs is considered. Furthermore, it is noted in [15] that a data center can serve as a potential battery in a super–grid system. However, such a notion has not been considered in [11].

The discussion in this aspect has demonstrated that the role of cloud computing systems in the future power grid has been recognized. However, the role of computing platforms such as virtual big batteries in HRS power grids requires further research consideration. Such a role requires a fusion between the data center's role as a communications and computing node alongside being an entity in an HRS power network.

III. PROBLEM DESCRIPTION

The evolution of power systems to incorporate multiple RESs has led to the emergence of the supergrid. The supergrid integrates HRSs and should be able to provide power in different contexts. A useful context that should be considered is one in which data centers with multiple RESs can potentially contribute power to the grid. This enable data centers to be capable of functioning as entities in computing networks and power networks. However, there is a need to design mechanisms to enable this co-functional capability in the multiple contexts associated with power systems. In this case, data centers should be able to meet own energy deficit and the energy deficits of other data centers. The mechanism being proposed also meets this performance requirement.

Let υ_1 and υ_2 denote the set of terrestrial data centers and modular data centers, respectively.

$$\upsilon_1 = \{\upsilon_1^1, \dots, \upsilon_1^A\} \quad (1)$$

$$\upsilon_2 = \{\upsilon_2^1, \dots, \upsilon_2^B\} \quad (2)$$

The a^{th} terrestrial data center $\upsilon_1^a, \upsilon_1^a \epsilon\, \upsilon_1$ is being operated by computing platforms operator with a renewable energy farm or an operator that engages in the purchase of electricity derived from renewable energy on a large scale. The operator deploying modular data centers does not engage in the acquisition of renewable energy farm systems or purchase of renewable energy-based electricity in large amounts. Instead, the modular data center operator uses simple low-cost set–up of renewable energy systems.

Each of the data centers in υ_1 comprise multiple servers and υ_1^a can be expressed as:

$$\upsilon_1^a = \{\upsilon_1^{a,1}, \upsilon_1^{a,2}, \dots, \upsilon_1^{a,C}\} \quad (3)$$

The b^{th} modular data center $\upsilon_2^b, \upsilon_2^b \epsilon\, \upsilon_2$ also comprises multiple servers such that:

$$\upsilon_2^b = \{\upsilon_2^{b,1}, \upsilon_2^{b,2}, \dots, \upsilon_2^{b,D}\} \quad (4)$$

The power required by the c^{th} server in the a^{th} terrestrial data center $\upsilon_1^{a,c}, \upsilon_1^{a,c} \epsilon\, \upsilon_1^a$ at the epoch t_y is denoted as $P_1(\upsilon_1^{a,c}, t_y)$. In addition, the power required by the d^{th} server in the b^{th} modular data center $\upsilon_2^{b,d}, \upsilon_2^{b,d} \epsilon\, \upsilon_2^b$ at the epoch t_y is denoted as $P_1(\upsilon_2^{b,d}, t_y)$. Given that the power accessible to the terrestrial data center system and modular data center system are denoted υ_1^{req} and υ_2^{req}, respectively. An operational challenge arises when:

$$\sum_{b=1}^{B} \sum_{d=1}^{D} \sum_{y=1}^{Y} P_1(\upsilon_2^{b,d}, t_y) \ \geq\ \upsilon_2^{req} \quad (5)$$

$$\sum_{a=1}^{A} \sum_{c=1}^{C} \sum_{y=1}^{Y} P_1(\upsilon_1^{a,c}, t_y) \ <\ \upsilon_1^{req} \quad (6)$$

$$\sum_{j=1}^{J} \sum_{y=1}^{Y} e(j, t_y) I(j, t_y) \ >\ E_D \quad (7)$$

$e(j, t_y)$ is the amount of electricity derivable from the source j at the epoch t_y.
$I(j, t_y), I(j, t_y) \epsilon \{0,1\}$ is the active status of the source j at the epoch t_y. The source j is inactive and active at the epoch t_y when $I(j, t_y) = 0$ and $I(j, t_y) = 1$, respectively.
E_D is the amount of electricity available to end–users of the power utility.

The scenario in (5) describes a case where the servers in the modular data centers require more power than that which is accessible as described by the parameter υ_2^{req}. In addition, the scenario in (6) describes a case where the energy demand by servers in the terrestrial data centers fall short of the accessible power from the renewable energy farm as described by the parameter υ_1^{req}. In this case, there is an occurrence of an energy surplus and energy deficit in the terrestrial data center and modular data center, respectively. The case in (7) is one in which there is a significant demand (exclusive of data centers) on the group of energy sources that are not directly linked to the grid. In this case, the grid cannot be used to meet the energy deficit observed in (5) and the surplus in (6) is not being utilized.

Hence, a solution and an architecture enabling the modular data centers to meet their deficit from the surplus of the terrestrial data center is required.

IV. PROPOSED SOLUTION

The solution being presented meets the energy deficit of terrestrial data centers (TDCs) and modular data centers (MDCs). The concerned scenario comprises TDCs with each having a renewable energy farm having multiple solar and wind farms. Alternatively, the TDC is owned by a platform service provider that purchases electrical energy from entities owning and operating renewable energy farm systems. In this capacity, the TDC can function as either a primary energy user (PEU) or a secondary energy user (SEU). As a PEU, the platform service provider owns and operates its renewable energy farm. In its capacity as an SEU, the TDC platform service provider sells excess energy to entities requiring power provisioning. In the context of the proposed solution, the entities being considered are communication and computing entities.

In the proposed solution, the TDC comprises a cognitive energy gateway (C–GW). The C–GW processes energy requests received from the MDC. In addition, the C–GW enables communications between the grid context arising between the TDC, MDC and a smart grid system. Furthermore, each MDC has a mini-C–GW (MC–GW). The MC–GW sends energy requests of the MDC to the C–GW.

The relations between the C–GW, MC–GW and the smart grid communications gateway (S–GW) is shown in Figure 1. In Figure 1, the S–GW enables communications between the C–GW and the MC–GW. The relations shown in Figure 1 also enables power flow between the power entities i.e., the TDC power entity (T–PE), smart grid power entity (S–PE) and the MDC power entity (M–PE).

The relations associated with the power entity enable bi–directional power flow. In Figure 1, C–GW (TDC) and MC–GW (MDC) belong to the computing service providers, CSP 1 and CSP 2, respectively.

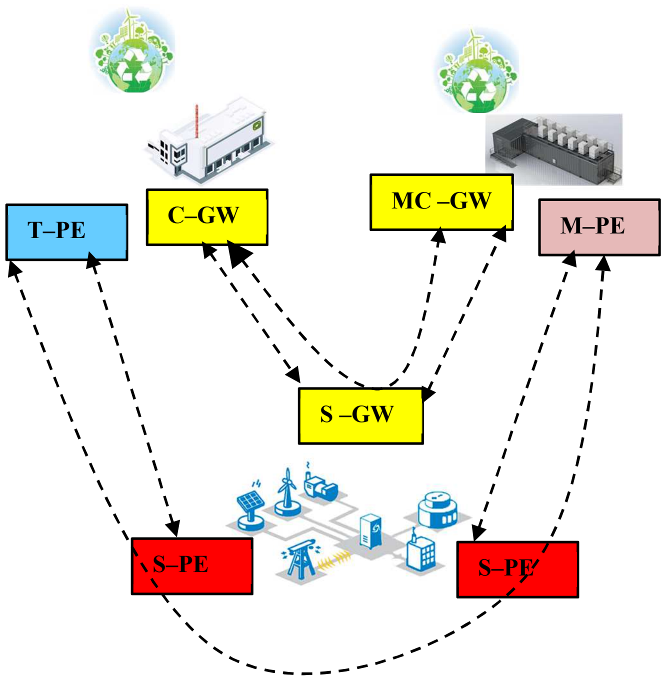

Figure 1: Relations between the interacting gateway (communication entities) alongside power entities in the proposed solution.

Let α and β be the set of computing entities owned and operated by CSP 1 and CSP 2, respectively.

$$\alpha = \{\alpha_1, \alpha_2, \dots, \alpha_N\} \tag{8}$$

$$\beta = \{\beta_1, \beta_2, \dots, \beta_M\} \tag{9}$$

In addition, the set of servers in $\alpha_m, \alpha_m \epsilon\, \alpha$ and $\beta_n, \beta_n \epsilon\, \beta$ are given as:

$$\alpha_m = \{\alpha_m^1, \alpha_m^2, \dots, \alpha_m^P\} \tag{10}$$

$$\beta_n = \{\beta_n^1, \beta_n^2, \dots, \beta_n^Q\} \tag{11}$$

The power required by $\alpha_m^p, \alpha_m^p \epsilon\, \alpha_m$ and $\beta_n^q, \beta_n^q \epsilon\, \beta_n$ at the epoch $t_y, t_y \,\epsilon\, t, t = \{t_1, \dots, t_Y\}$ are denoted $P_1(\alpha_m^p, t_y)$ and $P_1(\beta_n^q, t_y)$, respectively. In addition, let $I(x, t_y) \,\epsilon\, \{0,1\}, x \,\epsilon\, \{\alpha_m^p, \beta_n^q\}$ denote the functional status of computing entity x. The computing entity x is non-functional and functional at the epoch t_y when $I(x, t_y) = 0$ and $I(x, t_y) = 1$, respectively. Let the power required to operate the computing entities of CSP 1 and CSP 2 be denoted as P_1^{req} and P_2^{req}, respectively. A power deficit occurs when:

$$\sum_{p=1}^{P} \sum_{y=1}^{Y} I(x = \alpha_m^p, t_y)\, P_1(\alpha_m^p, t_y) \ \geq\ P_1^{req} \tag{12}$$

$$\sum_{q=1}^{Q} \sum_{y=1}^{Y} I(x = \beta_n^q, t_y)\, P_1(\beta_n^q, t_y) \ \geq P_2^{req} \tag{13}$$

The relations in (12) and (13) arise when there is a full utilization or oversubscription to the server capacity. A power surplus occurs when there is server underutilization and is described as:

$$\sum_{p=1}^{P} \sum_{y=1}^{Y} I(x = \alpha_m^p, t_y)\, P_1(\alpha_m^p, t_y) \ <\ P_1^{req} \tag{14}$$

$$\sum_{q=1}^{Q} \sum_{y=1}^{Y} I(x = \beta_n^q, t_y)\, P_1(\beta_n^q, t_y) \ <\ P_2^{req} \tag{15}$$

In the case that (12) holds true, the TDC (CSP 1) sends a power request message to the S–GW. The S–GW being the main power supplier provides the required energy via S–PE to T– PE relations. The amount of power provided, γ_1 is given as:

$$\gamma_1 = P_1^{req} - \sum_{p=1}^{P} \sum_{y=1}^{Y} I(x = \alpha_m^p, t_y)\, P_1(\alpha_m^p, t_y) \tag{16}$$

The amount of power (in a deficit case) associated with the MDC, γ_2 is given as:

$$\gamma_2 = P_2^{req} - \sum_{q=1}^{Q} \sum_{y=1}^{Y} I(x = \beta_n^q, t_y)\, P_1(\beta_n^q, t_y) \tag{17}$$

Given that (13) holds true, the MDC (CSP 2) sends a power request message to the S–GW. In this case, the S–GW probes the C–GW to verify the validity of (6) i.e., the occurrence of TDC power surplus. The TDC provides power to meet the MDC power deficit. The flowchart describing the proposed mechanism is shown in Figure 2.

In Figure 2, the entities CSP 1 and CSP 2 can act as either a PEU or SEU. As an SEU, each of the CSPs i.e., CSP 1 and CSP 2 negotiates with an external entity on deciding an agreed price for making a power transaction i.e., transaction enabling the exchange of power between TDCs and MDCs. In this case, the relations in (7) and (8) describing a power surplus holds true.

The C-GW verifies the validity of the deficit condition in (5). In addition, the C–GW verifies the validity of the power surplus condition in (7). Furthermore, the MC–GW associated with the MDC verifies the validity of the power deficit and power surplus conditions in (5) and (6), respectively.

In verifying the power surplus condition, the C–GW and MC–GW observes the server utilization. A low server utilization indicates that either of the MDC or TDC have a low computing workload. In this case, all the power allocated and planned for the servers in either the MDC or TDC is not utilized. Hence, there is idle power that can be used by external entities and applications. Furthermore, a power deficit condition occurs when either the MDC or TDC has a significant data workload requiring high power consumption. In this case, additional power is required to enable the realization of the intended data storage, data processing and algorithm execution functionality.

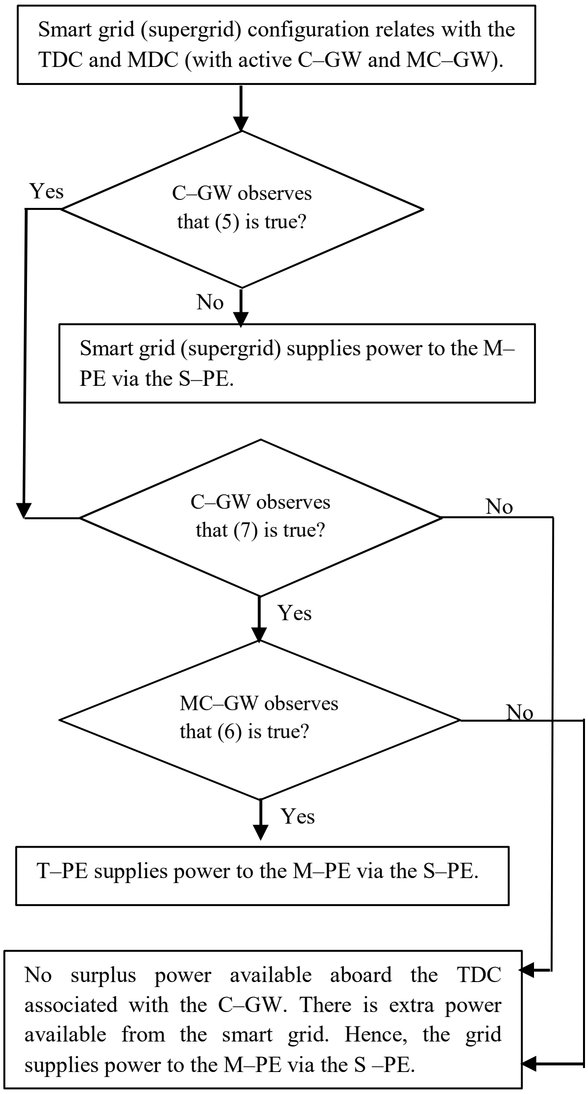

Figure 2: Flowchart showing the execution of computing functionality in the relations between the interacting gateway (communication entities) alongside corresponding power entities in the proposed solution.

V. PERFORMANCE FORMULATION

The performance metrics of MDC availability (associated with the number of epochs during which TDC surplus meets the power supply and demand associated with MDC deficit). In this regard, the number of communications epochs is formulated. The availability of CSP 2 before and after the incorporation of the proposed mechanism are denoted ς_1 and ς_2, respectively.

$$\varsigma_1 = \gamma_2 \left(\frac{1}{(Q-1)(Y-1)} \sum_{q=1}^{Q} \sum_{y=1}^{Y} I\left(\beta_n^q, t_y\right) P_1\left(\beta_n^q, t_y\right) \right)^{-1} \tag{18}$$

$$\varsigma_2 = \gamma_2 + B \tag{19}$$

$$B = (1+\zeta)\gamma_1 C^{-1} \tag{20}$$

$$C = \left(\frac{1}{(Q-1)(Y-1)} \sum_{q=1}^{Q} \sum_{y=1}^{Y} I\left(\beta_n^q, t_y\right) P_1\left(\beta_n^q, t_y\right) \right)^{-1} \tag{21}$$

In addition, the number of MDC communication epochs is formulated. Let $\eta_1(\beta_n^q, t_y)$ be the proportion of total power used for communication by the computing entity β_n^q at the epoch t_y. The amount of power required by the communication payload aboard the computing entity β_n^q at the epoch t_y is denoted $\eta_2(\beta_n^q, t_y)$. The number of communication epochs before and after the incorporation of the proposed mechanism are denoted A_1, and A_2, respectively.

$$A_1 = \left(\frac{1}{(Q-1)(Y-1)} \sum_{q=1}^{Q} \sum_{y=1}^{Y} \frac{\eta_1(\beta_n^q, t_y) I(\beta_n^q, t_y) P_1\left(\beta_n^q, t_y\right)}{\eta_2(\beta_n^q, t_y)} \right)^{-1} \tag{22}$$

$$A_2 = \left(\frac{\gamma_1(1+\phi)+\gamma_2}{(Q-1)(Y-1)} \sum_{q=1}^{Q} \sum_{y=1}^{Y} \frac{\eta_1(\beta_n^q, t_y) I(\beta_n^q, t_y) P_1\left(\beta_n^q, t_y\right)}{\eta_2(\beta_n^q, t_y)} \right)^{-1} \tag{23}$$

Where ϕ is the percentage increase in γ_1 due to the incorporation of the proposed mechanism and architecture.

VI. PERFORMANCE EVALUATION

The performance evaluation is conducted using the simulation parameters in Table 1. The server power for the terrestrial data center and the modular data center are considered using the information in [21]. In addition, the performance evaluation procedure is conducted using MATLAB stochastic simulation. The performance evaluation results obtained by simulation for the power and the number of communication epochs.

The presented results show that the use of the proposed mechanism outperforms the existing mechanism. Analysis shows that the power deficit occurring in the case of the MDC is met via the use of power surplus from the TDC facility. It can also be seen that the number of terrestrial communication epochs is improved using the proposed mechanism.

In the considered simulation context, the TDC comprises more servers than the MDC. Furthermore, MDCs are in remote location and provide computing capabilities where the deployment of large-scale facilities such as TDCs is deemed infeasible. Furthermore, MDCs require power to remotely communicate with larger capacity computing entities such as TDCs. Hence, they need power access to meet the demand for executing increased computational load and engage in communication within a computing and communication network. Hence, the context of the simulation is that of a communication network.

Further analysis shows that the use of the proposed mechanism (in proposed case) reduces the power deficit observed in the case associated with the existing mechanism (in existing case). This also improves the amount of power available for communications in the case of MDCs. The available power and the number of communication epochs are enhanced by 78.3% and 49.7% on average, respectively. The performance benefit is also investigated for a scenario where the power output from the NRESs of coal, nuclear and diesel are significantly reduced. Such a case models a scenario where the use of NRESs is being gradually reduced due to the need to incorporate more RESs with increasing contribution. In this case, the simulation parameters are presented in Table 1. The simulation results for the existing case and proposed case are presented in Figure 3 and Figure 4, respectively.

In this case, the inclusion of the proposed energy sources results in a reduction of the energy gap. A reduction of the energy gap is beneficial as it implies that RESs can meet the load demand previously satisfied by RESs being retired from use. Analysis shows that the energy gap is reduced by 36.6% on average in this case.

Table1: Simulation Parameters

Parameter	Value
Number of Terrestrial Data Centers (TDCs)	120
Number of Modular Data Centers (MDCs)	20
Required Power for operation by MDC	987 W
Maximum Server Power (TDC) [21]	289.6 W
Minimum Server Power (TDC)	186.3 mW
Average Server Power (TDC)	144.1 W
Maximum Server Power (MDC) [21]	241.1W
Minimum Server Power (MDC)	27.4 W
Average Server Power (MDC)	156.4W
Power contributions for Communications	
Maximum Power contribution in TDC	99%
Minimum Power contribution in TDC	0.83 %
Average Power contribution in TDC	53%
Maximum Power expended in MDC	925.5 mW
Minimum Power expended in MDC	66.5 mW
Average Power expended in MDC	492.6 mW
Number of Terrestrial Data Centers TDCs	120

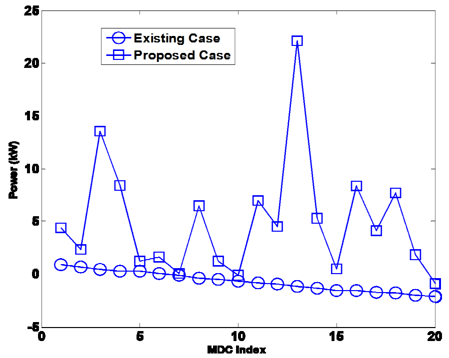

Figure 3: Performance simulation showing the results on the power accessible in the existing case and proposed case.

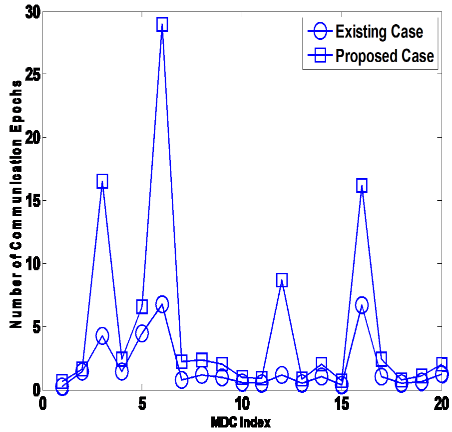

Figure 4: Performance simulation showing the number of communication epochs in the existing and proposed case.

VII. CONCLUSION

The need to make use of renewable energy has led to cases in data centers where power surplus and power deficit occur in segments of terrestrial data centers and centrally managed modular data center systems. The presented research proposes a data driven integrated networking architecture to address this challenge. The proposed solution makes use of power surplus in terrestrial data centers to address the power deficit in modular data center systems. This is beneficial and enables remotely located modular data centers to communicate and enable data access in a manner that meets subscriber demands in a communication network. The presented research evaluates the improvement in the power that is accessible to modular data centers and the resulting increase in the number of associated transmission (communication) epochs. Performance evaluation shows that the improvement in power and increase in number of communication epochs of 78.3% and 49.7% on average, respectively. Future work aims to examine additional scenarios such as one arising when there is an acute case of energy shortage in terrestrial data centers and modular data centers alongside a high demand on the grid.

ACKNOWLEDGMENT

The support of the Department of Electrical, Electronic and Computer Engineering of the Cape Peninsula University of Technology is highly acknowledged by the author.

REFERENCES

[1] L. Xing, G. Sizov, and O. E. Gundersen, "Digital Transformation in Renewable Energy: Use Cases and Experiences from a Nordic Power Producer," Digital Transformation in Norwegian Enterprises, pp. 63–89, 2022, doi: 10.1007/978-3-031-05276-7_5.

[2] I. Todd and D. McCauley, "An inter-disciplinary approach to the energy transition in South Africa," Discover Sustainability, vol. 2, no. 1, Jul. 2021, doi: 10.1007/s43621-021-00043-w.

[3] B. Tarekegne, K. Kazimierczuk, and R. O'Neil, "Communities in energy transition: exploring best practices and decision support tools to provide equitable outcomes," Discover Sustainability, vol. 3, no. 1, Apr. 2022, doi: 10.1007/s43621-022-00080-z.

[4] D. O. Aikhuele, A. Periola, and D. E. Ighravwe, "Wind turbine systems operational state and reliability evaluation: An artificial neural network approach," International Journal of Data and Network Science, pp. 323–330, 2019, doi: 10.5267/j.ijdns.2019.5.001.

[5] J. T. Dellosa and E. C. Palconit, "Artificial Intelligence (AI) in Renewable Energy Systems: A Condensed Review of its Applications and Techniques," *2021 IEEE International Conference on Environment and Electrical Engineering and 2021 IEEE Industrial and Commercial Power Systems Europe (EEEIC / I&CPS Europe)*, 2021, pp. 1-6.

[6] Z. Wu, G. Luo, Z. Yang, Y. Guo, K. Li, and Y. Xue, "A comprehensive review on deep learning approaches in wind forecasting applications," CAAI Transactions on Intelligence Technology, vol. 7, no. 2, pp. 129–143, Jan. 2022, doi: 10.1049/cit2.12076.

[7] A. V. Jha et al., "Smart grid cyber-physical systems: communication technologies, standards and challenges," Wireless Networks, Mar. 2021, doi: 10.1007/s11276-021-02579-1.

[8] F. E. Abrahamsen, Y. Ai, and M. Cheffena, "Communication Technologies for Smart Grid: A Comprehensive Survey," Sensors, vol. 21, no. 23, p. 8087, Dec. 2021, doi: 10.3390/s21238087.

[9] C. W. Gellings, "A globe spanning super grid," in *IEEE Spectrum*, vol. 52, no. 8, pp. 48-54, August 2015, doi: 10.1109/MSPEC.2015.7164402.

[10] M. Liaqat, Y. Ghadi and M. Adnan, "Multi-Objective Optimal Power Sharing Model for Futuristic SAARC Super Smart Grids," in *IEEE Access*, vol. 10, pp. 328-351, 2022, doi: 10.1109/ACCESS.2021.3137592.

[11] L. Reichenberg, F. Hedenus, N. Mattsson, and V. Verendel, "Deep decarbonization and the supergrid – Prospects for electricity transmission between Europe and China," Energy, p. 122335, Oct. 2021, doi: 10.1016/j.energy.2021.122335.

[12] A. A. Stephen, K. Musasa, and I. E. Davidson, "Voltage Rise Regulation with a Grid Connected Solar Photovoltaic System," Energies, vol. 14, no. 22, p. 7510, Nov. 2021, doi: 10.3390/en14227510.

[13] S. P. dos Santos, R. R. B. de Aquino, and O. N. Neto, "A proposal for analysis of operating reserve requirements considering renewable sources on supergrids," Electrical Engineering, vol. 103, no. 1, pp. 529–540, Sep. 2020, doi: 10.1007/s00202-020-01097-1.

[14] https://www.c2es.org/content/dominion-microsoft-teamup-to-build-solar-project

[15] "Can Microsoft's data centers become big batteries for the grid?," The Verge. https://www.theverge.com/2022/7/7/23197103/microsoft-data-center-dublin-batteries-electricity-grid-renewable-energy (accessed Sep. 18, 2022).

[16] https://businesstech.co.za/news/energy/534702/amazon-has-built-a-new-solar-plant-in-south-africa/

[17] N. Mishra, V. Kumar and G. Bhardwaj, "Role of Cloud Computing in Smart Grid," *2019 International Conference on Automation, Computational and Technology Management (ICACTM)*, 2019, pp. 252-255, doi: 10.1109/ICACTM.2019.8776750

[18] M. Ndiaye, G. P. Hancke, A. M. Abu-Mahfouz, and H. Zhang, "Software-Defined Power Grids: A Survey on Opportunities and Taxonomy for Microgrids," IEEE Access, vol. 9, pp. 98973–98991, 2021, doi: 10.1109/access.2021.3095317.

[19] P. D. Gurav, M. R. Hans and N. A. Kulkarni, "Review: Role of cloud computing in grid empowerment," *2016 International Conference on Automatic Control and Dynamic Optimization Techniques (ICACDOT)*, 2016, pp. 258-263, doi: 10.1109/ICACDOT.2016.7877590.

[20] H. A. M. Abobaker, J. Genci, M. Gamcova, and G. A. M. Ismeal, "Design and implementation of secured power grid system with information and communication technology," SN Applied Sciences, vol. 2, no. 12, Nov. 2020, doi: 10.1007/s42452-020-03820-w.

[21] https://medium.com/@zodhyatech/how-much-power-do-the-servers-consume-8f9620be71a

2023 SAUPEC Conference, Johannesburg, South Africa, January 24-26, 2023

A Nexus for Dispatching of Ancillary Services of Emergency Reserves in South African Networks

Ntanganedzeni Tshinavhe
Department of Electrical, Electronic and Computer Engineering
Cape Peninsula University of Technology
South Africa
tshinavhen@cput.ac.za/tshinavhen@gmail.com

Mukovhe Ratshitanga
Department of Electrical, Electronic and Computer Engineering
Cape Peninsula University of Technology
South Africa
RatshitangaM@cput.ac.za

Khaled Aboalez
Department of Electrical, Electronic and Computer Engineering
Cape Peninsula University of Technology
South Africa
AboalezK@cput.ac.za

***Abstract*—Power system (PS) networks with adequate operating reserves plays an important role in safeguarding the economies around the world. When PS has insufficient operating reserves, they could be prone to load-shedding or total black-outs. Operating reserves are mainly classified into three categories, which are regulation reserve, spinning, and non-spinning reserve. This paper reviews the provision of ancillary services and research opportunities for dispatching voltage and frequency ancillary services of emergency reserves in South African power networks. The voltage/frequency control of distribution and transmission grids are examined. This includes the current state of South African power networks in particular the existing load-shedding issue. Lastly, the opportunity for further study is identified in the provision of ancillary services to resolve the existing problems.**

Keywords—Ancillary services, voltage control, frequency regulation, operating reserves, South African electricity challenges, Variable renewable energy dispatch, Eskom.

I. INTRODUCTION

Ancillary Services (AS) are the various operations required to maintain the stability and security of the grid. They are features that help grid operators maintain a reliable power system, and can be provided by different resources [1]. These services ensure the proper flow and direction of power, correct supply and demand imbalances, and help the system recover from power system events. They need to maintain a momentary and continuous balance between power generation and load, manage transmission line flow, and provide grid operators with the resources necessary to implement control schemes. These systems are required in normal conditions and emergencies. It also provides the resources needed to restart the power system if the system operator fails to maintain power generation or load balancing and the system collapses [2]. These services include spare, black start and islanding [3, 4], power restoration [5, 6], restricted power generation, reactive power supply and voltage control, tuning and load tracking.

Electrical energy is an essential need as most activities require electrical energy for efficiency and effectiveness. Power utilities have the responsibility to ensure that they are providing continuous electrical energy to consumers. It is thus important to ensure the stability of the system and to prevent system blackouts that may occur due to disturbances such as loss of generator or loss of transmission line which then causes an imbalance of load and generation. In the event a blackout does occur operators must be prepared to restore power. The generating units should be able to restart without being connected to an energized grid. However, in some grids, most of the generating units cannot start autonomously and therefore should be connected to the energized grid [7]. Because of this, operators rely on Black Start Units (BS) which can start autonomously to restore power. The generating units are not available in some grids because they are expensive. It is thus important to find optimal solutions to allocate the BS units into the grid [8], [9].

South Africa has experienced load-shedding over the past years and is a problem that persists and affects all industries and households in the country. Lots of businesses have suffered losses due to this problem and some have resorted to finding alternative means to power up their buildings when load-shedding occurs. This has now become part of their business strategy to ensure they do not continuously lose profit as the problem has not shown any sign of being permanently resolved. Load-shedding is amongst the solutions that may be implemented to relive stress on the primary energy source, however, it has become the only solution to South Africa’s energy crises.

The paper discusses the dispatching of voltage and frequency ancillary services of emergency reserves in South African power and the opportunities availability to study alternatives of ancillary service provision. This will also include related research work that has been conducted in South Africa and other countries.

The rest of the paper is organized as follows, Section II reviews research on the provision of ancillary services in other countries and South Africa. Section III discusses the current state of the South African power network and the looming problem of load-shedding, its causes, and the effect it has on industries and households and Section IV addresses the gap in emergency reserves research in South Africa and the viable solutions that may be considered to guarantee a stable electricity supply.

II. ANCILLARY SERVICES PROVISSION IN SOUTH AFRICA

A. Ancillary servivces provission in South Africa

The defined ancillary services requirements of the System Operator in South Africa are the reserves, which includes instantaneous reserve, regulating reserve, Ten-minute reserve, emergency, and supplemental reserve. Other ancillary services are Reactive Power Supply and Voltage Control, Black-start [10]. As the penetration of renewable energy is introduced to the utility increases, [11]. It is also important that the trading of the ancillary services is technically possible and that it does not affect the reliability of the system.

III. OPERATING RESERVES

Operating reserves are mainly classified into three categories, which are regulation reserve, spinning and non-spinning reserve [12]. Reserves secure capacity and balancing of supply and demand and can be used in normal conditions or severe conditions. The reserve ancillary services can be provided by different resources, this has seen a rise in the use of distributed generation [13]. As the load increases, reserves should be dispatched to ensure there is sufficient energy generation to meet the load. They need to respond fast to the increase in demand when the generation is insufficient. Different methods for allocating reserves, requirements, and optimization are available and has been proposed by different authors.

In [14], a comparison of the different operating reserves and calculation of reserves was made. The results obtained show a significant difference because of the type of reserve, penetration level of variable generation, cost, and sensitivity to different conditions.

There is an increase in the level of penetration of renewable energy resources [15, 16], and as such are concerns with the power output. In [17, 18, 19], the authors proposed methods to determine the amount of operating and spinning reserves capacity to manage the wind power variability to address the uncertainties. In [18], the authors considered the geographical location of the wind power plants and how it affects the power output. The results show that wind plants that are at a windy site decrease the required reserve by 30% as compared to other sites. In [20], Hassan et al included the stability concerns, control strategies, existing challenges, trends, achievements, and new research opportunities.

IV. VOLTAGE CONTROL

A. Voltage Control Concepts

Voltage control is maintaining the system voltage to ensure it is kept at a predefined range. This can be achieved by controlling the reactive power on the AC (Alternating Current) power system. Generation and transmission equipment can produce or absorb reactive power. The voltage control equipment includes [21]:

- Generators
- Synchronous condenser
- Static VAR compensator (SVC)
- Distributed generation (DG)
- Capacitor
- Static synchronous compensator (STATCOM)

Generators and synchronous condensers have fast system response and have excellent ability to support voltage. In [22], Ma et al described that though the STATCOM, Distributed Generation, and Static VAR compensators have fast system, their ability to support voltage is fair as compared to generators and synchronous condensers [21]. Capacitors are much slower and have poor ability to support voltage as compared to the rest of the voltage control equipment.

The difference between the voltage control equipment is characteristics such as response speed, continuity of control, response to voltage change, and operating cost [21].

It is essential to control voltage for reliability and market. The voltage should always be preserved within the defined range to avoid system failure. Low voltage has potential to cause the equipment to fail as they are designed to operate within a particular percentage range of the nominal voltage, it is usually ±5% of the nominal voltage, the motor can overheat and get damaged and reactive power will be reduced [23]. High voltage may cause the equipment to overheat and break down insulation or cause a blackout.

Different approaches may be used for voltage control in the generation, distribution, and transmission systems using the voltage control equipment described above. The most popular equip used is the Distributed Generation (DG). The following subsections described the methods/approaches used in generation, distribution, and transmission systems. Most of the approaches described uses the DG unit to control the voltage of the system.

B. Voltage control methodologies

Different voltage control techniques have been proposed in [24]. The different voltage control techniques presented on electrical distribution networks connected with distributed generation. These methods consider the complexity of the network, and the number of distributed generations that could be connected [25]-[26]. When the DGs (Distributed Generation) are added to the network, a voltage rise may occur and as such different solutions will apply for different scenarios.

In [27], Li et al presents control methods to regulate voltage of the network. The papers focus on networks with distributed generation and use reactive power compensation to control the voltage. Voltage control can be accomplished by managing the reactive power, which can either be produced and absorbed by both the generation and transmission equipment. In [21], the several types of generation and transmission resources that can be used to supply reactive power and control voltage are examined. The equipment includes synchronous condensers, generators, capacitors, distributed generation, inductors, static VAR compensators, and transformers. From this list of equipment, [21] found that the generators, synchronous condensers, Static Var Compensators (SVSCs) and the STATCOM [28] provide fast reactive support and voltage control, while the other equipment is either slow or offers voltage control in large steps. Even though the generators and the synchronous condensers are favorable towards the voltage control characteristics, their capital and operating costs are extremely high. Though the costs are more favorable for capacitors and capacitor-based SVCs, their characteristics allow the output to drop the voltage low.

The system voltage needs to be kept at a predefined range, as high voltage can destroy the equipment and low voltages could cause the motor to stall and overheat equipment. [28] discussed the problems around voltage control on modern distribution networks. These problems are increasing load to the system which could either cause undervoltage or overvoltage. The suggested methods are using on-load tap changers [24]. STATCOM provides phase balancing, active filtering and reducing the flicker addition to the reactive compensation. The challenges to implementing the mentioned methods are dependent on the availability of funds

In [29], a method to control the voltage of the distribution networks with distributed generation using reactive power compensation is presented. The aim is to keep the voltage within the predefined range by regulating the reactive power of the compensators. This is achieved by deriving the voltage variation formula and then determining the reactive power compensation. Equation (1) and (2) shows the derived voltage variations ΔV_{ji} for small-scale systems and large systems, respectively.

$$\Delta V_{ji} \approx \frac{R_{ij}\left(P_{Gj} - P_{Lj}\right) + X_{ij}\left(\pm Q_{Gj} - Q_{Lj}\right)}{V_j} \qquad (1)$$

$$\Delta V_{ji} \approx \frac{R_{ij}\left(P_{Gj} - P_{Lj}\right) + X_{ij}\left(\pm Q_{Gj} \pm Q_{Cj} - Q_{Lj}\right)}{V_j} \qquad (2)$$

P_G *and* Q_G are the active power and reactive power respectively, supplied by the distributed generation and P_L and Q_L are the active and reactive power of the load respectively that is connected to the j^{th} bus of the system.

$$P_G \approx \frac{V_{GEN} - V_S + RP_L - X(\pm Q_C - Q_L \pm Q_G)}{R} \qquad (3)$$

For large distribution network

$$P_{Gj} \approx \frac{V_j - V_i + R_{ij}PL_j - X_{ij}\left(\pm QC_j - QL_j \pm QG_j\right)}{R_{ij}} \quad (4)$$

These equations depend on the voltage at the primary DES, at the receiving end, the size of conductors and load demand. The results obtained from simulations on a 15-bus Japanese system show that the voltage profile of the distribution network specified can be obtained by using reactive power compensation. In [30], Calderaro et al proposed a similar reactive power regulation approach for unbalanced distribution systems. This method is based on a sensitivity matrix which links the line-line voltage with the reactive power variation on each line. The reactive power in this case is obtained by solving the linear system. The proposed method is to measure the line-to-line voltages then calculate the reactive power variation to compensate for the voltage variation. [30] assumes that the distributed generation units are connected to the network by electronic power converters.

In [31] and [32], Su et al proposed a different method of controlling the secondary voltage and improving the voltage profile of the system using the Phasor Measurement Unit (PMU).Su in [32] presents an approach which uses PMU, measurements with timestamps as control feedback signals, to obtain an accurate and fast regulation of the voltage. The proposed algorithm acquires the time-synchronized measurements from the observed buses and compares the difference between the set-point voltage and that measured at each pilot bus. The adaptive secondary voltage control (ASVC) is triggered if the difference is greater than the desired value. The control actions are then computed and transmitted to the participating controllers. The author further explored the effect of an incoherent set of data such as different load disturbances on the SVC (Static Var Compensation) performance, and the effects of topology changes such as post-contingency situations like outages of transmission lines. Simulation results show that the proposed ASVC provides better results even under outage contingencies. In [31] however, more tests were done on the effects of an incoherent set of pilot voltage data such as different test systems, different number of pilot-bus, and different load disturbances. The approach considered a nonlinear optimal control model which considers unexpected disturbances.

In [33], Datta et al investigated the use of a battery energy storage system to improve the transient voltage and frequency stability of large power systems.

Recent research has focused on providing the voltage control in smart grids, as the transition from traditional grids to smart grids has been observed in different states. With different solutions to voltage stability, [34] has reviewed some of the challenges of voltage control in smart grids which also includes adaptation to wind and solar energy, voltage recovery, and delayed influenced by faults for the transmission grid, and the impact on distribution grids by high penetration of distributed energy resources.

V. FREQUENCY CONTROL

A. *Frequency Control Concepts*

The Frequency and voltage are the most important parameters of an electric power system. It is important to keep these parameters within the predefined constraints to avoid any disturbances to the system or even cause a system failure. The nominal/standard frequency in South Africa is 50 Hz. The system can operate at a certain allowed frequency range in its standard condition and cases where the system is in an emergency condition. The frequency in the power station varies because of imbalances that occur between generation and load. When such variations occur, it is important to initiate a control strategy to maintain the balance. There are three levels of control used to maintain this balance, and each level has its own purpose. The levels are:

Primary frequency control, an automatic function that restores balance between load and generation by adjusting the active power generation. It also stabilizes the frequency when there is a large generation or load outage [35, 36]. Secondary frequency control, which restores the frequency to its nominal value. This is after the frequency has been stabilized by the primary frequency control. There are designated generators to perform the secondary frequency control, and this is through a dedicated power reserve [37, 36]. And the final level is the tertiary frequency control also called the replacement reserve, its purpose is to restore the reserve margin used for the secondary control. The control level is not executed automatically, but upon request from the grid operator [36].

B. *Frequency control methodologies*

In [36], Rebours et al presented a document describing the frequency and voltage ancillary services in eleven power systems. This includes France, Australia, Belgium, Germany, Sweden, Great Britain, California, The Netherlands, New Zealand, PJM, and lastly Spain. The paper includes the technical features, requirements and a comparison of frequency and voltage control ancillary services across the eleven system. In part 2 of [37] the economic features are reviewed including the comparison of the ancillary market for the eight system.

In [38] and [39], Rijo and Wang discusses a control strategy to improve the performance of the primary frequency control, respectively. In [39], the strategy discussed involves using wind turbine generators with ancillary dynamic demand control. The strategy proposed through primary frequency control can provide rapid frequency support from timescale of inertial response. In [38], Rijo et al deploys PV sources and reviews the different control approaches of battery energy storage system to improve the inertial response.

Wu et al in [40] presented a method to control the secondary frequency and voltage for islanded microgrids which is based on distributed cooperative control. The presented method makes use of a sparse communication network. In this method, the distributed generation (DG) unit requires its local and neighbour information only to perform the control process.

VI. STATE OF SOUTH AFRICAN POWER NETWORKS

South Africa is currently facing challenges in generating sufficient electricity to meet the demand. Many plants are reported to be unavailable due to breaking down, maintenance, or repairs. Electricity consumption is continuously increasing with limited generation capacity [41], which causes a burden to the grid. As a result, South Africans have seen an increase in the implementation of load-shedding to avoid a total blackout. The increased unavailability of plants has seen extensive usage of emergency generation reserves, which are depleting faster than can be restored [42]. As it stands there are few generating plants available to cater for the whole country with the minimum solution available.

Load-shedding is caused when there is insufficient capacity to meet the demand. The generating capacity of ESKOM is lower than the load demand as such, some loads are sheds to accommodate for this instability [41]. The different stages implemented are associated with the amount of power to be shed for a set duration, ranging from two hours to six hours [43]. The sudden breakdowns in power stations also result in large capacity being unavailable [44]. The sudden breakdown could be due to delayed maintenance, outdated facilities, lack of skilled labour, or installations that degrade the delivery of the power to the consumers. These factors could lead to generators malfunctioning and losses in the transmission and distribution system which leads to loss of power.

The current plans for large scale variable renewable energy (VRE) resources are non-dispatchable and may not address these challenges since the system require voltage & frequency regulation and inertial response as additional power system quality service. Energy storage is an important means of delivering these services, but there are many uncertainties related to technology, market maturity, economics, and regulatory requirements [45]. In addition, South Africa earmarked these VRE for the reduction of carbon emissions due to the impact of fossil fuels to humanity [46].

It is evident from the literature presented that when it concerns the provision of ancillary services in South Africa, there is an opportunity to explore the different solutions taking into regard factors that affect the provision of services in South Africa. The presented solutions to dispatching voltage and frequency ancillary services have limitations when implemented in different states because of the policies, economic factors, technical, labour, capital, and politics, which plays a significant role in South Africa. There has not been an improvement in building new power stations to increase the generation capacity because of the costs involved and other factors. Therefore, solutions must be provided taking into consideration the resources available.

Many research opportunities may be explored such as the use of commercial buildings in providing ancillary services as well as exploring the integration of electric vehicles that has gained traction and has become an interest in different papers.

VII. CONCLUSION

In this paper, a literature review was done on the provision of ancillary services in different systems. This included power restoration, black start, and dispatching of voltage and frequency ancillary services in South Africa, with reference to other countries. Opportunities for further study have been identified in dispatching voltage and frequency control in the South African grid. Low generating capacity is still a problem in South Africa and the identified research opportunities such as utilizing commercial buildings for ancillary service provision could be further explored.

VIII. REFERENCE

[1] Y. Xiaoyan and L. Tolbert, "Ancillary services provided from DER with power electronics interface," *2006 IEEE Power Engineering Society General Meeting,* p. 8, 2006.

[2] Y.-T. Chou, C.-W. Liu, Y.-J. Wang, C.-C. Wu and C.-C. Lin, "Development of a Black Start Decision Supporting System for Isolated Power Systems," *IEEE Transactions on Power Systems,* vol. 28, no. 3, pp. 2202-2210, 2013.

[3] J. Zhao, Q. Zhang, Z. LIU and X. WU, "A Distributed Black-Start Optimization Method for Global Transmission and Distribution Network," *IEEE Transactions on Power Systems,* vol. 36, no. 5, pp. 4471-4481, 2021.

[4] A. A. Peña, S. A. Gómez, J. L. Rodriguez-Amenedo and M. Á. Cardiel-Álvarez, "Decentralized Frequency Control for Black Start of Full-Converter Wind Turbines," *IEEE Transactions on Energy Conversion,* vol. 36, no. 1, pp. 480-487, 2021.

[5] W. Feng, X. Xuanyi, S. Qiuqin, C. Chun, B. Feng, C. She and F. Jingmin, "Service restoration for distribution network with DGs based on stochastic response surface method," *International Journal of Electrical Power & Energy Systems,* vol. 107, pp. 557-598, 2019.

[6] Y. Hao, Z. Lin, Y. Ding, Y. Liu, L. Sun and Y. Yan, "A Model Predictive Control Based Generator Start-Up Optimization Strategy for Restoration With Microgrids as Black-Start Resources," *IEEE Transactions on Power Systems,* vol. 33, no. 6, pp. 7189-7203, 2018.

[7] G. Patsakis, D. Rajan, I. Aravena, J. Rios and S. Oren, "Optimal Black Start Allocation for Power System Restoration," *IEEE Transactions on Power Systems,* vol. 33, no. 6, pp. 6766-6776, 2018.

[8] P. Demetriou, M. Asprou and E. Kyriakides, "A Real-Time Controlled Islanding and Restoration Scheme Based on Estimated States," *IEEE Transactions on Power Systems,* vol. 34, no. 1, pp. 606-615, 2019.

[9] J. Li, H. You, J. Qi, M. Kong, S. Zhang and H. Zhang, "Stratified Optimization Strategy Used for Restoration With Photovoltaic-Battery Energy Storage Systems as Black-Start Resources," *IEEE Access,* vol. 7, pp. 127339-127352, 2019.

[10] ESKOM, "Ancillary Services Technical Requirements for 2022/23-2026-27," November 2021. [Online]. Available: https://www.eskom.co.za/wp-content/uploads/2022/04/Ancillary-Services-Technical-Requirements-2022_23-to-2026_27.pdf. [Accessed August 2022].

[11] C. van Dongen and B. Bekker, " Valuation of Pumped Storage in Capacity Expansion Planning-A South African Case Study," *Energies,* vol. 14, p. 6999, 2021.

[12] E. a. P. V. Kaushik, O. P. Mahela, B. Khan, A. El-Shahat and A. Y. Abdelaziz, "Comprehensive Overview of Power System Flexibility during the Scenario of High Penetration of Renewable Energy in Utility Grid," *Energies,* vol. 15, no. 2, 2022.

[13] F. D. Moya, G. D. M. Jannuzzi and L. C. P. Da Silva, "Distributed generation for the provision of operating reserves," in *2008 IEEE/PES Transmission and Distribution Conference and Exposition: Latin America*, 2018.

[14] E. Ibanez, I. Krad and E. Ela, "A systematic comparison of operating reserve methodologies," in *2014 IEEE PES General Meeting | Conference & Exposition*, 2014.

[15] M. Talaat, M. Elkholy and M. Farahat, "Operating reserve investigation for the integration of wave, solar and wind energies," *Energy ,* vol. 197, p. 117207, 2020.

[16] L. Bongers, N. Mararakanye and B. Bekker, "Operating Reserve Dimensioning Methodologies for Renewable Energy Aligned Power Systems," in *2021 56th International Universities Power Engineering Conference (UPEC)*, 2021.

[17] J. Chen, W. Wu, B. Zhang, B. Wang and Q. Guo, "A Spinning Reserve Allocation Method for Power Generation Dispatch Accommodating Large-Scale Wind Power Integration," *Energies,* vol. 6, pp. 5357-5381, 2017.

[18] D. Gezer, A. Nadar, C. Şahin and N. Özay, "Determination of operating reserve requirements considering geographical distribution of wind power plants," 2011.

[19] J. Xiao, B.-M. S. Hodge, J. F. JPekny and G. V. Reklaitis, "Operating reserve policies with high wind power penetration," *Computers & Chemical Engineering,* vol. 35, no. 9, pp. 1876-1885, 2011.

[20] B. Hassan, G. Hêmin, A. R. Messina, N. Hatziargyriou, F. Milano and T. Ise, "Power system frequency control: An

updated review of current solutions and new challenges," *Electric Power Systems Research,* vol. 194, 2021.

[21] E. HIRST and B. Kirby, "Ancillary Services Detail: Voltage Control," 1997. [Online]. Available: http://www.consultkirby.com/files/con453_Voltage_Control.pdf.

[22] Y. Ma, A. Huang and X. Zhou, "A review of STATCOM on the electric power system," in *2015 IEEE International Conference on Mechatronics and Automation (ICMA)*, 2015.

[23] J. d. A. Barros and R. I. Diego, "A review of international limits for rapid voltage changes in public distribution networks," *Renewable and Sustainable Energy Reviews,* vol. 144, p. 110966, 2021.

[24] T. Xu and P. Taylor, "Voltage Control Techniques for Electrical Distribution Networks Including Distributed Generation," *IFAC Proceedings Volumes,* vol. 41, no. 2, pp. 11967-11971, 2008.

[25] P. a. G. P. S. a. H. N. D. Moutis, "Voltage Regulation Support Along a Distribution Line by a Virtual Power Plant Based on a Center of Mass Load Modeling," *IEEE Transactions on Smart Grid,* vol. 9, no. 4, pp. 3029-3038, 2018.

[26] V. Calderaro, V. Galdi, F. Lamberti and A. Piccolo, "A Smart Strategy for Voltage Control Ancillary Service in Distribution Networks," *IEEE Transactions on Power Systems,* vol. 30, no. 1, pp. 494-502, 2015.

[27] H. Li, F. Li, Y. Xu, D. T. Rizy and J. D. Kueck, "Adaptive Voltage Control With Distributed Energy Resources: Algorithm, Theoretical Analysis, Simulation, and Field Test Verification," *IEEE Transactions on Power Systems,* vol. 25, no. 3, pp. 1638-1647, 2010.

[28] R. O'Gorman and M. A. Redfern, "Volatge Control Problems on Modern Distribution Systems," in *IEEE Power Engineering Society General Meeting*, 2004.

[29] M. A. a. H. M. J. a. P. H. R. a. N. A. B. M. Mahmud, "Voltage control of distribution networks with distributed generation using reactive power compensation," in *IECON 2011 - 37th Annual Conference of the IEEE Industrial Electronics Society*, 985-990, 2011.

[30] V. Calderaro, V. Galdi, F. Lamberti, A. Piccolo and G. Graditi, "Voltage support control of unbalanced distribution systems by reactive power regulation," in *IEEE PES Innovative Smart Grid Technologies, Europe*, Europe, 2014.

[31] H.-Y. Su and C.-W. Liu, "An Adaptive PMU-Based Secondary Voltage Control Scheme," *IEEE Transactions on Smart Grid,* vol. 4, no. 3, pp. 1514-1522, 2013.

[32] H.-Y. Su, F.-M. Kang and C.-W. Liu, "Transmission Grid Secondary Voltage Control Method Using PMU Data," *IEEE Transactions on Smart Grid,* vol. 9, no. 4, pp. 2908-2917, 2018.

[33] U. Datta, A. Kalam and J. Shi, "Battery Energy Storage System to Stabilize Transient Voltage and Frequency and Enhance Power Export Capability," *IEEE Transactions on Power Systems,* vol. 34, no. 3, pp. 1845-1857, 2019.

[34] H. Sun, Q. Guo, J. Qi, V. Ajjarapu, R. Bravo, J. Chow, Z. Li, R. Moghe, E. Nasr-Azadani, U. Tamrakar, G. N. Taranto, R. Tonkoski and G. Valverde, "Review of Challenges and Research Opportunities for Voltage Control in Smart Grids}," *IEEE Transactions on Power Systems,* vol. 34, no. 4, pp. 2790-2801, 2019.

[35] G. Chown and B. Wigdorowitz, "A methodology for the redesign of frequency control for AC networks," *IEEE Transactions on Power Systems,* vol. 19, no. 3, pp. 1546-1554, 2004.

[36] Y. G. Rebours, D. S. Kirschen, M. Trotignon and S. Rossignol, "A Survey of Frequency and Voltage Control Ancillary Services—Part I: Technical Features," *IEEE Transactions on Power Systems,* vol. 22, no. 1, pp. 350-357, 2007.

[37] Y. G. Rebours, D. S. Kirschen, M. Trotignon and S. Rossignol, "A Survey of Frequency and Voltage Control Ancillary Services—Part II: Economic Features," *IEEE Transactions on Power Systems,* vol. 22, no. 1, pp. 358-366, 2007.

[38] R. Rijo, M. F. Francis and Y. Yongheng, "Primary frequency control techniques for large-scale PV-integrated power systems: A review," *Renewable and Sustainable Energy Reviews,* vol. 144, p. 110998, 2021.

[39] S. Wang and K. Tomsovic, "Fast Frequency Support From Wind Turbine Generators With Auxiliary Dynamic Demand Control," *IEEE Transactions on Power Systems,* vol. 34, no. 5, pp. 3340-3348, 2019.

[40] X. Wu, C. Shen and R. Iravani, "A Distributed, Cooperative Frequency and Voltage Control for Microgrids," *IEEE Transactions on Smart Grid,* vol. 9, no. 4, pp. 2764-2776, 2018.

[41] M. Smit, D. Schoeman and F. Rust, "Forecasting Photovoltaic Electricity Generation at a Private Dwelling in Tshwane, South Africa: A Case Study," *International Journal of Science and Research (IJSR),* vol. 9, no. 9, pp. 1014-1027, 2020.

[42] ESKOM, 24 June 2022. [Online]. Available: https://www.eskom.co.za/to-conserve-emergency-generation-reserves-loadshedding-will-be-implemented-to-stage-4-from-1100-am-until-midnight-tonight/. [Accessed September 2022].

[43] N. E. Mabunda, "Use of Photovoltaic Energy to Minimize the Impact of Load-shedding in South Africa," *2021 International Conference on Electrical, Computer and Energy Technologies (ICECET),* pp. 1-4, 2021.

[44] Eskom, 20 May 2022. [Online]. Available: https://www.eskom.co.za/to-preserve-the-emergency-generation-reserves-the-implementation-of-stage-2-loadshedding-will-now-start-at-0800-until-2200-both-on-saturday-and-sunday/. [Accessed 28 September 2022].

[45] N. McIlwaine, A. M. Foley, D. J. Morrow, D. Dlzar Al Kez, C. Zhang, X. Lu and R. J., "A state-of-the-art techno-economic review of distributed and embedded energy storage for energy systems," *Energy,* vol. 229, p. 120461, 2021.

[46] M.-A. Mutombo and B. Numbi, "Assessment of renewable energy potential in Kwazulu-Natal province, South Africa," *Energy Reports,* vol. 5, pp. 874-881, 2019.

Artificial Intelligence Solution for Energy Management

AA Yusuff*, T Mosetlhe*
*Department of Electrical Engineering
University of South Africa
Johannesburg, South Africa
Email: yusufaa,mosettc@unisa.ac.za

***Abstract*—This paper discusses energy management and areas of application of artificial intelligence to energy management. World electricity and total final consumption by sector (i.e Industry, Transport, Commercial, etc) as well as electricity consumption of two top economic power in Africa, South Africa and Nigeria were presented.**

***Index Terms*—Energy management, total final energy consumption, energy transportation, artificial intelligence.**

I. Introduction

Right from time immemorial access to sources of energy and energy management have occupied a place of prime importance in affairs of homo sapiens. Humans have domesticated animals to till the ground for farming, as well as for transportation. Likewise humans have put fetters and chains on other humans to work in sugar cane farms, build temples or pyramids.

The prosperity of nations is closely related to the amount of energy they use, and in some cases, the sales of primary sources of energy.

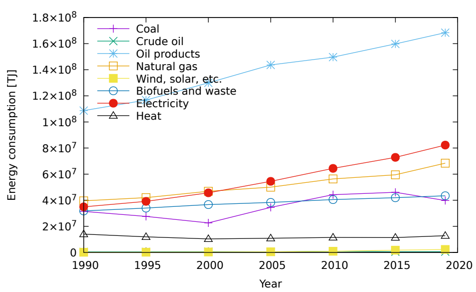

Fig. 1: World total final consumption by source [2].

It is evident from Figure 1 that oil products and electricity are the major sources of energy in the world. Is energy the root of good or evil? In recent time, possession of a large abundance of primary sources of energy may be more of a curse than blessing - Iraq, Nigeria, Libya, Syria.

A. The militarization of energy security

Energy is a necessity for socioeconomic development. Nations, corporate bodies, people seek for vantage positions, so that they can make other entities do things for them at little cost or if possible no cost at all.

Large-scale conflict among developed, developing and underdeveloped states is a possibility as a result of energy security or market share. Developed and powerful states may not be reluctant to use force to ensure energy security. One example that easily comes to mind is Iraq and Libya. Energy security is central to national security, and any threats to energy security of any nation is tantamount to national security. In essence, energy security is *casus belli*.

B. Energy management

The term energy management means different things to different people [1]. We will define it as: An effective and judicious use of energy in order to minimise the cost of energy utilisation, power generation and environmental impact.

Some desirable subobjectives of energy management from end users perspective include:

- Energy efficiency, reduction of energy use and consequently reduction of required total installed generation capacity.
- Effective monitoring, report and presentation of energy usage in an easily accessible manner.
- Reduction of environmental pollution and global warming.

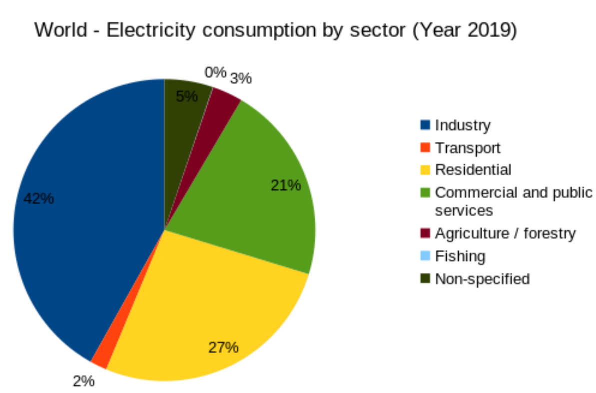

Fig. 2: World electricity consumption by sector 2019 [2].

The major targets of energy management are:

- Commercial and public services
- Industry

- Transport
- Residential
- Agriculture/forestry
- Fishing

The World electricity consumption by sector in year 2019 is shown in Figure 2. from the figure, the major consumers are (1) Industry, (2) Residential & (3) commercial and public services. The targets will generally vary from one country to another, depending on many factors.

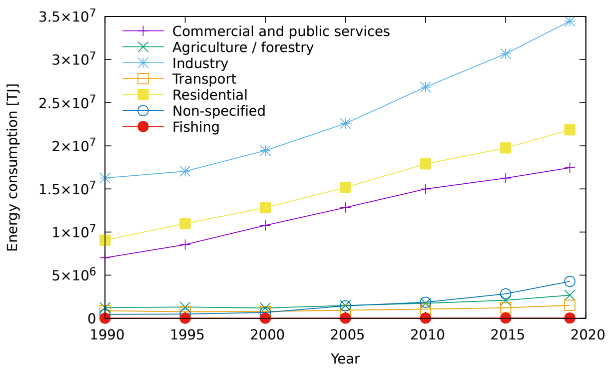

(a) Electricity consumption.

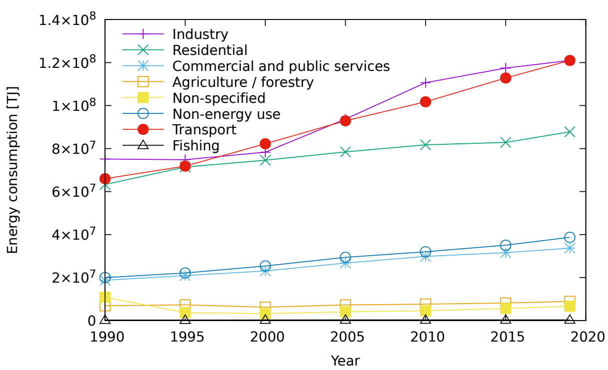

(b) Total energy consumption.

Fig. 3: World electricity and total final consumption by sector [2].

Over the past 30 years, the major consumer of electricity in the world are industry, residential and commercial & and public services. Similarly, if one considers World total final consumption of electricity as shown in Figure 3, industry, transport and residential are at the top. These are the sectors that energy management schemes should focus on.

The consumption of electricity in South Africa and Nigeria is depicted in Figure 4. The major consumption in Nigeria is from residential loads, while for the case of South Africa (SA), it is the industry. The first three major consumers in SA , which are, industry, residential, and commercial consume considerably higher than Nigeria. The flattening of consumption from year 2021 is as a result of energy management roll out (Demand side management.

Total final consumption (TFC) by sector for Nigeria and South Africa is depicted in Figure 5. The major consumption

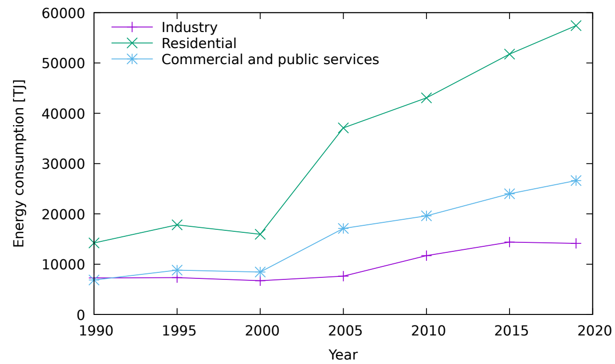

(a) Nigeria.

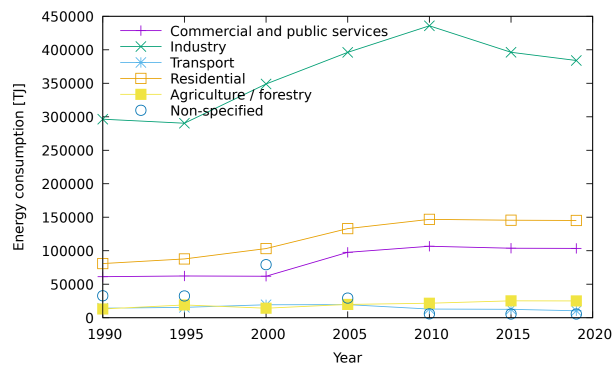

(b) South Africa.

Fig. 4: Electricity consumption in South Africa and Nigeria [2].

in Nigeria and South Africa are still residential and industry respectively. The TFC for industry in SA has flattened and it is already on the negative trend. The TFC at year 2019 for residential in Nigeria is more than the sum of TFC of industry, transport and residential in SA.

Total final consumption (TFC) by sources Nigeria and South Africa is depicted in Figure 6. The major sources of energy in Nigeria are biofuels & waste and oil products. Oil products, coal and electricity are the major sources of energy in South Africa. Although use of oil products and coal are on the rise, however, electricity usage is on the negative trend.

An example of breakdown of total final consumption on the basis of electricity, energy utilisation by sector and energy consumption by sources for a country in a year, in this case, Nigeria, are shown in Figure 7, Figure 8 and Figure 9 respectively. In Figure 9, although the percentage contribution of electricity is small, energy management can still be implemented in residential loads. Energy management can substantially reduce energy costs and energy consumption. The saved energy can be used elsewhere. Energy available from energy management is economical compared to a large-scale energy production. It leads to less consumption of energy resources which are scarce commodities.

Electric power is the easiest mode of energy delivery. Once an electric network is in place, electric power can be delivered

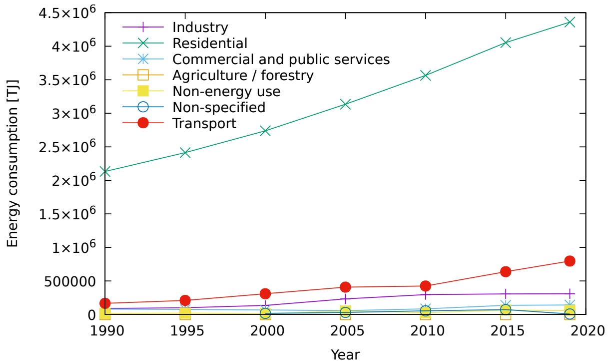

(a) Nigeria.

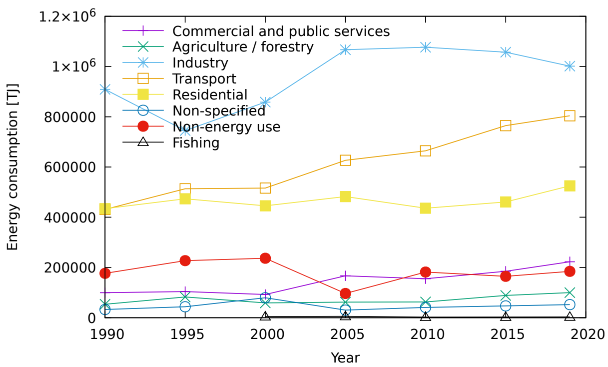

(b) South Africa.

Fig. 5: Total final consumption by sector in South Africa and Nigeria [2].

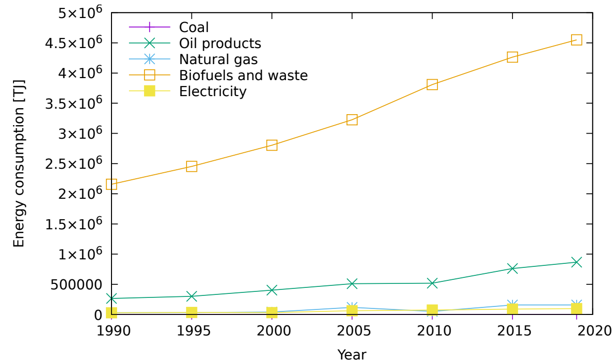

(a) Nigeria.

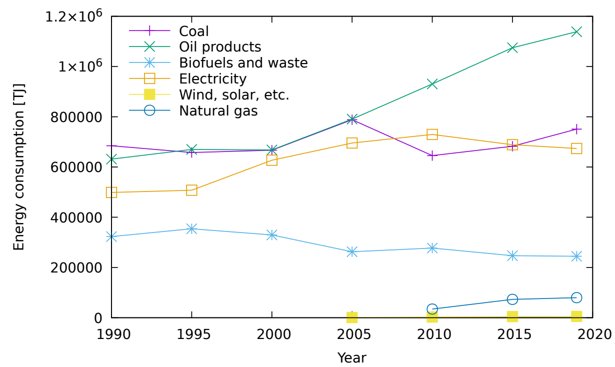

(b) South Africa.

Fig. 6: Total final consumption by source in South Africa and Nigeria [2].

in a twinkle of an eye. The electrical energy at its point of end-use always contains 3412 Btu per kWh. When electrical energy is generated from fossil fuels such as coal, oil or gas, it takes about 10,000 Btu of primary fuel to produce one kWh of electrical energy as a result of thermal losses.

Another reason for energy management is population explosion, especially in Africa. The expected World population in 2020 and 2050 [3] is presented in Table I. Africa is the only continent that has a positive growth in population, i.e 17.43% in 2020 to 30.45% growth in 2050.

Electricity generations per capital in different regions of Africa and the World are presented in Table II. Despite the fact that the population of Africa constitute 17.40% of the World population, however the total electricity generation in Africa is 3.22% of the World.

II. Economy of Energy Transportation

The purpose of energy delivery system is to reduce the cost of energy transportation. Electric transmission network, pipelines for natural gas or hot water are examples of delivery infrastructure. It determines the number of entities that can use or tap energy simultaneously. Energy delivery systems are expensive to build, especially when they cover large geographical area, hence it is essential to use energy efficiently or minimise its use.

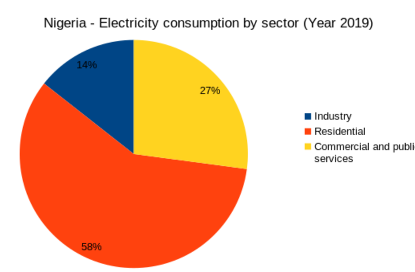

Fig. 7: Nigeria electricity consumption by sector 2019 [2].

Electric power system is a secondary energy delivery system. Its prevalence lies in the amalgamation of most primary sources through transmission network to ease energy delivery. The bulk of energy management schemes have been implemented by consumers of electricity. This is understandable because electricity is the second major source of energy in the world. In addition, the speed and its easy of transportation is not comparable to any other energy source.

III. Artificial Intelligence

It is of no doubt that, the most important asset of human beings is our brain (Intelligence). Over thousand of years, we have extended our human capacity or capability limits by developing machines, devices and maybe entities that can supplement our inadequacy.

TABLE I: Expected World population in 2020 with percentage (Numbers are in million) [3]

	Year 2020	%	Year 2020 age < 60 year	%	Year 2050 age < 60 year	%
Africa	1339.5	17.43	1265.10	19.06	2298.50	30.35
Asia	4539.6	59.08	3936.40	59.29	3895.80	51.44
Europe	749.3	9.75	558.20	8.41	469.70	6.20
Latin Am.& Carib	644.3	8.38	561.70	8.46	559.20	7.38
N. America	370.5	4.82	283.70	4.27	309.90	4.09
Oceania	41.1	0.53	33.80	0.51	40.00	0.53
World	7684.3	100.00	6638.9	100.00		100.00

TABLE II: Electricity generation per capital in Africa[4]

Region	Population	%	TW-hours	%	kWh per capital
Northern Africa	250083818	3.18	382.1	1.41	1527.89
Eastern Africa	455270262	5.79	115.3	0.43	253.26
Western Africa	410798807	5.22	75.4	0.28	183.54
Southern Africa	68263781	0.87	257.1	0.95	3766.27
Central Africa	184111505	2.34	40.3	0.15	218.89
Sub Sahara Africa	1118444355	14.22	488.1	1.81	436.41
Total Africa	1368528173	17.40	870.1	3.22	635.79
Total World	7865412337	100.00	27004.7	100.00	3433.35

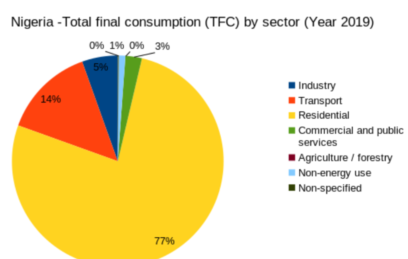

Fig. 8: Nigeria total final consumption by sector 2019 [2].

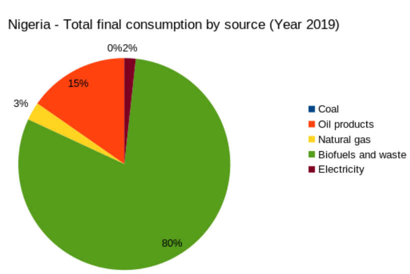

Fig. 9: Nigeria total final consumption by source 2019 [2].

- Mechanical and electric machines were developed to overcome the limit of force, torque that we can apply as humans.
- Motor vehicle, aeroplane, ships were developed to reduce amount of time required to travel over a long distance.
- If there is no need for material transportation, telecommunication and information communication technology can even reduce the needed travel time further.

If there is any positive thing about Covid-19, it has accelerated the adoption of certain digital technologies.

Artificial Intelligence (AI) is a big field. It encompasses logic, probability, and continuous mathematics, computer science [5]. Artificial intelligent algorithms include artificial neural networks, evolutionary computation, swarm intelligence, artificial immune systems, fuzzy systems, logic, deductive reasoning, expert systems, case-based reasoning and symbolic machine learning systems. AI can be seen as a combination of several research disciplines, such as, computer science, physiology, philosophy, and biology.

AI is currently being used in the following areas of applications:

- Robotic vehicles, commercial robotic taxi service.
- Autonomous planning and scheduling.

- Machine translation.
- Speech recognition.
- Recommendations.
- Medicine.
- Predictive modelling and control.
- Machine fault diagnosis, prognosis.

A. *Artificial Intelligence in energy management*

AI techniques are generally used in formulating high fidelity energy consumption models from data. The predictive models are then combined with additional AI schemes that can be used in real-time or near real time operation of appliances or devices. Good data are prerequisite for good models. Nevertheless, there are algorithms that are tolerant to missing data or bad data. The only consequence of bad data is the large training time that will be needed to get good or satisfactory performance. Bad data are like bad study materials. They are difficult to understand.

Some of the areas where AI solutions have been proffered in energy management are:

- short-term forecast of load consumption, daily forecast of load consumption prediction and a year ahead forecast of load consumption prediction [6]
- appliance load signature extraction
- development of load data-driven models
- Heating, Ventilation, and Air Conditioning (HVAC) control optimisation [7]
- charging of electric vehicle and vehicle travel time minimisation [8]
- optimal train control, scheduling and timetable optimisation
- Demand Response Management
- Coordinated Energy Management of Prosumers [9]

B. *Artificial Intelligence solution for energy management*

Some of schemes that are have been used for effective energy management are:

- Artificial neural network (ANN)
- Random forest (RF) model
- Emotional neural networks (ENNs)
- Support vector machine (SVM) and support vector regression
- Genetic algorithm (GA)
- Extreme learning machine (ELM)
- Convolutional Neural Networks (CNN)
- Adaptive Neuro-Fuzzy Inference System (ANFIS)

There are couples of companies that are already marketing AI solutions for energy management. AI solutions should be adaptive to context.

C. *Risks consideration*

The potential of using AI to free man from menial repetitive work sounds great. Even much more is the associated increase production of goods and services, as well as profit margins. Although AI can reduce or manage energy consumption and a host of other things, nevertheless, we should be aware of the risks if something goes wrong. It is not even impossible to subvert individual independence and democratic values, given the amount of data that are constantly collected just in the name of training AI schemes. Cybersecurity is also a concern that should be addressed when implementing solutions that use AI framework.

IV. SUMMARY

Energy management is a necessity in view of population explosion and non-renewable energy sources being limited. The world total final consumption of energy from non-renewable energy sources is linear, this will lead to a non-linear depletion rate. AI based solutions have been extensively used other fields, hence is not by accident that AI has been incorporated in to energy management. AI has a great potential in reducing energy consumption, but it is equally important not to overlook the risks associated with implementing AI-based solutions.

REFERENCES

[1] W. J. K. Barney L. Capehart, Wayne C. Turner, *Guide to energy management*, 5th ed. Fairmont Press; Distributed by CRC/Taylor and Francis, 2006.

[2] International Energy Agency, "IEA World Energy Balances," "https://www.iea.org/data-and-statistics/data-product/world-energy-statistics-and-balances", 2019, accessed: 2021-11-08.

[3] U.S. Census Bureau, "International data base," "https://www.census.gov/data-tools/demo/idb/informationGateway.php", 2019, accessed: 2021-05-25.

[4] United Nations Environment Programme (UNEP), "Atlas of africa energy resources," "https://energypedia.info/images/c/c7/Atlas_Africa_Energy_Resources.pdf", 2017, accessed: 2021-05-25.

[5] P. N. Stuart Russell, *Artificial Intelligence: A Modern Approach (Pearson Series in Artifical Intelligence)*, 4th ed. Pearson, 2020.

[6] Z. Chen, Y. Sun, X. Ai, S. M. Malik, and L. Yang, "Integrated demand response characteristics of industrial park: A review," *Journal of Modern Power Systems and Clean Energy*, vol. 8, no. 1, pp. 15–26, January 2020.

[7] R. Kannan, M. S. Roy, and S. H. Pathuri, "Artificial intelligence based air conditioner energy saving using a novel preference map," *IEEE Access*, vol. 8, pp. 206 622–206 637, 2020.

[8] Y. Zheng, J. Luo, X. Yang, and Y. Yang, "Intelligent regulation on demand response for electric vehicle charging: A dynamic game method," *IEEE Access*, vol. 8, pp. 66 105–66 115, 2020.

[9] J. Hu, J. Wu, X. Ai, and N. Liu, "Coordinated energy management of prosumers in a distribution system considering network congestion," *IEEE Transactions on Smart Grid*, vol. 12, no. 1, pp. 468–478, Jan 2021.

Comparative Study of Deep Learning Techniques for Breakdown Prediction in Pump Sensor Systems

Simba Chawanda and Peter Olukanmi
simbachawanda@gmail.com; polukanmi@uj.ac.za

Department of Electrical and Electronic Engineering Technology (DEEET),
Faculty of Engineering and the Built Environment,
University of Johannesburg

***Abstract*—In the current fourth industrial revolution, data plays a crucial role in providing insights about engineering systems. This paper studies artificial intelligence techniques for predicting the occurrence of anomalies, which are breakdowns in pump sensors. Among artificial intelligence techniques, deep learning methods are in high demand due to their ability to perform automated feature engineering. The techniques studied in this work belong to this class. They include the Long short-term memory (LSTM), Temporal Convolutional Network (TCN) and the Multi-Layer Perceptron(MLP).**

Keywords—Anomaly detection, Predictive Maintenance, Long Short-Term Memory (LSTM), Temporal Convolutional Network (TCN), Multi-Layer Perceptron (MLP)

I. INTRODUCTION

There are three types of maintenance exercises. The first and most rudimentary form is known as reactive maintenance which is maintenance done only once the machine has broken [1]. The second type of maintenance is known as planned maintenance where maintenance is at certain intervals to lessen the chance of a breakdown [1]. Research has shown that maintenance accounts for anywhere between 15% to 70% of the net production costs [2]. Most manufacturing industries continue to rely on traditional maintenance (reactive & planned) practices that emphasise inefficient run-to-failure strategies or statistically trend-driven maintenance intervals [2]. While these traditional maintenance strategies undoubtedly help with preventing breakdowns, maintenance studies show that about 33 cents for every dollar spent on maintenance are lost due to redundant maintenance tasks [2]. The combination of well-developed sensors and predictive algorithms enables a pretty accurate estimate of plant equipment's remaining useful life [2].

In the manufacturing industry prices of products tend to be incredibly competitive. These prices are heavily influenced by manufacturing efficiency and dependability. Machines and automatons are critical components of the production process [3]. This implies that if a device breaks, it will result in financial losses due to production downtime [3]. Examples of predictive maintenance as follow [4]:

- Equipment vibrations may indicate bearing wear or mechanical part damage.
- A motor's temperature and current changes may suggest that friction and possibly mechanical fault are reducing performance.
- The particle count in a lubricant shows the excessive wear caused by friction from contact components.

· Industrial big data analysis, medical and health big data analysis, financial big data analysis, and even aerospace big data analysis all benefit from time series anomaly detection [5]. The size of time series data grows dramatically as information technology advances, increasing the complexity of detecting time series anomalies [5]. Deep learning has seen a lot of success in the last decade and is now frequently employed in the field of anomaly detection [5].

Solving the problem of anomaly detection can be divided into three categories: statistical modelling, data mining-based techniques, and machine learning-based methods [6].

Statistical modelling algorithms include the Gaussian mixture model, regression-based models, histogram-based outlier detection. The disadvantage of these techniques is that they rely on the assumption that the data is generated in a certain statistical distribution. [6].

Using data mining techniques such as clustering or classification to improve anomaly detection is one solution [6]. For grouping comparable data points, researchers have largely employed K-means clustering [6]. In smaller datasets These techniques they may not provide reliable insights at the appropriate degree of detail [6].

Various neural network models, such as recurrent neural network (RNN)and back propagation neural network (BPNN), were designed to monitor the abnormalities of a sophisticated system as artificial intelligence progressed [6]. These techniques perform well in some niche applications, but generality remains a major difficulty [6]. The generative adversarial network (GAN) , Long Short-Term Memory (LSTM), convolutional neural network (CNN) as well as other autoencoders are among the most often used deep learning methods [6]. Almost all of the above models have been used to classify anomalies in previous research [6].

A. *LSTM autoencoders*

LSTM networks are a subset of recurrent neural networks, which are more generally known as (RNN) [5]. The ability of RNNs to save information, or cell state, for subsequent usage in the network is a critical feature [5]. As a result, they're especially well-suited to learning time-series data that tends to evolve as time progresses [5]. "Speech recognition, text translation [5]." and, in our scenario, the processing of sequential sensor data for anomaly detection, all use LSTM networks [5].

The input to RNNs consist of the current data point and the previously observed data point [6]. That means the prediction the RNN makes at time t is influence by the prediction that was made at time $t-1$ [6]. In essence, RNNs contain internal memory that keeps information about the computations that were made from a previous input [6]. This internal memory – in the simplest form - consists of a single hidden vector $\mathrm{h_t}$, with the equation $\mathrm{h_t} = \tanh(\mathrm{W_{hh}h_{t-1}} + \mathrm{W_{xh}x_t})$ [7]. Notice there are two terms inside the hyperbolic tan function, with one being dependent on the past hidden state $\mathrm{h_{t-1}}$ and the other being based on the current input $\mathrm{x_t}$ [7]. These terms are added together and the hyperbolic tan function ensures that the output stays within the [-1, 1] [7].

The LSTM was created to deal with the drawbacks of using RNNS [8]. The $\mathrm{x_t}$ and $\mathrm{h_{t-1}}$ work together in a more intricate manner that include multiplicative interactions in order to make the recurrence formula far more superior to the RNN. Furthermore, the LSTM recurrence employs additive interactions over time steps to more effectively backpropagate gradients in time [8]. The LSTM also has an additional memory vector $\mathrm{c_t}$ and can therefore choose to read from a cell, write to a cell, or reset a cell using explicit gating techniques [8].

The LSTM can be expressed mathematically as follows [8]:

$$\mathrm{c_t} = \mathrm{f} \odot \mathrm{c_{t-1}} + i \odot \mathrm{g}$$
$$\mathrm{h_t} = o \odot \tanh(\mathrm{c_t})$$

$\odot$ is elementwise multiplication

$$\begin{pmatrix} i \\ f \\ o \\ g \end{pmatrix} = \begin{pmatrix} sigm \\ sigm \\ sigm \\ tanh \end{pmatrix} W\left(\begin{matrix} \mathrm{x_t} \\ \mathrm{h_{t-1}} \end{matrix}\right)$$

The three vectors $i, f, o \in \mathbb{R}^H$ can be interpreted as binary gates that regulate the manner in which the memory cell is updated, reset to zero, or has its local state exposed in the hidden vector [8]. Because the activations of these gates are based on the sigmoid function, they may vary smoothly between zero and one to maintain the model distinguishable [8]. Furthermore, because the activations of these gates are based on the sigmoid function, their values vary fluidly between 0 and 1 to maintain the models distinguishability [8]. The vector $g \in \mathbb{R}^H$ has a value between negative one and one and is used to alter the memory contents additively [8]. Because a sum operation only evenly distributes gradients during backpropagation, this additive interaction is a crucial component of the LSTM's architecture which permits gradients on memory cells c to flow backwards through time indefinitely, or at least until disturbed by the multiplicative interaction of an active forget gate [8].

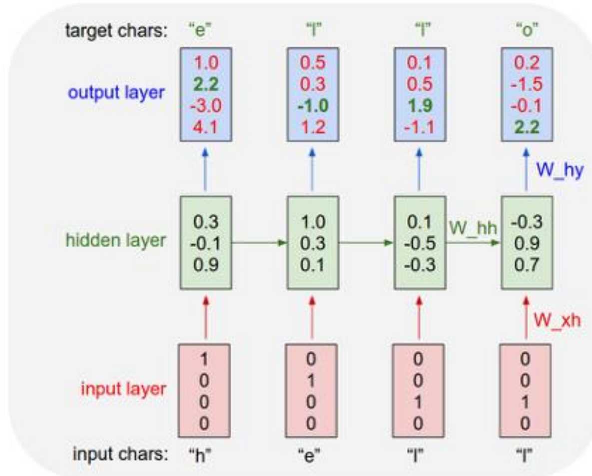

Fig 1. An example of an RNN being used to predict a sequence of characters [8]

We can see from the figure 4, a RNN as a character level model, where the goal is to predict the next character of the word at e ach time stamp. Notice that the input is a vector of 4 elements, this is because the vocabulary the model can use contains 4 different possible characters: h, e, l, o. The model can only understand numeric data so the characters are converted using one hot encoding. So the model can distinguish letters by checking where the "1" is in the input vector. In our example:

$$\begin{matrix}1\\0\\0\\0\end{matrix} = "h", \begin{matrix}0\\1\\0\\0\end{matrix} = "e", \begin{matrix}0\\0\\1\\0\end{matrix} = "l", \begin{matrix}0\\0\\0\\1\end{matrix} = "o"$$

Our output also has a vector of 4 elements and it works similarly to the input with the only difference being that instead of returning a binary digit for each element it returns a score which acts as a prediction for which character the model thought should come next. Notice that the numbers highlighted in green represent what the output should've been and so the RNN uses the loss function and gradients to incentivise the scores of the correct characters to become higher and the scores of the wrong characters to become lower [8].

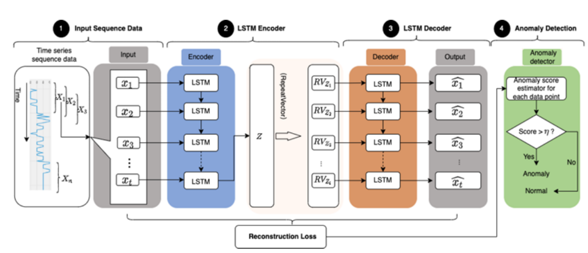

Fig 2. LSTM Autoencoder working principle to detect anomalies [9]

As we can see in figure 5, once we've created an LSTM autoencoder model that can predict data points in the future we can define an anomaly as an observation that deviates from the norm of the data as set by a certain threshold [9]. The threshold can be set as a selection point to determine how much an observation deviates from the norm. Anomalies are defined as observations that exceed the threshold [9].

B. Temporal Convolutional Networks

Given a time series X, where each point $x_t \in R^m$ is a vector representing the input variables at time step t. A prediction model attempts to forecast the future l values given a window of length L of previous time series values as input variables [10]. So to forecast the next l values of an input time series, a temporal convolutional network can be trained. After training the Temporal Convolution Network (TCN) model on a normal time series, the residuals between the predicted values and the real values are obtained, and a multivariate Gaussian distribution model is fitted [10]. The prediction errors are then utilized to determine the likelihood of anomalous points in the test time series.

TCN have piles of casual convolutional networks that ensure that the TCN model doesn't scan values in the future, which in turn encourage the model to make prediction instead of 'cheating' [11]. TCNs also have residual connections(which also increase the models stability) and dilated convolutions to help the model remember information it saw in the past [11].

A 1-dimensional convolution can be expressed mathematically as follows [11]:

$$g[i] = \sum_{l=1}^{L} f[i + d \cdot l]h[l]$$

Where $g[i]$ and $f[i]$ are the output and input respectively [11]. The TCN has two major constraints: the network's output should be the same length as its input, and the network may only use information from previous time steps [10]. To meet these temporal criteria, TCN employs a 1-D fully-convolutional network design, in which all convolution layers are the same length, with zero padding to ensure that higher layers are the same length as preceding ones [10].

One paper proposed using not only a TCN but also a gaussian mixture model in conjunction with the convolutional network as seen in figure 3 [12]. The Gaussian mixture model (GMM) is a weighted linear combination of numerous Gaussian components that is frequently used to handle the problem of data with various distributions [12]. GMM may be used to simulate intricate structures and can seamlessly approximate the density distribution of any forms [12]. We can see an example of this figure 6.

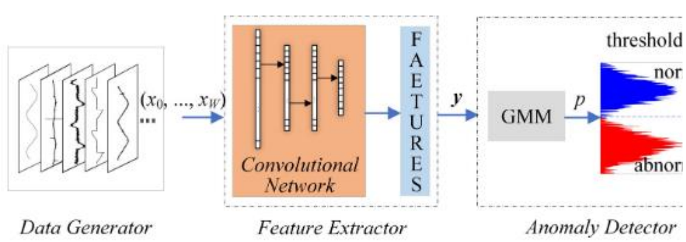

Fig 3. TCN with GMM [12]

Using a sliding window, samples of datasets are taken from time series, and the dataset is partitioned into training and testing datasets in a 1:4 ratio [12]. Then we undertake supervised TCN training using focal loss and centerloss [12]. A basic cross-validation approach is utilized to verify the model's performance during the training phase [12].

C. Multi-Layer Perceptron

The most popular and widely used kind of neural network is the multilayer perceptron. The signals are typically sent inside the from input to output in a single direction. There is no loop, and each neuron's output has no effect on the neuron itself. This design is known as feedforward. Additionally, there exist feed-back networks that, thanks to reaction links within the network, are capable of transmitting impulses in both ways. These networks have a lot of power and may be highly intricate. They are dynamic, always altering until the network finds an equilibrium state, and with each change in input, a new equilibrium is sought. Non-linear activation functions are precisely where the multilayer perceptron's power lies. Except for polynomial functions, almost every non-linear function may be utilized for this.

Usually, learning networks is accomplished under supervision. L earning generally relies on the reduction of misclassification between the results of the model and the expected outputs. This suggests a back propagation via a network that is analogous to learning. For this reason, back-propagation is the term for algorithm learning.

II. METHODOLOGY

A. Dataset

The data studied contains pump sensor readings for some unknown manufacturing industry. It contains time-series data with sensor readings sampled every minute, moreover it has labelled instances where the machine was either broken, normally working or under repair. The machine contains precisely 7 instances where the machine was broken. The goal was to feed our machine learning models a sequence of input sensor data and with this our models had to make a prediction on whether or not the machine would breakdown. Where "1" represents a breakdown will occur in the output window and "0" representing the machine will work normally.

The study compared three models: Temporal Convolutional Network(TCN) and Long Short Term Memory(LSTM) and Multi-Layer Perceptron(MLP) models to make these predictions.

B. Data preparation

Our input window was 60 minutes of data. And the output window in this case were predictions for the next 24 hours. Again this was is easy to prepare because data samples were taken after exactly one minute. Next we create a helper function to check if the machine broke in window after the input window. So a 1 represented the machine did break and a 0 represented the machine didn't break. We also used this helper function to make sure that the machine was working normally during the input window, because we obviously don't want the machine to have been broken during the input window. With this we can create as much training data as we want by randomly picking any starting point for the input window, because we can check if the input window is valid with our helper function. If it isn't valid we simply pick another random starting point until we find valid input windows.

1) Training and Testing data:

LSTM and TCN models need a sequence of data points as inputs to make predictions. In our case, the sequence of data points is the pump sensor readings. Our chosen sequence/window length is 100, so there were 100 sequentially different data points for each sensor reading fed into the models to make one prediction. Put differently, 100 minutes worth of input data is fed into the models to predict if a breakdown will occur in the next 30 minutes.

So for the LSTM and TCN models the training and testing data had to be reshaped into a 3D array in the format (total data points, sequence length, number of sensors). The training and testing data were 3D arrays.

LSTM model:

The input of the LSTM model took the shape (batch size, sequence length, number of sensors). And the output of the LSTM model was passed to a neural network with the output of the neural network having just one node because we were trying to solve a binary classification problem

TCN model:

The input of the TCN model took the shape (batch size, sequence length, number of sensors). And the output of the TCN model was passed to a neural network with the output of the neural network having just one node because we were trying to solve a binary classification problem

MLP model:

Unlike the LSTM and TCN model the MLP model takes a 1D array so what we did was flatten the sequence length and number of sensors before passing it into the model. The output also contained just one node to make a binary prediction.

C. Tools and Software

The implementation of the algorithms will be done using Python this is because Python has various data science frameworks and libraries such as Tensorflow, Keras, PyTorch, and Sci-Kit that we can use to implement our algorithms/models. This study used Google Collaboratory, a cloud computer offered by google that allows users to write and run Python code in a web browser. Furthermore, Google Collaboratory already comes pre-installed with a vast majority of data science frameworks/libraries needed to implement our algorithms. And last but certainly not least, we can exploit the use of their free GPU to train the models.

The data will conveniently be collected from Kaggle here. It contains pump sensor for some unknown manufacturing industry. It of course contains time-series data, and moreover it has labelled instances where the machine was either broken, normally working or under repair.

Below are the Google Collaboratory system specifications used for the experiments:

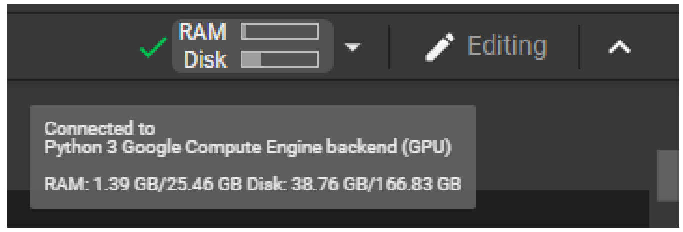

Figure 4 RAM and Disk space from Google colaboratory premium subscription

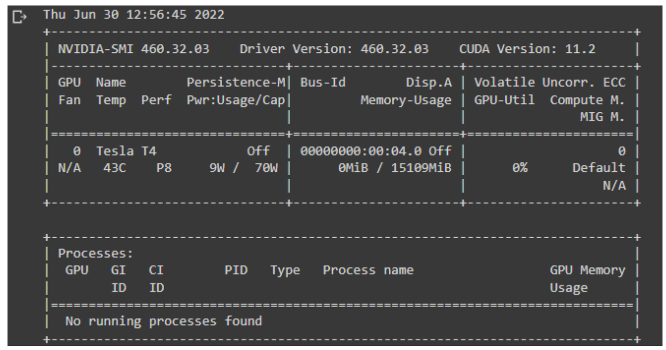

Figure 5 GPU specs from Google Collaboratory premium subscription

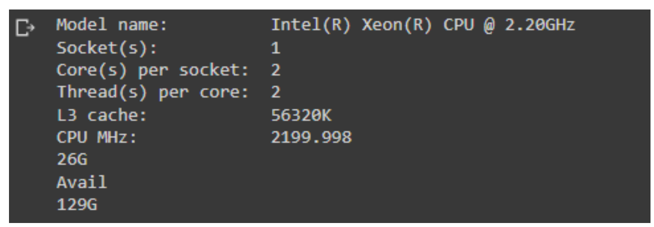

Figure 6 CPU and System specs from Google Collaboratory premium subscription

D. Model building

As we can see from Fig 1, the study uses two LSTM layers and one dense layer for our output. The first LSTM layer had 100 units and the second LSTM layer had 50 units. The dense layer had 1 neuron, being treated as a classification problem. The input to the LSTM was a window of 60 for the 50 sensor readings. The LSTM had 90651 tunable parameters.

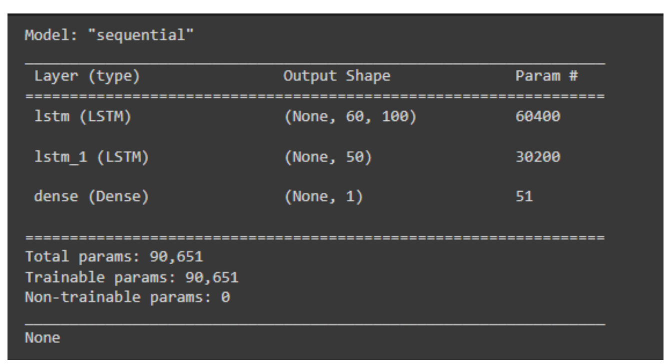
Model: "sequential"

Layer (type)	Output Shape	Param #
lstm (LSTM)	(None, 60, 100)	60400
lstm_1 (LSTM)	(None, 50)	30200
dense (Dense)	(None, 1)	51

Total params: 90,651
Trainable params: 90,651
Non-trainable params: 0

None

Figure 7 LSTM architecture

Figure 2 shows the architecture of the TCN model. One TCN was used, and similar to the LSTM its input contained a 2D array: a window of 60 samples for the 50 sensor readings. The TCN model had 148865 trainable parameters.

```
Model: "model"
_________________________________________________________________
 Layer (type)                Output Shape              Param #
=================================================================
 input_1 (InputLayer)        [(None, 60, 50)]          0

 tcn (TCN)                   (None, 64)                148800

 dense_1 (Dense)             (None, 1)                 65

=================================================================
Total params: 148,865
Trainable params: 148,865
Non-trainable params: 0
_________________________________________________________________
```

Figure 8 TCN architecture

Figure 3 shows the architecture of the MLP model, which uses three dense layers. The first layer had 200 neurons, the second had 40 and finally the last layer had one neuron because this is a classification problem. All in all, the MLP model had 608281 trainable parameters.

```
Model: "sequential_1"
_________________________________________________________________
 Layer (type)                Output Shape              Param #
=================================================================
 dense_2 (Dense)             (None, 200)               600200

 dense_3 (Dense)             (None, 40)                8040

 dense_4 (Dense)             (None, 1)                 41

=================================================================
Total params: 608,281
Trainable params: 608,281
Non-trainable params: 0
_________________________________________________________________
```

Figure 9 MLP architecture

E. Assessment metrics

We needed a system that can predict a breakdown sometime in the future by feeding the system a sequence of time-series data. Common metrics for evaluating the performance of anomaly detection algorithms include calculating the precision, precision and F1 which are all metrics derived from a confusion matrix [13]. The confusion matrix contains counts of samples categorised as True Positive (TP), True Negative (TN), False Positive (FP), and False Negative (FN) [13]:

$$Precision = \frac{TP}{TP+FP}$$

$$Recall = \frac{TP}{TP + FN}$$

$$F_1 = \frac{2 \times Precision \ \times Recall}{Precision + Recall}$$

To calculate the confusion matrix our test data will have to be labelled in two distinct classes: Normal data vs Anomalous data [13].

To evaluate predictive maintenance we use the Precision, Recall, and F1 scores which are common metrics because they evaluate the models' ability to predict machine failure and not create false alarms [1].

III. TESTING AND RESULTS

Confusion matrix

$$LSTM_{1000\ epochs}\ Confusion\ matrix = \begin{bmatrix} 938 & 7 \\ 15 & 40 \end{bmatrix}$$

$$TCN_{1000\ epochs}\ Confusion\ matrix = \begin{bmatrix} 941 & 4 \\ 14 & 41 \end{bmatrix}$$

$$MLP_{1000\ epochs}\ Confusion\ matrix = \begin{bmatrix} 939 & 6 \\ 47 & 8 \end{bmatrix}$$

Table 1 Evaluation after 1000 epochs

Model	**Precision**	**Recall**	**F1**	**Training time**
LSTM	0.851	0.727	0.784	106.49 seconds
TCN	0.911	0.745	0.820	155.54 seconds
MLP	0.571	0.145	0.232	60.51 seconds

IV. Discussion

The study shows that the LSTM and TCN models outperform the MLP models when comparing the F1 score. We use the F1 score as the deciding metric because it takes into account the precision and recall.

When comparing the LSTM and TCN against each other, the TCN(0.820) perform slightly better than the LSTM model(0.784). However, the LSTM model only trained for about 2/3 amount of time compared to the TCN.

The LSTM and TCN models performed well on the training data but when given the test data their performance drops a bit. This is most likely due to overfitting. The models are probably learning to predict certain breakdowns/anomalies but they are unable to generalize sufficiently to predict other types of breakdowns. In other words, the warning signs for certain breakdowns/anomalies are different for others.

V. Conclusion

We looked at how we can format a dataset from an industrial plant and use it to predict when the machine will have a breakdown 24 hours in advance. We compared three machine learning models, the LSTM, TCN and MLP and saw that the TCN outperformed the LSTM which is commonly believed to be the go-to model to make predictions on temporal data. For future work, it will be interesting to see how these models perform on a multiclass dataset.

REFERENCES

[1] V. M. Z. Wickern, "Challenges and Reliability of Predictive Maintenance," *Rhine-Waal University of Applied Science,* pp. 9-13, 2019.

[2] C. Krupitzer, T. Wagenhals, M. Zufle, V. Lesch, D. Schafer, A. Mozaffarin, J. Edinger, C. Becker and S. Kounev, "A Survey on Predictive Maintenance for Industry 4.0," *arXiv,* 5 February 2020.

[3] J. B. Gęca, "PERFORMANCE COMPARISON OF MACHINE LEARNING ALGORITHMS FOR PREDICTIVE MAINTENANCE," *IAPGOŚ,* p. 2, 2020.

[4] M. Paolanti, L. Romeo, A. Felicetti, A. Mancini, E. Frontoni and J. Loncarski, "Machine Learning approach for Predictive Maintenance in Industry 4.0," *MESA,* vol. 2018, no. 8449150, p. 3, 2018.

[5] B. Larzalere, "LSTM Autoencoder for Anomaly Detection," Towards Data Science, 25 September 2019. [Online]. Available: https://towardsdatascience.com/lstm-autoencoder-for-anomaly-detection-e1f4f2ee7ccf. [Accessed 18 April 2022].

[6] M. Mohammadi, A. Al-Fuqaha, S. Sorour and M. Guizani, "Deep Learning for IoT Big Data and Streaming Analytics: A Survey," *IEEE COMMUNICATIONS SURVEYS & TUTORIALS,* vol. X, no. 10, 5 June 2018.

[7] A. Karpathy, "The Unreasonable Effectiveness of Recurrent Neural Networks," GitHub, 21 May 2015. [Online]. Available: http://karpathy.github.io/2015/05/21/rnn-effectiveness/. [Accessed 14 May 2022].

[8] A. Karpathy, "CONNECTING IMAGES AND NATURAL LANGUAGE," *Stanford University,* August 2016.

[9] Y. Wei, J. Jang-Jaccard, W. Xu, F. Sabrina, S. Camtepe and M. Boulic, "LSTM-Autoencoder based Anomaly Detection for Indoor Air Quality Time Series Data," *arXiv,* 14 April 2022.

[10] Y. He and J. Zhao, "Temporal Convolutional Networks for Anomaly Detection in Time Series," *IOPscience,* vol. 1213 , 2019.

[11] Y. Zhang, P. J. Thorburn and P. Fitch, "Multi-task Temporal Convolutional Network for Predicting Water Quality Sensor Data," *Springer,* December 2019.

[12] J. Liu, H. Zhu, Y. Liu, H. Wu, Y. Lan and X. Zhang, "Anomaly detection for time series using temporal convolutional networks and Gaussian mixture model," *Journal of Physics Conference Series,* vol. MCLXXXVII, no. 4, April 2019.

[13] S. Gopali, F. Abri, S. Siami-Namini and A. S. Namin, "A Comparative Study of Detecting Anomalies in Time Series Data Using LSTM and TCN Models," *arXiv,* 17 December 2021.

Using the Multilayer Perceptron (MLP) Model in Predicting the Patterns of Solar Irradiance at Several Time Intervals

Chibuzor N Obiora, Ahmed Ali, and Ali N Hasan
Department of Electrical and Electronic Engineering Technology
Faculty of Engineering and the Built Environment, University of Johannesburg
Johannesburg, South Africa
chibuzorobiora58@gmail.com, aali@uj.ac.za, alin@uj.ac.za

***Abstract*— Fossil fuels, widely used to produce electricity and power industries, have significantly increased greenhouse gas emissions and led to current global warming. Many countries now allocate considerable resources to Renewable Energy Sources (RES) to produce clean electricity because of the adverse effects of these fossil fuels on the climate. Solar energy is currently one of the most naturally abundant renewable energy sources. Despite being cost-free, solar energy has always been unreliable. The Photovoltaic (PV) panels trap the radiative energy released by the sun, which is expressed in Watts per square meter ($Watts/m^2$). This solar radiation is highly stochastic. It fluctuates during the day before going away entirely at night. This study used Multilayer Perceptron (MLP), a deep learning model, to forecast solar radiation at five different horizons: five, ten, fifteen, thirty, and sixty-minute intervals. The model was trained with two years of meteorological data collected from Johannesburg. The best result was when data collected at five minutes intervals was used to train the model. The model recorded a normalized Root Mean Square Error (nRMSE) of 3.25%. This MLP performance was compared with the results obtained using the SVR model. The best result obtained using the SVR model was 6.26. It is suggested that utilizing this model would make it easier for solar plant operators to predict how much solar energy will be produced at different times of the day. This information will aid in planning failsafe outcomes during cascading solar irradiance, which negatively impacts the electrical energy supply to the power grid.**

***Keywords*—** *Deep Learning, Multilayer Perceptron (MLP)), Support Vector Regression (SVR), Solar irradiance, Prediction, Time Intervals.*

1. INTRODUCTION

Industrialization depends a great deal on electricity. After the first industrial revolution's advancements, the world's economy would have stagnated without electricity [1]. The commercialization of electricity propelled the second industrial revolution, which remained crucial during the third industrial revolution, which was ushered in by developments in Information and Communication Technology (ICT).

In the current fourth Industrial Revolution (4IR), Artificial Intelligence (AI) and any devices that use its technology depend on electricity [2]. For several years, many nations have relied on producing electric power from fossil fuels because of the significance of electricity to the development of the global economy [3],[4]. Presently, there is an upsurge in the production of electrical power from Renewable Energy Sources (RES) to minimize the effects of fossil fuels on the climate. Due to their minimal environmental impact, RES are typically considered a clean energy source [5]. However, even though most RES are free and naturally abundant, their unpredictability makes them unattractive to consumers at various levels [6]. For instance, it is well known that solar radiation varies throughout the day until finally falling to zero at night. Photovoltaic (PV) or solar panels primarily use this solar radiation to harvest and convert it into electrical energy. The unit of measurement for solar irradiance. $Watts/m^2$. It is essential to predict solar radiation accurately because it gives solar farm engineers an idea of how much electricity will be produced. They can use this information to assess how much energy needs to be safely delivered via the power grid to satisfy customers' demands. Also, with this information, they will arrange for backup if the estimated electricity is less than the quantity needed to prevent power outages. Several techniques are now being used to forecast solar radiation. Predictive models come in statistical and Artificial Intelligence (AI)-based methods. The accuracy of prediction techniques based on AI has increased over time.

In this paper, the Multilayer Perceptron (MLP), a deep learning model, was employed to forecast solar radiation for the electrical energy production of PV cells. Because their accuracy rises with the increasing size of the training dataset, deep learning models typically outperform classical machine learning models [7]. This behavior differs from most conventional machine learning algorithms, which typically overfit when the input data reaches a certain level.

The data for the MLP model used in this study were collected from meteorological weather data for Johannesburg that was made accessible on Solcast [9]. Error metrics such as the Root Mean Square Error (RMSE) were used to assess the model's performance after training at five different time intervals. Regression plots, which show how the data fit into the model, were also used to illustrate the models' performance.

Some of the similar works the authors reviewed are listed in the next section. The methodology is covered in Section 3. The results obtained from the simulations are presented in section 4. The paper's contribution to the field of solar energy forecasting is discussed in the conclusion section.

2. RELATED WORKS

Similar to how temperature varies by region, the location of solar plants is crucial in determining the pattern of solar radiation. It explains why the models' accuracy relies so heavily on the data gathered from the location. The nature of the input parameters of the training data is an additional factor that affects the models' accuracy. Additionally, the data collection horizons or time intervals impact how accurately the models forecast the future. For example, data acquired at shorter intervals produce more accurate forecasts than data collected at longer intervals. This is primarily due to the intermittent, brief fluctuations in solar radiations. As a result, data taken at longer intervals may not reflect the radiation pattern as precisely as those collected at shorter intervals. Overall, the studies reviewed in the literature demonstrate that algorithms for estimating solar irradiance based on AI outperform those based on conventional statistical techniques.

For example, a 2016 study conducted in Paris utilized sunshine duration as the sole input parameter. The study was conducted to estimate hourly solar radiation using machine learning methods such as Artificial Neural Networks (ANN), Support Vector Regression (SVR), Nave Bayes, and Autoregressive Inference Moving Average (ARIMA) [10]. The models' outcomes demonstrated that ANN outperformed the others. They used the normalized Root Mean Square Error (nRMSE) as an evaluation measure. Some researchers in Indonesia used temperature, sunshine duration, and historical solar radiation as training datasets to forecast solar irradiance. They used the Multiple Linear Regression (MLR) and Extreme Learning Machine (ELM) models for their experiment [11]. They gathered training data over five years. Their findings demonstrated that the ELM model outperformed the MLR model. Additionally, Extreme Gradient Boosting (XGBoost) exceeded Random Forest (RF), and Artificial Neural Networks (ANN) in another experiment carried out by researchers in India [12].

Before the authors discovered a gap in utilizing the MLP model to estimate solar radiation using data acquired from Johannesburg meteorological information, several previous comparable works were evaluated [13],[14],[15],[16],[17],[18],[19]. The gap from the available literature points that solar farm engineers may successfully handle the issues brought on by variations in solar radiation in electrical energy generation by using the MLP model in solar power forecasting.

3. METHODOLOGY

Data for the experiment were collected from Solcast's weather reports for Johannesburg [9]. The data were gathered at five different time intervals. After data cleansing and preprocessing, the data were ready for use in training the models. Datasets for training and testing were obtained by splitting the total data after preprocessing and scaling. Eighty percent of the entire data constitutes the training datasets. The model's code was developed using the Python programming language. Only the historical solar radiation was employed as an input parameter because the models are time series. The epochs were set to 100 during the MLP model fitting, and the batch size was 32. The model run in three (3) timesteps. The Adam optimizer and Rectified Linear Unit (ReLU) activation function were also applied to eliminate model overfitting and obtain optimal outcomes. To display its performance, the model automatically generated regression plots. Figure 1 shows the general process or methodology to train the model using input data collected at five intervals.

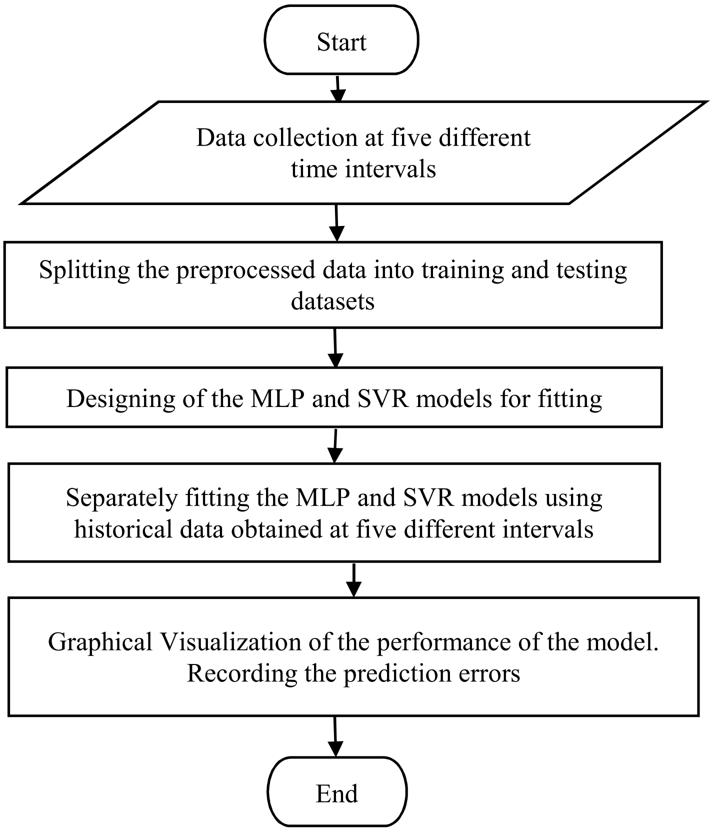

Fig. 1: A chart illustrating the procedure for predicting solar irradiance using the MLP and SVR models.

Brief Description of the Models

3.1 Multilayer Perceptron (MLP) model

The MLP is a deep artificial neural network. It is made up of many perceptrons. They consist of an input layer to receive the signal, an output layer to decide or forecast based on the input, and any number of hidden layers that make up the true computational engine between the two [20]. A series of input-output pairings are used to train multilayer perceptions, which then learn to represent the dependencies between those inputs and outputs. Training involves tampering with the model's parameters, weights, and biases to reduce errors. Backpropagation is used to manipulate the bias and weight to minimize the training error, and the Root Mean Square error (RMSE) is one approach to measure the error [21]. MLPs and other feedforward networks primarily entail two motions: a continuous back and forth (forward and backward passes).

3.2 Support Vector Regression (SVR) model

SVR is a kernel-based machine learning model. Support Vector Machines, a machine learning model used for data classification on continuous data, expanded the regression function known as Support Vector Regression (SVR) to encompass all regression functions [22]. SVRs, a collection of connected supervised learning algorithms for pattern recognition, regression, classification, estimation, and operator inversion, are utilized for complicated regression problems. It has shown great success when applied to time-series prediction tasks [13].

3.3 Evaluation Metrics

Evaluation metrics produce models' performance, record prediction errors, and evaluate the effectiveness of machine learning algorithms. It calculates the discrepancies between the values of expected and predicted. They also show how well the predicted and actual values fit during training. The expected and actual solar radiation errors are measured after the model's training. In this study, the Root Mean Square Error (RMSE) metric was used to determine the performance of the two models after each simulation. The coefficient of determination (R^2), which ranges from zero to one, expresses how accurately a model forecasts solar radiation. The R^2 is the percentage of variation in the dependent variable that the model predicts. A coefficient of determination value close to 100% denotes that the model is very efficient for the task, whereas a value close to 0% implies that it is not. A mathematical expression demonstrates how these metrics are calculated automatically by the model. Equations (1), (2), and (3) show the computation of the coefficient of determination, Mean Absolute Error (MAE), and RMSE values.

$$R^2 = 1 - \frac{RSS}{TSS} \qquad (1)$$

Where,

RSS = sum of squares of the residuals

TSS = total sum of squares.

$$\text{Mean Absolute Error, } MAE = \left(1/_N\right) \sum_t |A_t - F_t|$$

$$Mean\ square\ error, MSE = \left(1/_N\right) \sum_t (A_t - F_t)^2 \qquad (2)$$

$$\text{Root Mean Square Error, } RMSE = \sqrt{MSE}$$

$$Normalized\ root\ mean\ squared\ error = nRMSE$$

$$nRMSE = \sqrt{MSE}/\rho \qquad (3)$$

Where,

$mean\ of\ observed\ values, \rho = \mu = (A_{max} - A_{min}),$

$A = actual\ data\ solar\ radiation\ time\ series,$

$F = predicted\ solar\ radiation\ time\ series,$

$N = number\ of\ observations(non - missing\ data)$

4. RESULTS AND DISCUSSION

This section presents the performance of the MLP and SVR models after training. The actual or observed solar radiation values used during training are plotted against the predicted or forecasted values to graphically illustrate the model's performance. A good fit means that the data cluster along the regression lines of the plots.

4.1 Results from the MLP model trained with data collected at five different time intervals.

Fitting the MLP model involved setting the epochs at 100 and the batch size at 32. Adam optimizer was used, while the activation function was Rectified Linear Unit (ReLU). The regression plots visualize the model's performance, as indicated in the methodology. Figures 2a, 2b, 2c, 2d, and 2e show the graphs generated by the model after fitting it separately with data obtained at five different time intervals over two years.

(a)

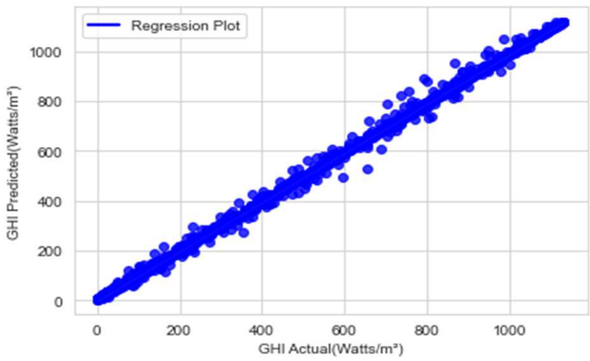

(b)

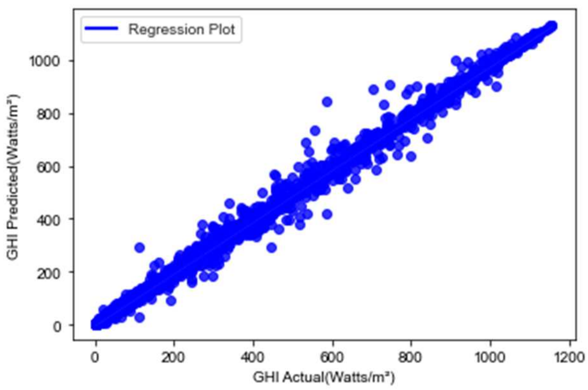

(c)

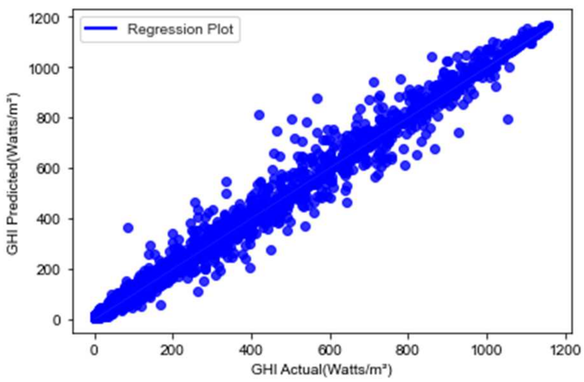

(d)

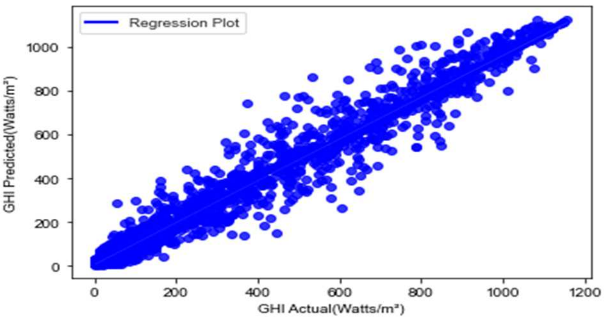

(e)

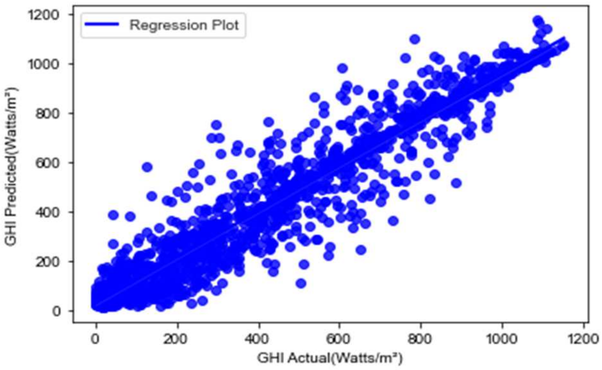

Fig. 2: Plots of the performance of solar radiation forecasting using the MLP model trained with historical data collected at five different time intervals. Figures 2a, 2b, 2c, 2d, and 2e represent the regression plots obtained after training the model with historical data obtained at 5-minute, 10-minute, 15-minute, 30-minute, and one-hour intervals, respectively.

The regression plots in figure 2 indicate that the data points clustered more along the regression lines when training the model with historical data obtained at five minutes intervals. As the time intervals of training datasets widen, the regression plots continuously present regression lines that are not well-fitted with the data points. Table I shows the values of error metrics recorded after training the MLP model. It shows that the prediction errors increase as training involves using data having longer time intervals. For instance, the RMSE error obtained when the model was trained with data obtained at 5-minute intervals is lower than that obtained at 10-minute intervals. The same can be observed for the Mean Absolute error (MAE). However, with the coefficient of determination, the values decreased with increasing time intervals, indicating that a good fit is closer to a value of 1.

Table I: The performance metrics of the MLP model

Horizon of Prediction	**Error Metrics**			
	MAE	**R^2**	**RMSE**	**nRMSE(%)**
5-minute	9.78	0.9983	15.32	3.25
10-minute	22.84	0.9910	32.64	6.80
15-minute	35.28	0.9767	52.75	11.00
30-minute	51.88	0.9550	73.47	15.88
1-hour	67.97	0.9136	96.95	23.00

4.2 Results from the SVR model trained with data collected at five different time intervals.

Fitting the SVR model involved training the model one after the other with the data obtained at five different time intervals. The regression plots are to visualize the model's performance, as indicated in the methodology. Figures 3a, 3b, 3c, 3d, and 3e show the graphs generated by the model after fitting it separately with data obtained at five different time intervals over two years.

(a)

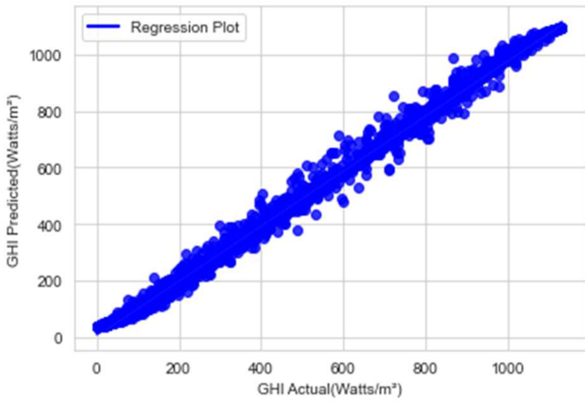

(b)

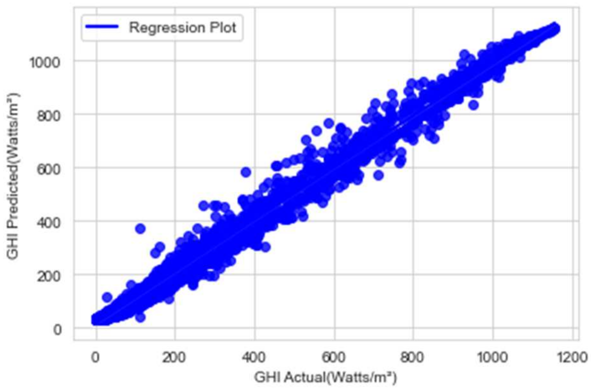

(c)

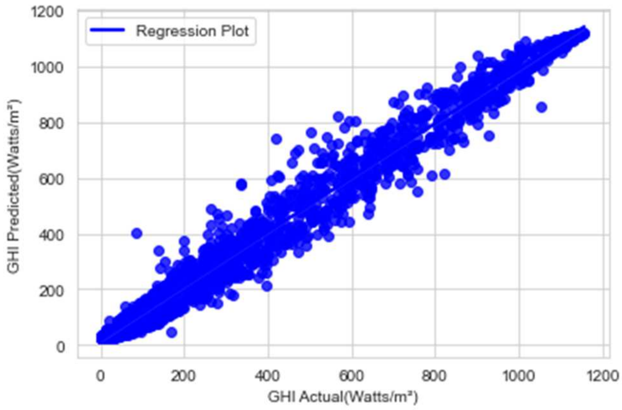

(d)

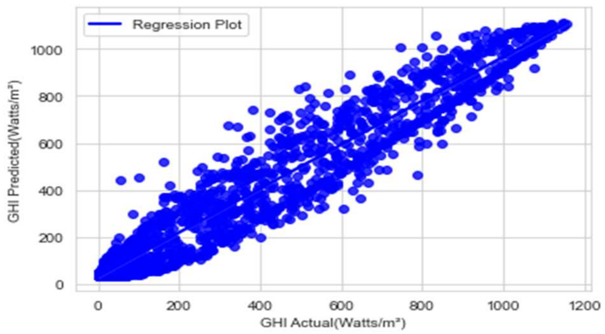

(e)

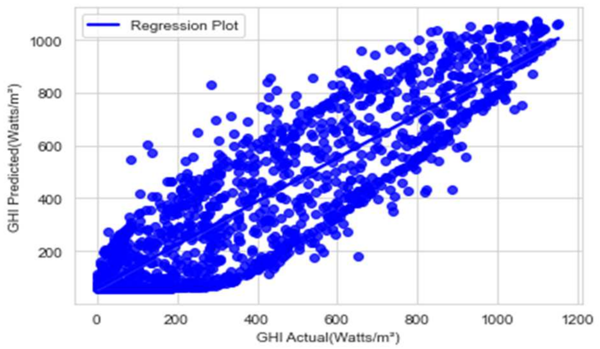

Fig. 3: Plots of the performance of solar radiation forecasting using the SVR model trained with historical data collected at five different time intervals. Figures 3a, 3b, 3c, 3d, and 3e represent the regression plots obtained after training the model with historical data obtained at 5-minute, 10-minute, 15-minute, 30-minute, and one-hour intervals, respectively.

The regression plots in figure 3 indicate that the data points clustered more along the regression lines when the model was trained with historical data obtained at five minutes intervals. With the widening time intervals of training datasets, the regression plots continuously present regression lines that are not well-fitted with the data points. Table II shows the values of error metrics recorded after training the SVR model. It shows that the prediction errors increase as training involves using data having longer time intervals. For instance, the RMSE error obtained when the model was trained with data obtained at 5-minute intervals is lower than that obtained at 10-minute intervals. The same can be observed for the Mean Absolute error (MAE). However, with the coefficient of determination, the values decreased with increasing time intervals, indicating that a good fit is closer to a value of 1.

Table II: The performance metrics of the SVR model

Horizon of Prediction	Error Metrics			
	MAE	R²	RMSE	nRMSE(%)
5-minute	23.34	0.9937	29.45	6.26
10-minute	33.36	0.9843	43.11	9.00
15-minute	46.74	0.9690	60.96	12.74
30-minute	79.48	0.9196	98.28	21.26
1-hour	127.79	0.7753	156.29	37.09

Records from Tables I and II show that the prediction errors obtained in fitting the MLP and SVR models with data obtained at five minutes intervals produced the least errors. The prediction errors increase gradually as the models' training involves data obtained at longer intervals. This was because solar radiation is characteristically stochastic. Overall, the RMSE obtained at five minutes intervals of training data with the MLP gave the nRMSE of 3.25. This is the best result obtained from the experiment conducted. The chart in figure 4 illustrates the comparison between the prediction errors obtained when training the models with datasets obtained at five different time intervals.

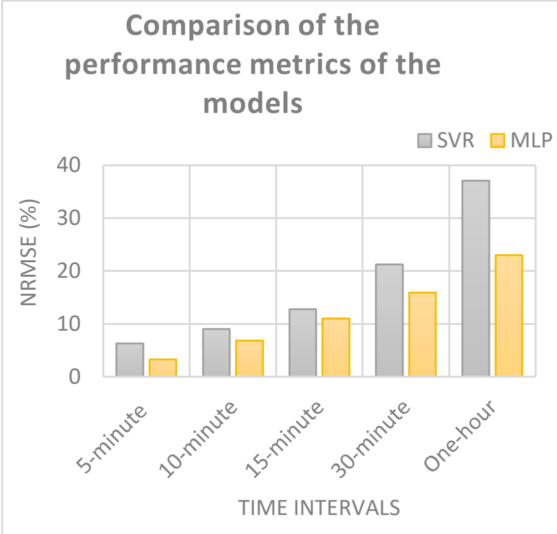

Fig. 4: A chart showing the nRMSE values obtained after training the MLP and SVR models with data collected at five different time intervals.

5. CONCLUSION

Stable electrical power production from solar energy requires reliable solar radiation. Sadly, solar radiation is inherently very stochastic. In order for solar farm engineers to plan for failsafe results during cascading drops in solar radiation, reliable prediction of the patterns of solar irradiance is the efficient way to generate solar power to satisfy consumers' demands at various levels. There are numerous techniques used to forecast solar radiation. Some of these techniques, particularly those using machine learning, are effective. However, the predictive models' accuracy still must be increased for improved efficiency.

In this study, the deep learning time series model MLP was utilized to accurately predict solar radiation using historical training datasets independently collected from Johannesburg city at five different time intervals. The simulation results demonstrated that the MLP model performed better than the SVR model, a traditional machine learning model. When the model was trained using data gathered at five minutes, the RMSE value was 3.25%. It represents a tremendous improvement. It is recommended that utilizing this model to estimate fluctuations in solar radiation would help make plans for producing dependable electricity that would satisfy consumers' demands at various levels.

REFERENCES

1. N. Rashied and M. Bhamjee, "Does the Global South Need to Decolonise the Fourth Industrial Revolution? In *The Disruptive Fourth Industrial Revolution*, Springer, Cham, pp. 95-110, 2022.

2. Z. Ullah, F. Al-Turjman, L. Mostarda, and R. Gagliardi, "Applications of artificial intelligence and machine learning in smart cities," *Computer Communications*, *154*, 313-323, 2020.

3. L. Cheng and T. Yu, "A new generation of AI: A review and perspective on machine learning technologies applied to smart energy and electric power systems," *International Journal of Energy Research*, *43*(6), 1928-1973, 2019.

4. C. N. Obiora, A. N. Hasan, A. Ali and N. Alajarmeh, "Forecasting Hourly Solar Radiation Using Artificial Intelligence Techniques," in IEEE Canadian Journal of Electrical and Computer Engineering, vol. 44, no. 4, pp. 497-508, Fall 2021, DOI: 10.1109/ICJECE.2021.3093369.

5. C. N. Obiora, A. Ali and A. N. Hasan, "Estimation of Hourly Global Solar Radiation Using Deep Learning Algorithms," 2020 11th International Renewable Energy Congress (IREC), 2020, pp. 1-6, DOI: 10.1109/IREC48820.2020.9310381.

6. C. N. Obiora and A. Ali, "Effective Implementation of Convolutional Long Short-Term Memory (ConvLSTM) Network in Forecasting Solar Irradiance," IECON 2021 – 47th Annual Conference of the IEEE Industrial Electronics Society, 2021, pp. 1-5, DOI: 10.1109/IECON48115.2021.9589934.

7. R. Zhang, M. Feng, W. Zhang. S. Lu, and F. Wang (2018). Forecast of solar energy production – A deep approach, IEEE International Conference on Big Knowledge, 2018, pp. 73-81.

8. Z. Wu, Q. Li, and X. Xia, Multi-timescale forecast of solar irradiance based on multi-task learning and echo state network approaches. *IEEE Transactions on Industrial Informatics, 2020 April 13*.

9. Solcast weather history, can be accessed at https://toolkit.solcast.com.au/historical/1b819b3e-dffb-4cd4-8e3b-5b93705e8402/download.

10. F.N. Melzi, T. Touati, A. Same, L. Oukhellou, Hourly solar irradiance forecasting based on machine learning models. 15th IEEE International Conference on Machine Learning and Applications, 16, (2016), pp. 441-446. DOI: 10.1109/ICMLA.2016.186.

11. H. Suyono, H. Santoso, R.N. Hasanah, U. Wibawa, and I. Musirin, prediction of solar radiation intensity using extreme learning machine, Indonesian Journal of Electrical Engineering and Computer Science. Vol. 12, no. 2, 2018, pp. 691-698.

12. A. Moosa, H. Shabir, H. Ali, R. Darwade, and B. Gite, Predicting solar radiation using machine learning techniques. Proceedings of the second International Conference on Intelligent Computing and Control Systems, IEEE Xplore.,18, 2018, 1693-1699. ISBN: 978-1-5386-2842-3.

13. C. Voyant, G. Notton, S. Kalogirou, M-L. Nivet, C. Paoli, F. Motte, and A. Fouilloy, Machine learning methods for solar radiation forecasting: A review, Renewable Energy, Vol.105, 2017, pp. 569-582.

14. J. Li, J.K. Ward, J. Tong, L. Collins, and G. Platt, Machine learning for solar irradiance forecasting of the photovoltaic system, Renewable Energy, Vol. 90, 2016, pp. 542-553. http://dx.doi.org/10.1016/j.renene.2015.12.069 0960-1481/.

15. A. Khosravi, R. Koury, L. Machado, and J. Pabon, Prediction of hourly solar radiation in Abu Musa Island using machine learning algorithms, Journal of Cleaner Production, 176, 2018, pp. 63–75.

16. C. N. Obiora and A. Ali, "Hourly Photovoltaic Power Forecasting Using CNN-LSTM Hybrid Model," 2021 62nd International Scientific Conference on Information Technology and Management Science of Riga Technical University (ITMS), 2021, pp. 1-6, doi: 10.1109/ITMS52826.2021.9615335.

17. M. De Felice, M. Petitta and P.MRuti, Short-term predictability of photovoltaic production over Italy, Renewable Energy, Vol. 80, 2015, pp. 197-204.

18. A. Sharma and A. Kakkar, Forecasting daily global solar irradiance generation using machine learning. Renewable and Sustainable Energy Reviews, Issue 82, 2018, pp. 2254-2269. http://dx.doi.org/10.1016/j.rser.2017.08.066.

19. H. Long, Z. Zhang and Y. Su, Analysis of daily solar power prediction with data-driven approaches, Applied Energy, Vol. 126, 2014, pp. 29-37.

20. A. Botalb, M. Moinuddin, U. M. Al-Saggaf, and S. S. Ali, "Contrasting convolutional neural network (CNN) with multilayer perceptron (MLP) for big data analysis." In *2018 International conference on intelligent and advanced system (ICIAS)*, pp. 1-5. IEEE, 2018.

21. C. Aicher, N. J. Foti, and E. B. Fox, "Adaptively truncating backpropagation through time to control gradient bias." In *Uncertainty in Artificial Intelligence*, pp. 799-808. PMLR, 2020.

22. C. N. Obiora, A. Ali and A. N. Hassan, "Predicting Hourly Solar Irradiance Using Machine Learning Methods," 2020 11th International Renewable Energy Congress (IREC), 2020, pp. 1-6, doi: 10.1109/IREC48820.2020.9310444.

Study of Fault Detection on a 230kV Transmission Line Using Artificial Neural Network (ANN)

Z.I Sobhuza & B.A Thango
Dept. of Electrical and Electronic Engineering Technology
University of Johannesburg
Johannesburg, South Africa
217094952@student.uj.ac.za; bonginkosit@uj.ac.za

***Abstract*—In the Southern African Development Community (SADC), transmission lines facilitate power utilities in distributing a considerable amount of electricity from generation stations to end users. Long conductors used in transmission lines can cover great distances. However, they are susceptible to various environmental and weather conditions which can have adverse effects such as power outages, and equipment malfunctions, posing a serious threat to the reliability of the system. Hence constant monitoring of the performance characteristics of this system is crucial. The main objective of this work is to propose an Artificial Intelligent (AI) based technique, which is the Artificial Neural Network (ANN) to detect and classify faults on a transmission line. In contrast to the most common approach viz. the protective relay system, a five-layer feed-forward-back propagation neural network architecture is proposed in this work to detect and classify faults on a 230kV transmission line system. A set of 12 fault conditions have been predefined viz. No fault, AB, AC, BC, ABC, AG, BG, CG, ABG, ACG, BCG and ABCG conditions. The results indicate that the proposed ANN approach with Levenberg-Marquardt (LM) algorithm, 5-Layers and TANSIG transfer function yield an output of 0.8927, 0.8882, 0.905 and 0.8938 in the training, validation, testing and overall accuracy respectively. To corroborate these results, a comparative study of the proposed network and other neural networks was also carried out.**

Keywords— Southern African Development Community (SADC), transmission line, faults, artificial neural network (ANN), Levenberg-Marquardt (LM) algorithm

I. INTRODUCTION

The sudden and unexpected failures of power system infrastructure in the Southern African Development Community (SADC) may be caused by the rising demand for electrical energy in almost every area of the economy. Protection relays that can identify and isolate faulty system sections and components in real time must be provided to maintain continuity in the delivery of electric power [1]. A power system facility is made up of numerous cooperating parts. Therefore, it is impossible to rule out the possibility of a defect or short-circuit. The system may suffer damage to crucial system components and other key system equipment if a short circuit current is allowed to flow continuously [2]. The demand for high-speed fault detection on power system infrastructure, more specifically transmission lines, is increasingly moving away from electromechanical and solid-state relaying devices that primarily rely on voltage and current ratios as well as phase comparison of sinusoidal quantities. There are Shunt faults in transmission lines, namely symmetrical (balanced) and unsymmetrical (unbalanced), with a likelihood of 95% to 98% for unsymmetrical faults [2].

The percentage contribution of various fault occurrences in the power system can be tabulated as shown in TABLE I.

TABLE I. FAULT OCCURRENCE

Fault Types	Occurrence (%)
Line to Ground (L-G)	70-80%
Line to line (L-L)	8-10%
Double Line to Ground (LL-G)	10-17%
3-phase	2-5%

Modern power system facilities strongly require instantaneous fault detection to improve transient stability. One cannot overstate the importance of creating and implementing an intelligent fault monitoring system that is capable of detecting faults on the transmission lines as the conventional electric grid system gradually gives way to the concepts of the smart grid system [3]. The selection of digital technology for power system protection has allowed for the realization of quick decision-making for system problem detection and resolution [4]. The deployment of digital relays for power system protection has increased as a result of this development in digital technology [5]–[7]. The construction of a quicker and more reliable method of identifying the various fault types happening in the system by employing a robust and reliable algorithm has become necessary due to the rapid expansion of the electric power system in both complexity and expanse [8]. The ANN-based relay-based transmission line protection technique presented in [9] and [10] has substantial drawbacks that restrict how well it can operate and react to a specific transmission line. As a result, modifications to the transmission line's characteristics would necessitate repeating the ANN training process, reintroducing the major constraints of those methods.

Because of the 230kV transmission line's size and dimensions, the effectiveness of the fault detection mechanism in the power system becomes crucial. Furthermore, it is imperative to create and implement an intelligent fault monitoring system that is capable of accurately identifying faults on transmission lines given the ongoing transition from the conventional electric grid system to the principles of the smart grid system.

The following sections make up this work: Section II gives an overview of the fundamental principle of ANN and studies power system modelling. Section III presents the results of the

ANN development, training and testing for the selected algorithm. Section IV provides the study's conclusion.

II. ANN And Power System Modelling

A. The fundamental principle of ANN

In the last few decades, the artificial neural network has been regarded as a significant component of artificial intelligence due to the introduction of the back-propagation algorithm, which allows the adjustment of network hidden layers of neurons under supervised network training. Some of the outstanding features of the artificial neural network (ANN) include nonlinear mapping, parallel processing, online and offline learning propensity, and nonlinear mapping. An artificial neural network is highly helpful for applications involving power systems due to the viability of offline data training. ANN can be used to prevent the false tripping of distance relays caused by overreach or underreach faults [8].

Transmission line fault detection using ANN with improved zone-reaching capabilities was presented in [9]. A 3-phase transmission line module was used as an experimental configuration for the implementation of an ANN fault detection algorithm [10]. A pattern-based ANN technique was given in [10] for reducing the influence of fault resistance on distance relays. The network was found to be able to adapt to changes in the power system network after intense training using a variety of fault patterns. In this work, the authors used the feed-forward back-propagation neural network for fault detection on a three-phase transmission line shown in Fig. 1.

Fig. 1. Transmission line (230kV).

The corresponding technical specifications of the conductors for this transmission line are tabulated in TABLE II.

TABLE II. TECHNICAL SPECIFICATION OF CONDUCTORS

Conductor Type	TACSR/AC 610 mm2
Stranded wires component	Al 53.9/3.78, AC 6.9/3.78
Conductor area	691.8 mm2
Conductor diameter	34.20 mm
Weight	2,198 kg/km
Ultimate Tensile strength	180,000 N
Modulus of elasticity	71.8 kN/mm2
Coefficient of linear expansion	20.6 × 10-6/°C
Maximum working tension	Less than 72,000N
DC resistance at 20°C	0.0458 ohm/km

A fault must be found in two steps: first, it must be identified when an excessive amount of fault current flows through the line, and second, it must be cleared by using the circuit breaker. After detecting a breakdown on the transmission line, it must also swiftly determine the type of faulty fault. The training data set is the only one that the ANN model will utilize [11].

Advantages

- Data storage over the entire network
- Machine learning capabilities through training
- Faster when detecting faults
- Offer smart protection to the system
- Tolerance for mistakes

Although the technique that ANN programming has numerous benefits, it also has several very complex drawbacks. The decision about the type of network, the network's architecture, the termination standards, etc. are some of the crucial elements. The Back Propagation Neural Network (BPNN) uses feedback from the output to the input to evaluate how the weight values should change. By starting from the previous step and computing the error backwards, the error for each iteration and each point is determined [12]. The weights used in the neural network's back-error- propagation algorithm are selected at random, and they feed back a pair of inputs to produce the output. The method is repeated for every possible combination of inputs and outputs accessible in the developer's training data set after updating the weights with the new ones after each step. This method is continued until the network converges for the specified goal values for the specified level of error tolerance [12]. The error in each iteration of the proposed algorithm is calculated using the Mean Square Error (MSE) method. By using the optimal weights at every stage, the ANN's learning rate can be accelerated [13]. A considerable portion of the system network could be disconnected from the electric power supply because of relay and circuit breaker malfunction.

B. Proposed project design

Fig. 2 below shows the flowchart of the project setup of the ANN method on the transmission line for fault detection and classification. The faults are simulated. Then the faulty voltage and current value of 11 types of fault conditions will be stored. These values will be used as the ANN input for fault detection and classification.

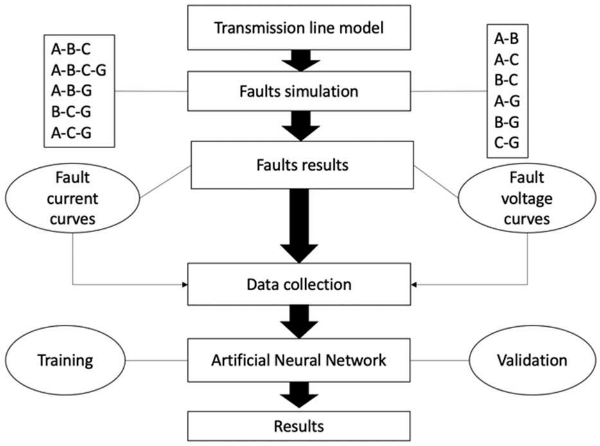

Fig. 2. Project setup.

A 230kV transmission line system is designed using the MATLAB/Simulink platform as shown in Fig. 3. Using a mathematical calculation and MATLAB programming, the faults are generated between bus 7 (B7) and circuit breaker 1 (CB1) 11 different types of fault conditions are simulated on the system, which includes line-to-ground (a-g, b-g, c-g), line-to-line (a-b, b-c, a-c), double line-to-ground (a-b-c-g), triple line-to-ground (a-b-c-g), three-phase (a-c-b-c), and no fault.

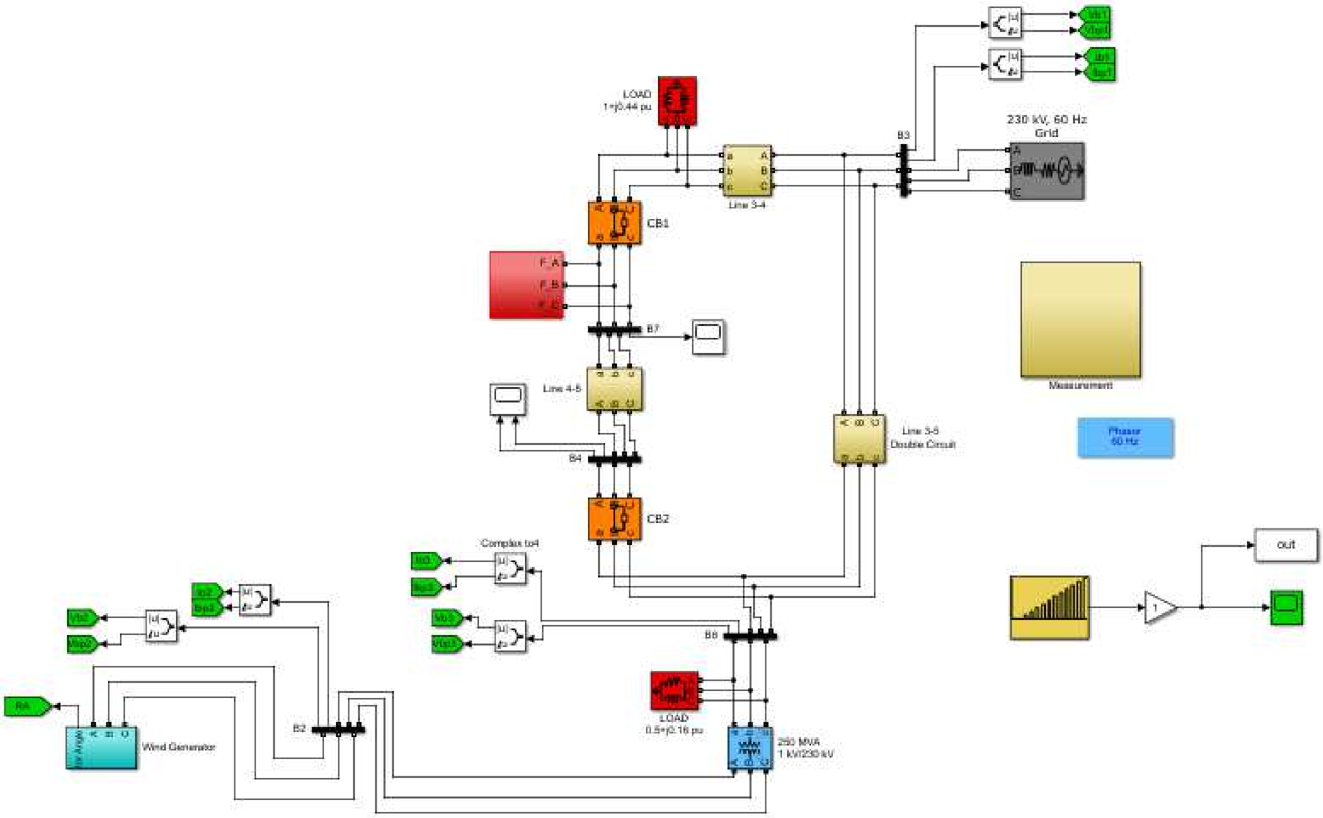

Fig. 3. Transmission line model.

The faults are simulated for 145 seconds, one after the other. The reason for simulating these faults in this manner is for data acquisition, we need as many data points as possible to train the ANN network. When a fault occurs on the line it causes an undesired voltage to drop and the current to rise. Fig. 4, shows the block diagram where all the faults are simulated and the voltage and current of each phase will be recorded. The recorded data will be plotted on a graph, with Voltage vs Time and Current vs Time graph, then be displayed on the scopes.

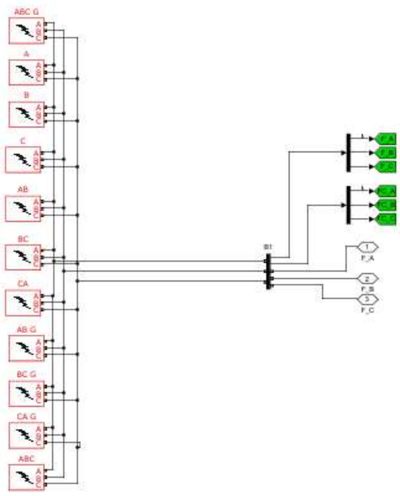

Fig. 4. Fault block simulation.

The waveforms in Fig. 5 depict the phase voltages of each phase after fault simulation. Where the first waveform is the output waveform for phase A, the second waveform is the output waveform for phase B, and the third waveform is the output waveform for phase C. the voltage is in per unit because Ann works well with data values that are between zero and one. For the voltage in phase A the data is stored in the workspace as A, for voltage in phase B stored in the workspace as B and the voltage in phase C is stored in the workspace as C. 14 501 data sets are collected for each phase voltage. More data will quite often expand the precision of a defined model.

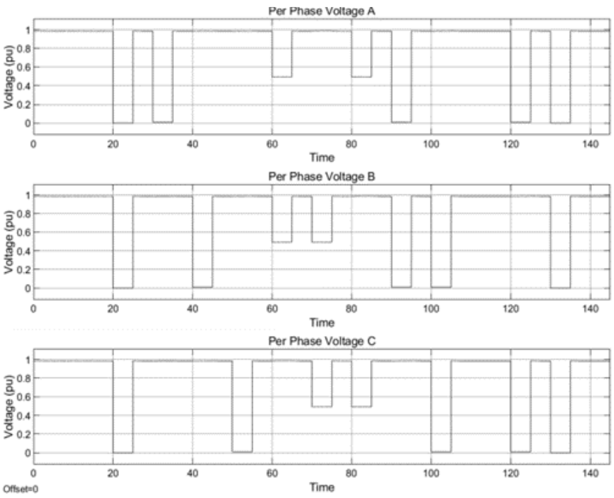

Fig. 5. Voltage results waveforms.

A fault code was created to distinguish between the different fault types as shown in Fig. 6.

0 ---> No-Fault condition
1 ---> A-B-C-G (LLLG)
2 ---> A-G (LG)
3 ---> B-G (LG)
4 ---> C-G (LG)
5 ---> A-B (LL)
6 ---> B-C (LL)
7 ---> C-A (LL)
8 ---> A-B-G (LLG)
9 ---> B-C-G (LLG)
10 ---> C-A-G (LLG)
11 ---> A-B-C (LLL)

Fig. 6. Fault code and fault types.

For certain input values, the predefined output will be the values from 0 to 11. Because ANN can only recognize values, one cannot get an output of alphanumeric. TABLE III is a sample of the data used and its associated output. The data set is big to be displayed in this document. When the input values are 0.1 for phase A voltage, 0.983774 for phase B voltage, and 0.983985 the output should be 1 and the fault type associated with is the ABCG fault.

TABLE III. SAMPLE DATA AND RESULTS

V(A)	V(B)	V(C)	Output value	Fault Type
0.985	0.985	0.985	0	No-Fault
0.1	0.984	0.984	1	ABCG
0.982	0.1	0.983	2	AG

III. RESULTS AND DISCUSSION

A five-layer feed-forward back propagation neural network architecture designed is shown in Fig. 7, with 3 inputs of three-phase voltage values, the hidden layers consisting of 10 neurons each and one output layer. The training data set contains 14501 training input data sets for each input and one output for 11 faults and no-fault. A supervised learning rule will be used by the neural network. In the supervised learning rule, the neural network will be trained using the output's predefined values. The weights are initialized with suitable values. The input is then collected from training data and compared to the predefined output. The error is then calculated. The Mean Squared Error (MSE), which measures the amount of error in statistical data, is the calculated error. When the MSE is equal to 0, the data is considered error-free.

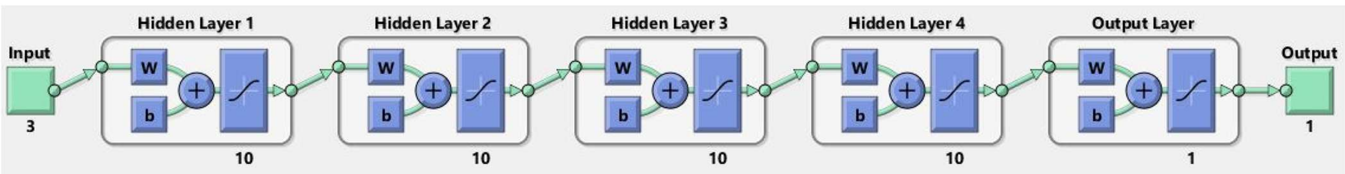

Fig. 7. Artificial neural network architecture.

The first step in the training process of the neural network is to train the data set by evaluating gradients and updating network weights until the network converges for a specific set of errors [1]. The second step is validating the data set, the validated data set is used by the neural during the training process, and the validation process error for the fully validated data set will be traced throughout the training process. During this step, the data set will only be used as inputs, with no output values assigned. The third stage involves testing the data set, which is typically not done during training.

The validation errors rise when the neural network starts to overfit the provided data during validation. When the number of validation processes fails and rises above a certain value, the training process is terminated to prevent further overfitting of the data, and the neural network is brought back to the minimum number of validation errors [3]. The third stage involves testing the data set, which is typically not done during training. The third stage is where the final trained neural network's overall performance is evaluated.

Since the Levenberg-Marquardt (LM) training method has the quickest training time, it is recommended by the

MATLAB platform as the preferred supervised algorithm. Several simulations were carried out using different network types, different transfer functions and changing the number of layers of the network. The network that produced the best result was a five-layer neural network, using the Feed-Forward-Back-Propagation and the TANSIG transfer function. The performance plot shows an MSE of 2.2405 at 613 epochs ash shown in Fig. 8.

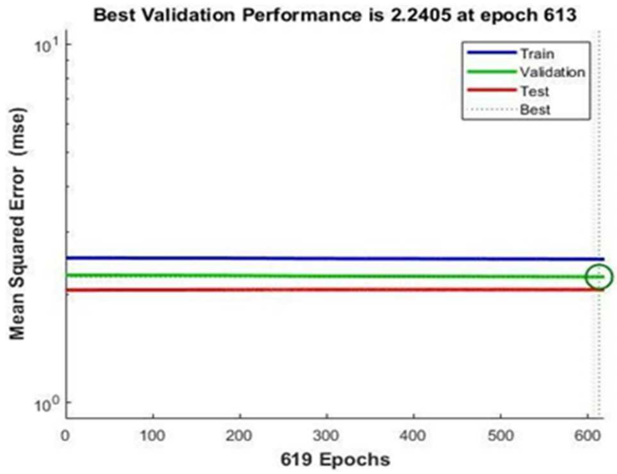

Fig. 8. Performance plot.

The data set that is utilized to train the ANN. After the neural network has been trained, its performance is evaluated by generating a linear regression plot as shown in Fig. 9 that simultaneously links the targets and outputs. How closely the targets of the neural network can monitor changes in the outputs is determined by the correlation coefficient. This network's overall correlation coefficient, which measures correlation across all variables, was found to be 0.896763, which is quite high.

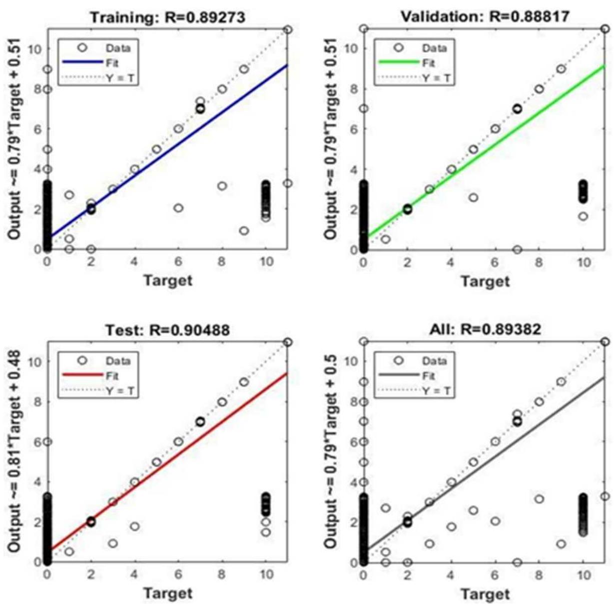

Fig. 9. Regression plot.

TABLE IV shows a summary of other results that were obtained after changing a few parameters on the ANN architecture. When the network type is a Feed-forward back propagation it's simple to change the number of layers and observe the MSE. But when the number of layers was increased to no results were obtained, the network gave a message of Gradient reached no simulation cannot be continued. The Perceptron network type did not have the obtain to choose the number of layers, its MSE was fairly good but the training time was 1h47sec, regression plot was not obtained. which is why this network type was not used for this project. In the Radial basis network type, the number of layers has defaulted at 2. This network did not show any results hence Not available (N/A). when comparing the results of the trained networks. The network which showed the best results was the 5-layered FFBP network. When using the TANSIG transfer function.

TABLE IV. SUMMARY OF OTHER RESULTS

Network type	Layers	Transfer function	MSE & Epochs	Regression results
FFBP	2 L	TANSIG	4.4814 @epoch 858	R = 0.81776
	5 LA	TANSIG	2.240 5 @Epoch 613	R = 0.89382
	10 LA	TANSIG	N/A	N/A
Radial basis exact	2	N/A	N/A	N/A
Perceptron	N/A	N/A	2.5171 @Epoch 0	N/A

IV. CONCLUSION

To detect and classify transmission line faults, an artificial neural network (ANN) model based on multilayer feedforward back-propagation has been developed in this study. The three-phase voltages are used as inputs to the neural networks in the described approach.

The simulation results show that the suggested neural networks have attained adequate performance and are practically implementable. In this work, emphasis has been placed on the significance of selecting the ideal ANN configuration to maximize network performance. The application of ANN is broad enough to warrant further investigation. By creating appropriate intelligent procedures, fault detection and categorization can become naturally intelligent.

REFERENCES

[1] N. A. M. Leh, F. M. Zain, Z. Muhammad, S. A. Hamid and A. D. Rosli, "Fault Detection Method Using ANN for Power Transmission Line," *2020 10th IEEE International Conference on Control System, Computing and Engineering (ICCSCE)*, 2020, pp. 79-84, doi: 10.1109/ICCSCE50387.2020.9204921.

[2] U. Uzubi, A. Ekwue and E. Ejiogu, "Artificial neural network technique for transmission line protection on Nigerian power system," *2017 IEEE PES PowerAfrica*, 2017, pp. 52-58, doi: 10.1109/PowerAfrica.2017.7991199.

[3] B. K. Sahoo, S. Pradhan, B. K. Panigrahi, B. Biswal, N. C. Patel and S. Das, "Fault detection in Electrical Power Transmission System using Artificial Neural Network," *2020 International Conference on Computational Intelligence for Smart Power System and Sustainable Energy (CISPSSE)*, 2020, pp. 1-4, doi: 10.1109/CISPSSE49931.2020.9212274.

[4] A. Elnozahy, K. Sayed and M. Bahyeldin, "Artificial Neural Network Based Fault Classification and Location for Transmission Lines," *2019 IEEE Conference on Power Electronics and Renewable Energy (CPERE)*, 2019, pp. 140-144, doi: 10.1109/CPERE45374.2019.8980173.

[5] A. Pandey, P. S. Gadekar and C. B. Khadse, "Artificial Neural Network based Fault Detection System for 11 kV Transmission Line," *2021 International Conference on Advances in Electrical, Computing, Communication and Sustainable Technologies (ICAECT)*, 2021, pp. 1-4, doi: 10.1109/ICAECT49130.2021.9392433.

[6] H. Khorashadi-Zadeh, "Artificial neural network approach to fault classification for double circuit transmission lines," *2004 IEEE/PES Transmision and Distribution Conference and Exposition: Latin America* (IEEE Cat. No. 04EX956), 2004, pp. 859-862, doi: 10.1109/TDC.2004.1432494.

[7] E. B. M. Tayeb and O. A. A. Rhim, "Transmission line faults detection, classification and location using artificial neural network," *2011 International Conference & Utility Exhibition on Power and Energy Systems: Issues and Prospects for Asia (ICUE)*, 2011, pp. 1-5, doi: 10.1109/ICUEPES.2011.6497761.

[8] P. Ray, D. P. Mishra, K. Dey and P. Mishra, "Fault Detection and Classification of a Transmission Line Using Discrete Wavelet Transform & Artificial Neural Network," *2017 International Conference on Information Technology (ICIT)*, 2017, pp. 178-183, doi: 10.1109/ICIT.2017.24.

[9] M. R. Bishal, S. Ahmed, N. M. Molla, K. M. Mamun, A. Rahman and M. A. A. Hysam, "ANN Based Fault Detection & Classification in Power System Transmission line," *2021 International Conference on Science & Contemporary Technologies (ICSCT)*, 2021, pp. 1-4, doi: 10.1109/ICSCT53883.2021.9642410.

[10] K. S. Swarup and H. S. Chandrasekharaiah, "Fault detection and diagnosis of power systems using artificial neural networks," *Proceedings of the First International Forum on Applications of Neural Networks to Power Systems*, 1991, pp. 102-106, doi: 10.1109/ANN.1991.213505.

[11] Eisa Bashier M Tayeb “Faults Detection in Power Systems Using Artificial Neural Network”, *American Journal of Engineering Research (AJER)*, Volume-02, Issue-06, pp-69-75, 2013.

[12] Jamil, M., Sharma, S.K. & Singh, R. Fault detection and classification in electrical power transmission system using artificial neural network. *SpringerPlus 4,* 334 (2015). https://doi.org/10.1186/s40064-015-1080-x.

[13] Thango, B.A. On the Application of Artificial Neural Network for Classification of Incipient Faults in Dissolved Gas Analysis of Power Transformers. *Mach. Learn. Knowl. Extr.* 2022, *4*, 839-851. https://doi.org/10.3390/make4040042.

Internet of Things (IoT) based Microgrid System for Optimal Scheduling: Case Study Kadoma-Zimbabwe

O.C.P Munemo, B.A Thango, P.N Bokoro,
Dept. of Electrical and Electronic Engineering Technology
University of Johannesburg
Johannesburg, South Africa
217084407@student.uj.ac.za; bonginkosit@uj.ac.za; pitshoub@uj.ac.za

***Abstract*— The electricity demand is increasing day by day due to industrial growth and the rise in the living standards of human beings in Kadoma, Zimbabwe. Electricity generation cannot only be dependent on fossil fuels because of carbon dioxide emissions to the atmosphere, which causes global warming and its devastating effects. In the context of distributed generation, renewable energies (RE)-based Microgrids (MGs) could be sourced to meet the electricity demand. However, the unpredictable nature of RE resources may pose a significant risk of unavailable and/ or unreliable electricity supply. This paper proposes optimal scheduling by making use of Internet of Things (IoT) devices in the MG. The MG system comprised a solar farm, wind farm, battery storage system (BSS), diesel generator, and a residential load. The proposed decision-making algorithm was developed using python and was implemented to improve scheduling in the MG system. Additionally, a comparison between three machine learning algorithms (Artificial Neural Network, Random Forest and Extreme Gradient Boosting) was implemented to determine the superior algorithm when it comes to accurately predict the sources to give power at a certain time to satisfy the load. The results indicated that the availability of electricity was enhanced by the use of IoTs in the microgrid. For accuracy prediction, the Extreme Gradient Boosting machine learning algorithm outperformed the Artificial Neural Network and Random Forest machine learning algorithms.**

Keywords—Microgrid, Optimal scheduling, Internet of Things, Artificial Neural Network, Random Forest and Extreme Gradient Boosting

I. INTRODUCTION

The Internet of Things (IoT) is a developing paradigm that aims to link various intelligent physical components for multi-domain modernization [1]. Sustainable development works to make sure that the three pillars of development environmental, social, and economic are all in balance. In 2015, the UN summit endorsed the 2030 Development Agenda and a new indicator framework for international collaboration to achieve sustainable development [2]. This agenda set forth 17 new Sustainable Development Goals (SDGs) [2]. The SDGs extend and consolidate the Millennium Development Targets while strengthening the environmental goals to make them more sustainable [2].

The United Nations Sustainable Development Goals (SDGs) give a framework for humanity to respond to a variety of essential challenges. Because of our growing demand for energy and more strict environmental quality criteria, SDG 7 prioritizes access to clean and affordable energy. Renewable energy development is one strategy to attain this goal [3]. SDG 7 aims to provide sustainable, dependable, affordable, and modern energy for all, accelerating decarbonization and reducing carbon emissions [4]. In Sub-Saharan Africa, around 55% of people lack access to electricity. According to the International Energy Agency (IEA), 860 million people globally lacked access to electricity in 2017, with 600 million of those people residing in Sub-Saharan Africa [5]. Lack of access to electricity affects Sub-Saharan Africa's environment, economy, quality of education and health care [5]. Energy demand in Africa is predicted to rise dramatically because of industrialization and population development. Most of Sub-Saharan Africa's energy comes from renewable sources, but South Africa, Nigeria, Morocco, Algeria, and Egypt rely heavily on fossil fuels. The replacement of fossil fuels with renewable energy sources is a key strategy in the fight against climate change [7]. A microgrid (MG) is a self-contained electrical grid made up of an energy storage system (ESS), loads and electrical generation, which can be connected to the main power grid or run independently. In comparison to the main grid, MG appears as a single component managed by control signals [8]. Wind, biomass, solar PV, and hydro energy are the primary sources of power in a MG [9]. It has been mentioned that MGs play a significant role in establishing universal access to electricity. However, difficulties must be resolved for MG electrification to attain its full potential [10]. MGs handle distributed energy resources (DERs) such as distributed generators (DGs) and energy storage systems. MG operators are responsible for efficient and reliable operation. To reach this goal, DGs must be generated using intermittent primary energy sources and demand [11]. Several works have been reported in the literature on MGs that use IoT for optimization purposes. The performance of MGs can be significantly improved using the Internet of Things (IoT). This is abundantly evident in modern MG infrastructure. From generation to consumption, the Internet of Things (IoT) plays a key role in the operation, control, and management of MGs.

In this paper, an off-grid MG system was developed using the MATLAB software platform. The MG comprises a solar farm, wind farm, battery storage system (BSS), diesel generator, and a residential load. A decision-making algorithm was proposed to enhance the energy management system in the MG system based on the data sent to ThingSpeak (cloud) through the IoT sensors, thus, achieving optimal scheduling. For predicting the combination of different sources in the MG at a certain time which can be classified under the load curve, ANN, Random Forest and Extreme

Gradient Boosting machine learning algorithms were applied. The accuracy of the predictions was used to determine the superior machine learning algorithm between the compared algorithms.

II. Hybrid Microgrid IoT Architecture

The MG system consists of the energy sources, a step-down transformer, and the residential load to be met. The sources produce electricity to satisfy the load. The sensors around the sources and the load measure the power being produced and the demand to be met for 24hrs. The values are sent to the cloud server (ThingSpeak) to display the real-time load demand and power data from the MG's energy sources for 24 hours. After every 10 seconds, the sensors' data was uploaded to the cloud server. The proposed architecture of the MG system to meet the residential homes in Kadoma is shown in Fig 1. The MG shows the solar PV, battery energy, diesel generator, wind turbine and residential load.

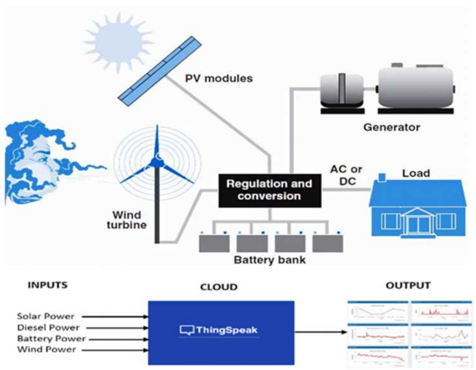

Fig. 1. System architecture [12]

The proposed hybrid MG-IoT system comprises multiple power sources and the IoT sensors measure the power being produced by the sources and send the values to the cloud. The output of the sources will be visualized on the graphs in ThingSpeak.

A. *System flowchart*

A decision-making algorithm was implemented. Python language was used to develop the algorithm. Based on the load to be satisfied, the algorithm selected the source or sources to supply. When the load demand to be met is identified, the system will select individual or combinations of power sources to meet the load. TABLE I provides the individual sources and possible combinations of the sources.

TABLE I. Individual sources and the possible combinations of sources

Sources	
S1	Battery
S2	Diesel Wind
S3	Diesel
S4	Wind
S5	Battery Wind
S6	Diesel Solar Wind
S7	Battery Diesel
S8	Battery Diesel Solar
S9	Solar
S10	Battery Solar Wind
S11	Battery Solar
S12	Solar Wind
S13	Battery Diesel Solar Wind

The proposed MG system consists of load L1 which represents the residential load. S1 to S13 represent the individual sources and the possible combinations of sources to meet the demand. The inputs to the decision-making algorithm are the sources. Fig. 2 shows the proposed decision-making algorithm, which enables users to visualize the power sources to be delivered to the load.

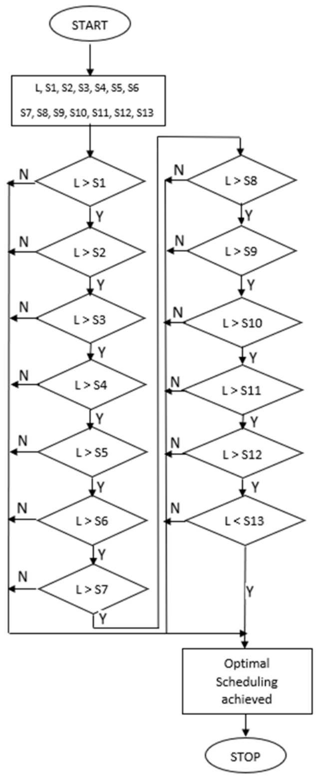

Fig. 2. Proposed decision-making flowchart

B. *Machine learning*

A comparison between three machine learning algorithms was implemented to determine the superior algorithm when it comes to predicting the sources to give power at a certain time to satisfy the load. The machine algorithms were ANN, Random Forest and Extreme Gradient Boosting algorithm. The possible combinations were input into the dataset. The data was split into 20% testing data and 80% training data. The classification was performed using machine learning algorithms, and the prediction accuracy of the techniques was determined.

1) *XGBoost*

XGBoost is an algorithm library for distributed gradient boosting that has been optimized. It provides machine learning techniques based on the Gradient Boosting Decision Tree (GBDT) architecture [13]. XGboost is developed for performance and speed. It aims to push boosted tree techniques' computational limits. The newly created tree continuously learns the differences between the actual value and the anticipated value of the current tree, and eventually collects the learning outcomes of various trees as the prediction outcomes [14]. It's faster than previous gradient-boosting random forest implementations. It is also more accurate and memory efficient. XGBoost is highly efficient in terms of resource utilization and processing speed [15].

2) *Random Tree*

Random forest is a well-known machine-learning technique that can be used to build prediction models [16]. It's a classification and regression tree-based ensemble learning algorithm. Random forest is an effective method for avoiding overfitting, which frequently occurs with a deep decision tree [13]. By using a put-back sample and randomly altering the predictor combinations in several tree evolutions, the model broadens the diversity of the decision trees. Random Forests are commonly employed in forecasting because they tolerate weak data and fit well [17].

3) *ANN*

An artificial neural network (ANN) is a model that can perform tasks such as decision-making, classification and prediction. It operates by adopting the system of operation of the human nervous system [18]. The neuron activities build a neural network. Each neuron is connected and given a weight during a training phase; the sum of these weights determines the projected output [19]. Because it is data-driven, this approach needs a lot of data in order to make accurate predictions [20]. Three layers make up a neural network. Input is the first layer. It consists of the neurons that transmit information to the layer that is hidden. The hidden layer processes incoming data and passes the results to the output layer. It contains the weight, activation and cost functions.

III. RESULTS AND ANALYSIS

In section, the results and analysis of the Internet of Things (IoT) based Microgrid for Optimal Hybrid Energy Systems Scheduling: A Kadoma, Zimbabwe Case Study. Fig. 3 illustrate the off-grid MG system that was used for the research. It consisted of the solar farm, wind farm, diesel generator, battery energy storage system, step-down transformer and the residential load.

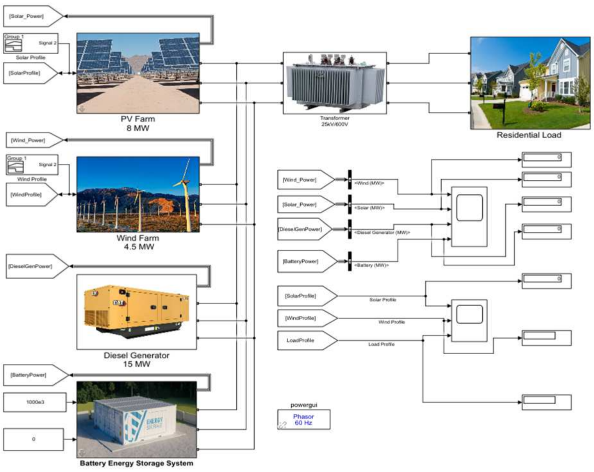

Fig. 3. Off-grid MG

The sensors measured the power produced by the DGs (solar farm, wind farm, diesel generator, and battery storage system (BSS) to meet the 24hr load profile. The sensor data was transmitted to the cloud, which is ThingSpeak. Fig. 4, Fig. 5, Fig. 6 and Fig. 7 show the solar (PV), wind turbine (WT), Battery Storage System (BSS), and diesel generator (DG) output power for 24 hours (hrs) respectively.

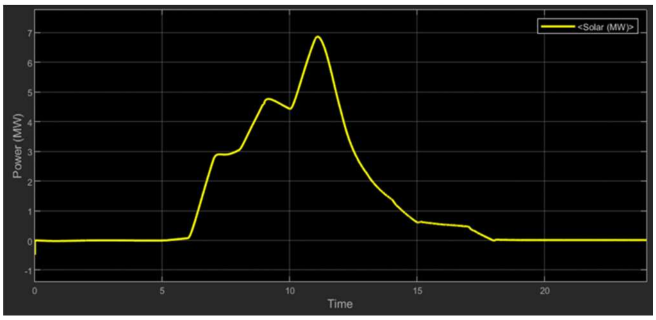

Fig. 4. Solar power source

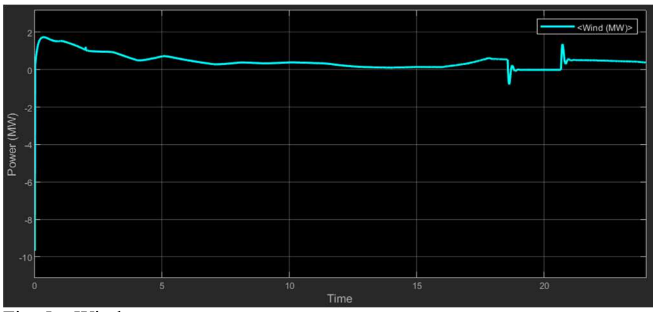

Fig. 5. Wind power source

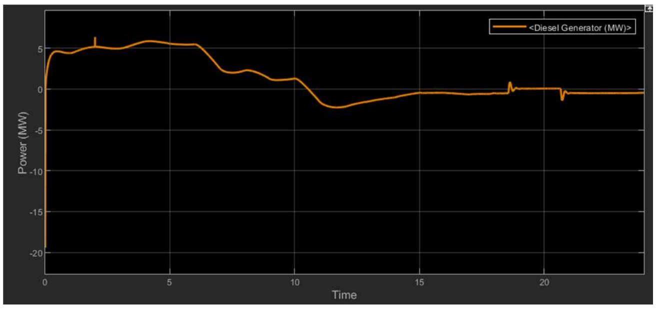

Fig. 6. Diesel generator power source

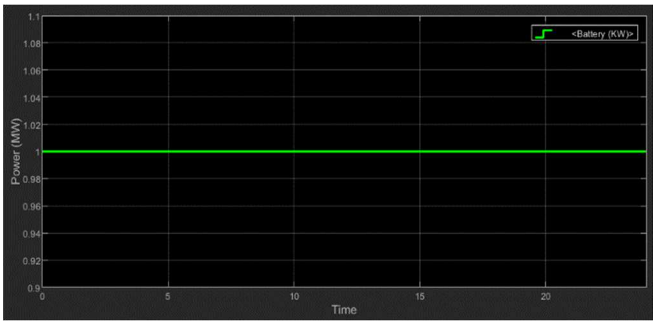

Fig. 7. Battery power source

Based on the average solar irradiation data collected in Kadoma, the solar panels are exposed to sunlight from 0700hrs to 1700hrs, resulting in the production of electricity during those hours, with the highest output occurring between 1100hrs and 1200hrs. The wind speed is often encountered between 1800hrs and 0200hrs the next day, resulting in the wind turbine providing power during that interval. In order to meet the load demand, the generator runs from 0000hrs to 1100hrs. As a result of the unreliable output of renewable energy sources and to prevent running the diesel generator for 24 hours due to expenses, the battery storage system is constantly supplied throughout the day to avoid total blackouts. The load profile of Kadoma over a 24hrs period is shown in Fig. 8.

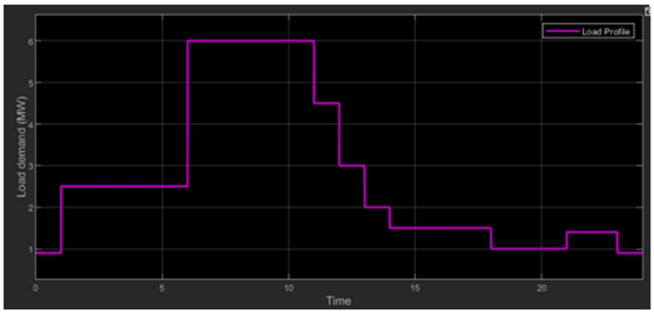

Fig. 8. Load profile

Throughout the day, the load requirement varies, with the peak demand experienced from 0600hrs to 1100hrs due to people requiring more power in that timeframe. The power data (in MW) sent to the cloud for the PV, WT, BSS, DG, and load demand are shown in Fig. 9, Fig. 10, Fig. 11, Fig. 12, and Fig. 13.

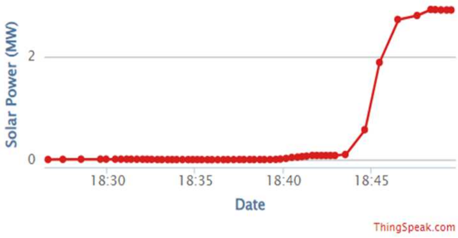

Fig. 9. Solar power data sent to the cloud

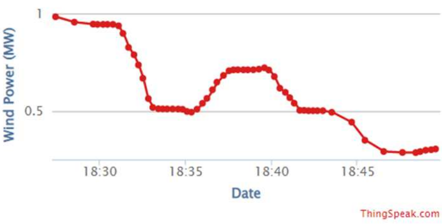

Fig. 10. Wind power data sent to the cloud

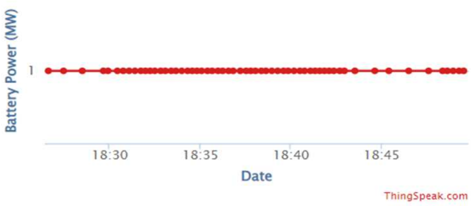

Fig. 11. Battery power data sent to the cloud

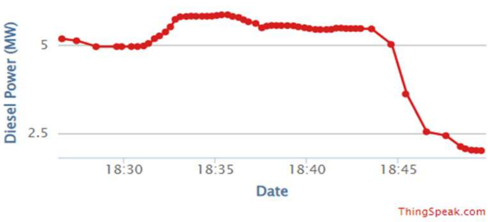

Fig. 12. Diesel generator power data sent to the cloud

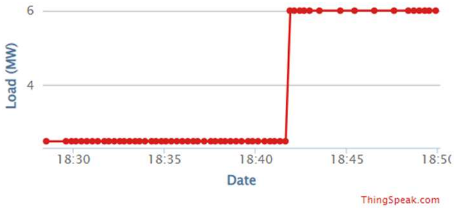

Fig. 13. Load demand data sent to the cloud

The sensors collect data from the sources and the load and send them to the cloud. The channels show the behaviour of the sources and the load demand in real-time.

A. *TEST CASES*

The decision-making algorithm will be tested using 6 different MG system cases, i.e., Case 1 at 0600hrs, Case 2 at 0700hrs, Case 3 at 1100hrs, Case 4 at 1200hrs, Case 5 at 1600hrs, and Case 6 at 1700hrs. The proposed smart MG system will make an intelligent decision that is based on the required power from the total load and the electricity available from MG sources. TABLE II demonstrate the decision-making outcomes for the different case scenarios for the total loads to be satisfied. It shows the available electricity from the solar farm, diesel generator, battery, and wind farm.

TABLE II. OPTIMAL SCHEDULING RESULTS FOR CASE SCENARIOS

Cases	**S**	**DG**	**B**	**W**	**RL**	**DM**	**TPP**
Case 1	0.08	5.48	1	0.51	6	S, DG,W	6.07
Case 2	2.71	2.55	1	0.29	6	B, DG, S	6.26
Case 3	6.78	-1.55	1	0.35	4.5	S	6.78
Case 4	4.39	-2.17	1	0.24	3	S	4.39
Case 5	0.53	-0.46	1	0.14	1.5	S, B	1.53
Case 6	0.47	-0.66	1	0.33	1.5	W, B, S	1.8

NB: S - Solar power, DG-Diesel generator power, B-Battery power, W- Wind power, RL- Required load, DM-Decision made, TPP -Total power produced

The results in case 1 indicate that the S-W-DG combination was utilized to fulfil the load demand of 6MW by producing a total power of 6.07 MW. The optimal DM for all the case scenarios can also be observed by comparing the RL with the DM and TPP.

B. *Optimum scheduling*

Fig. 14 shows how the MG is a result of the implementation of IoT sensors in it. The sensors communicated to exchange information and provided the best energy resources to provide for that certain load.

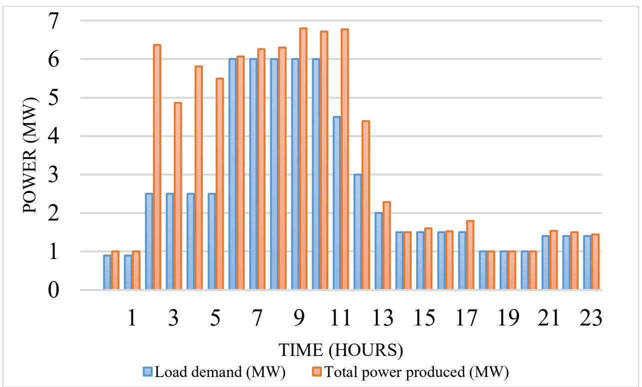

Fig. 14. Optimal Scheduling

The proposed micro-grid system made intelligent decisions based on how much power was needed by the load and how much power was available from the micro-grid, Fig.14 shows that optimum scheduling was achieved because the load demand was satisfied during the 24hrs.

C. *Comparison of prediction algorithms*

For predicting the combination of different sources in the MG at a certain time which can be classified under the load curve, the ANN, XGBoost and the Random Forest machine learning algorithms were used for classification. The accuracy results of the predictions were used to determine the superior machine learning algorithm between the two. TABLE III shows the individual and power combinations that were obtained as a result of IoT sensors communicating and achieving optimal scheduling.

TABLE III. POSSIBLE POWER SOURCE COMBINATIONS

POSSIBLE COMBINATIONS
Battery
Diesel Wind
Diesel
Wind
Battery Wind
Diesel Solar Wind
Battery Diesel
Battery Diesel Solar
Battery Diesel Solar Wind
Battery Solar Wind
Battery Solar
Solar Wind
Solar

The first algorithm used was the ANN classification algorithm, the confusion matrix was obtained as shown in Matrix 1, which summarizes the number of correct and incorrect predictions yielded by the ANN classification model.

$$\begin{bmatrix}
531, & 7, & 0, & 0, & 0, & 0, & 0, & 0, & 0, & 0, & 0, & 0 \\
0, & 0, & 0, & 0, & 0, & 0, & 0, & 0, & 0, & 0, & 0, & 0 \\
23, & 0, & 0, & 0, & 0, & 0, & 0, & 0, & 0, & 0, & 0, & 0 \\
14, & 0, & 0, & 0, & 0, & 0, & 0, & 0, & 0, & 0, & 0, & 0 \\
299, & 0, & 0, & 0, & 0, & 0, & 0, & 0, & 0, & 0, & 0, & 0 \\
0, & 0, & 0, & 0, & 0, & 0, & 0, & 0, & 0, & 0, & 0, & 0 \\
180, & 0, & 0, & 0, & 0, & 0, & 0, & 0, & 0, & 0, & 0, & 0 \\
47, & 0, & 0, & 0, & 0, & 0, & 0, & 0, & 0, & 0, & 0, & 0 \\
32, & 0, & 0, & 0, & 0, & 0, & 0, & 0, & 0, & 0, & 0, & 0 \\
1, & 0, & 0, & 0, & 0, & 0, & 0, & 0, & 0, & 0, & 0, & 0 \\
100, & 0, & 0, & 0, & 0, & 0, & 0, & 0, & 0, & 0, & 0, & 0 \\
18, & 0, & 0, & 0, & 0, & 0, & 0, & 0, & 0, & 0, & 0, & 0 \\
1, & 0, & 0, & 0, & 0, & 0, & 0, & 0, & 0, & 0, & 0, & 0
\end{bmatrix} \tag{1}$$

TABLE IV illustrates the ANN classification model performance and it had a prediction accuracy of 39%.

TABLE IV. ANN PREDICTIVE ANALYSIS REPORT

Combinations	Precision	Recall	F1-score	Support
0	0.40	0.99	0.57	538
2	0.00	0.00	0.00	23
3	0.00	0.00	0.00	14
4	0.00	0.00	0.00	299
5	0.00	0.00	0.00	78
6	0.00	0.00	0.00	180
7	0.00	0.00	0.00	83
8	0.00	0.00	0.00	32
9	0.00	0.00	0.00	1
10	0.00	0.00	0.00	100
11	0.00	0.00	0.00	18
12	0.00	0.00	0.00	1
Accuracy	-	-	0.39	1367
Macro avg	0.03	0.08	0.04	1367
Weighted avg	0.16	0.39	0.22	1367

The second classification model that was used was the Random Forest classification model. The confusion matrix shown in Matrix 2 showed the summary of how the Random Forest algorithm performed.

$$\begin{bmatrix}
538, & 0, & 0, & 0, & 0, & 0, & 0, & 0, & 0, & 0, & 0, & 0 \\
0, & 0, & 0, & 23, & 0, & 0, & 0, & 0, & 0, & 0, & 0, & 0 \\
0, & 0, & 0, & 14, & 0, & 0, & 0, & 0, & 0, & 0, & 0, & 0 \\
0, & 0, & 0, & 299, & 0, & 0, & 0, & 0, & 0, & 0, & 0, & 0 \\
0, & 0, & 0, & 4, & 0, & 74, & 0, & 0, & 0, & 0, & 0, & 0 \\
0, & 0, & 0, & 0, & 0, & 180, & 0, & 0, & 0, & 0, & 0, & 0 \\
0, & 0, & 0, & 0, & 0, & 3, & 80, & 0, & 0, & 0, & 0, & 0 \\
0, & 0, & 0, & 20, & 0, & 0, & 12, & 0, & 0, & 0, & 0, & 0 \\
1, & 0, & 0, & 0, & 0, & 0, & 0, & 0, & 0, & 0, & 0, & 0 \\
0, & 0, & 0, & 100, & 0, & 0, & 0, & 0, & 0, & 0, & 0, & 0 \\
0, & 0, & 0, & 18, & 0, & 0, & 0, & 0, & 0, & 0, & 0, & 0 \\
1, & 0, & 0, & 0, & 0, & 0, & 0, & 0, & 0, & 0, & 0, & 0
\end{bmatrix} \tag{2}$$

TABLE V illustrates the Random Forest classification model performance and it had a prediction accuracy of 80% which is significantly higher than the ANN classification model.

TABLE V. RANDOM FOREST ALGORITHM PREDICTIVE ANALYSIS REPORT

Combinations	Precision	Recall	F1-score	Support
0	1.00	1.00	1.00	538
2	0.00	0.00	0.00	23
3	0.00	0.00	0.00	14
4	0.63	1.00	0.77	299
5	0.00	0.00	0.00	78
6	0.70	1.00	0.82	180
7	0.87	0.96	0.91	83
8	0.00	0.00	0.00	32
9	0.00	0.00	0.00	1
10	0.00	0.00	0.00	100
11	0.00	0.00	0.00	18
12	0.00	0.00	0.00	1
Accuracy	-	-	0.80	1367
Macro avg	0.27	0.33	0.29	1367
Weighted avg	0.67	0.80	0.73	1367

The third classification model that was used was the Extreme Gradient Boosting classification model, a confusion matrix was obtained as shown in Matrix 3 and it was used to quantify the performance of the algorithm and to visualize important predictive analytics like precision, recall, F1-score and support data as shown in TABLE VI.

$$
\begin{bmatrix}
538 & 0 & 0 & 0 & 0 & 0 & 0 & 0 & 0 & 0 & 0 & 0 \\
0 & 23 & 0 & 23 & 0 & 0 & 0 & 0 & 0 & 0 & 0 & 0 \\
0 & 0 & 14 & 14 & 0 & 0 & 0 & 0 & 0 & 0 & 0 & 0 \\
0 & 0 & 0 & 298 & 0 & 0 & 0 & 1 & 0 & 0 & 0 & 0 \\
0 & 0 & 0 & 0 & 78 & 0 & 0 & 0 & 0 & 0 & 0 & 0 \\
0 & 0 & 0 & 0 & 0 & 180 & 0 & 0 & 0 & 0 & 0 & 0 \\
0 & 0 & 0 & 0 & 0 & 0 & 83 & 0 & 0 & 0 & 0 & 0 \\
0 & 1 & 0 & 0 & 1 & 0 & 0 & 30 & 0 & 0 & 0 & 0 \\
1 & 0 & 0 & 0 & 0 & 0 & 0 & 0 & 0 & 0 & 0 & 0 \\
0 & 0 & 0 & 0 & 0 & 0 & 0 & 0 & 0 & 99 & 1 & 0 \\
0 & 0 & 0 & 0 & 0 & 0 & 0 & 0 & 0 & 0 & 18 & 0 \\
1 & 0 & 0 & 0 & 0 & 0 & 0 & 0 & 0 & 0 & 0 & 0
\end{bmatrix} \tag{3}
$$

TABLE VI. XGBOOST PREDICTIVE ANALYSIS REPORT

Combinations	Precision	Recall	F1-score	Support
0	1.00	1.00	1.00	538
2	0.96	1.00	0.98	23
3	1.00	0.86	0.92	14
4	1.00	1.00	1.00	299
5	0.99	0.00	0.99	78
6	1.00	1.00	1.00	180
7	1.00	1.00	1.00	83
8	0.91	0.94	0.92	32
9	0.00	0.00	0.00	1
10	0.99	1.00	1.00	100
11	1.00	0.94	0.97	18
12	0.00	0.00	0.00	1
Accuracy	-	-	0.99	1367
Macro avg	0.82	0.81	0.82	1367
Weighted avg	0.99	0.99	0.98	1367

The Extreme Gradient Boosting classification model had an accuracy of 99% when it came to predicting the sources to give power at a certain time to satisfy the load. For ANN and Random Forest respectively, the first column represents the possible combinations of the power sources and the remaining 4 columns represent precision, recall, F1-score and support data of the sources. ANN is designed for big sample sizes which is why the predictive accuracy was relatively small as compared to the other two. The Extreme Gradient Boosting outperformed the Random Forest algorithm because the Extreme Gradient Boosting is designed to correct errors and capture complex patterns in the data.

IV. CONCLUSION

An Off-grid MG system was successfully developed which linked the load and distributed generating sources together. The cloud server stored the data (ThingSpeak). As a result, users will find it easier to retrieve and monitor micro-grid data. From the system, a decision-making algorithm was constructed that led to optimal scheduling, which enhanced electricity availability in Kadoma. Three machine learning classification methods, ANN, Random Forest and Extreme Gradient Boosting, predicted the combination of MG sources under the load curve. The Extreme Gradient Boosting algorithm outperformed the other two as it had a superior prediction accuracy.

V. REFERENCES

[1] B. Sinha and R. Dhanalakshmi, "Recent advancements and challenges of Internet of Things in smart agriculture: A survey," *Future Generation Computer Systems,* Vol. 126, 2022, pp: 169-184.

[2] M. Muntean , D. Danaiata, L. Hurbean and C. Jude, "A Business Intelligence & Analytics Framework for Clean and Affordable Energy Data Analysis," *Sustainability,* Vol. 13, Issue 2, 2021, pp: 1-25.

[3] J. He, Y. Yang, Z. Liao and A. Xu , "Linking SDG 7 to assess the renewable energy footprint of nations by 2030," *Applied Energy,* vol. 317, 20222, pp: 1-13.

[4] [3] M. R. Mawla and M. Z. R. Khan, "A Study on Sustainable Development Goal 7: Future Plan to Achieve the Affordable and Clean Energy - Bangladesh Perspective," in *2020 IEEE Region 10 Symposium (TENSYMP), 2020,* pp. 421-426.

[5] H. Kuffar, "The Profitability and Affordability of Smart Renewable Microgrid in Sub-Saharan Africa," in *2020 IEEE Electric Power and Energy Conference (EPEC), 2020,* pp: 1-4.

[6] G. Mutezo and J. Mulopo, "A review of Africa's transition from fossil fuels to renewable energy using circular economy principles," *Renewable and Sustainable Energy Reviews,* vol. 137, 2021, pp: 1-15.

[7] J. Gómez, J. Rodriguez, C. Garcia , L. Tarisciotti, F. Flores-Bahamonde, J. Pereda, F. Nuñez, A. Z. Cipriano and J. C. Salas, "An overview of Microgrids challenges in the mining industry," *IEEE Access,* vol. 8, 2020, pp: 1-16.

[8] V. K. Garg, and S. Sharma, "Overview on Microgrid System," in *2018 Fifth International Conference on Parallel, Distributed and Grid Computing (PDGC), 2018,* pp:1-6.

[9] M. Hannan, S. Tan, A. Al-Shetwi, K. Jern and R. Begum, "Optimized controller for renewable energy sources integration into Microgrid: Functions, constraints and suggestions," *Journal of Cleaner Production,* Vol. 256, 2020, pp: 1-21.

[10] T. Raji, F. Aleotti, A. Bharadwaj, and N.J. Williams, "Challenges of Microgrid project development in sub-Saharan Africa: an industry perspective," in *2021 IEEE PES/IAS PowerAfrica*, 2021, pp: 1-3.

[11] M. Ebrahimi and N. Amjady, "Adaptive robust optimization framework for day-ahead Microgrid scheduling," *International Journal of Electrical Power & Energy Systems,* vol. 107, 2019, pp: 213-223.

[12] S. Ramoji and B. Kumar, "Optimal economical sizing of a PV-wind hybrid energy system using genetic algorithm and teaching learning based optimization," *International Journal of Advanced Research in Electrical, Electronics and Instrumentation Engineering,* Vol. 3, Issue 2, 2014, pp: 7352-7367.

[13] W. Wang , G. Chakraborty and B. Chakraborty , "Predicting the risk of chronic kidney disease (ckd) using machine learning algorithm " *Applied Sciences,* Vol. 11, Issue 1, 2020, pp: 1-17.

[14] Z. Yan, H. Chen, X. Dong, K. Zhou and Z. Xu, "Research on prediction of multi-class theft crimes by an optimized decomposition and fusion method based on XGBoost" *Expert Systems with Applications,* Vol. 207, 2022, pp: 1-10.

[15] S. Jhaveri, I. Khedkar, Y. Kantharia and S. Jaswal, "Success prediction using random forest, catboost, xgboost and adaboost for kickstarter campaigns," in *2019 3rd International Conference on Computing Methodologies and Communication (ICCMC)*, 2019, pp 1-4.

[16] J. Speiser, M. Miller, J. Tooze and E. Ip, "A comparison of random forest variable selection methods for classification prediction modeling" *Expert systems with applications,* Vol. 131, 2019, pp: 93-101.

[17] D. Liu and K. Sun, "Random forest solar power forecast based on classification optimization" *Energy,* Vol. 187, 2019, pp. 1-11.

[18] E. Wahyuni , "Arabic speech recognition using MFCC feature extraction and ANN classification," in *2017 2nd International conferences on Information Technology, Information Systems and Electrical Engineering (ICITISEE)*, 2017, pp 1-4.

[19] D. Saquib, M. Nasser and S. Ramaswamy, "Image Processing Based Dust Detection and prediction of Power using ANN in PV systems," in *2020 Third International Conference on Smart Systems and Inventive Technology (ICSSIT)*, 2020, pp 1-7.

[20] A. Kumar, M. Rizwan and U. Nangia, "Artificial neural network based model for short term solar radiation forecasting considering aerosol index," in *2018 2nd IEEE International Conference on Power Electronics, Intelligent Control and Energy Systems (ICPEICES)*, 2018, pp 1-6.

Optimal Positioning and Sizing of Distributed Generation to Reconfigure Power Network Using Artificial Intelligent Algorithm

Mlungisi Ntombela
Faculty of engineering and built environment, Department of electrical power engineering
Durban university of technology
Durban, South Africa
mlungisi390@gmail.com

Kabeya Musasa
Faculty of engineering and built environment, Department of electrical power engineering
Durban university of technology
Durban, South Africa
MusasaK@dut.ac.za

Moketjema Clarence Leoaneka
Faculty of engineering and built environment, Department of electrical power engineering
Durban university of technology
Durban, South Africa
Moketjemal@dut.ac.za

Abstract: --- **In distribution systems, voltage instability and power loss are key issues. However, effective network reconfiguration, which includes integrating distributed generation (DG) units in the distribution network, often mitigates these issues. The appropriate positioning and sizing of DGs are essential in this regard. The goal of this study is to determine where and how many DGs should be placed in a radial distribution network before and after reconfiguration. The ideal positioning and sizing of the DGs both before and after the radial network's reconfiguration are determined using artificial intelligent algorithm (AI) which is hybrid genetic algorithm particle swarm optimization (HGAPSO). Power losses are eliminated, voltage profiles are elevated, and system stability is increased with the use of hydro power DG coordination in an active distribution network. With the addition of DG units to the test system, the simulation results demonstrated a significant improvement in the percentage power loss reduction. Similar improvements are made to the system's minimum bus voltage. The findings of the comparison analysis demonstrated that the suggested approach is successful at lowering the voltage variation and power loss of the distribution system.**

Keywords: *voltage deviation, power loss minimization, particle swarm optimization, network reconfiguration, voltage stability enhancement, distributed generation.*

1. INTRODUCTION

For all energy utilities, meeting the growing demand for electricity presents a considerable challenge. 75% of the world's energy needs is met by burning fossil fuels. A prospective energy plan involving renewable resources has become necessary due to rising greenhouse gas emissions, global warming, the depletion of fossil fuels, and rising fuel prices. Over the past ten years, many nations have placed a high priority on developing renewable energy technologies. The power losses and voltage instability that result from their various networks present a significant issue for electrical distribution businesses [1]. As a result of these issues, their operating expenses rise and their profits fall.

There are many difficulties facing the current distribution networks. Customers place a high value on voltage profiles since they are a must for high-quality voltage-controlled electrical equipment. At the end of a feeder, DGs can offer voltage support to raise the voltage. Due to the presence of DGs, distribution grids may experience significant changes in network dependability, power flow, relay safety, voltage profile, and stability. Power stability and improved distribution network reliability, along with a number of operational and cost-effective benefits, are the main benefits of DG integration in power systems. Better voltage profiles, lower power loss, peak load shaving, fewer transmissions, and network expansion are a few of the advantages for both utilities and customers [2].

In order to reduce power loss to the lowest possible level, limit branch current, and improve voltage stability both before and after the distribution network was reconfigured, a multi-objective PSO-based strategy was used in this research to determine the placement and size of multiple DG units. In terms of the bus voltage magnitude, line current limitation, minimizing voltage variation, and energy losses, the network's performance is improved to some extent by the integration of multi-DGs. Performance of a self-contained micro-grid can be improved by further distribution system modification. When analyzing the effects of DG units, the main restrictions voltage profile, voltage variation, current, and power losses are taken into account [3].

2. PROBLEM FORMULATION

This study's main focus is on how to best integrate distributed energy resources (DER) and new energy sources (NR) into micro-grids to minimize voltage dips and energy losses. To resolve the multi-objective optimization issue, a PSO algorithm is suggested. Typically, radial, the distribution network has a very high R/X ratio when compared to a transmission system.

The distribution system's load-flow issues can be solved using the Newton-Raphson load flow approach. Calculating the bus voltage, line current, and PQ losses at each bus is the major goal of the load flow. In order to increase voltage profile and minimize loss in the base and modified distribution system, our suggested solutions handled DG sizing and placement [4].

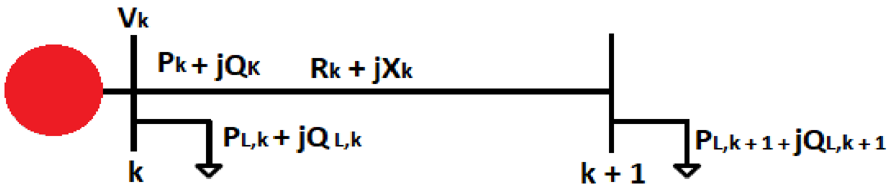

Figure 1: Load flow distribution system

- A line section between k and k + 1 with an impedance of Rk + jXk
- Loads at bus k and k + 1, as shown in figure 1.
- Pk and Qk are the real and reactive power flows from bus k to k + 1, respectively
- Vk and Vk + 1 are the complex voltages.

2.1. Test System Description

This study's examination of the IEEE-33 bus radial system includes 33 nodes, 37 lines overall, 32 loads, 32 PQ buses, 1 feeder, and 1 slack bus. 32 closed switches and 5 open switches are often employed. Substation Bus 1 in the network serves as the main power supply, providing a constant voltage of 12.66 kV. The 33-bus test system's line and load data are taken from [6]. Figures 2a and 2b illustrate the IEEE-33 bus network before and after reconfiguration, respectively. All loads are taken into account as a continuous load of active power at 3715 kW and reactive power at 2300 kVAr, respectively. For the purpose of examining the effects of the DGs factors like voltage profile and power losses are taken into account.

2.2. System Reconfiguration

Switches that can be divided into sections make up the distribution system. This uses the network resources most effectively for the current state of loading. By locating and sizing DGs through reorganizing the feeder, we proposed a minimizing of active and reactive power loss in the redesigned network. To keep the switch state open or closed, the feeder makes the decision. NR is the method of changing the distribution network's topology by utilizing switches in various states. To modify a network from its initial setup to an ideal state, the switching states are altered. As a result, NR aims to lower the distribution system's overall power losses and voltage variation. Figure 2a illustrates how to open switches, such as to get the system's ideal configuration [5].

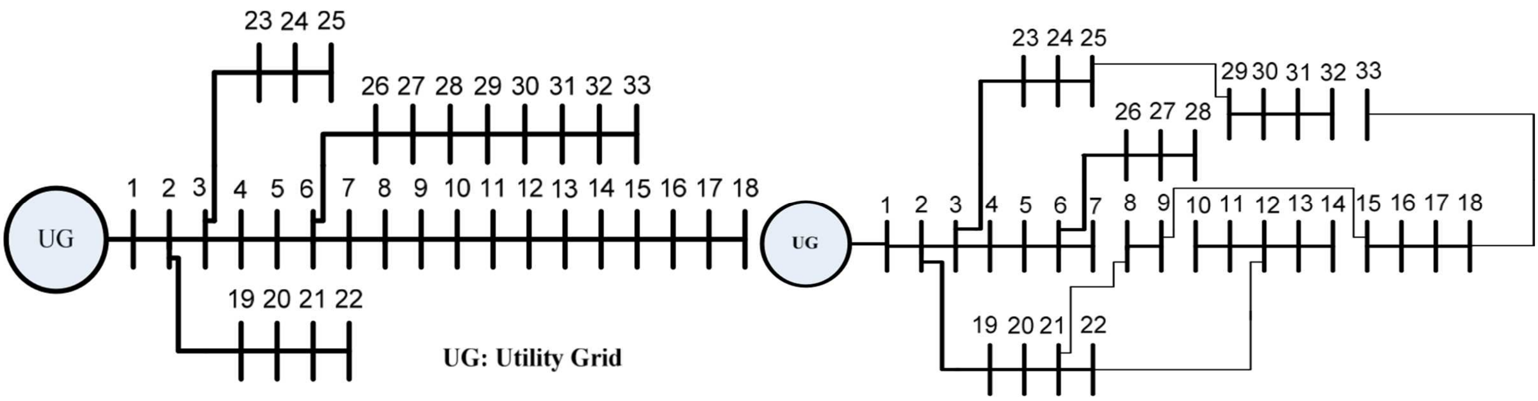

(a) (b)

Figure 2 (a, b): IEEE-33 bus test system before and after reconfiguration respectively

3. DG PLACEMENT OF THE DISTRIBUTION SYSTEM

The main driving forces behind the integration of DGs into distribution networks are the depletion of energy resource assets, increases in load demand, and the requirement for clean power generation. DGs might be extremely important in converting traditional distribution networks into active distribution networks [7]. The best DG sizing and placement are necessary for the conversion of a conventional radial distribution network into an independent micro-grid network. Current capacity of the feeder, voltage profile of the system, and operating limitations to reduce network power loss and control voltage variations in each bus (within prescribed limits) need all be met simultaneously [8].

3.1. Implementation of Genetic Algorithm

GA is when the population represents candidate solutions due to n chromosomes. Each chromosome represents a real value vector with m dimensions, where m is the quantity of variables that were optimized.

3.2. PSO Algorithm

PSO is artificial intelligent optimization technique that draws its initial inspiration from the social behavior of fish schools and flocks of birds. The PSO algorithm creates a population of particles that positioned randomly throughout the search space. Particles represent solutions to the problem and have fitness values. It optimized based on its fitness [10]. Eventually, particles will move towards the optimal position as they will have experienced their best position and the best solution. An updated velocity of particles was based on three factors, namely its past velocity; its best position to date and the best position the entire swarm has reached in the past [11]

3.3. Power Generation Limit

This upper and lower real and reactive power generation limits also apply to generators and other reactive sources [12].

$$P_{gi}^{min} \leq P_{gi} \leq P_{gi}^{max}, i = 1,2, \dots Ng \quad (1)$$

$$Q_{gi}^{min} \leq Q_{gi} \leq Q_{gi}^{max}, i = 1,2, \dots Ng \quad (2)$$

P_{gi}^{min} and P_{gi}^{max} are the real power generation limits, both minimum and maximum; and Q_{gi}^{min} and Q_{gi}^{max} are the reactive power generation's minimum and maximum limitations.

3.4. Voltage Limit

The magnitude limits for upper and lower voltages, as well as at bus-i, are included. In actual practice, the generator voltage will be equal to the load or bus voltage and some values related to the line impedance and the power flowing along the line. It is important to maintain a standard voltage on each line [13,14].

$$V_i^{min} \leq V_i \leq V_i^{max}, i = 1,2, \dots Ng \quad (3)$$

Where: V_i^{min} and V_i^{max} are the minimum and maximum voltage limits.

3.5. DG Power Generation Limit

Upper and lower limits on their real and reactive power production must be satisfied by distribution generators (DGs) linked at bus-i [15].

$$P_{DGi}^{min} \leq P_{DGi} \leq P_{DGi}^{min}, i = 1,2, \dots Ng \quad (4)$$

$$Q_{DGi}^{min} \leq Q_{DGi} \leq Q_{DGi}^{min}, i = 1,2, \dots Ng \quad (5)$$

P_{DGi}^{min} and P_{DGi}^{min} are the minimum and maximum real power generation limits of the distributed generators.

Q_{DGi}^{min} and P_{DGi}^{min} are the minimum and maximum reactive power generation limits of the distributed generators.

4. RESULTS AND DISCUSSION

4.1. POWER LOSS REDUCTION

Based on the columns in Table 1 that represent fitness and DG size, four optimal locations for the DGs of hydro power and their corresponding optimal sizes were selected. The minimal fitness values and corresponding DG sizes were allocated at these locations. The four most effective locations, together with their optimum DG sizes, are as follows:

- Bus number 19 with a DG which is generating 11.7872MW and 2.9609MVar;
- Bus number 23 with a DG which is generating 11.7548MW and 3.0002MVar;
- Bus number 24 with a DG which is generating 12.0001 MW and 1.3702MVar; and
- Bus number 30 with a DG which is generating 11.8308MW and 1.5817MVar.

Table 1: Comparison of Bus Voltage using hydro power DG

Method	Bus Number	DG Size	Power Losses		Power Loss Reduction		%Power Loss Reduction	
		MW	MW	MVar	MW	MVar	%MW	%MVar
Power Loss without DG			17.8798					
GA	10	11.35+j1.22	12.2260	-	5.6538	-	31.5890	-
	23	11.47+j1.17						
	24	11.92+j2.04						
	30	11.816+j1.468						
PSO	10	11.474+j2.159	12.1060	-	5.7738	-	32.2923	-
	17	11.981+j0.919						
	20	11.67+j2.309						
	30	11.349+j3						
IPSO	10	11.83+j0.001	11.9500	-	5.9298	-	33.1648	-
	21	11.433+j3						
	24	11.739+j3						
	30	11.995+j0.001						
HGAIPSO	19	11.7872+j2.9609	11.4001	-	6.4797	-	36.2403	
	23	11.7548+j3.0002						
	24	12+j1.3702						
	30	11.8308+j1.5817						

According to table 1 and figure 3, using the HGAIPSO method to optimize the location and size of this type of DG results in a 36.2403% reduction in real power losses. As compared to GA, PSO and IPSO, HGAIPSO method shows a higher percentage. the GA shows a reduction of 31.5890%; PSO shows a reduction of 32.2923%; and IPSO shows a reduction of 33.1648%. It is also comparable to the sizes determined using the other techniques that were chosen for the DGs sizing and allocation for power loss minimization. Since the overloads of the main transformer and feeder line play different roles with respect to the load balancing weight, the objective function is the load balancing weight.

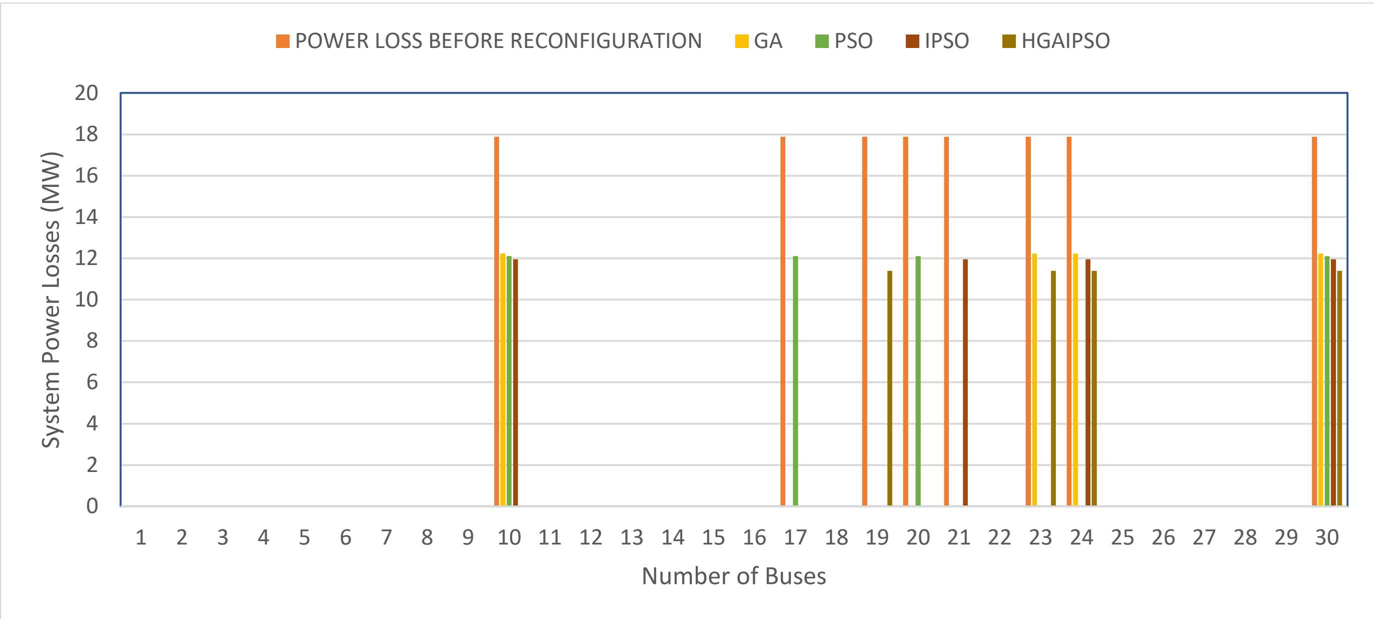

Figure 3: A comparison of Results for power loss obtained using hydro power DG

4.2. VOLTAGE PROFILE

An analysis of the voltage profile of the IEEE-30 bus system was performed after the placement and sizing of the hydro power DGs were optimized. Below is a table showing the results of the bus voltage levels under this condition. A comparison is also given in the table between this case and the one without DGs, and with DGs placed and sized using other methods. This comparison was also done using a bar chart, as shown in figure 6 below.

The voltages for the cases with and without DGs are compared in figure along with their ideal placement and sizing based on GA, PSO, IPSO, and HGAIPSO. Even when the voltages in an IEEE-30 bus system are within the allowed range, namely 0.95 pu to 1.1 pu, a DG might still have an impact on the voltage stability of the system. Figure 4 and both show this. The addition of DGs does not cause voltage levels to exceed permissible thresholds. It is evident that all the bus voltages were within a range of 0.95pu to 1.1pu. Thus, the HGAIPSO method improved the voltage levels of the bus that had voltages, and no voltage exceeded the acceptable limit

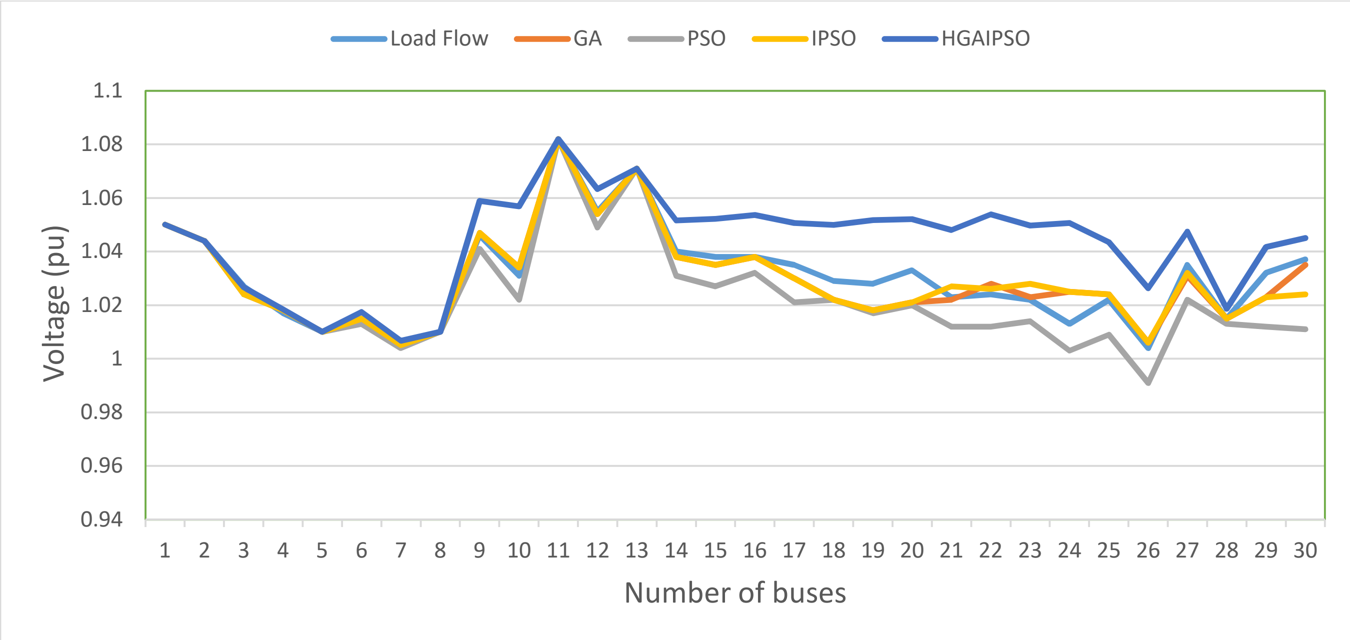

Figure 4: Bus voltage profile comparison using hydro power DG

5. CONCLUSION

By optimizing the location and size of DGs, the problem of power losses in systems was solved because power losses are reduced and voltage profiles are improved. This study presented a hybridized algorithm (HGAIPSO) to reduce system power losses and improve voltage profiles. Combining the sensitivity factors and tests on the IEEE-30 bus test system was effective in reducing the number of iterations for algorithms. 14 buses were chosen as the best DG locations for the IEEE-30 bus test system. Comparing the HGAIPSO method to the GA, PSO and IPSO methods in three types of DGs using the IEEE-30 bus shows that it can be reduced. According to hydro power DG real power losses were reduced by 36.2403%. This reconfiguration produced the highest bus voltage of 1.01pu, which shows that the voltage profile is generally improved.

6. REFERENCES

[1] Minnan Wang and Jin Zhong, "A Novel Method for Distributed Generation and Capacitor Optimal Placement considering Voltage Profiles", 978-1-4577-1002-5/11/©2019 IEEE, Vol. 7, pp. 47-55, 2019.

[2] Satish Kansal, B.B.R. Sai, Barjeev Tyagi, Vishal Kumar "Optimal placement of distributed generation in distribution networks", International Journal of Engineering, Science and Technology, Vol. 3, pp. 47-55, 2011.

[3] Ackermann, T., Anderson, G. and Soder, L., "Distributed Generation: A Definition", Electric Power System Research, Vol. 8, pp.195-204, 2018.

[4] Soroudi. An and M. Ehsan.: "Multi objective distributed generation planning in liberized electricity market", in IEEE Proc., Vol.9, pp.1-7, 2011.

[5] S. Chandrashekhar Reddy, P. V. N. Prasad and A. Jaya Laxmi, “Power Quality Improvement of Distribution System by Optimal Placement and Power Generation of DGs using GA and NN”, European Journal of Scientific Research ISSN 1450-216X, Vol.69, pp. 326-336, 2012.

[6] An D.T. L et al. “Maximising Voltage Support in Distribution Systems by Distributed Generation”, Australian Research Council and Aurora Energy, Tasmania, Vol.12, 2015.

[7] Andrew Keane, Member, Luis (Nando) F. Ochoa, Eknath Vittal, Chris J. Dent and Gareth P. Harrison, “Enhanced Utilization of Voltage Control Resources with Distributed Generation”, ©2011 IEEE, Vol.15, pp.456-564, 2011.

[8] W. El-Khattam, K. Bhattacharya, Y. H. Hegazy, et al.: "Optimal investment planning for distributed generation in a competitive electricity market" (Abstract), IEEE Trans. Power Syst., Vol.5, pp. 1674-1684, 2018.

[9] Ault, G.W. and J.R. McDonald, “Planning for distribution generation within distribution networks in restructuted electricity markets”. IEEE Power Eng. Rev., Vol.20, pp.52-54, 2016.

[10] Caisheng, W. and M.H. Nehrir. “Analytical approaches for optimal placement of distributed generation sources in power systems.” IEEE Trans. Power Sys. Vol.19(4): pp.27-34, 2013.

[11] Rahmat-Allah Hooshmand — Mohammad Ataei, “Optimal capacitor placement in actual configuration and operational conditions of distribution systems using RCGA”, Journal of Electrical Engineering, Vol. 58, pp.189–199, 2019.

[12] Yustra, Mochamad Ashari and Adi Soeprijanto, “Optimal Distributed Generation (DG) Allocation for Losses Reduction Using Improved Particle Swarm Optimization (IPSO) Method”, J. Basic. Appl. Sci. Res., Vol.2(7), pp 7016-7023, 2012.

[13] M. Vatankhah and S.M. Hosseini, “PSO based voltage profile improvement by optimizing the size and location of DGs”, IJTPE, issue 11, Vol.4, pages 135-139, February 2012.

[14] M. M. Aman, G. B. Jasmon, K. H. Solangi, A. H. A. Bakar, and H. Mokhlis, “Optimum Simultaneous DG and Capacitor Placement on the Basis of Minimization of Power Losses”, International Journal of Computer and Electrical Engineering, Vol.5, No.5, October 2013.

[15] Nasim Ali Khan, S. Ghosh, S. P. Ghoshal, “Optimal siting and sizing of shunt capacitors in radial distribution systems using Novel BPSO algorithm”, International Journal of Emerging Technology and Advanced Engineering, Vol.3, Issue 2, February 2013.

2023 SAUPEC Conference, Johannesburg, South Africa, January 24-26, 2023

Development of Dissolved Gas Analysis-based Fault identification System using Machine Learning with Google Colab

Nkululeko L.Z Msomi & Bonginkosi A. Thango
Dept. of Electrical and Electronic Engineering Technology
University of Johannesburg
Johannesburg, South Africa
218067205@student.uj.ac.za; bonginkosit@uj.ac.za

***Abstract*—Due to its high sensitivity to small amounts of electrical faults, dissolved gas analysis (DGA) is a popular method for identifying faults in power transformers. The early prediction of fault type in transformers is a crucial part of power system reliability. As a result of this, it is extremely essential to keep a close eye on the behaviour of the power transformer while in service. Periodic monitoring of the condition of power transformers is important to prevent power outages. Early fault detection can result in substantial operational and maintenance cost savings, as well as the prevention of any early breakdown or failure. The current research study aims to assist experts in precisely diagnosing power transformer faults by providing an alternative to the drawbacks that classical DGA methods viz. Dornensburg ratio, Rogers' ratio, IEC ratio, and Key gas possess i.e., the lack of a proper diagnosis for instances that do not fall under the usual DGA codes. This work proposes an artificial intelligence (AI)-based fault diagnoses algorithm, which is a Support Vector Machine (SVM) for improving the diagnostic accuracy of existing DGA methods. According to the author's knowledge, there are no existing research works that have developed an SVM-based fault classification approach using Google Colab. As a result, the proposed work contributes to the fault diagnostics of power transformers. The results presented in this research showed that the proposed method SVM has high accuracy in diagnosing faults in power transformers as compared to the four methods presented.**

Keywords—SVM, DGA, methods, power transformers, faults

Nomenclature:

NF	No fault
PD	Partial discharge
D1	Electrical discharge of low energy
D2	Electrical discharge of high energy
T1	Thermal faults of temperature T < 300° C
T2	Thermal faults, 300°C < T < 700° C
T3	Thermal faults, T > 700 C
UD	Undetermined fault
TO	Thermal Oil
TC	Thermal Cellulose
DGA	Dissolved Gas Analysis
IRM	IEC Ratio Method
RRM	Roger's Ratio Method
DRM	Dornenburg Ratio Method
KGM	Key Gas Method

I. INTRODUCTION

Power transformers are essential components of power systems. Failures of power transformers are frequently caused by a lack of electrical properties in oil insulation, which will have a detrimental effect on electrical power systems [1]. Early diagnosis of power transformer failures can significantly minimize the cost of restoring damaged transformers while preserving the system's stability. Dissolved gas analysis is a frequently used diagnostic technology for detecting impending defects in power transformers based on the association between the concentration of dissolved gases in oil transformers and a specific problem [1].

Dissolved gas analysis (DGA) in oil is recognized as a credible and widely used technique for identifying faults in oil-filled power transformers. Different electrical and thermal stresses will cause the oil that insulates transformers to break down, letting out and dissolving many gases [2]. The concentration of these gases is measured in parts per million (ppm): hydrogen (H_2), methane (CH_4), ethane (C_2H_6), ethylene (C_2H_4), acetylene (C_2H_2), carbon monoxide (CO), and carbon dioxide ($C0_2$). For dissolved gas analysis to understand the onset of transformer faults, the IEC ratio method, Rogers' method, Dornenburg ratio method, and key gas method are frequently employed [2]. Several DGA interpretation techniques rely on gas ratios between the previously stated gases, except for the key gas method, which employs individual key gases. All of these traditional methods are simple to execute, but their accuracy and stability with DGA data uncertainties are limited [2].

Many studies have been conducted on transformer fault diagnoses using Python [3] – [4], MATLAB [5] – [6], WEKA [7] et cetera. However, no related works have explored Google Colab in this research field.

The most significant part of fault gas analysis is the accurate diagnosis of the fault that produced the observed gases. In this work, the four traditional DGA methods for interpreting fault gas are examined. Microsoft Excel was used to design an Excel sheet of these DGA methods presented that can be used to automatically find faults and the results of each method were compared with the results of the proposed Google Colab-based SVM diagnostic algorithm.

II. MATERIALS AND METHODS

A. DGA interpretation Methods

Under abnormal electrical or thermal stress, insulating oils decompose and release minute quantities of gases. The makeup of these gases depends on the type of problem. Using dissolved gas analysis (DGA), faults such as partial discharge (corona), thermal, and arcing can be distinguished in a wide variety of oil-filled equipment [1]. Similar to a blood test or a scan of the human body, DGA can provide an early diagnosis and boost the likelihood of locating the proper treatment. DGA contains numerous techniques. In this research, four of the most popular techniques were examined.

a) IEC Ratio Method

This method was derived from Roger's Ratio, with the exception that the ratio C_2H_6/CH_4 was eliminated because it indicated only a narrow temperature range of breakdown [1]. As indicated in the table below, the remaining three gas ratios have distinct code ranges compared to Roger's ratio approach. As can be seen in TABLE I and TABLE II, the following method involves a total of seven different fault types, five different gases, and four different gas ratios.

TABLE I. GAS RATIOS [1].

Ratios	Gases
R_1	CH_4/H_2
R_2	C_2H_2/C_2H_4
R_3	C_2H_4/C_2H_6

TABLE II. FAULT INTERPRETATION [1].

Case	C_2H_2/C_2H_4	CH_4/H_2	C_2H_4/C_2H_6
PD	<0.1	<0.1	<0.2
D1	>1.0	0.1-0.5	>1.0
D2	0.6-2.5	0.1-1.0	>2.0
T1	<0.1	>1.0	<1.0
T2	<0.1	>1.0	1.0
T3	<0.1	>1.0	>3

b) Roger's Ratio Method

This approach was refined further to become an IEC standard for diagnosis, the classic Rogers ratio method used four gas ratios: CH_4/H_2, C_2H_6/CH_4, C_2H_4/C_2H_6, and C_2H_2/C_2H_4. The revised Rogers approach employs two tables, one of which defines the ratio's code as shown in TABLE III and the other the diagnosis criteria as shown in TABLE IV. The ratio C_2H_6/CH_4 pretty much shows a restricted temperature range of breakdown and did not aid in further fault identification [3].

TABLE III. ROGER'S GAS RATIOS [3].

Ratios	Gases
R_1	CH_4/H_2
R_2	C_2H_2/C_2H_4
R_3	C_2H_4/C_2H_6
R_4	C_2H_2/CH_4

TABLE IV. ROGER'S GAS RATIOS INTERPRETATION [3].

Case	Fault diagnosis	C_2H_2/C_2H_4	CH_4/H_2	C_2H_4/C_2H_6	C_2H_6/CH_4
0	NF	<0.5	≥0.1 <1.0	<1.0	<1.0
1	PD	<0.5	<0.1	<1.0	<1.0
2					
	D1	≥0.5≤3 .0	≥0.1 <1.0	<1.0	<1.0
3	D2	≥0.5≤3 .0	≥0.1 <1.0	>3.0	<1.0
4	T1	<0.5	>3.0	<1.0	<1.0
5	T2	≥0.5≤3 .0	≥0.1 <1.0	≥1.0≤3.0	≥1.0
6	T3	>3.0	≥0.1 <1.0	>3.0	≥1.0

c) Dornenburg Ratio Method

The method initially analyses each gas and proposes a test if any gas exceeds the preset limit in parts per million, as given in TABLE V. This method can identify three faults, while TABLE VI shows that five gases and four ratios are used to detect faults. Dornenburg's interpretation is presented in TABLE VII [4].

TABLE V. DORNENBURG LIMITS FOR INDIVIDUAL GAS [4].

Gas	Limit, ppm
H_2	100
CH_4	120
C_2H_4	50
C_2H_2	35
C_2H_6	1
CO	350

TABLE VI. DORNENBURG GAS RATIOS [4].

Ratios	Gases
R_1	CH_4/H_2
R_2	C_2H_2/C_2H_4
R_3	C_2H_2/CH_4
R_4	C_2H_6/C_2H_2

TABLE VII. DORNENBURG FAULT INTERPRETATION [4].

Fault diagnosis	CH_4/H_2	C_2H_2/C_2H_4	C_2H_2/CH_4	C_2H_6/C_2H_2
NF	<0.1	<0.75	<0.3	<0.4
PD	<0.1	-	<0.3	<0.4
TD	>1.0	<0.75	<0.3	>0.4
D2	≥0.1≤1	>0.75	>0.3	<0.4

d) Key Gas Method

The key gas method examines the onset of faults in a transformer by assigning four typical fault classes based on specific significant gases. These gases are referred to as "key gases" [5] and are shown in Fig. 1 to Fig. 4 [3].

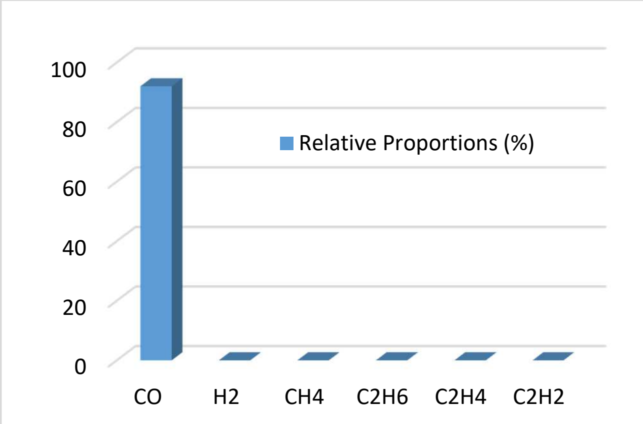

Fig. 1. Overheated Cellulose.

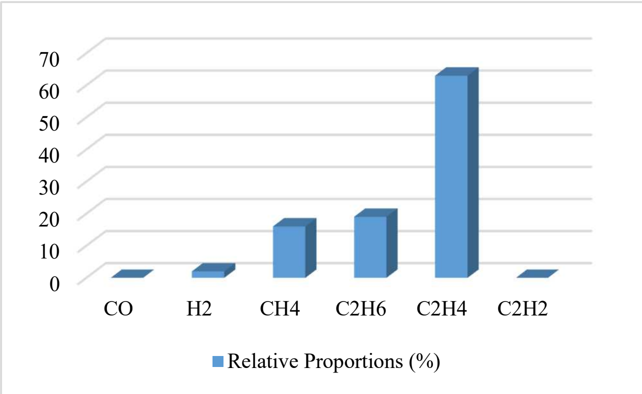

Fig. 2. Overheated Oil.

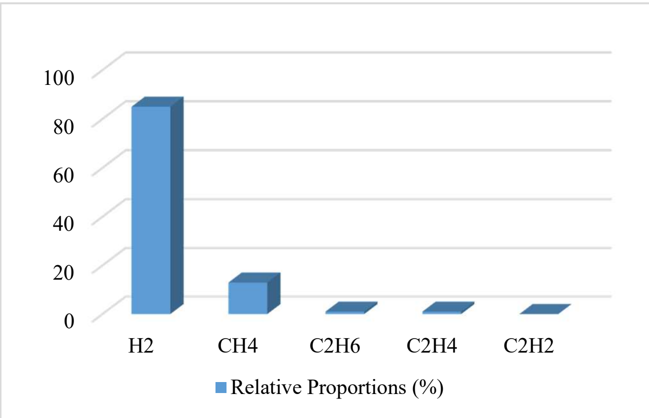

Fig. 3. Corona in Oil.

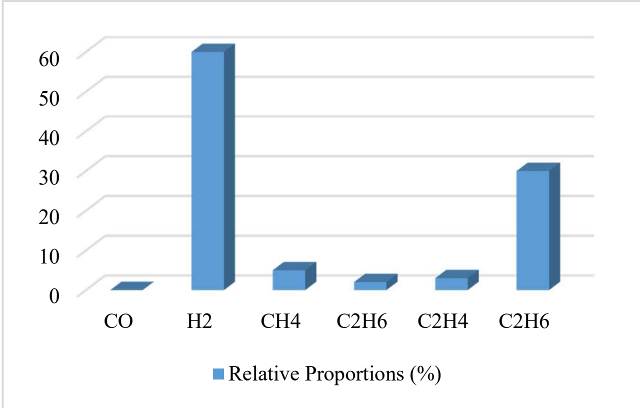

Fig. 4. Arcing in Oil.

e) Proposed method

i. Data preparation

The proposed SVM algorithm is used to identify normal operating conditions and faults in power transformers. As a training dataset for the SVM method, 306 DGA data from Oil Filled power transformers under varying conditions were obtained from other researchers to develop the DGA model. The gas concentrations, i.e., H_2, CH_4, C_2H_4, C_2H_6 and C_2H_6 in volume, are employed as discriminating features (input) of the method; the input vector for training the algorithm is a data array with dimensions of 306 by 5. Fig. 5 Show the project setup.

ii. Data Validation

Before the data were delivered to Google Collaboratory, validation was a critical stage in the process. This was accomplished by uploading each Excel data sheet to MATLAB and running it through a variety of SVM machine-learning models to determine the data's validity. The models were provided with a confusion matrix. The data is subsequently uploaded as a CSV file into the framework on Google Collaboratory. Pandas is a function that permits the import of data. The information was then separated into input columns and target columns. The objective was the column labelled "fault type." The input column contains H_2, CH_4,C_2H_2,C_2H_4, and C_2H_6. Fig. 5 show the data pre-processing stage.

Data preparation

Split data into inputs and outputs

```
[ ] input_cols = ['H2', 'CH4','C2H2', 'C2H4', 'C2H6']
    target_col = ['Fault Type']
```

```
[ ] inputs = df[input_cols].copy()
    targets = df[target_col].copy()
```

Fig. 5. Data preparation.

The detailed process flow chart of the proposed work is shown in Fig. 6.

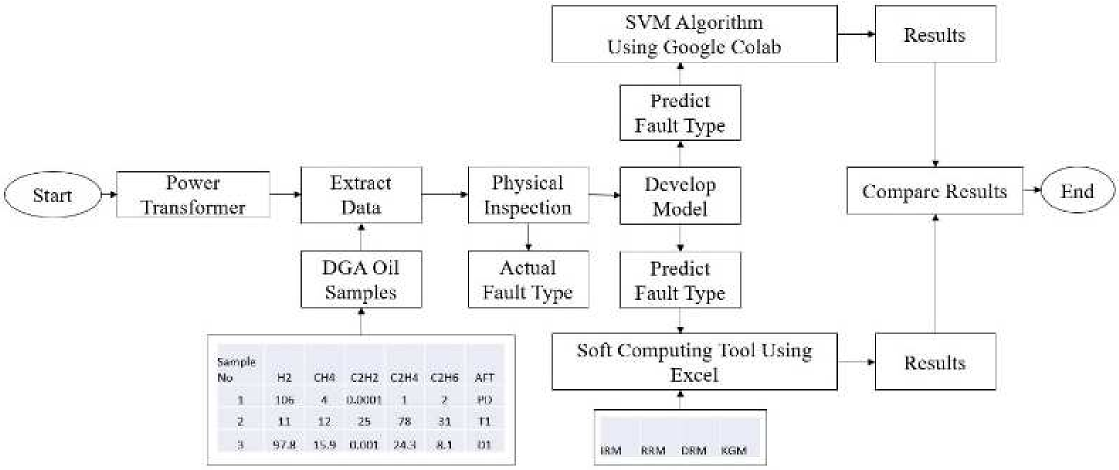

Fig. 6. Process flow chart of proposed work.

iii. Support Vector Machine Model

The proposed SVM algorithm utilized a kernel in the research. A kernel converts an input data space to the necessary format. SVM employs a method known as the kernel trick. In this research, the kernel transforms a low-dimensional input space into a higher-dimensional space. In other words, it transforms an inseparable problem into a separable one by adding extra dimensions. It is mainly beneficial for nonlinear separation issues. The kernel trick enables you to construct a more precise classifier. The polynomial kernel is utilized because it is a more generalized variant of the linear kernel. The polynomial kernel may discriminate between input space that is curved or nonlinear.

iv. Importing Libraries

Importing all necessary libraries was the initial step. Fig. 7 shows how the libraries were imported.

```
[ ]  import pandas as pd
```

Fig. 7. Import Libraries.

v. Importing the dataset

The data from the CSV file were loaded. Which uploads or saves the file to the local system or drive. The read_csv is a method file is utilized to load the data file. Then, variables corresponding to X and Y were assigned. Finally, the first five rows of the dataset are displayed in Fig. 8.

```
[ ]  df.head()
```

	H2	CH4	C2H2	C2H4	C2H6	Fault Type
0	4566.0	671.0	683643.0	434322.0	45482.0	D2
1	2323.0	782.0	545454.0	342233.0	4343.0	D2
2	2118.0	844.0	540711.0	449264.0	4443.0	D2
3	2285.0	706.0	546779.0	435718.0	4303.0	D2
4	2238.0	826.0	537988.0	335279.0	4008.0	D2

Fig. 8. Importing the dataset.

vi. Splitting the dataset into the Training set and Test set

There are 305 rows contained inside this dataset. The data was divided into a training set and a test set. 33% of the data were stored as the Test set, while the remaining 67% was used for training as the Training set. Therefore, around 100 data points form the test set. Fig. 9 show the splitting of data.

```
[ ]  from sklearn.model_selection import train_test_split
     X_train, X_test, y_train, y_test = train_test_split(
      inputs, targets, test_size=0.33, random_state=42)
```

Fig. 9. Splitting Data.

vii. Training the SVM Classification model on the Training Set

Once the training testing has been completed, the SVM Classification Class imports the training data and adjusts the model, accordingly, showed in Fig. 10. The variable classifier was given the class SVC. The kernel utilized here was the polynomial kernel, denoted by the "poly.".

```
Support Vector Machine

Train model

[ ]  # import support vector classifier
     # "Support Vector Classifier"
     from sklearn.svm import SVC
     clf = SVC(kernel='poly')

     import time
     t0 = time.time()
     # fitting x samples and y classes
     clf.fit(X_train, y_train)
     print("Training took "+str(time.time() - t0)+" seconds")

     Training took 0.010410785675048828 seconds
     /usr/local/lib/python3.7/dist-packages/sklearn/utils/validation.py:993:
```

Fig. 10. Training the SVM Classification model.

viii. Predicting the Test set results

The model of the support vector machine was developed by importing the SVM module and giving kernel as the polynomial kernel parameter to SVC(), and a support vector classifier object is created. In this phase, the classifier.predict() method was used to forecast the Test set values, and the predicted values were saved in the variable y pred as shown in Fig. 11.

```
[ ] # make predictions for test data
    y_pred = clf.predict(X_test)
```

Fig. 11. Predicting the Test set result.

ix. Confusion Matrix and Accuracy

This is the most common stage in classification methods. In this research, we analyzed the model's Accuracy and plotted the confusion matrix. When the actual values of the Test Set are known, the confusion matrix is a table used to display the number of correct and incorrect classification predictions as shown in Fig. 12. True values are formatted as the number of accurate forecasts made. Fig. 13 show the results of the accuracy score.

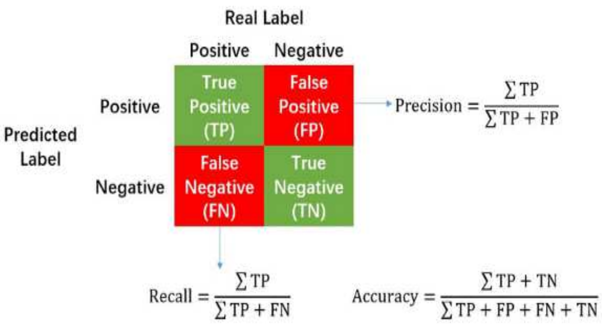

Fig. 12. Accuracy score.

```
Support Vector Machine Confusion matrix
- x-axis is true labels.
- y-axis is predicted labels
array([[10,  0,  0,  0,  2,  0,  0],
       [ 0, 12,  0,  0,  5,  0,  0],
       [ 0,  0,  0,  0,  1,  0,  0],
       [ 0,  0,  0,  0,  3,  0,  0],
       [ 0,  0,  0,  0, 56,  0,  0],
       [ 0,  0,  0,  0,  3,  0,  0],
       [ 0,  0,  0,  0,  9,  0,  0]])
```

Fig. 13. Confusion Matrix.

x. Evaluating the Model

They measured the accuracy with which the classifier or model can predict power transformer breakdowns. By comparing actual test set values to expected values, accuracy can be calculated. The output of prediction is a one-dimensional array. Using precision, recall, and f1-score which is a decisive element of the model how the model can predict the accuracy of 0.77 for the model with support of Fig. 14.

```
from sklearn import metrics
print(metrics.classification_report(y_test, y_pred))

              precision    recall  f1-score   support

          D1       1.00      0.83      0.91        12
          D2       1.00      0.71      0.83        17
          NF       0.00      0.00      0.00         1
          PD       0.00      0.00      0.00         3
          T1       0.71      1.00      0.83        56
          T2       0.00      0.00      0.00         3
          T3       0.00      0.00      0.00         9

    accuracy                           0.77       101
   macro avg       0.39      0.36      0.37       101
weighted avg       0.68      0.77      0.71       101
```

Fig. 14. Evaluating the Model.

III. Results and Discussion

The TABLE VIII comparative analysis displayed the results of fault identification using a sample size of ten and observed the several faults that were identified using DGA methods. The model was able to identify faults that, the traditional methods failed to detect. Fig. 14 displays the Excel-based soft computing tool results for DGA methods. Fig. 15 illustrated the creation of a Pandas DataFrame to compare the classified values of the original Test set (y test) with the forecasted results (y predict) in this stage. Using a ‘single prediction’, each data point was predicted.

TABLE VIII. Comparison between the results from the SVM model method and the results from literature and lab analysis

Sample No.	*H2*	CH4	C2H2	C2H4	C2H6	Fault
1	600	400	281	400	250	T1
2	102	6	10	7	6	D1
3	124	14	13	0.0001	4	D1
4	24	109	0.0001	0.0001	69	T1
5	10	26	0.0001	6	147	T1
6	5.8	2.7	0	0.8	1.8	NF
7	11	12	22	78	31	T1
8	56	5.5	27.5	34.5	92	D1
9	32	11.38	3.9	30.6	8.2	NF
10	17.01	13.75	26.59	39.5	3.06	D2

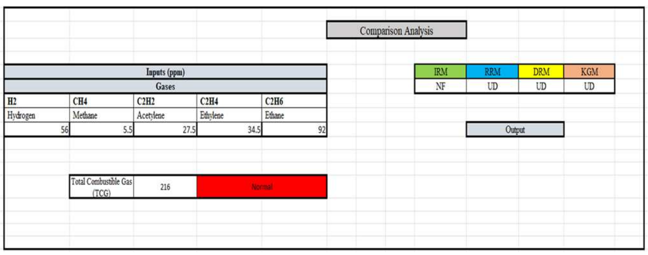

Fig. 15. Evaluating the Model

TABLE IX. COMPARISON BETWEEN THE PROPOSED SVM MODEL METHOD AND TRADITIONAL METHODS

Sample No.	*IRM*	RRM	DRM	KGM	SVM
1	D1	UD	UD	UD	DT
2	T2	UD	UD	D2	DT
3	UD	UD	UD	D2	DT
4	UD	UD	TD	UD	PD
5	UD	UD	UD	UD	T1
6	UD	UD	UD	NF	NF
7	D1	UD	UD	UD	T1
8	NF	UD	UD	UD	D1
9	D2	UD	UD	UD	NF
10	D2	UD	D2	UD	D2

The single prediciton model is shown in Fig. 16.

Fig. 16. Model Predicting.

IV. CONCLUSION

Power transformers form the backbone of the electrical system and are frequently at risk of failure, particularly during load shedding. These failures can leave entire regions without power for extended periods or even days after load shedding has stopped. This can have a negative influence on the livelihoods of many individuals. These transformers are subjected to large switching transients and periods of Oil Short delay due to load shedding. Preventative maintenance is essential to ensuring that these transformers do not fail prematurely due to insulation failure.

Inconclusive traditional methods presented in the research, including the Dornenburg ratio, Roger's ratio, key gas ratio, and IEC ratio, which are used to detect power transformer faults based on dissolved gas analysis, proven that in some instances, these methods do not correspond with the types of fault. Compared to traditional methods, a proposed method using a Support vector machine showed more accuracy in identifying faults in power transformers.

According to the author's knowledge, there is no existing research work that has developed an SVM-based fault classification approach using Google Colab. As a result, the proposed work contributes to the fault diagnostics of power transformers.

REFERENCES

[1] M. M. Emara, G. D. Peppas and I. F. Gonos, "Two Graphical Shapes Based on DGA for Power Transformer Fault Types Discrimination," in *IEEE Transactions on Dielectrics and Electrical Insulation*, vol. 28, no. 3, pp. 981-987, June 2021, doi: 10.1109/TDEI.2021.009415.

[2] N. Pattanadech and W. Wattakapaiboon, "Application of Duval Pentagon Compared with Other DGA Interpretation Techniques: Case Studies for Actual Transformer Inspections Including Experience from Power Plants in Thailand," *2019 5th International Conference on Engineering, Applied Sciences and Technology (ICEAST)*, 2019, pp. 1-4, doi: 10.1109/ICEAST.2019.8802523.

[3] Benmahamed, Y.; Kherif, O.; Teguar, M.; Boubakeur, A.; Ghoneim, S.S.M. Accuracy Improvement of Transformer Faults Diagnostic Based on DGA Data Using SVM-BA Classifier. *Energies* 2021, *14*, 2970. https://doi.org/10.3390/en14102970

[4] S. B. Wanjare and P. S. Swami, "DGA Interpretation for Increasing the Percent of Accuracy by Different Methods: A Review," *2018 International Conference on Computation of Power, Energy, Information and Communication (ICCPEIC)*, 2018, pp. 458-461, doi: 10.1109/ICCPEIC.2018.8525179.

[5] A. Basuki and Suwarno, "Online Dissolved Gas Analysis of Power Transformers Based on Decision Tree Model," *2018 Conference on Power Engineering and Renewable Energy (ICPERE)*, 2018, pp. 1-6, doi: 10.1109/ICPERE.2018.8739761.

[6] N. K. Bhatia, A. H. El-Hag and K. B. Shaban, "Machine Learning-based Regression and Classification Models for Oil Assessment of Power Transformers," *2020 IEEE International Conference on Informatics, IoT, and Enabling Technologies (ICIoT)*, 2020, pp. 400-403, doi: 10.1109/ICIoT48696.2020.9089647.

[7] Thango, B.A. On the Application of Artificial Neural Network for Classification of Incipient Faults in Dissolved Gas Analysis of Power Transformers. *Mach. Learn. Knowl. Extr.* 2022, *4*, 839-851. https://doi.org/10.3390/make4040042.

[8] T. Buchacz, J. Buchacz and M. Duval, "Stray Gassing of Oil in HV Transformers," in *IEEE Transactions on Dielectrics and Electrical Insulation*, vol. 28, no. 5, pp. 1729-1734, October 2021, doi: 10.1109/TDEI.2021.009520.

2023 SAUPEC Conference, Johannesburg, South Africa, January 24-26, 2023

AI Edge Processing – A Review of Distributed Embedded Systems

Matthew Sibanda
Discipline of Electrical, Electronic and Computer Engineering
University of KwaZulu-Natal
Durban, South Africa
sibanda.matthew@mut.ac.za

Ernest Bhero
Discipline of Electrical, Electronic and Computer Engineering
University of KwaZulu-Natal
Durban, South Africa
bhero@ukzn.ac.za

John Agee
Discipline of Electrical, Electronic and Computer Engineering
University of KwaZulu-Natal
Durban, South Africa
ageej@ukzn.ac.za

***Abstract*—The age of cybernetics is underway, with a lot of systems being computerized leading to the generation of a lot of data. Sending this data to remote systems and the cloud for analysis and/or processing introduces latency, reliability, and privacy issues. These issues are generally not acceptable to systems that need to respond in real-time or near real-time. Local processing of data is an alternative. Hence there is a need for high performance embedded computing systems to be employed at the edge. This paper proposes and reviews distributed embedded computing systems as a possible architecture for edge AI processing.**

Keywords—Distributed Embedded Systems, High Performance Embedded Computing, Embedded systems, Edge computing

I. INTRODUCTION

As early as 2002, Borcea *et al* [1] predicted an era of cyber-physical systems where incorporating computing capabilities in products is a norm. This was also echoed by Dixon [2] in his 2016 article discussing the progress in the computing industry as well as the future. The inclusion of computing capabilities in products is a norm, as such, the era of cyber-physical systems is upon us [3]–[7]. The reality of this situation is that the embedding of computers in devices is generating a lot of data [3], [8]. Traditionally the data would be transferred to a local server and to the cloud for processing (Fig. 1) [3], [9], [10]. This setup pushed the demand for High-Performance Computing (HPC). However, this process of transmitting data from the point of origin to a remote server for processing is time consuming, thus introducing latency in some systems [3], [11], [12]. At the same time, data transmission opens the door for security breaches, affecting privacy and security [3], [4], [9], [12], [13]. Also, transmitting data consumes energy and the further it needs to move the more energy and bandwidth is required. Thus making overall system costs high [3], [9], [13]. Hence, a need to reduce communication and computational latencies as well as improve data security was noted.

This need led to the adoption of a different paradigm - local processing of data by the resource constrained embedded systems [3], [10], [12], [14]. This, however, pushed the high-performance computing into the world of embedded systems giving rise to the field of high-performance embedded computing (HPEC) [15], [16]. The demand for HPEC systems has been further intensified by the advent of the internet of things (IoT) which further advocates for the introduction of intelligence at the edge of computing [4], [9], [12], [17]–[20]. Improved cognition at the edge of computing is making the historically separate and/or different fields of HPC and embedded computing to converge [4], [16], [20]. The improvement of cognition at the edge of computing, further, adds to the high performance requirements on embedded systems. There is, thus, a need for, and/or shift towards high performance embedded computing [4], [13], [21].

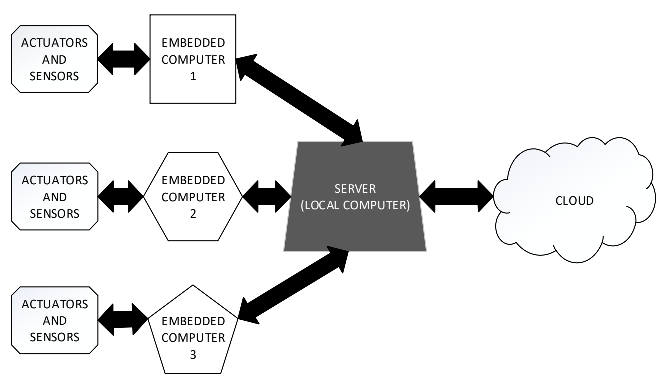

Fig. 1. Traditional approach to processing data from embedded systems

This paper reviews the distributed embedded processing and distributed embedded systems (DESs) as used achieve better performance that is required for local processing of data. The DESs characteristics are highlighted, and the paper ends with proposing some possible work to be done in the future.

II. BACKGROUND ON DISTRIBUTED SYSTEMS

Distributed processing allows simultaneous and collaborative data processing on different processing elements [22]. Generally, distributed systems (DSs) have higher scalabilities, reliabilities, and flexibilities than centralized systems [17]. Traditional DSs consist of resourceful (storage, compute and connectivity) systems but with high latency [14]. Instead of powerful computers, embedded computers can be used to process edge data faster, avoiding network latency and security issues introduced by centralised data processing of cloud-based systems [10], [11], [23]. Distributed embedded systems (DESs) refers to a collection of extremely resource constrained computing devices that cooperate to achieve a common goal. Traditional DSs are the precursors to the DESs. As such it is import to understand some of the general aspects of DSs that are common with DESs. These include the following [22], [24]:

- Low latency – processing happens closer to data source.
- Dependability – high reliability since distribution allows for independence of failures among nodes.
- Composability – chosen components can be assembled in a variety of ways.
- Scalability – system can be grown simply by addition of new nodes with new or replicated functionality.
- Maintainability – systems are modular thus allowing for easy node replacement.
- Fault tolerance – ability to remain in operation during and/or after occurrence of a fault.
- Transparency – hides the complexity of the DS to the user & application programmes, thus making a collection of computers appear as a single computer.

Despite being composed of a collection of homogeneous or heterogeneous cooperating components, a DS should appear to operate as a centralised system. This hiding of the complexity of distribution is the basis of a distributed architecture and is referred to as transparency. Transparency has different dimensions or forms which represent properties that a DS should have [17], [25]–[29]:

- Access transparency – hiding the way in which resources are retrieved, thus allowing local and remote access using identical operations.
- Location transparency – hiding where resources are located, hence enabling access without resource location knowledge.
- Performance transparency – ensuring system performance, from user's point of view, is not affected by system configuration or reconfiguration. This allows system reconfiguration to improve performance with varying loads.
- Migration/Relocation transparency – hiding that resources may change location during use. It allows the movement of information objects within a system without affecting the operations of users or application programs.
- Replication transparency – ensuring users cannot tell how many copies of resources exist. This enables multiple instances to be used to achieve fault tolerance and increase reliability as well as performance without user knowledge of replicas.
- Concurrency transparency – hiding that resources may be shared therefore enabling several processes to operate concurrently using the shared resources with no interference between them.
- Failure transparency – concealing failure and recovery of resources, hence allowing for tasks to be completed despite a component failure.
- Scaling transparency – ensuring the system and applications are able to scale up or down with no change to the structure of the system or the application algorithms.

III. Designing Distributed Embedded Systems

As stated by Wolf [24], the design of embedded systems (distributed or otherwise) relies heavily on three pillars, namely applications, architectures and methodologies. Applications define what the system will be doing and how, that is, the specifications, characteristics and design references. The architecture defines the major components, their connections and how they work together [30]. The desired system architecture is described by hardware (CPUs – single core, dual core or multi core including homogenous or heterogeneous, networks, co-design, etc.) and software (processes, scheduling, real time constraints, reliability etc.) level parameters [31]. On the other hand, methodologies look at the modelling, analysis, simulation, synthesis and verification of the system against the set performance and other criterion.

The basic units of DESs are the processing elements (PEs) and the network (CAN, I^2C, USB, PCI, etc.) [32], [33]. The PEs are the computing components and/or devices which can be, amongst others, microcontrollers, application specific integrated circuits (ASICs) and single-board computers (SBCs). Networking of embedded systems is achieved using a serial (e.g., CAN, I^2C, USB, etc.) or parallel (e.g., ISA, PCI, PCI-X, etc.) bus or wireless protocol software with appropriate hardware [34], [35]. There are many ways of organising DES to achieve the required goal(s) and, amongst others, these will depend on requirements of the application, as well as other system constraints. How the networking of the PEs is done depends on the communication standard as well as the microcontroller types used [36]. When the same PEs are networked a homogenous DES is formed and using dissimilar PEs results in a heterogeneous DES. Heterogeneity is the standard for distributed embedded systems thus making interoperability a key concern [32], [37], [38]. Object-Attribute architecture is introduced as a simple and consistent approach to designing DESs [38].

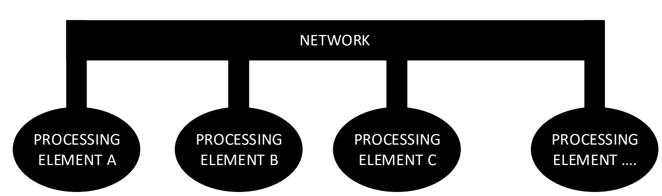

Fig. 2. Idealised DES design/structure

Wolf [39], notes that the design of DES is an example of hardware/software co-design because of the need to design the network topology in conjunction with the software running on the nodes. According to G. Coulouris *et al* [25], there are three ways in which the design of DSs can be described and discussed, namely: physical models, architectural models and fundamental models. The physical model is concerned with the type of computers and devices that make up the DS without specifics on technologies. The architectural model deals with the organisation of components across the network and their relationships, e.g. client-server or peer-to-peer model. Whilst the fundamental model is concerned with description of the properties that are present in all the architectural models e.g. interaction, failure and security.

Kumar *et al* [40] discuss a DES for IoT image processing based on Raspberry Pi and FPGA. Their focus is on the application and not the DES. Hajjar *et al* [41] also discuss a DES using Raspberry Pi and FPGA, however, they focus on the network connection implementation. Both articles show the potential of heterogenous HPECs.

A. *Embedded Hardware for Edge AI*

Generally machine learning is a computing intensive process thus requiring high performance computers. There are many, and diverse, categories of processors to consider when selecting one for deep learning, and all have their strengths and weaknesses as highlighted in Table 1 [7].

The hardware requirements will vary based on the application and selection of the appropriate embedded edge hardware, for AI processing, should consider [7], [9], [15]:

- Performance – can the hardware provide the speed needed by complex, data-intensive edge AI applications at the same time operating consistently and reliably, even in some harsh surroundings?
- SWaP (Size, Weight, and Power) – Can the hardware meet the specifications for size and weight, thus conforming to the physical constraints of the application? Does it make the most sense from a power-consumption standpoint?
- Cost – which hardware provides the functionality and specifications the project needs at the best price point?

TABLE I. PROCESSING ELEMENTS TYPES FOR EDGE AI HARDWARE

Core Type			ASIC	FPGA	GPU	CPU
Custom ASIC	TPU	VPU				
Typical Power Consumption	Low to medium	Ultra-low	Low	Medium	High	High
Description	Custom ASIC developed by Google	Image and vision processor/co-processor	Custom logic designed with libraries	Configurable logic gates	Parallel cores for high quality graphics rendering	Flexible, general purpose processing units
Strengths	• Specialised tool support • Optimised for TensorFlow	• Low power and small footprint • Dedicated to image and vision acceleration	• Fast and low power consumption • Small footprint	• Flexible • In-field reprogrammability	• High performance AI processing • Highly parallel core with 100's or 1000's of cores	• Complex instructions and tasks • System management
Constraints	• Proprietary design • Very limited framework support	• Limited dataset and batch size • Limited network support	• Fixed function • Expensive custom design	• High power consumption • Programming complexity	• High power consumption • Large footprint	• Possible memory access bottlenecks • Few cores (4 - 16)

B. *DESs Software Architecture*

As previously mentioned, DESs are generally designed to ensure transparency. This requires that the system performance be independent of the underlying low-level system software and hardware components. A widely used approach is that of middleware [42]–[44]. Middleware refers to a software layer that provides a programming abstraction, as well as masking the heterogeneity of the underlying networks, hardware, operating systems and programming languages [25], [45]. Middleware speeds up the development of distributed systems through the simplification of communication between the applications and the various components making up the system [42]–[44], [46]. There are many types of middleware with some focusing on specific connectivity types, others on specific applications, application components and devises. There are also some that combine different capabilities for explicit tasks [43]. Some of the most common types of middleware software include [43], [45], [47]:

- Message-oriented middleware (MoM) [48]
- Remote procedure call (RPC) middleware
- Data or database middleware
- Application programming interface (API) middleware
- Object request broker (ORB) middleware
- Transactional middleware
- Asynchronous data streaming middleware
- Device/component middleware
- OpenCL [33]
- Portal middleware
- Robotics middleware
- ScOSA system software [44]

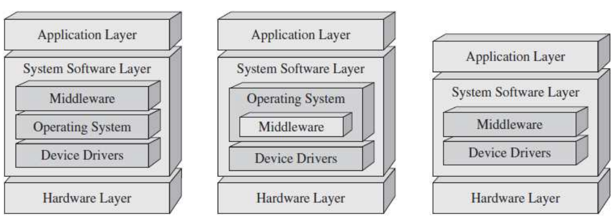

Fig. 3. Middleware within the Embedded Systems Model [49]

For middleware to be practical in the setting of embedded systems, it needs to be very efficient. Depending on the nature of the DES, efficiency can involve adaptability, flexibility, minimum use of the CPU, memory, battery power, network bandwidth, fault-tolerance etc.[44], [46], [49].

IV. Conclusion

The paper has confirmed the move towards processing at the edge as way of reducing latency that is introduced when cloud processing is involved. At the same time, it built a case for DESs as a form of HPEC platform for computing at the edge. There is a need to develop a generic DES platform (hardware and software) that can be used across various edge applications including machine learning, IoT and cyber-physical systems applications. Thus, there is a big scope of work for the future look into the development of HPEC systems based on DESs hardware, system software (including middleware). There is also a need to evaluate the performance, effectiveness and efficiencies of the developed DESs and middleware combination.

References

[1] C. Borcea, D. Iyer, P. Kang, A. Saxena, and L. Iftode, "Cooperative computing for distributed embedded systems," *Proc. - Int. Conf. Distrib. Comput. Syst.*, pp. 227–236, 2002, doi: 10.1109/icdcs.2002.1022260.

[2] C. Dixon, "What's Next in Computing?. The computing industry progresses in… | by Chris Dixon | Software Is Eating the World | Medium," 2016. https://medium.com/software-is-eating-the-world/what-s-next-in-computing-e54b870b80cc (accessed Nov. 20, 2020).

[3] X. Wang, Y. Han, V. C. M. Leung, D. Niyato, X. Yan, and X. Chen, "Convergence of Edge Computing and Deep Learning: A Comprehensive Survey," *IEEE Communications Surveys and Tutorials*, vol. 22, no. 2. Institute of Electrical and Electronics Engineers Inc., pp. 869–904, Apr. 01, 2020, doi: 10.1109/COMST.2020.2970550.

[4] M. Duranton *et al.*, Eds., *The HiPEAC Vision 2019*. 2019.

[5] R. Giorgi, M. Procaccini, and F. Khalili, "AXIOM: A Scalable, Efficient and Reconfigurable Embedded Platform," in *Proceedings of the 2019 Design, Automation and Test in Europe Conference and Exhibition, DATE 2019*, 2019, pp. 480–485, doi: 10.23919/DATE.2019.8715168.

[6] B. Zuberi, "The Future of Computing: Distributed, Deep Learning, Embedded Intelligence. | by Editor | Lux Capital | Medium," 2016. https://medium.com/lux-capital/the-future-of-computing-distributed-deep-learning-embedded-intelligence-d8d0b28e0ab1 (accessed Nov. 19, 2020).

[7] Z. Tsai, "Embedded Hardware for Processing AI at the Edge: GPU, VPU, FPGA and ASIC Explained." https://www.automation.com/en-us/articles/march-2021/embedded-hardware-processing-ai-edge-gpu-vpu-fpga (accessed Apr. 09, 2021).

[8] Gartner, "Gartner Says 8.4 Billion Connected 'Things' Will Be in Use in 2017, Up 31 Percent From 2016," 2017. https://www.gartner.com/en/newsroom/press-releases/2017-02-07-gartner-says-8-billion-connected-things-will-be-in-use-in-2017-up-31-percent-from-2016 (accessed Oct. 23, 2020).

[9] M. Nadeski, "Bringing machine learning to embedded systems," 2019. Accessed: Apr. 13, 2021. [Online]. Available: https://www.ti.com/lit/wp/sway020a/sway020a.pdf?ts=1620412861047&ref_url=https%253A%252F%252Fwww.google.com%252F.

[10] M. Meribout, A. Baobaid, M. O. Khaoua, V. K. Tiwari, and J. P. Pena, "State of Art IoT and Edge Embedded Systems for Real-Time Machine Vision Applications," *IEEE Access*, vol. 10, pp. 58287–58301, 2022, doi: 10.1109/ACCESS.2022.3175496.

[11] S. Bhave, M. Tolentino, and H. Zhu, “Embedded Middleware for Distributed Raspberry Pi Device to Enable Big Data Applications,” pp. 103–108, 2017, doi: 10.1109/CSE-EUC.2017.204.
[12] “Fog Computing and the Internet of Things: Extend the Cloud to Where the Things Are - DocsLib.” https://docslib.org/doc/7133745/fog-computing-and-the-internet-of-things-extend-the-cloud-to-where-the-things-are (accessed Sep. 27, 2022).
[13] C. P. Filho *et al.*, “A Systematic Literature Review on Distributed Machine Learning in Edge Computing,” *Sensors*, vol. 22, no. 7, pp. 1–36, 2022, doi: 10.3390/s22072665.
[14] C. Mwase, Y. Jin, T. Westerlund, H. Tenhunen, and Z. Zou, “Communication-efficient distributed AI strategies for the IoT edge,” *Futur. Gener. Comput. Syst.*, vol. 131, pp. 292–308, 2022, doi: 10.1016/j.future.2022.01.013.
[15] R. Ben Atitallah and K. M. A. Ali, “FPGA-Centric High Performance Embedded Computing: Challenges and Trends,” *Proc. - 20th Euromicro Conf. Digit. Syst. Des. DSD 2017*, pp. 390–395, 2017, doi: 10.1109/DSD.2017.88.
[16] L. M. Pinho *et al.*, Eds., *High-Performance and Time-Predictable Embedded Computing*. River Publishers, 2018.
[17] C. W. Leung, “Architecture of distributed real-time embedded system,” KTH, 2013.
[18] D. Belkacemi, Y. Bouchebaba, M. Daoui, and M. Lalam, “Network on Chip and Parallel Computing in Embedded Systems,” *Proc. - IEEE 10th Int. Symp. Embed. Multicore/Many-Core Syst. MCSoC 2016*, vol. 1, no. 1, pp. 146–152, 2016, doi: 10.1109/MCSoC.2016.53.
[19] X. Zhang, J. Zhan, W. Jiang, and Y. Ma, “Design Optimization of Energy- and Security-Critical Distributed Real-Time Embedded Systems,” 2013, doi: 10.1109/IPDPSW.2013.24.
[20] R. Giorgi, “Scalable Embedded Systems : Towards the Convergence of High-Performance and Embedded Computing,” pp. 148–153, 2015, doi: 10.1109/EUC.2015.34.
[21] A. Munir, A. Gordon-Ross, and S. Ranka, *Modeling and optimization of parallel and distributed embedded systems*. 2016.
[22] M. Törngren, “Distributed Embedded Systems: An Introduction.” https://www.academia.edu/4792637/Distributed_Embedded_Systems_Distributed_Embedded_Systems_An_Introduction_An_Introduction (accessed Oct. 23, 2020).
[23] A. Sehmi, “On Distributed Embedded Systems,” *Microsoft Archit. J.*, no. 8, pp. 1–12, 2009, Accessed: Oct. 22, 2020. [Online]. Available: https://docs.microsoft.com/en-us/previous-versions/dd129911(v=msdn.10)?redirectedfrom=MSDN.
[24] M. Wolf, *High-Performance Embedded Computing: Applications in Cyber-Physical Systems and Mobile Computing*, Second. 2014.
[25] G. Coulouris, J. Dollimore, T. Kindberg, and G. Blair, *Distributed Systems: Concepts and Design*, Fifth. Addison-Wesley, 2012.
[26] “CORBA-based Architecture.” https://www.ece.uvic.ca/~itraore/seng422-06/notes/arch06-6-1.pdf (accessed Dec. 22, 2020).
[27] “Explain the different forms of Transparencies in distributed systems.” https://www.ques10.com/p/24028/explain-the-different-forms-of-transparencies-in-d/ (accessed Dec. 22, 2020).
[28] “Transparencies.” https://www.cl.cam.ac.uk/~jac22/books/ods/ods/node18.html (accessed Dec. 22, 2020).
[29] “Introduction to Distributed Systems.” http://www.se.rit.edu/~se442/slides/class/01-Introduction.pdf (accessed Dec. 22, 2020).
[30] “Software Architecture & Design Introduction.” https://www.tutorialspoint.com/software_architecture_design/introduction.htm (accessed Apr. 13, 2021).
[31] S. Safari *et al.*, “A Survey of Fault-Tolerance Techniques for Embedded Systems From the Perspective of Power, Energy, and Thermal Issues,” *IEEE Access*, vol. 10, pp. 12229–12251, 2022, doi: 10.1109/ACCESS.2022.3144217.
[32] J. K. R. Sastry, J. V. Ganesh, and J. S. Bhanu, “I2C based Networking for Implementing Heterogeneous Microcontroller based Distributed Embedded Systems,” vol. 8, no. July, 2015, doi: 10.17485/ijst/2015/v8i15/68739.
[33] O. Rafique and K. Schneider, “Employing OpenCL as a Standard Hardware Abstraction in a Distributed Embedded System: A Case Study,” *2020 9th Mediterr. Conf. Embed. Comput. MECO 2020*, Jun. 2020, doi: 10.1109/MECO49872.2020.9134270.
[34] R. Kamal, *Embedded systems: Architecture, Programming and Design*. Tata McGraw-Hill, 2008.
[35] R. Lu, G. Xie, J. Jiang, R. Li, and K. Li, “Security-AwareReal-Time Transmission for Automotive CAN-FD Networks,” in *Cybersecurity and High-Performance Computing Environments: Integrated Innovations, Practices, and Applications*, vol. 4, no. 1, K.-C. Li, N. Sukhija, E. Bautista, and J.-L. Gaudiot, Eds. CRC Press, 2022, pp. 229–260.
[36] S. Sairohith, S. Sairohith, B. N. K. Venkatesh, J. K. R. Sastry, and J. Rajasekhar, “Inter-Networking Heterogeneous Embedded Networks through Universal Bus,” vol. 9, no. 2, 2020.
[37] J. Rajasekhar and J. K. R. Sastry, “Building Composite Embedded Systems Based Networks Through Hybridisation and Bridgig I2C and CAN,” vol. 15, no. 2, pp. 858–881, 2020.
[38] S. Salibekyan and P. Panfilov, “A new approach for distributed computing in embedded systems,”

Procedia Eng., vol. 100, no. January, pp. 977–986, 2015, doi: 10.1016/j.proeng.2015.01.457.

[39] W. Wolf, *High-Performance Embedded Computing: Architectures, Applications, and Methodologies*, vol. 97, no. 2. Morgan Kaufmann Publishers, 2007.

[40] S. Kumar, M. Shah, and A. Singh, "FPGA – Raspberry pi Interface for low cost IoT based image processing," *Invertis J. Sci. Technol.*, vol. 10, no. 4, p. 219, 2017, doi: 10.5958/2454-762x.2017.00034.8.

[41] H. Hajjar and H. Mourad, "Implementation of an FPGA-Raspberry Pi SPI Connection," in *The Twelfth International Conference on Advances in Circuits, Electronics and Micro-electronics*, 2019, pp. 7–12.

[42] T. Noergaard, *Demystifying Embedded Systems Middleware*, vol. 4, no. 3. Newnes, 2010.

[43] IBM, "Middleware." https://www.ibm.com/cloud/learn/middleware (accessed Apr. 16, 2021).

[44] A. Lund *et al.*, "ScOSA system software: the reliable and scalable middleware for a heterogeneous and distributed on-board computer architecture," *CEAS Sp. J.*, vol. 14, no. 1, pp. 161–171, 2022, doi: 10.1007/s12567-021-00371-7.

[45] R. E. Schantz and D. C. Schmidt, "Middleware for Distributed Systems."

[46] N. Medvidovic, S. Malek, and M. Mikic-Rakic, "Software Architectures and Embedded Systems."

[47] T. A. Bishop and R. K. Karne, "A Survey of Middleware."

[48] G. Lilis and M. Kayal, "A secure and distributed message oriented middleware for smart building applications," *Autom. Constr.*, vol. 86, pp. 163–175, Feb. 2018, doi: 10.1016/j.autcon.2017.10.030.

[49] T. Noergaard, *Embedded Systems Architecture*. 2013.

2023 SAUPEC Conference, Johannesburg, South Africa, January 24-26, 2023

Performance Analysis of Cascode Configuration 3T Pixel Structure Detectors Using y-parameter Representation

Johan Venter
Dept. of Electrical and Electronic Engineering Technology
University of Johannesburg
Johannesburg, South Africa
johanv@uj.ac.za

***Abstract*—In this paper, the standard 3T pixel structure detector using BJTs as pixels were replaced with cascode configured BJTs and several key parameters were compared. This work can be used to develop and optimise detectors before it is manufactured saving design time and cost. This was accomplished by inserting the diode-connected BJT in cascode configuration in the place of the normal diode connected BJT in the standard 3T pixel structure. Two different cascode configurations were analysed (the first is the BJT only one and the second one is a BJT MOSFET combined one). Furthermore, the *y*-parameter representation of the full 3T pixel structure is provided and subsequent mathematical model of both circuits was used to perform the comparison. The modified cascode configuration was found to have increased gain compared to the normal structure. The disadvantage is that the modified cascode configuration was found to be sensitive to β and Early Voltage where the standard structure is insensitive to these parameters. All three configurations were found to be temperature insensitive. Using this work, the designer can determine mathematically if the cascode configuration would perform better as opposed to standard 3T pixel structure detectors. The designer can also use this to optimise for a specific set of circumstances.**

Keywords*—*Image sensors, CMOS image sensors, integrated circuit modeling, analytical modeling, phototransistors.

I. INTRODUCTION

Radiation detecting applications and implementations have shown significant progress recently [1] – [5]. Implementations of detectors have been done in literature [6] – [9]. Readout circuitry of detectors have been published [10] [11], however generic mathematical modeling is somewhat lacking. Modeling can be done in multiple ways which can save on design time and costs. One such method is through the use of *y*-parameters and shunt-shunt feedback modeling. The inclusion of feedback results in more accurate results since the system would be deemed stable.

II. SHUNT-SHUNT FEEDBACK MODELLING IN DETECTORS

In 3T pixel structure detectors, one method that can be used to compare performance is *y*-parameter representation. The input is a current owing to the current flow as a result of incoming photons hitting the exposed part of a diode connected BJT connected since the diode is reverse-biased. The output is a voltage that is fed into a next stage where the impedance is expected to be very large such that negligible current would flow into the next stage.

III. DEVELOPMENT OF THE MODIFIED 3T PIXEL STRUCTURE

The 3T pixel structure was thoroughly analysed in [12]. The standard circuit is given below.

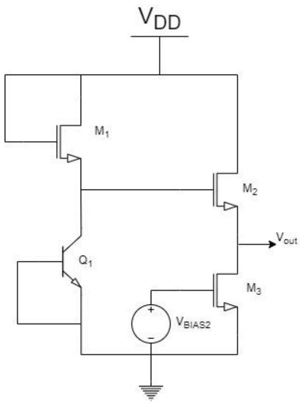

Fig. 1. Standard 3T pixel structure.

Although this structure performs quite well in terms of noise and temperature, one drawback is that the gain is relatively low which is seen in fig. 6(a). One way to increase the output voltage whilst keeping the rest of the specifications the same is to add another BJT and configure it in cascode configuration. Cascode configuration increases output resistance and reduces unwanted capacitive feedback. The modified 3T pixel structure using cascode configured pixels is given below.

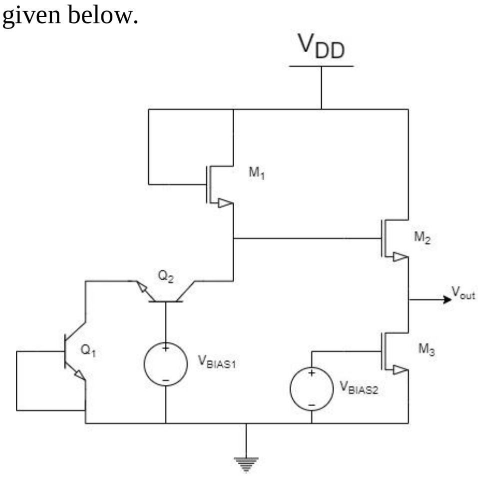

Fig. 2. Modified 3T pixel structure using cascode configured pixels (BJT only).

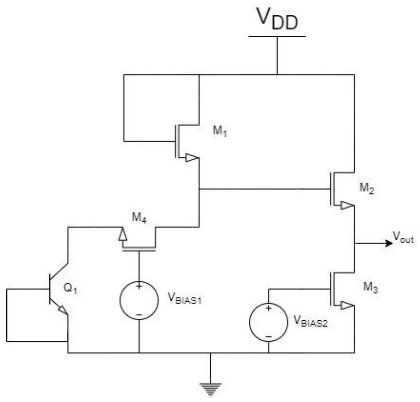

Fig. 3. Modified 3T pixel structure using cascode configured pixels (BJT and MOSFET combination).

As seen in fig. 2, a second transistor is required which will change the characteristics of the input resistance which is r_{opixel} in eq. 1. In the standard configuration, the pixel's small signal model consists of an output resistance only since it is diode connected [13]. The well-known cascode configuration's small signal model contains two output resistances and two current generators for the BJT only version. The BJT MOSFET combination cascode configured version contains two output resistance and one current generator only. To determine the output resistance of the cascode configuration, the input should be shorted to ground. This results in Q1's current generator to be 0 and thus it could be removed. The resulting small signal model that was used in this work is given in fig. 4.

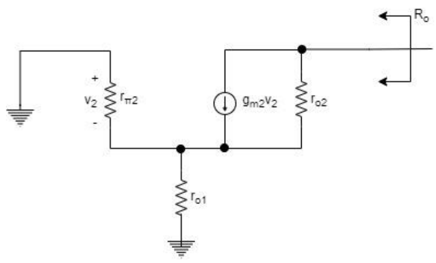

Fig. 4. Small signal model of the cascode configuration for the pixel only (BJTs only).

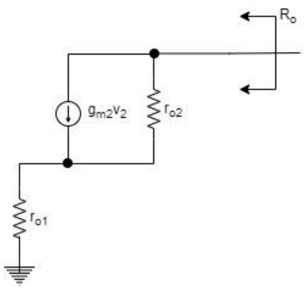

Fig. 5. Small signal model of the cascode configuration for the pixel only (BJT and MOSFET combination).

The current generator for Q_1 is missing since the input is shorted to ground to create a reverse biased diode. The admittance of this output resistance of the cascode amplifier is used as seen in eq. 2

A. *Standard 3T pixel structure model*

In eq. 1, the standard model used in performance analogy is given.

$$\frac{v_o}{i_s} = \frac{a}{\frac{1}{r_{o_{pixel}}} \times b} \tag{1}$$

where

$$a = \frac{1}{r_{o1}\left(1 + g_{m1}v_{gs1}\right) + r_{o2}\left(1 - g_{m2}v_{gs2}\right)}$$

and

$$b = \frac{r_{o1} + r_{o2} + r_{o3}}{r_{o3}\left(r_{o2}\left(1 + g_{m2}v_{gs2}\right) + r_{o1}\left(1 - g_{m1}v_{gs1}\right)\right)}$$

Assuming $g_{m1}v_{gs1} \ll 1$ and $g_{m2}v_{gs2} \ll 1$ and manipulating, eq.1 can be reduced to:

$$\frac{v_o}{i_s} \approx \frac{r_{o_{pixel}} r_{o3}}{(r_{o1} + r_{o2} + r_{o3})} \tag{2}$$

The parameter r_{opixel} is the small signal equivalent of the base emitter shorted BJT which then acts as the reverse biased diode forming the pixel. The circuit equivalent of r_{opixel} is merely the output resistance of the pixel BJT [12]

B. *Modified 3T pixel structure model*

In this section, a detailed description of the modified 3T pixel structure model is given. The output resistance of the cascode configuration is given in eq. 3.

$$R_o \cong r_{o2}\left(1 + \frac{g_{m2}r_{o1}}{1 + \frac{g_{m2}r_{o1}}{\beta_o}}\right) \tag{3}$$

Traditionally if $g_{m2}r_{o1} \gg \beta_o$ and $\beta_o \gg 1$, the output resistance equation is reduced to

$$R_o \cong \beta_o r_{o2} \tag{4}$$

However since it could be difficult to ensure that $g_{m2}r_{o1} \gg \beta_o$ since the pixel BJT and common base connected BJT specifications can differ significantly, the full equation was used in this work. The full mathematical model where *y*-parameter representation was employed is given in eq. 5:

$$\frac{v_o}{i_s} \approx \frac{r_{o2}r_{o3}}{(r_{o1} + r_{o2} + r_{o3})}\left(1 + \frac{g_{m2casbjt}r_{o1casbjt}}{1 + \frac{g_{m2casbjt}r_{o1casbjt}}{\beta_o}}\right) \tag{5}$$

The combined BJT and MOSFET cascode configuration mathematical model is:

$$\frac{v_o}{i_s} \approx \frac{r_{o2}r_{o3}}{(r_{o1} + r_{o2} + r_{o3})} \times g_{m2casmos} r_{o1casbjt} r_{o2casmos} \tag{6}$$

As seen in eqs. 5 and 6 several extra parameters are included. These refer to the applicable MOSFETs and BJTs in the cascode configurations.

In the section IV, these three models were compared to establish the performance and tradeoffs if one decides to use the modified structures.

IV. SIMULATIONS OF THE STANDARD AND MODIFIED 3T PIXEL STRUCTURE DETECTORS

Several characteristics were analysed and compared in this work to show the similarities and difference between the three configurations. This was done using simulations where several parameters were fixed and one was varied. In this way, the characteristics can be clearly seen.

The first simulation is a comparison between the gains of the two circuits (standard configuration and BJT only cascode configuration).

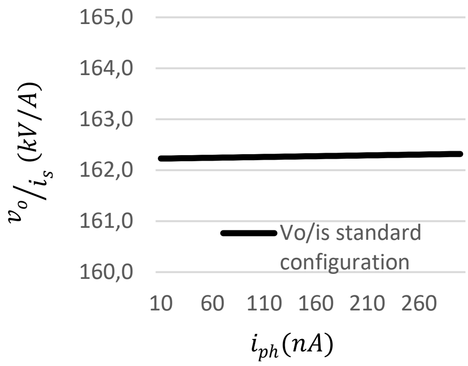

(a)

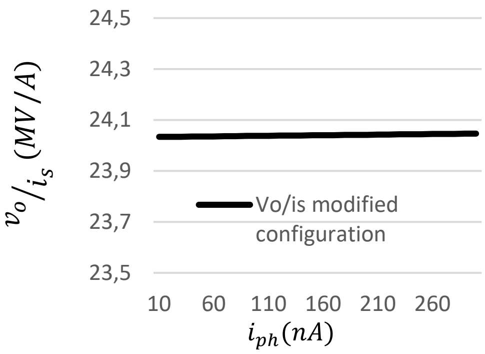

(b)

Fig. 6. Gains of both structures (a) standard configuration and (b) modified configuration (BJT only).

As it can be seen in figs. 6 (a) and (b) there is a considerable increase in overall gain. The same specification BJT that is used as a pixel was used as the common base transistor. Imperatively it would mean that the common base transistor should not be exposed to possible incoming radiation. Approximately 43 dB improvement is seen in the modified configuration. However, one should not just use this configuration due to the increase output voltage as there are some tradeoffs that will have to be considered in conjunction with the improved gain. A number of these parameters that would influence the output was simulated and the results presented.

The first of these parameters of concern is temperature. In the standard configuration, the BJT that acts as the pixel consists of an output resistance only as previously mentioned. There is no direct temperature parameter seen and thus makes it temperature insensitive in ideal circumstances. With the inclusion of the cascode configured pixel, transconductance parameters appear which is directly linked to temperature. Fig. 7 shows the temperature influence in the output voltage when the pixel is illuminated.

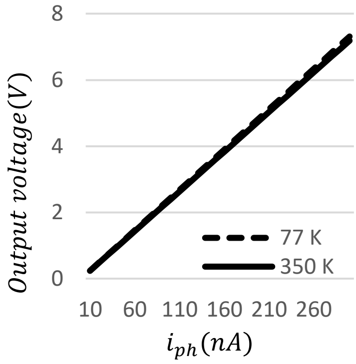

Fig. 7. Temperature effect on output voltage

As seen in fig. 7 there is no significant difference between 350 K operating temperature of the modified configuration compared to 77 K which is typically used in space applications in ideal circumstances. For practical implementation, this would align with Si BJT detecting applications. However, should a designer use SiGe HBTs as the detecting pixel, this would not be the case as carrier freezeout would influence the current flow at about 186 K and lower where current flow would be restricted [13].

The pixel output resistance would change significantly with the introduction of the cascode configuration which influences β and Early Voltage. The following graphs show the impact of this on the output resistance of the pixel and the resulting dB voltage increase of the overall circuit. The following parameters were set for the output circuit in conducting these simulations:

- V_{DD} = 5 V
- All MOSFET Early Voltages = 200 V
- All MOSFET Threshold Voltages = 0.66 V
- $k' = \mu_n C_{ox}$ = 200 µA/V^2
- All aspect ratios of MOSFETs = 2

The pixel output resistance changes significantly with the introduction of the cascode configured pixel. Both output resistances under the same illumination conditions are shown in fig. 8.

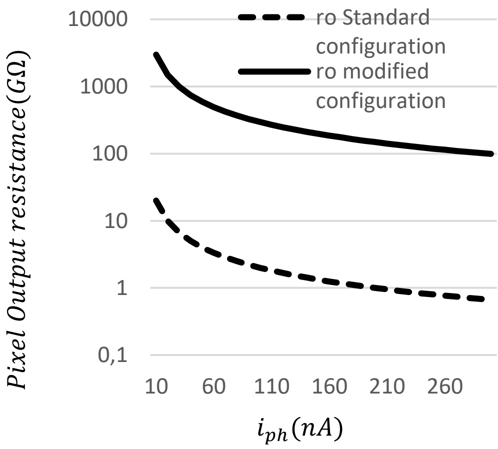

Fig. 8. Pixel output comparison between standard and modified configuration.

As it can be seen in fig. 8, the output resistance increases significantly with the inclusion of the extra common base transistor (from 20 GΩ to about 3000 GΩ). This reduces input current flow and will increase output voltage hence the significant improvement seen in the overall gain as shown in fig. 4. The next two graphs show how β and Early Voltage affect the output resistance of both configurations.

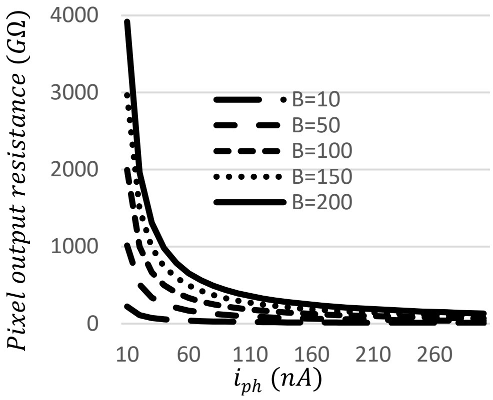

(a)

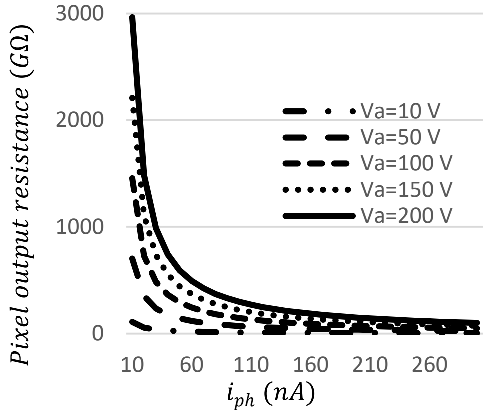

(b)

Fig. 9. Pixel output resistance vs photon generated current for varying (a) β and (b) Early Voltage.

It can be seen in figs. 9 (a) and (b) that an increase β and increase in Early Voltage has the same effect on the output resistance of the modified conguration (BJT only cascode configuration). Both results in an increased output resistance (4000 GΩ and 3000 GΩ maximum resistance respectively). The important aspect of this is how does this increase in output resistance affect the output voltage seen of the circuit. That is illustrated in figs. 10 (a) and (b).

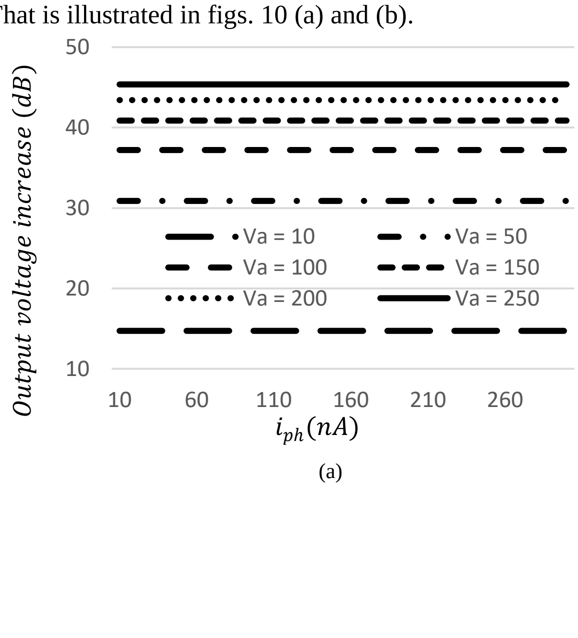

(a)

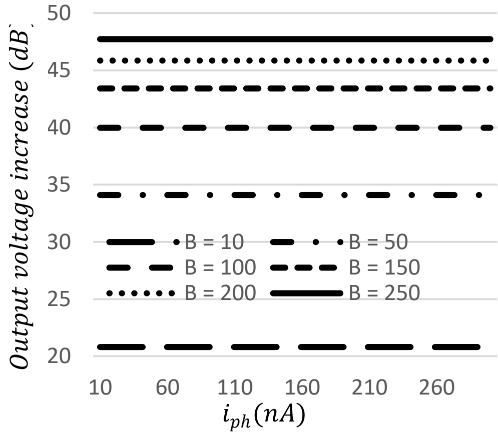

(b)

Fig. 10. dB output voltage increase using the modified structure compared to the standard 3T pixel structure vs photon generated current for varying (a) Early Voltage and (b) β.

In both figs. 10 (a) and (b), it can be seen that an increase in output voltage is observed with an increase in Early Voltage and β (maximum 45 dB and 47 dB respectively). Since r_o is proportional to ΔV_{CE}, this explains why there is a large increase in output voltage since the input voltage is also increased significantly. Since β is a measure of amplification in a BJT transistor, an increase in β results in larger current flow. This, in turn, will result in a larger voltage drop as seen in normal common-emitter circuit. Since the common-base part of the cascode configuration exhibits a series resistance, a larger voltage drop is seen resulting in a larger output voltage.

For the MOSFET-BJT cascode configuration, the following graphs depict the performance of the configuration:

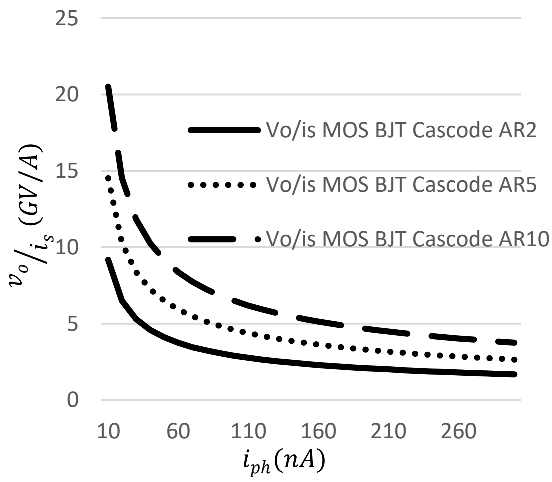

Fig. 11. Gain of modified configuration (BJT and MOSFET combination).

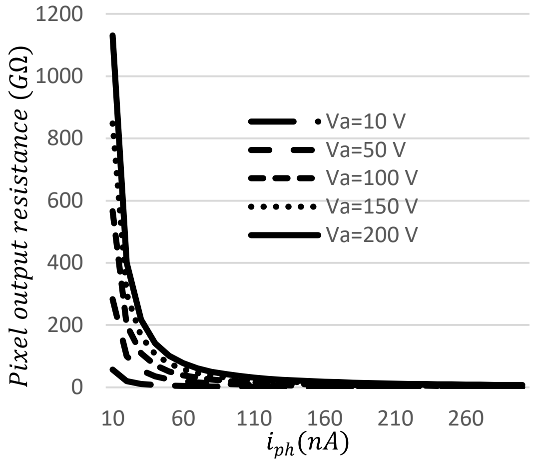

Fig. 12. Pixel output resistance vs photon generated current for varying Early Voltage for BJT and MOSFET combination configuration.

Comparing figs. 11 and 12 with the BJT only version of the cascode configuration, it is observed that the gain is increased (from 24 MV/A to 20 GV/A). Additionally the larger the common gate transistor's aspect ratio (AR), the larger overall gain is seen.

It must be noted that one should not just use values and configurations to increase the output as much as possible, since the maximum output voltage is constrained to the supply voltage minus some transistor voltage drops. However the benefits of using these modified configurations are still worthwile considering the tradeoffs. Power supply voltage variation does not affect any of these parameters analysed in this work.

V. Conclusion

In this work, a cascode configured diode connected pixel was inserted in the standard 3T pixel structure detector to obtain improved performance. This improved performance was in the form of much larger output voltage.

However, this improvement comes with some tradeoffs where the standard 3T pixel structure is not sensitive to β and Early Voltage. With the inclusion of the cascode configured diode-connected BJT acting as a pixel, the detecting element (pixel), is sensitive to β and Early Voltage. Lastly, with the inclusion of a common gate configured MOSFET in the place of the common base configured BJT increases the gain and pixel output resistance more than the BJT only cascode configured version. However, since 3T pixel structure detectors are usually powered using low voltages (typically 1.8 V to 5 V), the MOSFET-BJT combined cascode configured pixel would not be advisable to use since the resolution of the detector is large resulting in information loss.

This work can be used by a designer to develop much improved 3T pixel structure detectors in simulation without the need to prototype and incur large amounts of cost. This will also save on design time.

Acknowledgment

The author of this article would like to thank University of Johannesburg of making use of their computers to perform the simulations.

References

[1] G. C. Holst and R. G. Driggers, "Small detectors in infrared system design," *Optical Engineering Journal*, vol. 51, no. 3, pp. 1-6, Sept. 2012.

[2] S. Lee, K. Yasutomi, M. Morita, H. Kwanishi and S. Kawahito, "A Time-of-Flight Range Sensor Using Four-Tap Lock-In Pixels with High near Infrared Sensitivity for LiDAR Applications," *Sensors journal*, vol. 20, no. 1, art. no. 116, pp. 1-16, 2020.

[3] G. E. Smith, "The invention and early history of the CCD," *Nucl. Instruments Methods Phys. Research*, section A, vol. 607, no. 1, Aug. 2009.

[4] N. Bassler, "Radiation damage in charge-coupled devices," *Radiation, Environment and Biophysics*, vol. 49, no. 3, pp. 373-378, Mar. 2010.

[5] H. Tran et al., "Si-Based GeSn Photodetectors toward Mid-Infrared Imaging Applications," *ACS Photonics*, vol. 6, no. 11, pp. 2807-2815, 2019.

[6] E. Vilella, A. Comerma, O. Alonso and A. Dieguez, "Low-noise pixel detectors based on gated Geiger mode avalanche photodiodes," *Electronic Letters*, vol. 47, no. 6, pp. 397-398, Jan. 2011.

[7] A. D. Mora et al., "Fast-Gated Single-Photon Avalanche Diode for Wide Dynamic Range Near Infrared Spectroscopy," *IEEE J. of Selected topics in Quantum Electronics*, vol. 16, no. 4, Jul. 2010.

[8] M. Uzunkol and G.M. Rebeiz, "A Low-Noise 150-210 GHz Detector in 45 nm CMOS SOI," *IEEE Microwave and Wireless Components Letters*, vol. 23, no. 6, pp. 309-311, Jun. 2013.

[9] N. Namekata, S. Adachi and S. Inoue, "Ultra-low-Noise Sinusoidally Gated Avalanche Photodiode for High-Speed Single-Photon Detection at Telecommunication Wavelengths," *IEEE Photonics Tech. Lett*., vol. 22, no. 8, Apr. 2010.

[10] P. M. Santos, D. W. L. Monteiro and L. P. Salles, "Current-Mode Self-Amplified CMOS Sensor Intended for 2D Temperature Microgradients Measurement and Imaging," *Sensors*, vol. 20, no. 18, 5111, pp. 1 – 21, Sept. 2020.

[11] J. Gao, D. Zhang, K. Nie and J. Xu, " Analysis and Optimization design of the column bus parasitic effects on large-array CMOS image sensor," *Microelectronics Journal*, vol. 96, no. 1, pp. 1-8, Feb. 2020.

[12] J. Venter, S. Sinha and J.W. Lambrechts, "Characterization of diode-connected heterojunction bipolar transistors for near-infrared detecting applications," *Optical Engineering Journal*, vol. 57, no. 11, pp. 1 – 7, Nov. 2018.

[13] J. Venter, "Mathematical Modelling of Low-Frequency BiCMOS Near-Infrared Detectors" Ph.D. Thesis, Dept. of Electrical, Electronic and Computer Engineering, Univ. of Pretoria, Pretoria, RSA, 2020.

The Use of Digital Image Processing for Investigating Vulture Streamer Lengths to better understand Power Line Fault Mechanisms

Nishanth Parus
School of Electrical & Information Engineering
University of the Witwatersrand.
Johannesburg, South Africa
Email: nishanth.parus@students.wits.ac.za

Nishal Mahatho
Research Testing and Development
Eskom Holdings SOC Ltd
Johannesburg, South Africa
Email: MahathN@eskom.co.za

Dante Matlou
Eskom Transmission
Eskom Holdings SOC Ltd
Johannesburg, South Africa
Email: MatlouT@eskom.co.za

Andreas Beutel
Research Testing and Development
Eskom Holdings SOC Ltd
Johannesburg, South Africa
Email: BeutelAA@eskom.co.za

Kaajial Durgapersad
Research Testing and Development
Eskom Holdings SOC Ltd
Johannesburg, South Africa
Email: DurgapK@eskom.co.za

Chandima Gomes
School of Electrical & Information Engineering
University of the Witwatersrand.
Johannesburg, South Africa
Email: chandima.gomes@wits.ac.za

***Abstract*—This paper explores the measurement of vulture streamer lengths that contribute to power line faults. Digital image processing techniques were utilized to measure the streamer lengths of captive vultures with the aim of developing a practical measurement system to study the streamers of naturally occurring vultures. Various image processing options considered in this study are discussed and the setup of a camera system at a test site is described. Finally, some of the initial measurement results are provided. The maximum streamer length captured and evaluated with the proposed measurement methodology was determined to be 77 cm.**

Keywords— power line faults, line performance, bird streamer, digital image processing, vulture, artificial intelligence, camera calibration.

I. Introduction

Power line faults caused by bird excrement are categorised into two different mechanisms. Firstly, bird excrement that directly short circuits the electrical clearance at the towers are known as streamer faults (i.e. directly – at time of discharge), and secondly, excrement deposited on insulators over time may result in pollution related flash-overs (i.e. indirectly – sometime after the streamer is discharged). Bird faults due to streamers and pollution account for approximately 38 % of faults on Eskom's Main Transmission System [1].

This paper focuses only on the streamer faults that occur directly at time of discharge, with emphasis on transmission lines, i.e. lines operating at greater than 132 kV. Faults due to bird electrocutions and nesting are not addressed in this paper.

Previous research has documented broad estimates of expected streamer lengths from birds [2]. Laboratory experiments have shown that streamer volumes of between 50-60 cm^3 could potentially result in flashovers [1]. Taylor [3] also performed laboratory testing of streamer induced flashover. To date, however, actual streamers produced by birds have not been scientifically measured – although they have been visually observed and estimated to be as long as 3 m [4]. As part of ongoing research, the measurement of actual vulture streamer lengths is an important input for the design and development of new fault mitigation solutions. Mitigation of such faults are important to reduce unnecessary electrical stresses on network equipment such as transformers and to ensure better network reliability.

Digital image processing has gained popularity for practical engineering applications and significant strides have been made in algorithm development and optimization. For this research, simple digital image structure analysis has been used to infer the vulture streamer lengths.

II. Background

Generally, larger birds produce longer and thicker streamers than smaller birds. The longer the streamer, the greater is the probability of shorting-out the electrical safety clearance at the tower. Current research is considering the size range at which a bird is capable of producing a streamer long enough to cause a flashover. Observations of bird streamers indicate that species ± 50 cm in height are potential culprits of streamer faults [5]. Vultures are one of the large bird species (78-98 cm in height) that are known to roost on transmission towers. For high voltage lines (greater than 132 kV) the typical electrical clearance ranges between 2.8 m and 6 m, and is dependent on the line voltage. For lower voltage lines, the electrical clearances are smaller and are more susceptible to smaller streamers bridging a larger portion or the entire clearance distance.

Figure 1 shows examples of vulture streamer events on an Eskom Transmission line. The streamer was captured using a wildlife camera trap.

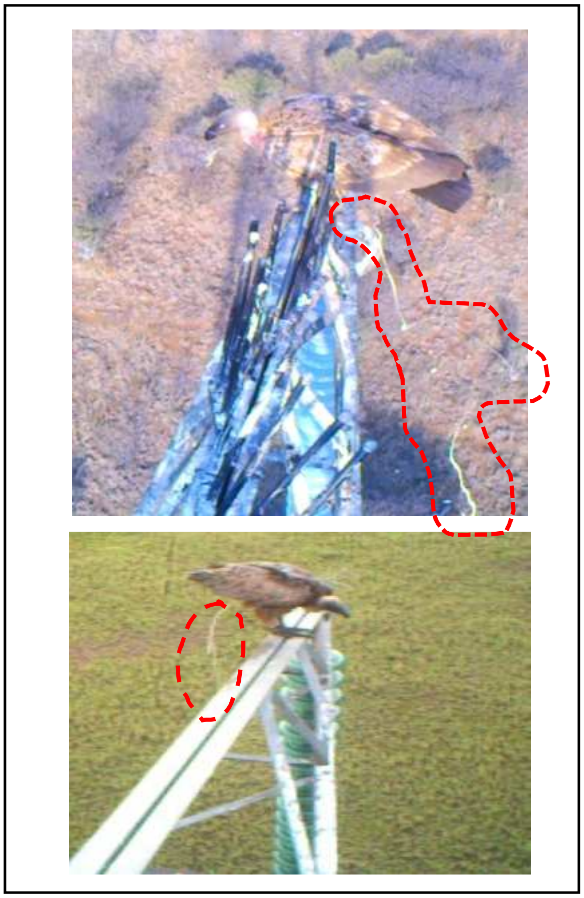

Figure 1: Vulture streamer events on a power line (bottom [1])

The lines were live at the time these images were captured; however, the streamer events shown here did not result in a line fault. The red dashed polygon lines highlight the streamer discharges.

Hobby type digital cameras used to capture the images shown in Figure 1 are generally not regarded as precision measuring instruments. This project was conceived as an initial investigation into the use of available wildlife trap cameras to obtain an estimate of vulture streamer lengths. For this phase of the research, an assessment of the sensitivity and measurement accuracy of this type of camera was investigated. Figure 2 is an example of a wildlife camera trap used for this research

Figure 2: Example of a wildlife camera trap [6]

III. Power line bird faults

Polat et al [7], reports that bird faults on transmission lines can cause significant outages, sometimes with severe financial consequences – even into millions of dollars (China was specifically cited as an example). Having said that, it is very difficult to conclusively verify that a streamer caused a fault [8,9].

Restani et al [10] performed a study into faults on a 500 kV transmission line due to bird droppings (contamination) on insulator strings. The contamination was caused by large flocks of ravens roosting on the transmission line towers. Gregarious species that gather in groups to roost on towers (e.g. vultures) are more vulnerable to electrocutions than solitary birds, as clearances are reduced by individuals of a flock making physical contact with one another [5].

Mitigation measures include spikes to discourage perching in critical locations on towers and insulating covers above insulators to prevent streamer and contamination problems [11,12]. Spikes have been found to be effective in many cases [2,12], but care needs to be taken in their selection and placement. Spikes also have to be maintained as they have been observed to slide-about or are damaged by bird activity over time.

IV. Test site and investigation methodology

The research methodology involved the following:

- Calibrate the camera sensor (i.e. pixel distance) to a reference measurement;
- Install the cameras at the test site;
- Data capture for a period of 1 month; and
- Analyse the saved videos to determine the streamer lengths.

A wildlife camera trap was setup in a vulture enclosure at a vulture rehabilitation facility near Hartbeespoort, west of Pretoria, South Africa. Figure 3 shows the rehabilitation enclosure. Ethical clearance for this research was not required as the work only involved video recording of the birds' behaviour inside the enclosure.

Over a one-month period, the cameras captured video footage of vulture behaviour in the enclosure. The cameras were motion-triggered and thirty second video clips were saved. The camera footage was downloaded and the video footage was manually reviewed. Only clips with streamers were further evaluated.

The cameras that were previously installed on Eskom's power lines (see Figure 1) were not intended for streamer length calculation, but rather for bird behaviour monitoring. Parameters such as the installation angle, the relative field of view, distance to the bird and other reference measurements were not documented during that project. The streamer imagery obtained from the initial research provided the motivation to conduct the research presented in this paper.

Two cameras were attached to the outside of the enclosure fence, facing inside the enclosure. One was set up along the width (i.e. 'A axis' in Figures 3 and 4) and one along the length of the enclosure (i.e. the 'B axis').

Figure 3: Vulture enclosure

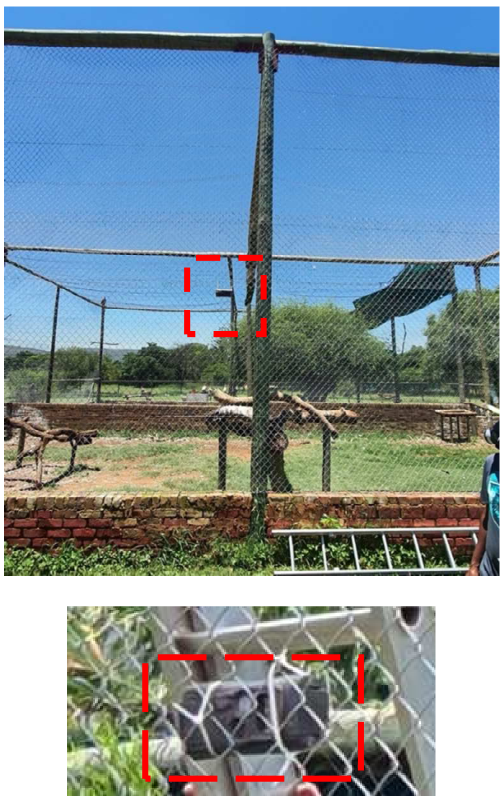

Figure 4: Camera mounted on enclosure fence

The camera specifications and photography settings are: Resolution 5184x4000 pixels, F Stop 2.7 and ISO 800. The manufacturer did not publish the lens specifications. The camera was positioned to capture streamer events occurring between 1 m to 9 m away from the camera. Both cameras were focused on a perch beam that spanned the width of the enclosure, giving both side and front views of the perch beam. The field of view was adjusted so that the perch beam and the area directly beneath it was in-frame. The field of view for both axes are shown in Figure 5.

V. DIGITAL IMAGE PROCESSING TECHNIQUES

A. Measurement Principle

Several imaging processing techniques are applicable as a potential solution. However; due to time constraints, only a simple image structure analysis solution using pixel length inference could be implemented. For accurate measurements, a camera calibration is required. A normal camera calibration is required to determine various physical parameters of the lens and sensor combination [13,14].

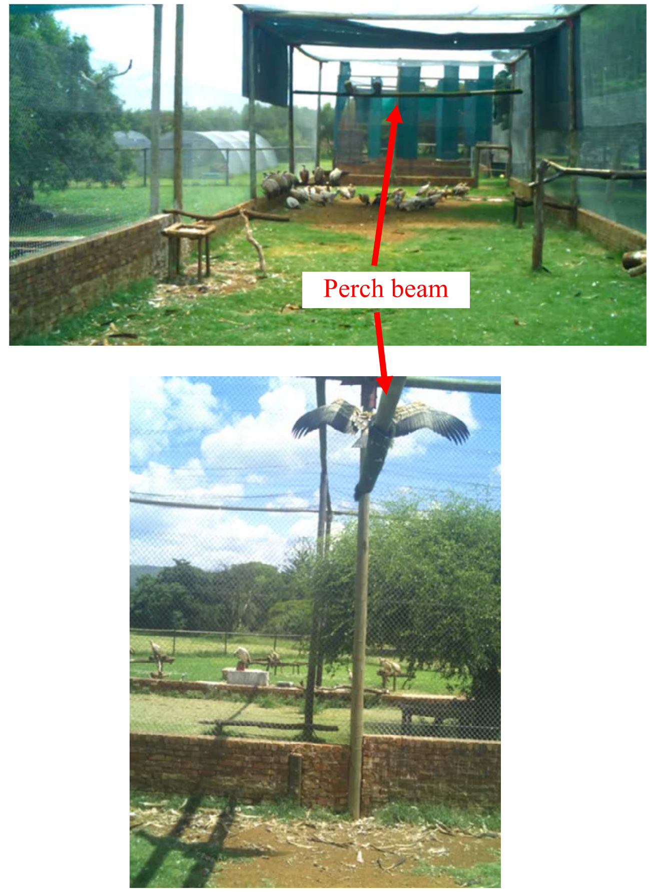

Figure 5: View from camera along enclosure length ('A' axis – top) and width ('B' axis – bottom)

A camera captures an image with each pixel representing a point in 3-D space with its projection into a 2-D space. Further, due to minor imperfections in the construction of the lens and sensor, the saved image may have distortions [14]. Improved measurement accuracy may be obtained if the camera's extrinsic and intrinsic parameters are computed, and the final image is corrected for these distortions.

The intrinsic parameters relate to the camera's focal length, optical centre and skew coefficients. These parameters are specific to each camera and lens combination. Extrinsic parameters relate to the rotation and translation vectors that translate a 3-D scene into a 2-D coordinate. The calibration process generates matrix coefficients that may be applied to a saved image to correct the distortions [14]. The radial distortion coefficients model the radial distortions that cause straight lines to appear curved in the saved image. This usually occurs when light waves entering at the periphery of the lens bend more than they do at its optical centre. The tangential distortion coefficients model the tangential distortion that occur when the lens and the image plane are not absolutely parallel with one another. To determine the projection of a 3-D point onto the flat 2-D image plane, the point from the real world must be transformed to the camera coordinate system. This is achieved using the extrinsic parameters (i.e. the Rotation R and Translation T) parameters. The equations that relate a 3-D point (X_w, Y_w, Z_w) in real world coordinates to its projection (u, v) in the image coordinates are [14]:

$$\begin{bmatrix} u', \\ v', \\ z' \end{bmatrix} = P \begin{bmatrix} Xw \\ Yw, \\ Zw, \\ 1 \end{bmatrix} \tag{1}$$

$$u = u' \div w' \tag{2}$$

$$v = v' \div w' \tag{3}$$

Where: P is a 3x4 Projection matrix consisting of the intrinsic matrix (K) that contains intrinsic parameters and the extrinsic matrix ([R | t]) – which is a combination of the 3x3 Rotation matrix R and 3x1 Translation vector t.

$$P = \underbrace{K}_{\text{Intrinsic Matrix}} \times \underbrace{[R \mid \;\; t]}_{\text{Extrinsic Matrix}} \tag{4}$$

$$K = \begin{bmatrix} fx & \gamma & cx \\ 0 & fy & cy \\ 0 & 0 & 1 \end{bmatrix} \tag{5}$$

Where: f_x and f_y are the focal lengths. These are generally the same value. c_x and c_y are the coordinates of the optical centre of the image plane. ϒ relates to the skew deviation between the axis (usually taken as 0).

The most common type of camera calibration is the checkerboard pattern calibration technique [15]. This process requires taking pictures of a reference checkerboard pattern (with known dimensions) from different angles and distances away from the camera. The OpenCV camera calibration library may be used to generate the calibration data [15]. The pre-compiled python function 'findChessboardCorners()' is used to process the checkerboard pictures to compute the calibration data. An example of the resultant checkerboard detection is illustrated in Figure 6.

Using this data, the various intrinsic and extrinsic matrices and coefficients may be computed. The rotation and translation calibration can then be applied to each new image to obtain a corrected image. The corrected image can then be used for more accurate measurement. More complex calibration techniques such as the Geometric Clues or Deep Learning based techniques may also be used; however, they are not covered in this paper.

Figure 6: Camera calibration using checkerboard technique [15]

B. Pixel-to-length inference

The first stage of this research utilized a simpler inference measurement to determine streamer lengths. The results of the streamer length computation using the camera calibration technique will be published as part of further work done on this project. It was therefore decided to use the basic inference technique for the initial stage and the checkerboard technique for subsequent stages of this project.

Pixel-length inference was achieved using the principle of triangle similarity. This technique involves pixel calibration against a target image of known width (W) at a distance (D) from the camera (i.e. a reference image). From the picture of the reference object, the apparent distance in pixels (P) can be measured. This 'measurement factor' can then be applied to the image containing the streamer event and the length thereof can be inferred. Although less accurate, it allowed for simple data analysis for the initial stage of this project. Figure 7 shows the camera reference pictures that were used. The camera's focus is best between 1 m to 6 m away from the lens. Images further away tend to be blurry or out of focus.

The reference image consisted of black coloured rectangles of dimensions 5 x 4 cm, 10 x 4 cm and 25 x 4 cm. The images were captured at distances from 7 m to 1 m away from the camera. The images were captured in the horizontal orientation of the camera (i.e. as shown in Figure 4). The pixel length was measured using the Mac 'Preview' Application and the results are plotted in Figure 8.

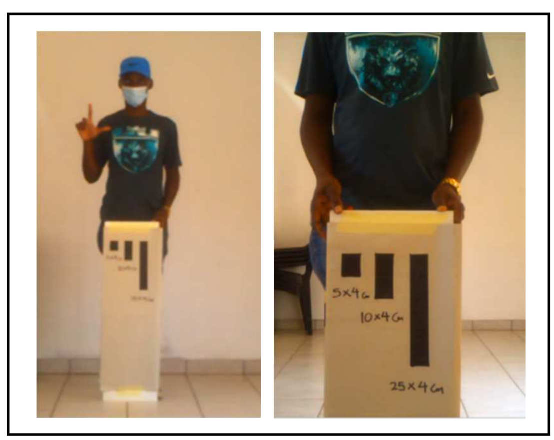

Figure 7: Reference images used for inference calibration (left - 7 m and right - 1 m away from camera).

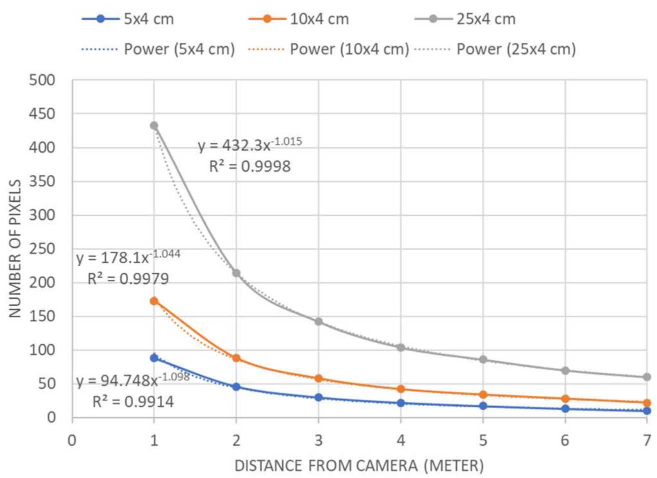

Figure 8: Inference calibration graphs

From Figure 8, the pixel length for the specific sized rectangle may be obtained at a specific distance away from the camera. When the pixel length for the streamer is compared to the pixel length of the reference rectangle, the actual streamer length may be obtained.

A power regression curve was fitted to the calibration data. The coefficient of determination (R^2) is very high (i.e. approx. 0.99 in all cases). This indicates that good accuracy can be achieved between the pixel to distance inference. The accuracy at a distance of 1 m away from the camera is 6 mm/pixel, at 5 m the accuracy is 29 mm/pixel and at 7m, it is 41 mm/pixel. The millimetre level accuracy was deemed acceptable for this initial work as the main clearances are in the order of meters. The power function for the larger 25 x 4 cm data was used for determining the streamer lengths in this report as it yielded a better pixel-to-length ratio. A limitation of this technique is that the distance of the streamer from the camera needs to be known to infer the actual length. Using the equation of the fitted curve, the apparent pixel length of the 25 cm reference may be obtained. From this value, a single pixel length may be calculated. The single pixel length is then multiplied by the number of pixels of the streamer picture to infer the streamer length.

VI. Results

Figure 9 is a 2-D representation of the scenario under investigation. The streamer length is determined using the direct linear distance between the tips of the streamer, i.e. the hypotenuse length (h). Of interest to this work, however, is the reduction of the electrical clearance distance (d) by the streamer, and therefore, the vertical distance (y) is also calculated. The hypotenuse length does not contribute to the reduction of the electrical clearance in 2-D space. In other words, if a streamer is ejected at an angle (θ), only the 'y' parameter contributes to a reduction of the electrical clearance and therefore this distance is of interest for the engineering study. Only images from the 'B' axis (i.e. the enclosure length) were obtained. The camera installed on the 'A' axis (i.e. width section) did not record any video that could be correlated with the streamer events triggered by the 'B' Axis camera. Five streamer events have been captured and analysed as part of this study. The width of the enclosure is 9 m and the length of the green perch mat is approximately 3 m in the camera's field of view. From these measurement references, the distance of the streamer from the camera may be estimated.

Table I lists the streamer events recorded and their inferred lengths. Figure 10 shows the streamer with the longest calculated length (event 1).

VII. Discussion

The initial data only yielded footage from the 'B' axis. The streamers are however projected in 3-D space. To obtain greater accuracy, the 3-D projection length should be considered. For this installation, however, the birds are forced to perch on the width-length beam. This configuration should result in streamers that are most accurate in the 'B' axis and the data obtained from this initial study is therefore considered to be suitable for the analysis.

For this initial review, assumptions were made relating to the position of the bird on the perch beam. This distance assumption will impact the absolute length calculations. For further work, it is recommended that the perch beam be graduated with fixed measuring reference markers so that the birds distance can be better assessed. From review of the camera video footage, the shape of streamer was observed to distort as it travels ground-ward. The effect of this distortion of the streamer should be considered in determining the reduction of the electrical clearance.

The cameras were mounted on the fence using cable ties. The footage from the 'A' axis camera showed that the camera position shifted after installation. This was attributed to the vultures flying directly the side of the fence as they were able to get a run-up before taking to flight. The vibrations from collisions with the fence caused the cable ties to slip and the camera shifted position. Consequently, the 'A' axis footage was unusable.

Captive birds are fed with dead animal carcasses, prompting the question that their dietary patterns may be different to that of naturally occurring vultures as they may experience some stress while in captivity.

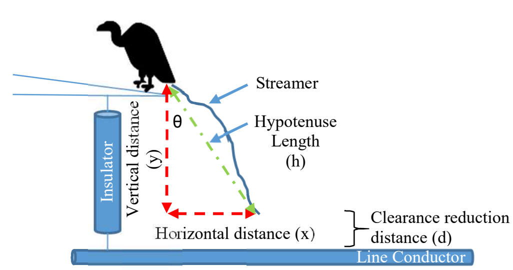

Figure 9: Graphic representation of the streamer path

TABLE 1: STREAMER EVENTS RECORDED

Event	Estimated distance from camera (m)	Estimated vertical electrical clearance distance (cm)	Estimated hypotenuse streamer length (cm)
1	7	76	77

2	7.5	34	34
3	2	24	25
4	5	12	12
5	4	41	48

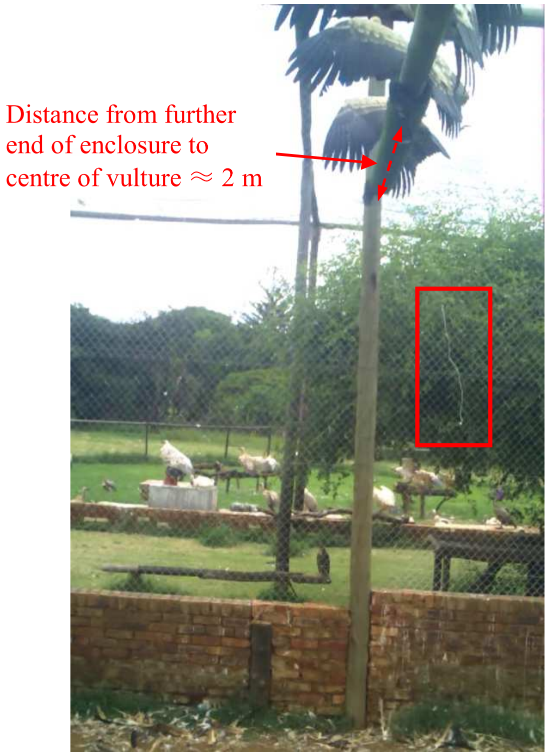

Figure 10: Vulture streamer event 1

It is unknown if the streamers of captive birds are comparable to that of naturally occurring birds. The vulture handlers at the rehabilitation facility have indicated that the food provided to the captive vultures is generally the same that they will consume in the wild. Further work is required to investigate the streamer lengths of wild vultures as compared to birds in captivity.

The camera was motion triggered, and as such, many hours of video that did not contain vulture streamers were captured. The footage had to be manually reviewed to extract the frames that had streamers. There is an opportunity to train a deep learning object detector to automatically identify a streamer and only capture those specific frames.

VIII. Conclusions and Recommendations

The initial work presented herein has provided acceptable results and is a good basis for future work that will be required to refine the measurement technique. The initial video footage used has yielded several streamer events. The maximum length streamer calculated from the initial video footage was determined to be 77 cm. Further events have been recorded since the analysis reported in this paper. The analysis of future events should include a fixed reference measurement indicator (such as a stick graduated at regular intervals and installed in the camera's field of view) to provide greater confidence in the calculated values.

Better mounting of the camera could also be considered. A stable tripod or any camera mount not fixed to the fence should yield better footage.

Obtaining streamer lengths measurements from an operating power line could be considered to account for differences between naturally occurring and captive birds. Once a sufficiently large data set has been obtained, electrical modelling should be conducted to determine the probability of flashover.

IX. References

[1] N. Mahatho, N. Parus, T. Govender, W.S. Miya, H. F. Vosloo and G. Sibilant, "The Effect of Bird Streamers on the Insulation Strength of HVDC Lines," Cigré Paris Session, 2016.

[2] C. van Rooyen, H. Vosloo, R. Harness, "Watch the birdie! Eliminating bird streamers as a cause of faulting on transmission lines," IEEE Ind. Appl. Mag., vol. 9, no. 5, pp. 55–60, Sep./Oct. 2003.

[3] P.V. Taylor, "Case study of bird streamer caused transient earth faults on a 275-kV transmission grid," M.S. thesis, Dept. of Electr. Eng., Univ. of Natal, Durban, South Africa, 2001.

[4] H. F. Vosloo, A. C. Britten, A. A. Burger, "The susceptibility of 400 kV transmission lines to bird streamers and bush fires: a definitive case study", Proceedings of the 2009 Cigré Regional Conference.

[5] M. Pretorius, T. Galloway-Griesel, L. Leeuwner, 2021. Eskom Research Report: Observations of Nocturnal Bird Activity at Eskom Transmission Towers Experiencing Bird-Related Faults. RES/RR/21/1961737.

[6] https://www.dreamstime.com/photos-images/wildlife-infrared-camera.html, last accessed 16 Nov 2022.

[7] Ö. Polat, K. Yumak, N. E. Atilla, M. Bağrıyanık, " An overview of bird related issues in electrical power systems", Proceedings of the 20th Innovative Manufacturing Engineering and Energy Conference (IManEE 2016), IOP Conf. Ser.: Mater. Sci. Eng. 161 012091.

[8] IEEE Std 1651-2010, "IEEE Guide for Reducing Bird-Related Outages".

[9] R. Harness, G. Kratz, "Bird streamer as the probable cause of a Bald Eagle electrocution", Colorado Birds, Vol. 14, No. 2, Apr 2007, pp. 86-90.

[10] M. Restani, J. S. Lueck, "The emerging conflict of common ravens roosting on electric power transmission line towers in Montana, USA", Human–Wildlife Interactions, Vol. 14, No. 3, pp. 451–460, Winter 2020, digitalcommons.usu.edu/hwi.

[11] CIGRE TB 876, "Interactions between Electrical Infrastructure and Wildlife", Aug 2022.

[12] P. Taklaja, P. Hyvönen, J. V. Klüss, J. Niitsoo, I. Palu, " Preventing Bird Streamer Outages Using Alternative Tower Configurations", IEEE Transactions on Power Delivery, Vol. 29, No. 5, Oct 2014, pp. 2402-2409.

[13] https://medium.com/vacatronics/3-ways-to-calibrate-your-camera-using-opencv-and-python-395528a51615, last accessed 16 Nov 2022.

[14] https://learnopencv.com/camera-calibration-using-opencv/, last accessed 16 Nov 2022.

[15] https://docs.opencv.org/4.x/dc/dbb/tutorial_py_calibration.html, last accessed 16 Nov 2022.

Distributed Hybrid Power-Sharing Control Strategy within Islanded Microgrids

G. Wanlongo Ndiwulu[1], M. Matalatala[1], A. Kuti Lusala[1] and P. Ntambu Bokoro[2]
[1]Département de Génie Electrique et Informatique, Faculté Polytenique, Université de Kinshasa, RD Congo
[2]Electrical Engineering Technology, Faculty of Engineering and the Built Environment, University of Johannesburg
guy.wanlongo@unikin.ac.cd, michel.matalatala@unikin.ac.cd, vital.kutilusala@unikin.ac.cd and pitshoub@uj.ac.za

***Abstract*—The stable operation of an islanded microgrid powered by multiple distributed energy sources (DESs) depends on the control of the voltage magnitude, the frequency and the power-sharing among the DESs. Uncontrolled power-sharing among sources can lead to voltage and frequency stability issues characterized by poorly damped oscillations. To achieve efficient power-sharing, a level-one control strategy is required. This paper proposes a communication-less hybrid control strategy to implement power-sharing regardless of the inverter output impedance. In this strategy, the power-sharing control is achieved with the inverters in both grid-forming and grid-following control modes—in particular, for the sources interfaced with rotating machines. Simulation results show that the instantaneous power-sharing is correctly carried out while maintaining the RMS voltage at the required value. Furthermore, the voltage drops remain within the 10% admissible range.**

***Index Terms*—AC microgrid, inverter, grid-forming, grid-following, power-sharing control**

I. Introduction

Microgrids can be considered as a better approach to ensure an efficient integration of distributed energy sources (DESs) into the main grid. They can be operated in both grid-connected and islanded modes. While operating in islanded mode, microgrids can be adopted for local generation of affordable, reliable and resilient power as an alternative to the main grids in islanded areas [1]. This provides more flexibility to communities living in areas with inadequate electrical infrastructures (like rural environments) to meet their electricity needs. However, the integration of DESs within a microgrid may give rise to critical voltage and frequency stability if the power-sharing among the sources is not addressed accordingly [1], [2]. The control strategy based on droop control is widely applied to carry out the proper power sharing among the sources [3]. However, in the droop control approach, the power-sharing control is dependent on the inverter output impedance, which requires a trade-off between voltage and frequency deviations and accurate power-sharing [4]. Furthermore, communication-based control strategies while achieving good power-sharing often result in increased cost of the system [5].

This paper proposes a communication-less distributed hybrid control strategy to carry out the power-sharing regardless of the inverter output impedance (Fig. 1). The inverters are used in both grid-forming and grid-following control modes. Unlike the conventional droop control method, the proposed control strategy decouples power-sharing control from the references of the voltage and current applied to the inner voltage and current control loops. This allows the inverters with the fastest dynamics to be most closely controlled. In addition, it can be applied even to islanded microgrids with different DES unit interfaces such as inverters and a directly connected synchronous machine.

Recent studies addressed the communication-less power-sharing challenges within islanded microgrids. In [1], the authors proposed an accurate power-sharing method for the control of a multi-Distributed Generation (DG) microgrid by employing low-bandwidth digital communications. However, this study was limited to two DG units. The study undertaken in [2] proposed a distributed integral controller based on averaging algorithms, which dynamically regulate the system frequency during a time-varying load. However, a secondary control level is required. In this work, the proposed power-sharing control strategy appears to be a more efficient method of performing the instantaneous power-sharing irrespective of the frequency droop control and the inverter output impedance, in comparison with the approaches based on the conventional droop control.

The remainder of this paper is organized as follows: Section II describes the challenges of the power-sharing of VSI-based microgrids. Section III presents the details of the proposed hybrid power-sharing control method, while in Section IV the performance of the proposed power-sharing method is analyzed and discussed. Finally, Section IV concludes the paper.

II. Power-sharing control of VSI-based microgrids

In an islanded mode, each power source must be able to supply its share of the total load in proportion to its rated power. The power-sharing concept is illustrated in the particular case of the islanded microgrid shown in Fig. 1. In this simplified representation, the power sources are represented by voltage sources. R_{line1} and R_{line2} are the feeder resistance of $line1$ and $line2$, respectively. X_{line1} and X_{line2} are the reactance feeder impedance associated with the $line1$ and $line2$, respectively. $V_i\angle\delta_i$ is the voltage of power energy source (i represents the i^{th} power source). δ_i represents the phase angle difference between V_i and V_M. V_M is the microgrid voltage at busbar M where loads are connected.

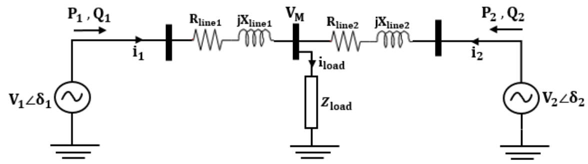

Fig. 1. Power-sharing principle in islanded microgrids.

The active and reactive power generated by the sources are given by the following equations [6]:

$$P_i = \frac{X_{linei}\left(V_i V_M \cos\delta_i - V_M^2\right) + R_{linei} V_i V_M \sin\delta_i}{X_{linei}^2 + R_{linei}^2} \quad (1)$$

$$Q_i = \frac{X_{linei}\left(V_i V_M \cos\delta_i - V_M^2\right) - R_{linei} V_i V_M \sin\delta_i}{X_{linei}^2 + R_{linei}^2} \quad (2)$$

The power angle δ_i is small in the case of a microgrid and it can be assumed that $\sin\delta_i \approx \delta_i$ and $\cos\delta_i \approx 1$. Equations (1) and (2) can then be rewritten as

$$P_i = \frac{X_{linei} V_M \left(V_i - V_M\right) + R_{linei} V_i V_M \delta_i}{X_{linei}^2 + R_{linei}^2} \quad (3)$$

$$Q_i = \frac{X_{linei} V_M \left(V_i - V_M\right) - R_{linei} V_i V_M \delta_i}{X_{linei}^2 + R_{linei}^2} \quad (4)$$

Equations (3) and (4) show that the flow of active and reactive power between sources and loads depends on the terminal voltages of the sources V_i and the power angle δ_i that is the representation of frequency in the microgrid based on the inverters, assuming that we know the feeder impedance parameters (X_{linei} and R_{linei}) and voltage of loads (V_M).

According to Fig. 1 and to the corresponding equations, the effective control of active and reactive power sharing dictates the stable operation of the microgrid. The load demand should be shared among sources according to their power ratings to ensure the power supply and balance stability. The power-sharing stability can be defined as the ability of the microgrid to maintain the power balance and effective load sharing among the sources. Poor power-sharing among sources can lead to voltage and frequency stability issues characterized by poorly damped oscillations.

III. Proposed microgrid control architectures

To decouple frequency control from power sharing control, We propose a hybrid grid-forming and grid-following control scheme. In this architecture, specific control roles are assigned to voltage source inverters (VSIs) connected to the microgrid. One VSI should act as a grid-forming VSI to control the voltage magnitude and set the adequate frequency (V-f control mode) for the entire microgrid, the other VSI is controlled in grid-following mode (PQ control mode) as a constant current source to inject a controlled current in amplitude and phase into the microgrid.

To identify the grid-following and grid-forming converters in a microgrid, we are calling "$GF\ node$" the particular microgrid busbar where a grid-following converter is connected, through its LC filter and connection impedance. "$Slack\ node$" is used to identify a microgrid busbar where a grid-forming converter is connected, through an LC filter and connection impedance. Finally, we call "$PQ\ node$" the particular microgrid busbars where the loads are connected.

A particular identification of microgrid busbars is given in Fig. 2 [7]. Thus, the considered islanded microgrid is composed of one "$GF\ node$", one "$PQ\ node$" and one "$Slack\ node$".

The power balance in the microgrid given in Fig. 2 can be established on the *Slack node* as follows:

$$P_s = P_1 - P_{PQ} - \sum P_{loss_i} \quad (5)$$

$$Q_s = Q_1 - Q_{PQ} - \sum Q_{loss_i} \quad (6)$$

where

- P_s and Q_s are the active and reactive power generated by the grid-forming VSI,
- P_1 and Q_1 represent respectively the active and reactive power injected by the grid-following VSI according to the $GF\ node$,
- P_{PQ} and Q_{PQ} represent the active and reactive power of loads, connected at the $PQ\ node$, respectively,
- Q_{ci} is the reactive power generated by the filter capacitance related to the i^{th} VSI, and
- P_{loss_i} and Q_{loss_i} are the loss of active and reactive power due to the i^{th} feeder impedance lines.

Equations (5) and (6) specify the active and reactive power that the grid-forming converter can exchange in the islanded microgrid.

A. Instantaneous active and reactive power-sharing

The proposed instantaneous power sharing as defined in this paper is independent of the frequency stability but is rather dictated by the voltage variation on the *Slack node*. In this approach, all the voltage fluctuations on the $Slack\ node$ are translated as an immediate power variation, and this means that the grid-forming source takes action to compensate for the power mismatch. Fig. 3 illustrates the proposed power-sharing approach. The instantaneous power-sharing can be analyzed through a model composed of a controlled voltage source connected to the $Slack\ node$. This voltage source models the grid-forming VSI, while a current source models the grid-following VSI. The current through the inductance of the LC filter, i_{l1} is equal to the current at the LC filter output i_{M1} since an ideal filter capacitance is assumed (see Fig. 2). As a result, i_{M1} represents the injected current into the $GF\ node$. In addition, loads are connected to the $PQ\ node$. i_{load} is the current absorbed by the loads.

By applying Kirchhoff's law at the *Slack node*, the voltage drop on the line impedance between the $PQ\ node$ and the $Slack\ node$ in sinusoidal steady-state is given by

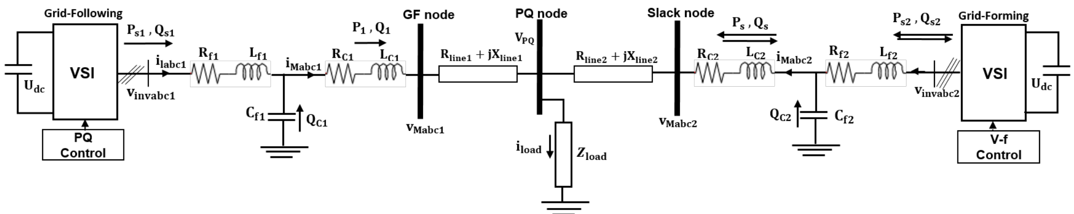

Fig. 2. Identification of "$GF\ node$", "$PQ\ node$" and "$Slack\ node$" in islanded microgrid powered by one grid-forming VSI and one grid-following VSI.

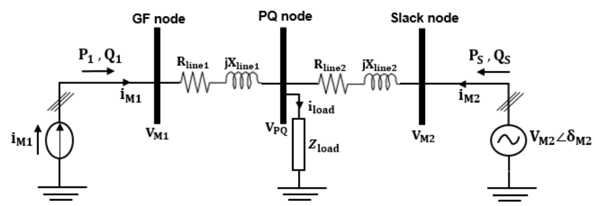

Fig. 3. Schematic diagram of modeling the proposed power-sharing approach.

$$V_{M2} - V_{PQ} = Z_{line2} i_{M2} \tag{7}$$

where

- V_{M2} is the voltage on the $Slack\ node$,
- V_{PQ} represents the voltage on the $PQ\ node$,
- Z_{line2} is the feeder impedance of the $line2$, and
- i_{M2} is the current generated by the voltage source V_{M2}.

Since $i_{GF} = i_{M1}$, the current i_{M2} is modeled by equation (8):

$$i_{M2} = i_{load} - i_{GF} \tag{8}$$

If the length of the feeder $line2$ is short and the voltage V_{M2} is set constant by the grid-forming inverter, this induces the voltage V_{PQ} close to the V_{M2}. As a result, the voltage drop across the feeder impedance of the $line2$ can be expressed as $V_{M2} - V_{PQ} = gV_{M2}$, where g ($g \leq 0$) is a proportional factor which can be dictated by the injected power generation on the PQ busbar. Equations (7) and (8) can be rewritten as

$$i_{load} - i_{GF} = \frac{gV_{M2}}{Z_{line2}} \tag{9}$$

Equation (9) can be rewritten as a function of the real and reactive power as

$$i_{dload} + ji_{qload} - (i_{dGF} + ji_{qGF}) = \frac{gV_{M2}\angle\delta_2}{R_{line2} + jX_{line2}} \tag{10}$$

$$P_{load} + jQ_{load} - (P_{GF} + jQ_{GF}) = \frac{gV_{M2}\angle\delta_2 V_{M1}\angle\delta_1}{R_{line2} + jX_{line2}} \tag{11}$$

Equations (10) and (11) show that the fluctuating voltage on the $Slack\ node$ is associated with the power deviation between generation and demand.

B. Control structure

Fig. 4 gives an overview of the proposed hybrid power-sharing control strategy applied to an islanded microgrid powered by one grid-following VSI and one grid-forming VSI. The proposed control approach is implemented in the $dq-$synchronous reference frame from the Park-Clarke transformation of the measured current and voltage.

The current i_{labci} (i_{Mabci}) and voltage V_{Mabci} are measured in abc natural frame at the output of VSIs. Current signals i_{labc1} and i_{labc2} are measured on the inductances of the LC filters (grid-following VSI and grid-forming VSI, respectively). i_{Mabc2} is measured at the LC filter output of the grid-forming VSI. V_{Mabc1} and V_{Mabc2} are the voltage signals measured at the LC filter output of the grid-following VSI and of the grid-forming VSI, respectively.

Regarding the grid-following VSI, the current signals i_{labc1} are transformed into i_{ld1} and i_{lq1} components of the current by using Park-Clarke's transformation [7]. The rotation angle θ_1 is generated by phase-locked-loop (PLL) from the measured voltage signals V_{Mabc1} at the output of the grid-following VSI. The signals of i_{ld1} and i_{lq1} are compared to the set point currents i^*_{ld1} and i^*_{lq1}. The proportional-integral (PI) controllers handle the error $i^*_{ld1} - i_{ld1}$ and $i^*_{lq1} - i^*_{lq1}$ from two comparators. The output voltage signals generated by the PI controllers are added to the feedforward signals V_{Md1} and V_{Mq1}, and to the decoupling signals of $-\omega_1 L_{f1} i_{lq1}$ and of $\omega_1 L_{f1} i_{ld1}$. The voltage signals V^*_{invd1} and V^*_{invq1} at the output of controllers are transformed in the abc natural frame for controlling the grid-following VSI in voltage $V^*_{invabc1}$.

Furthermore, a similar approach is chosen for the grid-forming VSI, however with several differences. Two measurements of the current signals i_{labc2} and i_{Mabc2} are performed to account for the current on the LC filter capacitance. Current signals i_{labc2} and i_{Mabc2}, and voltage signals of V_{Mabc2} are also transformed into i_{ld2} and i_{lq2}, i_{Md2} and i_{Mq2}, and V_{Md2} and V_{Mq2} components of the current and of the voltage, respectively. Compared to the grid-following control, the grid-forming control requires a rotating angle θ_2 which corresponds to the nominal frequency ω^* of the system ($\omega^* = \omega_2 = 2\pi f_n$, where f_n is equal to 50 Hz or 60 Hz). The direct and quadrature components of voltage signals V_{Md2} and V_{Mq2} are compared with the set point voltages V^*_{Md2} and V^*_{Mq2}. Error signals $V^*_{Md2} - V_{Md2}$ and $V^*_{Mq2} - V_{Mq2}$ are controlled through the PI controllers. The voltage controllers generate the current signals that are added

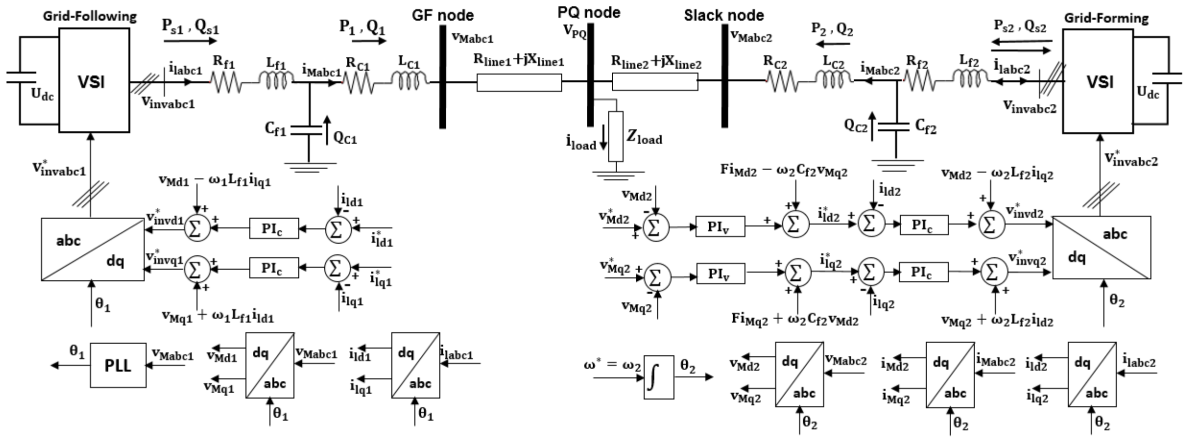

Fig. 4. Control structure of level-one control applied to an islanded microgrid based on VSIs.

to the feedforward signals Fi_{Md2} and Fi_{Mq2} and to the decoupling signals $-\omega_2 C_{f2} V_{Mq2}$ and $\omega_2 C_{f2} V_{Md2}$. Current signals resulting from this sum are considered as set points of filter inductance current i^*_{ld2} and i^*_{lq2}, and they are compared to the measured current signals i_{ld2} and i_{lq2}. The error signals $i^*_{ld2} - i_{ld2}$ and $i^*_{lq2} - i_{lq2}$ of current from these comparators are controlled via PI controllers. These controllers generated the voltage signals that are combined with the feedforward signals V_{Md2} and V_{Mq2}, and the decoupling signals $-\omega_2 L_{f2} i_{lq2}$ and $\omega_2 L_{f2} i_{ld2}$. Voltage signals V^*_{invd2} and V^*_{invq2} resulting from this summation are transformed in the abc natural frame by using Park-Clarke's inverse transform.

Finally, the presented control structure does not ensure any control of the reactive current produced by the LC filter capacitance.

C. Reactive circulating current

The general voltage drop relationship between the grid-following VSI and grid-forming converter (Fig. 2) can be assessed using the following equation [7].

$$V_{M1} = V_{M2} + \frac{R_{line}}{V_{M2}} \left(P_1 - P_{load}\right) + \frac{X_{line}}{V_{M2}} \left(Q_1 - Q_{load}\right) \tag{12}$$

where

- V_{M1} and V_{M2} are respectively the measured voltage magnitude on the $GF\ node$ and $Slack\ node$,
- P_1 and Q_1 are the injected active and reactive power into the $GF\ node$,
- P_{load} and Q_{load} represent the active and reactive power of loads, respectively and
- $R_{line} = R_{line1} + R_{line2}$ and $X_{line} = X_{line1} + X_{line2}$ are the equivalent resistance and reactance of the feeder impedance between $Slack\ node$ and $GF\ node$, respectively.

Assuming that the active power generated by the grid-following source is equal to the load demand $P_1 = P_{load}$ and no reactive power demand from the local loads ($Q_{load} = 0$), Equation (12) can be rewritten:

$$V_{M1} = V_{M2} + \frac{X_{line}}{V_{M2}} Q_1 \tag{13}$$

$$V_{M1} = V_{M2} + \frac{X_{line}}{V_{M2}} \left(Q_{s1} + Q_{C1}\right) \tag{14}$$

Equation (13) shows that if $V_{M1} - V_{M2} \neq 0$, i.e. there is a reactive current flowing between the two inverters. The flow direction depends on the voltage difference. If V_{M1} is greater than V_{M2}, the reactive current flows from the grid-following VSI to the grid-forming VSI. This can reduce voltage microgrid stability.

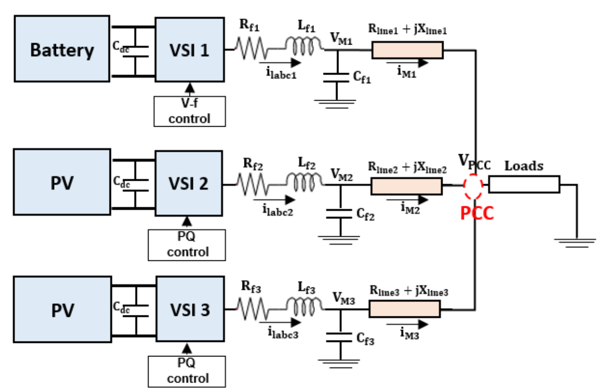

Fig. 5. Microgrid control architecture based on the grid-forming VSI and grid-following VSI.

IV. Results

To test and evaluate the efficiency of the proposed control strategy, the islanded microgrid shown in Fig. 5 is used [8] and simulated with Matlab/SimscapePowerSystems. It is composed of three different VSI and their corresponding energy sources or distributed generators (DGs) connected to the PCC through power lines of different lengths. We assumed a constant impedance load of 8 kW - 5 $kVar$ connected at the PCC. A simplified schematic of the islanded microgrid is shown in Fig. 6 [8]. The energy sources are modeled using an average model. Battery inverter (VSI_1) is acting as a grid-forming inverter to maintain the voltage magnitude and frequency at 230 V RMS and 50 Hz. Meanwhile, Photovoltaic (PV) inverters VSI_2 and VSI_3 are acting as grid-following inverters that inject 3 kW and 5 kW, respectively. The power line parameters are shown in Table I. The PI controller parameters and LC filter parameters are given in Table II.

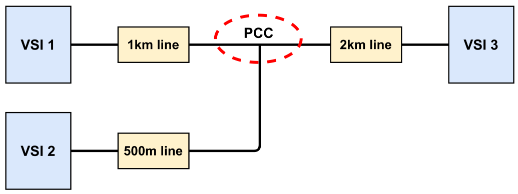

Fig. 6. Test microgrid layout

TABLE I
TYPICAL LINE PARAMETERS [9]

Type of line	**R'** Ω/km	**X'** Ω/km	I_N A	$\frac{R'}{X'}$
Low voltage line	0.642	0.083	142	7.7
Medium voltage line	0.161	0.190	396	0.85
High voltage line	0.06	0.191	580	0.31

TABLE II
PI CONTROLLER AND LC FILTER PARAMETERS

PI controller and LC filter	K_P	K_I	L_f mH	C_f μF
VSI_1: **Voltage control loop**	1.1	2.8	19.2	11.7
VSI_1: **Current control loop**	120	6000	19.2	11.7
VSI_2: **Current control loop**	120	6000	40.6	5.6
VSI_3: **Current control loop**	120	6000	9.6	23.4

A. Steady-State conditions of constant impedance load

The first scenario consists in testing the performance of the proposed control strategy in the steady-state conditions of a constant impedance load. Fig. 7 gives the obtained results for the RMS voltage at the outputs of VSI_1, VSI_2, VSI_3, and the PCC where a constant impedance load of 8 kW - 5 $kVar$ is connected. We can note that the VSI_1 sets the RMS voltage at 230 V within the microgrid, thus assuming the assigned role. This can be observed through RMS voltage at the outputs of VSI_2 and VSI_3 and at the PCC. Futhermore, a mismatch can be noted when comparing the output voltages between VSI_1 and VSI_3 or VSI_2 (2% between VSI_1 and VSI_3 and 0.4% between VSI_1 and VSI_2). This mismatch remains within the 10% admissible range and is due to the voltage drop along the power line.

Fig. 8 and Fig. 9 show the instantaneous active and reactive power-sharing among the DGs. It can be noticed that the power-sharing among the DGs is performed according to the assigned control roles. VSI_2 and VSI_3 act as constant current sources, they inject 3 kW and 5 kW, respectively into the PCC as shown in Fig. 8. It is noted that the active power at the output of VSI_1 is maintained at zero because the total active power of constant impedance load connected at the PCC is supplied by VSI_2 et VSI_3.

Fig. 9 gives the instantaneous reactive power-sharing within the microgrid. The reactive power load at the PCC is mainly supplied by the VSI_1 because VSI_2 and VSI_3 are controlled to inject only active power. The observed reactive powers are generated by the output LC filters of VSIs according to the voltage across each capacitance.

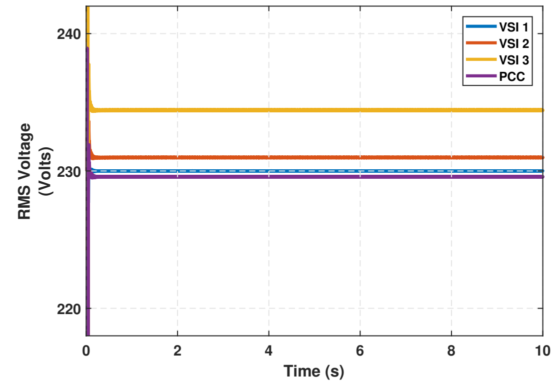

Fig. 7. RMS voltage at the output of the connected VSIs to the PCC.

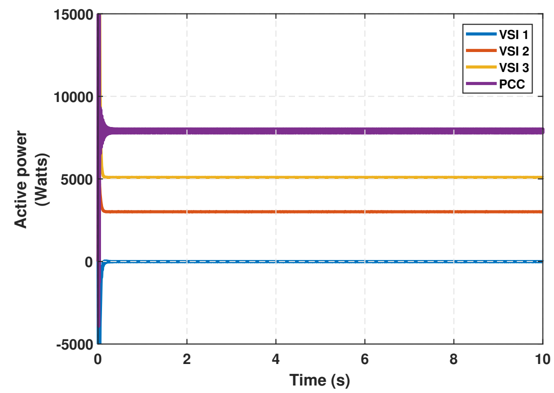

Fig. 8. Active power at the output of the connected VSIs to the PCC.

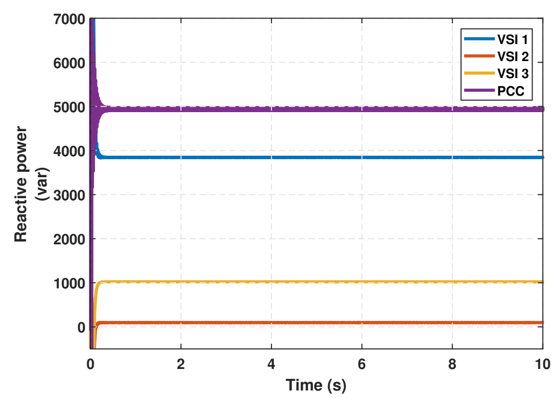

Fig. 9. Reactive power at the output of the connected VSIs to the PCC.

B. Change conditions of constant impedance load

The second scenario consists in analyzing the performance of the proposed distributed hybrid control strategy by adding a constant impedance load of 4.5 kW at the PCC and by the reducing reactive power at the same busbar. Fig. 10 shows the obtained results for the RMS voltage at the output of VSI_1, VSI_2, and VSI_3, and the PCC. VSI_1 also maintains the RMS voltage within the islanded microgrid. This is illustrated through RMS voltage values at the busbars VSI_2, VSI_3 and PCC. These voltages are also close to that imposed by the VSI_1. The observed small voltage mismatch concerning the RMS voltage at the VSI_1 busbar is also caused by the length between grid-forming VSI_1 busbar and grid-following VSIs busbars (VSI_2 and VSI_3).

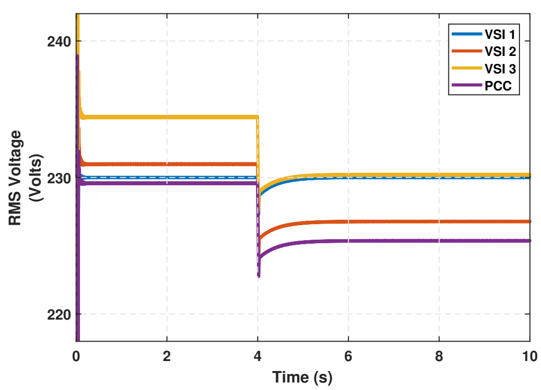

Fig. 10. RMS voltage with load change to the PCC at $t = 4s$.

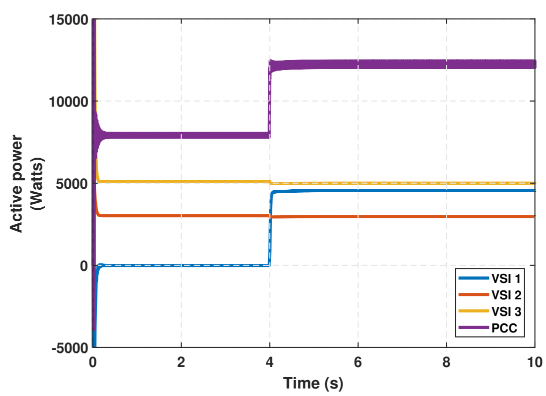

Fig. 11. Active power with load change to the PCC at $t = 4s$.

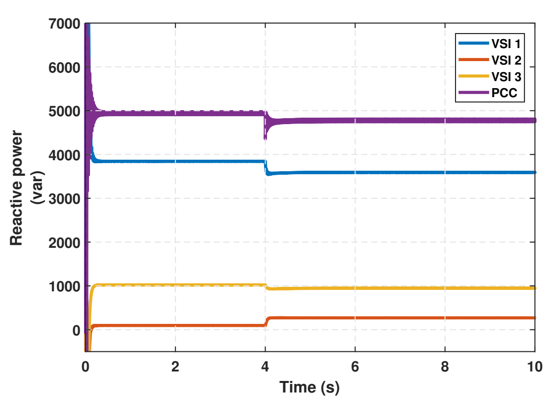

Fig. 12. Reactive power with load change to the PCC at $t = 4s$.

Fig. 11 and Fig. 12 illustrate the instantaneous power-sharing within the islanded microgrid. The active power-sharing is shown in Fig. 11. The increase of the constant impedance load at 4 s leads VSI_1 to compensate the active power change at the PCC busbar by increasing its active power (+ 100%). Whereas the VSI_2 and VSI_3 act as constant current sources according to the assigned control roles (grid-following VSIs). Fig. 12 depicts the instantaneous reactive power-sharing within the microgrid when the reactive power change at the PCC. VSI_1 reduces its reactive power (- 6.6%) to compensate for the observed reactive power change at the PCC. The reactive power change at VSI_2 and VSI_3 leads to a reactive current which flows from VSI_1 and VSI_3 to VSI_2.

V. Conclusion

This paper presents a communication-less hybrid control strategy to ensure power-sharing and balancing in an islanded multi-sources microgrid. The proposed control strategy consists in achieving power-sharing control by using the inverters in both grid-forming and grid-following control modes. Furthermore, this control scheme allows decoupling power-sharing control from the references of the voltage and current applied to the inner voltage and control loops. In this way, it allows to overcome the limitations of the conventional droop control method. Simulation results show the efficiency of the proposed method. The instantaneous power-sharing is correctly carried out while maintaining the RMS voltage at the required value. Furthermore, the voltage drops remain within the 10% admissible range. In future work, the proposed power-sharing control strategy will be compared with other power-sharing control methods.

References

[1] M. Hamzeh, H. Karimi, H. Mokhtari, and M. Popov, "An accurate power sharing method for control of a multi-dg microgrid," in *Proceedings of the International Conference on Power Systems Transients 2011*, 2011, pp. 1–6.

[2] J. Simpson-Porco, F. Dorfler, B. Francesco, Q. Shafiee, and J. Guerrero, "Stability, power sharing and distributed secondary control in droop-controlled microgrids," in *2013 IEEE International Conference on Smart Grid Communications*, 2013, pp. 672–677.

[3] A. Rosini, A. Labella, A. Bonfiglio, R. Procopio, and G. JM., "A review of reactive power sharing control techniques for islanded microgrids," in *Renewable and Sustainable Energy Reviews*, vol. 141, 2021, p. 110745.

[4] T. Vandoorn, J. De Kooning, B. Meersman, and L. Vandevelde, "Review of primary control strategies for islanded microgrids with power-electronic interfaces," in *Renewable and Sustainable Energy Reviews*, vol. 19, 2013, pp. 613–628.

[5] H. Han, X. Hou, J. Yan, J.and Wu, M. Su, and J. M. Guerrero, "Review of power sharing control strategies for islanding operation of ac microgrids," no. 4, pp. 1–16.

[6] Y. Han, H. Li, P. Shen, E. A. Alves Coelho, and J. M. Guerrero, "Review of Active and Reactive Power Sharing Strategies in Hierarchical Controlled Microgrids," in *IEEE IEEE trans. on Power Electronics*, vol. 32, no. 3, 2017, p. 2427–2451.

[7] G. Wanlongo Ndiwulu, "Control and stability analysis of islanded microgrids based on inner control loops approach," Ph.D. dissertation, Université catholique de Louvain, 2020.

[8] E. Vasquez Mayen, G. Wanlongo Ndiwulu, E. De Jaeger, and A. Kuti Lusala, "Voltage unbalance compensation for islanded microgrids with hybrid control approach," in *ICEET*, 2021, pp. 1–6.

[9] A. Engler and N. Soultanis, "Droop control in lv-grids," in *2005 International Conference on Future Power Systems*, 2005, pp. 6 pp.–6.

Effects of Upside Risk on Microgrids' Reliability Considering the COVID-19 Pandemic

A. K. Onaolapo, E. E. Ojo
Dept. of Electrical Power Engineering
Durban University of Technology
Durban, 4000, South Africa.
adeniyio@dut.ac.za
evanso@dut.ac.za

***Abstract*—The power systems in the areas of human resources and customer demand were greatly impacted by COVID-19 due to a series of restrictions on human movements, lockdowns of factories, and several job losses during the period. In situations like this, the use of microgrids may help attain a balance in the consumption and generation of power, thereby leading to customer satisfaction. The energy resources' optimal power scheduling in a standalone microgrid, taking into consideration the upside risk (UR), is proposed in this work. The standalone microgrid is made up of different energy resources such as a diesel generator (DSG), photovoltaic (PV), wind turbine (WT), and battery storage system (BSS). In this paper, the energy not supplied (ENS) is minimized in standalone mode by considering the effects of COVID-19. The UR is the change between the actual and target ENS when the target ENS is greater than the actual. Also, COVID-19 led to a significant reduction in the ENS.**

Keywords—upside risk, microgrids, reliability, COVID-19, pandemic.

I. INTRODUCTION

As of late 2022, reliable information from the World Health Organization (WHO) [1] revealed that there have been over 600 million confirmed cases, over 6 million confirmed deaths, and over 12 billion confirmed vaccine doses, of COVID-19 globally. COVID-19 impacted the power system greatly, particularly in customer demand. Moreover, the attention of industries and researchers has been recently drawn to microgrids. The implementation of microgrids has led to an increase in reliability [2, 3] and a decrease in losses in the power system [4]. Microgrids have been designed to combine resources from diesel generators (DSGs), renewable energy resources (RERs), and battery storage systems (BSSs) to have the smallest possible energy not supplied (ENS).

A lot of research has been conducted on microgrids [5, 6], but there is room for more research, particularly in assessing the effects of pandemics such as COVID-19. Authors in [7] assessed the microgrid utilities investment risk in Rwanda's rural electrification project using the Stochastic Technical and Economic Microgrid Model (STEMM) to determine the economic feasibility of microgrid projects and the impact of technical design decisions. In [8], Li et al. investigated the downside risk and upside potential of the optimal economic dispatch of microgrids using the group search optimizer. A Pareto solution trade-off was obtained among the downside risk, the upside potential, and the expected generation cost. And the final economic dispatch solution was chosen using a fuzzy decision-making method. A stochastic planning program was conducted for the data center microgrid considering risk management and batch workload scheduling [9]. The microgrid consisting of conventional resources, renewable resources, and energy storage, was modeled to improve its carbon footprint and electricity cost. The associated operation risk was measured using volatility risk. The strategy on the unit commitment of conventional resources, batch workload allocation, energy storage operation, and power procurement, was formulated using a stochastic planning scheme. Alford, in [10] posited that the acquisition and development of microgrid technology should be a political objective to satisfy national security and environmental protection concerns; thereby concluding that microgrids have assisted the USA's Department of Defense (DoD) in achieving its goals of sustainability and energy security through its ability to facilitate clean energy production and save energy. An analysis of power systems investment, transport, and mining, conducted in [11] to solve the power problems in the state of Bihar, India, showed that the deployment of microgrids is a cheaper and better option than the use of coal sourced from Australia. Sortino ratio was adapted for microgrid optimization in [12] to maximize aggregate profit per unit risk by optimally distributing the total load demand to different micro-sources. A risk estimate was then found by consolidating the change in the target profit of the reserve market and energy for diverse levels of uncertainties in electric vehicles and renewable energy. Zakaria et al. reviewed the stochastic optimizations of microgrid applications in [13]. The aspects of information, sampling, uncertainties modeling, and the merits and demerits of stochastic optimization techniques were covered; and it concluded that the deterministic optimization techniques do not perform as the stochastic optimization techniques in terms of economic, technical, and social aspects of microgrid systems. Authors in [14, 15] concluded, based on the data analyzed, that COVID-19 brought about an economic downturn, a decrease in electricity demand, and a decrease in carbon emission during the period.

In this paper, ENS minimization in the standalone mode and optimal power scheduling of microgrids (containing DG and RERs) is implemented with the aim of evaluating risk. The Weibull, Beta, and normal distribution functions are used due to the uncertainties in the load profile and generation of the RERs. An increase in ENS leads to dissatisfaction with the parts of consumers and microgrid operators. A phenomenon referred to as upside risk (UR) is caused when the ENS violates the expected limit. The simulations are carried out in MATLAB environments for five different sample cases. Optimal power scheduling (for different resources of the microgrid) and the UR were evaluated. And the impact of COVID-19 on the ENS (as it affects the standalone microgrids) was examined.

The rest of the paper is arranged as follows: The description of study area features in Section II, and model development featuring system modeling and problem formulation is highlighted in Section III. Section IV features the results and discussion, and the conclusion is highlighted in section V.

II. DESCRIPTION OF THE STUDY AREA

South Africa (30.5595° S, 22.9375° E), the most industrialized country in Africa, is the study area for this research. South Africa, the southernmost country in Africa, is projected as of June 2022 to be about 60,6 million in the population [16]. Currently, the major source of energy for South Africa is coal, comprising a whopping 80 percent of the total energy mix. South Africa experiences periodic outages in the form of scheduled interruptions, usually referred to as load shedding. Lack of maintenance of power system infrastructures, aging infrastructure, lack of technical skill experts, sabotage, and vandalization of power infrastructure, are the causes of the current load shedding in South Africa. Load shedding is practiced whenever there is an overload on the country's electricity system, which usually happens between 40-50 days a year [17]. COVID-19 infected millions of people and caused excessive deaths within a short period. The recorded cases and deaths are shown in Fig. 1, while the active cases and recovery are shown in Fig. 2 [18]. Load demand decreased during the pandemic and the average power generation dropped because of COVID-19 [19].

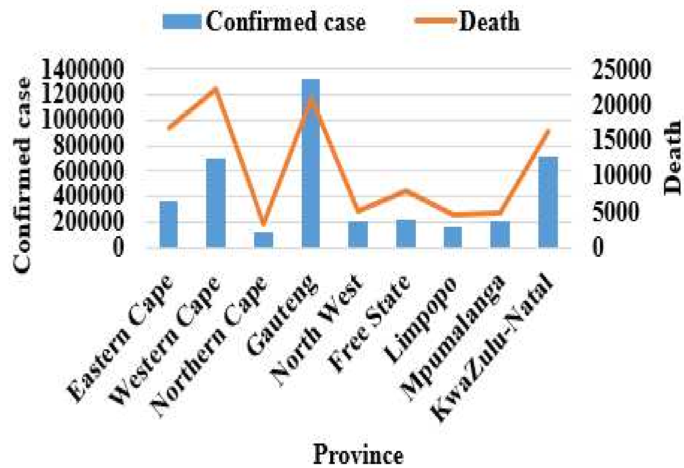

Fig. 1. COVID-19 confirmed cases and death in South Africa (September 21, 2022).

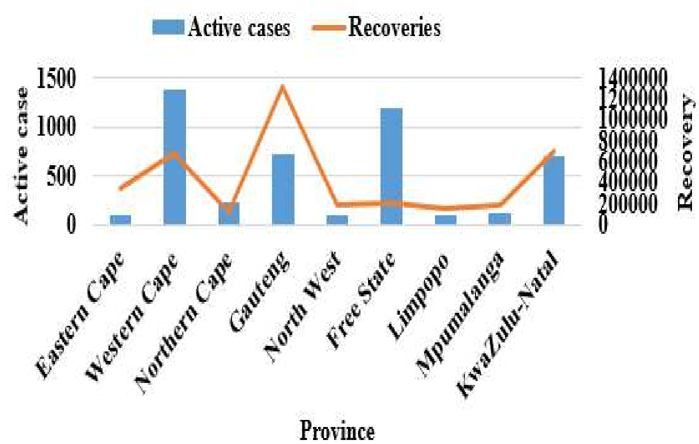

Fig. 2. COVID-19 active cases and recovery in South Africa (September 21, 2022)

III. MODEL DEVELOPMENT

A. System Modeling

The proposed model used for this research is shown in Fig. 3. The microgrid structure is made up of DSGs, photovoltaics (PVs), wind turbines (WTs), and BSSs. The stochastic behavior of the power generation and the load are modeled using Normal, Beta, and Weibull distribution functions due to the uncertainties in the load profile and generation; and the simulations are done for five sample cases.

B. Problem Formulation

Here, we discuss the objective function and the system constraints.

1) Objective Function

This aspect deals with the impact of *UR* when the *ENS* is minimized. As the total *ENS* (*TENS*) is minimized, the objective function is [4]:

$$TENS_S = \sum_{t=1}^{N_a} ENS_{t,s} \tag{1}$$

$$TENS = \sum_{s=1}^{N_b} \left(prob_s \times TENS_s \right) \tag{2}$$

where N_a and N_b are the numbers of microgrid resources on buses *a* and *b* respectively, at the t^{th} hour and s^{th} case (scenario). And $prob_s$ which is the probability of the s^{th} case is assumed the same for all cases with no loss of generality.

2) Constraints

The following constraints were considered from the different power equipment of the microgrid:

i). *DSGs Constraints:* The Constraints here are made up of the minimum decrease rate (down rate) and maximum increase rate (up rate) of the *DSGs*' power, the *DSGs*' maximum and minimum power generation [20].

$$P_{g,t,s} - P_{g,t-1,s} \le up\,rate_g \tag{3}$$

$$P_{g,t-1,s} - P_{g,t,s} \le down\,rate_g \tag{4}$$

$$P_{g,t,s} \le P_g^{\max} \times v'_{g,t,s} \tag{5}$$

$$P_{g,t,s} \ge P_g^{\min} \times v'_{g,t,s} \tag{6}$$

where $P_{g,t,s}$ is the power output of g^{th} DSG, and *v* denotes the inputs of the function.

ii). *BSSs Constraints:* The constraints for BSSs' minimum and maximum rate of charge or discharge and state of charge (*SOC*) are [20]:

$$SoC_{\min} \le SoC_{t,s} \le SoC_{\max} \tag{7}$$

$$0 \le P_{t,s}^{ch,bat} \le P_{\max}^{ch,bat} \times b_{t,s}^{bat} \tag{8}$$

$$0 \le P_{t,s}^{disch,bat} \le P_{\max}^{disch,bat} \times (1 - b_{t,s}^{bat}) \tag{9}$$

$$SoC_{t,s} = SoC_{t-1,s} + \eta^{ch} \left[\frac{P_{t,s}^{ch,bat}}{S_{base}} - \frac{P_{t,s}^{disch,bat}}{\eta^{disch} S_{base}} \right] \tag{10}$$

$$\sum_{t=1}^{T=N_a} \left(SoC_{t,s} - SoC_{t-1,s} \right) \ge 0 \tag{11}$$

where *b* is the upper limit of the function and η is the battery efficiency.

iii). *UR Constraints:* The possibility of value or asset increasing beyond the expectations is referred to as *UR*. This concept is considered a positive risk by giving the operators the liberty of reaching their goals in managing the system using different options, methods, and tools. But when a variable is taking lots of risks, the *UR* concept can show a red flag. *UR* is associated with the microgrid operator's disposition to take risks and use the maximum system's capacity in keeping the highly prioritized variables within certain reasonable margins. Managers with high-risk tolerance choose high *UR* and vice versa. Meanwhile, choosing high *UR* may hurt the microgrid during uncertainties because the system finds it difficult to respond to unexpected shocks, as the focus of the system is on some predetermined objectives. Considering a target ($target_s$) for each case (*s*) of *UR* (for UR_s) [4]:

$$\begin{aligned} &if\ TENS_s \le target_s,\ UR_S = target_s - TENS_s \\ &otherwise,\ UR_S = 0 \end{aligned} \tag{12}$$

and,

$$\sum_{s=1}^{N_a} \left(prob_s \times UR_s \right) \le \lambda \times EUR \tag{13}$$

where *λ*, a range of numbers between 0 and 1, is used for risk adjustment when operating and *EUR* is the standalone microgrid's expected UR.

iv). *Power balance constraints:* The power balance constraints are expressed as [4]:

$$\sum_{g=1}^{N_e} P_{g,t,s} + \sum_{i=1}^{N_c} PV_{i,t,s} + \sum_{j=1}^{N_d} WT_{j,t,s} + P_{t,s}^{ch,bat} + P_{t,s}^{disch,bat} + ENS_{t,s} = PL_{t,s} \tag{14}$$

where $P_{g,t,s}$ is the power output of g^{th} DSG, $PV_{i,t,s}$ is the power output of i^{th} PV, and $WT_{j,t,s}$ is the power output of j^{th} WT, at the s^{th} case and t^{th} hour. The charge and discharge power of the battery are $P^{ch,bat}$ and $P^{disch,bat}$, respectively. While the *ENS* and *PL* are the *ENS* and the demanded load of the system.

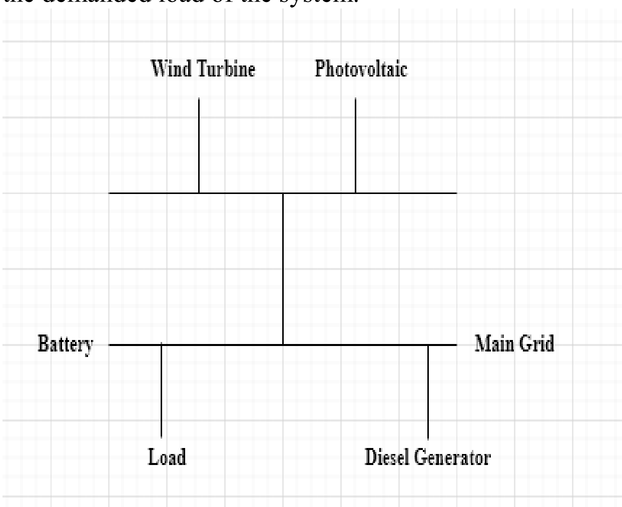

Fig. 3. Studied system.

v). *COVID-19 constraints:* The effects of COVID-19 on the power system are factored into the research leading to the definition of a new coefficient (*CVD*). *CVD* is the average percentage change in the load during the COVID-19 pandemic in comparison to the pre-COVID period. Therefore, we have [4]:

$$PL_{t,s}^{CVD} = (1+CVD) \times PL_{t,s} \quad (15)$$

C. Optimization Method

Mixed-integer programming (MIP) is used in the optimization work of this research. The problem is solved in the MATLAB environment to get optimal results. The proposed method is explained as follows:

Step 1: Input independent data into the system.
Step 2: Generate stochastic microgrid load (DSGs, RERs, and BSSs outputs).
Step 3: Analyze the ENS value first with *UR*, then without *UR*, and compare the results.
Step 4: Analyze the *ENS* value with *UR*, then without *UR*; consider different cross elasticities and compare the results.
Step 5: Investigate the microgrid's *ENS* value by applying the *COVID-19* impact, first with *UR*, then without *UR*, and compare the results.

IV. RESULTS AND DISCUSSION

COVID-19 impacts and *UR* are applied to minimize *ENS* in a standalone microgrid in this research. The total installed outputs of all *PVs*, *WTs*, and *DSGs* are 50kW, 48kW, and 22kW, respectively. All variables are computed in the simulation but only the necessary outputs are reflected in the results section. The $P^{bat}{}_{\min}$, $P^{bat}{}_{\max}$, $SoC_{\min}$, and $SoC_{\max}$ are -52 kW, 52 kW, 10%, and 90%, respectively. The *BESS's* charge and discharge efficiency are set at 90%. Table I presents the *ENS* of the microgrid's system as calculated without the impact of the *UR* on the system. The target *ENS* is shown, and for comparison, the passive *URs* (i.e., *UR* values without activating its constraints) were calculated.

Table I: The ENS and passive UR [kWh]

Case	ENS	Target	Passive UR
Case 1	0	8.725	8.725
Case 2	7.345	8.725	1.38
Case 3	12.423	8.725	0
Case 4	12.257	8.725	0
Case 5	5.736	8.725	2.989
Average	7.552	8.725	2.619

As can be seen from Table I, the value of the passive *UR* reaches the maximum when the *ENS* of the system is zero, indicating maximum positive risk. Conversely, the values of the passive *UR* tend to zero when the *ENS* values of the system are more than the target values indicating minimum positive risk. Then the *UR* constraints are initiated and diverse λ values are used to acquire a complete perception of the proposed system, as shown in Figure 4.

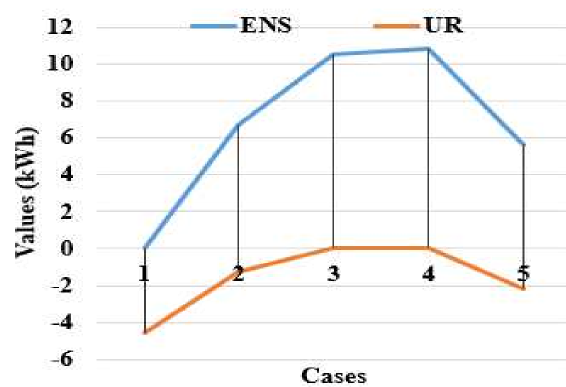

Fig. 4. Change in UR and ENS with λ variation.

Fig. 4 shows that a stepwise increase in λ between 0.5 and 0.95 leads to a decrease of between 15.67% to 1.33% in the average percentage of *ENS* as compared to Table I (the base case). Moreover, when the *UR* constraints are employed, there is a decrease in the average *UR*. The average *UR* ranges between -47.46% to -4.52% lesser than the base case.

Table II shows the results of *COVID-19's* implementation on the passive *UR* and *ENS* of the microgrid system. The *ENS* of the system considerably decrease by about 77.1% as compared to the base case (Table I).

Table II: The COVID-19 effect on ENS and passive UR [kWh]

Case	ENS	Target	Passive UR
Case 1	0	3.525	3.525
Case 2	1.002	3.525	2.523
Case 3	3.634	3.525	0
Case 4	4.028	3.525	0
Case 5	0	3.525	3.525
Average	1.733	3.525	1.714

It is observed that there was a considerable reduction in the load profile due to COVID-19 and the related events, hence, the reduction in the system's ENS. The UR constraints are then activated, and the results of the simulation are obtained and reported in Fig. 5.
Fig. 5 shows that the effects of COVID-19 on the system's ENS are more considerable than in Fig. 4 with the same λ variation.

V. CONCLUSION

The optimal power scheduling for minimizing ENS in a standalone microgrid is proposed in this research. The UR was evaluated with the implementation of COVID-19's effects on the load profile.

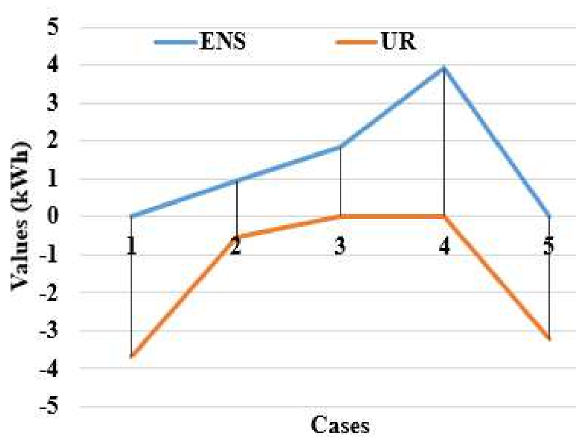

Fig. 5. The *COVID-19* effect on *ENS* and *UR* with λ variation

The simulations were conducted in a MATLAB environment. The studies were conducted with and without UR and the results were analyzed. Analysis revealed that the average COVID-19 effects on the ENS of the microgrid system are as remarkable as 77.1%. The proposed method can be adopted by microgrid operators to manage policies more beneficially for system operations.

ACKNOWLEDGMENT

This research was funded by the Durban University of Technology Ph.D. Training/Support program: 2022 (RFA-Smart Grids). The authors acknowledge the Smart Grid Research Centre, the Durban University of Technology, for providing facilities for this research.

REFERENCES

[1] World Health Organisation, "Coronavirus disease (COVID-19)," *WHO website*, 2022. [Online]. Available: https://www.who.int/emergencies/diseases/novel-coronavirus-2019?adgroupsurvey={adgroupsurvey}&gclid=EAIaIQobChMI0v3HqJqc-gIVGODtCh16Swc2EAAYASAAEgKUIPD_BwE [Accessed: 17-Sept-2022].

[2] A.K. Onaolapo, R. Pillay Carpanen, D.G. Dorrell, and E.E. Ojo "Assessment of Sustainable Development: A Nexus between Reliability, Greenhouse Gas Emissions, and Renewable Energy Technologies," Southern African Universities Power Engineering Conference (SAUPEC), DOI: 10.1109/SAUPEC55179.2022.9730748, 2022.

[3] A.K. Onaolapo, R. Pillay-Carpanen, D.G. Dorrell, and E.E. Ojo "Event-Driven Power Outage Prediction using Collaborative Neural Networks," IEEE Transactions on Industrial Informatics, ISSN: 1941-0050, DOI: 10.1109/TII.2022.3178695, pp1-9, 2022.

[4] T. Khalili, S. I. Habibi, S. A. G. K. Abadi, S. Ahmadi, and A. Bidram, "Upside Risk Effect on Reliability of Microgrids Considering Demand Response Program and COVID-19: An Investigation on Health System and Power System Interactions". [Online]. Available: https://scholar.google.co.za/scholar?hl=en&as_sdt=0%2C5&q=Upside+Risk+Effect+on+Reliability+of+Microgrids+Considering+Demand+Response+Program+and+COVID-19%3A+An+Investigation+on+Health+System+and+Power+System+Interactions&btnG= [Accessed: 17-Sept-2022].

[5] T. Adefarati, G. Sharma, A. K. Onaolapo, A. Njepu, K. T. Akindeji, S. O. Oladejo, G. D. Obikoya, and I Adeyanju, "Optimal Design and Techno-Economic Analysis of a Grid-Connected Photovoltaic and Battery Hybrid Energy System," *International Journal of Engineering Research in Africa*, vol. 60, no. 1, pp. 125–154, 2008.

[6] A.K. Onaolapo, R. Pillay-Carpanen, D.G. Dorrell, and E.E. Ojo "Reliability evaluation and financial viability of an electricity power micro-grid system with the incorporation of renewable energy sources and energy storage: A case study of KwaZulu-Natal, South Africa." *IEEE Access*, 9: 159908 – 159924, 2021.

[7] N. J. Williams, P. Jaramillo, and J. Taneja, "An investment risk assessment of microgrid utilities for rural electrification using the stochastic techno-economic microgrid model: a case study in Rwanda," *Energy for Sustainable Development*, vol. 42, no. 1, pp. 87–96, 2017.

[8] Y. Li, J. Huang, Y. Liu, Z. Ni, Y. Shen, W. Hu, and L. Wu, "Economic Dispatch with High Penetration of Wind Power Using Extreme Learning Machine Assisted Group Search Optimizer with Multiple Producers Considering Upside Potential and Downside Risk," *Journal of Modern Power Systems and Clean Energy*, pp. 1–13, 2020.

[9] Z. Ding, L. Xie, Y. Lu, P. Wang, and Shiwei Xia, "Emission-Aware Stochastic Resource Planning Scheme for Data Center Microgrid Considering Batch Workload Scheduling and Risk Management," *IEEE Transactions on Industry Applications*, vol. 54, no. 6, pp. 5599–5608, 2018.

[10] T. J. Alford, "Off the Grid: Facilitating the Acquisition of Microgrids for Military Installations to Achieve Energy Security

and Sustainability," *George Washington Journal of Energy & Environmental Law*, vol. 8, no. 2, pp. 97–120, 2017.
[11] L. Molyneaux, L. Wagner, and J. Foster, "Rural electrification in India: Galilee Basin coal versus decentralized renewable energy microgrids," *Renewable Energy*, vol. 89, no. 1, pp. 422–436, 2016.
[12] V. Mohan, J. G. Singh, and W. Ongsakul, "Sortino Ratio Based Portfolio Optimization
Considering EVs and Renewable Energy in Microgrid Power Market," *IEEE Transactions on Sustainable Energy*, vol. 8, no. 1, pp. 219–229, 2017.
[13] A. Zakaria, Firas B. Ismail, M.S. Hossain Lipu, and M.A. Hannan, "Uncertainty models for stochastic optimization in renewable energy applications," *Renewable Energy*, vol. 145, no. 1, pp. 1543–1571, 2020.
[14] C. Bertram, G. Luderer, F. Creutzig, N. Bauer, F. Ueckerdt, A. Malik, and O. Edenhofer, "COVID-19 induced low power demand and market forces starkly reduce CO_2 emissions," *Nature Climate Change*, vol. 11, no. 1, pp. 193–196, 2021.
[15] A. Navon, R. Machlev, D. Carmon, A. E. Onile, J. Belikov and Y. Levron, "Effects of the COVID-19 Pandemic on Energy Systems and Electric Power Grids—A Review of the Challenges Ahead," *Energies*, vol. 14, no. 1, pp. 1056, 2021.
[16] Stats SA, "Census 2022," [Online]. Available: https://www.statssa.gov.za/?p=15601#:~:text=The%20population %20of%20South%20Africa,growth%20year%2Don%2Dyear. [Accessed: 18-Sept-2022].
[17] US AID, "Power Africa Fact Sheet," [Online]. Available: https://www.usaid.gov/powerafrica/south-africa. [Accessed: 18-Sept-2022].
[18] Coronavirus SA, "COVID-19 online resource and news center," [Online]. Available: https://sacoronavirus.co.za/latest-vaccine-statistics/. [Accessed: 22-Sept-2022].
[19] J. V. B. Andrade, R. S. Salles, M. N. S. Silva, and B. D. Bonatto, "Falling Consumption and Demand for Electricity in South Africa - A Blessing and a Curse," *IEEE PES / IAS Power Africa, IEEE PES/IAS PowerAfrica*, pp. 1-6, 2020.
[20] T. Khalili, H. G. Ganjehlou, A. Bidram, S. Nojavan, S. Asadi, "Financial Risk-Based Scheduling of Microgrids Accompanied by Surveying the Influence of the Demand Response Program," IEEE/IAS 57th Industrial and Commercial Power Systems Technical Conference, pp. 1–9, 2021.

A Modified Droop Control Technique for Accurate Power-Sharing of a Resilient Stand-Alone Micro-grid

Peter Anuoluwapo Gbadega, Yanxia Sun
Dept. of Electrical and Electronic Engineering Science
University of Johannesburg,
Johannesburg, 2006, South Africa.
perosman4real1987@gmail.com and ysun@uj.ac.za

Kayode Timothy Akindeji
Dept. of Electrical Power Engineering
Durban University of Technology,
Durban, 4001, South Africa.
kayodea@dut.ac.za

***Abstract*— This paper proposes a modified droop control technique for accurate power-sharing of a resilient stand-alone microgrid. Two cases were presented in this study; In case 1, a stand-alone microgrid system with a single inverter operating as a voltage source and a local load is presented. A conventional droop-based control strategy was used to modify the voltage magnitude and frequency in relation to reactive and active power signals in order to employ an inner current loop and an outer voltage loop. Although the control scheme accomplishes high flexibility and reliability, the only drawback is that the sharing is realized via frequency and voltage variations in the system, which has motivated the case-2 study to solve these problems. The islanded micro-grid system considered in case 2 consists of two inverters operating as voltage sources (also known as network-forming converters) and a shared load. The load is shared between the first and second converter after a specified period. Therefore, since case- 2 aims to solve the problems of frequency and voltage variations induced by the primary control in case-1, centralized secondary control (modified droop control technique) is implemented in the micro-grid in case-2 to reinstate the nominal frequency and voltage amplitude value in the micro-grid. Additionally, case 2 considered the integration of virtual impedance in the converter's output using an additional closed-loop control to attenuate distortion, minimize the influence of circulating current, and ensure the sharing of harmonic current under unbalanced and non-linear loads. The system model was simulated using the MATLAB/Simulink environment.**

Keywords*— *Micro-grid modeling, network-forming converter, transient stability, droop-based control, virtual impedance, and MATLAB/Simulink.

I. Introduction

Flexibility and reliability are the fundamental properties of the enabling microgrids, which are connected with power flow control into the main grid. Such properties are designed to allow a system to respond rapidly and efficiently to variations in load demand and distributed generating output while maintaining system performance and stability. Therefore, the design of micro-grid control strategies must be stable to operate adequately alongside and independently of the utility power network, maintaining service quality requirements [1]. Multi-layer control strategies ensure disturbance rejection and power quality in microgrids by regulating and providing stable voltage amplitude and frequency via control loops that adjust active and reactive power flow, as well as filtering, harmonic current sharing, and reactive power compensation capabilities [2]. By comparison, planned islanding may occur during scheduled maintenance or when the network's power level compromises the microgrid operation. At the same time, unintentional islanding happens because of faults, uncertainties, or other unplanned occurrences. Islanded operating mode enables continuity of supply (at least for higher priority loads), reflecting cost savings and enhanced reliability [1]. More so, at least one converter will act as a voltage source to control the microgrid's network voltage conditions and power quality, followed by network-feeding converters in the stand-alone operating mode. Owing to the power disparity between distributed generators (DGs) and loads when a microgrid is operating in islanded mode, the voltage and frequency may exceed their permitted limitations, causing the microgrid to become unstable. The microgrid requires an accurate control approach in this mode of operation to ensure improved power-sharing among different DGs and to balance the power shortfall. Droop control using the V–F control method is used to control the voltage and frequency. It's worth noting that when more than one converter is functioning autonomously as a network, it must be synced using the Phase Lock Loop (PLL) feature, and the additional power needed by the loads should be delivered collectively [3].

Maintaining energy balance in any mode of microgrid operation is critical for improved management of voltage and frequency levels in the microgrid network. Any mismatch between generation and load demand results in a voltage and frequency deviation, which has a detrimental influence on energy supply quality and, as a result, affects the operation of sensitive loads linked to the microgrid network. In on-grid micro-grid operation mode, the utility grid regulates voltage and frequency, whereas, in off-grid operation mode, all distributed generations are responsible for power balance as well as voltage and frequency regulation via active coordinated power management and power-sharing control strategies [4]. Hence, to manage power requirements, power converters are controlled as network forming, operating in the same way as voltage sources, which are particularly used in islanded operating mode [5].

Several studies on droop control strategies for distributed generation sources integrated into a low voltage network of the micro-grid power system have recently been published in the literature. Ping et al. [6] used a novel virtual impedance consisting of a virtual negative resistor (VNR) and a virtual inductor incorporated into a micro-grid power system to investigate the coupling effect and dynamic instability of active and reactive power control in the resistive nature of the LV network. This enhances grid-connected inverter control stability in the case of line parameter drift. Satish [7] gave an insight into microgrid control and its various control aspects. They discussed the details of the necessity, objectives, features, and modes of operation of the microgrid. Jae-Jin Sao et al. Ref. [8] present an effective and reliable voltage control approach based on modified voltage droop control in a low voltage (LV) distribution system when a major voltage problem develops. The proposed method changes the droop control mode from conventional droop control to modified droop control and vice versa. It determines the mode change condition to maintain the point of common coupling (PCC) voltage within the voltage dead band. To lessen the effect of line impedance, Zhou et al. [9] offer a modified Q-V droop-control approach. The precision of reactive power-sharing has increased, but the voltage restoration procedure continues to have an impact. Its impact on power distribution is described and examined theoretically. Li and Kao [10] proposed that the droop ratio be dynamically adjusted to compensate for the voltage loss caused by the huge virtual inductor. This procedure necessitates complex computations and has an impact on the system's reliability. Guerrero et al. [11] changed the inverter output impedance profile from predominantly resistive to inductive by adding a large virtual inductor to the inverter voltage control loop. Despite this, the inverter's output voltage decreased dramatically owing to the massive virtual inductance.

Therefore, to address the drawbacks of the conventional technique (droop control) and also improve the droop control response, this paper presents a modified droop control to implement a virtual-impedance output-control strategy for inverter control of LV microgrid. The control technique is used to enhance the accuracy of the power balance. The proposed modified droop-control scheme offers excellent steady-state and dynamic efficiency, even when there is a significant impedance mismatch between the parallel inverters. The following are the main contributions of this paper:

- A systematic modeling approach of the network-forming converters for transient stability of a stand-alone micro-grid.
- Investigation of the transient behaviors of the grid-forming control scheme under signal disturbances.
- The droop control technique is used to implement an inner current loop and an outer voltage loop.
- Centralized secondary control was modeled to restore the frequency and voltage variations generated by the primary control, in addition to the droop-based primary control that was implemented above.
- The fine-tuning of the shunt capacitor and damping resistor values to mitigate noise and improve the power output during the period of disturbances in the load currents.

This paper discusses the following: The description of the methodology used in the paper (hierarchical control techniques of the micro-grids), the dynamic model of the micro-grid, the modeling of the control techniques, the simulation, and the discussions of the results obtained, and finally, the conclusions.

II. METHODOLOGY

This section describes the two control techniques used in the stand-alone micro-grid considered in this paper. Case 1 utilizes the Conventional droop control technique (primary control loop) whose goal is to deal with the change of active and reactive power with a change in frequency and supply voltage, respectively. The primary control loop caused a deviation in the nominal value of the frequency and voltage amplitude. Hence, this poses the need to eliminate such deviations in these two system parameters. Therefore, a secondary control loop (modified droop control technique) was introduced in the second case study to decrease or, better still, eliminate the frequency and voltage deviations caused by the droop control technique, hence, shifting them to their nominal values. The control techniques used in this paper are discussed in detail in the following subsections.

A. Hierarchical Control Techniques of the Micro-grids

The droop approach is frequently used on hierarchical controls to facilitate the simultaneous operation of several voltage sources sharing network loads while ensuring power quality [12]. Multilayer control schemes regulate and provide stable voltage amplitude and frequency via control loops that adjust active and reactive power flow, as well as add filtering, harmonic current sharing, and reactive power compensation functionality, to guarantee disturbance rejection and power quality in microgrids [13]. By adding virtual inertia that matches the physical properties of traditional power networks through voltage amplitude and frequency control, the main layer provides exact power-sharing between the inverters. Therefore, the secondary control was able to correct the droop control's voltage amplitude and frequency abnormalities. At the PCC, the tertiary layer controls the flow of power between the microgrid and the utility grid [5]. The major features of each hierarchical level of control are depicted in Fig. 1. The droop approach is used to derive the primary control layer to properly regulate the power delivered by each converter via voltage frequency and amplitude regulation. The secondary control layer reduces the frequency and voltage amplitude variations generated by droop control in the steady state, then restores their values to particular references while maintaining the power-sharing achieved by the primary layer [14].

The inertia property of synchronous generators is electronically mimicked in network-forming converters by the droop-based control technique to improve microgrid stability and coordination of voltage sources operating in parallel, thereby regulating the voltage amplitude and frequency correspondingly to the active and reactive power components. The primary and secondary control actions are depicted in Fig. 2. The primary layer is expressed using the droop approach with the following fundamental equations:

$$\omega_i = \omega_{nom} - m_i P_i \qquad (1)$$

$$V_i = V_{nom} - n_i Q_i \qquad (2)$$

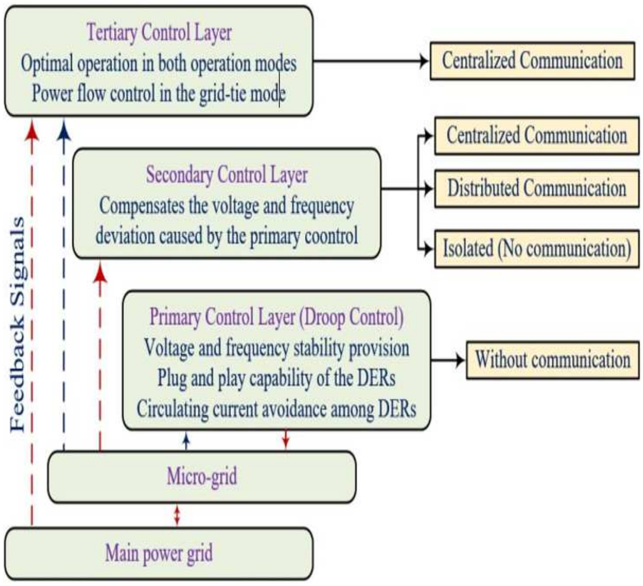

Fig. 1. The requirements at each hierarchical control level

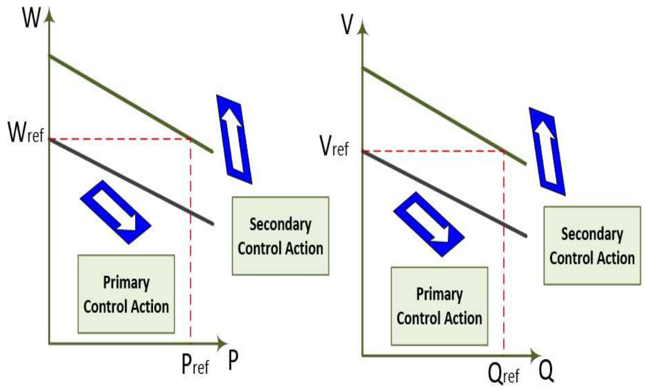

Fig. 2. The primary and secondary control actions

where ω_i denotes the inverter angular frequency i (i = 1, 2, 3 …n), which corresponds to the measured active power P_i, ω_{nom} is the network nominal frequency, and m_i is the coefficient for the active power for the droop technique. V_i denotes the output voltage amplitude of the converter, which corresponds to the measured reactive power Q_i. Similarly, V_{nom} is the nominal voltage amplitude, and ni is the coefficient related to the reactive power for the droop technique. The active and reactive power-sharing relationships between two network-forming converters are as follows [14]:

$$m_1 P_1 = m_2 P_2 \tag{3}$$

$$n_1 Q_1 = n_2 Q_1 + V_2 - V_1 \tag{4}$$

The voltage amplitude and angular frequency from the droop equations are used to generate the sinusoidal voltage reference of each converter, as shown in Eq (5).

$$V_{ref} = V_i \sin(\omega_i t) \tag{5}$$

In the angular frequency droop equation, a feed-forward component is incorporated with regard to the active power to enhance the dynamic transient response in the reference voltage, which is given as:

$$\omega_i = \omega_{nom} - m_i P_i - m_{ip} \frac{dP}{dt} \tag{6}$$

The droop compensation is equivalent to a proportional derivative (PD) controller, in which the gain, m_{ip} adds to a quicker transient response to active power fluctuations, and the derivative term is the feedforward signal. Hence, this parameter can improve the location of the system's closed- loop poles, increasing variability and lowering damping. The droop approach emulates impedance at the converter output by additional closed-loop control, known as virtual impedance, to decrease distortion, lessen the influence of circulating current, and assure harmonic current sharing under non-linear and unbalanced loads. Hence, the voltage reference signal includes the virtual impedance as a new variable dependent on the output current, which is given as [15]:

$$V_{ref} = V_i \sin(ph) - \left(R_v i_o + L_v \frac{di_o}{dt}\right) \tag{7}$$

The integral over time of Eq. (7) is denoted by ph, i_o corresponds to the converter output current. R_v and L_v denote the resistive and reactive inductive components of the virtual impedance, Z_v, respectively. The virtual impedance admits expression as:

$$Z_v = R_v + jL_v \tag{8}$$

Moreso, the virtual impedance variable is adjusted to offer primarily an inductive network to ensure enough controllability of the active and reactive power by the droop equations of (1) and (2). Fig. 3 shows the virtual output impedance loop for the droop control, voltage, and inner current loops. The virtual output impedance can also perform other purposes, such as providing a soft-start operation by designing a larger impedance value at first and then gradually reducing it [16].

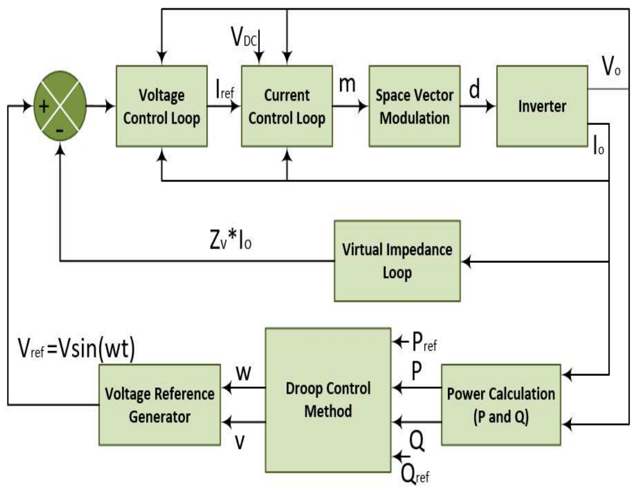

Fig. 3. The droop control with virtual output impedance control loop [5]

In primary control, the droop control approach achieves an acceptable power balance between network-forming converters. However, it produces an inaccuracy in the steady- state voltage's frequency and amplitude, which is corrected by secondary control [15].

III. THE DYNAMIC MODELLING OF THE MICRO-GRID

Due to planned or unplanned occurrences, the microgrid is not linked to the electricity utility when operating in an isolated mode. As a result, network feeders are provided by network-forming converters. This study investigates two cases. The first case presents an off-grid operation mode with a single inverter operating as a voltage source, and one local load is supplied. The second case presents an off-grid operation mode with two inverters operating as a voltage source, also known as network-forming converters, and one common load. Case 1 intends to implement an inner current loop and an outer voltage loop based on the droop control technique, which modifies the magnitudes of both frequency and voltage with regard to active and reactive power signals, respectively. The micro-grid model design of Fig. 4 presents a DC source that emulates the distributed generator, three- phase half-bridge insulated bipolar transistor (IGBT) switches from S1 to S6, electrical components, and a control system. The modulation signal is controlled by this series of switches, which represents a DC/AC converter. Figure 4 also shows how the filter connects the converter output to the load. More specifically, the filter's shunt capacitor and damping resistor values were fine-tuned to reduce noise and enhance power output during periods of load current fluctuations. Thus, the filter capacitor's low impedance acts as a harmonic bypass, preventing harmonic currents from entering the load and providing voltage support at the node [16], [17].

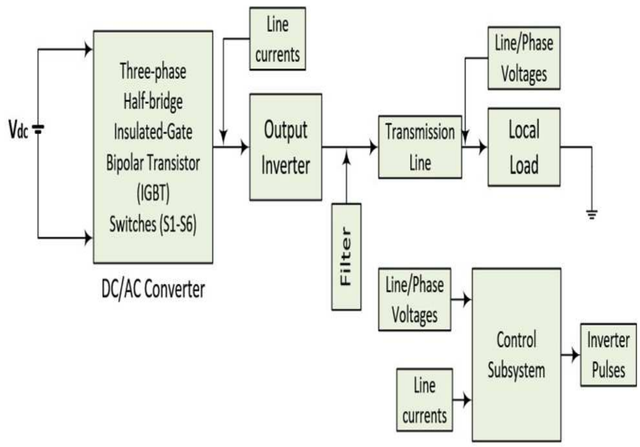

Fig. 4. Micro-grid with network-forming converter and one local load

The model design of Fig. 5 includes an additional converter, which will share the load with the other inverter after a specified period. The inverters are designed to be gradually connected to the micro-grid. Hence, when inverter 1 starts operating initially, inverter 2 will start operating after the specified period has passed. The design of the compensator control parameters will essentially vary with different operation points, sampling rates, and power ranges. The developed control values are equal for the two cases conducted and tuned while running the simulations based on the parameters' core functions and characteristics [18], [19], [20].

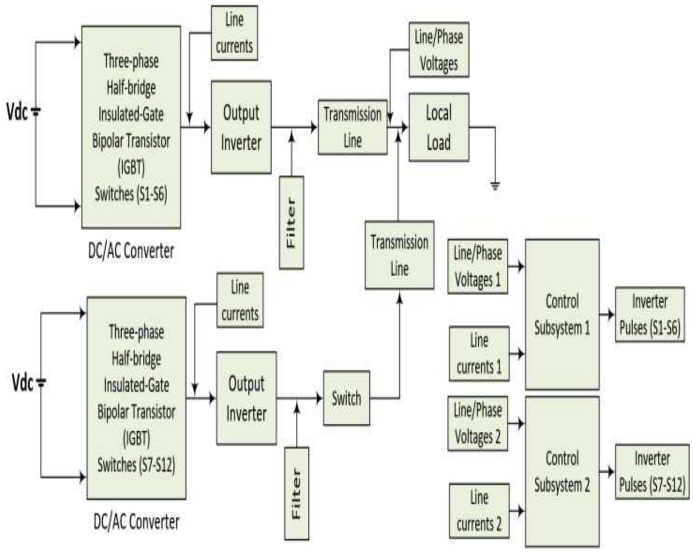

Fig. 5. Micro-grid with two network-forming converters and one common load

IV. SIMULATION RESULTS AND DISCUSSIONS

This section presents the simulation results and discussions on modeling the network-forming converters for transient stability of a stand-alone micro-grid. In this paper, two cases are considered; case-1 presents an off-grid operation mode with only one inverter operating as a voltage source and a local load. The case-2 presents two inverters operating as voltage sources, also known as network-forming converters, and a common load. The stand-alone micro-grids shown in Figs. 4 and 5 are simulated in Simulink/MATLAB environment, as shown in the Appendices. Table I presents the micro-grid system parameters.

TABLE I. MICROGRID SYSTEM PARAMETERS

Parameter Description		Value
	Nominal frequency, f_{nom}	50Hz
	Nominal angular frequency, ω_{nom}	$2\pi \times f_{nom}$
	DC-link voltage, V_{DC}	800V
	Load resistance, R_L	25Ω
	Load inductance, L_L	5mH
Inverter 1	Output resistance, R_{01}	0.5Ω
✓	Output inductance, L_{01}	5mH
✓	LC filter capacitance, C_{f1}	10μF
✓	LC filter damping resistor, R_{f1}	20Ω
✓	Line resistance, R_{L1}	70mΩ
✓	Line inductance, L_{L1}	1mH
Inverter 2	Output resistance, R_{02}	0.7Ω
✓	Output inductance, L_{02}	7mH
✓	LC filter capacitance, C_{f2}	15μF
✓	LC filter damping resistor, R_{f2}	50Ω
✓	Line resistance, R_{L2}	85mΩ
✓	Line inductance, L_{L2}	1.5mH

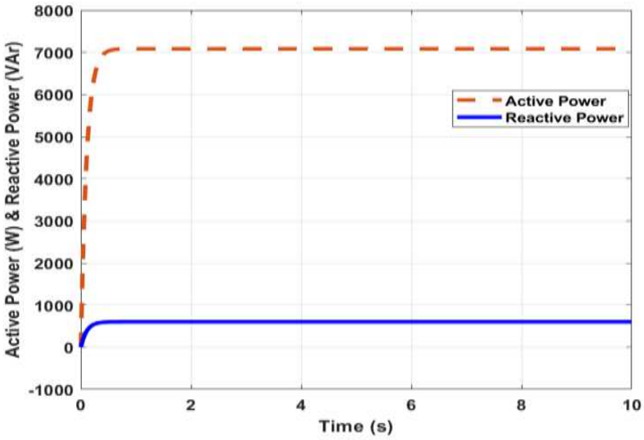

Fig. 6. Active and reactive power for case1

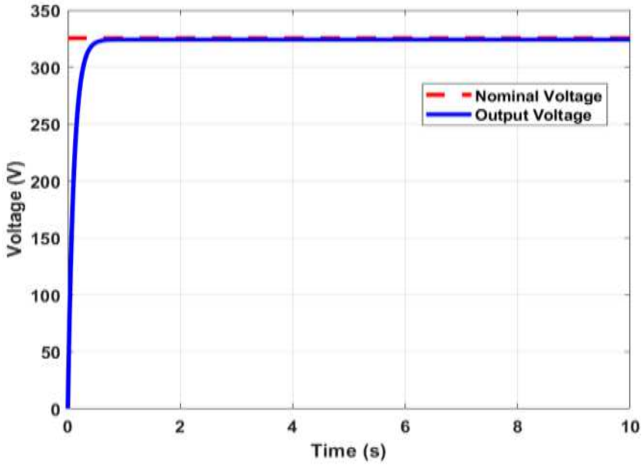

Fig. 7. Nominal and output voltage for case1

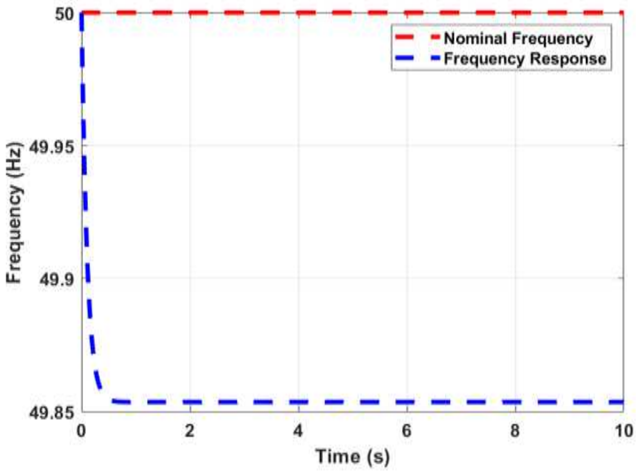

Fig. 8. Nominal and output frequency for case1

The load used in case 1 is resistive; therefore, the reactive power component shown in Fig. 6 is almost negligible, while the active power is calculated to be 7200 W. Fig. 7 demonstrates the stable system operation, which results in acceptable signal performance for the voltage response, which reaches its nominal value. Fig. 8 shows the consequence of employing just the primary control loop with a deviation in the output frequency response. The introduction of this steady-state needs the inclusion of the secondary control loop to restore this problem.

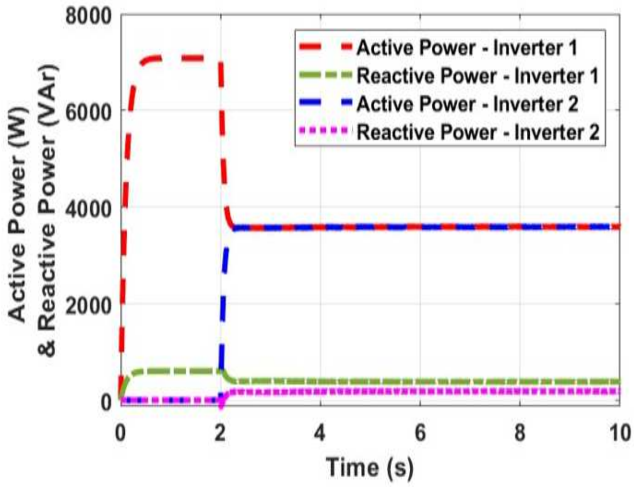

Fig. 9. Active and reactive power of inverters 1 and 2 for case 2

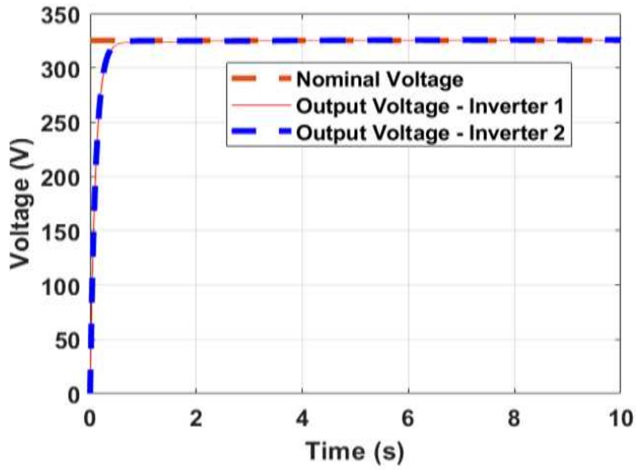

Fig. 10. Nominal and output voltage of inverters 1 and 2 for case 2

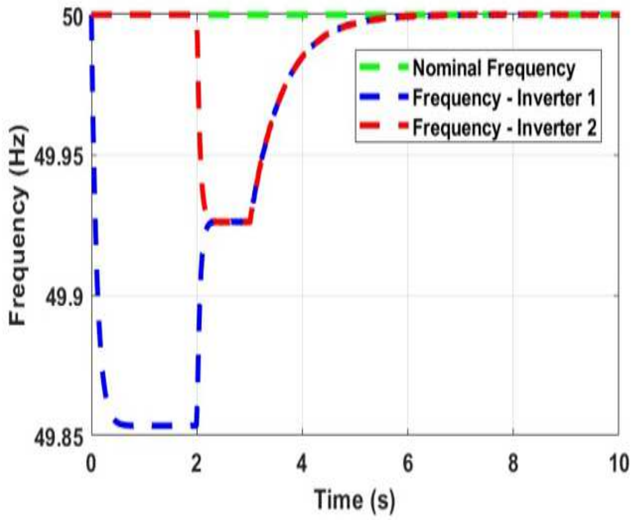

Fig. 11. Nominal and output frequency of inverters 1 and 2 for case 2

The active and reactive power-sharing between the two micro-grid inverters is illustrated in Fig. 9, which is obtained via the droop control process. The inverter 1 starts working on its own at $t = 0\ s$, providing the maximum power needed, and at $t = 2\ s$, the inverter 2 starts sharing the power. Moreover, because the frequency is a global variable and all micro-grid nodes have the same frequency, the active power accomplishes complete power-sharing, as illustrated in Fig. 9. On the other hand, reactive power-sharing is not fully accomplished since the voltage amplitude is a local variable with distinct values at each node. Notice that these power- sharing results have been obtained by finding them to be ideal, lossless, and without any network connectivity constraints. Similarly, Fig. 10 illustrates the stable system operation, which reaches the voltage nominal value. It is evident in Fig. 10 that the outputs of both inverters track the nominal voltage value, which results in system stability. Fig. 11 illustrates how the secondary control loop restores the deviation in the output frequency response caused by the primary control loop. This results in an excellent transient response with a soft start, resulting from the PLL synchronization function implemented with the LPF and the time derivative term included in the droop control scheme.

V. Conclusion

The proper implementation of micro-grids and their control systems is crucial to ultimately reap the benefits of lowering operating costs, increasing grid reliability and efficiency, and alleviating environmental impacts. More so, the implementation of control techniques is needed to accomplish excellent grid efficiency and integration between the conventional grid and micro-grid systems. Hence, this paper presents the modeling of the network-forming converters for the transient stability of an autonomous microgrid. Therefore, to address the transient stability problem common to the standalone microgrid, the network converters used in this study operate in the network-forming mode. The network-forming converters work as voltage sources, which are primarily used to manage the power requirements in an islanded operating mode of the microgrid. Network-forming converters control the voltage amplitude and frequency at the point of common coupling. In this paper, the droop control technique (primary control loop) was implemented to control the first case study which consists of the micro-grid with a network-forming converter with a local load. The primary control loop caused a variation in the nominal value of the frequency and voltage amplitude. Hence, this poses the need to eliminate such deviations in these two system parameters. Therefore, a secondary control loop was introduced in the second case study to decrease or, better still, minimize the frequency and voltage variations induced by the droop control technique, hence, moving them to their nominal values. The simulation results show that the control strategies used are efficient in the microgrids under consideration for maintaining power quality requirements and even power flow stabilization against the variations in power generation that are typical of renewable energy sources.

Acknowledgments

This study is partially funded by a grant from the South African National Research Foundation (No. 132159).

Reference

[1] F. De Andrade, M. Castilla, and B. D. Bonatto, *Basic Tutorial on Simulation of Microgrids Control Using MATLAB® & Simulink® Software*. Springer Nature, 2020.

[2] J. M. Guerrero, P. C. Loh, T.-L. Lee, and M. Chandorkar, "Advanced control architectures for intelligent microgrids—Part II: Power quality, energy storage, and AC/DC microgrids," *IEEE Transactions on industrial electronics,* vol. 60, no. 4, pp. 1263-1270, 2012.

[3] P. A. Gbadega and A. K. Saha, "Model predictive controller design of a wavelength-based thermo-electrical model of a photovoltaic (PV) module for optimal output power," in *International Journal of Engineering Research in Africa*, 2020, vol. 48: Trans Tech Publ, pp. 133-148.

[4] N. Hajilu, G. Gharehpetian, S. Hosseinian, M. Poursistani, and M. Kohansal, "Power control strategy in islanded microgrids based on VF and PQ theory using droop control of inverters," in *2015 International Congress on Electric Industry Automation (ICEIA 2015)*, 2015: IEEE, pp. 37-42.

[5] J. M. Guerrero, M. Chandorkar, T.-L. Lee, and P. C. Loh, "Advanced control architectures for intelligent microgrids—Part I: Decentralized and hierarchical control," *IEEE Transactions on Industrial Electronics,* vol. 60, no. 4, pp. 1254-1262, 2012.

[6] P. Zhang, H. Zhao, H. Cai, J. Shi, and X. He, "Power decoupling strategy based on 'virtual negative resistor'for inverters in low-voltage microgrids," *IET Power Electronics,* vol. 9, no. 5, pp. 1037-1044, 2016.

[7] B. Satish and S. Bhuvaneswari, "Control of microgrid—A review," in *2014 International Conference on Advances in Green Energy (ICAGE)*, 2014: IEEE, pp. 18-25.

[8] J. J. Seo, H.-J. Lee, W.-W. Jung, and D.-J. Won, "Voltage control method using modified voltage droop control in LV distribution system," in *2009 Transmission & Distribution Conference & Exposition: Asia and Pacific*, 2009: IEEE, pp. 1-4.

[9] J. Zhou and P.-T. Cheng, "A Modified $ Q-\dot {V} $ Droop Control for Accurate Reactive Power Sharing in Distributed Generation Microgrid," *IEEE Transactions on Industry Applications,* vol. 55, no. 4, pp. 4100-4109, 2019.

[10] Y. W. Li and C. N. Kao, "An accurate power control strategy for power-electronics-interfaced distributed generation units operating in a low-voltage multibus microgrid," *IEEE Transactions on Power Electronics,* vol. 24, no. 12, pp. 2977-2988, 2009.

[11] J. M. Guerrero, L. G. De Vicuna, J. Matas, M. Castilla, and J. Miret, "A wireless controller to enhance dynamic performance of parallel inverters in distributed generation systems," *IEEE Transactions on power electronics,* vol. 19, no. 5, pp. 1205-1213, 2004.

[12] P. A. Gbadega and O. A. Balogun, "Modeling and Control of Grid-Connected Solar-Wind Hybrid Micro-Grid System with Multiple-Input Ćuk DC-DC Converter for Household & High Power Applications," in *International Journal of Engineering Research in Africa*, 2022, vol. 58: Trans Tech Publ, pp. 191-224.

[13] J. C. Vasquez, J. M. Guerrero, J. Miret, M. Castilla, and L. G. De Vicuna, "Hierarchical control of intelligent microgrids," *IEEE Industrial Electronics Magazine,* vol. 4, no. 4, pp. 23-29, 2010.

[14] P. Martí, M. Velasco, E. X. Martín, L. G. de Vicuña, J. Miret, and M. Castilla, "Performance evaluation of secondary control policies with respect to digital communications properties in inverter-based islanded microgrids," *IEEE Transactions on smart Grid,* vol. 9, no. 3, pp. 2192-2202, 2016.

[15] J. M. Alcala, M. Castilla, L. G. De Vicuña, J. Miret, and J. C. Vasquez, "Virtual impedance loop for droop-controlled single-phase parallel inverters using a second-order general-integrator scheme," *IEEE Transactions on Power Electronics,* vol. 25, no. 12, pp. 2993-3002, 2010.

[16] J. M. Guerrero, J. C. Vasquez, J. Matas, L. G. De Vicuña, and M. Castilla, "Hierarchical control of droop-controlled AC and DC microgrids—A general approach toward standardization," *IEEE Transactions on industrial electronics,* vol. 58, no. 1, pp. 158-172, 2010.

[17] P. A. Gbadega and A. K. Saha, "Impact of incorporating disturbance prediction on the performance of energy management systems in micro-grid," *IEEE Access,* vol. 8, pp. 162855-162879, 2020.

[18] Gbadega, Peter Anuoluwapo, and Yanxia Sun. "Centralized peer-to-peer transactive energy market approach in a prosumer-centric residential smart grid environment." *Energy Reports* 8 (2022): 105-116.

[19] Gbadega P. A, Sun Y. A hybrid constrained Particle Swarm Optimization-Model Predictive Control (CPSO-MPC) algorithm for storage energy management optimization problem in micro-grid. Energy Reports. 2022 Nov 1; 8:692-708.

[20] Gbadega, Peter Anuoluwapo, and Yanxia Sun. "Primal–dual interior-point algorithm for electricity cost minimization in a prosumer-based smart grid environment: A convex optimization approach." *Energy Reports* 8 (2022): 681-695.

Using LSTM To Perform Load Modelling For Residential Demand Side Management

Kyppy N. Simani
Electrical & Information Engineering
University of the Witwatersrand
Johannesburg, South Africa
simanikyppy@gmail.com

Yuval O. Genga
Electrical & Information Engineering
University of the Witwatersrand
Johannesburg, South Africa
ORCID-0000-0001-5467-8317

Yu-Chieh J. Yen
Electrical & Information Engineering
University of the Witwatersrand
Johannesburg, South Africa
ORCID-0000-0002-1379-1572

***Abstract*—Energy consumption from the residential sector forms a large portion of the grid demand. The growing accessibility of residential load profile data presents an opportunity for improved residential load forecasting and more effective demand side management strategies. However, the stochastic nature of residential power usage limits the effectiveness of traditional load forecasting techniques. Machine learning is a tool well-suited for predicting processes containing stochastic elements. Long short-term memory (LSTM) neural networks are especially suited for predicting time-series data such as electrical load profiles. This paper investigates the efficacy of an LSTM to perform residential load forecasting. Two LSTM-based prediction strategies are compared by forecasting the load profile for a set of five simulated, periodic, temperature profiles representing a population of electric water heaters (EWH). In Method A an aggregated load profile representing a feeder-point measurement is applied to a single LSTM model to forecast the load. In Method B each simulated temperature profile, representing appliance-level measurements, is applied to its own LSTM temperature prediction. The predicted temperature profiles are combined and used to determine the load forecast. Method A outperforms Method B and is able to predict the EWH energy with a percentage error of approximately 0.76%.**

***Index Terms*—load forecasting, LSTM, periodic signal, Monte Carlo simulation, electric water heater (EWH)**

I. Introduction

Residential energy consumption forms a significant portion of electrical energy demand, ranging from 14% to 57% of the national consumption depending on the country [1]. Thus, managing residential energy demand is important for maintaining grid stability and performance. Demand side management (DSM) strategies aim to manipulate consumption profiles to the benefit of the utility as well as the consumer/prosumer. For the utility it is important to minimise the demand during peak usage times to maintain grid stability and power quality [2]. As a consumer, changing the pattern of their home electricity usage can help reduce costs and take advantage of time-of-use (TOU) tariffs [3].

To implement effective DSM strategies it is important to anticipate future load demand [4]. However, performing accurate residential load forecasting remains a challenge due to the stochastic nature of residential power usage [5]. A proposed solution is to use a machine learning tool to perform residential load forecasts. Machine learning is an effective tool for predicting processes which involve stochastic events [6].

This paper aims to investigate to what extent machine learning can be used to forecast residential load profiles. The residential load is represented using large, temperature regulated devices such as electric water heaters (EWH). A combination of periodic profiles, produced by a small population of simulated, steady-state EWHs, constitute the load profile. LSTM prediction models are used to evaluate two load prediction strategies, each implementing a different residential load model. Method A uses a single prediction model, with an aggregate load representing a feeder-point level measurement. Method B uses multiple prediction models, with individual loads representing appliance-level measurements.

The rest of the paper is structured as follows: Section II describes challenges in predicting residential demand as well as literature detailing various applications of machine learning to electrical load forecasting. Section III details the methodology used to perform this investigation. In Section IV the results from each of the prediction strategies are illustrated and discussed. Section V discusses recommendations for future work, and in Section VI the paper is concluded.

II. Background

A. Demand Side Management

An important aspect of demand side management is the ability to predict load demand and profile patterns. These forecasts inform investment decisions and planning for future electrical infrastructure, and minimises the risk of electrical supply shortages. Traditionally, electric utilities have performed short to long-term demand forecasts on the distribution/generation level [4]. In recent years there has been a transition towards the installation and use of digital meters for measuring household power consumption [5]. Residential consumption information is becoming increasingly more accessible, and therefore presents an opportunity to perform load profiling and forecasting on the residential level with a higher degree of data resolution and detail [6].

Despite the increased accessibility to consumption data, performing accurate residential load forecasting remains a challenge. Residential usage patterns can vary widely depending on the socio-demographic conditions, seasonal patterns, geographical location, residents' lifestyle, habits etc [8], [9]. Additionally, this variability presents a problem for prosumers who must analyze and predict their own loading and generation in order to effectively participate in energy exchange programs.

B. Machine Learning for Load Forecasting

Machine learning presents a suitable tool for analysing residential load data because of its ability to detect latent patterns as well as estimate future outcomes based on previous information. A Deep Q neural network is used by Tai et al. [10] to implement an adaptive, appliance management system that adapts to human behaviour and comfort. A semi-supervised learning approach is used by Li et al. [11] to identify residential user profiles i.e number and type of home residents, based on their smart meter data. Wijesingha et al. [12] proposed a residential load priority system that predicts solar power generation using Artificial Neural Networks, and selects between the grid and battery storage for load demand using reinforcement learning. Henri et al. [13] conduct a comparison of four different machine learning approaches for the prediction and scheduling of residential photovoltaic (PV) battery operations. Ahmadiahangar et al. [14] examine the performance of a mixed-effects regression model in forecasting consumption for a single household.

The memory retention capabilities of LSTMs make them a particularly suitable tool for this application. The use of LSTM networks is shown to demonstrate high accuracy for single variate and multivariate time-series predictions [15], [16]. Research carried out by Bouktif et al. [17] used an LSTM neural network to forecast the electrical load of a metropolitan area in France. Additionally, work by Siami-Namini et al. [18] demonstrated that LSTM neural networks outperform traditional autoregressive integrated moving average (ARIMA) models for predictions on time-series data.

III. Methodology

For this investigation, Monte Carlo simulations are used to generate load profiles for a population of temperature regulated, steady-state, residential EWHs with distinct but periodic patterns. Two sets of LSTM models are used to implement two different prediction strategies to determine future loading. The investigation consists of three main components: EWH temperature modelling, generation of Monte Carlo simulations, and load profile prediction with LSTM neural networks. An outline of the methodology components is illustrated in Fig. 1.

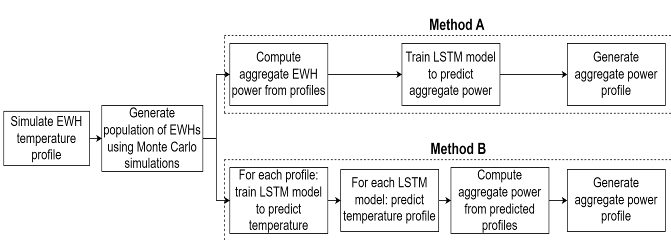

Fig. 1: Outline of methodology components.

A. EWH Temperature Simulation

Before forecasting the EWH load profile using LSTM it is necessary to first develop a means of simulating the changes in internal temperature using a steady-state, one-node EWH model proposed by Dolan in [19]. The simulation environment assumes a full, 150 litre tank with a 3 kW heating element and uniform, instantaneous heat distribution with no draw events. It is also assumed that all the energy inside the tank is sourced from the heating element and heat lost due to standing losses only.

The EWH temperature change during cooling is simulated using a standing loss model as described by Nel [21]:

$$T_{inside}[n+1] = T_{amb}[n] + (T_{inside}[n] - T_{amb}[n])e^{a} \quad (1)$$

Where T_{inside} and T_{amb} are the internal EWH temperature and ambient temperature at samples $[n+1]$ and $[n]$ respectively, and a is a temperature decay constant formulated as:

$$a = \frac{-t_n}{cm_{tank}R} \quad (2)$$

Where t_n is the interval between samples $[n]$ and $[n+1]$, c is the specific heat capacity of water, m_{tank} is the EWH mass and R is a thermal conductivity constant of the EWH.

The change in EWH temperature during heating is determined using:

$$\Delta T_{inside}[n] = \frac{E_{input}[n]}{cm_{tank}} \quad (3)$$

Where E_{input} is the energy input to the EWH, derived from the EWH element rating.

Using the initial conditions and EWH characteristics from Yen et al. [20], Equation (1) and (3) are used to generate a EWH temperature profile by simulating EWH heating and cooling cycles over a 24-hour period. The accuracy of the simulation is determined using the mean absolute error (MAE) which is formulated as:

$$\frac{\sum_{i=1}^{n} |y_i - x_i|}{n} \quad (4)$$

Generally, y_i is a predicted value, x_i is the actual value and n is the total number of data points. A smaller MAE value indicates fewer prediction errors.

The MAE of the simulation is calculated by taking y_i as the simulated temperature values, x_i as the actual temperature values and n as the total number of simulated and actual temperature data points. The MAE between the simulated and actual temperatures, is determined to be 0.26 °C. Fig 2. compares a single, simulated temperature profile against actual EWH temperature measured in [20].

B. EWH Population Generation

The simulation model is used to generate five steady-state, periodic internal temperature profiles each representing a different EWH in a population. To introduce randomly distributed attributes and ensure a distinct set of temperature patterns, each

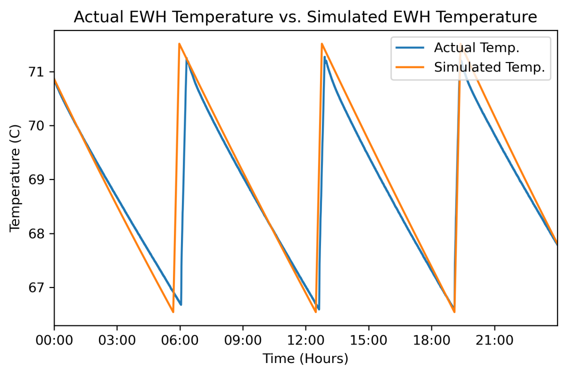

Fig. 2: Validation of simulated EWH temperature profile.

simulation is performed by varying EWH characteristics using Monte Carlo sampling. For each EWH simulation the tank volumes, element power ratings and ambient conditions are kept constant, but the upper and lower temperature thresholds as well as thermal conductivity characteristics are varied. Finally, to generate a sufficiently large set of training data for the LSTM, each temperature profile is made to span a period of twenty-five days.

C. Load Profile Prediction

The five temperature profiles are applied to LSTM neural networks that develop models to predict the loading for each of the simulated EWHs. Two prediction model strategies, Method A and Method B as outlined in Fig. 1, are implemented.

a) Method A: The five temperature profiles are used to calculate load profiles for each EWH. These load profiles are aggregated to produce a single, time-series profile. Power and time data points from the aggregate profile are used as the feature set for an LSTM to train a load prediction model. Using this model, a forecast for the loading over a 24-hour period is performed. To compare the output of the forecast, an additional load profile comprising a 24-hour period is produced. This profile is determined using only Equation (3) and the simulated EWH temperature profiles. The accuracy of Method A is measured by determining the MAE where: y_i is the predicted load value from simulation, x_i is the actual load value determined using the models described by Nel [21] and n is the total number of predicted and actual data points.

b) Method B: The internal temperature, ambient temperature and time data points from the five temperature profiles are used as feature sets for an LSTM to train individual temperature prediction models, one for each EWH. For n simulated EWHs this approach requires at least n LSTM models. Each of the temperature prediction models is used to forecast the temperature over a 24-hour period. A load profile is then determined from each of the predicted temperature profiles. These five load profiles are aggregated to produce a single, combined, load profile. To compare the resultant load profile, an additional load profile comprising a 24-hour period is produced. This profile is also determined using only Equation (3) and the simulated EWH temperature profiles. The accuracy of Method B is measured by determining the MAE between the aggregated and temperature derived load profiles.

IV. Results & Discussion

A comparison of the predicted EWH load profiles from Method A and Method B to the actual EWH load profile is presented in Fig. 3. The actual EWH load profile has a total energy of 6.56 kWh.

For Method A the difference between the actual and predicted EWH energy is 0.050 kWh with a percentage error of 0.76%. The MAE between the actual and predicted load profiles is 0.013 kW.

For Method B the difference between the actual and predicted EWH energy is 0.104 kWh with a percentage error of 1.59%. The MAE between the actual and predicted load profiles is 0.036 kW.

A summary comparison of the Method A and Method B results are illustrated in Table 1.

The load profile predictions of Method A result in a lower MAE value and are therefore more accurate than those of Method B. This is likely due to the use of a single prediction model, thereby preventing the accumulation of errors resulting from the use of multiple prediction models. In addition, although the temperature simulations have distinct patterns, each of them is periodic with no stochastic variations. The use of repetitive data points likely aided the development of the LSTM prediction model despite the lack of comprehensive training features.

The load profile predictions for Method B contained more errors. In Method B, the load profile forecast is determined using the output of several predictive models. Each predictive model will forecast a load profile with some amount of error included. As a result the combined load profile will contain the cumulative errors from each of the individual forecasts. For Method B, as the number of simulated EWHs and subsequent prediction models increases, there will be an increase in the accumulation of prediction errors in the resultant load profile.

The LSTM model development and forecasting approach used in Method B is more computationally intensive than Method A. For each simulated EWH an additional temperature prediction model must be trained. Furthermore, each model must perform an additional temperature forecast to determine an associated EWH load profile. In comparison, Method A requires the development of only one LSTM prediction model with a single forecast to predict the load profile.

V. Future Work & Recommendations

The ability of an LSTM to accurately predict a periodic pattern is demonstrated, but it is unknown how well it will

TABLE I: Prediction Method Comparison

Method	Models	Δ Energy (kWh)	Percent Error	MAE (kW)
A	1	0.050	0.76%	0.013
B	5	0.104	1.59%	0.036

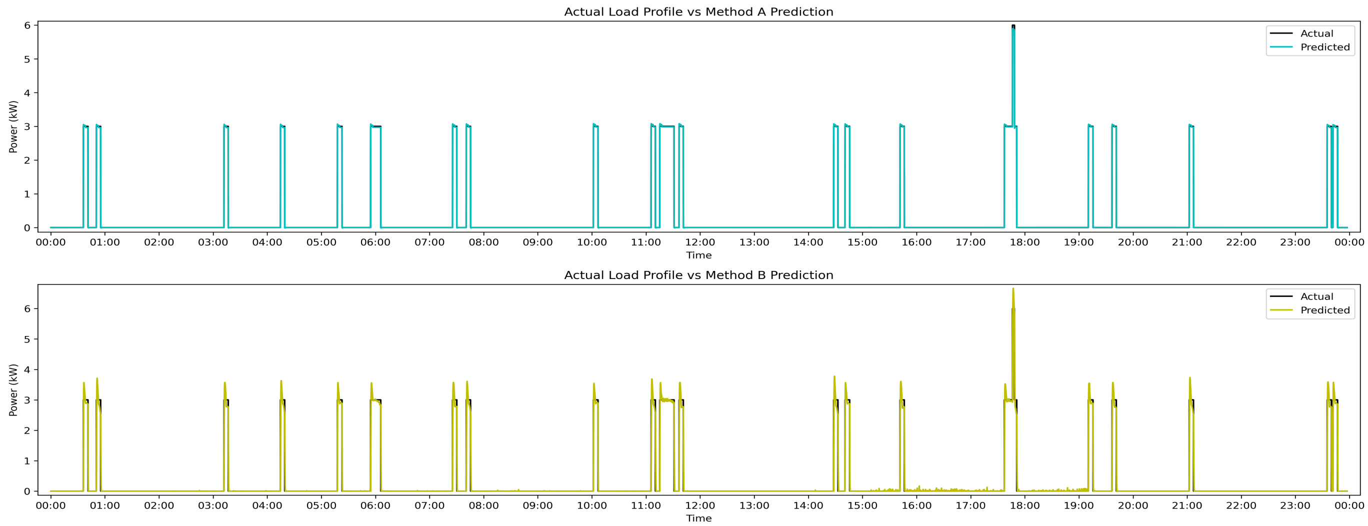

Fig. 3: Comparison of the actual load profile to the predicted load profiles.

perform when predicting load patterns that include human activity such as EWH draw events and expanded to include other residential loads. Future work should examine the effects of such stochastic events on the LSTM load prediction performance. This could be achieved by adding random draw events to the temperature profile simulations, or including simulations for appliances with more complex power profiles such as a washing machine or refrigerator.

VI. Conclusion

The stochastic nature of residential power usage presents a challenge in performing accurate residential load profile forecasts. It is proposed that a machine learning tool be used to accurately predict these stochastic processes. To investigate the efficacy of machine learning in forecasting residential loads, an LSTM neural network is used to evaluate and compare two residential load prediction strategies. The residential loads are represented using a population of periodic, simulated load profiles similar to those of domestic EWHs. In Method A the residential load forecast is performed using a single aggregated load profile. In Method B multiple EWH temperature predictions are combined to produce the residential load forecast. Based on the results it is found that Method A is able to most accurately predict the residential load energy with a percentage error of 0.76%. It is demonstrated that an LSTM can be used to predict the profiles of periodic, steady-state residential loads with a high degree of accuracy. The results indicate that a residential load forecast using an aggregate load model based on a single feeder-point measurement, represented by the Method A approach, is likely to be more accurate than a collection of individual, appliance-level measurements as shown in Method B.

References

[1] Ratio of Household Electricity Use to National Electricity Consumption by Country — Center for Global Development — Ideas to Action. (n.d.). Retrieved September 29, 2022, from https://www.cgdev.org/media/ratio-household-electricity-use-national-electricity-consumption-county.

[2] Kirui, G. K., Chiloane, L. L., Yen, Y. C. J. (2021). Remote Mechanical Switch to Regulate Electricity Consumption in a Household. 2021 Southern African Universities Power Engineering Conference/Robotics and Mechatronics/Pattern Recognition Association of South Africa, SAUPEC/RobMech/PRASA 2021. https://doi.org/10.1109/SAUPEC/ROBMECH/PRASA52254.2021.9377208

[3] Chiloane, L. L., Kirui, G. K., Yen, Y. C. J. (2021). Demand reduction of electric water heaters for load-shedding recovery using stochastic control. IEEE AFRICON Conference, 2021-September. https://doi.org/10.1109/AFRICON51333.2021.9571019

[4] Zhao, H., Tang, Z. (2016). The review of demand side management and load forecasting in smart grid. Proceedings of the World Congress on Intelligent Control and Automation (WCICA), 2016-September, 625–629. https://doi.org/10.1109/WCICA.2016.7578513

[5] Kong, W., Dong, Z. Y., Hill, D. J., Luo, F., Xu, Y. (2018). Short-term residential load forecasting based on resident behaviour learning. IEEE Transactions on Power Systems. https://doi.org/10.1109/TPWRS.2017.2688178

[6] Abdufattokhov, S., Muhiddinov, B. (2019). Stochastic Approach for System Identification using Machine Learning. 13th International IEEE Scientific and Technical Conference Dynamics of Systems, Mechanisms and Machines, Dynamics 2019 - Proceedings. https://doi.org/10.1109/DYNAMICS47113.2019.8944452

[7] Carvallo, J. P., Larsen, P. H., Sanstad, A. H., Goldman, C. A. (2018). Long term load forecasting accuracy in electric utility integrated resource planning. Energy Policy, 119, 410–422. https://doi.org/10.1016/J.ENPOL.2018.04.060

[8] Sovacool, B. K., Hook, A., Sareen, S., Geels, F. W. (2021). Global sustainability, innovation and governance dynamics of national smart electricity meter transitions. Global Environmental Change, 68, 102272. https://doi.org/10.1016/j.gloenvcha.2021.102272.

[9] Yildiz, B., Bilbao, J. I., Dore, J., Sproul, A. B. (2017). Recent advances in the analysis of residential electricity consumption and applications of smart meter data. Applied Energy, 208, 402–427. https://doi.org/10.1016/J.APENERGY.2017.10.014

[10] Lusis, P., Khalilpour, K. R., Andrew, L., Liebman, A. (2017). Short-term residential load forecasting: Impact of calendar effects and forecast granularity. Applied Energy, 205, 654–669. https://doi.org/10.1016/J.APENERGY.2017.07.114

[11] Fahad, M. U., Arbab, N. (2014). Factor Affecting Short Term Load Forecasting. Journal of Clean Energy Technologies, 2(4), 305–309. https://doi.org/10.7763/JOCET.2014.V2.145

[12] Tai, C. S., Hong, J. H., Fu, L. C. (2019). A real-time demand-side management system considering user behavior using deep q-learning in home area network. Conference Proceedings - IEEE International Conference on Systems, Man and Cybernetics, 2019-October, 4050–4055. https://doi.org/10.1109/SMC.2019.8914266.

[13] Li, H., Fu, F., Bai, X., Yan, S., Lu, X., Li, K., & Wang, F. (2020). A Graph Label Propagation Semi-Supervised Learning-Based Residential User Profiles Identification Method Using Smart Meter Data. 2020 IEEE Student Conference on Electric Machines and Systems, SCEMS 2020, 550–556. https://doi.org/10.1109/SCEMS48876.2020.9352420.

[14] Wijesingha, J. R., Hasanthi, B. V. D. R., Wijegunasinghe, I. P. D., Perera, M. K., & Hemapala, K. T. M. U. (2021). Smart Residential Energy Management System (REMS) Using Machine Learning. Proceedings of 2nd IEEE International Conference on Computational Intelligence and Knowledge Economy, ICCIKE 2021, 90–95. https://doi.org/10.1109/ICCIKE51210.2021.9410779.

[15] Henri, G., & Lu, N. (2020). A Supervised Machine Learning Approach to Control Energy Storage Devices. 1–1. https://doi.org/10.1109/pesgm41954.2020.9281748.

[16] Ahmadiahangar, R., Häring, T., Rosin, A., Korõtko, T., & Martins, J. (2019, June 1). Residential Load Forecasting for Flexibility Prediction Using Machine Learning-Based Regression Model. Proceedings - 2019 IEEE International Conference on Environment and Electrical Engineering and 2019 IEEE Industrial and Commercial Power Systems Europe, EEEIC/I and CPS Europe 2019. https://doi.org/10.1109/EEEIC.2019.8783634.

[17] Siami-Namini, S., Tavakoli, N., & Namin, A. S. (2019). The Performance of LSTM and BiLSTM in Forecasting Time Series. Proceedings - 2019 IEEE International Conference on Big Data, Big Data 2019, 3285–3292. https://doi.org/10.1109/BigData47090.2019.9005997.

[18] Karim, F., Majumdar, S., Darabi, H., & Harford, S. (2019). Multivariate LSTM-FCNs for time series classification. Neural Networks, 116, 237–245. https://doi.org/10.1016/j.neunet.2019.04.014.

[19] Bouktif, S., Fiaz, A., Ouni, A., & Serhani, M. A. (2018). Optimal deep learning LSTM model for electric load forecasting using feature selection and genetic algorithm: Comparison with machine learning approaches. Energies, 11(7). https://doi.org/10.3390/en11071636The Technical Writer's Handbook. Mill Valley, CA: University Science, 1989.

[20] Siami-Namini, S., Tavakoli, N., & Siami Namin, A. (2019). A Comparison of ARIMA and LSTM in Forecasting Time Series. Proceedings - 17th IEEE International Conference on Machine Learning and Applications, ICMLA 2018, 1394–1401. https://doi.org/10.1109/ICMLA.2018.00227.

[21] Nel, P. J. C., Booysen, M. J., & van der Merwe, B. (2018). A computationally inexpensive energy model for horizontal electric water heaters with scheduling. IEEE Transactions on Smart Grid, 9(1), 48–56. https://doi.org/10.1109/TSG.2016.2544882.

[22] Y. C. J. Yen, K. J. Nixon and W. A. Cronjé, "Maximum Demand Comparison of Aggregated Load Profiles for Vertical and Horizontal EWHs Due to a Fixed Draw Event," in SAIEE Africa Research Journal, vol. 110, no. 3, pp. 167-174, Sept. 2019, doi: 10.23919/SAIEE.2019.8732788

Load Shedding to Load Hedging - Evaluating Load Shedding Mitigation Options for Residential Customers within eThekwini Municipality

Leshan Moodliar
Department of Electrical Power Engineering
Faculty of Engineering and the Built Environment
Durban University of Technology
Durban, South Africa
22289297@dut4life.ac.za

Innocent E. Davidson
Department of Electrical Power Engineering
Faculty of Engineering and the Built Environment
Durban University of Technology
Durban, South Africa
InnocentD@dut.ac.za

***Abstract*—South Africa's current energy crisis is exemplified by regular periods of load-shedding, as electricity supply falls behind demand. Failure to conduct rotational load shedding risks destabilizing the entire national power grid. In 2021, the load-shedding hours increased by 32% compared to 2020. Consequently, the requirement for backup supplies by customers has increased. The study assessed the viability of installing alternate electricity generation supplies to mitigate load shedding for residential customers within eThekwini Municipality and discusses the impact on the municipality. The techno-economic assessment was carried out using the Hybrid Optimization of Multiple Energy Resources (HOMER) tool. Mitigating load shedding with a diesel generator was the cheapest option. However, the overall levelized cost of energy (LCOE) was R 3.70 /kWh. While not capital intensive, the generator's disadvantages included being noisy and requiring frequent refueling. While batteries were quiet and offered a more convenient solution, it costs nine times more than the generator with an LCOE of R 4.19/kWh, which is 13% higher than the generator. Incorporating solar PV panels reduced carbon emissions; however, it increased the initial capital expenditure by R 15000 / kW installed. The type of backup supply selection for the residential customer will be primarily influenced by the customer's objectives, including their ability to accommodate the technology's installation and operating procedure. In addition, the customer's access to capital and carbon reduction goals will impact their ultimate technology choice of a backup supply to mitigate load shedding.**

Keywords—Battery energy storage, load shedding, techno-economic modelling, residential solar

I. INTRODUCTION -THE PARADIGM CHANGE IN ELECTRICITY USE

Due to the enabling environment for PV and developing storage options, there will be a shift in the topology of how electricity is consumed by customers, which will be different from legacy methodologies. Fig. 1 summarises the changing landscape and potential technology uptakes within the electricity sector [1].

A. The Past

South Africa started electricity generation in 1882. With limited capacity and high costs, reticulated electricity was only utilized by those that could afford it. In 1923, Eskom was created as the national electricity generator [2]. At the time, the cheapest form of electricity was grid-supplied electricity. Fossil fuel-fired generators were used as an alternative during grid failure. Renewable energy technology options were limited and considered expensive and unreliable. After the turn of the century, South Africa became more cognizant of renewable energy and established more policy instruments, notably the Renewable Energy Policy White Paper, which aimed to introduce 10 000 GWh of renewable energy into South Africa's energy mix by 2013 [2]. In addition, the Renewable Energy Independent Power Producer Program (REIPPP) was introduced to promote renewable energy nationally. The program is an auction-based power procurement programme aiming to increase renewable power generation at the cheapest possible cost through a bidding program [3]. According to the IRP, 800 MW of renewable energy projects per annum are envisaged for commissioning in South Africa [4].

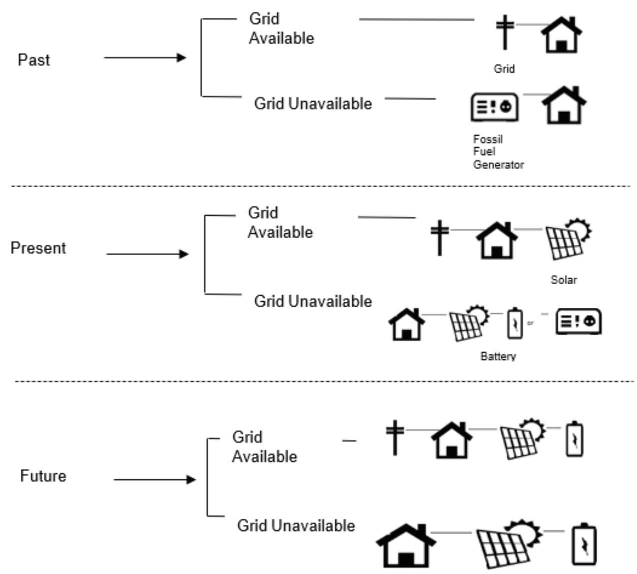

Fig. 1. Change in electricity supply topology – adopted from [1]

B. The Present

Due to enabling policy instruments, renewable energy technologies have become more prevalent. As the demand increased, the prices started to decline. In 2018 Solar PV was 63% cheaper relative to prices in 2010 [5]. Solar PV is now at comparable grid prices and is a feasible supply configuration while the grid is available. With the inclusion of solar PV, a customer could consume and occasionally provide electricity back to the network. The current trend is that solar PV becomes the primary energy source while the grid acts as a backup supply. Depending on the customer's loading, a fossil fuel generator or a battery could be used to ensure supply continuity when the grid is unavailable. Currently, South Africa, like many African nations, is faced with power deficits and inconsistent electricity supply. The main reasons include insufficient generating sources and poorly maintained infrastructure [6]. South Africa has a load-shedding schedule to manage the supply shortages better. In 2021, 1136 hours of load shedding resulted in a total load reduction of 2455 GWh [7]. Depending on the number of stages and block allocation, customers could experience between one and four events of load shedding per day [8].

C. The Future

South Africa's Government policy embraces the inclusion of distributed energy resources [4]; therefore, the widespread installation of PV is expected to continue. The rapid price drop in batteries will also play a key role in future supply configurations. The change in supply topology will ultimately bring change in the way customers would interact with the grid. Past interactions were limited to the unidirectional flow of electricity from the producer to the consumer. However, future interactions would allow for a bidirectional flow of electricity [1]. Contrary to the lowering cost curve of PV technology, electricity prices in South Africa have risen by 150% when comparing 2018 with 2010. According to Eskom's Fifth Multi-Year Price Determination (MYPD) revenue application for 2023/24, the proposed tariff increase is 38.10%, further elaborating on the rising electricity pricing trend within the country. [9].

A revision to Schedule 2 of the Electricity Regulation Act (ERA) permits the generation and trading of up to 100 MW of electricity through a regulatory registration process instead of a licensing process [10]. This amendment represents a partial liberation of the generating and retail sectors within South Africa. Without the need to follow a licencing process, significant time is saved in introducing generation to the market. Further, under the United Nations Framework Convention on Climate Change (UNFCCC) and its Paris Agreement (PA), South Africa has pledged to contribute to global climate change efforts [11], [12]. However, electricity usage accounts for 40% of all carbon emissions in eThekwini. As a result, the city adopted the Durban Climate Action Plan, which aims to transition to 40% renewable energy by 2030 and 100% renewable energy by 2050 [13]. As a result, some customers may be inclined to install cleaner energy sources to support these ambitious goals.

The transition from past to present is in line with the real-life scenarios that eThekwini Municipality is currently experiencing. However, while promoting widespread local generators is deemed to strengthen the security of supply, it would also introduce technical, planning and human resource challenges that must be carefully managed [4]

II. Research Method

A typical residential load profile was constructed, averaging 900 kWh per month. After that, techno-economic assessments were carried out utilising the Hybrid Optimisation Model for Electric Renewable (HOMER) tool. Key inputs include, among other things, the loading profile, the amount of solar irradiation and technical performance parameters. The inputs also considered financial and modelling parameters. Technology and electricity costs were included as financial inputs, while discount and inflation rates were included as modelling inputs. The simple payback period, the internal rate of return (IRR), the levelized cost of electricity (LCOE), and the net present cost (NPC) were some of the important outputs.

III. Modelling and Analysis and Scenario Setting

The scenarios are intended to evaluate the use of a diesel generator, solar PV and storage technology in conjunction with the grid to offer a backup supply for a typical residential dwelling (30 kWh per day). Each scenario was subject to 48 load-shedding events, each lasting 2 hours. Further, the scenarios were optimised according to the lowest net present costs (NPC) over the project's lifetime. Fig. 2 depicts the various scenarios.

Scenario 1 includes utilising a diesel generator as a backup supply when load shedding occurs.

Scenario 2 involves using lithium-ion batteries as a backup supply when load shedding occurs.

Scenario 3 (a) considers Scenario 1, with the integration of solar photovoltaic panels.

Scenario 3 (b) considers Scenario 2, with the integration of solar photovoltaic panels.

TABLE I. Input Parameters Applicable to the Modelling.

PV System		**Battery Energy Storage**	
Total PV installed cost	R 15 000 / kW	Battery Storage Type	Lithium Ion
Replacement inverter cost	R 7 500 / kW	Battery Storage Costs	R 7 000 / kWh
Replacement inverter year	Every 10 years	Replacement battery year	Every 10 years
PV degradation per annum	0.8%	Round trip efficiency	90%
Diesel Generator			
Generator installed costs	R 2240 / kW	Minimum load ratio	25%
Generator lifespan	15 000 hours	Lifetime	15 000 hours
Minimum generator load	25 %	Fuel Curve Slop	0.273 L / hr / kW
Diesel price	R 20 / Per Litre	Diesel price escalation	8% per annum
General Modelling Inputs		**Electricity Price**	
Modelling period	10 Years	Energy price	R 2.60 / kWh
Nominal discount/inflation rate	12% / 5%	Yearly electricity price escalation	8%

Loading: The loading has been split into critical and non-critical loads. Non-critical loads (50%) would not be electrified during load shedding.

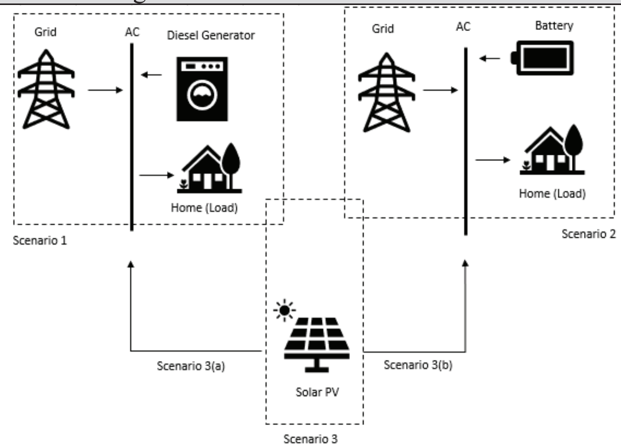

Fig. 2. Graphical representation of scenarios 1,2 and 3(a), 3(b)

IV. Discussion and Summary of Results

A. Scenario 1

Scenario 1 represents the case where a diesel generator was used to provide continuity of the supply during load-shedding events. Forty-eight random load-shedding events have been considered, each for 2 hours. The optimum generator size was 2.5 kW with an NPC of R 287 752 over the project lifespan. The LCOE was R 3.70 / kWh considering regular operation and outages. The initial investment required was R 5 600. Without a renewable energy source, none of the carbon emissions could be mitigated, and they remained at 6 916 kg/year. As illustrated in Figure 3, the generator would only function during load shedding as the cost per kWh of generator operation was R 7.56 /kWh while the grid-supplied electricity was R 2.60 /kWh. Therefore, the generators' sole purpose is to provide a backup supply during load shedding.

B. Scenario 2

Scenario 2 represents the case where a battery is used in place of the diesel generator with the primary aim of providing continuity of supply during loading shedding. The optimum battery storage required was 7 kWh, producing an NPC of R 325 187 over the project lifespan. The LCOE was R 4.19 / kWh. The initial investment required was R 52 000. Without a renewable energy source, none of the load could be fed from renewable energy resulting in zero improvements in carbon emissions.

Furthermore, without a time-of-use tariff, the battery energy storage system cannot leverage the potential of energy arbitrage. Therefore, the battery will only discharge during a load-shedding event, similar to the generator in scenario 1. However, scenario 1 has an advantage because it could accommodate more load-shedding events in closer succession as it would only require more diesel. On the other hand, in the case of the battery energy storage, it would need to charge before discharging; therefore, its ability to accommodate significantly more events of load shedding or longer durations are limited, especially after load shedding in the peak loading periods. While the use of batteries to mitigate load shedding is more expensive and limited in its ability to respond in the event the frequency and duration of load shedding increases, it can operate without the hassle of diesel purchases, storage and refills. Further, battery energy storage is a silent operation while generators produce noise that could affect neighbours and may not be allowed in apartments and communal living areas.

C. Scenario 3(a)

Scenario 3 represents 3 kW of solar PV panels connected to the diesel generator. The inclusion of solar improves the NPC to R 242 373 however requires an additional investment of R 45000 for the solar PV panels. The investment would pay itself off in 4.62 years and generate an IRR of 21.5%. The LCOE has also improved to R 2.75 / kWh. The customer would save R 8 577 in the first year of operation from installing solar PV panels. As illustrated in figure 4, the solar PV energy production and the load do not fully coincide. The lack of coincidence produces excess energy. However, this energy is of no financial value without suitable energy storage and an export tariff mechanism. Further, if load shedding does not occur when excess energy is available, the diesel generator would need to be used to supplement the loading. The carbon emissions have reduced to 4812 kg/year, an improvement of 30%.

D. Scenario (3b)

Introducing 1 kW of solar PV panels in conjunction with the battery energy storage improves the NPC to R 297 797 however requires an additional investment of R 15 000 for the solar PV panels. The investment would pay itself off in 9.29 years and generates an IRR of 3.7%. The LCOE has improved by 8.6% to R 3.83 kWh. The project generated savings of R 4061 in the first year of operation due to reduced grid purchases. As illustrated in figure 5, with a smaller PV size, the solar PV energy production and the load better coincide, resulting in less energy exported to the grid. Sizing the generation to align with the load is the correct methodology to adopt without an export tariff, as excess energy is of no financial value. Despite the small solar PV size, the carbon emissions have reduced to 5856 kg/year. Further, without a time-of-use pricing signal to the customer, there is no incentive to plan for battery charging in off-peak periods. Battery charging in peak periods adds to the total peak loading, which only exacerbates the load constraints of the country.

E. Cost of unserved energy (COUE)

Understanding the cost of unserved energy is crucial, as it defines and influences future policy decisions on electricity markets, regulations, network developments and investment decisions [14]. A method to quantify the COUE as approved by the National Energy Regulator of South Africa (NERSA) for the residential sector is to express the proportion of household expenditure on electricity to the household's total income and, after that, divide it by the total electricity usage. [15].

$$COUE_{residential} = \sum_{1}^{n} \left(\frac{H_{\% elec\ exp} \times H_{income}}{kWh} \right) \quad (1)$$

$COUE_{residential}$ = Cost of unserved energy
n = Number of households

$H_{\% \, elec \, exp}$	= Portion of household expenditure on electricity
H_{income}	= Household Income
kWh	= Household electricity consumption

By considering the national dataset relevant to 2015, the COUE for the residential sector in South Africa was calculated to be R 6.77 / kWh [15]. Similarly, considering the 2020 dataset, the COUE was calculated to be R 9.03 / kWh [16]. Not having electricity at a household level inhibits access to communications, leisure activities and security systems [15]. The LCOE of all the scenarios is lower than the estimated COUE of 2015 and 2020. The lower LCOE indicates that the alternate generation investment benefits the customer compared to not having access to that electricity during load shedding.

F. *Impact of load shedding on municipal financials: tariff dynamics*

As illustrated in Fig. 6, load shedding impacts the financial recovery mechanism of the municipality. Considering the residential, retail tariffs against the bulk purchasing tariff, load shedding sometimes prevents a loss to the municipality. While in other cases, it creates a loss. Prevention of the loss verse the creation of the loss happens due to the pricing dynamics on the time of use bulk tariff. Load shedding during the winter peak periods prevents losses, while all other periods create a loss for the municipality. The losses due to load shedding range between 72 c/kWh and 151 c/kWh, while the savings (not incurred) due to load shedding in the winter peak is 219 c/kWh. Promoting battery charging during off-peak periods is prudent, as it won't contribute to the national peak loading. Further, the municipality can generate the highest return during that time.

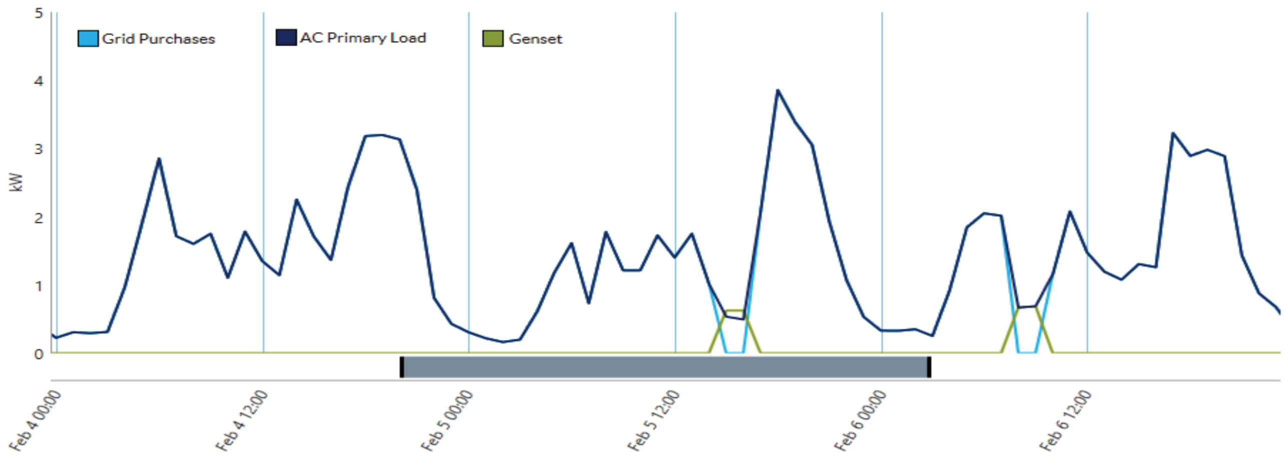

Fig. 3. Time series plot highlighting energy usage analysis with generator and grid

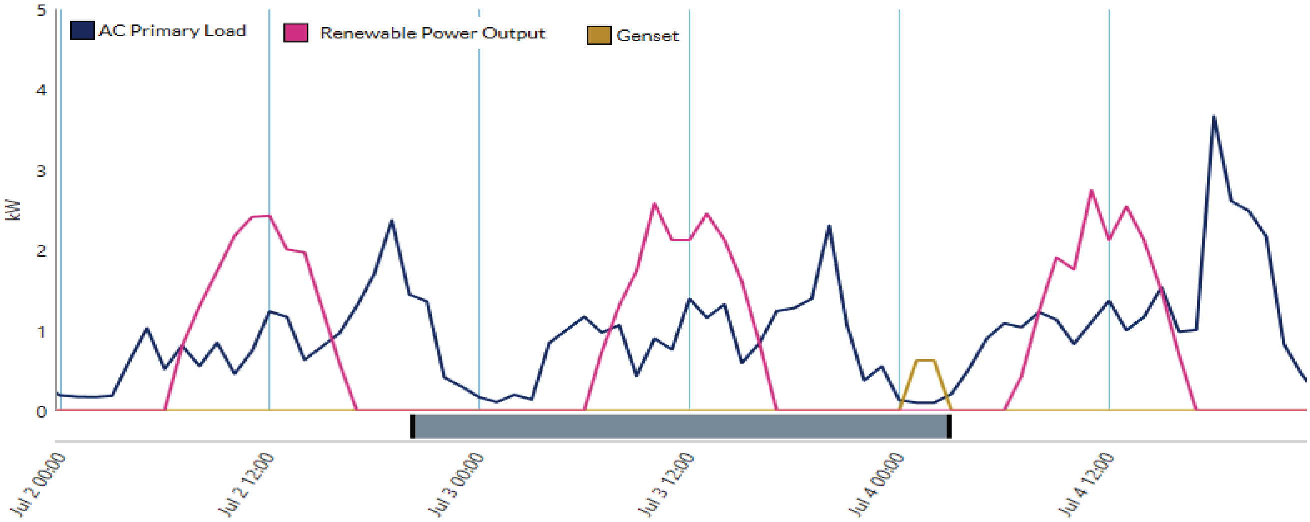

Fig. 4. Time series plot highlighting energy usage analysis with generator, solar PV and the grid

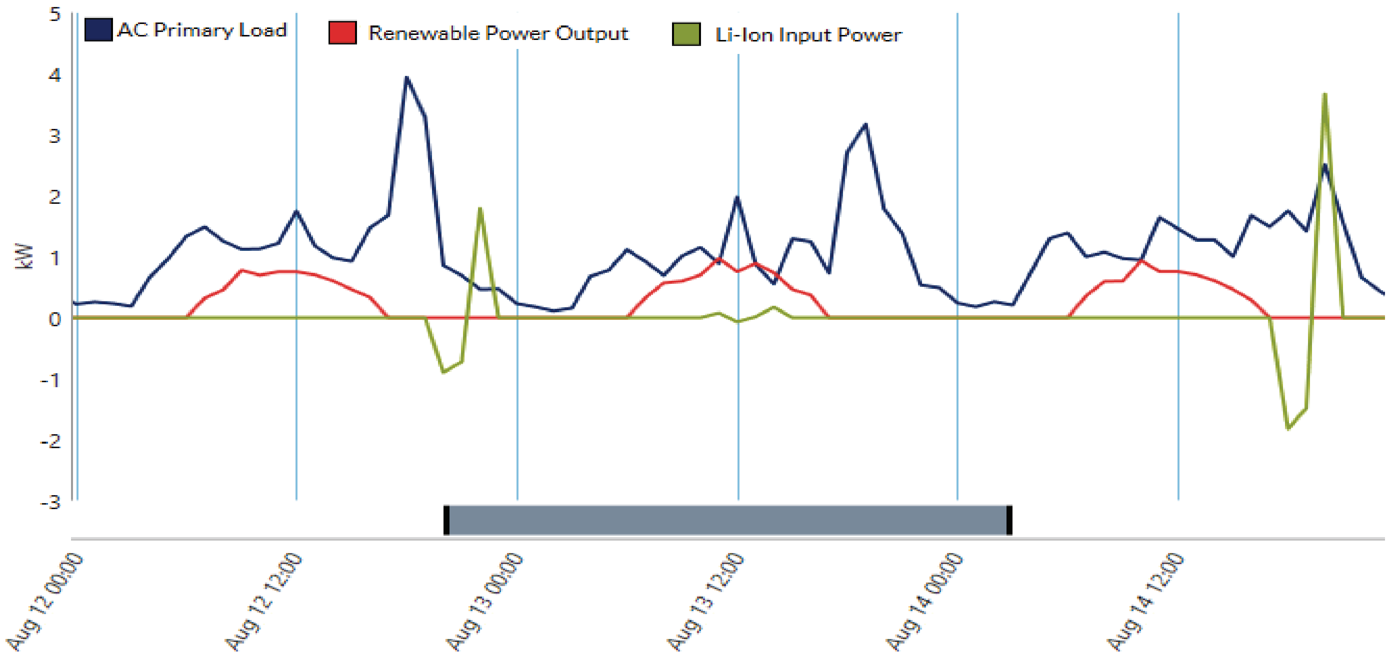

Fig. 5. Time series plot highlighting energy usage analysis with battery energy storage, solar PV and the grid

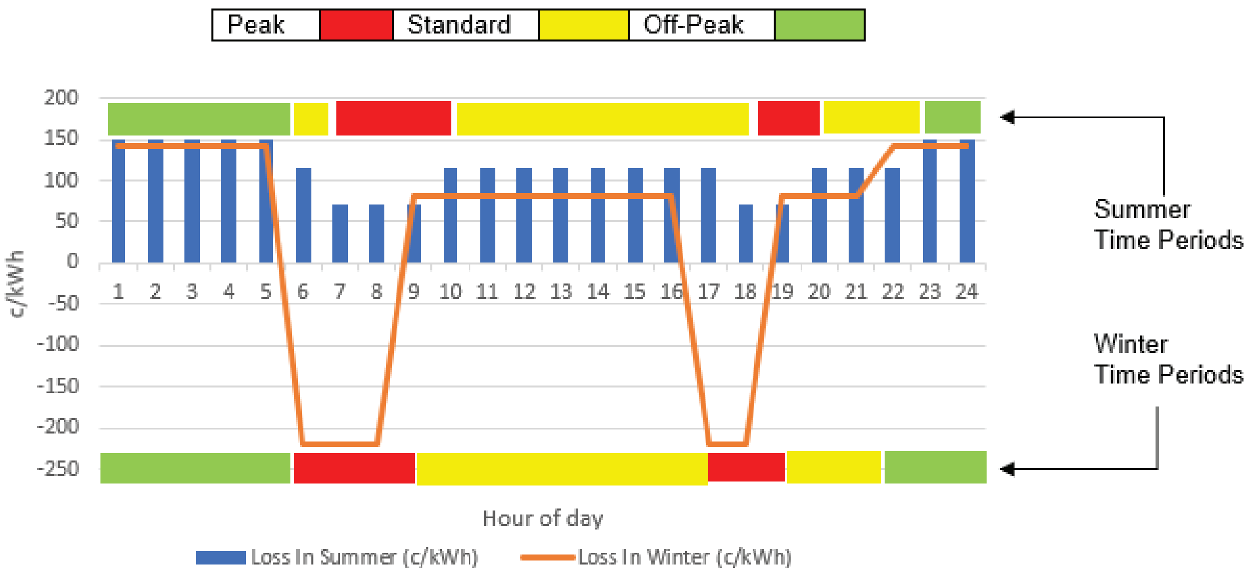

Fig. 6. Financial loss per kWh / per hour for the municipality

V. Discussion and Summary of Results

The cost competitiveness of solar PV has made it a rival competitor with a smaller carbon footprint than traditional fossil fuel generators. As a result, it has become popular and is being adopted by many residential customers to strengthen their electricity supply.

Residential consumers with minimal up-front capital who want to back up their electricity supply could purchase a small portable generator. A 2.5 kW generator could be acquired for an investment of R 5 600. However, the customer must manage the noise levels and prepare fuel purchases and storage. On the other hand, batteries offer a convenient alternative as they are quiet to operate without refuelling. However, a 7-kWh battery at R 52 000 is required to mitigate against 48 load-shedding events per annum. This investment is nine times higher when compared to the diesel generator scenario. In addition to the high initial costs, the levelized costs were reduced to R 4.19 / kWh. Without time-of-use tariffs, the battery could not harness the cost-saving benefits derived from energy arbitrage and further reduce the LCOE. The lowest LCOE of R 2.75 /kWh was generated by the scenario combining 3 kW of solar PV panels and a 2.5kW generator. The inclusion of solar PV reduced 2104 kg of carbon per annum and assisted with offsetting 38.1% of the load during the day, producing a savings of R 8577 in the first year of operation. Combining solar PV with batteries resulted in the highest investment cost of R 67 000. Without the time of use and feed-in tariffs, battery energy storage and solar benefits are underutilised.

Customers who aspire to minimise their carbon footprint would be required to install a renewable energy source. As observed in Scenarios 3(a) and 3(b), incorporating solar PV lowered emissions between 15% and 30%. The cost of unserved energy in the residential sector as of 2020 was R 9.03. All the alternate generation scenarios produced an LCOE below the COUE. The LCOE, less than the COUE, indicates that the customer benefits from alternate-generation investments. Load shedding reduces electricity sales during the 2-hour outage. Except for the winter peak period, all other times of load shedding results in a loss per kWh ranging between 72 c/ kWh to 151 c/kWh for the municipality.

There must be a multidisciplinary effort by all parties to promote the most optimal supply arrangement in households. The municipality must be able to provide time-of-use and feed-in tariffs. The technology exists for the customer to choose an alternative generation for their homes, but the ideal solution to mitigate load shedding will depend on the customer's specific circumstances, such as their affordability and level of commitment to contribute to a low-carbon future.

ACKNOWLEDGMENT

The authors wish to thank eThekwini Municipality: Electricity Unit for their support and the data provision during the research study.

REFERENCES

[1] R. Khalilpour and A. Vassallo, "Leaving the grid: An ambition or a real choice?," *Energy Policy,* vol. 82, pp. 207-221, 2015, doi: 10.1016/j.enpol.2015.03.005.

[2] O. J. Ayamolowo, P. T. Manditereza, and K. Kusakana, "South Africa power reforms: The Path to a dominant renewable energy-sourced grid," *Energy Reports,* vol. 8, pp. 1208-1215, 2022, doi: 10.1016/j.egyr.2021.11.100.

[3] A. Eberhard, J. Leigland, and J. Kolker, *South Africa's renewable energy IPP procurement program*. World Bank Publications, 2014.

[4] M. Bello, R. Smit, C. Carter-Brown, and I. E. Davidson, "Power Planning for renewable energy grid integration-Case Study of South Africa," in *2013 IEEE Power & Energy Society General Meeting*, 2013: IEEE, pp. 1-5.

[5] R. Fu, R. M. Margolis, and D. J. Feldman, "US Solar Photovoltaic System Cost Benchmark: Q1 2018," National Renewable Energy Lab (NREL), Golden, CO (United States), 2018.

[6] S. J. T. Mwale, "The Southern African Power Pool (SAPP) steady state security assessment using contigency analysis," MSc Thesis, University of KwaZulu-Natal, 2015.

[7] Council for Scientific and Industrial Research. "South Africa load shedding statistics.". Available at: https://www.csir.co.za/sites/default/files/Documents/Loadshedding%20plot.pdf

[8] EThekwini Municipality. "Load Shedding Schedule." www.durban.gov.za (accessed 02 February 2022).

[9] *Eskom's Fifth Multi-Year Price Determination Revenue Application For 2023/24 And 2024/25 Financial Years*.2022.[Online] Available: https://www.nersa.org.za/wp.content/uploads/2022/07/consultation-paper-mypd5.pdf

[10] South African Government, "Licensing Exemption and Registration Notice," 2017.

[11] *South Africa's First Nationally Determined Contribution under the Paris Agreement*.2021.[Online] Available: https://www.dffe.gov.za

[12] K. B. Mantlana, M. A. Maoela, and G. Nhamo, "Mapping South Africa's nationally determined contributions to the targets of the sustainable development goals," in *Natural Resources Forum*, 2021, vol. 45, no. 1: Wiley Online Library, pp. 3-17.

[13] Environmental Planning and Climate Change Protection Department, "Durban Climate Action Plan 2019," www.durban.gov.za, 2019.

[14] G. Timilsina and J. Steinbuks, "Economic costs of electricity load shedding in Nepal," *Renewable and Sustainable Energy Reviews,* vol. 146, 2021, doi: 10.1016/j.rser.2021.111112.

[15] U. Minnaar and J. Crafford, *Cost of Unserved Energy in South Africa*. 2017.

[16] NERSA. *Decision: The Review of Eskom's Cost of Unserved Energy Methodology*. 2020. [Online] Available: https://www.nersa.org.za

Improving Stability Through Adaptive Under-Frequency Load Shedding: the Zambian Scenario

Fred Kanjelesa[1]
fkanjelesa@gmail.com

Anthony Chobela Mumba[2]
mumbaanthony@gmail.com

Kabwe Mulenga[2]
kabwemulenga88@gmail.com

Clement Siame[2]
malamba74@gmail.com

Pitshou Ntambu Bokoro[1]
pitshoub@uj.ac.za

[1]*Department of Electrical and Electronic Engineering Technology, Faculty of Engineering and the Built Environment, University of Johannesburg, 5131 John Orr Building Doornfontein Campus, Johannesburg, South Africa*
[2]*ZESCO Limited, Head Office, Great East Road, Stand Number 6949, Lusaka, Zambia*

Abstract— ***Under-frequency load shedding (UFLS) is one of the interventions employed for power system frequency stabilization and has the potential to increase grid flexibility. Such flexibility is necessary to accommodate the integration of variable renewable energy sources (VRES) such as Solar. This paper presents a summary of a study that was undertaken to evaluate the frequency response of the Zambian integrated power system for different under-frequency load shedding (UFLS) scenarios and contingencies using the steep gradient strategy. With the power system simulation for engineering (PSS/E) tool, the islanded and interconnected scenarios of the system were simulated. The study showed that, while 10% UFLS gave the best response in all scenarios, the system frequency recovered at a better nadir and had no overshoot in the modified-interconnected compared to the islanded and interconnected scenarios.***

Keywords— *frequency stability, renewable energy sources, rate-of-change-of-frequency, under frequency load shedding*

I. INTRODUCTION

"Frequency stability refers to the ability of the power system to maintain steady frequency following a severe system disturbance resulting in a significant imbalance between generation and load" [1]. It is one of the critical requirements for stable operation of power systems and an important consideration in planning, especially as the load demand increases [2] and more variable renewable energy systems, such as solar photovoltaic (PV) and wind, are integrated to the grid [3]. For stable operation of the power system, it is required that there is an active power balance between the load and generation which is measured using frequency. Therefore, a demand-generation imbalance resulting from a loss of generation or load manifests itself as a variation in the system frequency [2].Synchronous machines influence and play a significant role in frequency stability since their rotational speed is directly proportional to the frequency of the system. In view of this, control applications such as the governor systems, droop, etc., are employed to regulate the frequency of the power grid to acceptable operational levels [1]. These methods however, require a spinning reserve [4], which at times may not be adequate for the size of the disturbance or dispatched fast enough in relation to the rate of frequency decay. In such circumstances, other means such as under-frequency load shedding (UFLS) and Over-frequency Generator Tripping (OFGT) are employed to regulate frequency [5], [6].

This study was motivated by the disturbances and provides insights into the frequency response of the Zambian power system and the optimal levels of load to shed in improving system stability. Zambia experienced several system disturbances in 2021 which led to a significant loss of power, the UFLS was one of the interventions that was applied to stabilize the system. This paper shares the experience of the Zambian scenario. The plans to increase generation through an energy mix by integrating more of VREs on the Zambian grid comes with concerns that could affect the grid stability which require to be addressed as a mitigation measure.

II. PRINCIPLES OF UNDERFREQUENCY LOAD SHEDDING

The UFLS is largely influenced by the inertia of the power system because a power system's frequency response and characteristics at the instance of a disturbance depends on level of inertia [5].

A. Power System Inertia

Power system inertia is related to the stored energy in the rotating masses of generators and loads connected to the power system. It is defined as the period in which the stored energy in the rotating masses could be used to supply the total rated power [7] and for a generator, it is given by

$$H = \frac{\frac{1}{2}J\omega_n^2}{S_n} \tag{1}$$

where J (kgm^2) is the generator's moment of inertia including its turbine, ω_n (rad/s) is the rotor angular speed and S_n (VA) is generator rated power. The major contributors to the system inertia are the generators and turbines of synchronized conventional power plants. Others are loads like motors connected to the grid [7]. The total system inertia is essential for the frequency stability and is given by [8]:

$$H_{sys} = \frac{\sum_{i=1}^{N} S_{ni} H_i}{S_{n,sys}} \tag{2}$$

where S_{ni} (MVA) is the rated apparent power of the *i*-th generator, $S_{n,sys}$ is system rated power equal to the sum of S_{ni} and H_i is the inertia constant of *i*-th turbine-generator in MVA [8].

B. Rate of change of frequency

The rate-of-change-of-frequency (ROCOF) is the derivative of the power system frequency with respect to time (df/dt) and it is given by [5]:

$$RoCoF|_{t=0^+} = \frac{\Delta P_{imbalance}}{P_{load}} \cdot \frac{f_0}{2 \cdot H} \tag{3}$$

where 0^+ is the moment just after disconnection of the load/generation, $\Delta P_{imbalance}$ is the difference between generation and load, P_{load} is the system load, f_0 is the nominal frequency, and H is the system inertia. As shown in the equation [3], the ROCOF is proportional to the size of the generation-load imbalance and inversely proportional to the inertia, H. The initial value of the df/dt is the instantaneous ROCOF just after an imbalance of power, before any control action [5].

C. Underfrequency Load Shedding

When large generating units trip or there is a considerable loss of power infeed, the resultant swing in frequency is relative to the size of loss [9]. Under circumstance of such severe disturbances, unless sufficient generation with the ability to rapidly increase output is available, the decline in frequency may reach levels that may lead to tripping of generation units on under frequency thus aggravating the situation further and may cause the power system to island or worse still cause a total blackout. To prevent extended operation at lower-than-normal frequency, underfrequency load shedding (UFLS) is employed to achieve a coordinated reduction of the connected load to the level that can safely be supplied by available generation, thus restore power equilibrium [1]. According to Rudez and Mihalic (2009), UFLS is one of the most important protection systems, which in many scenarios represents the last chance to prevent a system blackout after a serious disturbance occurs in a power system [5].

UFLS schemes are implemented to shed (trip) selected loads for pre-determined underfrequency scenarios. The instant of tripping a load is determined by under-frequency relays that continuously compares the actual frequency and ROCOF to the set thresholds [10]. Rudez and Mihalic (2009) categorized the UFLS schemes as traditional, semi-adaptive and adaptive. The steep gradient UFLS scheme belongs to the adaptive group [5]. Hassan Alhelou (2020) grouped them into conventional, adaptive, and computational intelligence-based techniques [11].

Alhelou presented that traditional UFLS, considered most common and basis of all other approaches, depend on relays which use locally measured frequency constantly compared against set threshold. While they are simple and easy to implement, they don’t provide optimum load shedding. They simply follow a preset rule in which a fixed amount of load is shed when frequency deviates from the nominal value [11]. In [8], the authors described an adaptive approach based on the wide-area monitoring system (WAMS) and aimed at performing situation-conditioned actions achieved by obtaining a few-seconds-in-advance prediction of frequency to obtain the most suitable frequency response while addressing frequency measurement related challenges. In [12], a pattern-recognition based system frequency response model capable of detecting less severe frequency deviations and thus disconnect fewer consumers than the conventional under-frequency load shedding approach was proposed owing to the complexity and communication needs associated with WAMS. Alhelou in [11] presented computational intelligence techniques such as artificial neural networks (ANN), genetic algorithms (GA), fuzzy logic control (FLC), adaptive neuro-fuzzy inference system (ANF), and particle swarm optimization (PSO) which have the advantage of being robust and flexible in dealing with complex non-linear systems. In [13], the authors discussed the future effectiveness of UFLS in systems with increased penetration of renewable energy sources (RESs) and associated reduced rotating mass. They argued that this would imply higher frequency gradients and higher harmonics and could make frequency measurements and short relay operation times more challenging.

In practice, disconnection stages are derived from appropriate dynamic studies based on applicable scenarios and realistic operational concerns. Planning for a UFLS scheme considers geographical distribution of load to shed, use of the common reference for frequency and load shedding steps across the network, the need to avoid over frequency (overcompensation) as this can lead to further generation loss, the rate of frequency decay for different magnitudes of generation deficiencies, the system's ability to increase power generation, possible emergencies that can occur, and the load shedding program required [9], [14].

III. Zambian Interconnected Power System

The Zambian Interconnected Power System (IPS) consists of hydro and thermal generating stations as major sources of power, with about 2% of Solar (PV) and 3% of Heavy Fuel Oil generation out of approximately 3,500MW generation capacity. The power system stretches across the country, with major power stations (hydro and thermal) and the interconnection to the Southern African Power Pool (SAPP) network located in the southern part, while the bulk load centers and connection to Democratic Republic of Congo are in the northern part [15].

Research has shown that systems with significant integration of variable renewable energy systems (VRES), such as Solar PV and wind, have been facing reduced inertia leading to frequency stability related challenges [3], [16], [17] [18]. While the Zambian IPS currently has relatively low amounts of VRES integration, being a predominantly hydro-generation system, available generation is mainly affected by hydrological conditions and therefore impacts the reserve carrying capacity of the system. Besides the traditional interventions for frequency control involving synchronous generators ZESCO Limited, the national utility owning and operating over 80% of the system, implemented the steep gradient UFLS.

IV. SAPP UFLS Settings

The Southern African Power Pool (SAPP) is an electricity power pool whose main purpose is to coordinate power system and market operations on the southern Africa IPS. The Zambian IPS is interconnected to the SAPP IPS through Zimbabwe and Namibia [19]. SAPP requires that the frequency should not deviate to outside 49.50Hz and 50.50Hz for a credible single contingency, such as a trip of a largest generating unit or instant loss of load equal to the largest generating unit on the interconnected system [20]. Currently, the largest generating unit on the SAPP IPS is 930MW at Koeberg nuclear power station in South Africa [Source: SAPP], [21].

In the SAPP the System Operators are required to implement mandatory first level automatic under-frequency load-shedding for frequencies lower than 48.75Hz with time delay of 800ms targeting 8% load for shedding [20]. However, ZESCO implemented a tighter 5-stage UFLS scheme from 49 – 48.5Hz with time delays of 100ms and 5% targeted load shedding at each stage. The generating units in the system are set to trip between 46 Hz and 47.5 Hz with time delay ranging from 2 to 10 seconds.

V. Study Approach

To evaluate the appropriateness of an associated UFLS scheme, it becomes necessary to simulate disturbances that are sufficiently large such that spinning reserves are not sufficient to maintain frequency stability and thus activate UFLS [22].

In this study, the loss of generating units at the major power stations in the Zambian IPS was first evaluated using the power system simulation for engineering (PSS/E) tool and contingencies at Kafue Gorge (KGPS) were observed to be more severe than at Kariba North Bank (KNBPS). KNBPS has 6 x 180MW (1080MW) hydro-generating units while KGPS has 6 x 165MW (990MW). The following scenarios were simulated.

A. *Islanded Scenario*

For the Islanded Scenario, i.e. the Zambian IPS not connected to any other system including the SAPP IPS, incremental losses of generation were simulated as contingencies, i.e. loss of 1 unit up to all the 6 units at KGPS. For each contingency, pre-selected varying percentages of load to disconnect (UFLS) was simulated, i.e. 0%, 10%, 12% and 15% of UFLS.

B. *Interconnected Scenario*

In the interconnected scenario, the Zambian IPS was connected to the SAPP network, which is the usual mode of operation as this enhances system security and economic operation. Based on results from the islanded scenario, 10% UFLS scenario was selected and investigated further under the interconnected and modified-interconnected scenarios. The contingencies with loss of 4 and 6 units at KGPS were selected, mainly due to the banked arrangement of the units at the station and these being severe scenarios.

C. *Modified-Interconnected Scenario*

The Modified-Interconnected scenario is simply the interconnected scenario with modified UFLS settings aimed at improving the frequency response of the system with respect to the contingencies.

D. *Contingencies for the Simulations*

In each scenario, two contingencies were simulated by tripping 4 and 6 units at KGPS at $t = 1$ second and further running the simulation for 30 seconds, i.e. 4 x 145MW = 580MW and 6 x 145MW = 870MW.

E. *Dynamic Simulations*

To simulate the stability of the system, using PSS/E, the load/power flow was first run to achieve convergence before converting the static data file to dynamic. The flow chart shows the detailed process. The results obtained from the simulation was used to observe frequency stability response of the system for different scenarios under study.

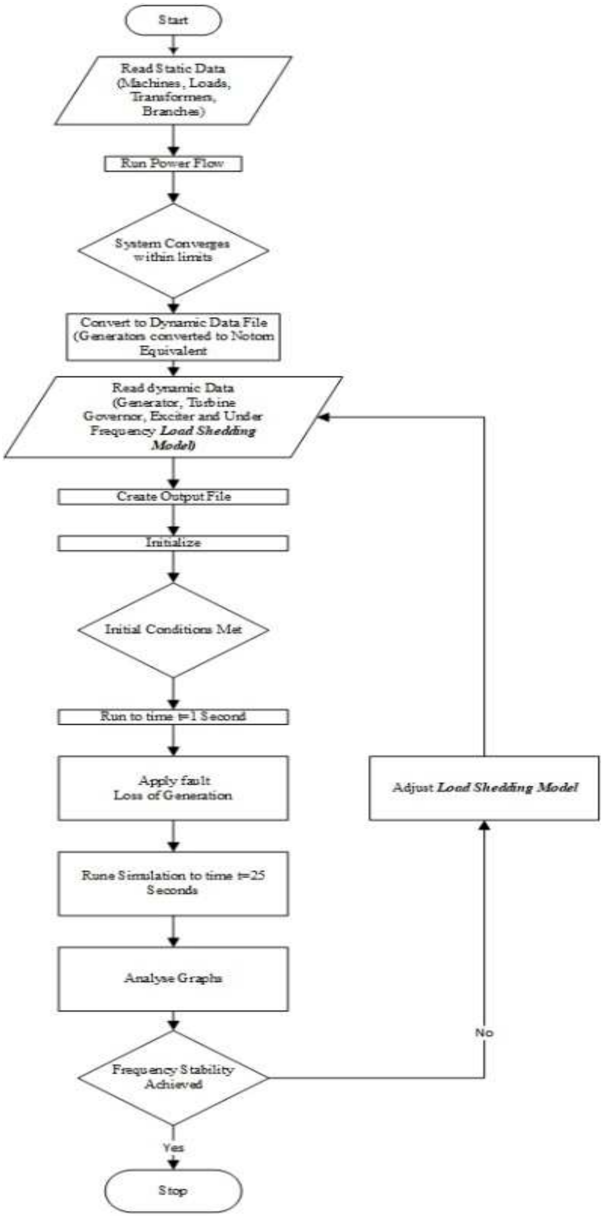

Fig. 1: Flowchart for the stability simulation and analysis using PSS/E.

The Load shedding parameters adjusted were pick up setting and the trip time of the load until frequency stability was achieved for a generation load imbalance.

VI. Assumptions

It is necessary to identify key assumptions that inform the basis of the PSSE model utilised in the screening process [9]. A Peak Scenario representing a peak demand scenario was prepared with total load of 2343.9 MW and generation of 2641.0 MW. The difference in the total load and generation is mostly attributed to exports and losses.

A. *Model Description*

The model consisted of Zambian and Societe Nationale d'Electricite (SNEL) Katanga Networks, SNEL Katanga network is considered part of the Control Area Covered by the Zambian National utility. The model contained 335 buses and 82 Machines.

B. *External Grid*

The SAPP network was modelled as an external generator using the PSS/E classical GENCLS model with an Inertia Constant (H) of 4.5MW.s/MVA and damping constant (D) of 0 per unit.

C. *Synchronous Machine Dynamic Model*

Largest generators are Hydro units located at Kariba North Bank Power Station with 180MW capacity. The turbine governors for KNBPS and KGPS were modeled using the PIDGOVD in the simulation tool, PSS/E, as shown below.

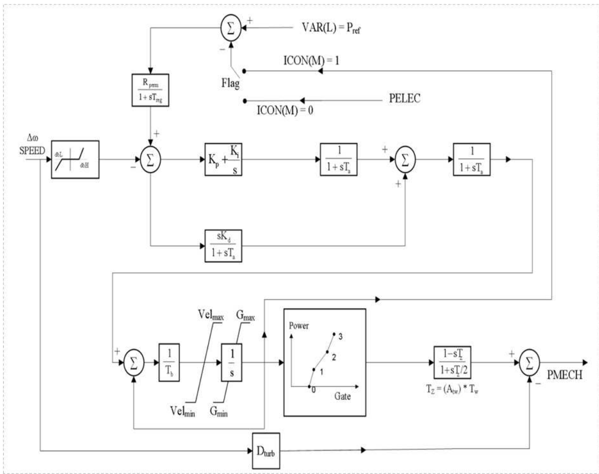

Fig. 2: PIDGOVD parameters for Kariba North Unit 6

D. *Generator Loading at KGPS*

For this simulation, each unit at KGPS was loaded at 145MW which is close to the actual mode of operation for purposes of meeting the reserve requirements.

The governor Dead Band for units was taken as -0.15 Hz to +0.15 Hz. (-0.003 to +0.003 in per unit).

VII. Results and Analysis

A. *Islanded Scenario - Loss of KGPS Units*

- ***Loss of 4 KGPS Unit***

For the loss of 4 units at KGPS, these units were tripped at $t = 1$ second and the frequency response observed for 30 seconds for each pre-selected % UFLS. Figure 3 below shows system frequency response for the loss of 4 units at KGPS giving a value -0.8 Hz/s as ROCOF.

- ***Loss of 6 KGPS Unit***

For the loss of 6 units, at $t = 1$ second, 6 units at KGPS were tripped and the system frequency response was observed for 30 seconds for each pre-selected % UFLS. Figure 4 below shows the resulting response giving a value -1.3 Hz/s as ROCOF.

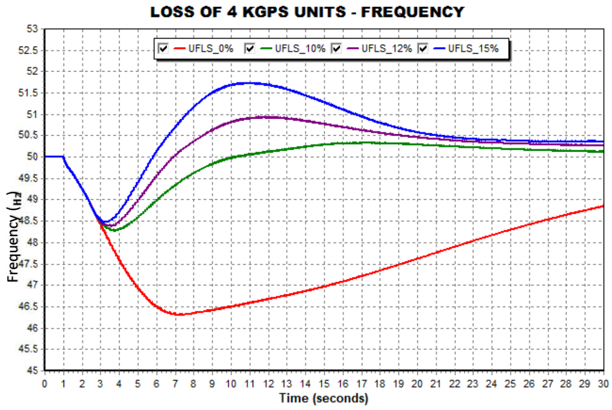

Fig. 3: System frequency response for the islanded scenario following the loss of 4 units at KFG power station

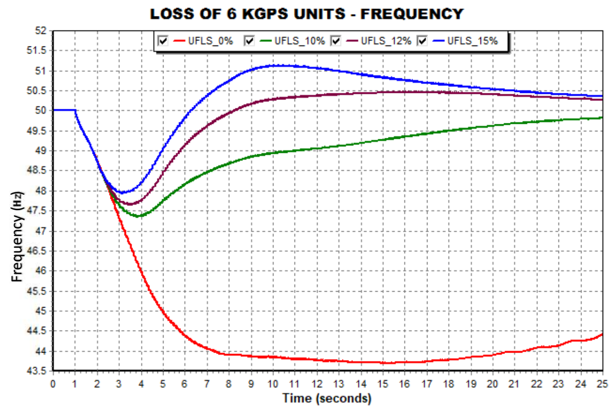

Fig. 4: System frequency response for the islanded scenario following the loss of 6 units at KFG power station

- ***Results Analysis***

The results for the islanded scenario showed that 10% UFLS gives the best frequency recovery for the selected worst contingencies of losing 4 and 6 machines at KGPS, because it had the lowest frequency overshoot and an acceptable nadir of about 48.3Hz and 47.3Hz respectively. The ROCOF under loss of 6 units was higher than the value for loss of 4 units. It is seen here that the larger the contingency, the steeper the ROCOF. As presented in [23] this aspect is utilized to make UFLS adaptive to different system contingencies.

B. *Interconnected Scenario - Loss of KGPS Units*

Under this scenario, the contingencies and % UFLS remained the same as for the islanded case, except that the Zambian grid was modelled to be interconnected to the SAPP grid.

- ***Loss of 4 KGPS Unit***

As earlier highlighted, at $t = 1$ second, 4 units at KGPS were tripped and response observed for 30 seconds for each pre-selected % UFLS. Figure 5 below shows system frequency response giving a value -0.5 Hz/s as ROCOF.

- ***Loss of 6 KGPS Unit***

At t = 1 second, 6 units at KGPS were tripped and response observed for 30 seconds for each pre-selected % UFLS. Figure 6 below shows system frequency response giving a value -0.8 Hz/s as ROCOF.

- ***Results Analysis***

The results for the interconnected scenario showed that for the loss of 4 and 6 units at KGPS, the frequency recovers with frequency nadirs of 48.5Hz and 48Hz respectively. However, for the loss of 4 units at KGPS, the frequency response had an overshoot reaching 50.6 Hz while the loss of 6 units did not.

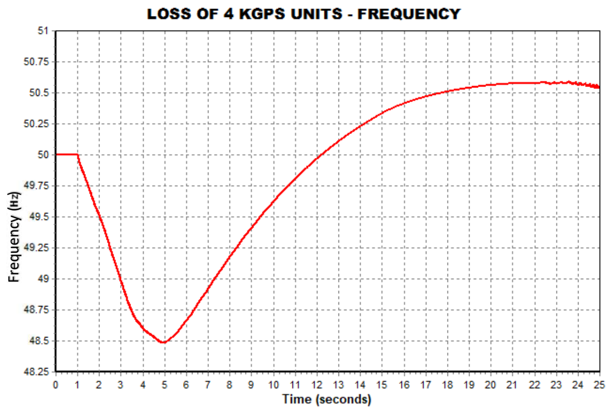

Fig. 5: System frequency response for the interconnected scenario following the loss of 4 units at KFG power station

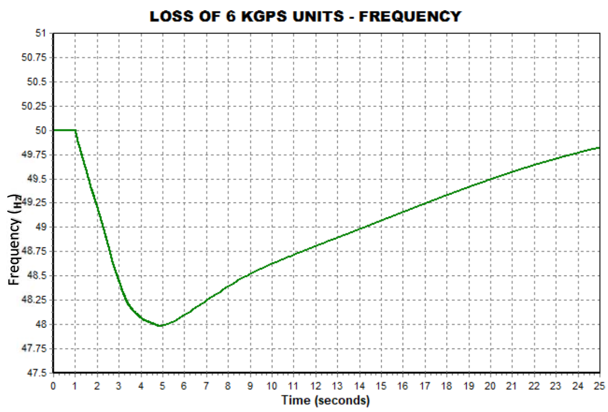

Fig. 6: System frequency response for the interconnected scenario following the loss of 6 units at KFG power station

C. *Modified-Interconnected Scenario - Loss of KGPS Units*

In this scenario, the interconnected scenario was modified by changing the pickup frequency from 48.5Hz to 48.6Hz, time delay from 200ms to 100ms with the amount of load to shed was unchanged. The following figures 7 and 8 show results of the modified-interconnected scenario compared to the interconnected one.

- ***Results Analysis***

It can be seen from the results that the frequency of the system under the modified scenario recovered at a better frequency nadir of about 48.5Hz than 48Hz for the 6 units contingency and had no overshoot.

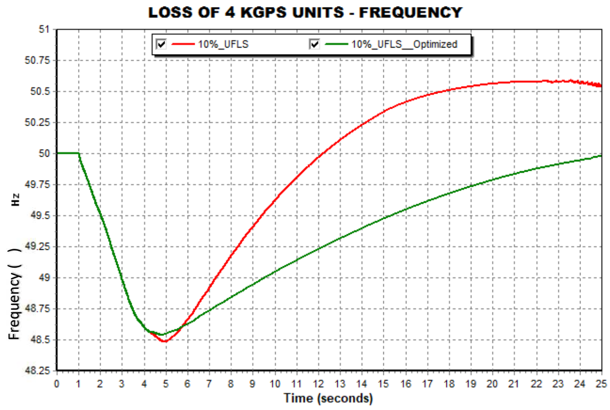

Fig. 7: System frequency response for the modified-interconnected scenario following the loss of 4 units at KFG power station

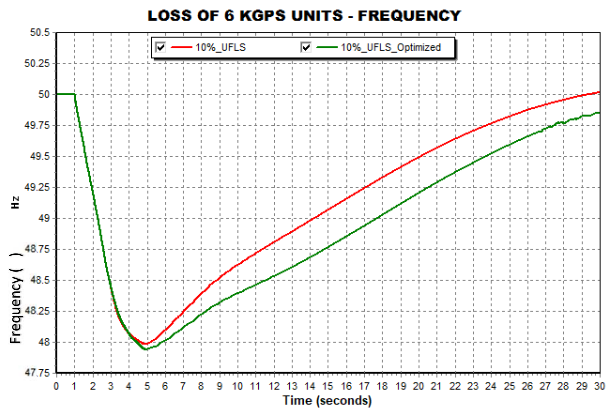

Fig. 8: System frequency response for the modified-interconnected scenario following the loss of 6 units at KFG power station

VIII. CONCLUSION

This study was undertaken to evaluate the frequency response of the Zambian IPS under contingencies resulting in the loss of 4 and 6 units at Kafue Gorge (KFG) power station for the islanded and interconnected scenarios.

The results showed that the system under the modified-interconnected scenario, with 10% UFLS, recovered with a lowest frequency nadir and had no overshoot compared to the other two scenarios. It is recommended that this be considered for implementation. It was also generally observed that the larger the contingency, the steeper the rate-of-change-of-frequency (ROCOF) which confirms the importance of considering ROCOF in UFLS schemes.

On the other hand, with numerous literatures confirming several advantages of approaches based on data-driven predictive models, which include mitigation of challenges related to measurements, easier to implement and configure, etc., it is recommended that a study on these approaches be undertaken on the Zambian IPS.

The voltage response of the system and the impact of significant penetration of variable renewable energy sources (VRES) on under-frequency load shedding (UFLS) requirements were not considered in the study. It is recommended that these are considered for future study owing to increasing penetration of VRES in power systems.

ACKNOWLEDGMENT

The authors wish to acknowledge and thank the management of ZESCO Limited for the support rendered during the study period.

REFERENCES

[1] A. Jovi and A. Ibrahim, "Impact of the generation system parameters on the frequency response of the power system: A UK grid case study," *Electricity,* vol. 2, pp. 143-157, 20 April 2021.

[2] N. Amjady and F. Fallahi, "Determination of frequency stability border of power system to set the thresholds of under frequency load shedding relays," *Energy Conversion and Management,* vol. 51, p. 1864–1872, 12 March 2010.

[3] L. Li, H. L. M.-L. Tseng, H. Feng and A. S. F. Chiu, "Renewable energy system on frequency stability control strategy using virtual synchronous generator," *Symmetry,* vol. 12, no. 10, 15 October 2020.

[4] U. Cetinkaya and R. Bayindir, "Impact of increasing renewable energy sources on power system stability and determine optimum demand response capacity for frequency control," *2022 10th International Conference on Smart Grid (icSmartGrid),* 18 August 2022.

[5] U. Rudez and R. Mihalic, "Analysis of underfrequency load shedding using a frequency gradient," *IEEE Transactions on Power Delivery,* vol. 26, no. 2, pp. 565 - 575, 28 December 2009.

[6] Y. Guo, H. Nan, X. Guan and L. Wu, "Discussion on the over-frequency generator tripping scheme of the power grid," *Journal of Physics: 2018 International Conference on Energy, Electrical and Power Engineering,* vol. 1072, 18 June 2018.

[7] P. Kundur, Power system stability and control, New Delhi: McGraw-Hill, 1993.

[8] U. Rudez and R. Mihalic, "WAMS-based underfrequency load shedding with short-term frequency prediction," *IEEE Transactions on Power Delivery,* vol. 31, no. 4, pp. 1912 - 1920, 25 November 2015.

[9] ENTSO-E, "Frequency based emergency disconnection policy review for the Nordic region," ENTSO-E, Brussels, 2017.

[10] S. Padron, M. Hernandez and A. Falcon, "Reducing under-frequency load shedding in isolated power systems using neural networks. Gran Canaria: A case study," *IEEE Transactions on Power Systems,* vol. 31, no. 1, pp. 63 - 71, 4 February 2015.

[11] H. H. Alhelou, "Under frequency load shedding techniques for future smart power systems," in *Handbook of research on smart power system operation and control*, IGI Global, 2019, pp. 188 - 202.

[12] T. Škrjanc, R. Mihalič and U. Rudež, "Pattern recognition-based predictive under-frequency load shedding scheme," *2020 IEEE PES Innovative Smart Grid Technologies Europe (ISGT-Europe),* 10 November 2020 2020.

[13] P. Favre-Perrod, W. Sattinger, P. Korba, M. Ramirez-Gonzalez, F. R. S. Sevilla and B. Wartmann, "Experimental and HIL investigation of under-frequency and rate of change of frequency load shedding schemes in interconnected networks with high penetration of renewable generation," *CIRED 2021 - The 26th International Conference and Exhibition on Electricity Distribution ,* 25 January 2022.

[14] N. Aparicio, S. Añó-Villalba, E. Belenguer and RamonBlasco-Gimenezc, "Automatic under-frequency load shedding mal-operation in power systems with high wind power penetration," *Mathematics and Computers in Simulation,* vol. 146, pp. 200-209, 16 January 2017.

[15] ZESCO Limited, "ZESCO Limited," 2022. [Online]. Available: https://www.zesco.co.zm/. [Accessed 01 September 2022].

[16] E. G.-L. E. M. A. M.-G. Ana Fernandez-Guillamon, "Power systems with high renewable energy sources: A review of inertia and frequency control strategies over time," *Renewable and Sustainable Energy Reviews,* vol. 115, 9 September 2019.

[17] B. Tan, J. Zhao, M. Netto, V. Krishnan, V. Terzija and Y. Zhang, "Power system inertia estimation- Review of methods and the impacts of converter-interfaced generations," *Electrical Power and Energy Systems,* vol. 134, 28 July 2021.

[18] D. Remon, A. M. Cantarellas, J. M. Mauricio and P. Rodriguez, "Power system stability analysis under increasing penetration of photovoltaic power plants with synchronous power controllers," *IET Renewable Power Generation,* vol. 11, no. 6, pp. 733-741, 21 March 2017.

[19] Southern African Power Pool (SAPP), "Southern African Power Pool (SAPP)," StarBright, 2022. [Online]. Available: https://www.sapp.co.zw/. [Accessed 01 September 2022].

[20] Southern African Power Pool (SAPP), "Operating guidelines," Southern African Power Pool (SAPP), 2013.

[21] Eskom, "Eskom," Eskom SA, March 2022. [Online]. Available: https://www.eskom.co.za/eskom-divisions/gx/nuclear/. [Accessed 22 September 2022].

[22] L. Sigrist, L. Rouco and F. M. Echavarren, "A review of the state of the art of UFLS schemes for isolated power systems," *International Journal of Electrical Power & Energy Systems,* vol. 99, pp. 525-539, 20 February 2018.

[23] P. Lakra and M. Kirar, "Load shedding techniques for system with cogeneration: A review," *Electrical and Electronics Engineering: An International Journal (ELELIJ),* vol. 4, no. 3, pp. 83-96, August 2015.

[24] Z. A. Obaid, L. M. Cipcigan, L. Abrahim and M. T. Muhssin, "Frequency control of future power systems: reviewing and evaluating challenges and new control methods," *Journal of Modern Power Systems and Clean Energy,* vol. 7, no. 1, pp. 9 - 25, January 2019.

[25] C. Collados-Rodriguez, M. Cheah-Mane, E. Prieto-Araujo and O. Gomis-Bellmunt, "Stability and operation limits of power systems with high penetration of power electronics," *Electrical Power and Energy Systems,* vol. 138, 13 January 2022.

[26] Y. Cheng, R. Azizipanah-Abarghooee, S. Azizi, L. Ding and V. Terzija, "Smart frequency control in low inertia energy systems based on frequency response techniques: A review," *Applied Energy,* vol. 279, 12 September 2020.

[27] U. Rudež and R. Mihalič, "Trends in WAMS-based under-frequency load shedding protection," *IEEE EUROCON 2017 - 17th International Conference on Smart Technologies,* 17 August 2017.

[28] European Network of Transmission System Operators for Electricity (entsoe), "Inertia and rate of change of frequency (RoCoF)," ENTSO-E AISBL, Brussels, 2020.

[29] C. Collados-Rodriguez, Cheah-Mane, E. Prieto-Araujo and O. Gomis-Bellmunt, "Stability analysis of systems with high VSC penetration: Where is the limit?," *IEEE Transactions on Power Delivery,* vol. 35, no. 4, pp. 2021-2031, 19 December 2019.

[30] P. Fernández-Bustamante, O. Barambones, I. Calvo, C. Napole and M. Derbeli, "Provision of frequency response from wind farms: A review," *Energies,* vol. 14, no. 20, 15 October 2021.

[31] B. Kroposki, B. Johnson, Y. Zhang, V. Gevorgian, P. Denholm, B.-M. Hodge and B. Hannegan, "Achieving a 100% renewable grid: Operating electric power systems with extremely high levels of variable renewable energy," *IEEE Power and Energy Magazine,* vol. 15, no. 2, pp. 61 - 73, 2 March 2017.

[32] M. Torres and L. A. C. Lopes, "Virtual synchronous generator: A control strategy to improve dynamic frequency control in autonomous power systems," *Energy and Power Engineering,* vol. 5, no. 2A, 15 April 2013.

Framework for ancillary services design for low inertia power systems

Azeez O. Olasoji
Electrical engineerig department
University of Cape Town
Cape Town, South Africa
olsazez001@myuct.ac.za

D.T.O. Oyedokun
Electrical engineerig department
University of Cape Town
Cape Town, South Africa
davoyedokun@ieee.org

***Abstract*— Increased penetration of renewable generation units may lead to the displacement of conventional synchronous generators, and consequently, reduce the system inertia. The decline in the system inertia increases the demand for primary frequency response (PFR) needed to system stability, with the expected surge in PFR demand; this research discusses a new approach for PFR electricity market ancillary service design. The design proposed in this study co-optimises energy, inertia and PFR while considering uncertainties in renewable energy production. The approach proposed caters to the temporal and heterogeneous nature of system inertia expected in low-inertia power systems and presents a new market design that allows synchronous and non-synchronous inertia sources to participate in the frequency response market. The outcome of this research will contribute to medium to long term reliable operation of power systems with prevalent non-synchronous generation.**

Keywords—electricity market, inertia, PFR, SCUC, MILP

I. INTRODUCTION

Conventional power systems are changing globally towards cleaner energy through the increasing penetration of renewable energy sources (RES) and the use of power electronic converters to interface with the grids. This development has been further fast-tracked by the Paris climate change agreement. In Europe, wind and solar energy have an installed capacity of 128.8GW and 87.9GW respectively, representing 14.1% and 9.7% of the entire European electricity production [1], [2]. Due to the concerted effort stemming from the Paris agreement to make electricity generation more sustainable, coupled with ageing electricity infrastructure being phased out, there has been an expected increase in electricity generated from renewable energy which is projected to continue [3]. In south Africa, Eskom [4] projects by 2030 RES would take up approximately 46% of its generation capacity. Bumping up RES installed capacity to 36GW [5]. This increased penetration of RES brings about increased operational challenges, that is, system inertia decline which inherently leads to an increased demand for primary frequency response (PFR).

The differing characteristics of RES from conventional units, that is, the stochastic nature and mode of connection via power electronic converters removes the buffers offered by synchronous generators in the event of a disturbance is greatly reduced [6]. The consequences are -

(a) It slows down the natural reaction of the system, and,

(b) It no longer gives the controllers and the operator the needed time to implement adjustments, because the resulting rate of change of frequency (RoCoF) is steeper and decline in frequency nadir becomes much higher in systems with reduced system inertia.

Thus, to ensure adequate provision of PFR, we must ensure there is enough incentive for PFR provision in the ancillary service (AS) electricity market. However, current products in the AS markets only cater to services such as, spinning/non-spinning reserves, regulation up/down. The AS markets do not have products that cater to PFR and system inertia. Hence this study proposes a new framework for AS electricity markets that cater to PFR and system inertia, considering the temporal and heterogenous nature of inertia.

II. POWER SYSTEM INERTIA

A. Characteristics of inertia in conventional power systems

System inertia has a huge impact on frequency stability—where frequency stability is the ability of the power system to maintain or restore a steady and stable frequency after a severe system disturbance (short term / long term). Maintaining system frequency within an acceptable operating range (~50Hz or 60Hz) is an important requirement in ensuring system reliability and security. Tielens [6] defined the inertia of an object in motion as the resistance to its change in state of motion, and changes in its displacement. Hence, in conventional power systems, the objects in motion refer to the rotating masses (turbines and synchronous generators) connected to the grid [7]. Their resistance to change in speed is indicated by the moment of inertia of the rotating mass. System inertia is one of the essential system factors on which the synchronized operation of present-day power systems is based. Inertia is mostly estimated using the swing equation in (1). The swing equation characterises the dynamic behaviours of the power system with respect to the change in active power and rate of change of frequency (RoCoF). [7]–[10].

$$\frac{\left(2SH_{sys}{}^{df(t)}/_{dt}\right)}{f_o} = P_m\text{-}\ P_e \tag{1}$$

Where - f_o is the nominal system frequency, H_{sys} is the system inertia, S is the apparent power of the system, f is the measured system frequency, P_m *and* P_e being the mechanical and electrical power respectively.

B. Inertia in Future Power Systems

It is anticipated that most synchronous generators will be replaced or switched off in favour of renewable energy generation sources with lower levelized cost of energy and lower marginal costs [3], [6]. Within the context of inertia, as discussed in section I, these renewable energy sources are markedly different from traditional generation units. With an increase in renewables, reduced inertial response in future power systems is inevitable. This will increase the susceptibility of power systems to a steeper RoCoF [3]. Higher RoCoF could trigger anti-islanding RoCoF relays and disconnect generating units from the grid. Hence, saving the system from reaching an unacceptable level of RoCoF that might trigger the UFLS scheme as experienced in the black system event in Southern Australia on the 28th of September 2016, or the power outage in the United Kingdom on the 9th of August, 2019, that disconnected a million customers due to the system's inability to resist disturbance [11], [12]. In Southern Australia the generation mix showed that wind energy had the largest infeed into the grid and the inability of the wind farms to resist deviations in voltage led to the triggering of the UFLS scheme, with a RoCoF value of 6.25 Hz/s, leading the system frequency to decline to 47Hz in 0.4s. However, the thermal generation plants in the mix were able to resist the deviations [11].

Another theme that pervades increased penetration of RES into power grids is the heterogenous nature of inertia that follows [13]. Variations in RoCoF and inertia at different location of the power system has been observed in South Africa, as well as Germany [3], [13], [14].

Many studies highlight the need to pay attention to differences in RoCoF values at different nodes on the network in future power systems with lower synchronous inertia [3], [11]–[15]. All of these have led to the degradation of frequency stability and an increased demand for primary frequency response (PFR) or primary frequency control (PFC) which is needed to maintain frequency stability and grid integrity. Hence, a need arises to ensure that low-inertia interconnected power systems can acquire the required primary frequency response services needed to maintain frequency stability and curtail contingencies associated with under-frequency load-shedding events.

1) *Electricity Markets*

Since the unbundling of electricity infrastructure from vertically integrated utilities, electricity markets have been designed to ensure competition for providing various services, that is, ancillary services (AS), needed to maintain/support power systems operations. Most electricity market designs operate with efficient economic principles coupled with the improved technology of modern power systems[16]. The stochasticity of RES and lack of inertia associated with these resources, impose a considerable demand for additional flexibility, particularly for the ancillary services needed to maintain real-time generation/demand balance[17]. The AS market products include spinning reserve, non-spinning reserve, and regulation up and down. At the moment, prevailing AS market designs do not cater to the peculiarities of PFR and inertia in low-inertia power systems [18].

Due to the unbundling of the electricity infrastructure which has incentivized competition in the electricity industry, most regions or countries operate with a pool-based market structure, to cater to and simultaneously clear (i.e. co-optimise) energy, and ancillary service [16]. In this setup, you have a day-ahead market, which can be a single or multi-period security-constrained unit commitment (SCUC) complimented with a real-time market, which can either be a single or multi-period security-constrained economic dispatch (SCED). To cater to PFR and inertia within this market structure, the peculiar requirement of PFR must be included in the market clearing formulation. Because, like other services, PFR and inertia must be simultaneously cleared in tandem with AS and energy.

III. Primary Frequency Response

North American Electric Reliability Corporation (NERC) termed primary frequency response (PFR) as "the response designed to cope with severe exigencies such as large generators tripping off-line" [19]. It involves generators in automatic and quick action to change their output in accordance to a significant frequency deviation (usually within seconds) [18]. It is the first measure to arrest system frequency. NERC divided frequency control into three categories based on response time window: primary, secondary, and tertiary control [18]. This control comes from automatic governor response, load (motors), and other devices that provide an instant response based on local control systems. The three stages of control work together to impede, stabilize and return system frequency to its pre-contingency state after an imbalance.

After the loss of a generator, at this stage, all synchronous generators supply extra MW relative to their size [7], [19]. The primary frequency response then jumps in, with the hope of halting and steadying frequency before under-frequency load shedding (UFLS) is initiated.
This stage is known as the "arresting period"[18]. Once the decline is arrested, primary frequency control will ensure stability by continuing to respond. After the frequency is stabilized, the secondary frequency control then reinstates the, system frequency back to the regular operation range. Eventually, Tertiary control will restore the reserved capacities. The response of the power system in the event of a contingency can be aptly summarize with Fig. 1.

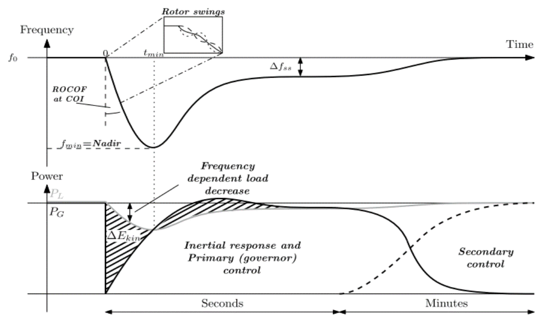

Figure 1:Frequency response pattern in the event of a generation demand imbalance. [7]

A. *Reserves and Ancillary service*

System operators require sufficient operating reserve to control and maintain system frequency to ensure there is enough room to maneuver in severe disturbances pertaining to primary, secondary, and tertiary frequency control. However, the most viable mechanism (market) to procure operating reserves is the ancillary services (AS) market [20]. The present AS market products includes spinning reserve, non-spinning reserve, and regulation up and down. The present AS market design does not include or cater to PFR and inertia constraints in power systems with high renewable penetration [18].

B. *Reserve requirements*

Different methodologies to determine reserve requirement has been discussed extensively in the past to ensure system reliability; N-1 rule, NREL 3+5 rule, NREL 2.5 rule, and wind variability modification AIGS [21]–[23]. Thus, when a reserve rule is established, it is modelled as a constraint in the unit commitment model for energy and reserve scheduling to maintain reliability levels against uncertainties that could occur [20]. Li [20] and Lew *et. al.* [21] tried navigating the stochasticity in renewables by using 3% of forecast load, as well as 5% of wind forecast to handle the intermittent nature of renewables. To handle the issue of forced outages Bouffard in [23], and [24] employed a stochastic SCUC multi-period market-clearing approach. Their approach was modelled in such a way that the reserve constraint was not implemented as a hard constraint, and any reserve violation was reflected in the expected load not served (ELNS). In the optimization problem formulation, generators and transmission lines with high failure rates were selected apriori. O'Sullivan [26] utilized a frequency-based response constraint approach to determine optimal dispatch. Their approach ensured the dispatch obtained did not result in a frequency below stipulated values irrespective of a contingency event, which was the loss of the single largest unit. In [27] the authors included the probability of load shedding in their frequency-based response approach. However, their model was executed using sequential programming, which sequentially clears products within an electricity market structure. This system leads to price reversals amongst the products being cleared sequentially.

In [28] the authors formulated and solved a multiperiod UC that simultaneously accounts for both primary & tertiary reserve constraints. Their formulations used simplified frequency model to cater to the dynamic frequency response during energy and AS scheduling process. The authors in [16] [29] focused on a more detailed model of governor responses to determine the PFR prices, catering to the peculiar dynamic behaviors of governors during frequency response. Bhana and Overbye [30] employed an iterative approach to dispatch interruptible loads to provide primary frequency response. During each iteration, the dynamic simulation results are used to update parameters in the problem formulation. The approach, however, falls short at its applicability to large power systems. Padraig *et. al.* [31] attempted to solve the problem of simultaneously clearing energy and PFR by developing two forms of inertial constraints in their problem formulation, a static and dynamic time-invariant constraint. The static constraint sets the online system stored rotational energy above a constant level, specified by the largest infeed/outfeed to the system, whilst the dynamic constraint sets the minimum rotational energy requirement as a function of the largest infeed or outfeed at each economic dispatch. Li [18]– [20] in their study designed a new primary frequency market that hosts offers from both loads and generators simultaneously. They developed a method to quantify PFR requirements on an hourly basis. The authors implement an electricity market model where load resources equipped with UFLS relays can participate in a PFR market alongside generator sources in real-time with the commitment of generators fixed. Their study was the only study that was able to utilise the full network model of large interconnected systems, that is, the electric reliability council of Texas (ERCOT). Thus, their model was able to cater to dynamic frequency response for different system inertia conditions, then obtain the required PFR requirements at the varying system inertia levels. Because of the full network model ERCOT used in the study, they were able to capture the interplay between unit commitment statuses of generating units, inertia and PFR requirements. Their study however fails to cater to non-synchronous sources participating in their new PFR market design.

In the literature studied, there exist common themes and gaps, which are aptly summarized below, some of which have not yet been tended to:

(a) There is a gap between current reliability requirements needed to maintain grid integrity and the corresponding AS products. Most utilities use the spinning reserve as a substitute for PFR, however, PFR and spinning reserve are two distinct products. This difference is much more exacerbated in low-inertia power grids as PFR requirement increases.

(b) In the unbundled electricity market structure where competition is incentivized, there is a need to cater to more resources to provide PFR, as against the current electricity market structure where core focus is on co-optimizing energy and AS, thus creating an inadequate product market fit for PFR.

(c) There is also a need to ensure electricity market design caters to non-synchronous resources providing PFR response, that is, battery energy storage systems (BESS), wind farms (providing virtual inertia).

(d) There also exist the possibility of frequency measurements not being adequately assessed, as such rolling over to the objective function of the problem formulation.

(e) Also, most electricity market designs, do not cater to the heterogeneity and temporal of inertia in low-inertia power grids, whilst evaluating PFR requirements.

(f) Most electricity market designs studies catering to PFR designs mostly derive their frequency response from simplified dynamic models. These models provide a close to accurate depictions of frequency response. However, these models might still fall short in large, interconnected power systems, such as ERCOT's or South Africa's power network.

IV. Energy, PFR, & Inertia Scheduling

Identifying the system's inertia condition is crucial for a power grid with a significant level of renewable energy penetration. If the system's inertia is known, it can be used to model a hard constraint into a Day-Ahead unit commitment or Real-Time economic dispatch problem to ensure sufficient inertia support available for the next day. The amount of PFR needed should be determined based on system inertia. Previous market structures operated from the assumption that the amount of reserve should equal the amount of generation lost [32]. However, in low inertia systems, conditions like this do not hold true as RoCoF differs as a function of system inertia and size of power imbalance, as well as the fact that system inertia varies with system load demand. Hence, in low inertia conditions, the reserve needed to cater to the contingency might be more than the loss. As such, this research leverages the methodology implemented in [32] by utilizing full system dynamics to determine PFR requirements. As stated prior, simplified dynamic models implemented in literature may provide a decent approximation of frequency response for a relatively simple system [16], [29], [33], [34]. However, for a large system, such as the South African network, frequency characteristics can be affected by factors such as turbine-governor models, contingency location, and the number of governors available to provide frequency response.

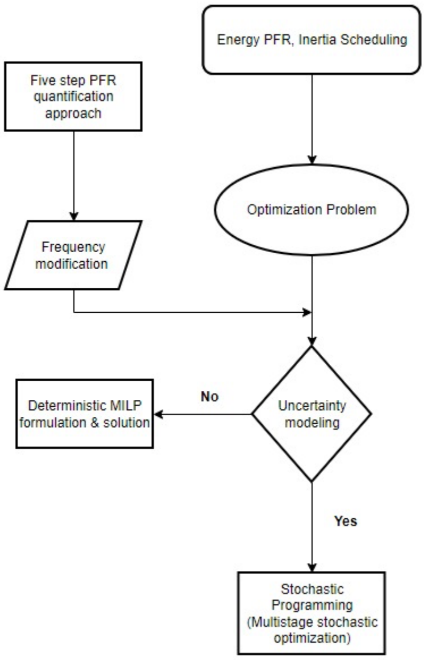

Figure 2: Framework of proposed PFR electricity market AS design

The pseudo model of the SA network developed at the university of Cape Town (UCT) is intended to be used for simulations in this research. The pseudo model includes detailed information on turbine-governor models, which is responsible for activating PFR provision in the event of a large contingency. As such, utilizing a full system dynamic model gives a full picture of the non-linear frequency response provided by synchronous machines. This provides an edge over simplified frequency models implemented in other studies. The overarching structure to be used in this study is shown in Fig. 2.

A. PFR Quantification

The PFR quantification method proposed in this study has five main procedures:

(a) Select representative conditions: Utilizing varying net load levels as seen in South Africa to conduct frequency stability studies for evaluating PFR requirements at different net load levels. Whilst catering to the different system inertia values expected at different load demand levels.

(b) The study also proposes evaluating the impact of varying load types on PFR requirements.

(c) Selection of dynamic models of the power system equipment: The pseudo–South African dynamic network model which mimics the South African network is to be employed.

(d) Simulations for quantifying the minimum PFR requirement: In the event of a large contingency, i.e., the loss of the largest units is simulated. The frequency response criterion is that frequency excursions are impeded before the first layer of under frequency load shedding (UFLS) relays are breached.

(e) Determine the ratio of PFR sources within that node on the grid to satisfy PFR requirements: The novelty of this study is to combine traditional and non-traditional energy sources. This is a first-of-its-kind approach or combination in literature as most studies only use PFR from generators or load resources equipped with under-frequency relays.

B. Frequency Measurements

PFR requirement is evaluated using the disturbance-based estimation approach. An inertia estimate is obtained under the assumption that the RoCoF and the size of the power imbalance are available. The inertia estimation should take place immediately after a disturbance before frequency containment responses are initiated, as such the changes in load due to frequency and voltage variations will not influence the power imbalance [35]. This study proposes to mitigate the rollover issue of frequency measurements impacting RoCoF and inertia estimations and inherently PFR requirements. The approach employed in [36] is proposed. Equation 2 shows frequency can be calculated from the time derivative of the voltage phase angle. A method of curve fitting would be used to impede the impacts of measured transients in the measured frequency following a power imbalance, to reduce the possibility of obtaining inaccurate RoCoF. Using a lowpass Butterworth filter with a corner frequency appropriately selected to eliminate undesired transients in the measured frequency, as well as noise and oscillations.

$$\hat{f} = f_n + \frac{d\delta}{dt} \cdot \frac{f_s}{360} \qquad (2)$$

Where- δ is the voltage phase angle, f_s is the sampling frequency, f_n is the nominal frequency.

C. PFR-Inertia Constraints Modelling

In the new PFR electricity market AS design framework being proposed in this study, we propose a new market model that makes procuring PFR services and energy co-optimisable. However, it is important to cater to the differing nature of PFR, as this service is different from other AS products. PFR requirements vary for varying system inertia levels, and system inertia varies for different load demand levels and the size of power imbalance. To account for those dependencies, a scheduling model is to be developed over the course of this study to co-optimise energy, PFR requirements, and the system inertia in both day-ahead and real-time system operations. The scheduling model works based on traditional unit commitment formulations and includes the PFR requirement obtained from the PFR quantifications approach highlighted in section V, sub-section A.

A 2-step procedure is implemented. The first step is the PFR quantification approach, including PFR constraints into the co-optimization problem formulation and extending the formulation to include non-synchronous sources providing PFR responses. In the first step, PFR required is calculated in response to realistic system dynamics. However, the scheduling problem is anticipated to be difficult to solve because of the nonlinearity of frequency response, as the optimization problem is to be formulated as a mixed integer linear programming (MILP) problem [37]. The nonlinearity of frequency response in a MILP approach is time-consuming and computationally inefficient. Thus, the anticipated second step envisaged in this study is to evaluate appropriate linearisation techniques. This intended modification makes it possible to formulate unit commitment problems catering to PFR needs at varying levels of system inertia conditions to be formulated as a MILP problem. The intended MILP formulation must be able to handle to handle uncertainties pertaining to RES, as well as equipment contingencies. Hence a stochastic unit commitment (UC) model is proposed to be employed.

D. Stochastic Unit commitment

Stochastic optimisation technique is an advanced methodology to handle uncertainties in scheduling processes [34]. The study proposes a multi-stage stochastic scheduling model be employed to optimally schedule energy, PFR and inertia considering augmented levels of uncertainties associated with renewable energy sources. The PFR-system inertia quantification approach discussed in section V, sub-section A, provides an alternative, to modelling system frequency dynamics in unit commitment problem formulation. The objective of the scheduling problem is to minimize the expected operation costs, expected cost of obtaining PFR, and load shedding costs. The proposed formulation of the PFR-INERTIA constrained stochastic unit commitment model in (3) is an offshoot of traditional unit commitment models bounded by PFR-INERTIA constraints as discussed in sub-section C. The traditional unit commitment model used here follows the formulation as seen in [19], [38]. In this study, the stochastic UC formulation would be modelled as a two-stage decision process. This aligns with how electricity markets are operated in practice. The first stage would depict the day-ahead market operation and the second stage would show the real-time (economic dispatch) operation of the market. The here-and-now decision variables in the first stage do not depend on any particular scenario realizations. The wait-and-see decision variables of the second stage however, depends on the scenario's realized in real-time. However, the anticipation of several possible outcomes in the second stage is deemed to have an impact on the scheduling decisions in the first stage.

Where- $C_{energy}(t,i,s)$is the cost of generator i at hour t in scenario s, $C_{PFR}\ (t,i)$ is the PFR cost or offering price from source i at time $(\$/MW)$, $ll(t,s)$ load shed during time t in scenario s (MW), $pfr\ (t,i,s)$ PFR response from generator i at time t in scenario s MW, $VOLL$ is the values of load loss $(\$/MWh)$

$$\sum_{s} prob(s)\left\{\sum_{t,i}[C_{energy}(t,i,s) + C_{PFR}\ (t,i).pfr\ (t,i,s)] + \sum_{t} VOLL\,.\,ll(t,s)\right\} \tag{3}$$

V. Conclusion

To achieve a much more viable electricity market ancillary service design for primary frequency reserves, needed to maintain grid integrity in an unbundled electricity market structure where competition is encouraged.

This paper discusses a new approach for PFR electricity market design that would host offers from both synchronous and non-synchronous sources. Whilst adhering to gird requirements and catering to the peculiar nature of system inertia and RoCoF in RES dominated power systems. The new framework proposes a PFR quantification approach that utilizes inertia estimates determined from varying system load demands and load types. Whilst not neglecting frequency drifts when determining inertia estimates, the PFR estimates obtained is then proposed to be modelled as a hard constraint into stochastic UC MILP formulation.

The next phase of this research is to detail the linearization technique to be employed to linearize PFR-inertia requirements at different system inertia levels, and preliminary SCUC MILP analysis are ongoing to ensure the proposed framework is computationally efficient and meets the computation time desired during electricity market operation.

References

[1] I. Pvps, "2016 Snapshot of global photovoltaic markets," 2016. [Online]. Available: https://iea-pvps.org/wp-content/uploads/2020/01/IEAPVPS-A_Snapshot_of_Global_PV-1992-2015-Final.pdf

[2] GWEC, "Annual market update 2017,"2017. [Online]. Available:https://gwec.net/wp-content/uploads/2020/11/GWEC_Global_Wind_2017_Report.pdf.

[3] M. J. Rainey and D. T. O. Oyedokun, "Transmission line damping effects on power system inertia response," 2020 International SAUPEC/RobMech/PRASA Conference, SAUPEC/RobMech/PRASA 2020, no. 978, pp. 1–6, 2020, doi:10.1109/SAUPEC/RobMech/PRASA48453.2020.9040925.

[4] E. H. Limited, "The Eskom transmission development plan 2022-2031," 2008.

[5] Department of Energy, "Integrated Resource Plan," 2019. doi: http://dx.doi.org/9771682584003-32963.

[6] P. Tielens and D. Van Hertem, "The relevance of inertia in power systems," Renewable and Sustainable Energy Reviews, vol. 55, no. 2016, pp. 999–1009, 2016, doi: 10.1016/j.rser.2015.11.016.

[7] P. Tielens, "Operation and control of power systems with low synchronous inertia," PhD thesis, Faculty of Engineering Science, KU Leuven, 2017.

[8] F. Milano, F. Dorfler, G. Hug, D. J. Hill, and G. Verbič, "Foundations and challenges of low-inertia systems ," 20th Power Systems Computation Conference, PSCC 2018, pp. 1–25, 2018, doi: 10.23919/PSCC.2018.8450880.

[9] P. Tielens and D. Van Hertem, "Grid inertia and frequency control in power systems with high penetration of renewables," in Young researcher Symposium, 2012, vol. 39. doi: 10.1101/sqb.1974.039.01.121.

[10] J. Fang, H. Li, Y. Tang, and F. Blaabjerg, "On the Inertia of Future More-Electronics Power Systems," IEEE J Emerg Sel Top Power Electron, vol. 7, no. 4, pp. 2130–2146, 2019, doi: 10.1109/JESTPE.2018.2877766.

[11] AEMO, "Preliminary report - Black system event in South Australia,"2016.[Online].Available: http://www.pfbach.dk/firma_pfb/references/aemo_sa_blackout_2016_09_28_preliminary.pdf

[12] Ofgem, "Investigation into the power outage that occurred on 9 August," 2020.

[13] A. Ulbig, T. S. Borsche, and G. Andersson, Impact of low rotational inertia on power system stability and operation, vol. 19, no. 3. IFAC, 2014. doi: 10.3182/20140824-6-za-1003.02615.

[14] M. J. Rainey and D. T. O. Oyedokun, "Load Modelling Effects on Power System Inertia Response," in 2020 IEEE

PES/IASPowerAfrica,2020,pp1-5,doi:10.1109/power africa49420.2020.9219951.
[15] D. Doheny and M. Conlon, “Investigation into the local nature of rate of change of frequency in electrical power systems,” 2017 52nd International Universities Power Engineering Conference, UPEC 2017, vol. 2017-Janua, pp. 1–6, 2017, doi: 10.1109/UPEC.2017.8231982.
[16] E. Ela, V. Gevorgian, A. Tuohy, B. Kirby, M. Milligan, and M. O’Malley, “Market designs for the primary frequency response ancillary service-Part II: Case studies,” IEEE Transactions on Power Systems, vol. 29, no. 1, pp. 432–440, 2014, doi: 10.1109/TPWRS.2013.2264951.
[17] G. Strbac and F. A. Wolak, “Electricity Market Design and Renewables Integration in Developing Countries,” 2017.
[18] W. Li, P. Du, and N. Lu, “PFR ancillary service in low-inertia power system,” IET Generation, Transmission and Distribution, vol. 14, no. 5, pp. 920–930, 2020, doi: 10.1049/iet-gtd.2019.1536.
[19] W. Li, “Primary frequency response ancillary service in low inertia power systems,” PhD thesis, North Carolina State University, 2018.
[20] W. Li, P. Du, and N. Lu, “Design of a new primary frequency control market for hosting frequency response reserve offers from both generators and loads,” IEEE Trans Smart Grid, vol. 9, no. 5, pp. 4883–4892, 2018, doi: 10.1109/TSG.2017.2674518.
[21] D. Lew, G. Brinkman, E. Ibanez, B. Hodge, and J. King, “The western wind and solar integration study phase 2,” 2013.
[22] R. Doherty and M. O’Malley, “A new approach to quantify reserve demand in systems with significant installed wind capacity,” IEEE Transactions on Power Systems, vol. 20, no.2, pp. 587–595, 2005, doi:10.1109/TPWR S.2005.846206
[23] C. Lowery and M. O’Malley, “Reserves in Stochastic Unit Commitment: An Irish System Case Study,” IEEE Trans Sustain Energy, vol. 6, no. 3, pp. 1029–1038, 2015, doi: 10.1109/TSTE.2014.2364520.
[24] F. Bouffard and F. D. Galiana, “An Electricity Market With a Probabilistic Spinning Reserve Criterion,” IEEE Transactions on Power Systems, vol. 19, no. 1, pp. 300–307, 2004.
[25] F. Bouffard, S. Member, F. D. Galiana, and A. J. Conejo, “Market-Clearing With Stochastic Security —Part II : Case Studies,” vol. 20, no. 4, pp. 1827–1835, 2005.
[26] J. W. O’Sullivan and M. J. O’Malley, “Economic dispatch of a small utility with a frequency based reserve policy,” IEEE Transactions on Power Systems, vol. 11, no. 3, pp. 1648–1653, 1996, doi: 10.1109/59.535710.
[27] J. W. O’Sullivan and M. J. O’Malley, “A new methodology for the provision of reserve in an isolated power system,” IEEE Transactions on Power Systems, vol. 14, no. 2, pp. 519–524, 1999.
[28] K. A. Papadogiannis and N. D. Hatziargyriou, “Optimal Allocation of Primary Reserve Services in Energy Markets,” IEEE Transactions on Power Systems, vol. 19, no.1,pp.652-659,2004,doi:10.1109/TPWRS.2003.820702.
[29] E. Ela, V. Gevorgian, A. Tuohy, B. Kirby, M. Milligan, and M. O’Malley, “Market designs for the primary frequency response ancillary service-Part I: Motivation and design,” IEEE Transactions on Power Systems, vol. 29, no. 1, pp. 432–440, 2014, doi: 10.1109/TPWRS.2013.2264951.
[30] R. Bhana and T. J. Overbye, “The Commitment of Interruptible Load to Ensure Adequate System Primary Frequency Response,” IEEE Transactions on Power Systems, vol. 31, no. 3, pp. 2055–2063, 2016, doi: 10.1109/TPWRS.2015.2458936.
[31] P. Daly, D. Flynn, and N. Cunniffe, “Inertia considerations within unit commitment and economic dispatch for systems with high non-synchronous penetrations,” in 2015 IEEE Eindhoven PowerTech, PowerTech 2015, 2015. doi: 10.1109/PTC.2015.7232567.
[32] W. Li, P. Du, and N. Lu, “PFR ancillary service in low-inertia power system,” IET Generation, Transmission and Distribution, vol. 14, no. 5, pp. 920–930, 2020, doi: 10.1049/iet-gtd.2019.1536.
[33] M. Paturet, U. Markovic, S. Delikaraoglou, E. Vrettos, P. Aristidou, and G. Hug, “Stochastic unit commitment in low-inertia grids,” IEEE Transactions on Power Systems, vol. 35, no. 5, pp. 3448–3458, 2020, doi: 10.110 9/TPWRS.2020.2987076.
[34] F. Teng, V. Trovato, and G. Strbac, “Stochastic Scheduling with Inertia-dependent Frequency Regulation,” IEEE Transactions on Power System, pp. 1–10, 2015.
[35] D. Zografos, “Power system inertia estimation and frequency response assessment,” KTH, 2019.
[36] A. G. Phadke, J. S. Thorpe, and M. G. Adamiak, “A new measurement technique for tracking voltage phasors, local system frequency, and rate of change of frequency,” IEEE Transactions on Power Apparatus and Systems, vol. PAS-102, no. 5, pp. 1025–1038, 1983.
[37] L. Montero, A. Bello, and J. Reneses, “Techniques , and Resolution Methods,” MDPI Energies, vol. 15, no. 4, 2022.
[38] D. S. Kirschen and G. Strbac, Fundamentals Of Power System Economics, Second. New Jersey: John Wiley & Sons, Ltd, 2019.
[39] A. J. Wood, B. F. Wollenberg, and G. B. Sheble, Power generation, operation, and control, Thrid. New Jersey: John Wiley & Sons, Inc, 2014.

Critical Assessment of the Feasibility of Shielding Overhead Medium Voltage Lines in South African Conditions

Charmaine Mathopo
Eskom Research Testing and Development
Johannesburg, South Africa
Email: MathopCM@eskom.co.za

Andreas Beutel
Eskom Research Testing and Development
Johannesburg, South Africa
Email: BeutelAA@eskom.co.za

Bruce McLaren
Eskom Distribution
Technology and Engineering
East London, South Africa
Email: mLarenB@eskom.co.za

Willem Dirkse Van Schalkwyk
Eskom Distribution
Central East Cluster
Bloemfontein, South Africa
Email: vSchalWJ@eskom.co.za

Abstract—Lightning is one of the most common causes of power outages on overhead medium voltage (MV) power lines. Lines located in areas with high ground flash density or in open country are particularly susceptible to being struck by lightning. The current design of overhead MV lines in South Africa has a more than adequate lightning performance, but one may be able to optimize this performance. One possible way of doing so is to install shield wires. This paper studies some of the key aspects that should be considered for practical shielding of overhead MV lines, such as ground flash density, line structure footing impedance, number of shield wires, performance when compared to unshielded lines and capital cost. The effect of soil ionization is also considered. It was found that for shielding to be effective on overhead MV lines in South Africa, the footing impedance must be very low, and the basic insulation level (BIL) of the line must be sufficiently high. If the footing impedance cannot be lowered any further, then the line insulation* must be over-designed to give a BIL of a line of much higher voltage, assuming that the structure is fully bonded and earthed and that the poles are unseasoned. The costs of shielding MV lines are not likely to be justified in South African conditions.

Keywords— Basic insulation level, footing resistance, lightning, medium voltage lines, shield wires, soil ionization, soil resistivity

I. Introduction

The safe and reliable supply of electricity is crucial to the day-to-day running of businesses, hospitals, industries and households. In rural areas of South Africa, electricity is distributed to customers using overhead medium voltage (MV) power lines, which commonly operate at 11, 22 or 33 kV phase-to-phase voltage. The most common is 22 kV. The South African MV distribution network operated by Eskom is over 300 000 km [1]. Regulatory requirements mean that it is imperative that electricity be delivered with as few interruptions as possible. Lightning is one of the common causes of interruptions on overhead MV lines [2]. A lightning flash can be defined as an electrical discharge that may originate in a charged cloud or from the ground. These electrical discharges are caused by charge imbalances between storm clouds and the ground or within the clouds themselves [3]. Lightning flashes can have single or multiple strokes, with either positive or negative polarity and negative polarity strokes occurring more often [4]. Lightning performance of an overhead MV line may be improved by adjusting its Basic Insulation Level (BIL), installing surge arresters or introducing one or two shield wires to intercept lightning flashes that would otherwise have terminated on a phase conductor or gap-earthed structure [5]. Shield wires are routinely used on transmission lines, but are not as commonly used on distribution lines.

South Africa has a wide range of climates and experiences half the global rainfall average per year. It is classified as a semi-desert country with soils having varying resistivities [6]. The soil in the country varies seasonally as in other countries with the peak soil resistivity being in the months June, July and August [6]. The objective of this study is to determine the feasibility of shielding overhead MV distribution lines in South African conditions. This study also seeks to determine under which circumstances shielding of an MV line could be beneficial. This is achieved by covering the following:

- The design of MV lines, practicalities involved and how these lines perform in lightning conditions.
- The following factors that make using shield wires effective:
  - Ground Flash Density (GFD).
  - Footing resistance and impedance.
  - The number of shield wires.
- Predicted performance of shielded overhead MV lines.
- Costs associated with shielding MV lines in South Africa.

II. Current design of South African MV lines

The main components of an overhead MV line are phase conductors, insulators, woodpoles and – if used – cross-arms. The current practice in Eskom is to also include electrical bonding of the unenergized pole-top hardware and to earth that bonding via an earth wire that runs down the pole, and that includes an insulation coordination gap on the pole. Examples of pole-top hardware are insulators, bolts, bracing straps and the upper ends of stays [7]. A typical intermediate structure configuration and a shielded wishbone structure are illustrated in Fig. 1.

Fig. 1. Bonded (steel cross-arm) and earthed overhead MV structure (left) [8], shielded wishbone structure (right)

This configuration has been shown over many years to provide acceptable pollution and lightning performance and acceptable safety for humans and birds [8].

Aluminium conductors are preferred in South Africa due to their good strength-to-weight ratio and lower theft risk than copper. Aluminium Conductor Steel Reinforced (ACSR) conductor is mostly used in inland areas while All-Aluminium Conductor (AAAC) is commonly used in high marine pollution areas [4]. Polymer composite and porcelain insulators are most commonly used in South Africa.

The pole material of choice for overhead MV lines in South Africa is wood – as it is in many other parts of the world. One reason is that it allows for the insulation coordination gap which helps in preventing flashover due to lightning-induced overvoltages. This gap increases the insulation level from that of the insulator (approximately 170 kV) to approximately 300 kV. The wood in the gap also assists in quenching arcs [9].

III. Lightning performance of Eskom MV lines

Lightning affects overhead MV lines by direct strikes to the phase conductors or by surges induced by strikes to nearby objects such as trees. When lightning strikes a conductor directly, the current divides into two equal parts that travel in opposite directions on the line [10]. Due to the short rise time of a lightning current surge, the resultant voltage on the phase conductors also rises very quickly and mostly causes flashovers to earth on the pole nearest to the strike [11].

Overhead MV lines are mostly 8-10 m high, therefore voltages induced from nearby strikes do not often exceed 200 kV, with a rare maximum being 250 kV [11]. A line with a height of 18 m can expect induced surges to not usually exceed 300 kV [12]. In Eskom, MV lines do not usually exceed 15 m, a BIL of 300 kV therefore ensures that induced surges very rarely cause flashover. Conversely, all direct lightning strikes to an MV line are expected to result in flashover, but not all cause power interruptions [8].

Eskom has found that the 300 kV BIL structure configuration gives very acceptable lightning performance, while also providing acceptable performance with respect to pollution (pole-top fires) and bird safety [8]. However, there may be room for optimizing the length of the insulation coordination gap, which is discussed in detail in [13].

IV. Options for lightning performance optimization

Lightning performance of overhead MV lines may be improved by changing the BIL of the structures, installing line surge arresters or introducing one or two shield wires to intercept lightning strikes that would have otherwise hit the phase conductors [5].

A lightning strike of 10 kA to a line with a surge impedance of 500 Ω can result in a peak voltage of 2.5 MV. This is significantly greater than the BIL of a typical overhead MV structure. If the BIL of this structure is increased to 500 kV, the strike would still result in a flashover. Therefore, increasing the BIL of a structure only would not dramatically decrease the number of flashovers that occur on MV lines due to direct lightning strikes. This, however, remains the most effective way of reducing or even completely eliminating the flashovers that occur due to induced surges [14].

A surge arrester is a protective device that diverts lightning current to earth while limiting the voltage across its terminals – and hence on the line [15]. The use of surge arresters is most effective for protection against induced surges when they are installed on every phase, at every 300 m and on structures that have a BIL of lower than 300 kV. Surge arresters are not effective for protection against direct lightning strikes when used on their own, because their energy rating is too low [16].

Shield wires are earthed conductors placed above the phase conductors to intercept direct lightning flashes. A stroke that terminates on the shield wire of an overhead MV line is very likely to result in a back-flashover occurring from the structure to the conductor. This is because the voltage from the lightning flash that develops across the line insulation is likely to exceed the BIL of the line [17]. The likelihood increases even further because the bonded hardware on shielded lines must be solidly earthed, i.e., the wood gap shown in Fig. 1 must be bridged. Shield wires have been used extensively on transmission lines with great success due to the naturally high BIL provided by the insulators required at transmission voltages and the control of the footing resistance. With the current overhead MV line design in South Africa, the footing resistance is not controlled by use of chemicals or earth electrodes, the "earth electrode" used on overhead MV lines involves simply wrapping the earth downwire around the pole on the underground portion of the pole. Simply adding one or more shield wires to an unshielded line is therefore not effective, because additional measures are required. The following section presents an analysis of the factors that need to be considered for effective shielding of MV lines.

V. Factors determining effective shielding

There are two main parameters that can be used to determine the effectiveness of shielding. These are Back-Flashover Rate (BFR) and Shielding Failure Rate (SFR). These two parameters are impacted by several design factors.

A. Shielding Failure Rate (SFR)

SFR describes the rate at which lightning flashes strike the phase conductors instead of the shield wires at a specific lightning peak current [18]. This rate depends on the area formed by the uncovered width (X in m), the length of the line in km (L) and the GFD of the area in Flashes/100 km/year. X is the horizontal width of the line perpendicular to the conductors, which is not covered by the shield wire(s). In South Africa, GFD ranges from 0 to 23, with the Western part of the country having the least number of flashes per year and the north-eastern part having the greatest number of flashes per year [19]. SFR (Flashes/100 km/year) can be calculated using equation (1) [4]. When using two shield wires, this value is halved. Fig. 2 shows the effect of the uncovered width and GFD on a structure's SFR. The greater the uncovered width and the GFD, the greater the probability of shielding failure occurring. Installing two shield wires reduces the uncovered width, this then decreases the SFR. In South Africa, most intermediate overhead MV structures are a single pole with a cross-arm as shown in Fig. 1. Where the relatively few shielded MV structures exist, they would typically be of single pole wishbone configuration, with only one shield wire. This is due to the special configurations required in terms of BIL, earthing, structural and related considerations. Lines that are in open country are more susceptible to being struck by lightning than those that are shielded by tall buildings and trees. The protection provided by these objects can be accounted for by using a shielding reduction factor of 0.6 in equation (1) [4].

$$\mathrm{SFR(I)} = 2 \cdot \mathrm{N_g} \cdot \mathrm{L} \cdot \mathrm{X} \tag{1}$$

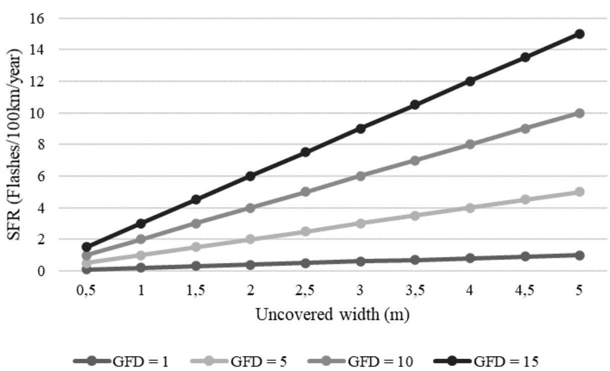

Fig. 2. Effect of the uncovered width and GFD on the SFR

B. Back Flashover Rate (BFR)

The effective footing impedance and BIL of a line are the major determinants of whether back flashover is likely to occur.

1) Effective footing impedance

This is a series combination of the impedances of the earth electrode and the structure. The soil resistivity impacts the footing impedance of the structure, which is largely dependent on the footing resistance. If the lightning current and the footing impedance are high, then the resultant voltage occurring on the shield wires will be high, resulting in a high probability of back flashover [20].

To calculate the BFR of an overhead MV line equation (2) is used [17]. N_L is the approximate number of flashes that terminate on the shield wires in flashes/100 km/year and can be calculated using equation (3) [17]. P(I) is the probability that the lightning strike will have a current magnitude that can cause a flashover on the structure. For a conductor with surge impedance (Z_C) of 500 Ω, the critical current is calculated to be 2.42 kA using equation (4) [17]. This value is below the average lightning strike current magnitude in South Africa; therefore, it can be assumed that most lightning strikes terminating on the shield wire will cause a flashover, and hence that P(I) ≈ 1. BFR can then be calculated using equation (5).

$$\mathrm{BFR} = \mathrm{N_L} \cdot \mathrm{P(I)} \tag{2}$$

$$\mathrm{N_L} = {}^{\mathrm{GFD}}/_{10} \cdot (28 \cdot \mathrm{h}^{0.6} + \mathrm{b}) \tag{3}$$

$$\mathrm{I_C} = {}^{2 \cdot \mathrm{LI}^-}/_{\mathrm{Z_C}} \tag{4}$$

$$\mathrm{BFR} = \mathrm{N_L} \tag{5}$$

Where:

h = Height of the structure (m).

b = Distance between shield wires (m), this is assumed to be zero when using a single shield wire.

LI^- = 605 kV/m (Standard lightning impulse flashover voltage for negative lightning strokes).

I_C = Critical current required to cause a flashover (kA).

To determine the relationship between the BFR and footing resistance, the IEEE method of estimating the percentage of direct strokes causing back flashover is used [20]. This gives the results shown in Fig. 3. It can be noted that the footing resistance and the GFD play a significant role in determining the BFR of a structure. This shows that in areas where the GFD is high, the footing resistance must be kept as low as possible to limit the BFR of the structure. This can be a challenge to achieve without implementing a more complex earthing system than simply installing an earth downwire.

2) Improving the footing impedance of the structure

To maximize the effectiveness of the shielding, the effective footing impedance must be as low as possible. One way of contributing to this, is to limit the resistance of the earth electrode by installing a deliberate and suitable earth electrode – instead of simply wrapping the earth downwire around the pole as is the practice on unshielded lines. The earthing system can also be improved by chemically treating the soil around the structure, but this is not preferred by Eskom [4].

One way of minimizing the earth electrode resistance is by combining different earth electrode configurations, e.g. single or multiple vertical rods, horizontal wires, ring electrode or star electrodes. The following electrode designs were investigated: single vertical rod, multiple vertical rods and eight-point star. The impedance of each of these electrodes was estimated by calculating the inductance of a single vertical rod using equation (6) [21] and calculating the effect of placing the requisite number of rods in parallel.

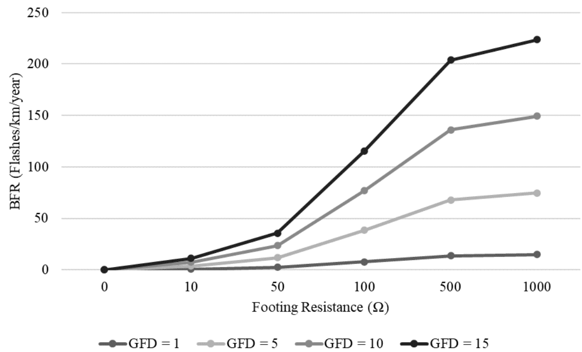

Fig. 3. Effect of footing resistance and GFD on BFR

Equation (7) was used to calculate the impedance due to this inductance. The total impedance was then calculated using equation (8), taking into account the resistance of the electrodes and the series combination of the inductance of the earth downwire and the earth electrodes as shown in Fig. 4. The capacitance of earth rods was found to be negligible. A frequency of 4 MHz was used in the impedance calculation as this is the average time it takes for a typical lightning strike current to reach 90 % of its peak magnitude [22].

$$L = \frac{\mu_0 \cdot l}{2\pi} \cdot \log\frac{2 \cdot l}{d} \tag{6}$$

$$X_L = 2\pi f L \tag{7}$$

$$Z = \sqrt{R^2 + X_L^2} \tag{8}$$

Where: L = inductance (H), μ_0 = permeability constant $(4\pi \times 10^{-7}\ \mathrm{H/m})$, l = length of electrode (m), d = diameter of the earth electrode (m), X_L = inductive reactance (Ω), f = frequency (Hz), Z = impedance (Ω), R = earth electrode resistance (Ω).

Fig. 5 shows the impedances of the different earthing electrode configurations compared. The eight-point star gives the least impedance when compared with the single vertical rod and multiple vertical rod configurations. The dimensions of the electrodes used for the calculations: d = 10 mm, l = 1 m, distance between rods = 1 m [21]. A peak lightning current of 10 kA was used to calculate the voltage across the impedances. This makes the eight-point star the best technical choice for improving the footing resistance of a structure and is therefore used as the earthing system for the structure cost and performance assessment in the upcoming sections of this paper.

3) Soil ionization

At high stroke current, earth resistance becomes non-linear. There is usually no effect at low currents in the order of 1 kA. However, at in the order of 7 kA, the effective size of the earthing system starts to increase, which decreases the resistance – and hence soil ionization occurs. This makes soil ionization a favourable condition, as it makes the ground a more favourable path for lightning current [23]. During soil ionization, the soil resistivity decreases by an average of 60 %, which in turn decreases and causes the voltage across the earthing system to decrease by the same factor, reducing the probability of back flashovers. This can be seen in Fig. 6, when using an eight-point star electrode configuration as an earthing system.

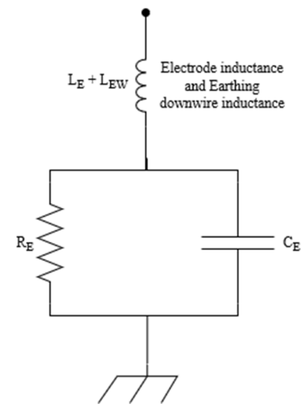

Fig. 4. Circuit diagram modelling the single vertical rod impedance and the earthing downwire inductance

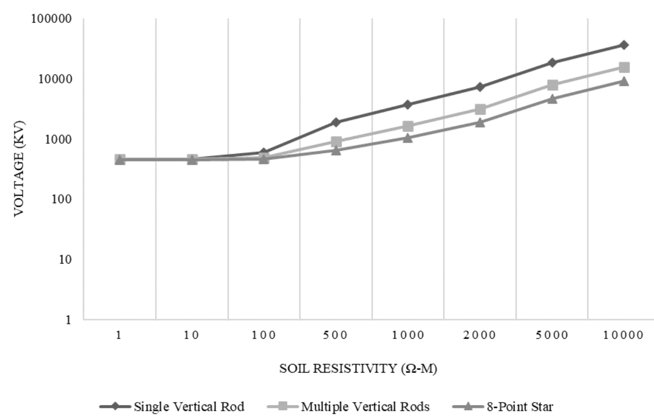

Fig. 5. Impedance comparison of different earthing electrodes

During a lightning strike with a peak magnitude lightning current of 10 kA, soil ionization would cause the voltage across the electrode configuration to drop from 302 kV to 120 kV. This would reduce the probability of back flashover occurring, as the voltage would be less than the BIL of the structure.

VI. Performance of Shielded Lines in South Africa

It is clear from the preceding sections that for shielding to be effective, structure BIL and footing impedance must be intentionally set. Footing impedance can be controlled using deliberate earth electrodes such as the eight-point star. The BIL can be increased by using longer insulators or by employing different structure types. TABLE I lists different structure types with their typical BIL. This table also includes the allowable maximum footing impedance and soil resistivity for effective shielding, using an eight-point star earth electrode configuration. A peak lightning current of 10 kA was used.

The BIL can be increased by using longer insulators or by employing different structure types. TABLE I lists different structure types with their typical BIL. This table also includes the allowable maximum footing impedance and soil resistivity for effective shielding, using an eight-point star earth electrode configuration. A peak lightning current of 10 kA was used.

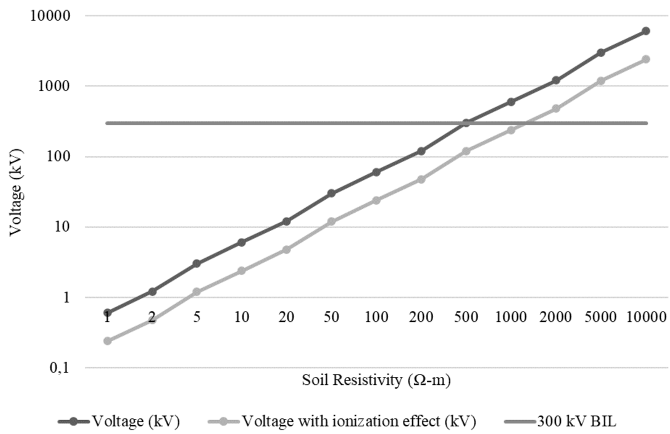

Fig. 6. Soil ionization effect

TABLE I shows that for a shielded woodpole structure with a BIL of 300 kV, the soil resistivity and footing resistance must be less than 1 Ω for effective shielding. This is practically impossible to achieve. A woodpole structure with a steel cross-arm and a BIL of 170 kV also has the same predicted lightning performance. It further shows that the higher the structure BIL, the greater the allowable footing impedance. This also emphasizes that for shielding to be feasible on overhead MV lines, the BIL of the structure must at least be 550 kV, the soil resistivity should not exceed 200 Ω-m and the maximum effective footing impedance is 49 Ω. In areas where a low footing impedance cannot be achieved, a structure with a higher BIL should be considered.

Using a polymer cross-arm provides a reduced number of flashovers due to its high BIL, which results in fewer power interruptions and fewer back flashovers [8]. This type of structure also allows shielding to be used in areas with higher soil resistivity than the standard Eskom MV line design.

VII. ESITMATED COSTS FOR SHIELDING OVERHEAD MV LINES

Fig. 7. lists the estimated per unit prices of different shielded structures in South Africa, using the standard 22 kV unshielded configuration as the reference. The prices include the anticipated material, installation and maintenance costs of the structures. This is an estimated lifecycle cost of adding the shield wire, increasing the BIL, adding an earthing system to every structure and line maintenance.

Fig. 7 shows that adding a shield wire to an unshielded line would more than double the cost. Overdesigning the insulation by building the line to a 132 kV shielded design would increase the cost by a factor of almost ten but only brings the BIL to the minimum value required for effective shielding. Overdesigning the insulation of the line to 66 kV costs four times more than the standard line but falls short of the minimum 550 kV mark required for the BIL. This design can work for lightning strikes of a lesser current magnitude. Using a polymer cross-arm instead of the usual wood or steel cross-arm would cost twice as much as the unshielded structure but would offer a higher BIL and would enable line to be shielded in areas with higher soil resistivity. Adding two shield wires would cost almost eight times the unshielded structure as it would require the installation of an additional pole, two shield wires and two deliberate earthing systems.

VIII. FEASIBILITY OF SHIELDING MV LINES IN SOUTH AFRICA

Eskom, South Africa's biggest power utility, has been using the unshielded overhead MV line design shown in Fig. 1 as its standard for some time. This philosophy has been found to perform more than adequately. The cost of any improvement in performance therefore needs to be well justified. Fig. 7 shows that the additional cost of shielding is significant. The benefits of shielding include a reduced number of lightning flashes terminating on the phase conductors, since these would be intercepted by the shield wires.

TABLE I. REQUIRED FOOTING IMPEDANCE FOR DIFFERENT OVERHEAD MV STRUCTURE TYPES

Structure Type	Structure BIL (kV)	Soil Resistivity (Ω-m)	Footing Resistance (Ω)	Effective Footing Impedance (Ω)
22 kV Bonded and earthed	300	< 1	< 1	30
66 kV design	450	1	1	45
Steel Cross-arm (effectively fully bonded and earthed)	170	< 1	< 1	17
132 kV design	550	200	18	49
Polymer Cross-arm (Unbonded)	>655	500	46	64

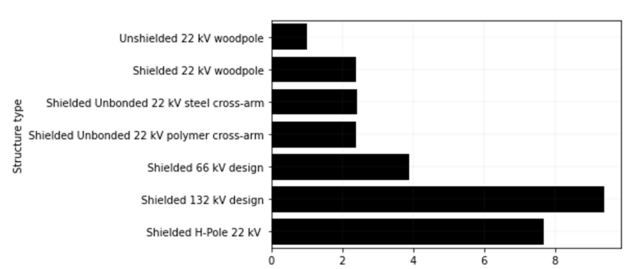

Fig. 7. Per unit prices of different structures per km

Shield wires would also reduce the number of power interruptions on the line due to lightning. Shielding would also reduce the number of equipment failures. The power utility loses revenue by not supplying electricity as agreed with customers and bears the expenses of fixing and replacing damaged MV overhead line equipment due to lightning strikes. The National Energy Regulator may also penalise the utility for not meeting electricity supply agreements [24]. These are some of the expenses that may be reduced if the power interruptions due to lightning strikes are reduced.

These benefits need to be weighed against the cost of shielding for each particular case, as the cost – and hence the cost-benefit ratio – varies with soil conditions and with the cost of interruptions. For example, shielding would likely not be necessary in areas with very low GFD, but it may be beneficial in areas with a very high GFD and where quality and reliability of electricity supply is crucial, i.e. where any loss of continuity of supply is very costly.

IX. Conclusion

The results show that shielding of overhead MV lines can be effective when the footing impedance is sufficiently low and the BIL of the structure is sufficiently high. This presents the challenge of designing an earthing system to reduce the effective structure footing impedance and increasing the structure BIL. This is currently not usually done for MV lines in South Africa. This presents a financial challenge as the addition of shield wires, the increase of structure BIL and a suitable earthing system at least doubles the lifecycle cost of a typical overhead MV line in South Africa.

Effective shielding can only be achieved if the BIL is at least 550 kV and if the effective footing impedance is 49 Ω or less. A shielded woodpole structure with a polymer cross-arm has the best lightning performance of the configurations considered. It costs twice as much as the overhead MV line structure that is currently in use in South Africa. Its use would therefore need to be well justified but could be considered for areas with high GFD and have a requirement for high quality and reliability of supply.

References

[1] Eskom Holdings SOC Ltd, "Plant information: Power lines and substations in service," in Integrated report 2021 for the year ended 31 March 2021, Johannesburg, Eskom Holdings SOC Ltd, 2021, p. 137.

[2] W. J. Dirkse van Schalkwyk, C. Gomes and J. M. Van Coller, "The Effect of Cloud-to-Cloud Lightning on Medium Voltage Lines," in International Conference on Lightning Protection, Cape Town, October 2022.

[3] M. Z. Mohyedin, "Lightning, the electrical phenomenon in Nature," in PHY 580 Electricity and Magnetism, Selangor, Malaysia, Universiti Teknologi Mara, 2017, pp. 3-4.

[4] S. Bisnath, A. Britten, M. D. Cretchley DH, P. T and V. R, in The Planning, Design and Construction of Overhead Lines, Johannesburg, Eskom Holdings Ltd, Crown Publications CC, 2005, pp. 357-367.

[5] A. Piantin, "Analysis of the effectiveness of shield wires in mitigating lightning-induced voltages on power distribution lines," Electric Power Systems Research, vol. 159, pp. 9-16, 2017.

[6] C. Thomas, "Seasonal variation of soil resistivity and the correction factor," Earthing Africa Symposium & Exhibition, p. 2, 2017.

[7] A. Beutel, H. Geldenhuys, J. Van Coller and B. McLaren, "Insulation coordination of medium voltage power lines: South African experiences," in 23rd International Conference on Electricity Distribution, Lyon, 2015.

[8] A. Beutel, B. McLaren, H. Geldenhuys, W. Dirkse Van Schalkwyk and J. Van Coller, "Lightning protection of unshielded overhead medium voltage power lines in South Africa," CIRED 25th International Conference on Electricity Distribution, vol. 253, pp. 1-5, 2019.

[9] A. Beutel, B. McLaren, H. Geldenhuys and W. Dirkse Van Schalkwyk, "Advantages and disadvantages of low insulation level on overhead MV power lines," 9th Cigre Southern Africa Regional Conference, pp. 1-11, October 2019.

[10] S. Agrawal and K. M. Nigam, "Lightning phenomena and its effect on transmission lines," Recent Research in Science, pp. 183-187, 2014.

[11] C. T. Gaunt, A. C. Britten and H. J. Geldenhuys, "Insulation co-ordination of unshielded distribution lines from 1 kV to 36 kV," South African Institute of Electrical Engineers, pp. 8-12, 1989.

[12] M. Darvenzia, G. J. Limbourn and S. A. Prentice, "Line design and electrical properties of wood," IEEE Transactions on Power Apparatus and Systems, Vols. PAS-86, no. 11, pp. 1344-1356, 1967.

[13] A. Beutel, B. McLaren and W. Dirkse Van Schalkwyk, "Characterization of a Medium Voltage Test Line in the Free State Province of South Africa," in 36th International Conference on Lightning Protection, Cape Town, 2022.

[14] A. Piantini, "Protection of overhead power distribution lines," in 29th International Conference on Lightning Protection, Uppsala, Sweden, 2008.

[15] H. J. Geldenhuys, R. B. Lagese, A. C. Britten, K. Sadurski and W. C. Van der Merwe, "Practical insulation co-ordination of woodpole distribution lines in high lightning areas," in 3D Africon Conference, 1992.

[16] T. E. McDermott, T. A. Short and J. G. Anderson, "Lightning Protection of Distribution Lines," IEEE Transactions on Power Delivery, vol. 9, no. 1, pp. 138-152, 1994.

[17] B. Alqahtani and M. H. Shweldi, "Calculation of lightning flashovers and backflash level on 230 kV transmission lines," in Power and energy Systems Conference, Marina delrey, USA, October 2005.

[18] A. R. J. Araujo, C. M. Sexias, S. Kurokawa, V. Okhmatouski and B. Kordi, "Analysis of Soil Resistivity and Tower Footing Characteristics on Overvoltages Caused by Lightning in power Transmission Towers," in The 12th Latin-American Congress on Electricity Generation and Transmission, 2017.

[19] C. R. Evert and M. Gijben, "Official South African lightning ground flash density map 2006 to 2017," in Earthing Africa Inaugural Symposium and Exhibition, Johannesburg, 2017.

[20] "IEEE Guide for improving the lightning performance of electric power overhead distribution lines. IEEE std 1410-2010," 2010.

[21] D. R. Stockin and S. Knyazeva-Johnson, "Electrode Calculations," in McGraw-Hill's guide to UK wiring standards for Earthing & bonding, United Kingdom, McGraw-Hill Education, 2017, p. Chapter 8.

[22] "SANS 62305-2011 Protection against lightning - Part 1: General Principles," 2011, pp. 30-31.

[23] K. J. Nixon, "The lightning transient behaviour of a driven rod esrth electrode in multi-layer soil," PhD Thesis, Faculty of Engineering and the Built environment, University of the Witwatersrand, Johannesburg, 2006.

[24] R. Herman, L. Talt and C. T. Gaunt, "On the adequacy of electricity reliability indices in South Africa," South African Universities Power Engineering Conference, vol. 1, pp. 1-12, 2015.

2023 SAUPEC Conference, Johannesburg, South Africa, January 24-26, 2023

Integrated Monitoring and Control System Architecture for 11 kV Substation

Daniel E. Okojie
department of electrical engineering,
Tshwane University of Tecnology
Pretoria, South Africa
OkojieDE@tut.ac.za

Siboniso Mhlongo
department of electrical engineering,
Tshwane University of Tecnology
Pretoria, South Africa
sbomhlongo8@gmail.com

Udochukwu B. Akuru
department of electrical engineering,
Tshwane University of Tecnology
Pretoria, South Africa
AkuruUB@tut.ac.za

***Abstract*—It is essential to have an integrated system architecture for monitoring and controlling substation so as to ensure the safety of people and equipment. This paper presents an architectural design and technique that is used for monitoring and controlling 11 kV substation. The proposed architecture is based on the IEC 61850 standard and is designed to provide a safe and reliable system for real-time monitoring and control of substations. The design incorporates multiple substation communication protocols to create a completely digital substation. Primary and secondary devices are employed to reduce the number of potential failure points. Components are deployed to acquire data from various constituents within a switchgear board. This arrangement contains a process to manage older devices, wherein a data concentrator is utilized to communicate with other devices such as an intelligent electronic device. These are combined to collect and deliver the necessary data at the station level for different system users. Furthermore, the architecture is designed to be scalable and flexible, allowing for the integration of additional components and equipment. The results show that the proposed architecture can respond to remote IEC 61850 commands by above 90%.**

Keywords—control, communication, digital, integrated monitoring, protocols, substation, system architecture.

I. INTRODUCTION

The difficulty of overseeing and regulating system machinery, distribution of system apparatus in power systems, production plants, and industries will continue to be a challenge for a considerable amount of time [1]. In many situations, inefficient and outdated operating procedures that are not beneficial to business, risky for personnel, and require a lot of energy and effort are still being utilised. Furthermore, engineers rely heavily on data to identify problems, decide what new machinery or substations need to be installed, and control existing resources. [2], [3]. In this regard, integrated monitoring and control systems (IMCS) are becoming increasingly important in the operation of medium voltage (MV) substations [4]. These systems provide real-time information on the state of the substation and enable operators to make informed decisions about the operation and maintenance of the substation. Substations are important components of the electric power system and are responsible for the efficient and reliable distribution of electricity to consumers. Substation automation and monitoring systems are used to ensure that electricity is delivered within the required quality and safety standards. An IMCS for an 11 kV substation provides the means to monitor and control electrical parameters and hardware from a single central location. The 11kV substation is a critical interface point between the transmission and distribution systems and provides a reliable and efficient means of supplying electricity to consumers. The control and monitoring of the 11kV substation requires an integrated system that offers features such as real-time monitoring, remote data access, secure access, fault detection and protection, and energy management. Modern power system monitoring and control systems provide advanced features such as distributed control, local and remote access, secure communication, and intelligent data processing [5].

Conversely, in older systems like the supervisory control and data acquisition (SCADA) and legacy substations, data transmission has proven not to be reliable as per engineering expectations [6]. There are no effective data transfers due to varied reasons; for example, in direct current (DC) system, the data gets lost due to control cable theft, cable damages and electrical interferences affecting the SCADA signals transmitted with use of copper cables [7], [8]. Also, the performance of high-speed control and protection signals is not easily achievable [9]. For example, sending protection trip signal from the downstream equipment is not easy and it requires extensive hardwiring or getting the status of downstream electrical equipment for interlocking purposes.

However, studies have shown that digital substations provide more benefits and less shortcomings compared to other legacy substations [10], [11]. In digital substations, reliability and availability of data is improved. Substation automation is the use of information technology (IT) and operational technology (OT) to optimise the operation, maintenance and management of MV substations. This includes the use of intelligent electronic devices (IEDs) to monitor, control and protect the substation equipment. Substation automation systems can be used to improve the reliability, safety and efficiency of MV substations. The automation of MV substations has become increasingly important in recent years due to the growing complexity of the power system and the need for more accurate and reliable data to support decisions [11]. Thus, during integration and commissioning, results now show significant improvement in the way data is collected and delivered to the station level equipment for monitoring and control compared to the old mimic systems that were used in the substations. Thus, introduction of an IMCS architecture that is compliant with digital substations may be the solution to the problems faced by utilities and industries today. Nonetheless, the underlining questions of "how to do?", and "how to implement?" without neglecting compliance with standard implementation practises of substation automation system (SAS), IEC 61850 compliances, SCADA, Station level, Bay level and Process Level models still linger [12].

Hence, this paper presents an integrated monitoring and control system architecture (IMCSA) designed for 11 kV substations. The IMCSA is capable of monitoring and controlling multiple 11 kV substations from a single location. The system is designed to provide an effective means to monitor and control the power flow, voltage, and frequency in the 11 kV substation. Additionally, the system is capable of providing real-time information regarding the operational status of the 11 kV substations. The outline of the paper is such that the introduction is presented in section I. Sections II and III comprise the system architecture and practical design, while sections IV and V contain implementation of the proposed design and the concluding remarks, respectively.

II. System Architecture

An IMCSA consists of a combination of hardware, software, and communication technologies. The hardware components include sensors, actuators, and controllers. Sensors are used to monitor the electrical parameters such as current, voltage, and power. The IMCSA consists of a combination of hardware, software, and communication technologies. The hardware components include sensors, actuators, and controllers. Sensors are used to monitor the electrical parameters such as current, voltage, and power. Actuators are used to control the various substation components, such as circuit breakers, transformers, and switches. A controller is used to process the sensor data, control the actuators, and communicate with the outside world. The software components of an IMCSA include a human machine interface (HMI) to provide a user-friendly graphical interface for monitoring.

The design is such that it is required to meet expectations and comply with all statutory requirements and specifications. The operator can visualise, supervise, and control the substation through simplified design of the HMI, gateways, and engineering workstations (EWS). This means that the IMCS can collect data and present it to a normal HMI. The system design is such that there is self-diagnosis and presentation of system issues to an operator, while the operator can operate the reticulation system by no more than five keystrokes or button clicks. When the circuit breakers are closed, or opened, the operator is automatically blocked from issuing open command to an already opened circuit breaker or close command to already closed-circuit breaker. The operator can leave notes or tag equipment on the monitoring screen during shift hours.

Also, logging in and out is recorded by the system automatically. Notifications about any malfunctions with the 11 kV reticulation system are sent out promptly when they happen, so that operators, technicians, and engineers can take appropriate action. As regards other functions of the system; Integrated monitoring system can interpret and present data to the operators, technicians, and engineers in simple and unambitious manner. The system overall is capable of processing IEC 61850 data to station level or upper level. The system can process data that is defined by open standards. Distributed network protocol (DNP) 3.0 and IEC 101 protocol are available for devices requiring this type of communication. Modbus protocol is also available for devices requiring this type of communication. The system is similarly able to process normal information or raw data or transfer of files; for example, using file transfer protocol (FTP).

III. Practical Design

In the 11 kV substation, 14 devices were IEC 61850 compliant, and 3 devices were non-IEC 61850 compliant. As shown in Fig. 1, the design presented in this paper monitors and controls the 11 kV substation by reading data (breaker and isolator statuses, current and voltage transformer measurements, transformer trip signals and alarms, etc.) from each bay and write data (breaker, isolator and control commands) to the primary plant equipment. These signals are hardwired to the digital inputs and outputs of the selected digital intelligent electronic device (IED) for indication, interlocking and tripping purposes. Data (plant status and IED internal functions) is then shared amongst IEDs over substation automation system (SAS) local area network (LAN) or serial bus (SBUS) network.

The data are from the IEDs or devices to the application software running IEC 61850 HMI Server/Client over the SAS LAN or SBUS network. Non IEC61850 devices have data flowing to the gateway and then to the application software running IEC 61850 driver. The data from the HMI Client/Server is displayed on the station HMI / EWS and control commands. These signals are then sent from the HMI to the IEDs or devices and from the IEDs to the primary plant equipment to execute the plant controls. As presented in Fig. 1, HMI 1 of the system is used as main human machine interface for monitoring and control. While HMI 2 of the system is used as backup interface for monitoring and control. This means when HMI 1 is down, the system can still be monitored and controlled using HMI 2, vice versa. Equally, EWS 1 of the system is used as main engineering workstation interface for monitoring and diagnosis by operators. Whereas EWS 2 of the system is used as backup engineering workstation interface for monitoring and diagnosis.

Furthermore, gateway / remote terminal unit (RTU) is used for station input/output (I/O) and other legacy data and build monitoring. Redundant ethernet switches are used for data reliability, availability and ensuring no common point of data loss. Global positioning system (GPS) clock is used to time synchronise internal clocks of 11kV substation devices. Data can be printed at station level for analysis. More users can use the system concurrently when logged in different workstations but only one can operate the electrical reticulation network. Data is converted by the gateway from IEC 61850 to IEC 101 to be read by the Master Station or Control Centre over IEC 101 protocol. Control commands are also sent by the Master Station or Control Centre over IEC 101 to the gateway/RTU from the RTU then to the IEDs and to the primary plant equipment [12].

IV. Implementation of Proposed System Architecture

The IMCSA for 11 kV substation design flow chart is shown in Fig. 2. The engineering, testing, and commissioning process from the 11 kV substation to the control center is presented. The design provides a complete solution of an IMCSA for the 11 kV substation. The presented solution is based on requirements for modern technology and in IEC 61850 compliance with accommodation for legacy standards.

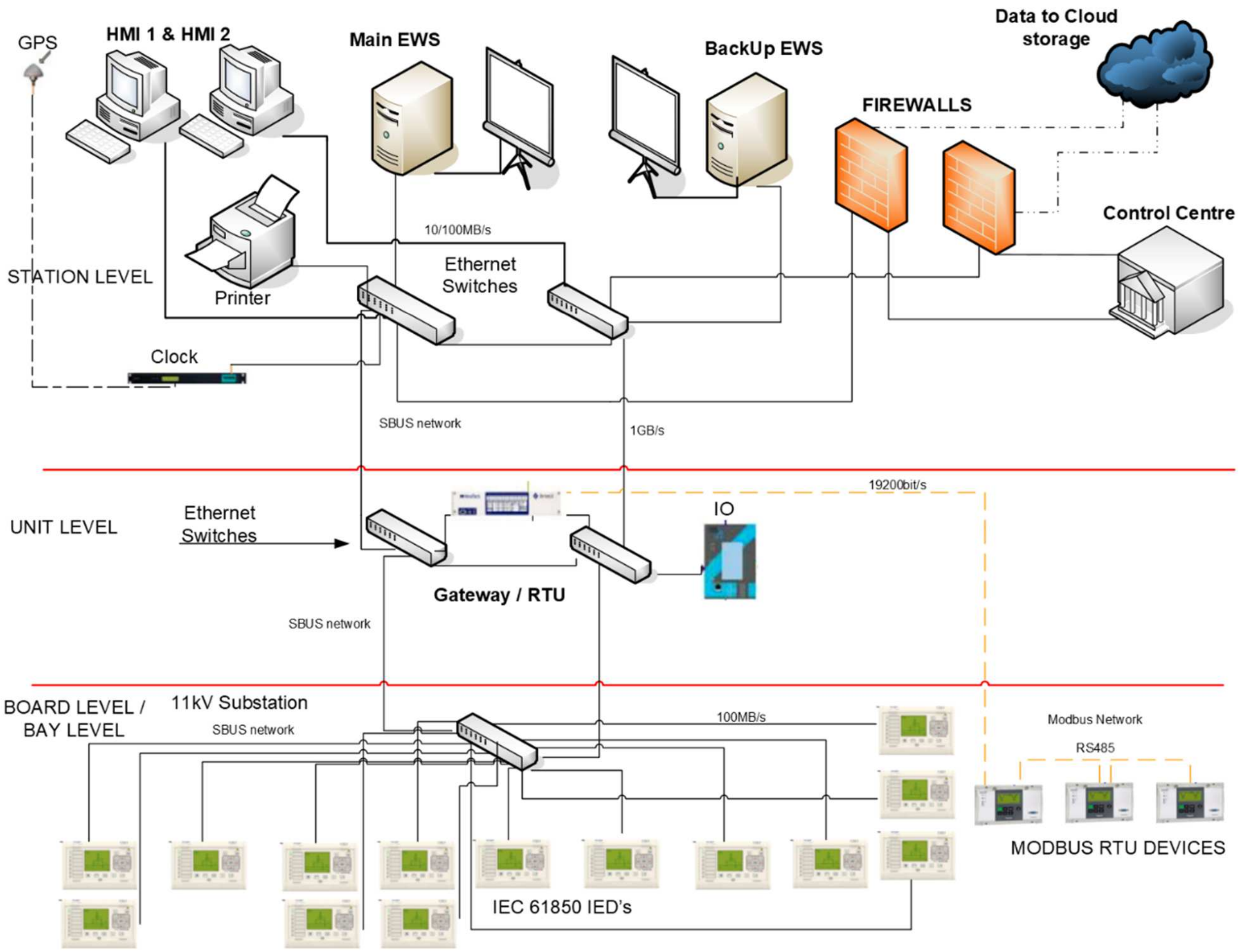

Fig. 1. Architecture overview [12].

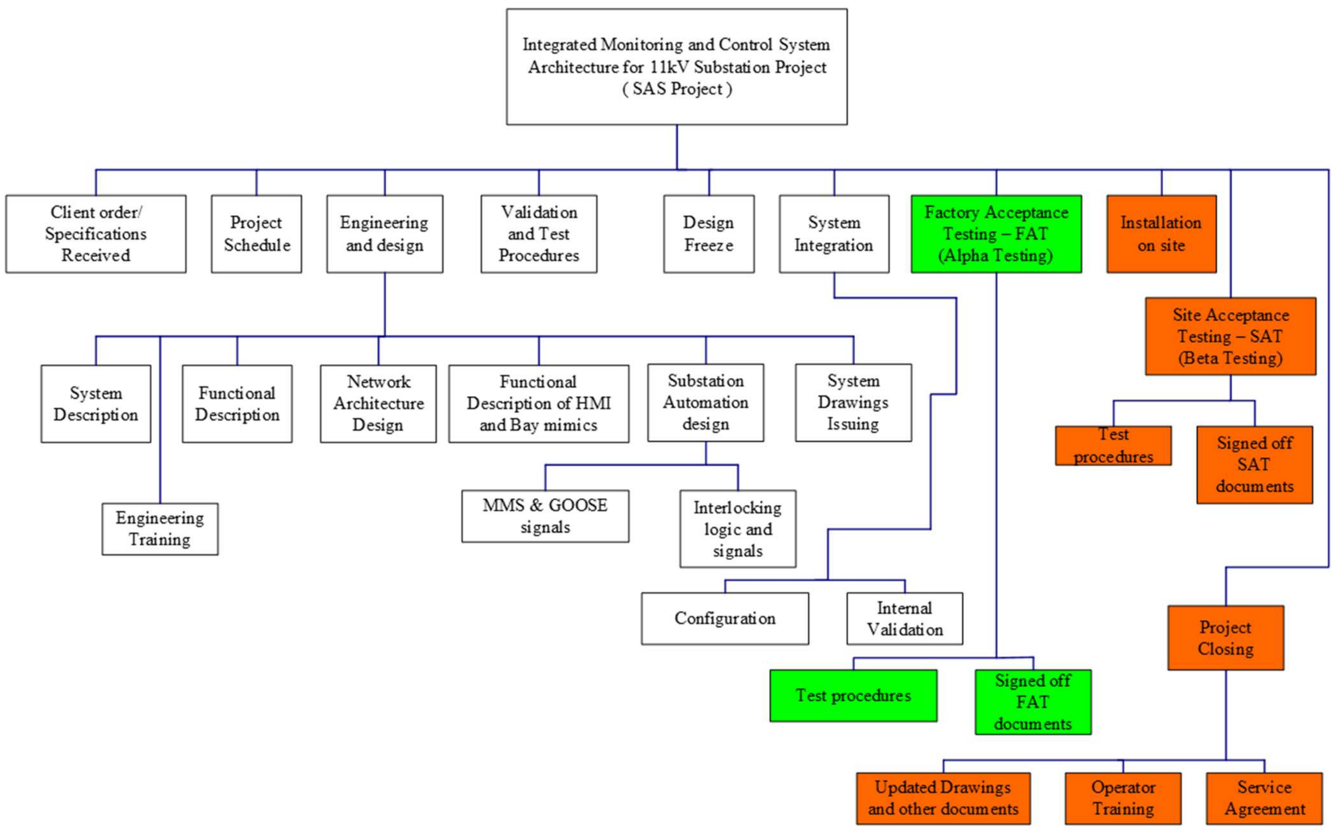

Fig. 2. IMCSA flowchart for 11 kV substation.

A. Three System Levels

The overall IMCSA for 11 kV substation shown in Fig. 1 may be divided into three levels [12];

- Bay level – low level
- Unit level – middle level
- Station level – top level

The bay level consists of protection, monitoring, and control units such as protective relays and voltage regulators. With the IEC 61850 generic object-oriented substation event (GOOSE) messaging, the bay level devices can communicate between different bays. Therefore, the bay-to-bay communication is called horizontal communication as defined in IEC 61850 [12], [13]. The unit level consists of layer 3 network switches and gateway devices. Unit level connects bay level with station level. The routing of specific tagged massages is done at the unit level. The station level consists of the station computer, EWSs, alarm unit and features, database, and remote communication. Most of the station level functions are often integrated in to the station computer. The design in this paper utilised DNP 3.0 as a communication protocol from the gateway to the SCADA control center. Whereas the data exchange between the IEDs and the HMI, EWSs, gateway is based on IEC 61850 multimedia messaging service (MMS).

B. Selecting and Implementation Phase

Two IEC 61850 devices were compared (device A and B) and all two IEDs meet the system and functional requirements. However, device A was selected since device A is an IEC 61850 certified one box solution for both protection and control. As a requirement to have ethernet switch at bay or board level. Again, two types of switches were compared (A and B). Although both options meet the requirements, however, ethernet switch A is selected based on the following additional features, including low cost:

- The ethernet switch A is certified for use in power substation automation systems (IEC 61850-3, IEEE 1613), traffic control systems (NEMA TS 2), and railway applications (EN 50121-4).
- It can be used for Gigabit or Fast ethernet backbones and supports redundant ring topologies.
- It also supports dual power inputs (24/48 VDC or 110/220 VDC/VAC) to increase the reliability of communication.
- The ethernet switch A has a modular design that makes network planning easy and allows greater flexibility.
- Installation of up to 4 Gigabit ethernet ports and 24 fast ethernet ports.
- Optional front or rear wiring makes it suitable for different applications.
- Built-in MMS server based on IEC 61850-90-4 switch data modelling for power SCADA that complies with a portion of EN 50155 specifications.
- Only exclusive to it brand the turbo ring and turbo chain redundancy technology (recovery time < 20 ms @ 250 switches).
- The ethernet switch A is robust, built for harsh temperatures which makes it a reliable cost-effective option for industrial applications.
- Easy configuration through a web browser or telnet.

Two brand options of ethernet switches are compared again as A and B. However, option B is chosen since it is a layer 3 switch. Layer 3 switches provide extra capability of routing messages using both MAC and IP addresses compared to layer 2. Other features for unit level switch are the same as those for the bay level ethernet switch.

Furthermore, as a requirement to have a gateway at unit level in the design, two brands were compared technically and one product that met all design requirements was selected. The selected gateway is a multi-port automation platform. It is designed to operate all ports independently of one another. Each port can support a unique communications protocol:

- Master mode - connected to IEDs or other slave devices.
- Slave mode - connected to SCADA Masters, or HMI. I/O can be added in the same unit without the need to purchase a separate I/O unit.

A suitable GPS clock unit was also added as a need described on user requirements. For simplicity, station level computer with HMI application software selected for implementation is of the same original equipment manufacturer as that of the selected protection and automation devices. The computer machine selected has great functionality with a personal computer (PC) combined with a touch screen also at a cheaper price than other brands in the market. The housing is a standard international unit, 19-inch wide, rack-mounted rugged enclosure. This robust, rack-mountable design provides the hardened protection needed for industrial environment applications. This type of industrial PC allows for remote access for operators. This was used for station level servers – EWS and HMI.

C. Test Results

After the design configuration and testing was done, the results and outcomes were documented. The results and comparison to the requirements are briefly discussed in this section of the paper.

In Fig. 3, the first test with the use of a Wireshark tool was successful in validating that IEDs can respond to station level user requirements in IEC 61850 MMS protocol. This proved that the IEC 61850 compliant IEDs drivers are working. Hence all devices can respond to remote IEC 61850 user requests.

Results shown in Fig. 3 is found to have met the user requirements by above 90%. The necessary variations and improvements were done on site upon user requests. After the tests were conducted and results recorded the following conclusions were reached:

- Different monitoring and control screens are required by the operator to be in a friendly and unambitious manner.

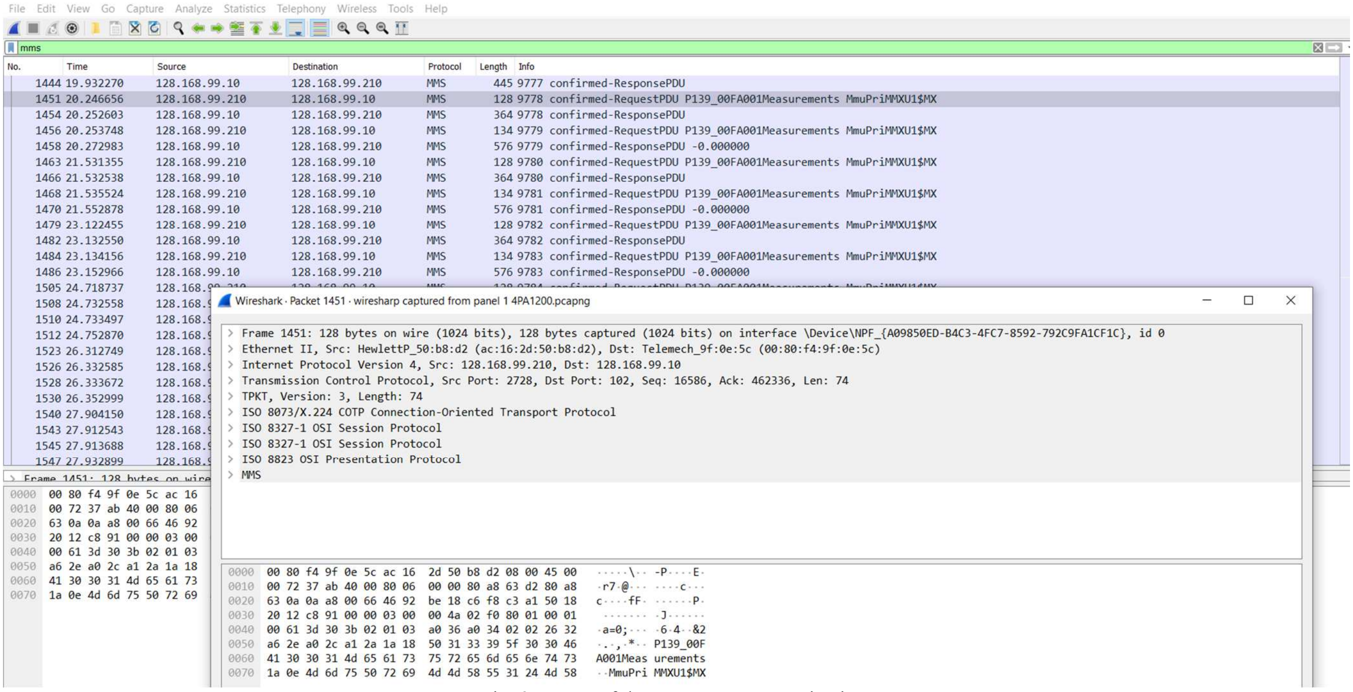

Fig. 3. Successful IED MMS communication.

- A lot of unnecessary signals (alarms and events) were filtered out to ensure that the operator can visualise important substation signals.
- Also, it was noted that it is important to get all system deliverables approved by the customer before testing to avoid many changes requested by customer during testing at no cost.

In terms of products, different vendors are still trying to block access of others into the IED being used. This is to ensure sales and competitiveness. Also, it is a way to make users go for the specific vendor products so as to avoid interoperability challenges. Finally, the IEC 61850 is beneficial to the user as a standard, but manufactures compliance certificates need to be considered, by undergoing the interoperability tests that are necessary to improve substation automation system.

V. Conclusion

This paper presented an integrated monitoring and control system architecture for 11kV substations. The proposed architecture is based on the IEC 61850 standard and is designed to provide a secure and reliable system for real-time monitoring and control of substations. The proposed architecture consists of three level: the station level, the unit level, and the bay level, and it is designed to provide real-time data acquisition and analysis, secure communication, fault detection and diagnosis capabilities. Furthermore, the architecture is designed to be scalable and flexible, allowing for the integration of additional components and equipment. In conclusion, it is found that legacy devices are still a big challenge; thus, they require complete replacement to ensure substation reliability and availability. Upon design configuration and testing of the proposed substation architecture (IMCSA), the user requirements are met by above 90%

References

[1] F. Lamnabhi-Lagarrigue, A. Annaswamy, S. Engell, A. Isaksson, P. Khargonekar, R. M. Murray, H. Nijmeijer, T. Samad, D. Tilbury, and P. Van den Hof, "Systems & control for the future of humanity, research agenda: Current and future roles, impact and grand challenges", Annual *Reviews in Control* 43, pp. 1-64, 2017.

[2] M. W. Hoffmann, S. Wildermuth, R. Gitzel, A. Boyaci, J. Gebhardt, H. Kaul, I. Amihai, B. Forg, M. Suriyah, T. Leibfried, and V. Stich, "Integration of novel sensors and machine learning for predictive maintenance in medium voltage switchgear to enable the energy and mobility revolutions", *Sensors* 20(7), pp. 2099, 2020.

[3] S. Koziel, P. Hilber, P. Westerlund, and E. Shayesteh. "Investments in data quality: Evaluating impacts of faulty data on asset management in power systems", *Applied Energy*, no. *281*, pp. 116057, 2021.

[4] S. Robson, "An integrated monitoring and communication device for use on 11 kV overhead lines", PhD diss., *Cardiff University*, 2012.

[5] H. Bevrani, M. Watanabe, and Y. Mitani. *Power system monitoring and control*. John Wiley & Sons, 2014.

[6] V. M. Igure, S. A. Laughter, and R. D. Williams. "Security issues in SCADA networks", *Computers & Security* 25(7), pp. 498-506, 2006.

[7] D. E. Okojie, A. A. Jimoh, H. Yskandar, and A. A. Yusuff, "Identification of vulnerable transmission lines in power system switching operations," *4th International Conference on Electric Power and Energy Conversion Systems (EPECS)*, pp. 1-5, 2015.

[8] F. de Souza Savian, J. C. M. Siluk, T. B. Garlet, F. M. do Nascimento, J. R. Pinheiro, and Z. Vale, "Non-technical losses: A systematic contemporary article review", *Renewable and Sustainable Energy Reviews* 147, 2021, pp. 111205.

[9] S. Sarangi, B. K. Sahu, and P. K. Rout, "Distributed generation hybrid AC/DC microgrid protection: A critical review on issues, strategies, and future directions", *International Journal of Energy Research* 44, 2020, no. 5, pp. 3347-3364.

[10] A. Waleed, U. S. Virk, M. T. Riaz, S. B. Mehmood, S. A. Muhammad Rameez, and A. R. Javed, "Effectiveness and comparison of digital substations over conventional substations", *Advances in Science, Technology and Engineering Systems Journal* 4(4), 431-439, 2019.

[11] T. E. Johnson, M. D. Hoefle, and A. K. Jain, "A hierarchical distributed architecture for monitoring and control of electric power substations," *Int. Journal of Elect Pwr & Eng Sys*, 2000, 22(7), pp. 639–643.

[12] IEC, IEC. "61850-1: Communication networks and systems in substations-Part 1: Introduction and overview." *IEC.–2003*.

[13] S. M. S. Hussain, T. S. Ustun, and A. Kalam, "A review of IEC 62351 security mechanisms for IEC 61850 message exchanges", *IEEE Transactions on Industrial Informatics* 16(9), pp. 5643-5654, 2019.

Modelling CSIR Long-term Electricity Least-cost Proposition

Unarine Bridget Mudau[1]
Department of Electrical & Electronic Engineering Science
University of Johannesburg (UJ)
Johannesburg, South Africa
unarine0958@gmail.com

Mamahloko Senatla[2]
Department of Electrical & Electronic Engineering Science
University of Pretoria (UP)
Pretoria, South Africa
msenatla@gmail.com

Prof. Antoine F. Mulaba-Bafubiandi[2]
Department of Mineral Processing and Technology Research Centre
University of Johannesburg
Johannesburg, South Africa
antoinemulaba1@gmail.com

Prof. Johan Meyer[2]
Department of Electrical & Electronic Engineering Science
University of Johannesburg (UJ)
Johannesburg, South Africa
Johanm@uj.ac.za

***Abstract*— The drive towards net-zero strategy has resulted in the global energy systems shifting from generating electricity from technologies which emit more emissions to renewable technologies that emit less emissions. The research question for this paper is "What is the least cost electricity supply technology mix for the Council of Scientific and Industrial Research (CSIR) main campus in the year 2040?". The bottom-up methodology was applied using PLEXOS-tool framework. Two scenarios were analyzed, Business as Usual (BAU) scenario, which considers the existing supply options to the CSIR, with City of Tshwane (CoT) supplying more than 80% of the electricity. No additional capacity investment was included on this scenario for the energy planning time horizon from 2018 to 2040. Least cost (LC) scenario, considers BAU scenario assumptions, however new supply options are added, and the model selects the least cost supply options. The additional capacity investment was solar photovoltaic, biogas and wind. The least cost scenario results, indicates that both wind and biogas were proven not to be financially viable for the CSIR to implement. The technology which was chosen to be financially viable for the CSIR was to add more rooftop solar PV to meet 50% of the CSIR energy demand. This will enable the CSIR to spend less, as the average cost of electricity is less than the average cost of electricity for BAU. However, the system indicates that a balanced energy mix is required to provide CSIR with the least cost electricity.**

Keywords—energy demand, least cost electricity, solar photovoltaic, wind,

I. Introduction

Unreliable electricity supply in South Africa (SA) is due to an increase in electricity demand and low Availability Factor (AF) of the generating units, which has impacted the economy negatively. This has open minded South Africans to transition from centralized energy systems to decentralized energy system to ensure electricity security and reliability is strengthened. The Department of Mineral Resources and Energy (DMRE) has gazetted the Integrated Resource Plan (IRP) in 2019 which stipulated the envisaged electricity demand and how it will be met by diversifying energy sources to provide least-cost option while minimizing negative emissions and water usage. ESKOM, which supplies 80% of South Africa's electricity, increases electricity tariffs annually after National Energy Regulator of South Africa (NERSA) has approved, unfortunately this has led to consumers feeling the pinch of the sky rocketing electricity price. This has led to residential and commercial customers installing the least cost electricity supply technologies such as solar systems to reduce reliance on the electricity from ESKOM or municipalities which comes with exorbitant electricity bill at the end of the month. This paper focuses on modelling electricity least cost options for CSIR Pretoria main campus in the year 2040.

II. Background

A. Research Site

The research was conducted at the CSIR Pretoria Campus, which is an organization which initiates directed, multidisciplinary research and technological innovation that contributes to the improved quality of life of South Africans. The organization was established in 1945 and is composed of 51 buildings which consist of offices, workshops, and laboratories.

B. Energy Systems

An energy systems planning is described as an energy network which include energy generation, storage, transportation, conversion, and supplying to the consumers[1] An energy systems planning can be conducted for short term, medium- and long-term period, depending on what the modeller is trying to reach. For this research, a long-term electricity planning was opted for since it was conducted from 2018 to 2040. There are different types of energy systems models and are classified as Integrated Assessment Models (IAM), Energy-economy models, Energy system planning models and Power system planning models. The IAM models are mostly used to assess the policies implemented by government to assist to mitigate the climate change. This model includes macro-economic interactions, demographics, and resource availability restrictions such as land and water usage as well as greenhouse gas emissions. The energy-economy model focusses on the interlinkages between the energy systems and the economic system. The model takes into consideration the impact of policies implemented on employment, trading, and welfare of the society. The energy system planning model covers the entire series from extracting the primary resources to refining, conversion and consuming of the energy. The model results give the policy makers to set the policy target, to assess the feasibility and boundary conditions to achieve policy targets and guide to develop the Research and Development(R&D) policy. The power system planning models restrict the scope of the electrical power sector such as including investments in generation capacities. This model can assist in decarbonizing the power system by determining the cost-optimal capacity mix to achieve certain policy targets[2].

C. Electricity energy system softwares

The long-term electricity capacity expansion models are used to analyse the least cost electricity supply mix from both non-renewable and renewable resources and storage[3].The energy systems models are defined as a model that has a mathematical representation of the energy system, which are used to quantify the impacts of the energy transition and plan potential pathways based on the country's, or individual needs[4].There has been an advancement in the energy system models due to electricity supply security and environmental reasons which led to decarbonizing of the energy system; however the major cause of the energy system advancement is the increase share of the decentralized and intermittent generation units from renewable energy sources[5]. There are open-source energy modelling tools and closed source tools which requires licenses. Several energy modelling tools that are mostly used are MARKAL, The Integrated MARKAL-EFOM System (TIMES), Open-Source Energy Modelling System (OSeMOSYS), PLEXOS Integrated Energy Model, BALMOREL, etc.

III. METHODOLOGY

The bottom-up methodology was applied using the PLEXOS-tool framework to determine the least cost electricity pathways for CSIR. The long-term expansion model in PLEXOS indicates the optimal combination of new electricity technology generation plant, economic generation retirements of the new plants and the existing electricity generation plants and the development of input scenarios to test different policy drivers.

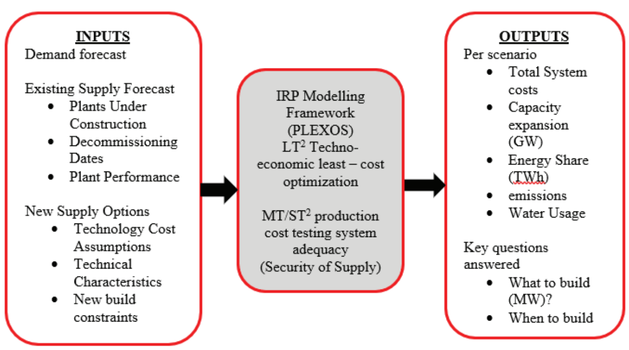

Figure 1 PLEXOS Framework[6]

The time horizon for this research was an hourly time horizon with the forecast from 2019 to 2040, using the year 2018 as a baseline before the COVID-19 pandemic. Therefore, the time horizon was longitudinal based on the Saunders research onion concept. The model optimizes the existing supply side generators and new build investments, and the model chooses the least-cost supply options.

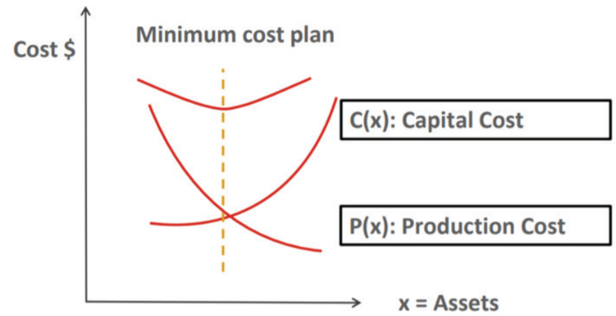

Figure 2 Least-cost plan[7]

The principle is that the production cost decreases with an increase in assets, whereas the capital cost increases with the increase in assets. Then the PLEXOS optimization tool generates the minimum cost plan.

A. Scenarios

A scenario in this context, is defined as a description of possible actions or events that could occur in future and they are used to tell a story. The scenarios were used in this research to assist to answer the research questions in the simplest manner. The following scenarios were analysed:

Business as Usual (BAU): The BAU scenario considers the existing supply options to the CSIR with the CoT supplying more than 80% of the electricity. No additional capacity investment was included on this scenario for the energy planning time horizon from 2018 to 2040. The results of the scenario included the installed generators capacity, total generation cost, CO2 emissions, and water consumption.

Least cost (LC): The Least cost scenario applied the BAU scenario assumptions, however new supply options are added, and the model selects the least cost supply options. The additional capacity investment was solar photovoltaic, biogas and wind. The results of the scenario included the installed generators capacity, total generation cost, CO2 emissions, and water consumption.

B. Model Exclusions

Power flows in the distribution and transmission network were excluded. The Network integration studies is broad, therefore, to limit the scope of the paper, it was excluded.

C. Model Inputs

The following input assumption parameters were deployed in the electricity planning model for all the scenarios: Demand forecast, Existing Technology , New supply technology cost, Technology learning rate, Economic parameters.

Demand Forecast

The CSIR demand data used for this research was for a year, from the 1st of January to the 31st of December 2018. A pre-COVID data was used as it reflects the business-as-usual (BAU) demand profile properly. Energy demand forecast predicts the amount of demand which will be consumed by the CSIR from 2019 to 2040. The energy demand used was the natural energy demand as it shows the true energy consumed by the CSIR, which is netted against energy from the PV plants. The top-down forecast method was used to forecast the electricity demand for the duration of the model. It was assumed that the electricity demand will reduce by 2% from 2019 to 2030, and from 2031 to 2040 the demand will be constant. The assumptions were based on the energy audit results (outside scope of work) which took place in 2017. The energy audit indicated that the CSIR can reduce the electricity demand by 30% by implementing the Demand Side Management (DSM) options which considers the behavioral measures, install the demand control module and building management systems (BMS) and the Energy Efficiency (EE) which caters for the installation of more efficiency lightning systems and insulation of geysers.

For sensitivity analysis the second demand forecasting was analysed. The second assumptions took into consideration the COVID-19 impact, where the CSIR demand dropped by 50% in the year 2020 to the end of 2022. However, from the year 2023 to 2040 it was assumed that the demand remained the same as in 2019, without any DSM and EE interventions.

Existing supply forecast

City of Tshwane (CoT) is still the main electricity supplier at the CSIR supplying more than 80% of the demand while the rest is supplied by solar Photovoltaic (PV). The existing solar photovoltaic capacity is shown in Table *1* below. The solar PV energy data used was for a reference year, from the 1st of January to the 31st of December 2018. The data format received from the energy monitoring systems was in 30 minutes intervals, therefore average energy was determined by transforming 30 minutes data into an hourly data format.

Table 1 Existing Supply Technologies

	Single-axis tracker	Dual-axis tracker	Building 17	PV phase 1
			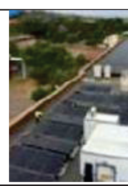	
Installed capacity (kWp)	558	202	250	911
LCOE (R/kWh)	0.83	1	0.87	0.77

Energy supply forecast predicts the amount of energy which will be generated by the current installed solar PV plants at the CSIR from 2019 to 2040. The commissioning and decommissioning data was considered during the forecast. For example, the single-axis solar plant was commissioned in 2015, with the expected life span of 25 years, therefore the last year of operation will be 2040 December. For the year 2041 going forward there won't be any energy generated by this plant. The same methodology applied to the rest of the plants.

Different modules have different annual degradation, expressed in percentage. Degradation is defined as an accurate quantification of a PV module power decline[8] The module degradation for single-axis tracker plant was 0.3%[9], dual-axis tracker was 0.7%[10], building 17 rooftop solar plant was 0.5%[11] and PV phase 1 rooftop solar plant was 0.7%[12]. The degradation for the solar PV plant module differs due to different types of modules and materials used to create a solar module. The degradation was included in the forecast to enhance the accuracy of the energy supply. Each plant module degradation was included while forecasting the energy supply output to the year 2040. Up to date, no additional solar PV capacity has been confirmed or in the pipeline, therefore the model included only the existing capacities.

New technology supply options

As much as there are different electricity supply technologies, only the technologies which can be installed at the CSIR campus were considered. The new technology options which were included into the model were solar PV technology, wind technology, biogas technology. Most of the operational model input values were influenced by the inhouse cost of the existing solar plants at the CSIR and the information from the literature review. Each technology had the following parameters: Rated capacity MW, Maximum Units Built, Total Overnight Cost R/KW (January 2018) , Lead-times and Project Schedule, years, Expense (% per year) , Fixed O&M Cost (R/KW/Year), Variable O&M Cost (R/MWh), Availability Factor %, Planned Outage %, Economic life year and the Capacity factor %.

Technology learning rate

Learning rate is defined as log-linear equation relating the unit cost of a technology to its cumulative installed capacity[13] The learning rate can also be referred as learning curve or experience curve. The Renewable Energy Independent Power Producer Procurement Programme (REIPPPP) has shown a significant cost reduction from round 1 to round 4 as shown in Figure *3*. According to the NREL Annual Technology Baseline (ATB) costs for solar PV and Wind are expected to decline globally due to declines in the value of system components such as solar panels, inverters, cables, racking, and turbines [14]

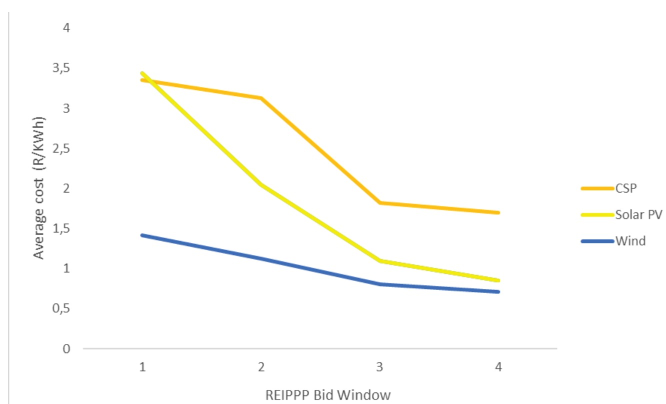

Figure 3 REIPPPP Bid window cost[15]

Economic parameters

The economic parameters used on this study were:

- The January 2018 exchange rate R15.80 to $1 (USD)
- All technology costs shown in Table 7 are in January 2018 Rands
- Post-tax real discount of 10%

Cost of Unserved Energy (COUE) of R87.85/kWh as per the National Energy Regulator of South Africa[16]. The COUE is referred as a The COUE is the value (in Rands per kWh) that is placed on a unit of energy not supplied due to an unplanned outage of short duration[17]. The inclusion of COUE ensures that an acceptable system reliability is achieved in the model as the model will ensure that this high cost is avoided by building additional capacity and dispatching the supply options optimally to meet the expected demand.

IV. RESULTS

A. Demand Forecasting

The CSIR natural demand profile for 2018 indicates that during December and January, the demand is low because of the holidays when the company closes, and most employees are on leave, and fewer laboratory experiments are being run. The natural demand profile in Figure *4* shows that, high demand season results in high natural demand.

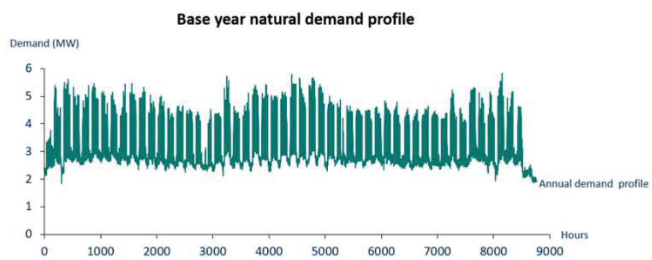

Figure 4 Base year natural demand

The energy modelling demand forecasting was categorized into two demands. The first demand takes into consideration the energy efficiency intervention, where the annual 2% demand reduction takes place until the year 2030 and the demand remains constant until the year 2040. The second demand takes into consideration the COVID-19 impact on the demand as well as no changes brought by energy efficiency intervention. The two demand forecasting profiles are shown in Figure *5*.

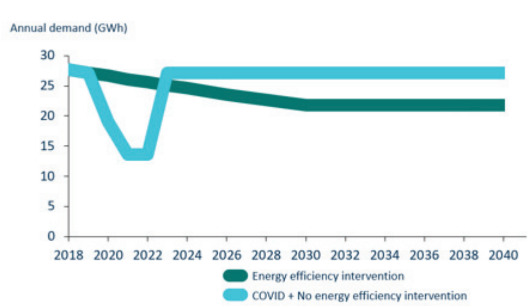

Figure 5 Forecasted Energy Demand

B. Business as Usual Scenario results

a) BAU installed capacity

The installed capacity for CoT and solar PV technologies remained the same throughout, as the scenario does not allow new investments.

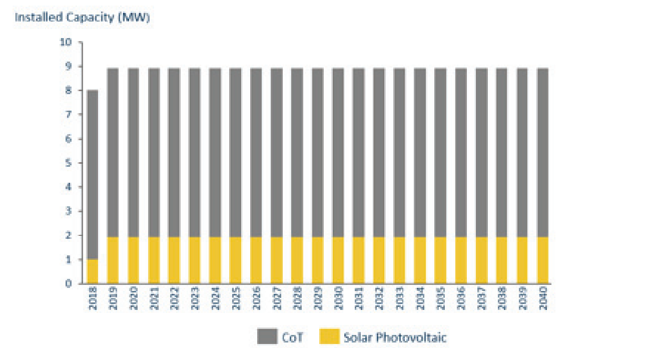

b) Energy Generation

For BAU CoT still supplies 80% of the demand as no new investments were made. However, for COVID-19 demand, CoT provided less than 50% of the usual demand, due to employees working from home as shown in Figure *6* and Figure *7*.

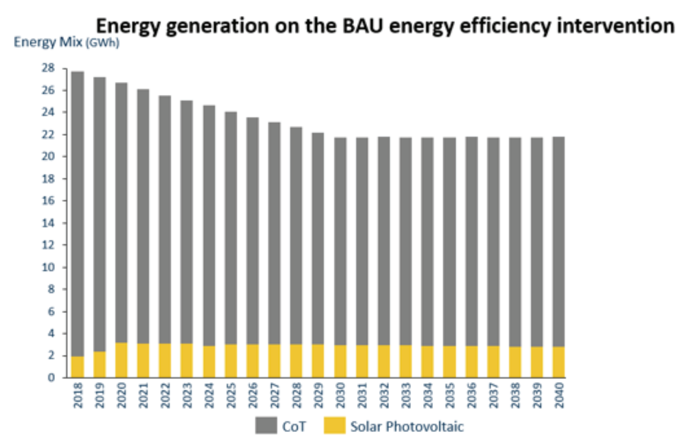

Figure 6 BAU Energy Generation with EE interventions\

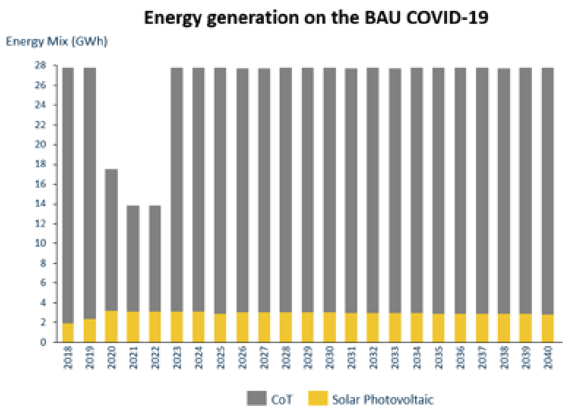

Figure 7 BAU Energy Generation with COVID-19

c) BAU Average electricity cost

The average electricity cost is expected to increase in the future. This is due to the annual electricity tariff imposed by the CoT on the first of July each year. The average electricity cost for the simulated time horizon is shown in Figure *8*.

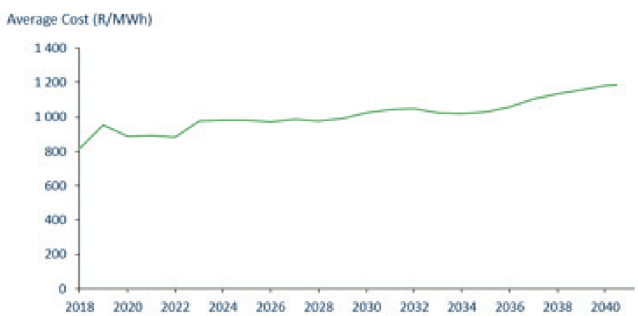

Figure 8 BAU Average electricity cost

d) BAU Net Present Value

The Net Present Value (NPV) of BAU COVID scenario is R263 406 247.05 with an annuity of R24 270 576.09. The Net Present Value of BAU energy efficiency scenario is R248 833 931.49 with an annuity of R22 927 864.98

C. Least cost Scenario result

a) Least Cost (LC) installed capacity

The least cost scenario has additional capacity technologies which can be installed at the CSIR as shown in Figure *9*. However, both wind and biogas technologies were not selected as one of the least cost options for the CSIR, this mainly because of their high CAPEX and OPEX cost compared to other technologies and the wind resource availability in Pretoria.

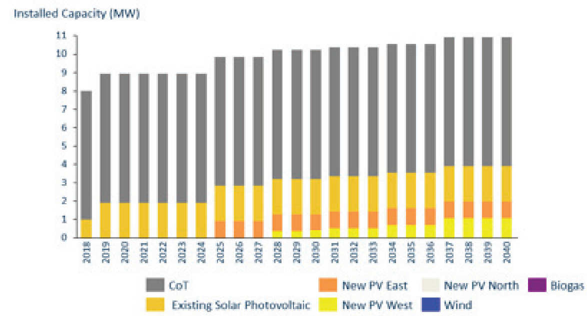

Figure 9 LC installed capacity

b) Energy Generation

The electricity generation from the solar photovoltaic technology supplies more than 50% of the demand by the year 2028. The contribution of electricity from CoT has decreased from 80% to 50% as shown in Figure 10 and Figure *11* due to new least cost technology investments.

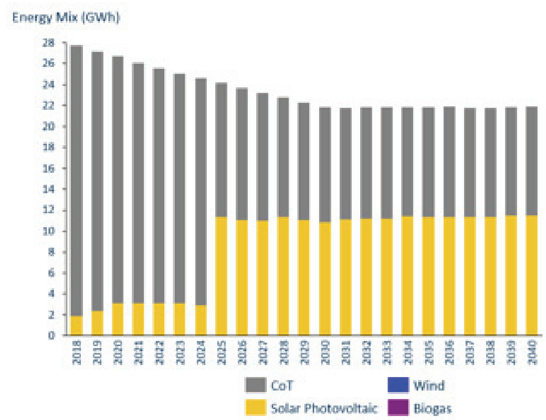

Figure 10 LC energy generation with EE interventions

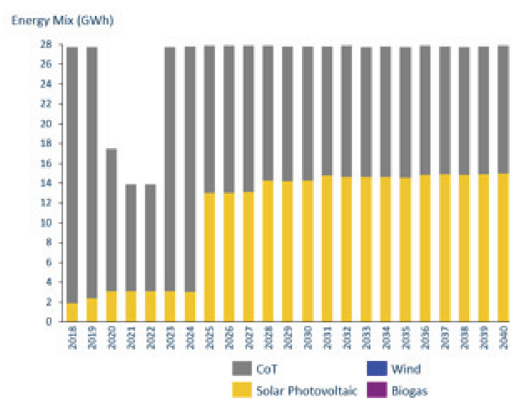

Figure 11 LC Energy generation with COVID-19 demand

c) LC Average Cost

The electricity average cost for least cost scenario does not increase as compared to the BAU scenario. This constant average cost indicated in Figure *12* is due to the penetration of photovoltaic technology which has a low generation cost.

Figure 12 LC Average electricity cost

d) LC Net Present Value

The LC COVID-19 scenario Net Present Value is R202 566 727.23 with an annuity of R18 664 747.78. However, the LC EE scenario has Net Present Value is R196 187 457.4 with an annuity of R18 076 954.00.

CONLCUSION

The deployment of renewable energy sources to the current traditional systems requires a significant energy planning to ensure the energy demand is met. The energy model results for both least cost and business usual has significant differences. The business-as-usual scenario results shows that if CSIR continues with the current systems, the average cost of electricity will increase, as an impact of annual tariffs increase.

The least cost scenario results, indicates that both wind and biogas were proven not to be financially viable for the CSIR to implement. The technology which was chosen to be financially viable for the CSIR was to add more rooftop solar PV of east - west facing to meet 50% of the CSIR energy demand. This will enable the CSIR to spend less, as the average cost of electricity is less than the average cost of electricity for BAU scenario.

The research question, “What is the least cost electricity supply technology mix for CSIR main campus in the year 2040?” has been answered. In conclusion, the combination of electricity from Tshwane municipality and solar Photovoltaic technologies are the least cost energy mix for the CSIR.

ACKNOWLEDGMENT

I would like to acknowledge my former Research Group Leader (RGL) Dr. Brian North from the CSIR for providing consent to conduct this research, as part of my thesis at the University of Johannesburg.

REFERENCES

[1] Y. N. D. P. Meisam Farrokhifar, “Energy systems planning: A survey on models for integrated power and natural gas networks coordination,” *ELSEVIER Applied Energy*, 2020.

[2] K. Poncelet, “Long-term energy-system optimization models,” no. January, 2018.

[3] W. Is and C. Expansion, “Power System Planning : Advancements in Capacity Expansion Modeling,” 2021.

[4] M. Chang *et al.*, “Trends in tools and approaches for modelling the energy transition,” *Appl Energy*, vol. 290, 2021, doi: 10.1016/j.apenergy.2021.116731.

[5] F. Wiese, S. Hilpert, C. Kaldemeyer, and G. Pleßmann, “A qualitative evaluation approach for energy system modelling frameworks,” *Energy Sustain Soc*, vol. 8, no. 1, 2018, doi: 10.1186/s13705-018-0154-3.

[6] J. Wright and J. Calitz, “Systems analysis to support increasingly ambitious CO2 emissions scenarios in the South African electricity system,” *Tech. Rep.*, vol. 27, no. July, p. 129, 2020, [Online]. Available: https://naturaljustice.org/wp-content/uploads/2021/05/FA-13-CSIR-Meridian-Report.pdf

[7] R. de Janeiro, “PLEXOS for modeling hydrothermal systems with strong presence of renewable and pumped storage plants . Table of Contents,” no. August, 2019.

[8] D. C. Jordan and S. R. Kurtz, “Photovoltaic degradation rates - An Analytical Review,” *Progress in Photovoltaics: Research and Applications*, vol. 21, no. 1, pp. 12–29, 2013, doi: 10.1002/pip.1182.

[9] A. Byd, “P6C-30-SERIES-4BB P6C-30-SERIES-4BB”, [Online]. Available: https://sg.byd.com/wp-content/uploads/2017/10/combine-4-1.pdf

[10] T. U. v Power, “Sw 285 Mono,” pp. 3–4, [Online]. Available: https://rexel-cdn.com/Products/SolarWorld/SW285M33MM.pdf?i=6ACC4EE1-81A5-4948-A26F-676B92BA3CAC

[11] M. Module, “Dual Glass 60-Cell Module,” 1997, [Online]. Available: https://static.trinasolar.com/sites/default/files/PS-M-0472 B Datasheet_Duomax M Plus_DEG5.XX%28II%29_US_Jan2018_TS4_0.pdf

[12] ArtSolar, “ArtsolarModule Warranty.” https://artsolar.net/linear-output-guarantee/

[13] E. S. Rubin, I. M. L. Azevedo, P. Jaramillo, and S. Yeh, “A review of learning rates for electricity supply technologies,” *Energy Policy*, vol. 86, pp. 198–218, 2015, doi: 10.1016/j.enpol.2015.06.011.

[14] NREL, “Annual Technology Baseline,” 2021. https://atb.nrel.gov/electricity/2021/commercial_pv

[15] M. D. Sklar-Chik, “System Cost of Energy Generation Scenarios for South Africa: Understanding the real cost of integrating energy generation technologies,” no. March, p. 130, 2017, [Online]. Available: scholar.sun.ac.za

[16] A. Preprint and M. Eje-, “Cost of Unserved Energy NERSA,” no. December, pp. 1–18, 2008.

[17] Department of Energy, “Cost of Unserved Energy (COUE) - IRP 2010 Input Parameter information sheet (Supply input),” *Department of Energy SA*, p. 3, 2010.

2023 SAUPEC Conference, Johannesburg, South Africa, January 24-26, 2023

Network Analysis and Compensation of Underground Cable Capacitive Effects

Hilary K. Chisepo
Department of Electrical Engineering
University of Cape Town
Cape Town, South Africa
hilary.chisepo@uct.ac.za

C. Trevor Gaunt
Department of Electrical Engineering
University of Cape Town
Cape Town, South Africa
ct.gaunt@uct.ac.za

***Abstract*— Various reports of problems associated with cable networks, light loads, and voltage control have identified different mechanisms of the disturbances and different solutions. The underlying problem appears to be associated with the understanding of capacitive reactive power. We have studied the problems using time-domain simulation and a physics-consistent analytical power theory applied to a representative model of the distribution network. This paper tests two compensation approaches: conventional inverter-based volt-var control (VVC), and control according to the general power theory (GPT). The results show that lightly loaded dense cable networks can cause unwanted network conditions consistent with reports from the literature. The GPT-based compensation reduced delivery loss and non-active backfeeding currents to a minimum, thus improving the performance of the network. The study gives novel insight into the modeling of such power systems.**

Keywords*— *distribution networks, underground cables, general power theory, power system, capacitive current

I. Introduction

Changes in the way that power is delivered and in the dominant types of loads in residential and commercial sectors affect the performance of distribution networks. These changes include the increased integration of inverter-based renewable energy sources as distributed generators (DG), and the extensive use of underground (UG) cables [1], [2].

Factors influencing the increased installation of UG cables and/or the replacement of overhead (OH) lines with cables include the need for increased reliability, such as under extreme weather conditions that have been experienced in Europe [3], [4], [5]. After Sweden's Gudrun storm in 2005, regulation changes resulted in an increase in total cable installation, with improved reliability performance [3]. However, potential problems are associated with the increased use of UG cables. A notable decline in the export of reactive power from the transmission network (TN) to the distribution networks (DNs) has been reported in the United Kingdom during minimum load, resulting in voltage rise excursions caused by UG cable capacitance. Even though shunt reactors have been used to minimize the voltage rise, "there is a need to understand the main factors [of voltage rise due to cables] and their trends" and investigate other cost-effective solutions to offset the high cost of reactors [1].

In another analysis [6], heavily meshed UG cable networks are identified as the cause of capacitive backfeeding currents at transmission and distribution (T-D) interfaces. (This Ferranti effect occurs because lightly loaded cables behave like capacitive loads.) Overvoltage mitigation was performed using either shunt reactors or zig-zag grounding transformers. Others investigated the detection of capacitive backfeeding currents initiated by lightly loaded cables using directional fault passage relays [7]. A recent study reported Dutch distribution networks were experiencing reverse flows of reactive power at T-D interfaces [8]. Photovoltaic (PV) inverter volt-var control (VVC) was used for compensation.

While some studies attribute the adverse capacitive effects at T-D interfaces to the increased use of nonlinear and/or less inductive loads [8], consistent evidence from the literature points to UG cables as the source of the problem [1], [6], [7] Limited studies, however, investigate from this point of view and even fewer studies focus on cost-effective compensation approaches different from traditional shunt compensation requiring significant capital investment.

With increasing network cable installation and capacitive effects at T-D interfaces [1], [5], it is crucial to investigate low-cost compensation strategies, assess the network losses due to capacitive backfeeding, and compare compensation approaches to the problem.

This study, therefore, analyzes a physically representative MV network model with unbalance and harmonics adapted from [9] with a lightly loaded heavily meshed cable network typical of a European urban area. Network compensation with the new general power theory (GPT) [10] is compared against inverter-based VVC.

The rest of the paper is organized as follows. Section II gives a background to the modeling considerations and the two approaches to be compared. Section III describes the test circuits used to assess the capacitive effects of UG cables on network performance and the time domain simulation protocol implemented using an electromagnetic transients (EMT) program. The results are presented in Section IV and discussed in Section V before some conclusions are drawn.

II. Background

A. *Inverter volt-var control (VVC)*

VVC implemented by PV inverters is controlled by a custom curve with capacitive and inductive regions to compensate for low voltage levels and voltage rise, respectively [11]. Different approaches to VVC are described in an early study by [12] using OpenDSS software highlighting the promising outlook on how smart inverters can provide voltage support for voltage variations at a point of connection (PoC).

More recently [13] further analysis using the same software revealed that PV inverter VVC capability is limited by inverter kVA capacity which can be supplemented with energy storage (batteries) if available. Another study using multiple inverters in a grid indicated that there could be 'harmful interactions' between inverters' VVC controllers due to 'excessive reactive power cycling' [14]. In the same study, however, physical measurements with power hardware-in-the-loop (PHIL) experiments did not replicate the 'harmful interactions' predicted by the simulation modeling.

In this study, VVC will be implemented by modeling the inductive region of the VVC curve [11], [13] to clamp voltage rise. Even though PV inverters are limited by their kVA capacity, it is assumed in the modeling that sufficient energy storage is available to supplement the VVC capacity up to the desired level as described in [10].

B. *The general power theory (GPT)*

The development and application of the GPT were described in [9]. Unlike, conventional power theory e.g., the *pq* theory [15], the formulation of the GPT [10] does not identify any parameter for reactive power Q (an adjacent comparative analysis also highlights the differences between these approaches [16]). This is because the GPT is based on linear vector algebra and its objective function brings delivery loss to a minimum. The absence of Q was an unexpected result in the derivation of GPT in vector space. It has to do with orthogonality with Q, i.e, identifying that the dot product of two vectors is zero means that treating voltages and currents as vectors $\boldsymbol{V}$ and $\boldsymbol{I}$, the dot product between them is zero. This implies that Q is an arbitrarily scaled ($\sin\varphi$) zero-valued parameter; an approximation that can sometimes give inconsistent results, especially in complex practical power systems (*vide supra* subsection A: *Inverter volt-var control* – conflicting results between simulated VVC and physical measurements with PHIL [14]).

The GPT uses the principle of network equivalence (through the network Thévenin equivalent) at a PoC and compensates the network by adjusting the voltages and currents and their harmonics there to achieve optimum power delivery, i.e., keeping delivery losses at a minimum. First, an optimal active current vector $\boldsymbol{I}_{A(m,h)}$ in each wire m and for harmonic h delivering real power to a load is identified. The optimal compensation currents to be injected at the PoC are then computed by subtracting $\boldsymbol{I}_{A(m,h)}$ from the current source vector $\boldsymbol{I}_{S(m,h)}$ as depicted in (1) [10]:

$$\boldsymbol{I}_{C(m,h)} = \boldsymbol{I}_{S(m,h)} - \boldsymbol{I}_{A(m,h)} \tag{1}$$

III. SIMULATION PROTOCOL

Time domain simulations were performed in EMT-based MATLAB/Simulink. First, a description of the network is given after which the protocol for a comparative analysis with GPT-controlled compensation and VVC is described.

A. *Medium Voltage (MV) test network*

The test network in Fig. 1 is adapted from the three-phase three-wire (3p3w) circuit with unbalance and distortion used to demonstrate the application of the GPT in [9]. The overhead (OH) lines were replaced by 185 mm^2 three-core cross-linked polyethylene (XLPE) underground cables 10 km long. To increase the cable capacity, three cables were connected in parallel in each phase. In this paper, these will be referred to as 10 km 3*3c185mm2CuXLPE. A 2000 kW variable speed drive (VSD) at Bus 2 represents a typical industrial area activity. It has an impedance factor (IF) of 0.85 (IF is a physical representation of power factor) and its controller produces some voltage and current harmonics at the PoC. There is a single-phase (1ph) unbalancing load of 300 kW @ 0.95 IF across the red and blue phases.

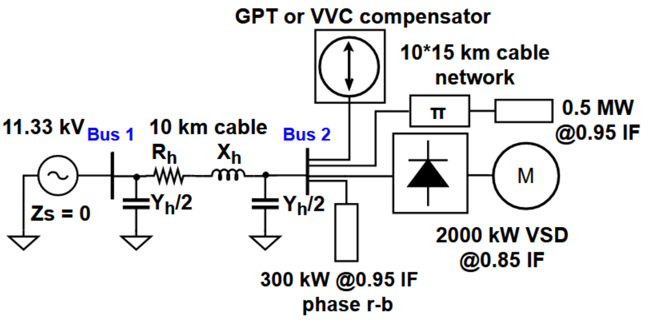

Fig. 1 A simplified diagram of the test network. The full load ratings of the VSD and 1ph loads are shown. The 10*15 km cable network represents an urban area with a lightly loaded heavily meshed cable network.

At the same PoC of Bus 2 is a connection to a dense cable network representing a modern European urban area. The network is represented by ten 15 km long cables in parallel supplying a very light total load of 0.5 MW @ 0.95 pf. The full load capacity of this cable network could be 20 MW. The cables in this network will be referred to as 10*15 km 3*3c35mm2CuXLPE in this study. All the cables in the simulations were modeled as a π-model of a transmission line with uniformly distributed R, L, and C components. The frequency dependency of the cables in Fig. 1 is represented by R_h, X_h, and $Y_h/2$ where R is the resistance corrected to a 50°C operating temperature, X is the inductive reactance, Y is the capacitive admittance, and h is the harmonic frequency.

Even though all the physical properties of the cables were considered in modeling, i.e., cable length, conductor diameter, input insulation dielectric constant, insulation sheath thickness, etc., only the key parameters are given in Table I.

TABLE I. CABLE PHYSICAL PROPERTIES FOR 3CORE XLPE

CABLE SIZE (mm^2)	35	185
OPERATING VOLTAGE (kV)	11	11
TOTAL CAPACITANCE (μF/km)	0.15085	0.27948
CHARGING CURRENT (A)	0.3008	0.5573
INDUCTANCE (mH/km)	0.41473	0.3185
AC RESISTANCE @50°C (Ω)	0.76434	0.14638
CONDUCTOR X/R RATIO	0.17	0.68
SURGE IMPEDANCE (Ω)	52.43	33.76

B. *Network modeling*

Using the setup shown in Fig. 1, the objectives of the simulation protocol were to:

1. determine the capacitive effects of the UG cables with the VSD and the 1ph loads at full load (FL)
2. determine the effect of GPT-controlled compensation
3. determine the effect of VVC
4. compare the compensation performed by 2 and 3

Steps 1 – 4 were repeated for a light load (LL) condition represented by the 0.5 MW on the urban network and 50% of the of the VSD and 1ph load at Bus 2.

The modeling followed the protocol in [9] whereby a simulation of the model in Fig. 1 is run in Simulink to determine the set of harmonics contributing the highest harmonic power injection at the PoC. After that, using the frequency-dependent Thévenin equivalent impedance ($\boldsymbol{Z_{th(m,h)}}$) of the 10 km delivery cable and the measured complex root mean square (CRMS) $\boldsymbol{V}$ and $\boldsymbol{I}$ at each harmonic, the GPT compensation currents $\boldsymbol{I_{C(m,h)}}$ were calculated. Some key network performance parameters were recorded before and after GPT-controlled compensation. The compensation was performed by injecting $\boldsymbol{I_{C(m,h)}}$ at the PoC.

Inverter VVC was implemented by simulating the inductive region of the custom curve described in [10] without any restrictions on inverter kVA capacity.

IV. Results and Discussion

A. Cable modeling

The cable modeling in Simulink was validated by comparing open circuit tests against the charging currents of the 35 mm^2 and 185 mm^2 cables calculated in Table I. The calculated and modeled values matched with a percentage difference of only 0.058% and 0.057%, respectively. The accurate modeling of the total charging current of a cable is important because it determines the extent to which the Ferranti effect occurs in the networks [5].

It is noteworthy that accurate modeling of the cables was achieved using elemental models with explicit R, L, and C (2*Y/2 as shown in Fig. 1) elements uniformly distributed over the cable length. Surprisingly, the inherent Simulink π-model of a cable could not be utilized because it exhibited errors in the total capacitive charging currents and significantly underestimated the actual network losses. It exhibited even greater errors when determining its frequency-dependent $\boldsymbol{Z_{th(m,h)}}$ (an essential input into the GPT algorithm) with Simulink's impedance measurement tool. Therefore, the $\boldsymbol{Z_{th(m,h)}}$ of the elemental 10 km 3*3c185mm2CuXLPE model was performed analytically through network reduction.

B. Delivery losses with VSD and 1ph loads at full load (FL)

Fast Fourier Transform (FTT) analysis of $\boldsymbol{V}$ and $\boldsymbol{I}$ up to 1 kHz at the PoC (Bus 2) resulted in the highest harmonic power contributions being h = 5, 7, 11, and 13. Higher harmonic orders became increasingly insignificant and so they could be neglected. The first set of experiments was performed at FL for the VSD and 1ph loads in the presence of the lightly loaded 10*15 km 3*3c35mm2CuXLPE network. Table II shows the results of the simulation modeling.

TABLE II. Full Load Mv Network Results

EXP.	P_del loss(kW)	Loss %redxn	Vbus2 (pu)	%THDv	%THDi
Base case	73.54	-	1.0243	0.55	6.33
GPT comp.	55.19	24.95	1.0198	0.68	9.23
VVC comp.	58.91	19.89	1.0198	0.55	7.16

From Table II, the base case is the state of the network in Fig. 1 without any compensation. P_del loss represents the system delivery loss in kW and as a percentage in loss reduction from the base case. Vbus2 is the pu voltage of the highest line-to-line voltage at the PoC in pu. %THDv,i are the average voltage and current total harmonic distortion (THD) at the PoC. The voltage harmonics at the PoC are negligible and the current (THD) is 6.33%. When the GPT-controlled compensation currents are injected (see Fig. 2), delivery losses are reduced by 24.95% and the terminal voltage decreases because the backfeeding capacitive currents lifting the voltage are offset.

Using VVC to achieve the same terminal voltage that was achieved by the GPT after compensation (1.0198 pu) yields a smaller loss reduction of 19.89%. It is important to note that the $\boldsymbol{Z_{th(m,h)}}$ of the delivery cable was calculated analytically offline. During the simulation, capacitance-induced voltage rise from the meshed UG cable network upstream may change the offline $\boldsymbol{Z_{th(m,h)}}$ but only very slightly.

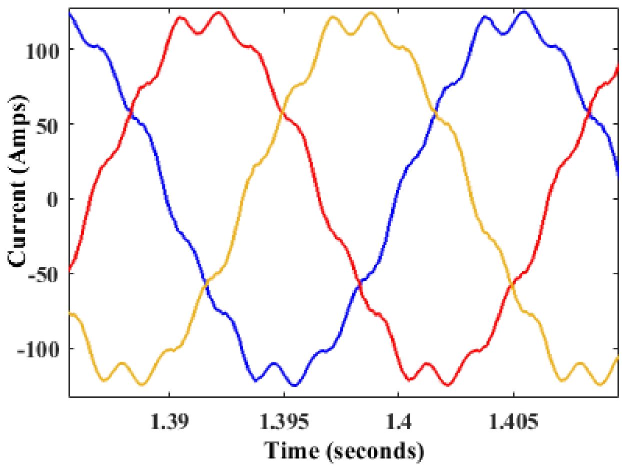

Fig. 2 GPT-calculated compensation currents injected at Bus 2 for the FL network model.

After GPT compensation, the voltage harmonics were still negligible, but the current THD increased to 9.23%. Compensation with VVC to the same level of PoC terminal voltage as the one achieved by the GPT also yields a reduction in delivery but to a lesser extent as can be seen in Table II. A similar trend is observable with voltage and current THD after compensation.

C. Delivery losses with VSD and 1ph loads at 50% of FL

Next, a light load (LL) condition was investigated under the same network conditions of the lightly loaded 10*15 km 3*3c35mm2CuXLPE network. Fig. 3 shows the GPT-calculated compensation currents performed with (1).

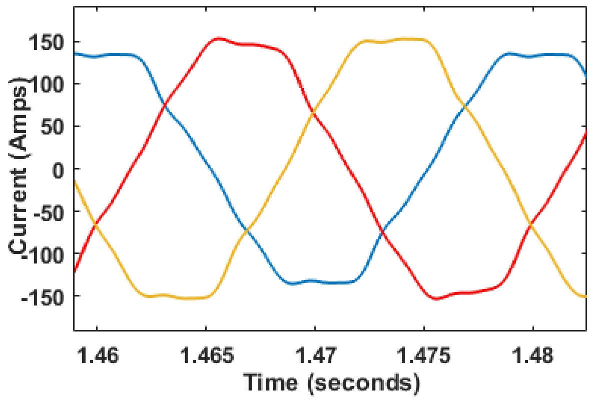

Fig. 4 GPT-calculated compensation currents injected at Bus 2 for LL network model.

TABLE III. MV NETWORK RESULTS WITH LL = 50% OF FL

EXP.	P_del loss(kW)	Loss %redxn	Vbus2 (pu)	%THDv	%THDi
Base case	61.72	-	1.0300	0.2	3.8
GPT comp.	22.35	63.78	1.0243	0.32	6.24
VVC comp.	37.38	39.44	1.0243	0.26	6.06

From Table II, comparing the two approaches to compensation against the base case (no GPT or VVC compensation), the GPT reduces delivery losses significantly better than VVC at same voltage level that was reached by the GPT (1.0243 pu). Both compensation techniques appear to increase current THD after compensation but are measured on different bases.

V. DISCUSSION

There is a need to mitigate the capacitive effects caused by UG cables with cost-effective approaches different from traditional ancillary equipment which comes at a high cost [1], [8]. This paper has applied two converter-based approaches to compensate for unwanted conditions caused by the extensive use of cables in distribution networks. The first is a novel power theory that works on the principle of minimum power delivery loss by optimal compensation at a PoC [9], [10], [16], [17]. The second is a widely used volt-var control function in inverters [11], [12], [13], [14].

It is evident from the results that the GPT approach reduces delivery loss to a minimum by eliminating the capacitive non-active currents which do not deliver any real power to the load but incur losses. Even though loss reduction is optimized by the GPT, current harmonic distortion appears to increase at the PoC after compensation. This is caused by the system having multiple voltage sources, i.e., the generator at Bus 1 and the capacitive generator at Bus 2 fed by a dense UG network. This highlights the operation of the GPT when different sources are applied to the network. For instance, when the GPT is applied to a network with a linear, balanced source it results in optimum loss reduction and total elimination of all voltage and current harmonics [9]. Another scenario is when the GPT is applied to a network with a nonlinear supply, like a transformer experiencing part-wave saturation due to geomagnetically induced currents (GIC) [17]. After compensation, the voltage drop caused by the GIC is removed and the new terminal voltage sits slightly above the knee-point of the transformer B-H characteristic causing a slight increase in current THD.

In this study, the GPT is applied to a non-ideal composite capacitive voltage source and a nonlinear unbalanced load. A possible solution is the use of harmonic filters at the PoC to stay within the recommended harmonic limits for MV networks according to IEEE 519-2022 [18] where necessary.

VI. CONCLUSIONS

The performance of MV networks with already existing non-ideal conditions of unbalance and harmonic distortion can be detrimentally affected by a dense network of lightly loaded UG cables. As an alternative to traditional shunt compensation with reactors, inverter-based compensation can be used.

The new general power theory not only eliminates the non-active capacitive backfeeding currents but also reduces delivery losses to a minimum, with technical and financial benefits. VVC can clamp the voltage rise caused by cables, but this comes at the cost of more delivery losses in the network – a parameter that is seldom analyzed in mitigation studies.

This research shows that GPT-controlled compensation of capacitive load currents can provide more efficient, more stable power systems under conditions of distortion and unbalance that exceed the capabilities of most other power theories. Several other network models have been tested for compensation with the GPT [9], [16], [17] with consistent results.

A GPT-controlled three-level inverter was proposed [19]. Future work involves physical experiments in a laboratory setting with control and hardware in the loop.

ACKNOWLEDGMENT

The research was supported in part by a grant from the Open Philanthropy Project for GIC research.

REFERENCES

[1] C. G. Kaloudas, L. F. Ochoa, B. Marshall, S. Majithia, and I. Fletcher, “Assessing the future trends of reactive power demand of distribution networks,” IEEE Trans. Power Syst., vol. 32, no. 6, pp. 4278–4288, 2017. DOI: https://doi.org/10.1109/TPWRS.2017.2665562

[2] F. Jiang, Z. Zhang, T. Cao, B. Hu, Z. Piao, “Impact of distributed generation on voltage profile and losses of distribution systems,” *in IEEE 32nd Chinese Control Conf*., Xi’an. 2013.

[3] P. Bengtsson, L. Persson, K. Oberger, & J. Hasselstrom, “Reliability-based planning in rural areas; goals, methods prioritization, and follow-up at Fortum Distribution,” *in 20th Int’l CIRED*, Prague. 2009.

[4] G. Kjølle, R. H. Kyte, M. Tapper, & K. Hänninen, “Major storms – main causes, consequences and crisis management,” *in 22nd Int’l CIRED*, Stockholm. 2013.

[5] O. Papailiou. *Springer Handbook of Power Systems*, 1st ed. Singapore: Springer, 2021, pp 770-801. DOI: https://doi.org/10.1007/978-981-32-9938-2

[6] R. Salcedo, X. Ran, F. de León, D. Czarkowski, & V. Spista, “Long duration overvoltages due to current backfeeding in secondary networks,” IEEE Trans. Pow. Del., vol 28. no. 4, pp. 2500-2508, October 2013. DOI: https://doi.org/10.1109/TPWRD.2013.2273897

[7] C. González de Miguel, T. De Rybel, & J. Driesen, “Enhancing reliability in medium voltage distribution networks with directional fault passage indicators without voltage sensors,” *in Int’l Elec. Eng. Conf. for Young Research*, Cluj-Napoca. 2013.

[8] A. H. Javed, J. G. H. Slootweg, P. H. Nguyen, & J Morren, "Issues of capacitive reactive power flow in electricity networks," *in IEEE UPEC*, Istanbul. 2022. *In press.*

[9] H. K. Chisepo, C. T. Gaunt, & P. Jankee, "Applying and comparing the general power theory compensation for unbalance and harmonics," *in IEEE UPEC,* Istanbul. 2022. *In press.*

[10] M. Malengret & C. T. Gaunt, "Active currents, power factor, and apparent power for practical power delivery systems," IEEE Access, vol. 8, 2020, pp. 133095-133113. DOI: https://doi.org/10.1109/ACCESS.2020.3010638

[11] L. C. Ribeiro Jnr., F. L. Vieira, B. D. Bonatto, A. C. Z. de Souza, & P. F. Ribeiro, *Decision-making applications in modern power systems, Chapter 5: Modeling and simulation of active electrical distribution systems using the OpenDSS*, Elsevier, 2020, pp. 133-134. DOI:

[12] J. W. Smith, W. Sunderman, R. Duga, & B. Seal, "Smart inverter vol-var control functions for high penetration of PV on distribution systems, in *IEEE PES/PSCE*, Phoenix. 2011. DOI: https://doi.org/10.1109/PSCE.2011.5772598

[13] L. C. Ribeiro Jnr., J. P. O. S Minami, B. D. Bonatto, P. F. Ribeiro, & A. C. Z. de Souza, "Voltage control simulations in distribution systems with high penetration of PVs using the OpenDSS," *in 2018 Simposio Brasileiro de Sistemas Eletricos (SBSE)*, Niteroi. 2018. DOI: https://doi.org/10.1109/SBSE.2018.8395639

[14] S. Chakraborty, A. Hoke, & B. Lundstrom, "Evaluation of multiple inverter volt-var control interactions with realistic grid impedances," in *IEEE PES Meeting*, Denver. 2015. DOI: https://doi.org/10.1109/PESGM.2015.7285795

[15] H. Akagi, S. Ogasawara, & H. Kim, "The theory of instantaneous power in three-phase and four-wire systems: a comprehensive approach," in IEEE IAS, Phoenix. 1999. DOI: https://doi.org/10.1109/IAS.1999.799991

[16] P. Jankee, D. T. O. Oyedokun, & H. K. Chisepo, "Network unbalance compensation: conventional pq theory vs the general power theory," *in IEEE PES/IAS PowerAfrica*, Kigali. 2022. DOI: https://doi.org/10.1109/PowerAfrica53997.2022.9905291

[17] H. K. Chisepo & C. T. Gaunt, "Towards asymmetrical modelling of voltage stability in the presence of GICs," *in IEEE PES/IAS PowerAfrica,* Kigali. 2022. DOI: https://doi.org/10.1109/PowerAfrica53997.2022.9905396

[18] *IEEE Std 519-2022*, "Standard for harmonic control in eletric power systems, Institute of electrical and electronics engineeris, Inc. 2022.

[19] P. Jankee, M. Malengret, D. T. O. Oyedokun, & C. T. Gaunt, "An inverter controlled by the general power theory for power quality improvement," in *IEEE SAUPEC*, Durban. 2022. DOI: https://doi.org/10.1109/SAUPEC55179.2022.9730729

Online Education Poverty: A Multidimensional Approach

Mohammed Raees Dangor
School of Electrical & Information Engineering
University of the Witwatersrand, Johannesburg
South Africa
ORCID 0000-0003-4478-046X

Estelle Trengove
School of Electrical & Information Engineering
University of the Witwatersrand, Johannesburg
South Africa
ORCID 0000-0002-1343-1753

Martin Bekker
School of Electrical & Information Engineering
University of the Witwatersrand, Johannesburg
South Africa
ORCID 0000-0001-8766-937X

***Abstract*—The COVID-19 pandemic prompted universities to shift to emergency remote teaching. This shift foregrounded previously underappreciated dimensions of poverty. Poverty is a complex and multidimensional phenomenon. When considering the needs of university students, conceptions and measures of poverty should include the lack of the resources required to access online education. This research seeks to create a multidimensional poverty index, that can be used to assess the poverty of students with respect to online education. This index will be useful when planning interventions that can assist students. The index is created by combining the well-known Alkire-Foster method with concepts emanating from the digital divide, energy poverty and educational technology. The work will focus on students at the University of the Witwatersrand in South Africa.**

***Keywords*—energy, education, poverty index, emergency remote teaching**

I. Introduction

The COVID-19 pandemic forced universities to shift to emergency remote teaching (ERT). It soon became evident that many students did not have appropriate access to ERT by virtue of their living conditions and access to amenities [1]. This phenomenon can be described as online education poverty. The aim of this research is to create an index that can measure online education poverty. It will be possible for policymakers to use the index as a tool to decide on interventions that could alleviate online education poverty to ensure that all students have fair and equal access.

Poverty measures are necessary to aid the efforts to reduce the effects of poverty, by providing information that is used to better understand the multidimensionality of the phenomenon. A poverty measure can identify the deprivations that are being suffered, the extent to which they are suffered and by whom. This information gives direction for what resources need to go where and on whom efforts need to be focused. The progress and effectiveness of policy aimed at reducing poverty can also be determined by measuring poverty over time. A poverty measure thus paints a broad picture that gives insight into the magnitude of poverty and how it varies and affects different groups over time. While the proposed poverty measure would have been invaluable during the shift to ERT, there is increasing evidence that an increasing amount of higher education content will remain online in future as universities start to adopt blended learning approaches, so this work will have importance well beyond times of crisis.

Section II gives a background on online education which expands on the resources required to access online education; Section III discusses the Alkire-Foster methodology and lists the methodological steps; Section IV discusses the choice of variables for the proposed index.

II. Online Education

This research investigates the dimensions of poverty that create a barrier to accessing online education. Online education is an umbrella term used to describe any education that uses an online format such as ERT or online learning. Emergency remote teaching was a temporary shift of instructional delivery to an online format due to crisis circumstances. This is in contrast to online learning which is well planned from the outset and designed in a manner that fully exploits the affordances of the online format [2]. ERT provides temporary online access to material and instruction, keeping in mind that the format will return to normal once the crisis has ended [3]. The resources that are required by a student to access online education need to be explored. The remainder of this section examines what these resources are and categorizes them as either digital, energy or learning environment resources.

A. Digital Resources

To access online education, the digital resources that students need are an internet connection and a computer. Literature shows that digital deprivation creates a barrier to accessing online education and a digital divide among students [1], [4], [5], [6]. [7] and [8].

During the COVID-19 pandemic, South African universities sought to address digital deprivations by partnering with mobile networks to provide a monthly 30 Gb stipend of mobile data to all students for accessing ERT. The National Student Financial Aid Scheme (NSFAS), implemented the Digital Learning Device Project. This project provided NSFAS-funded students with laptops paid for from their learning material allowance. The University of the Witwatersrand also loaned laptops to full-time students with an annual family income of less than R600 000 and to students that did not have access to a computer [9].

A smartphone is also considered to be an important, but non-essential tool for accessing online education. Smartphones are mainly used for communication but also offer accessibility to the internet and mobile applications. Smartphones allow students to multitask with a single device and they can be used for tethering. Tethering is the process of connecting a device to the internet via the smartphone's mobile connection and using its mobile data.

B. Energy Resources

Electricity benefits online learning by providing electrical lighting and power for internet connectivity, computers and smartphones [10]. Literature shows that energy deprivations create a barrier to accessing online education and an energy divide among students [1], [5], [11], [12] and [13].

Eskom is South Africa's electricity public utility. Students who have access to a utility grid connection reported that power interruptions caused by load shedding are one of the main issues faced preventing them from accessing online education [12]. Load shedding is the controlled curtailment of the electricity supply by disconnecting the utility supply to households for several hours. During 2020, 859 hours and a total of 1269 GWh of electricity were shed [14].

According to the 2021 South African General Household Survey, the rate of electrification in South Africa in 2021 is 89,3% [15]. This means that there are approximately two million South African households that live off-grid.

C. Home Learning Environment

It is important that the physical space in which a student works should be conducive to learning [4]. For online learning, the student should have a space that is comfortable, private, and quiet, with adequate lighting and a well-regulated temperature [16], [17], [18], [19], [20], [21] and [22].

According to the 2021 South African General Household Survey, 83,6% of South African households live in formal dwellings, 11,7% live in informal dwellings, and 4,2% live in a traditional dwelling [15]. Pillay et al. [22] explored how the home learning environment shaped South African university students' experience of ERT. Findings indicated that online education at home was negatively impacted by poor internet, home responsibilities, a cramped environment, lack of safety and financial and psycho-social stress.

III. Creating a Multidimensional Online Education Poverty Index

It is clear from Section II that a multidimensional online education poverty index will need to take three factors into account, namely digital resources, energy resources and the learning environment.

The proposed index is based on the Alkire-Foster methodology (AFM). The AFM was developed by Sabina Alkire and James Foster at Oxford University as a part of the Oxford Poverty and Human Development Initiative (OPHI) [23]. The AFM counts the number of deprivations that may be suffered at the same time in multiple dimensions of poverty. It uses this data to build a deprivation profile that is used to identify the poor and to construct a multidimensional poverty index. The extent of poverty is measured by the proportion of deprivations that are faced [24]. Other notable applications based on the AFM include the Global Multidimensional Poverty Index (GMPI), which is used by the United Nations [25], the Multidimensional Energy Poverty Index and the South African Multidimensional Poverty Index which is based on the GMPI [26] and [27].

This research is a novel application of the AFM to measure a set deprivations that are cumulatively viewed as online education poverty. The following steps are summarised from the AFM which was conceptualised by [24]:

1) Select the dimensions of poverty and the set of deprivation indicators for each dimension that will be considered.
2) Set the deprivation cut-off for each indicator and apply the cut-off to determine whether a student is deprived or not with respect to an indicator.
3) Assign a relative weighting to each dimension and indicator according to its contribution to the overall poverty being measured and ensure that the sum of weights equals 1.
4) Calculate the weighted sum of deprivations for each student. This deprivation score reflects the breadth of a student's deprivation across all indicators. A student's deprivation score will increase as the number of deprivations they experience increases and will reach a maximum value of 1 if a student is deprived in all indicators. A student that experiences no deprivations will have a score of 0.
5) Identify the poor by setting a poverty cut-off. The poverty cut-off is the number of weighted deprivations that a student needs to experience in order to be considered multidimensionally poor.
6) Calculate the incidence of poverty which is the proportion of students from the population that have been identified as multidimensionally poor. The incidence of poverty is represented by the headcount ratio.
7) Calculate the intensity of poverty by summing the deprivation scores of all poor students and dividing this by the total number of poor students to calculate the average deprivation score across the poor.

8) Calculate the adjusted headcount ratio, which is an aggregated measure that combines the incidence and intensity of poverty. The adjusted headcount ratio is the focal point of the AFM. It condenses information that can be unpacked to compare the levels of poverty and the dimensional composition of poverty across the population.

IV. Proposed Index

The multidimensional nature of online education poverty needs to be reflected in the choice and structure of the dimensions, deprivation indicators, deprivation cut-offs and weightings of the proposed index shown in Table 1. Preliminary weights are assigned to this model and statistical methods will be used to assign weights in the final model.

The dimensions of the index are derived from the literature presented in Section II. An equal weight is assigned to each dimension which suggests an equal contribution to the overall poverty being measured by each dimension.

A. Digital and Energy Dimension Indicators

An exploratory research survey was conducted to inform the choice of the deprivation indicators and cut-offs for the digital dimension and energy dimension. The survey was administered online and to the students enrolled at the Faculty of Engineering at Wits University. The survey received 1043 responses. The key findings of the survey are:

- 63% of students use the mobile data provisioned by the university as their main data to access the internet;
- 9% of students do not have access to a computer.
- 13% of students do not have access to a handheld device (smartphone or tablet).
- 2% of students do not have access to a utility electricity supply.
- 93% of students do not have access to an alternative to utility electricity supply.
- 68% of students indicated that planned interruptions of their utility electricity supply is a barrier to accessing online education.
- 46% of students indicated that unplanned interruptions of their utility electricity supply is a barrier to accessing online education.

The majority of students rely on the mobile data provisioned by the university. Reliance on the mobile data provisioned implies that a students does not have access to a reliable, personal internet connection that may be used for working online. The index, therefore, indicates that a student is deprived if they rely on the mobile data provisioned by the university. A small proportion of students do not have access to a computer. This is expected due to interventions discussed in Section II. The index, therefore, indicates that a student is deprived if they do not have access to a computer. A small proportion of students do not have access to a handheld device. Despite a handheld device being considered to be a non-essential tool for accessing online education, the proposed index still measures this because a handheld may be used for tethering since the majority of students rely on mobile data. The index, therefore, indicates that a student is deprived if they do not have access to a handheld device. The weight of having access to a handheld device is set to be less than the weight of having access to a computer and internet, which are set to be equal. This suggests that access to a handled device is of least importance and that access to a computer and internet are equally important when considering the digital dimension.

The majority of students have access to a utility electricity supply. This is expected based on the electrification statistics of South Africa discussed in Section II. However, most students are negatively affected by interruptions to their utility electricity supply. Most students do not have access to a utility alternative electricity supply. This suggests that when the utility supply is interrupted, these students cannot power their devices. The index, therefore, indicates that a student is deprived if they do not have access to a utility or utility alternative electricity supply. The weight of having access to a utility alternative is set to be greater than the weight of having access to a utility electricity supply. This suggests that having access to a utility alternative electricity supply is more important under the South African context when considering the energy dimension.

B. Learning Environment Dimension Indicators

Reference [15] suggests that formal dwellings indicate greater well-being of the household members than informal and traditional dwelling units. The index, therefore, indicates that a student who lives in an informal dwelling is deprived. However, the dwelling type does not provide information on whether or not a student has access to a private working space within their dwelling. The index, therefore, indicates that a student is deprived if they do not have unrestricted access to private working space. The index also indicates that a student is deprived if they do not have access to earphones. Earphones are an important technology that aids audio-visual learning content [28]. The weight of having access to earphones and the weight of the dwelling type is set to be less than the weight of having access to a private working space. This suggests that access to a private workspace is most important when considering the learning environment dimension.

V. Conclusion

This paper discusses the resources required to access online education. This insight is used to identify three dimensions that should be included in a multidimensional online education poverty index, namely a digital dimension, energy dimension and a learning environment dimension. A case for the phenomenon of online education poverty was made and a set of deprivations that may be suffered by a student in each dimension, which cumulatively may be viewed as online education poverty, were established and validated with supporting literature. The Alkire-Foster method (AFM) was introduced briefly. The AFM was chosen as the proposed methodology to develop a poverty measure for online education poverty. The paper showed how the AFM will be applied to develop

TABLE I
ONLINE EDUCATION POVERTY INDEX

Dimension (Weight)	Indicator	Deprivation cut-off (The student is derived if they...)	Weight
Digital (1/3)	Internet access	Rely on the mobile data provision	2/15
	Computer ownership	Do not own a computer	2/15
	Handheld device ownership	Do not own a smartphone or tablet	1/15
Energy (1/3)	Utility electricity supply	Do not have access to a utility electricity supply	1/9
	Alternative electricity supply	Do not have access to a utility alternative electricity supply	2/9
Learning environment (1/3)	Dwelling type	Live in an informal dwelling	1/15
	Workspace	Do not have unrestricted access to a private workspace	3/15
	Acoustics	Do not own earphones	1/15

the poverty measure and following this, the variables of the poverty measure were proposed. Work to refine the proposed index is ongoing.

REFERENCES

[1] J. Mhandu, S. Serpa, M. Evelyne and I. T. Mahiya, "The exclusionary character of remote teaching and learning during the COVID-19 pandemic. An exploration of the challenges faced by rural-based University of KwaZulu Natal students," Cogent Social Sciences, vol. 7, no. 1, 2021.

[2] R. M. Branch and T. A. Dousay, Survey of Instructional Design Models, Indiana: Association for Educational Communications and Technology, 2015.

[3] C. Hodges, S. Noore, B. Lockee, T. Trust and A. Bond, "The Difference Between Emergency Remote Teaching and Online Learning," Educase Review, 27 March 2020. [Online]. Available: https://er.educause.edu/articles/2020/3/the-difference-between-emergency-remote-teaching-and-online-learning. [Accessed 14 February 2022].

[4] A. Haxell, S. Agarwal, H. Kath, L. Kelvin, G. Norina, G. Nick and G. D. Erlam, "What Really Matters: Experiences of Emergency Remote Teaching in University Teaching and Learning During the COVID-19 Pandemic," Frontiers in Education , vol. 6, p. 397, 2021.

[5] A. Cahyadi, Hendryadi, S. Widyastuti, V. N. Mufidah and Achmadi, "Emergency remote teaching evaluation of the higher education in Indonesia," Heliyon, vol. 7, no. 8, 2021.

[6] T. Guzzo, P. Grifoni and F. Ferri, "Online Learning and Emergency Remote Teaching: Opportunities and Challenges in Emergency Situations," Societies, vol. 10, no. 4, 2020.

[7] D. Thurab-Nkhosi, C. Maharaj and V. Ramadhar, "The impact of emergency remote teaching on a blended engineering course: perspectives and implications for the future," SN Social Sciences, vol. 159, no. 1, 2021.

[8] J. Pete and J. J. Soko, "Preparedness for online learning in the context of Covid-19 in selected SubSaharan African countries," Asian Journal of Distance Education, vol. 15, no. 2, pp. 37-47, 2020.

[9] J. September, "Process to apply for mobile computing devices," Wits University, 15 April 2020. [Online]. Available: https://www.wits.ac.za/news/latest-news/general-news/2020/2020-04/process-to-apply-for-mobile-computing-devices.html. [Accessed 31 October 2021].

[10] B. Sovacool and I. Vera, "Electricity and education: The benefits,barriers, and recommendations for achieving the electrification of primary and secondary schools," United Nations Department of Economic and Social Affairs, 2014.

[11] O. I. Ikwuka, A. C. Okoye, S. A. Olanikawu, V. C. Udenwa, C. C. Okoye and D. C. Ikwuka, "Emergency remote teaching during COVID-19 pandemic lockdown: Nigeria University students' perspective," Global Biosecurity, vol. 3, no. 1, 2021.

[12] L. Czerniewicz, N. Agherdien, J. Badenhorst, D. Belluigi, T. Chambers, M. Chili, M. de Villiers, A. Felix and et al., "A Wake-Up Call: Equity, Inequality and Covid-19 Emergency Remote Teaching and Learning," Postdigital Science and Education, vol. 2, p. 946–967, 2020.

[13] A. N. Hazaea, W. R. Ali Bin-Hady and M. M. Toujani , "Emergency Remote English Language Teaching in the Arab League," Computer-Assisted Language Learning Electronic Journal, vol. 22, no. 1, pp. 201-222, 2021.

[14] J. Calitz and J. Wright, "Statistics of utility-scale power generation in South Africa in 2020," The Council for Scientific and Industrial Research, 2021.

[15] Statistics South Africa, "Statistical Release P0318: General Household Survey 2021," Stats SA, Pretoria, 2021.

[16] L. Scannell, M. Hodgson, J. G. M. Villarreal and R. G. Gifford, "The role of acoustics in the perceived suitability of, and well-being in, informal learning spaces," Environment and Behavior, vol. 48, no. 6, p. 769–795, 2016.

[17] S. Kärnä , P. Julin and S. Nenonen, "User satisfaction on a university campus by students and staff," Intelligent Buildings International, vol. 5, no. 2, pp. 69-82, 2013.

[18] L. Chatzidiakou , D. Mumovic and A. J. Summerfield, "What do we know about indoor air quality in school classrooms? A critical review of the literature," Intelligent Buildings International , vol. 4, no. 4, pp. 228-259, 2012.

[19] Z. Yang, B. Becerik-Gerber and L. Mino, "A study on student perceptions of higher education classrooms: Impact of classroom attributes on student satisfaction and performance," Building and Environment, vol. 70, pp. 171-188, 2013.

[20] N. Van Note Chism, "A tale of two classrooms," New Directions for Teaching and Learning, no. 92, pp. 5-12, 2002.

[21] L. Morieson, G. Murray, R. Wilson, B. Clarke and K. Lukas, "Belonging in space: Informal learning spaces and student experience," Journal of Learning Spaces, vol. 7, no. 2, pp. 12-22, 2018.

[22] N. Nyika, B. Mthembu, B. Campbell, A. Sheik, M. Khosa and A. Pillay, "How Home Contexts of South African University Students Shape their

Experiences of Emergency Remote Teaching and Learning," Student Success, vol. 2, no. 2, 2021.
[23] S. Alkire, J. Foster, S. Seth, M. E. Santos, J. M. Roche and P. Ballon, Multidimensional Poverty Measurement and Analysis, Oxford University Press, 2015.
[24] S. Alkire, J. E. Foster, S. Seth, M. E. Santos, J. M. Roche and P. Ballon, Multidimensional Poverty Measurement and Analysis: Chapter 5, Oxford: Oxford University Press, 2015.
[25] N. Suppa, S. Alkire and U. Kanagaratnam, The global Multidimensional Poverty Index (MPI) 2020, University of Oxford: Oxford Poverty and Human Development Initiative, 2020.
[26] P. Nussbaumer, M. Brazilian and V. Modi, "Measuring energy poverty: Focusing on what matters," Renewable and Sustainable Energy Reviews, vol. 16, no. 1, pp. 231-243, 2012.
[27] P. Lehohla, "The South African MPI," Statistics South Afric, Pretoria, 2014.
[28] S. M. Yousof, "The possible negative effects of prolonged technology-based online learning during the COVID-19 pandemic on body functions and wellbeing: a review article", JMS, vol. 90, no. 3, p. e522, Sep. 2021.

Educating the Future Engineer Towards Realizing the Powering of the Future Internet

A.A. Periola
Department of Electrical, Electronic and Computer Engineering
Cape Peninsula University of Technology
periolaa@cput.ac.za

A.A. Alonge
Department of Electrical and Electronics Engineering Technology
University of Johannesburg
aalonge@uj.ac.za

K.A Ogudo
Department of Electrical and Electronics Engineering Technology
University of Johannesburg
kingsleyo@uj.ac.za

Abstract— **The increasing role of the internet in society and enterprise necessitates that future engineers be trained in aspects enabling continued internet access in different contexts. An important context in this regard is that of training future engineers to be proficient in the aspect of integrating renewable energy technologies into the cloud data center. The cloud data center plays an important role in hosting content and enabling content access. However, this aspect has not received sufficient attention in the design of suitable teaching approaches with a focus on students in Electronics and Computer Engineering. The discussion here addresses this problem and proposes novel approaches to deriving a multi-disciplinary curriculum and conducting interactive content delivery sessions. The multi-disciplinary curriculum is designed using the proposed approach of module descriptive programming. The interactive content delivery session is realized via the proposed approach of the classroom which fuses content on lecturer and student perspectives.**

Keywords – Cloud Data Center, Renewable Energy Sources, Future Internet, Future Engineer

I. INTRODUCTION

There is an increasing need and recognition of the need to increasingly incorporate renewable energy sources instead of non–renewable energy sources (fossil fuel sources) due to the environmental preservation motive. The necessity of using renewable energy sources plays an important role in enabling the operation of future systems that enable content accessible via the internet. This can be seen in the provisioning of power to operate data centers as seen in [1–4].

The use of renewable energy in a manner that is sustainable requires the satisfaction of multiple criteria such as organization adoption, governmental support, and engineering training. Enterprises delivering cloud computing services have been identified to signify interest in adopting the use of renewable energy [5–8]. In addition, there is increasing governmental and municipal support for the use of renewable energy as seen in [9–11]. However, it is important to redesign engineering education to train future engineers. This requires the design of an engineering education curriculum to train future engineers. The redesign of the curricula should consider the multidisciplinary relations between the previously separate domains of cloud computing and power systems. Cloud computing receives significant consideration in the areas of Computer Engineering, Electrical engineering, and Electronic Engineering. In addition, the subject of power systems receives significant consideration in the domain of Electrical Engineering and Power Systems Engineering.

The curricula design should also consider meeting the need to equip undergraduate, and postgraduate (students in Computer Engineering, Electrical Engineering, Electronic Engineering, and Power Systems Engineering. It is also important to consider that future engineers in these disciplines have varying mathematical skills, aptitudes, and capabilities. In addition, each of the considered disciplines requires existing students to make use of software and computing tools to different extents.

The development of the required engineering curricula should also consider lecturer preferences, competencies, and the emergence of multimedia platforms [12] and advances in internet technology [13]. This is important as lecturers in computer science or computer engineering may have a focus that differs from lecturers in electrical and power systems engineering. Nevertheless, the design of multi–disciplinary engineering curricula that consider existing lecturer preferences should also be considered. This is the challenge being addressed. The contributions are:

The discussion here makes the following contributions:

1) First, the design and provisioning of engineering education in the areas of Electronics and Computer Engineering (ECE) is presented. The curriculum is intended to equip engineering students in ECE to have more awareness of designing computing platforms that use renewable energy systems. The use of non–terrestrial data centers is beginning to increasingly receive attention [14–17]. These data centers significantly use renewable energy. Hence, the need to provide education on the use of renewable energies. This is important due to interest in the use of novel paradigms such as the super-grid [18–20]. The new contents to be included in the undergraduate and postgraduate aspects of the ECE curriculum are presented.
2) Secondly, different modes of content delivery are considered. This has been defined considering student preferences for internet technology-based education [21 – 22]. Each mode is described by the composition of integrated technical data and subject content. These modes are (1) Passive Internet history mode (PIHM), (2) Active Internet history mode (AIHM), (3) Passive Internet–Mobile Mode (PIMM), and (4) Active Internet–Mobile Mode (AIMM). In addition, the transition between the identified PIHM, AIHM, AIMM, and PIMM is discussed.

The discussion is organized as follows: Section II discusses background work. Section III discusses the merge of cloud computing (conventional terrestrial and non-terrestrial) and power engineering education with a focus on the use of renewable energy. In addition, the concerned contents are identified, discussed, and integrated. Section IV presents the model of the proposed classroom enabling the ECE curriculum delivery. Section V presents the merge of cloud computing and renewable energy usage in a classroom.

II. PROPOSED DISCIPLINARY MERGE

The proposed merge between cloud computing systems and power systems is presented in this section. The cloud computing system is recognized to comprise four subsystems namely the computing subsystem, communication subsystem, cooling subsystem, and power subsystem. The power subsystem provides the operational power that enables the computing platform to execute the functionalities of data storage, algorithm execution, and data transmission.

The power subsystem in the computing platform interacts with the components found in either renewable or non–renewable energy systems or components. In this case, the interactions associated with the power systems span five aspects. These are (1) power–cooling subsystem relations, (2) power–communication system relations, (3) power–cooling subsystem relations, (4) cloud computing platform power–cooling subsystem relations, and (5) cloud computing platform–power–external power system relations. The first four relations focus on the interaction between subsystems within the cloud computing platform comprising multiple networked data centers. The design of the communications, networking and power systems alongside the information networks in the data center utilizes the concept that is already incorporated in the existing ECE engineering curricula.

For example, courses in communication networks significantly have coverage in the aspects of wired networks making use of copper and fiber optic cables. In addition, there are courses that focus on the design of power electronic circuits which are covered in modules within the ECE curricula. In a similar manner, the basics of computer logic and computer engineering also receive consideration and coverage for undergraduate and post-graduate ECE students.

The relations in the aspect of the interaction between cloud computing power subsystem–external power system relations are the aspect being considered in this paper. In this case, the power system providing power to the cloud computing system can comprise renewable or non–renewable energy sources. In this case, renewable energy sources comprise either solar, wind (onshore), wind (offshore), or a hybrid power system. Each power system option has its own components, unique design aspects, and trade-offs that should be incorporated in the education of the future engineer.

The design of hybrid systems has received attention as seen in [23–24]. However, the focus on the design has been done with a focus on addressing the challenge of power insecurity i.e., increasing and improving power availability. This does not consider the goal of enhancing the quality of education provided to the future ECE engineer and computing systems.

The rest of the discussion has three aspects. The first aspect presents an approach utilizing the object-oriented approach to describe the components and role of the power systems associated with the provisioning of electricity for data center operation. The use of the object–oriented programming (OOP) approach is deemed appropriate as both computer scientists and ECE students already take modules and courses in computer programming. The second aspect presents a new module of descriptive systems programming as an additional module to be included in future curricula for ECE and computer science students. The third aspect describes the logical foundations enabling the extension of the proposed descriptive systems programming approach to other aspects of engineering arising due to advances in technology.

A. Proposed OOP Approach

The use of the OOP approach in designing multi-disciplinary education as being proposed receives consideration in [25–26]. However, the focus in [25] and [26] is not on the context of describing component relations about power systems as is being considered here. In addition, the use of the OOP approach provides a logical framework that enhances the clarity of students during the education provisioning process.

Furthermore, the use of the OOP approach is suitable for mathematically deficient students. This is because it makes of syntactic statements, and commands without any use of intensive mathematical symbols, notations and complex closed-form mathematical relations.

In the use of the proposed OOP approach, each component is considered an object with defined properties (global and local) and associated methods. This allocation of attributes is done for the components that are identified to be associated with the realization of power flow between the external power systems (renewable or non-renewable) and the computing subsystems of the cloud computing system.

For example, a solar panel is a component in a solar power system. In this context, the properties of the solar panel is the number of solar cells, efficiency of the solar panel and maximum power output. These properties constitute the attributes of the solar panel. Furthermore, the OOP approaches advocates the execution of methods that describe tasks being executed by an identified component. In this regard, the method associated with the solar panel component is that of aligning and tracking. This method ensures that the solar panel intercepts the maximum solar radiation.

The proposed OOP approach treats concepts in the computing platform subsystem and the domain of external power systems as objects where allowable functionalities are regarded as methods or functions. In this case, properties are defined to describe parameters associated with a given power system component or device. This manner of adoption enables a logical definition of the capabilities of all components associated with different components of the power system. In addition, it fosters a modular approach that improves student understanding of workshop exercises at a later stage.

B. Proposed Module Descriptive Programming

The adoption of the OOP approach enables the development of a module descriptive programming (MDP) format. The MDP is developed with the goal of enhancing the provisioning of education to future engineers. This is done in the context of a multi–disciplinary education for ECE students. The proposed MDP integrates the knowledge from prerequisite courses that have been taken by a student and adopts them into the provisioning and presentation of the new engineering curricula. The adoption of the MDP considers the background and course prerequisites that have been taken and passed by the students. In addition, the development of the MDP considers the professional experience of students enrolled in post–graduate programs like taught MSc programs. In addition, the interests of students in other areas are integrated into the curricula being developed.

In addition, the MDP can be updated to reflect advances and the need to consider the needs of the industry for future engineers. In this case, the MDP is updated by lecturers and professors in a higher education institution. The MDP is defined for a given module and the need to accommodate the needs of the cloud computing industry as regards training future ECE graduates in the aspect of using renewable energy in computing platforms.

The MDP is defined for a given module and receives contributions from multiple faculty members. This enables the benefits of diversity to be derived in its definition and realization. In addition, it reduces the workload on faculty members as is observed in the faculty workload. In the current approach, a faculty member is expected to execute the tasks associated with defining a module's outcomes, assessment patterns and topics to be considered. The use of the MDP in this manner enables multi-disciplinary module content development. It is also beneficial because it enables a concerned department to increasingly benefit from diversity among its faculty. Currently, departments and faculties benefit from diversity via the feedback approach of internal and external moderation. In this approach, the work of the module developer is reviewed by internal and external academics. The proposed MDP is integrated into this approach. However, it enables the module developer to obtain additional content and enables the easy recognition of resources to be used in the phase of module development.

The existing case of module development by academics opines that the developer academic is a subject matter expert. Being a subject matter expert puts the academic in the role of identifying the key components and subjects to be included in a module. However, this does not consider the emergence of new knowledge and data explosion. In the existing approach of module development, the internal moderators and external moderators fulfill the critical role of ensuring that new subject areas and concepts are embedded alongside the module during the development phase. This approach is deemed inefficient.

In the proposed MDP, the process of identifying new subject areas, and associated concepts are executed in an automated manner. This is done during the process of module development by the subject matter expert. The automated agent that is active within the MDP. The automated agent is realized as a subject bot that enables the identification of new concepts and subjects that are associated with the subject of concern in the module being developed. The new concepts are integrated into the MDP as a form of intelli-sense. The IntelliSense capabilities appear during the module development phase to indicate a concept that is aligned with a subject aspect. The use of an IntelliSense capability has been motivated by its incorporation in software development kits and platforms. This capability enables the developer to rapidly develop software by providing intelligent assistance and support during the coding process. In a similar manner, the IntelliSense capability being proposed can provide guidelines on the necessary features to be included in the subject guide to ensure conformance with the accreditation process.

The automated agent i.e. subject automaton becomes active only after the identification of trusted resources associated with a given subject area.

The module developed in this manner is presented for internal moderation and external moderation after the module development process. In addition, the internal moderators and external moderators are able to see the subject automatons that have been used. This helps in verifying the quality of the developed subject module as the automated agent has a verification process prior to use. The key benefit of using the automated agent in the proposed manner is two-fold. The first is that the use of automated agents can function in finding new content in an autonomous manner. This enables the module developer to devote more time to the generation of new knowledge. The second is that it provides a framework that enables module developers to inform students of trusted and verified online sources of technical content. This is also beneficial for the concerned higher education institution as it provides a basis for reaching the modern student who is increasingly savvy and provides timely and needed guidance on the use of online materials.

C. *Module Descriptive Programming – Architecture*

The functionality of the proposed module descriptive programming is realized using a crawler-driven Intellisense architecture. In the proposed MDP, crawlers are used to conduct a search over a defined database to acquire information regarding the module associated with the module developer or academic in a given context. In this case, the database can be defined by an accreditation authority, institution, or industrial partner. In this case, the industrial partners seek to ensure that the developed curricula meet the needs of the industry. The developed database comprises different module areas associated with a given industry and linked with a target role. In the case of an institution, the database comprises the list of modules alongside their subject areas, the year of development, and notes on module implementation (in delivery to students). In addition, the institutional database also hosts information on the comments that have been made by different accreditation bodies. The industrial partner's database hosts information on expectations as regards skills and knowledge competencies for an engineering graduate. In this case, the competencies are linked to that of an ECE graduate (completion of undergraduate or postgraduate program) with relation to working in the area of integrating renewable energies or other forms of electrical power sources to the operation of cloud data centers.

These three databases communicate with the automation agent. The automation agent receives its input as regards curricula development from the module developer and subject matter expert. In addition, the automation agent is also linked to a semantic analytic entity. The semantic analytic entity executes the function of determining if the data obtained from the databases meet the requirements specified in the input of the automation agent as defined by the module developer and subject matter expert. The semantic analytic entity also enables the development of IntelliSense keywords associated with different module aspects using the input from the automation agent–database interaction that meets the specifications and intents of the module developer and subject matter expert.

The implementation of the proposed MDP architecture showing the relations between the databases, the automation agent and the semantic analytic entity is shown in Figure 1.

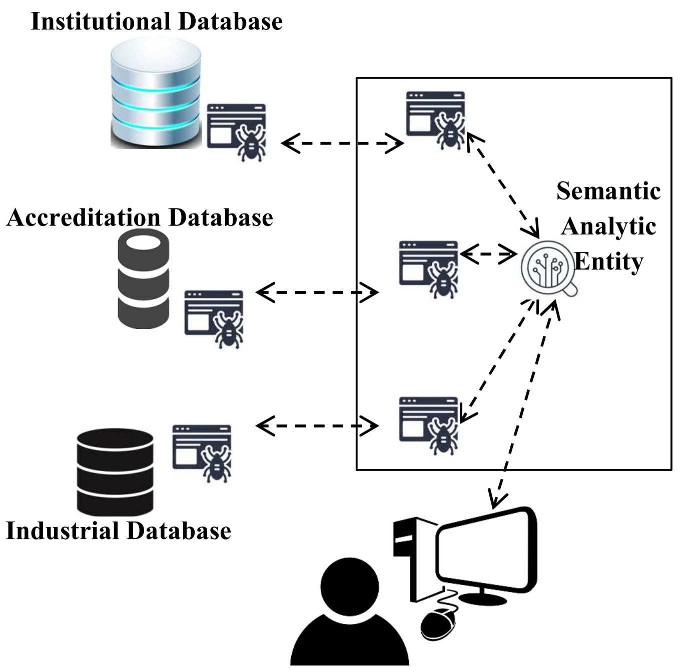

Figure 1: Relations between entities in the proposed MDP.

III. CLASSROOM AND LEARNING SPACE

The classroom is an important aspect of lecture and content delivery in higher education institutions. The modern classroom is equipped with computing entities enabling the delivery of lecture content in multiple modes. Currently, lecturers can be delivered using presentation slides, digital presentations of scanned handwritten notes, and conventional lecture methods (using chalk and board or markers). The use of crawlers in enabling the lecturer to gain an increased awareness of student preferences is presented in [13]. However, the lecture delivery, in this case, does not consider the developed subject guide and the needs of accreditation boards, and industry.

In addition, the lecture delivery is not done in a manner that the industry needs, and the need to prepare ECE graduates is not considered. However, the classroom enables the integration of industry preparedness outcomes and the delivery of subject content during lecture sessions. This directly helps the student to have more industry preparedness.

In addition, the outcomes of the crawler with regard to new advances in the aspects of integrating renewable energy into the cloud data centers are also integrated into the classroom. The classroom comprises multiple computing entities. In the discussion here, two computing units are considered. Each computing unit comprises a laptop or desktop personal computer. The first computing unit is used to project lecture slides to a wall-mounted projector screen during the lecture session. The second computing unit is used to host content on new aspects and advances in the use of renewable energy within cloud data centers. The content from the second computing unit is cached and projected during the lecturing session. This projection after the delivery of the scheduled content serves to educate students on advances in the domain of using renewable energies in cloud data centers.

The classroom is realized in three modes. These modes have been defined considering the use of the internet history data associated with student subject searches. These operational modes are the passive internet history mode (PIHM), active internet history mode (AIHM), passive internet–mobile mode (PIMM), and the active internet–mobile mode (AIMM). These modes have been defined considering the source of data describing learning preferences and new content.

The PIHM makes use of the internet history of the academic and the student with regard to deriving new content. In this case, the new content describes advances in renewable energy sources and their use in cloud data centers. The PIHM makes use of the filtered content of the internet history of academics. In this case, participating academics are not only limited to the lecturer that is handling a module or course. Multiple lecturers, academics, and subject matter experts with expertise in the applications of renewable energy sources to the operation of future cloud data centers participate in this regard. In this case, the computing devices where participants want the internet history to be utilized are specified before launching the application i.e., enabling the classroom in the PIHM mode.

The AIHM mode is similar to the PIHM in making use of only the internet history of the participating lecturer, academics, and subject matter experts. However, the internet history content is utilized in a manner that considers only recently accessed content. In this case, the recently accessed content is defined to be content in the history which has been accessed within a specified time period. Furthermore, the PIHM does not consider the case of subject matter experts who are willing to provide real-time insights during the module development process. Examples of such insights in this case arise from entrepreneurs who are involved in the commercialization of innovative ideas on the application of advances in renewable energy sources to enable the operation of cloud data centers.

The PIMM mode is similar to of the PIHM in the proposed classroom. However, it differs by incorporating the internet history of non–academics and non–subject matter experts. In this case, non–academics could comprise students. The consideration of students in this regard enables the lecturer and academic to have an increased awareness of the student perspective on the aspect of the use of renewable energies to enable the operation of the data center. Besides students, non–academic entities can also imply tutor roles in the context of applying renewable energy sources in powering cloud data centers.

In this case, tutors execute the role of providing additional explanations to students in the concerned module. The inclusion of tutors (who may not be necessarily subject matter experts) in this case enables the further explanation of taught subject contents to occur in an environment that is not exclusive of the consideration of the advances in renewable energy and their usage in cloud data centers.

The AIMM mode is like the AIHM but specifies the extent and the period of the internet history of non–academic entities that will be considered in the course of subject content delivery by non–academic entities such as the tutors and non–subject matter experts.

The transition between the PIHM, AIHM, PIMM, and AIMM modes is determined by the lecturer (or tutor) during a content delivery session. In determining the transition, the lecturer or subject session coordinator determines the content that will be considered during the delivery of lecture sessions at different stages. A description of the transition between the operational modes of the PIHM, AIHM, PIMM and AIMM associated with the proposed classroom is presented in Figure 2.

The transition in Figure 2 comprises 10 transition paths. These are (1) PIHM to AIMM, (2) AIMM to PIHM, (3) PIHM to AIHM, (4)AIHM to PIHM, (5) AIHM to PIMM, (6) PIMM to AIHM, (7) AIHM to AIMM, (8) AIMM to AIHM, (9) PIMM to AIMM, and (10) AIMM to PIMM. Each transition path is activated and deactivated via the inclusion and non–inclusion of different data from the internet history of academic entities, non–academic entities, and students. In Figure 2, the academic or coordinating lecturer can start from any operational mode i.e. PIHM, PIMM, AIHM, and AIMM in the classroom. The relations presented in Figure 2 mainly focus on the transition between each classroom's operational mode.

The transition from the PIHM operational mode to the AIHM operational mode is realized by specifying that only a portion of the internet history is used. This specification is deemed necessary when the computational resources aboard the involved computing entities are limited or when history contents that have been accessed beyond a given time epoch are no longer suitable for use in the classroom context. In addition, the transition from the AIHM operational mode to the PIHM operational mode is considered important when more subject-related accessed contents from the history content of the computing entity are deemed necessary for illustration by the academic or coordinating academic. This can be useful when delivering courses where new components and systems have evolved from pre–existing systems. Such a case can be found in the context of wireless communications (involving progression from the first generation, second generation, third generation, fourth generation, and now fifth generation). Another case where new systems have evolved from pre–existing systems can be found in power systems in which case the evolution to the smart grid from the conventional power systems is an important case.

The direct transition from the PIHM operational mode to the AIMM operational mode is necessitated when the history contents from a single student or multiple students are incorporated in the content delivery, lecture or tutorial session. The inclusion is determined by the coordinating lecturer, tutor, or academic. This transition only considers the history window of the concerned student(s) and the coordinating academic(s) up to a certain epoch in time. The entire history window is not considered. The non – consideration of the entire history window is set in the context where the processing capability and computational resources aboard computing entities are limited. This consideration makes it feasible for capital-constrained higher education institutions that may not have all the resources required to acquire high-capacity computing entities. The transition from the AIMM operational mode to the PIHM operational mode occurs when student internet history sources and the history window limitation on the coordinating academic history's sources are removed.

The transitions from the PIHM operational mode to the PIMM operational mode and the transition from the PIMM operational mode to the PIHM operational mode occur via the AIHM operational mode. However, the AIHM operational mode is not activated in the case of this transition. In this case, the internet history of other subject matter experts is included during the transition from the PIHM operational mode to the PIMM operational mode. The inclusion of the AIHM in this transition path is to provide a check on the need to include components from the student's accessed content before incorporating the third party in a content delivery session.

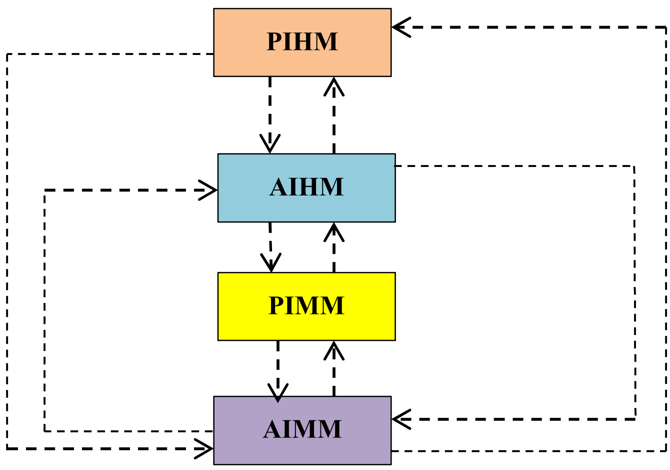

Figure 2: Transition between different operational modes associated with the classroom.

IV. CLASSROOM IN THE ENGINEERING EDUCATION CONTEXT

In the context of the provisioning education to ECE graduates in the aspects of using renewable energy to power the systems that drive the internet i.e., cloud data centers. Integration of the classroom in a manner that enables the provisioning of engineering education in the proposed manner requires accessing the related history content of the coordinating academic and students during a lecture session.

The history contents are accessed via a wireless local area network with coverage in the concerned lecture venue. The accessed history contents are in the form of universal resource locator links that enable content accessible via the web. Each accessed link is associated with the concerned time epoch of time and date. In addition, the accessed links are ranked based on the time and date of access. This ranking is done by an intelligent agent aboard the computing entity being used by the coordinating academic. In addition, the coordinating academic is able to select the suitable operational mode via a user interface that is designed for this purpose.

The inclusion of the user interface, accessing the history content via the wireless local area network in the lecture venue, and ranking of the accessed resource locator links enables the realization of the proposed educational solution and integration within the classroom context. The integration is done aboard a client that is active aboard the coordinating academic computing entity.

V. CONCLUSION

The discussion focuses on designing engineering curricula that train future graduates of Electronics and Computer Engineering in the aspect of integrating renewable energy sources with the future cloud data centers that drive the internet. The proposed engineering curriculum is interactive and makes significant use of advances in mobile device usage alongside internet technology in the classroom context. In this regard, it presents the context of the classroom as one that is capable of enabling the integration of multiple contents from different sources in a manner that enhances the content delivery session. Furthermore, the discussion describes an online approach to designing engineering curricula (in the considered context). This approach incorporates the proposed module descriptive programming. Future work aims to derive quantitative measures and metrics that describe how the proposed approach enhances the content delivery sessions and student learning in the context of Electronics and Computer Engineering.

ACKNOWLEDGMENT

The support of the Department of Electrical, Electronic, and Computer Engineering of the Cape Peninsula University of Technology and the Department of Electrical and Electronic Engineering Technology is acknowledged by the authors.

REFERENCES

[1] M.Xu, A.N.Toosi, B.Bahrani, R.Razzaghi and M.Singh, 'Optimized Renewable Energy Use in Green Cloud Data Centers', n: Yangui, S., Bouassida Rodriguez, I., Drira, K., Tari, Z. (eds) Service-Oriented Computing. ICSOC 2019. Lecture Notes in Computer Science(), 2019, Vol. 11895. Springer, Cham. https://doi.org/10.1007/978-3-030-33702-5_24

[2] C. Dupont, 'Renewable Energy-Aware Data Centres: The Problem of Controlling the Applications Workload.' In: Klingert, S., Hesselbach-Serra, X., Ortega, M.P., Giuliani, G. (eds) Energy-Efficient Data Centers. Lecture Notes in Computer Science, vol 8343. Springer, Berlin, Heidelberg. https://doi.org/10.1007/978-3-642-55149-9_2

[3] J.Guitart, 'Toward sustainable data centers: a comprehensive energy management strategy. 'Computing 99, 597–615 (2017). https://doi.org/10.1007/s00607-016-0501-1

[4] M. D. M. da Silva, A. Gamatié, G. Sassatelli, M. Poss and M. Robert, "Optimization of Data and Energy Migrations in Mini Data Centers for Carbon-Neutral Computing," in IEEE Transactions on Sustainable Computing, 2022, DOI: 10.1109/TSUSC.2022.3197090.

[5] A.Agarwal, J.Sun, S.Noghabi, S.Iyengar, A.Badam, R.Chandra, S.Seshan, S.Kalyanaraman, 'Redesigning Data Centers for Renewable Energy, 2021, [Online] Available: https://www.microsoft.com/en-us/research/uploads/prod/2021/10/VirtualBattery.pdf

[6] M.Oman, and I.F.Stearns, '24/7 Carbon-Free Energy: Powering up new clean energy projects across the globe', April 21, 2022, [Online] Available: https://cloud.google.com/blog/topics/sustainability/clean-energy-projects-begin-to-power-google-data-centers

[7] Amazon, 'Renewable Energy Methodology', [Online] Available: https://sustainability.aboutamazon.com/renewable-energy-methodology.pdf

[8] A.S.Brown, 'Keep it Cool ! Inside the World's Most Efficient Data Center', Spring 2014, pp 12 – 16.

[9] J.Grafstrom, P.Soderholm, E.Gawel, P.Lehmann and S.Strunz, 'Government support to renewable energy R&D: drivers and strategic interactions among EU Member States', Economics of Innovation and New Technology, https://doi.org/10.1080/10438599.2020.1857499.

[10] F.Chien, C.Hsu, Y.Zhang, T.D.Tran and L.Liu, 'Assessing the impact of green fiscal policies and energy poverty on energy efficiency', Environmental Science and Pollution Research volume 29,2022, pp. 4363–4374.

[11] O.M.Akinbami, S.R.Oke and M.O.Bodunrin, 'The state of renewable energy development in South Africa: an overview', Alexandria Engineering Journal, Vol. 60, No. 6, Dec 2021, pp. 5077 – 5093.

[12] L.Yu, and W.Lizhi. "Construction of multimedia assisted legal classroom teaching model based on data mining algorithm.", 2021, Scientific Programming, Volume 2021 |Article ID 9948800 | https://doi.org/10.1155/2021/9948800.

[13] A. A. Periola, A. A. Alonge and K. A. Ogudo, "Internet Driven Dynamic Question Analysis and Response for Engineering," 2022 45th Jubilee International Convention on Information, Communication and Electronic Technology (MIPRO), 2022, pp. 1351-1356, doi: 10.23919/MIPRO55190.2022.9803679.

[14] B. Cutler, S. Fowers, J. Kramer and E. Peterson, "Dunking the data center," in IEEE Spectrum, vol. 54, no. 3, pp. 26-31, March 2017, doi: 10.1109/MSPEC.2017.7864753.

[15] Z.Hu, Y.Zheng and Y.Wang, 'Packing computing servers into the vessel of an underwater data center considering cooling efficiency', Applied Energy, Vol. 314, 15 May 2022, 118986.

[16] A. A. Periola, A. A. Alonge and K. A. Ogudo, "Intelligent Scheduling for Stratosphere Cloud Platforms," 2020 International Conference on Artificial Intelligence, Big Data, Computing and Data Communication Systems (icABCD), 2020, pp. 1-7, doi: 10.1109/icABCD49160.2020.9183856.

[17] S.Moss, 'NTT and SKY Perfect JSAT to launch 'space data center' in 2025', May 19, 2021, [Online] Available: https://www.datacenterdynamics.com/en/news/ntt-and-sky-perfect-jsat-to-launch-space-data-center-in-2025/

[18] H.A.M.Abobaker, J. Genci, M. Gamcova and G.A.M.Ismeal, 'Design and implementation of secured power grid system with information and communication technology.' SN Appl. Sci. 2, 2016 (2020). https://doi.org/10.1007/s42452-020-03820-w

[19] P. Kuhn, M. Huber, J. Dorfner and T.Hamacher, 'Challenges and opportunities of power systems from smart homes to super-grids. ' Ambio, 45 (Suppl 1), 2016, pp. 50–62. https://doi.org/10.1007/s13280-015-0733-x

[20] L.Xing, G.Sizov and O.E.Gundersen, 'Digital Transformation in Renewable Energy Use Cases and Experiences from a Nordic Power Producer', In: Mikalef, P., Parmiggiani, E. (eds) Digital Transformation in Norwegian Enterprises . Springer, Cham. https://doi.org/10.1007/978-3-031-05276-7_5.

[21] A. Tatnall, and A. Fluck, 'Twenty-five years of the Education and the Information Technologies journal: Past and future.' Educ Inf Technol 27, 1359–1378 (2022). https://doi.org/10.1007/s10639-022-10917-9

[22] C.Coman, L.G.Tiru, L.Mesean-Schmitz, C.Stanciu and M.C.Bularca, 'Online Teaching and Learning in Higher Education during the Coronavirus Pandemic: Students' Perspective', Sustainability 2020, 12, 10367; doi:10.3390/su122410367

[23] P.K.Sannidhi, V.R.Mandla, S.S.V.Saladi, N.Chokkavarapu and V.S.S.Peddinti, 'An integrated hybrid renewable energy system: potential of electricity—a geospatial approach', SN Appl. Sci. 2, 1642 (2020). https://doi.org/10.1007/s42452-020-03329-2

[24] S.Ferahtia, A.Djerioui, S.Zeghlache and A. Houari, 'A hybrid power system based on fuel cell, photovoltaic source and supercapacitor', SN Appl. Sci. 2, 940 (2020). https://doi.org/10.1007/s42452-020-2709-0

[25] D.Petkovic, S.Jovic and Z.Golubovic, 'Object-oriented modeling approach of universal education software', Computer Applications in Engineering Education, 2018;Vol. 26, pp. 543–558.

[26] F.Buitrago-Florez, M.Sanchez, V.P.Romanello, C.Hernandez and M.H.Hoyos, 'A systematic approach for curriculum redesign of introductory courses in engineering: a programming course case study', Kybernetes, DOI 10.1108/K-10-2021-0957

Transformer Differential Protection System Testing for Scholarly Benefits Using RTDS Hardware-in-the-Loop Technique

Sinawo Nomandela
Electrical, Electronic, and Computer Engineering
Cape Peninsula University of Technology (CPUT)
Cape Town, South Africa
NomandelaS@cput.ac.za

Mkhululi Mnguni
Electrical, Electronic, and Computer Engineering
Cape Peninsula University of Technology (CPUT)
Cape Town, South Africa
MnguniM@cput.ac.za

Mukovhe Ratshitanga
Electrical, Electronic, and Computer Engineering
Cape Peninsula University of Technology (CPUT)
Cape Town, South Africa
RatshitangaM@cput.ac.za

Sikho Ntshiba
Electrical, Electronic, and Computer Engineering
Cape Peninsula University of Technology (CPUT)
Cape Town, South Africa
NtshibaS@cput.ac.za

***Abstract*—The hardware-in-the-loop (HIL) test for a transformer differential protection system is presented in this paper, to prove the validity of the settings configuration of the relay. A step-by-step configuration is done up to the testing part, which proves and validates the concept of differential calculations. The steps and configuration procedures presented in this paper will help other scholars understand the configuration and the operating principle of the transformer differential protection system and its elements. The focus of this study is not limited to the protected transformer, it also considers the system in which the transformer is employed. The obtained simulation results demonstrate that the configuration of the protection system is successful. This was observed through the human-machine interface (HMI) of the relay.**

Keywords—Power systems, power transformers, transformer protection, differential protection system, inrush currents, current transformer saturation, hardware-in-the-loop.

I. INTRODUCTION

It has been discovered that 10% of the power system faults occur in power transformers, and 70% of these faults are a result of short circuits occurring in the transformer's windings. As the result, continuous monitoring and fast operating protection techniques are some of the requirements for power transformers [1]. Power transformer failures have been occurring in power systems, mostly at the transmission level. One of the major causes at the transmission level is the maloperation of protection systems [2]. Some of the protection system maloperations result from incorrect configuration during the design and configuration of the protection system.

Power transformer differential protection system requires high-standard methods of testing for functionality test and validation of multiple protection elements' response for each type of fault.

The literature work has been discovered with power transformer differential protection system tests. To review some of the work discovered, the authors in reference [3] proposed a differential protection system that uses the calculated power. Their system can discriminate between the inrush and internal fault of the protected transformer. They tested their system using a two-winding 667 MVA transformer on the Electromagnetic Transients including DC (MTDC) simulation platform. Their algorithm prevents the relay's maloperation. The authors in [4] provided essential knowledge about transformer differential protection. In their study, they did theoretical work and considered transformer differential examples up to the current transformer (CT) and relay connections. In reference [5], the authors proposed an algorithm that utilizes both currents and voltages to enhance the reliability of the differential protection system. Their algorithm was tested on a 225 kVA transformer using MATLAB/Simulink. In [6], a relay that rapidly detects all internal faults is proposed. In their protection technique, the relay remains stable for external faults and inrush currents due to transformer energization. Their results show that their technique is faster and smarter. The algorithm developed by these authors was tested using the PSCAD/EMTD simulation platform.

The transformer differential protection technique that uses the dead angle wavelet energy waveform to discriminate between the differential currents due to over-excitation and differential currents due to internal faults is also proposed in [7]. The authors in [8] proposed a transformer differential protection technique based on Clarke's transform with Fuzzy sets. Their technique can distinguish between differential currents due to internal faults and other forms of operation. The differential currents in this technique are the result of Clarke's transform. The fuzzy-based relay inputs are measured from the primary and secondary sides of the protected transformer. The operating time for this technique is less than 200 ms because the relay's decision is independent of the harmonic component. [1] proposed the transformer differential protection system that works with the boundary wavelet transform to discriminate between internal faults and other forms of disturbances. Their technique provides real-time disturbance faster than conventional differential protection techniques. Also, this technique intended to use the principle of differential protection that recreates the phase differential element (87T) and the negative sequence differential element (87Q) using the boundary wavelet coefficient energy.

The authors in [9] enhanced the power transformer differential protection system to improve security and dependability. In their study, they included early detection of current transformer saturation and a directionality check to provide security against external faults. They did their experiments on the Real-Time Digital Simulator (RTDS). [10] looked at various complications transformer differential protection relays have for both testing and commissioning. The authors did a review on numerical relays for phase differential protection principles to guide their applications and guide test personnel in conducting their test methods that can be applied in testing all transformer differential protection functions easily and effectively.

Since the development of power system protection has begun, different protection systems were applied to the protection of power transformers. However, some of the discovered work does not take into consideration the MVA size of the power transformer used for testing the protection system. Moreover, very few researchers test their methods using the hardware in the loop test, whose implementation is fairly accurate as it mimics the real power system networks to which the power transformers are connected. Some of their testing methods do not provide strong validation of the operation of the protection system since they neglect normal operating conditions of power systems. The type of circuit breakers (CBs) used as well as the current transformer (CT) location are critical when testing power transformer differential protection systems since the CTs used also depend on the type of circuit breakers used. The proposed algorithms in the existing literature do not include in-depth theory about the design and operation of power transformer differential protection relays and their operating elements.

The hardware-in-the-loop (HIL) test for transformer differential protection system is studied in this research, using the power system network to accommodate well the normal loading conditions of the transformer. The HIL test increases the chances of accurate test results since it allows the physical interface of the protective devices with the modeled protected unit. Furthermore, the protection system test done in this study uses a numerical relay that protects the transformer against all types of faults. Mostly for scholarly benefits, an in-depth theory about the operating principle of the transformer differential protection system is covered, as well as the configuration procedures.

The first section of this paper highlights the challenges of power transformers and their importance in the power system. Section II of this paper describes the operating principle of the transformer differential protection system. Section III presents the proposed testing technique. The preliminary results and discussion are presented in Section IV. The last section is conclusions and future work for this research.

II. Transformer Differential Operating Principle

The transformer differential protection system disconnects the power transformer from the circuit, whenever there is a non-zero differential current between the currents measured from the terminals of the protected transformer. In the past, challenges were experienced in the operation of the power transformer differential protection system, where the relays used to mal-operate due to the transformer inrush currents during the transformer energization. This challenge was solved by the numerical protective devices that have additional elements such as harmonic restraint and harmonic blocking elements. These additional features increased the security of the protection system when the transformer is exposed to inrush currents [1].

Power transformer differential relays consist of differential elements that compare the operating current with the restraining current. The operating current, also termed the differential current, is the phasor sum of the currents entering and leaving the protected transformer [11]. To analyze the operating principle of the power transformer differential protection system, Fig. 1 and Fig. 2 are used and are adopted from [11]. There are two conditions presented by the circuits shown in these figures, namely, external and internal fault conditions.

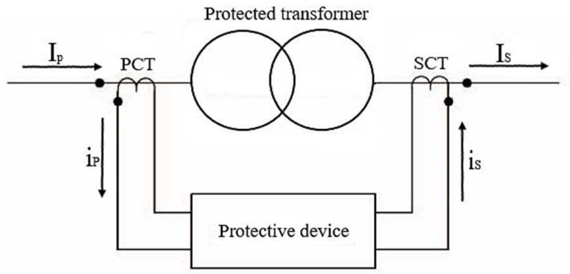

Fig. 1. Current flow on the transformer differential protection relaying circuit under steady-state conditions

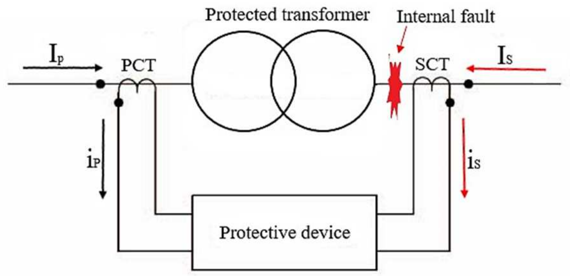

Fig. 2. Current flow on the transformer differential protection relaying circuit under internal fault conditions

External fault: The primary current (I_P) that flows to the transformer is equal to the secondary current (I_S) leaving the transformer. Kirchhoff's current principle applies to this, even for the CTs' secondary currents. The differential protection system is not allowed to operate for this condition, as there are other forms of protection systems dedicated to that.

The CTs' arrangement plays a crucial role in achieving the same principle on their secondary terminals, and this is through the significance of the CT polarity.

Internal fault: Any fault that occurs between the primary and the secondary current transformers is internal. When this fault occurs, the direction of the current changes. If the fault occurs on the secondary side of the transformer, the current on the secondary terminals of the secondary CT will change direction, thereby approaching and summing up to the secondary current of the primary side CT, to make a current that will flow on the differential element of the transformer differential protection relay.

Numerical transformer differential protection relays generate a signal to trip a breaker for disconnecting the protected transformer if the amount of the differential current (I_{Op}) exceeds the amount of the pick-up current (I_{PU}) and is greater than the percentage slope of the restraining current (I_{Res}) [11]. The common way to determine the restraining (I_{Res}) and the differential (I_{Diff}) current is by using the equations

$$I_{Res} = k(|i_P| + |i_S|) \tag{1}$$

$$I_{Diff} = |i_P| + |i_S| \tag{2}$$

In equation (1), **k** is the compensating factor of 1 or 0.5 and is vendor-dependent.

Digital or numerical relay's operation is fulfilled by the description, TRIP = 1 if $I_{Op} > I_{PU} > SLP(I_{Res})$ [12].

Two percentage slopes exist for most of the numerical transformer differential protection relays. The first slope (SLP1) is for normal operation, and the second one (SLP2) is for security and sensitivity.

One of the problems when it comes to differential protection for power transformers is that of the falsely generated differential currents, which occurs when one of the current transformers saturates. When CTs saturate, unbalanced currents flow in the relaying circuit, making the differential element pick up the differential current and operate.

III. The Proposed Transformer Differential System

To perform a suitable simulation study with more accuracy, it is advisable in reference [13] to choose the system with all the necessary parameters. This study puts its focuses on the transformer to be protected. The IEEE 9 Bus Power System shown in Fig. 3 was selected and suits the modeling requirements [14].

The RSCAD draft load flow was run to see the initial load conditions of the system. The results are presented in Table I, and they form part of the modeling requirements.

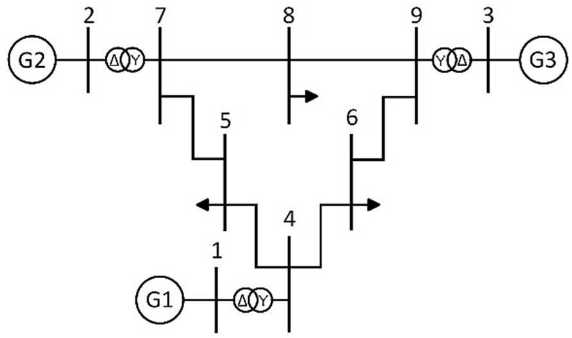

Fig. 3. The IEEE Nine-Bus System adopted from RTDS literature

TABLE I. RSCAD Draft Load Flow Results

Bus	Bus Type	Voltage	P_G	Q_G	P_L	Q_L
		PU	*MW*	*MVar*	*MW*	*MVar*
Gen1	Slack	1.04∠0°	71.78	36.28	-	-
Gen2	PV	1.03∠ 8.36°	163	11.23	-	-
Gen3	PV	1.025∠4.02°	85	-3.72	-	-
Bus1	PQ	1.02∠27.76°	-	-	-	-
Bus2	PQ	0.99∠26.32°	-	-	125.0	50.0
Bus3	PQ	1.01∠26.57°	-	-	90.0	30.0
Bus4	PQ	1.02∠32.79°	-	-	-	-
Bus5	PQ	1.01∠30.29°	-	-	100.0	35.0
Bus6	PQ	1.03∠31.31°	-	-	-	-

a. P_G and Q_G represents the true and reactive power generated during the draft load flow in megawatts (MW) and megavars (MVARs).

b. P_L and Q_L represents the true and reactive power demanded by the loads during the draft load flow in megawatts (MW) and megavars (MVARs)

A. *Current Transformer Selection*

According to the IEEE Guide for the selection of protection CTs, the primary CT turns ratio should be within the range of 120% to 150% of the normal load current [15]. The first side to be considered is the high-current side. In our case, the current was monitored under normal load conditions and the value of 2.744 kA and 0.1888 kA normal load currents were found on the primary side of the transformer, and the secondary side respectively. The minimum CT ratio was calculated, therefore 120% is considered for calculating both the primary current transformer ratio (PCTR) and the secondary current transformer ratio (SCTR).

$$\mathrm{PCTR} = 120\%(2.744\ \mathrm{kA})$$

$$\mathrm{PCTR} = 3.2928\ \mathrm{kA}$$

$$\mathrm{SCTR} = 120\%(0.1888\ \mathrm{kA})$$

$$\mathrm{SCTR} = 0.22656\ \mathrm{kA}$$

However, the ratio of 3 300 for primary and 240 for secondary CT turns is chosen from the standards, which makes the CT turns ratios 3 300/1 and 230/1.

The protection system presented in this paper makes use of external protective device hardware. To make the analog signal available to the external hardware, the giga-transceiver analog output (GTAO) card was configured in the RSCAD draft. This processor card converts the digital simulated signals to a +/-10 VDC signal which is amplified to the instrument transformers' secondary values for use by the external protective device.

After the current transformer parameter settings were done, the load flow was run, and the primary and secondary currents were monitored on runtime.

TABLE II. Current Monitoring Across The Protected Transformer Under Normal Load Conditions

Signal Names	Description	Values
TRF1PriCurr	Transformer 1 primary current	2.746 kA
TRF1SecCurr	Transformer 1 secondary current	0.189 kA
PriCTCurr	Primary current transformer output terminal current	0.832 A
SecCTCurr	Secondary current transformer output terminal current	0.8197 A

Moreover, using an electronic multimeter, the output currents from the amplifiers were also measured, and are recorded in Table II. The test bench setup for the proposed testing of the protection system is shown in Fig. 4. In the figure, the RTDS, Omicron Amplifiers, and the SEL-487E Station Phasor Measurement Unit device are shown. The configuration of the SEL-487E is presented in Section B.

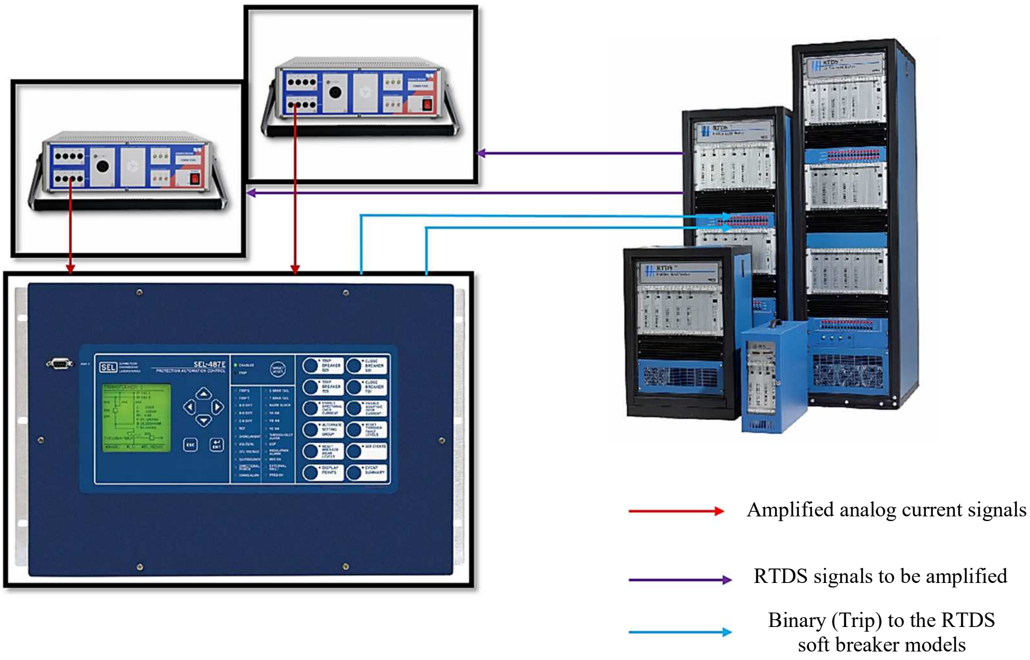

Fig. 4. Hardware-In-the-Loop power transformer differential protection system test setup

B. *The SEL-487E Station Phasor Measurement Unit*

There are three types of faults transformers need to be protected against. These faults are phase-to-phase faults, phase-to-ground faults, and turn-to-turn faults. The current trend of transformer differential protection relays protects power transformers against these types of faults at once, using the elements, phase percentage-restrained differential elements (87R), negative-sequence percentage-restrained differential elements (87Q), and unrestrained phase differential elements (87U). The phase percentage-restrained differential elements (87R) use the adaptive percentage slope for security and sensitivity [16].

Inrush currents occur in the transformer during its energization and the relay may see differential currents. Therefore, the security of the differential element in the relay is added by applying the percentage slope characteristic in element 87R, and this is to provide harmonic blocking, harmonic restraint, or both. The second and third harmonics provide security during the transformer energization, and the fifth harmonic provides security for overexcitation conditions. The adaptive slope in the phase percentage-restrained characteristic provides security for CT saturation under external faults [17].

Also, transformer differential protection relays operate using the differential characteristic curve which consists of two slopes and regions as shown in Fig. 5. Since the differential calculation occurs on a per-phase basis, the characteristic curve shown in the figure is derived from one of the phases. In this plot, the characteristic curve with Slope 1 is effective under normal internal fault conditions, and Slope 2 becomes effective only when the fault detection logic detects the external fault [17], [18].

The CTs are more vulnerable to saturation when the fault occurs externally from the protected transformer, therefore the saturation security mode is also included as part of the through fault detection.

The CT values that were calculated for RTDS CT models are set in the protective device as well.

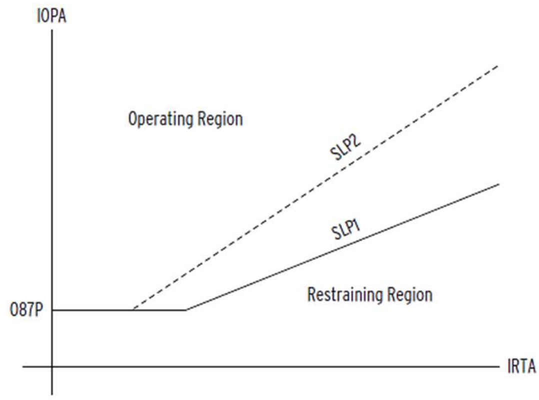

Fig. 5. Differential protection characteristic plot

O87P - Restrained differential minimum operating pick-up settings: This element is set so that the minimum current, which is 10% of the nominal current (1A or 5A) is less than the product of the minimum TAP value and O87P. The relay used in this study has a nominal current rating of 1 A. According to [19], the value of this element should be kept as low as possible to increase the sensitivity in the case of the power transformer's winding faults.

Reference [17] uses the following method to calculate the value of this element:

$$O87P \geq 10\% \left(\frac{I_{NominalRMS}}{TAPS}\right)$$

$$\text{O87P} \geq 10\% \left(\frac{\frac{S_{TRFRating}}{\sqrt{3}(V_{TRFPrimaryRating})}\left(\frac{1}{CT_{Ratio}}\right)}{TAPS} \right)$$

$$\text{O87P} \geq 10\% \left(\frac{0.10603 \text{ Amps}}{1.06} \right)$$

$$\text{O87P} \geq 0.10003 \text{ p.u}$$

We are using the value to confirm whether the statement is fulfilled.

$$\text{O87P}(TAP_{Min}) > I_{Min}$$

$$\text{O87P}(TAP_{Min}) > 10\%(I_{Nominal})$$

$$0.1(1.05 \text{ A}) > 10\%(1 \text{ A})$$

$$0.105 > 0.1$$

Because this value satisfies equation (2), the value is set in the relay's configuration as 0.11 per unit for the O87P settings block.

U87P - Unrestrained differential pick-up settings: Reference [19] states that the settings range for this element is between 8 and 10 per unit. The same reference mentions the case of inrush current during the transformer energization, that the inrush current is usually 10 times higher than the transformer's rated MVA. Moreover, the same reference raises concerns about the security and sensitivity of the percentage restrained element. To accommodate this feature, they increase the U87P by 167%. For this study we first calculate the U87P settings based on [17], then we apply the 167% from [19].

$$\text{U87P}_1 = \left(\frac{200\%(I_{NormalLoadSRMS})\left(\frac{1}{CT_{Ratio}}\right)}{TAPS} \right)$$

$$\text{U87P}_1 = \left(\frac{\left(\frac{200\%(2.714 \text{ kA})}{\sqrt{2}}\right)\left(\frac{1}{3\,300}\right)}{1.06} \right)$$

$$\text{U87P}_1 = 0.8959 \text{ p.u}$$

We made U87P 167% of U87P_1, which gives us U87P = 1.496153 and we set this value as 1.50 per unit in the relay's configuration settings block for U87P.

Differential protection relays operate on a per-phase per-unit basis. Therefore, the actual currents input to the transformer differential device terminals is converted into per unit by using the base currents for both sides of the protected transformer. Base current is the current that would flow through the power transformer when it is 100% loaded. To calculate this, we first considered the primary side of the power transformer. On the primary side, the transformer has a voltage rating of 16.5 kV. The current at 100% loading on the primary side is then calculated using the equation

$$\text{TAPS} = I_{BS} = \left(\frac{S_B}{\sqrt{3}V_{SB}}\right)\left(\frac{1}{PCT}\right)$$

where S on TAP states the primary winding of the protected transformer, as stated in transformer differential relays from Schweitzer Engineering Laboratories (SEL), I_{BS} is base current on the primary side of the protected transformer, S_B is the rated complex power of the transformer in MVA, and V_{BS} is the rated voltage of the transformer's primary side.

$$\text{TAPS} = I_{BS} = \left(\frac{100 \text{ MVA}}{\sqrt{3}(16.5 \text{ kV})}\right)\left(\frac{1}{3\,300}\right)$$

$$\text{TAPS} = I_{BS} = 1.06 \text{ A}$$

For the secondary side of the transformer, secondary rated values are used, and this calculates as follows:

$$\text{TAPT} = I_{BT} = \left(\frac{S_B}{\sqrt{3}V_{BT}}\right)\left(\frac{1}{SCT}\right)$$

T on TAP represents the secondary winding of the power transformer protected.

$$\text{TAPT} = I_{BT} = \left(\frac{100 \text{ MVA}}{\sqrt{3}(230 \text{ kV})}\right)\left(\frac{1}{230}\right)$$

$$\text{TAPT} = 1.09 \text{ A}$$

The per-unit current values were also calculated. To calculate these values, only one phase (Red-phase) is presented. However, this calculation is the same for all phases under normal system conditions.

$$I_{RSPU} = \left(\frac{I_{PCTCurrRMS}}{TAPS}\right)$$

I_{RSPU} is the S winding CT red-phase secondary per unit current, and $I_{PCTCurrRMS}$ is the S winding CT red-phase secondary current in RMS amps.

$$I_{RSPU} = \left(\frac{0.81576 \text{ A}}{1.06 \text{ A}}\right)$$

$$I_{RSPU} = 0.7696 \text{ pu}$$

$$I_{RTPU} = \left(\frac{I_{PCTCurrRMS}}{TAPS}\right)$$

I_{RSPU} is the T winding CT red-phase secondary per unit current, and $I_{SCTCurrRMS}$ is the S winding CT red-phase secondary current in RMS amps.

$$I_{RTPU} = \left(\frac{0.7996 \text{ A}}{1.09 \text{ A}}\right)$$

$$I_{RTPU} = 0.7336 \text{ pu}$$

The relay wordbits for the elements configured in Section B were assigned to the physical output terminals OUT101 and OUT102 for circuit breakers 1 and 2 through the combined trip logic of the transformer differential relay.

IV. Results and Discussion

The normal load flow was simulated for the above-protected system, and monitoring was done. Results were viewed on the relay's human-machine interface (HMI). In the same HMI, the results of the differential metering of currents were obtained. Table III shows the terminal currents of the protected transformer, and Table IV shows the differential metering of currents.

The results recorded in tables III and IV complement the theory, settings, and configuration of the differential protection relay [12]. For instance, in Table IV, the restrained currents are greater than the differential currents.

TABLE III. FUNDAMENTAL METERING FOR S AND T WINDING OF THE PROTECTED TRANSFORMER UNDER NORMAL LOAD CONDITIONS USING THE PROTECTIVE RELAY'S HMI

Windings	Phase	Magnitude	Phase Shift
Winding S	R	2 740.43 A	-159.59
	Y	2 742.04 A	-39.56
	B	2 741.87 A	80.42
Winding T	R	188.44 A	0.14
	Y	188.26 A	120.23
	B	188.36 A	-119.87

TABLE IV. DIFFERENTIAL METERING

Types of Current	Phase	Per Unit Value
Differential Currents	R	0.39
	Y	0.38
	B	0.38
Restrained Currents	R	1.53
	Y	1.53
	B	1.52

V. CONCLUSIONS

In this paper, the transformer differential protection system was configured and tested using the IEEE 9 Bus Power System. The configuration of the current transformers (CTs) was done based on the IEEE standards. The protection system was tested on a 100 MVA transformer, which falls in the category of transformers to be protected using the dedicated differential protection system. For scholarly benefits, the configuration of the protection system used was explained, making it easier for other scholars to follow and apply. Furthermore, the practical information gained in this research work will assist protection engineers in how to configure and deploy hardware-in-the-loop testing of power transformer differential protection and minimize the maloperation of the differential protection relay under normal conditions. The results obtained thus far shows a successful interface of the protective device with the RTDS.

VI. FUTURE WORK

The next part of this study will look at the operation of the transformer differential protection system under the influence of current transformer saturation due to inrush currents. An in-depth theoretical analysis will be done, in support of simulation studies. Furthermore, the IEC 61850 communication standard will be used for the reduction of hardwiring between the protection system and the protected unit.

REFERENCES

[1] R. P. Medeiros, F. B. Costa, and K. M. Silva, "Power Transformer Differential Protection Using the Boundary Discrete Wavelet Transform," *IEEE Trans. Power Deliv.*, vol. 31, no. 5, pp. 2083–2095, 2016, doi: 10.1109/TPWRD.2015.2513778.

[2] J. Jagers and S. Tenbohlen, "Differences Approaches for the Acquisition of Reliability Statistics," 2009.

[3] L. Wang and X. Wang, "Transformer differential protection using calculated power," in *APAP 2011 - Proceedings: 2011 International Conference on Advanced Power System Automation and Protection*, 2011, vol. 1, pp. 363–367. doi: 10.1109/APAP.2011.6180428.

[4] L. Sevov, Z. Zhang, I. Voloh, and J. Cardenas, "Differential protection for power transformers with non-standard phase shifts," in *2011 64th Annual Conference for Protective Relay Engineers*, 2011, pp. 301–309. doi: 10.1109/CPRE.2011.6035631.

[5] A. H. Hamouda, F. Q. Al-Anzi, H. K. Gad, and A. Gastli, "Numerical differential protection algorithm for power transformers," in *2013 7th IEEE GCC Conference and Exhibition, GCC 2013*, 2013, pp. 440–445. doi: 10.1109/IEEEGCC.2013.6705819.

[6] H. Dashti and M. Sanaye-Pasand, "Power transformer protection using a multiregion adaptive differential relay," *IEEE Trans. Power Deliv.*, vol. 29, no. 2, pp. 777–785, 2014, doi: 10.1109/TPWRD.2013.2280023.

[7] M. Tripathy and N. Nirala, "Power transformer differential protection algorithm based on dead angle of Wavelet Energy Waveform," *IEEE Reg. 10 Annu. Int. Conf. Proceedings/TENCON*, vol. 2016-Janua, pp. 5–6, 2016, doi: 10.1109/TENCON.2015.7372813.

[8] D. Barbosa, U. C. Netto, D. V Coury, and M. Oleskovicz, "Power transformer differential protection based on Clarke's transform and fuzzy systems," *IEEE Trans. Power Deliv.*, vol. 26, no. 2, pp. 1212–1220, 2011, doi: 10.1109/TPWRD.2010.2097281.

[9] L. Sevov, S. Member, U. Khan, Z. Zhang, and S. Member, "Enhancing Power Transformer Differential Protection to Improve Security and Dependability," *IEEE Trans. Ind. Appl.*, vol. 53, no. 1, pp. 2642–2649, 2017, doi: 10.1109/TIA.2017.2670525.

[10] Q. Verzosa and W. A. Lee, "Testing Microprocessor-Based Numerical Transformer Differential Protection," *IEEE Trans. Ind. Appl.*, vol. 53, no. 1, pp. 56–64, 2017, doi: 10.1109/TIA.2016.2609402.

[11] S. M. Saad, A. Elhaffar, and K. El-arroudi, "Optimizing Differential Protection Settings for Power Transformers," in *2015 Modern Electric Power Systems (MEPS)*, 2015, pp. 1–6. doi: 10.1109/MEPS.2015.7477186.

[12] SEL, "SEL-487E-3, -4 Transformer Protection Relay: Instruction Manual," 2022

[13] B. M. Weedy, B. J. Cory, N. Jenkins, J. B. Ekanayake, and G. Strback, *Electric power systems*, Fifth Edit. Wiley, 2012. doi: 10.1016/B978-0-12-804448-3.00018-9.

[14] S. Nomandela, M. Ratshitanga, and M. Elvis, "IEC 61850 Standard-Based Protection of the Coupling Point between a Wind Farm and the Power Grid," Cape Peninsula University of Technology (CPU), 2021. [Online]. Available: http://ir.cput.ac.za/handle/20.500.11838/3424

[15] IEEE, *IEEE Guide for the Application of Current Transformers Used for Protective Relaying Purposes - Redline*, vol. 2007, no. April. 2008.

[16] P. Jankee and K. Awodele, "Design Of An IEC 61850 Based Substation Automation and Protection Panel: Including Peer to Peer Relay Communication," in *2019 Southern African Universities Power Engineering Conference/Robotics and Mechatronics/Pattern Recognition Association of South Africa (SAUPEC/RobMech/PRASA)*, 2019, pp. 570–575. doi: 10.1109/RoboMech.2019.8704775.

[17] Schweitzer Engineering Laboratories, "SEL-487E Transformer Protection," 2020.

[18] P. Ngema, E. Buraimoh, and I. Davidson, "A New Technique for Improvement Differential Relay Performance in Power Transformers," in *2022 30th Southern African Universities Power Engineering Conference (SAUPEC)*, 2022, pp. 1–5. doi: 10.1109/SAUPEC55179.2022.9730768.

[19] S. Uddin *et al.*, "Application Considerations for Protecting Transformers With Dual Breaker Terminals Application Considerations for Protecting Transformers With Dual Breaker Terminals," no. December, pp. 1–25, 2018.